Topics in Applied Physics 132

Junko Habasaki
Carlos Leon
K.L. Ngai

Dynamics of Glassy, Crystalline and Liquid Ionic Conductors

Experiments, Theories, Simulations

EXTRAS ONLINE

Springer

Topics in Applied Physics

Volume 132

Topics in Applied Physics is a well-established series of review books, each of which presents a comprehensive survey of a selected topic within the broad area of applied physics. Edited and written by leading research scientists in the field concerned, each volume contains review contributions covering the various aspects of the topic. Together these provide an overview of the state of the art in the respective field, extending from an introduction to the subject right up to the frontiers of contemporary research.

Topics in Applied Physics is addressed to all scientists at universities and in industry who wish to obtain an overview and to keep abreast of advances in applied physics. The series also provides easy but comprehensive access to the fields for newcomers starting research.

Contributions are specially commissioned. The Managing Editors are open to any suggestions for topics coming from the community of applied physicists no matter what the field and encourage prospective editors to approach them with ideas.

Managing Editor

Dr. Claus E. Ascheron
Springer-Verlag GmbH
Tiergartenstr. 17
69121 Heidelberg
Germany
claus.ascheron@springer.com

Assistant Editor

Adelheid H. Duhm
Springer-Verlag GmbH
Tiergartenstr. 17
69121 Heidelberg
Germany
adelheid.duhm@springer.com

More information about this series at http://www.springer.com/series/560

Junko Habasaki • Carlos León • K.L. Ngai

Dynamics of Glassy, Crystalline and Liquid Ionic Conductors

Experiments, Theories, Simulations

Springer

Junko Habasaki
Tokyo Institute of Technology
Yokohama, Kanagawa
Japan

Carlos León
Facultad de Fisica
Universidad Complutense Madrid
Madrid, Spain

K.L. Ngai
IPCF, CNR
Pisa, Italy

Additional material to this book can be downloaded from http://extras.springer.com.

ISSN 0303-4216 ISSN 1437-0859 (electronic)
Topics in Applied Physics
ISBN 978-3-319-42389-0 ISBN 978-3-319-42391-3 (eBook)
DOI 10.1007/978-3-319-42391-3

Library of Congress Control Number: 2016946978

© Springer International Publishing Switzerland 2017
This work is subject to copyright. All rights are reserved by the Publisher, whether the whole or part of the material is concerned, specifically the rights of translation, reprinting, reuse of illustrations, recitation, broadcasting, reproduction on microfilms or in any other physical way, and transmission or information storage and retrieval, electronic adaptation, computer software, or by similar or dissimilar methodology now known or hereafter developed.
The use of general descriptive names, registered names, trademarks, service marks, etc. in this publication does not imply, even in the absence of a specific statement, that such names are exempt from the relevant protective laws and regulations and therefore free for general use.
The publisher, the authors and the editors are safe to assume that the advice and information in this book are believed to be true and accurate at the date of publication. Neither the publisher nor the authors or the editors give a warranty, express or implied, with respect to the material contained herein or for any errors or omissions that may have been made.

Printed on acid-free paper

This Springer imprint is published by Springer Nature
The registered company is Springer International Publishing AG Switzerland

Preface

Transport of mobile ions in ionic conductors of many kinds is the key to performance in a wide variety of applications, including portable energy sources from primary and secondary batteries, chemical sensors, ionic switches, electrochromic displays, power generators, fuel cells, component in electronic devices, and electric car technology. These applications have become a major part of the world economy, and their advances in research and development in the future may shape the way of life of the present and future generations. Thus the field of research on ionic motions in ionic conductors has practical implications particularly in the search and discovery of materials with desired or optimal properties for applications in the bulk form and in the nanometer scale.

The dynamics of mobile ions leading to conductivity and diffusivity in various kinds of ionic conductors are interesting from the basic research perspective. In most ionic conductors, liquid and solid, the density of the mobile ions are considerable, and non-negligible is the effect of ion-ion interaction on the ion dynamics as well as interaction between the ions and the matrix in which the ions are embedded. Randomness and disorder in liquid and glassy ionic conductors may also complicate the dynamics. Brownian diffusion or random walk of particles without interaction is a well-known solved problem, but ceases to apply in most ionic conductors of interest. The presence of ion-ion interactions poses difficulty in visualizing the motion of the ions and in explaining the properties. This is because it requires the solution of a many-ion problem of irreversible process (conductivity or diffusion) in statistical mechanics, which does not exist at the present time. The nonexistence of a universally accepted solution to the problem is remarkable in view of the fact that more than a century has gone by since 1905 when Einstein solved the Brownian diffusion problem. Actually over the years very few attempts have been made just to attack the problem theoretically. This unique situation offers a fantastic opportunity at the present time for someone to make a great contribution in science by solving this fundamental problem.

However, an acceptable solution must be able to explain satisfactorily *all* known essential and critical experimental facts or at least be consistent with *all* of them.

By now many experimental techniques have been applied in the study of the ion dynamics over time scales ranging from microscopic times to macroscopic times and experimental data abound in the literature. They need to be collected, categorized, and summarized so the essentials can be brought out without neglecting any. This task is attempted by us in this book with the purpose of benefitting the research community engaged in solving this centuries-old problem in condensed matter physics. If a theory can account for the collection of properties of ionic conductors in general, it can be considered to be close to a final solution of the problem. Another purpose is to make those involved in applications aware of the properties and limitations of typical ionic conducting materials. This knowledge will help them in the search for new materials to suit the purpose of the application or for better performance.

By extracting the results from experiments and molecular dynamics simulations of ionic conductors with diverse chemical and physical structures (crystalline, liquid, and glassy), we are able to present overwhelming evidences of universal dynamics and properties of ions in many different ionic conductors. The universal properties found suggest they originate from some fundamental physics governing the motion of the ions. The universal behavior makes the problem more exciting and inspiring for others to solve the problem. Moreover, the universal dynamics of ions has analogs in the relaxation of structural units of glass-forming substances and systems. The analogy links the two research areas together, and it suggests that understanding the dynamics of ions can have impact on the research field of glass transition, which is currently also considered as an unsolved problem. Some of the ionic conductors are not glass-forming, and even the glass-forming ones have the ionic conductivity relaxation decoupled from the structural relaxation. Notwithstanding, the analogy continues to hold. This means that glass transition is just an effect with the cause being the universal dynamics shared with ionic conductivity relaxation in ionic conductors.

The authors of this book come from different backgrounds and have different but complementary expertise. Junko Habasaki is an expert and leader in molecular dynamics simulations of ionic conductors, ionic liquids, and porous ionic conductors. Carlos León has been engaged in experimental study of various ionically conducting materials for years and now leads a pioneering effort in nanoionics in his group. K.L. Ngai is a theoretician who works closely with experiments and simulations in the broad fields of relaxation and diffusion in complex systems. He is the originator of the Coupling Model, which has been applied with success to many different phenomena and materials in various research disciplines. In the book, we have combined our individual expertise in writing most of the chapters with participations to various degrees from all three of us. The chapters are linked to each other by their contents, which are either developments of the same subject in a different light or by a different technique, or specialization to a particular system. We deem that this book will be useful in various ways to readers with widely different interest ranging from physicists, chemists, materials scientists, and engineers, as well as for teaching a course of ionics in academic institutions. As far as we know, a book of this kind does not exist at the present time.

Junko Habasaki thanks many of her collaborators in the field of ionics and molecular dynamics simulations, especially Kia L. Ngai, Carlos León, Akira Ueda, and Yasuaki Hiwatari. The technical part of MD simulations (Chap. 8) in this book was kindly checked by Akira Ueda. She also thanks Isao Okada for collaboration in the early stage of works. She also thanks Takashi Odagaki, Frederic Affouard, Philipp Maass, Akira Takada, Masamichi Ishikawa, and Anna Gubarevich for discussion for related problems and encouragement. Thanks are extended to the members of the Department of the Electronic Chemistry, Department of Innovative and Engineered Materials and School of Materials and Chemical Technology in Tokyo Institute of Technology. She is grateful for the assistance for the preparation of an accelerated MD program using GPU given by the Global Scientific Information and Computing Center, Tokyo Institute of Technology. (A main part of the program code is attached in the Appendix.) Last but not the least, she thanks her family especially her daughter Chika for encouragement.

Carlos León thanks all his collaborators in the field of ionics for the last 20 years, especially Jacobo Santamaría, Kia Ngai, Junko Habasaki, Alberto Rivera-Calzada, Jesús Sanz, Alejandro Várez, Emilio Morán, Miguel Angel Alario-Franco, Antonio Fernández-Fuentes, Javier García Barriocanal, Karla Moreno, Mario Díaz-Guillén, Oscar Juan Durá, and Marisa Frechero. He also thanks his family, especially his wife for her patience and understanding.

K.L. Ngai thanks his collaborators in the field of ionics over the past three decades, particularly Connie Moynihan (deceased), Otmar Kanert, Himanshu Jain, Neville Greaves, Steve Martin, Paul Heitjans, Apostolos Rizos, Peter Lunkenheimer, Ian Hodge, Ron Rendell, Jacobo Santamaria, Zaneta Wojnarowska, and Marian Paluch. I thank especially Junko Habasaki and Carlos León for collaborations in research over the years and in writing this book.

Yokohama, Japan Junko Habasaki
Madrid, Spain Carlos León
Pisa, Italy K.L. Ngai

Contents

Chapter 1
Introduction

By now the study of ion transport and conductivity in ionically conducting materials is a subject of interest to physicists, chemists, materials scientists, and engineers. The interest of physicists is to understand the complex motion of ions leading to steady state diffusion and conductivity. This is a challenging endeavor because of the large number of ions in most ionic conductors of practical interest. The motions of the ions are not independent due to mutual ion interactions as well as interactions with the matrix ions. For this reason the problem of diffusion and electrical conductivity of interacting many-ion system has remained unsolved up to the present time. Historically it was Michael Faraday who discovered ionic transport in electrolytes in the years after 1830 [1]. Following Faraday, it was Kohlrausch [2] in Göttingen, Germany who made the first measurement of electrical relaxation of alkali ions in the Leyden jar (a glass) in 1854. For experimental data, see [3]. He found the relaxation has time-dependence given by

$$\phi_K(t) = \exp\left[-(t/\tau)^{1-n}\right], \text{ where } 0 < (1-n) \leq 1, \tag{1.1}$$

the stretched exponential functions, or the Kohlrausch decay function, which continues to be relevant in conductivity relaxation of ionic conductors, structural relaxation of glass-forming liquids, and other research areas. By the way, the stretched exponential function (1.1) was found to describe well the mechanical relaxation in the natural polymer, silk, in 1863 and 1866 by F. Kohlrausch [4, 5], the son of R. Kohlrausch. Nowadays, the function is known to fit well the structural relaxation of glass-forming materials and systems in general. However, since the times Faraday or Kohlrausch started the field, 180 years have gone by and remarkably the problem has not been solved in the physics world. Surprisingly few theoretical attempts have been made in the past years to solve the problem.

One purpose of this book is to make the readers aware of this unusual situation in physics research, and therefore the opportunity for anyone to make a significant contribution towards solving this fundamental and important problem. Many ionic

J. Habasaki et al., *Dynamics of Glassy, Crystalline and Liquid Ionic Conductors*,
Topics in Applied Physics 132, DOI 10.1007/978-3-319-42391-3_1

conductors with different physical and chemical structures have been discovered or fabricated. A variety of experimental techniques have been applied to elucidate the structures, and characterize the dynamics of ions over many orders of magnitude of frequency/time from vibration of ions to d.c. conductivity. By this time, the wealth of experimental data accumulated and the contrasting interpretations given in the literature can overwhelm anyone entering the field. Chapter 2 gives a brief description of each of the theories and models of ion dynamics that are currently active. Chapter 3 introduces the various experimental techniques utilized in the research of ionic conductivity relaxation and diffusion. We make it easier for the readers to grasp the essentials of the knowledge gained in experimental research in Chap. 4 by organizing the facts and phenomena into general categories, and systematically bringing out the salient and general features or properties of the ion dynamics. The different methods of analyzing the data advocated by different workers, and the interpretations resulting from the analyses are critically discussed.

In physics, veracity of theory is not judged by how intuitively appealing it is or by the degree of mathematical complexity and rigor. Rather it is judged by agreement of predictions with experiments, and more such predictions a theory has, the better is the theory. Therefore in this book, we emphasize comparisons of theory or models with all experimental findings that are well established. This practice is followed in Chaps. 4–7, where data of widely different materials from different experimental techniques are brought out to challenge any theory to explain, much more than contained in the old reviews [6–8]. Other review articles in the literature will be cited in the chapters. In this way the limitation and/or validity of any theory/model/interpretation becomes so transparent that the readers can make their own judgements.

Despite the fact that many ionic conductors with widely different physical and chemical structures are considered in Chaps. 4–7, the many-ion dynamics in them conform to the same pattern. In other words, for most of all the ionic conductors discussed in this book the many-ion dynamics are similar, suggesting some common but fundamental physics is at work. The universal behavior is an outstanding phenomenon in condensed matter physics challenging anyone to provide a theoretical explanation. Awareness of the universal ion dynamic properties may help as a guide in the research of new materials. Therefore, to make it convincing, plenty of examples showing similar properties or the universality of ion dynamics in diverse materials are given, item by item, in the chapters of this book. In the literature, others have proposed universal scaled frequency dependence of ionic conductivity, which we show is faulty and should not be considered anymore.

Molecular dynamics (MD) simulations of ion dynamics can bring out properties and provide information with details that are not obtainable by experiments. The results can be additional critical tests of theory. These days realistic interaction potential of ions in some archetypal ionic conductors are known and the dynamics obtained by the MD simulations can faithfully reproduced the ion dynamics, albeit the drawback from time scale limitation in simulation is unavoidable. Notwithstanding, MD simulations are playing important role in the research on the ion dynamics in many different types of material. Moreover, MD simulations can be used to explore the feasibility of ionic conductor with certain desired properties, but that material has not yet been synthesized or fabricated. In view of the importance of MD simulations in ionics, Chap. 8 introduces the general methodology of MD simulations. In Chaps. 9–11, MD simulations of alkali silicate glasses and room temperature ionic liquids are shown, and they can be used as examples of how to use MD simulations in the research of ionic conductivity relaxation. The results from the MD simulations are compared with experimental data presented before in Chaps. 4–7. In Chap. 12, a practical introduction to perform MD simulations is given to show the art and technique of MD simulations, the set-up of the simulations, the execution of the program, and the extraction of information from the data, such that the reader can learn step by step in how to perform MD simulations on their own.

The rapid growth of research and application of ionic conductors we witness in recent years would not be possible without the contributions of chemist and material scientists who synthesize or fabricate new materials, and characterize them for potential applications. The activities are driven by the search of materials of high ionic conductivity to serve as the electrolyte in many electrical and electrochemical devices including primary and secondary batteries, fuel cells, memristors, sensors, smart windows, and electrochromic displays. New materials enable innovations in the electrode and electrolyte components, critical in the development of batteries with high energy density suitable for large scale everyday applications [9–13].

Examples of recent developments in new materials are the room temperature ionic liquids (RTILs) and nanoionics materials [14–24]. The RTILs are molten salts composed of bulky, asymmetric organic cations and inorganic anions, and have many beneficial properties such as low vapor pressure, environmentally friendly, non-flammability, high electrical conductivity, excellent thermal and electrical stability. Some RTILs have been used as electrolytes for lithium-ion batteries. In principle many RTILs can be obtained by different combinations of organic cations and inorganic anions, and this is the reason why new materials appear every now and then. RTILs are usually glass-formers, and thus they can be used to study not only ion conductivity relaxation but also the structural relaxation and glass transition on cooling. The relation between the two distinctly different relaxations is also of interest. Therefore the study of RTILs and ionic liquids in general span two currently active research areas, glass transition and ionics. Some RTILs have properties of ion conductivity relaxation not found in solid amorphous and crystalline ionic conductors, and these properties are instrumental in acquiring a deeper understanding of the dynamics of ions.

Nanoionics is another new field outgrown from bulk ionic conductors to explore how structure and dynamics are changed when one or more dimensions of the material are reduced to the nanometer length-scale [25–32]. The studies of ion dynamics in nanoionics have found changes of the bulk properties, which demand any theory proposed for the bulk to explain further. Observed in many nanoionics materials is significant increase in ionic conductivity, and this beneficial change makes possible some novel and rapidly developing technological applications.

The book is written with the intent that the content can be useful for a broader readership and different purposes. Topics including basic concepts, theories/ models, experimental techniques, experimental data, interpretations and explanations, methods of and sample results in molecular dynamics simulations are all covered in the book. Thus it can be used for teaching a special course by academics. If some topics are chosen to be the emphasis of the course, the materials in the book on these topics can be easily expanded in details and coverage by consulting the references cited.

For those readers who are interested in materials engineering, the choice of ionic conductors with optimal properties for specific applications is the major concern. For example, although there are many ionic conductors that can be used as electrolytes in solid-state batteries, in some cases they are unstable against typical negative electrodes such as graphite and metallic lithium, or may react easily with positive electrode materials and give rise to poor charge-transfer kinetics [9–13]. Trying to maximize the ionic conductivity of the electrolyte is another example. It is known that increasing the concentration of mobile ions results in higher activation energy for ion diffusion and consequently in a decrease of ion mobility. It is necessary to follow new strategies to find materials showing lower activation energies for ion diffusion, exploiting size effects, space-charge effects, controlling and modulating structural disorder, and etc. This is in fact one of the current challenges in solid state ionics. The variety of ionic conductors and their properties discussed in this book provide easy access to the characteristics as well as limitations of the materials available for their specific applications. Despite the lack of fundamental understanding of the dynamics of mobile ions in ionically conducting materials, the book provides insights into the possible mechanisms for ion diffusion, examples of how tuning structure to enhance ionic conductivity by changing composition in materials with different structures, and also useful trends observed in ionic conductivity for different families of materials that, overall, are intended to pave the way towards the design of novel and optimized ionic conductors.

For scientists entering the field of ionic conductors for basic research and applications, the book is perhaps one of the best media to be brought to the forefront proficiently by the critical review of the available experimental tools and methods, the phenomena, the salient experimental findings, the theoretical considerations and explanations, and guidance to perform molecular dynamics simulations and analyze the results.

With the multiple purposes of the book in mind, the chapters are organized and arranged in order as given in the Table of Contents. Ionic conductivity relaxation is one of the dissipative or irreversible processes. Chapter 2 introduces the basic concepts and general formalism of treating irreversible process in statistical mechanics. Specializing to ionic conductivity relaxation, we introduce the phenomenological approaches based on the assumption of a distribution of exponential time correlation functions with different ionic conductivity relaxation times can account for some of the observed experimental data. These are followed by brief descriptions of theories and models of ionic conductivity relaxation and diffusion to let the reader be familiar with the various attempts to explain the ion dynamics.

More detailed description of some will be given in Chap. 4. Any theory will be mentioned again wherever it makes contact with or is relevant to experiment findings and simulation results in all following chapters.

Techniques derived from nuclear magnetic resonance have been profitably applied to the study of ion dynamics, and the accomplishments are summarized in Chap. 5. The emerging field of nanoionics is reviewed in Chap. 6. Ionic liquids and especially the room temperature ionic liquids have attracted much attention in recent years because their properties are not only beneficial in technological applications but also having impact on fundamental understanding of ion dynamics. For this reason, Chap. 7 is devoted entirely to the discussion of this class of ionic conductors.

Brought out by a multitude of experiments discussed in Chaps. 4–7 in a wide variety of ionic conductors, the properties of ion dynamics turn out to be universal. Even more remarkable is that the universal ion dynamics are analogous to the universal structural relaxation dynamics of glass-forming substances and systems [33]. It is hoped that the overwhelming evidences of universality of ion dynamics and structural relaxation of glass-formers could stimulate some readers to identify the underlying fundamental physics and solve these basic problems in condensed matter physics in the near future.

Methodology of molecular dynamics (MD) simulations explained in Chap. 8 are used in the studies of alkali silicate glasses, including mixed alkali system and room temperature ionic liquids in Chaps. 9–11. The results of MD are compared with experiments and theories. Characteristics of complex (heterogeneous) jump (hopping) motions of ions obtained by MD simulations, which are briefly described in Chap. 2 with the related theories, are explained in details there. More practical introduction of MD explaining methods for the fundamental setting of simulations, preparation of initial configurations, available programs and examples of analysis is given in Chap. 12. An exercise of MD simulation for a lithium silicate glass and following analysis and visualization will be useful for starting and understanding MD simulations by others.

In Chap. 13, several applications of ionics to related fields are described. The ionics discussed in the present book will give hints for designing several properties of materials, such as high conductivity. Fabrication of porous materials in MD is a topic closely related to nanoionics discussed in Chap. 5. Increase of conductivity in porous materials has been reported for several systems. Acceleration of the ionic motion is predicted by MD simulation of porous lithium disilicate and further studies will be useful for material designs of electric devices.

The studies of ions are closely related to the field of glass transition. Especially, insights obtained from the studies of ionic liquid, which can be glass forming, are useful to understand the glass transitions. Some hints to consider the problems are also discussed in this chapter.

Some concepts and methods used for the studies by MD simulations, such as Lévy distribution and multifractal are explained separately in Appendixes 1–7. The main part of the MD code (CUDA, FORTRAN) for GPGPU (General-purpose computing on graphics processing units) is found in the Appendix A.8. The usage of Excel file for Fast Fourier Transform (FFT) included in Electronic Supplementary Materials (ESM) is explained in the Appendix A.9

Electronic Supplementary Materials (ESM) are available online. (http://extras.springer.com/). A short MD program, which works on Windows machine, initial configuration of lithium silicate glass and some related files used in the exercise of MD simulation mentioned in Chap. 12 are included. Several interactive free Computational Document Format (CDF) files (CDF player is freely available) for manipulation of parameters of Lévy distribution, MD simulation of a small soft-sphere system and some examples of analysis of jump motions of ions are also included. Some movie clips for the motion of ionically conducting glass and a crystal, as well as ionic liquid can be found there.

"Data Tables for the Fourier Transform of the Time Derivatives of the Stretched Exponential Functions" as well as Excel files for performing FFT, explained in Appendix A.9, are included. The reader is welcome to use these files but at his/her own risk.

References

1. M. Faraday, *Experimental Researches in Electricity Art. 1339* (Taylor and Francis, London, 1839)
2. R. Kohlrausch, Pogg. Ann. Phys. Chem. **91**, 179 (1854)
3. R. Kohlrausch, Pogg. Ann. Phys. Chem. **91**, 56 (1854)
4. F. Kohlrausch, Pogg. Ann. Phys. Chem. **119**, 337 (1863)
5. F. Kohlrausch, Pogg. Ann. Phys. Chem. **128**, 1, 207, 399 (1866)
6. C.A. Angell, Annu. Rev. Phys. Chem. **43**, 693 (1992)
7. K.L. Ngai, J. Non Cryst. Solids **203**, 232 (1996)
8. K.L. Ngai, C.T. Moynihan, Bull. Mater. Res. Soc. **23**(11), 51 (1998)
9. J.K. Feng, L. Lu, M.O. Lai, J. Alloys Compd. **501**, 255 (2010)
10. C.P. Sandhya, B. John, C. Gouri, Ionics **20**, 601 (2014)
11. M. Park, X.C. Zhang, M.D. Chung, G.B. Less, A.M. Sastry, J. Power Sources **195**, 7904 (2010)
12. Y.-C. Jung, S.-K. Kim, M.-S. Kim, J.-H. Lee, M.-S. Han, D.-H. Kim, W.-C. Shin, M. Ue, D.-W. Kim, J. Power Sources **293**, 675 (2015)
13. J.C. Bachman, S. Muy, A. Grimaud, H.-H. Chang, N. Pour, S.F. Lux, O. Paschos, F. Maglia, S. Lupart, P. Lamp, L. Giordano, Y. Shao-Horn, Chem. Rev. **116**, 140 (2016)
14. M. Freemantle, Chem. Eng. News **78**, 37 (2000)
15. R.D. Rogers, K.R. Seddon, Science **302**, 792 (2003)
16. T. Welton, Ionic liquids in catalysis. Coord. Chem. Rev. **248**, 2459 (2004)
17. P. Wasserscheid, T. Welton, *Ionic Liquids in Synthesis*, 2nd edn. (Wiley-VCH, Weinheim, 2007)
18. C. Roosen, P. Müller, L. Greiner, Appl. Microbiol. Biotechnol. **81**, 607 (2008)
19. H. Ohno, *Electrochemical Aspects of Ionic Liquids* (Wiley, New York, 2005)
20. A. Lewandowski, A. Swiderska-Mocek, J. Power Sources **194**, 601 (2009)
21. M. Armand, F. Endres, D.R. MacFarlane, H. Ohno, B. Scrosati, Nat. Mater. **8**, 621 (2009)
22. H. Olivier-Bourbigou, L. Magna, D. Morvan, Appl. Catal. A **373**, 1 (2010)
23. S. Werner, M. Haumann, P. Wasserscheid, Annu. Rev. Chem. Biomol. Eng. **1**, 203 (2010)
24. E.W. Castner Jr., J.F. Wishart, Chem. Phys. **132**, 120901 (2010)
25. H. Tuller, Solid State Ion. **131**, 143 (2000)
26. J. Maier, Solid State Ion. **175**, 7 (2004)

27. J. Maier, Nat. Mater. **4**, 805 (2005)
28. R. Waser, M. Aono, Nat. Mater. **6**, 833 (2007)
29. J. Garcia-Barriocanal, A. Rivera-Calzada, M. Varela, Z. Sefrioui, E. Iborra, C. Leon, S.J. Pennycook, J. Santamaria, Science **321**, 676 (2008)
30. S. Kim, S. Yamaguchi, J.A. Elliott, Solid-state ionics in the 21st century: current status and future prospects. MRS Bull. **34**, 900 (2009)
31. P. Heitjans, M. Wilkening, MRS Bull. **34**, 915 (2009)
32. I. Kosacki, C.M. Rouleau, P.F. Becher, J. Bentley, D.H. Lowndes, Solid State Ion. **176**, 1319 (2005)
33. K.L. Ngai, *Relaxation and Diffusion in Complex Systems* (Springer, New York, 2011)

Chapter 2
Theories and Models of Ion Diffusion

This chapter describes some models that are often used in trying to understand experimental data and fundamental questions in ion diffusion in ionically conducting materials. The basics of linear response theory are introduced first, with the definition of the linear response function, the Kramers-Kronig relations, and the Fluctuation-Dissipation theorem. The second section is devoted to present the Debye model and several other phenomenological descriptions of dielectric relaxation in materials whose electrical response is dominated by bound charges. This helps to understand the conductivity relaxation that occurs in materials with mobile charges like ionic conductors, and to introduce the so called conductivity formalism and electric modulus formalism for the analysis of experimental data of ion diffusion dynamics. A simple model of ion hopping is introduced that accounts for the thermally activated behavior often found in ionic conductivity data. The relationship between non-Debye relaxation and non-Gaussianity of the dynamics in the real space is also discussed in this chapter. Finally, three different models for ion diffusion are described in some detail. These are the Random Barrier Model, the MIGRATION concept, and the Coupling Model.

2.1 Linear Response Theory

In physics and material science we often encounter the problem of understanding, and even predicting how the system of interest will respond when an external force or perturbation is applied to drive it away from equilibrium. Response theory is devoted to this goal [1]. For example, if a temperature gradient is applied to a material, the response is heat transport through it, and this response is determined by the thermal conductivity of the material. Or when we apply an electric field as an external force to the same material, the free electrical charges will flow and give

J. Habasaki et al., *Dynamics of Glassy, Crystalline and Liquid Ionic Conductors*,
Topics in Applied Physics 132, DOI 10.1007/978-3-319-42391-3_2

rise to a current density in response. The magnitude of the current density is determined by the electrical conductivity of the material, and, if the response is *linear*, the current density will be proportional to the magnitude of the applied electric field.

We may be interested in the *stationary* response of the system when applying a time independent external force on it, or in the *transient* response of the system. The latter is how the system evolves with time to reach a stationary state under a time independent external force or, conversely how it returns to equilibrium with time after the external force is removed. We may be also interested in the response of the system if the applied external force is time dependent. In this case, if the response is *linear*, we can use Fourier analysis to obtain the response of the system as a superposition of the responses to sine waves of different frequencies that are the Fourier components of the time dependent applied force. This is why the study of the response of a system at different frequencies is relevant. In the following, we shall present a general introduction to linear response theory, and then specialize it to the case of ionically conducting materials.

2.1.1 Linear Response Function

Let us consider a small perturbation or external force $x(t)$ acting on an isotropic system in causing a response $y(t)$. If we assume *linearity* (i.e. the reaction of the system to the sum of two different perturbations is the sum of the two reactions separately to each perturbation) and *causality* (that is, only forces applied in the past contribute to the response at a given time t), the response can be related to the perturbation by [2]:

$$y(t) = \int_{-\infty}^{t} J(t-t')\frac{dx(t')}{dt'}dt', \tag{2.1a}$$

where $J(\tau)$ is known as the material function. This material equation is often written also as

$$y(t) = y_{\infty} + \int_{-\infty}^{t} J(t-t')\frac{dx(t')}{dt'}dt', \tag{2.1b}$$

where the magnitude y_{∞} accounts for the instantaneous response of the system (or its response for very short times, entirely due to fast processes, which are not related to the response from processes that we are interested in, and may not be accessible by experiment). The material function can be determined by measuring the response of the system to a step-like perturbation, $x(t) = x_0$ for $t \geq 0$ and

$x(t) = 0$ before. In this case, $dx(t)/dt = x_0\delta(t)$, with $\delta(t)$ the delta function, and substituting in Eq. (2.1b) we obtain the material function $J(t) = [y(t) - y_\infty]/x_0$. Equation (2.1a) describes the response of the system as a convolution of the material function with the time derivative of the applied external force. Note that the time dependence of the system only depends on the time interval between the application of the force and the observation time t. We can then define a time interval, $\tau = t - t'$, and write Eq. (2.1a) as

$$y(t) = \int_0^\infty J(\tau)\frac{dx(t-\tau)}{d\tau}d\tau, \tag{2.1c}$$

Partial integration of Eq. (2.1c) results in the following alternative expression relating the response and the external force signals in the time domain:

$$y(t) = \int_0^\infty \frac{dJ(\tau)}{d\tau}x(t-\tau)d\tau = \int_0^\infty R(\tau)x(t-\tau)d\tau, \tag{2.1d}$$

where $R(\tau) = dJ(\tau)/d\tau$ is the so-called response function (linear response function, or impulse response function). This means that, in general, the value of $y(t)$ will depend not only on the present value of $x(t)$, but also on past values, and we can approximate $y(t)$ as a weighted sum of the previous values of $x(t-\tau)$, with the weights given by the response function $R(\tau)$. Note that for an impulse or delta function perturbation, $x(t) = x_0\delta(t)$, the response of a system will be proportional to the (impulse) response function, $y(t) = x_0R(t)$.

By inverting Eq. (2.1) we obtain:

$$x(t) = \int_{-\infty}^{t} G(t-t')\frac{dy(t')}{dt'}dt', \tag{2.2}$$

where $x(t)$ and $y(t)$ are a pair of conjugated variables. If $y(t)$ is an extensive quantity, the material function $J(\tau)$ is a generalized compliance, and the time dependent process is defined as retardation. If $y(t)$ is an intensive quantity, the material function $G(\tau)$ is a generalized modulus, and the time dependent process is relaxation. It follows from Eqs. (2.1) and (2.2) that

$$\int_{-\infty}^{\infty} J(t-t')G(t')dt' = \delta(t). \tag{2.3a}$$

$$J^*(\omega)G^*(\omega) = 1. \tag{2.3b}$$

Equation (2.3b) is obtained by Fourier transformation of Eq. (2.3a) and relates the complex functions $J^*(\omega)$ and $G^*(\omega)$ in the frequency domain. If we are interested in relating the response of the system to the external perturbation as a function of frequency, we consider a stationary periodic time dependent perturbation of the form, $x(t) = x_0 e^{-j\omega t}$, where ω is the angular frequency. We obtain by Fourier transform both sides of Eq. (2.1d) that

$$\int_{-\infty}^{\infty} y(t)e^{-j\omega t}dt = \int_{-\infty}^{\infty}\left[\int_{0}^{\infty} R(\tau)x(t-\tau)d\tau\right]e^{-j\omega t}dt, \tag{2.4a}$$

$$\int_{-\infty}^{\infty} y(t)e^{-j\omega t}dt = \int_{-\infty}^{\infty} x(t')e^{-j\omega t'}dt\int_{0}^{\infty} R(\tau)e^{-j\omega\tau}d\tau, \tag{2.4b}$$

with $t' = t - \tau$. The quantities, $x\ (\omega)$ and $y(\omega)$, which are respectively the Fourier transforms of $x(t)$ and $y(t)$, satisfies the relation,

$$y^*(\omega) = \chi^*(\omega)\, x^*(\omega), \tag{2.4c}$$

where the susceptibility function, $\chi^*(\omega)$, is the one-sided Fourier transform (Laplace transform) of the impulse response function, $R(\tau)$:

$$\chi^*(\omega) = \int_{0}^{\infty} R(\tau)e^{-j\omega\tau}d\tau. \tag{2.5}$$

While the impulse response function is real, the susceptibility is complex,

$$\chi^*(\omega) = \chi'(\omega) - j\chi''(\omega), \tag{2.6}$$

and the real and imaginary parts of the susceptibility can be obtained from the response function by

$$\chi'(\omega) = \int_{0}^{\infty} R(\tau)\cos\omega\tau\, d\tau, \tag{2.7a}$$

$$\chi''(\omega) = \int_{0}^{\infty} R(\tau)\sin\omega\tau\, d\tau. \tag{2.7b}$$

It follows straightforwardly from these relations that $\chi'(\omega)$ is an even function of frequency and $\chi''(\omega)$ is an odd function of frequency.

2.1.2 *The Kramers-Kronig Relations*

Since $\chi'(\omega)$ and $\chi''(\omega)$ are cosine and sine transforms of the same function, the real and imaginary parts of the susceptibility are not independent of each other. Provided that: (1) the response function is real and analytic, (2) the system response at a given time only depends on the forces applied before that time (causality), and (3) the susceptibility converges to zero stronger than $1/\omega$ at high frequencies (i.e. there is not time for the system to respond if the applied force oscillates at enough high frequencies), it can be shown that $\chi'(\omega)$ and $\chi''(\omega)$ are related by the Kramers-Kronig relationships [3–6]:

$$\chi'(\omega) = \frac{1}{\pi}\,\mathcal{P}\int_{-\infty}^{\infty} \frac{\chi''(\omega)}{\omega' - \omega}\,d\omega', \tag{2.8a}$$

$$\chi''(\omega) = -\frac{1}{\pi}\,\mathcal{P}\int_{-\infty}^{\infty} \frac{\chi'(\omega)}{\omega' - \omega}\,d\omega', \tag{2.8b}$$

where the symbol $\mathcal{P}$ denotes the Cauchy principal value. Usually valid in most physical situations, these relations show that the full susceptibility function can be obtained if we just know its real (or imaginary) part at every frequency. An alternate form for the Kramers-Kronig relations can be derived that involves only the response of the system at positive frequencies. If we multiply the numerator and denominator in Eq. (2.8) by $(\omega' + \omega)$ we obtain:

$$\chi'(\omega) = \frac{1}{\pi}\,\mathcal{P}\int_{-\infty}^{\infty} \frac{\omega'\chi''(\omega)}{\omega'^2 - \omega^2}\,d\omega' + \frac{1}{\pi}\,\mathcal{P}\int_{-\infty}^{\infty} \frac{\omega\chi''(\omega)}{\omega'^2 - \omega^2}\,d\omega', \tag{2.9a}$$

$$\chi''(\omega) = -\frac{1}{\pi}\,\mathcal{P}\int_{-\infty}^{\infty} \frac{\omega'\chi'(\omega)}{\omega'^2 - \omega^2}\,d\omega' - \frac{1}{\pi}\,\mathcal{P}\int_{-\infty}^{\infty} \frac{\omega\chi'(\omega)}{\omega'^2 - \omega^2}\,d\omega'. \tag{2.9b}$$

Since $\chi''(\omega)$ and $\chi'(\omega)$ are odd and even functions of frequency respectively, the second integral in Eq. (2.9a) and the first integral in Eq. (2.9b) vanish, and we can finally write:

$$\chi'(\omega) = \frac{2}{\pi}\mathcal{P}\int_{0}^{\infty} \frac{\omega'\chi''(\omega)}{\omega'^2 - \omega^2}\,d\omega', \tag{2.10a}$$

$$\chi''(\omega) = -\frac{2}{\pi}\mathcal{P}\int_{0}^{\infty} \frac{\omega\chi'(\omega)}{\omega'^2 - \omega^2}\,d\omega'. \tag{2.10b}$$

The imaginary part of the susceptibility function is out of phase with the applied force and therefore determines how energy is dissipated by the system. From the Kramers–Kronig relations we can conclude that it is sufficient to measure the dissipative response of a system in order to determine its in-phase response (and vice versa).

2.1.3 The Fluctuation-Dissipation Theorem

We can further examine the relationship between the susceptibility, or the linear response function, and the dissipation of energy in a system, by introducing the Fluctuation Dissipation Theorem (FDT) [7, 8]. The FDT is a general result of statistical thermodynamics that relates the microscopic fluctuations in a system at thermal equilibrium and the response of the macroscopic system to applied external perturbations. In other words, the FDT relates non-equilibrium dynamics of a system driven away from (or relaxing towards) equilibrium to the existing fluctuations and dynamics in the equilibrium state. The FDT thus allows the use of microscopic or molecular models to predict material properties in the context of linear response theory.

Thermodynamic quantities characterizing a macroscopic system are described in statistical physics by their average values. These quantities actually fluctuate around their mean value due to the stochastic motions of the particles in the system. For instance, for a given quantity $y(t)$ with average value, $\langle y \rangle$, the fluctuations of the quantity are defined as $\Delta y(t) = y(t) - \langle y \rangle$. The correlation function $\varphi(\tau)$ is introduced in order to describe the dependence of the fluctuations at a given time $\Delta y(t+\tau)$ on their value $\Delta y(t)$ at a previous time separated by the time interval τ, and it is defined as the average of the product of these two values of the fluctuations at two times separated by τ, $\varphi(\tau) = \langle \Delta y(t) \Delta y(t+\tau) \rangle$. In the case of a *stationary process* the time t is irrelevant and the correlation function can be written as:

$$\varphi(\tau) = \langle \Delta y(0) \Delta y(\tau) \rangle. \tag{2.11}$$

A normalized correlation function, $\phi(\tau) = \varphi(\tau)/\varphi(0)$, is often considered,

$$\phi(\tau) = \langle \Delta y(0) \Delta y(\tau) \rangle / \langle \Delta y(0) \Delta y(0) \rangle, \tag{2.12}$$

so that $\phi(0) = 1$. Note also that it is expected that the correlation function tends to zero for long enough τ, i.e. $\phi(\infty) = 0$.

It is worthwhile to emphasize that every correlation function of an observable quantity can be expressed in terms of the so-called memory function $K(t)$ by [9]

$$\frac{d\phi(t)}{dt} = -\int_0^t K(t-\tau)\phi(\tau)d\tau. \tag{2.13}$$

From the expression above, the time dependence of the correlation function is obtained if the memory function can be calculated by using a microscopic or molecular model or if the memory function can be described by an empirical function.

Again for the case of stationary processes, the so called spectral density function (or the power spectral density function, or simply the power spectrum), $\mathrm{S}_y(\omega)$, is defined as the Fourier transform of the correlation function:

$$\mathrm{S}_y(\omega) = \int_{-\infty}^{\infty} \varphi(\tau) e^{-j\omega\tau} d\tau. \tag{2.14}$$

The spectral density function is a measure of the frequency distribution of the fluctuations. It can be shown that the response function is related to the correlation function by:

$$R(\tau) = -\frac{1}{kT}\frac{d\varphi(\tau)}{d\tau}, \tag{2.15}$$

and therefore, the spectral density function in the classical limit (no quantum effects) is related to the imaginary part of the susceptibility by:

$$\mathrm{S}_y(\omega) = \frac{2kT}{\omega}\chi''(\omega). \tag{2.16}$$

Within the approximations of the linear response theory, the Fluctuation Dissipation Theorem means that the relaxation dynamics of a macroscopic non-equilibrium disturbance is governed by the same mechanisms as the regression of spontaneous microscopic fluctuations in the equilibrium state [10, 11].

2.2 Dielectric Relaxation

Before analyzing relaxation dynamics driven by mobile ions in ionically conducting materials, it is instructive to describe the case of dielectric relaxation in materials with polarization charge. The dielectric relaxation that takes place in a dielectric material with bound electric charges at small electric field strengths can be analyzed within the framework of the linear response theory. In dielectrics the external perturbation is an applied electric field $E(t)$, and the response of the system is the polarization $P(t)$, or the electric displacement $D(t)$ [12]. Let us consider an isotropic system and a homogeneous electric field. We can then describe the time dependence of the magnitude of the polarization inside the material as:

$$P(t) = \varepsilon_0 \int_{-\infty}^{t} \chi(t - t')E(t')dt', \tag{2.17a}$$

$$P(t) = \varepsilon_0 \int_{0}^{\infty} \chi(\tau)E(t - \tau)d\tau, \tag{2.17b}$$

where $\chi(\tau)$ is the corresponding response function for the polarization and ε_0 the permittivity of a vacuum. Since the polarization is an intensive thermodynamic quantity, the function $\chi(\tau)$ is a generalized compliance. In the frequency domain, the polarization and the electric field are related through the complex dielectric susceptibility, $\chi^*(\omega)$, which is the one sided Fourier transform of $\chi(\tau)$ (see Eq. (2.5)), and

$$P^*(\omega) = \varepsilon_0 \chi^*(\omega) E^*(\omega). \tag{2.18}$$

Since the polarization can only depend on the electric field at previous times, a consequence of causality, the real and imaginary parts of the complex susceptibility must satisfy the Kramers–Kronig relations (see previous section).

Analogously, we can obtain the following relation between the electric displacement, D, and the electric field amplitudes if the electric field oscillates periodically at a given frequency, by using the complex dielectric permittivity, $\varepsilon^*(\omega) = 1 + \chi^*(\omega)$,

$$D^*(\omega) = \varepsilon_0 E^*(\omega) + P^*(\omega) = \varepsilon_0 \varepsilon^*(\omega)\, E^*(\omega). \tag{2.19}$$

Note that the frequency dependence of the susceptibility leads to frequency dependence of the permittivity, and characterizes the *dispersion* properties of the material.

2.2.1 Debye Relaxation

Debye theory of dielectric relaxation is the simplest model of rotational Brownian motion of spherical dipoles in a viscous medium where inertia effects are neglected [13, 14]. In this case it is found that the response function has the exponential time dependence. The same behaviour can be explained by assuming that, in the absence of an electric field, if there exists a polarization due to the occurrence of a field in the past, the decrease rate of the polarization at a given instant is independent of the history of the material and depends only on the value of the polarization at that instant, with which it is proportional. The proportionality constant has the dimension of a reciprocal time and is often denoted by $1/\tau_D$, giving rise to the following first order differential equation:

$$-dP(t)/dt = P(t)/\ \tau_D, \tag{2.20}$$

the solution of which is

$$P(t) = P(0)e^{-t/\ \tau_D}. \tag{2.21}$$

It follows that the impulse response function can be written as

$$\chi(t) = \frac{1}{\tau}e^{-t/\ \tau_D}, \tag{2.22}$$

with τ_D the so called (Debye) relaxation time (see Fig. 2.1). The frequency dependence of the complex dielectric permittivity is given by

$$\varepsilon^*(\omega) = \varepsilon_\infty + \frac{\Delta\varepsilon}{1 + j\omega\tau_D}\ . \tag{2.23}$$

Figure 2.2 shows the frequency dependence of the real and imaginary parts of the dielectric permittivity of a system with a Debye relaxation. It can be observed that the real part shows an increase of $\Delta\varepsilon$ with decreasing frequency below the characteristic frequency $\omega_D = 1/\tau_D$, while the imaginary part shows a symmetric peak with the maximum at ω_D. The relaxation time is usually found to be thermally

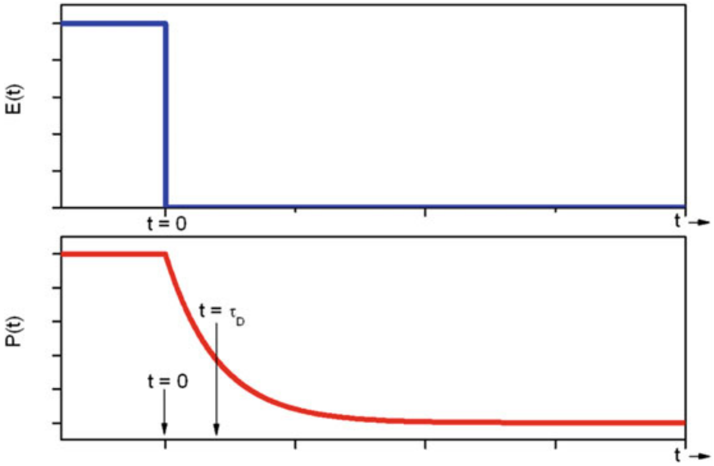

Fig. 2.1 Sketch showing the exponential time dependence of the polarization P(t) for an ideal Debye relaxation in a dielectric material. The polarization starts to decrease after removing the application of an external electric field, E(t), at t = 0. The time τ_D is the Debye relaxation time (see text)

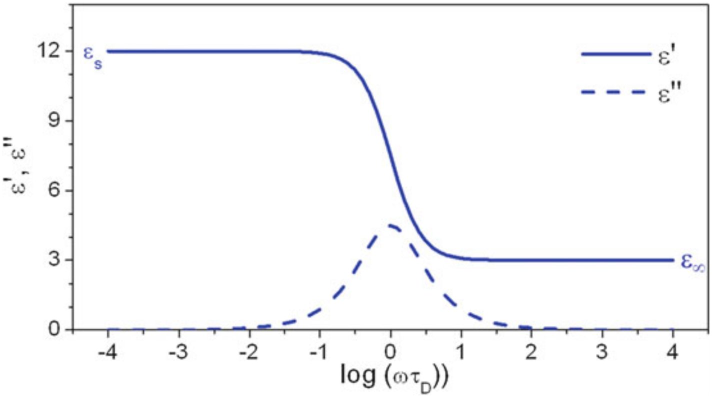

Fig. 2.2 Sketch of the frequency dependence of the real and imaginary parts of the dielectric permittivity ($\varepsilon^* = \varepsilon' - j\varepsilon''$) for a dielectric material showing a Debye relaxation with relaxation time τ_D. The values of the real part of the dielectric permittivity at low and high frequencies are taken as $\varepsilon_s = 12$ and $\varepsilon_\infty = 3$, respectively

activated, which can be explained in terms of a potential barrier for the dipoles to rotate in the system [2].

Within the framework of the memory function formalism (see Eq. (2.13)), the Debye relaxation is obtained by using

$$K(t-\tau) = \frac{\delta(t-\tau)}{\tau_D}, \tag{2.24}$$

which implies that the orientational rotations of the electric dipoles are random and uncorrelated (independent) events in the Debye relaxation model and characterized by one and the same relaxation time.

2.2.2 Non-Debye Relaxation

Although the Debye model provides a simple understanding of the relaxation phenomena, in most cases the measured dielectric relaxation spectra is more complex and show departures from the behavior expected from Eq. (2.23). In particular, it is usually found that the relaxation peak in the imaginary part of the susceptibility or dielectric permittivity functions is asymmetric and broader than expected for a Debye response. This behaviour is known as non-Debye (or sometimes non-ideal) dielectric relaxation. While the ultimate reason for the observed non-Debye relaxation is still a matter of scientific debate and may be different for different systems, there are usually two different approaches in the several proposed models to account for the non-Debye response. One approach is based on considering that the individual dipole rotations are not independent but correlated, and the relaxation is thus the result of a cooperative process such as that proposed by Adam and Gibbs from configurational entropy arguments [15]. Cooperative relaxation also arises from interaction between the relaxation units, and the many-body relaxation is dynamically heterogeneous [16–18]. The other approach relies on considering that the individual dipole rotations take place as random and independent events, and each can be described as true Debye-like process, but that they are characterized by different relaxation times due to an inhomogeneous or disordered environment in the system giving rise to an energy landscape.

While the validity of the different approaches or models for the dielectric relaxation remains a subject of scientific debate, the non-Debye response of the relaxation process is often described in terms of phenomenological functions either in the time or frequency domains which can be used to obtain information about the dynamics and eventually to discriminate between the different theoretical models. One of the most used empirical functions to describe a relaxation process from long time ago is the so-called Kohlrausch-Williams-Watts (KWW) function [19–22]. Its time dependence is a stretched exponential decay of the form

$$\phi(t) = e^{-(t/\ \tau_{KWW})^{\beta_{KWW}}} \tag{2.25}$$

for the correlation function. The exponent or stretching parameter β_{KWW} is a fractional number between 0 and 1, what leads to an asymmetric broadening of the susceptibility spectra compared to the case of an ideal Debye exponential decay ($\beta_{KWW} = 1$). The corresponding memory function for a correlation function of the KWW type can be estimated to be [2, 9]

$$K(t-\tau) = \frac{\delta(t-\tau)}{\zeta(\tau)}\ , \quad \text{with}\ \ \zeta(\tau) \sim \tau_{KWW}{}^{1-\beta_{KWW}}. \tag{2.26}$$

Since the KWW function usually represents experimental data quite well, there has been a long standing search for realistic models that lead to KWW behavior [23, 24]. In particular, Ngai's Coupling Model (CM) [25, 26] provides a physical basis for the KWW behavior in the relaxation of complex systems with many applications. It assumes that at short times, before a crossover time t_c of the order of a few picoseconds, the relaxing species are independent from each other, and this primitive relaxation process is Debye-like with a characteristic primitive relaxation time τ_0. The onset of cooperativity after t_c would give rise to the slowing down of the relaxation dynamics and the corresponding KWW behavior of the correlation function. The important relationship derived in the CM model,

$$\tau_{KWW} = \left[\tau_0 t_c^{(\beta_{KWW}-1)}\right]^{1/\beta_{KWW}} \tag{2.27}$$

between the primitive relaxation time τ_0 and the experimentally determined values of τ_{KWW} and β_{KWW} allows the experimental verification of the model [18].

While the KWW function allows for a fairly good description of many experimental relaxation data in the time domain, there are other important and widely used empirical descriptions of the relaxation processes that describe the susceptibility or permittivity function in the frequency domain. Among these empirical functions is the so called Havriliak-Negami function [27] which reads

$$\varepsilon^*(\omega) = \varepsilon_\infty + \frac{\Delta\varepsilon}{\left(1 + (j\omega\,\tau_{HN})^\alpha\right)^\beta} \ . \tag{2.28}$$

The fractional parameters α and β describe the symmetric ($\beta = 1$) or asymmetric $(\beta < 1)$ broadening of the relaxation peak in the dielectric spectra. These parameters being less than 1 account for the experimentally observed fractional power-law frequency dependence of the dielectric permittivity, the so-called Jonscher's law or universal dielectric response [28], since the limiting behavior of the dielectric loss at low and high frequencies is given by $\varepsilon''(\omega) \sim \omega^\alpha$ and $\varepsilon''(\omega) \sim \omega^{-\alpha\beta}$ respectively. The memory function which leads to a relaxation behavior according to the Havriliak-Negami function can be approximated by [9]

$$K(t-\tau) = \frac{\Omega_0 \tau^{-\alpha}(t-\tau)^{\beta-2}}{\Gamma(\beta-1)} \quad . \tag{2.29}$$

The case $\beta = 1$ in the Havriliak-Negami function leads to the so-called Cole-Cole (CC) function [29],

$$\varepsilon^*(\omega) = \varepsilon_\infty + \frac{\Delta\varepsilon}{\left(1 + (j\omega\,\tau_{CC})^\alpha\right)} \ , \tag{2.30}$$

which describes the case of a symmetric relaxation spectra, with the dielectric loss given by $\varepsilon''(\omega) \sim \omega^\alpha$ and $\varepsilon''(\omega) \sim \omega^{-\alpha}$ in the limit of low and high frequencies respectively. It accounts for broader spectra compared to the Debye case, which is in fact the limiting case for $\alpha = 1$. Another phenomenological expression that is often used to describe relaxation spectra was given by Davidson and Cole [30]. The Cole-Davidson (CD) function reads

$$\varepsilon^*(\omega) = \varepsilon_\infty + \frac{\Delta\varepsilon}{(1 + j\omega\,\tau_{CD})^\beta} \ , \tag{2.31}$$

and results from setting the parameter $\alpha = 1$ in the HN function. Although there are other empirical descriptions of dielectric relaxation, the Havriliak-Negami, Cole-Cole and Cole-Davidson functions in the frequency domain, together with the KWW function in the time domain, are most often used in the literature to describe non-Debye relaxation spectra or response function [12].

2.3 Conductivity Relaxation

2.3.1 Electric Modulus Formalism

While in the case of dielectric relaxation the response of the system is due to bound electric charge, when analyzing conductivity relaxation dynamics in ionically conducting materials, it is important to bear in mind that it is driven by mobile electric charge carried by the ions. In this case the relaxation process is the decay of the electric field $E(t)$ inside the conductor after applying an electric displacement $D(t)$. Analogous to the description of dielectric relaxation, let us assume an isotropic system and a homogeneous electric displacement. If an ionic conductor is placed between the charged plates of a condenser at time $t = 0$, the displacement vector can be described by a step-function with amplitude D_0. It gives rise to an electric field that causes the mobile ions to diffuse and accumulate, which results in an additional and opposite electric field that increases with time until the total electric field that mobile ions feel inside the material cancels out. Therefore, the electric field inside the ionic conductor decays with time (see Fig. 2.3), and we can describe the time dependence of this electric field after $t = 0^+$ as:

$$E(t) = \frac{D_0}{\varepsilon_0 \varepsilon_\infty} \Phi(t), \tag{2.32}$$

where $\varepsilon_0 \varepsilon_\infty$ is the “high frequency” value of the dielectric permittivity, and $E(t = 0^+) = D_0 / \varepsilon_0 \varepsilon_\infty$. The “high frequency” permittivity accounts for all possible contributions to the decay of the electric field between $t = 0$ and $t = 0^+$ and always before the mobile ions start to move. Thus, the correlation function for the electric field relaxation due to mobile ions is given by $\Phi(t)$.

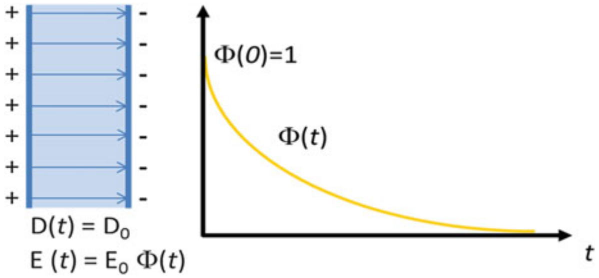

Fig. 2.3 Sketch showing the relaxation of the electric field inside an ionic conductor placed at time $t = 0$ between the charged plates of a condenser where the displacement vector can be described by a step-function with amplitude D_0. The electric displacement gives rise to an electric field that causes the mobile ions to diffuse and accumulate, which results in an additional and opposite electric field that increases with time until the total electric field that mobile ions feel inside the material cancels out. The electric field inside the ionic conductor decays with time as $E(t) = E_0\Phi(t)$

By using the time derivative of Eq. (2.32) we can write

$$E(t) = \frac{1}{\varepsilon_0 \varepsilon_\infty}\left[D(t) + \int_{-\infty}^{t} \frac{d\Phi}{dt}(t - t')D(t')dt'\right] \tag{2.33a}$$

and therefore

$$E(t) = \frac{D_0}{\varepsilon_0 \varepsilon_\infty}\left[1 + \int_{0}^{t} \frac{d\Phi}{d\tau}(\tau)d\tau\right]. \tag{2.33b}$$

In the frequency domain, the relation between the electric field and the electric displacement is obtained by performing the Fourier transform of Eq. (2.33), resulting in

$$E^*(\omega) = \frac{\left[1 + \dot{\Phi}^*(\omega)\right]}{\varepsilon_0 \varepsilon_\infty} D^*(\omega). \tag{2.34}$$

where $\dot{\Phi}^*(\omega)$ accounts for the Fourier transform of the time-derivative of the correlation function describing the electric field relaxation. By using the electric modulus $M^*(\omega) = 1/\varepsilon*(\omega)$ and Eq. (2.19) we can write

$$E^*(\omega) = \frac{M^*(\omega)}{\varepsilon_0} D^*(\omega), \tag{2.35}$$

and therefore

$$M^*(\omega) = M_\infty\left[1 + \dot{\Phi}^*(\omega)\right], \tag{2.36a}$$

$$M^*(\omega) = M_\infty\left[1 + \int_{0}^{\infty} \frac{d}{dt}\Phi(t)e^{-j\omega t}dt\right], \tag{2.36b}$$

where $M_\infty = 1/\varepsilon_\infty$. Equation (2.36) means that the correlation function $\Phi(t)$ for the time decay describing the relaxation of the electric field (often referred to as electrical conductivity relaxation), which is governed by the dynamics of the mobile ions, can be obtained from the electric modulus as a function of frequency. By using the relation $1 + \dot{\Phi}^*(\omega) = j\omega\Phi^*(\omega)$, we can relate the Fourier transform of the correlation function, $\Phi*(\omega)$, to the experimental impedance spectra $Z^*(\omega) = 1/\sigma*(\omega) = 1/j\omega\varepsilon_0\varepsilon*(\omega) = M^*(\omega)/j\omega\varepsilon_0$ as

$$\Phi^*(\omega) = \varepsilon_0 \varepsilon_\infty Z^*(\omega) \tag{2.37}$$

2.3.2 Conductivity Formalism

Alternatively, we can think of the ion diffusion process in ionic conductors in terms of the successive jumps of the ions from their sites to neighboring empty sites in the structure. According to linear response theory, the frequency dependent complex electrical conductivity due to ion hopping is proportional to the Fourier transform of the current density autocorrelation function:

$$\sigma^*_{hop}(\omega) = \frac{V}{3k_BT}\int_0^\infty \langle J(0)J(t)\rangle e^{-j\omega t}dt\,, \tag{2.38}$$

where V is the volume of the sample, and k_B denotes Boltzmann's constant. The current density is given by

$$J(t) = \frac{1}{V}\sum_i q_i v_i(t) \tag{2.39}$$

with q_i and v_i the charge and velocity of the ion i and the sum performed for all the mobile ions in the sample. The combination of Eqs. (2.38–2.39) shows that the electrical conductivity is related to velocity correlation function of the hopping ions, $\left\langle \sum_{i,j} v_i(0)v_j(t)\right\rangle$, as

$$\sigma^*_{hop}(\omega) = \frac{q^2}{3Vk_BT}\int_0^\infty \left\langle \sum_{i,j} v_i(0)v_j(t)\right\rangle e^{-j\omega t}dt\,. \tag{2.40}$$

Similarly, the frequency dependence of the complex self-diffusion coefficient due to ion hopping is proportional to the Fourier transform of the velocity autocorrelation function:

$$D^*_{hop}(\omega) = \frac{1}{3}\int_0^\infty \langle v(0)v(t)\rangle e^{-j\omega t}dt\,, \tag{2.41}$$

and it is related to the complex electrical conductivity through the generalized Nernst-Einstein equation:

$$\sigma^*_{hop}(\omega) = \frac{Nq^2}{Vk_BT\,H^*(\omega)}D^*_{hop}(\omega), \tag{2.42}$$

with N the total number of mobile ions and $H^*(\omega)$ the so-called Haven ratio. When correlations between the velocities of different ions can be neglected, the velocity correlation function is proportional to the velocity autocorrelation function,

$$\left\langle \sum_{i,j} v_i(0)v_j(t) \right\rangle = N\langle v(0)v(t)\rangle \tag{2.43}$$

and the Haven ratio is real and equal to 1. But if cross correlations cannot be neglected, then the Haven ratio is a complex function of the frequency.

In the particular case that the ions behave as random walkers, they have no memory and their velocities are uncorrelated, so the velocity correlation function is proportional to a delta function at time $t = 0$,

$$\left\langle \sum_{i,j} v_i(0)v_j(t) \right\rangle_{random\ hops} = \frac{N\,\Gamma\,x_0^2}{2}\delta(t), \tag{2.44}$$

where, Γ and x_0 are the hopping rate and the elementary jump distance of the ions, respectively. Thus, random hopping yields a hopping conductivity which is real and constant that is given by

$$\sigma^*_{hop}(\omega) = \frac{n\,q^2\,x_0^2\,\Gamma}{6k_BT} = \frac{n\,q^2\,D_0}{k_BT} \tag{2.45}$$

with $n = N/V$ as the concentration of mobile ions, and a frequency independent diffusion coefficient given by $D_0 = \frac{x_0^2\,\Gamma}{6}$. However, experimental data usually shows a dispersive (frequency dependent) complex conductivity, which is interpreted in terms of the non-random nature of the ion hopping events. As in the case of dielectric relaxation, there are models that consider the dispersive behavior arises from the existence of a distribution of hopping rates because the different ions experience different environments at a given time, and other models where the dispersive conductivity is a consequence of the cooperative hopping of mobile ions due to ion-ion interactions.

It is important to remark that independently of using the conductivity or electric modulus formalism in order to analyze or interpret experimental data of the electrical response of ionic conductors, they are just different representations of the same data, that are related through

$$Z^*(\omega) = M^*(\omega)/j\omega\varepsilon_0 = 1/\sigma^*(\omega) = \frac{1}{\sigma^*_{hop}(\omega) + j\omega\varepsilon_0\varepsilon_\infty}, \tag{2.46}$$

and therefore contain the same information about ion dynamics.

2.3.3 Empirical Description of Ion Dynamics. Distribution of Relaxation Times

The experimental data of electrical conductivity relaxation (ECR) from admittance spectroscopy measurements can be represented in terms of the complex conductivity or the electric modulus. The two alternative representations of the same data have proven to be very useful in the study of ion diffusion dynamics in ionically conducting materials [26, 31]. Similar to the case of dielectric relaxation in polarizable insulating materials, a Debye response function, i.e. exponential time decay with a single relaxation time, is rarely observed [32]. The usual behavior is a rather strongly non-Debye response, characterized by a frequency dispersive electrical conductivity and therefore by a broader, and usually asymmetric, peak in the imaginary part of the electric modulus spectra compared to that expected from a Debye relaxation. The observed departure from a simple Debye behavior in ECR has been mainly considered as due to either the presence of structural disorder and randomness in the material [33], or to the effect of interactions among ions in their cooperative motion [18, 34–37]. Before entering in the description of some of these models that have been proposed to explain the non-Debye character of the conductivity relaxation, we describe the main features of the relaxation in the frequency and time domains and an empirical approach to study the dynamics of mobile ions by using an analysis based on distributions of relaxation times. Although it is a mathematical tool, it may offer hints in the search of the physics behind the relaxation process. The ac conductivity $\sigma'(\omega)$ of these materials shows a constant value at low frequencies, the so called dc conductivity value, and a crossover to a power law dependence with frequency at high frequencies, so that the real part of the conductivity can be expressed as [28, 38, 39]

$$\sigma'(\omega) = \sigma_{dc} + A\omega^n \tag{2.47}$$

where σ_{dc} is the dc conductivity, A is a temperature dependent parameter and n is a fractional exponent which usually lies between 0.6 and 1 [28, 40]. This universal behavior is shown in Fig. 2.4. Equation (2.47) and Kramers-Kronig relations lead to a frequency dependence of the complex conductivity which can be written as

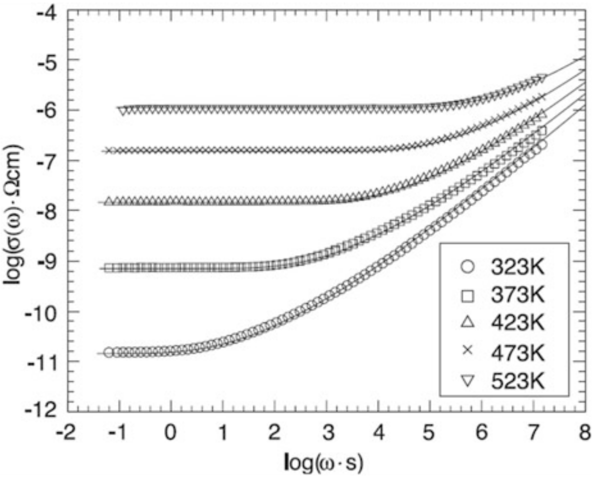

Fig. 2.4 Frequency dependent conductivity of a sodium germanate glass of composition $0.2Na_2O \cdot 0.8GeO_2$ at several temperatures. Reproduced from [41] with permission

$$\sigma^*(\omega) = \sigma_{dc}[1 + (j\omega/\omega_c)^n] + j\omega\varepsilon_0\varepsilon_\infty \tag{2.48a}$$

$$\sigma^*(\omega) = \overset{*}{\sigma}_{hop}(\omega) + j\omega\varepsilon_0\varepsilon_\infty \tag{2.48b}$$

where included is the high frequency permittivity term, $j\omega\varepsilon_0\varepsilon_\infty$, due to the contributions from all the polarization at higher frequencies, and ω_c represents a crossover frequency from the dc conductivity plateau (at $\omega < \omega_c$) to the power law frequency dependence (at $\omega > \omega_c$).

Some authors [42–44] have argued the advantage of using the $\sigma'(\omega)$ representation of the measurements since it allows to separate the hopping dynamics from the high frequency permittivity term due to other different physical processes occurring at shorter times. However, it is important to note that the characteristic crossover frequency characterizing ion hopping dynamics is always of the order of $\omega_c \approx \sigma_{dc}/\varepsilon_0\varepsilon_\infty$ [33, 45], which shows that in fact ion dynamics are influenced by the dielectric permittivity of the medium, in particular the time dependence of the corresponding correlation function. It is also relevant to point out that the physical significance arising from the additive character of the two contributions in Eq. (2.47) has been questioned [46–48]. Equation (2.47) implies that both terms contribute to the conductivity at all frequencies, like two independent conduction mechanisms simultaneously present at every time. And this is actually at odds with the finding of a crossover frequency proportional to the value of the dc conductivity ($\omega_c \approx \sigma_{dc}/\varepsilon_0\varepsilon_\infty$), and also with the fact that experimental data of the imaginary part of the complex conductivity do not usually increase indefinitely as the frequency decreases. However, Eq. (2.47) is widely used in the literature in order to describe empirical conductivity data of ionic conductors, since it describes rather well the conductivity spectra, $\sigma'(\omega)$, particularly in the limits of low and high frequencies.

An alternative description of ECR has been made in the time domain [49–52] in terms of electric field decay with the Kohlrausch-Williams-Watts (KWW) function [19–22]. As previously stated, at constant displacement vector, the electric field inside an ionic conductor shows a time decay $\Phi(t)$ well approximated by a KWW function or stretched exponential function,

$$\Phi(t) = e^{-(t/\tau^*)^{1-n}} \tag{2.49}$$

where τ^* is a temperature activated relaxation time and $0 < n < 1$. Although the physical significance of the KWW function is not generally agreed by researchers in the field, it has been interpreted in terms of the slowing of the relaxation process due to cooperative many-ion dynamics, with the parameter n as an index of correlations between the ions in motion. The case $n = 0$ would thus correspond to the completely uncorrelated ion motion giving rise to a Debye response characterized by exponential time decay function.

Experimental conductivity data are usually obtained in the frequency domain from Admittance Spectroscopy, and the time decay $\Phi(t)$ is calculated from the electric modulus data according to Eq. (2.36). The calculation of the decay function, $\Phi(t)$, involves a numerical Fourier transform of the measured data in the frequency domain from which the parameters n and τ^* that best characterize the relaxation process by the KWW decay function can be obtained. However, it is well known that the calculation of the Fourier transform by numerical methods from real data in the frequency domain is affected by numerical errors arising from the fact that the experimental data set is usually discrete and finite. An alternative procedure has been proposed in order to calculate the time decay function without evaluating any numerical Fourier transform [52]. It consists of finding the coefficients g_i of a distribution of discrete relaxation times τ_i so that the measured frequency response may be approached as a superposition of Debye-like processes according to

$$\dot{\Phi}^*(\omega) \approx \sum_1^n g_i[1/(1 + j\omega\tau_i)] \tag{2.50}$$

The time decay function can then be calculated as

$$\Phi(t) \approx \sum_1^n g_i \exp(-t/\tau_i) \tag{2.51}$$

Assuming a KWW dependence for the time decay, one can fit the parameters n and τ^* describing the conductivity relaxation in the time domain. Other methods based on a complex non-linear least squares fitting of experimental data to equivalent circuit models [53–55] can also be used in order to obtain the time decay function from admittance spectroscopy data avoiding the numerical Fourier transform.

A different approach has been reported based on an analysis of the frequency dependence of the electric modulus. The electric modulus spectra in ionic conductors can be usually well described by one of the empirical relaxation functions in the frequency domain like the Cole-Cole, Cole-Davidson, or Havriliak-Negami. These functions, described in the subsection devoted to dielectric relaxation, can also be used to describe phenomenologically the electrical conductivity relaxation in ionic conductors [56]. The advantage is that an analytical expression exists for the distribution of relaxation times once the parameters characterizing the empirical function (CC, CD or HN) in the frequency domain is obtained. This procedure allows then a description of the decay function in the time domain by using Eq. (2.51). Figure 2.5 shows experimental data of the electric modulus at different temperatures for several ionic conductors. Since the plot is in a double logarithmic scale, the linear behavior at both sides of the peaks is indicative of the power law frequency dependence of the complex conductivity. Modulus plots are usually presented in a linear scale, showing asymmetric peaks for the imaginary part ($M''(\omega)$) shifting to lower frequencies when temperature is decreased. However, the linear scale obscures relevant features of the modulus spectra, like, for example, the mentioned power law dependences. The asymmetric power law behavior of the electric modulus data at low and high frequencies, suggests that conductivity relaxation may be described using a Havriliak-Negami (HN) relaxation function

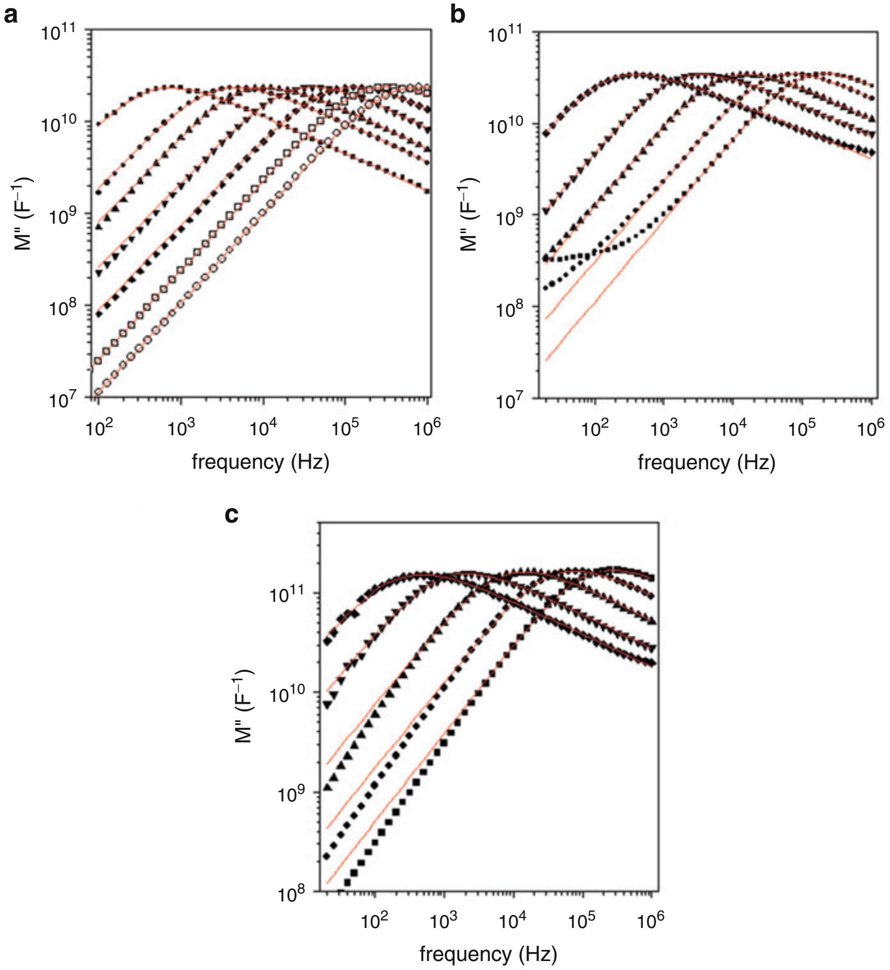

Fig. 2.5 Imaginary part of the dielectric modulus against frequency presented in a double logarithmic scale for (**a**) single-crystal YSZ at 480, 514, 532, 560, 587, 615 and 639 K (from *left to right*), (**b**) $Li_{0.5}La_{0.5}TiO_3$, at 179, 193, 206, 221 and 245 K (from *left to right*) and (**c**) $Li_{0.5}Na_{0.5}La(CrO_4)_3$, at 262, 275, 296, 317 and 336 K (from *left to right*). The *solid curves* are fits to Havriliak-Negami functions according to Eq. (2.53) (see text). Reproduced from [56] with permission

(see Eq. (2.28)), and it is indeed the case as shown by the lines in Fig. 2.5 that are fits of experimental data to a HN function [56].

The discrepancies observed between experimental data of $Li_{0.5}La_{0.5}TiO_3$ and the corresponding fitting functions at low frequencies and high temperatures, are due to blocking effects. Blocking appears as a consequence of charge built ups at grain boundaries or electrodes and do not affect experimental data at high frequencies. This is further discussed in Chap. 4.

The parameters τ_{HN}, α and β in Eq. (2.28) that best fit experimental data can be used to construct an analytical distribution of relaxation times ($\rho(\tau)$) according to the following expressions:

$$\rho(\tau) = \frac{1}{\pi}\frac{(\tau/\tau_{HN})^{\alpha\beta}\sin(\beta\theta)}{\left[(\tau/\tau_{HN})^{2\alpha} + 2(\tau/\tau_{HN})^{\alpha}\cos(\alpha\pi) + 1\right]^{\beta/2}}, \tag{2.52a}$$

where θ is

$$\theta = \arctan\left|\frac{\sin(\alpha\pi)}{(\tau/\tau_{HN})^{\alpha} + \cos(\alpha\pi)}\right|. \tag{2.52b}$$

According to Eq. (2.36) we can relate the dielectric modulus to the Havriliak-Negami function $F^*_{HN}(\omega)$ through :

$$1 - M^*(\omega)/M_\infty = F^*_{HN}(\omega) = -\dot{\Phi}^*(\dot{\omega}). \tag{2.53}$$

And from the distribution of relaxation times obtained from the fitting to a HN function and using Eq. (2.52), the frequency dependence of the Fourier transform of the time derivative of the decay function can be expressed as a superposition of Debye-like processes of the form:

$$-\dot{\Phi}^*(\omega) = \int_0^\infty \frac{\rho(\tau)}{1 + j\omega\tau}d\tau. \tag{2.54}$$

So that in the time domain the following expression holds,

$$\Phi(t) = \int_0^\infty \rho(\tau)e^{-t/\tau}d\tau, \tag{2.55}$$

which allows determining the time decay function from $\rho(\tau)$ by numerical integration. In order to evaluate numerically the integral in Eq. (2.55) it is better to use $\ln\tau$ as integration variable instead of τ, because of the smoother dependence of the integrand on $\ln\tau$. Note also that since the contribution due to small and large values of τ compared to τ_{HN} is negligible, the infinite range of integration do not pose a problem, and it is enough to perform the numerical integration at a finite interval around τ_{HN} to obtain a good approximation to the time decay function $\Phi(t)$.

Finally, once the time decay function $\Phi(t)$ has been obtained from experimental electric modulus data using the procedure explained above, it is possible to verify whether or not this function is well approximated by assuming a KWW dependence (see Eq. (2.49)), and eventually obtain the parameters τ^* and n which describes the relaxation process in the time domain. The time decay functions and their fittings to stretched exponential functions with a KWW behavior are presented in Fig. 2.6 at different temperatures for the three systems analyzed. The insets of the figures show

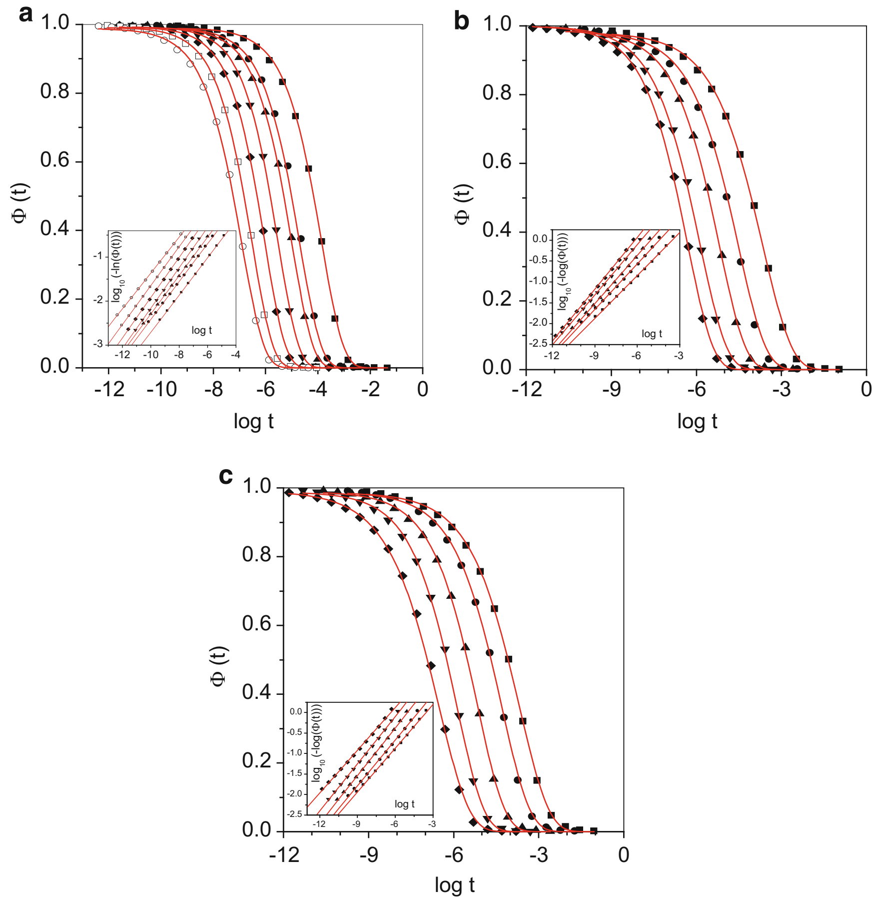

Fig. 2.6 Time decay functions Φ(*t*) obtained for (**a**) single-crystal YSZ at 480, 514, 532, 560, 587, 615 and 639 (from *right to left*), (**b**) Li$_{0.5}$La$_{0.5}$TiO$_3$, at 179, 193, 206, 221 and 245 K (from *right to left*) and (**c**) Li$_{0.5}$Na$_{0.5}$La(CrO$_4$)$_3$, at 262, 275, 296, 317 and 336 K (from *right to left*). The *solid curves* are fits to KWW functions. The *insets* show log (-ln [Φ(*t*)]) against log t plots, and the *solid lines* are linear fits. Reproduced from [56] with permission

the corresponding linear log[-ln(Φ(*t*))] versus log *t* plots from which parameters τ^* and n were obtained by a linear least-squares fitting.

Although an analytical relationship does not exist between the HN function in the frequency domain and the KWW in the time domain because they are not exactly Fourier transforms of each other, a connection among the parameters of both descriptions has been proposed in the past for dielectric relaxation in polymeric systems [57]. It has been shown that the empirical relation $\alpha\,\beta = (1-n)^{1.23}$ that approximately holds in those systems is also valid naturally in the case of ionic conducting materials, at least for a limited range of values of the parameter n in the KWW function [56]. The relaxation time τ_{HN}, on the other hand, is thermally activated with the same activation energy than τ^* and the dc conductivity.

Once we have obtained the parameters τ^* and n that best fit the conductivity relaxation to a KWW function in the time function, an average relaxation time $\langle\tau\rangle$ can be defined in terms of the integrated area of the KWW function as

$$\langle\tau\rangle = \int_0^\infty \Phi(t)dt = \frac{\Gamma(1/(1-n))}{1-n}\tau^*, \tag{2.56}$$

where Γ refers to the Euler's gamma function [58]. This average relaxation time $\langle\tau\rangle$ is related to the dc conductivity through the following expression:

$$\langle\tau\rangle = \varepsilon_0\varepsilon_\infty/\sigma_0. \tag{2.57}$$

The relaxation time $\langle\tau\rangle$ results to be temperature dependent according to the expression

$$\langle\tau\rangle = \tau_\infty \exp(E/kT) \tag{2.58}$$

so the dc conductivity is also temperature activated and can be expressed as

$$\sigma_0 = \frac{\varepsilon_0\varepsilon_\infty}{\tau_\infty}\exp(-E/kT) \tag{2.59}$$

since the high frequency permittivity $\varepsilon_0\varepsilon_\infty$ usually shows weak temperature dependence. The temperature dependence of the dc conductivity thus obtained is presented in Fig. 2.7 in an Arrhenius plot (open symbols), where the thermally activated behavior results in an apparent linear behavior with slopes determined by the activation energy E. Figure 2.7 also shows the values of the dc conductivity

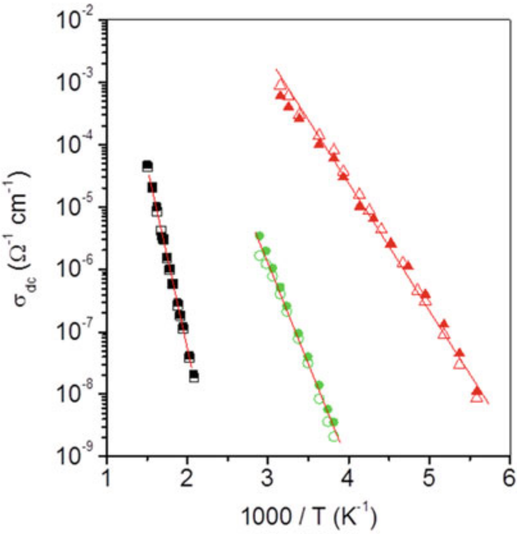

Fig. 2.7 Arrhenius plot of dc conductivities of YSZ (*open squares*), $Li_{0.5}La_{0.5}TiO_3$ (*open triangles*) and $Li_{0.5}Na_{0.5}La(CrO4)$, (*open circles*), obtained assuming a KWW behaviour for the time decay functions. The *solid lines* are fits according to Eq. (2.59). Dc conductivities obtained from complex impedance plots are also displayed as *solid symbols*. Reproduced from [56] with permission

obtained at each temperature from the fitting of the frequency dependent ac conductivity to Eq. (2.47) (solid symbols). A very good agreement can be observed between these results and those deduced from the time decay functions assuming a KWW dependence, which may be considered as an additional evidence for the KWW behavior of the conductivity relaxation in the time domain and the validity of Eq. (2.57).

2.3.4 Ion Diffusion Mechanisms

In crystalline ionic conductors, ion diffusion takes place by the hopping of mobile ions from site to site in the lattice. This explains the temperature dependence of the dc conductivity due to long range ion transport, which, with few exceptions, is found to be thermally activated. The thermal activation results from the energy barrier that ions need to overcome in order to jump to an available neighbouring site in the structure. The existence of different types of structural defects gives rise to several possible diffusion mechanisms for the ions [59]. For example, the diffusion is said to take place by the *vacancy mechanism* if ions jump into an adjacent unoccupied lattice site (vacancy). These vacancies can be point defects, or structural vacancies, that can be created in large amounts for example by doping of CeO_2 or ZrO_2 by substituting Ce and Zr for aliovalent cations as Gd, Sm, Y..., resulting in a large concentration of oxygen vacancies that are responsible of the ionic conductivity in these fluorite structures. Note that vacancies move in the direction opposite the oxide ions. The vacancy mechanism is most often found in fast ionic conductors but there are other different mechanisms that can give rise to high ionic conductivity, like the *interstitial mechanism* that occurs when an ion occupying an interstitial site moves to one of the neighbouring interstitial sites (see Fig. 2.8). In order such a jump to happen between interstitial sites, a large distortion of the lattice is usually required, so its probability is higher the smaller the size of the mobile interstitial ions compare to the ions in lattice sites.

$La_2NiO_{4+\delta}$ is an example of an ionic conductor showing oxide ion diffusion by an interstitial mechanism. In this and other materials with the perovskite related structure of the K_2NiF_4 type, excess oxide ions can be easily accommodated in interstitial sites, giving rise to high oxide ion conductivity. Materials where ion diffusion takes place by interstitial mechanism have the advantage that mobility is not limited by the vacancy-dopant association that usually occurs in materials showing the vacancy mechanism. However, interstitial occupancy usually gives rise to changes in the oxidation state of ions in the lattice and thus to an additional electronic conductivity. In fact, all materials known up to date showing ion conductivity by interstitial mechanism are not pure ionic conductors but they show also electronic conductivity.

Other mechanisms for ion diffusion in solids have been proposed. In the case that interstitial diffusion would require a lattice distortion too large, this mechanism becomes improbable and interstitial ions may move by pushing one of its nearest

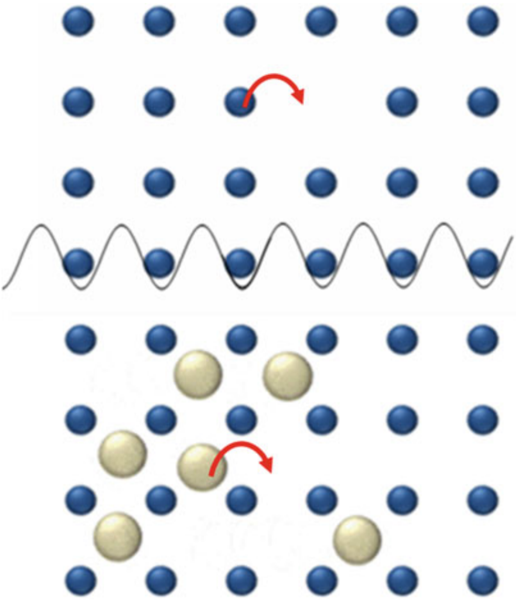

Fig. 2.8 (*Top*) Sketch of the vacancy mechanism for ion diffusion, where the diffusion takes place if ions are able to jump into adjacent unoccupied lattice sites (vacancies). The *line* represents the potential energy barrier that ions must overcome in order to jump. (*Bottom*) Sketch of the interstitial mechanism for ion diffusion, where an ion occupying an interstitial site moves to one of the neighbouring interstitial sites. A large distortion of the lattice is usually required in order such a jump to happen between interstitial sites

neighbours on a lattice site into another interstitial position and itself occupies the lattice site of the displaced atom. This is known as the *interstitialcy mechanism*. Note that it is necessary for an ion to move that there is an interstitial atom on a neighbouring site, and consequently the diffusion coefficient is proportional to the concentration of interstitial ions. A variation of the interstitialcy mechanism is the so called crowdion, where an ion is assumed to be crowded into a line of other ions, causing them to move along the line from their equilibrium sites.

In the last years, the combination of experimental data and computer modelling techniques have led to deeper understanding of the relationships between ion transport mechanisms and the local structure and defect types of ionically conducting materials, allowing materials optimisation for specific applications [60–63].

For the special case of proton diffusion in solids, two different mechanisms have been proposed: the free transport mechanism and the vehicle mechanism. The free transport, also known as Grotthuss mechanism, is usually the way protons diffuse in oxides. For a review see Ref. [64]. The protons jump from one oxygen ion to a neighbouring one, and after each jump the proton in the hydroxide rotates such that the proton reorients in the electron cloud and becomes aligned for the next jump. The rotation and reorientation may involve small activation energy, but it is believed that the jump itself accounts for most of the activation energy required in the diffusion process. In the vehicle mechanism the proton moves as a passenger on an oxide ion, and thus it actually consists of transport of hydroxide ions. These hydroxide ions may diffuse by an oxygen vacancy mechanism or as an interstitial hydroxide ion. It is worthwhile to remark that the hydroxide ion has a smaller radius and charge than the oxide ion and it is thus expected to have smaller activation energy for diffusion than the oxide ion. Other species such as hydronium ions, H_3O^+ , or water molecules may serve as vehicles for proton diffusion, particularly in open structures [59, 65].

The mechanisms described above are for ion diffusion in crystals. But microstructure in crystals can play a major role in ion diffusion. For example, lower activation energy for ion diffusion is often found along certain dislocations and along the grain boundaries in polycrystalline materials compare to bulk values. In general, surface diffusion occurs much faster than grain boundary diffusion, and grain boundary diffusion occurs much faster than lattice diffusion. Thus, in polycrystalline materials an effective diffusion coefficient is introduced which is a combination of the diffusion coefficients along the different regions. This is particularly relevant in the case of nanocrystalline materials, where the grain boundaries may be a significant fraction of the material, and thus result in an enhancement of ion diffusion (see Chap. 5). Finally, amorphous, glassy or liquid ionic conductors are often described as disordered lattices with a landscape of energy barriers for ion hopping, and where pathways for enhanced ion transport may exist compared to the crystalline structure with same chemical composition.

2.3.5 Temperature Dependence of Ion Diffusion

Independently of which is the mechanism involved in ion diffusion through the material, the mobile ions have to overcome a potential (energy) barrier of height ΔH_m in order to jump from site to site in the structure. This is schematically shown in Fig. 2.9. At a given temperature, ions are vibrating within their cages and have a finite probability of jumping outside the cage which is proportional to $\exp(-\Delta H_m/k_BT)$. The diffusion will be thermally activated and the energy barrier ΔH_m represents the activation energy for ion hopping. If one considers the equilibrium state for the ion, the energy minimum and its activated state at the maximum energy between equilibrium sites, it can be shown that the transition rate between equilibrium sites is given by [66]:

$$\Gamma = \nu_0 e^{-\Delta G_m/k_BT} = \nu_0 e^{-\Delta S_m/k_B} e^{-\Delta H_m/k_BT} \tag{2.60}$$

where ν_0 represents the vibration or "attempt" frequency of the mobile ion within the potential cage, of the order of $\nu_0 \sim 10^{13}$ Hz, and ΔG_m, ΔS_m, and ΔH_m represent the Gibbs free energy, entropy and enthalpy change respectively, characterizing the

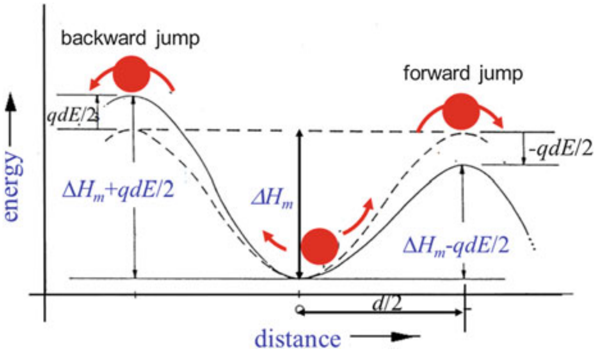

Fig. 2.9 One dimensional model for jump diffusion in an ionic conductor. In the absence of an applied electric field, the probability of the ion of jumping in either forward or backward direction is the same. The activation energy for ion hopping is always ΔH_m and the transition rate (jump frequency) for forward and backward jumps will be the same. When an electric field of magnitude E is applied, the jump frequency in the forward direction is increased, while the jump frequency in the backward direction is decreased. Figure adapted from reference [59]

ion displacement from its equilibrium state to its activated state at the top of the potential barrier. Assuming the vibration of the ion can be described as a harmonic oscillator, the attempt frequency can be estimated to be of the order of $\nu_0 \sim \left(\sqrt{\Delta H_m/M}\right)/x_0$, with x_0 the jump distance and M the reduced mass of the oscillator. Therefore, it is expected that the smaller the value of the enthalpy change ΔH_m, the lower the value of the preexponential factor in the diffusion coefficient in Eq. (2.42–2.45). This behaviour gives rise to a compensation effect that is in fact observed in experimental data and that it is known as the Meyer-Neldel rule. However, it is often found experimentally that a decrease in ΔH_m results in a value of the preexponential factor much lower than predicted by this simple effect of the Meyer-Neldel rule [67].

Another factor determining the temperature dependence of the diffusion coefficient is the concentration of available sites where the mobile ions can jump to. However, for the sake of simplicity we will consider here that this concentration is temperature independent, which is often the case for fast ionic conductors in the experimental temperature range of interest.

2.3.6 One Dimensional Random-Hopping Model for Ionic Conductivity

Figure 2.9 illustrates a simple one dimensional model for jump diffusion in an ionic conductor [59]. In the absence of an applied electric field, the probability of the ion of jumping in either forward or backward direction is the same. The activation energy for ion hopping is always ΔH_m and the transition rate (jump frequency) for forward and backward jumps will be the same. Therefore, in a given time interval, the number of jumps in both directions will be the same. If the material is homogeneous, we can conclude that there will be no net transport of ions in the material. When an electric field of magnitude E is applied, the jump frequency in the forward direction is increased since the activation energy is decreased by an energy *qdE*/*2* (see Fig. 2.9),

$$\Gamma_f = \nu_0 e^{\frac{\Delta S_m}{k_B}} e^{-\left(\frac{\Delta H_m - qdE/2}{k_B T}\right)}, \tag{2.61a}$$

with q the electric charge of the hopping ion and $d = x_0$ the jump distance. Similarly the jump frequency is decreased in the backward or reverse direction since the activation energy is increased by an energy *qdE*/*2*,

$$\Gamma_r = \nu_0 e^{\frac{\Delta S_m}{k_B}} e^{-\left(\frac{\Delta H_m + qdE/2}{k_B T}\right)}. \tag{2.61b}$$

We can calculate the current density from the difference of the forward and reverse directions,

$$j = \tfrac{1}{2} nqd\left(\Gamma_f - \Gamma_r\right), \tag{2.62a}$$

where n is the concentration of hopping ions. Therefore, by using Eq. (2.61) we can write

$$j = \tfrac{1}{2}\, nqd\nu_0 \exp\left(\frac{\Delta S_m}{k_B}\right) \exp\left(\frac{-\Delta H_m}{k_B T}\right) \left[\exp\left(\frac{qdE}{2k_B T}\right) - \exp\left(\frac{-qdE}{2k_B T}\right)\right]. \tag{2.62b}$$

If, as it is usually the case, the electrostatic term is much lower than the thermal energy of the ion, $qdE << k_B T$, we can use the approximation $e^x - e^{-x} \approx 2x$ for $x << 1$, and get

$$j = \tfrac{1}{2} nqd\nu_0 \exp\left(\frac{\Delta S_m}{k_B}\right) \exp\left(\frac{-\Delta H_m}{k_B T}\right) \frac{qdE}{kT}. \tag{2.63a}$$

$$j = \frac{nq^2 d^2 \Gamma}{2kT} E. \tag{2.63b}$$

The factor 1/2 in our one dimensional model becomes 1/6 for a three dimensional diffusion in a cubic structure.

$$j = \frac{nq^2 d^2 \Gamma}{ZkT} E = \frac{nq^2 d^2 \Gamma}{6kT} E. \tag{2.63c}$$

The factor Z may be different in materials with other structures where ion diffusion is favoured in some particular directions.

The expressions for the electrical conductivity and for the diffusion coefficient in a 3D cubic structure are finally given by

$$\sigma_0 = \frac{nq^2d^2\Gamma}{6kT} = \frac{nq^2D_0}{kT}, \tag{2.64a}$$

$$D_0 = \frac{d^2\Gamma}{6}. \tag{2.64b}$$

Note that this simple random-hopping model for ion diffusion results in the Nernst-Einstein equation introduced above (see Eq. (2.42–2.45)), and it also explains the thermally activated behaviour of the diffusion coefficient in ionic conductors.

Before ending this section, we discuss the case when the electric field that the ions feel is so large that the approximation $qdE << k_BT$ does not hold. At room temperature, for ions with charge $q = \pm e$, and for typical jump distances of a few angstroms, it involves that the electric field must be larger than $\sim 10^8$ V/m which is extremely high. In fact, the opposite condition $qdE >> k_BT$ can sometimes be fulfilled, and Eq. (2.63) can then be approximated by

$$j = \tfrac{1}{2}\, nqd\nu_0 \exp\left(\frac{\Delta S_m}{k_B}\right)\exp\left(\frac{-(\Delta H_m - qdE/2)}{k_BT}\right). \tag{2.65}$$

These large electric fields, of the order of ~10^8 V/m or larger, may easily exist in nanostructured materials (see Chap. 5). If a voltage difference of just a few volts is applied for example to a thin film of an ionic conducting material with a thickness of just a few nanometers, the term $qdE/2$ can be as large as hundreds of millielectron-volts and then, not only it is larger than the thermal energy, but even comparable to ΔH_m in Eq. (2.65). In this case, non-linear ion diffusion occurs, even at low temperatures, since the effective activation energy can be very small under the application of such large electric fields.

2.4 Non-Gaussianity of Dynamics

The intermediate scattering function, $F_s(\mathrm{k},t)$, obtained by neutron scattering and/or molecular dynamics simulations (see Sect. 8.3.3.2) also shows stretched exponential decay and this is known to be a common character of the slow dynamics observed in many glass forming materials. The functional form is closely related to the Non-Gaussianity of the diffusive motion. In this subsection the relationship between non-Debye relaxation and non-Gaussianity of the dynamics in the real space is discussed.

The intermediate scattering function, $F_s(\mathrm{k},t)$ is connected to the self-part of the van Hove function (see Sect. 8.3.3.1) by the Fourier transform [68]

$$F_s(k,t) = \int 4\pi r^2 G_s(\mathbf{r},t)\frac{\sin(\mathbf{k}\bullet\mathbf{r})}{\mathbf{k}\bullet\mathbf{r}}dr. \tag{2.66}$$

When the van Hove function spreads to a distance r_c, the mean squared displacement (MSD) $<r_i(t)^2>$ is represented by

$$<r_i(t)^2>=\int_0^{r_c} r^2 \bullet 4\pi r^2 G_s(r,t)dr \tag{2.67}$$

Therefore, the functional form of the stretched exponential is connected how the mean squared displacement of particle changes with an elapse of time (see Sects. 9.4 and 11.3).

The function $F_s(k,t)$ can be approximated by the following equations [69].

$$F_s(k,t) \approx exp\left[-\frac{k^2}{2d}<r_i{}^2(t)> + \frac{k^4}{2}\left(\frac{r_i{}^2(t)}{2d}\right)^2\alpha_2(t)\right], \tag{2.68}$$

where α_2 is the non-Gaussian parameter and d is the spatial dimension. The value α_2 becomes 0, when the Dynamics has a Gaussian form and therefore, the parameter represent the deviation from the Gaussian form. On the other hand, k^2 dependence of the $F_s(k,t)$ mean the Debye type decay of the function. Therefore, Non-Debye functional form is closely related to the non-Gaussianity of the dynamics in the real space. That is, to examine the origin of the power law dependence found in MSD is equivalent to examine the origin of stretched exponential decay.

Non-Gaussianity of the dynamics is thus observed by using deviation from the Gaussian function of self-part of the van-Hove functions, wave number dependence of $F_s(k,t)$, and non-Gaussian parameters. In the self-part of the van Hove function, obviously the tail part with inverse-power law (with exponential truncation) exists and it means the existence of the longer length scale of the motion, related to the Lévy distribution of wider sense [see A.2.2]. This feature is commonly appeared in ionic systems and in other glass forming materials. Therefore, the motion of particles has the distribution of distances, which is different from the Gaussian dynamics. Thus the non-Gaussianity is also a signature of the cooperative dynamics.

2.4.1 Relation Between Jump Rate and Relaxation Rate in the Stretched Exponential Decay: From the Modeling by the Molecular Dynamics Simulations

It is noteworthy to mention that the time scale of the elementary ion jump motion is not the same as that of the diffusive motion as will be shown in the several characteristic time regions in the mean square displacement (MSD) of ions in glassy ionic conductors (see Sects. 9.4.1, 9.4.4 and 11.3). For example, the first successful jump motion of ion at 700 K of the lithium metasilicate (Li_2SiO_3) system in the glassy state is found at around 10–20 ps region, while the diffusive region starts at around 500 ps. This situation is made clear in this subsection by the result of MD simulations. It also means that the activation energy of each jump motion is different from those for diffusive and/or conduction. Similar discussion also holds for several relaxation functions such as $F_s(k,t)$. Namely, the distribution of jump rates is different from the relaxation rate of the stretched exponential functions. Waiting time distribution assumed in some theories are also observed in the MD simulations of ionic systems, and this distribution partially explain the various events found at the different time scales. However, the difference of time scales is coming from not only by the wide distribution of jump rates but also by the geometrical correlation among successive jumps, where both the back and forward correlated motions of ions contribute.

Frequency dependent behavior of the conductivity [see Sect. 8.3.2.2] can also be connected to the MSD in the real space by the following relation [70, 71]:

$$\sigma^*(\omega) = -\omega^2 \frac{Nq^2}{6H_R kT} \int_0^\infty < r^2(t) > e^{-i\omega t} dt, \tag{2.69}$$

where N is the number density of mobile ions, q the ion charge, k the Boltzmann constant, H_R the Haven ratio and T the temperature.

Each of the variety of ionic motions is not simple as shown in the following examples. In Fig. 2.10, examples of two dimensional projections of trajectories of one Li ion observed by MD for glassy Li_2SiO_3 at 700 K during 500 ps run (This time scale corresponds to the beginning of the diffusive regime ($=t_{\mathrm{dif}}$, see Sect. 9.4.2)) are shown for three cases. In the upper panel, trajectory is projected on XY plane, while in the lower panel, it is projected on YZ plane. Several kinds of jump motions are found in MD of ionic systems including strong localized motion within the neighboring sites and forward correlated jumps which are highly cooperative.

In Fig. 2.11 a three dimensional plot of the same trajectories is shown. The complexity of the motion is clear when you compared it with the simple three dimensional random walk shown in the lower panel. The dense part of the trajectory means that the ion is caged by the surrounding particles for a long time at the so called ion site. This situation is consistent with the existence of clear peaks in the pair correlation functions, $g(r)$ for Li-Li pair. The site represented by the localization of the trajectory shows a variety in size, shape and density, indicating the existence of multifractality. One can see the both long ranged motion and localized motion, and the mixing of them.

During this period, some ions tend to be localized for long times, while some other ions continued many back correlated jumps and a limited number of ions tends to show an accelerated dynamics and such motions are accompanied of cooperative jumps of several ions. Among these different type of motions, contribution of the fast (accelerated) ions to MSD is large, because the displacement is

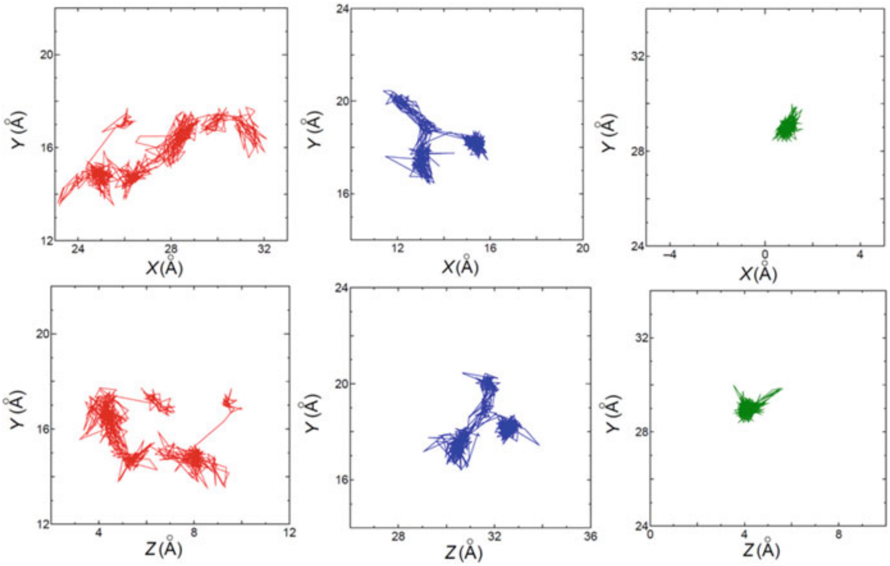

Fig. 2.10 Examples of trajectory of Li^+ ion in Li_2SiO_3 system at 700 K during 500 ps obtained by MD simulations. This time scale corresponds to the beginning of the diffusive regime, t_{dif}. *Upper panel* is for XY projections and *lower panel* is for ZY projections. In the *left panel* (*red curves*), starting position of the motion is (X = 29.8, Y = 17.4, Z = 6.2), while ending position is (X = 26.2, Y = 17.2, Z = 9.3) (in Å). In the *middle panel* (*blue curves*), starting position of the motion is (X = 13.2, Y = 17.0, Z = 30.4), while ending position is (X = 15.4, Y = 18.3, Z = 32.6) (in Å). In the *right panel* (*green curves*) starting position of the motion is (X = 1.1, Y = 28.4, Z = 4.0), while ending position is (X = 1.1, Y = 29.1, Z = 4.2) (in Å). Squared displacement, r_i^2 at the end positions of *left*, *middle*, and *right* examples are, 23.7, 11.0 and 0.5 $Å^2$, respectively. The contribution of accelerated dynamics is large. The dynamics are extremely heterogeneous. Accelerated jumps, localized jumps and long time localization and mixing of such motions are found as discussed in Chaps. 9 and 11. That is, the time scale of the power law dependence of MSD (or stretched exponential decay) is not for a single jump process. Note that the motions are just examples. Note that if the observation time was short, only localized motion might be found

squared in calculation of it. An example of cooperative motions is shown in Fig. 2.12. The ion tends to show further successive jumps.

Similar situation is also found for the system with lower diffusivity. Another example for the motions of Li ions and atoms for a slice of MD cell in lithium disilicate ($Li_2Si_2O_5$) glass at lower temperature of 600 K for longer scale 8 ns runs is shown in Fig. 2.13. Heterogeneous dynamics of Li ions and partial formation of ion channels, which are formed dynamically by cooperative jumps along the networks formed by SiO_4 units, are observed. For the calculation of mean square displacement (MSD), one needs to use many numbers of ions and many initial times to average it [see Sect. 8.5].

Thus ionic motion of ions itself is highly heterogeneous and one needs to consider effect of heterogeneity caused by cooperativity of motions. We will discuss the characteristics of several theories and models here with the aid of MD

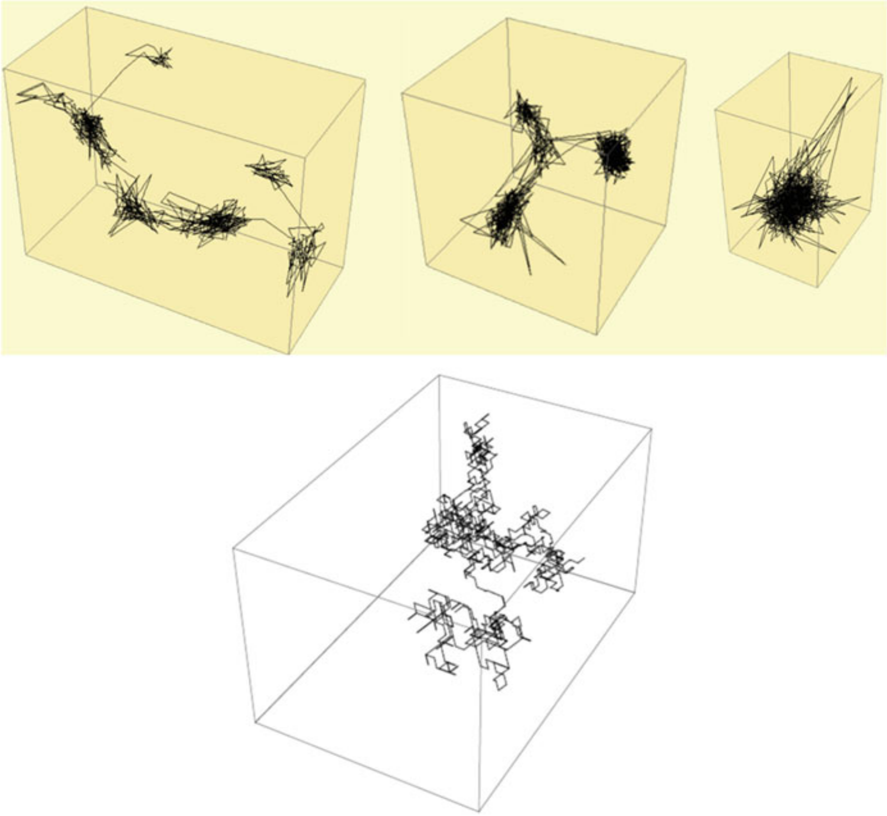

Fig. 2.11 (*Upper panel*) Three dimensional plot of the trajectories of Li ions shown in Fig. 2.10. Ionic motion is a complex one with mixing of strong back correlated motions, waiting time distribution and existence of accelerated motion. (*Lower panel*) Three dimensional plot of an example of 3D random walk (1000 steps). One can see the ionic motion in the glassy state is quite different from the random walk

simulations. These complex behaviors of ions can be well characterized by considering the fractal nature of the motion represented by both temporal (related to the distributions of jump rate or waiting time) and spatial terms (related to the correlation among successive motions and distribution of length scale).

2.4.2 Relation Between Power Law Exponent of MSD and Characteristics of Jump Motions

In this subsection, we consider the cause of power law behavior of MSD based on the characteristics of jump motions. As already shown in Sect. 2.3.4, non-Debye character of the relaxation of the ionic motion are often explained by the temporal

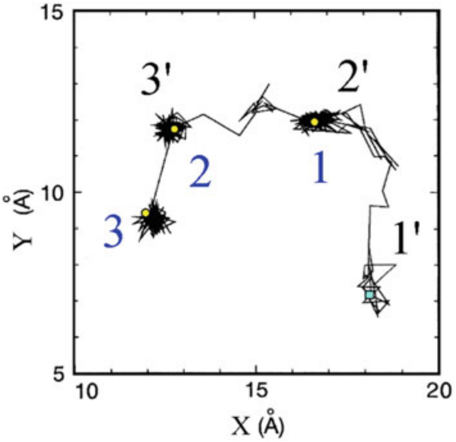

Fig. 2.12 Example of cooperative jumps of Li ions in the Li_2SiO_3 glass at 700 K projected on X-Y plane. Initial positions of three Li ions are 1, 2 and 3 (marked by *yellow circles*), while the last position of the ions after 16 ps run is 1', 2' and 3'. The last position of the first ion is marked by a *pale blue square*. The first ion shows a long jump (~twice of the typical distance among ion sites) without a clear trapping. The second ion is found to be located between two sites for a while, until the vacant site is available. Thus availability of the vacancy is closely related to the cooperative jumps

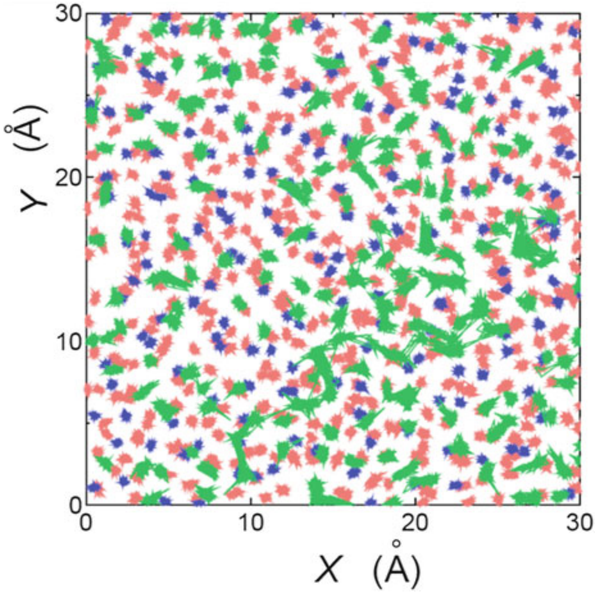

Fig. 2.13 Trajectories of ions and atoms represented for 10 Å in a slice in thickness of MD cell for Lithium disilicate at 600 K, during 8 ns run. *Green*: Li ions, *Blue*: Si atoms, *Red*: O atoms. Motion of Si and O atoms are essentially localized. The dynamics of Li ions is heterogeneous. Formation of a part of the ion channels is observed, while many ions are showing localized motions. In this case, t_{dif} is longer than 15 ns

and/or spatial terms of jump motions and therefore, this is also related to the non-Gaussian character of the diffusive dynamics. In real space, the relation between jump motions and behavior of the MSD is connected by the theory of fractal and/or percolations, and the power law dependence of MSD is argued to be related to the fractal dimension of walks or jumps and their paths contributing to the MSD. Therefore the concept of fractal [72] is useful to consider the relationship between characteristics of jump motions and the functional forms of the MSD. In the following, we discuss the approaches that are related to the characteristics of jump motions in ionic system and related materials. (See Sect. 2.3.4 for related mechanisms suggested for crystals and see also Sect. 9.10 for the comparison of crystal and glass by MD simulations.)

Elliott has discussed [73] the two possible mechanisms of the AC conduction, which corresponds to the power law behavior of MSD (see Sect. 9.4.2) of ions. In the parallel conduction, ion jumps independently with the distribution of the relaxation rate, while in the series conduction, the site causes a relaxation coupled with other sites.

AC hopping conductivity of the one dimensional bond percolation was discussed by Odagaki and Lax [74] based on the distribution of the random interruptions. Odagaki [75] also discussed the stochastic trapping transport assuming the waiting time distribution of jump motions with the use of the generalized coherent medium approximation.

Strong localization in the solid state can be also explained by the fractal dimension of the motion and paths. Alexander and Orbach discussed the vibrational excitation by “fracton” [see Appendix A.2.1 for details], determined by fractal dimension of walks and that of their paths. The mode is discussed as an origin of the “boson peak” [76], which is one of the characteristics commonly found in glasses. On the basis of the relaxation mode theory, Ishii [77] has discussed the hopping on the fractal lattice and found the “fracton” of the hopping version. The approach was expanded to the many particle problem of weak coupling case [78] and the appearance of the both diffusive and non-diffusive mode was discussed.

Bunde et al. [79] have examined the localized excitation on the incipient infinite percolation cluster and discussed the relation to the multifractality.

2.4.3 Relation Between the Theory of Fractal and the Characteristics of Jumps

These theories mentioned in the above explain well some parts of findings by experiments and/or simulations. However, the mechanisms assumed therein are not necessarily the same. Here we introduce some fractal dimensions (exponents) to characterize the dynamics of ions by the fractal nature of the jump motions, where waiting time distribution, distribution of length scale, fractal dimensions of paths and/or their combinations are taken into account. Then we consider how we can distinguish these contributions by MD simulations.

Readers may not be familiar with technical terms such as fractal, fracton, multifractal, Lévy flight and Lévy distribution (and its truncation) used in the following subsections. Details of such terms are explained separately in the Appendix. By using the CDF files included in ESM, the readers also can manipulate the parameters of Lévy distribution and examine the example of the analysis of such motions. [See Sect. 12.2 for the explanation of Example 2 in ESM.]

If one fractal dimension governs the system, the exponent of the power law behavior of the MSD, θ is connected to the fractal dimension of the random walks, d_{w}, as a first approximation [72] by,

$$\left\langle r^2(t)\right\rangle \sim t^{\theta},\ \ \theta = 2/d_w \tag{2.70}$$

For regular diffusion, $d_{\mathrm{w}} = 2$ is expected. However, if the dynamics are beyond random walks, d_{w} does not equal 2. Specifically, if the motions of the ions involve localized motions, the trajectory becomes more complex and the exponent θ becomes smaller. On the contrary, when ion shows forward correlated jumps with the trajectory becoming linear like, this resulted in the decrease of d_{w} and increase of θ. The former situation retards the time scale for the start the diffusive regime, while the latter situation causes an opposite case. The exponent d_{w} of the trajectory of ions can be determined by MD simulations [see Sects. 9.5.4, 11.5.2 and Appendix A.1 for more details] and this can be a direct measure of the power law behavior in MSD of the ionic motion. Although the relation between the complexity of the trajectory and the power law exponent is clear from Eq. (2.70), result of MD simulations reveals that the motion is extremely heterogeneous and not monofractal. In the case of coexistence of fast and slow ions, two length scale regions are found in MD. Therefore, the expansion of the situation to the multifractal walks [80], where two length scales are concerned, is necessary. The large scale motion is found to be caused by cooperative jumps of several ions and successive motions. Therefore, even for the single particle motion, the dynamic heterogeneity affects the exponent connecting different time scale motions. In the collective mode such as conductivity, this relation is further modified by the Haven ratio as shown in Eq. (2.69).

2.4.4 Distribution of Length Scales and Lévy Distribution

Another factor related to the jump motions is concerned with the distribution of the length scales. Lévy distribution and related Lévy flight dynamics is experimentally known to exist in several physical phenomena such as turbulent [81] and Josephson junction [82]. By MD simulation of lithium silicates and in an ionic liquid, we have found that in the power law region of MSD, the dynamics is well represented by the Lévy distribution [83] or Lévy flight [84] (with a Lévy index $\alpha < 2$) related to this distribution, as shown in the inverse-power law tail of the self-part of the van Hove functions. (See Sects. 9.5, 11.2, 11.5.3 and 11.12.2, see also files in ESM and 12.2 for examples of motions and manipulation of parameters of distributions. See also Appendix A.2–A.4)

2.4.5 Heterogeneity and Multifractal Mixing of Different Length Scales

The observed Lévy distribution by MD is accompanied with an exponential truncation and strong back-correlated motion, and occurrence of the infinite variance of the distribution is avoided by these mechanisms. The Lévy distribution combined with the exponential truncation [see Sect. 11.5.3] shows a multifractal character in a long time region. This view is consistent to the existence of multifractal density profile of ions (see Appendix A.3) formed by such motions.

2.4.6 Separation of Exponents Having Different Origins

As observed in the trajectories of Li ions obtained by MD, both temporal (waiting time distribution) and spatial character (distribution of length scale and back and forward correlated motions) contribute to the dynamics. When the exponent α concerned with distribution of length scale and the exponent γ characterizing the waiting time distribution are coexisting, the relevant question is how the dynamics are modified.

Blumen and coworkers [85] considered the situation where the both temporal and spatial terms contribute to the diffusive motion and obtained the following relation.

$$D(t) \sim d\left\langle r^2(t)\right\rangle/dt \sim t^{\alpha\gamma-1}, 0 < \alpha\gamma < 1 \tag{2.71}$$

Similar argument holds for the exponent of the stretched exponential relaxations. They pointed out that the combination of the exponents giving the same behaviors of the stretched exponential (and time dependence of MSD) is infinitive and it is difficult to separate them if it is overlapped in the time region. They also suggested that the separation of temporal and spatial terms might be possible when the long time behavior is governed by the temporal term. However, this condition of the long time might be difficult to fulfill and to judge within the limited time scale of the observation in the case of MD simulations.

Habasaki and coworkers [86] tried to distinguish temporal and spatial contribution of the dynamics using MD simulations (see Sect. 9.5 for more details, where the same analysis was done with better statistics) by another method. That is, MSD is separated into two plots. In the first plot, the accumulated jump numbers is plotted against time and in the second plot, MSD was plotted against the accumulated number of jumps. By this analysis, it was clarified that the cause of the power law dependence of MSD is due to the spatial term (geometrical correlation among successive jumps), although waiting time distribution exists and contribute to the slow dynamics through a mean jump rate. (See Sect. 9.5.5 for different view for the contribution of the temporal and spatial terms and cause of the difference.) Even for the motion of a tracer ion (single particle motion), the geometrical correlation found there is affected one by the cooperative motions of surrounding ions (collective motions).

This kind of analysis is useful to clarify the effect of interactions among ions at the same time. This is because, if there was no interaction with surrounding particles, we can expect only the random single jumps. Of course, direct analysis of cooperative motions is also informative as well as fractal dimension analysis of the trajectories.

The method used to separate the terms is applicable to other systems and will be useful to understand the role of temporal and spatial factors. As shown in the present section, the short time behavior of the system is connected by the exponent (fractal dimension) to the long time behavior. We note that this connection is represented well by the Coupling Model by one of the authors, but is not necessarily clearly included in other theories or models. For further details of heterogeneous dynamics observed by MD, see Chaps. 9–11.

2.5 Models of Ion Dynamics

In the following we present a brief discussion of some of the more relevant theoretical models of ion dynamics. Among all the existing models proposed in the literature we have tried to choose those most highly cited. In Chap. 4 we present a further discussion of the models where we have tried to bring out, when possible, their relations with experimental data as well as the extent of their predictions and applications, in order to emphasize the relevant ideas behind the models and also their possible deficiencies. This is relevant since, as Karl Popper said [87], any theory can claim it is correct by choosing its own list of experiments to verify.

2.5.1 *Random Barrier Model*

As in the simple one dimensional model sketched in Fig. 2.9, other hopping models [88–91] are defined by specifying the allowed transitions and their transition rates for the hopping particles (ions in the case considered here). In order to simplify the models it is usually assumed that the allowed sites for the ions define a regular lattice and that interactions among ions can be neglected, so that it is enough to consider the motion of just one ion. The random barrier model starts by assuming the particles can take positions only on a simple cubic lattice in d dimensions. The basic quantity characterizing such an ensemble of particles is the probability P_s to be at site $\boldsymbol{s}$. If $\Gamma(\boldsymbol{s} \to \boldsymbol{s}')$ is the probability per unit time for jumps from site $\boldsymbol{s}$ to site $\boldsymbol{s}'$, the "equation of motion" is the well known master equation [90, 92]

$$\frac{dP_s}{dt} = \sum_{s'} [\Gamma(\boldsymbol{s}' \to \boldsymbol{s}) P_{s'} - \Gamma(\boldsymbol{s} \to \boldsymbol{s}') P_s]. \tag{2.72}$$

Equation (2.72) determines the equilibrium dynamics, and from equilibrium fluctuations the velocity autocorrelation function may be calculated where v is the projection of the velocity in a fixed direction. This quantity determines the frequency dependence of the diffusion coefficient $D^*(\omega)$ and the electrical conductivity $\sigma^*(\omega)$ (see Eqs. (2.41–2.42)). In the following, for simplicity of the expressions derived from the model, a unit system is chosen so that $\sigma^*(\omega) = D^*(\omega)$ and where moreover both quantities are normalized such that on a lattice with uniform jump frequency Γ one has $\sigma^*(\omega) = D^*(\omega) = \Gamma$ (note that for a uniform jump frequency the conductivity is frequency independent and given by Eq. (2.64)). It is also useful to define a dimensionless frequency-dependent conductivity by $\widetilde{\sigma^*}(\omega) = \sigma^*(\omega)/\sigma(0)$.

The **random barrier model** (RBM) is defined by a special case of Eq. (2.72) where all sites have equal energy [93]. Figure 2.14 illustrates the random energy landscape of this microscopic model in one dimension. Whenever site energies are equal, by the principle of detailed balance (a consequence of time-reversal invariance) the jump rates are symmetric, i.e. $\Gamma(\boldsymbol{s}' \to \boldsymbol{s}) = \Gamma(\boldsymbol{s} \to \boldsymbol{s}')$. This is why the random barrier model is also referred to as symmetric hopping model. It is assumed that, if the energy barrier height is E, the jump rates are given by the attempt frequency times $e^{-\beta E}$ $(\Gamma = \nu_0 e^{-\beta E})$, with $\beta = 1/k_B T$. The model is then completely defined in terms of the energy barrier probability distribution, $p(E)$. In the so called

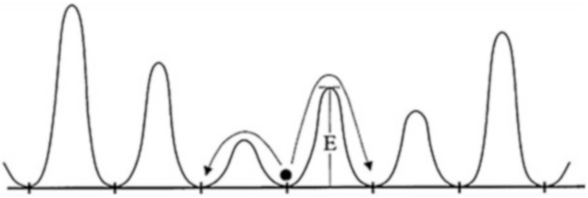

Fig. 2.14 Sketch of a typical potential for a system described by the random barrier model in one dimension. The *arrows* indicate the two possible jumps for the charge carrier shown. At low temperatures most time is spent close to energy minima but, occasionally, a charge carrier by chance acquires enough energy from the surrounding heat bath to jump into a neighboring site. If the barrier height is E, the probability per unit time for a jump is given by $\Gamma = \nu_0 e^{-E/k_B T}$. At low temperatures the charge carrier almost always chooses the lowest barrier. This implies that after one jump the next jump most likely goes back again. Reproduced from [94] with permission

extreme disorder limit, $\beta \rightarrow \infty$, the jump rates vary many orders of magnitude and the random barrier model describes a highly inhomogeneous (heterogeneous) situation.

Because of the broad range of barrier energies that are involved in long range dc transport, a priori one would not expect any particular temperature dependence of the dc conductivity $\sigma_{dc} = \sigma(0)$. However, for strong enough disorder, percolation determines dc conductivity and results in its Arrhenius (thermally activated) temperature dependence [95], which is often observed experimentally. If one considers all the lattice links with barriers below a certain energy, for low energy values, these links form small separated clusters. As the energy value is increased, eventually, for an energy E_c, a fraction of links p_c (the percolation threshold) is reached and an infinite cluster forms, allowing dc conduction. Thus, the activation energy for dc conductivity is the largest barrier on the percolation cluster, E_c, which determines the bottleneck for long range transport and is given by [94].

$$\int_0^{E_c} p(E)dE = p_c. \tag{2.73}$$

The frequency dependence of the ac conductivity can be obtained by solving the master equation in Eq. (2.72) using numerical methods [33]. Figure 2.15 shows computer simulations for different barrier distributions $p(E)$ at large values of the β parameter. These results show that, according to the RBM, the frequency dependence of the ac conductivity is expected to show universal behavior in the extreme disorder limit, i.e. it is independent of the details of the distribution of energy barriers in the material. The best available analytical approximation to this universal ac conductivity response is the diffusion cluster approximation (DCA) [96], which reads

$$ln\tilde{\sigma} = \left(\frac{j\omega}{\tilde{\sigma}}\right)^{d_0/2}, \tag{2.74}$$

where the exponent $d_0 = 1.35$ fits the results from computer simulations of diffusion in three dimensions (see solid line in Fig. 2.15). It is important, however, to note that DCA does not give the same frequency dependence than computer simulations for the imaginary part of the conductivity at low frequencies. Figure 2.15 shows also the prediction of the effective medium approximation (EMA) [33], as given by the expression $ln\tilde{\sigma} = (j\omega/\tilde{\sigma})$, (dashed line), which gives a qualitatively reasonable good fit to computer simulation results, but worse than the diffusion cluster approximation.

The RBM is based on the existence of disorder at a microscopic scale, which seems to be the case for ionic conducting glasses and liquids, although there is no guarantee of whether the disorder is actually relevant for ionic dynamics and conductivity. A macroscopic model has been proposed [33] for systems that are

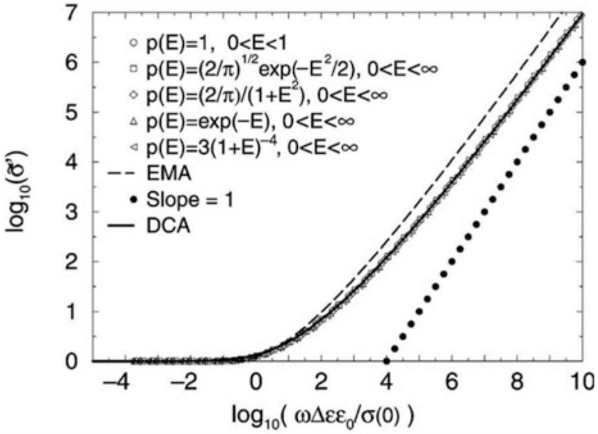

Fig. 2.15 Frequency dependence of the real part of the ac conductivity obtained from computer simulations of the random barrier model for several energy barrier probability distributions at large β, showing ac universality in a scaled frequency representation. The diffusion cluster approximation (DCA) and the effective medium approximation (EMA), *solid and dashed lines* respectively, are also shown. *Dots* mark a line with slope unity, i.e. a linear frequency dependence, as the limiting behaviour at high frequencies. Reproduced from [94] with permission

characterized by disorder only at a macroscopic scale, which might apply for crystalline ionic conductors. In this case, both the diffusion cluster approximation and the effective medium approximation results in the same expression, $ln\tilde{\sigma} = (j\omega/\tilde{\sigma})$, for the frequency dependence of the ac conductivity.

The random barrier model accounts for a universal frequency dependence of the ac conductivity in the extreme disorder limit, but no rigorous proof of this behavior exist. In fact, the RBM scaling function is close to, but rarely identical to those of experiments. Experimental data often show deviations for the claimed ac universality that are not addressed by the model [43, 48]. Even assuming ac universality, there remain also other important problems not able to address by the model: [33, 94]

- In the diffusion cluster approximation, it is necessary to characterize more precisely the diffusion cluster and its dimension, either by independent simulations or by using analytical arguments.
- It is necessary to determine how realistic is the approximation made by linearizing a hopping model with random site energies and Fermi statistics.
- Is ac universality also obtained, at least in some particular cases, by solving the master equation in Eq. (2.72) without assuming the condition of symmetric hopping?
- The RBM does not deal with the well-known mixed alkali-effect, as well as the observed changes in activation energies when changing the concentration of mobile ions in glasses (see Chap. 4 for a description of these experimental facts). The simplest models accounting for these effects are hopping systems with site

exclusion [97], i.e. where there can be at most one ion at each site, but a conclusive picture of the scaling properties of this type of models remains to be established.

- It is important to clarify how the scaling function and time-temperature superposition are affected by including Coulomb interactions in hopping models [98].
- The RBM predicts characteristic length-scales in ionic glasses to be larger than the values of order 1 Å that have been determined from experimental data [99]. It has been proposed that the reason for this discrepancy is that ion diffusion in glasses takes place by a vacancy mechanism [100], but further studies are needed to clarify this issue.

2.5.2 The MIGRATION Concept

The so called MIGRATION concept (MC) [41] is an evolution of the previously developed "Jump Relaxation Model" (JRM) [37] and "Concept of Mismatch and Relaxation" (CMR) [101] by Klaus Funke. The acronym stands for MIsmatch Generated Relaxation for the Accommodation and Transport of IONs. As mentioned in previous section, the dynamics of mobile ions can be expressed in terms of time correlation functions such as the velocity autocorrelation function, $\langle v(0)v(t)\rangle$. Its normalised integral, $W(t)$, which is often called the time-dependent correlation factor, represents the probability for the ion to be (still or again) at its new position after a hop (see Fig. 2.16). Note that, while $W(0)$ is unity by definition, its limiting value at long times, $W(\infty)$, is just the fraction of "successful" hops.

Under the assumption that the cross terms in the velocity correlation function of the hopping ions, $\left\langle \sum_{i,j} v_i(0)v_j(t) \right\rangle$, may be neglected, i.e. $\left\langle \sum_{i,j} v_i(0)v_j(t) \right\rangle = N\langle v(0)v(t)\rangle$, then $\sigma^*_{hop}(\omega)$ becomes proportional to the Fourier transform of the time derivative of $W(t)$ (see Eqs. (2.40–2.43)), denoted by $\dot{W}(t)$. Introducing $W_s(t) = W(t)/W(\infty)$, Eq. (2.40) can be written as [41]

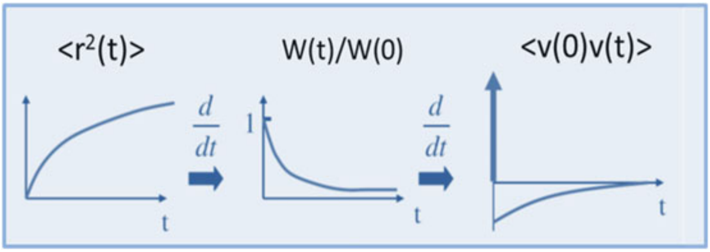

Fig. 2.16 Sketch of the time dependence of the mean square displacement, correlation factor in the MIGRATION concept, and the velocity autocorrelation function of hopping ions, showing the relationships between them. Figure adapted from reference [102]

$$\sigma^{*}_{hop}(\omega)/\sigma(0) = 1 + j\omega\int_{0}^{\infty}[W_s(t) - 1]e^{-j\omega t}dt. \tag{2.75}$$

In the physical picture conveyed by the MIGRATION concept, it is emphasized the mismatch introduced by any hop of an ion, the resulting relaxation (rearrangement) of the neighbourhood and, as a consequence of the relaxation, the accommodation (stabilisation) of the ion at its new position. Once accommodation at the new site is achieved, an elementary step of macroscopic transport is completed by the ion. In this model treatment, a simple set of rules is introduced in order to describe the essence of the ion dynamics in terms of a physical picture of the most relevant elementary processes. The rules are expressed in terms of three coupled rate equations, which form the basis for deriving frequency-dependent model conductivities as well as mean square displacements. The set of rules that constitute the MIGRATION concept are:

$$-\frac{\dot{W}(t)}{W(t)} = -B\dot{g}(t), \tag{2.76}$$

$$-\frac{\dot{g}(t)}{g(t)} = \Gamma_0 W(t)N(t), \tag{2.77}$$

$$N(t) = N(\infty) + [\mathrm{B}g(t)]^{\lambda}, \tag{2.78}$$

In these equations, $g(t)$ represents a normalised mismatch function, taking values $g(0) = 1$ and $g(\infty) = 0$. This mismatch function describes the decay of the (normalised) distance between the (new) position of the "central" ion and the position where its neighbours expect it to be. The mismatch created by the hop of the "central" ion is experienced by an effective number of neighbours, $N(t)$, a function that may depend on time. Γ_0 is the elementary hopping rate, while B and λ are parameters. In Eq. (2.76), the rates of relaxation along the single-particle route, with the ion hopping backwards, and on the many-particle route, with the other ions rearranging, are both proportional to the same driving force, $g(t)$, and hence proportional to each other (see Fig. 2.17). According to Eq. (2.77), the rate of decay of $g(t)$, is proportional to the driving force $g(t)$, to the elementary hopping rate, Γ_0, and to the number function, $N(t)$. It is also proportional to $W(t)$, since the mobile neighbours perform correlated forward–backward jumps in the same fashion as the "central" ion does.

Model conductivity spectra can be obtained from Eqs. (2.76–2.78) and compared with experimental ones [104]. The shape of the conductivity spectra depends on the value of the parameters B and λ, but it is not clear what their physical significance is. Figure 2.18 shows frequency-dependent conductivities of the supercooled glass-forming melt $0.4\mathrm{Ca(NO_3)_2}$–$0.6\mathrm{KNO_3}$ (CKN) at 393 K and 353 K, respectively, above and below the coupled-to-decoupled transition

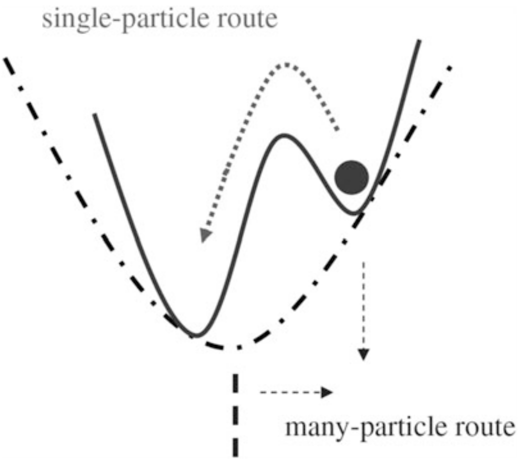

Fig. 2.17 Sketch of the MIGRATION concept. The backward hop of the ion implies the possible relaxation on the single-particle route, while the shift of the caged potential indicates the possible relaxation along the many-particle route. The *solid line* represents the effective potential experienced by the hopping ion. Reproduced from [103] by permission

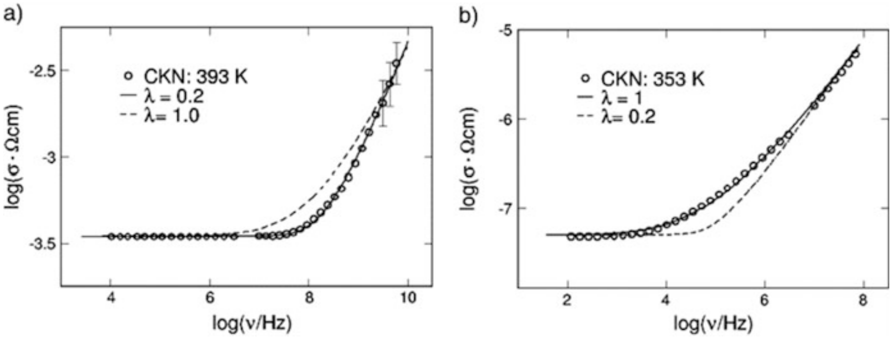

Fig. 2.18 Real part of the conductivity vs frequency of a supercooled melt of CKN (**a**) above and (**b**) below the coupled-to-decoupled transition temperature. In the model curves, the value of the parameter λ is found to change from 0.2 to 1.0. Reproduced from [104] by permission

temperature reported at 378 K [105]. It can be observed that both conductivity isotherms are well reproduced by the equations of the MIGRATION concept, but different values are found for the parameter λ. At the higher temperature, in the fluid melt, a 'successful' displacement of an individual ion only seems to require suitable movements of its immediate neighbours, and hence there is no need to consider any significant time dependence of their number. At the lower temperature, in the viscous melt, a solid-like conduction mechanism seems to prevail. The system is now decoupled, with mobile ions moving from site to site in a comparatively immobile structure. In such a scenario, long-range Coulomb forces between the ions become important, the mismatch of a "central" ion exerting dipole forces on its mobile neighbours, thus inducing their rearrangement by suitable hops and thereby reducing the mismatch [41]. More discussion of the MC and relation to experimental data are given in Chap. 4.

2.5.3 The Coupling Model

The Coupling Model (CM) was proposed in 1979 with the purpose of providing a general theoretical treatment of relaxation and diffusion in systems where the relaxing or diffusing units are interacting with each other, i.e. the many-body problem of irreversible processes in classical statistical mechanics. Exploring the effect that interaction between the relaxing or diffusing units has on the dynamics ranging from microscopic to macroscopic times and the transport coefficients is the objective of the CM. Surprisingly no such theory or model exists at least before 1979 despite the fact that most condensed matter including glass-forming liquids, glasses and ionic conductors are interacting systems, and relaxation and diffusion are the major properties of interest.

The first version of the Coupling Model (CM) [34, 106–108] on relaxation of interacting systems was published in 1979. In retrospect, this model is based on semiclassical quantization of nonlinear Hamiltonian mechanics, i.e. classical chaos [109–113]. The interacting system is semiclassically quantized and the energy levels distribution is described by Wigner's statistical theory [114–116]. This theory of Wigner originated from his idea that the complex Hamiltonians of many-body interacting systems (in the original case considered by Wigner, it is that of heavy atom nuclei such as uranium) could be approximated by a random Hamiltonian representing the probability distribution of individual Hamiltonians for the purpose of finding the energy levels. This idea was then further developed with advances in random matrix theory and statistics [117]. For systems invariant under time reversal, it is given by the Gaussian Orthogonal Ensemble (GOE) in random matrix theory. It makes sense to use GOE because it has been shown to apply to a variety of atomic, molecular, nuclear systems. [113–117] In GOE, the distribution of level spacings E is given by the expression, $p(E/D) = (\pi/2)(E/D)\exp\left[-(\pi/4)(E/D)^2\right]$, and D is the average spacing. In the absence of interactions, the level spacings follow the Poisson distribution, drastic different from the GOE (see Fig. 2.19). GOE has the characteristic linear dependence of $p(E/D) \propto E/D$ which originates from energy level repulsions, and this dependence holds up to a cut-off high energy, E_c. When considering relaxation and diffusion, frequency ω or time t varies over many orders of magnitude, and $\log\omega$ or $\log t$ is the appropriate variable. Since energy E correspond to ω or time $1/t$, we replot $p(E/D)$ vs. $\log(E/D)$ in Fig. 2.20, and put $\log(\omega/\omega_c)$ or $\log(t/t_c)$ under $\log(E/D)$, as label of the abscissa, to indicate the corresponding variables when considering relaxation. Like D, the magnitudes of $\omega_c = E_c/\hbar$, where $\hbar$ is the Planck's

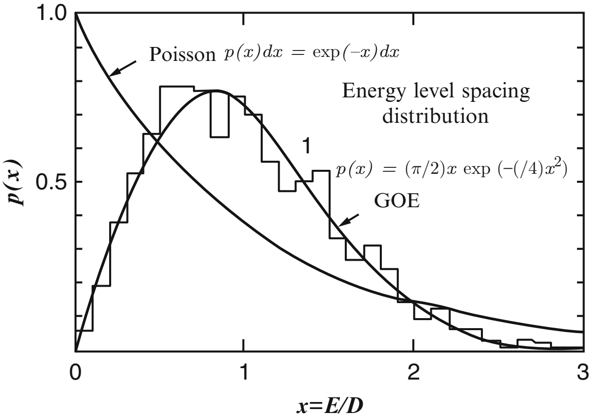

Fig. 2.19 A Wigner distribution fitted to the spacing distribution of 932 s-wave resonances in the interaction $^{238}U + n$ at energies up to 20 keV. The Poisson distribution is shown for contrast

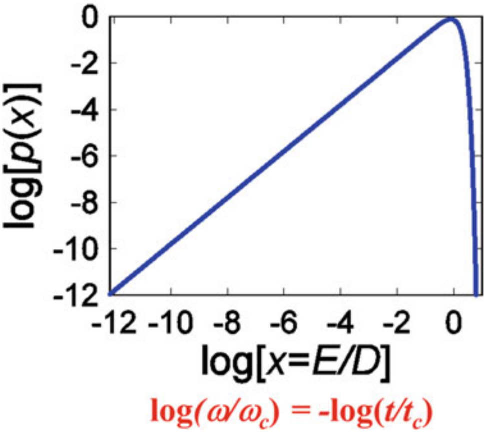

Fig. 2.20 Replotting the GOE in Fig. 2.19 as log vs. log

constant, and t_c depends on the interaction strength determined by the potential of interaction, and it is insensitive to temperature or pressure. Stronger is the interaction strength, larger is D and ω_c and shorter is t_c.

The results given above brings out the physics that interactions has no effect on relaxation and diffusion at frequencies higher than ω_c or at times shorter than t_c. This is because the linear dependence of the level spacing distribution on E no longer holds for $E > E_c$, which corresponds to times shorter than $t_c \equiv (\omega_c)^{-1}$. So, if ion-ion interaction is the cause of the non-exponential time correlation function of many-body conductivity relaxation such as that given by the Kohlrausch function of Eq. (2.49), it is ineffective at times shorter than t_c, and the normalized correlation function is simply the one-body exponential function, $\Phi(t) = \exp(-t/\tau_0)$, of Debye in relaxation and of Einstein in Brownian diffusion.

Therefore, in the CM, at times shorter than $t_c \equiv (\omega_c)^{-1}$ the relaxation is a primitive or one-body (single ion) relaxation with constant rate $W_0 \equiv (\tau_0)^{-1}$, and the correlation function is given by $\exp(-t/\tau_0)$. Due to interactions and the onset of the linear level spacings distribution or correlations between the ions, the many-body relaxation takes over after crossing t_c. It is the response of the GOE energy level structure to the primitive relaxation that is used to account for the many-body relaxation which necessarily slows down its primitive relaxation rate W_0 [106–108]. Calculated by perturbation theory, the response coming from $p(E)$ with the linear dependence on E slows down the relaxation rate W_0 to have the time dependent form of

$$W(t) = W_0(w_c t)^{-n}, \quad t > t_c, \tag{2.79}$$

and the correlation function to have the Kohlrausch form given by Eq. (2.49), for times longer than t_c. The power, n, called the coupling parameter, is a fraction of unity which increases with the strength of interaction. Thus, the relaxation rate of interacting many-body systems is time dependent. It is the primitive relaxation rate, $W(t) = W_0$ for $t < t_c$, and the many-body relaxation rate, $W(t) = W_0(\omega_c t)^{-n}$, when $t > t_c$. This crossover from the primitive to the many-body relaxation rate does not occur necessarily sharply at t_c but rather smoothly in a neighborhood of t_c, so that the correlation function and its derivatives are continuous across t_c. The factor, $\exp\left[-(\pi/4)(E/D)^2\right]$, in $p(E)$ effects the transition between the two rates. Its width parameter D suggests that the width of the neighborhood is of the order of t_c itself, and hence narrow, if there is no other factor like polydispersity of relaxation units entering into the problem. Some of the experimental data to be introduced later show that the crossover is quite sharp. In view of this and in the absence of reliable way to account quantitatively for the narrow crossover, the sharp crossover of the two relaxation rates at t_c is used to generate predictions. The correlation function in Eq. (2.32), $\phi(t)$ obtained from the CM rate equation, $\partial\phi(t)/\partial t = -W(t)\phi(t)$, by integration with $\tau_0 \equiv 1/W_0$ is given by

$$\phi(t) = \exp(-t/\tau_0), \quad t < t_c, \tag{2.80}$$

$$\phi(t) = A \exp\left[-(t/\tau^*)^{1-n}\right], \quad t > t_c, \tag{2.81}$$

and continuity of $\phi(t)$ at t_c leads to the relation,

$$\tau^*(T, P, Q, m, U, \cdots) = \left[(1-n)(t_c)^{-n}\tau_0(T, P, Q, m, U, \cdots)\right]^{\frac{1}{1-n}}, \tag{2.82}$$

and

$$A = \exp\{[n/(1-n)](t_c/\tau_0)\}. \tag{2.83}$$

In Eq. (2.82) the dependences of τ^* and τ_0 on temperature T, pressure P, isotope mass m, neutron scattering vector Q, and any other variable U are written out explicitly to show how the two are related.

When τ_0 is much longer than t_c, $A \rightarrow 1$, and

$$\phi(t) = \exp\left[-(t/\tau^*)^{1-n}\right], \quad t > t_c, \tag{2.84}$$

$$\tau^*(T, P, Q, m, U, \cdots) = [(t_c)^{-n}\tau_0(T, P, Q, m, U, \cdots)]^{\frac{1}{1-n}} \tag{2.85}$$

There is no difference between Eqs. (2.82) and (2.85) when the CM is used merely to predict the relation between the dependence of the many-body relaxation time τ^* with that of the primitive τ_0 on some variable U. For example if τ_0 has Arrhenius T-dependence with activation energy E_a, then both equations predict that the activation energy of τ is given by $E_a/(1-n)$. From the Q^{-2}-dependence of τ_0, Eq. (2.85) predicts that the τ^* has the $Q^{-2/(1-n)}$-dependence. Thus the CM Eq. (2.85) spawns many predictions to compare with experiments. Quantitatively for the relation between τ_0 and τ^*, the two expressions make some difference particularly when n becomes larger. In that case, Eq. (2.82) should be used when τ_0 is not much longer than t_c for the sake of accuracy, as demonstrated in comparing prediction [118] with molecular dynamics simulation data [119] where n has unusually large value. When using the prediction to deduce quantitatively τ_0 from the experimentally observed τ^* with known values of n and t_c, Eqs. (2.82) and (2.85) leads respectively to $\tau_0 = (t_c)^n(\tau^*)^{1-n}/(1-n)$ and

$$\tau_0 = (t_c)^n(\tau^*)^{1-n}. \tag{2.86}$$

The difference between the two expressions for τ_0 is not large, only a factor 2 for $n = 0.5$, and lesser for smaller values of n. For this reason, Eq. (2.86) is often used.

The significance of the CM equation Eqs. (2.82) and (2.85) is that it makes a connection between the many-body relaxation time τ^* usually endowed with anomalous properties and the primitive one-body relaxation time τ_0, the properties of which are normal and known. Thus, the connection provides falsifiable explanations/predictions of the anomalous properties of τ from the known or familiar properties of τ_0. The connection is made via the Kohlrausch exponent n, and the crossover time t_c. These two parameters of the many-body relaxation naturally are ultimately determined by the interaction potential and its strength.

The Eqs. (2.82) and (2.85) coupled with the Kohlrausch function of the CM spawns many predictions that can be tested by experiments and used to explain anomalous properties. Many such tests and applications are given in Chap. 4. Since it was derived for complex Hamiltonians in general, the predictions form these equations should apply to relaxation and diffusion in interacting many-body systems of many kinds, and the dynamics of ionic conductors is only a special case. Thus, ever since the inception of the CM in 1979, the expected existence of universal relaxation and diffusion properties of interacting many-body systems has led to concurrent explorations of several fields using the two coupled equations (2.84) and (2.85) as the tool [18]. It must be borne in mind that these equations hold strictly for systems in which all relaxation/diffusing units are identical and monodisperse, and heterogeneity is not introduced by boundaries, randomness, mixing, and etc. If extrinsic heterogeneity is present, these equations have to be modified by incorporating extraneous factors, and the test of applicability of the CM become less precise and direct, but nevertheless can be done. Moreover, the two coupled equations (2.84) and (2.85) strictly apply to the terminal many-body relaxation leading to steady state transport coefficients. Before reaching the terminal relaxation, the dynamics of ions have passed through several stages. The first stage is the dissipation of ions mutually confined in cages through the interionic potential, manifesting as the nearly constant loss (NCL) in $\varepsilon''(\omega)$ and $\sigma'(\omega)$ (see Chap. 4). The caged ion dynamics has no characteristic time and continues with time indefinitely until the onset of the primitive ion relaxation corresponding to ion hop out of the cage singly or independently, which is the second stage. Thereafter, increasing number of ions cooperatively relax continuously with time (this is the third stage), until the maximum number (or length-scale L) of the heterogeneous ion dynamics is reached. The latter is the terminal or primary many-ions relaxation with time correlation function and relaxation time governed by Eqs. (2.84) and (2.85).

The CM does not provide description of the motion of ions in space at the third and the final stage. Notwithstanding, the CM had anticipated that these processes in interacting many-body systems is dynamically heterogeneous by pointing out [120] the analogy of the CM to the heterogeneous process in the solution of the ‘Dining Philosophers Problem’ in computer science [121], 1 year before the first experimental evidence of dynamic heterogeneity of structural α-relaxation was published [16]. In the CM, dynamic heterogeneity and Kohlrausch non-exponentiality, Eq. (2.84), are regarded as parallel consequences of the cooperative many-body molecular dynamics, but the former is not emphasized in the applications of the CM. Description of the motions as a function of time is best obtained by special experiment techniques like confocal microscopy for colloidal suspensions [17, 122] or by molecular dynamics simulations of ions [123] and especially designed computer simulation method for molecular liquids such as the Dynamic Lattice Liquid Model [124, 125]. Such description is worthwhile as well as pleasing to acquire, but being able to describe motions as a function of time does not necessarily mean that it can explain the anomalous properties of the terminal many-ion relaxation time, τ, while the CM equation can do just that via Eq. (2.85). Ever since it was first derived in 1979, this problem-solving capability of the CM continues to apply in the field of ionic conductivity relaxation and other areas, particularly the dynamics of glass-forming materials and systems [18]. Plenty of examples from ionic conductivity relaxation will be given in Chaps. 4–7.

References

1. L. Landau, E. Lifschitz, *Textbook of Theoretical Physics, Vol. V. Statistical Physics* (Akademie-Verlag, Berlin, 1979).
2. F. Kremer, A. Schönhals (eds.), *Broadband Dielectric Spectroscopy* (Springer, Berlin, 2012), p. 729

3. R. de L. Kronig, J. Opt. Soc. Am. **12**, 547 (1926)
4. H. Kramers, *Atti Del Congr. Internazionale Dei Fis*, 2nd edn. (Bologna Zanichelli, 1927), p. 545
5. C.F. Bohren, Eur. J. Phys. **31**, 573 (2010)
6. J.D. Jackson, *Classical Electrodynamics* (Wiley, New York, 1999)
7. H. Nyquist, Phys. Rev. **32**, 110 (1928)
8. H.B. Callen, T.A. Welton, Phys. Rev. **83**, 34 (1951)
9. G. Williams, J. Fournier, J. Chem. Phys. **104**, 5690 (1996)
10. L. Onsager, Phys. Rev. **37**, 405 (1931)
11. L. Onsager, Phys. Rev. **38**, 2265 (1931)
12. C.J.F. Böttcher, P. Bordewijk, *Theory of Electric Polarization, Vol. II: Dielectrics in Time-Dependent Fields* (Elsevier, Amsterdam/Oxford/New York, 1978)
13. P. Debye, Phys. Z. **13**, 97 (1912)
14. P. Debye, Ber. Deut. Phys. Ges. **55**, 777 (1913)
15. G. Adam, J.H. Gibbs, J. Chem. Phys. **43**, 139 (1965)
16. K. Schmidt-Rohr, H. Spiess, Phys. Rev. Lett. **66**, 3020 (1991)
17. E. Weeks, J. Crocker, A. Levitt, A. Schofield, D. Weitz, Science **287**, 627 (2000)
18. K.L. Ngai, *Relaxation and Diffusion in Complex Systems* (Springer, New York, 2011), p. 835
19. R. Kohlrausch, Ann. Der Phys. Und Chemie **167**, 179 (1854)
20. G. Williams, D.C. Watts, Trans. Faraday Soc. **66**, 80 (1970)
21. G. Williams, D.C. Watts, S.B. Dev, A.M. North, Trans. Faraday Soc. **67**, 1323 (1971)
22. M. Cardona, R.V. Chamberlin, W. Marx, Ann. Phys. **16**, 842 (2007)
23. G. Williams, IEEE Trans. Electr. Insul. **EI-17**, 469 (1982)
24. G. Williams, IEEE Trans. Electr. Insul. **EI-20**, 843 (1985)
25. K. Tsang, K. Ngai, Phys. Rev. E **56**, R17 (1997)
26. K.L. Ngai, J. Habasaki, Y. Hiwatari, C. Leon, J. Phys. Condens. Matter **15**, S1607 (2003)
27. S. Havriliak, S. Negami, J. Polym. Sci. Part C Polym. Symp. **14**, 99 (1966)
28. A. Jonscher, *Dielectric Relaxation in Solids* (Chelsea, London, 1983)
29. K.S. Cole, R.H. Cole, J. Chem. Phys. **9**, 341 (1941)
30. D.W. Davidson, R.H. Cole, J. Chem. Phys. **19**, 1484 (1951)
31. I.M. Hodge, K.L. Ngai, C.T. Moynihan, J. Non-Cryst. Solids **351**, 104 (2005)
32. C. Angell, Annu. Rev. Phys. Chem. **43**, 693 (1992)
33. J. Dyre, T. Schrøder, Rev. Mod. Phys. **72**, 873 (2000)
34. K.L. Ngai, A.K. Jonscher, C.T. White, Nature **277**, 185 (1979)
35. K.L. Ngai, J. Habasaki, C. León, A. Rivera, Z. Phys. Chem. **219**, 47 (2005)
36. C. León, J. Habasaki, K.L. Ngai, Zeitschrift Für Phys. Chemie **223**, 1311 (2009)
37. K. Funke, Prog. Solid State Chem. **22**, 111 (1993)
38. A.K. Jonscher, Nature **267**, 673 (1977)
39. D.P. Almond, A.R. West, R.J. Grant, Solid State Commun. **44**, 1277 (1982)
40. C. Cramer, K. Funke, T. Saatkamp, Philos. Mag. Part B **71**, 701 (1995)
41. K. Funke, Solid State Ionics **169**, 1 (2004)
42. D. Sidebottom, B. Roling, K. Funke, Phys. Rev. B **63**, 024301 (2000)
43. J.C. Dyre, P. Maass, B. Roling, D.L. Sidebottom, Rep. Prog. Phys. **72**, 046501 (2009)
44. D. Sidebottom, Phys. Rev. Lett. **82**, 3653 (1999)
45. C. León, M. Lucia, J. Santamaria, Phys. Rev. B **55**, 882 (1997)
46. C.T. Moynihan, J. Non-Cryst. Solids **172–174**, 1395 (1994)
47. C. Moynihan, Solid State Ionics **105**, 175 (1998)
48. K.L. Ngai, C.T. Moynihan, MRS Bull. **23**, 51 (1998)
49. P.B. Macedo, C.T. Moynihan, R. Bose, Phys. Chem. Glas. **13**, 171 (1972)
50. T.J. Higgins, L.P. Boesch, V. Volterra, C.T. Moynihan, P.B. Macedo, J. Am. Ceram. Soc. **56**, 334 (1973)
51. F.S. Howell, R.A. Bose, P.B. Macedo, C.T. Moynihan, J. Phys. Chem. **78**, 639 (1974)
52. C.T. Moynihan, L.P. Boesch, N.L. Laberge, Phys. Chem. Glas. **14**, 122 (1973)

53. J.R. Macdonald, J. Chem. Phys. **102**, 6241 (1995)
54. B.A. Boukamp, Solid State Ionics **20**, 31 (1986)
55. B. Boukamp, J.R. Macdonald, Solid State Ionics **74**, 85 (1994)
56. C. León, M.L. Lucía, J. Santamaría, Philos. Mag. Part B **75**, 629 (1997)
57. F. Alvarez, A. Alegra, J. Colmenero, Phys. Rev. B **44**, 7306 (1991)
58. K.L. Ngai, J. Chem. Phys. **98**, 6424 (1993)
59. P. Kofstad, T. Norby, *Defects and Transport in Crystalline Solids* (University of Oslo, Oslo, 2007)
60. M.S. Islam, C.A.J. Fisher, Chem. Soc. Rev. **43**, 185 (2014)
61. G. Ceder, MRS Bull. **35**, 693 (2011)
62. L. Malavasi, C.A.J. Fisher, M.S. Islam, Chem. Soc. Rev. **39**, 4370 (2010)
63. Y. Wang, W.D. Richards, S.P. Ong, L.J. Miara, J.C. Kim, Y. Mo, G. Ceder, Nat. Mater. **14**, 1026 (2015)
64. Z. Wojnarowska, M. Paluch, J. Phys. Condens. Matter **27**, 073202 (2015)
65. T. Norby, Mater. Res. Soc. Bull. **34**, 923 (2009)
66. C. Zener, Proc. R. Soc. A Math. Phys. Eng. Sci. **137**, 696 (1932)
67. K. Ngai, Solid State Ionics **105**, 231 (1998)
68. L. Van Hove, Phys. Rev. **95**, 249 (1954)
69. A. Rahman, K.S. Singwi, A. Sjölander, Phys. Rev. **126**, 986 (1962)
70. R. Kubo, J. Phys. Soc. Jpn. **12**, 570 (1957)
71. T. Odagaki, M. Lax, Phys. Rev. B **24**, 5284 (1981)
72. D. Ben-Avraham, S. Havlin, *Diffusion and Reactions in Fractals and Disordered Systems* (Cambridge University Press, Cambridge, 2000), p. 316
73. S. Elliott, Solid State Ionics **27**, 131 (1988)
74. T. Odagaki, M. Lax, Phys. Rev. Lett. **45**, 847 (1980)
75. T. Odagaki, Phys. Rev. B **38**, 9044 (1988)
76. T. Nakayama, Rep. Prog. Phys. **65**, 1195 (2002)
77. T. Ishii, J. Phys. Soc. Jpn. **61**, 924 (1992)
78. T. Ishii, Solid State Ionics **40–41**, 244 (1990)
79. A. Bunde, H. Roman, S. Russ, A. Aharony, A. Harris, Phys. Rev. Lett. **69**, 3189 (1992)
80. E. Bacry, J. Delour, J.F. Muzy, Phys. Rev. E. Stat. Nonlin. Soft Matter Phys. **64**, 026103 (2001)
81. M. Shlesinger, B. West, J. Klafter, Phys. Rev. Lett. **58**, 1100 (1987)
82. T. Geisel, J. Nierwetberg, A. Zacherl, Phys. Rev. Lett. **54**, 616 (1985)
83. J. Habasaki, K.L. Ngai, J. Chem. Phys. **129**, 194501 (2008)
84. J. Habasaki, I. Okada, Y. Hiwatari, Phys. Rev. B **55**, 6309 (1997)
85. A. Blumen, J. Klafter, B.S. White, G. Zumofen, Phys. Rev. Lett. **53**, 1301 (1984)
86. J. Habasaki, I. Okada, Y. Hiwatari, J. Phys. Soc. Jpn. **67**, 2012 (1998)
87. K. Popper, *Conjectures and Refutations: The Growth of Scientific Knowledge* (Routledge Classics, New York, 1963)
88. J.C. Kimball, L.W. Adams, Phys. Rev. B **18**, 5851 (1978)
89. J.C. Dyre, T.B. Schroeder, Phys. Status Solidi **230**, 5 (2002)
90. P.N. Butcher, J. Phys. C Solid State Phys. **7**, 879 (1974)
91. D.L. Stein, C.M. Newman, Phys. Rev. E **51**, 5228 (1995)
92. J.W. Haus, K.W. Kehr, Phys. Rep. **150**, 263 (1987)
93. J.C. Dyre, J. Appl. Phys. **64**, 2456 (1988)
94. T.B. Schrøder, J.C. Dyre, Phys. Chem. Chem. Phys. **4**, 3173 (2002)
95. V. Ambegaokar, B.I. Halperin, J.S. Langer, Phys. Rev. B **4**, 2612 (1971)
96. T. Schrøder, J. Dyre, Phys. Rev. Lett. **84**, 310 (2000)
97. S.D. Baranovskii, H. Cordes, J. Chem. Phys. **111**, 7546 (1999)
98. W. Dieterich, P. Maass, Chem. Phys. **284**, 439 (2002)
99. B. Roling, C. Martiny, K. Funke, J. Non-Cryst. Solids **249**, 201 (1999)
100. J.O. Isard, J. Non-Cryst. Solids **246**, 16 (1999)

101. K. Funke, R.D. Banhatti, S. Brückner, C. Cramer, C. Krieger, A. Mandanici, C. Martiny, I. Ross, Phys. Chem. Chem. Phys. **4**, 3155 (2002)
102. K. Funke, R.D. Banhatti, J. Non-Cryst. Solids **353**, 3845 (2007)
103. K. Funke, R.D. Banhatti, D.M. Laughman, L.G. Badr, M. Mutke, A. Santic, W. Wrobel, E.M. Fellberg, C. Biermann, Zeitschrift Für Phys. Chemie **224**, 1891 (2010)
104. K. Funke, R.D. Banhatti, Solid State Ionics **177**, 1551 (2006)
105. P. Singh, R.D. Banhatti, K. Funke, Phys. Chem. Glas. **46**, 241 (2005)
106. K.L. Ngai, Comment Solid State Phys. **9**, 141 (1980)
107. K.L. Ngai, C.T. White, Phys. Rev. B **20**, 2475 (1979)
108. K.L. Ngai, Comment Solid State Phys. **9**, 127 (1980)
109. M. Gutzwiller, *Chaos in Classical and Quantum Mechanics* (Springer, Berlin, 1990)
110. M.V. Berry, Proc. R. Soc. A Math. Phys. Eng. Sci. **413**, 183 (1987)
111. M. Berry, Phys. Scr. **40**, 335 (1989)
112. O. Bohigas, Chaos Phys. Quantique Chaos Quantum Phys. 87 (1989)
113. O. Bohigas, M.J. Giannoni, C. Schmit, Phys. Rev. Lett. **52**, 1 (1984)
114. E.P. Wigner, *Proceedings of Fourth Canadian Mathematical Congress* (University Toronto Press, Toronto, 1957), p. 174
115. M.L. Mehta, *Random Matrices*, 2nd edn. (Academic, New York, 1991)
116. F.J. Dyson, J. Math. Phys. **3**, 140 (1962)
117. L. Gor'kov, G. Eliashberg, JETP **21**, 940 (1965)
118. K.L. Ngai, S. Capaccioli, J. Phys. Condens. Matter **19**, 205114 (2007)
119. D. Bedrov, G.D. Smith, Macromolecules **39**, 8526 (2006)
120. I.A. Campbell, C. Giovannella (eds.), *Relaxation in Complex Systems and Related Topics* (Springer, Boston, 1990)
121. G. Kolata, Science **223**, 917 (1984)
122. E. Weeks, D. Weitz, Phys. Rev. Lett. **89**, 095704 (2002)
123. J. Habasaki, K.L. Ngai, J. Non-Cryst. Solids **352**, 5170 (2006)
124. T. Pakula, J. Mol. Liq. **86**, 109 (2000)
125. P. Polanowski, T. Pakula, J. Chem. Phys. **117**, 4022 (2002)

Chapter 3
Experimental Probes for Ion Dynamics

Impedance Spectroscopy (IS) is by far the most commonly used technique to investigate experimentally the dynamic response of mobile ions in ionic conductors. Although other techniques, like NMR, light scattering, and neutron scattering, are also used to gain some insights into the ion diffusion process, they are mainly useful to probe high frequency dynamics since their spectral range is much more limited than in the case of IS. Due to its unparalleled broad frequency ν (or time t) range, IS is an ideal tool to study the dynamics of species with electric charge (mobile or bound) in materials [1]. It is based on the interaction of the electric charge of the species inside the sample with an applied electric field, and essentially consists of measuring the magnitude of this interaction and its characteristic frequency or time scale. Nowadays, by combining different experimental techniques, the total frequency range spans from a few nHz ($\tau \sim 1$ year) to above 1 THz ($\tau \sim 10^{-1}$ ps) [2–7]. Thus, we will focus here on the use of IS and pay particular attention to its applications to measurements of the electrical response of ionically conducting materials.

3.1 Impedance Spectroscopy

3.1.1 Description of the Technique

Although Impedance Spectroscopy (IS) is not a new technique, and it has been used to characterize the electrical properties of materials for many years [8–10], significant improvements have been introduced in the last decades mainly due to the advent of microelectronics that had extended and generalized its applications. The most common experimental setup allows determining the impedance of a test sample by the application of a sinusoidal (ac) voltage (current) signal with known amplitude and frequency, and the measured phase shift and amplitude of the

J. Habasaki et al., *Dynamics of Glassy, Crystalline and Liquid Ionic Conductors*,
Topics in Applied Physics 132, DOI 10.1007/978-3-319-42391-3_3

Fig. 3.1 Current response to a sinusoidal voltage excitation in a linear system

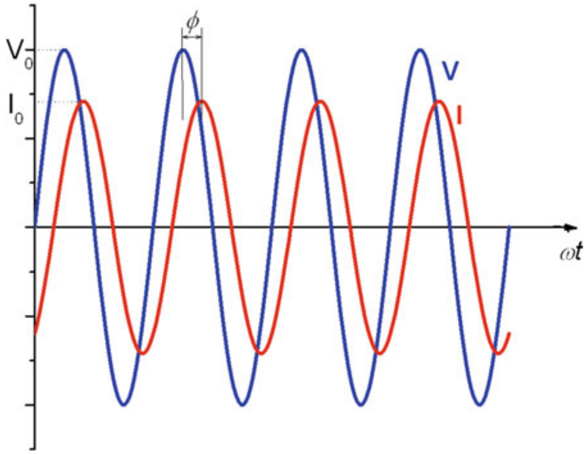

resulting current (voltage). Assuming the response is linear, which we will discuss below in more detail, if a sinusoidal time dependent voltage, $V(t) = V_0 sin\ (\omega t)$, is applied, the current will be a sinusoidal signal with the same frequency but shifted in phase, $I(t) = I_0 sin\ (\omega t - \phi)$ (see Fig. 3.1). The angular frequency ω (measured in rad/s) is related to the frequency f (in Hz) by $\omega = 2\pi f$.

The analysis of the response to a periodic voltage or current excitation is usually very complex in the time domain, requiring in general the solution of differential equations. In the case of sinusoidal excitations, the use of Fourier Transforms of the signals to the frequency domain allows simplifying the problem since the differential equations are converted to simple algebraic equations. By using the relationship, $e^{i\omega t} = cos\ \omega t + i \sin \omega t$, it is possible to express the impedance as a complex function of frequency. The voltage is the real part of the complex function, $V = V_0 e^{i\omega t}$, and similarly, the current is the real part of $I = I_0 e^{i(\omega t - \delta)}$. The impedance is defined as the complex function $Z = \frac{V}{I} = Z_0 e^{i\delta} = Z_0 cos\delta + iZ_0 sin\delta$. It is worthwhile to remark that Fourier transformation only reduces differential equations to simple algebraic equations under conditions of linearity, causality, and stationarity of the system, and therefore impedance is properly defined only for systems satisfying these conditions [9]. We can represent the impedance, $Z = Z' + iZ''$, as a vector in the complex plane (see Fig. 3.2), with rectangular coordinates $Z' = Z_0 cos\delta$ and $Z'' = Z_0 sin\delta$ as its real and imaginary parts. The polar coordinates of the impedance can be expressed as its phase

$$\delta = \tan^{-1}\left(\frac{Z''}{Z'}\right), \tag{3.1a}$$

and its modulus

$$|Z| = Z_0 = \left[\left(Z'\right)^2 + \left(Z''\right)^2\right]^{1/2} \tag{3.1b}$$

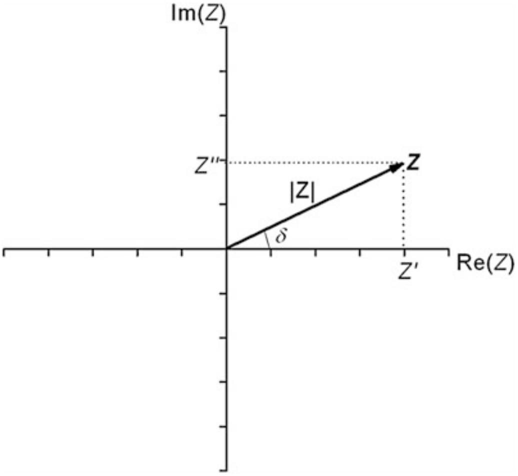

Fig. 3.2 Representation of impedance Z in the complex plane

As shown above, the impedance is in general a function of frequency, $Z = Z(\omega)$, and IS consists of the determination of the frequency dependence of $Z(\omega)$ by measuring its value for different frequencies in a given experimental frequency range. It is from this frequency dependence of the impedance that we would be able to characterize the physical (or chemical) properties of a material or a material-electrode interface. Today, commercial instruments allow varying the frequency of the applied signal in a broad frequency range, typically from 10^{-5} Hz up to 10^{9} Hz, and even lower frequencies (below 10^{-8} Hz) by using time-domain measurements of the electric modulus [3, 11], or higher frequencies (above 10^{12} Hz) by using microwave and infra-red techniques [12, 13]. This experimental frequency range spanning more than 20 decades in frequency allows the characterization of electrical properties of materials for many different applications and also helps understanding the underlying physics behind each particular electrical response [1]. In IS measurements, besides the frequency range, the most important parameters in order to evaluate the performance of an instrument are the impedance (|Z|) range and the phase accuracy or tan(δ). Currently it is possible to cover an impedance range from 10^{-2} to 10^{14} Ω, or even broader, by using just one single instrument, and with an accuracy in the determination of the impedance phase of $\tan(\delta) > 10^{-4}$.

The experimental setup to perform time-domain measurements of the electric modulus is based on polarizing the sample under "constant charge" condition [14], instead of the more common electric polarization under "constant voltage" condition used in the time domain experiments with a lower limiting frequencies of about 10^{-6} Hz [15–17]. On the other hand, network analyzers are used to measure transmission and reflection coefficients in the frequency domain and thus allow determining the impedance of a sample at microwave frequencies above 10^{9} Hz, usually filling a coaxial cable segment or with the sample in contact with the inner and outer conductors of the cable at its end. In the frequency domain, impedance analyzers or LCR meters based on ac auto balancing bridge circuits are commonly used to measure impedance in the range 10 Hz–10^7 Hz. This technique, which is most often used to study the dynamics of mobile ions in ionic conductors, will be discussed below in more detail. For these materials which usually show low frequency dependence, impedance analyzers based on current-voltage (I-V) method can be used. They directly measure the voltage applied to the sample and the current through the sample, and allow extending the low frequency range down to the order of 10^{-3} Hz. Typical impedance analyzers are able to measure an impedance range 10^{-2}–10^8 Ω, and with phase accuracy $\tan(\delta) > 10^{-3}$, which is often enough to measure impedance spectroscopy of ionic conductors without major problems, at least in a temperature range useful for applications.

Although nowadays the instruments are able to generate and apply a sinusoidal signal with almost any frequency value within the available range, measuring the impedance at a few selected frequencies, typically between 5 and 10 logarithmically spaced values per frequency decade, is often enough to obtain the relevant data to characterize the electrical response of the material. The use of logarithmically spaced frequency values allows the determination of the impedance in a broad dynamic range of several decades in a reasonable time. However, impedance measurements at very low frequencies, usually below a value of 10^{-2}–10^{-3} Hz, are very rarely performed since they are time consuming and do not usually result in an additional relevant information. Note that the measurement of the impedance requires at least a full sinusoidal cycle of the applied signal. If, for any reason, one needs to determine the impedance at such low frequencies, it is more convenient to use a different experimental setup to measure in the time domain the transient current in response to the application of a step function in the applied voltage ($V(t) = 0$ for $t < 0$ and $V(t) = V_0$ for $t > 0$) [14, 16, 18]. A Fourier or Laplace Transform algorithm is required to determine the impedance in the frequency domain. While the need to perform the numerical integration might be a disadvantage, the whole impedance spectra is obtained in an amount of time similar than that required for measuring the impedance in the frequency domain just at a single frequency (the lowest frequency). This becomes an increasingly important advantage of the Impedance Spectroscopy (IS) in the time domain when extending the measurements to lower frequency values. On the other hand, extending the impedance measurements at frequencies above a few MHz is also cumbersome, requiring careful calibration and correction procedures to remove any contributions to the impedance arising from cables and measurement cell and not from the sample itself. In the microwave (GHz) frequency range, it is usually necessary to use coaxial lines filled with the material under test as the dielectric between the internal and external conductors. In the case of liquid samples one has to avoid the presence of bubbles and impurities, and it is even more difficult to fill the coaxial line with a solid ceramic sample. It may require sintering the sample after filling the coaxial line, since using a ceramic powder usually result in measuring an impedance dominated by the grain boundary response instead of that from the bulk. In addition, measuring the impedance in the microwave range requires the use of specific instrumentation which is much more uncommon in the research and industrial laboratories worldwide than that used to measure impedance at lower frequencies. For all these reasons, most of the impedance measurements reported in the literature are in the frequency range from about 10 mHz to 1 MHz. This is not a severe limitation since, as discussed below, the impedance spectra usually shifts to lower (higher) frequencies when decreasing (increasing) temperature, following the shifts of the temperature dependent (usually thermally activated) electric responses of the conductor. Thus, one can access experimentally to several dynamical processes contributing to the electrical response of the system not only by increasing the measurement frequency range but also by increasing the experimental temperature range.

Impedance Spectroscopy (IS) allows measuring the complex impedance Z of our sample, as well as any other immittance function such as the complex admittance $Y = Z^{-1}$, or the complex capacitance $C^* = Y/i\omega$, and from them, by using a geometrical factor C_0, one can determine the dielectric permittivity $\varepsilon^* = C^*/C_0$, the complex conductivity $\sigma^* = i\omega\varepsilon^*$, or the electric modulus $M^* = 1/\varepsilon^* = i\omega C_0 Z$, of the material under test. The relations of these equally valid representations of the measured electrical response are discussed in details in Chap. 4. The advantage of some representation in bringing out the characteristic of the ion dynamics can be found in this chapter. Note that since the instrument measures the phase shift and amplitudes ratio between voltage and current sine waves, it is straightforward to obtain the value of any immittance function. Table 3.1 summarizes the relationships between some of these immittance functions that are often used in the analysis and description of experimental data, particularly for the case of ionically conducting materials. The geometrical factor C_0 is known as the capacity of the empty cell, and it is especially easy to determine when measuring a sample in a parallel-plate capacitor geometry. In this case it is obtained that $C_0 = \varepsilon_0\ (A/d)$, with A is the area of the electrodes, d the distance separating the (parallel) electrodes, $(A/d^2) \gg 1$, and $\varepsilon_0 = 8.85 \times 10^{-12}$ Fm^{-1} the dielectric permittivity of a vacuum. To fulfill this parallel-plate capacitor geometry requirement, the sample to be measured is usually shaped as a cylindrical pellet with a thickness as lower as possible (typically $d < 1$ mm) and large top and bottom areas with metal electrodes painted or evaporated on them (typically $A > 10\ \mathrm{mm}^2$).

Table 3.1 Relationships between several immittance functions

	Z	Y	σ^*	ε^*	M^*
$Z =$	–	Y^{-1}	$(C_0\sigma^*)^{-1}$	$(i\omega C_0\varepsilon^*)^{-1}$	$M^*/i\omega C_0$
$Y =$	Z^{-1}	–	$C_0\sigma^*$	$i\omega C_0\varepsilon^*$	$i\omega C_0/M^*$
$\sigma^* =$	Z^{-1}/C_0	Y/C_0	–	$i\omega\varepsilon^*$	$i\omega/M^*$
$\varepsilon^* =$	$Z^{-1}/i\omega C_0$	$Y/i\omega C_0$	$\sigma^*/i\omega$	–	$(M^*)^{-1}$
$M^* =$	$i\omega C_0 Z$	$i\omega C_0/Y$	$i\omega/\sigma^*$	$(\varepsilon^*)^{-1}$	–

C_0 refers to the capacity of the empty cell (see text)

3.1.2 IS Data Analysis

As previously stated, different formalisms are used in the analysis of the electrical response of ionically conducting materials, and there is no consensus from researchers in the field on which is the best one. While those interested mainly in the bulk response of materials for applications as solid electrolytes use the conductivity or the electric modulus formalisms, those studying the electrode-electrolyte interfacial response rather use the impedance representation in the so called Nyquist or Argand plots. Of course, no matter of the formalism chosen to analyze the experimental data, one must know that these are just different representations of the same data. A detailed discussion on the advantages and disadvantages of using different formalisms is given in Chap. 4. Many graphical methods have been proposed for the analysis of impedance or dielectric data [19–22]. Here we will describe briefly the use of the impedance plots to obtain information on the ion diffusion process. We will also describe the use of electric circuits to model the response of ionic conductors measured by the Impedance Spectroscopy techniques.

Since ionic conduction is a thermally activated process, we can think of an ideal ionically conducting material at enough low temperature as an insulator or dielectric material with no dielectric losses. Its response can be represented by a pure capacitor characterized by a real capacitance C, whose value would be proportional to the dielectric permittivity of the material. At higher temperatures, as ionic conduction increases, it eventually becomes measurable. This conduction mechanism can be ideally represented by just an ideal resistor of resistance R. Since the conduction process is independent of the dielectric response, the total electrical response of the material at a given temperature could be represented (see inset to Fig. 3.3) by a parallel combination of these two circuit elements (a resistor R and a capacitor C). The admittance of such a parallel circuit will be given by

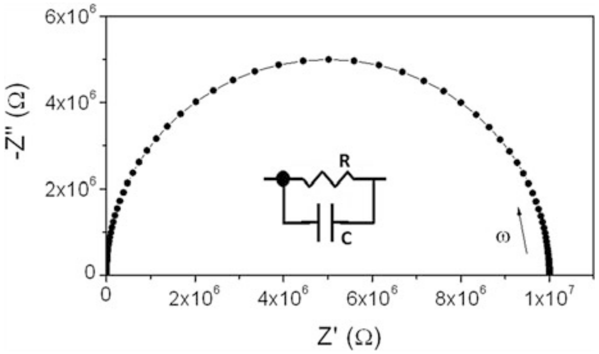

Fig. 3.3 Nyquist plot of the impedance for a parallel RC circuit representing the electrical response of an "ideal" ionic conductor. The values $R = 10$ MΩ and $C = 10$ pF are used in the plot. Each point represents the impedance at a single frequency from 10^{-2} to 10^{6} Hz, increasing frequency from right to left in the plot. Note that the frequency dependence of the impedance gives rise to a semicircle in this representation (see Eq. (3.3) in the text)

$$Y = Y' + iY'' = 1/R + i\omega C, \tag{3.2}$$

and consequently, the impedance by

$$Z = Z' + iZ'' = Y^{-1} = \left(Y' - iY''\right)/\left(Y'\right)^2 + \left(Y''\right)^2, \tag{3.3a}$$

with

$$Z' = (1/R)/\left[(1/R)^2 + (\omega C)^2\right], \tag{3.3b}$$

$$Z'' = (-\omega C)/\left[(1/R)^2 + (\omega C)^2\right]. \tag{3.3c}$$

Impedance is thus a complex quantity with both the real and imaginary parts frequency dependent. If the (negative) imaginary part of the impedance, $-Z''$, is plotted on the Y-axis of a chart against the real part, Z', plotted on the X-axis, we get the so called Nyquist plot, sometimes simply referred as impedance plot (see Fig. 3.3). Note that each point in this plot is the impedance at one frequency. The low frequency data are on the right side of the plot ($Z \rightarrow R$) and high frequency data ($Z \rightarrow 0$) are on the left.

From simple inspection of the experimental impedance spectra of an ideal ionic conductor in the Nyquist plot we can obtain the resistance R from the intersection with the X-axis at low frequencies, and thus obtain the resistivity, and the conductivity σ' of the material if the geometrical factor C_0 is known. As shown in the figure, and easily derived from Eqs. (3.3a–3.3c), the impedance data of an RC circuit are represented in a Nyquist plot by a semicircle, with a maximum value of Z'' at the characteristic frequency $\omega = 1/RC$, when $Z'' = Z' = R/2$. Note that in the time domain, if a step function voltage V_0 is applied to this circuit, the current will decreases exponentially towards a value $I = V_0/R$ at long enough times with a relaxation time $\tau = RC$. The impedance spectra is characterized by an ideal Debye behavior with Z' and Z'' varying with frequency as represented in Fig. 3.4, and characterized by the relaxation time constant $\tau = RC$. Since the dielectric permittivity, and therefore the capacitance C, usually shows weak temperature dependence, the characteristic relaxation time will be thermally activated with the same activation energy as the value of the resistance R, or the activation energy of the ionic conduction process. By increasing temperature, the characteristic relaxation time (frequency) will decrease (increase). Thus, by changing temperature, one can "tune" the characteristic relaxation frequency to be inside the available experimental frequency window, particularly if it is not very broad.

However, the electrical response of a "real" ionically conducting material shows deviations from this ideal Debye behavior. As already discussed in Chap. 2, the electrical conductivity relaxation is usually well described by a Kohlrausch-Williams-Watts (KWW) function in the time domain, giving rise to an apparent power law dependence in the conductivity. This is emphasized by some researchers

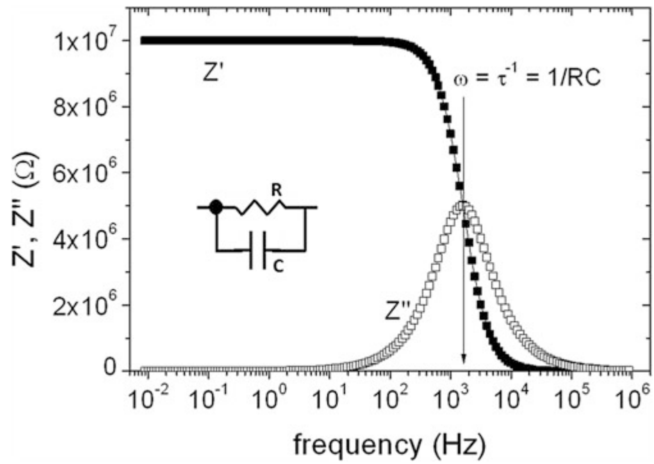

Fig. 3.4 Representation of the frequency dependence of the real and imaginary parts of the impedance Z for a parallel RC circuit representing the electrical response of an "ideal" ionic conductor. The values $R = 10$ MΩ and $C = 10$ pF are used in the plot. The impedance shows an ideal Debye spectra characterized by a relaxation time $\tau = RC$

by calling it the "universal response" in accordance with the Jonscher's expression for the real part of the conductivity, $\sigma'(\omega) = \sigma + A\omega^n$, where n is a fractional exponent [23, 24]. However, Moynihan [25] showed that the Jonscher's expression is unphysical or pathological because its imaginary part [24] rewritten as the real part of $\varepsilon'(\omega)$ is given by $\varepsilon'(\omega) = \varepsilon_\infty + [A/\epsilon_0 \cot(n\pi/2)]\omega^{n-1}$, which diverge at low frequencies rather than level off to a constant value for the bulk material.

Nevertheless, this power law dependence in the conductivity is usually described in electrical circuit models by using a so called universal capacitor (Q) instead of the pure capacitor (C). The circuit element known as universal capacitor is characterized by a complex admittance given by $Y_Q = Q(i\omega)^n$, where n is a fractional exponent. Since both the real and imaginary parts of the admittance Y_Q of a universal capacitor are proportional to ω^n, the phase angle of its admittance, $\theta = \tan^{-1}\left(Y''/Y'\right) = n\pi/2$, is independent of frequency. In fact, the universal capacitor is often referred to as constant-phase element (CPE) in equivalent circuit models. The real part of this admittance Y_Q accounts for the power law frequency dependence of the conductivity at high frequencies that is usually observed experimentally for ionic conductors. The use of this circuit element to fit the experimental data is rather extended in the literature, particularly in Impedance Spectroscopy studies in the electrochemistry field. However, although it may be useful for a phenomenological analysis of the electrical response in ionic conductors, it is worthwhile to note that its validity has been criticized in the past [25–28].

Figure 3.5 shows Nyquist plots at several temperatures of a single crystal yttria stabilized zirconia (YSZ), which is an emblematic oxide-ion conductor. At the lowest temperatures, the Nyquist plots are well described by depressed semicircles, and the experimental data can be reasonably fit to an electrical circuit model

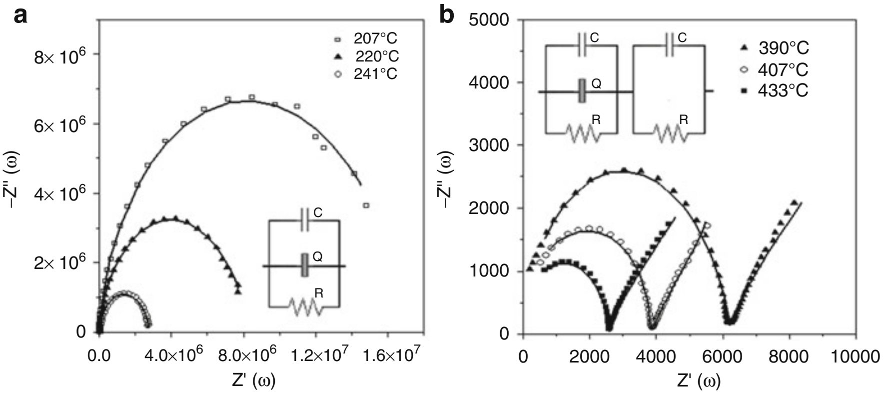

Fig. 3.5 Nyquist plots at several temperatures, and for frequencies ranging between 20 Hz and 1 MHz, for a single crystal yttria stabilized zirconia (YSZ) sample (0.09 Y_2O_3 : 0.91 ZrO_2). (**a**) It can be observed that semicircular arcs appear depressed due to the existence of dispersive, i.e. frequency dependent, conductivity. (**b**) At enough high temperature, an additional arc or semicircle is visible at the lowest frequencies due to the onset of ion blocking effects at the sample-electrode interface. *Solid lines* in both figures are fits of the experimental data to the electrical circuit models shown as insets in each case

including a universal capacitor *Q* in parallel with a resistor *R* and a capacitor *C* (see inset to Fig. 3.5a). On the other hand, Fig. 3.5b shows that at higher temperatures, the presence of an additional semicircle becomes evident at low frequency (right side). This is due to the onset of ion blocking effects at the sample-electrode interface. At sufficiently low frequencies (i.e. long times) the diffusing (oxygen) ions under the applied electric field eventually arrive at the sample-electrode interface and accumulate there if the electrode is not as good ion conductor as the bulk sample, which is usually the case for silver, gold or platinum electrodes that are often used in Impedance Spectroscopy experiments with ionic conductors. The blocking of ions at the electrodes leads to a decrease of the electric field inside the sample and thus to an apparent decrease of the bulk conductivity.

The total electrical response can be modeled by including an additional *RC* circuit in series with the bulk response, to account for the electrode effects, as shown in the inset to Fig. 3.5b. However, note that the bulk resistance, and therefore the bulk ionic conductivity, can be obtained from the intersection of the bulk semicircle with the X-axis at the right side. Sometimes the semicircle due to the bulk response is not well defined at low frequencies due to the presence of the additional semicircle arising from blocking effects, and then it is not possible to obtain a bulk resistance value from the extrapolation towards the real axis in the Nyquist plot. Then it is useful to fit the experimental data to electric circuit models to determine the physical quantities like the bulk resistance or capacitance. Solid lines in the plots of Fig. 3.5 are fits of the experimental data to the electrical circuit models shown as insets in each case. There are different software programs to perform these fits by means of complex non-linear least-squares (CNLS) fitting algorithms, like ZVIEW® from Scribner Associates, LEVM developed by J. Ross

Macdonald, or EQIVCT developed by Bernard Boukamp [29–33]. Again, although the use of fitting software may be useful in a particular case, it is often found that several different circuit models can be used to describe the experimental data, and it is not always straightforward to assign a physical meaning to the circuit elements in the model used. It is then important to use the least possible number of parameters in the fits and a model with a clear physical meaning in order to interpret the fit results to the experimental data.

In the case of polycrystalline samples of ionically conducting materials, ion blocking effects at the grain boundaries contribute also to the electrical response and therefore these effects are evident in the experimental data from the corresponding impedance plots. Grain boundaries usually act as blocking interfaces for the transport of ions between the different grains (or bulk) regions in the sample, giving rise to charge accumulation as in the case of electrodes and consequently to an apparent decrease of the conductivity when decreasing the frequency (increasing the diffusing time for the ions), as the accumulated ions at the boundary create an electric field within the grains with opposite direction to that of the applied electric field. Thus, the impedance associated to the grain boundaries can be thought as "in series", in terms of an electrical circuit model, to the bulk response, and results in an additional semicircle in the Nyquist plot, between the bulk semicircle at higher frequencies and the electrode arc or spike at lower frequencies (see Figs. 3.6 and 3.7). Figure 3.6 shows complex impedance (Nyquist) plots of Z'' vs Z' at

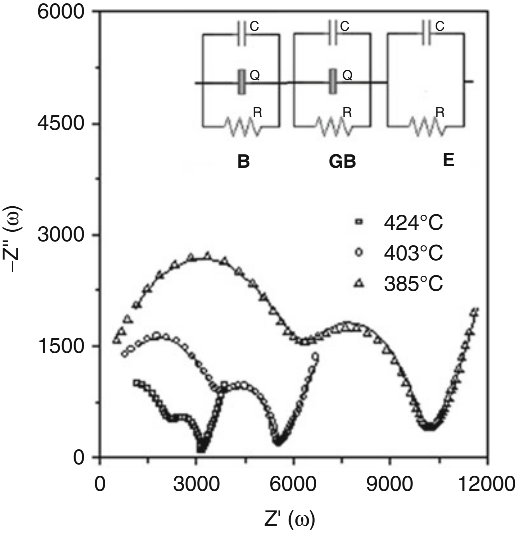

Fig. 3.6 Nyquist plots at several temperatures, and for frequencies ranging between 20 Hz and 1 MHz, for a polycrystalline ceramic yttria stabilized zirconia (YSZ) sample (0.09 Y_2O_3: 0.91 ZrO_2). At each temperature, the presence of an additional semicircle is evident at intermediate frequencies, which is related to the electrical response of the grain boundaries (GB), between the bulk (B) response at high frequencies (*left*) and the electrode (E) response at lower frequencies (*right*). *Solid lines* in the figure are fits of the experimental data to the electrical circuit model shown as an inset

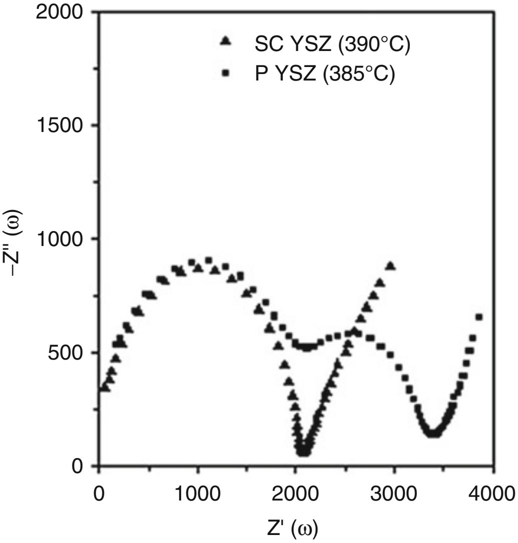

Fig. 3.7 Nyquist plots for single crystal and polycrystalline ceramic YSZ samples (0.09 Y_2O_3: 0.91 ZrO_2) measured at a similar temperature. The comparison evidences the presence of an additional semicircle at intermediate frequencies due to the electrical response of the grain boundary. For a better comparison, experimental data have been normalized to account for the different geometrical factors of each sample

several temperatures where the electrical response of the bulk, grain boundary and electrodes can be separated due to their different relaxation times and are observed at the highest, intermediate and lowest frequencies respectively (from left to right in the plots). In order to obtain the dc bulk (R_b) and grain boundary (R_{gb}) resistances at each temperature, it is possible to fit the experimental impedance data to an equivalent circuit where bulk, grain boundary, and electrode contributions to the total impedance Z^* are in series:

$$Z^* = Z_b^* + Z_{gb}^* + Z_e^*. \tag{3.4}$$

Each separate contribution ($i = b$ for bulk, $i = gb$ for grain boundary, and $i = e$ for electrode) can be modelled using a complex equivalent circuit component based on a parallel resistor-capacitor-universal capacitor combination [9, 10]:

$$\frac{1}{Z_i^*} = \frac{1}{R_i} + Q_i(i\omega)^{n_i} + i\omega C_i. \tag{3.5}$$

The results from the fits to Eqs. (3.4) and (3.5) are shown as solid lines in Fig. 3.6. The equivalent electrical circuit model is shown as an inset in the same figure. Note that the data at the lowest frequencies, affected by electrode blocking effects, do not show a full semicircle but an arc or spike, and therefore a parallel RC circuit is usually enough to fit the electrode response and Q_e is taken as zero.

Although one is mainly interested in determining the bulk ionic conductivity values of a material, the presence of grain boundaries may be unavoidable when using the material in a practical device, and therefore it is the total dc conductivity which is relevant in that case. The total dc conductivity is obtained as the inverse of the total resistivity, which is the sum of the bulk resistivity and the grain boundary resistivity. It can be determined by using fitting software to electrical circuits or directly from inspection of the Nyquist plots, from the value of the real part of the impedance at the intersection of the grain boundary semicircle with the X-axis at the right side.

From a structural point of view, a grain boundary is a crystallographic mismatch zone in the material with a high density of defects, what gives rise to an increase of the free energy compared to the bulk region. It has been shown that impurity atoms are preferentially accommodated at grain boundaries in ordered defect structures in order to reduce its free energy [34, 35], leading to profound changes in electrical properties [36, 37]. In the case of ionic conductors there is a large compositional flexibility due to a high density of mobile ions, which offers additional degrees of freedom to reduce the free energy of the grain boundary through the stabilization of correlated composition changes in its neighbourhood. The interplay between elastic (strain) and chemical free energies gives rise to a redistribution of atoms at the grain boundary, and this may result in the formation of a space charge region to restore electrochemical equilibrium [37, 38]. The nature of the space charge depends on the formation free energies of point defects and the effective charge of the dopants and/or impurities that accumulate in the space charge region [39].

It is well established that the accumulation of defects and impurities at the grain boundaries gives rise to a barrier for ionic diffusion through the material, and the ionic transport across the grain boundaries takes place through the grain-to-grain contacts, while the impurity phase at the grain-boundary results in a blocking effect by decreasing the width of the ion conduction path. It has been also proposed that the formation of a space charge layer adjacent to the grain boundary core would also result in a barrier for charge transport as in the case of Mott-Schottky junctions in semiconductors [40]. The contribution of a space-charge layer to the electrical properties of the grain boundary can be described by assuming a conduction mechanism similar to that of the bulk but introducing an effective charge carrier (mobile ions) concentration and an effective width for the space-charge layer [41]. Guo and Maier have proposed a Schottky barrier model to explain the ion transport across grain boundaries in acceptor-doped ZrO_2 and CeO_2 [42, 43]. As discussed in details in Chap. 6, Frechero et al. [44] have shown that this might not always be the case.

A usual model to describe the electrical response of polycrystalline ionic conductors is the brick layer model (BLM) proposed by Van Dijk and Burggraaf [45]. It is assumed in this model that ceramic samples consist of grains with a high conductivity, separated by relatively thin, uniform grain boundaries (see Fig. 3.8). The grain boundary consists of a homogeneous layer and the conduction along the grain boundaries is negligible. The BLM model assumes that the permittivity value at the grain boundary is similar to the bulk one, $\varepsilon_{gb} = \varepsilon_b$, a reasonable

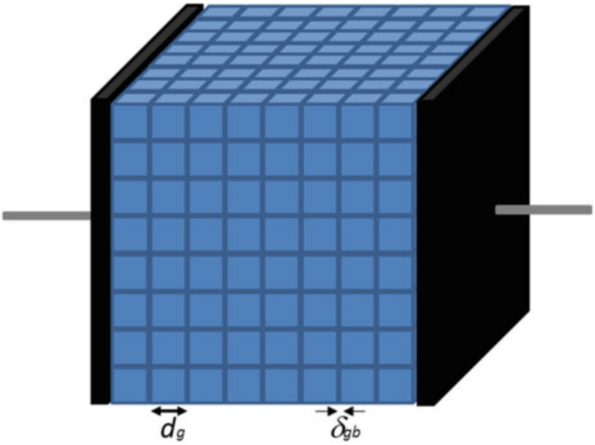

Fig. 3.8 Brick Layer Model representation of a polycrystalline sample with an average grain size d_g and an average thickness of the grain boundary δ_{gb}

approximation since in most ionic conductors the dielectric constant does not change significantly with the concentration of mobile ions. Assuming cubic grains of the same size d_g, the average grain-boundary thickness δ_{gb} can be estimated from the brick layer model in terms of the ratio of bulk and grain boundary capacitances, $\delta_{gb} = C_b/C_{gb}d_g$. The BLM approximates the thickness of the SCL in polycrystalline ceramics to half the width of the grain boundary region since it is shared by the two neighbouring grains at the boundary [40], and thus the thickness of the space charge layer $\lambda*$ is estimated as $\lambda^* \approx \delta_{gb}/2$. A value for the specific grain boundary conductivity can be also estimated by $\sigma_{sgb} = \sigma_{gb}$ $(\delta_{gb}/d_g) = \sigma_{gb}$ (C_b/C_{gb}) from the measured bulk and grain boundary capacitance and conductivity values.

3.1.3 Experimental Considerations

As in any other experimental technique, a relevant issue in Impedance Spectroscopy measurements is to check that the experimental data obtained are valid, consistent, and free of experimental artifacts. One possibility is the use of CNLS fitting of impedance data to a linear response or circuit model. If a model is found that describes appropriately and simultaneously the experimental data for the real and imaginary parts of the impedance, one can be reasonably sure of the validity of the data. However, when dealing with experimental data a suitable model is not always known, i.e., no analytical expressions nor equivalent electrical circuits can be used to obtain a good description of the complex impedance data. In this case, an alternative method is the use of Kramers-Kronig (KK) transforms [24, 46–49]. Real and imaginary components of any susceptibility function $\chi^*(\omega)$ are related by the following expressions:

$$\chi'(\omega) = \frac{2}{\pi}\int_0^\infty \frac{x\chi''(x)}{x^2-\omega^2}dx \tag{3.6a}$$

$$\chi''(\omega) = -\frac{2}{\pi}\int_0^\infty \frac{\omega\chi'(x)}{x^2-\omega^2}dx \tag{3.6b}$$

which are known as the Kramers–Kronig relations, and that allows to obtain the imaginary part of the susceptibility from the frequency dependence of the real part, and vice versa. It is important to note that the Kramers–Kronig relations are derived as a pure mathematical result, provided the following four general requirements are fulfilled: (1) causality: the response of the system must be only due to the applied perturbation; (2) linearity: the response of the system must be described by a set of linear differential laws, and consequently independent of the magnitude of the perturbation; (3) stability: system must return to its original state after the perturbation is removed; and (4) continuity: susceptibility must be continuous and finite valued for all frequencies and finite valued at the limits $\omega \to 0$ and $\omega \to \infty$.

If the experimental data are correct, they must obey the K-K relations. One can use for example the dielectric susceptibility $\chi^*(\omega) = (\varepsilon^*(\omega) - \varepsilon_0)/\varepsilon_0$ in order to perform the test. Expressions for the KK relations involving other immittance functions can be also used [9, 24, 50, 51]. Therefore, by comparing the real part of the susceptibility spectrum with the transform of the imaginary part by using Eq. (3.6a), and vice versa by using Eq. (3.6b), the validity and consistency of the experimental data can be checked. If there is any discrepancy between the actual and transformed values (within the range of experimental error) then the data must be considered invalid and affected by experimental artifacts that need to be solved [51]. Note also that numerical integration of any of the KK relations requires the knowledge of the susceptibility function in the whole frequency spectrum but the measured data are obtained as a discrete and finite set. This problem is however approximately solved by using appropriate algorithms [29, 51, 52].

In order to avoid experimental artifacts affecting the Impedance Spectroscopy measurement, as well as to improve the accuracy of the measurements, it is important to take into account two main issues. First, the instrument must be correctly calibrated. It is important to perform regularly a calibration of the instrument according to the manufacturer's procedures. It is also convenient to check if the calibration is correct before measuring each sample. Moreover, any contribution to the measured impedance not due to the sample but to the cables used, the sample holder or measurement cell should be considered and removed. How to deal with this second issue is described in more detail in the following paragraphs.

As it was previously described in this chapter, determining the impedance of a sample requires applying a known current (voltage) signal through the sample and an independent voltage (current) measurement. Commercial impedance analyzers usually have the possibility to use four different connections to the sample cell: the

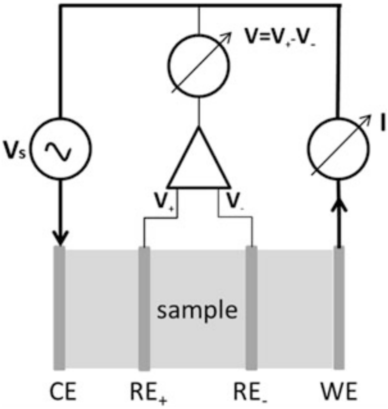

Fig. 3.9 Sketch of the set-up of a 4-terminal configuration for impedance measurements of materials. The four electrodes are the counter electrode (CE) to inject the current to the sample, the working electrode (WE) to measure the current through the sample, and the two reference electrodes (RE) to measure the voltage difference between them

counter electrode to provide current to the sample and the working electrode to determine the current through the sample; and two reference electrodes to measure voltage. It is possible then to use 2, 3 or 4-terminal configuration tests of the impedance of the sample cell [9, 10]. In the case of samples of ionic conductors used as electrolytes, their impedance is usually much higher than that of the cables used for the measurement, at least at low frequencies, and it is possible then to use 2-terminal test connections to the sample without introducing significant errors to the measurement due to not considering the (small) voltage drops in the cables. The 4-terminal configuration, with separate contacts for the reference electrodes to the sample cell, avoids these problems, and must be used to measure the impedance of batteries and fuel cell devices since they have low impedance values (see Fig. 3.9). By using the 4-terminal configuration the voltage drop measured between the reference electrodes is not influenced by any voltage drop in the counter electrode or working electrode connections due to bad electrode-sample contacts. If the differential voltage between the references electrodes is measured by an instrument with high (ideally infinite) input impedance, a negligible current will flow through the voltage electrodes and the current through the sample will be that measured at the working electrode. Due to the almost zero current, the voltage drop due to the contacts or cables used will be also negligible in the measured voltage.

The 3-terminal configuration can be used to determine the impedance of the electrode/electrolyte interface (see Fig. 3.10). The counter electrode provides current to the cell, the working electrode allows measuring this current, and a reference electrode close to the working electrode measures the voltage drop due to any electrochemical activity or to the accumulation of ions (double layer capacity) at the working electrode interface. While this configuration is useful to characterize the electrode/electrolyte interface and thus the performance of

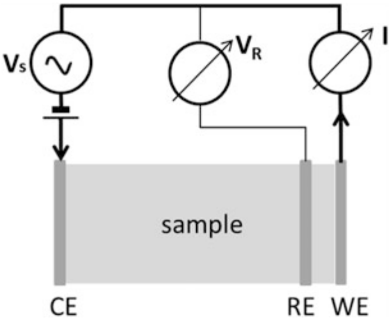

Fig. 3.10 Sketch of the set-up of a 3-terminal configuration for impedance measurements of electrochemical cells. The three electrodes are the counter electrode (CE) to inject the current to the sample, the working electrode (WE) to measure the current through the sample, and the reference electrode (RE) placed close to the working electrode for the voltage measurement

different materials used as electrodes in batteries, fuel cells or other electrochemical devices, the 2- or 4-terminal configurations are used to characterize ionically conducting materials as electrolytes by impedance spectroscopy techniques. In this case, electrodes are just used to provide good electrical contact to the material, and inert metals must be used not only for the counter electrode but also for the working electrode, in order to prevent chemical reactions at the electrode/electrolyte interfaces that would affect the impedance measurement. It is important also to have an inert gas environment in this case, usually achieved by a nitrogen gas flow that helps also in thermal stabilization of the sample. Inert electrodes are usually made by depositing a thin layer of platinum, gold, or even silver by sputtering or thermal evaporation. Platinum and silver paints are also much often used as electrodes for impedance spectroscopy of ionic conductors. It is worthwhile to remark here that platinum and gold electrodes are generally preferred since silver electrodes might result in non-negligible electrochemical activity and even silver ion diffusion for some ionic conductors, especially at elevated temperatures [10].

When using the 2-terminal or even the 4-terminal configurations for an impedance spectroscopy measurement, there might be important contributions to the measured impedance arising from undesired voltage drops or leakage currents due to the series or shunt resistances, residual inductance and stray capacitance arising from the test cables and the sample holder used. All these parasitics or spurious contributions can be largely eliminated from the measured experimental data by performing the so called "open-short" correction to the data. Most commercial instruments allow performing automatically this correction to the experimental data. The "open" correction helps to eliminate the stray admittance in "parallel" due to the sample holder and connections. It is especially important when measuring samples with high impedance values. It requires the measurement of the impedance spectra in an open circuit condition, that is, without the sample connected to the instrument but otherwise using the same cables and sample holder configuration that will be used to measure the impedance spectra of the sample. In this way, the leakage currents are determined as a function of frequency, and they can be subtracted afterwards from the measured current with the sample connected. The “short” correction helps to eliminate the residual “series” impedance due to the cables and connections to the sample. It is on the contrary especially relevant when measuring samples with low values of impedance. It requires the measurement of the impedance spectra in a short circuit condition, that is electrically connecting the test leads that will be used later to contact the sample, and also using the same cables and sample holder that will be used to measure the impedance spectra of the sample. In this way, the voltage drops arising from other sources different from the sample are obtained as a function of frequency, and they can be subtracted afterwards from the measured voltage with the sample connected. The open-short correction consists of applying both corrections to the measured data, and largely improves the accuracy in the determination of the true impedance spectra of a given sample. The open and short measurements should be performed immediately before connecting the sample to the test leads for its measurement. Most commercial instruments allow performing an additional “load” correction that consists of measuring the impedance spectra of a calibrated reference sample with known impedance (and whose value is similar to that of the sample). This allows referencing the impedance measurements to a standard. However, since ionic diffusion is a thermally activated process, impedance values change by orders of magnitude when changing temperature for samples of ionically conducting materials, and the load correction is not very useful in this case. Note that open, short and load impedance spectra measurements should be ideally performed by using the same frequency values that will be used later for the impedance spectra measurement of the sample. Otherwise, the instrument will interpolate and extrapolate the measured data for the impedance at open, short and load conditions in order to calculate the values of the impedance for each of these conditions at the corresponding frequencies used in the measurement of the sample, which might introduce errors in the correction procedure if the impedance in open, short or load conditions is not a smooth function of frequency or the spectra has been measured in a narrower frequency range than that used for the measurement of the sample. One should consider also that parasitics to the measured impedance are not completely removed by performing the open-short correction, since additional contributions arise just by connecting the sample. In order to minimize these additional undesired effects on the measurements, such as fringing and stray capacitance, it is important to consider the design of the sample holder, with a guarding electrode and shielded cables as close to the sample as possible, and a Faraday cage to prevent interferences in the measured signal from the outside [9].

Another relevant issue to consider in an IS measurement is the amplitude of the input signal. Although the electrical response of ionically conducting materials is usually linear, this is not true for the case of the interface between the sample and electrodes, or even for the response of the grain boundaries, which are “in series” with the bulk response. For nonlinear systems like most real “electrode/ionic conductor” systems, IS measurements are useful and meaningful only for small-signal stimuli of magnitude such that the overall electrode–material system to ensure that the overall response is electrically linear. Therefore, it is important to check for the linearity of the total response of our system before performing an IS experiment. This requires that the response to the sum of two given signals applied simultaneously be the sum of the responses of the signals applied separately. A consequence of this requirement is that if a monochromatic input signal is applied, it results in negligible generation of harmonics in the output signal. In practice, linearity can be assessed by checking that there is no significant changes in the immittance spectra by increasing the magnitude of the applied input voltage (or current) signal. It can be shown that as far as the amplitude of the applied voltage is less than the thermal voltage $V_{th} = kT/e$, with k the Boltzmann's constant, T the absolute temperature, and e the magnitude of the electron charge (V_{th} is about 25 mV at 20 °C), the differential equations describing the response of the system become linear to an excellent approximation [9]. However, in order to increase the signal-to-noise ratio and thus the accuracy in the measurement of the impedance data, it is desirable to apply an input signal with amplitude as large as possible. A good practice is to start the impedance spectroscopy measurement of a given sample by taking several impedance spectra at a limited set of frequencies, at room temperature (or at a different temperature in the temperature range of interest), but at different, increasing, amplitudes of the input voltage (or current) until any change in the spectra can be detected due to the onset of nonlinear effects in the measurement. In this way it is possible then to use a large enough amplitude value for the input signal but keeping the linear response of the system.

3.2 Nuclear Magnetic Resonance

Nuclear Magnetic Resonance (NMR) is another powerful, reliable, and widely used technique to study ion diffusion dynamics in ionic conductors. Since the pioneering work by Bloembergen, Purcell and Pound (BPP) [53], it is well established that ion motion in a material has a significant influence on its measured NMR properties, and consequently NMR becomes an experimental tool in order to study the dynamics of mobile ions in these materials [54–57]. An important difference between NMR and Impedance Spectroscopy techniques is that while IS measures a macroscopic electrical response due to mobile ions, NMR is a local probe that allows studying the microscopic dynamics of mobile ions. The use of NMR spectroscopy to study ion mobility in ionic conductors is based on the existence of a non-zero spin of the nuclei of the mobile ions. Almost every element in the periodic table has an isotope with a non-zero nuclear spin, but NMR requires that the natural abundance of these isotopes is high enough to be detected. When a group of spins is placed in a static magnetic field, each spin aligns in one of the two possible orientations. According to Boltzmann statistics, the number of spins in the lower energy level, N^+, is related to the number in the upper level, N^-, by a simple ratio $N^-/N^+ = e^{-\Delta/kT}$ where Δ is the energy difference between the spin states; k is Boltzmann's constant, and T is the absolute temperature. At high temperatures the ratio is close to 1, and as the temperature decreases, so does the ratio N^{-}/N^{+}. The measured signal in NMR spectroscopy results from the difference between the energy absorbed by the spins making a transition from the lower energy state to the higher energy state, and the energy radiated by the spins making a transition from the higher energy state to the lower energy state. The signal is thus proportional to the population difference between both states, and NMR is capable of detecting very small population differences. It is the resonance, or exchange of energy between the spins and the spectrometer, that occurs when a radio frequency field is applied at a specific frequency determined by the intensity of the static magnetic field, which gives NMR its sensitivity (http://www.cis.rit.edu/htbooks/nmr/bnmr.htm). In a microscopic view, each nuclei actually experiences a slightly different magnetic field strength. We can think of spin packets formed by groups of spins experiencing the same magnetic field strength. Each spin packet can be represented by a magnetization vector whose magnitude is proportional to ($N^{+}-N^{-}$), and the net magnetization will be the sum of the magnetization vectors of every spin packet. At equilibrium, the net magnetization vector is parallel to the external magnetic field. It is customarily assumed that the external magnetic field $\mathbf{B_0}$ and the net magnetization vector $\mathbf{M_0}$ at equilibrium are both along the z-axis ($M_z = M_0$, $M_x = M_y = 0$ at equilibrium).

There are several NMR techniques that can be applied to study ion dynamics, and they can be divided into two generic classes: wideline and transient studies [58]. In wideline or continuous wave studies, a static magnetic field is applied to the sample and the absorption of a small radio frequency field simultaneously applied is measured. The interaction of the nuclei with the microscopic local environment determines the position, width and shape of the absorption spectra at resonance. In basic transient studies, a brief and intense pulse of radio frequency radiation is applied to the sample under a static magnetic field. The pulse results in an energy transferred to the nuclei and a phase correlation that decay with relaxation times T_1 and T_2 respectively. The spin-lattice relaxation (SLR) time T_1 and the spin-spin relaxation (SSR) time T_2 are determined from the decay of the longitudinal and transverse components of the magnetization (parallel and perpendicular to the static magnetic field) respectively [59, 60]. Note that the energy transferred to the nuclei results in an excess magnetic moment in the direction of the static magnetic field, and its decay is possible due to the thermal bath of the lattice. The magnetic moment gained in the perpendicular direction results in no additional magnetic energy but in a correlated phase in the precession motion around the magnetic field. By adjusting the duration of the pulse, it is possible for example to place the net magnetization in the xy-plane, and then the equation that describes the return of the net magnetization to equilibrium is

$$M_z(t) = M_0 \left(1 - e^{-t/T_1} \right). \tag{3.7}$$

Simultaneously, once the net magnetization is placed in the xy-plane, it precesses about the z-axis at the Larmor frequency determined by the static magnetic field (equal to the resonance frequency of the photons which would cause a transition between the two energy levels of the spin). Since each spin packet experiences a slightly different magnetic field and thus rotates at its own Larmor frequency, in addition to precession the net magnetization starts to dephase. Assuming the net magnetization vector is initially along the y-axis, the equation that describes the return to equilibrium of the transverse magnetization, M_{xy}, is

$$M_{xy}(t) = M_{xy}(0)\, e^{-t/T_2}\ . \tag{3.8}$$

Besides of these basic transient studies of the T_1 and T_2 processes, there are other more complex experimental procedures in NMR measurements, like the spin-lattice relaxation time in the rotating frame $T_{1\rho}$ [61], or the use of pulse field gradients [62]. Moreover, it has been recently shown that the use of NMR multi-time correlation functions enables new insights into the understanding of the dynamics of mobile ions in solid ion conductors [63].

Figure 3.11a shows a schematic view of the basic idea behind an NMR-SLR measurement. Under an applied constant magnetic field B_0 along the z direction, the magnetization along the field direction will reach an equilibrium value $M_z = M_{eq}$. By using a series of radio frequency magnetic field $(\pi/2)_{x'}$ pulses along the x direction (a so called saturation comb) the initial magnetization along the z direction can be fully destroyed (the prime $'$ axes are those in the rotating frame of reference, rotating with the Larmor frequency along the magnetic field B_0 direction (z axis)). After that, the magnetization will tend to recover again its value at thermal equilibrium, and this relaxation usually follows exponential time dependence with a relaxation rate $1/T_1$, which is a measure of the transition probability of the spins between distinct Zeeman levels. Resonant fluctuations of spin interactions due to ion motion result in induced Zeeman transitions, and the

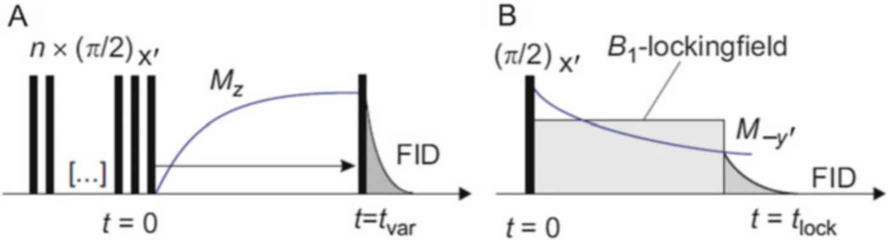

Fig. 3.11 (**a**) Simplified view of an NMR T_1 measurement: under an applied dc magnetic field in the z direction, a series of n closely spaced magnetic field rf-pulses $(\pi/2)_{x'}$ ($n \approx 10$) are applied to destroy any longitudinal equilibrium magnetization so that $M_z = 0$ at $t = 0$. The recovery of $M_z(t)$ towards equilibrium is then probed with a single $\pi/2$-pulse which is applied after a variable relaxation delay $t = t_{var}$. In most cases, M_z (t_{var}) can be approximated by using an exponential function with a characteristic relaxation time T_1. (**b**) Simplified picture of a $T_{1\rho}$ measurement: After a $\pi/2$-pulse the magnetization M_{-y} is locked by a B_1-field. Compared to the preparation pulse, the corresponding locking pulse is phase-shifted by $-\pi/2$. The decay of M_{-y} is then probed as a function of the locking pulse length t_{lock}. Reproduced from [60] by permission

transition probability (and thus the rate $1/T_1$) will be maximum when the correlation time τ_c for the motional process is of the order of the inverse of the Larmor frequency ω_L characterizing the Zeeman splitting of the energy levels under the application of the magnetic field B_0. The Larmor frequency is related to the magnetic field through the expression, $\omega_L = \gamma B_0$, with γ the gyromagnetic ratio. At magnetic fields lower than 1 Tesla, the signal to noise ratio is usually not enough for reliable measurements, and therefore NMR $1/T_1$ is most useful to characterize fast ion motions, with characteristic correlation time of the order of nanoseconds, corresponding to apply magnetic fields of several Tesla. Slower ion motions can be studied by using the spin-locking technique in the rotating frame of reference [60, 61]. The basic idea behind a $T_{1\rho}$ measurement is shown in Fig. 3.11b. First, the magnetization is aligned parallel to the y'-axis by using a $(\pi/2)_{x'}$ pulse along the x' direction. Following this pulse a locking magnetic field B_1 is applied along the y' direction, typically of a few mT, so that the corresponding Zeeman splitting in this rotating frame of reference is much smaller than that in the laboratory frame. While this locking magnetic field B_1 is applied, the magnetization along the y'-axis relaxes towards equilibrium with a characteristic rate $1/T_{1\rho}$. Therefore, this rate can be determined by varying the length, t_{lock}, of the locking magnetic field pulse, and measuring afterwards the residual magnetization along the y'-axis. Note that a maximum in the temperature dependence of $1/T_{1\rho}$ is expected when $\tau_c^{-1} \approx \gamma B_1$. Thus, by using this technique, much slower diffusion processes with correlation times τ_c of the order of 10^{-5} s can be explored.

The ion diffusion process in an ionic conductor is due to the hopping of mobile ions, and this thermally activated ion hopping, with a characteristic time τ at a given temperature, results in the averaging of the dipolar interactions between the nuclei and also of the quadrupolar interactions of the nuclei with their environment when $1/\tau$ is comparable to the interaction strength. In wide-line NMR studies, this averaging due to the motion of ions reduces the width of the resonance line in the absorption spectra, and it is known as “motional narrowing effect”. A hopping rate can be estimated from these measurements of the linewidth as a function of temperature. However, it is important to note that the observation of a line narrowing does not always guarantee that the material is an ionic conductor, since the hopping of ions may be restricted to a local environment and thus may not result in a long range diffusion process and a dc ionic conductivity. Ion hopping has also an important effect on the relaxation times T_1, $T_{1\rho}$ and T_2, and more importantly, these transient NMR measurements allow exploring a much broader range of the hopping rate $1/\tau$ and its quantitative determination as a function of temperature. Fluctuating interactions result in different shifts values $\Delta\omega$ of the Larmor frequencies of the interacting spin. Since these interactions depend on the position of the spin(s), they are altered by possible ion hopping processes, resulting in changes of $\Delta\omega$. The relaxation times T_1, $T_{1\rho}$ and T_2 depend on spectral density functions $J^*(\omega)$ that are proportional to the Fourier transforms of the autocorrelation function of the fluctuating magnetic dipole interactions,

$$G(t) =< \Delta\omega(0) \cdot \Delta\omega(t) >= G(0)g(t). \tag{3.9}$$

The brackets in this expression denote an ensemble average of the fluctuations in the sample, $G(0)$ is a measure of the interaction strength of the spins with the local magnetic field, or electric field gradient, and $g(t)$ represents a normalized decay function from 1 to 0, whose shape or exact time dependence is determined by the relevant spin interactions in each case, as well as by the ion diffusion mechanism. As mentioned above, the spectral density function $J^*(\omega)$ is readily obtained from Fourier transformation of the correlation function $g(t)$,

$$J^*(\omega) = \int_{-\infty}^{\infty} g(t)e^{-i\omega t}dt. \tag{3.10}$$

It is important to remark that the NMR correlation function is in general different from the electrical conductivity correlation function [64, 65]. The angular dependencies of the interactions have an effect on the function $g(t)$ which may be relevant, particularly in the case of anisotropic diffusion, and it is then useful to interpret the experimental data in terms of the predictions of appropriate models that take into account the geometric properties of the diffusion. In the BPP model developed by Bloembergen, Purcell and Pound [53] for three dimensional isotropic random diffusion, the autocorrelation function of the microscopic fluctuations causing the relaxation is assumed to be proportional to an exponential decay $g(t) = e^{-t/\tau_c}$, where τ_c is called the correlation time. This results in a Lorentzian shaped spectral density $J^*(\omega)$. By using this theory for magnetic dipolar relaxation, one can write the following expressions relating the correlation time τ_c, the Larmor frequencies $\omega_L = \gamma B_0$ and $\omega_1 = \gamma B_1$, and the relaxation times T_1, $T_{1\rho}$ and T_2:

$$T_1^{-1}(\omega_L, T) = \frac{G(0)}{3}\left[J'(\omega_L, T) + 4J'(2\omega_L, T)\right], \tag{3.11a}$$

$$T_1^{-1}(\omega_L, T) = \frac{G(0)}{3}\left[\frac{\tau_c}{1 + (\omega_L\tau_c)^2} + 4\frac{\tau_c}{1 + (2\omega_L\tau_c)^2}\right], \tag{3.11b}$$

$$T_{1\rho}^{-1}(\omega_L, T) = \frac{G(0)}{2}\left[J'(2\omega_1, T) + \frac{5}{3}J'(\omega_L, T) + \frac{2}{3}J'(2\omega_L, T)\right], \tag{3.12a}$$

$$T_{1\rho}^{-1}(\omega_L, T) = \frac{G(0)}{2}\left[\frac{\tau_c}{1 + (2\omega_1\tau_c)^2} + \frac{5}{3}\frac{\tau_c}{1 + (\omega_L\tau_c)^2} + \frac{2}{3}\frac{\tau_c}{1 + (2\omega_L\tau_c)^2}\right], \tag{3.12b}$$

$$T_2^{-1}(\omega_L, T) = \frac{G(0)}{2}\left[J'(0, T) + \frac{5}{3}J'(\omega_L, T) + \frac{2}{3}J'(2\omega_L, T)\right], \tag{3.13a}$$

$$T_2^{-1}(\omega_L, T) = \frac{G(0)}{2}\left[\tau_c^{-1} + \frac{5}{3}\frac{\tau_c}{1 + (\omega_L\tau_c)^2} + \frac{2}{3}\frac{\tau_c}{1 + (2\omega_L\tau_c)^2}\right]. \tag{3.13b}$$

Figure 3.12 shows a simulation of this temperature dependence for the relaxation times T_1, $T_{1\rho}$ and T_2 assuming as in BPP theory an ideal exponential decay of the autocorrelation function with a thermally activated correlation time $\tau_c = \tau_{c,0}\exp(-E_A/kT)$. The relaxation rate $1/T_2$ behaves as the linewidth in the continuous wave experiments due to the motional narrowing effect. It is constant at low temperatures and starts to fall as the correlation time decreases and approaches the inverse of the Larmor frequency. At enough high temperature, the relaxation rate $1/T_2$ becomes equal to the relaxation rate $1/T_1$. It can be also observed from Fig. 3.12 that the relaxation time T_2 is always shorter or equal to the relaxation time T_1. The relaxation rate $1/T_1$ shows a maximum when the correlation time is close to the inverse of the Larmor frequency ($\tau_c \approx 10^{-9}$ s). This allows a quantification of the correlation time with considerable precision. Furthermore, the activation energy E_A for the ion hopping process can be obtained from the slope of $1/T_1$ in this Arrhenius plot. The SLR rate $1/T_{1\rho}$ in a rotating frame of reference shows a maximum when the correlation time is close to the inverse of the applied locking frequency ($\tau_c \approx 10^{-5}$ s). Finally, NMR-SSR rates allow probing even slower ion diffusion processes. Therefore, in order to obtain as much quantitative information as possible from NMR-SLR experiments, it is desirable to cover a wide enough temperature range to resolve the peaks maximum and slopes with good accuracy.

Despite the usefulness of the BPP model in explaining the qualitative temperature and frequency dependence of the NMR-SLR rates, it is often found that experimental data deviate from those expected according to a single exponential decay for the NMR correlation function. These deviations can often be satisfactorily described by using a stretched exponential of the Kohlrausch-Williams-Watts (KWW) form for the decay function, $g(t) = e^{(-t/\tau_C)^\beta}$, with the KWW exponent β between 0 and 1. When the KWW exponent is different from 1, the Arrhenius plots of the SLR rates are asymmetric peaks, where the slope at the high temperature side ($\omega_L\tau_c \ll 1$) is still given by E_A but the slope at the low temperature side ($\omega_L\tau_c \gg 1$) is lower and given by the product βE_A (see Fig. 3.12). In a separate chapter on NMR we shall fully explore the results obtained on realistic ionic conductors by the techniques, and bring out the microscopic information on the dynamics of ions different from that provided by Impedance Spectroscopy. The difference turns out to be another critical test of validity of any theoretical account of ion dynamics. Thus, the combined consideration of IS and NMR experimental data confers the bonus of a deeper and microscopically theoretical understanding.

As an example, we show in Fig. 3.13 the temperature dependence of the ^{7}Li NMR spectra in the lithium ionic conducting $Li_{0.18}La_{0.61}TiO_3$. Samples were pressed as pellets, heated at 1623 K during 6 h, and then quenched into liquid nitrogen to favor A-site (and vacancy) disorder in the perovskite structure. Below 160 K, the spectra display a Gaussian shape with constant linewidth (rigid lattice). At increasing temperatures, the linewidth is motionally narrowed and the line shape becomes Lorentzian. Note the existence of a plateau in $1/T_2$ curves between 230 and 350 K, which has been ascribed to an intermediate stage in which only a partial

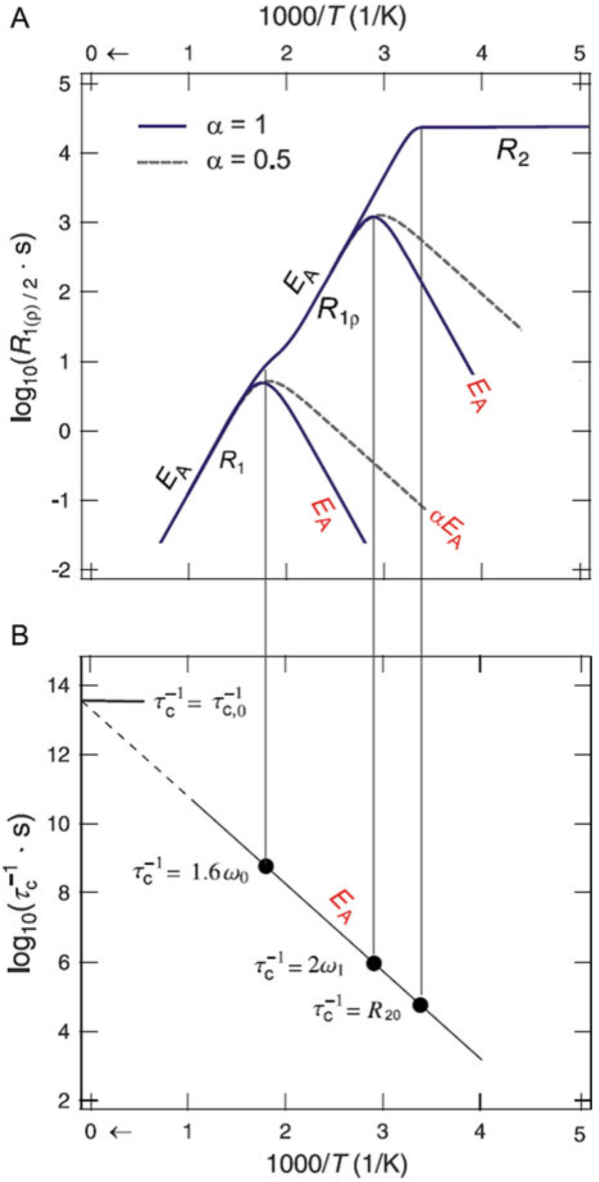

Fig. 3.12 (**a**) Calculated relaxation rates $R_1 = 1/T_1$, $R_{1\rho} = 1/T_{1\rho}$, and $R_2 = 1/T_2$, for homonuclear dipolar relaxation and isotropic 3D diffusion. Parameters used in the simulation are $\omega_0/2\pi = 77.7$ MHz, $\omega_1/2\pi = 80$ kHz and an Arrhenius temperature dependence of the correlation time $\tau_c = \tau_{c,0}\,\exp(-E_A/kT)$, with $\tau_{c,0} = 2.10^{13}$ s and activation energy $E_A = 0.5$ eV. The rate R_2 in the rigid lattice was chosen $R_{2,0} = 2.10^4\ \mathrm{s}^{-1}$. *Solid lines* represent BPP behaviour ($\alpha = 1$), and *dashed lines* show the case of a stretched exponential time dependence, $\exp[-(t/\tau_c)^{\alpha}]$, for the correlation function with $\alpha = 0.5$. (**b**) Arrhenius plot of the correlation times showing how they can be determined from NMR relaxation rates. Reproduced from [60] by permission

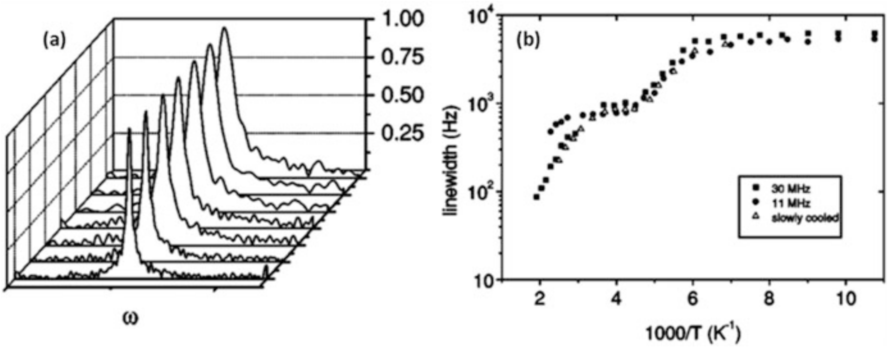

Fig. 3.13 (**a**) Normalized NMR spectra of $Li_{0.18}La_{0.61}TiO_3$ at temperatures 133, 143, 155, 167, 175, 191, and 200 K from back to front. Above 160 K, the line narrowing indicates the onset of hopping diffusion processes. (**b**) Temperature dependence of ^{7}Li NMR linewidths of static spectra in $Li_{0.18}La_{0.61}TiO_3$ at Larmor frequencies of 11 and 30 MHz (*circles* and *squares*, respectively). Samples were heated at 1623 K during 6 h and then quenched into liquid nitrogen. Data reported on slowly cooled sample (*open triangles*) are included as reference (see text). Reproduced from [66] by permission

cancellation of dipolar Li-Li interactions is achieved [66], since similar observations have been reported in NMR studies of slowly cooled samples of the same composition, where vacancy ordering occurs in alternated planes along the *c*-axis [67]. In fact, the observation of this plateau in $1/T_2$ curves has been interpreted as due to the existence of two-dimensional local motions of lithium in the *ab*-plane, that would take place also in the case of quenched $Li_{0.18}La_{0.61}TiO_3$ samples.

Figure 3.14 shows the temperature dependence of SLR $1/T_{1\rho}$ and $1/T_1$ rates for the same sample. It can be observed that $1/T_1$ values remain almost constant below 125 K, decreasing when the resonance Larmor frequency is increased. This behavior observed at low temperatures, when lithium ions can hardly jump to neighboring sites, would be related to the nearly constant loss (NCL) regime observed in the electrical response of ionic conductors [65, 66, 68], and amply discussed in Chap. 4. Increasing temperature, when lithium diffusion starts to contribute significantly to spin-lattice relaxation, $1/T_1$ values increase with temperature, reaching a maximum and finally decreasing. The position of the maximum shifts towards higher temperatures and the intensity decreases when the Larmor frequency is increased. Note that $1/T_1$ data taken at different frequencies in the high temperature range where $\omega_L \tau_c \ll 1$ (long range motions) do not collapse and show a monotonous frequency dependence. This is also an indication of the highly anisotropic lithium ion diffusion in these samples, which would take place preferentially along two-dimensional *ab*-planes in the perovskite structure. It is known that the dimensionality of the long range ion diffusion process can be detected from measurements of the SLR $1/T_1$ rate at high temperatures and several frequencies, since ion motion along 1D, 2D or 3D structures give rise to different frequency dependence of the spectral density function, and therefore of the $1/T_1$ values, when $\omega_L \tau_c \ll 1$ [56, 69–71]. While translational diffusion in three-dimensional systems results in a frequency

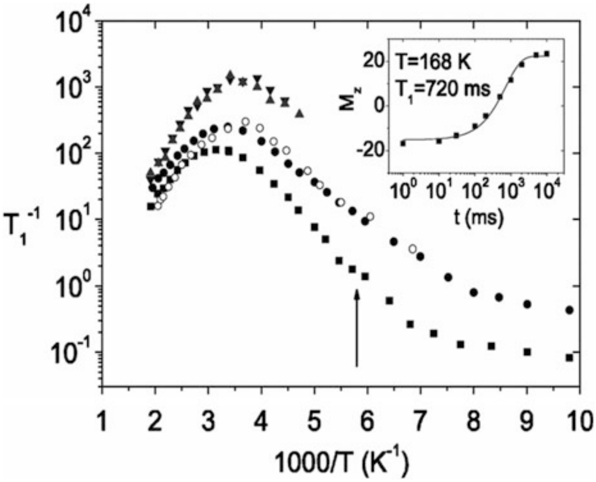

Fig. 3.14 Temperature dependence of SLR $1/T_{1\rho}$ rates at 60 (*up triangles*) and 78 kHz (*down triangles*), and $1/T_1$ rates at 11 MHz (*circles*) and 30 MHz (*squares*) for the lithium ion conductor $Li_{0.18}La_{0.61}TiO_3$. The exponential relaxation of the magnetization at $T = 168$ K is shown in the inset in a semilog plot, together with the fit used to determine the value of the $1/T_1$ rate at this temperature, marked with an *arrow* in the main plot. Data reported on slowly cooled sample are included as reference (*open circles*). Reproduced from [66] by permission

independent spectral density function ($J'(\omega) \propto \tau_c$) at low frequencies or high temperatures, in two-dimensional systems it is expected a logarithmic dependence on frequency ($J'(\omega) \propto \tau_c \ln[\omega_L \tau_c]^{-1}$), and a square root frequency dependence in one dimensional systems ($J'(\omega) \propto \tau_c[\omega_L \tau_c]^{-1/2}$).

References

1. F. Kremer, A. Schönhals (ed.), *Broadband Dielectric Spectroscopy* (Springer Science & Business Media, 2012), p. 729
2. J. Wong, C. Angell, *Glass: Structure by Spectroscopy* (Dekker, New York, 1976), p. 750
3. H. Wagner, R. Richert, Polymer (Guildf). **38**, 255 (1997)
4. R. Richert, in *Advances Chemical Physics*, ed. by S.A. Rice, A.R. Dinner (Wiley, Hoboken, 2015), pp. 101–195
5. U. Schneider, P. Lunkenheimer, R. Brand, A. Loidl, J. Non Cryst. Solids **235–237**, 173 (1998)
6. J.G. Berberian, E. King, J. Non Cryst. Solids **305**, 10 (2002)
7. M.R. Pradel, A.G. Taillades, C. Cramer, Solid State Ionics **105**, 139 (1998)
8. J.R. Macdonald, Ann. Biomed. Eng. **20**, 289 (1992)
9. J.R.M. Evgenij Barsoukov, *Impedance Spectroscopy: Theory, Experiment, and Applications* (Wiley, KGaA, 2005)
10. J.R. Macdonald, W.R. Kenan, *Impedance Spectroscopy: Emphasizing Solid Materials and Systems* (Wiley, 1987), p. 368
11. R. Richert, Phys. A Stat. Mech. Its Appl. **287**, 26 (2000)

12. P. Lunkenheimer, A. Pimenov, A. Loidl, Phys. Rev. Lett. **78**, 2995 (1997)
13. F. Kremer, J. Non Cryst. Solids **305**, 1 (2002)
14. R. Richert, H. Wagner, Solid State Ion. **105**, 167 (1998)
15. F.I. Mopsik, Rev. Sci. Instrum. **55**, 79 (1984)
16. F. Qi, T. El Goresy, R. Böhmer, A. Döß, G. Diezemann, G. Hinze, H. Sillescu, T. Blochowicz, C. Gainaru, E. Rössler, H. Zimmermann, J. Chem. Phys. **118**, 7431 (2003)
17. R. Nozaki, S. Mashimo, J. Chem. Phys. **87**, 2271 (1987)
18. A. Rivera, J. Santamarıa, C. León, T. Blochowicz, C. Gainaru, E.A. Rössler, Appl. Phys. Lett. **82**, 2425 (2003)
19. J.R. Macdonald, J. Chem. Phys. **61**, 3977 (1974)
20. C.J.F. Böttcher, P. Bordewijk, *Theory of Electric Polarization, Vol. II: Dielectrics in Time-Dependent Fields* (Elsevier, Amsterdam, 1978)
21. J.R. Macdonald, J. Electrochem. Soc. **124**, 1022 (1977)
22. J.R. Macdonald, J. Electroanal. Chem. Interfacial Electrochem. **53**, 1 (1974)
23. A.K. Jonscher, Nature **267**, 673 (1977)
24. A. Jonscher, *Dielectric Relaxation in Solids* (Chelsea, London, 1983)
25. C. Moynihan, Solid State Ion. **105**, 175 (1998)
26. K.L. Ngai, C.T. Moynihan, MRS Bull. **23**, 51 (1998)
27. C.T. Moynihan, J. Non Cryst. Solids **172–174**, 1395 (1994)
28. I.M. Hodge, K.L. Ngai, C.T. Moynihan, J. Non Cryst. Solids **351**, 104 (2005)
29. B.A. Boukamp, Solid State Ionics **20**, 31 (1986)
30. B. Boukamp, Solid State Ion. **62**, 131 (1993)
31. J.R. Macdonald, J. Chem. Phys. **102**, 6241 (1995)
32. B. Boukamp, Solid State Ion. **169**, 65 (2004)
33. J. Macdonald, Phys. Rev. B **66**, 064305 (2002)
34. R.F. Klie, J.P. Buban, M. Varela, A. Franceschetti, C. Jooss, Y. Zhu, N.D. Browning, S.T. Pantelides, S.J. Pennycook, Nature **435**, 475 (2005)
35. Z. Wang, M. Saito, K.P. McKenna, L. Gu, S. Tsukimoto, A.L. Shluger, Y. Ikuhara, Nature **479**, 380 (2011)
36. J. Maier, J. Electrochem. Soc. **134**, 1524 (1987)
37. J. Maier, Prog. Solid State Chem. **23**, 171 (1995)
38. J. Maier, Berichte Der Bunsengesellschaft Für Phys. Chemie **88**, 1057 (1984)
39. W.D. Kingery, J. Am. Ceram. Soc. **57**, 74 (1974)
40. X. Guo, R. Waser, Prog. Mater. Sci. **51**, 151 (2006)
41. J. Maier, Berichte Der Bunsengesellschaft Für Phys. Chemie **90**, 26 (1986)
42. X. Guo, J. Maier, J. Electrochem. Soc. **148**, E121 (2001)
43. X. Guo, W. Sigle, J. Fleig, J. Maier, Solid State Ion. **154–155**, 555 (2002)
44. M. Frechero, Sci. Rep. **5, 17229; doi: 10.1038/srep17229** (2015)
45. T. Dijk van, A.J. Burggraaf, Phys. Status Solid A Appl. Res. **63**, 229 (1981)
46. R.de L. Kronig, H.A. Kramers, Zeitschrift Fuer Phys. **48**, 174 (1928)
47. R.de L. Kronig, J. Opt. Soc. Am. **12**, 547 (1926)
48. M. Urquidi-Macdonald, J. Electrochem. Soc. **133**, 2018 (1986)
49. M. Urquidi-Macdonald, S. Real, D.D. Macdonald, Electrochim. Acta **35**, 1559 (1990)
50. J.R. Macdonald, M.K. Brachman, Rev. Mod. Phys. **28**, 393 (1956)
51. B.A. Boukamp, Solid State Ionics **62**, 131 (1993)
52. C. Leon, J.M. Martin, J. Santamaria, J. Skarp, G. Gonzalez-Diaz, F. Sanchez-Quesada, J. Appl. Phys. **79**, 7830 (1996)
53. N. Bloembergen, E. Purcell, R. Pound, Phys. Rev. **73**, 679 (1948)
54. O. Kanert, Phys. Rep. **91**, 183 (1982)
55. D. Brinkmann, Prog. Nucl. Magn. Reson. Spectrosc. **24**, 527 (1992)
56. R. Böhmer, K.R. Jeffrey, M. Vogel, Prog. Nucl. Magn. Reson. Spectrosc. **50**, 87 (2007)
57. J. Bjorkstam, J. Listerud, M. Villa, Solid State Ion. **18–19**, 117 (1986)

58. M.S. Whittingham, B.G. Silbernagel, in *Solid Electrolytes*, ed. by P. Hagenmuller, W. Van Gool (Elsevier, 1978), pp. 93–108
59. E. Hahn, Phys. Rev. **80**, 580 (1950)
60. A. Kuhn, M. Kunze, P. Sreeraj, H.D. Wiemhöfer, V. Thangadurai, M. Wilkening, P. Heitjans, Solid State Nucl. Magn. Reson. **42**, 2 (2012)
61. D.C. Look, I.J. Lowe, J. Chem. Phys. **44**, 2995 (1966)
62. O.J. Żogal, R.M. Cotts, Phys. Rev. B **11**, 2443 (1975)
63. C. Brinkmann, S. Faske, B. Koch, M. Vogel, Zeitschrift Für Phys. Chemie **224**, 1535 (2010)
64. K.L. Ngai, J. Chem. Phys. **98**, 6424 (1993)
65. K. Ngai, C. León, J. Non Cryst. Solids **315**, 124 (2003)
66. A. Rivera, J. Sanz, Phys. Rev. B **70**, 094301 (2004)
67. M.A. París, J. Sanz, C. León, J. Santamaría, J. Ibarra, A. Várez, Chem. Mater. **12**, 1694 (2000)
68. C. León, A. Rivera, A. Várez, J. Sanz, J. Santamaria, K.L. Ngai, Phys. Rev. Lett. **86**, 1279 (2001)
69. H.C. Torrey, Phys. Rev. **92**, 962 (1953)
70. W. Kuchler, P. Heitjans, A. Payer, R. Schollhorn, Solid State Ion. **70–71**, 434 (1994)
71. C.A. Sholl, J. Phys. C Solid State Phys. **14**, 447 (1981)

Chapter 4
Electrical Response of Ionic Conductors

4.1 Electrical Conductivity Relaxation in Glassy, Crystalline and Molten Ionic Conductors

In spite of the vast amount of studies devoted during the past decades to understand the dynamics of ions in ionically conducting materials, it is still unsettled to remain an open and challenging problem [1–4]. Since the charge transport in these materials is mainly due to the mobile ions, the measurement, analysis, and theoretical interpretation of their response to an applied electric field constitute the method as well as the key to gain insights into the dynamics of the mobile ions [1–6], which ultimately determines the conductivity. Most remarkable is the fact that, overall, the electrical response in all molten, glassy, liquid, or even crystalline ionically conducting materials, shows similar properties and universal features [3, 7, 8]. Though at the present time there is not a generally accepted theory for the description of the microscopic motion of ions, it is generally agreed that a disordered structure and Coulomb interactions among ions play an essential role in determining the dynamics of mobile ions and its complex properties and behaviour [1, 9–11]. Note that even in the case of crystalline ionic conductors the mobile ions experience a disordered potential landscape since there are significantly fewer ions than available sites with similar energies for them to occupy, and the mobile ions are usually randomly distributed in the structure, like in an ionic glass or molten salt [1]. This is true at least for fast ionic conductors with a high density of mobile ions and vacant available unoccupied sites.

Since the mobile ions have to overcome an energy barrier to jump to neighboring unoccupied sites, their transport and consequently the measured values of the dc conductivity are thermally activated, and show either an Arrhenius behaviour or a super-Arrhenius dependence over wide temperature ranges [4, 8, 12]. The influence of Coulomb interactions between ions may also enhance the effective activation energy for the ions to successfully jump in a cooperative manner [13, 14]. Enhanced values of these activation energies determined by experiment are in the range

J. Habasaki et al., *Dynamics of Glassy, Crystalline and Liquid Ionic Conductors*,
Topics in Applied Physics 132, DOI 10.1007/978-3-319-42391-3_4

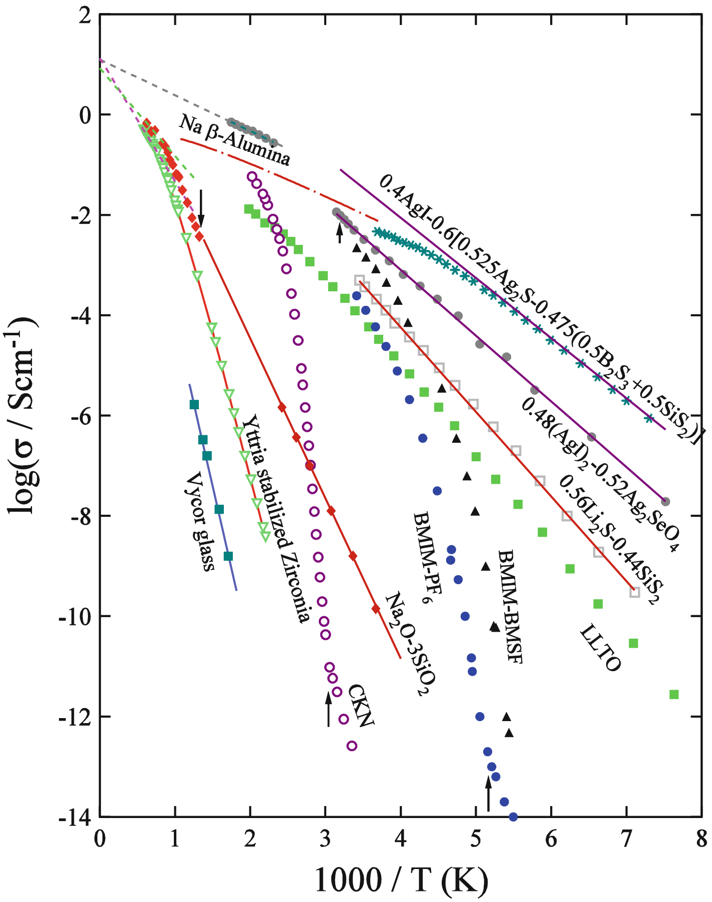

Fig. 4.1 The temperature dependence of the d.c. conductivities, σ, of several ionically conducting materials shown in the form of Arrhenius plots of logσ vs. 1/T(K) to illustrate the tremendous variation of σ with temperature and materials

0.5–1 eV, although lower and higher values are also observed. Therefore a huge range of dc conductivities are usually accessible for a given material by varying the temperature in typical experimental range between 100 and 1000 K.

The temperature dependence of the d.c. conductivities, σ, of archetypal ionically conducting materials are shown in Fig. 4.1 in the form of Arrhenius plots of logσ vs. 1/T to illustrate the tremendous variation of σ with temperature and materials. Shown on the right are three "superionic" glasses which have very high conductivities below the ambient temperature and reach large values, ~10^{-2} Scm^{-1}, at the glass transition temperature, T_g (indicated by vertical arrows for a few ionic glasses in Fig. 4.1). In the case of 0.48(AgI)$_2$-0.52Ag$_2$SeO$_4$, some data for the melt above T_g are also shown [7]. For most ionic glasses the temperature dependence of σ remains strictly Arrhenius in the glassy state, i.e. $\sigma = \sigma_\infty^* \exp(-E_\sigma/kT)$, where E_σ is the activation energy. Exceptions to this sub-T_g Arrhenius behavior exist, such as that exhibited by $0.4AgI \cdot 0.6[0.525Ag_2S \cdot 0.475(0.5B_2S_3 + 0.5SiS_2)]$ [15]. The data for another superionic conductor that does not contain silver ions, $0.56Li_2S \cdot 0.44SiS_2$ [16], are also shown. In the middle of Fig. 4.1 is the data for the glass-forming molten salt, $0.4Ca(NO_3) \cdot 0.6KNO_3$ (CKN) [17], which has a very low conductivity at T_g. High above T_g, σ for the CKN melt shows non-Arrhenius behavior, but returns to Arrhenius behavior well before T_g is reached. At and below T_g, a weaker Arrhenius temperature dependence prevails. $Na_2O \cdot 3SiO_2$ [18, 19], a typical alkali oxide glass, has a much higher T_g, but again σ shows non-Arrhenius behavior in the melt and Arrhenius behavior in the glassy state. An oxide glass containing very few ions, Vycor glass ($0.00044Na_2O \cdot 0.04B_2O_3$-$0.96SiO_2$) [20] has the lowest conductivity and the highest activation energy, E_σ. Included are conductivity data of two room temperature ionic liquids, BMIM-PF6 and BMIM-BMSF [21], which are non-Arrhenius at all temperatures above T_g, and Arrhenius below it.

Finally we have included in Fig. 4.1 data for three crystalline ionic conductors, yttria-stabilized zirconia (YSZ) [For references, see 22] in which the vacancies at oxide sites are responsible for oxide ion conductivity, $Li_xLa_{1-x}TiO_3$ (LLTO) [23], and Na β-alumina [24]. There is no structural phase transition and certainly no glass transition in these crystalline materials but nevertheless their conductivity temperature dependencies become non-Arrhenius at temperatures where σ exceeds ~10^{-2} S cm^{-1}. At still higher temperatures where σ approaches 1 S cm^{-1}, the conductivity seems to return to Arrhenius behavior, $\sigma = \sigma_\infty \exp(-E_a/kT)$, indicated by the dashed lines. As evidenced by the intercept of the dashed lines at infinite temperature ($1/T = 0$), the prefactors σ_∞ for the high temperature Arrhenius equation all have approximately the same value, ~10 S cm^{-1}, independent of whether the material is an ionic crystal or a molten ionic glass-former. The electric field Maxwell relaxation time, τ_σ, defined by the relation [3–6, 25]

$$\sigma = \varepsilon_o \varepsilon_\infty / \tau_\sigma, \tag{4.1}$$

where ε_o is the permittivity of free space, ε_∞ is the high frequency dielectric constant typically having order of magnitude of 10, one finds that σ_∞ corresponds to a relaxation time $\tau_{\sigma\infty}$ of about 1×10^{-13} s and a corresponding frequency ($=1/2\pi\tau_{\sigma\infty}$) of about 2×10^{12} Hz. The latter value is close to vibrational frequencies of mobile ions in glasses.

Since the prefactor σ_∞ is usually close to 10 S/cm [4, 13], lower activation energies give rise to higher dc conductivity values at room temperature, which is a technological objective. The high temperature limit of the dc conductivity is related to the vibrational modes associated with the mobile ions and thus with electrical relaxation. In fact, the temperature dependence of the dc conductivity is related to the absorption of energy from the oscillating ac electric field, and this absorption shows its maximum at frequencies characteristic of the quasi-lattice vibrations in the far-infrared region of the electromagnetic spectrum [4]. Figure 4.2 shows such a relation between vibrational and relaxational modes under an applied ac electric

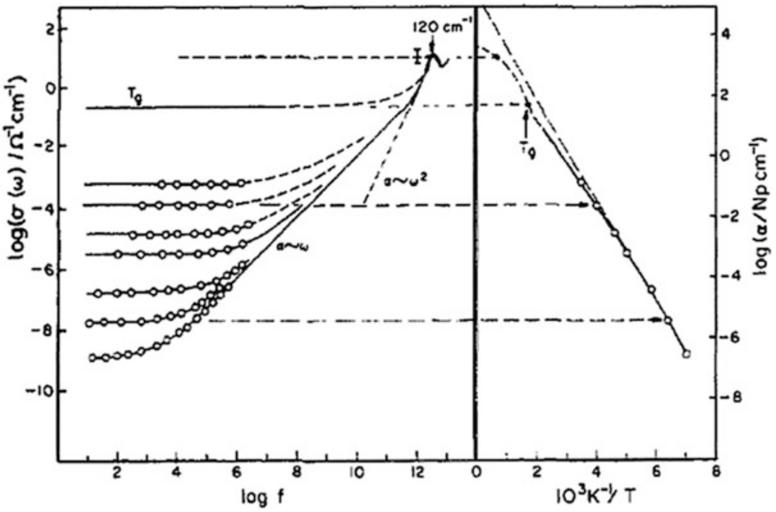

Fig. 4.2 (*Left panel*) Double logarithmic representation of the frequency dependence of electrical conductivity at different temperatures for the fast ion conducting glass $0.6\mathrm{AgI}\cdot0.4(\mathrm{Ag_2O}\cdot2\mathrm{B_2O_3})$. (*Right panel*) Arrhenius plot showing the temperature dependence of the absorption coefficient α for the same glass. Reproduced from [4] by permission

field for the fast ion conducting glass $0.6\mathrm{AgI}\cdot0.4(\mathrm{Ag_2O}\cdot2\mathrm{B_2O_3})$. It can be observed that the dc conductivity, and consequently the low frequency absorption coefficient, increases with temperature towards a limit set by the absorption due to the vibrating ions in the THz regime.

4.1.1 Frequency Dependence of Ionic Conductivity Relaxation

The most commonly used experimental technique to study the dynamics of ions in ionically conducting materials is electrical relaxation. A thin plate or a disc-shaped specimen with thin film metal electrodes deposited on its two parallel faces is prepared. An admittance bridge is used to measure the conductance, G, and capacitance, C, of the specimen as a function of frequency, f. or angular frequency $\omega(=2\pi f)$. Alternatively, the sample impedance $|Z|$ and the phase angle δ between the input and output signals are measured by an impedance spectrometer. Results from these direct measurements are referred to as ionic conductivity relaxation data. The real part of the complex conductivity, σ', and the real part of the complex permittivity, ε', are obtained from the measurements by the expressions $\sigma'(\omega)=G(L/A)=L\sin\delta/A\omega|Z|$ and $\varepsilon'(\omega)=(C/\varepsilon_o)(L/A)$ or $\varepsilon'=L\cos\delta/A\ \varepsilon_o\omega|Z|$, where L is the thickness, A the cross-sectional area of the sample and ε_o is the permittivity of a vacuum. These measurements give immediately the imaginary part

$$\varepsilon''(\omega) = \sigma'(\omega)/\omega\varepsilon_o \tag{4.2}$$

of the complex permittivity,

$$\varepsilon^*(\omega) = \varepsilon'(\varepsilon) - i\varepsilon''(\varepsilon), \tag{4.3}$$

and the complex conductivity,

$$\sigma^*(\omega) = \sigma'(\omega) + i\sigma''(\omega) = i\omega\varepsilon_o\varepsilon^*(\omega). \tag{4.4}$$

The complex electric modulus $M^*(\omega)$ is related to the more familiar $\varepsilon^*(\omega)$ and $\sigma^*(\omega)$ by [25]

$$\varepsilon^*(\omega) = 1/M^*(\omega) \quad \text{and} \quad \sigma^*(\omega) = i\omega\varepsilon_o/M^*(\omega) \tag{4.5}$$

The dc conductivity, σ_{dc}, due to long range displacement of mobile ions is defined by $\sigma_{dc} = \lim_{\omega \to 0} \sigma'(\omega)$, if there is no contribution from the electrode polarization caused by layers of surface charge to be discussed later.

A plot of $\log[\sigma'(f)]$ vs. $\log f$ is matched point by point by $\log[M''(f)]$ or $\log[\varepsilon''(f)]$ vs. $\log f$ and $\log[M'(f)]$ or $\log[\varepsilon'(f)]$ vs. $\log f$ plots. There is nothing special about $\sigma^*(f)$ in comparison with $M^*(f)$ or $\varepsilon^*(f)$. They are just different representations of the *same* macroscopically measured quantities, $G(f)$ and $C(f)$. The electric modulus in the time domain, $M(t)$, has also been measured directly [26] and is not an artificial construct. Let us now introduce some examples of experimental data of ionic conductors to elucidate the points to be made in the following sections. We chose the classic study of the molten salt, $0.4Ca(NO_3)_2$-$0.6KNO_3$ (CKN) by Howell et al. [17]. This historically important publication in 1974 demonstrated the benefit in understanding the dynamics of ions by considering the conductivity relaxation data in all three representations without bias. Advance in experimental technique has made possible measurements over a wider frequency range. This is brought out by combining the $\sigma'(f)$ data of Howell et al. (black closed symbols) and those of Lunkenheimer et al. [27, 28] taken at much higher frequencies (open color symbols) in Fig. 4.3. The $\sigma'(f)$ at high frequencies have very different temperature dependences than σ_{dc}, indicating different ionic dynamic processes are present at higher frequencies before the dc conductivity is reached.

The data of for $0.4Ca(NO_3)_2$-$0.6KNO_3$ from Howell et al. represented by $M^*(f)$ are shown by the imaginary part, $M''(f)$, in Fig. 4.4. The data from Lunkenheimer et al. are shown in Fig. 4.5. The same data of Howell et al. are represented by ε' plotted against frequency f in Fig. 4.6.

One representation of the measurements can be more advantageous over the other ones in revealing some features of the ion dynamics. Different representations of the same experimental data provide additional, rather than subtractive or contradictive insights into the difficult problem of understanding ionic conductivity in melts, glasses and crystals. Insistence of using one representation and either

Fig. 4.3 Conductivity vs. frequency for 0.4Ca$(NO_3)_2$–0.6KNO_3 melt above the glass transition temperature

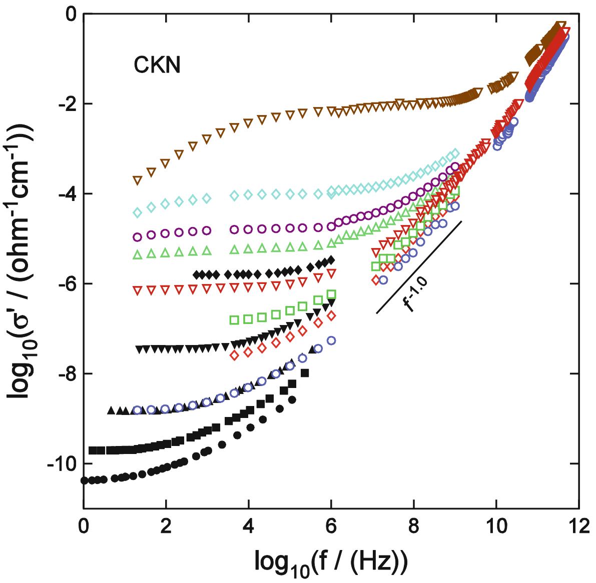

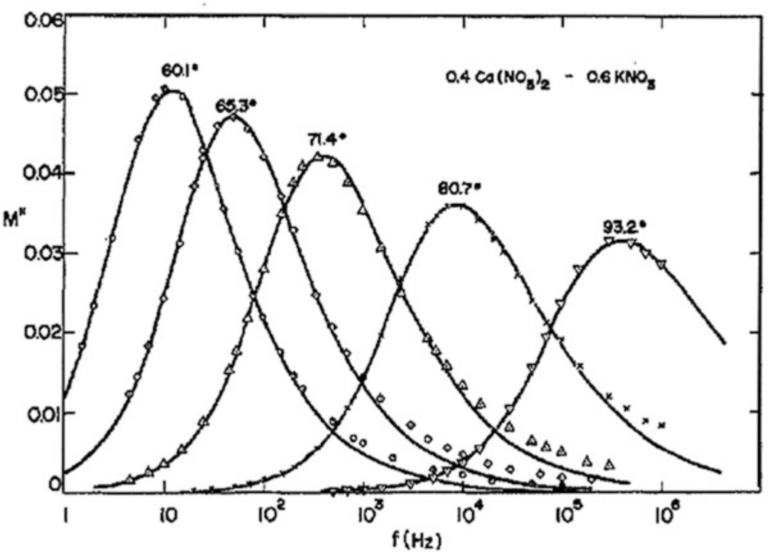

Fig. 4.4 The imaginary and real part of $\varepsilon^*(\omega)$ from Howell et al

ignoring or totally dismissing the others has no justification. A theoretical idea or interpretation of the data proposed can appear to be reasonable and acceptable in one particular representation, but becomes questionable or even unacceptable in another representation. For the sake of preserving their own point of view, some proponents of the theoretical idea/interpretation chose to attack the verity of another

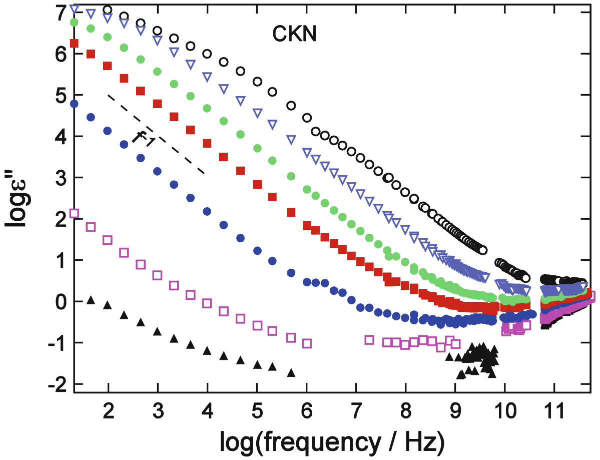

Fig. 4.5 Plot of $\log \varepsilon''$ versus $\log f$ of CKN at different temperatures. From top to bottom: 468, 417, 393, 379, 361, 342 and 326 K. Data from Lunkenheimer and coworkers

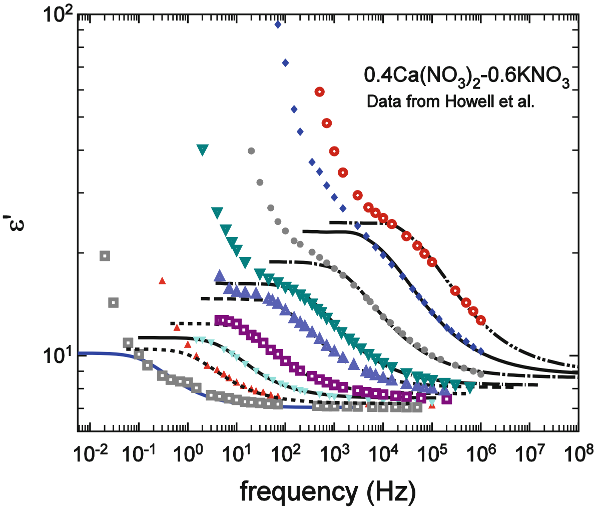

Fig. 4.6 The data points are measured ε' plotted against frequency f for $0.4Ca(NO_3)_2{-}0.6KNO_3$ from *left* to *right* at nine different temperatures $T = 35.3$, 54.3, 60.1, 65.3, 71.4, 74.6, 80.7, 86.8, and 93.2 C. Experimental data after Howell et al. to be discussed in a later section, the curves through the data points at each temperature are $\varepsilon'(f)$ calculated from the fit to $M^*(\omega)$ by the stretch exponential functions, previously obtained by Howell et al.

representation not supporting it. The attack is not justified and does nothing but impeding progress [29–32]. This unfortunate situation happened before, and examples will be given later. On the other hand, the positive and correct outlook for any proposed interpretation of the data is to require that it is consistent with any of the equivalent representations. If not, the interpretation is either outright wrong or at least questionable.

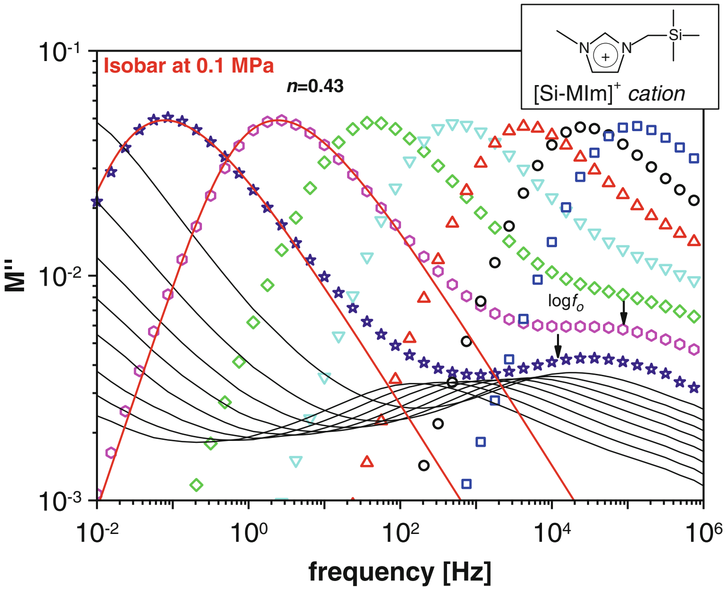

Fig. 4.7 $M''(f)$ of $[\text{Si-MIm}]^+[\text{BF}_4]^-$ versus frequency at ambient pressure and constant temperature with temperature in the range 243 to 173 K, spanning across T_g. The spectra were measured at intervals of 5 K each. The data represented by *symbols* range from 243 to 213 K. Data from 208 to 173 K are not shown by *symbols*, otherwise they overlap and the features cannot be clearly discerned. To avoid this undesirable situation, the data are interpolated by *black lines* to show the shift of the secondary β-conductivity relaxation on decreasing temperature. The *red lines* are fits to the slower primary α-conductivity relaxation loss peak at two temperatures by the Fourier transform of the Kohlrausch function. The secondary β-conductivity relaxation are resolved above and below T_g. The *arrows* indicate the locations of the logarithm of the primitive conductivity relaxation frequencies, $\log f_0$, which are in agreement with the most probable β-conductivity relaxation frequencies within a factor of about 2

Naturally one representation gives more direct information of some specific quantity than the other. For example, if one is interested only in the value of the d.c. conductivity and nothing else, then it suffices to have the data represented by $\sigma'(f)$. However if the purpose is to understand the mechanism of ionic conduction and diffusion, and how it determines the magnitude of σ_{dc}, it is advantageous and in many cases necessary to consider the frequency dependence of not only $\sigma'(f)$. but also $M^*(f)$ or $\varepsilon^*(f)$.

These differences in the quality and richness of information conveyed differently by $M^*(\omega)$, $\varepsilon^*(\omega)$, and $\sigma'(\omega)$ are brought out by the conductivity relaxation data of a room temperature ionic liquid, 1-methyl-3-trimethylsilylmethylimidazolium tetrafluoroborate, ($[\text{Si-MIm}][\text{BF}_4]$), in Figs. 4.7 and 4.8 [33]. The data represented by $M^*(\omega)$ has $M''(\omega)$ showing not only the primary α-loss peak at low frequencies related to dc conductivity but also a secondary β-loss peak at higher frequencies. The data expressed as $\varepsilon^*(\omega)$ also has in the $\varepsilon''(\omega)$ representation a corresponding secondary loss peak with approximately the same peak frequency of $M''(\omega)$ at the same temperature. The low frequency response from the mobile ions shown in $\varepsilon'(\omega)$

Fig. 4.8 Spectra in different representations of the same measurements of $[\mathrm{Si\text{-}MIm}]^+[\mathrm{BF}_4]^-$ at ambient pressure in various temperature ranges as indicated in the figures. From top to bottom: ε', ε'', M', M'', and σ'

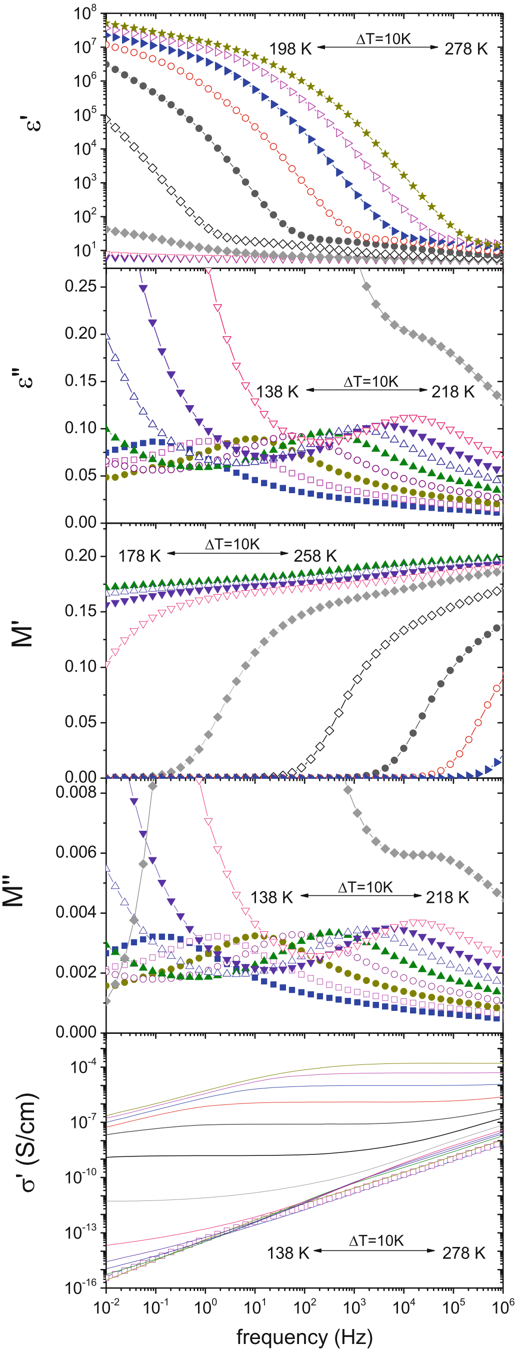

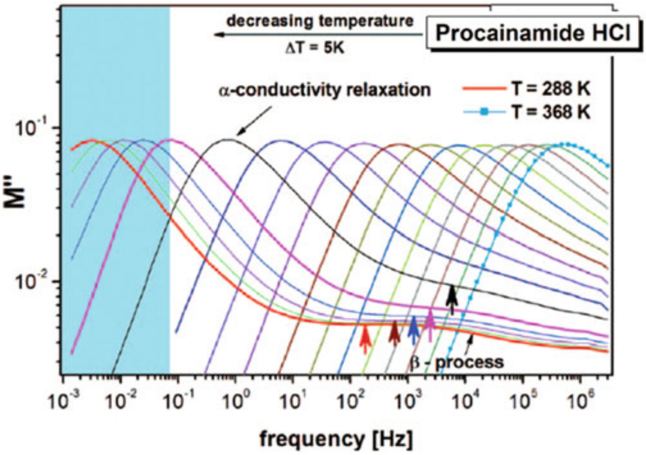

Fig. 4.9 Isothermal electric loss modulus spectra of procainamide HCl at ambient pressure in temperature range indicated in the figures. *Each arrow* with the *same color* as the spectrum indicates the logarithm of the primitive ion conductivity relaxation frequency, logf_0, calculated by the CM equation

is obscured by the presence of the electrode polarization [29, 32], while $M'(\omega)$ decreases towards zero value as low frequencies [32]. The $\sigma'(\omega)$ show the usual monotonic increase with frequency and provide no evidence of the secondary conductivity relaxation process (see Fig. 4.8). The lack of any indication of a new process at higher frequencies in $\sigma'(\omega)$ is a clear warning to those insisting that $\sigma'(\omega)$ is the only right choice and sufficient to understand the dynamics of ions. Since the secondary loss peak appears in $M''(\omega)$ and $\varepsilon''(\omega)$, the presence of the secondary conductive relaxation is real and cannot be dismissed by antagonists of the electric modulus representation as an artifact.

Another example is procainamide HCl, a pharmaceutical, but nevertheless a typical ionic conductor [34]. Its $M''(\omega)$ in Fig. 4.9 show the primary loss peak and a secondary loss peak at higher frequencies, but the latter does not appears in Fig. 4.10 when the same data are presented as $\sigma'(\omega)$. This problem of $\sigma'(\omega)$ shows one of its shortcomings in representing data.

The temperature dependences of the relaxation times of the primary α-loss and secondary β-loss peaks, τ_α and τ_β, determined for of [Si-MIm]$^+$[BF4]$^-$ and procainamide HCL are plotted against 1000/T in Fig. 4.11 (left) and (right) respectively.

4.1.2 Dissection into Contributions from Different Time/Frequency Regimes

By inspection of Figs. 4.3, 4.4, and 4.5 for CKN and Figs. 4.7, 4.8, 4.9, and 4.10 for the ionic liquid ([Si-MIm][BF$_4$] and procainamide HCl, it can be seen that the data at higher frequencies have properties different from the primary conductivity

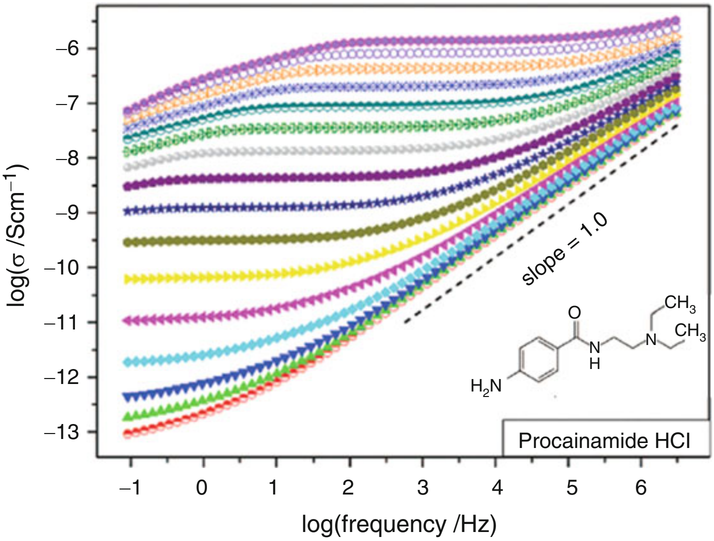

Fig. 4.10 The same measurements for procainamide HCl as in Fig. 4.9 at higher temperatures but now presented in terms of log$\sigma(f)$ vs. log$f$. The secondary conductivity relaxation seen in the log$M''(f)$ vs. log$f$ representation is no longer visible in the log$\sigma(f)$ vs. log$f$ representation

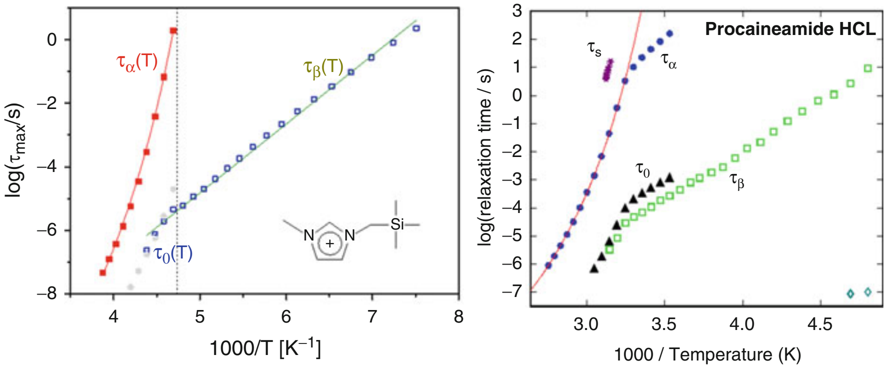

Fig. 4.11 (*left*) Temperature dependences of the α- and β-conductivity relaxation times in [Si-MIm]$^+$[BF4]$^-$ obtained at ambient pressure. Predictions for the JG relaxation times above T_g according to Coupling Model (to be discussed in a later section) are plotted as the *solid grey circles*. The *solid lines* are fits to the Vogel-Fulcher dependence of τ_α, and the Arrhenius law for τ_β. (*right*) Relaxation map of procainamide hydrochloride. *Closed blue circles* denote conductivity relaxation times, τ_α, *open green squares* represent the β-conductivity relaxation times, τ_β. The *stars* are the structural relaxation times, τ_s, determined from TMDSC measurements. *Solid line* is Vogel-Fulcher fit to the data of τ_α. The *closed black triangles* are the primitive conductivity relaxation times, τ_0, calculated from the CM equation

relaxation at lower frequencies responsible for dc conductivity, including the temperature and frequency dependences. The contribution from vibration of ion and molecule is obviously different, but it is not what we are concerned in here. The dielectric loss $\varepsilon''(f)$ in Figs. 4.5 and 4.8 at high frequencies/low temperatures decreases very slowly with frequency to become a nearly constant loss (NCL)

$$\varepsilon''(f) = Af^{-c}, \quad c << 1 \tag{4.6}$$

This in turn gives rise to a frequency dependence of ε' related to $\varepsilon''(f)$ by the approximate expression [35], $\varepsilon''(f) = -(\pi/2)d\varepsilon'(f)/d\ln f$. The temperature dependence of the intensity A of the NCL at a fixed frequency is very weak in comparison with dc conductivity. The NCL in $\varepsilon''(f)$ is another NCL in $M''(f)$ as can be seen in Fig. 4.8. However, in $\sigma'(\omega)$ it corresponds to

$$\sigma'(f) = (A/2\pi\varepsilon_0)f^{1-c}, \quad c << 1 \tag{4.7}$$

which is evident from Fig. 4.3 in the range $7 < \log f < 9$ for CKN, and from Figs. 4.8 and 4.10 at lower frequency range for the ionic liquid and procainamide HCl because these data were taken at lower temperatures.

In the case of fast ionic conductors, glassy or crystalline, the NCL is a well-known and well-observed contribution to the dielectric loss that goes back to 1946 [36–38]. It is discussed in the 1976 book by Wong and Angell [35], extended to a gigahertz range for the first time by Robert Cole and coworkers in 1989, and is the subject of many other studies [39–48]. Nowick et al. [40] were the first to draw attention that this linear frequency dependence of the real part of the conductivity is a general feature of ion dynamics in ionic conductors. Since then, in ionic conductors it is referred to by some workers [49] as "second universality". The NCL of Eq. (4.6) associated with Eq. (4.7) is also generally found in non-ionic glasses and non-conducting materials [39, 50, 51], and hence it is more general than the presence in ionic conductors.

The NCL in $\varepsilon''(f)$ and $M''(f)$ or the f^{1-c}-dependence of $\sigma'(\omega)$ extends to lower frequencies as temperature is decreased, and this trend continues on indefinitely. It has no characteristic time constant and hence the NCL is not a normal relaxation process. This feature of $\sigma'(f)$ is general and found in most ionic glasses, in melts such as CKN [17, 28, 52, 53] and in ionically conducting crystals including Na β-alumina [54] and YSZ [55] and LLTO [56]. There are a number of indications that the *nearly* $Af^{1.0}$ dependence of $\sigma'(f)$ at high frequencies is distinctly different in physical origin from the a.c. conductivity frequency dependence at lower frequencies due to the long-range motions of mobile ions [57]. For example, the temperature dependence of the A parameter is extremely weak compared to the temperature dependence of the d.c. conductivity σ and of the frequency where $\sigma'(f)$ first begins to rise above σ_{dc} [41, 57–59]. Likewise, as discussed in Sect. 4.8 below, changes in the alkali oxide mole fraction x in glasses have a much weaker effect on the value of A than they do on the d.c. conductivity and the low frequency relaxation. The same is true for substitution of one alkali for another (the mixed alkali) [57]. Finally, changes in the thermal history of the same glass which change the d.c. conductivity σ_{dc} by nearly half an order of magnitude have no effect on the value of A [57; C.T. Moynihan, K.L. Ngai, unpublished results].

NCL is found by dielectric and mechanical relaxation spectroscopy at high frequencies/low temperatures of non-ionic glass-formers without any trace of conductivity [53, 60–63]. Thus the NCL is a general feature of relaxation and diffusion of interacting systems, and ionic conductors are just a particular case. The origin of the NCL is traced to caged ion or caged molecules dynamics [53, 60–63] to be elaborated after the Coupling Model [60–63] of ion dynamics has been introduced. Molecular dynamics simulations [45, 64–66] of Li silicate glasses have also found the NCL from the mean square displacements of the ions at times much shorter than the long range diffusion of the ions, and explicitly showed the anharmonic motions of the ions within anisotropic and fluctuating cages. The results will be shown in details in chapters to follow.

The secondary $M''(f)$ loss peaks in Figs. 4.7 and 4.9 evidently shift less to lower frequencies on decreasing temperature and also with increasing pressure [33] than the primary $M''(f)$ loss peak, and hence it has weaker temperature dependence. The intensity of the NCL also has weak temperature dependence either as power law of T or some other functional form [65]. Thus, any serious attempt to understand the ion dynamics must make clear distinctions of the three processes; namely the NCL, the secondary ion relaxation, and the primary ion relaxation/dc conductivity.

In the Chap. 9 on molecular dynamics simulations, details of motions of ions in the NCL regime of glassy $x\text{Li}_2\text{O-}(1\text{-}x)\text{SiO}_2$ with $x = 0.5$ are presented. Here we give the essential of the results that ions in the NCL region are undergoing anharmonic motions in anisotropic cages. The density distribution of Li ions in each cage (i.e., the shape of the cage) tends to have strong anisotropy, and the cage is not static but fluctuating.

4.2 Comparison of Methods for Analysis of Data

4.2.1 *The Electric Modulus*

The simplest ion dynamics is the case when G and C are constants independent of frequency. The specimen can be treated as a parallel resistance-capacitance (RC) circuit, where $C = \varepsilon_\infty C_\text{o}$, $C_\text{o} = \varepsilon_\text{o} A/l$, $R = Gl/A$, and σ' is the dc conductivity σ_{dc}. The time constant of a simple RC circuit element, τ, is given by the product RC, which may be expressed as

$$\tau = \varepsilon_\infty \varepsilon_o / \sigma_{dc} \tag{4.8}$$

The complex permittivity is given by

$$\varepsilon^*(\omega) = C/\varepsilon_o - iG/\omega\varepsilon_o \equiv \varepsilon_\infty - i\sigma_{dc}/\omega\varepsilon_o = \varepsilon_\infty[1 - i/\omega\tau] \tag{4.9}$$

The corresponding $M^*(\omega)$ from Eq. 4.5 is

$$M^*(\omega) = \frac{1}{\varepsilon_\infty}[i\omega\tau/(1+i\omega\tau)] = \frac{1}{\varepsilon_\infty}\left[1 - \int_0^\infty e^{-i\omega t}\left(-\frac{d\exp(-t/\tau)}{dt}\right)dt\right] \quad (4.10)$$

A plot of M'' vs $\log\omega$ will be a Debye peak at $\omega\tau = 1$.

However, the experimental data of most ionic conductors except at very low ion concentrations rarely agree with this description, thus suggesting that the specimen cannot be treated as a parallel resistance-capacitance circuit with an exponential decay $\exp(-t/\tau)$ with a single time constant τ. A nonexponential decay function $\Phi(t)$ has to replace $\exp(-t/\tau)$ in Eq. (4.10) which can always be formally written in terms of distribution of time constants as

$$\Phi(t) = \int_0^\infty g(\tau)\exp(-t/\tau)d\tau, \quad (4.11)$$

where $g(\tau)$ is the normalized probability function for τ. In this manner, Macedo, Moynihan and coworkers [5, 6, 17, 25, 30] have generalized the electric modulus representation of experimental data by

$$M^*(\omega) = \frac{1}{\varepsilon_\infty}\left[1 - \int_0^\infty e^{-i\omega t}\left(-\frac{d\Phi}{dt}\right)dt\right] \quad (4.12)$$

The mean relaxation time $<\tau>$ is related to σ_{dc} by

$$<\tau> = \int_0^\infty g(\tau)\tau d\tau = \varepsilon_o\varepsilon_\infty/\sigma_{dc} \quad (4.13)$$

and

$$\varepsilon_s \equiv \lim_{\omega\to 0}\varepsilon' = \varepsilon_\infty <\tau^2> / <\tau>^2 \quad (4.14)$$

Of all the well behaved one parameter distributions of relaxation times, the one which gives good fit to typical data is that corresponding to the stretched exponential function, Eq. (4.15), proposed by Kohlrausch [67] in 1854 in fitting his own experimental data of decay of static electricity stored between two electrodes on the inside and outside of a glass Leyden jar. His data were published in the same year in Ref. [68]

$$\Phi(t) = \exp\left[-(t/\tau^*)^\beta\right]. \quad (4.15)$$

It is remarkable that R. Kohlrausch not only studied ion conductivity relaxation in the glass but also characterized the time decay function by his stretched exponential function, which accurately account for his own data, a large volume of data up to the present time, and several properties to be presented below.

From the $M_\beta^*(\omega)$ calculated by Eq. (4.12) with this Kohlrausch relaxation function, it can be shown by straightforward mathematics that the quantities in Eqs. (4.13) and (4.14) are given by

$$<\tau>= [\Gamma(1/\beta)/\beta]\tau^*, \tag{4.16}$$

$$\sigma_{dc} = \varepsilon_o\varepsilon_\infty / <\tau>= \varepsilon_o\varepsilon_\infty/[\Gamma(1/\beta)/\beta]\tau^* \tag{4.17}$$

and

$$\varepsilon_s \equiv \lim_{\omega\to 0}\varepsilon' = \beta\frac{\Gamma(2/\beta)}{[\Gamma(1/\beta)]^2}\varepsilon_\infty, \tag{4.18}$$

where Γ is the gamma function.

It is worthwhile to emphasize the result from Eqs. (4.14) or (4.18) that the ratio $\varepsilon_s/\varepsilon_\infty$ is determined solely by the distribution of relaxation times $g(\tau)$ or the fractional exponent β of the stretched exponential function From Eq. (4.18), the permittivity change $\Delta\varepsilon$ caused by the relaxation of mobile ions is given by

$$\Delta\varepsilon = \left[\langle\tau^2\rangle/\langle\tau\rangle^2 - 1\right]\varepsilon_\infty = \left[\beta\frac{\Gamma(2/\beta)}{[\Gamma(1/\beta)]^2} - 1\right]\varepsilon_\infty, \tag{4.19}$$

Thus the value of $\varepsilon_s/\varepsilon_\infty$ that can be calculated by the right-hand-side of Eq. 4.18 is a sensitive test of both the $M^*(\omega)$ formalism and the Kohlrausch function fit to it [32, 69].

4.2.1.1 Accurately Calculating ε′(ω) from Kohlrausch Fit to M*(ω)

In the literature, usually shown are fits to the frequency dependence of σ' and M^* data. The fit to the latter is by the $M_\beta^*(\omega)$ calculated according to Eq. (4.12) with the Kohlrausch stretched exponential function (Eq. 4.15) as the decay function $\Phi(t)$. For example, Howell et al. [17] have given the fits to such M^* data of $0.4Ca(NO_3)_2$-$0.6KNO_3$ (CKN) at different temperatures shown before in Fig. 4.4. Seldom shown are the corresponding fits to $\varepsilon'(\omega)$. In Fig. 4.6, we show the Kohlrausch function fits, $\varepsilon'_\beta(\omega)$, to the $\varepsilon'(\omega)$ data of CKN for nine temperatures, 35.3, 54.3, 60.1, 65.3, 71.4, 74.6, 80.7, 86.8, and 93.2 °C, below and above $T_g = 60$ °C. The $\varepsilon'_\beta(\omega)$ are calculated directly from the relation, $\varepsilon_\beta^*(\omega) = 1/M_\beta^*$, using exactly the same parameters, ε_∞, β and τ^*, as given by Howell et al. [17]. The values of β decreases monotonically with temperature, and the values for the nine temperatures in the same order as given above are 0.74, 0.74, 0.72, 0.69, 0.64, 0.61, 0.58, 0.53, and 0.52.

Starting from the high frequency end and on decreasing frequency, the ε' data in Fig. 4.6 monotonically increase from ε_∞ and show tendency of leveling off to plateau, before the appearance of a final rapid rise. The calculated $\varepsilon'_\beta(\omega)$ shown by lines [32] fit well the data up to the plateau with the value exactly given by Eq. (4.19).

The continued and rapid rise of $\varepsilon'(\omega)$ above the plateau at lower frequencies is contributed by the electrode surface polarization capacitance which is much larger than the sample capacitance. As a result, the time constant of electrode polarization can be much larger than the conductivity relaxation time $<\tau>$ and allows us in some cases to separate the two contributions.

The plateau level ε_s, together with the decrease of $\varepsilon'(\omega)$ at higher frequencies down to ε_∞, come from the contribution of electrical relaxation in the bulk sample. On the whole, the frequency dependence of $\varepsilon'(\omega)$ is reproduced at all temperatures, although the fits tends to overestimate the high frequency limits of ε'. These deviations are inherited from the fits by Howell et al. to the same M^* data, which invariably show the well-known deviations at high frequencies. It has been proposed that these deviations are due to the presence of a nearly constant loss contribution that dominates the ion hopping contribution to the dielectric response at high frequencies [1, 8, 32, 43, 44, 53, 57]. Based on experimental facts, it is generally believed that this nearly constant loss (NCL) contribution originates from a process that is unrelated to the hopping relaxation of ions. It is possible in Fig. 4.6 that the calculated $\varepsilon'(\omega)$ may slightly underestimate the plateau level. However, any conclusion cannot be made until the electrode polarization contribution has been removed from the data. On increasing temperature, the increase of the plateau level is explained quantitatively by ε_s calculated from Eq. (4.18) with the corresponding decreasing β values required to fit the broadening dispersion of the $M^*(\omega)$ data (see Fig. 4.4). The origin of this temperature dependence of β has been explained by the increasing coupling of ionic conductivity relaxation to structural relaxation with increasing temperature in CKN [70–72]. This is a general property found in other ionic conductors, and will be elaborated in other places of this treatise.

The success of the electric modulus in accounting for $\varepsilon'(\omega)$ is general the case for all ionic conductors. The generality is demonstrated by the conductivity relaxation data of some glassy ionic conductors with large difference of ion concentrations. One example is the Vycor glass ($0.00044Na_2O$-$0.04B_2O_3$-$0.96SiO_2$) with low concentration of Na ions [20], showing $M^*(\omega)$ having narrow dispersion and $\beta = 0.95$ in the Kohlrausch fit M^*_β. The $\varepsilon'(\omega)$ data at 358 °C are presented in Fig. 4.12. The development of a plateau is observed at low frequencies but the contribution of electrode polarization is not present within the experimental frequency window. The entire dispersion observed can be associated with the ionic hopping contribution, except for a small correction to $\varepsilon'(\omega)$ due to the nearly constant loss $\Delta\varepsilon''$. The $\varepsilon'_\beta(\omega)$ calculated from M^*_β are in good agreement with the data [32]. The ratio $\varepsilon_s/\varepsilon_\infty$ calculated from Eq. (4.18) for $\beta = 0.95$ is equal to 1.2, in approximate agreement with the small permittivity change $\Delta\varepsilon$ observed in this alkali ion glass with low ion concentration. The $\varepsilon'(\omega)$ data at 350 °C of the sodium germanate glass containing 0.0079 mol% Na_2O measured by Cordaro and Tomozawa [73] are shown also in Fig. 4.12. These authors have determined

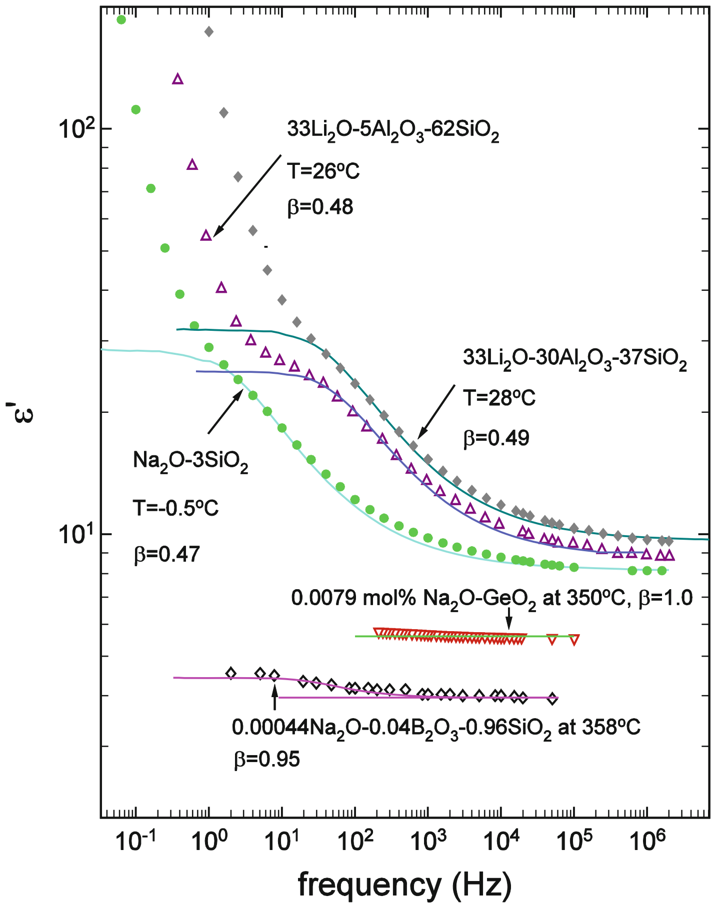

Fig. 4.12 The data points are the measured $\varepsilon'(\omega)$ plotted against frequency $\nu = \omega/2\pi$ for five alkali oxide glasses. Sodium germanate glass containing 0.0079 mol% Na_2O measured by Cordaro and Tomozawa [73], Vycor glass ($0.00044Na_2O$-$0.04B_2O_3$-$0.96SiO_2$) measured by Simmons et al. [20], two lithium aluminosilicate glasses measured by Saad [N. Saad, Ph.D. Thesis, Catholic University of America, Washington, DC (1974).] and a sodium trisilicate glass [1, 18]. The *solid curves* through the data points are $\varepsilon'_\beta(\omega)$ calculated from M^*_β. The measurement temperature and the stretch exponent β for each case are indicated

$\varepsilon_\infty = 5.5$, $\varepsilon_s = 5.7$ and a small value of $\Delta\varepsilon$ equal to 0.2. Compared with ε_∞, this small value of $\Delta\varepsilon$ implies that ε' is nearly dispersionless. Their $M''(\omega)$ data have a half-width at half-maximum nearly equal to the Debye value of 1.144 decades and hence corresponds to $\beta = 1.0$. The $\varepsilon'(\omega)$ calculated from this fit has no dispersion and is shown by the solid curve through the data points. It describes well the small permittivity change observed.

Data of $\varepsilon'(\omega)$ of several other oxide glasses with higher alkali concentrations are also shown in Fig. 4.12. All these data sets exhibit a pseudo-plateau before the electrode polarization starts to take over at lower frequencies, and are chosen for consideration here because the ionic hopping contribution therein can be identified approximately. Also the fits to the complete data in the $M^*(\omega)$ representation by M^*_β have been made previously. The parameters, ε_∞, β and τ^*, that give these good fits to the $M^*(\omega)$ data are taken from the published works and used to calculate $\varepsilon'(\omega)$. The calculated results shown as solid curves in Fig. 4.12 fit the $\varepsilon'(\omega)$ data including the plateau level well. The values of β for these glasses with large concentration of alkali ions are considerably smaller than unity. Consequently, the ratios $\varepsilon_s/\varepsilon_\infty$ calculated from Eq. (4.18) are much larger than for glasses containing few ions and have $\beta \approx 1.0$.

Good agreement between the $\varepsilon'(\omega)$ data and $\varepsilon'_\beta(\omega)$ calculated from M^*_β, the fit to $M^*(\omega)$, were obtained in non-oxide glasses. Three examples are shown in Fig. 4.14, which are $0.10AgI + 0.90[0.525Ag_2S + 0.475(0.5B_2S_3 + 0.5SiS_2)]$, $0.35Li_2S\text{-}0.65GeS_2$, and $0.48(AgI)_2\text{-}0.52Ag_2SeO_4$.

Finally, in Fig. 4.14 we summarize all the values of $\varepsilon_s/\varepsilon_\infty$ obtained from the fits to the data shown in Figs. 4.6, 4.12, and 4.13 by plotting them against (1-β), where β is the stretch exponent previously determined from the fits of the Kohlrausch functions to the conductivity relaxation data in the electric modulus representation. Naturally, these values lie exactly on the solid line defined by Eq. 4.19. Although we have made no attempt to determine the experimental ε_s by subtracting off the electrode polarization contribution in any of the data shown in Figs. 4.6, 4.12, and 4.13, it is clear by inspection of the quality of the fits that they cannot be far from the theoretical values. In addition, we show the value of $\varepsilon_s/\varepsilon_\infty$ of 0.30 mol% $Na_2O\text{-}GeO_2$ (open diamond) determined by Sidebottom [74] after subtracting off the electrode polarization contribution, the values of $\varepsilon_s/\varepsilon_\infty$ of the Vycor glass at 358 °C (open triangle) and the 0.0079 mol% $Na_2O\text{-}GeO_2$ glass at 350 °C (filled triangle) both determined directly from the experimental data of Simmons et al. [20] and Cordaro et al. [73] respectively. These independently determined experimental values of $\varepsilon_s/\varepsilon_\infty$ do not exactly lie on the theoretical curve but close to it. For the 0.0079 mol% $Na_2O\text{-}GeO_2$ at 350 °C (filled triangle) the difference is so small that it cannot be seen by eye. One purpose of Fig. 4.14 is to show the large range of variation of $\varepsilon_s/\varepsilon_\infty$, $1 \le \varepsilon_s/\varepsilon_\infty < 10$, in the ionic glasses considered in this work and its dependence only on β but not on chemical structure and composition.

The monotonic decrease of $n = (1\text{-}\beta)$ with falling temperature found for the molten salt CKN in transit from the liquid to the glassy state is due to decoupling of the conductivity relaxation from the structural relaxation [34, 70]. This property of $n = (1\text{-}\beta)$ due to decoupling is general and found in other ionic conductors including $CdF_2\text{–}LiF\text{–}AlF_3\text{–}PbF_2$ melt and glass, and the pharmaceuticals procaine HCl and procainamide HCl [70]. Accompanying this unusual T-dependence of $n = (1\text{-}\beta)$ is the corresponding decrease of $\varepsilon_s/\varepsilon_\infty$. In contrast, in the case of glassy ionic conductors at temperatures far below T_g, such as those shown in Figs. 4.12 and 4.13 [75], the value of $n = (1\text{-}\beta)$ increases slightly with decrease in temperature, and the ratio $\varepsilon_s/\varepsilon_\infty$ also increases, opposite to the trend shown by CKN. Thus $\varepsilon_s/\varepsilon_\infty$

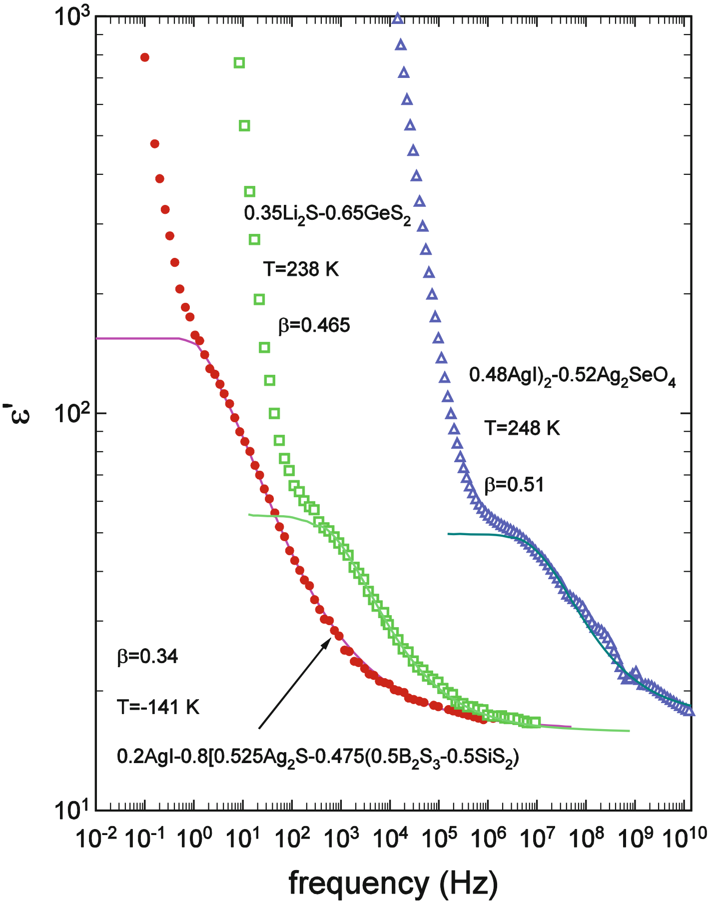

Fig. 4.13 Non-oxide glasses. 0.35Li$_2$S-0.65GeS$_2$, 0.48(AgI)$_2$-0.52Ag$_2$SeO$_4$, and 0.10AgI + 0.90 [0.525Ag$_2$S + 0.475(0.5B$_2$S$_3$ + 0.5SiS$_2$)]. The data points are the measured $\varepsilon'(\omega)$ plotted against frequency $\nu = \omega/2\pi$. The data of the third set have been shifted uniformly by one decade to the left. The *solid curves* through the data points are $\varepsilon'_\beta(\omega)$ calculated from M^*_β. The measurement temperature and the stretch exponent β for each case are indicated

is a sensitive test for validation of both the $M^*(\omega)$ formalism and the Kohlrausch function.

From Eq. (4.14), it is clear that the ratio $\varepsilon_s/\varepsilon_\infty$ is a direct reflection of the breadth of conductivity relaxation times and vice versa [29, 72]. Thus, if $\varepsilon_s/\varepsilon_\infty$ changes on varying temperature of an ionic conductor, or on varying the concentration of ions in the same ionic conductor, then *by fiat* the breadth of conductivity relaxation times has to change as well as the frequency dispersion of the data in any representation $\sigma^*(\omega)$, $\varepsilon^*(\omega)$, or $M^*(\omega)$.

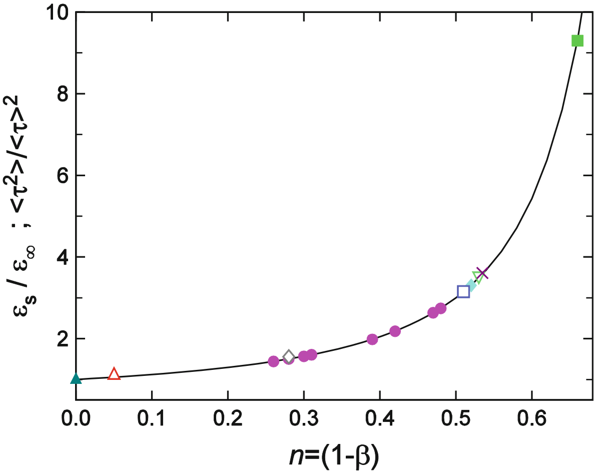

Fig. 4.14 The ratio $\varepsilon_s/\varepsilon_\infty$ calculated by using the value of the stretch exponent β obtained from the fit to the electric modulus data is plotted against (1-β) for $0.4Ca(NO_3)_2$-$0.6KNO_3$ at different temperatures (*filled circles*); lithium aluminosilicate glasses (*filled diamond*); sodium trisilicate glass (*open inverted triangle*); $0.35Li_2S$-$0.65GeS_2$ (*times*), $0.48(AgI)_2$-$0.52Ag_2SeO_4$ (*open square*); and $0.10AgI + 0.90[0.525Ag_2S + 0.475(0.5B_2S_3 + 0.5SiS_2)]$ (*filled square*). For the sodium germanate glass containing 0.0079 mol% Na_2O (*filled triangle*), 0.30 mol% Na_2O-GeO_2 (*open diamond*) and $0.00044Na_2O$-$0.04B_2O_3$-$0.96SiO_2$ Vycor glass (*open triangle*), these three data points are obtained from the experimental data (see text). The *solid curve* is the theoretical value of $\varepsilon_s/\varepsilon_\infty$ calculated from Eqs. (4.14) and (4.18) as a function of β

4.2.1.2 Unwarranted Fixation with Scaling of log[σ′(f)/σ$_{dc}$] to a Master Curve

In the past years, there are various suggestions that data of logσ'(f) vs. log$f$ of diverse glassy ionic conductors, or the same glassy ionic conductor with different ion concentrations, and at various temperatures can be scaled to form approximately a master curve. Although the scaling results are still empirical, if true it implies some physics behind it, and this is the reason why we consider it here. However, the same data represented in term of log$M$*(f) vs. log$f$ of the ionic conductors cannot be scaled to form a master curve, and this conundrum left the proponents of scaling data logσ'(f) vs. log$f$ no choice but to attack the electric modulus representation of data [76–80]. This attack needs to be answered and is refuted in this section later on when electric modulus is further discussed in detail.

In all these scaling schemes, data of $\sigma'(f)$ from different samples and at different temperatures are scaled by σ_{dc}, and frequency f is scaled by a factor f_0, which a function of the parameters of the sample. Success of scaling means that a single master function $F(f/f_0)$ can fit all data sets in the form $\sigma'(f)/\sigma_{dc} = F(f/f_0)$, and it implies that the frequency dispersion of σ' is the same despite significant changes in ion concentration (accompanied by changes of the chemical and physical structures) and temperature. Roling [76] and Roling et al. [77] showed that scaling holds over the range, $0 \leq \log\sigma'(f) \leq 2.5$, in a series of alkali borate glasses $(Na_2O)_x(B_2O_3)_{1-x}$, with $x = 0.10$, 0.15, 0.20, 0.25, and 0.30, by the choice of $f_0 = \sigma_{dc}T/x$. Roling [76] did not show the data of $\varepsilon'(f)$, and instead gave a plot of $T\Delta\varepsilon$, but the values of T in $f_0 = \sigma_{dc}T/x$ to scale data were not specified. However, $\sigma'(f)$ data of sample with smaller x were taken at higher temperatures because of lower ion mobility. Hence we expect larger value of T in the product $T\Delta\varepsilon$ was used for samples with lower ion concentration x. Taking this consideration into account, we can deduce that $\Delta\varepsilon$ increases with x even more than shown by $T\Delta\varepsilon$ in Fig. 4.4 of Ref. [76]. The value of ε_∞ was not given by Roling, but it is reasonable to assume the change of ε_∞ with x is minor compared with that of $\Delta\varepsilon$. Thus the ratio $\Delta\varepsilon/\varepsilon_\infty$ increases with x, and from Eq. (4.19) the breadth of the conductivity relaxation times has to increase. This result derived from $\varepsilon'(f)$ contradicts the invariance of the breadth of the conductivity relaxation times concluded from the success of obtaining a master curve by horizontal shifts of the $\sigma'(f)$ data of samples with different x.

Data plotted as $\log\sigma'(f)$ vs. $\log f$ are often fitted by the Jonscher's expression [39], $\sigma'(f) = \sigma_{dc} + Af^n = \sigma_{dc}[1 + (f/f_2)^n]$, where f_2 is a characteristic ion hopping frequency. It emphasizes the importance of the frequency dispersion of $\sigma'(f)$ at frequencies of the order of f_2 at which $\sigma'(f_2)$ is equal to $2\sigma_{dc}$. The slope of $\log\sigma'(f)$ increases monotonically with f and departs from the power law with exponent n. If performed, fits of the $\log\sigma'(f)$ data in Fig. 4.4 of Ref. [77] by the Jonscher's expression will give values of n that increases with x, which is indication of different breadths of conductivity relaxation times. Notwithstanding, shifting $\sigma'(f)$ data of different x by scaling f according to $f_0 = \sigma_{dc}T/x$ for some T, Roling et al. did get reasonably satisfactory superpositioning and a master curve. This feat is made possible by the monotonically increasing slope of $\log\sigma'(f)$ with $\log f$ continuing to frequencies higher than f_2. Data of $\log\sigma'(f)$ of sample with smaller x and n can be made to approximately superpose with data with larger x and n simply by shifting the former more to lower frequencies to use the data at higher frequencies than f_2 to compensate for the less rapid rise of the Jonscher fit. This procedure can hide the differences in frequency dispersion from the Jonscher fits of the samples with different n values. On close inspection of the master curve in Fig. 4.5 of Ref. [77], the data do not superpose that well in the region of $\log(\sigma'/\sigma_{dc})$ where the Jonscher expression fits the data well. This is evidenced by the conspicuously thicker master curve formed by the data from different samples, and this is because the frequency dispersions in the important Jonscher fits region are different.

The same comment applies to the $\sigma'(f)$ data of CKN of Howell et al. [17], as can be seen by comparing the data above T_g in their Fig. 4.2 and the data below T_g in Fig. 4.4. The best Jonscher fits of data in Fig. 4.2 will yield a larger n than in Fig. 4.4. Actually in demonstrating invariant scaling of $\sigma'(f)$ of CKN, the $\sigma'(f)$ data was fitted with the Jonscher expression by Sidebottom et al. [81]. They scaled $\sigma'(f)$ by σ_{dc} and frequency f by f_2 for data taken at nine temperatures. The results shown in Fig. 4.1b of their paper are used by them to claim that they have demonstrated temperature invariant scaling of $\sigma'(f)$ (with $n = 0.61$) both above and below T_g. If one examines their Fig. 4.1b, it is evident that the scaled data at 319, 325 and 330 K below T_g fail to superpose at the most important region of σ'/σ_{dc} with values near 1 and slightly above it. The frequency f_2 in the Jonscher expression is near the peak frequency f_{max} of the $M''(f)$. From their Fig. 4.1a, it can be seen that the $M''(f/f_2)$ peaks at 319, 325 and 330 K are narrower on both sides of f_{max}. The difference of frequency dispersion at frequencies in the neighborhood of $f_2 \sim f_{max}$ appears less important in the log-log plot of $\log[\sigma'/\sigma_{dc}]$ vs. $\log(f/f_2)$ because the data extend to about 3 decades above $\log[\sigma'/\sigma_{dc}]$. In this plot, deviations from superposition in the neighborhood of $f_2 \sim f_{max}$ look insignificant. Had the superposition of data were presented in a semi-log plot of σ'/σ_{dc} vs. $\log(f/f_2)$, the deviations will become more alarming. Therefore the lack of superposition of the σ'/σ_{dc} data at frequencies below $f_2 \sim f_{max}$ is a reflection of narrower $M''(f/f_2)$ peaks at lower temperatures. There is no temperature invariant scaling of $\sigma'(f)$ (with $n = 0.61$) both above and below T_g as claimed.

Sidebottom et al. [78] examined the Roling et al. [77] scaling with $f_0 = \sigma_{dc}T/x$ for another glass system, $(Na_2O)_x(GeO_2)_{1-x}$ over a much wider range of Na ion concentration ($0.003 < x < 0.1$) and found it fails to collapse their $\sigma'(f)$ data sets to a master curve. He [74] had proposed another scaling of f with the choice of $f_0 = \sigma_{dc}/e_0\Delta\varepsilon$. The new scaling parameter f_0 scales the $\log[\sigma'(f)/\sigma_{dc}]$ data sets of the glassy systems $(Na_2O)_x(GeO_2)_{1-x}$, for x from 0.003 to 0.1, and $(K_2S)_x(B_2S_3)_{1-x}$ for x from 0.0005 to 0.05, as well as the molten salt $0.4Ca(NO_3)_2$-$0.6KNO_3$ (CKN) [79, 80] at temperatures in the same range as we considered before in Fig. 4.6.

To rationalize the scaling, $\sigma'(f)/\sigma_{dc} = F(f/f_0)$, with $\Delta\varepsilon$ appearing in $f_0 = \sigma_{dc}/e_0\Delta\varepsilon$, Sidebottom [74] suggested an analogy of the hop of the cation between anionic sites to the rotation of a permanent dipole. The assumed analogy led him to propose the permittivity change $\Delta\varepsilon$ caused by the relaxation of mobile ions is given by $\Delta\varepsilon = n(qd)^2/3\varepsilon_o kT$, where n is the mobile ion concentration, q is the charge of the mobile ions, d is the jump length, and the product qd is the effective dipole of the hopping ion. A similar expression for $\Delta\varepsilon$ has been suggested by Roling [76].

In 2001, León et al. [82] used electrical relaxation data of a crystalline ionic conductor [83], yttria stabilized zirconia (YSZ), in which the mobile ion density n and the ionic hopping distance d are known, to perform a critical test of the validity of $\Delta\varepsilon = n(qd)^2/3\varepsilon_o kT$. It was found that the magnitude of $\Delta\varepsilon$ is nearly independent of temperature and also of the ion mobile density, which is at odds with a large change predicted by $\Delta\varepsilon = n(qd)^2/3\varepsilon_o kT$ in the temperature range of 500–780 K, where the value of ε_s can be determined from the experimental data. This result from León et al. clearly dismisses the relation $\Delta\varepsilon = n(qd)^2/3\varepsilon_o kT$ assumed by Sidebottom, and should be sufficient to stop using it. Inexplicably, the disproof is ignored and its usage was continued in the 2009 review [79].

Like the previous results of CKN in scaling f by f_2, the ion hopping frequency in the Jonscher fit [81], the superpositions of data are far from perfect. Noticeable is the deviations of $\log[\sigma'(f)/\sigma_{dc}]$ data taken at lower temperatures in the important region $\sigma_{dc} < \sigma'(f) < 2\sigma_{dc}$. Sidebottom ignored the T-dependence of the breadth of the conductivity relaxation times that follows directly from Eq. (4.14) and the experimental fact that $\varepsilon_s/\varepsilon_\infty$ changes on varying temperature (see Fig. 4.6). Instead the change is hidden by considering the ratio, $(\varepsilon'\text{-}\varepsilon_\infty)/\Delta\varepsilon$, and the data at different temperatures are superposed by scaling f by $f_0' = \sigma_{dc}/2\pi e_0\Delta\varepsilon$, which is an ansatz rationalized but had not been justified. As discussed before and validated in Fig. 4.6, the T-dependence of $\varepsilon_s/\varepsilon_\infty$ implies that the frequency dispersion of $\sigma^*(f)$, $\varepsilon^*(f)$, or $M^*(f)$ changes with temperature. This is clearly supported by the narrowing of the $M''(f)$ loss peak on cooling from the melt found by Howell et al. in CKN. There is obvious contradiction of T-dependence of $\varepsilon_s/\varepsilon_\infty$ and width of $M''(f)$ to his universal scaled frequency dependence of $\log[\sigma'(f)/\sigma_{dc}]$. The contradiction led Sidebottom to suggest that $M^*(f)$ is defined in such a way as to include the nonionic high-frequency permittivity, in addition to the ionic contributions, and thus $M^*(f)$ cannot be expected to obey time-temperature superpositioning. Hodge et al. [29] have answered this attack on the electric modulus. It is also clear from the fact that the mean relaxation time $< \tau >$ calculated from $M^*(f)$ by Eq. 4.13 or by Eq. 4.17 with β from the Kohlrausch fit accounts for σ_{dc} quantitatively very well.

Patel and Martin [84, 85] published ionic conductivity relaxation of sodium thioborate glasses, $(Na_2S)_x(B_2S_3)_{1-x}$, with the concentration of ions varying over an extremely wide range from $x = 0.001$ to 0.15. For some reason, Sidebottom [79, 80] did not analyse these published data and instead considered that of a similar series of potassium thioborate glasses, $(K_2S)_x(B_2S_3)_{1-x}$, purported in the thesis of Patel [86]. He show the scaling of $\log[\sigma'(f)/\sigma_{dc}]$ and $(\varepsilon'\text{-}\varepsilon_\infty)/\Delta\varepsilon$ with $f_0 = \sigma_{dc}/e_0\Delta\varepsilon$ can be obtained for the series of $(K_2S)_x(B_2S_3)_{1-x}$, ranging from $x = 0.0005$ to 0.05 mole fraction. The data obtained for all compositions and taken at different temperatures superimpose to produce a single master curve. This impressive scaling result is touted by him as clearly demonstrating the shape of the curve (i.e., the nature of the correlated ion motion) is not influenced by even two orders of magnitude change in the ion density. He went on to claim that 'this finding proves conclusively that the correlated motion is not a consequence of any interaction between mobile ions'. However, the same data represented by $M''(f)$, show the breadth of dispersion increases or the Kohlrausch exponent β decreases with increase of ion concentration x. Moreover, $\Delta\varepsilon$ increases monotonically with x and its value for $x = 0.05$ is a factor of about 6 larger than that for $x = 0.0005$ (see Fig. 4 of Ref. [80]). These other experimental facts give the opposite conclusion that the breadth of the conductivity relaxation time by Eq. (4.14) is changing. Also the σ_{dc} as well as $\varepsilon'(f)$ is expected to be well described by Eqs. (4.17) and (4.18) with the β values from fits to $M''(f)$, although Sidebottom did not check this out. Without resolving these contradictory experimental facts from the other side, it is premature to accept or reject the conclusion made by him based on $\sigma'(f)/\sigma_{dc}$.

We do not understand why Sidebottom did not consider the data of sodium thioborate glasses, $(Na_2S)_x(B_2S_3)_{1-x}$, with x ranging from 0.001 to 0.15 published in the open literature in great details [84, 85]. The raw data are presented in both $\sigma'(f)$ and $M^*(f)$, analysed and discussed by Patel and Martin (PM). On the other hand, the raw $\sigma'(f)$ data of $(K_2S)_x(B_2S_3)_{1-x}$ were not shown by him except the final scaled master curve. In the following, we recapture some of data of

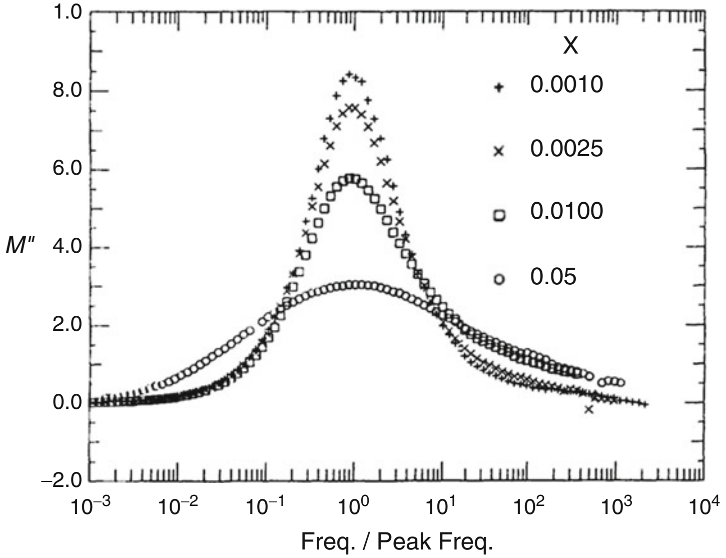

Fig. 4.15 The imaginary part of the electrical modulus plotted against normalized frequency for a few selected glasses in the series $x(Na_2S) + (1-x)B_2S_3$

$(Na_2S)_x(B_2S_3)_{1-x}$ and the discussions by PM to show the log[σ′(*f*)/σ_{dc}] data for different x cannot be scaled to a master curve, and actually the difference in frequency dispersions are consistent with that shown by $M''(f)$.

The $M''(f)$ data of several glasses from PM are reproduced in Fig. 4.15 here. The temperature for each glass was chosen such that the peak relaxation frequency is about the same at ~1 kHz. The shape of $M''(f)$ of each glass does not change with temperature. As pointed out by PM, we see the dramatic narrowing of $M''(f)$ with decreasing x or the average Na-Na separation distance, suggesting diminishing ion-ion correlations is the cause. The fits of the frequency dependence of $M''(f)$ by the Fourier transforms of the Kohlrausch function yield the parameter $\beta \equiv (1-n)$ for each glass. For the x =0.001 glass, the value of β is 0.93, corresponding to a nearly single exponential relaxation. The width of $M''(f)$ increases and β decreases with x. For $x = 0.0025$, the value of β_x is 0.86; for $x = 0.005$, $\beta_x = 0.82$; for $x = 0.01$, $\beta_x = 0.71$; for $x = 0.02$, $\beta_x = 0.65$; and for $x = 0.05$, $\beta_x = 0.35$.

In Fig. 4.16 we reproduced the raw data of log[σ′(*f*)/σ_{dc}] for $x = 0.001$, 0.0025, 0.005, 0.01, and 0.03 presented by PM in their Fig. 4.5. Like in previous figure, the temperatures were chosen such that each glass has approximately the same peak relaxation frequency ~1 kHz of $M''(f)$. In this way, each curve covers about the same data region above and below the peak frequency f_{max} of $M''(f)$. In Fig. 4.16 we use solid magenta lines to estimate the slope of increase of log[σ′(*f*)/σ_{dc}] at its lower values, and the dashed red lines the slopes at the higher values of log[σ′(*f*)/σ_{dc}]. The dashed lines have different slopes. Sidebottom's scaling merely shifts the data of log[σ′(*f*)/σ_{dc}] horizontally by normalizing *f* by f_0. Since the slopes of the increase

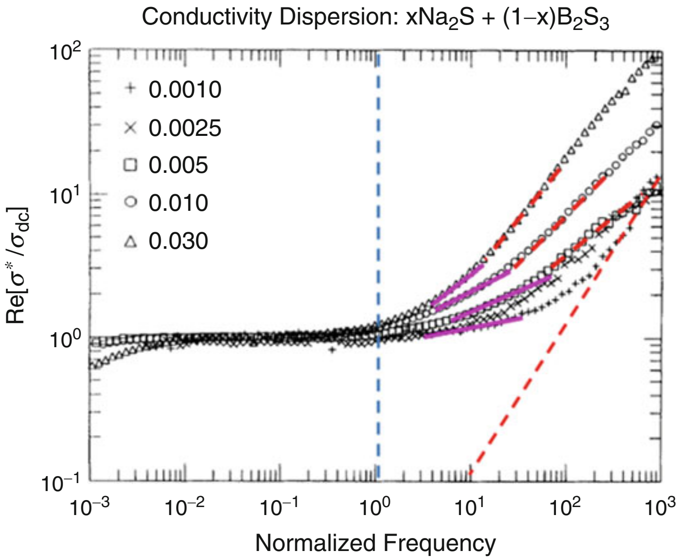

Fig. 4.16 Conductivity for a series of $x(Na_2S) + (1\text{-}x)B_2S_3$ glasses from Patel and Martin

of log[σ′(f)/σ_{dc}] over the same range of values are different for the glasses in Fig. 4.16, it is impossible to obtain a well defined master curve by him using his $f_0 = \sigma_{dc}/e_0\Delta\varepsilon$, or by anyone else using a different f_0. Thus, the fully published log[σ′(f)/σ_{dc}] data of the $(Na_2S)_x(B_2S_3)_{1-x}$ glasses of different compositions show different frequency dependences and cannot be scaled, just like the same data expressed in terms of $M''(f)$ in Fig. 4.15.

The slopes of the magenta solid lines, n_x, in Fig. 4.16 can be taken as approximately the value of the exponent n in the Jonscher expression, $\sigma'(f) = \sigma_{dc}[1 + (f/f_2)^n]$ had it been used to fit the data of the $(Na_2S)_x(B_2S_3)_{1-x}$ glasses. From the lines drawn in Fig. 4.16, values of the slopes are: $n_x = 0.10$ for $x = 0.0010$; $n_x = 0.17$ for $x = 0.0025$; $n_x = 0.27$ for $x = 0.005$; $n_x = 0.30$ for $x = 0.01$; and $n_x = 0.50$ for $x = 0.03$. The large differences between these approximate values for n of the Jonscher fits are direct evidence of the sensitive dependence of the frequency dispersion on x. Moynihan [72] compared the fit to logσ′(f) data by the Jonscher expression and the fit to the same data derived from the fit to $M^*(f)$ by the Kohlrausch function with fractional exponent β. The values of n and $(1-\beta)$ are comparable, with n being slightly larger. This relation leads us to compare n_x with $(1-\beta_x)$ in Table 4.1, where we find good correspondence between these two parameters. These results indicate consistency of the conclusion of change of frequency dispersion of ion dynamics with composition based on either $M^*(f)$ or σ′(f)/σ_{dc} representation.

PM noted that in Fig. 4.16 for $x = 0.001$ and $x = 0.0025$ glass, there is a range of frequencies above $f/f_{max} \approx 1$ where the conductivity remains nearly frequency independent. These weak frequency dependences for small x glasses correspond

Table 4.1 Comparison of n_x with $(1-\beta_x)$ for several $(Na_2S)_x(B_2S_3)_{1-x}$ glasses

x	β_x	n_x	$(1-\beta_x)$
0.0010	0.93	0.10	0.07
0.0025	0.87	0.17	0.13
0.0050	0.82	0.26	0.18
0.010	0.71	0.30	0.29
0.03	0.55[a]	0.48	0.45

[a] Estimated by linear interpolation between the values of β_x given by PM for $x = 0.02$ and $x = 0.05$

[b] Line not shown in Fig. 4.16 to avoid crowding

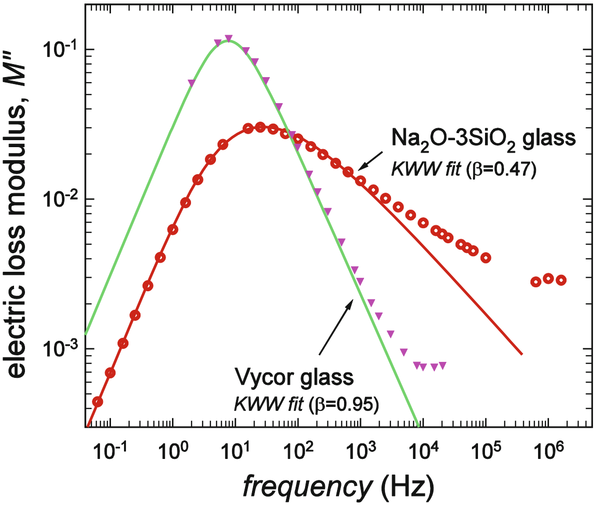

Fig. 4.17 Log-log plots of the imaginary part of the electric modulus $M''(f)$ of the two glasses in Fig. 4.2. For details see text

to the small exponents n of the fits by the Jonscher expressions and are approximately given by $n_x = 0.10$. for $x = 0.001$, and $n_x = 0.17$ for $x = 0.0025$. Such weak frequency dependence of $\log[\sigma'(f)/\sigma_{dc}]$ found in $(Na_2S)_x(B_2S_3)_{1-x}$ glasses with very low ion concentrations were observed in other glasses. One example is the Vycor glass ($0.00044Na_2O$-$0.04B_2O_3$-$0.96SiO_2$) measured by Simmons et al. [20]. We have considered the frequency dependence of its $\varepsilon'(f)$ and the small value of $\Delta\varepsilon$ (see Fig. 4.12). This property of $\varepsilon'(f)$ is corroborated by the narrow width of $M''(f)$ with $\beta = 0.95$ via Eq. (4.19), and are in stark contrast to those of the sodium trisilicate glass, $0.25Na_2O$-$0.75SiO_2$. Figure 4.17 shows the difference in the width of $M''(f)$ between the Na_2O-$3SiO_2$ glass at −0.5 °C and the Vycor glass at 313 °C, and their Kohlrausch β parameter. The value of $\beta = 0.95$ and $\beta = 0.47$ respectively of the Vycor glass and the trisilicate glass is nearly the same as $\beta = 0.93$ and $\beta = 0.55$ respectively of $(Na_2S)_x(B_2S_3)_{1-x}$ with $x = 0.0010$ and $x = 0.030$. Figure 4.18 is a plot of $\log[\sigma'(f)/\sigma_{dc}]$ against f/f_{max}, where f_{max} is the $M''(f)$ peak frequency of the two sodium silicate glasses. The data of Vycor glass and the trisilicate glass resembles respectively the $(Na_2S)_x(B_2S_3)_{1-x}$ with $x = 0.0010$ and $x = 0.030$. The dashed lines having different slopes of $\log[\sigma'(f)/\sigma_{dc}]$

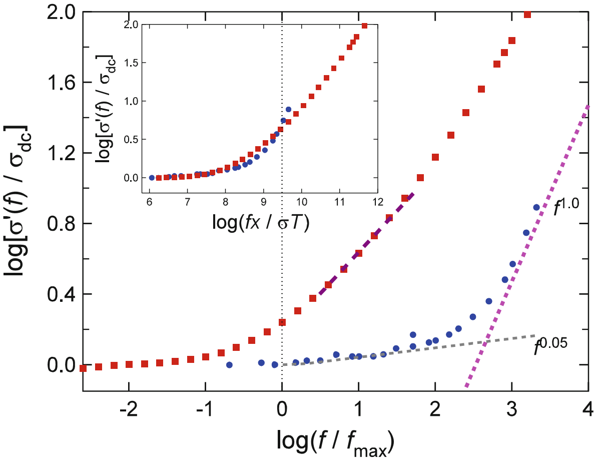

Fig. 4.18 Isothermal electrical relaxation data shown as plots of log[$\sigma'(f)$] vs. log f for a Na_2O-$3SiO_2$ glass at −0.5 °C, and for a Vycor glass $x$$Na_2O$-(1-$x$)[$0.04B_2O_3$-$0.96SiO_2$] at 313 °C with $x = 0.00044$. For details see text. The *inset* shows the scaling of frequency by $f_0 = \sigma_{dc}T/x$ fails to obtain a master curve, or by any additional horizontal shift of either data set

indicate that the data of the two Na silicate glasses cannot be scaled to form a master curve. The inset of Fig. 4.17 shows the results of scaling f by $f_0 = \sigma_{dc}T/x$ suggested by Roling [76]. The different scaled frequency dependence clearly show a master curve cannot be obtained no matter what additional horizontal shift is applied. The failure of obtaining a master curve by scaling frequency happens also for $\sigma'(f)/\sigma_{dc}$ instead of log[$\sigma'(f)/\sigma_{dc}$], although the results are not shown here.

The distinctly different frequency dependences of either log[$\sigma'(f)/\sigma_{dc}$] or $M''(f)$ between glasses containing very low and high concentrations of mobile ions are general and are found in other glasses [73, 87, 88]. A similar situation was found in the comparison of the dependence of log[$\sigma'(f)/\sigma_{dc}$] on f/f_0 from two $x$$K_2O$-(1-$x$) GeO_2 glasses with $x = 0.20$ and 0.0023 by Jain et al. [88] (see Fig. 6 in this reference and note the similarity to Fig. 4.18 in here). The difference in the slope of increase of log[$\sigma'(f)/\sigma_{dc}$] above the 0 value between the $x = 0.20$ and 0.0023 glasses dashes any hope of obtaining a master curve by any horizontal shift of data. Surprisingly, this result published in 1998 was not cited in the 2000 paper of Sidebottom and Zhang (SZ) [80], and in the 2008 review by Sidebottom [79].

Changes of $M^*(f)$ and $\Delta\varepsilon$ with composition were shown by SZ in $(K_2S)_x(B_2S_3)_{1-x}$ and by PM in $(Na_2S)_x(B_2S_3)_{1-x}$ glasses, indicating changes of breadth of ionic conductivity relaxation times with composition. Consistently, we find the frequency dispersion of log[$\sigma'(f)/\sigma_{dc}$] also changes with composition in the $(Na_2S)_x(B_2S_3)_{1-x}$ glasses. Therefore it is a mystery that SZ [80] can produce a nearly perfect master curve from the data of $(K_2S)_x(B_2S_3)_{1-x}$ for x in a similar range from 0.0005 to 0.05. The mystery cannot be solved until SZ show the raw log[$\sigma'(f)/\sigma_{dc}$] data separately they took from Patel's thesis to construct the master curve.

Better if they compare them under the same condition as done by PM in Fig. 4.16 here. It is important to know whether all data of $(K_2S)_x(B_2S_3)_{1-x}$ in Patel's thesis had been considered to obtain the scaling. The assertion of Sidebottom based on scaling of $(K_2S)_x(B_2S_3)_{1-x}$ that "This finding proves conclusively that the correlated motion is not a consequence of any interaction between mobile ions." is at odds with Monte Carlo computer simulations of electrical relaxation in a disordered Coulomb lattice gas of ions, when analyzed in the modulus representation, reproduce just such an decrease in width of dispersion with decreasing strength of ion–ion interactions [89–91]. Similar conclusions were drawn from Monte Carlo simulation of the spin lattice relaxation time of another disordered Coulomb lattice gas [92, 93], where again it was found that a decrease of Coulomb interaction strength is accompanied by an decrease in width of dispersion.

4.2.1.3 Reaching a Dead End After Scaling

In the previous section we have shown, except for the glasses $(K_2S)_x(B_2S_3)_{1-x}$ with x ranging from 0.0005 to 0.05 that Sidebottom took from the thesis of Patel, no other case support that a genuine master curve can be obtained for $\log[\sigma'(f)/\sigma_{dc}]$ data from glasses with orders of magnitude difference in ion concentration. Also in all cases including $(K_2S)_x(B_2S_3)_{1-x}$, the change of $M^*(f)$ and $\varepsilon'(f)$ with composition contradicts perfect scaling of $\log[\sigma'(f)/\sigma_{dc}]$. Changes of $M^*(f)$ and $\varepsilon'(f)$ can be seen in plotting these quantities linearly vs. $\log f$. Success in scaling of $\log[\sigma'(f)/\sigma_{dc}]$ is not complete until success in scaling $\sigma'(f)/\sigma_{dc}$ is also demonstrated at least for some range of $\sigma'(f)/\sigma_{dc}$ from 1 and up to a few tens times larger. In general the physical and chemical structure of the glasses as well as the ion-ion separation change a lot with orders of magnitude change of ion concentration. If indeed the shape of the frequency dispersion of $\log[\sigma'(f)/\sigma_{dc}]$ were independent of the enormous change in ion density, then this finding is spectacular, and deserve theoretical explanation. Disappointingly, none of the scaling proponents or anyone else has given explanation to this spectacular 'finding', or even just a physical reasoning. For CKN, the change of frequency dispersion of $M^*(f)$ and $\Delta\varepsilon$ with temperature is companying the decoupling of ion dynamics from structural relaxation [17] and also with glass transition, and there is an explanation given [34, 70]. By scaling $\log[\sigma'(f)/\sigma_{dc}]$ data of CKN at different temperatures to obtain a master curve, Sidebottom not only denies the physics involved with decoupling [17], but also leads to no further application, except the assertion that somehow his scaling works. From all papers published to demonstrate the purported scaling, we have not seen any theoretical explanation, connection with any other property or established phenomenon of ion dynamics, or any applications. Therefore, the scaling studies leads to a dead end, serving no purpose except adding distraction to retard real progress of the field.

4.2.1.4 Accurately Calculated σ_{dc} from the Kohlrausch Fit to M*(ω)

The stretched exponential fit to the $M^*(\omega)$ data deviates only at high frequencies. Since high frequency corresponds to short τ which makes negligible contributions to $<\tau>$ and $<\tau^2>$, the results calculated by Eqs. (4.17) and (4.18) are excellent approximations to σ_{dc} and ε_s respectively. The value of σ_{dc} calculated from Eq. (4.17) with β, in the Kohlrausch function used in conjunction with Eq. (4.12) to fit the experimental data of $M^*(\omega)$, agrees with the measured dc conductivity to within a few percent for a wide variety of materials [17, 18, 25, 30]. It has also been shown for an ionic glass that the KWW function accounts for over 80 % of the conductivity relaxation strength [5, 6].

In actual experiments, often there is an additional capacitive contribution to $\varepsilon'(\omega)$ from the layers of surface charge referred to as the electrode surface polarization. This unwanted contribution complicates the $\varepsilon'(\omega)$ data, and makes the analysis of the measurements in the $\varepsilon^*(\omega)$ representation uninviting and the interpretation ambiguous. Besides, $\varepsilon''(\omega)$ data show monotonic decrease with increasing frequency and it is not clear how to deduce a characteristic τ or average $<\tau>$ of the mobile ions. This comment applies also to the $\sigma'(\omega)$ data. Although σ_{dc} can be obtained from $\sigma'(\omega)$ at sufficiently low frequencies, on further increase of frequency $\sigma'(\omega)$ increases monotonically. Some model has to be used to fit the frequency dependence of $\sigma'(\omega)$ in order to deduce τ or average $<\tau>$. Moreover, the imaginary part of complex conductivity, $\sigma''(\omega)$, has received no attention by those workers who consider exclusively data in the form of $\sigma'(\omega)$. In contrast, measurements represented by $M^*(\omega)$ provides, via the peak frequency ω_p of $M''(\omega)$, a characteristic conductivity relaxation time, $\tau = 1/\omega_p$, without the need of any fit. Alternatively, τ^* can be obtained from the fit to $M^*(f)$ by the Fourier transform (Eq. 4.10) of the Kohlrausch function (Eq. 4.15), and $<\tau>$ from Eq. 4.16.

To be demonstrated by the results from many experimental studies throughout this chapter and chapters to follow, the value of τ^* and its properties are correlated or determined by the value of $(1-\beta) \equiv n$, or alternatively the full-width at half-maximum (FWHM) of the $M''(\omega)$ loss peak. These relations between n and properties of τ^* lead to deeper insight into the microscopic dynamics of the ions, and are in agreement with predictions of a theoretical model emphasizing the importance of ion-ion correlation through their interaction.

4.2.1.5 Making Easier for Anyone to Fit M*(ω) and Determine β

A relation exists between n and W, ratio the full widths at half-maximum of the observed loss peak to that of an ideal Debye loss peak (=1.144). It is given by

$$n \equiv (1 - \beta) = 1.047\left(1 - W^{-1}\right) \tag{4.20}$$

from Dixon [94]. Thus, without actually fitting $M''(\omega)$ by the Fourier transform of the Kohlrausch function, the value of n or β can be determined from W. There is a relation between τ^* and the peak frequency ω_{max} of $M''(\omega)$ given by $\log_{10}(\omega_{max}\tau^*) = -0.263(1\text{-}\beta)$] [95; D. Lellinger et al., 1994, unpublished]. Since β of most ionic conductors is larger then 0.40, ω_{max} is practically equal to $1/\tau^*$.

One problem faced by others in fitting their data expressed as $M^*(\omega)$ by the Fourier transforms of the Kohlrausch functions is that the latter are not readily available. This problem is alleviated by providing the Fourier transforms of the time derivative of the Kohlrausch functions with different values of the exponent $n = (1-\beta)$. These can be downloaded from Additional Material of this book from http://extras.springer.com. In this way, anyone can easily fit the experimental $M^*(\omega)$ data to Eqs. (4.12) and (4.15) and determine the exponent. We also provide in the Additional Material a method of how to perform Fast Fourier Transforms. The interested reader can use the method to generate the Fourier transforms of the Kohlrausch functions themselves.

In fitting these transforms to data of $M^*(\omega)$, emphasis should be placed in obtaining good fit at lower frequencies. This is because low frequency data dominates the contribution to the dc conductivity as can be understood from Eqs. (4.13) or (4.16) and (4.17), and certainly the parameters, β and τ^*, from such fits will give by Eq. (4.17) a value of σ_{dc} close to the one measured experimentally. Moreover the deviations at high frequencies from such fits are natural, and actually are coming from faster processes including the secondary ion dynamics (resolved or unresolved) included in $M''(\omega)$ and the NCL from caged ion dynamics.

We have seen from the discussions in the above that data in the $M^*(\omega)$ representation reveals more features of ion dynamics, not possible if the same data are represented by $\sigma'(\omega)$ or $\varepsilon^*(\omega)$. There is yet another advantage of data presented as $M^*(\omega)$. It turns out there is the Coupling Model (CM) of relaxation and diffusion of complex interacting systems [12, 31, 53, 60, 62, 63, 70, 87, 96–104] which predicts the primary ion relaxation showing up in the $M^*(\omega)$ representation of data is given by Eq. (4.12) with the decay function $\Phi(t)$ assuming the Kohlrausch stretched exponential time dependence in Eq. (4.15). Furthermore, in the CM, the parameters, β and τ^*, are consequences of the correlation between ions in conductivity/diffusion due to ion-ion interaction. The narrowing of width of $M''(\omega)$ or increase of β with decreasing ion concentrations discussed before is clear indication that ion-ion interactions, and is the basis of the CM. Interactions and correlations determine ion dynamics and properties in ionic glasses, melts and crystals containing higher concentration of mobile ions. Since τ^* is determined by many-ion dynamics, its properties are often found to be anomalous. The CM has a time honored result for the many-ion dynamics that relates τ^* to the microscopic single ion (primitive) relaxation time τ_0 by the CM equation involving β. The relation spawns many applications to explain a multitude of properties of ionic conductivity and diffusion to be discussed later, many of which are anomalous and difficult to explain. The successes have provided insight of the many-ion conductivity relaxation originating from ion-ion interaction, which is the crux of the CM and supported by molecular dynamics simulations where all model potentials used has the ion-ion interaction term

[45, 64–66, 105, 106], and Monte Carlo simulations of a disordered Coulomb lattice gas model of the ionic conductor [89–93]. The CM is general and applicable to relaxation and diffusion in other interacting systems, one of which is the glass-forming liquids and glasses [53, 60]. Successes in explaining the properties of these other interacting systems by the predictions of the CM are worth noticing by readers who are interested mainly in the conductivity of ionic systems.

The anomalous properties of ionically conducting systems and the explanations given by the CM will be presented later in this chapter and in other chapters. We hasten to point this out in order to justify the attention and preference we give to the electric modulus and the CM. As we shall see in the next section on the $\sigma'(\omega)$ representation of data, results from model analysis of $\sigma'(\omega)$ have made little or no headway in explaining the same anomalous properties.

4.2.2 *Jonscher Expression and Augmented Jonscher Expression to Fit $\sigma'(f)$*

Other expressions to fit the frequency dependences of σ' and ε' were proposed by Jonscher [39, 107]:

$$\sigma'(\omega) = \sigma_{dc} + A\omega^n = \sigma_{dc}[1 + (\omega/\omega_2)^n] \tag{4.21}$$

$$\varepsilon'(\omega) = \varepsilon_\infty + [A/\varepsilon_0 \cot(n\pi/2)]\omega^{n-1} \tag{4.22}$$

In Eq. (4.21), the parameter ω_2 is the frequency at which $\sigma'(\omega_2)$ is equal to $2\sigma_{dc}$, and it has no deeper physical meaning other than that. If the consideration is restricted to the $\sigma'(\omega)$, the Jonscher expression given by Eq. (4.21) is easy to use. However, as pointed out by Moynihan [72], Eq. (4.22) predicts that ε' diverges as ω^{n-1} with decreasing frequency. This diverging ε' is associated with the ion dynamics, and should not be confused with the electrode surface polarization mentioned before. Hence the Jonscher's expression is *unphysical*, and certainly it cannot predict ε_s and $\Delta\varepsilon$.

As evident from the log-log plot of $\sigma'(f)$ vs. f in Figs. 4.3, 4.8, 4.10 and 4.11, the slope increases monotonically with increasing f. The Jonscher expression, Eq. (4.21) with a constant fractional exponent n fails to account of the $\sigma'(f)$ data at high frequencies and/or low temperatures. Furthermore, at sufficiently high frequencies and/or low temperatures, $\sigma'(f)$ tends to assume the f^{1-c} frequency dependence with c a positive number and value close to zero. This behavior was seen in alkali silicate glasses for the first time in the GHz range by Robert Cole and coworkers in 1989 [108]. Noticing this behavior in their study, Nowick and coworkers [42] were led to suggest an augmented form of the Jonscher expression,

$$\sigma'(\omega) = \sigma_{dc} + A\omega^n + A'\omega \tag{4.23}$$

to fit the data. The term $A\omega^n$ fits the lower frequencies part of the data, while the $A'\omega$ term accounts for the high frequency part. The $\varepsilon'(\omega)$ accompanying the augmented $\sigma'(\omega)$ has not been given. By inspection of Fig. 4.3, it is clear that experimentally A is highly temperature dependent, but A' is weakly temperature dependent. The Jonscher expression as well as the augmented Jonscher expression are specifically proposed to fit only $\sigma'(\omega)$. The imaginary part $\sigma''(\omega)$ accompanying the real part of the augmented Jonscher $\sigma'(\omega)$ has not been given, and hence the functional forms of $\varepsilon^*(\omega)$ and $M^*(\omega)$ related to the augmented Jonscher $\sigma^*(\omega)$ by Eqs. (4.4) and (4.5) are unknown. This is a drawback of the augmented Jonscher expression. In a special section on the nearly linear dependence of $\sigma'(\omega)$ on ω to be presented much later, we shall show by experimental data that the term $A'\omega$ representing the caged dynamics is not an *additive* contribution as proposed in Eq. (4.23) by the augmented Jonscher expression. Thus Eq. (4.23) is fundamentally incorrect, although it is commonly used to fit data.

We have seen from Figs. 4.8 and 4.10 in the case of the ionic liquid and procainamide HCl that the plots of $\log\sigma'(f)$ vs. $\log f$ totally miss the secondary ionic relaxation found in $M^*(f)$ and $\varepsilon^*(f)$. Therefore, fitting conductivity relaxation data in terms of $\sigma'(f)$ by the Jonscher expression or the augmented Jonscher expression runs the risk of missing an important process of the ion dynamics found in $M''(f)$ and $\varepsilon''(f)$.

At the end of the previous section on electric modulus, mention is made on the scanty use of the parameters A or ω_2 and A' in the expressions (4.21) and (4.23) to explain properties. This weak link will become clear when we come to examine those remarkable properties later. Before that, we can see this deficiency from the contents of a recent review of ionics [2] by authors (except P. Maass) who are advocates of representation of conductivity relaxation data by $\sigma'(f)$. Despite in this review the ionic conductivity data are given exclusively in terms of $\log\sigma'(f)$ vs. $\log f$, these authors are fair in showing the limitations. For example they pointed out the problem of using Eq. (4.21) to obtain the density of mobile ions N by others in the literature. The crossover frequency $f_2 = \omega_2/2\pi$ in Eq. (4.21) was identified with a 'hopping rate' in the Nernst-Einstein relation, which gives a formal expression, $N = (6k_BT/q^2a^2)(\sigma_{dc}/f_2)$, to determine N, where a is the jump length assumed to be constant. The authors of the review pointed out that even if one accepts that the Jonscher expression Eq. (4.21) fits well $\sigma'(f)$ in the low-frequency regime, it generally fails at higher frequencies. From this they concluded that the estimate of an effective number density of 'mobile ions' based on the equation above is questionable.

In the review [2], the authors discuss electrode polarization effects, which is extraneous to the dynamics and mechanism of ion conduction/diffusion and the core problem. They discuss the mixed alkali effect which is germane, but hardly the experimental facts considered have specific relation to $\sigma'(f)$. In contrast the electric modulus representation of the data in conjunction with the change of ion-ion correlation in mixed alkali glasses had been used to give an explanation of the mixed alkali effect [109], and confirmed by molecular dynamics simulations (see Chap. 10). The importance of ion–ion correlation/interaction in considering the MA effect was also pointed out by Maass [110].

They discuss time-temperature superposition (TTS) of $\sigma'(f, T)$ data taken at different temperatures. TTS means $\sigma'(f,T)$ for all T can be written as $\sigma'(\omega, T) = \sigma_{dc}(T)f[\omega/\omega^*(T)]$, where $f(u)$ is the so called scaling function [74, 77–79]. If the Jonscher expression given by Eq. (4.21) is applicable to describe $\sigma'(\omega,T)$, then $\omega^*(T)$ is to be identified with $\omega_2(T)$. In demonstrating the TTS, not included are data of $\sigma'(f,T)$ at higher frequencies and lower temperatures where the $\sigma'(f,T)$ assumes the dependence given by Eq. (4.7), corresponding to the NCL of Eq. (4.6). This is because the temperature dependence of the NCL are so different from $\omega^*(T)$ as can be seen in Figs. 4.3, 4.5 and 4.10. If TTS holds for data in $\sigma'(f,T)$, it will hold also for data presented in $M''(f,T)$ and $\varepsilon''(f,T)$ because they represent the same measurements. So this property, if it holds, is not uniquely possessed by $\sigma'(f,T)$. In glassy ionic conductors and if the range of temperature considered is far below T_g, change of the structure of the glassy matrix is insignificant. Therefore TTS is expected to hold if the many-ion dynamics due to ion-ion interaction is the principal cause of the frequency dependence of $\sigma'(f,T)$, and thus TTS is unsurprising or a trivial property. However TTS can be surprising as well as a problem to those believing that the frequency dependence of $\sigma'(f,T)$ originates simply from a distribution of energy barriers because it can change with temperature. Actually more interesting and challenging are the case where TTS does not work such as CKN [17] and CdF_2–LiF–AlF_3–PbF_2 (CLAP) [111] above T_g and the crystalline lithium ionic conductor $Li_{0.18}La_{0.61}TiO_3$ (LLTO) [112, 113]. There must be new physics behind the breakdown of TTS in these ionic conductors, like that found in polymer viscoelasticity [60, 114, 115]. Exploring the physics that cause the failure of TTS is more constructive and meaningful [34, 113] an endeavor than just providing a plausibility to rationalize the failure [2].

The authors of the review [2] also put emphasis on a relation between the parameters ω_2 and σ_{dc} that came out from the use of the Jonscher expression (4.21) to fit data. Referred to in the literature as the Barton-Nakajima-Namikawa (BNN) relation [116–118], it is given by

$$\omega^* = \sigma_{dc}/[p\varepsilon_0\Delta\varepsilon] \tag{4.24}$$

where p is a constant of order of unity, $\Delta\varepsilon = (\varepsilon_s - \varepsilon_\infty)$ is the dielectric strength, and ω^* is a frequency the definition of which varies from authors to authors. The importance of the BNN relation is overblown because we can trace its origin to the basic Maxwell relation, $\sigma_{dc} = \varepsilon_0\varepsilon_\infty/<\tau>$. The latter can be rewritten in the form $\sigma_{dc} = \varepsilon_o\varepsilon_\infty/<\tau>= \left[\varepsilon_o\Delta\varepsilon/(\omega^*)^{-1}\right](1/\omega^* <\tau>)(\varepsilon_\infty/\Delta\varepsilon)$. Comparing this with the BNN relation rewritten as $\sigma_{dc} = p\varepsilon_o\Delta\varepsilon/(\omega^*)^{-1}$, it follows that we have the relation, $p = (1/\omega^* < \tau >)(\varepsilon_\infty/\Delta\varepsilon)$. The first factor, $(1/\omega^* <\tau>)$, of p has value of order 1 because ω^* is the reciprocal of a conductivity relaxation time whatever is its definition. Demonstrated before in Fig. 4.6 is the accurate account of $\Delta\varepsilon$ by the expression in Eq. (4.19) where β and τ^* are the parameters of the Kohlrausch

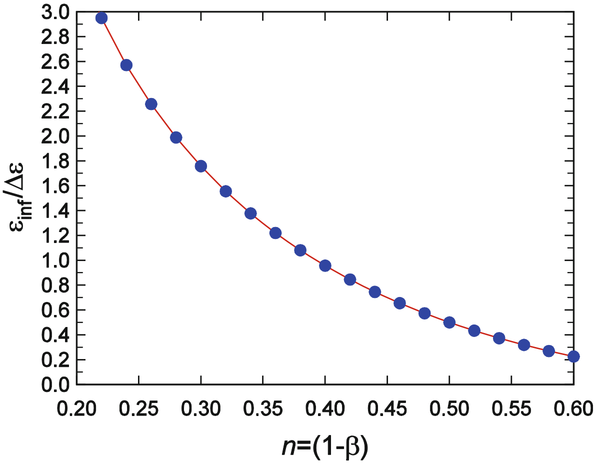

Fig. 4.19 The ratio $\varepsilon_\infty/\Delta\varepsilon$ calculated as a function of $n = (1-\beta)$

function that fits the data represented by $M''(\omega)$. The second factor of p, $(\varepsilon_\infty/\Delta\varepsilon)$, from Eq. (4.19) is given by $\varepsilon_\infty/\Delta\varepsilon = 1/\left\{\beta\Gamma(2/\beta)/[\Gamma(1/\beta)]^2 - 1\right\}$, and its values have been calculated as a function of $(1-\beta)$ and shown in Fig. 4.19. The range of $(1-\beta)$ is restricted from 0.30 to 0.60 because the ionic glasses considered for the BNN relation in Refs [116–118]. have β values within this range. The values of $(\varepsilon_\infty/\Delta\varepsilon)$ is of order 1. Thus p, as the product of the two factors, is also of order 1.

The purpose of discussing the contents of the recent review [2], which exclusively consider conductivity relaxation data in $\sigma'(f)$, is to show as an example the parameters deduced from $\sigma'(f)$ have not been used to tackle any significant and anomalous properties of ion dynamics to be presented and discussed in the remainder of this chapter. There is no theory or model based on $\sigma'(f)$ we know of that can explain many of the properties. On the other hand, there is the Coupling Model which can explain the anomalies by utilizing the parameters of the data in the $M^*(\omega)$ representation. For these reasons, if the purpose of the reader is fundamental understanding of the ion dynamics through the anomalous properties, then conductivity relaxation data must be considered primarily in the $M^*(\omega)$ representation.

4.3 Relevance of Theories and Models to Experimental Findings

Brief reviews of theories and models of ionic conductivity, diffusion, and relaxation have been given in a previous chapter. Here we critique them in terms of their range of applicability and validity to established phenomena and important experimental findings that we know of today. Theories and models proposed a long time ago naturally cannot address many new experimental facts discovered since then. However we separate them into two classes. In one class are those that have not been developed any further since they were proposed years ago, have limited applications, and hence need not be taken into detailed consideration in this chapter. In the other class are those maintained by their proponents to be still viable for understanding ion dynamics up to the present time. More attention is paid to theories and models that continue to be applied to address experimental results. Although molecular dynamics and Monte Carlo simulations are computer experiments performed to explore and observe some specific property and are not theory, the results are of interest because the relevance depends on the either the potentials or the model Hamiltonian chosen in molecular dynamics simulations and/or in Monte Carlo simulations. Therefore we also mention the results of some simulations as well.

Among theories belonging to the first class, one is based on random walk diffusion, yielding the following result of the dc conductivity [119],

$$\sigma_{dc} = \left(Ne^2a^2/kT\right)\gamma c(1-c)\omega_h. \tag{4.25}$$

Here N is the number of equivalent sites, γ a geometrical factor, c the concentration of mobile ions, a the jump distance, and ω_h is the jump rate. Obviously this theory does not address the dynamics of ions. To account for the frequency dispersion of the dynamics, others have modified the theory by assuming a distribution of jump rates. Another notable theory of conductivity in glass is by Anderson and Stuart [120]. The theory proposes that the energy barrier opposing motion between sites consist of an electrostatic work term, and a short range repulsion term. The number of sites is fixed and the mobile ion concentration is temperature independent as in the so-called 'strong electrolyte' view of electrical conduction. There is the 'weak electrolyte' view which postulates the existence of two types of sites, and conduction is dominated by the ions thermally activated to the higher energy sites. All these models are principally concerned with dc conductivity and have no predictions on dynamics of ions. In the present days, advances in molecular dynamics can calculate the energy barrier of ion conduction [121], and the interatomic potential chosen in computation basically replace the postulates of Anderson and Stuart.

In the second class of theories and models, surprisingly there are only a few that are still maintained by the proponents to be relevant, or are applied continuously to new research results of the present time. They have been introduced before in Chap. 2.

4.3.1 Random Barrier Models

The random barrier model (RBM) [9, 122–125] considers jumping of a single particle to neighboring sites on a lattice with identical site energies, but the energy barriers for jumps are randomly drawn from a smooth probability distribution that is static in time. Long range motion leading to dc conductivity is accomplished by percolation [126, 127]. Thus the RBM and its generalizations are all single-particle dynamics models without considering ion-ion interactions. The RBM can generate the frequency dependence of $\sigma'(f)$ to resemble the experimental data, consistent with the BNN relation, and in scaled units becomes independent of both temperature and activation energy probability distribution, as shown by computer simulations [124, 125]. The results and predictions of the RBM are limited to these few items. Moreover, the constructs (or assumptions) of the RBM, i.e. barrier energy distribution and the critical percolation energy barrier, have not been validated for any realistic ionic conductor. Even if the constructs were valid for a particular ionic conductor, these constructs are not known quantitatively and hence the results from the RBM cannot be compared with experimental data. This limitation of the RBM is honestly admitted by the proponent with the statement "The RBM scaling function is close to, but rarely identical to those of experiments" when comparing with experiment in Fig. 4.6a in Ref. [2]. The Fig. 4.6a of Ref. [2] shows the RBM function not fitting the frequency dependence of $\sigma'(f)$ with values less than a factor of 2 above σ_{dc} of the lithium phosphate glass. Despite its long history, the RBM has no serious applications beyond the ability to generate the frequency dependence of $\sigma'(f)$ resembling the experimental ones. Even so, the RBM is academic because its constructs and assumptions have not been verified microscopically for any specific ionic conductor, and the fit have not been used to address additional property in any realistic ionic conductor.

4.3.2 Jump Relaxation Models and the MIGRATION Concept

The Jump Relaxation Models was proposed by Funke [128, 129] and coworkers [130, 131]. In the collection of Jump Relaxation Models, the most recent version is called the MIGRATION concept (MC) [14, 131–135]. The physical picture of the series of jump relaxation models by Funke et al. is related to the Debye–Falkenhagen-type arguments for dilute and strong liquid electrolytes [136], but the effect is more pronounced due to the high number density of mobile charge carriers in ionic conductors and stronger Coulomb interactions between them. The consideration starts from a hop of the ion to neighboring site at time zero. The hop creates a mismatch in the sense that its momentary position and the minimum of its cage-effect potential no longer coincide. The mismatch causes the system to respond. There are two competing processes to reduce the mismatch. One is the single-particle route, with the ion hopping backwards. The other is the many particle route, with the neighbouring ions rearranging, thus stabilising the ion at its new position. When this is achieved, an elementary step of macroscopic transport has been completed by the ion. As stated by Funke in a review [137]: ". . .. the high number density of mobile charge carriers implies that the Coulomb interactions between them can no longer be ignored", the frequency dispersion of $\sigma^*(\omega)$ predicted by his different versions of jump relaxation models in ion conductor with very low concentrations of ions will be different from that with high concentration.

Funke gave a historical perspective of the development of the science and technology of solid state ionic in an article [137] with the title “Solid State Ionics: from Michael Faraday to green energy—the European dimension”. Surprisingly, there is no mention of the study of ionic conductivity relaxation in a Leyden glass jar by R. Kohlrausch in 1854 published in Ref. [67], where the stretched exponential function (now known by his name) was proposed to fit the experimental data.

In the latest version of Funke’s models, MC [14, 134], three coupled rate equations were formulated to describe the ion dynamics based on the time-dependent correlation factor, $W(t)$. They are given by:

$$-\frac{\dot{W}(t)}{W(t)} = -B\dot{g}(t); \quad -\frac{\dot{g}(t)}{g(t)} = \Gamma_0 W(t)N(t); \quad N(t) = N(\infty) + [Bg(t)]^K \tag{4.26}$$

where Γ_0 is the elementary hopping rate while B and K are parameters. $N(t)$ is the effective number of mobile neighbors that, in spite of ongoing shielding, still notice the dipole at time t. For the decay of $N(t)$ described by the last one in (4.26), an empirical function has been chosen that yields excellent agreement with experimental conductivities and permittivities. $N(\infty)$ is the effective number of nearest neighbors, i.e., of those ions that never get shielded. This number determines the low-frequency limiting value of the permittivity.

Once $W(t)$ is obtained by solving the three equations in (4.26), the complex conductivity $\sigma^*(\omega)$ scaled by σ_{dc} (another parameter of the model) is obtained via

$$\sigma^*(\omega)/\sigma_{dc} = 1 + \int_0^\infty [W(t)/W(\infty) - 1]\exp(-i\omega t)dt \tag{4.27}$$

where

$$W(\infty) = \sigma_{dc}/\sigma_{HF} = \exp(-B) \tag{4.28}$$

and σ_{HF} is the high frrequency limiting conductivity.

The value of the parameter K has an effect on the shape of the conductivity spectra close to the onset of the dispersion above $\sigma'(\omega)/\sigma_{dc} = 1$. There is an additional result for $\varepsilon'(\omega)$ from the MIGRATION concept given by

$$\varepsilon'(\omega_s) = \int_0^\infty [W(t_s)/W(\infty) - 1]\cos(\omega_s t_s)dt_s \tag{4.29}$$

where $\omega_s = \omega/\omega_0$ and $t_s = t\omega_0$, and ω_0 marks the onset of the conductivity dispersion of $\sigma^*(\omega)$ obtained from Eq. (4.29) on the ω-scale. However, results of $\varepsilon'(\omega)$ are seldom given together with $\sigma^*(\omega)/\sigma_{dc}$.

Value of K that is smaller or larger has to be chosen in order to fit the experimental data of $\log[\sigma'(\omega)/\sigma_{dc}]$ having an onset of the dispersion which is less or more gradual respectively. Different values of K is needed to fit data of various ionic conductors. For example, CKN at 393 K requires $K = 0.2$, and $K = 1$ at 353 K, and $0.3Na_2O$-$0.7B_2O_3$ needs $K = 1$ [134]. For the 0.45 LiBr-0.56

$Li_2O \cdot B_2O_3$ glass, the fit requires $K = 2$ [131]. The value of $K = 2.3$ was used to fit the data of Ag_2S-GeS_2 at 273 and 183 K, albeit poorly [131]. For the γ-$RbAg_4I_5$ at 113 K, the fit requires $K = 2.6$. Fit to the conductivity spectra of the ionic liquid, BMIm-BF4, requires $K = 1.9$ [14]. Conductivity isotherms of powdered 0.78 $AgI \cdot 0.165\ Ag_2O \cdot 0.055\ B_2O_3$ glass, taken at −110 °C, −130 °C and −155 °C, were fitted with MIGRATION concept (MC) model spectra obtained with the values of the shape parameter K are 2.4, 2.7 and 3.0, respectively [138]. The parameter K is equal to 1 to fit data of a salt-in-polymer electrolyte, i.e., of 1 mole $NaPF_6$ dissolved into a crosslinked PEO-PPO random copolymer [139]. Hence the parameter K is a critical but adjustable fitting parameter in determining the shape of dispersion in the important range of the rise of $\sigma'(\omega)$ above σ_{dc} of ion dynamics, as discussed in connection with the Jonscher expression and the ion hopping frequency ω_2 in Eq. 4.21. In the fits to experimental data, the other parameters Γ_0 and B have to be chosen in addition to K.

At low temperatures, the conductivity spectra over a broad frequency range is composed of the dynamics of mobile ions described by MC at lower frequencies and the nearly constant loss (NCL) at higher frequencies. On further decrease in temperature, the mobile ion dynamics can be moved out of the experimental frequency window, and observed is entirely the NCL. An example is taken from the isothermal $\log\sigma'(\omega)$ vs $\log\omega$ spectra of $0.3Na_2O$-$0.7B_2O_3$ shown in Fig. 28 of Ref. [14]. Figure 4b in Ref. [134] or Figure 9 in Ref. [140] shows a master curve of $\log[\sigma'(\omega)/\sigma_{dc}]$ vs. $\log(\omega/\omega_0)$ after shifting data at different temperatures in the scaling of ω by ω_0, as done in the same manner as by Roling et al. [77] In the master curve [134, 140], the authors did not distinguish for the reader the data obtained at different temperatures, and the superposed data rises about 8.5 decades above the base line, $\log[\sigma'(\omega)/\sigma_{dc}] = 0$. For such a large range in values of log $[\sigma'(\omega)/\sigma_{dc}]$, the scaled data are composed of the mobile ion dynamics contribution at lower scaled frequency and the NCL at higher scaled frequencies. One can appreciate this point by examining the raw isothermal data of $\sigma'(\omega)$ to see that the data at 210 and 230 K in Fig. 28 of Ref. [14] had been used by Funke et al. to construct the master curve. The isothermal data at these two temperatures no doubt involves the NCL over broad range of frequencies. Notwithstanding, Funke and Banhatti has a solid line in the figure going through all the scaled data of $\sigma'(\omega)/\sigma_{dc}$ increasing by 8.5 decades. They stated [140] that the line comes from the "standard" model spectrum obtained from the MIGRATION concept. This is impossible because the results from the MC model is exclusively for mobile ion dynamics and long range ion conduction and diffusion, and cannot account for the NCL. The fact that the MC model can fit data not intended for raises doubt on the meaning of the fitting parameters, K, Γ_0 and B.

The same doubt arises in the excellent fit of the theory to the master curve of $\log[\sigma'(\omega)/\sigma_{dc}]$ with σ_{dc} increasing by 9 decades above σ_{dc} in $0.45LiBr \cdot 0.56\ Li_2O \cdot B_2O_3$ glass, shown in Fig. 13 in Ref. [131] or Fig. 1b in Ref. [141]. One can find the raw isothermal data at 148, 173, and 448 K in Fig. 1a used to construct the master curve in Fig. 1b of Ref. [141]. Obviously the $\sigma'(\omega)$ data at 148 K in some range of higher frequencies originate from the NCL. Furthermore, the NCL has

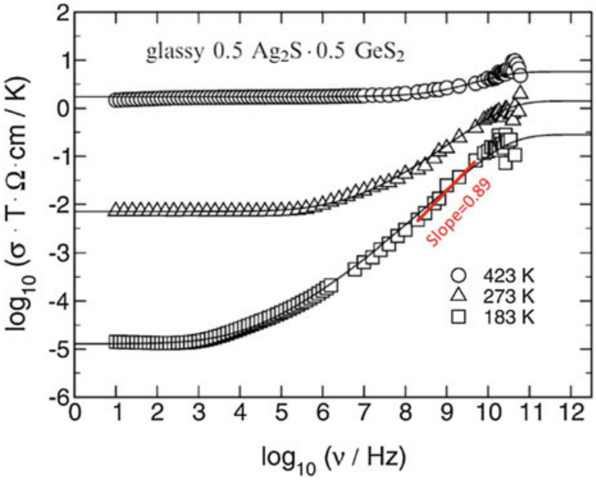

Fig. 4.20 Conductivity spectra of glassy $0.5Ag_2S–0.5GeS_2$. The *solid lines* are model spectra from MC [134]. The *red line* indicate the slope is 0.89, and should be considered as the NCL or the "second universality" and distinguished from the "first universality". Surprisingly the MC fits both

weak temperature dependence (compare data from 123 to 223 K at 10^6 Hz in Fig. 1a of Ref. [141]). On the other hand, the $\sigma'(\omega)$ spectra derived from the MIGRATION concept is thermally activated for all ω. This is because both σ_{dc} and the high frequency conductivity σ_{HF} of MC are Arrhenius activated, and hence also $\sigma'(\omega)$ for all intermediate frequencies. This large difference in temperature dependence means that if the spectrum from the MIGRATION concept can fit the $\sigma'(\omega)$ data including the NCL at one temperatures (i.e., $\sigma'(\omega)$ data at 148 K included into the master curve in Fig. 1b of Ref. [141]), then it should fail to fit the NCL data at another temperature higher than 148 K.

Keen examination of the fits of the MC model to some data published by Funke et al. reveals that the quality of the fits in the important range, $1 \leq \sigma'(\omega)/\sigma_{dc} \leq 3$, is not satisfactory. Examples are the fits with $K = 2.3$ to data of Ag_2S-GeS_2 at 273 and 183 K in Fig. 3b in Ref. [134], or Fig. 11 in Ref. [140] reproduced here as Fig. 4.20, where the large size symbols used to represent the data cannot hide the lack of good fits. The solid lines are model spectra derived from the MIGRATION concept with $K = 2.3$. The fit of the 183 K $\sigma'(\omega)$ data covers 4.5 decades of increase from the σ_{dc} level. The high frequency part has slope 0.89 and is the NCL.

Other examples are the fits to the data of CKN at 393 and 353 K shown in Fig. 7 of Ref. [134]. Since fitting dispersion of $\log[\sigma'(\omega)/\sigma_{dc}]$ is the main goal of MC, the lack of good agreement in the most important range makes one wonders what is the use of the MC model.

4.3.2.1 Limitations of MC

From the description of the structure of the MC by the equations in (4.26) and (4.27), it becomes clear that the results from MC are limited to fitting the frequency dependence of $\log[\sigma'(\omega)/\sigma_{dc}]$. This limitation is obvious because in all the papers on MC cited here and in the reviews of Funke [137] and coworkers [14], the main application is just that. Furthermore, the values of the three fitting parameters, K, Γ_0 and B have to be adjusted to fit experimental data. K, which critically determine the shape of the frequency dispersion, has no fundamental significance given. The dc conductivity σ_{dc} is left as yet an another parameter, unrelated to the calculated frequency dispersion of $\log[\sigma'(\omega)/\sigma_{dc}]$ or any of the parameters K, Γ_0 and B used in fitting the data. Except for the fact that MIGRATION concept is based on a theoretical idea, the scope of its predictions and applications to ionic conductivity relaxation is very limited despite the model had been developed continuously over the last two decades.

In the open literature, so far the use of the MC model spectra to fit data has been exclusively done by Funke and his coworkers. This is understandable because of the nontrivial procedure to obtain a model spectrum to fit data. The steps involve solving the three coupled equations in (4.26) to obtain $W(t)$, performing the Fourier transform in (4.27) to calculate $\sigma'(\omega)/\sigma_{dc}$, while adjusting the parameters K, Γ_0 and B, to fit the data. Moreover, even after one has carried out these multiple steps to obtain a fit, the results do not go any further. The best one can say is that the MC can account for the conductivity frequency dispersion of the ionic conductor. Objectively speaking, the MC is impracticable for others to use for fitting the dispersion. Even if used to fit data, the parameters obtained in the fit do not lead to any further prediction or explanation of other properties.

4.3.3 Comparison of MC with CM

In the 2010 review of the *MC* and *Jump Relaxation Models* by Funke et al. [14], they mention other concepts, models and computer simulations published over the years, and stated that ‘all of them aiming at a description and/or modelling of broadband conductivity spectra’. Those considered by Funke are the Jonscher’s *power law*, Ngai’s *Coupling Model* (CM), *Monte-Carlo* simulations by Maass et al. [89, 142, 143], Dieterich’s *Counter-Ion Model* [144–146] and the *Random Barrier/Random Energy Models* of Dyre [122]. The characterization of the other studies by Funke et al. [14] as ‘all of them aiming at a description and/or modelling of broadband conductivity spectra.’ is incorrect. Although the papers by Maass et al. and Dieterich and coworkers are based on Monte-Carlo simulations, the results addressed also properties other than conductivity spectra, including the nuclear spin relaxation and Haven’ ratio. When putting the

Coupling Model (CM) into the same category, Funke et al. reference only three papers published in 1980 and 1981 [70]. It is true that these published 35 years ago at the birth of the CM are concerned principally with the conductivity relaxation spectra. However the continued development of the CM in the intervening years and up to the present time have contributed advances in many different aspects of ionic dynamics in different classes of materials in the vast field of ionic conductivity relaxation. The accomplishments up to 2010 in ionics alone was summarized in a book [60] covering other fields. The theoretical structure of the CM for ion dynamics has been expanded to include caged ion dynamics, manifested as the nearly constant loss, and it is terminated by the onset of the primitive relaxation [46, 48, 53, 64–66], and the same for glass-forming liquids [61, 147–152]. Hundred or so papers on various applications to various aspects of ion dynamics by the CM have been published in the period of 1982–2016. These advances will be brought out later in this chapter after the theoretical basis and prediction have been presented, and also in Chap. 5 on NMR, Chap. 6 on nanoionics, and Chap. 7 on ionic liquids. Hence, it is hard to understand why Funke et al. cite only these 35 years old papers when they characterize the CM in their 2010 review [14] and elsewhere [153].

Even harder to comprehend is the Sect. 4.3.3 entitled ‘Mutual Mapping of MC and CM’ in the review [153] where Funke et al. compare their recent and up-to-date MC model with the not-yet-fully-developed 1980 and 1981 version of the CM for ionic conductivity relaxation. As will be presented in detail, the fully developed CM long before the year 2007 of Ref. [153] has the caged dynamics (NCL) and primitive conductivity relaxation/secondary conductive relaxation. These processes precede the terminal primary ion conductivity relaxation with its correlation function given by the Kohlrausch stretched exponential function. The NCL is terminated by the onset of the primitive conductivity relaxation, and in turn the primitive conductivity relaxation time is related to the primary conductivity relaxation time by the CM relation [60]. The experimental data shown before in Figs. 4.7, 4.8, and 4.9 as well as those in Refs [46, 48, 53, 60, 64–66]. support the results of the fully developed CM. Therefore, it is hard to understand why Funke et al. compare the MC with the CM using for the latter its 35 years old version and neglecting the later developments.

A factual comparison between MC and the CM was given by us in Ref. [154]. In this paper we give credit to Funke for also recognizing the importance of ion-ion interaction. One can see some examples of the broad applications of the CM in this paper but that cannot be matched by the MC, and these are just part of the total number of CM applications over the years. The predictions of the CM are not only successful in ionic conductivity relaxation, but also in dynamics of glass-forming materials and systems in the glass transition problem, and polymer viscoelasticity [60]. The reason why the predictions of the CM are applicable to different interacting systems is because it is based on a fundamental physical principle discussed later.

4.3.4 Monte Carlo and Molecular Dynamics Simulations

The Monte Carlo simulation of ion dynamics [89, 142, 143], and the Dieterich's *Counter-Ion Model* [144–146] are computer experiments performed to bring out the effects of ion-ion interactions in ionic conductivity relaxation. The results from the simulations all indicate that ion-ion interaction is the origin of the frequency dispersion of conductivity, and lend support to theories of ion dynamics based on ion-ion interaction, which include the MC and the CM but not the random barrier models with or without percolation. Although instructive, Monte-Carlo simulations are not theory in the sense that they have no well-defined quantitative predictions, and cannot be used for treatment of experimental data to extract values of meaningful parameters. Nevertheless we give credit to these simulations for their contributions to the advance in the research on ion dynamics, particularly on the importance of ion-ion interaction.

Molecular dynamics simulations of glassy [65, 66, 106, 155–164] and crystalline [165] ionic conductors, a molten salt [151, 166, 167], and ionic liquids [162, 168–177] are an important part of this book. The methodology, applications, and results will be the subjects of Chaps. 8–11. Success of molecular dynamics simulations to reproduce ion dynamics of real material depends on the choice of the potential. In conductors where ion concentration is large, inevitably ion-ion interaction potential term has to be included in order for the simulations to be successful, and also in the case of theory.

4.4 The Coupling Model (CM)

Before 1978, the research activity of one of us (KLN) was totally in electron physics. In that year he was first exposed to some experimental results in relaxation and diffusion of non-electronic materials and systems [50]. The materials and systems are mostly condensed matter composing of densely packed and interacting ionic, atomic, and molecular units or particles in general. Although lacking any background and experience in the research areas, he immediately recognized that this is a many-body problem in irreversible statistical mechanics, and the importance of considering interactions between the basic units, without which a fundamental understanding of the dynamics of relaxation and diffusion and the properties of the transport coefficients cannot be attained. He was surprised by not finding any theory or model specifically consider ion-ion interaction in conductivity relaxation and diffusion of ionic conductors, or unit-unit interactions in relaxation and diffusion in other fields including glass transition of glass-formers with widely different physical and chemical structures. The vacuum confers the opportunity for him to explore ways to incorporate interaction into relaxation and diffusion. Interactions in most complex materials, such as liquid, glassy, and crystalline ionic conductors, van der Waals glass-forming liquids, polymers, inorganic and metallic glass-formers, and dense colloidal particles, involve potentials (e.g., Coulombic, dipolar, Lennard–Jones, and hard sphere, and etc.) that are anharmonic. In classical mechanics, such anharmonic interactions cause non-linear Hamiltonian dynamics (i.e. *chaos*) in the phase space of the system. Since chaos is fundamental and universal property [178, 179], it is logical to investigate the effect of interaction on ion dynamics based on classical chaos. This was his choice in 1979, but in the first try the semiclassical quantization of classical chaos was used, resulting in four publications in the same year [50, 180–182]. Since then a number of studies based on classical chaos [183–189] and other considerations [190–195] have appeared, but the original results of the CM on the many-body and cooperative relaxation and diffusion remains unchanged till the present times. The papers cited have been reviewed in great details in the book "Relaxation and Diffusion in Complex Systems" published in 2011 [60], and only the essentials will be given here. The first paper dedicated to ionic conductivity relaxation was published in 1981 [70]. The CM is clearly the pioneer in incorporating many-body effects in relaxation and diffusion of interacting systems, proposed earlier than other models, Monte Carlo and molecular dynamics simulations.

Starting in 1998, the CM has been extended to cover the processes that transpire before the many-body and cooperative relaxation [45, 46, 48, 53, 147, 150, 151]. The extension has expanded the predictions of the CM to cover the caged dynamics (NCL in susceptibility), the secondary relaxation, and the primary many-body and cooperative relaxation, and the relations between them.

We believe a physical description of the theoretical basis of the CM with some qualitative justifications, and a presentation of its predictions are more suitable in this book than a replication of the formal mathematical physics used before to derive the predictions and given already in publications and the 2011 book [60]. Besides we expect the majority of readers of this book are mainly interested in ionic conductivity relaxation, and they may be more interested in the predictions and results of the CM rather than the details.

4.4.1 The CM Based on Universal Statistics of Energy Levels

The first version of the Coupling Model (CM) [50, 180–182] on relaxation of interacting systems was published in 1979. In retrospect, this model is based on semiclassical quantization of nonlinear Hamiltonian mechanics, i.e. classical chaos [179, 196–200]. The interacting system is semiclassically quantized and the energy levels distribution is described by Wigner's statistical theory [201–203]. This theory of Wigner originated from his idea that the complex Hamiltonians of many-body interacting systems (in the original case considered by Wigner, it is that of heavy atom nuclei such as uranium) could be approximated by a random Hamiltonian representing the probability distribution of individual Hamiltonians for the purpose of finding the energy levels. This idea was then further developed with advances in random matrix theory and statistics. For systems invariant under

Fig. 4.21 A Wigner distribution fitted to the spacing distribution of 932 s-wave resonances in the interaction 238U + n at energies up to 20 keV. The Poisson distribution is shown for contrast

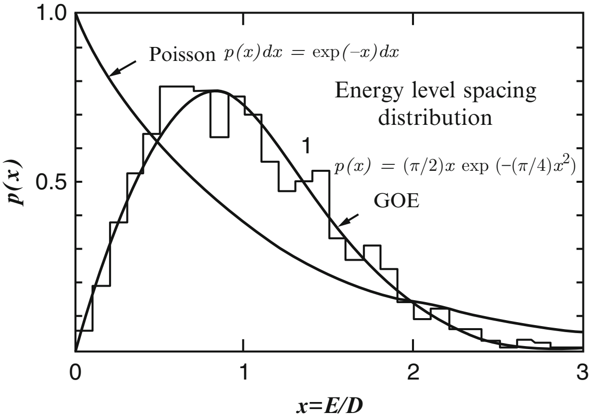

Fig. 4.22 Replotting the GOE in Fig. 4.21 as log vs. log

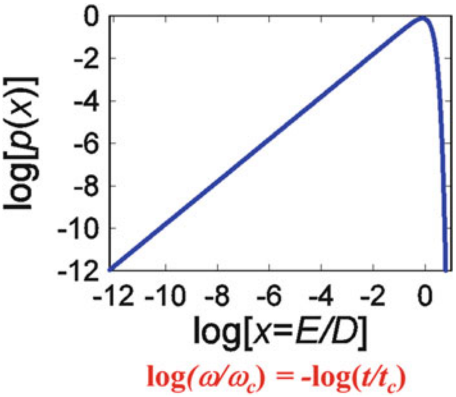

time reversal, it is given by the Gaussian Orthogonal Ensemble (GOE) in random matrix theory. It makes sense to use GOE because it has been shown to apply to a variety of atomic, molecular, nuclear systems [200–203] [A collection of original papers by E.P. Wigner and others on random matrices and applications can be found in refs. [204, 205]. In GOE, the distribution of level spacings E is given by the expression, $p(E/D) = (\pi/2)(E/D)\exp\left[-(\pi/4)(E/D)^2\right]$, of Wigner, where D is the average spacing (see Fig. 4.21). In the absence of interactions, the level spacings follow the Poisson distribution, drastic different from the GOE (see Fig. 4.21). GOE has the characteristic linear dependence of $p(E/D) \propto E/D$ which originates from energy level repulsions, and this dependence holds up to a cut-off high energy, E_c. When considering relaxation and diffusion, frequency ω or time t varies over many orders of magnitude, and logω or log$t$ is the appropriate variable. Since energy E correspond to ω or time $1/t$, we replot $p(E/D)$ vs. log(E/D) in Fig. 4.22, and put log (ω/ω_c) or log(t/t_c) under log(E/D), as label of the abscissa, to indicate the corresponding variables when considering relaxation. Like D, the magnitudes of

$\omega_c = E_c/\hbar$, where $\hbar$ is the Planck's constant, and t_c depends on the interaction strength determined by the potential of interaction, and it is insensitive to temperature or pressure. Stronger is the interaction strength, larger is D and ω_c and shorter is t_c.

The results given above brings out the physics that interactions has no effect on relaxation and diffusion at frequencies higher than ω_c or at times shorter than t_c. This is because the linear dependence of the level spacing distribution on E no longer holds for $E > E_c$, which corresponds to times shorter than $t_c \equiv (\omega_c)^{-1}$. So, if ion-ion interaction is the cause of the non-exponential time correlation function of many-body conductivity relaxation such as that given by the Kohlrausch function of Eq. (4.15), it is ineffective at times shorter than t_c, and the normalized correlation function is simply the one-body exponential function, $\Phi(t) = \exp(-t/\tau_0)$, of Debye in relaxation and of Einstein in Brownian diffusion.

Therefore, in the CM, at times shorter than $t_c \equiv (\omega_c)^{-1}$ the relaxation is a primitive or one-body (single ion) relaxation with constant rate $W_0 \equiv (\tau_0)^{-1}$, and the correlation function is given by $\exp(-t/\tau_0)$. Due to interactions and the onset of the linear level spacings distribution or correlations between the ions, the many-body relaxation governed by chaos takes over after crossing t_c. It is the response of the GOE energy level structure to the primitive relaxation that is used to account for the many-body relaxation which necessarily slows down its primitive relaxation rate W_0 [180–182]. Calculated by perturbation theory, the response coming from $p(E)$ with the linear dependence on E slows down the relaxation rate W_0 to have the time dependent form of

$$W(t) = W_0(\omega_c t)^{-n}, t > t_c, \tag{4.30}$$

and the correlation function to have the Kohlrausch form given by Eq. (4.15), for times longer than t_c. The power, n, called the coupling parameter, is a fraction of unity which increases with the strength of interaction. Thus, the relaxation rate of interacting many-body systems is time dependent. It is the primitive relaxation rate, $W(t) = W_0$ for $t < t_c$, and the many-body relaxation rate, $W(t) = W_0(\omega_c t)^{-n}$, when $t > t_c$. This crossover from the primitive to the many-body relaxation rate does not occur necessarily sharply at t_c but rather smoothly in a neighborhood of t_c, so that the correlation function and its derivatives are continuous across t_c. The factor, $\exp[-(\pi/4)(E/D)^2]$, in $p(E)$ effects the transition between the two rates. Its width parameter D suggests that the width of the neighborhood is of the order of t_c itself, and hence narrow, if there is no other factor like polydispersity of relaxation units entering into the problem. Some of the experimental data to be introduced later show that the crossover is quite sharp. In view of this and in the absence of reliable way to account quantitatively for the narrow crossover, the sharp crossover of the two relaxation rates at t_c is used to generate predictions. The correlation function $\phi(t)$ obtained from the CM rate equation, $\partial\varphi(t)/\partial t = -W(t)\varphi(t)$, by integration with $\tau_0 \equiv 1/W_0$ is given by

$$\phi(t) = \exp(-t/t_0), t < t_c, \tag{4.31}$$

$$\phi(t) = A\exp\left[-(t/\tau^*)^{1-n}\right], \quad t < t_c, \tag{4.32}$$

and continuity of $\phi(t)$ at t_c leads to the relation,

$$\tau^* = [(1-n)(t_c)^{-n}\tau_0]^{\frac{1}{1-n}} \tag{4.33}$$

and

$$A = \exp\{[n/(1-n)](t_c/\tau_0)\}. \tag{4.34}$$

When τ_0 is much longer than t_c, $A \to 1$, and

$$\phi(t) = \exp\left[-(t/\tau^*)^{1-n}\right], \quad t > t_c, \tag{4.35}$$

$$\tau^* = [(t_c)^{-n}\tau_0]^{\frac{1}{1-n}} \tag{4.36}$$

There is no difference between Eqs. (4.33) and (4.36) when the CM is used merely to predict the relation between the dependence of the many-body relaxation time τ^* with that of the primitive τ_0 on some variable U. For example if τ_0 has Arrhenius T-dependence with activation energy E_a, then both equations predict that the activation energy of τ^* is given by $E_a/(1\text{-}n)$. Quantitatively for the relation between τ_0 and τ^*, the two expressions make some difference particularly when n becomes larger. In that case, Eq. (4.33) should be used when τ_0 is not much longer than t_c for the sake of accuracy, as demonstrated in comparing prediction [206] with molecular dynamics simulation data [207, 208] where n has unusually large value. When using the prediction to deduce quantitatively τ_0 from the experimentally observed τ^* with known values of n and t_c, Eqs. (4.33) and (4.36) leads respectively to $\tau_0 = (t_c)^n(\tau^*)^{1-n}/(1-n)$ and

$$\tau_0 = (t_c)^n(\tau^*)^{1-n}. \tag{4.37}$$

The difference between the two expressions for τ_0 is not large, only a factor 2 for $n = 0.5$, and lesser for smaller values of n. For this reason, Eq. (4.37) is often used.

The significance of the CM equation (4.33) or (4.36) is that it makes a connection between the many-body relaxation time τ^* usually endowed with anomalous properties and the primitive one-body relaxation time τ_0, the properties of which are normal and known. Thus, the connection provides falsifiable explanations/predictions of the anomalous properties of τ^* from the known or familiar properties of τ_0. The connection is made via the Kohlrausch exponent n, and the crossover time t_c. These two parameters of the many-body relaxation naturally are ultimately determined by the interaction potential and its strength.

The equation (4.36) coupled with the Kohlrausch function (4.35) of the CM spawns many predictions that can be tested by experiments and used to explain anomalous properties. Many such tests and applications are given in the sections to follow. Since it was derived for complex Hamiltonians in general, the predictions form these equations should apply to relaxation and diffusion in interacting many-body systems of various kinds, and the dynamics of ionic conductors is only a special case. Thus, ever since the inception of the CM in 1979, the expected existence of universal relaxation and diffusion properties of interacting many-body systems has led to concurrent explorations of several fields using the two coupled equations (4.35), (4.36) as the tool [60]. It must be borne in mind that these equations hold strictly for systems in which all relaxation/diffusing units are identical and monodisperse, and heterogeneity is not introduced by boundaries, randomness, mixing, and etc. If extrinsic heterogeneity is present, these equations have to be modified by incorporating extraneous factors, and the test of applicability of the CM become less precise and direct, but nevertheless can be done. Moreover, the two coupled equations (4.35) and (4.36) strictly applies to the terminal many-body relaxation leading to steady state transport coefficients. Before reaching the terminal relaxation, the dynamics of ions have passed through several stages. The first stage is the dissipation of ions mutually confined in cages through the interionic potential, manifesting as the nearly constant loss (NCL) in $\varepsilon''(\omega)$ in Eq. (4.6), and $\sigma'(\omega)$ in Eq. (4.7). The caged ion dynamics have no characteristic time and continues with time indefinitely until the onset of the primitive ion relaxation corresponding to ion hop out of the cage singly or independently, which is the second stage. Thereafter, increasing number of ions cooperatively relax continuously with time (this is the third stage), until the maximum number (or length-scale L) of the heterogeneous ion dynamics is reached. The latter is the terminal or primary many-ions relaxation with time correlation function and relaxation time governed by Eqs. (4.35) and (4.36) [60].

The CM does not provide description of the motion of ions in space at the third and the final stage Notwithstanding, the CM had anticipated that these processes in interacting many-body systems is dynamically heterogeneous by pointing out [209] the analogy of the CM to the heterogeneous process in the solution of the ‘Dining Philosophers Problem’ in computer science [210], one year before the first experimental evidence of dynamic heterogeneity of structural α-relaxation was published [211].

In the CM, dynamic heterogeneity and Kohlrausch non-exponentiality, Eq. (4.35), are regarded as parallel consequences of the cooperative many-body molecular dynamics, but the former is not emphasized in the applications of the CM. Description of the motions as a function of time is best obtained by special experiment techniques like confocal microscopy for colloidal suspensions [212, 213] or by molecular dynamics simulations of ions [66] and especially designed computer simulation method for molecular liquids such as the Dynamic Lattice Liquid Model [214, 215]. Such description is worthwhile as well as pleasing to acquire, but being able to describe motions as a function of time does not necessarily mean that it can explain the anomalous properties of the terminal many-ion relaxation time, τ, while the CM equation can do just that via Eq. (4.36). Ever since it was first derived in 1979, this problem-solving capability of the CM continues to apply in the field of ionic conductivity relaxation and other areas, particularly the dynamics of glass-forming materials and systems [60].

4.4.2 Tracing the Key Result of the CM, $W(t) = W_0(\omega_c t)^{-n}$, Back to R. Kohlrausch

One of crucial results of the CM in the 1979 paper [180, 181], is the time dependent relaxation rate, $W(t) = W_0(t/t_c)^{-n}$. Nowadays, to many workers in the field of relaxation, R. Kohlrausch [67, 68] and his son and F. Kohlrausch [216, 217] are known for their introduction and use of the stretched exponential function to describe electrical and mechanical relaxations of materials. Not noticed or pointed out by others is that in the 1854 paper by R. Kohlrausch, on page 198 he actually started with the time dependent rate equation, $d(pQ_t - r_t)/dt = -bt^m(pQ_t - r_t)$, duplicated faithfully here. For the notations he used, m is a negative fraction of unity, b is a constant, and $(pQ_t - r_t)$ is the relaxing quantity he considered. By integration of the differential equation from $t = 0$ to $t = t$ and with $Q_t(t = 0) = Q_0$ and $r_t(t = 0) = 0$, he then arrived at $\log[(pQ_t - r_t)/pQ_0] = -[b/(m + 1)]t^{m+1}$. This is just the same as $(pQ_t - r_t)/pQ_0 = \exp(-Bt^{m+1})$, where $B = b/(m + 1)$. In other words, R. Kohlrausch derived the stretched exponential function from the time dependent relaxation rate bt^m, with $-1 < m < 0$. Using his own data, he deduced $m = -0.5744$, and $b = 0.4289$. F. Kohlrausch [216, 217] wrote down a similar equation, $dx/dt = -g \cdot x/t^n$, before getting the stretched exponential function. Now it becomes clear that the primary result of the CM, $W(t) = W_0(t/t_c)^{-n}$, is exactly the same as time dependent relaxation rate, bt^m, of R. Kohlrausch after putting $m = -n$, and $b = W_0(t_c)^n$. Notwithstanding, in the CM, from the rate equation, $d\phi/dt = -W(t)\phi$, and $W(t)$ given by $W_0 \equiv (\tau_0)^{-1}$ for $t < t_c$, and $W(t) = W_0(t/t_c)^{-n}$ for $t > t_c$, not only one can obtain the Kohlrausch function, $\exp[-(t/\tau)^{1-n}]$, but also the 2nd relation $\tau = [(1-n)(t_c)^{-n}\tau_0]^{1/(1-n)}$, where $\tau_0 \equiv 1/W_0$. This 2nd relation introduces new physics and immensely enhances the applications of the Kohlrausch function beyond an empirical function to fit data. In the CM, n is indicator of the slowing down and stretching to longer times of the many-body relaxation. As will be shown in many sections to follow, the 2nd relation can explain the experimentally observed anomalous and universal properties of τ of ion dynamics from the normal properties of the primitive ionic relaxation time τ_0 as well as the corresponding quantities of the dynamics in other interacting systems [60].

These important advances cannot be achieved without using the time dependent relaxation rate, $W(t) = W_0(t/t_c)^{-n}$, originally proposed in terms of bt^m with $-1 < m < 0$ by R. Kohlrausch phenomenologically. Therefore, when paying homage to Kohlrausch, I propose that it is more appropriate to cite Kohlrausch's fractional-power time dependent relaxation rate, bt^m with $-1 < m < 0$, instead of his widely known stretched exponential function, or at least together with it. The function follows as a consequence of the rate, bt^m, but not vice versa. Moreover, there can be different interpretations of the stretched exponential function, such as the more trivial one of distribution of linear exponentials due to randomness, while the interpretation of the rate, bt^m or $W_0(t/t_c)^{-n}$, is more restrictive and its origin has to be derived from some fundamental physics. This was done in the CM from quantum chaology [196], and the variety of consequences and predictions coming out from Eq. (4.36) have gone far beyond the Kohlrausch function alone.

Based on random-matrix behavior in the statistics of energy levels, the first version of the CM is a development under the field called *quantum chaology* by Berry [196, 197], who gave the following definition: "*Quantum chaology* is the study of semiclassical, but nonclassical, phenomena characteristic of systems whose classical counterparts exhibit chaos." From this definition of quantum chaology and the relation to the first version of the CM, it is clear that the results of the CM can be derived in model systems exhibiting classical chaos without resorting to random matix of quantum chaology as originally done in 1979. The next section briefly mention some examples of the derivations.

4.4.3 Coupling Model from Classical Chaos

In classical mechanics, it is well known systems with anharmonic interactions universally exhibit classical nonlinear dynamics (chaotic classical motion) [178, 179, 218]. In the 1980s, many publications show classically chaotic systems when quantized have quantum energy spectra characterized by the universal statistics of random matrix eigenvalue ensembles [179, 198, 199, 219, 220] [This subject is still actively being pursued at recent times, see 221]. Overwhelming experimental and numerical evidence supports this connection for systems as diverse as atomic nuclei, Rydberg atoms [204] and quantum billiards [222]. The relation between classical nonlinear dynamics and quantum energy spectra is natural because, in the macroscopic size regime, laws of classical mechanics are expected to emerge in the semiclassical limit, $\hbar \to 0$. It suggests that the many-body relaxation stems from classical nonlinear mechanics, and from which one can find another way to derive the CM equations applicable to relaxation/diffusion in systems exhibiting classical chaos. The first attempt in this direction involves the use of the characteristic of classical chaos, which is the emergence of complexity on infinitely fine scales in classical phase space. The structure of the infinitely fine phase space was used as basis of qualitative models to generate the Kohlrausch correlation function [184, 193]. Some residual order in phase space in terms of quasiperiodic motions (vague tori) was found to exist on a short time scale even in the chaotic regions of phase space for a large class of systems [223, 224]. The quasiperiodic motions are attributed to remnants of destroyed invariant tori in phase space This property ensures the relaxation/diffusion at short times is normal and its correlation function is given by the linear exponential of Eq. (4.31).

Starting from simple nonintegrable Hamiltonian models that exhibit classical chaos, the results of the CM have been reproduced [184–189, 225]. The crux of the CM is the existence of a rather sharp crossover of the relaxation function from linear exponential to the Kohlrausch stretched exponential, and this has been found from the numerical solutions of the simple models. Moreover, stretching (or n) increases with increase in nonlinearity (anhamonicity) or interaction strength of the Hamiltonian, consistent with the same expected heuristically from the CM on increasing the strength of coupling or constraints in glassforming substances, ionic conductors, and other interacting systems. In the following we reproduce one example.

4.4.4 Relaxation of Interacting Arrays of Phase-Coupled Oscillators

Consider an array of N oscillators, where the phase $\varphi_i(t)$ of the ith oscillator, $1 \leq i \leq N$, is coupled nonlinearly by a sine function to the phases of the other oscillators and obey the equation of motion [186, 189, 226],

$$\frac{d}{dt}\varphi_i = -\frac{K}{N}\sum_{j=1}^{N} \sin\left(\varphi_j - \varphi_i\right) \tag{4.38}$$

with uniform interaction K/N. We are interested in the decay of the phase coherence, r, which is the absolute value of the order parameter, $r\exp(i\psi)$, defined by

$$r = \left|re^{i\psi}\right| = \left|\frac{1}{N}\Sigma_j e^{i\varphi_j}\right| \tag{4.39}$$

It has been shown that the decay of r for an array of phase-coupled oscillators is exponential [226], like the primitive relaxation of an isolated molecule in a solvent such as described by the Debye model [227]. As an analogue of many-body systems interacting with anharmonic potential, we consider now a number M (larger than one) of such arrays and couple these arrays nonlinearly together, again by the sine function,

$$\frac{K'}{MN}\Sigma_{\beta=1,\beta\neq\alpha}^{M}\Sigma_{j=1}^{N} sin\left(\varphi_{j\beta} - \varphi_{i\alpha}\right) \tag{4.40}$$

where K'/MN is the inter-array interaction strength. The new equation of motion of the phase of the ith oscillator in the αth array, $1 \leq \alpha \leq M$, is now given by

$$\varphi'_{i\alpha} = \varphi_{i\alpha} - \frac{K}{N}\Sigma_{j=1}^{N} sin\left(\varphi_{j\alpha} - \varphi_{i\alpha}\right) + \frac{K'}{MN}\Sigma_{\beta=1,\beta\neq\alpha}^{M}\Sigma_{j=1}^{N} sin\left(\varphi_{j\beta} - \varphi_{i\alpha}\right). \tag{4.41}$$

The problem is simplified to a map by picking the appropriate time steps and rescaling the time, so that time t is now discrete and incremented by 1 after each iteration of the map. The effect of the interactions between the M arrays on r of each array is studied by considering the new map. The interacting arrays mimic an assembly of interacting molecules in a molecule liquid. In the absence of inter-array interaction (i.e., $K' = 0$), r of the non-interacting arrays of coupled oscillators decays exponentially to an incoherent state, i.e. $r = 0$, for $K > 0$, in analogy to the primitive Debye relaxation of isolated molecules in dilute solution. However, since the interacting arrays do not model translational or rotational motion, they cannot be identified exactly with the structural relaxation in a glass-forming liquid. A nonlinear Hamiltonian that resembles more closely interacting ions in a ionic conductor or interacting molecules in a glass-forming liquid has to be much more complicated than the interacting arrays, and likely its dynamics cannot be solved exactly. In spite of its limitations, the interacting arrays of oscillators model has the advantage that its dynamics can be obtained readily, as shown below, and is a prototype of the relaxation of interacting many-body systems.

With arrays of random initial oscillator phases, we iterate the map in Eq. (4.41) to obtain the evolutions of the coupled arrays numerically. The evolutions of three (i.e., $M = 3$) interacting arrays, each of $N = 32$ oscillators initially with random phases, are obtained by iteration of the map defined by Eq. (4.41). From the results we calculate the decay of the phase coherence $r(t)$ for each array. First for a fixed K we calculate $r(t)$ for four values of $K' = 0$, 0.6, 0.8, 1.0 and 1.2. The results are shown in Fig. 4.23 (left). The figure shows with increasing inter-array coupling strength K', the decay of $r(t)$ becomes slower and its time dependence more non-exponential. The accompanying Fig. 4.23 (right) is replotting the same results as $\log_{10}\{-\log_e[r(t)]\}$ versus $\log_{10}t$. At short times the slope is exactly 1, indicating that initially $r(t)$ is an exponential function of time, $\exp(-t/\tau_0)$, in analogy to the primitive relaxation of the CM, Eq. (4.31). However, the linear exponential decay does not hold at longer times. There exists a cross-over time t_c after which the slope becomes less than 1, and $r(t)$ departs from the $\exp(-t/\tau_0)$ time dependence. Actually, for $t > t_c$, the slope varies slightly with time but the result is still reasonably well approximated by a straight line having a constant slope equal to $\beta \equiv (1 - n) \leq 1$, indicating $r(t)$ has crossed over to assume the stretched exponential time dependence, Eq. (4.35), of the CM. Naturally, Eq. (4.36) of the CM is satisfied. The systematic decrease of the long time slope β (see insert in Fig. 4.23 right) with increase of K'/K supports the intuitively reasonable surmise that n, the coupling parameter in the CM, increases with the mutual interaction strength of the relaxing units in real materials. We observe that there is a slight increase of t_c with decrease in the interaction strength, which is also consistent with real materials.

In addition to the interacting arrays of oscillators, we have studied relaxation in other models of nonlinear Hamiltonian dynamics [184–189, 225] which reproduce the same results. All of them are systems exhibiting classical chaos governed by the nonlinear (anharmonic) Hamiltonian. We expect the crossover property found in these idealized models to be general and carried over to other Hamiltonians that describe more realistically the nonlinear interaction potentials in ionic conductors

Decay of phase coherence, $r(t)$, for different inter-array coupling strengths, K'

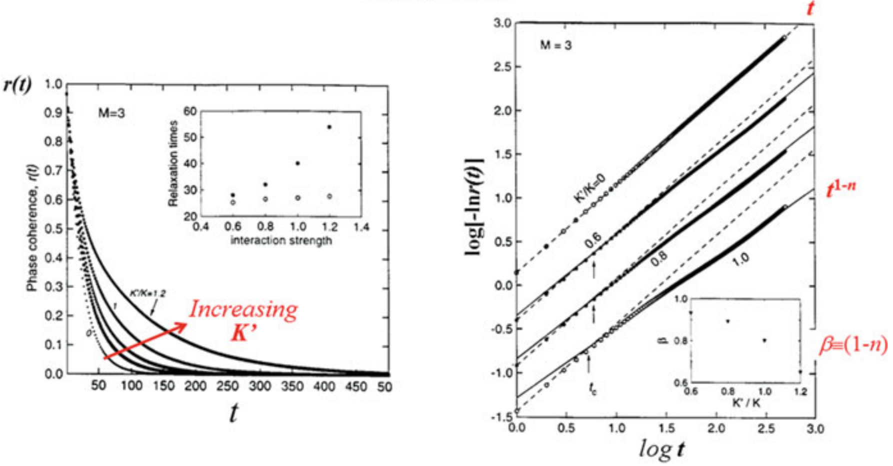

⇒ **Existence of** t_c: $r(t)=\exp(-t/\tau_0)$ *for* $t<t_c$; $r(t)=\exp[-(t/\tau)^{1-n}]$ *for* $t>t_c$

⇒ n *, the coupling parameter, increases with interaction strength,* K'

Fig. 4.23 (*left*) Decay of $r(t)$ calculated for $M = 3$, $K = -0.03$ and $K'/K = 0$, 0.6, 0.8, 1.0 and 1.2. The *inset* shows τ_0 (O) and τ (•) as a function of K'/K. (*right*) Plot of $\log_{10}\{-\log_e[r(t)]\}$ versus $\log_{10}t$ obtained numerically for $M = 3$, $K = -0.03$ and K'/K =0, 0.6, 0.8 and 1.0. The *dashed lines* are the exponential fits and the *solid lines* are the stretched exponential fits. Curves for K'/K =0.0, 0.6 and 0.8 are shifted vertically by multiples of 0.5 to avoid overlapping of results in the figure. The crossover time t_c is indicated by the *vertical arrows*. The calculated $r(t)$ conforms well to exp $(-t/\tau_0)$ for $t < t_c$ and to $\exp[(-t/\tau)^{\beta}]$ for $t > t_c$. The *inset* shows that the stretch exponent β decreases with increasing inter-array interaction strength

or molecular liquids as done in molecular dynamics simulations. Thus, the results from the idealized model systems can be considered as justification of the physical principle behind the CM when applied to many-body relaxation process in the ionic and molecular systems.

4.5 Experimental Verifications of the CM

Before we compare the results of the CM from the idealized models, either from semiclassical quantization of classical chaos or directly from classical chaos, with experimental data of conductivity relaxation in ionic conductor or structural relaxation in molecular systems, the following point has to be borne in mind. In real materials, the terminal or primary many-body relaxation or diffusion, which determines the transport coefficients, is preceded in time and in order by vibrations, caged dynamics (NCL in susceptibility), the primitive relaxation of the CM, and the secondary relaxation. In conductivity relaxation these faster processes appear at times shorter than the correlation time of the Kohlrausch function. Although Eqs. (4.31), (4.35) and (4.36) remain applicable to the terminal many-body relaxation with the Kohlrausch correlation function, and are useful to explain its properties, the faster processes must be taken into account when considering experimental data *in toto*. Such comprehensive consideration of the dynamics of all times was called at one time the *extended* Coupling Model [53]. Since then it is the version of the CM used whenever applied to real materials, and the word '*extended*' was dropped. The attention paid to the faster processes confer a bonus. The appearance of the secondary β-relaxation in the spectrum makes it possible to show its relaxation time τ_β is in agreement with the primitive relaxation time τ_0 (calculated by Eq. 4.36) in order of magnitude, which says that the primitive relaxation is the precursor of the secondary relaxation [7, 33, 34, 53, 60, 62, 63, 65, 148–152]. The secondary β-relaxation is composed of increasing number of units participating in relaxation with increasing time before the terminal many-body α-relaxation is reached. Moreover, the caged dynamics is terminated by the onset of the primitive relaxation and secondary relaxation. All these properties found from the processes transpired before the terminal many-body relaxation show connectivity of the processes in the evolution of the dynamics with time. Experimental data demonstrating these properties will be presented later in this chapter.

4.5.1 Direct Crossover

Caged dynamics do not exist at high temperatures where the primitive relaxation time τ_0 is comparable in order of magnitude to t_c. Observed processes are entirely relaxational because the ions or molecules are never caged. Under this condition, the correlation function directly crosses over at t_c from $\exp(-t/\tau_0)$ of the primitive relaxation to $\exp[-(t/\tau^*)^{1-n}]$ of the many-body relaxation, exactly as found in the idealized models. The crossover time t_c originate from the onset of chaos, which is governed by the interaction. Hence the magnitude of t_c is temperature insensitive and is determined by the strength of the interaction. In the following we show some examples of the direct crossover from $\exp(-t/\tau_0)$ to $\exp[-(t/\tau^*)^{1-n}]$ in ionic conductors and molecular glass-formers found by experiments. It should be mentioned that this property was first pointed out as one of the predictions of the Coupling Model (CM) [180–182] on relaxation of interacting systems, long before the experimental observations by others [228–232], and simulations for ortho-terphenyl (OTP) [233], polyisoprene [234], and polyisobutylene [235]. These experimental confirmations were obtained from quasielastic neutron scattering (QENS) studies of polymers. The magnitude of t_c found is about 1–2 ps for all these polymers. The dynamic incoherent structure factor, $S(Q,\omega)$, measured at scattering vector Q was transformed to time domain to obtain the incoherent intermediate scattering function (i.e., the self-correlation function) associated with local segmental relaxation, $I(Q,t)$. Here we show as an example the data of poly(ethylene oxide) (*h*PEO) in mixtures with poly(methylmethacrylate) in which

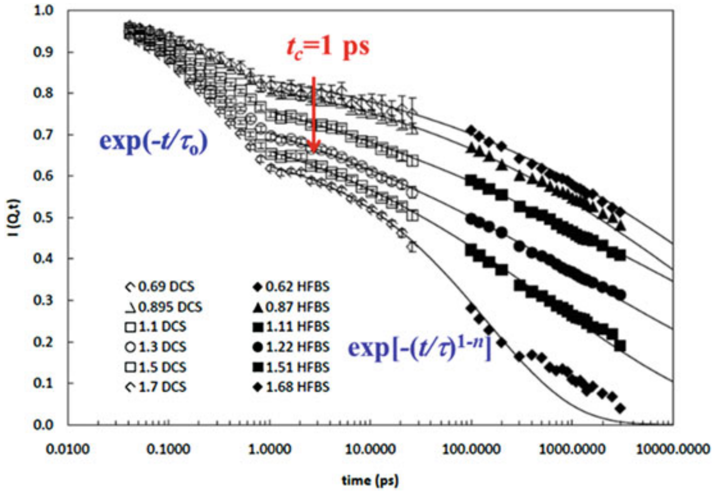

Fig. 4.24 Combined DCS and HFBS scattering decay curves for hPEO in dPMMA at 308 K for six Q values in Å^{-1} (from top to bottom) given in the figure. The values of Q are approximately the same for the two spectrometers. *Lines* represent a KWW fit with parameters falling within the *error bars* determined using the DCS data alone. The disk chopper time-of-flight spectrometer (DCS) was operated at an incident wavelength of 4.2 Å and an energy resolution of 81.6 μeV. A dynamic range of ±20 μeV was used for the high flux backscattering spectrometer (HFBS), with an energy resolution of 0.87 μeV. Data from Ref. [231] and redrawn

all hydrogen atoms are replaced by deuteron atoms (*d*PMMA) [231, 232]. The dynamics observed by neutron scattering comes from the local segmental relaxation of the *h*PEO. The $I(Q,t)$ measured at six different Q values and extended time range by use of two spectrometers DCS and HFBS are reproduced from the figure in Ref. [231] and shown in Fig. 4.24. A change of time dependence of $I(Q,t)$ from $\exp(-t/\tau_0)$ to $\exp[-(t/\tau^*)^{1-n}]$ at $t_c = 1$ ps is evident. The relaxation time τ_0 is found to have Q^{-2} -dependence of normal diffusion, indicating the relaxation is an independent or one-body in nature consistent with the so called primitive relaxation of the CM.

Triolo et al. [236] performed QENS measurements of the room temperature ionic liquid, 1-*n*-butyl-3-methylimidazolium hexafluorophosphate, [*bmim*][PF$_6$], and obtain the corresponding $I(Q,t)$ data. In Fig. 4.25, we reproduce the time dependence of the $I(Q,t)$ at a fixed value of $Q = 2.0$ Å^{-1} at several temperatures. Two relaxations occur over the experimental time range. The faster one with time dependence proportional to $\exp(-t/\tau_0)$ occurs on a time scale of the order of picosecond, and a slower process follows at longer times, thus [*bmim*][PF$_6$] exhibit the crossover as found in the structural relaxation in glass-formers [228–232]. Shown in Fig. 4.25 are not only the experimental data (symbols) but also the fits (solid lines) by Triolo et al. In fitting the data, they assume the time dependence of $I(Q,t)$ is the sum, $A\exp(-t/\tau_0) + (1-A)\ \exp[-(t/\tau)^{1-n}]$. This function is not exactly the same as the crossover from $\exp(-t/\tau_0)$ to $\exp[-(t/\tau^*)^{1-n}]$ predicted by the CM. Nevertheless, the data at the high temperature of 320 K, as well as the fit is consistent with the crossover at t_c slightly less than 2 ps.

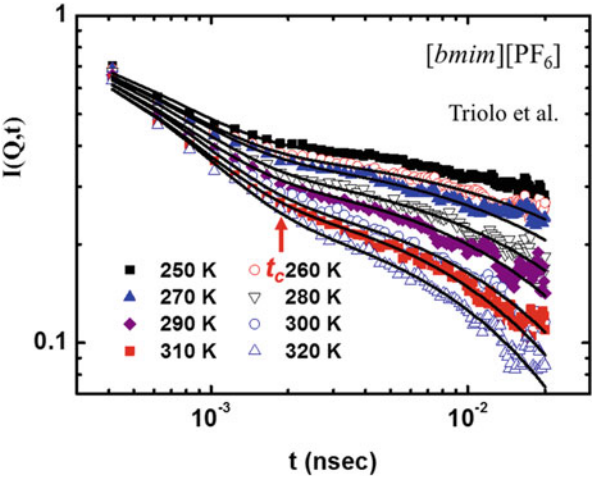

Fig. 4.25 Temperature dependence of $I(Q,t)$ for [*bmim*][PF$_6$] at $Q = 2.0\ \text{Å}^{-1}$. The *symbols* represent the experimental data, while the *lines* represent the fit in terms of the model mentioned in the text

At lower temperatures, there is no direct crossover from $\exp(-t/\tau_0)$ to $\exp[-(t/\tau^*)^{1-n}]$. The caged dynamics and the secondary or β-relaxation intervene and appear before the many-body relaxation with time dependence of $\exp[-(t/\tau^*)^{1-n}]$. This is evidenced by the very slow decrease of $I(Q,t)$ with time after t_c at 250 K in Fig. 4.25. If $I(Q,t)$ is Fourier transformed to frequency domain, this slow decrease becomes the nearly constant loss (NCL) in susceptibility. In some cases, a β-loss peak is resolved at frequencies in between the NCL and the terminal α-relaxation as shown before in Figs. 4.7, 4.8, and 4.9. If the Gaussian approximation holds and the incoherent elastic intensity $I(Q,t)$ can be expressed in terms of the mean square displacement, $<u^2>$, by $I(Q,t) = I_0\exp\left(-\langle u^2\rangle Q^2/3\right)$, the caged dynamics responsible for the very slow decrease of $I(Q,t)$ at lower temperatures correspond to a very slow increase of $<u^2>$ with $\log t$. This will be amply shown in molecular dynamic simulations of ions in glassy ionic conductors [161, 163] to be presented later.

4.5.2 Q-Dependence of τ^* and τ_0

We have mentioned that the CM has many predictions besides the Kohlrausch correlation function, $\exp[-(t/\tau^*)^{1-n}]$, which provides good description of the time correlation function of the terminal many-body ionic or molecular relaxation. Here is one example from the relation of the Q-dependence of τ^* to that of τ_0 obtained from $I(Q,t)$ in neutron scattering experiments, where Q is the scattering vector. The Q-dependence of τ_0 is proportional to Q^{-2} because τ_0 is the relaxation time of the primitive relaxation. This is supported by the findings of neutron scattering experiments [228, 237–239] at $t < t_c$ that the intermediate scattering function is Gaussian and corresponds to a normal diffusion process, and the Q-dependence of the relaxation time $\tau_0(Q,T)$ is proportional to Q^{-2}. Writing out explicitly the Q- and

T-dependence of $\tau_0(Q,T)$ as the product $\tau_0(Q,T) = Q^{-2}\zeta_0(T)$, the Q- and T-dependence of $\tau^*(Q,T)$ is given via that of $\tau_0(Q,T)$ by the CM Eq. 4.36

$$\tau^*(Q,T) = [(t_c)^{-n}\tau_0(Q,T)]^{\frac{1}{1-n}} = Q^{-2/(1-n)}\left[t_c^{-n}\zeta_0(T)\right]^{1/(1-n)}. \tag{4.42}$$

If the temperature dependence of $\tau_0(Q,T)$ is Arrhenius with activation energy E_a and prefactor $\tau_{0\infty}$ such that $\tau_0(Q,T) \propto \tau_{0\infty}\exp(E_a/RT)$, the T-dependence of $\tau^*(Q,T)$ is also Arrhenius but with a larger activation energy,

$$E_a^* = E_a/(1-n). \tag{4.43}$$

The CM has two predictions for $\tau^*(Q,T)$, one is the $Q^{-2/(1-n)}$ dependence, and the other is the stronger T-dependence, $[\zeta_0(T)]^{1//(1-n)}$, than $\zeta_0(T)$ of $\tau_0(Q,T)$, or larger activation energy E_a^* than that of $\tau_0(Q,T)$. Both predictions can be tested quantitatively by using the value of the fractional exponent, $(1-n)$, of the Kohlrausch function obtained from the fit to $I(Q,t)$ at times $t > t_c$.

The $Q^{-2/(1-n)}$-dependence of the segmental α-relaxation time, $\tau^*(Q,T)$, in the range, $Q \leq Q_{\max}$, where $Q_{\max}$ is the value at which the static structure factor $S(Q)$ shows its first maximum, was first discovered by neutron scattering in the polymer, polyvinylchloride (PVC), by Colmenero and coworkers [230, 237] as early as in 1992. In the same year, the $Q^{-2/(1-n)}$ dependence was explained by the CM Eq. (4.42) [238] not only for PVC but also for polyisobutylene (PIB), poly(vinyl methyl ether) (PVME), poly(dimethyl siloxane) (PDMS) from data in the literature, and new data for poly(bisphenol A, 2-hydroxypropylether). The T-dependence of $\tau^*(Q,T)$ of these polymers, $[\zeta_0(T)]^{1//(1-n)}$, was shown to correlate with n, as predicted by Eq. (4.42). The property was found also in ortho-terphenyl, a small molecule van der Waals glass-former, and explained [239].

The CM explanation of the $Q^{-2/(1-n)}$-dependence of $\tau^*(Q,T)$ is the only one given by any theory despite its first observation since 1992. Justification of this claim will become clear from the discussion in the next paragraph. This is an important point because it shows the usefulness of the CM unrivaled by other theories. Since then more refined studies by neutron scattering [240–242] and simulations [234, 235] have confirmed the $Q^{-2/(1-n)}$-dependence of the segmental α-relaxation time of polymers. An example from polyisobutylene (PIB) is shown in Fig. 4.26a taken from Ref. [242], in which the fit to $I(Q,t)$ determined $\beta = (1-n) = 0.55$. These papers and more [241, 243, 244] also tried to rationalize this dependence by arguments, which we show immediately below is not an explanation on a theoretical basis, and instead is consistent with other observed properties including Kohlrausch time dependence and return to Gaussian form of both, the self-part of the van Hove correlation function $G_s(r,t)$ and its Fourier transform $S_{self}(Q,t)$. This is necessary because there is misconception in the literature that the $Q^{-2/(1-n)}$-dependence has been explained theoretically by these papers, and the true theoretical explanation by the CM is ignored. Moreover this is relevant for ionics because the $Q^{-2/(1-n)}$-dependence was found in neutron scattering of ionic liquids [236], and the accompanying prediction by Eq. (4.43) is valid for a fast glassy ionic conductor all to be discussed later.

In all papers by others [240, 241, 243–245] the crux of the arguments to rationalize the $Q^{-2/\beta}$-dependence of $\tau^*(Q,T)$ or $\tau_w(Q,T)$ is by combining two points. Point (1) is to take from experiment the empirical fact that $S_{\text{inc}}(Q,t)$ can be described by a KWW function $S_{inc}(Q,t) = A(Q,T)\exp\left[-(t/\tau_w(Q,T))^{\beta}\right]$. Point (2) is to assume that the van Hove function $G_s(r,t)$ and its Fourier transform, $S_{inc}(Q,t) = \int G(\vec{r},t) \quad \exp\left(-i\vec{Q}\cdot\vec{r}\right)d\vec{r}$, are Gaussian functions, i.e. $G(r,t) = [\alpha(t)/\pi]^{3/2}\exp[-\alpha(t)r^2]$, and $S_{inc}(Q,t) = A(Q,T)\exp\left[-\langle r^2(t)\rangle Q^2/6\right]$. By equating the two expressions for $S_{\text{inc}}(Q,t)$ from points (1) and (2), $S_{inc}(Q,t) = A(Q,T)\exp\left[-\langle r^2(t)\rangle Q^2/6\right] = S_{inc}(Q,t) = A(Q,T)\exp\left[-(t/\tau_w(Q,T))^{\beta}\right]$, the $Q^{-2/\beta}$-dependence of τ_w is deduced. Not made explicitly clear in Refs [240, 241, 243–245]. is that $\tau_w(Q,T)$ becomes very long for the small Q values in the Q-range where its $Q^{-2/\beta}$-dependence is found experimentally at fixed temperature. The deviations of $G_s(r,t)$ from the Gaussian form, quantified by the second-order non-Gaussian parameter, $\alpha_2(t) = (3/5)\langle r^4(t)\rangle/\langle r^2(t)\rangle - 1$, exhibits a peak with maximum at a Q-independent time $t^*(T)$, and α_2 becomes vanishingly small at long times. Therefore, the Gaussian forms are valid because $\tau_w(Q,T)$ is much longer than $t^*(T)$ for Q in the range where the $Q^{-2/\beta}$-dependence of $\tau_w(Q,T)$ holds. In the experiments, it turns out the condition is satisfied for Q below Q_{max} (at which the static structure factor shows its first maximum), where the assumption in point (2) is justified. By these steps we have shown that the observed $Q^{-2/\beta}$-dependence of τ_w is a necessary consequence of consistency with the other properties. Alternatively one [244] can take the empirical observation of the $Q^{-2/\beta}$-dependence of $\tau_w(Q,T)$ and substitute it into the empirical $S_{inc}(Q,t) = A(Q,T)\exp\left[-(t/\tau_w(Q,T))^{\beta}\right]$ of point (1). The result is $S_{\text{inc}}(Q,t)$ having the Gaussian form, and hence also $G_s(r,t)$ in the Gaussian form.

However, since point (1), i.e. $S_{inc}(Q,t) = A(Q,T)\exp\left[-(t/\tau_w(Q,T))^{\beta}\right]$, is empirical, the best one can conclude from this approach is that the $Q^{-2/\beta}$-dependence of τ_w is consistent with other experimental properties, but is not derived from a theory. This approach does not have bearing on the temperature dependence of the relaxation time. On the other hand, not only the $Q^{-2/\beta}$-dependence is derived from the CM Eq. (4.42) but also is the accompanying temperature dependence given by Eqs. (4.42) and (4.43), which has been applied for polymers in Ref. [238]. Later on we discuss another application of Eq. (4.43) to quasielastic neutron scattering measurements of ionic diffusion coefficient in several superionic glasses as a function of temperature at short times (in the picosecond and sub picoseconds range) [8, 101, 246–249].

In Fig. 4.25 we have shown $I(Q,t)$ of [*bmim*][PF$_6$] at $Q = 2.0$ Å^{-1}, exhibiting the cross over from $\exp(-t/\tau_0)$ to $\exp[-(t/\tau^*)^{1-n}]$ at $t_c \sim 2$ ps [236]. The inset of Fig. 4.26b gives the values of the Kohlrausch exponent, $\beta = (1\text{-}n)$, as a function of Q at $T = 300$ K. The main figure presents in a log-log plot of the average

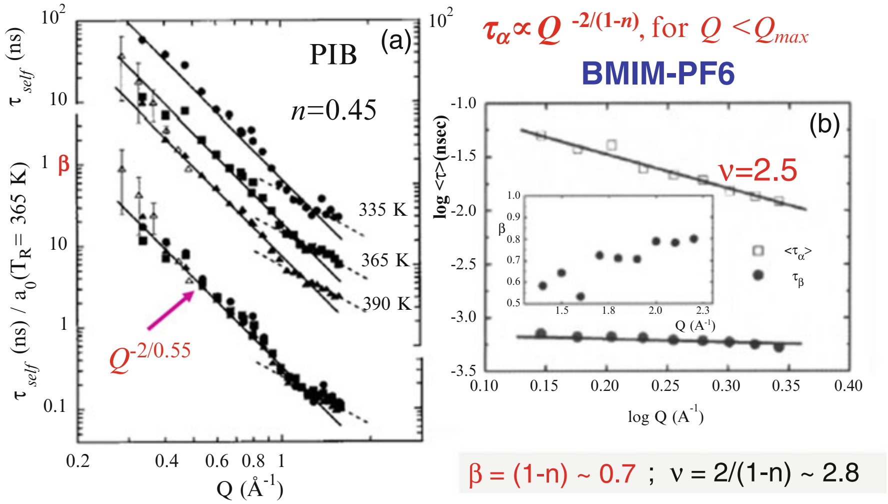

Fig. 4.26 (**a**) PIB (*upper part*): Momentum transfer dependence of the characteristic time of the KWW functions describing the self-correlation function at 335 (*circles*), 365 (*squares*), and 390 K (*triangles*). *Lower part*: Scaling representation: 335 and 390 K data have been shifted to the reference temperature 365 K applying a shift factor corresponding to an activation energy of 0.43 eV. *Full symbols* correspond to results from measurements performed with incoming wavelength $\lambda = 6$ Å and empty symbols to $\lambda = 10$ Å. *Solid (dotted) lines* through the points represent $Q^{-2}/0.55$ (Q^{-2}) power laws. (**b**) [*bmim*][PF$_6$]: Momentum transfer dependence of the characteristic times of the fast (τ_β) and slow ($<\tau>$) relaxations for $T = 300$ K. In the *inset* the Q-dependence of the stretching parameter β is reported for the same temperature

relaxation time, $<\tau> = [\Gamma(1/\beta)/\beta]\tau^*$, vs. Q at the same temperature. The slope ν is about 2.5. The predicted $Q^{-\nu}$-dependence from Eq. (4.42) has $\nu = 2/(1-n)$. Taking the value of $\beta = (1-n) \sim 0.7$, Triolo et al. gave the value $\nu \sim 2.85$, close to 2.5. The lack of Q-dependence of the fast relaxation time in Fig. 4.26b is the consequence of the assumed sum, $A\exp(-t/\tau_0) + (1-A)\ \exp[-(t/\tau)^{1-n}]$ for the time dependence of $I(Q,t)$ in fitting the data in Ref. [236].

The observed $Q^{-2/(1-n)}$-dependence of the α-relaxation time of glassforming liquids is also found in other systems by dynamic light scattering including suspensions of colloidal particles [250], semidilute polymer solutions [251–254], associating polymer solutions [255, 256], and polymer cluster solutions [252, 257]. This rather universal dependence of relaxation time on the scattering vector is the exemplification of many-body relaxations that are common to these systems all having mutual interaction between the basic relaxation units. The anomalous $Q^{-2/(1-n)}$-dependence of τ_α is derivable from the CM Eq. (4.42) simply by substituting the known Q^{-2}-dependence of τ_0 into it. Again in these other interacting systems, the CM not only predicts correctly the $Q^{-2/(1-n)}$-dependence but also other properties. For example, the concentration and molecular weight dependences of polymer dynamics in solution are predicted together with the scattering vector $Q^{-2/(1-n)}$-dependence of the light scattering field correlation function $g^{(1)}(t)$, and all are verified in experiments [251, 252, 257].

4.5.3 *Evidence of Crossover from Other Experiments in Ionic Conductors*

Like glassformers and other interacting systems, there are experimental evidences in various ionically conducting materials supporting the crossover of the ionic conductivity correlation function from $\exp(-t/\tau_0)$ to $\exp[-(t/\tau)^{1-n}]$ in a neighborhood of a temperature insensitive time t_c.

4.5.3.1 Fast Glassy Ionic Conductors

There are many fast glassy ionic conductors where the mobility of the ions are so high that the conductivity relaxation time τ_σ can become very short and comparable to t_c by raising temperature but still staying within the glassy state. These are examples of relaxation of interacting systems which remain in the glassy state because T here is always significantly below T_g. At lower temperatures where τ_σ is longer than t_c, but if the difference is not large, there is a chance to see the direct crossover of the correlation function of the ion conductivity relaxation from $\exp(-t/\tau_0)$ to $\exp[-(t/\tau_\sigma)^{1-n}]$ via $\sigma(\omega)$. The $\sigma(\omega)$ corresponding to $\exp(-t/\tau_0)$ for $t < t_c$ from Eq. (4.8) is σ_0 a constant given by

$$\sigma_0 = \varepsilon_\infty \varepsilon_o / \tau_0. \tag{4.44}$$

The $\sigma_n(\omega)$ corresponding to the $M^*(\omega)$ obtained with $\exp[-(t/\tau_\sigma)^{1-n}]$ has the d.c. conductivity σ_{dc} in the low frequency limit when $\omega\tau_\sigma \ll 1$ given via Eqs. (4.13) and (4.16) by

$$\sigma_{dc} = \varepsilon_\infty \varepsilon_o / \langle \tau_\sigma \rangle = \varepsilon_\infty \varepsilon_o / [\Gamma(1/\beta)/\beta] \tau_\sigma \tag{4.45}$$

and increases with the ω^n-dependence at higher frequencies when $\omega\tau_\sigma \gg 1$. Direct crossover occurs at sufficiently high temperatures if $\sigma_n(\omega)$ increases with the same ω^n-dependence all the way and reaches σ_0 at $\omega_c \equiv (t_c)^{-1}$. If temperature is too low, the caged ion dynamics intervene between σ_{dc} and σ_0, changing the ω^n-dependence of the observed $\sigma(\omega)$ from $\sigma_n(\omega)$ to a stronger ω^{1-c}-dependence with $c << 1$ before reaching σ_0. The ω^{1-c}-dependence of $\sigma(\omega)$ corresponds to the NCL of caged ion dynamics with $\varepsilon''(\omega) \propto \omega^{-c}$.

One example showing the direct crossover from σ_{dc} to σ_0 is chosen from the work of Belin et al. on the fast glassy ionic conductors, $0.5\text{Ag}_2\text{S}$-0.5GeS_2 [258]. In inorganic glasses, the vibrational contribution $\sigma_{vib}(\omega)$ to $\sigma(\omega)$ extends from high frequencies down to low frequencies with an ω^2-dependence [259, 260], found also in this glassy ionic conductors as shown in Fig. 4.27. The Ag ion conductivity contribution $\sigma_{ion}(\omega)$ is obtained after the tail of the vibrational contribution with a ω^2-dependence has been subtracted off. This is demonstrated in Fig. 4.27 for the data at 437 K, where the ion contribution, $\sigma_{ion}(\nu) = [\sigma(\nu) - \sigma_{vib}(\nu)]$ at 473 K

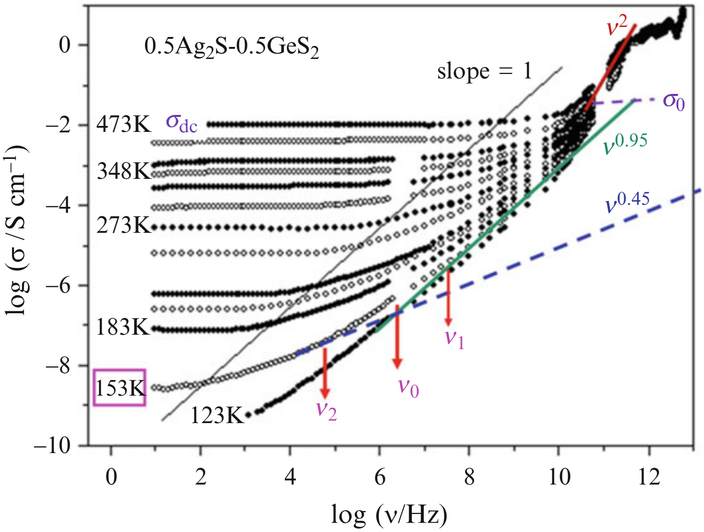

Fig. 4.27 Frequency-dependent conductivity, $\sigma(\nu)$, of $0.5Ag_2S\text{-}0.5GeS_2$ glass, from the work of Berlin et al. The ion contribution, $\sigma_{ion}(\nu)$ at 473 K crosses over from primitive ion conductivity relaxation with $\sigma_{ion}(\nu) = \sigma_o$ to $\sigma_n(\nu)$ at $\nu_c = 10^{10.7}$ Hz. The *solid line* with slope 0.95 indicates the NCL for $T = 153$ K and as well for 123 K. The *line* with slope 0.45 is the high frequency dependence of $\log_{10}\sigma'(\nu)$ corresponding to the Kohlrausch fit to the electric modulus data (not shown) with $n = 0.45$. The location of the independent relaxation frequency of the CM, $\nu_o \equiv 1/2\pi\tau_o$, at 153 K is indicated by one of the arrows. Reproduced from Ref. [258] by permission

exhibits a crossover from primitive ion conductivity relaxation with $\sigma_{ion}(\nu) = \sigma_o$ to $\sigma_n(\nu)$ at $\nu_c \sim 10^{10.7}$ Hz on decreasing frequency. The green line with slope equal to nearly one in the logσ-logν plot is drawn to show the low temperature 153 and 123 K data of $\sigma(\nu)$ at high frequencies have nearly such dependence, ν^{1-c}-dependence with $c = 0.05 \ll 1$, and originate from caged ion dynamics with the NCL for $\varepsilon''(\nu)$. The weak temperature dependence of $\sigma(\nu)$ in this caged dynamics regime is evident from the proximity of the two sets of data. The location of the independent ion-hopping frequency, $\nu_0 \equiv 1/(2\pi\tau_0)$, at 153 K is indicated by the longer downward arrow. The other arrows and labels ν_{x1} and ν_{x2} for 153 K will be explained much later when discussing the transitions of ion dynamics from NCL to the many-ion dynamics and dc conductivity.

Another example is taken from the $\sigma(\nu)$ data of $0.44LiBr\text{-}0.56Li_20\text{-}B_2O_3$ [261] in Fig. 4.28 at the high temperature of 573 K, where ionic conductivity contribution $\sigma_{ion}(\omega)$ to $\sigma(\nu)$ is deduced after subtracting the approximately ν^2-dependence of $\sigma_{vib}(\omega)$ from the measured $\sigma(\nu)$. Like in the previous example, the ion contribution, $\sigma_{ion}(\nu) = [\sigma(\nu) - \sigma_{vib}(\nu)]$ at 573 K exhibits a crossover from primitive ion conductivity relaxation with $\sigma_{ion}(\nu) = \sigma_o$ to $\sigma_n(\nu)$ at $\nu_c \sim 10^{11}$ Hz. The leveling off of $\sigma_{ion}(f)$ to a plateau value σ_o at frequencies higher than ν_c is expected by both the MIGRATION concept of Funke and the CM. Because we are in the glassy state, σ_{dc} (or τ_σ) and the plateau value σ_o (or τ_0) at frequencies higher than ν_c both have

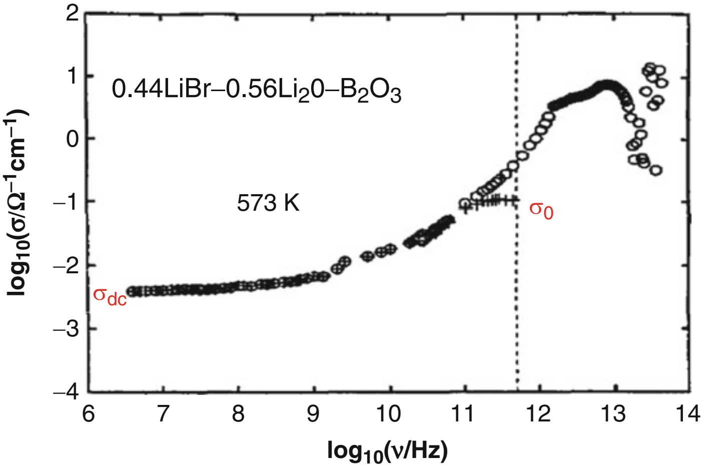

Fig. 4.28 Frequency-dependent conductivity, $\sigma(\nu)$, of 0.44LiBr-0.56$Li_2$0-B_2O_3 glass at 573 K from the work of Cramer et al. [261] by permission. The ion contribution, $\sigma_{ion}(\nu) = [\sigma(\nu) - \sigma_{vib}(\nu)]$ at 473 K exhibits a crossover from primitive ion conductivity relaxation with $\sigma_{ion}(\nu) = \sigma_o$ (+) to $\sigma_n(\nu)$ at $\nu_c \sim 10^{11}$ Hz (*dashed line*)

Arrhenius temperature dependence with activation energies E_{dc} and E_0 respectively. At high temperatures it was reported [261] that σ_o has an Arrhenius temperature dependence with an activation energy E_a of about 0.22 eV which is equivalent to 2553 K. On the other hand, the activation energy E_{dc} of σ_{dc} has the larger value of 0.49 eV or 5670 K. Actually this is the activation enthalpy of the product $\sigma_{dc}T$; the activation enthalpy for σ_{dc} would be slightly lower. The value of β_σ has not been determined by a fit to the electric modulus representation of the data using the Kohlrausch function. A fit to the Jonscher expression by Funke and coworkers has yielded $s = 0.6$. From an example of the comparison between the two methods of fitting the conductivity relaxation data [5, 6, 30] by Moynihan, β_σ determined from the electric modulus is larger than $1-s$. Thus, we can expect that $\beta_\sigma > 0.40$. Conductivity relaxation measurements on a similar glass, $(LiCl)_{0.6}(Li_2O)_{0.7}(B_2O_3)$, have yielded $E_{dc} = 5500$ K of σ_{dc} and $\beta_\sigma = 0.50$ [262]. The actual value of β_σ for Funke's sample will likely lie within the bounds: $0.40 < \beta_\sigma < 0.50$. The correlation between β_σ and $\beta_\sigma E_\sigma$ established for many families of glassy ionics [87, 104] would also place $\beta_\sigma \cong 0.48$ (from Fig. 8a of Ref. [12]) if we identify $E_a = 0.22$ eV with the product $\beta_\sigma E_\sigma$. With $\beta_\sigma = (1\text{-}n)$ estimated within the range $0.40 < (1 - n) < 0.48$, we can test the other CM prediction given by Eq. (4.43) and rewritten as

$$E_0 = (1 - n)E_{dc} \tag{4.46}$$

The product on right side of this equation lies within the bounds, $2268\ \text{K} < (1 - n)E_{dc} < 2721\ \text{K}$, and is consistent with the experimental value of $E_0 = 2553$ K.

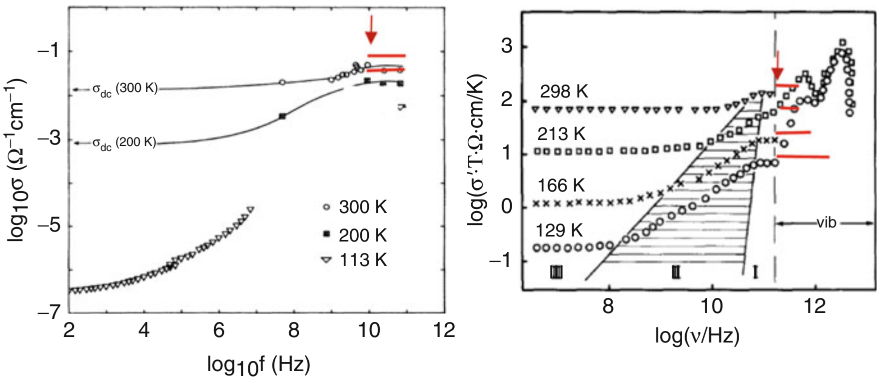

Fig. 4.29 (*Left*) Frequency dependence of $\sigma(\nu)$ of Na β-alumina at three temperatures showing crossover after 10^{10} Hz. Reproduced from Ref. [54] by permission. (*Right*) The product $\sigma(\nu)T$ of $RbAg_4I_5$ crystals at four different temperatures. The crossover is seen for 166 and 129 K. Reproduced from Ref. [264] by permission

4.5.3.2 Fast Crystalline Ionic Conductors

Many-body relaxation dynamics require the effect of interaction between the units necesarily to be included. Although randomness and disorder foster interaction, by no means they are essential to observe the vestige of many-body relaxation dynamics. Thus, we can expect to see the crossover to primitive conductivity relaxation in fast crystalline ionic conductors. In fact there are experimental evidences for the crossover in crystalline Na β-alumina [54, 101, 102], Na-β''-alumina [128, 263], and $RbAg_4I_5$ [101, 264]. The crossover of conductivity of Na β-alumina at $\nu_c \approx 10^{10}$ Hz and $RbAg_4I_5$ at about 10^{11} Hz can be seen by inspection of the data presented respectively in the left and right panels of Fig. 4.29. For Na β-alumina, the activation energy E_0 of $\sigma(\nu)$ for $\nu > \nu_c$ in the range, $200 < T < 300$ K, is ≈ 810 K. On the other hand, the activation energy of d.c. conductivity, E_{dc}, is ≈ 1600 K at 300 K and ≈ 1700 K at 200 K [54]. The coupling parameter n is ≈ 0.50 at 300 K and ≈ 0.53 at 200 K [54]. From these values, one can verify that the relation, $E_0 = (1 - n)E_{dc}$, of Eq. (4.47) is satisfied.

4.5.3.3 The Molten Salt CKN

The crossover behavior of the dynamics of ions in fast ionic conductors in the glassy or crystalline state at ν_c also was observed in the molten salt, $0.4Ca(NO_3)_2$-$0.6KNO_3$ (CKN), by high frequency dielectric relaxation [265]. The data shown in Fig. 4.30 taken at highest temperature of 478 K is close to directly observing the direct crossover from primitive ion conductivity relaxation with $\sigma_{ion}(\nu) = \sigma_o$ to $\sigma_n(\nu)$ at $\nu_c \sim 10^{11.7}$ Hz (see inset). However, at lower temperature the caged ion

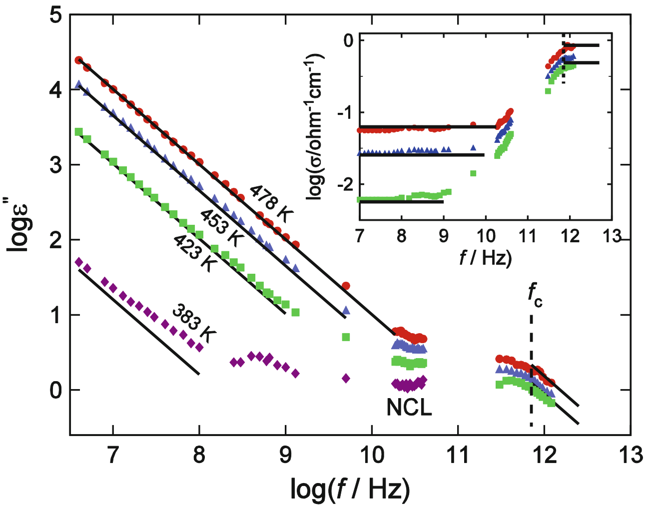

Fig. 4.30 Frequency dependence of the dielectric loss in CKN at high frequencies and several temperatures. The *vertical dashed line* indicates the crossover frequency $\nu_c \sim 10^{11.7}$ Hz. The *inset* is the log-log plot of the frequency dependence of the contribution by ionic motions to the a.c. conductivity in CKN. *Circles* (478 K); *triangles* (453 K); *squares* (423 K)

dynamics intervene, particularly clear at 383 K by the appearance of the NCL in the main figure.

4.5.4 Quasielastic Neutron Scattering Studies of Glassy Ionic Conductors

Quasielastic neutron scattering (time of flight) is a technique for measurements at short times (in the picosecond range) of the ionic diffusion coefficient as a function of temperature in superionic glasses. The fast ion glasses AgI-$AgPO_3$ and Ag_2S-GeS_2 with and without AgI have been studied by this techniques by two groups [246, 247, 266, 267]. The glass. Ag_2S-GeS_2, is the same as that studied by high frequency conductivity relaxation shown before in Fig. 4.27. It was found that the activation enthalpy of the short-time diffusion coefficient, E_0, is smaller than that of the d.c. conductivity, and approximately equal to the product βE_{dc} as predicted by Eq. (4.46) of the CM [45, 101, 102]. Here $\beta = (1 - - n)$ is the Kohlrausch exponent and E_{dc} is the d.c. conductivity activation energy observed at much lower temperatures and frequencies. These neutron scattering experiments measure the ion diffusion with correlation times of the order of ps, and correspond to the high frequency plateau of $\sigma_{ion}(\nu) = \sigma_o$ with activation energy E_0 in the glassy, crystalline and molten ionic conductors discussed

Table 4.2 Activation energies, E_0, of 0.5AgI-0.5AgPO$_3$ [246, 247] and Ag$_2$S-GeS$_2$ [266, 267] from short time ionic diffusion obtained by neutron time of flight measurements

Glass	E_{dc}	$\beta \equiv 1 - n$	$\beta\, E_{dc}$	E_0 (QENS)
AgI-AgPO$_3$	21 kJ/mol	0.44	9.2 kJ/mol	8.7 kJ/mol
Ag$_2$S-GeS$_2$	0.34 eV	0.45	0.153 eV	0.15 eV

The Kohlrausch exponent, $\beta \equiv (1\text{-}n)$, and the activation enthalpies, E_{dc}, of conductivity relaxation observed in the same glasses at lower temperatures and frequencies in the many-particles hopping region are also included. The near equality between E_0 and βE_{dc} is found as predicted, consistent with the change to independent relaxation at times shorter than $t_c \approx 2$ ps and probed by quasielastic neutron scattering (QENS)

before. The E_0 from neutron scattering are compared with the calculated βE_{dc} in Table 4.2. The good agreement between the two validates observation of the crossover of dynamics at t_c near 1 ps of the CM.

4.5.5 Change of Temperature Dependence of σ_{dc} at High Temperatures

Another way to see the crossover to primitive relaxation of ion dynamics in fast glassy or crystalline ionic conductors is by the change in T-dependence of σ_{dc} from its Arrhenius dependence at lower temperatures to a weaker Arrhenius dependence of σ_o by raising temperature till when the conductivity relaxation time τ_σ becomes comparable to or shorter than t_c. The Maxwell relation, $\sigma_{dc} = \epsilon_o \varepsilon_\infty / <\tau_\sigma>$, determines $<\tau_\sigma(T)>$, and hence $\tau_\sigma(T)$, from $\sigma_{dc}(T)$. Here $\varepsilon_o = 8.854 \times 10^{-14}$ F/cm is the permittivity of free space, ε_∞ the high frequency dielectric constant, and $<\tau_\sigma>$ is the mean relaxation time. If $\varepsilon_\infty = 10$, $<\tau_\sigma>$ will reach ~1 ps when $\sigma_{dc} \sim 1$ S/cm. At lower temperatures where $\tau_\sigma << t_c$ and the correlation function is $\exp[-(t/\tau_\sigma)^{1-n}]$, τ_σ has the Arrhenius T-dependence

$$\tau_\sigma(T) = \tau_\infty^* \exp\left(E_a^*/kT\right), \tag{4.47}$$

and $<\tau_\sigma> = [\Gamma(1/\beta)/\beta]\tau_\sigma$. The activation energy E_a* and the prefactor τ_∞* are usually anomalous because they originate from nontrivial many-ion relaxation due to ion-ion interactions. The temperature dependence of τ_σ is Arrhenius with a constant activation energy E_a* provided that n does not change with temperature. If n decreases with increasing temperature, the Arrhenius T-dependence no longer holds as seen in the crystalline ionic conductors, Na β-alumina [54] and LLTO [154], and in some very fast glassy ionic conductor such as 0.525Ag$_2$S + 0.475 (B$_2$S$_3$:SiS$_2$) at all temperatures below T_g [15, 103].

On raising temperature, τ_σ becomes shorter and when it is of the order of picoseconds or shorter, t_c is crossed and primitive motion of ions takes over with correlation function given by $\exp(-t/\tau_0)$ with

$$\tau_0(T) = \tau_\infty \exp(E_a/kT), \tag{4.48}$$

and now $<\tau_\sigma> = \tau_\sigma$. We use E_a and E_0, as well as τ_σ and τ^* interchangeably in this chapter. The primitive activation energy E_a that can be identified with a realistic energy barrier of an independent ion hop, and the reciprocal of its prefactor τ_∞ is the attempt angular frequency, which should correspond to some peak frequency of the infrared or Raman spectrum. Inserting the Arrhenius T-dependences of τ_σ and τ_0 in Eqs. (4.47) and (4.48) into the CM Eq. (4.36), it follows that

$$E_a = (1-n)E_a^*, \quad \tau_\infty = (t_c)^n \left(\tau_\infty^*\right)^{1-n}, \quad E_a^* = E_a/(1-n) \quad \tau_\infty^* = \left[(t_c)^{-n}\tau_\infty\right]^{1/(1-n)}. \tag{4.49}$$

The temperature dependence of conductivity relaxation time is mirrored by that of the measured σ_{dc}. Therefore, on increasing T, the T-dependence of σ_{dc} will eventually cross over to the Arrhenius T-dependence having the same activation energy E_a of τ_0, albeit may be slightly modified at the higher temperatures when $1/\tau_0$ approaches the vibration frequencies. These properties associated with the expected crossover of σ_{dc} at high temperatures have been found in many ionic conductors [13], including the molten salt, CKN, fast glassy ionic conductors such as $0.48(\mathrm{AgI})_2$-$0.52\mathrm{Ag_2SeO_4}$ [268], and $0.525\mathrm{Ag_2S} + 0.475(\mathrm{B_2S_3{:}SiS_2})$ [15, 103], and crystalline ionic conductors such as yttria stabilized zirconia, $(\mathrm{ZrO_2})_{1-x}(\mathrm{Y_2O_3})_x$ [22, 82, 83, 269, 270].

As an example, σ_{dc} data of yttria stabilized zirconia (YSZ) are shown in Fig. 4.31 [For references, see 22]. The high oxygen conductivity of yttria stabilized zirconia (1-x $\mathrm{ZrO_2}$: x $\mathrm{Y_2O_3}$) at elevated temperatures has been known since 1899 [275]. It takes values of about 0.1 $\mathrm{Scm^{-1}}$ at 1000 °C. Doping with $\mathrm{Y_2O_3}$ stabilizes the cubic fluorite structure of $\mathrm{ZrO_2}$ at room temperature due to the presence of oxygen vacancies, and these oxygen vacancies are also responsible for the ionic conduction in the material (see for example the review by Etsell and Flengas [276] and references therein). Because of its applications as electrolyte material in solid oxide fuel-cells and oxygen sensing devices, yttria stabilized zirconia, usually referred to as YSZ, is probably the most extensively studied fast oxide-ion conductor [82, 83, 270–274, 277–282]. These studies have provided us with a deep knowledge of many properties of the dynamics of oxygen ions in YSZ. In particular, the long range or dc conductivity is known to depend on the yttrium content, having a maximum at around $x = 0.08$–0.10, i.e. an 8–10 % mol yttria content and decreasing strongly for higher doping [276]. The exact position of this maximum depends on the temperature value chosen for the comparison, since the activation energy for the dc conductivity is found to increase by increasing the yttria content.

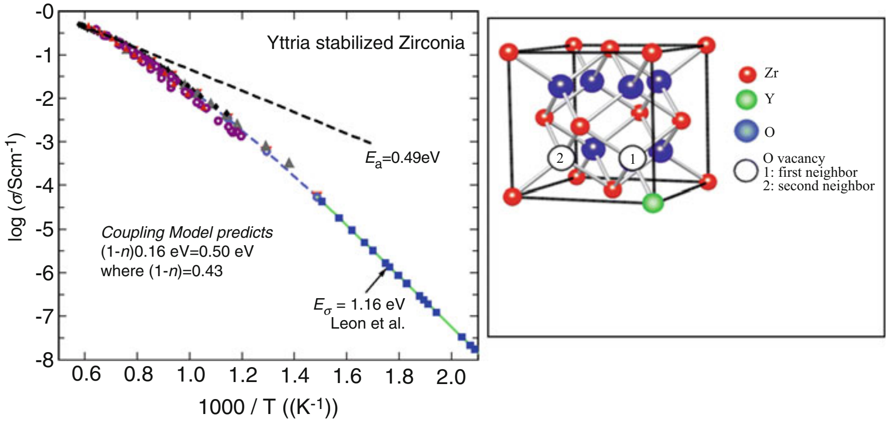

Fig. 4.31 Temperature dependence of d.c. conductivity data of bulk YSZ. *Blue squares* strung together by *green line* are lower temperature data from León et al. [270] of bulk YSZ with 9.5 mol % Y_2O_3. Higher temperature data: *black closed diamonds* from Casselton [271]; *purple open circle* from Dixon et al. [272]; *red closed triangles* from Stricker and Carlson [273], and *grey open triangles* from Näfe [274]. The *dashed line* indicates the high temperature activation energy of approximately 0.49 eV. The structure of YSZ is shown in the panel on the right

The measurements of $\sigma_{dc}(T)$ in YSZ shown in Fig. 4.31 were made by different groups [For references, see 22, 82, 83, 270–274, 277–282]. In the lower temperature regime where σ_{dc} has the Arrhenius T-dependence, $\sigma_{dc}(T) = \sigma_\infty{*}\exp(-1.16\ \mathrm{eV}/kT)$ $\Omega^{-1}\mathrm{cm}^{-1}$, from the experimentally measured frequency dispersion, the oxygen ion hopping correlation function was found to have the Kohlrausch function form with $n = 0.56$ [22, 82]. As temperature increases $\sigma_{dc}(T)$ becomes non-Arrhenius, but at the highest temperatures on approaching 1 $\Omega^{-1}\mathrm{cm}^{-1}$, it returns to another Arrhenius dependence described by $\sigma_{dc}(T) = 10^{3.6} \times \exp(-0.49\ \mathrm{eV}/kT)\ \Omega^{-1}\mathrm{cm}^{-1}$. Such behavior is evidence of crossover from many-ion conductivity relaxation to primitive conductivity relaxation because at the high conductivity levels approaching 1 $\Omega^{-1}\mathrm{cm}^{-1}$, the conductivity relaxation times are likely to be comparable with $t_c \approx 1$ to 2 ps. For YSZ, the value of ε_∞ is 28 [82], and hence from the Maxwell equation, $\sigma_{dc} = \epsilon_o\varepsilon_\infty/<\tau_\sigma>$, $\sigma_{dc} = 1$ $\Omega^{-1}\mathrm{cm}^{-1}$ corresponds to $<\tau_\sigma> = 2.5 \times 10^{-12}$ s. Oxygen-oxygen ions interaction slows down the conductivity at lower temperatures when $\tau_\sigma> > t_c$, and its higher activation energy $E_a{}^* = 1.16$ eV is correctly predicted from the smaller (primitive) activation energy, $E_a = 0.49$ eV, at high temperatures by Eq. (4.49). This can be verified by the equation, 0.49 eV= $(1 - n)1.16$ eV, being satisfied if $n = 0.57$, which is close to the value of 0.56 independently determined by fitting the frequency dependence of the conductivity relaxation data by the Kohlrausch function [22].

Figure 4.32 shows the d.c. conductivity of Na β-alumina also crosses over to a weaker Arrhenius T-dependence at high temperatures when σ_{dc} exceeds about 0.4 $\Omega^{-1}\mathrm{cm}^{-1}$, which corresponds to $<\tau_\sigma> = 1.0 \times 10^{-11}$ s because ε_∞ is 50 [54]. This indicates that t_c for Na β-alumina is about 1.0×10^{-11} s and

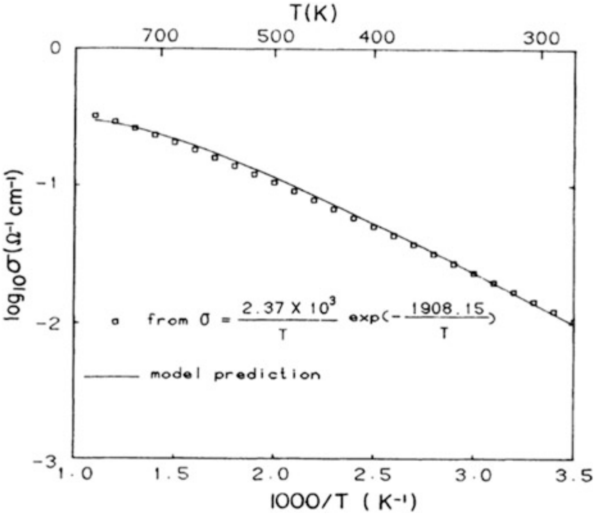

Fig. 4.32 σ_{dc} data of Na β-alumina (*open circles*). For details of the model calculation represented by the *line*, see Ref. [54]. Reproduced from Ref. [54] by permission of APS

$\nu_c = 1.6 \times 10^{10}$ Hz. Interestingly, this is nearly the same as the frequency at which the a.c. conductivity $\sigma(\nu)$ crosses over to the plateau value at higher frequencies (see the left panel of Fig. 4.29). Thus, there is consistency in determining the crossover to primitive relaxation from the temperature dependence of σ_{dc} and from the frequency dependence of isothermal $\sigma(\nu)$. Earlier in connection with the left panel of Fig. 4.29, the relation, $E_0 = (1 - n)E_{dc}$, has been verified for Na β-alumina. Except for the change in notation, this relation is the same as $E_a = (1 - n)E_a^*$ in Eq. (4.49).

The values of E_a calculated by Eq. (4.49) from the values of E_a* and n deduced from Arrhenius T-dependence of data at lower temperatures of many ionic conductors, glassy or crystalline, and in the same way as shown in Fig. 4.31, are given in Table 4.3.

Each of the calculated values of $E_a = (1-n)E_a$* is about the same as, or slightly larger than (but by no more than 20 %) the value of E_a obtained directly from the Arrhenius T-dependence of the σ_{dc} data at high temperatures where the corresponding values of τ_σ becomes comparable or shorter than t_c as described above. Furthermore, the reciprocal of the primitive attempt time τ_∞ calculated by Eq. (4.49) from the anomalous τ_∞^* is also in rough agreement with the value deduced from the high temperature σ_{dc} data after the crossover. It corresponds well to the peak angular frequency of vibrational spectrum. These good correspondences between the calculated τ_∞ and E_a from the experimentally determined parameters τ_∞*, E_a* and n in the glassy state with their counterparts at high temperature are expected because both sets of parameters are for independent diffusion of the ion, and the difference between them is caused only by the difference in density at lower and higher temperatures respectively. These changes should not have a large effect on the primitive attempt frequency and the activation energy of the primitive relaxation or independent hopping over energy barrier of the

Table 4.3 Ionic transport and conductivity relaxation parameters

Glass-forming ionic conductors	β	E_a^*	βE_a^*	E_a	E_a^{glass}	$\beta E_a^*/E_a$
$LiCl \cdot 7H_2O$	0.46	34	15.6	14.4		1.08
CdF_2-LiF-AlF_3-PbF_2	0.77	109	83.9	68.4		1.23
ZBLAN20	0.68	85	57.8	50		1.16
ZBLAN10	0.66	79	52.1	46		1.13
ZBLA	0.61	72	43.9	36		1.22
$(Li_2O) \cdot 3(B_2O_3)$	0.52	84	43.7	40		1.09
$(Na_2O) \cdot 3(SiO_2)$	0.55	64	35.2	33.5		1.05
$0.56Li_2O \cdot 0.45LiBr \cdot B_2O_3$	0.44	47.1	20.7		21.1	0.98[a]
$AgPO_3$	0.66	49.5	32.7	28.5		1.14
$(AgI)_{0.1} \cdot (AgPO_3)0.9$	0.59	43	25.4	22.5		1.13
$(AgI)_{0.2} \cdot (AgPO_3)0.8$	0.57	39.5	22.5	19.8		1.14
$(AgI)_{0.3} \cdot (AgPO_3)0.7$	0.54	32.9	17.8	15.6		1.14
$(AgI)_{0.4} \cdot (AgPO_3)0.6$	0.51	32.0	16.3	13.3		1.23
$(AgI)_{0.5} \cdot (AgPO_3)0.5$	0.48	26.9	12.9	10.1	8.7	1.27
$(AgI)_{0.6} \cdot (AgPO_3)0.4$	0.48	26.9	12.9	7.9		1.29
$(AgI)_{0.7} \cdot (Ag_2MoO_4)0.3$	0.44	19.3	8.5	9.0		0.95
$0.48\ (AgI)2^-$	0.51	25.1	12.8	13.6		0.94
$(Ag_2S)_{0.5}(GeS_2)0.5$	0.45	32.8	14.8		14.5	1.02[a]
Crystalline conductors						
Na β-Al_2O_3	0.5	13.4[b]	6.7	6.8[c]	6.74	0.99
$RbAg4I_5$	0.47[d]	9.8[c]	4.6		4.2[c]	1.09[a]
$(Y_2O_3)_{0.095}(ZrO_2)0.905$	0.43	111.9	48.2	48.2		1

For the glass-forming melts $\beta \equiv (1-n)$ and E_a^* were obtained in the glassy state from conductivity relaxation measurements, while the activation energies, E_a, were obtained from the high temperature melt dc conductivity data by $E_a = [-Rd\ln\sigma/d(1/T)]$ at $\sigma = 1\ \Omega^{-1}\text{cm}^{-1}$. For some glassy ionic conductors, the activation energies $E_a{}^{glass}$ were obtained from neutron scattering or high frequency microwave and far infrared conductivity data at temperatures all within the glassy state. All activation energies are in units of kJ/mol

[a] Calculated from the ratio $\beta E_\sigma/E_a^{glass}$

[b] At 300 K

[c] Obtained by plotting $\log\sigma$ against $1/T$

[d] Estimated from $\log\sigma$ versus $\log f$ data

ion. There are cases in which n decreases with increasing temperature and approaches zero value while τ_σ is still longer than t_c. This causes the crossover of T-dependence of σ_{dc} data to occur at temperature for which τ_σ is still longer than t_c, but the relations in Eq. (4.49) are still valid.

4.5.6 The Non-Arrhenius Intermediate Temperature Region

The reader may have already noticed in Fig. 4.31 of YSZ, and other glassy and crystalline ionic conductors in Fig. 4.1 that the crossover of $\sigma_{dc}(T)$ from the low temperature Arrhenius T-dependence to the high temperature Arrhenius

T-dependence is gradual. In fast ion conducting glasses, it was reported for the first time in 1982 by Ingram et al. [283] that the temperature dependence of the ionic conductivity becomes non-Arrhenius at enough high temperature. About 15 years later, trying to push the room temperature conductivity above 10^{-2} S/cm in "superionic" glasses of optimized composition and structure, Kincs and Martin [15] found that the conductivity at room temperature was systematically 1 to 2 orders of magnitude below that predicted from the Arrhenius behaviour of the conductivities at lower temperatures. One of these glasses is $0.4\mathrm{AgI}\cdot 0.6[0.525\mathrm{Ag_2S}\cdot 0.475(0.5\mathrm{B_2S_3} + 0.5\mathrm{SiS_2})]$ shown in Fig. 4.1. They reported this behavior as ubiquitous in fast ionic conducting glasses and thus as a fundamental limitation for their use in practical devices. Since then, the non-Arrhenius temperature dependence of the dc conductivity in ionic conductors has been confirmed experimentally as a characteristic feature arising when the conductivity exceeds a value of about 10^{-3} S/cm [13, 112, 284, 285], and several theoretical interpretations have been proposed to explain it [103, 142, 286].

A quantitative explanation for the non-Arrhenius temperature dependence of the ionic conductivity in glassy fast ion conductors was provided from the CM [103]. The d.c. conductivity, $\sigma_{dc}(T)$, is calculated by the expression, $\sigma_{dc}(T) = \epsilon_o \varepsilon_\infty / <\tau_\sigma(T)>$ where $<\tau_\sigma(T)>$ is the integral of the correlation function $\phi(t)$, i.e. $\langle \tau_\sigma \rangle = \int_0^\infty \phi(t)dt$. Although the correlation function $\phi(t)$ is given in two pieces by Eqs. (4.31) and (4.35), at lower temperatures where the condition τ_σ or $\tau^* \gg t_c$ holds, the decay of the exponential function of Eq. 4.31 is negligible for $t \leq t_c$. The intervening caged dynamics does not contribute to σ_{dc} and can be neglected. The decay in this time region given by $\exp-(t_c/\tau_o)$, when rewritten via Eq. 4.36 as $\exp-(t_c/\tau^*)^{1-n}$, is clearly small because $\tau^* \gg t_c$. The decay of $\phi(t)$ is carried out effectively from one to zero by the Kohlrausch function of Eq. 4.35 at times $t > t_c$, and $\sigma_{dc}(T)$ of glassy and crystalline ionic conductors has the Arrhenius T-dependence with activation energy, $E_a^* = E_a/(1-n)$. However, at high temperatures when τ^* (and also τ_o) becomes short and approaches t_c ($\approx$1 to 2 ps) significant decay of $\phi(t)$ has occurred by the exponential function (4.31) before t_c and $< \tau_\sigma(T) >$ picks up some partial contribution from $\tau_o(T)$. Since τ_o has a smaller activation energy E_a than that of $E_a{}^*$, this extra contribution is the cause of the non-Arrhenius behavior of $\sigma_{dc}(T)$ at the intermediate temperature range exhibited by many ionic conductors (see Fig. 4.1). In other words, on increasing temperature, the apparent activation energy of $\sigma_{dc}(T)$ decreases monotonically and assume the value of E_a when $\sigma_{dc}(T)$ is near $\epsilon_o \varepsilon_\infty / t_c \approx 1\ \mathrm{Scm}^{-1}$.

4.5.7 Anomalously Short Prefactor τ_∞^*

Here in Fig. 4.33, we show the low temperature conductivity relaxation data of (9.5 %)YSZ from León et al. [For references, see 22] [269, 270] in terms of $\tau_\sigma(T)$.

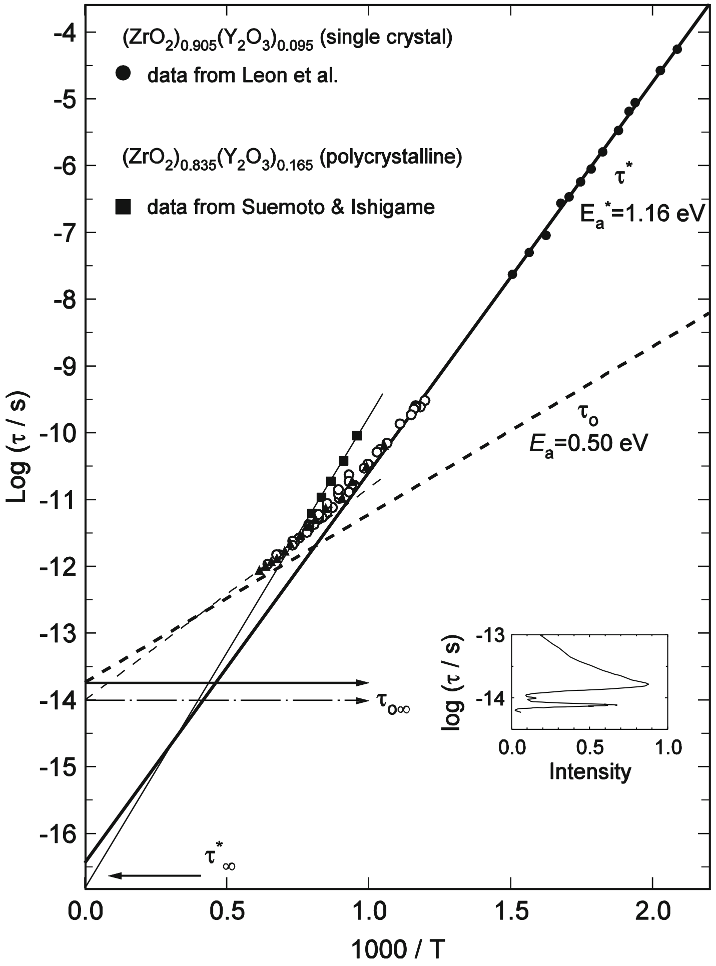

Fig. 4.33 *Closed circles* and *filled squares* are the relaxation times τ obtained from the oxygen ion conductivity relaxation data (by León et al. [270]) and quasielastic light scattering data (by Suemoto and Ishigami [279]) of YSZ. The *inset* shows the hyper-Raman spectrum from Shin and Ishigami [278]. *Open circles* are τ deduced from d.c. conductivity data in Fig. 4.31. The *thick solid* and *thin solid lines* through the data points are Arrhenius fits. The *thick* and *thin broken lines* represents respectively the independent relaxation time τ_0 calculated from τ of conductivity relaxation (*thick solid line* through *circles*) and from quasielastic light scattering (*thin solid line* through *closed squares*). The intercepts of the *broken lines* give prefactors $\tau_{0\infty}$ in good agreement with the frequencies in the narrow band at 690 cm^{-1} of the hyper-Raman spectra shown in the inset. Reproduced from Ref. [For references, see 22] by permission

Its temperature dependence is Arrhenius as indicated by the straight line through the data points in the figure, which corresponds to

$$\tau_\sigma(T) \equiv \tau_\infty^* \exp\left(E_a^*/kT\right) = 10^{-16.44} \exp(1.16\ eV/kT)\ \mathrm{s}. \tag{4.50}$$

The prefactor τ_∞^* of the experimentally observed $\tau_\sigma(T)$ is very short and its reciprocal corresponds to an unphysically high attempt frequency of the oxygen ions. On the other hand, the independent hopping relaxation times, $\tau_0(T)$, calculated from $\tau_\sigma(T)$ via Eqs. (4.37) or (4.49) with $t_c = 2$ ps, are given by

$$\tau_0(T) = \tau_\infty \exp(E_a/kT) = 10^{-13.74} \exp(0.50\ eV/kT)\ \mathrm{s}, \tag{4.51}$$

and it is represented by the thicker dashed line in Fig. 4.33. Remarkably, this calculated $\tau_0(T)$ has nearly the same value as well as temperature dependence as $\tau_\sigma(T)$ at high temperatures. This is no surprise because $\tau_\sigma(T)$ is reaching $t_c = 2$ ps at the high temperatures, and hence it crosses over to $\tau_0(T)$. The reciprocal of the prefactor τ_∞ of the calculated τ_0 now has the magnitude of an attempt frequency, as it should.

The actual attempt frequency of oxygen ions in YSZ was determined experimentally from the hyper-Raman spectrum obtained by Shin and Ishigame [278]. The vibrational modes shown have displacement of the oxygen ion towards the vacancy and are candidates for the vibrational frequency. Shin and Ishigame argued that the highest frequency narrow band located at 690 cm^{-1}, corresponding to time of $(\omega_\infty)^{-1} = 10^{-14.1}$s, contributes most effectively to the hopping of the oxygen ions and can be identified with their attempt frequency. Having determined the reciprocal of the true attempt (angular) frequency ω_∞ of the oxygen ions from experiment to be $10^{-14.1}$ s, comparison of it can be made in Fig. 4.33 with the prefactors τ_∞^* and τ_∞. The figure has $\tau_{0\infty}$ instead of τ_∞. The true angular attempt frequency $(\tau_{0\infty})^{-1}$ deduced from the CM is only 2.4 times smaller than the experimentally determined ω_∞. This small discrepancy between $(\tau_\infty)^{-1}$ and ω_∞ is well within the uncertainty in determining $\tau_0(T)$, from Eq. (4.49) due to experimental errors in determining n and $\tau_\sigma(T)$. The upper horizontal arrow in Fig. 4.33 indicates the good correspondence between τ_∞ and $(\omega_\infty)^{-1}$ from the hyper-Raman spectrum depicted by the inset. On the other hand as mentioned earlier, the angular frequency $1/\tau_\infty^* = 10^{16.4}\ \mathrm{s}^{-1}$ is unphysical because its value is more than 200 times higher than the vibrational frequency ω_∞.

Quasielastic light scattering (QELS) in YSZ by tandem Fabry-Perot interferometry was measured by Suemoto and Ishigame [279] using the same samples as in the hyper-Raman scattering experiment. Light scattering is due to fluctuation of the polarizability caused by ionic motion. They found that the shape of the scattered light intensity peak as a function of temperature taken at constant frequency, f, in the range from 1.8 to 24 GHz is non-Lorentzian and in good agreement with that coming from a correlation function that has the Kohlrausch form. The dependence of the temperature of the intensity maximum on f is converted to a dependence on $(2\pi f)^{-1} \equiv \tau_{QELS}^*$ and the data are shown in Fig. 4.33 by closed squares. The thinner straight line through the data point is the best fit to an Arrhenius temperature dependence

$$\tau^*_{QELS} \equiv \tau^*_{QELS,\infty}\exp\left(E^*_{a,QELS}/kT\right) = 10^{-16.82}\exp(1.40\ \ eV/kT) \tag{4.52}$$

The unphysically high apparent attempt frequency $\tau^*_{QELS,\infty}$ is again evident from the prefactor. The QELS correlation time τ^*_{QELS} has a slightly larger activation energy than the conductivity relaxation time $\tau_\sigma(T)$ obtained León et al. [270]. This difference arises because the concentration of yttria is higher in the sample studied by QELS than that by conductivity relaxation (16.5 vs 9.5 mol %) and it is known from conductivity measurement that E^*_a increases with yttria content when above roughly 8 mol %. The spectral shape is well fitted by an expression proportional to $\chi'(\omega)/\omega$, where $\chi'(\omega)$ is the imaginary part of the susceptibility function calculated [278] by a Fourier transform of the time derivative of the Kohlrausch function. In the process, the coupling parameter n_{QELS} was determined to have the value of 0.55. The independent ion hopping correlation time, $\tau_{QELS,\ o}$, calculated from τ^*_{QELS} has the Arrhenius dependence,

$$\tau_{QELS,o}(T) \equiv \tau_{QELS,\infty}\exp\left(E_{a,QELS}/kT\right) = 10^{-14.0}\exp(0.63\ \ eV/kT)\ \text{s} \tag{4.53}$$

and is plotted as a function of temperature in Fig. 4.33 (the thinner dashed line).

The situation in QELS is similar to conductivity relaxation in that the experimentally determined attempt frequency, $\left(\tau_{QELS,\infty}\right)^{-1}$, is too high to be real. However, the attempt frequency $\left(\tau_{QELS,\infty}\right)^{-1}$ of the independent ionic hopping motion deduced by the CM nearly coincides with the measured frequency of the vibrational mode (690 cm^{-1}). The near coincidence is indicated by the lower horizontal arrow located at the intercept of $\tau_{QELS,\ o}(T)$ with the y-axis at $(1000/T) = 0$. This horizontal arrow points almost at the 690 cm^{-1} -peak position of the observed vibrational band. Thus, the QELS data reaffirm the interpretation of the CM that $\tau_{QELS,\ o}$ and τ^*_{QELS} are respectively the ion hopping correlation time without and with the effects of many-body interactions between the ions.

The YSZ data presented and discussed in the above show how the anomalous activation energy and prefactor of the measured conductivity relaxation time can be explained by the CM equations (4.50)–(4.51) simultaneously. We mention in passing that the same equations had explained [97] the anomalous isotope mass dependence of ionic conductivity in a series of $(^6\text{Li},^7\text{Li})_2\text{O} - 2.88\text{B}_2\text{O}_3$ glasses found experimentally by Jain and coworkers [287, 288]. So far the CM is the only theory that has explained this observation.

4.5.8 The Meyer-Neldel Rule or Compensation Law

For a wide range of materials and relaxation phenomena, not just ionic conductivity [289–293], which have the effective relaxation time τ^* an Arrhenius temperature dependence, $\tau^* = \tau^*_\infty\exp\left(E^*_a/kT\right)$, often found is that the preexponential factor,

τ_∞^*, and the activation energy, E_a^*, are linked by an empirical relationship known as the Meyer-Neldel rule [289] or the Compensation Law which has the form:

$$\log\tau_\infty^* = -aE_a^* + b \tag{4.54}$$

where a and b are constants. It is important to note that a is positive so that Eq. 4.54 indicates that $\log\tau_\infty^*$ decreases with increasing E_a^*. There is a similar rule for the transport coefficient such as the conductivity, σ, or diffusivity, D. For example, written in the form, $\sigma = (\sigma_o/T)\exp(-E_\sigma/kT)$, there is a similar relation between the preexponential factors, σ_0, and the activation energies, E_σ:

$$\log\sigma_o = a'E_\sigma + b' \tag{4.55}$$

where a' and b' are constants and a' is positive. Almond and West [294] pointed out that the Meyer-Neldel rule applies to conductivity data for a variety of solid electrolytes including the Ag^+ ion conducting AgI-Ag oxysalt glasses and the polycrystalline Lisicon solid solutions of formula, $Li_{2+2x}Zn_{1-x}GeO_4$. Nowick et al. [295] further examined the Meyer-Neldel rule and concluded that there are exceptions in the solid electrolytes they considered.

The Meyer-Neldel rule has been rationalized by the CM equations (4.49) [296] for a family of ionic conductors that have approximately the same primitive energy barrier E_a and ion attempt frequency $1/\tau_\infty$, but different coupling parameters n. Variation in the magnitude of n can arise from different ionic concentrations, values of ε_∞ and structure. These factors affect the screened Coulomb interactions between the diffusing ions and therefore change n from one member of the family to another as borne out by Monte Carlo simulations [89]. If n is larger, via Eq. 4.49 the many-body effects simultaneously make the prefactor τ_∞^* unphysically shorter and the activation energy E_a^* larger than the true activation energy E_a. The dual effects when combined leads to the Meyer-Neldel rule or the compensation law. It makes repeated appearance in other interacting systems.

4.5.9 Anti Meyer-Neldel Rule

The behavior opposite to the Meyer-Neldel rule was found in the family $(AgI)_x(AgPO_3)_{1-x}$ [297, 298]. For this family, the coupling parameters n, the d.c. conductivity activation energy E_σ and the preexponential factor have been determined for all x by electric modulus analysis of conductivity relaxation measurements [298]. The values of these parameters are given in Table I of Ref. [296]. Although there is some scatter, the trend that the prefactor τ_∞^* decreases while E_σ also decrease is clear and is opposite to Eq. 4.54 or the MN rule.

The origin of this anti Meyer-Neldel behavior has also been rationalized by the CM [296]. As shown in Table I of Ref. [296], the values of the product $(1-n)E_\sigma$, which is to be identified with E_a, clearly show in the system $(AgI)_x(AgPO_3)_{1-x}$ that the true energy barrier E_a decreases by a large factor of 2.5 when x increases. The coupling parameter n increases with increasing x due naturally to increased interaction between the Ag^+ ions with concentration. Although n also increases with x, the increase is not sufficient to compensate the decrease in E_a and to make the ratio $E_a/(1-n)$, or E_σ from Eq. 4.49, increases with x. Consequently, E_σ decreases with increasing x. Far infrared spectra of $(AgI)_{0.5}(AgPO_3)_{0.5}$ has determined τ_∞ to be about $10^{-13.3}$ s. Since t_c is ~2 ps and is longer than τ_∞, Eq. 4.49 indicates that the apparent τ_∞^* will be shorter than τ_∞ and it decreases with increasing n (or x). This trend is in qualitative agreement with the experimental data shown in Table I of Ref. [296]. Combining the two results of the dependences of E_σ and on x from the CM, we explain the anti Meyer-Neldel rule observed in the system $(AgI)_x(AgPO_3)_{1-x}$.

4.5.10 Computer Simulations of Energy Barrier of YSZ

Apart from the many experimental studies, many groups have published results from computer simulations on the dynamics of oxide ions in YSZ, thus allowing a critical test for the predictions and interpretation of the CM described above. Kinetic Monte Carlo simulation with density functional theory has been used to calculate the migration energy barriers and the self-diffusion of oxygen at macroscopic time-scales [299]. This method assumes that oxygen diffusion is well-represented by oxygen vacancy hopping through the edges of cation tetrahedra. The advantage of this method is that it is not restricted to relatively short times like molecular dynamics simulations. For example, the smallest of all the activation barriers for oxygen vacancy migration is across the Zr–Zr edges, and it is 0.58 eV. Activation energy for oxygen self-diffusion, E_{Ka}, increases with x, the mol % of Y_2O_3, from nearly 0.58 eV for x less than 2.5 to ≈ 0.59 eV for $x = 8$, ≈ 0.60 eV for $x = 10$, and ≈ 0.61 eV for $x = 12$. It was pointed out [300] that these migration energy barriers were calculated without including ionic interactions. This may be the reason why the calculated migration energy barriers E_{Ka} are smaller than E_a^* and $E_{a,QELS}^*$ found in conductivity and quasielastic light scattering experiments, say for 8 mol% of Y_2O_3. It is however interesting that these smaller activation energies E_{Ka} calculated without ion-ion interaction is the actual energy barrier, and hence it can be identified with the energy barrier for independent oxygen hop, E_a, of the CM. In fact, the value $E_{Ka} \approx 0.59$ eV for $x = 8$ mol % lies close and in between the two values of the energy barrier for independent oxygen hop: $E_a \approx 0.52$ eV and $E_{a,QELS} = 0.63$ eV deduced from conductivity relaxation and quasielastic light scattering respectively, and supports the prediction of the CM that the true energy barrier E_a of oxygen ion hopping is in the range $0.52 \leq E_a \leq 0.63$ eV. Recognizing the importance of accounting for ionic interactions, Lee et al. used a kinetic Monte Carlo model based on combining density functional theory with the cluster expansion method to calculate ionic conductivity in single-crystal YSZ [300]. An increase of the activation energy to 0.74 eV at high T and 0.85 eV at low T, as compared with $E_{Ka} \approx 0.59$ eV, was found for the ionic conductivity of YSZ with 8 mol% of Y_2O_3. This enhancement of the activation energy found by including ion-ion interaction in the simulations is in fact expected according to the prediction of the CM, although its magnitude is still smaller than $E_a^* = 1.16$ eV found by conductivity relaxation data at low T.

Tarancón et al. have also published another molecular dynamics simulation in which the interaction between oxygen ions was included [301]. The potential energy chosen is a function of the distance between ions, Zr^{4+}, Y^{3+}, and O^{2-}. It is composed of a Born–Mayer–Buckingham potential for short range interactions, and Coulomb terms to describe the long-range electrostatic interactions between the ions of YSZ. These authors obtained the oxygen tracer diffusion coefficient of YSZ with 8 mol% Y_2O_3 at high temperatures ranging from 1159 K to 1959 K. From the Arrhenius temperature dependence, they obtained the activation energy of 0.68 eV, which is significantly smaller than $E_a^* = 1.16$ eV of d.c. conductivity at lower temperatures. Its apparent activation energy is significantly smaller than 1.16 eV, but still larger than $E_a \approx 0.52$ eV and $E_{a,QELS} = 0.63$ eV. Therefore, the activation energy of 0.68 eV found by Tarancón et al. is due to τ^* not long compared with $t_c \approx 1$ to 2 ps in the temperature range of simulations, consistent with the existence of the crossover from many-ion relaxation to independent ion hop in the CM. Similar molecular dynamics simulations of YSZ were carried out by Devanathan et al. with the same potential [302] and also at high temperatures from 1125 to 2500 K. The diffusion coefficients of oxygen obtained over this temperature range have activation energies of 0.59, 0.60, and 0.73 eV for YSZ with 6, 8, and 10 mol% Y_2O_3 respectively. Again, τ_∞^* is close to $t_c \approx 1$ to 2 ps in the measurement temperature range, and the activation energies obtained by Devanathan et al. are the actual energy barriers opposing oxygen hopping consistent with the values deduced by the CM. Chang et al. [303] have obtained mean square displacements of oxygen in YSZ over the temperature range, $873 \leq T \leq 1473$ K, and for times up to 500 ps, in another molecular dynamics simulation using the same potential. An activation energy of about 0.5 eV is obtained for the YSZ with 7 mol% Y_2O_3, and for the same reason as discussed in the above, the proximity of τ^* to $t_c \approx 1$ to 2 ps in the simulation temperature range justifies interpreting the deduced activation energy of 0.5 eV as the actual energy barrier of oxygen vacancy hopping. Lau and Dunlap [304] performed another similar molecular dynamics simulation up to 2.5 ns and reported d.c. conductivity of single crystal YSZ with 8 mol% Y_2O_3 having Arrhenius temperature dependence over about 15 orders of magnitude in the wide temperature range from 300 to 1400 K, and have activation energy of 0.59 ± 0.05 eV. This activation energy is similar to $E_a \approx 0.52$ eV and $E_{a,QELS} = 0.63$ eV and is consistent with the interpretation of actual energy barrier as long as temperature is higher than say 1000 K. However, the results of Lau and Dunlap at low temperature are at odds with the much larger activation energy, $E_a^* = 1.16$ eV, of d.c. conductivity observed by experiments of single crystal YSZ with 8 mol% Y_2O_3.

Pennycook et al. [305, 306], have reported results of finite-temperature dynamical simulations of the oxygen vacancy dynamics in bulk cubic zirconia where the oxygen vacancies were generated by applying 7 % strain to change the oxygen sublattice. At high temperatures the oxygen structure becomes disordered. The mean-square-displacements were calculated up to 6 ps, and hence the diffusion coefficients of oxygen in the strained structure were obtained from the simulations. The activation barrier extracted from an Arrhenius plot of the diffusivities is 0.4 ± 0.1 eV, identical to $E_a \approx 0.50$ to 0.52 eV within the error estimate. Since the simulations were carried out only up to 6 ps and close to $t_c \approx 1$ to 2 ps, this activation energy from simulation of strained bulk cubic zirconia can be taken as another source of information on the actual energy barrier for oxygen diffusion.

4.5.11 Temperature Independence of $\Delta\varepsilon$ in YSZ

The measurements of the real part of the permittivity $\varepsilon'(\omega)$ vs. frequency of YSZ at different temperatures offer critical test of the prediction from the electric modulus, $M^*(\omega)$, representation of the data that the ratio $\varepsilon_s/\varepsilon_\infty$ is given by Eq. (4.14). If the correlation function is the Kohlrausch function for the electric modulus $M_\beta^*(\omega)$, in conformity with the CM, $\varepsilon_s/\varepsilon_\infty$ and $\Delta\varepsilon$ are given by Eq. (4.18) and Eq. (4.19) respectively. Moreover, the $\varepsilon'_\beta(\omega)$ calculated from $M_\beta^*(\omega)$ is in good agreement with the frequency dispersion of the experimental data of $\varepsilon'(\omega)$, as shown before in Figs. 4.6 and 4.12 for various ionic conductors. Despite the demonstrative success of the electric modulus $M_\beta^*(\omega)$, there are others who ignored it. Instead, by analogy of the hop of the cation between anionic sites to the rotation of a permanent dipole, they [74] assumed that the permittivity change $\Delta\varepsilon$ caused by the relaxation of mobile ions is given by $\Delta\varepsilon = n(qd)^2/3\varepsilon_o kT$, where n is the mobile ion concentration, q is the charge of the mobile ions, d is the jump length, and the product qd is the effective dipole of the hopping ion. We have discussed this before in Sect. 4.2.1.2.

León et al. [82] used electrical relaxation data [83] of YSZ, in which the mobile ion density n and the ionic hopping distance d are known, to perform a critical test of the validity of $\Delta\varepsilon = n(qd)^2/3\varepsilon_o kT$, and the alternative expression for $\Delta\varepsilon$ given by Eq. (4.19) from the electric modulus. The frequency dependence of the real part of the permittivity, $\varepsilon'(\omega)$, is shown in Fig. 4.34 at several temperatures for YSZ samples with different yttria content. For each composition, data points have been shifted horizontally by using a normalization frequency for each temperature, f_p, in order to collapse all data in a single curve in the log-log scale. Despite the presence of strong electrode polarization effects at high temperature and low frequencies, the low frequency value of ε_s can be determined, and consequently the permittivity change from the high frequency permittivity ε_∞ towards ε_s. It is found that the magnitude of $\Delta\varepsilon$ is nearly independent of temperature and also of the ion mobile density, which is at odds with a change of ε_s by a factor of about 1.6 predicted by

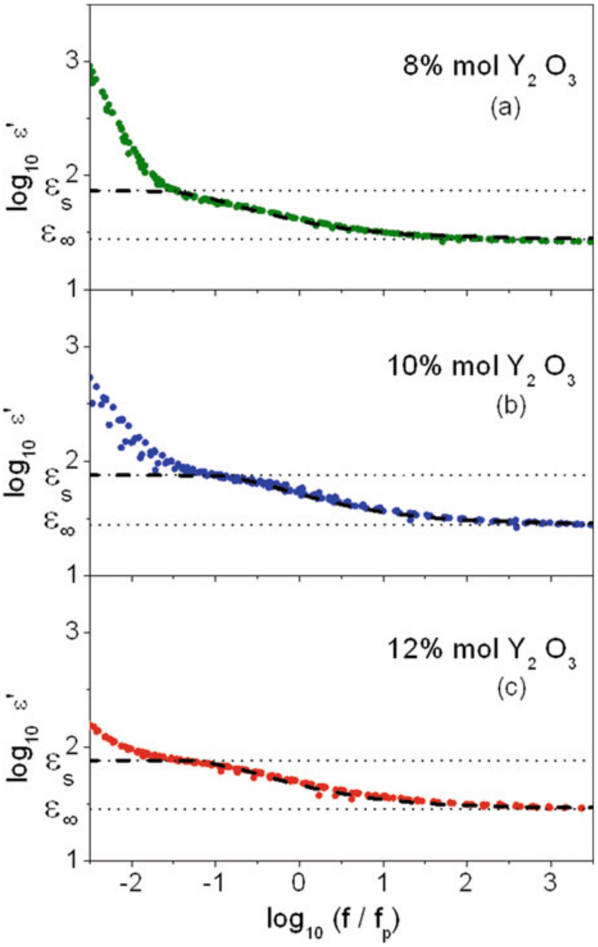

Fig. 4.34 Log-log plots of the real part of the permittivity $\varepsilon'(f)$ vs. frequency for: (**a**) 8 % mol Y_2O_3 –YSZ at temperatures between 300 K and 780 K (*green symbols*); (**b**) 10 % mol Y_2O_3 – YSZ at temperatures between 300 K and 775 K (*blue symbols*); (**c**) 12 % mol Y_2O_3 – YSZ at temperatures between 302 K and 774 K (*red symbols*). Frequency axis has been shifted for each data set in order to collapse permittivity data at different temperatures into a single curve. The normalization frequencies f_p used for each sample were calculated from the following expressions: $f_p = 11.75 - 4882/T$ in (**a**), $f_p = 11.13 - 5052/T$ in (**b**), and $f_p = 9.81 - 5577/T$ in (**c**). *Dashed lines* represent the real part of the permittivity $\varepsilon'(\omega)$ calculated from the fits of the electric modulus data by a KWW function with $1 - n = 0.52$. *Horizontal dotted lines* represent the limiting values, ε_∞ and ε_s, at high and low frequencies respectively. The permittivity change $\Delta\varepsilon = \varepsilon_s - \varepsilon_\infty$ is found to be independent of both temperature and mobile ion concentration. Data after León et al. [82]

$\Delta\varepsilon = n(qd)^2/3\varepsilon_o kT$ in the temperature range of 500 to 780 K, where the value of ε_s can be determined from the experimental data. On the other hand, according to the electric modulus formalism, and assuming a KWW stretched exponential (Eq. 4.15) for the relaxation function, $\Delta\varepsilon$ is given by Eq. (4.19). It is worthwhile to emphasize that the proportionality relationship between $\Delta\varepsilon$ and ε_∞ in Eq. (4.19) holds regardless of the exact time dependence of the relaxation function. Eq. (4.19) is obtained by the choice of a KWW function to describe the electrical relaxation data, but a similar expression, and a comparable value of the proportionality factor, would be obtained for any other choice.

León et al. [82] found that the electrical relaxation data of YSZ samples with yttria content between 8 % and 12 % are well described by using a single exponent $(1-n)=0.52$, independent of temperature. This finding, together to the fact that ε_∞ is almost constant, implies that if Eq. (4.19) from the CM is correct, the permittivity change $\Delta\varepsilon$ is also approximately independent of temperature and composition and its predicted value from the electric modulus analysis is $\Delta\varepsilon=1.75\varepsilon_\infty=49\pm2$. This is contrary to that expected from the validity of $\Delta\varepsilon = n(qd)^2/3\varepsilon_o kT$ used in the scaling analysis, since then the permittivity change $\Delta\varepsilon$ should depend on temperature and mobile ion concentration. Dashed lines in Fig. 4.34 represent the real part of the permittivity $\varepsilon'(\omega)$ calculated from the fits of the electric modulus data by the stretched exponential function with $1\text{-}n=0.52$. From these fits the values of $\varepsilon_\infty=28\pm1$ and $\varepsilon_s=77\pm2$ were obtained at high and low frequencies respectively, and there is good agreement with experimental data, not only in the magnitude of the permittivity change, but also in the frequency dependence. This strongly suggests the validity of Eq. (4.19) from the CM, instead of $\Delta\varepsilon = n(qd)^2/3\varepsilon_o kT$ to account for $\Delta\varepsilon$, supports the use of the electric modulus formalism to describe electrical relaxation in ionic conductors, and casts doubts on the use of a universal scaling law to analyse and interpret the ac conductivity spectra of ionic conductors by Sidebottom [74, 79].

Before we go to discuss other ionic conductor in the next section, it is worth pointing out the success of the CM in explaining quantitatively the multiple experimental facts of a single ionic conductor YSZ. To be discussed in Chap. 6 on nano-ionics is the dramatic change of oxygen ion conductivity relaxation in nanometer thin films of YSZ, which has been explained quantitatively as well by the CM [307]. YSZ is one example among many ionic conductors, and this feat is unmatched by any other theory of ionic conductivity relaxation.

4.6 Oxide-Ion Dynamics and Diffusion in $RE_2Zr_{2\text{-}y}Ti_yO_7$ Conductors

The success of the CM in quantitative explanation of oxygen ion dynamics in YSZ is not an isolated incident. The applications of the CM to similar ion dynamic properties have been equally successful in other glassy and crystalline ionic conductors [154]. Among these cases to be discussed in this section are the oxygen ion conductors of the pyrochlore structure [308] having compositions, $A_2Zr_{2-y}Ti_yO_7$, (A = Y, Dy, and Gd, the rare earths), which are directly related to YSZ with 33 mol % yttria, $Y_2Zr_2O_7$ ($0.33Y_2O_3$-$0.67ZrO_2$).

Oxide-ion conductors of pyrochlore structure $A_2B_2O(1)_6O(2)$ have been proposed as alternative electrolytes in solid oxide fuel cell devices [309–312]. The pyrochlore cubic crystal structure might be derived from that of an anion deficient fluorite by doubling the unit cell, removing one out of every eight anions and placing cations and anions in four crystallographically non-equivalent sites. Thus, A ($R_A \approx 1$ Å) and B ($R_B \approx 0.6$ Å) cations are respectively found at the 16*d* (8-coordinated) and 16*c* (6-coordinated) sites (origin choice 2 of space group 227) whereas anions are distributed between two tetrahedrally coordinated positions, 48*f* [O(1)] and 8*b* [O(2)] [313, 314]. There is in addition another tetrahedral site available for anions in the unit cell, 8*a*, which is systematically vacant in fully ordered pyrochlores, and which makes them poor oxygen ion conductors. However, *defect* pyrochlores such as $Gd_2Zr_2O_7$, which are intrinsically disordered and with the three aforementioned anion positions partially occupied, are good oxygen ion conductors at high temperatures. Different theoretical calculations have shown that the most stable intrinsic defect in these compounds is an oxygen Frenkel pair consisting of a vacant 48*f* position and an interstitial ion located at the 8*a* site [312, 315–317]. Thus, oxygen conductivity in pyrochlores depends essentially on the energy of formation of this defect. Since cation disorder increases the similarity between non-equivalent oxygen sites and promotes Frenkel defect formation, this energy is substantially reduced in defect pyrochlores by the presence of disordering in the cation sublattice. However, it is found that the most disordered pyrochlores are not the best oxygen ion conductors, usually showing higher activation energies E_{dc} for ion migration. Consequently, highest conductivity values are obtained in partially disordered materials.

Within the family of oxide-ion conductors with pyrochlore structure, rare-earth titanate-zirconates, and in particular the series $Gd_2Ti_{2-y}Zr_yO_7$ is of interest since the concentration of mobile oxygen vacancies can be largely increased by substitution of Zr for Ti [318, 319]. This is due to the oxygen disorder induced by the increase of the average ionic radius of the cation at the B site from $R_B = 0.74$ Å (for Ti^{4+}(VIII)) to $R_B = 0.84$ Å (for Zr^{4+}(VIII)). Moreover, for $y \approx 1.8$ the ionic conductivity is of the same order of magnitude as that of YSZ (10^{-2} S/cm at 700 °C) [309]. As already mentioned, previous theoretical calculations [312, 316, 317] have found that oxygen diffusion in $Gd_2Ti_{2-y}Zr_yO_7$ takes place by hopping from 48*f* site to 48*f* sites. This result was in fact confirmed later experimentally by XPS measurements [310]. The occupancy of 48*f* sites by oxygen ions is very close to 1 for those compositions with Zr contents up to $y = 0.6$, but decreases progressively as Zr content is increased further [320]. Similar to the case of YSZ presented in the previous section, the energy barrier for oxygen hopping from 48*f* to 48*f* sites had been calculated theoretically and found to be much smaller than that observed experimentally in d.c. conductivity [321].

These facts made the series $Gd_2Ti_{2-y}Zr_yO_7$ an ideal system to investigate the possible existence of cooperative effects in the oxygen ions dynamics and its influence in determining the activation energy of long-range ionic transport. In fact, this issue was investigated by using Impedance Spectroscopy, which allows determination of the complex electrical conductivity, $\sigma^*(\omega)$, and thus obtaining information on the oxygen dynamics from its frequency dependence [31, 322]. As it is usually found in ionic conductors, the electrical conductivity relaxation is well described by using a stretched exponential or Kohlrausch function of the form, $\Phi(t) = \exp\left(-(t/\tau_\sigma)^{1-n}\right)$, with $0 < (1-n) \leq 1$. The characteristic relaxation time τ_σ is thermally activated with the activation energy E_{dc} of the dc conductivity. The Coupling Model (CM) accounts for this time dependence of the relaxation function as a consequence of ion-ion cooperativity in the ion diffusion process, which results in the slowing down of the relaxation rate at times longer than t_c of the order of 1–2 ps, changing the correlation function from a pure exponential to the Kohlrausch function (see Eqs. 4.31 and 4.35). For ions vibrating in their cages and hopping to neighboring sites through barriers of energy E_a, the relaxation time for this independent ion hop is $\tau_0(T) = \tau_\infty \exp(E_a/kT)$. The reciprocal of τ_∞ is the attempt frequency of ions. It follows from the CM that the activation energy for the d.c. conductivity or τ_σ will be larger than the energy barrier and given by $E_{dc} = E_a/(1-n)$, i.e. Eq. (4.49). An increase of ion-ion interaction leads to higher degree of cooperativity in the ion diffusion process, which corresponds to a higher value of the coupling parameter n and consequently to a higher activation energy for long-range ionic transport.

The imaginary part of the electric modulus for samples with different Zr contents, as obtained by Moreno et al. [313], are presented in Fig. 4.35. It shows how the peak broadens when Zr content is increased, corresponding to higher

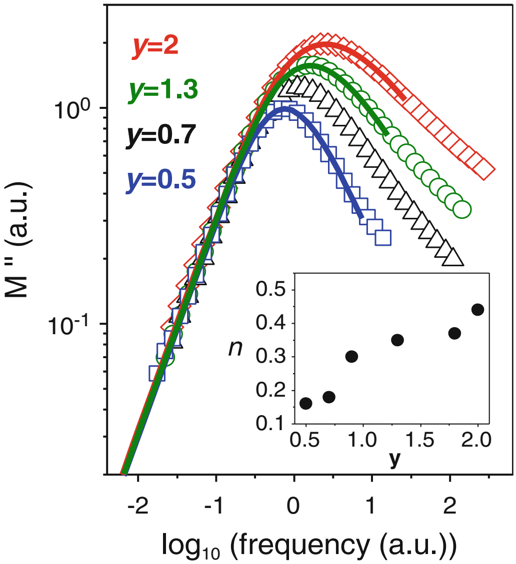

Fig. 4.35 Imaginary part of the electric modulus spectra for $Gd_2Ti_{2-y}Zr_yO_7$ samples with $y = 2$, 1.3, 0.9 and 0.5 (from *right* to *left*). Experimental data have been *horizontally* and *vertically* shifted for clarity. The *inset* shows the dependence of the exponent n as a function of Zr content, as obtained from fits of electrical conductivity relaxation data to a Kohlrausch function in the time domain

Fig. 4.36 Arrhenius plot of dc conductivity in the series $Gd_2Ti_{2-y}Zr_yO_7$ for different Zr contents ($y = 0.5$, 0.7, 0.9, 1.3, 2, and 1.8 (from bottom to top). The *inset* shows the increase of the activation energy for the dc conductivity as the Zr content increases

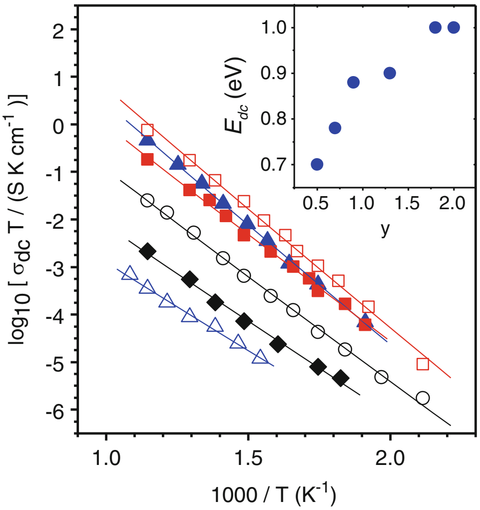

n values in the Kohlrausch function fit to electric modulus spectra. The inset to Fig. 4.35 shows there is a systematic and significant rise in the value of n, from $n = 0.16$ towards $n = 0.44$, as Zr content is increased from $y = 0.5$ to 2.0. As mentioned above, it is well known that increasing Zr content above $y \geq 0.5$ results in creating vacant 48*f* sites which are responsible for oxygen hopping motion [320]. On the other hand, XPS results have shown that increasing Zr content leads to higher disorder in both the cationic and anionic sublattices [310]. It is thus expected that the higher concentration of mobile oxygen vacancies at 48*f* sites enhances mutual interactions and the more disordered structure fosters correlations. The trend of increase of the coupling parameter n with ion concentration shown in Fig. 4.35 can be rationalized in terms of the CM as due to the enhancement of ion-ion interactions.

Figure 4.36 is an Arrhenius plot of the dc conductivity for different compositions in the series $Gd_2Ti_{2-y}Zr_yO_7$, showing the activated behavior of the temperature dependence. The activation energy E_{dc} is in the range 0.70–1.0 eV and increases systematically with Zr content above $y = 0.5$ (see inset to Fig. 4.36). According to the Coupling Model, E_a is the activation energy for independent ion hopping or the microscopic energy barrier for oxygen ions to hop into neighboring vacant sites. Since both n and E_{dc} have been obtained from experiment, we can use Eq. (4.49) to get an estimate of the energy barrier for oxygen ions to jump from 48*f* to 48*f* sites in the structure. In Fig. 4.37, the activation energy E_{dc} has been plotted as a function of $(1-n)^{-1}$ (see red squares), and a clear linear correlation is found. From the slope of a linear fit to these data, the microscopic energy barrier can be determined, and a value of $E_a = 0.60 \pm 0.03$ eV is obtained. Another way to show this result is given in Fig. 4.38. Interestingly, this value is in excellent agreement with 0.57–0.64 eV from molecular dynamics simulations [315] and 0.58 eV from static lattice energy minimization simulations [312] for the energy barrier oxygen ions must overcome to hop from 48*f* to 48*f* sites. Note that the increase in the activation energy E_{dc} occurs despite increasing cell volume when substituting Zr for Ti (e.g. $a = 10.185$ Å vs. 10.528 Å for $Gd_2Ti_2O_7$ and $Gd_2Zr_2O_7$ respectively).

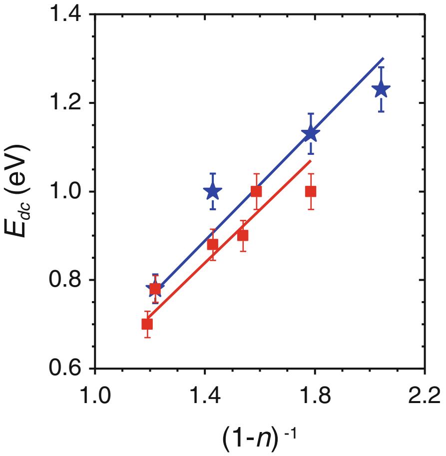

Fig. 4.37 Activation energy E_{dc} for the dc conductivity as a function of the coupling parameter obtained from electrical conductivity relaxation measurements: *red squares* are data from $Gd_2Ti_{2-y}Zr_yO_7$ samples with different Zr content between $y = 0.5$ and $y = 2$, where increasing activation energy is obtained by increasing the Zr content; and *blue stars* are from $Gd_2Ti_{1.3}Zr_{0.7}O_7$ samples but sintered at different temperatures (800, 1000, 1200 and 1500 °C), where increasing sintering temperature leads to lower E_{dc} values

Fig. 4.38 Activation energies E_{dc} (*open squares*) and $E_a = (1 - n)E_{dc}$ (*closed circles*) as a function of Zr content in $Gd_2Ti_{2-y}Zr_yO_7$. *Solid line* represents the average value $E_a = 0.60$ eV obtained for the energy barrier for oxygen hopping

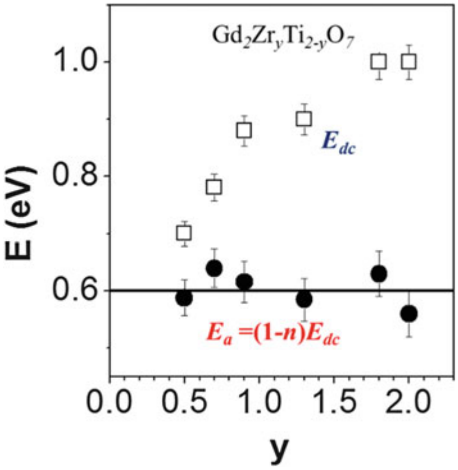

Furthermore, while the dc conductivity activation energy increases systematically with Zr content, the energy barrier seems to remain constant within experimental error, indicating that the difference between the observed E_{dc} and E_a is due to the slowing down of the oxygen ion hopping dynamics by the many-ions cooperative dynamics. Naturally, increasing ion concentration leads to enhanced cooperativity and larger coupling parameter n in the dynamics of the oxygen ions, and explains the larger difference between E_{dc} and E_a.

4.6.1 Cation Size Effects in Oxygen ion Dynamics

It is worth mentioning that for other lanthanides (Ln) like Y and Dy instead of Gd in the A sites of the $Ln_2Ti_{2-y}Zr_yO_7$ systems, both the exponent n and the activation energy E_{dc} have also found to increase as the average R_B increases (i.e. Zr content increases) [308, 313]. The increases of n and E_{dc} with R_B are shown in Figs. 4.39 and 4.40a respectively. Noticeably, as structural disordering in the Dy and Y containing series is higher than in the Gd one (both $Dy_2Zr_2O_7$ (DZT) and $Y_2Zr_2O_7$ (YZT), are nominally fluorites at all temperatures whereas $Gd_2Zr_2O_7$

Fig. 4.39 Dependence of the exponent n on the average cations size R_B for samples in the series of (DZT) $Dy_2Zr_{2-y}Ti_yO_7$, (YZT) $Y_2Zr_{2-y}Ti_yO_7$, and (GZT) $Gd_2Zr_{2-y}Ti_yO_7$

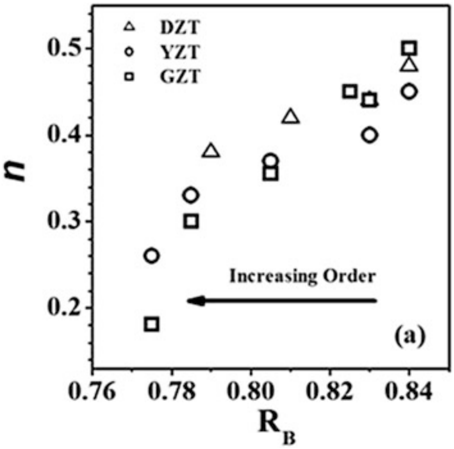

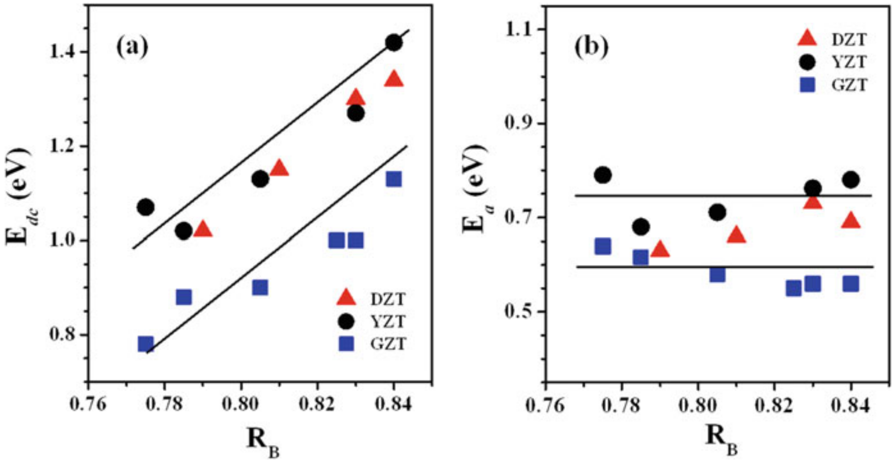

Fig. 4.40 Dependences of the values of (**a**) the dc conductivity activation energy E_{dc} and (**b**) microscopic activation energy E_a, on the average cations size R_B for samples in the series of (DZT) $Dy_2Zr_{2-y}Ti_yO_7$, (YZT) $Y_2Zr_{2-y}Ti_yO_7$, and (GZT) $Gd_2Zr_{2-y}Ti_yO_7$. *Solid lines* are only shown to emphasize the trends

(GZT) is pyrochlore below 1550 °C), lower dc activation energies E_{dc} were obtained for the latter (see Fig. 4.40a). As for the E_a, the energy barrier remains approximately constant for each series (see Fig. 4.40b), indicating that the difference between the observed E_{dc} and E_a is indeed primarily due to the increasing slowing down of the oxygen ion hopping dynamics by the many-ions cooperative effects. The degree of cooperativity in the dynamics of the mobile oxygen ions is enhanced by increasing R_B (higher Zr content), since the mobile ions concentration increases by almost two orders of magnitude by increasing Zr content from $y = 0$ to 1.5 [318, 323],and thus naturally it explains the increasing larger difference between E_{dc} and E_a. It can be observed also in Fig. 4.40b that the average E_a value decreases as A-site occupancy changes from Y to Gd accompanied by an increase in R_A. We will come back later to this point.

The influence of oxygen order on oxide ion dynamics have also been investigated by using samples with a fixed Zr content where structural disorder is thermally induced instead of chemically induced [55]. The composition $Gd_2Ti_{1.3}Zr_{0.7}O_7$ was selected for this study because it lies close to the boundary between the fully-ordered "*ideal*" and the "*defect*" pyrochlore stability fields observed for equilibrium phases in the $Gd_2Ti_{2-y}Zr_yO_7$ solid solution. It has been also shown the feasibility of preparing metastable anion deficient fluorite-type $Gd_2Ti_{1.3}Zr_{0.7}O_7$ samples by mechanical milling starting from constituent oxides [324]. These facts make this composition an appropriate system to investigate the possible influence of structural disorder on the oxygen hopping dynamics and thus on the long-range ionic transport. Moreno et al. [325] performed post-milling thermal treatments at four selected temperatures (800, 1000, 1200 and 1500 °C) that allow some ordering to take place. X-ray diffraction and Raman spectroscopy were used to characterize the structure of the samples, obtaining transient pyrochlores with a very unusual cation distribution. They report that both cation and anion substructures order at different rates: while the anion substructure orders mostly in a narrow temperature range around 860 °C, the ordering of the cation substructure is sluggish, and very high temperatures (1500 °C) are needed to complete the process. This has been related to the extremely slow rate of cation diffusion in fluorite-related stabilized zirconia based materials, which is well known [98]. Impedance spectroscopic measurements on these samples have allowed the analysis of electrical conductivity relaxation data as a function of structural disorder. Experimental data show that the activation energy for the *dc* conductivity, E_{dc}, decreases with increasing sintering temperature, thus leading to higher ionic conductivity values. It is also found in this series of samples that there is a concomitant decrease of the exponent n in the Kohlrausch functions characterizing the dynamics of oxygen ions.

Figure 4.41 shows the imaginary part of the electric modulus for $Gd_2Ti_{1.3}Zr_{0.7}O_7$ samples with different post-milling thermal treatments at temperatures of 800, 1000, 1200 and 1500 °C, as obtained by Moreno et al. [325] Peak narrowing corresponds to lower n values in the KWW fit to electric modulus spectra, and the exponent n decreases systematically from 0.51 ± 0.01 to 0.18 ± 0.01 when the sintering temperature increases from 800 to 1500 °C (see inset to Fig. 4.41). The characteristic relaxation time is found to be thermally activated with the

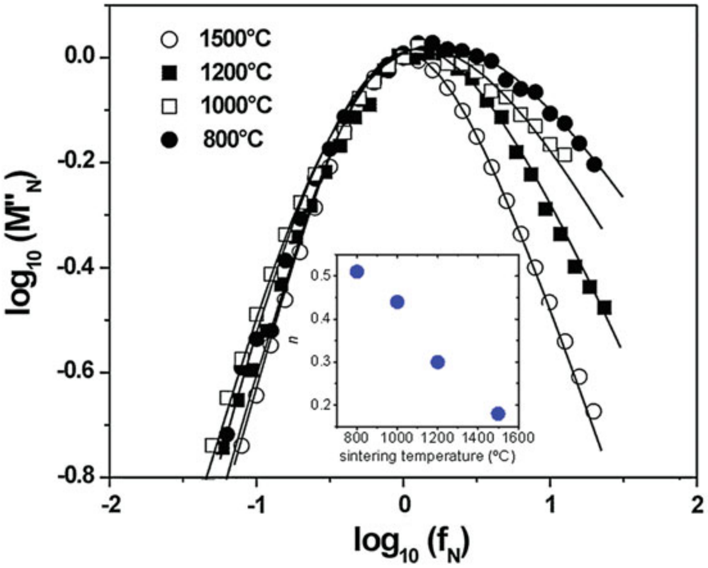

Fig. 4.41 Spectra of the imaginary part of the electric modulus for $Gd_2(Ti_{0.65}Zr_{0.35})_2O_7$ powders sintered at different temperatures. Experimental data have been *horizontally* and *vertically* shifted by normalizing to the corresponding peak frequency and peak height values in each curve. *Solid lines* are fits according to a Kohlrausch relaxation function. The *inset* shows the decrease in the value of the exponent n in the KWW fit as the sintering temperature increases from 800 °C to 1500 °C

same activation energy as the dc conductivity, whose temperature dependence is shown in Fig. 4.42.

All samples show a thermally activated behavior of the *dc* conductivity σ_{dc}, and the activation energy, E_{dc}, is found to decrease from 1.23 ± 0.04 to 0.78 ± 0.03 eV as the sintering temperature increases from 800 to 1500 °C (see Fig. 4.42). The activation energy E_{dc} obtained for these samples has been also plotted as a function of $(1\text{-}n)^{-1}$ in Fig. 4.37 (blue stars) where they can be easily compared with samples presenting a chemically induced disorder. The microscopic energy barrier $E_a = 0.64 \pm 0.03$ eV was also obtained from a linear fit to $E_{dc} = E_a/(1\text{-}n)$, i.e. Eq. (4.49). This behavior is also explained as due to the enhancement of ion-ion interactions. It is interesting to see again that a clear correlation is found, although in this case the enhancement of ion-ion interactions is related to the higher structural disorder induced by the lower sintering temperature in the preparation process instead of due to a higher Zr content as in the previous section.

The effect of increasing the A cation size on the oxide ion dynamics has been also reported by Díaz-Guillén and coworkers [308, 326, 327]. A similar analysis of the electrical relaxation data was performed on several samples: Gd-, Dy- and Y-zirconates (AZ samples: $A_2Zr_2O_7$ (A = Gd, Y, Dy)), and also on Gd-zirconates where Gd was partially replaced by La (GLZ samples: $Gd_{2-x}La_xZr_2O_7$ ($x = 0.2$; 0.3; 0.4; 0.8; 1) [308, 326, 327]. In this way, the average value of the ionic radius of A cation was changed between $R_A = 1.02$ and 1.10 Å.

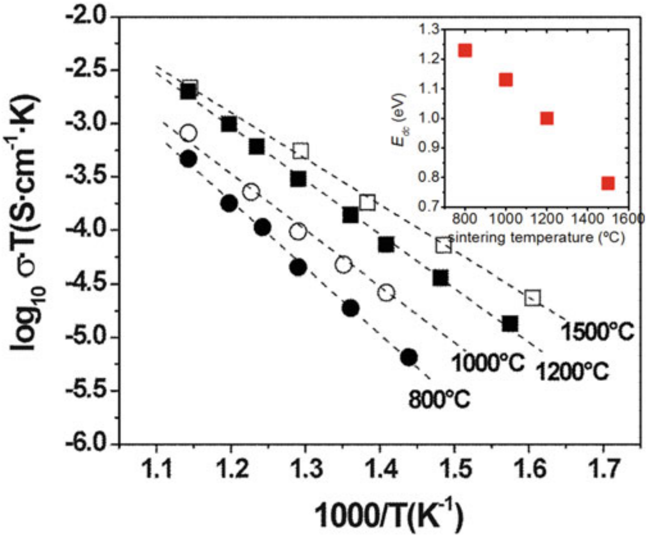

Fig. 4.42 Arrhenius plots showing the temperature dependence of the *dc* conductivity obtained for various $Gd_2(Ti_{0.65}Zr_{0.35})_2O_7$ samples sintered at different temperatures between 800 and 1500 °C. The *inset* shows the decrease of the activation energy for the dc conductivity as the sintering temperature increases

Figure 4.43 shows the evolution of the activation energy E_a with the A-site average cation size for the samples in the AZ and GLZ zirconate series all with constant R_B (R_{Zr}(VIII) = 0.84 Å). It is clearly observed from the figure that E_a systematically decreases when R_A increases. This trend was already pointed out when presenting the data in Fig. 4.40 for GZT, YZT and DZT samples. The observed lower energy barrier for mobile oxygen ions to hop to neighboring vacant sites as R_A increases might be explained by the increase in cell volume, since cell volume is to a good approximation linearly dependent on the ionic radius of the A-type cation [328]. Therefore, on replacing Gd in $Gd_2Zr_2O_7$ for La, the unit cell volume will increase ($a = 10.528$ Å vs. 10.805 Å for $Gd_2Zr_2O_7$ and $La_2Zr_2O_7$ respectively [314]) and one would expect larger free space available for mobile charge carriers and, consequently, a lower barrier for oxygen ions to hop into neighboring vacant sites, consistent with the experimental data shown in Fig. 4.42. The value of the exponent n obtained from the electric modulus spectra do not change significantly ($n = 0.47 \pm 0.03$), since structural ordering/disordering is similar for all these pure zirconate samples, and therefore, the variation of the E_{dc} with the A-cation size is basically determined by the change in E_a. This is also shown in Fig. 4.43. It is clear that the trend is similar to that of E_a. Solid symbols in Fig. 4.43 represent the activation energy values for oxygen migration in $Gd_2Zr_2O_7$ and $Y_2Zr_2O_7$ obtained by Pirzada et al. [312] by using atomic scale computer simulations; i.e. 0.58 and 0.65 eV respectively. The existing structural disordering was not considered in these calculations by assuming in both cases a fully ordered

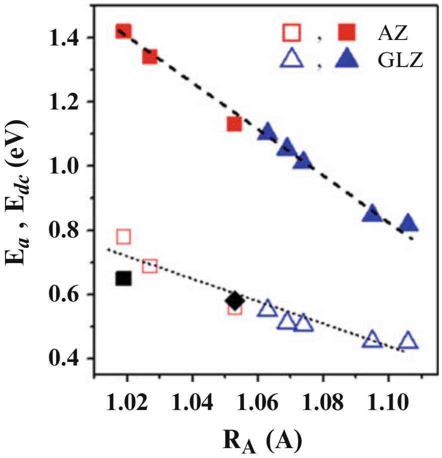

Fig. 4.43 Activation energies E_a (*open symbols*) and E_{dc} (*solid symbols*) for selected $A_2Zr_2O_7$ samples as a function of the average R_A cation radius. AZ and GLZ stand for the (A = Y, Dy and Gd) and $Gd_{2-x}La_xZr_2O_7$ samples respectively. *Lines* are guides for the eye to emphasize the drop in both activation energies as the size of the A-site cation increases. The (*diamond*) and (*square*) symbols represent activation energy values for oxygen migration in $Gd_2Zr_2O_7$ and $Y_2Zr_2O_7$ respectively calculated by atomic scale computer simulations (see text)

pyrochlore structure. The aforementioned activation energy values from computer simulations would correspond in fact to the energy barrier, E_a, deduced from experimental data. As shown, the computer simulation value for $Gd_2Zr_2O_7$ is quite similar to the experimental value, while that for $Y_2Zr_2O_7$ is somewhat lower than expected from experiment. However, it should be recalled that yttrium zirconate $Y_2Zr_2O_7$ does not exist as an ordered pyrochlore as assumed in the computer simulations but as an anion deficient fluorite, and this might explain the difference of activation energies from simulation and experiment for $Y_2Zr_2O_7$.

4.7 Li-Ion Dynamics and Diffusion in $Li_{3x}La_{2/3-x}TiO_3$

Besides the interest in oxide-ion conducting materials for application as electrolyte in solid oxide fuel cell devices discussed in the previous sections, there is also renewed interest in Li^+ ion conductors mainly driven by their extensive use in current solid-state batteries technology. Between the different materials exhibiting high lithium ion conductivity there are many metal oxides of interest, like Li_2SO_4 [329], Li_4SiO_4 [330], Li_3N [331], Li- β-alumina [332], $Li_{1+x}Ti_{2-x}Al_x(PO_4)_3$ [333], and $Li_{3x}La_{2/3-x}TiO_3$ [334]. In particular, extensive work has been devoted to the family of $Li_{3x}La_{2/3-x}TiO_3$ (LLTO), the lithium conducting oxides with perovskite structure [334–341].

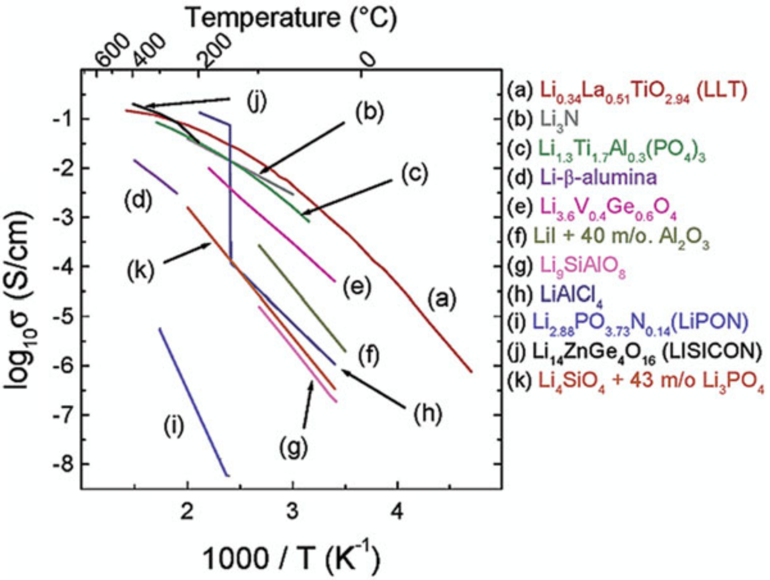

Fig. 4.44 Arrhenius plot of the electrical conductivity of several solid lithium ion conductors. Reproduced from Ref. [334] by permission

$Li_{0.18}La_{0.61}TiO_3$ (LLTO) is a crystalline lithium fast-ion conductor with very high dc conductivity σ_{dc} values of 10^{-3} S/cm at room temperature. The first study on the conducting properties of LLTO was reported by Belous et al. [336], who ascribe the stabilization of the perovskite structure to the lanthanum ions larger in ionic size, and interpret the high electrical conductivity measured as due to the mobility of the lithium ions. However, Inaguma et al. [339, 342] reported for the first time a bulk lithium ion conductivity of 10^{-3} S/cm at room temperature, and it is usually referred to as the first study on the ionic conductivity of LLTO. Since then, there has been much research work investigating the influence of the composition, pressure, and sintering conditions on the crystal structure, ion conductivity, and the mechanism for lithium ion conduction (for detailed information see the comprehensive review by Weppner et al. [334]). Figure 4.44 shows an Arrhenius plot for ionic conductivity of LLTO together with that of other solid Li^+ ion conductors [334]. The reason for the high mobility of Li ions in these oxides was understood as due to the fact that there are partially occupying equivalent A sites of the ABO_3 perovskite structure, and the presence of empty A sites facilitates Li ions to move easily through them. The perovskite structure can be regarded as a three-dimensional framework made up of vertex-sharing BO_6 octahedra with a large A cation in each of the 12-coordinated cavities of the framework. In the solid solution $Li_{3x}La_{2/3-x}TiO_3$ $(0 < x < 0.5)$ Li atoms were thought to replace La atoms at the A sites, leading to a progressive reduction of vacancies at these positions. The precise structure determination, and lithium ion location, of these oxides by XRD is particularly difficult because the superlattice reflections associated with the tilting

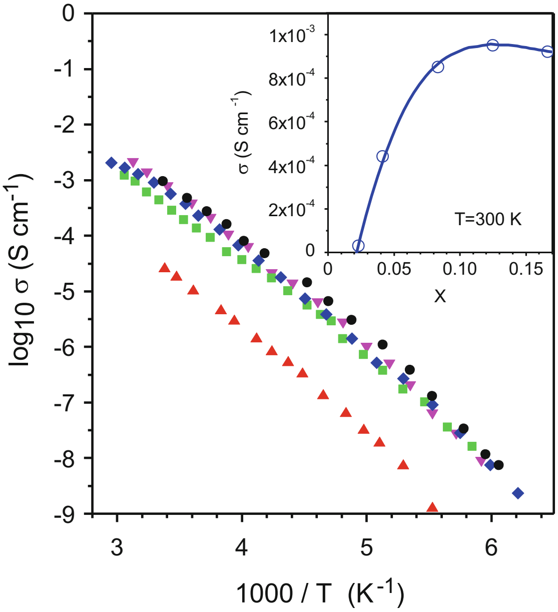

Fig. 4.45 Arrhenius plot of the bulk lithium ion conductivity of $Li_{3x}La_{2/3-x}TiO_3$ for samples with lithium content $x = 0.025$ (*red triangles*), $x = 0.042$ (*green squares*), $x = 0.083$ (*blue diamonds*), $x = 0.125$ (*black circles*) and $x = 0.167$ (*magenta down triangles*). The *inset* shows the conductivity value at room temperature as a function of the lithium content x of the sample. The *solid line* is a guide for the eye

of the TiO_6 octahedra arise from the oxygen atoms, which are weak scatterers when compared with La and Ti. In 2000, Alonso et al. [338] performed neutron powder diffraction (NPD) measurements of $La_{0.5}Li_{0.5}TiO_3$ and show its structure is constituted of a network of TiO_6 octahedra slightly tilted along the pseudocubic rhombohedral axes in order to optimize La-O distances. For this composition, La positions are half-occupied, leaving 0.5 vacancies per formula unit, distributed at random in the structure. The Li ions are fourfold coordinated to oxygen atoms, in square-planar configuration, and placed at the middle of windows formed by four TiO_6 octahedra. Since there are 0.5 Li atoms per formula unit (i.e., per pseudo-cubic unit cell), the occupancy factor of Li is only 1/6, and the unoccupied 5/6 equivalent sites provide the pathway for Li ion diffusion with large mobility through the structure. This location for the Li ions also explains that the maximum conductivity value at a given temperature is observed at relatively high Li content (about $3x = 0.35$) which can not be understood by assuming the Li atoms are located in the A sites as La atoms (see Fig. 4.45) [342–344]. Moreover, in the latter case, for a random distribution of Li, La and A vacancies in the A sites, a strong decrease of the dc conductivity would be predicted for $La_{0.5}Li_{0.5}TiO_3$ ($3x = 0.5$), which is not found [55, 340]. Figure 4.45 shows that dc conductivity is thermally activated, but shows a non-Arrhenius behavior. The activation energy, rather independent of the lithium content, decreases from about $E_\sigma \approx 0.4$ eV at the lowest temperatures

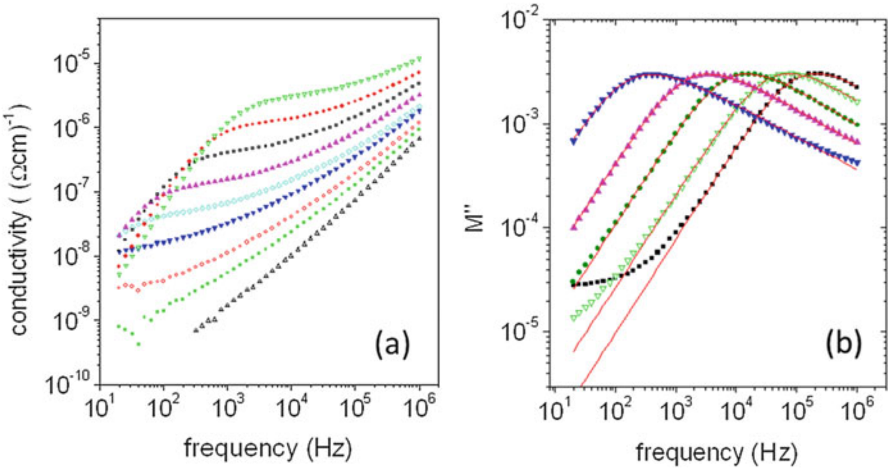

Fig. 4.46 (**a**) Frequency dependence of the real part of the conductivity of $Li_{0.5}La_{0.5}TiO_3$ at several temperatures (221, 211, 202, 193, 186, 179, 171, 164 and 153 K, from top to bottom). (**b**) Frequency dependence of the imaginary part of the electric modulus of $Li_{0.5}La_{0.5}TiO_3$ at several temperatures (179, 193, 206, 221 and 235 K, from *left* to *right*). *Solid lines* are fits to Fourier transforms of the Kohlrausch function

(160–250 K) to $E_\sigma \approx 0.3$ eV or lower at higher temperatures (250–360 K). This non-Arrhenius behavior of the ionic conductivity will be discussed in the next section.

Bulk dc conductivity values in Fig. 4.45 were obtained from impedance spectroscopy measurements [340, 344]. Figure 4.46a shows the frequency spectra of the real part of the conductivity at different temperatures. The rapid decrease of the conductivity observed at low frequencies and high temperatures is caused by blocking of ions at grain boundaries, and shifts to lower frequencies when the temperature is decreased. There is a plateau in the conductivity spectra that can be ascribed to the bulk dc conductivity and a crossover to a power law frequency dependence at the highest frequencies, as commonly observed in ionic conductors [39, 345]. Figure 4.46b shows the spectra of the imaginary part of the electric modulus for various temperatures, and the solid lines are fits to Fourier transform of the Kohlrausch correlation function of Eq. (4.15) or the CM Eq. (4.35), following the method proposed by other authors [18, 25]. The high frequency permittivity obtained from the fits takes a value of $\varepsilon_\infty = 85 \pm 5$ and is rather temperature independent. The values obtained for the fractional exponent 1-n of the Kohlrausch function are close to 0.4, showing a slight increase with temperature in this temperature range. Impedance spectroscopy measurements over a much wider temperature and frequency ranges also have been performed in LLTO, showing that the change in the fractional exponent 1-n is related to a non-Arrhenius temperature dependence of the dc conductivity (see next section). From the fits of the electric modulus data, shown as solid lines in Fig. 4.46b, the dc conductivity can be calculated by Eq. (4.13) as [97, 287, 288] $\sigma_{dc}(T) = \epsilon_o \varepsilon_\infty / {<}\tau_\sigma(T){>}$, where ${<}\tau_\sigma{>}$ is the mean relaxation time of the decay function obtained by

Eq. (4.16) as $<\tau_\sigma>=\int_0^\infty \Phi(t)dt = \tau_\sigma \Gamma\left(\frac{1}{1-n}\right)/(1-n)$, where Γ is the Euler's gamma function.

It has been reported that depending on the synthesis conditions and composition, LLTO crystallizes in simple cubic, tetragonal or orthorhombic perovskite-type structure. For the same lithium content, samples with a cubic structure exhibits slightly higher conductivity than the ordered tetragonal structure, which is probably due to the presence of alternating planes along the *c*-axis with a different amount of vacancies. In fact, NMR measurements have shown that two types of lithium ions with different mobility are present in orthorhombic samples, which would correspond to lithium located in these alternating planes. This is also likely in the case of tetragonal samples, although quadrupole constants decrease and resolution of two different sites become more difficult [344]. The ordering of A site vacancies in alternating planes along the *c*-axis should favor a 2D motion of Li in orthorhombic samples. In tetragonal samples, since vacancies turn progressively disordered, a 3D motion of Li ions is found at enough high temperature, while at temperatures below 200 K lithium ion hops between cages through the bottleneck in the *ab* plane (2D motion) have been reported [346, 347]. Although different conduction mechanisms have been proposed for LLTO in order to explain its high ionic conductivity at room temperature, the exact dimensionality (2D or 3D) of the lithium mobility in these compounds is still controversial [334].

Substitution of different cations for La gives rise to important changes in conductivity and activation energy, which have been attributed to the shrinking of lithium hopping due to the tilting and rotating of the TiO_6 octahedra [348]. Sr and Ba substitution for La should lead to a lattice expansion that would enhance the conductivity. This is in fact observed for the substitution of up to 5 % Sr for La [342]. However, substitution of a higher amount of Sr (>5 %) for La, or substitution of Ba for La, result in a decrease of the lithium ion conductivity, which has been related to local lattice deformation narrowing the bottleneck size [334]. Similar findings have been reported for other perovskite-type titanates, $M_{3x}Ln_{2/3-x}TiO_3$ (where Ln = rare-earth element and M = Li, Na, K, Ag) [349–351]. Inaguma et al. have compared the influence of pressure and the Ln cation substitution on the ionic conductivity of the LLTO in terms of activation volume, showing that the effect of lattice expansion is much smaller than that of lattice deformation [350–352].

Another interesting issue that determines the value of lithium conductivity in LLTO samples of different lithium content is the existence of site percolation. Diffusion of lithium ions in LLTO related materials have been shown to be limited by percolation effects. Since the presence of vacant sites allows the ions to hop from site to site through the structure, one would expect that ionic conductivity were proportional to the concentration of mobile ions, n_c, and also to their mobility, which should increase with the amount of vacant equivalent sites n_v for lithium ions. In fact, one of commonly used strategies in the search for novel ionically conducting materials consists of the optimization of the product $n_c n_v$ by the partial substitution of certain ions by others with different valences in structures with open conduction pathways. Thus, in the case of LLTO, La^{3+} ions in A sites of the perovskite (ABO_3) are substituted by Li^+ ions, and the number of nominal vacant A sites is given by $(1 - 2x)/3$. For a random distribution of vacant A sites, a maximum value of dc conductivity would be expected for a lithium content of $x = 0.25$ (maximum $n_c n_v$ product), while it should vanish at $x = 0$ and $x = 0.5$. However, as mentioned above and shown in Fig. 4.45, the highest value of dc conductivity at room temperature is found for a lithium content $x = 0.31$, and unexpectedly high dc conductivity values have been reported for samples with x close to 0.5 [344]. Inaguma and Itoh [353] were the first to propose the existence of a percolation limited motion of lithium ions as the reason for the shift observed in the maximum of the dc conductivity to higher lithium contents, but a quantitative explanation seemed elusive. Later on, a neutron diffraction study helped to provide an explanation for the high dc conductivity values measured in Li-rich LLTO perovskites. As already mentioned, it was found that lithium ions are not located at A sites but distributed at unit-cell faces of the perovskite [338]. Therefore, the amount of vacant A sites in the structure is actually higher than that deduced from the structural formula. This fact on its own can also explain the shift to higher lithium contents of the highest dc conductivity value, although the existence of percolation effects on lithium diffusion could not be discarded. A convincing evidence of the existence of percolation-limited ionic motion came with a study of structure and ionic mobility in the crystalline series $Li_{0.5-y}Na_yLa_{0.5}TiO_3$ $(0 \leq y \leq 0.5)$ (LNLTO) combining neutron diffraction, X-Ray diffraction, NMR and Impedance Spectroscopy [354]. It was already known that $Na_{0.5}La_{0.5}TiO_3$ is not an ionic conductor but behaves like an insulator [355]. The higher size of sodium compared to that of lithium results in a better coordination of sodium ions at A sites. The very different electrical properties of the end members of the solid solution LNLTO motivated the study. Structural characterization of LNLTO samples showed that Na and La ions occupy A sites, while Li ions, as in LLTO, are located at the center of unit cell faces of the perovskite. Thus, substitution of Li by Na ions reduces the amount of vacant A sites, and the local mobility of Li ions at room temperature was found to decrease by two orders of magnitude along the series. At the same time, long-range dc conductivity values show a sharp decrease at $y = 0.2$ (see Fig. 4.47), from almost 10^{-3} S/cm to values below 10^{-10} S/cm, which was explained in terms of a percolative blocking of the 3D conduction network. If all A sites were occupied by alkaline cations, dc conductivity values of LNLTO samples will be always close to zero. However, dc conductivity values are very high in samples with $y > 0.2$, suggesting that part of the A sites are not occupied. This is in agreement with neutron diffraction results. The amount of vacant A sites is thus higher than that deduced from the structural formula which could explain the high values of dc conductivity measured in Li-rich perovskites. On the other hand, LNLTO samples with low lithium contents ($y > 0.2$) show a much lower dc conductivity than those obtained in the LLTO series (see Fig. 4.47a). This can be explained in terms of the amount of vacant A sites, that is considerably reduced in LNLTO samples when sodium content is increased. The steep decrease

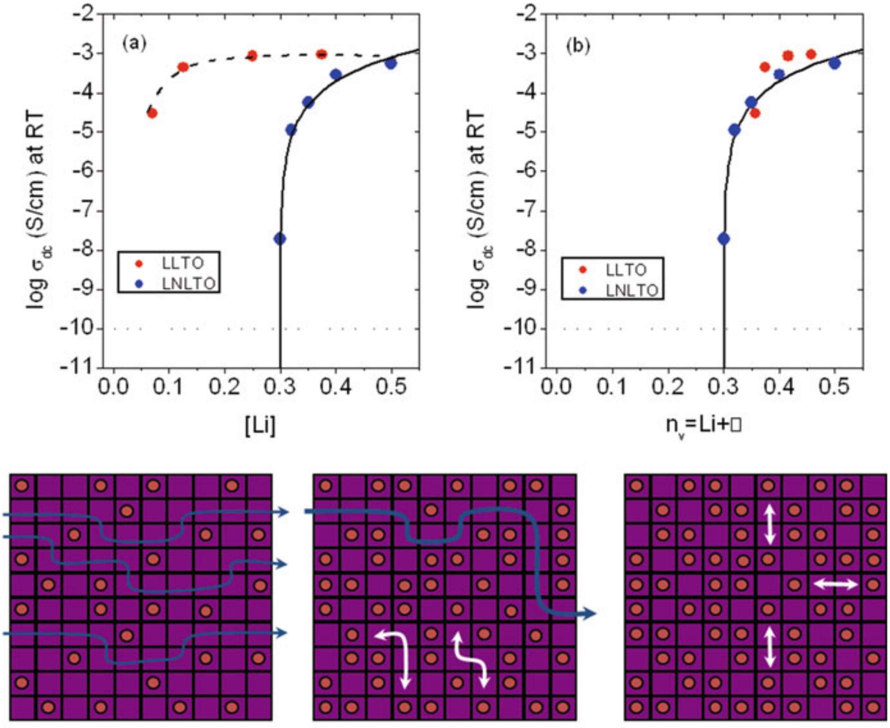

(c) p>p$_c$ **(d) p=p$_c$** **(e) p<p$_c$**

Fig. 4.47 (**a**) Room-temperature dc conductivity of $Li_{0.5-y}Na_yLa_{0.5}TiO_3$ versus lithium content of the samples (*blue circles*). The *solid line* is a fit of dc conductivity data to the expression $\sigma_{dc} = K(n - n_p)^2$, deduced for a percolation limited diffusion of lithium ions in a 3D perovskite structure. A value of the percolation threshold $n_p = 0.30 \pm 0.01$ is obtained, in remarkable agreement with that expected from the percolation model in a cubic lattice ($n_p \approx 0.31$). For $n < 0.3$ the dc conductivity values are below experimental resolution (10^{-10} S/cm). Room-temperature dc conductivity of $Li_{3x}La_{2/3-x}TiO_3$ samples are also plotted for comparison as a function of lithium content (*red circles*). (**b**) Same data as in (**a**) but plotted versus the number of vacant A sites per formula unit. (**c**–**e**) represent a schematic illustration of the percolation-limited motion above (**c**), at (**d**), and below (**e**) the percolation threshold for a two-dimensional square lattice. *White arrows* illustrate local mobility of Li in finite clusters

of the dc conductivity observed in LNLTO samples (Fig. 4.47a) is well described by considering a percolation model for the lithium diffusion. In this model, A sites associated with Li ions are vacant and participate in ionic diffusion, but A sites occupied by La or Na ions do not participate in ionic conduction and block lithium diffusion. Ionic transport is expected to give rise to a dc conductivity only for concentrations of vacant A sites above the percolation threshold, $n_p \approx 0.31$, and a composition dependence of the dc conductivity of the form $\sigma_{dc} = K(n\text{-}n_p)^2$, corresponding to the three-dimensional percolation of Li motion in the cubic network formed by A sites [356, 357]. Solid line in Fig. 4.47a shows the good agreement between the dc-conductivity values and those expected from the percolation model. The dc conductivity is very high when the number of vacant A sites per unit cell is higher than 0.3 ($y < 0.2$).

At $y = 0.2$, the amount of vacancies is very close to the percolation threshold, and the infinite percolation cluster is about to disappear, reducing drastically the value of the dc conductivity. For higher sodium contents, $y > 0.2$, all clusters are expected to be of finite size, and long-range ionic transport does not occur (see Fig. 4.46c–e). The results suggest that the amount of vacancies available for lithium diffusion is defined by the sum of nominal vacancies plus the Li content, $n_v = [\mathrm{Li}] + \square$, and it is n_v which rules the percolation threshold. This is shown in Fig. 4.47b, where room temperature dc-conductivity data for both the LLTO and LNLTO series are plotted as a function of n_v. In this plot, all points are placed in the curve deduced for a three-dimensional percolation of vacant A sites. Consequently, the amount of vacancies in LLTO increases with the Li content from 0.33 to 0.5, values that are always above the percolation threshold ($n_v = 0.31$). The decrease of two orders of magnitude in dc conductivity measured for Li-poor LLTO perovskites shows the proximity of the percolation threshold, while the composition dependence of the dc conductivity in LNLTO samples evidences the existence of a percolation process. Since Na ions are located at A sites of perovskites, they effectively block the pathways for lithium diffusion. NMR T_1 relaxation times of Li^+ and Na^+ ions are also consistent with this scenario [354]. The residence time of lithium at square windows is near 10^{-8} s at room temperature in $\mathrm{Li_{0.5}La_{0.5}TiO_3}$ [55]. Due to the high mobility of lithium, quadrupole interactions are averaged out in the ^{7}Li NMR spectra. As the Na content increases in LNLTO samples, the ^{7}Li NMR spectra progressively display quadrupole satellite transitions of less mobile species, whose intensity increases with the sodium content, and there is an increase of T_1 relaxation time, suggesting a decrease of the average Li mobility. Changes observed on T_1 values from the ^{23}Na signal are similar to those detected in the ^{7}Li signal, what has been ascribed to the relaxation induced by mobile Li ions at sites occupied by sodium cations [354].

4.7.1 Unusual Non-Arrhenius dc Conductivity of LLTO

In discussing the temperature dependence of $\sigma_{dc}(T)$ in YSZ (see Figs. 4.31 and 4.33) and some other glassy and crystalline ionic conductors (see Fig. 4.1 and Table 4.3), we point out the gradual crossover of $\sigma_{dc}(T)$ from the stronger Arrhenius dependence at lower temperatures to the weaker Arrhenius dependence at higher temperatures when $\sigma_{dc}(T)$ reaches levels of ~ 1 $\mathrm{Scm^{-1}}$. An exception or special case is the crystalline ionic conductor $\mathrm{Li_{0.18}La_{0.61}TiO_3}$ measured by Rivera et al. [112]. The T-dependence of $\sigma_{dc}(T)$ is Arrhenius at low temperatures above 120 K with $E_\sigma = 0.36$ eV, but on increasing temperature $\sigma_{dc}(T)$ shows a non-Arrhenius behavior starting at about $\sigma_{dc} \sim 10^{-4.5}$ S $\mathrm{cm^{-1}}$, as shown in Fig. 4.48. The apparent activation energy of σ_{dc}, defined by $E_\sigma(T) = d\ln\sigma_{dc}/d(kT)^{-1}$, decreases monotonically with increasing temperature after the onset of deviation

Fig. 4.48 Arrhenius plot of the dc conductivity of $Li_{0.18}La_{0.61}TiO_3$ showing a non-Arrhenius temperature dependence

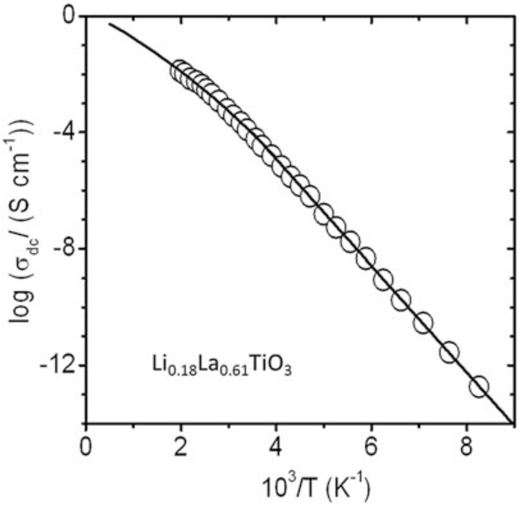

Fig. 4.49 Spectra of the real (*open squares*) and imaginary part (*open circles*) of the electric modulus of Li $_{0.18}$La $_{0.61}$$TiO_3$ obtained from 120 K, 130 K, 150 K, and 180 K from *left* to *right*

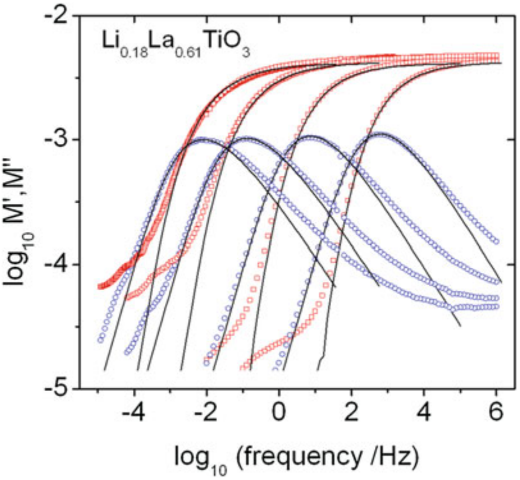

from the low temperature strictly Arrhenius dependence. This behavior of $\sigma_{dc}(T)$ or $\tau_\sigma(T)$ is surprising because there is no change of either the crystalline structure or the number of mobile Li ions.

Time and frequency domain measurements of ion dynamics in the wide frequency range of eleven decades (from 10^{-5}–10^6 Hz) with data expressed in terms of the complex electric modulus helped to shed light on this behavior. As shown in Fig. 4.49, there is a narrowing of the loss modulus peak as temperature is increased, indicating that the exponent, 1-$n(T)$, of the Kohlrausch relaxation function fitting the data increases with increasing temperature (see Fig. 4.50). In the CM, the decrease of the coupling parameter $n(T)$ reflects the decrease of many-ion

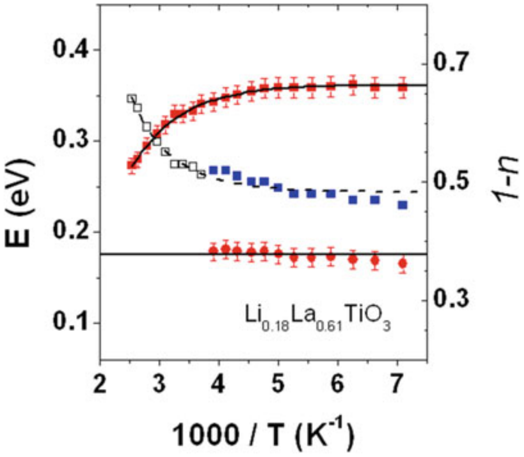

Fig. 4.50 Temperature dependence of the dc activation energy E_{dc} (*red squares*) and of the Kohlrausch exponent [1-$n(T)$] (*blue squares*) describing the dynamic response of ions in $Li_{0.18}La_{0.61}TiO_3$. *Circles* represent the microscopic activation energy E_a estimated by using the Coupling Model, and a constant value of 0.175 eV is obtained (*horizontal line*). *Open squares* are the predicted values of the exponent [1-$n(T)$] for temperatures higher than 256 K in order that the same constant value, $E_a = 0.175$ eV, is maintained at the higher temperatures according to the relation $E_a = [1\text{-}n(T)]E_{dc}$

cooperativity with increasing temperature. The primitive activation energy E_a, identified with the true or microscopic energy barrier, is independent of temperature since the structure of LLTO remains unchanged. If one uses the CM Eq. 4.50, $E_\sigma(T) = E_a/[1-n(T)]$, in conjunction with the observed decrease of the $n(T)$, it is possible to give a quantitative explanation of the concomitant decrease of $E_\sigma(T)$. Similar decrease of n with increasing temperature is found in the structural relaxation of many glassforming liquids, and it has effect on the T-dependence of the structural relaxation time [189, 358, 359]. The observed decrease of $E_\sigma(T)$ in LLTO is challenging for any theory to explain. It was used to put the CM to a test.

The primitive activation energy $E_a(T)$ calculated via Eq. (4.49) by the product $[1-n(T)]E_\sigma(T)$ are shown by the circles in Fig. 4.50. It can be seen that within errors the values of $E_a(T)$ obtained are independent of temperature as it should be since it corresponds to the microscopic energy barrier of the crystalline LLTO. This result is tantamount to verification of the CM explanation of the non-Arrhenius dependence of the $\sigma_{dc}(T)$ of LLTO. We do not know any other theory/model that can explain this property.

4.7.2 Accounting for the Non-Arrhenius T-Dependence of $\sigma_{dc}(T)$ from $n(T)$ by the CM

So far, the published electric modulus data of LLTO give $[1\text{-}n(T)]$ for T up to 256 K (blue filled squares in Fig. 4.50), while sizeable decrease of $E_\sigma(T)$ continues up to 385 K. If the CM explanation continues to hold at higher temperatures, $E_a(T)$ must still be temperature independent all the way up to 385 K. Assuming this is the case and taking the temperature independent value of $E_a = 0.175$ eV determined at temperatures lower than 256 K, $[1-n(T)]$ must have the values shown by open squares in order that the product $[1-n(T)]E_\sigma(T)$ remain constant and equal to $E_a = 0.175$ eV for all temperatures up to 385 K. This offers an additional critical test of the CM explanation by extending the measurement of the electric modulus at higher frequencies up to the GHz region to determine $[1-n(T)]$ directly at temperatures higher than 256 K. Measurements of the electric modulus at higher frequencies up to the GHz region are necessary to determine $[1-n(T)]$ directly at temperatures higher than 256 K. Such measurements have been made by Rivera et al., but so far unpublished, and the coupling parameter $n(T)$ obtained by fitting the electric modulus to a Kohlrausch function at temperatures above 256 K and up to 385 K are in agreement with the predicted values of the exponent (see Fig. 4.50). Using the experimentally obtained values of $E_{dc}(T)$ and $n(T)$, the calculated products $[1-n(T)]E_{dc}(T)$ should be good estimates of the primitive energy barrier E_a. An approximately constant value of $E_a = 175 \pm 10$ meV is obtained over the whole temperature range, which is remarkably similar to the value of 170 meV determined from electrical conductivity relaxation and NMR spin-lattice relaxation for the microscopic energy barrier [55, 340, 360]. These results strongly support the CM interpretation of a decrease in ion-ion interactions with increasing temperature as the origin of the observed decrease in the exponent n, which in turn explains the parallel decrease of E_{dc} at dc conductivity levels orders of magnitude below 10^{-2} S cm^{-1}.

4.8 Caged Dynamics and Nearly Constant Loss in Ionic Conductors

At sufficiently low temperatures, where not only the observed conductivity relaxation time, τ_σ, but also the primitive relaxation time, τ_0, of the CM is long, a new feature of the ion dynamics appears in the real part of the ac conductivity at higher frequencies having $\sigma'(f) \propto f^{1-c}$ with the exponent c being small but positive. This nearly linear frequency dependence of the real part of the conductivity $\sigma'(\omega)$ was given before by Eq. (4.7) and the associated nearly constant loss (NCL) given by Eq. (4.6) are commonly found at low temperatures/high frequencies in ionic conductors in general. Examples have been shown in Figs. 4.3, 4.5, 4.8, 4.10, 4.16, 4.18, and 4.20. Since these properties are the focus of the present section, Eqs. (4.7) and (4.6) are combined and reproduced here for convenience,

$$\sigma'(f) = (A/2\pi e_0)f^{1-c}, \quad \varepsilon''(f) = Af^{-c} \quad c << 1 \tag{4.56}$$

The NCL or the nearly linear frequency dependence of $\sigma'(\omega)$ (NLfDσ') can extend indefinitely to lower frequencies over as many decades as the experimental window can reveal on lowering temperature (see Fig. 4.8 for an example). Therefore, it has no characteristic time, and does not originate from ion hop from site to site whether local or long range. In the ionic liquids shown in Figs. 4.7, 4.8, 4.9, and 4.10, where a thermally activated secondary ion relaxation is present, the NCL or the NLfDσ' is the fastest process after vibrations. The intensity factor of the NCL, A, increases weakly with increasing temperature in the manner well described by either T^{γ} with γ not much larger than unity, or by $\exp(T/T_0)$ [361]. The NCL is present whether the ionic conductor is glassy, molten, or crystalline [41, 43–47], and glass-formers of different physical and chemical composition [53, 60, 61], even in insulators and semiconductors [39, 50, 51]. NCL is found in crystalline ionic conductors including Na β-alumina [54], yttria stabilized zirconia (YSZ) [270] and LLTO [362], and crystalline $LiAlSi_2O_6$ [47], indicating that the origin of NCL is not due to randomness or disorder.

From the connection between fluctuation and dissipation [363], the NCL corresponds to the $1/f$ noise [51] which is also commonly observed. The derivation of the $1/f$ noise by the CM in the 1980 paper [51] is tantamount to a first attempt to understand the origin of the NCL in some materials, although a more intuitively clear explanation by caged ion dynamics has emerged from the CM [43–45, 53]. The nature of the ubiquitous nearly constant loss is certainly a challenging problem in ionic conductors, but it has received more attention to understand it only very recently [1–10, 14, 40–43, 45]. In 1999, most of the experimental data of the constant loss in ionic conductors measured to that date were collected to extract its properties [43, 44]. The magnitude and temperature dependence of the NCL in 25 ionic conductors are shown in Fig. 4.51. All are either glassy or crystalline ionic conductors, except for CKN (#17) the data of which covers both the glassy state (17 g) and the molten liquid state (17 m) and a prominent increase on crossing $T_g = 333$ K. The straight line interpolating data points of each glassy and crystalline ionic conductor show the temperature dependence of NCL increases mildly with temperature and is proportional to $\exp(T/T_0)$. Many properties of the NCL have been reported in Ref. [43, 44], although in reconsideration we recognize anharmonicity of the inter-ion potential responsible for caged ions is ultimately the determining factor of the properties of the NCL. This will become clear from the results presented in Sect. 4.10.

In molecular dynamics simulations the NCL is found in the mean square displacement of the form, $<r^2(t)> \propto t^c$, $c \ll 1$, at times shorter than τ_0 [163]. The molecular dynamics simulation data show by either the van Hove function [45] or by the motions of all ions at times when $< r^2(t) > \propto t^c$ with $c \approx 0$ [66] that no ion or negligibly few ions have successfully hop to nearest neighbors. In other words, almost all ions remain caged. The weak T-dependence of A reflects the NCL is due to loss of ion confined within the anharmonic potential defining the cage. The ions

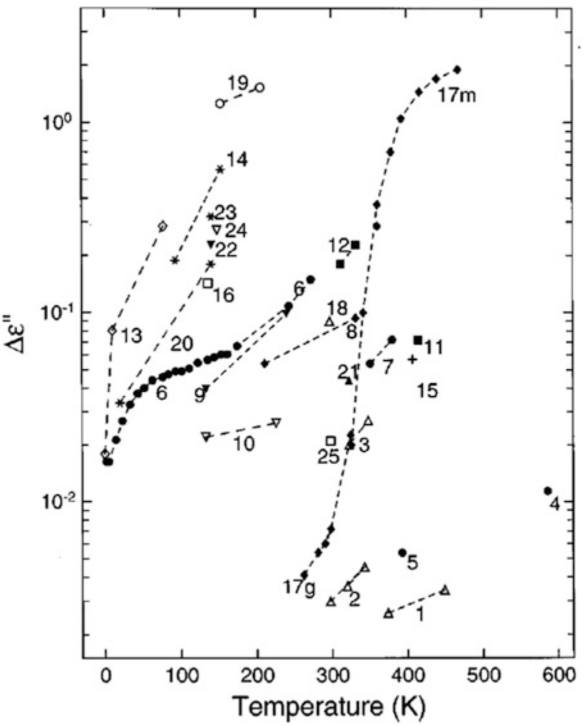

Fig. 4.51 Magnitudes and temperature dependencies of the NCL for many ionic conductors. Data sets 1, 2, and 3 are for xK$_2$O.(1-x)GeO$_2$ glasses with $x = 0.0023$, 0.02, and 0.20, respectively. Data set 4 is for 0.00044Na$_2$O.(0.99956)[0.04B$_2$O$_3$ –0.96SiO$_2$]. Data set 5 is for a quartz crystal with a few hundred ppm of ions. Data set 6 is for Na$_2$O.3SiO$_2$. Data points 11 and 12 are for xNa$_2$S.(1-x) B$_2$S$_3$ with $x = 0.001$ and $x = 0.005$, respectively. Others are 0.5Na$_2$O.0.5K$_2$O.3SiO$_2$ (set 7); YSZ (set 8); LiPO$_3$ (set 9); Li$_{0.5}$Na$_{0.5}$PO$_3$ (set 10); Na β–Al$_2$O$_3$ (set 13); 0.48(AgI)$_2$•0.52Ag$_2$SeO$_4$ (set 14); CdF$_2$ –LaF$_3$ –AlF$_3$ –PbF$_2$ (point 15); 0.5Li$_2$S–0.5SiS$_2$ (point 16); CKN glass (set 17); CKN melt (set 17 m); ZBLAN20 (point 18); LLTO (set 19); 0.30Ag$_2$S•0.70AgPO$_4$ (set 20); 0.03Li$_2$O.0.97Ge$_2$O (point 21); 0.625(0.5Ag$_2$S–0.5GeS$_2$)0.375AgI (point 22); 0.30AgI•0.70AgPO$_4$ (point 23); 0.35Li$_2$S•0.65GeS$_2$ (point 24), and (AgI)$_{0.70}$ (tetraehyltammonimiodide)$_{0.20}$ (tetrapropylammonium iodide)$_{0.10}$ (point 25). Reproduced from Ref. [43, 44] by permission

are no longer caged at long enough times starting when ions hop to neighboring sites singly and independently with high probability, which naturally can be identified with the primitive ion relaxation with relaxation time τ_0 of the CM. Consequently, the NCL no longer persists at times longer than τ_0, and it may undergo some changes at times when approaching τ_0. Thus the primitive relaxation performs another function of terminating the NCL, and τ_0 provides the time when the regime of caged ion dynamics has ended with certainty. More exactly, the primitive frequency, $f_0 \equiv 1/(2\pi\tau_0)$, is comparable in order of magnitude to the lower bound of the NCL frequency regime. This relation of the primitive relaxation to NCL have been demonstrated to be true by isothermal conductivity relaxation data of many different ionic conductors represented either as $\sigma'(f)$,

$\varepsilon''(f)$, or $M''(f)$ [43–45], and also as $\sigma'(T)$ at different fixed frequencies [46]. The examples include LLTO where termination of the NCL is indeed at frequencies having the same activation energy as E_a of the primitive relaxation time τ_0 calculated from E_σ of the conductivity relaxation time τ_σ by Eq. (4.49). Moreover, this relation enables us to derive the weak T-dependence of the NCL intensity, A [361]. The derivation confers a bonus of another prediction, which is the anti-correlation between A and the primitive activation energy, E_a. This prediction is consistent with experimental data [364].

It is important to realize that ion dynamics evolves with time essentially in four stages. Caged ion dynamics with NCL or nearly linear frequency dependence of σ' (NLfDσ') is the first stage. Termination of the caged ion dynamics by the onset of the primitive relaxation at $\sim t_{x1}$ less than but comparable in order of magnitude to the primitive relaxation time τ_0 is the second stage. After the onset of the primitive relaxation, the number of ions cooperatively relax increases continuously with time (this is the third stage), until reaching the final stage at $\sim t_{x2}$ in which the maximum number N of ions (or length-scale L) is involved in the terminal many-ions dynamics with the Kohlrausch function, $\exp[-(t/\tau_\sigma)^{1-n}]$, as the time relaxation function [43–45, 53]. The dc conductivity is determined by the terminal ion dynamics. The size of N or L as well as the coupling parameter n of the CM is governed by the strength of the inter-ion potential. The contributions from the processes at all four stages are not additive, instead the one before is replaced by the one that follows. Rivera et al. have shown by their experiment that the NCL or NLfDσ' is not an additive contribution to the total $\varepsilon''(f)$ or $\sigma'(f)$ [362]. More experimental data of the NCL or NLfDσ' to show its properties and its relation to the other processes will be given by some examples in the sections to follow.

4.8.1 Caged Ion Dynamics, Properties and Termination by the Primitive Relaxation

From the analysis of the frequency and temperature dependence of the conductivity data in two different lithium ionic conductors, and at enough low temperature, León et al. found strong experimental evidence of NLfDσ' [44, 154], originating from caged ion dynamics [46, 48, 362]. At the shortest time scale ions are vibrating in their potential wells of height E_a, with a frequency ν_{vib} usually associated with the attempt frequency of ion in thermally activated hopping. A microscopic residence time is defined, $\tau_o = (\nu_{vib})^{-1}\exp(E_a/k_BT)$, such that for times $t \ll \tau_o$ ions are caged within their sites. At times $t > \tau_o$, randomly the ions have hopped to the neighboring site, although statistically some of them return to the same site before τ_o [66]. Nevertheless, caging effectively disappears after τ_o [45]. Figure 4.52 shows the temperature dependence of $\sigma'(f)$ at several fixed frequencies (300 Hz, 1 kHz, 3 kHz, 10 kHz, 30 kHz and 100 kHz) from measurements on $Li_{0.18}La_{0.61}TiO_3$ by León et al. [46].

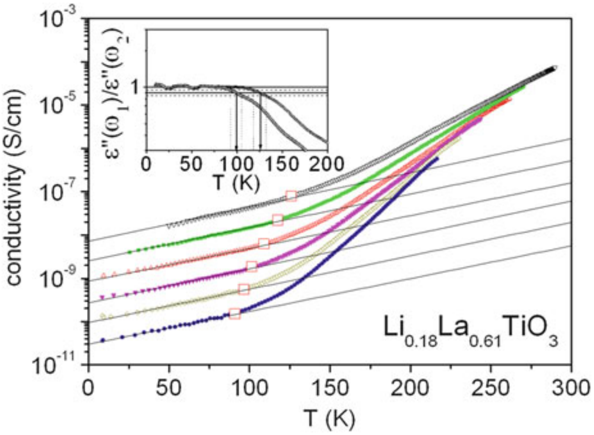

Fig. 4.52 Conductivity vs. temperature plots for $Li_{0.18}La_{0.61}TiO_3$. Conductivity data are shown for different frequencies (300 Hz, 1 kHz, 3 kHz, 10 kHz, 30 kHz and 100 kHz, from bottom to top). *Solid lines* are fits to an exponential temperature dependence of the magnitude of the NCL. *Open squares* represent the crossover to the linear frequency dependent conductivity (NCL regime) at enough low temperature. The *inset* shows the ratio of the permittivity values at two different frequencies, ω_1 and ω_2, which is equal to 1 at low temperatures, where the NCL is the dominant contribution, but starts to depart from 1 as temperature is increased. Displayed data are for $\omega_1 = 3$ kHz (*sqaure*) and 100 kHz (*circle*), with $\omega_2 = \omega_1/10$. Crossover temperatures were obtained for a departure of a 10 % (*arrows*) and *error bars* of ± 7 K were obtained from 5 % and 15 % decays (*dotted lines*)

At the highest temperatures shown and beyond (not shown), experimental data taken at different frequencies tend to collapse together to form a single curve, corresponding to the temperature dependent dc ionic conductivity. As the temperature is lowered (in the range 225–275 K) a different contribution to the conductivity due to the fractional power law frequency dependence of the ac conductivity is observed, first appearing for the highest frequencies. In this regime, some ions have already jumped over the potential barriers from their wells but the long range ionic transport has not been achieved yet. And when the temperature is further lowered down (below 90–125 K, depending on frequency), the NCL is observed to be the dominant contribution to the ac conductivity down to the lowest temperatures. Note that, at the low temperature region of Fig. 4.52, experimental isofrequency conductivity data sets are spaced according to a linear frequency dependence, which provides a criterion to determine, at each frequency, a crossover temperature where the NCL becomes the dominant contribution to the ac conductivity. The inset in Fig. 4.52 shows the criterion used to obtain the crossover temperature at each frequency. The ratio of the permittivity values at two different frequencies, ω_1 and ω_2, is equal to 1 at low temperatures, where the NCL is the dominant contribution, but decreases as temperature is increased and ion hopping contributes to ac conductivity. The crossover points, represented by open squares in Fig. 4.52, were obtained by León et al. from the highest temperature where the linear frequency dependence was still observed within a 10 % accuracy. The

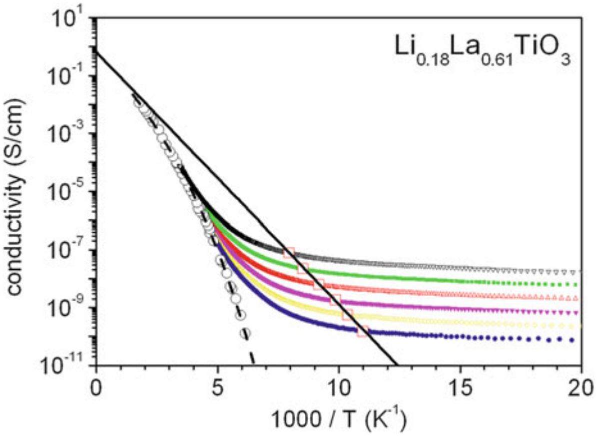

Fig. 4.53 Arrhenius plot of the conductivity for $Li_{0.18}La_{0.61}TiO_3$ at several frequencies (300 Hz, 1 kHz, 3 kHz, 10 kHz, 30 kHz and 100 kHz, from bottom to top). *Open circles* are dc conductivity data. *Open squares* represent the crossover to the NCL regime at the lowest temperatures. The *solid line* is a fit to an Arrhenius law for the crossover temperature dependence

magnitude of the NCL in Fig. 4.52 shows a weak temperature dependence, which is well described over a wide temperature range by an exponential form $\exp(T/T_a)$. Solid lines in Fig. 4.52 are fits to such an exponential temperature dependence of the ac conductivity at each frequency. It is readily observed that the exponential fits account perfectly for the temperature dependence of the ac conductivity at low temperatures up to the crossover points (open squares), which were calculated independently by the 10 % criterion in the frequency dependence. It is important to note that the crossover points were defined by using a criterion based on the frequency dependence of ac conductivity at a fixed temperature, and therefore without any consideration of the exact temperature dependence of the NCL, which is unknown “a priori”. It is only “a posteriori” that it is found that the crossover points also separate two different temperature dependences of the ac conductivity at a fixed frequency. There is excellent agreement between the temperatures at which ac conductivity starts to deviate from an exponential temperature dependence and the temperatures at which the crossover points are obtained. This result gives further support to the existence of a true crossover at these points between a NCL and a power law regime.

By replotting the ac conductivity data in an Arrhenius manner (see Fig. 4.53), León et al. realized that the crossover temperatures $T_x(f)$ as a function of frequency show a thermally activated behavior with an activation energy $E_x = 0.17 \pm 0.03$ eV, the same value as was previously obtained from spin-lattice and electrical conductivity relaxation [55] for the microscopic energy barrier (or the activation energy of the primitive relaxation in the CM) for single ion hopping, $E_a = 0.17 \pm 0.01$ eV, i.e., the height of the potential well. The reader may recall that the value of the primitive activation energy $E_a = 0.175 \pm 0.01$ eV is derived from the product (1-n) E_σ from Eq. (4.49) and given before in Fig. 4.50 with $E_\sigma = 0.36$ eV [112]. Exactly the same results are found in $Gd_2Zr_2O_7$ [193, 365]. The left and right panels of

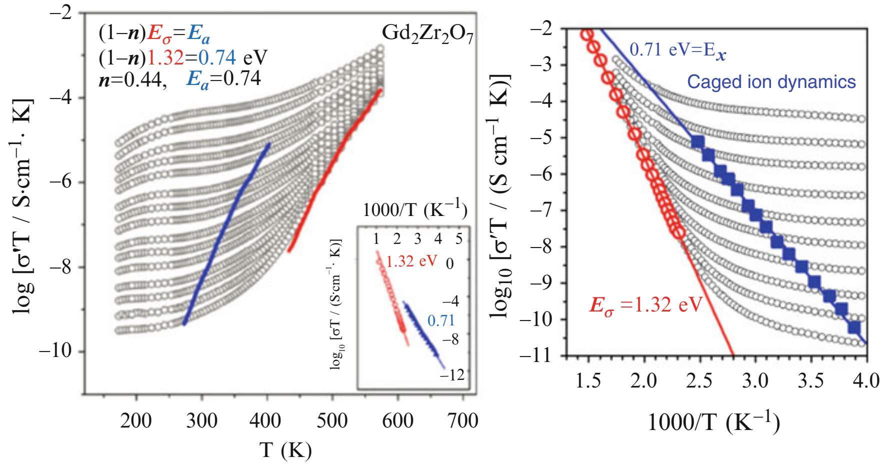

Fig. 4.54 Temperature dependence of the real part of the conductivity at several fixed frequencies (22 Hz, 48 Hz, 107 Hz, 210 Hz, 522 Hz, 1 kHz, 2 kHz, 5 kHz, 10 kHz, 20 kHz, 55 kHz, 110 kHz, 210 kHz, 525 kHz, and 1 MHz, increasing frequency from bottom to top). *Inset*: Arrhenius plot of the conductivity values at the crossover point between hopping conductivity and nearly constant loss behavior (*blue solid triangles*) and dc conductivity values (*red open circles*). *Solid lines* in *inset* and main panel are fits to an Arrhenius law for dc conductivity values (*red*), and crossover points between hopping conductivity and nearly constant loss behavior (*blue*)

Fig. 4.54 are the analogues of Figs. 4.52 and 4.53 respectively, and the same descriptions apply. In $Gd_2Zr_2O_7$, $E_\sigma = 0.132$ eV and $n = 0.44$, and therefore the primitive energy activation energy E_a calculated by the product (1-n)E_σ is 0.74 eV. On the other hand, $E_x = 0.71$ eV, which can be considered the same as $E_a = 0.74$ eV within the uncertainties involved in determining both activation energies.

It has been argued [46, 362, 366] that the solid line in Fig. 4.53 as well as in Fig. 4.54, obtained from the crossover points to the NCL regime, divides the plot roughly into two temperature regions. For any given frequency the right side is where the temperature falls below the crossover temperature and ions remain within their cages. On the other hand, the left side is the regime when enough thermal energy is available and mobile ions start to jump with a significant probability to adjacent sites, giving a new contribution that takes over to determine the ac conductivity.

4.8.2 Ruling Out the Augmented Jonscher Expression

A further consequence of the temperature dependence found for the crossover to the NCL regime is that it is at odds with the usual assumption [367–369] that the total ac conductivity in ionic conductors can be described by the augmented Jonscher expression discussed before in Sect. 4.2.2 and presented as Eq. (4.23). For convenience in the discussion here, it is given once again as

$$\sigma' (\omega) = \sigma_0[1 + (\omega/\omega_o)^{n_J}] + A\omega. \tag{4.57}$$

In Eq. (4.57) the ac hopping ionic conductivity and the NCL contribution $A\omega$ are considered to be additive terms, and therefore, the activation energy of the crossover should be close to the dc conductivity activation energy and much higher than that determined from experimental data. Note that the (Jonscher) fractional exponent n_J accounts for the power law frequency dependence observed in the dispersive ac conductivity but its value is in general different to that of the parameter n in the exponent of a Kohlrausch stretched exponential fitting the same electrical relaxation data according to the electric modulus formalism [5, 6, 29, 30]. Assuming the validity of Eq. (4.57), and following the 10 % criterion used to define the crossover, one expects that the crossover frequency ω_x at a given temperature satisfies the expression

$$\sigma' (\omega_x) = \sigma_0[1 + (\omega_x/\omega_o)^{n_J}] + A\omega_x = 1.1A\omega_x. \tag{4.58}$$

As shown by the experimental data in Fig. 4.53, at the frequency ω_x, the dc conductivity makes a negligible contribution to $\sigma'(\omega_x)$, so that the conductivity can be written as

$$\sigma' (\omega_x) \approx \sigma_0(\omega_x/\omega_o)^{n_J} + A\omega_x = 1.1A\omega_x. \tag{4.59}$$

Solving Eq. (4.59) for ω_x, we get

$$\omega_x = \sigma_0(0.1A)^{-1/(1-n_J)}(\sigma_0/\omega_0)^{n_J/(1-n_J)}, \tag{4.60}$$

and inserting Eq. (4.60) back into Eq. (4.59), one gets for the conductivity at the crossover frequency:

$$\sigma' (\omega_x) = 1.1A\omega_x = 1.1\sigma_0(0.1)^{-1/(1-n_J)}A^{-n_J/(1-n_J)}(\sigma_0/\omega_o)^{n_J/(1-n_J)}. \tag{4.61}$$

Since σ_0 and ω_o are thermally activated with the dc activation energy E_σ, it can be shown from Eq. (4.61) that, assuming the weak temperature dependence of the NCL of the exponential form $\exp(T/T_a)$, the activation energy for the crossover should be

$$E_x = -k_b\left[d\ln\sigma'(\omega_x)/dT^{-1}\right] = E_\sigma - (n_J/(1 - n_J))k_b\ T^2/T_a, \tag{4.62}$$

which is essentially equal to E_σ provided that $T/T_a \sim 1$ and k_bT is much smaller than E_σ which is indeed the case. The last Eq. (4.62), derived from the augmented Jonscher's law given by Eq. (4.57), is unphysical because none of the mechanisms on both sides of the crossover have anything to do with the long-range displacement of ions or its activation energy E_σ. In fact, the experimental data show that this crossover is thermally activated, but with a much lower activation energy, E_a, and its value is close to the microscopic energy barrier for a single ion to hop between adjacent wells [46, 362]. This apparent discrepancy is explained because the augmented Jonscher law cannot actually describe the frequency dependence of conductivity relaxation of ionic conductors over a wide temperature range. However, at a given temperature, a simple addition of the NCL term to the Jonscher expression can give a reasonable description of experimental data. The crossover from the NCL contribution (at times shorter than the microscopic residence time, τ_o, of ions in their wells) to the onset of ionic hopping between adjacent wells (at times longer than τ_o) is thus more complicated than a simple sum in the frequency domain. The experimental conductivity data cannot be described simply by a sum, as suggested by Eq. (4.57), because the sum implies continued existence of the NCL (caged ions) at times (frequencies) much longer (lower) than the residence (primitive relaxation in the CM) time (frequency) of the ions in the wells, which is not the case. The experimental data suggest a serial or evolution picture of ion dynamics in which NCL (caged ion dynamics) is automatically terminated when the ions leave their cages and start hopping to neighboring wells, and consequently that there is a genuine crossover from NCL to ion hopping ac conductivity.

4.9 Evidences of Evolution of Ion Dynamics with Time

Understandably, readers interested mainly in conductivity or diffusivity of ionic conductors may be surprised by the amount of coverage we give to processes (stages 1 to 3) that have transpired at times before the terminal conductivity relaxation and dc conductivity (stage 4). The reason for us doing this is the wealth of experimental evidence showing the terminal conductivity relaxation and dc conductivity are linked in their properties to those of the earlier processes including the caged ion dynamics. Therefore, in order to arrive at a fundamental and complete understanding of conductivity relaxation, these faster processes and the links need to be addressed. With the understanding of the processes and the links at hand, the search of ionic conductor with desired property and level of dc conductivity can be expedited. There is yet another reason for doing this is that these processes and their links in ionic conductors are found in other interacting systems, indicating at work is fundamental physics of great interest to explore for condensed matter physicists. We shall start with colloidal particles suspension by confocal microscopy experimental data. Although the colloidal particles are interacting with hard-spheres interaction, different from the Coulomb interaction between ions, it is instructive to see all the processes of ionic conductors appear and are related to each other in the colloidal system.

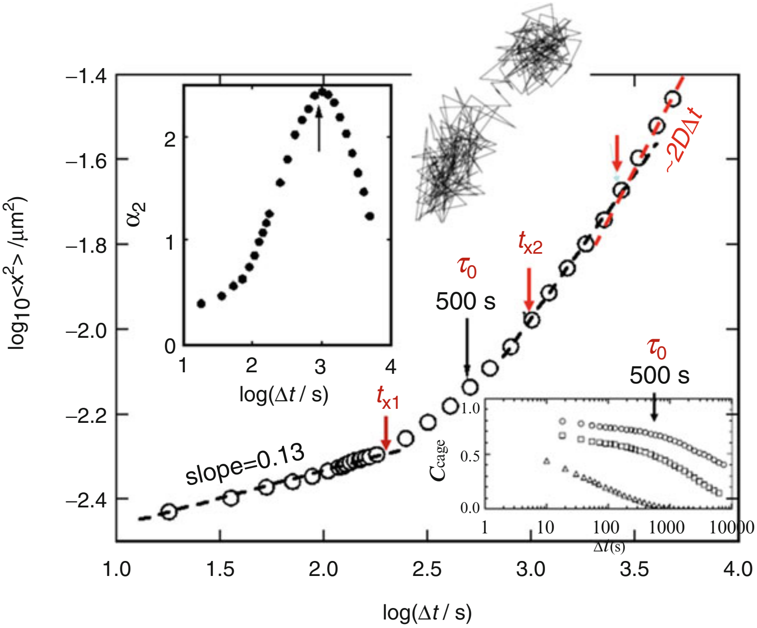

Fig. 4.55 Mean square displacement $< \Delta x^{2}(\Delta t) >$ for volume fractions $\phi = 0.56$ from Weeks et al. [212]. The *dashed line* has slope 0.13 indicates the NCL regime. The *first vertical arrow* indicates t_{x1}. The *second vertical arrow* indicate $\Delta t = 500$ s ~ τ_0, the time when a typical particle shifts position and leaves the cage determined by confocal microscopy experiment. The *last vertical arrow* indicates the time t_{x2} of the onset of the fractional power law (*black dashed line*) and is also the time when the non-Gaussian parameter $\alpha_2(\Delta t)$ assumes its maximum as shown in the inset on the upper-left corner. The *red dashed line* indicates $< x^2 > \sim 2D\Delta t$ or terminal diffusion. The *inset* on the lower-right corner [213] is a plot of the cage correlation function $C_{cage}(\Delta t)$ against Δt for three systems with $\phi = 0.56$, 0.52, and 0.46 (from *top* to *bottom*), and the *vertical arrow* indicates $\Delta t = 500$ s ~ τ_0. (*Upper middle inset*) A 2D representation of a typical trajectory in 3D for 100 min for $\phi = 0.56$ from Weeks et al. [212] to illustrate that particles spent most of their time confined in cages formed by their neighbors and moved significant distances only during quick rare cage rearrangements. The particle shown took ~500 s to shift position. Reproduced from Ref. [212] by permission

4.9.1 Colloidal Particles Suspension by Confocal Microscopy Experiment

To support the interpretation of NCL as the manifestation of caged molecular dynamics and the caged decay and termination of NCL as caused by the onset of primitive, we show the experimental results obtained on colloidal particles (hard spheres) suspension by confocal microscopy experiment by Weeks et al. [212], and by Weeks and Weitz [213]. Here we select the data in the case of volume fraction $\phi = 0.56$ and reproduce them in Fig. 4.55. This spectroscopy has the advantage that motions of all colloidal particles can be observed continuously as a function of time, and hence the change in dynamics are seen directly. It can be seen in the log-log plot of mean square displacement, $<\Delta x^2(\Delta t)>$, against logΔt in Fig. 4.55 that $< \Delta x^2(\Delta t) > \sim (\Delta t)^c$ with $c \approx 0.13$ at times shorter than 200 s ($\sim t_{x1}$), during which effectively the particles are all confined in cages because $\tau_c = \tau_0$ of 500 s has not yet been reached. The $< \Delta x^2(\Delta t) >$ for $\Delta t < 200$ s corresponds to susceptibility with frequency dependence $\chi''(\nu) \sim (\nu)^{-c}$ with $c \approx 0.13$, which is the NCL in the caged regime. This caged particles regime (*first stage*) ends at time $\sim t_{x1}$ indicated by the first arrow. The upper-middle inset shows the trajectories of particles that they spent most of their time confined in cages formed by their neighbors and moved significant distances only during quick and rare cage rearrangements. A typical particle takes average time τ_c of 500 s to shift position and leaves the cage. This time, identifiable with the primitive relaxation time τ_0 of the CM is indicated by the second vertical arrow. Termination of the caged ion dynamics at $\sim t_{x1}$ by the onset of the primitive relaxation with relaxation time τ_0 is the *second stage*.

The lower-right inset is a plot of the cage correlation function $C_{\mathrm{cage}}(\Delta t)$ against Δt for three systems with $\phi = 0.56$, 0.52, and 0.46 (from top to bottom), and the vertical arrow indicates Δt =500 s. It can be seen that for $\phi = 0.56$, $C_{\mathrm{cage}}(\Delta t)$ undergoes significant decay starting at Δt =500 s $\sim \tau_0$. After the primitive relaxation at τ_0, the number of ions cooperatively relax increases continuously until $\sim t_{x2}$ of about 1000 s (indicated by the third arrow) is reached. This is the *third stage*. The non-Gaussian parameter $\alpha_2(\Delta t)$ assumes its maximum at t_{x2} as shown in the inset on the upper-left corner. After t_{x2}. $<\Delta x^2(\Delta t) >$ assumes the fractional power law of Δt (black dashed line), which indicates the maximum number N of ions (or length-scale L) involved is reached and the start of the terminal many-ions heterogeneous dynamics with the Kohlrausch function, $\exp[-(t/\tau_\sigma)^{1-n}]$, as the time relaxation function. The extreme right dashed line indicates $< x^2 > \sim 2D\Delta t$ and the steady state diffusion is reached thereafter and at longer times. This is the *final stage*. At volume fraction $\phi = 0.60$ and higher, the colloidal particles are in the glassy state, and the change from $\phi = 0.56$ to $\phi = 0.60$ is the analogue of cooling an ionic conductor (see Figs. 4.8 and 4.10). The caged regime where $< \Delta x^2(\Delta t) > \sim (\Delta t)^c$ extends to longer times because the average time $\tau_c = \tau_0$ of particles leaving the cage is longer. There is concomitant decrease in the magnitude of $< \Delta x^2(\Delta t) >$ due to decrease in size of cage with increase in ϕ, and the exponent c becomes smaller. All these properties have analogues in the behavior of the NCL of ionic conductors and glassformers [7] on cooling. In the following section we present molecular dynamics simulations of lithium metasilicate (Li_2SiO_3) glass to show this trend and more.

4.9.2 Molecular Dynamics Simulations of Li_2SiO_3

Molecular dynamics simulations of the structure and dynamics of different kinds of ionic conductors are the main focus in a separate chapter. Here we take some of the results to support the evolution of ion dynamics in several stages from caged ion dynamics to the terminal many-ion dynamics and dc conductivity.

The mean square displacement, $<r^2(t)>$, of lithium metasilicate (Li_2SiO_3) glass obtained over a wide range of temperatures down to the very low temperature of

Fig. 4.56 Mean squared displacement of Li ions in Li_2SiO_3 at 100 K, 300, 500, 600, 700, 800, 900 K (from *bottom* to *top*)

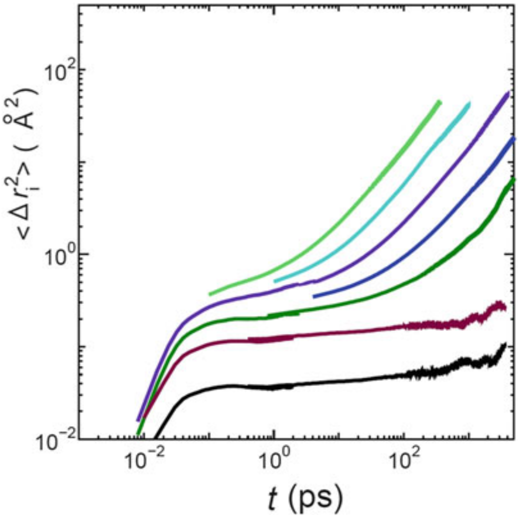

100 K are shown in Fig. 4.56 [370]. At short times but after the ballistic regime, it is evident from the plateau that $< r^2(t) >$ has the dependence $A(T)t^{c(T)}$ with $c(T) << 1$ at temperatures below 700 K. From the approximate relation between $< r^2(t) >$ and complex conductivity,

$$\sigma^*(\omega) = -\omega^2 \frac{Nq^2}{6kT} \int_0^\infty < r^2(t) > e^{-i\omega t} dt, \tag{4.63}$$

where N is the number density of mobile ions, q the ion charge, k the Boltzmann constant, and T the temperature. For $<r^2> = A(T)t^{c(T)}$, Eq. (4.63) gives $\sigma'(\omega) \propto \omega^{1-c}$ and $\varepsilon''(\omega) \propto \omega^{-c}$ and therefore a NCL if $c(T)$ is close to zero. As a limiting case, if the mean square displacement increased logarithmically with time as $< r^2 > \propto \log t$, the dielectric loss $\varepsilon''(\omega)$ would be practically flat, and $\sigma'(\omega) \propto \omega^{1.0}$. We found that the density distribution of Li ions in each cage tends to have strong anisotropy and the shape of the cage fluctuates. The details are given in Ref. [370]. The decrease of $A(T)$ and $c(T)$ with decrease of temperature are the same as in colloidal suspension with the increase of volume fraction ϕ.

We choose the $< r^2(t) >$ data at 700 K to illustrate the four stages in Fig. 4.57. The caged ion dynamics (1st stage) corresponding to $< r^2(t) > \propto t^{0.1}$ is terminated at $\sim t_{x1}$. The primitive ion relaxation time τ_0 had been located within the approximate range of $15 < t < 30$ ps from the linear dependence of $< r^2(t) > \propto t^{1.0}$ found over there (see Fig. 3 of Ref. [66]). The 2nd stage occurring at time $t_{x1} < t < \tau_0$ witnesses the decay of the cages. The 3rd stage at times from τ_0 to t_{x2} observes the increasing number of ions cooperatively hop. The maximum number has been reached at t_{x2}, thereafter the fractional power law, $<r^2(t) > \propto t^{0.64}$, becomes established and continue on until it changes to $< r^2(t) > = 6Dt^{1.0}$. This final stage

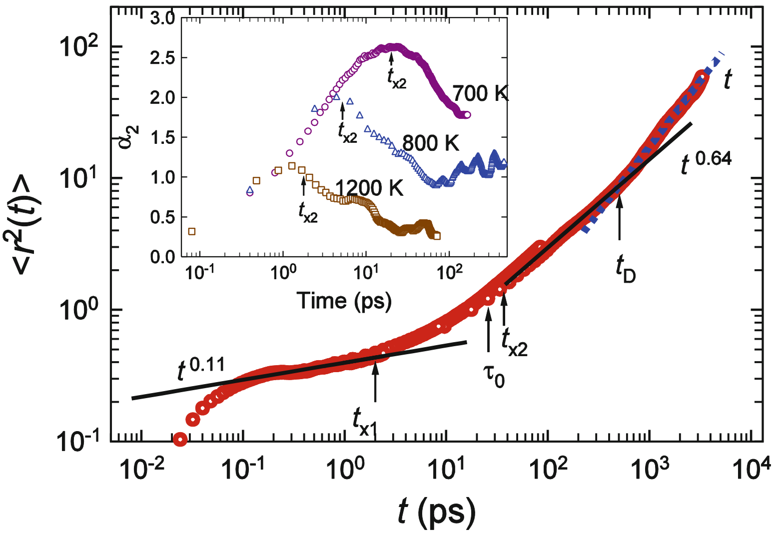

Fig. 4.57 MSDs of Li$^+$ ions in Li$_2$SiO$_3$ at 700 K. t_{x1}, $\tau_{0,}$ t_{x2} and t_D are crossover times that separate out the four time regimes explained in the text. The *inset* shows the time dependence of the non-Gaussian parameter

starting from t_{x1} is consistent with its correlation function given by the Kohlrausch stretched exponential function, exp[-$(t/\tau^*)^{0.64}$]. The inset of Fig. 4.57 shows the time dependence of the non-Gaussian parameter calculated to elucidate the ion dynamics in the NCL regime, the transition zone and the many-particles ion hopping regime. It peaks at t_{x2} like that of the colloidal particles in Fig. 4.55. The van Hove self-correlation function, $G_s(r,t)$, offers more insights into the ion dynamics, but it will be presented in the chapter on simulations.

The confocal microscopy of colloidal particles [212, 213] can follow all particles at all times to observe directly the kind of ion dynamics specifically in each of the four stages. So is molecular dynamics simulation of the Li ions in Li$_2$SiO$_3$. Space-time pictures have been generated to elucidate the motion of Li ions at 700 K at different times, equivalent to the real time pictures of motion of colloidal particles provided by confocal microscopy. These pictures of Li ions at progressively longer times of 4, 8, 16, 24, 48, 200, 400, and 1000 ps give clear information of the motions of Li ions in the different dynamic regimes separated by t_{x1}, τ_0, t_{x2}, and t_D as found from the time dependence of the $< r^2(t) >$ in Fig. 4.57.

The Fig. 4.58a–d show the displacements of the Li ions at four chosen times, $t = 4$ ps, 8 ps, 16 ps and 24 ps respectively at 700 K. The displacements of the Li ions are indicated by the vectors originating from the positions of the ions at an arbitrary chosen initial time 0 to the position at time t in three dimensions for a part of the basic cell of the simulation. The amplitudes of the vectors are coded according to the color scheme shown. These results are supposed to represent the behavior of the ions within the time regime bounded approximately by $t_{x1} \sim 2$–4 ps $< t < \tau_0 \sim 30$ ps. At 4 ps in Fig. 4.58a are within the time regime (4.1) in which the MSD in Fig. 4.57

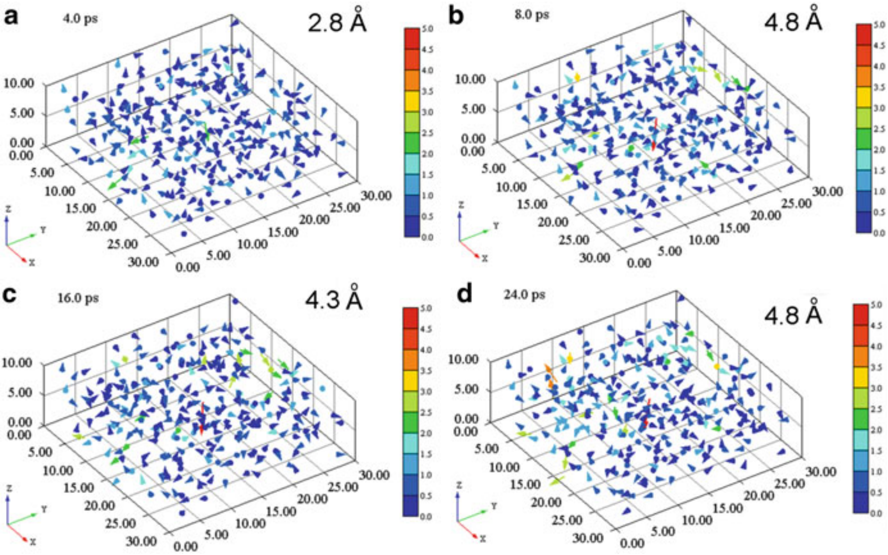

Fig. 4.58 Motion of Li ions in Li_2SiO_3 at 700 K at four different times, (**a**) 4 ps, (**b**) 8 ps, (**c**) 16 ps, (**d**) 24 ps. The positions of the Li ions at any of the indicated chosen times are represented by the vectors from the positions at an initial time in three dimensions for a part of the basic cell of the simulation. The values of axes are in Å. The *colors* are used to indicate the lengths of the vectors (the values shown in the legend are also in Å). In each case, the *arrow* help to indicate approximately the rare maximum displacement of the Li ions, and the value is recorded on top. It is 2.8, 4.8, 4.3, and 4.8 Å for 4, 8, 16, and 24 ps respectively. Note that this result fluctuates considerably, because of mixing of the back correlated motions and this vector field is just for one initial time. Many initial times are used for statistical treatment and even a longer length scale motion is found. Reproduced from Ref. [66] with permission

increases very slowly like t^c with $c \approx 0.1$ up to about 2 ps and with $c \approx 0.25$ from 2 ps to 4 ps. According to the color code of the figure, absolutely no ion makes jump to nearest neighboring Li sites with distance of about 3 Å or further. The maximum amplitude of motion is 2.5 Å. Thus, motion of all ions are confined within the cages, substantiating the interpretation of the caged ion dynamics with NCL in $\varepsilon''(f)$. At 8 to 16 ps in Fig. 4.58b, c, some rare jumps with distances larger than 3 Å are found. The colors of vectors in gold, orange and red represent such jumps with distances of 3.0–3.5 Å, 4.0–4.5 Å and 4.5–5.0 Å respectively. At 24 ps, which becomes comparable to $\tau_0 \approx 30$ ps, Fig. 4.58d show more such jumps with distance larger than 3 Å. These isolated or independent jumps are the primitive relaxation of the CM, and have been identified by their contribution to the MSD that is linearly proportional to time within the approximate range, $15 < t < 40$ ps. Cages decay by the onset of the primitive relaxation.

Figure 4.59a at 48 ps shows more jumps with distance larger than 3 Å, some of which are within the same neighborhood, and are no longer isolated events. The motions of the Li + ions are dynamically heterogeneous. There are fast and slow

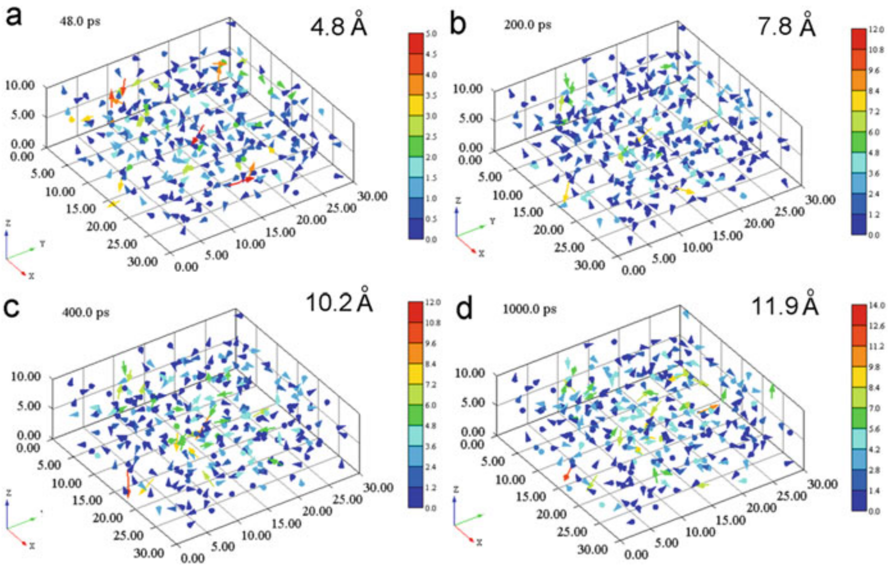

Fig. 4.59 Motion of Li ions in Li_2SiO_3 at 700 K at four times, (**a**) 48 ps, (**b**) 200 ps, (**c**) 400 ps, (**d**) 1000 ps. The positions of the Li ions at any of the indicated chosen times are represented by the vectors from the positions at an initial time in three dimensions for a part of the basic cell of the simulation. The values of axes are in Å. The *colors* are used to indicate the lengths of the vectors (the values shown in the legend are also in Å). Note that the code of the color scales for 48 ps and 200 ps, and for 400 ps and 1000 ps are different. In each case, the *vertical arrow* help to indicate approximately the maximum displacement of the Li ions, and the value is recorded on top. It is 4.5, 7.8, 9.0, and 11.8 Å for 48, 200, 400, and 1000 ps respectively. Of course most of the displacements have magnitudes smaller than the maximum value; however, contribution of longer length-scale motion to MSD is larger, because the value is squared. Reproduced from Ref. [66] with permission

ions classified as such by both temporal (waiting time of jumps) and spatial (back and/or forth correlation) behaviors [371, 372]. Back-correlated jumps return to the previous positions. Marked by $t_{x2} \approx 40$–50 ps in Fig. 4.57, this is the start of the heterogeneous dynamics regime in which increasingly number of ions cooperatively jump with increasing time, and the $< r^2(t) >$ has the fractional power law dependence $t^{0.64}$ in Fig. 4.57.

This trend is confirmed by Fig. 4.59b at $t = 200$ ps, and Fig. 4.59c at $t = 400$ ps, where it can be observed that the number of ions jumping cooperatively increases with time (note that the color code for jump distance is different in Fig. 4.59b–d). The ions undergoing these large amplitude motions form clusters and the vectors of their motions tend to be linked together, and the length-scale of the vectors linked together increase with time. Conversely the ions limited to local motions also form clusters. The increase with time of the length scale of the mobile ion clusters can be seen in going in succession from panels (a), (b), (c), and (d) at 48, 200, 400, and 1000 ps respectively. In Fig. 4.59d the ion dynamics at 1000 ps correspond to steady state ion diffusion because the time is past $t_D \approx 500–600$ ps in Fig. 4.57. As can be seen from the left panel of Fig. 4.57, at t_D the root MSD, $(<r^2(t)>)^{0.5}$, is about 3 Å, which is the average Li-Li ion sites separation distance, although even in a diffusive regime dynamics is still heterogeneous.

The reader can find a clip included in Additional material of this book which can be downloaded from http://extras.springer.com, entitled "0–1 ns vector-lithium metasilicate at 700 K.wmv" in the Folder Example 3, and can examine how vectors develop with an elapse of time in a cooperative manners.

The evolution of ion dynamics can be further substantiated by the time dependence of the self-part of the van Hove function for the Li ions defined by

$$G_s(r,t) = (1/N)\sum_{i=1}^{N} \langle \delta\big(r_i(t) - r_i(0) - r\big)\rangle, \tag{4.64}$$

where r is the distance traveled by the Li ion in a time t. The results in Fig. 10a–d of Ref. [45] show the evolution of $4\pi r^2 G_s(r,t)$ with time, which clearly can be separated into the different time regimes, same as done from $< r^2(t) >$ in Fig. 4.57, and from the vectors in Figs. 4.58a–d and 4.59a–d.

The evolution of ion dynamics with time elucidated by $< r^2(t) >$ in Fig. 4.57, and details of motion in Figs. 4.58a–d and 4.59a–d have exact analogues in the results of particle dynamics of colloidal suspensions by confocal microscopy [212]. It is also analogous to $< r^2(t) >$ of glass-forming liquids [373].

4.9.3 Experimental Conductivity Relaxation Data

Plenty of experimental data of frequency dependent conductivity relaxation can be cited to show the evolution of ion dynamics in the four stages separated by three characteristic times, t_{x1}, τ_0, and t_{x2}, as shown by the colloidal particles suspension and MD simulations of the Li_2SiO_3 glass. A few examples are given. The best example is the room temperature ionic liquid $[\text{Si-MIm}]^+[BF_4]^-$, the data of which are presented before in Fig. 4.8 for the purpose of contrasting different representations of the same data. Here the $M''(f)$ data are used to show the four stages. The secondary or β-conductivity relaxation is resolved and its peak frequency, f_β, is roughly in agreement with the primitive relaxation frequency, f_0, as predicted by the CM Eq. (4.37) via the identity $f_0 = 1/2\pi\tau_0$. The agreements are shown also in the lower panel of Fig. 4.60 (same as Fig. 4.11b). The black (magenta) arrows pointing at the data with the same color indicate $\log f_{x2}$, and $\log f_0$. The value of $f_{x2} = 1/2\pi t_{x2}$ is the frequency below which the $M''(f)$ of $[\text{Si-MIm}]^+[BF_4]^-$ becomes well fitted by the Fourier transform of the Kohlrausch function with $n = 0.43$ (lines in Fig. 4.60). The right panel show starting at some frequency ~$f_{x1} = 1/2\pi t_{x1}$ is the NCL regime with $M''(f) \propto f^{0.1}$. The four stages are clearly partitioned by f_{x1}, f_0, and f_{x2}.

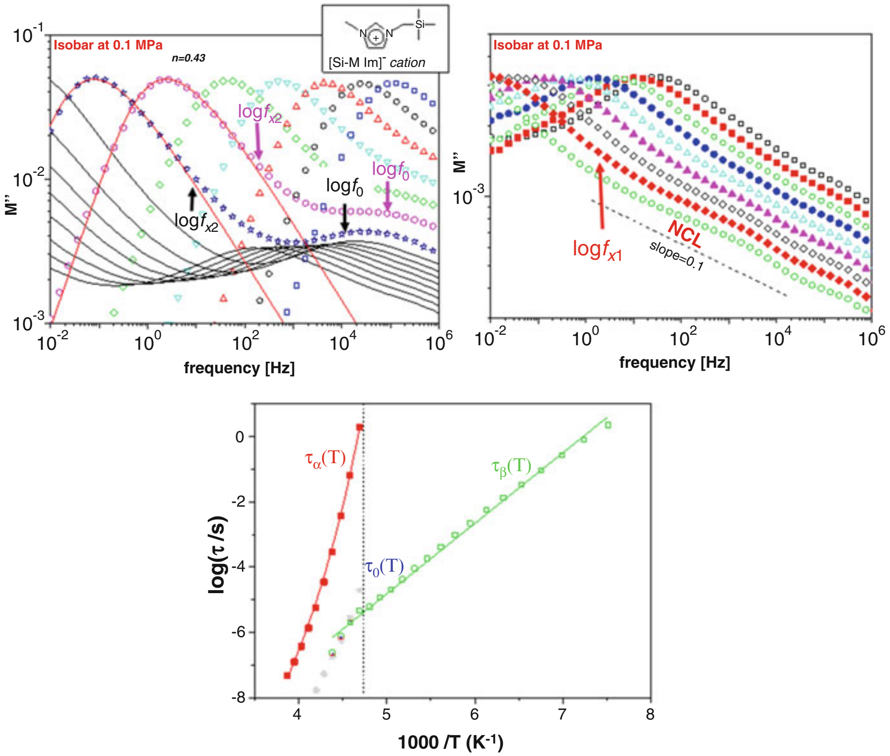

Fig. 4.60 (*Top left*) $M''(f)$ of [Si-MIm]$^+$[BF$_4$]$^-$ versus frequency at temperature in the range 243–173 K, spanning across T_g. The spectra, measured at every 5 K, show the presence of the slower structural α-relaxation and the well resolved secondary β-relaxation. (Top right) $M''(f)$ at temperatures in the range 163–123 K, way below T_g. The spectra, measured at every 5 K, show the presence of the slower well resolved secondary β-relaxation to be followed by the nearly constant loss (NCL) at higher frequencies. (*Bottom*) Temperature dependences of the α- and β-relaxation times. The primitive relaxation times τ_0 above T_g are plotted as the *solid blue circles*. The *solid lines* are fits to the VFT equation, $\log\tau_\alpha = -16.67 + 920/(T\text{-}159\ \text{K})$, and the Arrhenius law with $E_a = 41$ kJ/mol

The secondary or β-conductivity relaxation is resolved in $M''(f)$ data of this ionic liquid, presented in Fig. 4.60 and another one in Fig. 4.9. Moreover, there is good agreement of f_β with the primitive relaxation frequency, f_0. These two facts together provide direct validation of the CM.

4.9.3.1 Molten 0.4Ca(NO$_3$)$_2$-0.6KNO$_3$ (CKN)

Electrical relaxation measurements on CKN were made by Lunkenheimer et al. [27, 28] over unusually broad frequency and temperature ranges. In Fig. 4.61, we show their ε'' data at 342 K as a function of frequency ν. The data

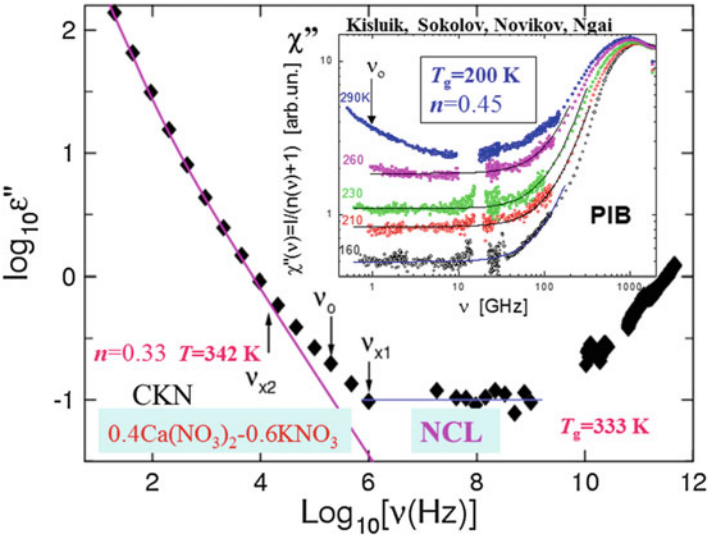

Fig. 4.61 Dielectric loss as a function of frequency of CKN at 342 K showing the existence of the NCL over 3 decades in frequency. The *horizontal dashed line* indicates the NCL. The *other dashed line* is the many-particles ion conductivity relaxation calculated from the Kohlrausch fit to the electric loss modulus, M'', data shown in the *inset* as the *dashed line* with $\beta = 0.67$. The deviation of the data from the Kohlrausch fit at higher frequencies is marked by one crossover frequency, ν_{x2}. The deviation of the data from the NCL at lower frequencies is marked by the other crossover frequency, ν_{x1}. The location of the independent relaxation frequency of the CM, $\nu_o \equiv 1/2\pi\tau_o$, is also indicated. τ_o is the independent relaxation time calculated from the CM. Data after Refs [67, 68]. The *inset* show the NCL from the light scattering data of PIB at temperatures below T_g from Ref. [374]

indicate the NCL that extends over about three decades and there is a cross over to a power law $\varepsilon''(\nu) \propto \nu^{-\beta}$ at lower frequencies, with $\beta = 1\text{-}n$, and eventually $\varepsilon'' \propto \nu^{-1}$ at even lower frequencies which corresponds to the dc conductivity regime from the relation, $\sigma'(\omega) + i\sigma''(\omega) = \mathrm{i}\omega\varepsilon_o\varepsilon^*(\omega)$, as illustrated in the figure. The line having ν^{-1} at low frequencies and $\nu^{-\beta}$ at higher frequencies is actually the $\varepsilon_\beta''(\nu)$ calculated from the fit to the electric modulus by the Fourier transform of the Kohlrausch function with exponent $\beta = 1 - n$, i.e. the loss from many-particle hopping of ions. The departure of the Kohlrausch fit at higher frequencies starting at ν_{x2} is indicated by an arrow. The primitive relaxation frequency, ν_0, calculated by the CM Eq. (4.37) via the identity $\nu_0 = 1/2\pi\tau_0$ is indicated by another arrow. Onset of the NCL at higher frequencies occurs quite distinctly at ν_{x1}. Thus the change in ion dynamics from the $\varepsilon''(\nu)$ data occurs in four stages separated by ν_{x1}, ν_0, and ν_{x2}.

The inset of the figure shows the susceptibility $\chi''(\nu)$ data of polyisobutylene, a non-ionic polymer, obtained by high frequency dynamic light scattering at temperatures below T_g. The presence of the NCL is clear. The primitive relaxation frequency, ν_0, calculated by the CM at 290 K and indicated by the arrow is effective in terminating the NCL regime.

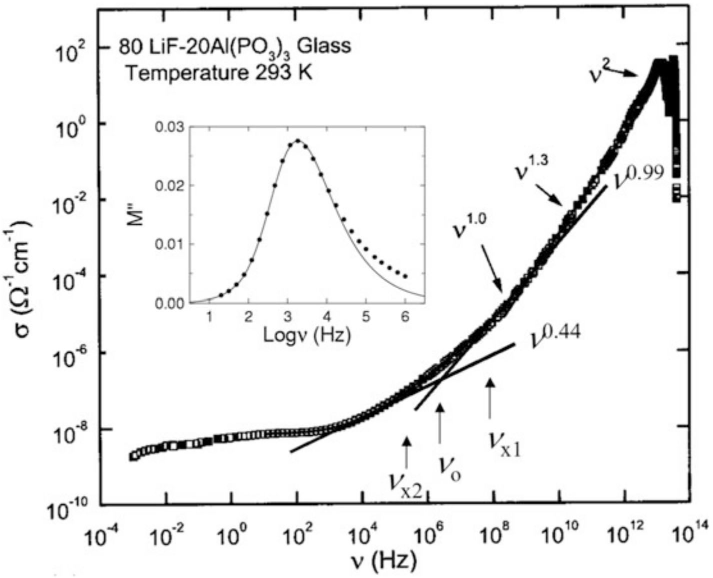

Fig. 4.62 $\log_{10}\sigma'(\nu)$ versus log(frequency/Hz) plot of data at 293 K of 0.80LiF-0.20Al(PO$_3$)$_3$ obtained by Kulkarni et al. [375] to show the near linear frequency dependence of the NCL by the line with slope equal to 0.99. The line with slope 0.44 is the high frequency dependence of $\log_{10}\sigma'(\nu)$ corresponding to the Kohlrausch fit to the electric modulus data (shown in the *inset*) with $n = 0.44$. The *dashed line* in the main figure is the many-particles ion conductivity relaxation. The crossover frequencies ν_{x1} and ν_{x2} as well as the independent hopping frequency ν_o are determined from the data in the same manner as explained in Fig. 4.61

4.9.3.2 Glassy 0.80LiF-0.20Al(PO$_3$)$_3$

Electrical relaxation data at 293 K of a glassy ionic conductor, 0.80LiF-0.20Al(PO$_3$)$_3$, was obtained by Kulkarni et al. [375] over unusually broad frequency range. In Fig. 4.62, we show their data as σ' as a function of frequency ν. The existence of the NCL is exemplified by a near linear frequency dependence of the σ' data over about two decades, which terminates starting at ν_{x1}. The inset of the same figure shows the *same* data only up to 10^6 Hz in terms of $M''(\nu)$ to isolate the contribution from many-particles ion hopping. The line is the Kohlrausch fit to the $M''(\nu)$ data with $\beta \equiv (1\text{-}n) = 0.56$ and $\tau_K = 8.7 \times 10^{-5}$ s. At high frequencies the Kohlrausch fit to M'' assume the $\nu^{-\beta}$-dependence and the corresponding $\sigma_\beta'(\nu)$ assumes the $\nu^{1-\beta}$-dependence, which is shown by the straight line with slope 0.44. The $\sigma'(\nu)$ data conform to the $\nu^{1-\beta}$-dependence of $\sigma_\beta'(\nu)$ at frequencies below ν_{x2}. The value of ν_0 is calculated by the CM Eq. (4.37) with $\beta \equiv (1\text{-}n) = 0.56$. Thus, just like CKN, the $\sigma'(\nu)$ data of 0.80LiF-0.20Al(PO$_3$)$_3$ crossover from NCL to $\sigma_\beta'(\nu)$ over several dynamics regimes defined by the frequency ranges separated by ν_{x1}, ν_0, and ν_{x2}.

4.9.3.3 $0.5Ag_2S$-$0.5GeS_2$

The data of glassy $0.5Ag_2S$-$0.5GeS_2$ from the work of Belin et al. [258] at many temperatures have been presented before in Fig. 4.27 for showing the presence of the NCL and its weak temperature dependence. We revisit Fig. 4.27 to consider the data taken at 153 K. The NCL over extensive frequency domain is indicated by the solid green line with $\nu^{0.95}$-dependence. The vertical arrow labeled by ν_{x1} pointing upwards indicate the location of ν_{x1} for 153 K. The blue dashed line with slope 0.45 is the continuation of the $\nu^{1-\beta}$-dependence of $\sigma_\beta'(\nu)$ to high frequencies. Here $\sigma_\beta'(\nu)$ is the correspondent of $M_\beta^*(\nu)$, the Kohlrausch fit to $M^*(\nu)$ data with exponent $\beta \equiv (1\text{-}n) = 0.55$ (not shown). The location of the independent relaxation frequency of the CM, $\nu_o \equiv 1/2\pi\tau_o$, at 153 K is indicated by one of the arrows. The NCL regime is terminated at ν_{x1}. The onset of the low frequency many-ion $\sigma_\beta'(\nu)$ is at ν_{x2}. The transition from NCL to many-ion $\sigma_\beta'(\nu)$ occurs by crossing over several dynamics regimes defined by ν_{x1}, ν_0, and ν_{x2}.

4.10 Properties of Caged Ion Dynamics, Primitive Relaxation, and Many-Ion $\sigma_\beta'(\omega)$ Are Related

The ample results from molecular dynamics simulations and experimental studies have shown convincingly the ion dynamics evolve from one regime to another in the manner described by the CM. Therefore the dynamics in the several regimes are connected, and their properties are related. In this section we consider some of the properties of the different regimes and demonstrate the relations. Also from the connection, property of ion dynamics in one regime can be deduced or inferred from the property in another regime. The existence of these relations means study confined to the terminal many-ion $\sigma_\beta'(\nu)$ is incomplete and may even leads to wrong interpretation.

4.10.1 Derivation of the Weak T-Dependence of the NCL

In the previous section shown is that the NCL exists in the short time (high frequency) regime, $t_{on} < t < t_{x1}$ where there is absolutely no thermally activated independent jumps of the ions out of their cages with the relaxation time $\tau_o = \tau_\infty \exp(E_a/kT)$. Here t_{on} is the onset time of the NCL. Experimental data extending to very high frequencies show that the NCL continues to exist up to about 10^{11} Hz, from which t_{on} is estimated to be of the order of 10^{-11} to 10^{-12} s. The crossover time t_{x1} has to be much less than τ_o in order to satisfy the condition for generation of the NCL that practically there is no successful independent ion jumps out of their cages throughout the period $t_{on} < t < t_{x1}$. Therefore $\exp(-t_{x1}/\tau_o)$ is still close to unity and the probability of an ion to have jumped out of its cage at time t_{x1}, given by $[1-\exp(-t_{x1}/\tau_0)]$, is small. It has the same value for all temperatures, as required by the same criterion used to determine that the NCL terminates at the time t_{x1}. Hence t_{x1} has the same temperature dependence as τ_0, i.e., $t_{x1}(T) = t_\infty \exp(E_a/kT)$, a result supported by experimental data [46, 376]. From the definition of t_{x1}, the mean square displacement $<r^2>_{\mathrm{NCL}}$ corresponding to the NCL increases by the *same* small amount in the period, $t_{on} < t < t_{x1}(T)$, at *all* temperatures. However, since t_{x1} is thermally activated, this same increase of $<r^2>_{\mathrm{NCL}}$ is spread over a number of decades of time given by $[\log t_{x1} - \log t_{\mathrm{on}}]$. Consequently the mean square displacement is inversely proportional to $\log(t_{x1}/t_{\mathrm{on}})$. From this and Eq. (4.63) relating the conductivity to mean square displacement, it is deduced that the intensity of the NCL, $\varepsilon''(\omega) = A\omega^{-c}$, measured by A is given by the proportionality relation [44, 364],

$$A \propto E_a^{-1}[1 - (T/T_o)]^{-1}. \tag{4.65}$$

This expression is well approximated by $A \propto \exp(T/T_o)$, at $T << T_o$, with

$$T_o \approx E_a/k\log_e(t_{on}/t_\infty) \tag{4.66}$$

T_{o} is a positive number because $\log(t_{\mathrm{on}}/t_\infty)$ is a positive number from the fact $t_{x1} < \tau_{\mathrm{o}}$ that t_∞ is even shorter than the prefactor τ_∞ of τ_{o}, which is the reciprocal of a vibrational attempt frequency. Thus the weak temperature dependence of the NCL is captured by the relation of the NCL to the primitive relaxation of the Coupling Model.

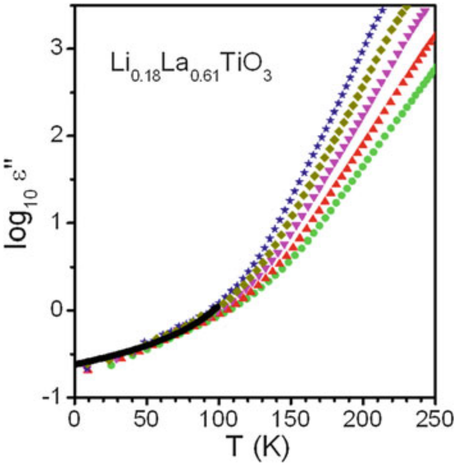

Fig. 4.63 Temperature dependence of the dielectric loss, $\varepsilon''(\nu)$, at fixed frequencies for $Li_{0.18}La_{0.61}TiO_3$. Experimental data are shown for different frequencies (300 Hz (*stars*), 1 kHz (*diamonds*), 3 kHz (*down triangles*), 10 kHz (*up triangles*) and 30 kHz (*circles*)). Below about 100 K, data are almost frequency independent, $\varepsilon''(\nu) \approx A\nu^{-c}$ with $c \approx 0$, showing a NCL behavior. *Solid line* is a fit to Eq. (4.65) (see text)

Figure 4.63 shows the temperature dependence of the almost frequency independent dielectric loss, $\varepsilon''(\nu) \approx A\nu^{-c}$ with $c \approx 0$, for $Li_{0.18}La_{0.61}TiO_3$ at several fixed frequencies, showing a NCL behavior below approximately 100 K. Also plotted in the figure is the best fit of the data to Eq. (4.65), and there is very good agreement down to the lowest temperatures. It is worthwhile to comment that since the deduced temperature dependence of the NCL comes from a qualitative theory, it is not expected that it will accurately describe the experimental data, particularly if considered over an extended temperature range where another source of contribution such as two-level systems or asymmetric double well potentials (ADWP) [377–379], and a broad $\varepsilon''(\nu)$ peak at low temperatures such as found in $Gd_2Zr_2O_7$ [380], which has a large concentration of mobile oxygen vacancies, may come into play at very low temperatures and high frequencies. These extra contributions have no bearing on the dynamics of ions leading to dc conductivity, and are not discussed any further.

4.10.2 Anti-Correlation of NCL with E_a or E_σ

Also from Eq. (4.65) is at constant temperature that the magnitude A of the NCL should decrease with increasing E_a, had other factors that determine the absolute value of A be the same for all ionic conductors. If this condition holds for many ionic conductors, then an approximate anti-correlation between A and E_a may exist at constant temperature. Figure 4.66 shows the remarkable anti-correlation from experimental data for a variety of ionic conductors as predicted by the model. The solid line in the figure represents an exact inversely proportional relation. It is indeed noteworthy that such a correlation holds since may be there are other factors which affect the magnitude of the NCL and have not been considered. It has been argued that the different ion jump distances and the chemical structures of the different ionically conducting materials might be responsible for the deviations from a perfect anti-correlation [364]. It has been shown [8, 104] that for different families of ionic conductors, smaller the activation energy E_a corresponds to smaller activation energy for the dc conductivity E_σ. This correlation is shown in the inset of Fig. 4.64 for the ionic conductors plotted in the main panel, and the values of both magnitudes are shown in Table 4.4.

Therefore, an anti-correlation is also expected between A_{NCL} and E_σ. Figure 4.65 shows that a strong correlation indeed exists between them. The inset to Fig. 4.65 shows a correlation is also observed between A_{NCL} and the logarithm of the dc conductivity σ_0 at room temperature. This finding is consistent with the observation by Ngai that superionic conductors show highest values of the magnitude of the NCL [43, 44]. Since $\sigma_0(T) = \sigma_\infty \exp(-E_\sigma/kT)$, and the prefactor σ_∞ takes not too different values in all ionic conductors, the rule that higher E_σ means smaller dc conductivity at room temperature is usually obeyed. Therefore, the correlation observed between A_{NCL} and the dc conductivities at room temperature can be

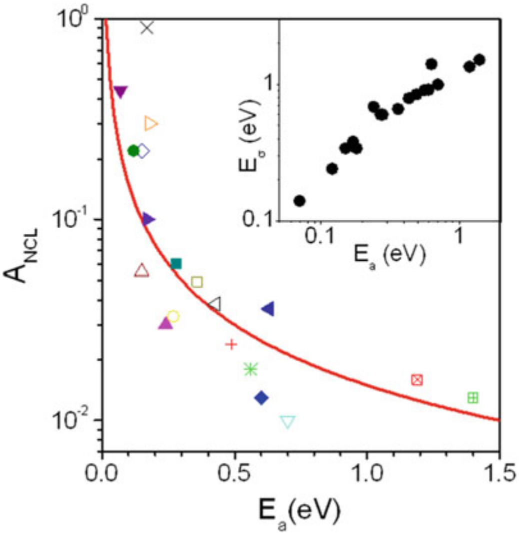

Fig. 4.64 The magnitudes A of the NCL at $T = 100$ K versus the activation energy E_a for a variety of ionic conductors. *Solid line* represents an exact inversely proportional relation as derived from the Coupling Model for the NCL (see text). The references from which the experimental data are taken are given in Table 4.4. Li_2O-$3B_2O_3$ (*plus*), Na_2O-$3B_2O_3$ (*asterisk*), K_2O-$3B_2O_3$ (*filled diamond*), Rb_2O-$3B_2O_3$ (*open inverted triangle*), $LiPO_3$ (*filled triangle*), $35Li_2O$-$61SiO_2$-$3Al_2O_3$-P_20_5 (*open circle*), $Li_{0.18}La_{0.61}TiO_3$ (*cross*), $(ZrO_2)_{0.84}(Y_2O_3)_{0.16}$ (*left pointing filled triangle*), Na_2O-$3SiO_2$ (*open square*), $(AgI)_{0.3}$-$(AgPO_3)_{0.7}$ (*right pointing open triangle*), $(AgI_2)_{0.48}$-$(Ag_2SeO_4)_{0.52}$ (*open diamond*), Na-βAl_2O_3 (*filled inverted triangle*), $(Li_2S)_{0.56}$-$(SiS_2)_{0.44}$ (*right pointing filled triangle*), $(Ag_2S)_{0.5}$-$(GeS_2)_{0.5}$ (*open triangle*), Ag_7GeSe_5I (*filled circle*), $(LiF)_{0.8}(Al(PO_3)_3)_{0.2}$ (*filled square*), xK_2O-$(1$-$x)GeO_2$ ($x = 0.2$) at $T = 381$ K (*right pointing open triangle*), xK_2O-$(1$-$x)GeO_2$ ($x = 0.02$) at $T = 367$ K (*squared times*), xK_2O-$(1$-$x)GeO_2$ ($x = 0.0023$) at $T = 374$ K (*squared plus*). The *inset* shows that the smaller is the value of E_a, the smaller is the activation energy E_σ for the dc conductivity for the set of ionic conductors shown in the main panel

considered simply to follow from the correlation between A and E_σ or between A and E_a deduced from Eq. (4.65) [364].

In general, the anti-correlation of the decrease of the magnitude of the NCL with the increase of the activation energy of the dc conductivity can be considered qualitatively by how tightly bound are the ions by the potential. More tightly bound ions naturally implies larger activation energies, E_a and E_σ. However, why NCL becomes smaller in more tightly bound ions is intriguing. We shall show shortly that the potential confining the ions is more harmonic and deeper in conductors where the ions are more tightly bound and have smaller mean square displacements in motion. Consequently the magnitude of NCL becomes smaller since it is determined by the anharmonicity of the potential. The terminology "tight" and "loose" was first introduced by Angell in glassy ionic conductors [384], but for different purpose and not in connection with NCL and (1-n) than we did. In the following we select some examples from Ref. [43, 44] to substantiate the points.

Table 4.4 Activation energies $E_a = (1\text{-}n)E_\sigma$ for the ionic conductors shown in Fig. 4.64

Ionic conductor	E_a (*eV*)	(1-*n*)	E_σ (*eV*)	*Ref.*
$Li_2O\text{-}3B_2O_3$	0.49	0.58	0.84	[48, 381]
$Na_2O\text{-}3B_2O_3$	0.56	0.62	0.90	[48, 381]
$K_2O\text{-}3B_2O_3$	0.60	0.66	0.91	[48, 381]
$Rb_2O\text{-}3B_2O_3$	0.70	0.71	0.99	[48, 381]
$LiPO_3$	0.24	0.35	0.68	[270]
$35Li_2O\text{-}61SiO_2\text{-}3Al_2O_3\text{-}P_2O_5$	0.27	0.45	0.60	[33, 382]
$Li_{0.18}La_{0.61}TiO_3$	0.17	0.45	0.38	[270]
$(ZrO_2)_{0.84}(Y_2O_3)_{0.16}$	0.63	0.54	1.40	[For references, see 22] [270]
$Na_2O\text{-}3SiO_2$	0.36	0.55	0.66	[40, 43, 44]
$(AgI)_{0.3}\text{-}(AgPO_3)_{0.7}$	0.18	0.54	0.34	[43, 44]
$(AgI_2)_{0.48}\text{-}(Ag_2SeO_4)_{0.52}$	0.15	0.45	0.34	[43, 44]
$Na\text{-}\beta Al_2O_3$	0.07	0.5	0.14	[43, 44]
$(Li_2S)_{0.56}\text{-}(SiS_2)_{0.44}$	0.17	0.48	0.35	[43, 44]
$(Ag_2S)_{0.5}\text{-}(GeS_2)_{0.5}$	0.15	0.45	0.34	[44]
Ag_7GeSe_5I	0.12	0.48	0.24	[44, 383]
$(LiF)_{0.8}\text{-}(Al(PO_3)_3)_{0.2}$	0.26	0.44	0.60	[44]
$xK_2O\text{-}(1\text{-}x)GeO_2$ $(x = 0.2)$	0.43	0.54	0.79	[88, 368]
$xK_2O\text{-}(1\text{-}x)GeO_2$ $(x = 0.02)$	1.19	0.89	1.34	[88, 368]
$xK_2O\text{-}(1\text{-}x)GeO_2$ $(x = 0.0023)$	1.40	0.93	1.50	[88, 368]

Reproduced by permission from Ref. [364]
E_σ and (1-*n*) were obtained from electrical conductivity measurements at temperatures where ionic hopping is the dominant contribution to the ac conductivity

(1) Shown in the first 4 rows of Table 4.4 are data from the family of alkali triborate glasses especially prepared to have exactly the desired compositions. The alkali ion ranges from Li, Na, K, to Rb. In Figs. 4.64 and 4.65, the data are shown by the symbols (red +) $Li_2O\text{-}3B_2O_3$, (asterisk) $Na_2O\text{-}3B_2O_3$, (blue diamond) $K_2O\text{-}3B_2O_3$, (pale blue inverted triangle) $Rb_2O\text{-}3B_2O_3$, the systematic decrease of the magnitude of the NCL observed in the family of alkali triborate glasses when changing the alkali ion from lithium to rubidium was reported as a mass dependence of the NCL [48]. From the perspective of the predictions from the Coupling Model, such a decrease in the NCL when increasing the mass of the alkali ion may just follow as a consequence of the more basic correlation between A and E_a, and arises from the increase of E_a when increasing the mass of the alkali ion in the alkali triborate glasses [361, 364].

(2) The last three rows of Table 4.4 are from the conductivity data of several potassium germanate glasses, $xK_2O\text{-}(1\text{-}x)GeO_2$ $(x = 0.2,\ 0.02,\ 0.0023)$ [88, 368], which have NCL decreases with decreasing concentration of mobile ions, and concomitantly with increasing E_a or E_σ shown in Figs. 4.64 and 4.65, and increasing (1-*n*). The same anti-correlations apply to the sodium thioborate glasses with different concentrations of Na ions [41].

(3) In alkali glasses, when replacing one alkali ion by another alkali ion at the same temperature, it is observed that there is a reduction of the magnitude of the NCL,

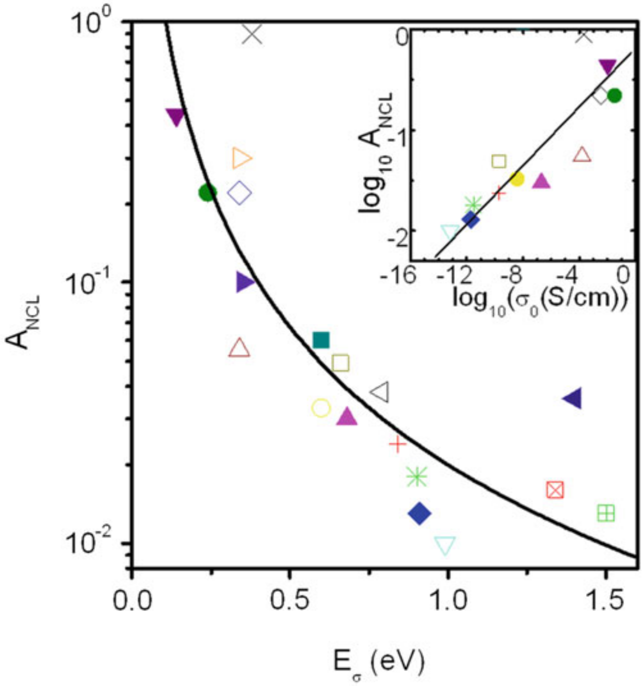

Fig. 4.65 A clear negative correlation holds between the magnitude A_{NCL} of the NCL at $T = 100$ K and the activation energy, E_σ, of the dc conductivity. *Symbols* are the same used in Fig. 4.64. References from which the experimental data are taken are given in Table 4.4. The *inset* shows the same NCL data vs. the dc conductivity at room temperature. *Lines* are guides for the eye

although the change is much smaller than the decrease of the dc conductivity due to the mixed alkali effect [43, 44, 109, 385]. This is exemplified by the comparison of $Na_2O.3SiO_2$ with $0.5Na_2O$-$0.5K_2O$-$3SiO_2$ [18], and $LiPO_3$ with $Li_{0.5}Na_{0.5}PO_3$ [386]. In both cases there is again a correlation of the decrease of the magnitude of the NCL with the increase of E_σ of the dc conductivity, and narrowing of the electric modulus loss peak and increase of (1-*n*).

(4) Loosening the binding of the mobile ion by modification of the glass structure leads to an increase of the magnitude of the NCL, decrease of E_a or E_σ, and decreasing (1-*n*). This was observed by halogenation in lithium borate glasses by addition of LiBr or LiCl [261, 262].

(5) The magnitude of the NCL of the superionic conductors with technological interest for their application as electrolytes in solid state batteries and fuel cells, as well as room temperature ionic liquids (see Figs. 4.8, 4.9, and 4.10) is much higher than in other ion conducting solids [23, 43, 44, 48, 364]. Again, this was related to the fact that in the former the mobile ions are loosely bound within more anharmonic potentials, and have larger mean square displacements in caged motion [43, 44]. They have smaller E_a or E_σ, and (1-*n*) as well.

(6) At comparable ion densities, the magnitude of the NCL is larger in glasses where the motion of the ions is more decoupled from the structural relaxation

[43, 44]. This means ions are more decoupled from the less mobile matrix atoms, and hence less tightly bound.

Some of examples given in the above NCL not only anti-correlates with E_a or E_σ, but also with $\beta = (1\text{-}n)$. Thus, this result implies that E_a or E_σ correlates with (1-n). Remarkably, this correlation had been found empirically earlier. The data are discussed in the next section.

4.10.3 Correlation of E_a or E_σ with $(1-n)$

The existence of a correlation between $\beta = (1-n)$ and E_σ for a family of ionically conducting glasses was first pointed out by Angell and Martin [387]. Later on, this correlation, as well as another correlation between β and E_σ and between β and the product βE_σ, have been established from data of many families of alkali oxide glasses [104]. This correlation between β and βE_σ is reproduced from the

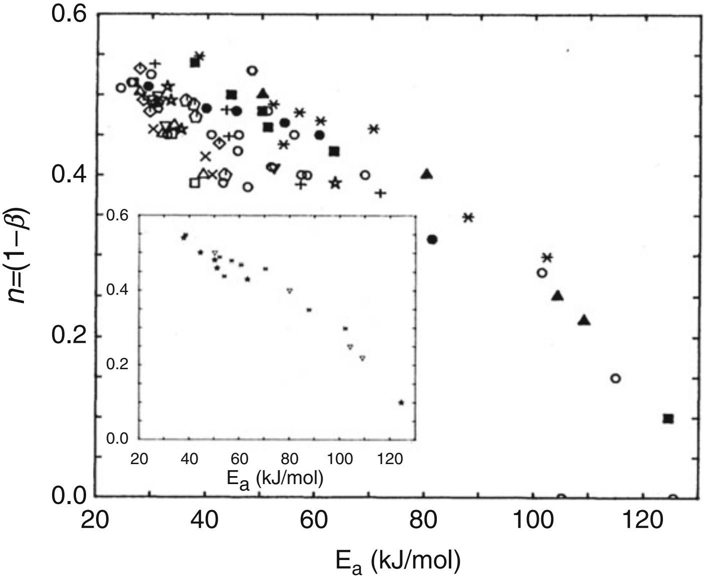

Fig. 4.66 A plot of the coupling parameter n vs E_a for alkali oxide glasses having total alkali oxide mole fraction of $c = 0.05$ (*filled square*), 0.075 (*filled triangle*), 0.10 (*asterisks*), 0.20 (*plus*), 0.25 (*circle*), 0.30 (*pentagon*), 0.35 (*star*), 0.40 (*inverted triangle*), 0.45 (*diamond*), 0.50 (*cross*), 0.55 (*open triangle*), 0.60 (*open square*), from Table 4.2 and 12 other tables in AIP documents (see Ref. [104]). *Open circles* are a collection of data from alkali oxide glasses in Table I of Ref. [104] that do not have c falling into the above 12 values. Two semicircular points on the x-axis are data from the very low alkali silicate and germanate glasses. The *inset* are the data from the family of the alkali aluminogermanate glasses only. By restricting consideration of glasses from the same family, the correlation is improved

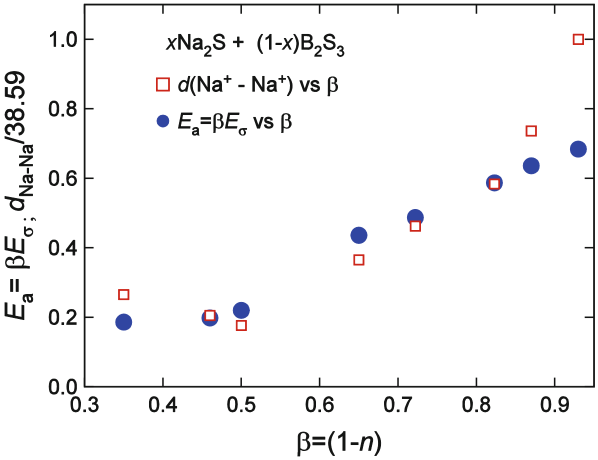

Fig. 4.67 The primitive activation energy $E_a = \beta E_\sigma$ of $x(Na_2S) + (I-x)$ B_2S_3 glasses plotted against β showing perfect correlation. The *open squares* are the average Na-Na ion separation distances, $d(Na^+ - Na^+)$ normalized by 38.59 Å, the value of d. for $x = 0.0010$. The plot of $d(Na^+-Na^+)/38.59$ Å vs. β shows no correlation

Ref. [104]. The source of data and the values of β and E_σ of the oxide glasses in Fig. 4.66 can be found in this figure caption. There are data from the alkali germanate glasses [87] which show that the correlation between β and E_σ is not maintained while the correlation between β and βE_σ continues to hold. Between these two correlations, the one between β_σ and $\beta_\sigma E_\sigma$ appears to be most robust.

Also, a more obvious correlation between β_σ and d, the ion-ion separation distance, has been proposed [387, 388]. Notwithstanding, from their data of the fast ionic conductors $x(Na_2S) + (1-x)B_2S_3$, Patel and Martin [85] found the correlation between β and $d(Na^+-Na^+)$ breaks down, as shown in Fig. 4.67 here. On the other hand, the correlation between β and βE_σ continues to hold (see Fig. 4.67).

4.10.4 Origin of Correlation of E_a with $(1-n)$, and Anti-Correlation with NCL

Before we address these correlations in the case of the ionic conductors, it is instructive to consider the findings from molecular dynamics simulations of binary Lennard-Jones particles by Bordat et al. [389–390]. As we shall see, the results of these simulations exhibit analogs of correlations found in ionic conductors. Furthermore, the anharmonicity of the potential is the origin of the characteristics of all the quantities and their correlations.

Molecular dynamics (MD) simulations were performed by Bordat et al. on binary Lennard-Jones (LJ) particles systems with three different interaction potentials [389, 390]

$$V(r) = [\Lambda_0/(q-p)]\{p(r_0/r)^q - q(r_0/r)^p\}. \qquad (4.67)$$

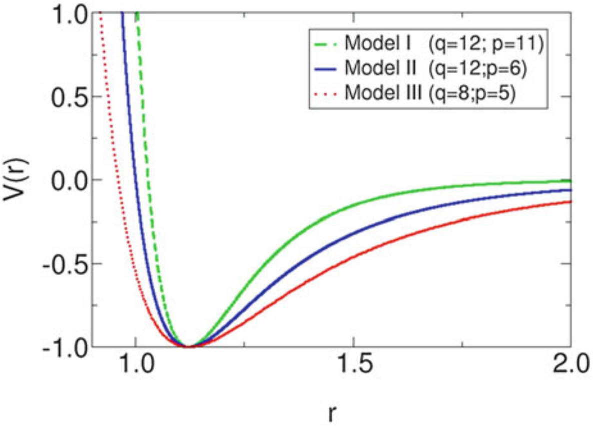

Fig. 4.68 Potential $V(r)$ governing the particles A–A interaction. The *dashed curve* is the (12, 11) LJ potential for model I, the *solid curve* is the (12, 6) LJ potential for model II and the *dotted curve* is the (8, 5) LJ potential for model III

The parameters r_0 and Λ_0 represent the position of the minimum of the well and its depth, respectively. The choice of $q = 12$ and $p = 6$ corresponds to the standard LJ potential used by Kob & Andersen [391, 392] and others for other studies by simulation. For the purpose of investigating the change of dynamics with controlled change of $V(r)$, Bordat et al. developed two other models by changing only the exponents, q and p, of the LJ potential for the species A–species A interactions. They are $(q = 8, p = 5)$ and $(q = 12, p = 11)$ and shown together with the (12, 6) LJ potential in Fig. 4.68.

The dynamics of Lennard-Jones particles is relevant for ionic conductors. The relevance is by the similarity of the results of the two systems from the MD simulations. We start from the MD simulation of glassforming binary Lennard-Jones system composed of 6400 particles of type A and 1600 particles of type *B* interacting with the (12, 6) LJ potential by Donati et al. [373] The $< r^2(t) >$ of A particles from this paper are reproduced here in Fig. 4.69a together with the non-Gaussian parameter $\alpha_2(t)$ in Fig. 4.69b. For all temperatures (in L-J unit), subdiffusion having the fractional power law dependence of $< r^2(t) > \propto t^{1-n}$ with $(1\text{-}n) = 0.77$ appears at earlier times before the terminal free diffusion with $< r^2(t) > = 6Dt$ takes over. The onset time of the subdiffusion is denoted by t_{x2}, its location for $T = 0.451$ is indicated approximately by the arrow in Fig. 4.69a. At lower temperatures, the particles are initially caged, and the caged dynamics contribute a power law $< r^2(t) > \propto t^c$ to the MSD with $c << 1$ or a nearly constant loss (NCL) with frequency dependence ω^{-c} to the susceptibility $\chi''(\omega)$. At the lowest temperature $T = 0.451$, c is about 0.1. In order of time, the caged dynamics term, $<r^2(t) > \propto t^c$, is followed after a short interlude by the subdiffusion term, $<r^2(t) > \propto t^{1-n}$, and in turn by the terminal diffusion term $< r^2(t) > = 6Dt$. The value of the fractional power $(1\text{-}n)$ of the subdiffusion is comparable to the stretch exponent β in the Kohlrausch function used to fit the intermediate scattering function $F_s(q,t)$ for $q = q_{\max}$. Donati et al. [373] fitted $F_s(q_{max},t)$ to the Kohlrausch function having stretched exponent $(1\text{-}n) = 0.75$ and $\tau = 655$. This together with t_c of the binary L-J particles is about 1, and the CM equation, $\tau = [(t_c)^{-n}\tau_0]^{1/(1-n)}$,

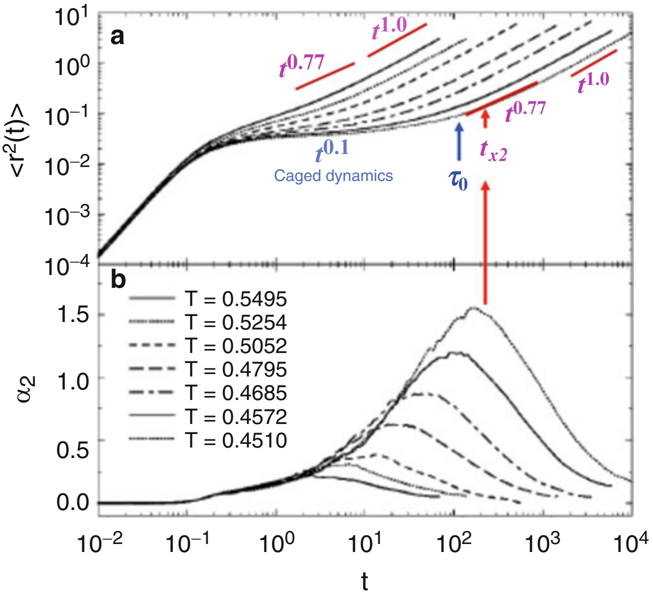

Fig. 4.69 (**a**) Mean square displacement $< r^2(t) >$ of the *A* particles vs time (L-J unit) for several values of *T*. For the definitions of the labels, *line* and *arrows* see text. (**b**) Non-Gaussian parameter $\alpha_2(t)$ vs time for the same values of *T* as in (**a**). Figure from Donati et al. [373] reproduced by permission

yields $\tau_0 \approx 129$. The maximum of $\alpha_2(t)$ occurs at about the same time as t_{x2}, the onset time of subdiffusion. On decreasing temperature, the term $< r^2(t) > \propto t^c$ persists to longer times, accompanied by decrease in both $< r^2(t) >$ and the exponent c reflecting increasing degree of caging.

The results from the MD simulations of the binary Lennard-Jones particles with the (12, 6) L-J potential shown and illustrated in Fig. 4.69 are similar in every respect to the dynamics of ions in the Li metasilicate glass shown in Figs. 4.56 and 4.57, as well as the colloidal particles from confocal microscopy in Fig. 4.55. Such similarity is clear evidence of universal dynamics of many-body interacting systems and evolution with time as described by the Coupling Model (CM). This implies that the understanding of the dynamics of ionic conductors can be directly transferred from that of the dynamics of the L-J systems given here as well as real glass-formers, and vice versa. It also explains why we give so much coverage to experimental data and simulations of molecular dynamics of glass-forming systems in a book on ionics.

Now we move on to see how the dynamics are modified on varying the L-J potential as done by Bordat et al. [389, 390]. The (12,11) L-J potential is more harmonic than the classical (12,6) LJ potential, while the (8,5) L-J potential is a flat well and the most anharmonic. Henceforth the (12,11), (12,6) and (8,5) potentials are referred to as Model I, II and III respectively, reminding us that anharmonicity is

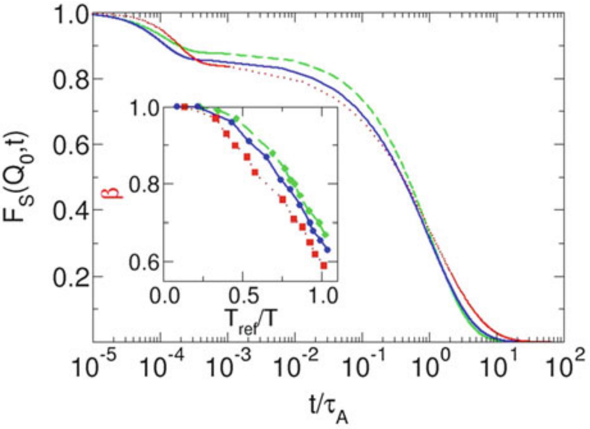

Fig. 4.70 $F_S(Q,t)$ versus scaled time t/τ_A, where τ_A is the relaxation time. *Dashed*, *continuous* and *dotted lines* are for Models I, II and III respectively. For all three models, $Q = 2\pi/r_0$ and $\tau_A(T_{ref}) =$ 46,435.8. The *inset* shows the stretch exponent $\beta = (1-n)$ as a function of the scaled reciprocal temperature T_{ref}/T for the three models. (*diamond*) Model I, (*circle*) Model II, (*square*) Model III

increasing in this order. By inspection of the shape of the potentials, one can also say that the particle is most tightly bound in Model I, lesser in Model II, and least in Model III. All models are composed of 1500 uncharged particles (1200 species *A* and 300 species *B*). Dynamics have been investigated by computing the self intermediate scattering functions $F_S(Q,t)$ of particles A at $Q = 2\pi/r_0$ for the three models. At high temperatures, $F_S(Q,t)$ decays linear exponentially to zero with a characteristic time of about 0.45 (L-J unit) close to the crossover time $t_c \approx 1$ to 2 ps of the coupling model (CM). When temperature is lowered, the dynamics slows down dramatically and a two-step process appears. Shown in Fig. 4.70 are $F_S(Q,t)$ versus t/τ_A of all three models for $Q = 2\pi/r_0$ at the reference temperature T_{ref} defined by $\tau_A(T_{ref}) = 46{,}435.8$, a very long time in our simulations and the analogue of T_g. The values of T_{ref} are 0.688, 0.431, and 0.263 for models I, II, and III, respectively.

From the relation, $F_S(Q,t) = \exp(-Q^2 < r^2(t)>$, the plateau in Fig. 4.70 correspond to the level of $< r^2(t) > = At^c$ with $c << 1$ or the NCL, $\chi''(\omega) = A_{\mathrm{NCL}}\omega^{-c}$, in the caged particles regime. The level of the plateau in $F_S(Q,t)$ is also called the nonergodicity parameter, $f(Q,T)$. Hence the magnitude of the NCL, A_{NCL}, or the level A of $< r^2(t) >$ in the caged particles regime is correlated with the reciprocal of $f(Q,T)$. From the $F_S(Q,t)$ at each of the lower temperatures, the relaxation time, $\tau_A(T)$, and the stretched exponent, $\beta(T)$, from the fit to the second step decay of $F_S(Q,t)$ by $f(Q,T)\exp[-(t/\tau_A)^\beta]$. These two parameters are plotted separately in the inset of Fig. 4.70 for β, and Fig. 4.71 for $\tau_A(T)$ as a function of the scaled reciprocal temperature T_{ref}/T for the three models. The results of interest are given as follows.

i. At any T_{ref}/T, the inset of Fig. 4.70 shows that $\beta = (1\text{-}n)$ is largest for model I and smallest for model III. At $T = T_{\mathrm{ref}}$, $\beta = 0.69$, 0.65 and 0.60 respectively for

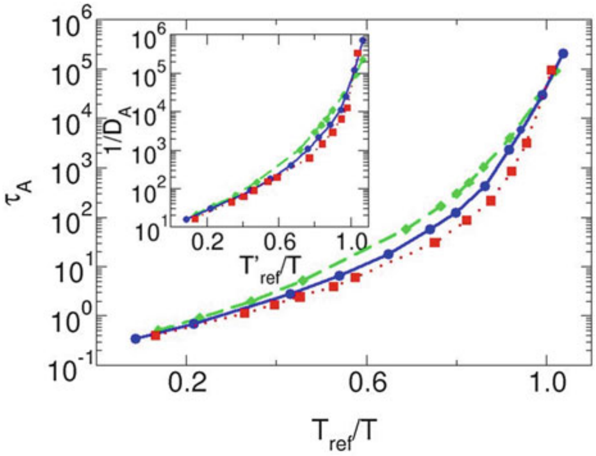

Fig. 4.71 The relaxation times τ_A obtained from $F_S(Q,t)$ for the three models as a function of T_{ref}/T where T_{ref} is defined as the temperature at which τ_A reaches 46,435.8. (*diamond*) Model I, (*circle*) Model II, (*square*) Model III. In the *inset*, the reciprocal of diffusivity D_A of A particles for the three models are given as a function of T'_{ref}/T. Here T'_{ref} is now defined as the temperature at which D_A is equal to 1.857×10^{-5}

models I, II and III. Thus, measured by $n=(1-\beta)$, the degree of non-exponentiality of the relaxation increases with anharmonicity or looseness of the potential. The same correlation between n and anharmonicity of intermolecular potential was found from dielectric relaxation data of molecular glass-formers by Paluch et al., Phys.Rev.Lett.116, 025702 (2016).

ii. The simulations found at some high temperature, $F_S(Q,t)$, decays exponentially to zero with a characteristic time of about 0.45. The fact that the primitive relaxation is observed at such temperature is because its relaxation time of 0.45 is shorter than $t_c \approx 1$ of the CM. Hence in Fig. 4.71, the relaxation times τ_A within the low T_{ref}/T-range, $0.1 < T_{ref}/T < 0.3$, are all primitive relaxation times with apparent primitive activation energy E_a. It can be seen that the slope of $\log\tau_A$ in this T_{ref}/T-range decreases slightly but monotonically in going from Model I to Model III. E_a is proportional to the product of the slope and T_{ref}. This trend of the slope together with the values 0.688, 0.431, and 0.263 of T_{ref} for models I, II, and III, respectively, leads to the result of larger decrease of E_a with anharmonicity or looseness of the potential. The slope of Model III is larger than Model I by a factor of 1.36 at $T_{ref}/T=1$. Notwithstanding, the product of the slope and T_{ref}, or E_a, is still smaller by a factor of 0.52 for Model III compared with Model I.

iii. We have shown that the reciprocal of $f(Q,T)$ is a measure of the magnitude of the NCL, $A_{NCL}\omega^{-c}$, or $<r^2(t)> = At^c$, with $c << 1$ in the caged particles regime. In Fig. 4.72, the results of $1/f(Q,T)$ from simulations are plotted against T/T_{ref} for the three models. The values of $1/f(Q,T)$ increase almost linearly with T/T_{ref} for all the three models, but the value of $1/f(Q,T)$ at the same T/T_{ref} and its

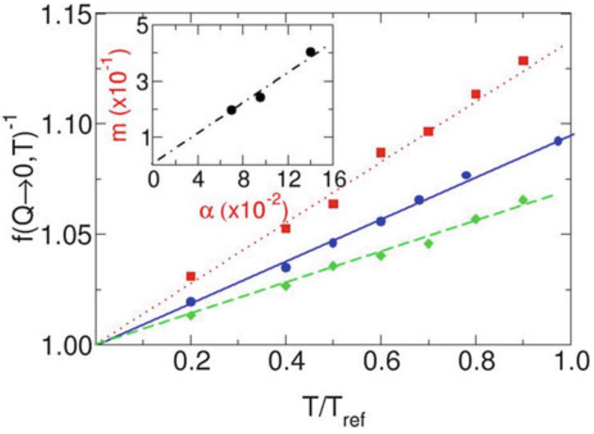

Fig. 4.72 1/*f*(*Q*,*T*) versus T/T_{ref} for the three models. (*diamond*) Model I, (*circle*) Model II, (*square*) Model III. 1/*f*(*Q*,*T*) is almost linear relative to T/T_{ref} with a slope noted α. The *inset* shows the correlation of the fragility m with α from the results of the three models

slope is largest for Model III, intermediate for Model II, and smallest for Model I. Considering that the values 0.688, 0.431, and 0.263 of T_{ref} for models I, II, and III, we can make the conclusion that 1/*f*(*Q*,*T*) of Model III is larger at a lower temperature than 1/*f*(*Q*,*T*) of Model II at a higher temperature, and even larger than 1/*f*(*Q*,*T*) of Model I at a even higher temperature. For example in Fig. 4.72 at $T/T_{ref} = 0.2$, which corresponds to $T = 0.0526$, 0.0862, and 0.137 for Model III, II, and I respectively, the value of 1/*f*(*Q*,*T*) is correspondingly 1.031, 1.0188, and 1.0125. From the monotonic increase of 1/*f*(*Q*,*T*) with temperature, if 1/*f*(*Q*,*T*) is compared at the same temperature, it is clear that 1/*f*(*Q*,*T*) is even larger for Model III than Model II, and much larger than Model I.

The inset shows the correlation of the fragility index *m* with the slope from the results of the three models. But since *m* correlates with $n = (1\text{-}\beta)$ for the three models, this is equivalent to correlation of *n* with the slope.

The results (*i*)-(*iii*) from the simulations of Bordat are all obtained by varying the anharmonicity of the potential and how tight the particle is bound by the potential. Therefore all correlations found originate from these two attributes of the potential, which can be summarized as follows. More harmonic (*anharmonic*) the potential and more (*less*) tightly bound the particle, larger (*smaller*) is the Kohlrausch exponent β and the primitive activation energy E_a, but smaller (*larger*) is the magnitude of the NCL or $< r^2(t) >$ of the caged particle dynamics. By not mentioning the potential at all, naturally the original correlations are reduced to the following corollaries or sub-correlations.

(1) Kohlrausch exponent β is correlated with the primitive activation energy E_a.
(2) The magnitude of the NCL or the level of $<r^2(t)>$ in the caged particle dynamics regime is correlated with E_a and β.

We have pointed out that Fig. 4.69 for the L-J particles is isomorphic to Figs. 4.56 and 4.57 from Li ions in the Li metasilicate glass, and to Fig. 4.55 for the colloidal particles. By the isomorphism, all the correlations originating from the potential as well as the corollaries (1) and (2) found in the L-J particles are directly transferrable to the dynamics of ionic conductors. In the context of ionic conductors, in fact corollary (1) is the correlation between β and the product $\beta E_\sigma = E_a$ established from data of many families of alkali oxide glasses [104] illustrated by Fig. 4.66, and from the family of $x(Na_2S) + (I\text{-}x)\ B_2S_3$ glasses in Fig. 4.67. Corollary (2) is the anti-correlation between A_{NCL} and E_a established from many ionic conductors in Table 4.4 and shown in Fig. 4.64. Notwithstanding, these two corollaries come from correlations (*i*)-(*iii*) all of which originate from the potential. Hence, ultimately the explanation of the corollaries is based on the anharmonicity or looseness of the potential, and it is theoretically consistent with the CM. More anharmonic the potential in the CM, more prominent is the chaos to slow down the many-ion relaxation and stretch it to longer times (i.e. smaller value of the Kohlrausch exponent β), as obtained from solution of models such as coupled arrays of oscillators (see Eq. 4.41), and the results presented in Fig. 4.23. It is also intuitively clear from the shapes of the potentials in Fig. 4.68 that more anharmonic the potential, lower is the energy barrier opposing an ion jumping to a neighboring site (i.e. smaller is E_a), and in the caged dynamics regime, the caged ions have larger amplitudes of fluctuation or larger $< r^2(t) >$ and larger nearly constant loss.

4.11 The Mixed Alkali Effect

It is frequently observed that the conductivity and physical properties of alkali oxide glasses vary in a extremely non-linear manner when the alkali ion is gradually replaced by a different one [200–203]. This is known as the “mixed-alkali effect” (MAE), and gives rise to pronounced changes in the expansion coefficient, viscosity, and in particular the electrical conductivity of mixed-alkali oxide glasses, which may decrease by several orders of magnitude when even a small amount of one kind of alkali (A) in a single alkali oxide glass is replaced by another kind (B). A similar decrease is observed if the roles of alkali ions A and B are exchanged, giving rise to a deep minimum in the conductivity of mixed alkali glasses at some intermediate composition. The MAE is exemplified in Fig. 4.73 by the composition dependence of the dc ionic conductivity for $0.2[xNa_2O \cdot (1-x)Rb_2O]{-}0.8B_2O_3$ mixed-alkali borate glasses with $x = 0.0$, 0.2, 0.4, 0.6, 0.8 after Imre et al. [393]. The dc conductivity of the sodium glass is about one order of magnitude higher than that of the rubidium borate glass. The dc conductivity shows a minimum near $x = 0.4$ where its value is around two orders of magnitude lower than the conductivity of the pure sodium borate glass. As often found in other mixed-alkali glasses, it can be observed that the minimum becomes deeper with decreasing temperature. This is related to a maximum occurring in the activation energy of the dc conductivity as one alkali ion is replaced by the other one. The lower panel shows tracer diffusion coefficients of ^{22}Na and ^{86}Rb at 653 K in the same sodium-rubidium borate glasses. The ^{22}Na-diffusion in the single-alkali sodium borate glass is about four orders of magnitude faster than that of ^{86}Rb present in low concentration. In the rubidium

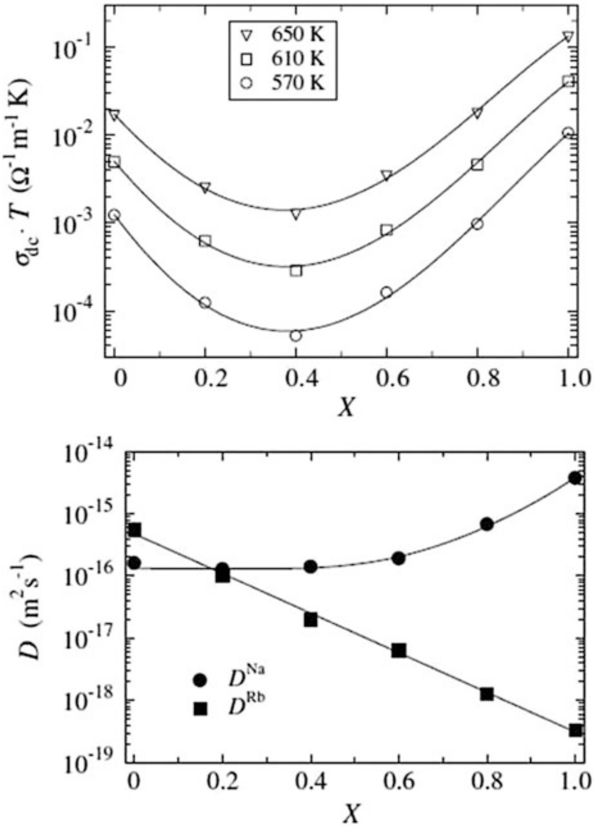

Fig. 4.73 (*Upper panel*) Composition dependence of the ionic conductivity for $0.2[x\mathrm{Na_2O} \cdot (1\text{-}x)\mathrm{Rb_2O}]$ $0.8\mathrm{B_2O_3}$ glasses at three different temperatures. (*Lower panel*) Composition dependence of the tracer diffusion coefficients of ^{22}Na and ^{86}Rb at 653 K in these glasses at 653 K. Reproduced from Ref. [393] by permission

borate glass the diffusivity of ^{86}Rb is larger than the diffusivity of ^{22}Na, even though the sodium ion is smaller than the rubidium ion. It is thus found in general that the self-diffusion coefficient of the alkali ion in the single-alkali glass is higher than the impurity-alkali diffusion coefficient [393]. Similar results for the composition dependence of ^{22}Na and ^{137}Cs tracer diffusion coefficients in sodium-cesium silicate glasses had been obtained by Jain et al. [394]. These changes in the diffusion coefficients are due to changes in the activation energies of the diffusivities of both species, A and B, upon mixing. The MAE occurs in all alkali ion conducting glasses and has been also reported in fluoride glasses [395] and even in crystalline ionic conductors such as alkali β-alumina [396–398]. The origin of the MAE in crystals and glasses might be similar, related to the fact that A and B ions have a different interaction with their local environment.

Several studies have shown that the local environments of the two different alkali ions in mixed alkali glasses are different by using X-ray absorption fine structure (XAFS) spectroscopy [399–401], spin echo double-resonance NMR spectroscopy [402, 403], neutron diffraction and Raman spectroscopy [404], or infrared spectroscopy [405]. These studies have revealed that alkali ions retain more or less the same local environment as in the respective single alkali glasses, and they are randomly distributed in the glass structure. Consequently, jumps of a given alkali ion to the sites of a different alkali ion cannot occur due to the large difference between the site energies for the two alkali ions [155, 216, 217, 408]. By molecular dynamics simulations of lithium-potassium metasilicate $(Li,K)_2SiO_3$ glass, Habasaki et al. [155, 156] clearly shows from the van Hove function (distinct part) that interception of the jump path among the unlike alkali ion sites occurs in the mixed alkali glass. The effect has been confirmed to be caused by the size differences of lithium and potassium ions. The cause for the interception leading to the mixed alkali effect has been studied in terms of the potential surfaces, and from which a site mismatch between the unlike ions is found with respect to the potential energies. Balasubramanian and Rao [406, 407] have shown similar MD results in $35(x\mathrm{Li_2O}(1\text{-}x)\mathrm{K_2O})\text{-}65\mathrm{SiO_2}$, glasses. More refined simulations by Habasaki et al. [64] subsequently show the number of fast ions, facilitated by cooperative jumps, decreases considerably when small amount of Li ions are frozen. Consequently there is a large overall reduction of the mobility of the Li ions. The result is also in accordance with the experimental finding in mixed alkali silicate glasses that the most dramatic reduction of ionic conductivity occurs in the dilute foreign alkali limit [409]. The effect found by simulations was described as ‘cooperativity blockage’. We shall defer presentations of the comprehensive results from simulation of Habasaki and coworkers, including the visualization of paths, to a chapter on studies of MAE using Molecular Dynamics Simulations (Chap. 10).

Reverse Monte Carlo modeling with the bond-valence method of mixed lithium-rubidium phosphate ($\mathrm{Li}_x\mathrm{Rb}_{1-x}\mathrm{PO}_3$) glasses have also found that ions of one kind tend to block the pathways for the other kind of ions and vice versa [410] and can explain the observed MAE in the experimental ionic conductivity data [411] (see Fig. 4.74). This blocking would be highly effective due to the low dimensionality of the conduction pathways.

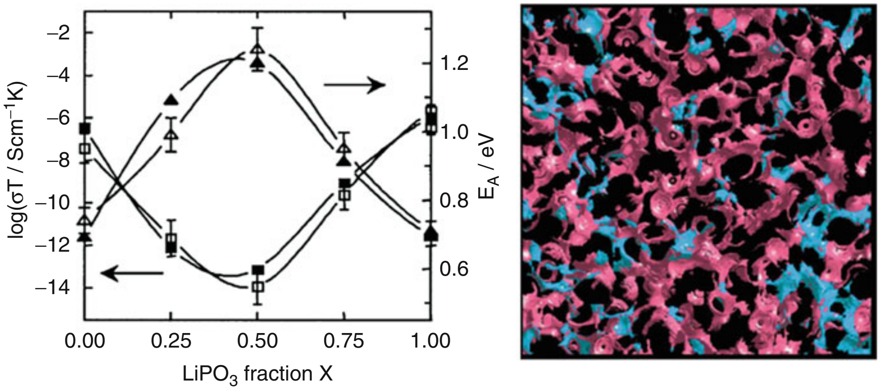

Fig. 4.74 (*Left panel*) Composition dependence of the dc conductivity and its activation energy for the glass system $\mathrm{Li}_x\mathrm{Rb}_{1-x}\mathrm{PO}_3$ at 300 K. *Open squares* are experimental data points by Karlsson et al. [411], and *filled squares* correspond to the values predicted from the pathway volume fractions of the structural models by Swenson et al. [410]. The *solid lines* are a guide to the eye. (*Right panel*) A thick slices through the Li conduction pathways in $\mathrm{Li}_{0.5}\mathrm{Rb}_{0.5}\mathrm{PO}_3$ (*blue*) and those regions that are blocked by Rb ions but otherwise would have a matching bond valence and therefore been conduction pathways for the Li ions (*pink*). Reproduced from [410] by permission

However, the microscopic mechanisms giving rise to the MAE are not generally agreed by various researchers. Theoretical model was proposed by Bunde and coworkers [412, 413]. This is a development of their dynamic structure model. Based on the results of EXAFS experiments [399], they included a site memory effect which introduces vacancies appropriate to each kind of mobile ion, and a mismatch energy which emerges whenever an ion attempts to enter a different kind of site. The dynamic structure model helped to elucidate some facets of the MAE but not all. Another theoretical development was achieved by Hunt [126], who suggested that the diffusion paths may be associated with a random energy landscape in the glass with the lower energy states for different types of ions located at different sites, and could identify the distinct diffusion paths. Further progress in a theory of the MAE was developed by Maass and coworkers [110] by taking the Coulomb interaction between the mobile ions into account. Greaves and Ngai [12] recognized the importance of taking into account the interaction among mobile ions and developed an empirical approach in order to explain the MAE by ascribing it to changes in alkali-alkali distances that lead to variations in Coulomb barriers for single ion jumps in an Anderson-Stuart like ansatz for the activation energies [120]. There is experimental evidence of the importance of the average distance between like alkali ions in determining the strength of the MAE and in particular the increase of the activation energy of ionic conductivity upon mixing [414]. According to them, mixing alkali ions in the glass results in a decrease of the concentration of mobile alkali ions of each kind (compared to the single alkali glass) and thus in an increase in the average distance between similar ions, which results in diminishing ion-ion interaction and correlation. Thus the MAE can be qualitatively understood by its similarity to the effect of decreasing the alkali ion concentration of a single alkali glass, which is well known to result in an increase of the activation energy of conductivity due to lower level of cooperativity between ions [1, 104]. In fact, molecular dynamics simulations by Habasaki et al. have shown such a reduction of cooperativity in the dynamics of mobile ions due to the presence of immobile ions of another kind [64]. More recently, Maass et al. [415] have shown that a small fraction of vacant sites in the glassy network might be also relevant in originating the anomalies in ionic transport associated with the mixed alkali effect. These authors proposed a trapping of vacancies to explain the vulnerability of the mobility of the majority ion at the beginning of replacement, and that short-range correlations between the site energies might give rise to such trapping effect.

A ubiquitous feature of the MAE is that the most rapid change of the dc conductivity, σ_{dc}, upon replacement of the majority ions occurs in the dilute limit of the foreign alkali region (see upper panel of Fig. 4.73). The derivative, $(\partial \log \sigma_{dc} / \partial x)$, with x the fraction of the majority ions, is an appropriate measure of how rapid the conductivity changes upon increasing the fraction $(1-x)$ of the minority ions. The rapid decrease in σ_{dc} by replacement of the host alkali ions by just a small amount of foreign alkali ions indicates that the introduction of a single foreign alkali ion largely decrease the mobility of many host ions. In 1980, Moynihan et al. [409] reported a study of the MAE in silicate glasses of composition $0.242[xK_2O+(1-x)Na_2O]-0.758SiO_2$ in the dilute sodium ion composition range ($x = 0.9$ to 1), and they found that the decrease in ionic conductivity when the majority alkali K^+ is replaced with the foreign alkali Na^+ is most rapid in the very dilute range $x = 0.98$ to 1 and becomes less rapid at larger Na^+ contents. They attempted to account for the decrease in conductivity by assuming that the foreign alkali complexes with and immobilizes the majority alkali, but concluded that calculated values of the number of majority alkali ions complexed by a single foreign-alkali ion were unreasonably large. It was difficult at that time for Moynihan et al. to understand how a single foreign alkali can immobilize as many as 50 host alkali ions. However, recent NMR chemical shift measurements of mixed alkali glasses by Eckert [228], and molecular dynamics simulations by Habasaki et al. [64], have confirmed that indeed many host alkali ions are affected by every single foreign ion. Thus, it appears to be true that a single foreign alkali ion can immobilize a large number of host alkali ions. This is an important experimental fact since some current models of the MAE do not predict a large number of host ions being immobilized by a single foreign ion in the dilute foreign alkali region. An explanation of largest value of $(\partial \log \sigma_{dc} / \partial x)$ at the dilute limit of the foreign alkali region was provided by Ngai et al. [109] by drawing the analogy to the simulation results of mobile particles confined by walls formed by immobile particles [416–418]. In the simulation all immobile and mobile particles interact with each other by the same Lennard-Jones potential, and the effects of immobile particles on the mobile particles are obtained. It is found that the particles in the layer closest to the wall have their relaxation time increased by orders of magnitude. This is due to interaction between the particles in the dead wall and the particles in first layer, can be explained by the CM from large increase of the coupling parameter. Although different in configuration and system the effect is similar to the large increase of relaxation time and T_g of the fast component when mixed with a slow component in binary mixtures of two glass-formers, and the explanation is again the increase of the coupling parameter [419]. The huge slowing down of the particles by the neighboring immobile particles does not stop at the first layer at the interface, and the effect of the immobilized particles in the first layer is passed on to the second layer and so on, albeit the effect is attenuated with distance from the wall. Thus a number of layers are effectively immobilized. If this result from Lennard-Jones liquid can be applied to a mixed alkali glass in the dilute foreign alkali limit, we are led to conclude that not just the nearest-neighbor host alkali ions will be severely immobilized by the foreign alkali ion, but also second nearest-neighbor host alkali ions will also be immobilized although to a lesser extent, and so on. The immobilizing effect propagates and dies off with distance away from the foreign alkali ion. It is now conceivable in the glasses of composition $0.242[xK_2O+(1\text{-}x)Na_2O]\text{-}0.758SiO_2$ studied by Moynihan et al. [409] in the dilute Na^+ ion composition range that an Na^+ ion can effectively immobilize as many as 48 K^+ ions. Furthermore, the temperature dependence of the dynamics of L-J particles confined by walls made of immobile L-J particles show that the observed degree of immobilization increases rapidly with decreasing temperature (see inset to Fig. 4.75). Again applying this result to the mixed alkali effect, the observed increase of

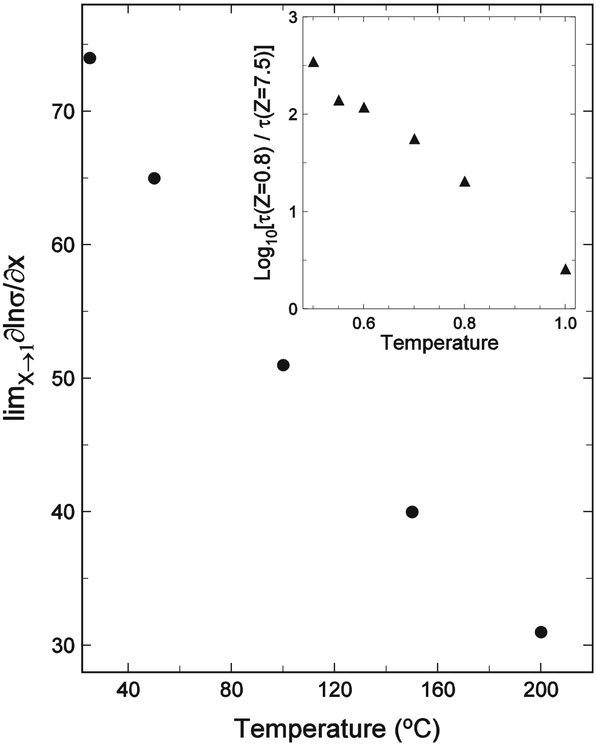

Fig. 4.75 Temperature dependence of the limiting slopes, $\lim_{x\to1}(\partial \ln\sigma_{dc}/\partial x)$, of dc conductivity vs x isotherms obtained for $0.242[x\mathrm{K_2O}+(1\text{-}x)\mathrm{Na_2O}]\text{-}0.758\mathrm{SiO_2}$ glasses by Moynihan et al. [409] in the dilute sodium ion composition range. As explained in the text, this slope is an indication of how many host potassium ions are immobilized by a single foreign sodium ion, and is a decreasing function of temperature. The *inset* shows ratio of the relaxation time $\tau(z=0.8)$ of particles in the L-J liquid located at $z=0.8$ close to the frozen L-J glass forming the wall to $\tau(z=7.5)$ far from the wall as obtained from data of molecular dynamics simulation result of Schneider et al. [416]. This ratio, an indication of the extent of the immobilization of particles in the L-J liquid, is also a decreasing function of temperature like $\lim_{x\to1}(\partial \ln\sigma_{dc}/\partial x)$in the main figure. Reproduced from [417] by permission

$\lim_{x\to1}(\partial \log\sigma_{dc}/\partial x)$ on decreasing temperature found by Moynihan et al. (see Fig. 4.75) can be rationalized by similar explanation as given before for the effect found in confined L-J liquid [417, 418].

4.11.1 Immobilization of Li Ions by Frozen Li Ions in the Confining Walls

The immobilization of more mobile ions by less mobile ions in the MA effect has been rationalized by analogy to similar effect found in L-J particles confined by frozen L-J particles forming the walls. To demonstrate the physics of two systems

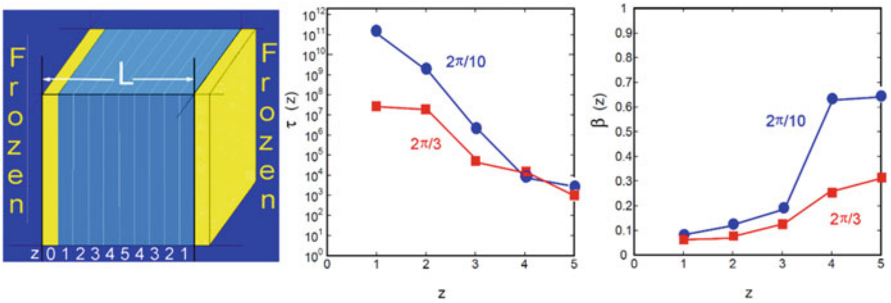

Fig. 4.76 (*Left*) Li metasilicate glass confined by two walls of the same Li metasilicate glass except the Li ions therein are frozen. (*Middle*) Plot of $\tau(z)$ against z for the stretched exponential region of $F_s(k,t)$ of Li ions in Li_2SiO_3 glass (in ps). *Filled circle*: $k = 2\pi/10$, *filled square*: $k = 2\pi/3$. (*Right*) $\beta(z)$ against z for the stretched exponential region of $F_s(k,t)$ of Li ions. *Filled circle*: $k = 2\pi/10$, *filled square*: $k = 2\pi/3$. (The values of $\beta(z)$ in the $z = 5$ region are close to the values for the bulk Li_2SiO_3, which are $\beta = 0.67$ and 0.32 for $k = 2\pi/10$ and $k = 2\pi/3$, respectively. Data from Ref. [64] are replotted in all figures here

closer, a molecular dynamics simulations was made on the dynamics of Li ions in Li_2SiO_3 glass confined by parallel walls formed by the same glass except the Li ions therein were frozen but still interacting with the Li ion in the confined Li_2SiO_3 glass [64]. The geometry of the systems is illustrated in the left panel of Fig. 4.76. The self-part of the density-density correlation function, $F_s(k,t;\, z)$ were obtained at any distance z from the wall for Li ions located at $z \leq 0$. The unit of z is $L/10$, where L is the side length of the basic cell of the simulation. The $F_s(k,t;\, z)$ obtained has the Kohlrausch stretched exponential time dependence, $\exp[-(t/\tau(k;z))^{\beta(k;z)}]$. The frozen Li ions in the walls cause slowing down of Li ion as seen by in the increase of $\tau(k;z)$ in the middle panel of Fig. 4.76, and the concomitant increase in stretching of $F_s(k,t;\, z)$ as seen by the decrease of $\beta(k;z)$ in the right panel for two chosen values of $k = 2\pi/10$ and $2\pi/3$. The effect is largest for the Li ions closest to the wall and decreases monotonically with distance from the wall. The values of $\tau(k;z)$ for Li ions residing in the innermost $z = 5$ region are close to those for the unmodified bulk Li_2SiO_3 glass, which are $\tau(k) = 1292$ ps for $k = 2\pi/10$ and 340 ps for $k = 2\pi/3$. Values of $\beta(k;z)$ in the innermost $z = 5$ region are also close to those for the unmodified bulk system, which are $\beta(k) = 0.67$ for $k = 2\pi/10$ and 0.32 $k = 2\pi/3$. The changes in the dynamics of Li ions interacting with the frozen Li ions in the confining walls are exact analogues of the L-J particles confined by frozen L-J particles in the confining walls obtained by Scheidler et al. [416], and the results explained by the CM in [417]. This becomes obvious when comparing the dependence of $\tau(k;z)$ and $\beta(k;z)$ on distance from the wall in Fig. 4.76 with those of the same quantities for the confined L-J particles in Ref. [416, 417].

The above discussion highlights the importance of ion-ion interaction in explaining the MAE. Therefore, models of ion dynamics of single alkali glasses without taking ion-ion interaction seriously will not be able to make any significant advance in understanding the MAE.

In glasses with low alkali content there is a negligible effect of ion–ion interaction on the dynamics of ion transport. A natural consequence is that the strength of the MAE should decrease on lowering the total alkali concentration in the glass (i.e. increasing the average ion-ion separation distance in the single alkali glass). This is confirmed by the experimental results by Tomozawa and coworkers [420, 421] in mixed alkali germanate glasses of composition 0.019[xK$_2$O+(1-x) Na$_2$O]-99.981GeO$_2$ with an extremely low (0.019 mol%) total alkali content. By the way, the nearly Debye-like dynamics of the single alkali germanate glass containing 0.0079 mol% Na$_2$O from Cordaro and Tomozawa [73] has been shown before in connection with the subject matter of Fig. 4.12, Th results of the mixed alkali germinate glass show that at 350 °C the logσ_{dc} vs. x plot does not exhibit the minimum associated with the MAE. After mixing the alkalis, the ions remain far apart and ion-ion interaction is negligible as supported by the normal semicircular trace of the data in a plot of Z'' vs. Z'. Hence there is no effect analogous to 'immobilization' of one kind of alkali ions by another kind.

This trend of decreasing magnitude of the MAE on increasing separation of the ions was verified by Voss et al. [414] in various series of Na–Rb alumino-germanate glasses and Na–Rb borate glasses that allow exploring a wide range of the value of $< d_{ion} >/< d_{network} >$, the ratio between the average Na–Na distance to the average separation between the network–former atoms. They defined a strength of the mixed alkali effect as the relative difference between the measured activation energy of the dc conductivity at a given (mixed alkali) composition and the activation energy one would expect for a linear interpolation between the activation enthalpies of the end-member (single alkali) compositions. Figure 4.77 shows that the strength of the mixed-alkali effect, Δ_{MAE}, decreases as a function of $< d_{ion} >/< d_{network} >$.

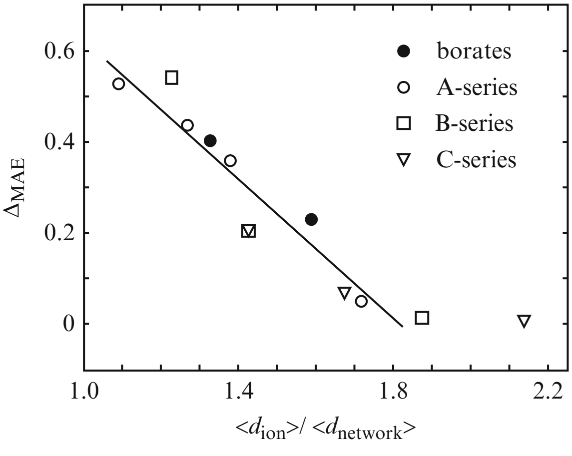

Fig. 4.77 Strength of the mixed-alkali effect, Δ_{MAE}, as a function of the ratio between the average Na–Na distance to the average separation between the network–former atoms, $< d_{ion} >/< d_{network} >$. *Open symbols* represent Na–Rb alumino-germanate glasses, whereas the two *filled circles* refer to Na–Rb borate glasses, respectively. Reproduced from Ref. [414] by permissiont

Besides the changes in the activation energies and isothermal dc conductivity associated to the MAE, several works have reported deviations in the ac conductivity spectra of mixed alkali glasses from the typical behavior of single alkali glasses. These deviations were first pointed out by Macedo et al. [234] and by Tomozawa et al. [233, 235]. Macedo and coworkers [422] studied the electrical conductivity relaxation of $0.5Na_2O \cdot 0.5K_2O \cdot 3SiO_2$ glass compared to that of the single alkali $Na_2O \cdot 3SiO_2$ glass, and found that the shapes of the electric modulus spectra for the single alkali and mixed alkali glasses differ significantly, and at all temperatures the distribution of conductivity relaxation times for the mixed alkali glass was narrower than that for the single alkali glass, i.e., they measured narrower peaks in the imaginary part of the electric modulus for the mixed alkali glass. Tomozawa and coworkers [423] found that the permittivity and impedance spectra of $Li_2O \cdot 2SiO_2$ and $[0.5Na_2O \cdot 0.5LiO_2] \cdot 2SiO_2$ glasses are remarkably different at low frequencies. It is well known that in these representations of the experimental data, and contrary to the case of the electric modulus representation, the low frequency contributions from the less mobile (or immobile) ions are emphasized [1, 5, 6, 17, 30], and the presence of immobile or less mobile ions in the mixed alkali glass can explain these differences observed. Roling et al. [424] have also reported electrical conductivity data for several mixed alkali borate and aluminosilicate glasses, and found that in mixed alkali glasses the crossover from dc to dispersive conductivity extends over a broader frequency range than in single alkali glasses. In that work the authors suggest that the difference observed might be in fact a fingerprint of faster and slower ions and due to an incomplete decoupling between the diffusion of both kinds of ions in the glass. More recently, Cramer et al. [141] have also reported these differences in the conductivity spectra of $0.3[xLi_2O \cdot (1\text{-}x)Na_2O] \cdot 0.7B_2O_3$ glasses, showing that the data for different compositions do not obey the time-temperature superposition principle (see Fig. 4.78), and suggest it might be due to differently activated mobilities of the two different ionic species. Cramer et al. [425] have also reported for the same borate glasses slight differences in the conductivity values at very high frequencies, close to the THz regime, where the conductivity shows linear and super linear frequency dependence. Since in their opinion these contributions to the dynamic conductivity would not result from ion hopping movements, they concluded their results show a new mixed alkali effect. However, they stressed that it is not clear the effect of the network contributions to the conductivity at such high frequencies, and that further studies on different kinds on glass systems with varying network modifier content would be necessary to prove their interpretation. It is worthwhile to remark that this claim by Cramer et al. might be at odds with the previous finding by Jain et al. [368] in sodium-rubidium germanate glasses that the MAE is essentially absent at enough high frequencies and low temperatures, consistent with the fact that the MAE arises from the long range motion of ions. It has been also reported that the static dielectric constant, ε_s, and thus the dielectric relaxation strength, $(\varepsilon_s\text{-}\varepsilon_\infty)$, of the mixed alkali glass is much higher than that of the corresponding single alkali glass [424, 426]. This result actually suggests that, in addition to the relaxation from mobile ions, there is an additional relaxation process contributing to the dielectric

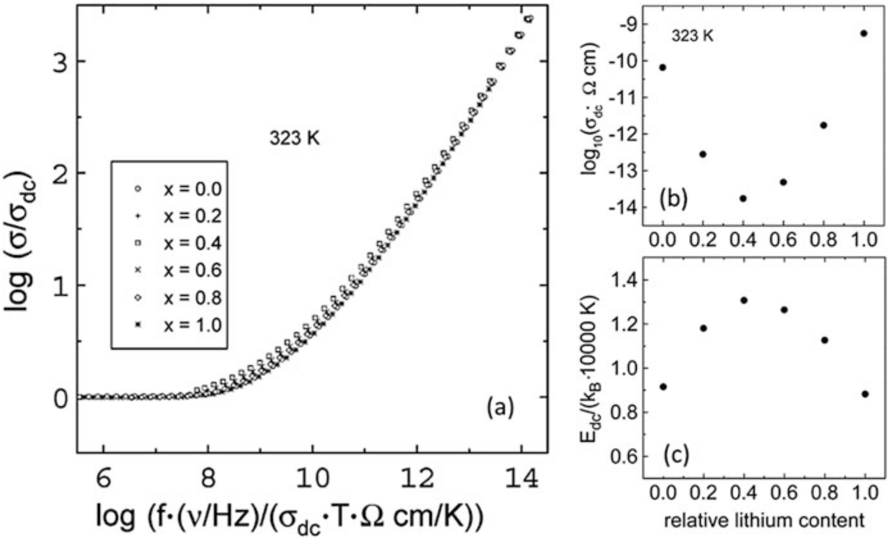

Fig. 4.78 (**a**) Scaled conductivity spectra of $0.3[xLi_2O \cdot (1\text{-}x)Na_2O] \cdot 0.7B_2O_3$ glasses at 323 K. Besides the Summerfield scaling, an additional scaling factor f (close to unity for all compositions) is used in the scaling plot to make the spectra coincide at high frequencies. (**b**) Composition dependence of the dc conductivity of $0.3[xLi_2O \cdot (1\text{-}x)Na_2O] \cdot 0.7B_2O_3$ glasses at 323 K. (**c**) Activation energy of the dc conductivity for the same glasses as a function of the lithium content x. Reproduced from Ref. [141] by permission

permittivity at low frequencies in the case of mixed alkali glasses. Tomozawa et al. [421, 423] showed that this additional relaxation was responsible for the large value of the dielectric permittivity at low frequencies in mixed alkali glasses and corresponded to a large polarization contributed by ions of low mobility, which are the alkali ions immobilized to various degrees in the neighborhoods of the other kind alkali ions as discussed in the above. These experimental facts can thus be taken as additional evidence of the immobilization of ions in mixed alkali glasses due to the MAE (Fig. 4.78).

In SA glasses all ions are equivalent and mobile, at least before the details of the evolution of the heterogeneous dynamics with time are considered, and their dynamics are well suited for the application of the coupling model. On the other hand, in MA glasses there is the coexistence of immobile, and more mobile ions. This possibility we have seen in the dilute foreign-alkali case and can be expected to be the case for all MA compositions. In the framework of the Coupling Model, for the most mobile ions of one alkali species there is reason to expect the Kohlrausch function may still be applicable in describing their correlated dynamics originating from their mutual interactions, although the complication now due to the presence of less mobile ions may make this only an approximation. However, the electric modulus representation is known to suppress low frequency contributions, not only from the electrode polarization, but also from the less mobile and the immobile ions in the MA glasses. Such suppression in effect makes the Kohlrausch fits to $M^*(f)$ data of MA glasses practical because only the mobile ions contribute to $M^*(f)$. The story is different, however, when the same MA data are shown in the $\varepsilon^*(f)$ or the complex impedance Z^* vs. log$f$ representation [423]. In these representations of the data, the low frequency contributions from less mobile and immobile ions are not deemphasized and show up prominently as large deviations from the prediction of the Kohlrausch relaxation fit to $M^*(f)$ at low frequencies well below the frequency maximum in the M'' vs. log f plot. The large deviations from Kohlrausch relaxation were first seen in the complex impedance plots of Z'' vs. Z' of MA glasses and later at lower frequencies in $\varepsilon'(f)$, the real part of $\varepsilon^*(f)$. Whereas Z'' vs. Z' plots of actual data for the single alkali glasses or Z'' vs. Z' curves predicted by the Kohlrausch fit to the SA glass electric modulus data display approximately the shape of a submerged semicircle, the data for MA glasses show large deviations from this shape. This deviation was pointed out by Moynihan and Boesch [427] and by Tomozawa and coworkers [421]. Tomozawa and coworkers further showed enormous differences between SA and MA glasses in $\varepsilon'(f)$ and $Z^*(f)$ at low frequencies by comparing the data of Li_2O-$2SiO_2$ and $[0.5Na_2O + 0.5LiO_2]$-$2SiO_2$ glasses. The dielectric relaxation strength, $(\varepsilon_s - \varepsilon_\infty)$, of the MA glass is much higher than that of the SA glass, due to the presence of an additional relaxation contribution in MA glasses contributed by ions of the alkali ions immobilized at lower frequencies.

Therefore, when shown as $\varepsilon'(f)$ vs. log f, the data of MA glasses support the presence of contributions to polarization from immobilized or partially immobilized alkali ions that are not accounted for by the Kohlrausch relaxation describing the dynamics of mobile ions. The reason why the Kohlrausch relaxation still gives acceptable, though approximate, fits to $M^*(f)$ data of MA glasses, as found by many workers (see references given in [109]), is the known suppression by the electric modulus of any low frequency polarizations, including those from the immobilized or partially immobilized ions. In effect, by showing the data as $M^*(f)$ one has selected only the faster dielectric response of the mobile ions in the MA glass. For these mobile ions, the description using the Kohlrausch relaxation is justified from the Coupling Model point of view. Unlike the case of SA glasses, there could still be deviations caused by the inherent presence of some distribution of mobility of the mobile ions or by mobile alkali ions of both kinds with comparable mobility in some compositions contributing to $M^*(f)$. The number of these mobile ions in a high alkali MA glass is significantly fewer than the total number of alkali ions because of the large number of ions that have been immobilized, as discussed earlier in Sect. 4.11. Structural studies of mixed alkali glasses [399, 400, 428–431] indicate that each kind of alkali ion maintains its characteristic local environment independent of the MA glass composition. The large difference in site energies of two alkalis excludes the use of sites of one kind of alkali ion by another, rendering effectively fewer sites available for conduction. Considering these factors in the comparison with SA glasses with same total alkali concentration, we see now in the MA glasses there are significantly fewer mobile ions, and on the average they are further apart. The situation suggests that the transport of mobile ions in the MA glass resembles a SA glass with reduced alkali concentration, which we know has a lower conductivity at the same temperature and a higher activation enthalpy, and these are exactly the changes when modifying a SA glass to a MA glass [409]. Thus the MA effect when considered in terms of the change in activation enthalpy and isothermal conductivity can be qualitatively understood by its similarity to the effect of decreasing the alkali ion concentration of a SA glass, a suggestion that was made earlier by Greaves and Ngai [12]. A concomitant consequence of the larger separation between the mobile ions is the reduction of ion-ion interaction and correlation. In the Coupling Model, this means that the coupling parameter n of the mobile ions is reduced, the Kohlrausch exponent is increased and the dispersion of $M^*(f)$ narrows as the MA effect increases. This narrowing of the dispersion is countered by the broadening due to the inevitable presence of some inherent distribution of mobility of even for the mobile ions. Thus, if experimentally there is indeed a narrowing of $M^*(f)$ with increasing MA effect, then the actual narrowing due to decreasing mobile ion interactions is dominating the data. From a survey of the published literature on MA glasses with high concentrations of alkali ions, we find that, in general, whenever the data is represented by the electric modulus, the dispersion of $M^*(f)$ narrows when more and more majority alkali ions are replaced by the minority alkali ions and exhibits a minimum width at some intermediate composition. When the $M^*(f)$ data are fitted to the Fourier transform of the Kohlrausch function, the Kohlrausch exponent $\beta \equiv (1\text{-}n)$ also displays an increase towards a maximum at some intermediate composition [12, 87, 409, 421, 422, 432–435]. The experimental observation is exemplified in Fig. 4.79 by the electric modulus data of the alkali silicate glasses $[x\mathrm{K_2O} \cdot (1\text{-}x)\mathrm{Na_2O}] \cdot 3\mathrm{SiO_2}$. The experimental data show that the KWW exponent β increases, or the dispersion narrows, with increasing amounts of foreign alkali in the dilute foreign-alkali region, leading to a maximum in β at an intermediate composition close to the

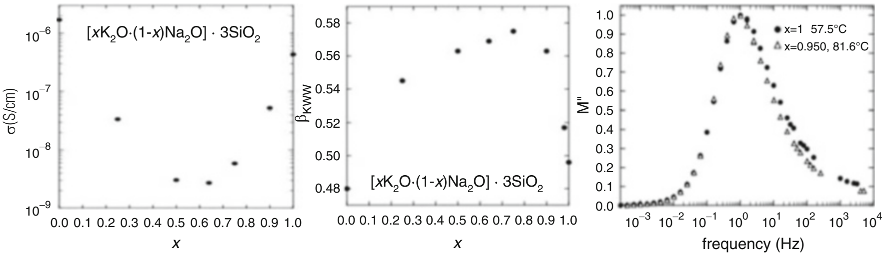

Fig. 4.79 (*Left*) Composition dependence of the d.c. conductivity for the alkali silicate glasses $[x\mathrm{K_2O} \cdot (1\text{-}x)\mathrm{Na_2O}] \cdot 3\mathrm{SiO_2}$. Data taken from Ref. [436] and re-plotted. (*Middle*) Value of the KWW exponent β obtained from fits to the electric modulus data by using the KWW function for the same glasses. Here β for all x have been obtained from electric modulus data that have similar values of the relaxation time τ ($\tau \approx 3 \times 10^{-3}$s within a factor of 2). The data show that β increases or the dispersion narrows with increasing amounts of foreign Na in the dilute foreign Na region, leading to a maximum in β at an intermediate composition. Data taken from Ref. [436] and re-plotted. (*Right*) Electric modulus spectra of the mixed alkali silicate glass $0.242[x\mathrm{K_2O} \cdot (1\text{-}x)\mathrm{Na_2O}] \cdot 0.758\mathrm{SiO_2}$ with $x = 0.950$, in the dilute $\mathrm{Na^+}$ ion composition range compared with the parent single alkali glass ($x = 1$) studied by Moynihan et al. [409]

minimum of d.c. conductivity. The right panel of Fig. 4.79 shows the narrower peak in the imaginary part of the electric modulus data of the mixed alkali glass (0.242[xK$_2$O · (1-x)Na$_2$O] · 0.758SiO$_2$ with $x = 0.950$, in the dilute sodium ion composition range compared with the parent single alkali glass with $x = 1$ studied by Moynihan et al. [409]. The same was found in mixed alkali Li$_x$Rb$_{1-x}$PO$_3$ glasses by Karlsson et al. [411, 435], and they also interpreted this result as indicating that the mixed alkali glasses behave as single alkali glasses of effectively lower concentrations. The observed decrease in the width of the relaxation spectra of the electric modulus in mixed alkali glasses can be considered as evidence for the reduced ion-ion interaction due to fewer mobile ions and wider separations between them [12], as mentioned before in this section.

4.11.2 Comparison of Electrical Relaxation with Mechanical Relaxation

Mechanical-relaxation (internal friction as a function of temperature at a fixed frequency) measurements on mixed alkai silicate, borate and phosphate glasses performed by many workers was reviewed by Day [437]. They show the same behavior as foreign alkali B is introduced into a single alkali A glass. On increasing the content of B, the internal friction peak associated with host A is rapidly reduced in intensity and shifted to higher temperatures. This trend indicate that it comes from diffusion of the mobile host ions. It is also in agreement with the reduction of electrode modulus loss and the increase of activation energy of diffusion of A, and consistent with the large number of A immobilized by B.

Simultaneously, starting at low concentration of B a new internal friction peak appears at higher temperatures, which rapidly increase in intensity. The new peak was called the “mixed alkali peak”, not found in the electric modulus spectrum. The origin of this mixed alkali peak comes the elastic dipoles formed by the immobilized A and B alkali ions. Again this is consistent with the interpretation given before on mixed alkali effect probed by electrical relaxation.

4.12 Haven Ratio, Breakdown of Nernst-Einstein Relation

The breakdown of the Stoke-Einstein relation in molecular glassformers has been considered to be one of the important and general characteristics by the glass transition research community. An analogue of this anomaly in glassforming systems can be found in glassy and crystalline ionic conductors by the fact that the self (tracer) diffusion coefficient, D^*, and the conductivity diffusion coefficient, D_σ, are not the same. In glassy single-alkali ionic conductors, D^* is measured by tracer diffusion of an radioactive isotope of the same alkali, and D_σ is calculated from the measured dc conductivity, σ_{dc}, via the Nernst–Einstein relation,

$\sigma_{\mathrm{dc}} = (Nq^2/k_BT)D_\sigma$ between conductivity and diffusion coefficient that holds for non-interacting systems. Here N is the number density of alkali ions, q the ion charge, k_B the Boltzmann constant, and T the temperature. The experimental fact that D^* is larger than D_σ in many glassy ionic conductors with large concentration of mobile alkali ions is evidence of breakdown of the Nernst-Einstein relation, which should be $\sigma_{\mathrm{dc}} = (Nq^2/k_BT)D^*$. The degree of breakdown is usually indicated by the Haven ratio, $H_R = D^*/D_\sigma$, which has values less than or equal to one [438]. The smaller H_R is, the larger is the breakdown. Since ion-ion interaction and many-ion dynamics have been identified as important in glassy and crystalline ionic conductors containing high concentration of mobile ions, it is natural to consider it as the cause of the breakdown. Simulation of Li ions motion in lithium silicate glasses by Heuer et al. [106] also have concluded that the inverse of the Haven ratio can be considered as a measure of the degree of "collectivity" in ionic motion. From molecular dynamics simulations, Habasaki et al. [156] had already pointed out that cooperative ion jumps induced by ion-ion interactions contribute to the Haven ratio. They cited the MD work of Na-β''-alumina of Hafskjold and Li [439], which pointed out that a small Haven ratio corresponds to highly correlated velocities of different conducting ions, indicating that ions move in the same direction simultaneously. Since the interception of jump paths on mixing found by Habasaki et al. [64, 156, 440] should affect co-operative motion of ions too, the larger value of the Haven ratio in the mixed alkali system can be explained in terms of a decreased number of the co-operative forward jumps.

One way to support this is consistency of the prediction that H_R should increases with decreasing ion-ion interaction strength as can be realized by increasing the average separation between ions. The limit of $H_R = 1$ is reached and Nernst-Einstein relation holds when ion-ion interaction becomes negligible. The equivalent of this in the CM description is the expected increase of H_R with decrease of the coupling parameter n on decreasing ion concentration, where n can be obtained from the fit to the electric modulus data by the Kohlrausch function, $\exp[-(t/\tau)^{1-n}]$. The decrease of n on decreasing ion concentration in the same family of glassy ionic conductors have been verified before in Refs [87, 104], and in crystalline ionic conductors in Ref. [318]. For glassy ionic conductors, the support of the ion-ion interaction is the cause of the breakdown of the Nernst-Einstein relation can be drawn from the collection of experimental data of the dependence of H_R on total alkali content of alkali borate, germinate, and silicate glasses by Kelly et al. [385] and Na alumino-germanate, and Na borate glasses by Voss et al. [414]. Kelly et al. have reported for each family of alkali oxide glass that H_R increases with decreasing total alkali content Y for alkali borate, germanate, and silicate glasses. Voss et al. combined their Haven ratio data of Na borate and Na alumino-germanate glasses with the data of Kelly et al., and plotted all data of H_R altogether against the ratio of the average Na–Na distance to the network distance, $<d_{\mathrm{Na}}>/<d_{\mathrm{network}}>$. This plot shown here in Fig. 4.80 verifies the expected increase of H_R on increasing ion-ion distance, and the limit $H_R = 1$ is attained at low alkali concentration.

The degree of breakdown of the Stokes-Einstein relation of glassformers increases on decreasing temperature towards T_g [60]. Similar T-dependence of the

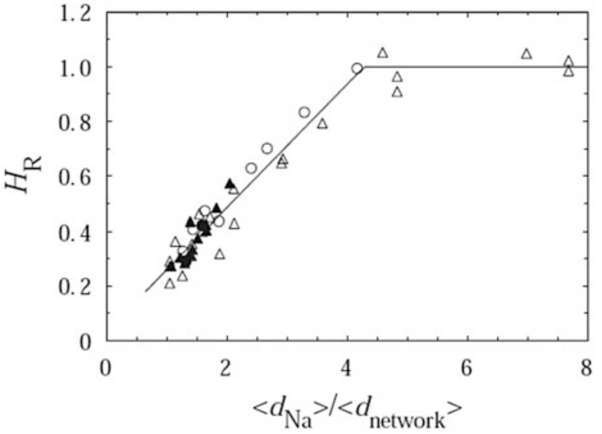

Fig. 4.80 Haven ratio H_R as a function of the ratio of the average Na–Na distance to the network distance, $<d_{Na}>/<d_{network}>$. Values for Na-borate glasses: *filled circle*—Voss et al. [441] ($T = 380$ C), *open circle*—Kelly et al. [385] ($T = 300$ C); Na-alumino-germanate glasses: *filled triangle*—from Ref. [414] ($T = 380$ C), *open triangle*—Kelly et al. [385] ($T = 300$ C). Reproduced from Ref. [414] by permission

degree of breakdown of the Nernst-Einstein relation was found by simulation and experiment. Decrease of the Haven ratio on decreasing temperature was found by Knödler et al. [146] by simulation of a stochastic lattice gas model with ion-ion interaction included into the Hamiltonian, and by experimental measurements in a Rb borate glass, $0.2Rb_2O \cdot 0.8B_2O_3$ [442]. However, H_R of the corresponding Na borate glass, $0.2Na_2O \cdot 0.8B_2O_3$, show no temperature dependence.

Explanation of the breakdown of the Stokes-Einstein relation in glassformers given by the CM was based on the correlation functions for center of mass diffusion and viscosity weigh differently the effects of the many-body relaxation, resulting in different coupling parameters and relaxation times. A similar reasoning was given to explain the difference in relaxation times between nuclear spin relaxation and conductivity relaxation of glassy ionic conductors to be discussed in Chapter 5. The origin of the Haven ratio being less than unity in glassy ionics may also be explained by the slight difference between the tracer diffusion correlation function, $C_D(t) = <\boldsymbol{r}_i(0)\boldsymbol{r}_i(t)>$ and the conductivity correlation function, $C_\sigma(t) = (1/N)\Sigma_{ij} < \boldsymbol{v}_i(0)\boldsymbol{v}_j(t)>$, where $\boldsymbol{r}_i$ and $\boldsymbol{v}_i$ are the position and velocity of the diffusing ions. The $i \neq j$ cross-correlation terms in $C_\sigma(t)$ do not appear in the $C_D(t)$.

4.12.1 The Haven Ratio for Mixed Alkali Glasses

Having shown for single alkali glasses that the Haven ratio H_R anti-correlates with ion-ion interaction and many-ion cooperative dynamics, here the ‘common’ Haven ratios of the mixed alkali glasses, $0.2[xNa_2O \cdot (1-x)Rb_2O] \cdot 0.8B_2O_3$, obtained by

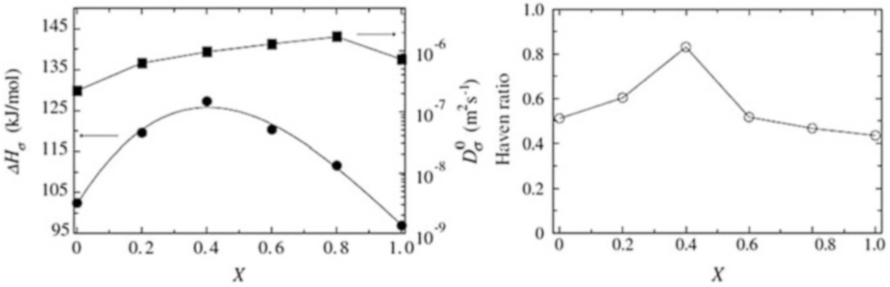

Fig. 4.81 (*Left*) Activation enthalpy ΔH_σ and pre-exponential factor D_σ^0 of the conductivity diffusion coefficient as a function of composition below the glass-transition temperature for 0.2 $[x\mathrm{Na_2O} \cdot (1\text{-}x)\mathrm{Rb_2O}] \cdot 0.8\mathrm{B_2O_3}$ glasses. (*Right*) Composition dependence of the common Haven ratio of the same glass. Reproduced from Ref. [393] by permission

Imre et al. [393] are used to further support the decrease of ion-ion interaction and many-ion dynamics in the mixed alkali effect.

The common $H_R(x)$ of the mixed alkali glass with composition x is defined by

$$H(x) = \left(\frac{Nq^2}{k_B T \sigma_{dc}(x)}\right)\left[xD^{Na}(x) + (1-x)D^{Rb}(x)\right], \tag{4.68}$$

where D^{Na} and D^{Rb} are the tracer diffusion coefficient of Na and Rb respectively. The right panel of Fig. 4.81 shows H_R increases on introducing foreign alkali into the host, and it peaks at the same composition ($x = 0.4$) as the activation enthalpy ΔH_σ of d.c. conductivity (see left panel). These properties of H_R and ΔH_σ corroborate in indicating the decrease of ion-ion interaction and many-ion dynamics as one of the manifestations of the mixed alkali effect. Actually, the maximum of the Haven ratio at some intermediate x value shown in the right panel of Fig. 4.81 was found earlier by Terai [443], and by Jain et al. [394]

4.13 Relating Macroscopic Electrical Conductivity to Microscopic Movements of Ions

The question of how to relate the macroscopic conductivity relaxation measurements in ionic conductors (either permittivity $\varepsilon^*(\omega)$, conductivity $\sigma^*(\omega)$, or electric modulus $M^*(\omega)$) to the microscopic movement of the ions, is a longstanding and relevant issue to solve. Here we compare the macroscopic electrical response with a stochastic transport theory of charged carriers, and find that the electric modulus, $M^*(\omega)$, is the most appropriate representation of the macroscopic data to describe the microscopic movement of the ions. It is found that $M^*(\omega)$ faithfully reproduces the spectral shape of the microscopic ionic movement except that the characteristic relaxation frequency is shifted away from the microscopic ionic hopping relaxation frequency by a frequency-independent factor that can be calculated [31].

In 1973, Scher and Lax (SL) [444] published a theory of stochastic transport of charged carriers (ions in the case presented here). They started from the Nyquist theorem which relates admittance and noise and generalizes the Einstein relation between mobility, μ, and diffusion constant, D, to nonzero frequency as

$$\mu^*(\omega) = (q/kT)D^*(\omega) \tag{4.69}$$

where q is the ion charge, k is the Boltzmann constant and T is the temperature [445, 446]. The real part of the frequency-dependent diffusion constant $D^*(\omega)$ is related to the velocity-velocity autocorrelation function, $<v(t)\ v(0)>$ by

$$\mathrm{Re}D^*(\omega) = \int_0^\infty \cos\omega t < v(t)v(0) > dt, \tag{4.70}$$

and to the mean squared displacement of the carrier, $< [\mathbf{r}(t) - \mathbf{r}(0)]^2 >$, by

$$D^*(\omega) = -\frac{1}{6}\omega^2 \int_0^\infty e^{-i\omega t} < [\mathbf{r}(t) - \mathbf{r}(0)]^2 > dt. \tag{4.71}$$

This form for $D^*(\omega)$ naturally obeys the Kramers-Kronig relationship,

$$-\mathrm{Im}\,D^*(\omega) = \frac{1}{\pi}\wp \int_{-\infty}^{\infty} \frac{\mathrm{Re}D^*(\omega)}{\omega' - \omega} d\omega' \tag{4.72}$$

The complex conductivity is given by the relations

$$\sigma^*(\omega) = Nq\mu^*(\omega) = \left(Nq^2/kT\right)D^*(\omega) \tag{4.73}$$

where N is the density of the mobile ions. Whatever the mechanism of ionic transport, a calculation of $\sigma^*(\omega)$ needs to determine the probability of finding a carrier at any point at time t if it was at the origin at $t = 0$. The model used by SL to calculate such a probability function is a generalization of the continuous time random walk (CTRW) of Montroll and Weiss [447]. In that model the basic quantity is the probability that the time between hops is in the interval $(t, t + \Delta t)$ and the displacement is $\mathbf{s}$, is equal to $\psi(\mathbf{s}, t)\ \Delta t$. Then, $\phi(t)$ defined by

$$\phi(t) = 1 - \int_0^t \psi(\tau)d\tau \tag{4.74}$$

with

$$\psi(t) = \sum_{\mathbf{s}} \psi(\mathbf{s}, t), \tag{4.75}$$

which is the probability that the ion remains fixed in the time interval [0,t]. From Eq. 4.74, it is clear that

$$\psi(t) = -\frac{d}{dt}\varphi(t) \tag{4.76}$$

If the spatial and temporal probability distribution of each hop of the ion is independent of each other such that $\psi(\mathbf{s},t)$ can be written as a product, $p(\mathbf{s})\psi(t)$ with $\sum_{\mathbf{s}} p(\mathbf{s}) = 1$, then calculating $< [\mathbf{r}(t) - \mathbf{r}(0)]^2 >$ by the CTRW method and substituting it into Eq. 4.70, SL finally obtained the key result:

$$D^*(\omega) = \frac{1}{6} r_{rms}^2 (i\omega) \widetilde{\psi}(\omega) / [1 - \widetilde{\psi}(\omega)], \tag{4.77}$$

where

$$r_{rms}^2 = \sum_{\mathbf{s}} s^2 p(\mathbf{s}) \tag{4.78}$$

and $\widetilde{\psi}(\omega)$ is the Laplace or causal Fourier transform of $\psi(t)$ defined by

$$\widetilde{\psi}(\omega) = \int_0^\infty e^{-i\omega t} \psi(t) dt. \tag{4.79}$$

Once the principal results of the stochastic transport theory of SL have been summarized in the above, we are able to show the relation between the electric modulus function, $M^*(\omega)$ and the theoretical expression for the conductivity of SL. We can rewrite Eq. 4.77 using Eqs. 4.76 and 4.79, as

$$D^*(\omega) = \left(r_{rms}^2/6\right)(i\omega) \frac{\widetilde{\psi}(\omega)}{1 - \widetilde{\psi}(\omega)} = \left(r_{rms}^2/6\right)(i\omega) \left\{ \frac{\int_0^\infty dt e^{-i\omega t}\left(-\frac{d}{dt}\phi(t)\right)}{\left[1 - \int_0^\infty dt e^{-i\omega t}\left(-\frac{d}{dt}\phi(t)\right)\right]} \right\} \tag{4.80}$$

Then, from Eqs. 4.72 and 4.80, the complex conductivity can be calculated from $\phi(t)$ by

$$\sigma_{STT}^{*}(\omega) = \left(Nq^2/kT\right)\left(r_{rms}^2/6\right)(i\omega)\left\{\frac{\int\limits_0^\infty dte^{-i\omega t}\left(-\frac{d}{dt}\phi(t)\right)}{\left[1-\int\limits_0^\infty dte^{-i\omega t}\left(-\frac{d}{dt}\phi(t)\right)\right]}\right\}. \tag{4.81}$$

The suffix STT is introduced in Eq. 4.81 to indicate the quantity is obtained from the stochastic transport theory, which is assumed to describe correctly the microscopic ion dynamics. This theoretical expression is to be compared with the macroscopic one, σ_{EM}^{*}, which can be written using the electric modulus formalism as

$$\sigma_{EM}^{*}(\omega) = \varepsilon_o \frac{i\omega}{M^{*}(\omega)} = (\varepsilon_o/M_\infty)(i\omega)\left\{\frac{1}{\left[1-\int\limits_0^\infty dte^{-i\omega t}\left(-\frac{d}{dt}\Phi(t)\right)\right]}\right\}, \tag{4.82}$$

with $M_\infty = 1/\varepsilon_\infty$ the inverse of the high frequency permittivity value. We can also write an expression for the macroscopic electrical conductivity as the sum of two different contributions,

$$\sigma_{EM}^{*}(\omega) = \sigma_{EM,ion}^{*}(\omega) + i\omega\varepsilon_o\varepsilon_\infty, \tag{4.83}$$

with $\sigma_{EM,ion}^{*}(\omega)$ the part coming entirely from ion diffusion, and $i\omega\varepsilon_o\varepsilon_\infty$ a pure imaginary part accounting for the permittivity at high frequencies. From Eqs. (4.82) and (4.83) we can obtain the following relation between $\sigma_{EM,ion}^{*}(\omega)$ and the macroscopic decay function $\Phi(t)$:

$$\sigma_{EM,ion}^{*}(\omega) = (\varepsilon_o/M_\infty)(i\omega)\left\{\frac{\int\limits_0^\infty dte^{-i\omega t}\left(-\frac{d}{dt}\Phi(t)\right)}{\left[1-\int\limits_0^\infty dte^{-i\omega t}\left(-\frac{d}{dt}\Phi(t)\right)\right]}\right\} \tag{4.84}$$

By inspection of the expressions inside the curly brackets in Eqs. 4.81 and 4.84, one finds that the frequency dependencies of the theoretical contribution of ionic diffusion to the conductivity from the Scher and Lax theory, $\sigma_{STT}^{*}(\omega)$, and of the ionic contribution to the macroscopic conductivity derived from the electric modulus formalism, $\sigma_{EM,ion}^{*}(\omega)$, have similar functional forms. In spite of the similarity in form, we hasten to mention that $\sigma_{STT}^{*}(\omega)$ and $\sigma_{EM,ion}^{*}(\omega)$ differ in their dependencies on ω because $\Phi(t)$ and $\phi(t)$ have different characteristic time scales, τ_{EM} and τ_{STT} respectively. Interestingly, this similarity leads to a relation between $\Phi(t)$ and $\phi(t)$, which gives from the microscopic $\phi(t)$ a more basic interpretation to the macroscopic $\Phi(t)$ than the decay of the electric field at constant displacement vector, as customarily done in the electric modulus formalism [5, 6, 17, 29, 30]. The pre-factors of the frequency dependent terms in Eqs. 4.81 and 4.84 are different. This is understandable because the theoretical expression (4.81) is obtained from the mean square displacement, the frequency dependent diffusion constant and the use of the Nyquist theorem, which generalizes the Nernst-Einstein relation between conductivity and diffusion constant to nonzero frequency. On the other hand, the route to expressions (4.82) and (4.84) of the electric modulus formalism is through the Maxwell relation. The two approaches, being based on sound physical principles, are legitimate ways to arrive at $\sigma^*(\omega)$. Both $\phi(t)$ and $\Phi(t)$ start from the initial (i.e., at $t = 0$) value of 1 and decrease monotonically towards zero with time. However, $\phi(t)$ and $\Phi(t)$ are characterized respectively by two different characteristic time constants, τ_{STT} and τ_{EM}. We can go a step further in relating the STT and the EM approaches by rewriting Eqs. 4.81 and 4.84 as

$$\sigma^*_{STT}(\omega) = \left(Nq^2/kT\right)\left(r^2_{rms}/6\right)(i\omega)\left\{\frac{1}{i\omega\ \ \tilde{\phi}_{STT}(\omega)} - 1\right\} \tag{4.85}$$

and

$$\sigma^*_{EM,\,ion}(\omega) = (\varepsilon_o/M_\infty)(i\omega)\left\{\frac{1}{i\omega\ \ \tilde{\Phi}_{EM}(\omega)} - 1\right\}. \tag{4.86}$$

Here we have introduced $\tilde{\phi}(\omega)$ and $\tilde{\Phi}(\omega)$ as the Laplace transforms of $\varphi(t)$ and $\Phi(t)$ respectively, and made use of the relationship between the Laplace transform of a function and that of its time derivative, i.e., $\int_0^\infty dt e^{-i\omega t}\left(-\frac{d}{dt}\phi(t)\right) = 1 - i\omega\tilde{\phi}(\omega)$. Writing out explicitly the time dependencies of $\Phi(t/\tau_{EM})$ and $\phi(t/\tau_{STT})$ to include their respective characteristic times, and using the identity, $\tilde{\phi}(\omega) = \tau\tilde{\phi}(\omega\tau)$, we arrive at the following expressions,

$$\sigma^*_{STT}(\omega\tau_{STT}) = \left(Nq^2/kT\right)\left(r^2_{rms}/6\right)\frac{1}{\tau_{STT}}\left\{\frac{1}{\tilde{\phi}_{STT}(\omega\tau_{STT})} - i\omega\tau_{STT}\right\} \tag{4.87}$$

and

$$\sigma^*_{EM,\,ion}(\omega\tau_{EM}) = (\varepsilon_o/M_\infty)\frac{1}{\tau_{EM}}\left\{\frac{1}{\tilde{\Phi}_{EM}(\omega\tau_{EM})} - i\omega\tau_{EM}\right\}. \tag{4.88}$$

Note that inside the curly brackets in Eqs. 4.87 and 4.88 the expressions have the same structure. If $\tilde{\varphi}_{STT}(\omega\tau_{STT})$ and $\tilde{\Phi}_{EM}(\omega\tau_{EM})$ are the *same* functions of the variables $\omega\tau_{STT}$ and $\omega\tau_{EM}$, then *a posteriori* they have the same value in the limits of $\omega\tau_{STT} \to 0$ and $\omega\tau_{EM} \to 0$ respectively. Thus $\sigma^*_{STT}(\omega\tau_{STT})$ and $\sigma^*_{EM,ion}(\omega\tau_{EM})$ will have equal d.c. conductivity if the factors outside the curly brackets in Eqs. 4.87 and 4.88 are the same, i.e.

$$\tau_{STT}/\tau_{EM} = \left(Nq^2 r_{rms}^2\right)/(6kT\varepsilon_o\varepsilon_\infty). \tag{4.89a}$$

If this relation between the macroscopic conductivity relaxation time, τ_{EM}, of EM and the microscopic ionic hopping correlation time, τ_{STT}, is satisfied, the two expressions for the complex conductivity, $\sigma^*_{STT}(\omega\tau_{STT})$ and $\sigma^*_{EM,ion}(\omega\tau_{EM})$, become isomorphic to each other. However, as a function of pure frequency ω, $\sigma^*_{STT}(\omega)$ differs from $\sigma^*_{EM,ion}(\omega)$. When plotted against log ω, $\sigma^*_{STT}(\omega)$ differs from $\sigma^*_{EM,ion}(\omega)$ only by a horizontal shift of the whole curve $\sigma^*_{EM,ion}(\omega)$ parallel to the logω-axis with a shift factor equal to log(τ_{STT}/τ_{EM}). The same relation holds between Re $\left[\sigma^*_{STT}(\omega)\right]$ and Re[$\sigma^*_{EM}(\omega)$] because from Eq. (4.83) it follows that Re[$\sigma^*_{EM}(\omega)$] is exactly equal to Re[$\sigma^*_{EM,ion}(\omega)$].

In general, τ_{EM} is not equal to τ_{STT} and they are related to each other by the ratio shown on the right-hand-side of Eq. 4.89. Hence, τ_{EM} cannot be identified with the microscopic ion hopping relaxation time, τ_{STT}. Depending on the material parameters on the right-hand-side of Eq. (4.89), the two relaxation times can be very different. In fact, two systems with identical microscopic ion dynamics and the same τ_{STT} but have different values of ε_∞ will have two different values of τ_{EM}, each related to the same τ_{STT} by Eq. 4.89. This dependence of τ_{EM} on ε_∞ is considered by some workers as a shortcoming of the EM [78]. We do not agree with this opinion because this invariably will occur in any representation of the electrical relaxation data because the latter are from macroscopic measurement where ε_∞ inevitably enters. Nevertheless, even considered as a shortcoming of the EM, this is a minor problem that can be overcome. From τ_{EM} the microscopic STT relaxation time can be readily calculated by the expression,

$$\tau_{STT} = \tau_{EM}\left(Nq^2 r_{rms}^2\right)/(6kT\varepsilon_o\varepsilon_\infty). \tag{4.89b}$$

In the EM, the d.c. conductivity, $\sigma_{\mathrm{EM,dc}}$ is calculated by the well known relation,

$$\sigma_{EM,dc} = \varepsilon_o\varepsilon_\infty/\tau_{EM}, \tag{4.89c}$$

in which ε_∞ appears explicitly in the numerator and also implicitly in the denominator. However, when substituting Eq. (4.89a) into Eq. (4.89c), the macroscopic d.c. conductivity turns out to give correctly the microscopic d.c. conductivity, i.e.,

$$\sigma_{EM,dc} = \varepsilon_o\varepsilon_\infty/\tau_{EM} = Nq^2 r_{rms}^2/6kT\tau_{STT} \tag{4.89d}$$

The consistency of $\sigma_{EM,dc}$ with the microscopic d.c. conductivity explains why $\sigma_{EM,dc}$ calculated by Eq. (4.89b) are always in good agreement with experimental values [4–6, 23, 270, 275]. Note also that except for the slowly varying T^{-1} factor in Eq. (89), the temperature dependence of τ_{STT} and τ_{EM} is the same. They have about the same activation energy as long as the activation energy in temperature unit is much larger than T.

It follows from $\widetilde{\phi}_{STT}(\omega\tau_{STT})$ and $\widetilde{\Phi}_{EM}(\omega\tau_{EM})$ being the *same* functions of the variables $\omega\tau_{STT}$ and $\omega\tau_{EM}$ respectively, that the normalized electric modulus $M^*(\omega\tau_{\mathrm{EM}})/M_\infty$ of Eq. 4.12 can be related to the microscopic $\widetilde{\phi}_{STT}(\omega\tau_{STT})$ by

$$M^*(\omega\tau_{EM})/M_\infty = i\omega\tau_{EM}\widetilde{\Phi}(\omega\tau_{EM}) = i\omega\tau_{EM}\widetilde{\phi}(\omega\tau_{STT}) \tag{4.90}$$

Since $\widetilde{\phi}_{STT}(\omega\tau_{STT})$ appears in the expression (Eq. 4.87) for $\sigma^*_{STT}(\omega)$, this result leads to the important conclusion that the shape of the dispersion of $[M^*(\omega\tau_{EM})/M_\infty]$ obtained from data analysis using the electric modulus formalism can be identified with the shape of the dispersion of $\widetilde{\phi}(\omega\tau_{STT})$, which originates from the microscopic movement of the ions and determines the frequency dependent transport coefficients in the stochastic transport theory (Eq. 4.87). Therefore, the shape of the observed loss peak of $\mathrm{Im}(M^*(\omega\tau_{EM})/M_\infty)$ is uniquely determined by the movement of the ions. This correspondence between the EM and the stochastic transport theory, though not totally exact (i.e., the difference in the relaxation times given by Eq. 4.89b) also justifies that the electric modulus has a theoretical basis, e.g. the stochastic transport theory of Scher and Lax. Although the τ_{EM} differs from τ_{STT} by the factor in Eq. 4.89b, the dispersion of $(M^*(\omega\tau_{EM})/M_\infty)$ and the quantity $i\omega\widetilde{\phi}_{STT}(\omega\tau_{STT})$ of the stochastic transport theory is exactly the same. Therefore, any dispersion coming from ion hopping and picked up by the stochastic transport theory in Eq. 4.87 will be seen exactly in the same shape or form in the EM representation of the data at frequencies in the neighborhood of $(\tau_{EM})^{-1}$. It is also worthwhile to point out from Eq. 4.89a that the ratio $(\varepsilon_\infty/\tau_{EM})$ is a constant independent of ε_∞. Hence, as a function of $\omega\tau_{EM}$, the ionic motion contribution to the conductivity, $\sigma^*_{EM,ion}(\omega\tau_{EM})$, given by Eq. 4.88 is independent of the value of the high frequency dielectric constant, ε_∞. For more discussion of this, see Appendix in Ref. 31.

Finally, some remarks on CTRW used by Scher and Lax (SL) are appropriate before closing this section. In the past, Tunaley [448] made a literal interpretation of the CTRW procedure of SL as an ongoing renewal process which led to frequency independent $D^*(\omega)$ and $\sigma^*(\omega)$. This difficulty is removed by a proper treatment of the CTRW problem as demonstrated by Lax et al. [449] and others [450, 451]. Also, a formal equivalence between averaged particle transport in disordered systems and the generalized master equation or the CTRW theory was established by Klafter and Silbey [452]. Although the CTRW as a theory is on firm grounds, it may not be general enough to describe any model of charged carrier transport as was found by Maass, Meyer and Bunde [143] for their model.

In summary, by comparing the results of a stochastic microscopic transport theory of the dynamics of ionic movement with the electric modulus representation of the macroscopic conductivity relaxation data, we have shown that the form of microscopic ion hopping correlation function is faithfully reproduced in the electric modulus formalism. This correspondence between microscopic description and the electric modulus analysis of macroscopic measurement of ionic motion indicate that the electric modulus, M^*, is the most suitable representation of macroscopic data compared with other alternatives, e.g. ε^* and σ^*. However, the macroscopic conductivity relaxation time obtained from the electric modulus analysis of the data differs from the microscopic ion hopping correlation time by a known factor, which is weakly temperature dependent. Consequently the two times have practically the same thermal activation energy and other dependencies on variables such as the isotope mass of the diffusing ion.

4.13.1 An Experimental Verification

Nuclear spin lattice relaxation and conductivity relaxation data of the crystalline ionic conductor $Li_{0.5}La_{0.5}TiO_3$ (LLTO) obtained by León et al. [55] have been employed [31] to demonstrate that in this crystalline conductor the nuclear spin relaxation correlation function is in every respect the same as the microscopic ion hopping conductivity correlation function. The latter has been calculated from the macroscopic electrical relaxation data, according to the relation between them established by Eq. (4.89). Thus, the nuclear spin relaxation data enable us to verify the relation between the macroscopic conductivity relaxation function and the microscopic ion hopping correlation function. For details see Ref. [31] and Chapter 5 of this book on NMR.

4.14 Relation to Other Chapters

The present chapter is intended to present the dynamics of ionic conductors as obtained from experimental measurements and compared with theoretical predictions. Many issues will be discussed again from different angles and amplified by additional experimental data and simulations in other chapters to follow. For example, the Chap. 5 on nuclear magnetic resonance, Chap. 6 on nanoionics, Chap. 7 on ionic liquids, and Chaps. 9–11 on molecular dynamics simulations will revisit the issues and provide additional information that corroborate the findings and interpretations of this chapter, and enhance the understanding. Efforts will be made to relate the results in the other chapters back to that in the present chapter.

References

1. K.L. Ngai, C.T. Moynihan, MRS Bull. **23**, 51 (1998)
2. J.C. Dyre, P. Maass, B. Roling, D.L. Sidebottom, Rep. Prog. Phys. **72**, 046501 (2009)
3. C. Angell, Annu. Rev. Phys. Chem. **43**, 693 (1992)

4. C. Angell, Chem. Rev. **90**, 523 (1990)
5. C.T. Moynihan, J. Non-Cryst. Solids **172–174**, 1395 (1994)
6. C.T. Moynihan, J. Non-Cryst. Solids **203**, 359 (1996)
7. K.L. Ngai, J. Habasaki, C. León, A. Rivera, Z. Phys. Chem. **219**, 47 (2005)
8. K.L. Ngai, J. Non-Cryst. Solids **203**, 232 (1996)
9. J. Dyre, T. Schrøder, Rev. Mod. Phys. **72**, 873 (2000)
10. W. Dieterich, P. Maass, Zeitschrift Für Phys. Chemie **223**, 1187 (2009)
11. R. Syed, D.L. Gavin, C.T. Moynihan, J. Am. Ceram. Soc. **65**, c129 (1982)
12. G.N. Greaves, K.L. Ngai, Phys. Rev. B **52**, 6358 (1995)
13. K.L. Ngai, G.N. Greaves, C.T. Moynihan, Phys. Rev. Lett. **80**, 1018 (1998)
14. K. Funke, R.D. Banhatti, D.M. Laughman, L.G. Badr, M. Mutke, A. Santic, W. Wrobel, E.M. Fellberg, C. Biermann, Z. Phys. Chem. **224**, 1891 (2010)
15. J. Kincs, S. Martin, Phys. Rev. Lett. **76**, 70 (1996)
16. M. Menetrier, A. Hojjaji, C. Estournes, A. Levasseur, Solid State Ionics **48**, 325 (1991)
17. F.S. Howell, R.A. Bose, P.B. Macedo, C.T. Moynihan, J. Phys. Chem. **78**, 639 (1974)
18. C.T. Moynihan, L.P. Boesch, N.L. Laberge, Phys. Chem. Glasses **14**, 122 (1973)
19. C.L. Babcock, J. Am. Ceram. Soc. **17**, 329 (1934)
20. J.H. Simmons, P.B. Elterman, C.J. Simmons, R.K. Mohr, J. Am. Ceram. Soc. **62**, 158 (1979)
21. A. Rivera, E. Rössler, Phys. Rev. B **73**, 212201 (2006)
22. K.L. Ngai, Phil. Mag. B **77**, 187 (http://www.tandfonline.com) (1998)
23. C. León, M.L. Lucia, J. Santamaria, F. Sanchez-Quesada, Phys. Rev. B **57**, 41 (1998)
24. M.S. Whittingham, R.A. Higgins, J. Chem. Phys. **54**, 414 (1971)
25. P.B. Macedo, C.T. Moynihan, R. Bose, Phys. Chem. Glasses **13**, 171 (1972)
26. R. Richert, H. Wagner, Solid State Ionics **105**, 167 (1998)
27. P. Lunkenheimer, A. Pimenov, A. Loidl, Phys. Rev. Lett. **78**, 2995 (1997)
28. P. Lunkenheimer, *Dielectric Spectroscopy of Glassy Dynamics* (Aachen, Shaker, 1999)
29. I.M. Hodge, K.L. Ngai, C.T. Moynihan, J. Non-Cryst. Solids **351**, 104 (2005)
30. C.T. Moynihan, Solid State Ionics **105**, 175 (1998)
31. K.L. Ngai, C. León, Phys. Rev. B **60**, 9396 (1999)
32. K.L. Ngai, R.W. Rendell, Phys. Rev. B **61**, 9393 (2000)
33. G. Jarosz, M. Mierzwa, J. Ziolo, M. Paluch, H. Shirota, K.L. Ngai, J. Phys. Chem. B **115**, 12709 (2011)
34. Z. Wojnarowska, A. Swiety-Pospiech, K. Grzybowska, L. Hawelek, M. Paluch, K.L. Ngai, J. Chem. Phys. **136**, 164507 (2012)
35. J. Wong, C. Angell, *Glass: Structure by Spectroscopy* (Dekker, New York, 1976), p. 750
36. G.C. Garton, Discuss. Farad. Soc. A **42**, 161 (1946)
37. A.E. Owen, Prog. Ceram. Sci. **3**, 77 (1963)
38. J.M. Stevels, Handbuch Phys. **20**, 372 (1957)
39. A.K. Jonscher, *Dielectric Relaxation in Solids* (Chelsea Dielectric Press, London, 1983)
40. A.S. Nowick, A.V. Vaysleyb, W. Liu, Solid State Ionics **105**, 121 (1998)
41. X. Lu, H. Jain, J. Phys. Chem. Solids **55**, 1433 (1994)
42. A.S. Nowick, B.S. Lim, A.V. Vaysleb, J. Non-Cryst. Solids **172–174**, 1243 (1994)
43. K.L. Ngai, J. Chem. Phys. **110**, 10576 (1999)
44. K.L. Ngai, C. León, Phys. Rev. B **66**, 064308 (2002)
45. K.L. Ngai, J. Habasaki, Y. Hiwatari, C. León, J. Phys. Condens. Matter **15**, S1607 (2003)
46. C. León, A. Rivera, A. Várez, J. Sanz, J. Santamaria, K.L. Ngai, Phys. Rev. Lett. **86**, 1279 (2001)
47. A.K. Rizos, J. Alifragis, K.L. Ngai, P. Heitjans, J. Chem. Phys. **114**, 931 (2001)
48. A. Rivera, C. León, C.P.E. Varsamis, G.D. Chryssikos, K.L. Ngai, C.M. Roland, L.J. Buckley, Phys. Rev. Lett. **88**, 125902 (2002)
49. K. Funke, R.D. Banhatti, L.G. Badr, D.M. Laughman, H. Jain, J. Electroceram. **34**, 4 (2015)
50. K.L. Ngai, A.K. Jonscher, C.T. White, Nature **277**, 185 (1979)
51. K.L. Ngai, Phys. Rev. B **22**, 2066 (1980)

52. A. Pimenov, P. Lunkenheimer, H. Rall, R. Kohlhaus, A. Loidl, Phys. Rev. E **54**, 676 (1996)
53. K.L. Ngai, J. Phys. Condens. Matter **15**, S1107 (2003)
54. K.L. Ngai, U. Strom, Phys. Rev. **B38**, 10350 (1988)
55. C. León, J. Santamaria, M.A. Paris, J. Sanz, J. Ibarra, L.M. Torres, Phys. Rev. **B56**, 5302 (1997)
56. C. León, M.L. Lucia, J. Santamaria, F. Sanchez-Quesada, Phys. Rev. **B57**, 41 (1998)
57. K.L. Ngai, J. Chem. Phys. **110**, 10576 (1999)
58. D.L. Sidebottom, P.F. Green, R.K. Brow, Phys. Rev. Lett. **74,** 5068 (1995)
59. D.L. Sidebottom, P.F. Green, R.K. Brow, J. Non-Cryst. Solids **203**, 300 (1996)
60. K.L. Ngai, *Relaxation and Diffusion in Complex Systems* (Springer, New York, 2011)
61. S. Capaccioli, M.S. Thayyil, K.L. Ngai, J. Phys. Chem. B **112**, 16035 (2008)
62. K.L. Ngai, AIP Conf. Proc. **708**, 515 (2004)
63. K.L. Ngai, Philos. Mag. **84**, 1341 (2004)
64. J. Habasaki, K.L. Ngai, Y. Hiwatari, J. Chem. Phys. **121**, 925 (2004)
65. J. Habasaki, K.L. Ngai, Y. Hiwatari, Phys. Rev. **E66**, 021205 (2002)
66. J. Habasaki, K.L. Ngai, J. Non-Cryst. Solids **352**, 5170 (2006)
67. R. Kohlrausch, Theorie des elektrischen Rückstandes in der Leidener Flasche; R. von Kohlrausch, Pogg. Ann. Phys. Chem. **91**, 179–214 (1854)
68. R. Kohlrausch, Pogg. Ann. Phys. Chem. **91**, 56 (1854)
69. K.L. Ngai, C. León, J. Non-Cryst. Solids **315**, 124 (2003)
70. K.L. Ngai, Solid State Ionics **5**, 27 (1981)
71. K.L. Ngai, J. Mundy, in *Physics of Non-Crystalline Solids*, ed. by L.D. Pye, W.C. LaCourse, H.J. Stevens (Taylor and Francis, Washington DC, 1992), p. 342
72. C.T. Moynihan, Solid State Ionics **105**, 75 (1998)
73. J.F. Cordaro, M. Tomozawa, J. J. Am. Ceram. Soc. **64**, 713 (1981)
74. D.L. Sidebottom, Phys. Rev. Lett. **82**, 3653 (1999)
75. L.P. Boesch, C.T. Moynihan, J. Non-Cryst. Solids **17**, 44 (1975)
76. B. Roling, Solid State Ionics **105**, 185 (1998)
77. B. Roling, A. Happe, K. Funke, M.D. Ingram, Phys. Rev. Lett. **78**, 2160 (1997)
78. D.L. Sidebottom, B. Roling, K. Funke, Phys. Rev. B **63**, 024301 (2000)
79. D.L. Sidebottom, Rev. Mod. Phys. **81**, 999 (2009)
80. D.L. Sidebottom, J. Zhang, Phys. Rev. B **62**, 5503 (2000)
81. D.L. Sidebottom, P.F. Green, R.K. Brow, Phys. Rev. B **56**, 170 (1997)
82. C. León, P. Lunkenheimer, K. Ngai, Phys. Rev. B **64**, 184304 (2001)
83. A. Pimenov, J. Ullrich, P. Lunkenheimer, A. Loidl, C.H. Rüscher, Solid State Ionics **109**, 111 (1998)
84. H.K. Patel, S.W. Martin, Solid State Ionics **53–56**, 1148 (1992)
85. H.K. Patel, S.W. Martin, Phys. Rev. B **45**, 10292 (1992)
86. H.K. Patel, Ph.D. thesis, Iowa State University, Ames, Iowa, 1993
87. K.L. Ngai, J.N. Mundy, H. Jain, O. Kanert, G. Balzer-Jöllenbeck, Phys. Rev. **B39**, 6169 (1989)
88. H. Jain, S. Krishnaswami, Solid State Ionics **105**, 129 (1998)
89. P. Maass, J. Petersen, A. Bunde, W. Dieterich, H.E. Roman, Phys. Rev. Lett. **66**, 52 (1991)
90. D. Knodler, W. Dieterich, Physica (Amsterdam) **191A**, 426 (1992)
91. J. Petersen, W. Dieterich, Philos. Mag. **65**, 231 (1992)
92. M. Meyer, P. Maass, A. Bunde, Phys. Rev. Lett. **71**, 573 (1993)
93. P. Maass, M. Meyer, A. Bunde, Phys. Rev. **B51**, 8164 (1995)
94. P.K. Dixon, Phys. Rev. B **42**, 8179 (1990)
95. G. Williams, D.C. Watts, S.B. Dev, A.M. North, Trans. Faraday Soc. **67**, 1323 (1971)
96. K.L. Ngai, Comment Solid State Phys. **9**, 127 (1979)
97. K.L. Ngai, R.W. Rendell, H. Jain, Phys. Rev. B **30**, 2133 (1984)
98. K.L. Ngai, J. Chem. Phys. **98**, 6426 (1993)
99. K.L. Ngai, Phys. Rev. **B48**, 13481 (1993)

100. K.L. Ngai, U. Strom, Phys. Rev. B **38**, 10350 (1988)
101. K.L. Ngai, O. Kanert, Solid State Ionics **53–55**, 936 (1992)
102. K.L. Ngai, J. Phys. (Paris) Colloq. C2, **2**, 61 (1992)
103. K.L. Ngai, A.K. Rizos, Phys. Rev. Lett. **76**, 1296 (1996)
104. K.L. Ngai, S.W. Martin, Phys. Rev. B **40**, 10550 (1989)
105. P. Jund, W. Kob, R. Jullien, Phys. Rev. B **64**, 134303 (2001)
106. A. Heuer, M. Kunow, M. Vogel, R.D. Banhatti, Phys. Chem. Chem. Phys. **4**, 3185 (2002)
107. A.K. Jonscher, J. Mater. Sci. **13**, 553 (1978)
108. A. Burns, G.D. Chryssikos, E. Tombari, R.H. Cole, W.M. Risen, Phys. Chem. Glasses **30**, 264 (1989)
109. K.L. Ngai, Y. Wang, C.T. Moynihan, J. Non-Cryst. Solids **307–310**, 999 (2002)
110. P. Maass, J. Non-Cryst. Solids **255**, 35 (1999)
111. W.C. Hasz, C.T. Moynihan, J. Non-Cryst. Solids **172–174**, 1363 (1994)
112. A. Rivera, J. Santamaría, C. León, T. Blochowicz, C. Gainaru, E.A. Rössler, Appl. Phys. Lett. **82**, 2425 (2003)
113. C. León, J. Habasaki, K.L. Ngai, Z. Phys. Chem. **223**, 1131 (2009)
114. D.J. Plazek, J. Rheology **40**, 987 (1996)
115. K.L. Ngai, D.J. Plazek, Macromolecules **47**, 8056 (2014)
116. J.L. Barton, Verres Refract. **20**, 328 (1966)
117. T. Nakajima, *Annual Report, Conference on Electric Insulation and Dielectric Phenomena* (National Academy of Sciences, Washington DC, 1972), p. 168
118. H. Namikawa, J. Non-Cryst. Solids **18**, 173 (1975)
119. R.A. Huggins, in *Diffusion in Solids, Recent Developments*, ed. by A.S. Nowick, J.J. Burton (Academic, New York, 1975), p. 445
120. O.L. Anderson, P.A. Stuart, J. Am. Ceram. Soc. **37**, 573 (1977)
121. P.J. Wilde, C.R.A. Catlow, Solid State Ionics **112**, 185 (1998)
122. J.C. Dyre, J. Appl. Phys. **64**, 2456 (1988)
123. S.D. Baranovskii, H. Cordes, J. Chem. Phys. **111**, 7546 (1999)
124. T.B. Schrøder, J.C. Dyre, Phys. Rev. Lett. **84**, 310 (2000)
125. T.B. Schrøder, J.C. Dyre, Phys. Chem. Chem. Phys. **4**, 3173 (2002)
126. A. Hunt, J. Non-Cryst. Solids **160**, 183 (1993)
127. T. Ishii, J. Phys. Soc. Japan **76**, 064603 (2007)
128. K. Funke, Prog. Solid State Chem. **22**, 111 (1993)
129. K. Funke, Solid State Ionics **94**, 27 (1997)
130. K. Funke, D. Wilmer, Solid State Ionics **136–137**, 1329 (2000)
131. K. Funke, R.D. Banhatti, S. Brückner, C. Cramer, C. Krieger, A. Mandanici, C. Martiny, I. Ross, Phys. Chem. Chem. Phys. **4**, 3155 (2002)
132. K. Funke, R.D. Banhatti, Solid State Ionics **169**, 1 (2004)
133. R.D. Banhatti, K. Funke, Solid State Ionics **175**, 661 (2004)
134. K. Funke, R.D. Banhatti, Solid State Ionics **177**, 1551 (2006)
135. K. Funke, P. Singh, R.D. Banhatti, Phys. Chem. Chem. Phys. **9**, 5582 (2007)
136. P. Debye, H. Falkenhagen, Phys. Z. **24**(121), 401 (1928)
137. K. Funke, Sci. Technol. Adv. Mater. **14**, 043502 (2013)
138. K. Funke, R.D. Banhatti, P. Grabowski, J. Nowinski, W. Wrobel, R. Dinnebier, O. Magdysyuk, Solid State Ionics **271**, 2–9 (2015)
139. S.J. Pas, R.D. Banhatti, K. Funke, Solid State Ionics **177**, 3135–3139 (2006)
140. K. Funke, R.D. Banhatti, Solid State Sciences **10**, 790–803 (2008)
141. C. Cramer, S. Bruckner, Y. Gao, K. Funke, Phys. Chem. Chem. Phys. **4**, 3214 (2002)
142. P. Maass, M. Meyer, A. Bunde, W. Dieterich, Phys. Rev. Lett. **77**, 1528 (1996)
143. P. Maass, M. Meyer, A. Bunde, Phys. Rev. B **51**, 8164 (1995)
144. W. Dieterich, D. Knödler, J. Petersen, Ber. Bunsenges. Physik. Chem. **95**, 964 (1991)
145. D. Knödler, P. Pendzig, W. Dieterich, Solid State Ionics **70/71,** 356 (1994)
146. D. Knödler, P. Pendzig, W. Dieterich, Solid State Ionics **86–88**, 29 (1996)

147. K.L. Ngai, J. Chem. Phys. **109**, 6982–6994 (1998)
148. K.L. Ngai, M. Paluch, J. Chem. Phys. **120**, 857 (2004)
149. K.L. Ngai, D. Prevosto, S. Capaccioli, C.M. Roland, Phys.: Condens. Matter **20**, 244125 (2008)
150. S. Capaccioli, M. Paluch, D. Prevosto, L.-M. Wang, K.L. Ngai, J. Phys. Chem. Lett. **3**, 735 (2012)
151. K.L. Ngai, J. Habasaki, D. Prevosto, S. Capaccioli, M. Paluch, J. Chem. Phys. **137**, 034511 (2012)
152. K.L. Ngai, J. Chem. Phys. **142**, 114502 (2015)
153. K. Funke, R.D. Banhatti, J. Non-Cryst. Solids **353**, 3845 (2007)
154. C. León, J. Habasaki, K.L. Ngai, Z. Phys. Chem. **223**, 1311 (2009)
155. J. Habasaki, I. Okada, Y. Hiwatari, J. Non-Cryst. Solids **183**, 12 (1995)
156. J. Habasaki, I. Okada, Y. Hiwatari, J. Non-Cryst. Solids **208**, 181 (1996)
157. J. Habasaki, Y. Hiwatari, Phys. Rev. **B69**, 144207 (2004)
158. H. Lammert, M. Kunow, A. Heuer, Phys. Rev. Lett. **90**, 215901 (2003)
159. M. Vogel, Phys. Rev. B **70**, 094302 (2004)
160. M. Kunow, A. Heuer, Phys. Chem. Chem. Phys. **7**, 2131 (2005)
161. J. Habasaki, K.L. Ngai, Phys. Chem. Chem. Phys. **9**, 4673 (2007)
162. J. Habasaki, K.L. Ngai, J. Chem. Phys. **129**, 194501 (2008)
163. J. Habasaki, K.L. Ngai, J. Chem. Phys. **129**, 034503 (2008)
164. J. Habasaki, K.L. Ngai, J. Chem. Phys. **139**, 064503 (2013)
165. J. Habasaki, K.L. Ngai, J Electroceram **34**, 43–56 (2015)
166. G.F. Signorini, J.-L. Barrat, M.L. Klein, J. Chem. Phys. **92**, 1294 (1990)
167. M.C.C. Ribeiro, Phys. Rev. B **63**, 094205 (2001)
168. J. Habasaki, K.L. Ngai, Anal. Sci. **24**, 1321 (2008)
169. M.G. Del Popolo, G.A. Voth, J. Phys. Chem. B **108**, 1744 (2004)
170. T.I. Morrow, E.J. Maginn, J. Phys. Chem. B **106**, 12807 (2002)
171. J.N.C. Lopes, J. Deschamps, A.A.H. Padua, J. Phys. Chem. **108**, 2038 (2004)
172. C.G. Hanke, S.L. Price, R.M. Lynden-Bell, Mol. Phys. **99**, 801 (2001)
173. C.J. Margulis, Mol. Phys. **102**, 829 (2004)
174. Y. Wang, S. Izvekov, T. Yan, G.A. Voth, J. Phys. Chem. B **110**, 3564–3575 (2006)
175. Y. Umebayashi, W.-L. Chung, T. Mitsugi, S. Fukuda, M. Takeuchi, K. Fujii, T. Takamuku, R. Kanzaki, S. Ishiguro, J. Comput. Chem. Jpn **7**(4), 125 (2008)
176. J. Habasaki, R. Casalini, K.L. Ngai, J. Phys. Chem. B **114**, 3902 (2010)
177. J. Habasaki, K.L. Ngai, J. Non-Cryst. Solids **357**, 446 (2011)
178. A.L. Lichtenberg, M.A. Lieberman, *Regular and Chaotic Dynamics* (Springer, New York, 1992)
179. M. Gutzwiller, *Chaos in Classical and Quantum Mechanics* (Springer, Berlin, 1990)
180. K.L. Ngai, Comment Solid State Phys. **9**, 127 (1980)
181. K.L. Ngai, Comment Solid State Phys. **9**, 141 (1980)
182. K.L. Ngai, C.T. White, Phys. Rev. B **20**, 2475 (1979)
183. A.K. Rajagopal, K.L. Ngai, S. Teitler, J. Phys. C **17**, 6611 (1984)
184. K.L. Ngai, S.L. Peng, K.Y. Tsang, Physica A **191**, 523 (1992)
185. K.L. Ngai, C.M. Roland, G.N. Greaves, J. Non-Cryst. Solids **182**, 172 (1995)
186. K.Y. Tsang, K.L. Ngai, Phys. Rev. E **54**, R3067 (1996)
187. K.Y. Tsang, K.L. Ngai, Phys. Rev. E **56**, R17 (1997)
188. R.W. Rendell, Phys. Rev. E **48**, R17 (1993)
189. K.L. Ngai, K.Y. Tsang, Phys. Rev. E **60**, 4511 (1999)
190. K.L. Ngai, A.K. Rajagopal, S. Teitler, J. Chem. Phys. **88**, 6088 (1988)
191. A.K. Rajagopal, K.L. Ngai, S. Teitler, Nucl. Phys. B (Proc. Suppl.) **5A**, 97 (1988)
192. K.L. Ngai, A.K. Rajagopal, S. Teitler, Nucl. Phys. B (Proc. Suppl.) **5A**, 103 (1988)
193. K.L. Ngai, R.W. Rendell, J. Non-Cryst. Solids **131–133**, 942 (1991)
194. A.K. Rajagopal, K.L. Ngai, S. Teitler, J. Non-Cryst. Solids **131–133**, 282 (1991)

195. A.K. Rajagopal, K.L. Ngai, S. Teitler, J. Chem. Phys. **92**, 243 (1990)
196. M. Berry, Phys. Scripta **40**, 335 (1989)
197. M.V. Berry, Semiclassical mechanics of regular and irregular motion, in *Chaotic Behavior of Deterministic Systems*, ed. by G. Iooss, R.H. Helleman, R. Stora. Les Houches Lectures, vol. XXXVI (North Holland, Amsterdam, 1983), pp. 171–271
198. O. Bohigas, M.J. Giannoni, C. Schmit, Phys. Rev. Lett. **52**, 1 (1984)
199. M.V. Berry, Proc. R. Soc. Lond. A **413**, 183 (1987)
200. O. Bohigas, Random Matrix Theories and Chaotic Dynamics, in Chaos and Quantum Physics, Les Houches Summer School Session **52**, 87 (1991)
201. E.P. Wigner, in *Statistical Properties of Real Symmetric Matrices with Many Dimensions*. Proceedings of the 4th Canadian Mathematical Congress, Toronto, pp. 174–184. Toronto, Canada: University of Toronto Press (1957)
202. M.L. Mehta, *Random Matrices*, 2nd edn. (Academic, New York, 1991)
203. J. Dyson, J. Mat. Phys. **3**, 140, 157, 166, 1191, 1199 (1962)
204. C.E. Porter, *Statistical Theories of Spectra: Fluctuations* (Academic, New York, 1965)
205. L.P. Gorkov, G.M. Eliashberg, Soviet Phys. JETP **21**, 940 (1965)
206. K.L. Ngai, S. Capaccioli, J. Phys.: Condens. Matter **19**, 205114 (2007)
207. D. Bedrov, G.D. Smith, Macromolecules **39**, 8526 (2006)
208. G.D. Smith, D. Bedrov, J. Polym, Sci.: Part B: Polym. Phys **45**, 627 (2007)
209. K.L. Ngai, R.W. Rendell, The symmetric and fully distributed solution to a generalized dining philosophers problem, in *Relaxation in Complex Systems and Related Topics*, ed. by I.A. Campbell, C. Giovannella (Plenum Press, New York, 1990), pp. 309–316
210. G. Kolata, Science **223**, 917 (1984). The Dining Philosophers Problem, a classic multi-process synchronization problem in computer science first set forth by E. Dijkstra in 1965, and reformulated by Sir Charles Anthony Richard Hoare
211. K. Schmidt-Rohr, H.W. Spiess, Phys. Rev. Lett. **66**, 3020 (1991)
212. E.R. Weeks, J.C. Crocker, A.C. Levitt, A. Schofield, D.A. Weitz, Science **287**, 627 (2000)
213. E.R. Weeks, D.A. Weitz, Phys. Rev. Lett. **89**, 095704 (2002)
214. T. Pakula, J. Teichmann, Mater. Res. Soc. Symp. Proc. **455**, 211 (1997)
215. P. Polanowski, T. Pakula, J. Chem. Phys. **117**, 4022 (2002)
216. F. Kohlrausch. Ueber die elastische Nachwirkung bei der Torsion. Pogg. Ann. Phys. Chem. **119**, 337–368 (1863)
217. F. Kohlrausch. Beiträge zur Kenntniss der elastischen Nachwirkung. Pogg. Ann. Phys. Chem. **128**, 1–20, 207–228, 399–419 (1866)
218. R.S. McKay, J.D. Meiss (eds.), *Hamiltonian Dynamic Systems* (Adam Hilger, Bristol, 1987)
219. S.W. McDonald, A.N. Kaufman, Phys. Rev. Lett. **42**, 1189 (1979)
220. G. Casati, F. Valz-Gris, I. Guarneri, Lett. Nuovo Cimento **28**, 279 (1980)
221. J.P. Keating, S. Müller, Proc. R. Soc. A **463**, 3241 (2007)
222. H.-J. Stöckmann, *Quantum chaos: an introduction* (Cambridge, University Press, Cambridge, UK, 1999)
223. C. Jaffe, W.P. Reinhardt, J. Chem. Phys. **77**, 5191 (1982)
224. R.B. Shirts, W.P. Reinhardt, J. Chem. Phys. **77**, 5204 (1982)
225. K.L. Ngai, J. Phys. C **12**, 6437 (2000)
226. S.H. Strogatz, R. Mirollo, P.C. Mathews, Phys. Rev. Lett. **68**, 2730 (1992)
227. P. Debye, *Polar Molecules* (Dover, New York, 1929)
228. J. Colmenero, A. Alegria, A. Arbe, B. Frick, Phys. Rev. Lett. **69**, 478 (1992)
229. R. Zorn, A. Arbe, J. Colmenero, B. Frick, D. Richter, U. Buchenau, Phys. Rev. E **52**, 781 (1995)
230. J. Colmenero, A. Arbe, G. Coddens, B. Frick, C. Mijangos, H. Reinecke, Phys. Rev. Lett. **78**, 1928 (1997)
231. V.G. Sakai, J.K. Maranas, Z. Chowdhuri, I. Peral, J.R.D. Copley, J. Polym. Sci. Part B Polym. Phys. **43**, 2914 (2005)
232. V.G. Sakai, J.K. Maranas, I. Peral, J.R.D. Copley, Macromolecules **41**, 3701 (2008)

233. G. Wahnström, L.J. Lewis, Phys. A **201**, 150 (1993)
234. J. Colmenero, F. Alvarez, A. Arbe, Phys. Rev. E **65**, 041804 (2002)
235. Y. Khairy, F. Alvarez, A. Arbe, J. Colmenero, Phys. Rev. E **88**, 042302 (2013)
236. A. Triolo, O. Russina, V. Arrighi, F. Juranyi, S. Janssen, C.M. Gordon, J. Chem, Phys. **119**, 8549–8557 (2003)
237. J. Colmenero, A. Arbe, A. Alegria, Phys. Rev. Lett. **71**, 2603 (1993)
238. K.L. Ngai, J. Colmenero, A. Arbe, A. Alegria, Macromolecules **25**, 6727 (1992)
239. J. Colmenero, A. Arbe, A. Alegria, K.L. Ngai, J. Non-Cryst. Solids **172–174**, 229 (1994)
240. A. Arbe, A. Moral, A. Alegría, J. Colmenero, W. Pyckhout-Hintzen, D. Richter, B. Farago, B. Frick, J. Chem. Phys. **117**, 1336 (2002)
241. A. Arbe, J. Colmenero, F. Alvarez, M. Monkenbusch, D. Richter, B. Farago, B. Frick, Phys. Rev. E **67**, 051802 (2003)
242. B. Farago, A. Arbe, J. Colmenero, R. Faust, U. Buchenau, D. Richter, Phys. Rev. E **65**, 051803 (2002)
243. D. Richter, A. Arbe, J. Colmenero, M. Monkenbusch, B. Farago, R. Faust, Macromolecules **31**, 1133 (1998)
244. J. Colmenero, A. Arbe, F. Alvarez, M. Monkenbusch, D. Richter, B. Farago, B. Frick, J. Phys.: Condens. Matter **15**, S1127–S1138 (2003)
245. A. Arbe, J. Colmenero, M. Monkenbusch, D. Richter, Phys. Rev. Lett. **81**, 590 (1998)
246. M. Tachez, R. Mercier, J.P. Malugani, A.J. Dianoux, Solid State Ionics **20**, 93 (1986)
247. A.J. Dianoux, M. Tachez, R. Mercier, J.P. Malugani, J. Non-Cryst. Solids **131-133**, 973 (1991)
248. A.P. Owens, A. Pradel, M. Ribes, S.R. Elliott, J. Non-Cryst. Solids **131-133**, 1104 (1991)
249. K.L. Ngai, O. Kanert, Solid State Ionics **53-56**, 936 (1992)
250. P.N. Segre, P.N. Pusey, Phys. Rev. Lett. **77**, 771 (1996)
251. K.L. Ngai, G.D.J. Phillies, J. Chem. Phys. **105**, 8385 (1996)
252. K.L. Ngai, Macromol. Symp. **146**(117), 776 (1999)
253. S.Z. Ren, W.F. Shi, W.B. Zhang, C.M. Sorensen, Phys. Rev. A **45**, 2416 (1992)
254. G.D.J. Phillies, C. Richardson, C.A. Quinlan, S.Z. Ren, Macromolecules **26**, 6849 (1993)
255. B. Nyström, H. Walderhaug, F.N. Hansen, J. Phys. Chem. **97**, 7743 (1993)
256. K.L. Ngai, Adv. Colloid Interf. Sci. **64**, 1 (1996)
257. M. Adam, M. Delasanti, J.P. Munch, D. Durand, Phys. Rev. Lett. **61**, 706 (1988)
258. R. Belin, G. Taillades, A. Pradel, M. Ribes, Solid State Ionics **136–137,** 1025–1029 (2000)
259. U. Strom, J.R. Hendrickson, R.J. Wagner, P.C. Taylor, Solid State Commun. **15**, 1871 (1974)
260. U. Strom, P.C. Taylor, Phys. Rev. B **16**, 5512 (1977)
261. C. Cramer, K. Funke, T. Saatkamp, Philos. Mag. **B71**, 701 (http://www.tandfonline.com) (1995)
262. M. Tatsumisago, C.A. Angell, S.W. Martin, J. Chem. Phys. **97**, 6868 (1992)
263. C. Cramer, R. Graeber, M.D. Ingram, T. Saatkamp, D. Wilmer, K. Funke, Mater. Res. Soc. Symp. Proc. **369**, 233 (1995)
264. R. Hoppe, T. Kloidt, K. Funke, Ber. Bunsenges. Phys. Chem. **95**, 1025 (1991)
265. K.L. Ngai, C. Cramer, T. Saatkamp, K. Funke, in *Non-Equilibrium Phenomena in Supercooled Fluids, Glasses and Amorphous Materials*, ed. by M. Giorano, D. Leporini, M.P. Tosi (World Scientific, Singapore, 1996), pp. 3–24
266. A.P. Owens, A. Pradel, M. Ribes, S.R. Elliott, J. Non-Cryst. Solids **131–133**, 1104 (1991)
267. A.P. Owens, A. Pradel, M. Ribes, S.R. Elliott, Mater. Res. Soc. Symp. Proc. **210**, 621 (1991)
268. C. Cramer, M. Buscher, Solid State Ionics **105**, 109 (1998)
269. K.L. Ngai, J. Non-Cryst. Solids **248**, 194 (1999)
270. C. León, L. Lucia, J. Santamaria, Phys. Rev. B **55**, 5302 (1997)
271. R.E.W. Casselton, Phys. Status Solidi **2**, 571 (1970)
272. J.M. Dixon, L.D. LaGrange, U. Merten, C.F. Miller, J.T. Porter, J. Electrochem. Soc. **110**, 276 (1963)
273. D.W. Strickler, W.G. Carlson, J. Am. Ceram. Soc. **47**, 122 (1964)

274. H. Nafe, Solid State Ionics **13**, 255 (1984)
275. C. León, L. Lucia, J. Santamaria, Philos. Mag. B **75**, 629 (1997)
276. T.H. Etsell, S.N. Flengas, Chem. Rev. **70**, 339 (1970)
277. J.E. Bauerle, J. Hrizo, J. Phys. Chem. Solids **30**, 565 (1969)
278. S. Shin, M. Ishigame, Phys. Rev. B **34**, 8875 (1986)
279. T. Suemoto, M. Ishigame, Phys. Rev. B **33**, 2757 (1986)
280. J. Solier, I. Cachadiña, A. Dominguez-Rodriguez, Phys. Rev. B **48**, 3704 (1993)
281. A. Rivera, J. Santamaría, C. León, Appl. Phys. Lett. **78**, 610 (2001)
282. M. Kilo, C. Argirusis, G. Borchardt, R.A. Jackson, Phys. Chem. Chem. Phys. **5**, 2219 (2003)
283. M.D. Ingram, C.A. Vincent, A.R. Wandless, J. Non-Cryst. Solids **53**, 73 (1982)
284. S. Murugavel, Phys. Rev. B **72**, 134204 (2005)
285. M. Malki, M. Micoulaut, F. Chaimbault, Y. Vaills, Phys. Rev. Lett. **96**, 145504 (2006)
286. C. Bischoff, K. Schuller, S.P. Beckman, S.W. Martin, Phys. Rev. Lett. **109**, 075901 (2012)
287. H. Jain, N.L. Peterson, Philos. Mag. A **46**, 351 (1982)
288. H.L. Downing, N.L. Peterson, H. Jain, J. Non-Cryst. Solids **50**, 203 (1982)
289. W. Meyer, H. Neldel, Z. Tech. **18**, 588 (1937)
290. G.J. Dienes, J. Appl. Phys. **21**, 1189 (1950)
291. T. Dosdale, R.J. Brooks, J. Mat. Sci. **13**, 167 (1978)
292. A. Schönhals, D. Wolff, J. Springer, Macromolecules **28**, 6254 (1995)
293. E. Marchal, J. Non-Cryst. Solids **172-174**, 902 (1994)
294. D.P. Almond, A.R. West, Solid State Ionics **18 &19**, 1105 (1986)
295. A.S. Nowick, W.-K. Lee, H. Jain, Solid State Ionics **28–30**, 89 (1988)
296. K.L. Ngai, Solid State Ionics **105**, 231–235 (1998)
297. C. Liu, C.A. Angell, J. Non-Cryst. Solids **83**, 162 (1986)
298. M.B.M. Mangion, G.P. Johari, Phys. Chem. Glasses **29**, 225 (1988)
299. R. Krishnamurthy, Y.-G. Yoon, D.J. Srolovitz, R. Car, J. Am. Ceram. Soc. **87**, 1821 (2005)
300. E. Lee, F.B. Prinz, W. Cai, Phys. Rev. B **83**, 052301 (2011)
301. A. Tarancón, A. Morata, F. Peiró, G. Dezanneau, Fuel Cells **11**, 26 (2011)
302. R. Devanathan, W. Weber, S. Singhal, J. Gale, Solid State Ionics **177**, 1251 (2006)
303. K.-S. Chang, Y.-F. Lin, K.-L. Tung, J. Power Sources **196**, 9322 (2011)
304. K.C. Lau, B.I. Dunlap, J. Phys. Condens. Matter **23**, 035401 (2011)
305. T.J. Pennycook, M.J. Beck, K. Varga, M. Varela, S.J. Pennycook, S.T. Pantelides, Phys. Rev. Lett. **104**, 115901 (2010)
306. T.J. Pennycook, M.P. Oxley, J. Garcia-Barriocanal, F.Y. Bruno, C. León, J. Santamaria, S.T. Pantelides, M. Varela, S.J. Pennycook, Eur. Phys. J. Appl. Phys. **54**, 33507 (2011)
307. K.L. Ngai, J. Santamaria, C. León, Eur. Phys. J. B **86**, 7 (2013)
308. M.R. Díaz-Guillén, K. Moreno, J.A. Díaz-Guillén, A.F. Fuentes, K.L. Ngai, J. Garcia-Barriocanal, J. Santamaria, C. León, Phys. Rev. B **78**, 104304 (2008)
309. P.K. Moon, H.L. Tuller, Solid State Ionics **28–30**, 470 (1988)
310. J. Chen, J. Lian, L. Wang, R. Ewing, R. Wang, W. Pan, Phys. Rev. Lett. **88**, 105901 (2002)
311. B.J. Wuensch, K.W. Eberman, C. Heremans, E.M. Ku, P. Onnerud, E.M.E. Yeo, S.M. Haile, J.K. Stalick, J.D. Jorgensen, Solid State Ionics **129**, 111 (2000)
312. M. Pirzada, R.W. Grimes, L. Minervini, J.F. Maguire, K.E. Sickafus, Solid State Ionics **140**, 201 (2001)
313. K.J. Moreno, A.F. Fuentes, U. Amador, J. Santamaría, C. León, J. Non-Cryst. Solids **353**, 3947 (2007)
314. M.A. Subramanian, G. Aravamudan, G.V. Subba Rao, Prog. Solid State Chem. **15**, 55 (1983)
315. R.E. Williford, W.J. Weber, R. Devanathan, J.D. Gale, J. Electroceram. **3–4**, 409 (1999)
316. P. Wilde, C. Catlow, Solid State Ionics **112**, 173 (1998)
317. P. Wilde, C. Catlow, Solid State Ionics **112**, 185 (1998)
318. K. Moreno, G. Mendoza-Suárez, A.F. Fuentes, J. García-Barriocanal, C. León, J. Santamaria, Phys. Rev. B **71**, 132301 (2005)

319. J. García-Barriocanal, K.J. Moreno, G. Mendoza-Suárez, A.F. Fuentes, J. Santamaría, C. León, J. Non. Cryst. Solids **351**, 2813 (2005)
320. C. Heremans, B.J. Wuensch, J.K. Stalick, E. Prince, J. Solid State Chem. **117**, 108 (1995)
321. T. van Dijk, A.J. Burggraaf, Phys. Status Solidi A Appl. Res. **63**, 229 (1981)
322. K.L. Ngai, C. León, Solid State Ionics **125**, 81 (1999)
323. J. García-Barriocanal, K.J. Moreno, A.F. Fuentes, J. Santamaría, C. León, J. Non. Cryst. Solids **352**, 5141 (2006)
324. K.J. Moreno, A.F. Fuentes, J. García-Barriocanal, C. León, J. Santamaría, J. Solid State Chem. **179**, 323 (2006)
325. K. Moreno, A. Fuentes, M. Maczka, J. Hanuza, U. Amador, J. Santamaría, C. León, Phys. Rev. B **75**, 184303 (2007)
326. J. Díaz-Guillén, M.R. Díaz-Guillén, J.M. Almanza, A.F. Fuentes, J. Santamaría, C. León, J. Phys. Condens. Matter **19**, 356212 (2007)
327. J. Díaz-Guillén, A.F. Fuentes, M.R. Díaz-Guillén, J.M. Almanza, J. Santamaría, C. León, J. Power Sources **186**, 349 (2009)
328. H. Yamamura, Solid State Ionics **158**, 359 (2003)
329. A. Kvist, A. Lunden, Zeitschrift Fuer Naturforsch. **20a**, 235 (1965)
330. A.R. West, J. Appl. Electrochem. **3**, 327 (1973)
331. B.A. Boukamp, R.A. Huggins, Phys. Lett. A **58**, 231 (1976)
332. J.T. Kummer, J. Inorg. Nucl. Chem. **29**, 2453 (1967)
333. H. Aono, J. Electrochem. Soc. **136**, 590 (1989)
334. S. Stramare, V. Thangadurai, W. Weppner, Chem. Mater. **15**, 3974 (2003)
335. M. Vijayakumar, Y. Inaguma, W. Mashiko, M.-P. Crosnier-Lopez, C. Bohnke, Chem. Mater. **16**, 2719 (2004)
336. A.G. Belous, G.N. Novitskaya, S.V. Polyanetskaya, Y.I. Gornikov, Neorg. Mater. **23**, 470 (1987)
337. M. Yashima, M. Itoh, Y. Inaguma, Y. Morii, J. Am. Chem. Soc. **127**, 3491 (2005)
338. J.A. Alonso, J. Sanz, J. Santamaría, C. León, A. Várez, M.T. Fernández-Díaz, Angew. Chemie **112**, 633 (2000)
339. Y. Inaguma, C. Liquan, M. Itoh, T. Nakamura, T. Uchida, H. Ikuta, M. Wakihara, Solid State Commun. **86**, 689 (1993)
340. C. León, M. Lucia, J. Santamaria, M. París, Phys. Rev. B **54**, 184 (1996)
341. D. Qian, B. Xu, H.-M. Cho, T. Hatsukade, K.J. Carroll, Y.S. Meng, Chem. Mater. **24**, 2744 (2012)
342. Y. Inaguma, L. Cchen, M. Itoh, T. Nakamura, Solid State Ionics **70–71**, 196 (1994)
343. H. Kawai, J. Electrochem. Soc. **141**, L78 (1994)
344. J. Ibarra, A. Varez, C. León, J. Santamarıa, L.M. Torres-Martinez, J. Sanz, Solid State Ionics **134**, 219 (2000)
345. A. Jonscher, C. León, J. Santamaria, J. Mater. Sci. **3**, 4485 (1998)
346. M.A. París, J. Sanz, C. León, J. Santamaría, J. Ibarra, A. Várez, Chem. Mater. **12**, 1694 (2000)
347. A. Rivera, C. Leon, A. Varez, M.A. Paris, J. Sanz, **310**, 992 (2002)
348. M. Itoh, Y. Inaguma, W. Jung, L. Chen, T. Nakamura, Solid State Ionics **70–71**, 203 (1994)
349. A.G. Belous, Ionics (Kiel). **4**, 360 (1998)
350. O. Bohnke, C. Bohnke, J. Ould Sid'Ahmed, M.P. Crosnier-Lopez, H. Duroy, F. Le Berre, J.L. Fourquet, Chem. Mater. **13**, 1593 (2001)
351. Y. Inaguma, J. Electrochem. Soc. **142**, L8 (1995)
352. G.A. Samara, Solid State Phys. **38**, 1 (1984)
353. Y. Inaguma, M. Itoh, Solid State Ionics **86–88**, 257 (1996)
354. A. Rivera, C. León, J. Santamarıa, A. Varez, O. V'yunov, A.G. Belous, J.A. Alonso, J. Sanz, Chem. Mater. **14**, 5148 (2002)
355. R.M.V. Rao, H. Munekata, K. Shimada, M. Lippmaa, M. Kawasaki, Y. Inaguma, M. Itoh, H. Koinuma, J. Appl. Phys. **88**, 3756 (2000)
356. A. Aharony, D. Stauffer, *Introduction to Percolation Theory*, 2003

357. J. Wicks, L. Börjesson, G. Bushnell-Wye, W. Howells, R. McGreevy, Phys. Rev. Lett. **74**, 726 (1995)
358. K.L. Ngai, G. Floudas, A.K. Rizos, J. Chem. Phys. **106**, 6957 (1997)
359. R. Casalini, K.L. Ngai, C.M. Roland, Phys. Rev. B **68**, 014201 (2003)
360. C. León, J. Santamaría, M.A. París, J. Sanz, J. Ibarra, A. Várez, J. Non. Cryst. Solids **235-237**, 753 (1998)
361. A. Rivera, J. Santamaría, C. León, K.L. Ngai, J. Phys.: Condens. Matter **15**, S1633 (2003)
362. A. Rivera, C. León, J. Sanz, J. Santamaría, C.T. Moynihan, K.L. Ngai, Phys. Rev. B **65**, 224302 (2002)
363. H.B. Callen, T.A. Welton, Phys. Rev. **83**, 34 (1951)
364. C. León, K.L. Ngai, A. Rivera, Phys. Rev. B **69**, 134303 (2004)
365. M.A. Frechero, O.J. Durá, M.R. Díaz-Guillén, K.J. Moreno, J.A. Díaz-Guillén, J. García-Barriocanal, A. Rivera-Calzada, A.F. Fuentes, C. León, J. Non-Cryst. Solids **407**, 349–354 (2015)
366. K.L. Ngai, R.W. Rendell, C. León, J. Non-Cryst. Solids **307–310**, 1039 (2002)
367. W. Lee, J. Liu, A. Nowick, Phys. Rev. Lett. **67**, 1559 (1991)
368. H. Jain, X. Lu, J. Non-Cryst. Solids **196**, 285 (1996)
369. J.R. Macdonald, J. Chem. Phys. **115**, 6192 (2001)
370. J. Habasaki, K.L. Ngai to be published (2016)
371. J. Habasaki, K.L. Ngai, Y. Hiwatari, J. Chem. Phys. **122**, 054507 (2005)
372. J. Habasaki, Y. Hiwatari, Phys. Rev. E **59**, 6962 (1999)
373. C. Donati, S.C. Glotzer, P.H. Poole, W. Kob, S.J. Plimpton, Phys. Rev. E **60**, 3107 (1999)
374. A.P. Sokolov, A. Kisliuk, V.N. Novikov, K. Ngai, Phys. Rev. B **63**, 172204–1 (2001)
375. A. Kulkarni, P. Lunkenheimer, A. Loidl, Ceram. Trans. **92**, 115 (1999)
376. M.R. Díaz-Guillén, J.A. Díaz-Guillén, A.F. Fuentes, J. Santamaría, C. León, Phys. Rev. B **82**, 174304 (2010)
377. S. Estalji, R. Kuchler, O. Kanert, R. Bolter, H. Jain, K.L. Ngai, J. Phys. (Paris) Colloq. C2 **2**, 159 (1992)
378. O. Kanert, R. Kühler, K.L. Ngai, H. Jain, Phys. Rev. B **49**, 76 (1994)
379. S. Estalji, O. Kanert, J. Steinert, H. Jain, K.L. Ngai, Phys. Rev. B **43**, 7481 (1991)
380. M.R. Díaz-Guillén, M.A. Frechero, J.A. Díaz-Guillén, A.F. Fuentes, C. León, J. Electroceram. (2014)
381. G. Chryssikos, L. Liu, C. Varsamis, E. Kamitsos, J. Non-Cryst. Solids **235–237**, 761 (1998)
382. C.H. Hsieh, H. Jain, J. Non-Cryst. Solids **203**, 293 (1996)
383. R. Belin, A. Zerouale, A. Pradel, M. Ribes, Solid State Ionics **143**, 445 (2001)
384. C.A. Angell, Solid State Ionics **105**, 15 (1998)
385. J.E. Kelly, J.F. Cordaro, M. Tomozawa, J. Non-Cryst. Solids **41**, 47 (1980)
386. D.L. Sidebottom, P.F. Green, R.K. Brow, J. Non-Cryst. Solids **183**, 151 (1995)
387. S.W. Martin, C.A. Angell, J. Non-Cryst. Solids **83**, 185 (1986)
388. S.W. Martin, Appl. Phys. A **49**, 239 (1989)
389. P. Bordat, F. Affouard, M. Descamps, K.L. Ngai, Phys. Rev. Lett. **93**, 105502 (2004)
390. P. Bordat, F. Affouard, M. Descamps, J. Non-Cryst. Solids **352**, 4630 (2006)
391. W. Kob, H.C. Andersen, Phys. Rev. E **51**, 4626 (1995)
392. W. Kob, C. Donati, S.J. Plimpton, P.H. Poole, S.C. Glotzer, Phys. Rev. Lett. **79**, 2827 (1997)
393. Á.W. Imre, S. Voss, H. Mehrer, J. Non-Cryst. Solids **333**, 231 (2004)
394. H. Jain, N.L. Peterson, H.L. Downing, J. Non-Cryst. Solids **55**, 283 (1983)
395. Z. Siujian, S. Sakka, J. Non-Cryst. Solids **112**, 347 (1989)
396. S. Nariki, Solid State Ionics **36**, 103 (1989)
397. J. Bruce, M. Ingram, Solid State Ionics **9–10**, 717 (1983)
398. G.V. Chandrashekhar, L.M. Foster, Solid State Commun. **27**, 269 (1978)
399. G.N. Greaves, S.J. Gurman, C.R.A. Catlow, A.V. Chadwick, S. Houde-Walter, C.M.B. Henderson, B.R. Dobson, Philos. Mag. A **64**, 1059 (2006)

400. G.N. Greaves, A.V. Chadwick, M.C. Jermy, M.E. Smith, R. Zhu, J. Non-Cryst. Solids **235–237**, 766 (1998)
401. G. Greaves, Solid State Ionics **105**, 243 (1998)
402. B. Gee, H. Eckert, J. Phys. Chem. **100**, 3705 (1996)
403. H. Eckert, Zeitschrift Für Phys. Chemie **224**, 1591 (2010)
404. J. Swenson, A. Matic, A. Brodin, L. Börjesson, W.S. Howells, Phys. Rev. B **58**, 11331 (1998)
405. C. Rau, P. Armand, A. Pradel, C.P.E. Varsamis, E.I. Kamitsos, D. Granier, A. Ibanez, E. Philippot, Phys. Rev. B **63**, 184204 (2001)
406. S. Balasubramanian, K.J. Rao, J. Phys. Chem. **97,** 8835 (1993)
407. S. Balasubramanian, K.J. Rao, J. Non-Cryst. Solids **181**, 157 (1995)
408. T. Uchino, T. Sakka, Y. Ogata, M. Iwasaki, J. Non-Cryst. Solids **146**, 26 (1992)
409. C.T. Moynihan, N.S. Saad, D.C. Tran, A.V. Lesikar, J. Am. Ceram. Soc. **63**, 458 (1980)
410. J. Swenson, S. Adams, Phys. Rev. Lett. **90**, 155507 (2003)
411. C. Karlsson, A. Mandanici, A. Matic, J. Swenson, L. Börjesson, Phys. Rev. B **68**, 064202 (2003)
412. A. Bunde, M.D. Ingram, P. Maass, J. Non-Cryst. Solids **172–174**, 1222 (1994)
413. P. Maass, A. Bunde, M.D. Ingram, Phys. Rev. Lett. **68**, 3064 (1992)
414. S. Voss, S.V. Divinski, Á.W. Imre, H. Mehrer, J.N. Mundy, Solid State Ionics **176**, 1383 (2005)
415. P. Maass, R. Peibst, J. Non-Cryst. Solids **352**, 5178 (2006)
416. P. Scheidler, W. Kob, K. Binder, G. Parisi, Philos. Mag. B **82**, 283 (2009)
417. K.L. Ngai, Philos. Mag. B **82**, 291 (2002)
418. K.L. Ngai, J. Polym. Sci. Part B Polym. Phys. **44**, 2980 (2006)
419. K.L. Ngai, S. Capaccioli, J. Chem. Phys. **138**, 054903 (2013)
420. J.F. Cordaro, M. Tomozawa, J. Am. Ceram. Soc. **65**, c50 (1982)
421. M. Tomozawa, J.M. Hyde, J.F. Cordaro, M. Yoshiyagawa, Phys. Chem. Glas. **33**, 69 (n.d.)
422. T.J. Higgins, L.P. Boesch, V. Volterra, C.T. Moynihan, P.B. Macedo, J. Am. Ceram. Soc. **56**, 334 (1973)
423. J.M. Hyde, M. Tomozawa, M. Yoshiyagawa, Phys. Chem. Glas. **28**, 174 (1987)
424. B. Roling, A. Happe, M.D. Ingram, K. Funke, J. Phys. Chem. B **103**, 4122 (1999)
425. C. Cramer, S. Brunklaus, E. Ratai, Y. Gao, Phys. Rev. Lett. **91**, 266601 (2003)
426. M. Tomozawa, J. Non-Cryst. Solids **196**, 280 (1996)
427. C.T. Moynihan, L.P. Boesch, Presented at the 79th Annual Meeting of the American Ceramic Society, Chicago, Paper 26-G-77
428. G.N. Greaves, C.R.A. Catlow, B. Vassal, J. Charnock, C.M.B. Henderson, R. Zhu, S. Qiao, Y. Wang, S.J. Gurman, S. Houde-Walter, IOP Conf. Proc. Ser. No. III (Institute of Physics and Physical Society, London, 1990), p. 411
429. F. Ali, A.V. Chadwick, G.N. Greaves, M.C. Jermy, K.L. Ngai, M.E. Smith, Solid State Nucl. Magn. Reson. **5**, 133 (1995)
430. B. Gee, H. Eckert, J. Phys. Chem. **100**, 3705 (1996)
431. J. Swenson, A. Matic, A. Brodin, L. Börjesson, W.S. Howells, Phys. Rev. B **58,** 11331 (1998)
432. K.L. Ngai, H. Jain, Solid State Ionics **18&19**, 362 (1986)
433. W.C. Huang, H. Jain, J. Non-Cryst. Solids **212**, 117 (1997)
434. A.R. Kulkarni, P. Lunkenheimer, A. Loidl, Mater. Chem. Phys. **63**, 93 (2000)
435. C. Karlsson, A. Mandanici, A. Matic, J. Swenson, L. Börjesson, J. Non-Cryst. Solids **307–310**, 1012 (2002)
436. L.P. Boesch, Ph.D. thesis, Catholic University of America, 1975
437. D.E. Day, J. Non-Cryst. Solids **21**, 343 (1976)
438. Y. Haven, B. Verkerk, Phys. Chem. Glass **6**, 38 (1965)
439. B. Hafskjold, X. Li, J. Phys.: Condens. Matter **7**, 2949 (1995)
440. J. Habasaki, K.L. Ngai, Y. Hiwatari, C.T. Moynihan, J. Non-Cryst. Solids **349**, 223 (2004)
441. S. Voss, F. Berkemeier, A.W. Imre, H. Mehrer, Z. Phys. Chem. **218**, 1353 (2004)
442. S. Voss, A.W. Imre, H. Mehrer, Phys. Chem. Chem. Phys. **6**, 3669 (2004)

443. R. Terai, J. Non-Cryst. Solids **6**, 121 (1971)
444. H. Scher, M. Lax, Phys. Rev. B **7**, 4491 (1973)
445. M. Lax, Rev. Mod. Phys. **32**, 25 (1960)
446. H. Scher, E. Montroll, Phys. Rev. B **12**, 2455 (1975)
447. E.W. Montroll, G.H. Weiss, J. Math. Phys. **6**, 167 (1965)
448. J. Tunaley, Phys. Rev. Lett. **33**, 1037 (1974)
449. M. Lax, H. Scher, Phys. Rev. Lett. **39**, 781 (1977)
450. A.A. Kumar, J. Heinrichs, J. Phys. C Solid State Phys. **13**, 2131 (1980)
451. J. Haus, K. Kehr, Phys. Rev. B **28**, 3573 (1983)
452. J. Klafter, R. Silbey, Phys. Rev. Lett. **44**, 55 (1980)

Chapter 5
NMR Experiments in Ionic Conductors

Nuclear Magnetic Resonance (NMR) has been shown to be a useful tool for the study of the structure [1–4] and dynamics [3, 5–11] of ionic conductors. While magic-angle spinning techniques are most often used for obtaining structural details, the dynamics of ion are usually explored by measuring spin-relaxation times [12]. Many of these NMR studies of ionically conducting materials have focused on lithium ion conductors. The reason is probably twofold: on one hand, the huge interest in these materials for their application in solid state batteries due to the usually high lithium mobility; and on the other hand, the existence of two stables isotopes, ^{6}Li and ^{7}Li, with different magnetic dipole and electrical quadrupole moments, that allow studying these ionic conductors from two different views since different NMR interactions are dominant for different probe nuclei [10, 11, 13, 14]. However, in many cases lithium NMR experiments are performed with the ^{7}Li ($I = 3/2$) nucleus rather than ^{6}Li ($I = 1$). This is because of the higher sensitivity of the former due to its higher natural abundance and gyromagnetic ratio, while ^{6}Li experiments require enrichment of the samples. Incidentally a series of $(^6\mathrm{Li},^7\mathrm{Li})_2\mathrm{O}$-$2.88\mathrm{B}_2\mathrm{O}_3$ glasses had been studied for the Li isotope mass dependence of conductivity by Downing et al. [15], and data were explained by the Coupling Model [16]. Recently, NMR spectroscopy has been also shown to be useful to probe the structural changes that occur in battery electrode materials during electrochemical cycling [17]. While most of these studies have been performed *ex situ*, providing considerable insight into the structural and dynamical processes that occur in battery materials at different (previously achieved) states of charge, *in situ* NMR now provides a non-invasive means to study the electrochemically-induced structural changes that occur on cycling a lithium ion battery [18].

In this chapter we will focus in particular on how NMR experiments can be used to study the dynamics of mobile ions in electrolytes, showing examples on different crystalline and glassy lithium ion conductors, and we will also show how the data obtained from these experiments can be compared to electrical conductivity relaxation (ECR) measurements.

J. Habasaki et al., *Dynamics of Glassy, Crystalline and Liquid Ionic Conductors*,
Topics in Applied Physics 132, DOI 10.1007/978-3-319-42391-3_5

5.1 Ion Dynamics Studied by NMR Techniques

The diffusion of ions in solids takes place by their hopping motion from one site to another available one in a discrete lattice. In a previous chapter we have described the use of NMR techniques to study the dynamics of mobile ions in ionic conductors. There are several works dealing with the spin–lattice relaxation (SLR) of interacting magnetic dipoles and quadrupole while ions are diffusing through particular types of crystal structures [19–24], and with the method to detect anisotropic diffusion from 2D or 1D ion transport in some cases [22, 25–30]. In crystalline lithium conductors, there is usually some form of disorder in the sublattice of mobile ions. The effects of disorder on the time dependence of the correlation function for ion diffusion have been also considered by different authors [31–35], trying to account for the different activation energies found experimentally on the low-temperature and high-temperature sides of the $1/T_1$ peak. This departure from the behavior of described by the Bloembergen-Purcell-Pound (BPP) behavior [36] can be the result from replacing the exponential time dependence by a stretched exponential time dependence for the correlation function [8].

Lithium lanthanum titanates, $Li_{3x}La_{2/3-x}TiO_3$, (LLTO) is a family of crystalline lithium ion conductors [37] that has been widely studied by NMR [38–43]. Since its discovery [44–47], this perovskite-type (ABO_3) oxide is among the fastest lithium ion-conducting solid electrolytes known at room temperature. Its conductivity as function of temperature can be seen from Fig. 4.1 in Chap. 4. Although there is often controversy on the exact structure of a particular member of the LLTO series, which seems to be strongly dependent on the details of sintering and quenching procedures of these ceramics, there is agreement that the basic structural unit is a cubic perovskite with titanium atoms at the corners of the cube (B sites), oxygen at the middle on the edges (forming octahedra with Ti at the center), and lanthanum or vacancies at the center of the cube (A sites) [37, 48]. Neutron diffraction experiments have shown that lithium ions are located at the center of the faces, and can thus easily move through the structure due to the presence of vacant A sites [48]. There is evidence of ordering of lanthanum and vacancies at A sites in alternate layers for $x < 0.1$, favoring a 2D motion of Li^+ ions. Such ordering would disappear for higher lithium contents, giving rise to a cubic phase and to a 3D Li^+ motion [41, 49–51].

^{7}Li spectra and relaxation times have been reported by Bohnké et al. for several LLTO samples with different lithium content [38, 40, 52], showing that there is a quadrupolar splitting that depends on composition at least at room temperature, (see Fig. 5.1). At high enough temperature, and if the correlation time is short enough and the ions sample many sites, this splitting depends on the average value of the electric field gradient (EFG). Thus, it is difficult to explain the observed changes in the quadrupolar splitting with composition since the correlation time at a fixed temperature may change with composition. For a given composition, it is found that the splitting increases and the lines broaden by decreasing temperature. At 150 K no satellite peaks are visible, and while the reason for this is not definitely answered, it

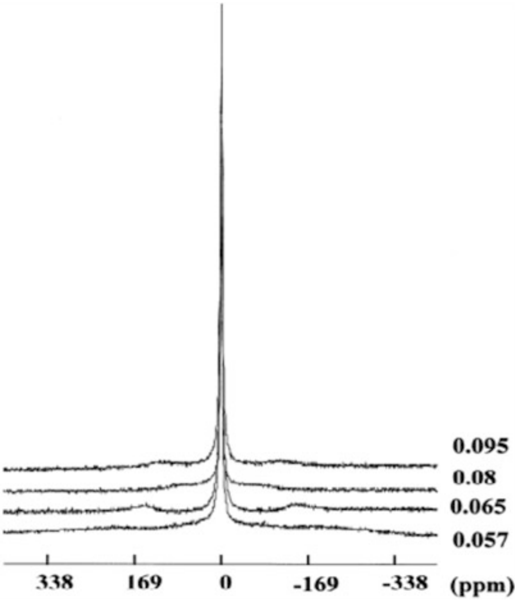

Fig. 5.1 Room temperature ^{7}Li spectra recorded at 116 MHz for $Li_{3x}La_{2/3-x}TiO_3$ samples with different lithium content ($x = 0.057$, 0.065, 0.08 and 0.095). Reproduced from [52] by permission

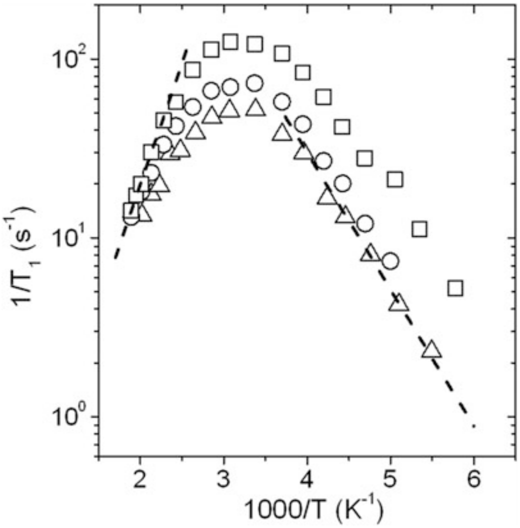

Fig. 5.2 Temperature dependence of $1/T_1$ at 10.6 MHz (*squares*), 20 MHz (*circles*) and 31 MHz (*triangles*) for $Li_{0.5}La_{0.5}TiO_3$. *Dashed lines* have slopes of 0.26 eV at high temperatures and 0.15 eV at low temperatures. Data after Sanz et al. [43]

is possible that satellites become too broad to be observed. The same authors have also reported that, for the sample $Li_{0.33}La_{0.56}TiO_3$ ($x = 0.11$), there is a change from 2D to 3D motion of Li^+ ions by increasing temperature above 200 K, and the onset of motional narrowing of the central transition [38].

Figure 5.2 shows the temperature dependence of the spin–lattice relaxation rate, $1/T_1$, at Larmor frequencies of 10, 20 and 31 MHz, for $Li_{0.5}La_{0.5}TiO_3$ [43]. The rate $1/T_1$ is related to the SLR correlation function $g(t)$ through the equation

$$\frac{1}{T_1(\omega_L, T)} = C\left[J'(\omega_L, T) + 4J'(2\omega_L, T)\right], \tag{5.1}$$

where ω_L is the Larmor frequency, C is a constant, and the spectral density function, $J^*(\omega)$, is the Fourier transform of the SLR correlation function $g(t)$,

$$J^*(\omega, T) = \int_{-\infty}^{\infty} g(t, T)e^{-i\omega t}dt. \tag{5.2}$$

Two different activation energies, E_h and E_l, are obtained, respectively, from the Arrhenius plots of $1/T_1$ at the high and low temperature sides of the peaks. This asymmetry of $1/T_1$ peaks would result from a non exponential correlation function, that is better described instead by a stretched exponential or Kohlrausch–Williams–Watts (KWW) function [53], $g(t) = \exp\left[-(t/\tau_s)^{\beta_s}\right]$ (see Fig. 5.3). According to Ngai's coupling model (CM), activation energies E_s and E_a are defined such that E_s is an activation energy for long range motion of ions and E_a is a microscopic activation energy for local motion free of the effect of cooperativity [31, 54–56]. If the correlation time for ionic motion has an Arrhenius temperature dependence, these activation energies E_s and E_a are directly obtained from the slopes of the high and the low temperature sides of the $1/T_1$ plot respectively, $E_s = E_h$ and $E_a = E_l$, and both energies are related through the β exponent in the KWW correlation function

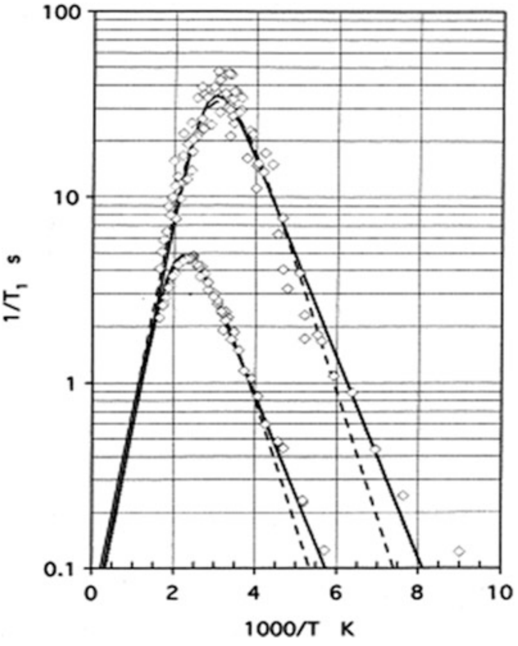

Fig. 5.3 Temperature dependence of $1/T_1$ at 16.1 MHz (*upper curve*), and 116.64 MHz (*lower curve*) for $Li_9B_{19}S_{33}$. Lines are descriptions by the Kohlrausch–Williams–Watts [53] model (*dashed*), and by a Cole–Davidson [58] distribution of correlation times (*solid*). Reproduced from [59] by permission

according to $E_a = \beta_s E_s$ [8, 31, 54, 55, 57]. However, in the case of a non-Arrhenius temperature dependence of the correlation time, activation energies for ionic motion depend on temperature and the relation $E_a = \beta_s E_s$ holds only if both energies are calculated in the same temperature range [43]. Experimental $1/T_1$ curves obtained for $Li_{0.5}La_{0.5}TiO_3$ show an activation energy $E_a = E_l = 0.15$ eV at low temperatures. The activation energy for the high temperature side of the peak cannot be estimated unambiguously except for data measured at 10 MHz, where a value of $E_s = E_h = 0.26$ eV is obtained in the higher temperature range (400 K $< T <$ 500 K). In fact, the same activation energy of 0.26 eV has been obtained for the dc conductivity from electrical conductivity relaxation measurements in this same temperature range (400 K $< T <$ 500 K), suggesting that long range activation energies might be the same if they are measured at this same higher temperature range. However, to compare with $E_a = E_l = 0.15$ eV determined at low temperatures, we must use E_s from NMR at low temperatures, which is not available. Thus the value of E_s is taken from the measured activation energy E_σ of the dc conductivity in the same temperature range (below 250 K), which is equal to 0.4 eV. Putting this value of $E_s = 0.40$ eV and $E_a = 0.15$ eV from the low temperature branches of $1/T_1$ curves into the prediction, $E_a = \beta_s E_s$, the result is $\beta_s = 0.38$. This value is consistent with the frequency dependence, at a fixed temperature, of $1/T_1 \approx \omega_L{}^{-1-\beta s}$ at the low temperature side of $1/T_1$ plots, that yields $\beta_s = 0.4$. The assumption of $E_s \approx E_\sigma$ made is justified because the correlation function of ion are nearly the same for NMR and conductivity relaxation in the case of $Li_{0.5}La_{0.5}TiO_3$. This was implied by the remarks on $Li_{0.5}La_{0.5}TiO_3$ made at the end of Sect. 4.13, and will be reaffirmed later in this chapter.

Lithium titanium sulfide (Li_xTiS_2) is a nice example of the influence that the dimensionality of the ion transport pathways has on the spin–lattice relaxation data [60]. Depending on the lithium content these compounds show a rich polymorphism, and different studies have found cubic ($x \approx 0.6$), trigonal ($x \approx 0.7$), and hexagonal ($x \approx 1$) phases [61, 62]. Figure 5.4 shows the spin-relaxation times T_1, $T_{1\rho}$ and T_2 together with the decay times τ_{SAE} of the stimulated-echo for $LiTiS_2$. Each of these quantities probes ionic dynamics at different time scales. Most remarkable is the fact that, for this hexagonal phase, the spin–lattice relaxation time T_1 is frequency dependent at the high temperature side of the peak, evidencing that the diffusion process is two-dimensional. In fact, the data follow as expected a logarithmic dependence on the Larmor frequency, i.e. on the magnetic field used, over several decades. Such a frequency dependence is absent in the cubic phase, as expected for a three-dimensional diffusion process [10, 60–62].

As mentioned before, the NMR data of crystalline and glassy ionic conductors show similar features. Despite the similarity, the non-exponentiality of the correlation function and the asymmetry in the Arrhenius plots of $1/T_1$, have been ascribed by other as mainly due to the disordered environment felt by the mobile ions even in crystalline materials. But NMR spectroscopy has been particularly useful to investigate the details of structure and dynamics of mobile ions in glasses. There are many works reporting motional narrowing of ^{7}Li or ^{6}Li spectra in glasses, but since it occurs in a relatively narrow temperature range in fast ion conductors,

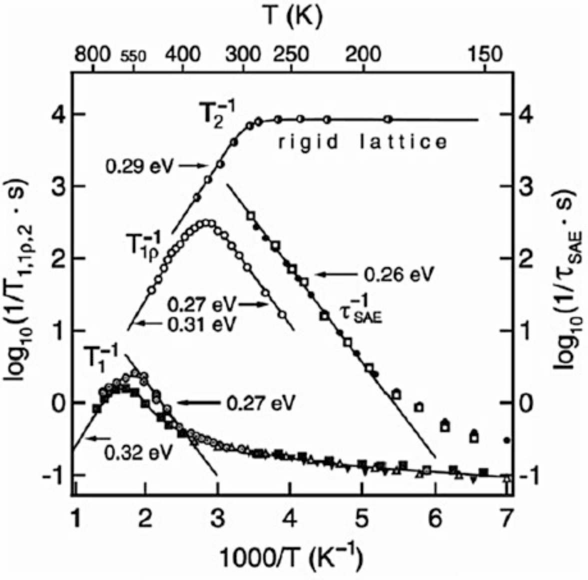

Fig. 5.4 Temperature dependence of several ^{7}Li NMR relaxation rates for $LiTiS_2$. The spin–lattice relaxation rates $1/T_1$ were measured at 9.97 MHz (*circle with dot*), 19.2 MHz (*crossed square*), 32.2 MHz (*open triangle*), and 77.7 MHz (*filled inverted triangle*), and the spin–spin relaxation rate $1/T_2$ at 77.7 MHz (*half filled circle*). The rate $1/T_{1\rho}$ (*open circle*) probes the dynamics in the kHz range, and the spin-alignment measurements (*filled circle* 32.2 MHz, *square* 77.7 MHz) are sensitive to ultra-slow motions of lithium ions. The lines are guides to the eye. Reproduced by permission from [62]

spin–lattice relaxation measurements are usually preferred in order to study the lithium ion dynamics [8, 63–70]. As an example, Fig. 5.5 shows an Arrhenius plot of the spin–lattice relaxation rate for the glassy fast lithium ion conductor $(Li_2S)_{0.56}(SiS_2)_{0.44}$ at several frequencies [70]. The large asymmetry of the $1/T_1$ peaks vs reciprocal temperature and its frequency dependence are indicative of strong non-exponential time dependence of the correlation function. In fact, also shown in the figure are the best fits to a KWW stretched-exponential function, with a value of $\beta_s = 0.35$ for the KWW exponent. The deviation of the NMR data from the curve of best fit was observed at the lowest temperatures, and expecially at the higher frequencies, could to be due to an additional frequency-independent contribution to relaxation. This discrepancy is generally found in fast ion conductors and has been ascribed in the past to be due to localized low frequency excitations arising from the disordered potential landscape [71, 72]. These low frequency excitations have been described by using a broad distribution of asymmetric double well potentials [73, 74] in several glasses [57, 75, 76]. In fact, the observed behavior at the lowest temperatures in the spin–lattice relaxation rate is reminiscent of the nearly constant loss (NCL) measured in electrical conductivity relaxation (ECR) experiments [75, 77–83], which has been recently explained in terms of caged ion

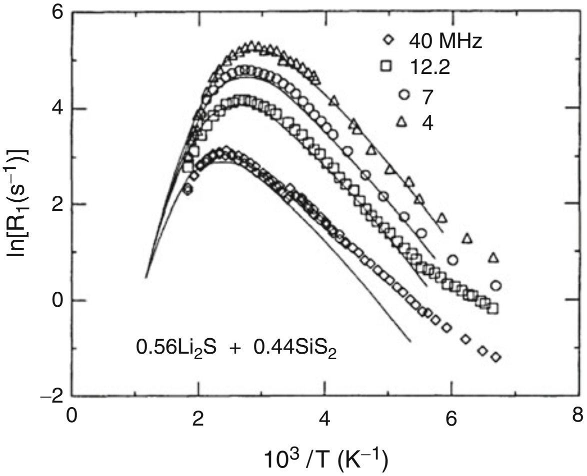

Fig. 5.5 Arrhenius plot of the ^7Li spin–lattice relaxation rate in $0.56Li_2S + 0.44Si_2S$ at several frequencies. *Solid lines* are fits to a KWW correlation function with $\beta s = 0.35$. Reproduced from [70] by permission

motion [84–86]. The properties of the NCL and relation to the conductivity relaxation are discussed at length in Sect. 4.8.

NMR multi-time correlation functions (MT-CF) have recently opened an interesting new avenue towards the understanding of the dynamics of mobile ions in solids [10, 11, 87, 88]. The analysis of NMR stimulated echo signals allows correlating the positions of an ion at two, three, or four points in time, thus providing new insight into the nature of ionic hopping motion. Since the resonance frequency of a nucleus associated with a mobile ion is determined by the local environment, and the environments are in general different for different sites in the solid, translational diffusion gives rise to a time dependence of the resonance frequency. By correlating the resonance frequencies at different times it is possible to obtain information about the ion diffusion process. NMR MT-CF are measured by using the stimulated pulse sequence (pulse - t_p - pulse - t_m - pulse - t_p) that define short evolution times between pulses, $t_p << \tau$, during which the resonance frequencies of the nuclei are probed, and long mixing times $t_m \approx \tau$, during which the resonance frequencies can change due to ion hopping events. Here τ is the correlation time of the ionic hopping motion [89, 90]. If the height of the echo is measured after the stimulated-echo pulse sequence for a constant value of t_p and several t_m, two-time correlation functions (2T-CF) are obtained. Similarly, three-time and four-time correlation functions can be obtained if 2 or 3 different mixing times are separated by corresponding evolution times in the pulse sequence. Actually, these pulse sequences can be considered as consecutive stimulated-echo pulse sequences. These higher order (three-time and four-time) correlation functions are useful when the diffusion process is characterized by non-exponential correlation functions [87].

In general NMR MT-CF depend on the value of the evolution time t_p, but they do not when the spectral widths associated with the quadrupole/chemical shift interactions, $\Delta\omega_i$, and with the dipole-dipole interactions between the nuclei, $\Delta\omega_d$,

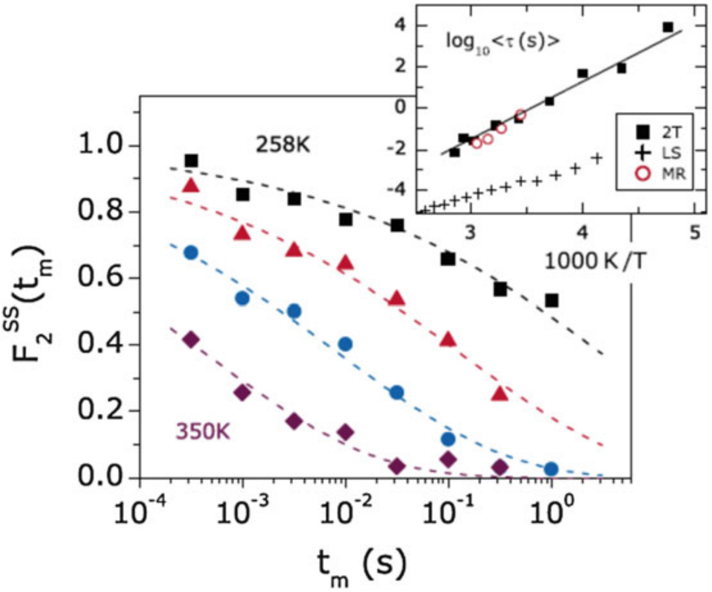

Fig. 5.6 ^{6}Li NMR two time correlation function of LiPO$_3$ glass (50 % ^{6}Li enrichment), obtained from stimulated-echo experiments at 350, 310, 275, and 258 K. All data were corrected for spin diffusion. The evolution time was set to $t_p = 100$ μs. The *dashed lines* are KWW fits with $\beta = 0.27$. The *inset* shows an Arrhenius plot of the mean correlation times obtained from the KWW fits (*solid squares*). The *solid line* is a fit with an Arrhenius law, yielding an activation energy of $E_a = 0.66$ eV. Results from ^{7}Li NMR line-shape analysis (*crosses*) and mechanical relaxation studies (*open circles*) [91] on LiPO$_3$ glass are included for comparison. Reproduced from [10] by permission

satisfy the relation $\Delta\omega_i t_p \gg 1 \gg \Delta\omega_p t_p$ [87]. Then the 2T-CF can be well described by using a Kohlrausch–Williams–Watts (KWW) decay as a function of the mixing time $t_m, F_2(t_p, t_m) \approx F_2(t_m) = (1 - C)\exp\left[-(t_m/\tau_{KWW})^{\beta_{KWW}}\right] + C$, and it represents the probability that an ion occupies the same site after the time t_m. Although dipole-dipole interactions favor the existence of spin diffusion in the case of ^{6}Li and ^{7}Li nuclei, its contribution to stimulated-echo decays can often be separated from that arising from ion dynamics since the former is rather independent of temperature while the latter is thermally activated with the activation energy of ion hopping. Figure 5.6 shows the time dependence of 2T-CF at several temperatures for the LiPO$_3$ glass, once corrected for spin diffusion [66]. It can be observed that indeed the decays are stretched exponentials and the KWW exponent, $\beta_{KWW} = 0.27$, is rather independent of temperature. The inset shows the Arrhenius temperature dependence found for the mean correlation time, which is in agreement with those obtained by mechanical relaxation measurements [91]. It is worth noting that, unlike NMR line-shape analysis, NMR stimulated-echo analysis yields an activation energy that agrees with that obtained from dc conductivity data [92], allowing long range ion transport properties to be probed microscopically. This has been observed also in other lithium ion conductors [93], providing evidence that stimulated-echo experiments probes the elementary steps (ion jumps) of the long range ion diffusion process.

5.2 Relation Between SLR and ECR in Ionic Conductors

Electrical conductivity relaxation (ECR) experimental data in ionic conductors, represented by either the complex conductivity or the complex electric modulus, are determined by how the mobile interacting ions respond to an applied electric field. Thus, these data provide information about the dynamics of mobile ions but are macroscopic in nature. In contrast, nuclear spin relaxation (NSR) is a more direct and microscopic probe of the ionic motion, and from the nuclear spin–lattice relaxation (SLR) experimental data one can directly infer the microscopic dynamics of the ions. Combined studies of ion dynamics using ECR and SLR were first reported at almost the same time by Tatsumisago et al. in Li chloroborate glasses [94, 95], and by Kanert and coworkers in heavy metal fluorozirconate glasses [55, 57, 96], and they all found large difference between the ECR and SLR results. At some temperatures, the NSR correlation time of the mobile ion, τ_s, are several orders of magnitude longer than the ECR time, τ_σ, while the thermal activation energy of τ_s, E_s, is significantly larger than E_σ of τ_σ. Since the two techniques are monitoring motion of the ions, it is puzzling that there is such a pronounced difference between SLR and ECR times and activation energies. Similar differences were subsequently observed in other superionic glasses including $(Li_2S)_{0.56}(SiS_2)_{0.44}$ [70], $x(Li_2S)+(1-x)GeS_2$ [97] and $x(Li_2S)+(1-x)B_2S_3$ [64], and in crystalline Naβ-Al_2O_3 [98], confirming that the effect can be considered as a general property of ionic conductors. Computer experiments by Monte Carlo simulation of ionic motion in disordered lattices, taking into account the Coulomb interactions between the mobile ions [99], found the same difference between SLR and ECR as in real experiments. The proposed explanations are limited to address the difference between the activation energies E_s and E_σ [97, 100–104]. We shall review the explanations given by the CM because they are quantitative and because the CM had successfully explained many properties of SLR and ECR, while explanation of others are qualitative and limited to this problem. However, these explanations in Refs. [97,100–104] did not explain quantitatively the large difference between the magnitudes of τ_s and τ_σ. Further development of the CM had led to the recognition that this difference arises not only from the different correlation functions characterizing ECR and SLR dynamics, but also from the macroscopic and microscopic nature, respectively, of the corresponding measurements [105]. The complete explanation of the difference between SLR and ECR are given next.

It is found in experiments that both the ECR and NSR correlation functions depart from a pure exponential behavior and have the Kohlrausch forms and Arrhenius T-dependences for their relaxation times:

$$\phi_M(t) = \exp\left[-(t/\tau_M)^{1-n_M}\right], \text{ where } \tau_M = \tau_{M,\infty}\exp(E_M/kT) \qquad (5.3)$$

and

$$\phi_s(t) = \exp\left[-(t/\tau_s)^{1-n_s}\right], \text{ where } \tau_s = \tau_{s,\infty}\exp(E_s/kT) \qquad (5.4)$$

As already mentioned, the relations $\tau_s \gg \tau_M$ and $E_s > E_M$ were reported to hold when comparing ECR and NSR data in ionic conducting glasses. Moreover, it was found that $n_s > n_M$. The effect was also found by a Monte Carlo simulation experiment of a disordered Coulomb lattice gas model of the ionic conductor [33, 34, 106, 107]. It is also present in the NMR and conductivity relaxation data of the non-glassy fast ionic conductor sodium β-alumina, Na-βAl$_2$O$_3$, found by Bjorkstam and Villa [108]. A relevant issue that was missed for long time is the fact that electrical conductivity relaxation is a macroscopic probe involving the measurement of capacitance $C(\omega)$ and conductance $G(\omega)$, from which the macroscopic quantities, $\varepsilon^*(\omega)$, $\sigma^*(\omega)$ or $M^*(\omega)$, are obtained. Therefore, the macroscopic electrical conductivity correlation function in Eq. (5.3) fitting the $M^*(\omega)$ is not the microscopic conductivity correlation function, $\phi_\sigma(t)$, for ion transport given by

$$\phi_\sigma(t) = \exp\left[-(t/\tau_\sigma)^{1-n_\sigma}\right], \quad \text{where } \tau_\sigma = \tau_{\sigma,\infty}\exp(E_\sigma/kT). \qquad (5.5)$$

It has been shown [109] that the correlation functions $\phi_M(t)$ and $\phi_\sigma(t)$ are isomorphic, i.e., the Kohlrausch exponents of $\phi_M(t)$ and $\phi_\sigma(t)$ are the same, $n_M = n_\sigma$, because the time dependence or frequency dispersion of the microscopic ion dynamics is faithfully reproduced by the macroscopic measurement (see Section 4.13). The macroscopic τ_M and the microscopic τ_σ are however in general different from each other. They have the same activation energy $E_M = E_\sigma$ but different pre-exponential factors $\tau_{\sigma,\infty}$ and $\tau_{M,\infty}$. On the other hand, nuclear spin–lattice relaxation is a microscopic probe of the dynamics of the mobile ions, and the SLR, $T_1^{-1}(\omega_L, T)$, corresponds to the microscopic correlation function $\phi_s(t)$.

In the following we describe examples of the differences found between ECR and SLR in ionic conductors. Figure 5.7a shows the temperature dependence of the relaxation times obtained from ECR and SLR measurements on a heavy metal fluorozirconate glass with the composition (in mol%): 27.4 ZrF$_4$, 27.4 HfF$_4$, 19.8 BaF$_2$, 3 LaF$_3$, 3.2 AlF$_3$, 20NaF (ZBLAN) [96, 110]. The ionic conductivity due to mobile F$^-$ ions was measured over ranges of frequencies and temperatures, and the ECR time τ_M, its activation energy, E_σ, and the coupling parameter n_σ from these measurements are shown in Fig. 5.7a and Table 5.1. The spin–lattice relaxation (SLR) times τ_s of ZBLAN were obtained from measurements of the ^{19}F spin lattice relaxation rate $T_{1\rho}^{-1}(\omega_L, T)$ in the rotating frame at Larmor frequencies of 28, 42, and 62 kHz. In order to compare the relaxation times obtained from both techniques, the Larmor frequencies were chosen to match those used to measure the conductivity

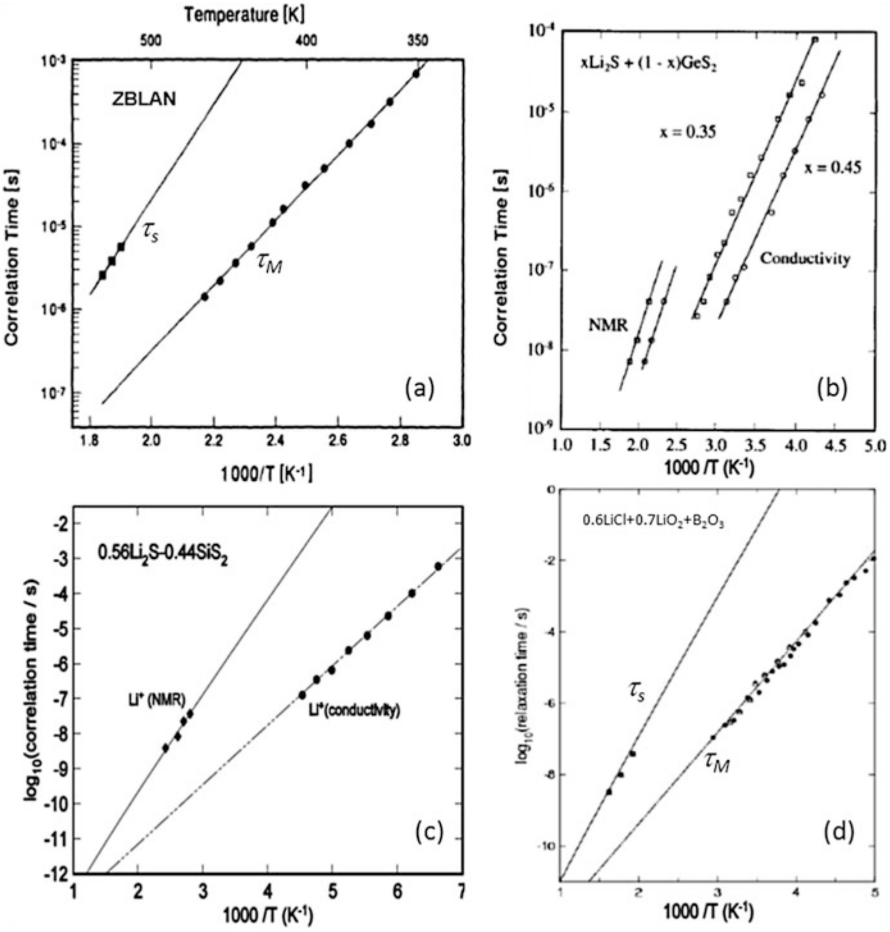

Fig. 5.7 (**a**) ZBLAN conductivity correlation times τ_M from data analysis of the electric modulus and NSR correlation time τ_s from frequency dependence of ^{19}F $1/T_{1\rho}$ maxima plotted against 1000/*T*. From Ref. [57], reproduced by permission. Panels (**b**–**d**) show similar Arrhenius plots of the correlation times, τ_s, deduced from ^{7}Li NMR spin–lattice relaxation measurement, and τ_M, from electrical conductivity measurement for $(Li_2S)_x(GeS_2)_{1-x}$, $(Li_2S)_{0.56}(SiS_2)_{0.44}$ and 0.6LiCl-0.7Li_2O-B_2O_3 respectively. Reproduced from Refs. [97, 100, 104] by permission

relaxation time τ_M [57]. The results of τ_s are shown in Fig. 5.7a, and n_s and E_s determined from fits to temperature dependence of $T_{1\rho}^{-1}(\omega_L, T)$ [57] are given in Table 5.1. All the measurements were performed at temperatures below the glass transition ($T_g = 553$ K) since in the glassy state the temperature dependences of τ_s and τ_M are undoubtedly Arrhenius. The difference between ECR and SLR times is clear from the data, although both measure the motion of the F$^-$ ions.

Another examples are the SLR and ECR experimental data by Kim et al. [64, 97] on Li$^+$ ion motion in the fast glassy ionic conductor $(Li_2S)_x(GeS_2)_{1-x}$ (x = 0.35 and

Table 5.1 The relaxation time τ_s, activation energy E_s and coupling parameters n_s for SLR, and the corresponding quantities, τ_M, E_σ, and n_s for ECR for three different glassy ionic conductors

Ionic conductor	Dynamic variable U	$\beta_U \equiv (1 - n_U)$	E_U^* (K)	$(1 - n_U)E_U^*$ (K)
$(Li_2S)_{0.56}(SiS_2)_{0.44}$	*spin* (SLR)	0.35	5845	2046
$(Li_2S)_{0.56}(SiS_2)_{0.44}$	σ (ECR)	0.52	3911	2034
$(Li_2S)_{0.45}(GeS_2)_{0.55}$	*spin* (SLR)	0.34	5750	1950
$(Li_2S)_{0.45}(GeS_2)_{0.55}$	σ (ECR)	0.44	4730	2080
$(LiCl)_{0.6}(Li_2O)_{0.7}(B_2O_3)$	*spin* (SLR)	0.35	7400	2590
$(LiCl)_{0.6}(Li_2O)_{0.7}(B_2O_3)$	σ (ECR)	0.50	5500	2750
ZBLAN[a]	*spin* (SLR)	0.30	13,346	3830
ZBLAN[a]	σ (ECR)	0.44	9284	4085

[a] 27.4 ZrF, 27.4 HfF, 19.8 BaF, 3 LaF, 3.2 $A1F_3$, 20 NaF (in mol%)

0.45), similar measurements of glassy Li^+ conductor $(Li_2S)_{0.56}(SiS_2)_{0.44}$, by Borsa et al. [70], and the study by Tatsumisago et al. [94, 95] on Li^+ ion motion in the fast glassy ionic conductor $0.6LiCl\text{-}0.7Li_2O\text{-}B_2O_3$. Panels (b-d) in Fig. 5.7 are, respectively, Arrhenius plots of the correlation times for these glasses of the mobile Li^+ ion, τ_s, deduced from ^7Li nuclear spin–lattice relaxation measurement, and the macroscopic electrical conductivity relaxation time, τ_M, from dielectric measurements. Note that in these works, unlike the rotating frame SLR measurements in the tens of kHz range of Kanert and coworkers, the Larmor frequencies of the SLR used are in the 10–100 MHz range, higher than the frequencies used in conductivity relaxation measurements. The activation energies E_s and E_σ, together with the KWW parameters n_s for SLR and n_σ for conductivity relaxation have been determined from the data and are given in Table 5.1.

These differences found experimentally between SLR and ECR have been explained and rationalized within the Coupling Model [100, 103–105]. The microscopic complex conductivity, $\sigma^*(\omega)$, related to the velocity-velocity correlation function of ions, can be written as (for derivation see Section 4.13)

$$\sigma^*(\omega) = \left(Nq^2/kT\right)\left(r_{rms}^2/6\right)(i\omega)\left\{\frac{1}{i\omega\tilde{\phi}_\sigma(\omega)} - 1\right\} \tag{5.6}$$

where N is the density of the mobile ions, q the ion charge, k the Boltzmann constant and T the temperature, and the quantity r_{rms}^2 represents the mean squared displacement of an ion due to a single hopping event. The function, $\tilde{\phi}_\sigma(\omega)$, is the Laplace-Fourier transform of the correlation function $\phi_\sigma(t)$, which is the probability that the ion remains fixed in the time interval $[0,t]$ in the microscopic stochastic transport theory by Scher and Lax [111, 112] discussed in Sect. 4.13. In the context of the coupling model, $\phi_\sigma(t)$ has the form [113, 114],

$$\phi_\sigma(t) = \exp\left[-(t/\tau_\sigma)^{1-n_\sigma}\right], \quad \text{for} \quad t > t_c. \tag{5.7}$$

On the other hand, in NMR measurements the ion-induced spin–lattice relaxation (SLR) is caused by time-dependent fluctuations of the nuclear spin coupling energy ω_{ij} between interacting ion pairs (i,j) [71]. The resulting SLR rate, $T_1^{-1}(\omega_L, T)$, as a function of temperature T at the Larmor frequency ω_L is given by the expression $C[J(\omega_L, T) + 4J(2\omega_L, T)]$. Here C is the coupling constant and $J(\omega,T)$, the spectral density function, is the real part of the Fourier transform, $J(\omega, T) \equiv \mathrm{Re}\int_0^\infty \phi_s(t/\tau_s)\exp(-i\omega t)dt\big)$ of the pair-pair correlation function $\phi_s(t) = \sum_{i,j} < \omega_{ij}(0)\omega_{ij}(t) >$ [105]. If the ion NSR is via magnetic dipole or quadrupolar interactions, it is governed by the correlation function,

$$\phi_s(t) = (1/N)\sum\nolimits_{i\neq j} (1/N)\sum\nolimits_{i\neq j} \left\langle F_{ij}^{(q)}(t)F_{ij}^{(q)}(0)\right\rangle, \tag{5.8}$$

where

$$F_{ij}^{(q)}(t) = q\sqrt{8\pi/15}\,Y_2(q)\Omega_{ij}/r_{ij}^3, \tag{5.9}$$

Y_2 is the spherical harmonics, r_{ij} is the distance between two ions, and $q = 1$, 2 [71]. It is important to note from Eq. (5.6) that $\phi_\sigma(t)$ is effectively a correlation function of an ion while $\phi_s(t)$ from Eq. (5.8) is a correlation function of a pair of ions [100, 104]. It is clear from the $1/r_{ij}^3$ dependence in Eq. (5.9) that $\phi_s(t)$ weighs more heavily on the contributions from ion pairs at smaller distance of separation r_{ij}. Therefore, it is expected that ion-ion interaction has a stronger effect on $\phi_s(t)$ than on $\phi_\sigma(t)$ and this translates in the Coupling Model to a larger SLR coupling parameter n_s in the stretched exponential function, $\phi_s(t) = \exp\left[-(t/\tau_s)^{1-n_s}\right]$ for $t > t_c$ [103]. This important deduction that can be written down explicitly as

$$n_s > n_\sigma, \tag{5.10}$$

follows from the conceptual basis of the Coupling Model. For shorter times, $t < t_c$, interactions have no effect on the correlation function according to the Coupling Model, and the ions are hopping independently of each other (see Sect. 4.4 in Chap. 4 for details). Since both conductivity relaxation and SLR are monitoring the independent hops of the ions at times shorter than t_c, $\phi_\sigma(t)$ and $\phi_s(t)$ are the same and given by $\phi_s(t) = \phi_\sigma(t) = \exp(-t/\tau_o)$ where $\tau_o = \tau_\infty\exp(E_a/kT)$ is the primitive relaxation time and E_a is the activation energy [105, 113]. At time longer than t_c, $\phi_\sigma(t)$ is given by Eq. (5.7). Continuity of $\phi_\sigma(t)$ at t_c leads to

$$\begin{aligned}\tau_\sigma &= \left[t_c^{-n_\sigma}\tau_o\right]^{1/(1-n_\sigma)} = \left[t_c^{-n_\sigma}\tau_\infty\right]^{1/(1-n_\sigma)}\exp\left[\frac{E_a}{(1-n_\sigma)kT}\right]\\ &\equiv \tau_{\sigma,\infty}\exp\left(\frac{E_\sigma}{kT}\right),\end{aligned} \tag{5.11}$$

where, by definition, $\tau_{\sigma,\infty}$ and E_σ are respectively the pre-exponential factor and activation energy of the conductivity relaxation time τ_σ. Similarly, continuity of $\phi_s(t)$ at t_c leads to

$$\tau_s = \left[t_c^{-n_s}\tau_{\mathrm{o}}\right]^{1/(1-n_s)} = \left[t_c^{-n_s}\tau_\infty\right]^{1/(1-n_s)}\exp\left[\frac{E_a}{(1-n_s)kT}\right] \equiv \tau_{s,\infty}\exp\left[\frac{E_s}{kT}\right], \quad (5.12)$$

where $\tau_{s,\infty}$ and E_s are respectively the pre-exponential factor and activation energy of the SLR time τ_s. It can be straightforwardly obtained from Eqs. (5.11) and (5.12) that τ_s and τ_σ are related by

$$\tau_s = \left[t_c^{(-n_s+n_\sigma)}\tau_\sigma{}^{(1-n_\sigma)}\right]^{1/(1-n_s)} \quad (5.13)$$

Therefore, the relation between the activation energies E_s and E_σ of the nuclear SLR times τ_s and conductivity relaxation times τ_M respectively is given by

$$E_s = E_\sigma(1-n_\sigma)/(1-n_s),\ or\ (1-n_s)E_s = (1-n_\sigma)E_\sigma, \quad (5.14)$$

From the relation $n_s > n_\sigma$ deduced within the Coupling Model (CM) framework as well as verified by experiment in glassy ionic conductors, the stronger temperature dependence of τ_s than τ_σ is explained. Moreover, a quantitative test is afforded by comparing the products $(1-n_s)E_s$ with $(1-n_\sigma)E_\sigma$. They should be equal according to the CM, and indeed this is the case (see Table 5.1).

5.2.1 Absence of Difference Between ^{11}B Spin Relaxation and Li Ion Conductivity Relaxation in $(LiCl)_{0.6}(Li_2O)_{0.7}(B_2O_3)$

In explaining the difference between E_s and E_σ, we have used the example of the $1/r_{ij}{}^3$ dependence in Eq. (5.9) that $\phi_s(t)$ of the mobile ion is a ion-ion pair correlation function weighing more heavily on the contributions from ion pairs at smaller distance of separation r_{ij}. By contrast the correlation function $\phi_\sigma(t)$ is essentially a one particle correlation function if ignoring the cross-correlation and the associated Haven ratio. The stronger effect of ion-ion interaction on $\phi_s(t)$ than in $\phi_\sigma(t)$ results in a larger n_s than n_σ, and the explanation of experimental findings by the CM Eq. (5.14). However, this is not the case if the SLR comes from the nucleus of an immobile atom in the glassy matrix, such as ^{11}B in $(LiCl)_{0.6}(Li_2O)_{0.7}(B_2O_3)$ [69]. The SLR correlation, $\phi_{sB}(t)$, of ^{11}B is contributed from the motion of Li ions sensed by the ^{11}B nucleus, similar to that of diffusion and ECR. Hence the coupling parameter n_B of $\phi_{sB}(t)$ is about the same as n_σ, and it follows from the CM that the ^{11}B SLR correlation time, τ_B, should be nearly the same as τ_σ and with the same activation energy. This additional prediction from the CM led to the examination of the ^{11}B SLR data of Trunnell et al. in Ref. [115]. From the analysis of the data, the additional prediction is verified. For more details and consideration of similar situation in Ag ion borate glass, see Ref. [115].

5.2.2 Quantitative Difference Between the Values of τ_s and τ_M

Notwithstanding the success in understanding the difference between E_s and E_σ, the large difference between the values of τ_s and τ_M has not been accounted for. The reason is that electrical conductivity relaxation measurement provides a macroscopic conductivity relaxation time, τ_M, which does not have the same value as the microscopic conductivity relaxation time τ_σ. Although the temperature dependence of τ_σ is the same as that of τ_M, and the coupling parameter obtained from the macroscopic data is exactly the same as n_σ [109]. However, it is possible to determine the microscopic conductivity relaxation time, τ_σ, from the macroscopic measurement [109], and thus to verify the predicted relation in Eq. (5.13).

As already mentioned in Chap. 4, the electric modulus is often written as $M^*(\omega) = M' + iM'' = M_\infty\left[1 - \int_0^\infty dt \exp(-i\omega t)(-d\Phi/dt)\right]$, a one-sided Fourier transform of a macroscopic decay function $\Phi(t)$ caused by migration of ions [116–118]. Here M_∞ is the reciprocal of the high frequency dielectric constant ε_∞. The ECR data in the electric modulus representation are fitted by $M^*(\omega)$ calculated with the Kohlrausch function $\Phi(t/\tau_M) = \exp\left[-(t/\tau_M)^{1-n_M}\right]$ and the macroscopic parameters, τ_M and $1-n_M$ are determined in the process [119, 120]. It is found that the macroscopic $\Phi(t/\tau_{EM})$ and the microscopic $\phi_\sigma(t/\tau_\sigma)$ are one and the same function of the two different scaled variables, t/τ_{EM} and t/τ_σ, respectively [121] (see Sect. 4.13). Hence, from the Kohlrausch expressions written down earlier for ϕ_σ and Φ respectively, we have $1 - n_\sigma = 1 - n_M$. However, τ_M and τ_σ have different values but they are related to each other by [109]

$$\tau_\sigma/\tau_M = \left(Nq^2 r_{rms}^2\right)/(6kT\varepsilon_o\varepsilon_\infty). \tag{5.15}$$

It is thus possible to calculate the microscopic ion hopping relaxation time, τ_σ, from the macroscopic τ_M, which can be obtained from the ECR experimental data. On combining Eqs. (5.13) and (5.15), the SLR relaxation time can be calculated quantitatively from the ECR relaxation time τ_M by

$$\tau_s = \left[t_c^{(n_M - n_s)}\left(\tau_M N q^2 r_{rms}^2/6kT\varepsilon_o\varepsilon_\infty\right)^{1-n_M}\right]^{1/(1-n_s)}. \tag{5.16}$$

Moreover, the activation energies of SLR times, E_s, and ECR times, E_M, are related by

$$E_s/E_M = (1 - n_M)/(1 - n_s), \tag{5.17}$$

a prediction that has previously been verified by experimental data (see Table 5.1).

In order to test the predicted quantitative difference given by Eq. (5.16) between τ_s and τ_M, we must have their experimental values as well as measured or estimated values of the parameters in the equation. The crossover time t_c of glassy, crystalline and molten ionic conductors has been determined to be about 1–2 ps from isothermal conductivity relaxation spectra at high temperatures [122–124] and temperature dependence of d.c. conductivity [56]. The mobile ion density N can be determined from the chemical composition and the density of the ionic conductor, assuming all ions contribute to conductivity. The quantity r_{rms} is not exactly known in glassy ionic conductors. If there is crystalline analogue to the glass, it can be estimated by the hopping distance of the ion in the crystalline analogue. Otherwise, it can be estimated simply by using the approximation $r_{rms} \approx N^{-1/3}$. The quantities ε_∞, n_M and τ_M are determined from fits of the electrical conductivity relaxation data in the usual manner [118–120] (see also Chap. 4). The theoretical values of τ_s calculated by the right-hand-side of Eq. (5.16) involves only a single parameter from SLR measurements, namely n_s. The experimental value of τ_s at the temperature where the SLR rate attains the maximum value is easily obtained without using any fitting procedure whatsoever from the Larmor measuring frequency ω_L by the relation $\omega_L \tau_s = 0.64$ [70]. Some workers [57, 94, 96] use the simpler relation, $\omega_L \tau_s = 1$ to obtain τ_s from the SLR rate data. Anyhow, the difference of τ_s obtained from the two definitions is small. The SLR Kohlrausch exponent $1-n_s$ in the stretched exponential function, $\phi_s(t) = \exp\left[-(t/\tau_s)^{1-n_s}\right]$ for each ionic conductor can be obtained by fitting the SLR rate, $T_1^{-1}(\omega_L, T)$, as a function of temperature T at the Larmor frequency ω_L as it is usually performed [57, 64, 69, 94, 97, 101, 102, 110]. The τ_M of ionic conductors shown in Fig. 5.7 are Arrhenius in the lower temperature range where conductivity relaxation measurements are made in the typical frequency range of $10^{-2} < \omega/2\pi < 10^6$ Hz. The stretch exponent $1-n_M$ used to fit the isothermal electric modulus data in this frequency range has only slight temperature dependence. It is worthwhile to remark here that the fit using Fourier transform of the Kohlrausch stretched exponential function should be carried out with emphasis of good fit to only the data taken at frequencies not too far above the M'' peak frequency. This practice is the same as that used by Moynihan and coworkers [116, 117, 125]. The reason for us doing this is that the deviation of the data from the Kohlrausch fit at higher frequencies is due to the presence of the unresolved or resolved secondary conductivity relaxation followed by the near constant loss contribution [120], which are processes distinctly different from the primary conductivity relaxation. On the other hand, Svare et al. [126] were not mindful of the faster processes contributing to the electric modulus at high frequencies, and they performed the Kohlrausch fits to electric modulus data of $0.35\mathrm{Li_2S}$

+ $0.65GeS_2$ by including these faster processes are part of the primary conductivity relaxation. Thus, the n_M values they obtained are inaccurate and has more appreciable temperature dependence for peak frequency in the range $10 < \omega_{max}/2\pi < 10^6$ Hz, which is an artifact of the fitting procedure used. It is interesting to note that in the paper by Borsa et al. [70], the real and imaginary parts of the electric modulus of $0.56Li_2S$-$0.44SiS_2$ taken in a similar frequency window as $0.35Li_2S + 0.65GeS_2$ at different temperatures superpose near perfectly on a master curve. Such near perfect superposition of raw data suggests before any fits are made that n_M will not have too much of a temperature dependence.

Since the Larmor frequency is typically about 10 MHz in SLR measurements, they are usually carried out at much higher temperatures than ECR measurements. At the high temperatures near the T_1^{-1} maximum, the measured σ_{dc} of the three glassy ionic conductors considered here show slight deviations from the extrapolation of the Arrhenius temperature dependence obeyed at lower temperatures. In the context of the coupling model, the deviations from Arrhenius extrapolation can originate from some decrease of n_M at high temperatures, compared with the approximately constant value at the lower temperatures of ECR measurements. Unfortunately, the measurement of ECR and hence n_M in most ionic conductors at the high temperatures of SLR measurement is not available because the peak frequency of the electric modulus is well above the high frequency limit of typical instruments. This uncertainty of the actual n_M at high temperatures in Eq. (5.16) can be avoided by using its near constant value at low temperatures and τ_M obtained by extrapolation of its Arrhenius temperature dependence also at low temperatures. Using the procedure explained above, the calculated τ_s of three ionic conductors by Eq. (5.16) are shown as solid lines (labeled in the Figures by "τ_s correctly calculated from τ_σ") in Figs. 5.8, 5.9, 5.10 and 5.11 for three glassy ionic conductors, $0.56Li_2S$-$0.44SiS_2$, $0.45Li_2S + 0.55GeS_2$, $0.6LiCl$-$0.7Li_2O$-B_2O_3, and the crystalline $Li_{0.5}La_{0.5}TiO_3$. The parameters used are listed in Table 5.2. Shown also are the measured τ_M and extrapolated by their Arrhenius dependence to higher temperatures, the τ_σ calculated from them by Eq. (5.15), and the experimental data points of τ_s obtained from the Larmor frequencies. Since r_{rms} is not exactly known, several values less than $N^{-1/3}$ are used to calculate τ_s. It can be observed that, within a reasonable range of possible values of r_{rms}, the calculated values of τ_s are in good agreement with the experimental values. The "primitive" or independent relaxation times τ_o and τ_{oM}, calculated by solving the equations,

$$\tau_\sigma = \left[t_c^{-n_\sigma}\tau_o\right]^{1/(1-n_\sigma)} \tag{5.18}$$

and

$$\tau_M = \left[t_c^{-n_M}\tau_{o,M}\right]^{1/(1-n_M)} \tag{5.19}$$

are also plotted in Fig. 5.8. Finally, the calculated SLR times (line labeled in the figures by "τ_s incorrectly calculated from τ_M") had we replaced the microscopic ion

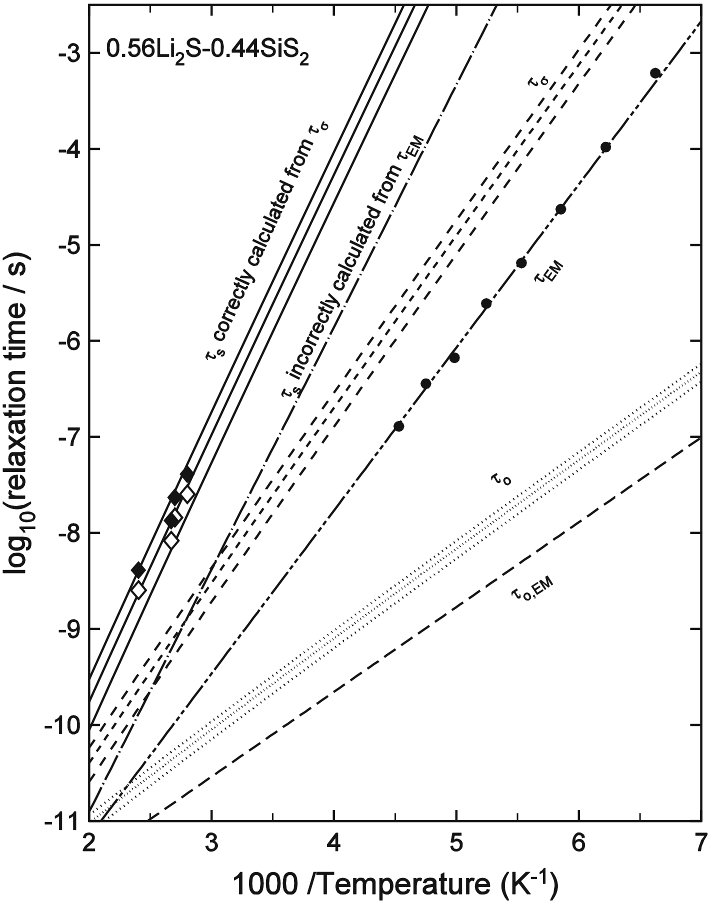

Fig. 5.8 Arrhenius plot of the correlation time of the mobile ion, τ_s, deduced from ^{7}Li nuclear spin–lattice relaxation measurement and the macroscopic electrical conductivity relaxation time, τ_M (labeled here by τ_{EM}), for $0.56Li_2S$-$0.44SiS_2$. Experimental data of τ_s (*filled diamonds* determined by $\omega_L\tau_s = 1$ and *open diamonds* determined by $\omega_L\tau_s = 0.64$), and τ_{EM} (*closed circles*). The three *dashed lines* in descending order are the corresponding microscopic ion hopping relaxation time τ_σ calculated by Eq. (5.15) for $r_{rms} = 3$, 2.5 and 2 Å and other known parameters [105]. The most probable value of r_{rms} is 2.5 Å. The three *dotted lines* in descending order are the corresponding microscopic ion hopping relaxation time τ_o calculated from τ_σ by solving Eq. (5.18) for the three cases of $r_{rms} = 3$, 2.5 and 2 Å. The three *full lines* in descending order are τ_s calculated by Eq. (5.16) with $r_{rms} = 3$, 2.5 and 2 Å respectively and other parameters [105]. There is good agreement with the experimental τ_s. Shown also is the primitive relaxation time $\tau_{o,EM}$ (*dashed line at the bottom*) calculated from τ_{EM} by solving Eq. (5.19). Note that τ_s calculated from $\tau_{0,EM}$ (*dashed-dotted line*) cannot explain the spin-relaxation time data for reason explained in the text. Reproduced from [105] by permission

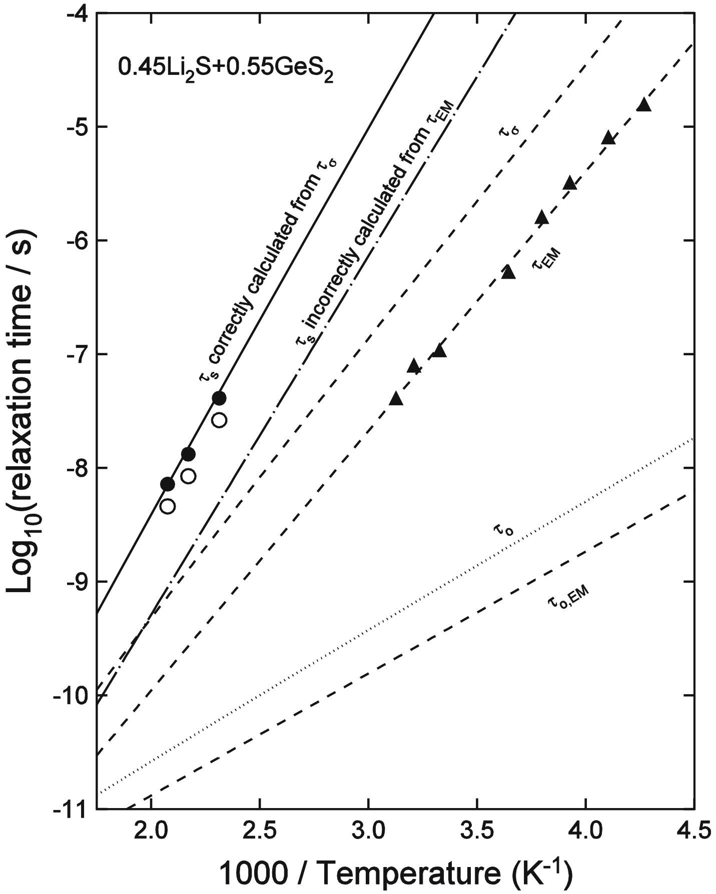

Fig. 5.9 Arrhenius plot of the correlation time of the mobile ion, τ_s, deduced from ^{7}Li nuclear spin–lattice relaxation measurement and the macroscopic electrical conductivity relaxation time, τ_M, for $0.45Li_2S + 0.55GeS_2$. Experimental data of τ_s (*filled and open circles*), and τ_M (*triangles*). The legends of other lines are the same as in the caption of Fig. 5.8, except here only results for $r_{rms} = 2.5$ Å are shown. Reproduced from [105] by permission

hopping time, τ_σ, in Eq. (5.13) by the macroscopic ECR time, τ_M, are also shown in the plots. Naturally, such τ_s does not explain the experimental data of τ_s. Although the inaccuracy in the determination of the quantity r_{rms}in ionic glasses is found to be not very relevant for estimating τ_s, a final example of the excellent agreement between the experimental and theoretically calculated values of τ_s is shown in Fig. 5.8 for the crystalline ionic conductor $Li_{0.5}La_{0.5}TiO_3$ [43, 105, 127], where the value of $r_{rms} = 3.87$ Å is known [45]. The success of Eq. (5.16) to account for the experimental τ_s can be considered as another reminder that τ_M is a macroscopic conductivity relaxation time, while τ_σ is the microscopic conductivity relaxation time. They differ, and the difference is about an order of magnitude for these

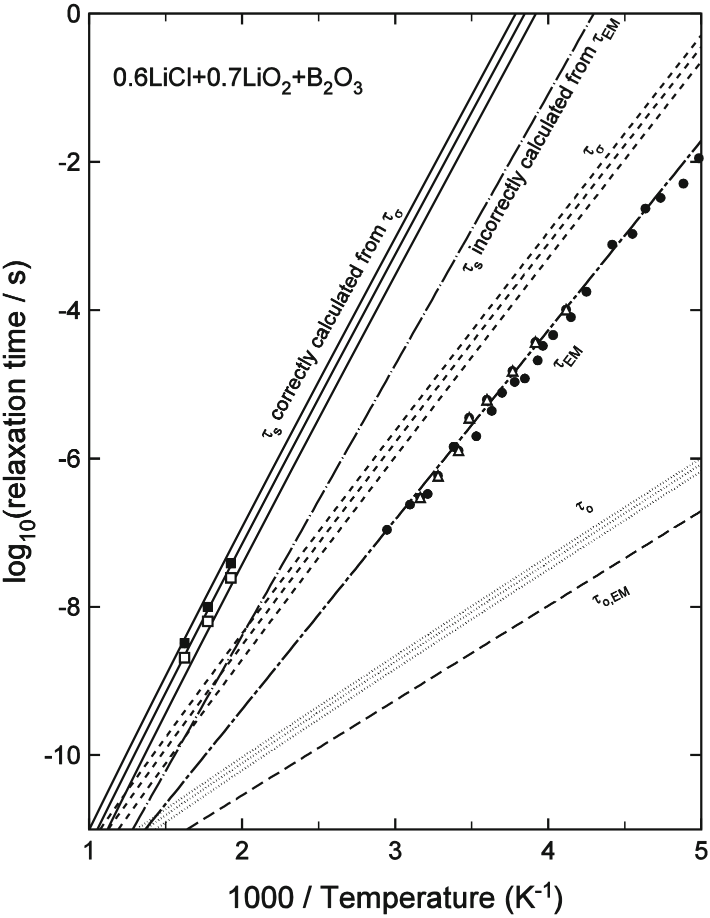

Fig. 5.10 Arrhenius plot of the correlation time of the mobile ion, τ_s, deduced from ^{7}Li nuclear spin–lattice relaxation measurement and the macroscopic electrical conductivity relaxation time, τ_M, for 0.6LiCl-0.7Li$_2$O-B$_2$O$_3$. Experimental data of τ_s (*filled and open squares*), and τ_M (*other symbols*). Legends of other lines are the same as in the caption of Fig. 5.8. Reproduced from [105] by permission

glasses. The difference between their corresponding independent relaxation times τ_o and $\tau_{o,M}$ is smaller. Nevertheless, the difference is important in calculating τ_s and in particular to get good agreement between the calculated τ_s with experimental data [105].

In summary, it is possible to obtain the microscopic conductivity relaxation time τ_σ from its macroscopic counterpart τ_M, and then, by using the Coupling Model (CM), to calculate theoretically τ_s from the parameters obtainable from the conductivity relaxation and spin–lattice relaxation experimental data. Good agreement between the experimental values of τ_s and the theoretical values calculated via Eq. (5.16) are obtained. The predictions from the CM can thus account

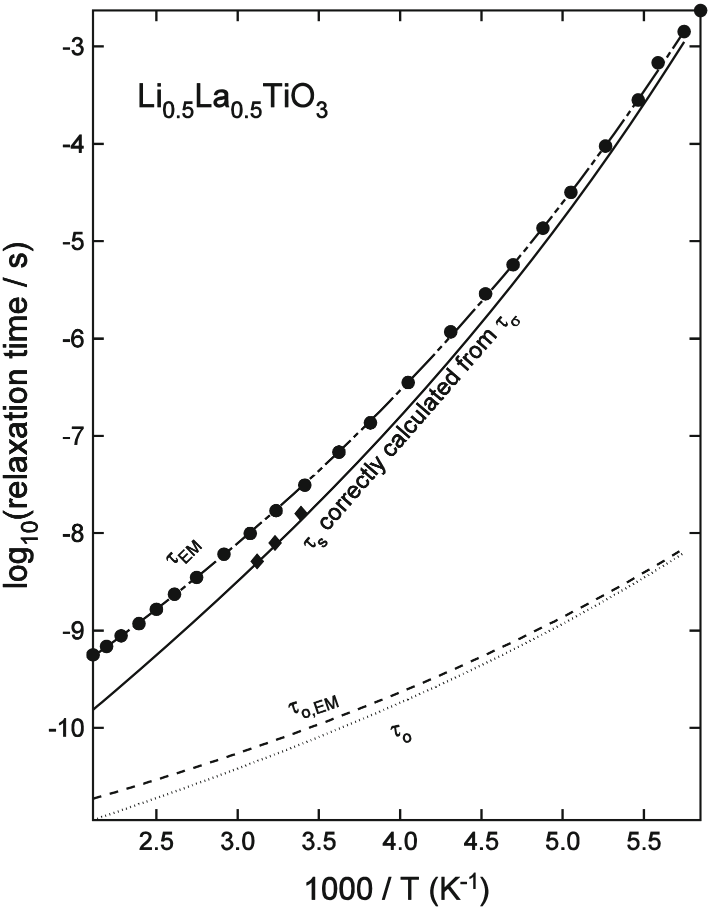

Fig. 5.11 Arrhenius plot of the correlation time of the mobile ion, τ_s, deduced from ^{7}Li nuclear spin–lattice relaxation measurement and the macroscopic electrical conductivity relaxation time, τ_M, for $Li_{0.5}La_{0.5}TiO_3$, a crystalline ionic conductor. Experimental data of τ_s (*filled diamonds*) and τ_{EM} (*filled circles*). The value of $r_{rms} = 3.87$ Å is known. Reproduced from [105] by permission

quantitatively for the large difference found experimentally between the correlation times of conductivity relaxation, τ_M, and of the mobile ion nuclear spin relaxation, τ_s, in ionic conductors. So far and 2 decades have elapsed of time since the publication of the experimental data, no other model has accomplished this feat. In Chap. 4 we have critically reviewed the developments of the works on ion dynamics by Funke and coworkers over the past decades. There we pointed out that despite their scholarly studies, the major accomplishments are limited to fitting the frequency dependence of conductivity $\sigma'(\omega)$. In their 2010 review, fits of $\sigma'(\omega)$ data of 0.45 $LiBr \cdot 0.56\, Li_2O \cdot B_2O_3$ glass [128] were shown as examples. Their Li ion borate glass [129] is similar to $(LiCl)_{0.6}(Li_2O)_{0.7}(B_2O_3)$ in chemical composition, which shows the ion dynamics probed by SLR are drastically different from

Table 5.2 Parameters used to calculate τ_s by the coupling model via Eq. (5.16)

Material	$N \times 10^{-28}$ (m)$^{-3}$	$N^{-1/3}$ (Å)	r_{rms} (Å)	ε_∞	$\beta_{EM} \equiv (1 - n_\sigma)$	$\tau_{EM,\infty}$ (s)	$E_{EM} = E_\sigma$ (K)	$\beta_s \equiv (1 - n_s)$
$0.56Li_2S–0.44SiS_2$	1.9	3.75	2[a], 2.5[a], 3[a]	14	0.48 ± 0.01[b]	4×10^{-15}	4000 ± 100	0.35 ± 0.02[c]
$0.6LiCl–0.7Li_2O–B_2O_3$	1.8	3.82	2[a], 2.5[a], 3[a]	12	0.50 ± 0.01	3×10^{-15}	5500 ± 150	0.35 ± 0.02
$0.45Li_2S–0.55GeS_2$	1.4	4.15	2.5	14.5	0.47 ± 0.01[d]	3×10^{-15}	4730 ± 200	0.34 ± 0.02
$Li_{0.5}La_{0.5}TiO_3$	0.216		3.87[e]	84.7	0.40 ± 0.01	2×10^{-15}	4600 ± 200	0.40 ± 0.02

[a] Arbitrarily chosen to be less than $N^{-1/3}$.

[b] There is a mistake in Table 2 of Ref. [100] in citing the value of β_{EM} determined in Ref. [70] to be 0.52. The present value 0.48 for β_{EM} is the correct one [105]

[c] The same value as given in Refs. [70, 100]

[d] The stretched exponential fits to the ECR data in the electric modulus representation, emphasizing the data at frequencies near and below the peak frequency in the spirit stated in Ref. [116–120], give an approximately constant value of $\beta_{EM} = 0.47 \pm 0.02$

[e] From jump distance of Li ion in the crystalline structure [45]

that by ECR. Explanation of this spectacular and general property of ion dynamics has not been attempted by anyone using Funke's model. This is one of many instances justifying our critique of Funke's model in the previous chapter.

References

1. H. Eckert, Zeitschrift Für Phys. Chemie **224**, 1591 (2010)
2. H. Eckert, Prog. Nucl. Magn. Reson. Spectrosc. **24**, 159 (1992)
3. D. Brinkmann, Prog. Nucl. Magn. Reson. Spectrosc. **24**, 527 (1992)
4. R.J. Kirkpatrick, R.K. Brow, Solid State Nucl. Magn. Reson. **5**, 9 (1995)
5. P. Heitjans, S. Indris, J. Phys. Condens. Matter **15**, R1257 (2003)
6. J.F. Stebbins, Chem. Rev. **91**, 1353 (1991)
7. J. Stebbins, in *Solid State NMR Spectroscopy: Principles and Applications*, ed. by M. Duer (Blackwell Science Ltd, Oxford, UK, 2002), p. 592
8. A. Kuhn, M. Kunze, P. Sreeraj, H.D. Wiemhöfer, V. Thangadurai, M. Wilkening, P. Heitjans, Solid State Nucl. Magn. Reson. **42**, 2 (2012)
9. O. Kanert, Phys. Rep. **91**, 183 (1982)
10. R. Böhmer, K.R. Jeffrey, M. Vogel, Prog. Nucl. Magn. Reson. Spectrosc. **50**, 87 (2007)
11. M. Graf, B. Kresse, A.F. Privalov, M. Vogel, Solid State Nucl. Magn. Reson. **51–52**, 25 (2013)
12. G. Brunklaus, H. Spiess, H. Eckert, in *Methods in Physical Chemistry*, ed. by R. Schäfer, P.C. Schmidt (Wiley-VCH Verlag GmbH & Co. KGaA, Weinheim, 2012), pp. 85–158
13. H. Hain, M. Scheuermann, R. Heinzmann, L. Wünsche, H. Hahn, S. Indris, Solid State Nucl. Magn. Reson. **42**, 9 (2012)
14. T. Hasiuk, K.R. Jeffrey, Solid State Nucl. Magn. Reson. **34**, 228 (2008)
15. H.L. Downing, N.L. Peterson, H. Jain, J. Non-Cryst. Solids **50**, 203 (1982)
16. K. Ngai, R. Rendell, H. Jain, Phys. Rev. B **30**, 2133 (1984)
17. C.P. Grey, N. Dupré, Chem. Rev. **104**, 4493 (2004)
18. N.M. Trease, L. Zhou, H.J. Chang, B.Y. Zhu, C.P. Grey, Solid State Nucl. Magn. Reson. **42**, 62 (2012)
19. H.C. Torrey, Phys. Rev. **92**, 962 (1953)
20. C.A. Sholl, J. Phys. C Solid State Phys. **21**, 319 (1988)
21. W.A. Barton, C.A. Sholl, J. Phys. C Solid State Phys. **13**, 2579 (1980)
22. C.A. Sholl, J. Phys. C Solid State Phys. **14**, 447 (1981)
23. C.A. Sholl, J. Phys. Condens. Matter **13**, 11727 (2001)
24. W.A. Barton, J. Phys. C Solid State Phys. **15**, 5123 (1982)
25. J.L. Bjorkstam, M. Villa, Phys. Rev. B **22**, 5025 (1980)
26. J.-P. Korb, M. Winterhalter, H.M. McConnell, J. Chem. Phys. **80**, 1059 (1984)
27. A.F. McDowell, P.A. Fedders, M.S. Conradi, Phys. Rev. B **58**, 248 (1998)
28. A. Avogadro, M. Villa, J. Chem. Phys. **66**, 2359 (1977)
29. P. Heitjans, M. Wilkening, MRS Bull. **34**, 915 (2009)
30. P.M. Richards, Phys. Rev. B **33**, 3064 (1986)
31. K.L. Ngai, O. Kanert, Solid State Ionics **53–56**, 936 (1992)
32. A. Rajagopal, K. Ngai, S. Teitler, J. Non-Cryst. Solids **131–133**, 282 (1991)
33. D. Knödler, P. Pendzig, W. Dieterich, Solid State Ionics **86–88**, 29 (1996)
34. M. Meyer, P. Maass, A. Bunde, J. Non-Cryst. Solids **172–174**, 1292 (1994)
35. K. Funke, Prog. Solid State Chem. **22**, 111 (1993)
36. N. Bloembergen, E. Purcell, R. Pound, Phys. Rev. **73**, 679 (1948)
37. S. Stramare, V. Thangadurai, W. Weppner, Chem. Mater. **15**, 3974 (2003)
38. O. Bohnke, Solid State Ionics **158**, 119 (2003)

39. O. Bohnke, Solid State Ionics **109**, 25 (1998)
40. J. Emery, O. Bohnké, J.L. Fourquet, J.Y. Buzaré, P. Florian, D. Massiot, J. Phys. Condens. Matter **14**, 523 (2002)
41. A. Rivera, C. Leon, A. Varez, M.A. Paris, J. Sanz, J. of Non-Cryst. Solids 307–310, 992 (2002)
42. C. Leon, J.M. Martin, J. Santamaria, J. Skarp, G. Gonzalez-Diaz, F. Sanchez-Quesada, J. Appl. Phys. **79**, 7830 (1996)
43. C. León, J. Santamaría, M. París, J. Sanz, J. Ibarra, L. Torres, Phys. Rev. B **56**, 5302 (1997)
44. M. Itoh, Y. Inaguma, W. Jung, L. Chen, T. Nakamura, Solid State Ionics **70–71**, 203 (1994)
45. Y. Inaguma, C. Liquan, M. Itoh, T. Nakamura, T. Uchida, H. Ikuta, M. Wakihara, Solid State Commun. **86**, 689 (1993)
46. Y. Inaguma, L. Cchen, M. Itoh, T. Nakamura, Solid State Ionics **70–71**, 196 (1994)
47. A.G. Belous, G.N. Novitskaya, S.V. Polyanetskaya, Y.I. Gornikov, Neorg. Mater. **23**, 470 (1987)
48. J.A. Alonso, J. Sanz, J. Santamaría, C. León, A. Várez, M.T. Fernández-Díaz, Angew. Chemie **112**, 633 (2000)
49. J. Ibarra, A. Rivera, C. Leon, J. Santamarıa, M.A. Laguna, M.L. Sanjuan, J. Sanz, Chem. Mater. **15**, 225 (2003)
50. M.A. París, J. Sanz, C. León, J. Santamaría, J. Ibarra, A. Várez, Chem. Mater. **12**, 1694 (2000)
51. A. Rivera, J. Sanz, Phys. Rev. B **70**, 094301 (2004)
52. J. Emery, J. Buzare, O. Bohnke, J. Fourquet, Solid State Ionics **99**, 41 (1997)
53. G. Williams, D.C. Watts, Trans. Faraday Soc. **66**, 80 (1970)
54. K. Ngai, Solid State Ionics **5**, 27 (1981)
55. K.L. Ngai, J.N. Mundy, H. Jain, O. Kanert, G. Balzer-Jollenbeck, Phys. Rev. B **39**, 6169 (1989)
56. K. Ngai, G. Greaves, C. Moynihan, Phys. Rev. Lett. **80**, 1018 (1998)
57. O. Kanert, R. Küchler, K.L. Ngai, H. Jain, Phys. Rev. B **49**, 76 (1994)
58. D.W. Davidson, R.H. Cole, J. Chem. Phys. **19**, 1484 (1951)
59. R. Bertermann, W. Müller-Warmuth, C. Jansen, F. Hiltmann, B. Krebs, Solid State Ionics **117**, 245 (1999)
60. W. Kuchler, P. Heitjans, A. Payer, R. Schollhorn, Solid State Ionics **70–71**, 434 (1994)
61. P. Heitjans, S. Indris, M. Wilkening, Diffus. Fundam. **2**, 1 (2005)
62. M. Wilkening, P. Heitjans, Defect Diffus. Forum **237–240**, 1182 (2005)
63. M. Wilkening, D. Bork, S. Indris, P. Heitjans, Phys. Chem. Chem. Phys. **4**, 3246 (2002)
64. K. Kim, D. Torgeson, F. Borsa, S. Martin, Solid State Ionics **90**, 29 (1996)
65. C. Angell, Chem. Rev. **90**, 523 (1990)
66. S. Faske, H. Eckert, M. Vogel, Phys. Rev. B **77**, 104301 (2008)
67. S. Faske, B. Koch, S. Murawski, R. Küchler, R. Böhmer, J. Melchior, M. Vogel, Phys. Rev. B **84**, 024202 (2011)
68. M. Storek, R. Böhmer, S.W. Martin, D. Larink, H. Eckert, J. Chem. Phys. **137**, 124507 (2012)
69. M. Trunnell, D.R. Torgeson, S.W. Martin, F. Borsa, J. Non-Cryst. Solids **139**, 257 (1992)
70. F. Borsa, D.R. Torgeson, S.W. Martin, H.K. Patel, Phys. Rev. B **46**, 795 (1992)
71. A. Abragam, *Principles of Nuclear Magnetism* (Oxford University Press, London, 1962)
72. G. Balzer-Jöllenbeck, O. Kanert, J. Steinert, H. Jain, Solid State Commun. **65**, 303 (1988)
73. W.A. Phillips, J. Low Temp. Phys. **7**, 351 (1972)
74. P.W. Anderson, B.I. Halperin, C.M. Varma, Philos. Mag. **25**, 1 (1972)
75. X. Lu, H. Jain, O. Kanert, R. Küchler, J. Dieckhöfer, Philos. Mag. Part B **70**, 1045 (1994)
76. J. Dieckhöfer, O. Kanert, R. Küchler, A. Volmari, H. Jain, Phys. Rev. B **55**, 14836 (1997)
77. W. Lee, J. Liu, A. Nowick, Phys. Rev. Lett. **67**, 1559 (1991)
78. C. León, A. Rivera, A. Várez, J. Sanz, J. Santamaria, K.L. Ngai, Phys. Rev. Lett. **86**, 1279 (2001)
79. X. Lu, H. Jain, J. Phys. Chem. Solids **55**, 1433 (1994)
80. A. Rivera, J. Santamarı́a, C. León, J. Sanz, C.P. Varsamis, G. Chryssikos, K. Ngai, J. Non-Cryst. Solids **307–310**, 1024 (2002)

81. A. Rivera, C. León, J. Sanz, J. Santamaria, C. Moynihan, K. Ngai, Phys. Rev. B **65**, 224302 (2002)
82. A.S. Nowick, A.V Vaysleyb, W. Liu, Solid State Ionics **105**, 121 (1998)
83. K. Ngai, J. Chem. Phys. **110**, 10576 (1999)
84. C. León, K. Ngai, A. Rivera, Phys. Rev. B **69**, 134303 (2004)
85. K. Ngai, C. León, Phys. Rev. B **66**, 064308 (2002)
86. J. Habasaki, K. Ngai, Y. Hiwatari, Phys. Rev. E **66**, 021205 (2002)
87. C. Brinkmann, S. Faske, B. Koch, M. Vogel, Zeitschrift Für Phys. Chemie **224**, 1535 (2010)
88. M. Vogel, C. Brinkmann, H. Eckert, A. Heuer, Phys. Rev. B **69**, 094302 (2004)
89. M. Vogel, C. Herbers, B. Koch, J. Phys. Chem. B **112**, 11217 (2008)
90. M. Vogel, T. Torbrügge, J. Chem. Phys. **125**, 164910 (2006)
91. P.F. Green, D.L. Sidebottom, R.K. Brow, J.J. Hudgens, J. Non-Cryst. Solids **231**, 89 (1998)
92. D.L. Sidebottom, P.F. Green, R.K. Brow, J. Non-Cryst. Solids **183**, 151 (1995)
93. M. Wilkening, C. Mühle, M. Jansen, P. Heitjans, J. Phys. Chem. B **111**, 8691 (2007)
94. M. Tatsumisago, C.A. Angell, S.W. Martin, J. Chem. Phys. **97**, 6968 (1992)
95. C. Angell, Annu. Rev. Phys. Chem. **43**, 693 (1992)
96. S. Estalji, O. Kanert, J. Steinert, H. Jain, K. Ngai, Phys. Rev. B **43**, 7481 (1991)
97. K. Kim, D. Torgeson, F. Borsa, J. Cho, S. Martin, I. Svare, Solid State Ionics **91**, 7 (1996)
98. K. Ngai, Solid State Ionics **61**, 345 (1993)
99. M. Meyer, P. Maass, A. Bunde, Phys. Rev. Lett. **71**, 573 (1993)
100. K.L. Ngai, Phys. Rev. B **48**, 13481 (1993)
101. I. Svare, F. Borsa, D. Torgeson, S. Martin, J. Non-Cryst. Solids **172–174**, 1300 (1994)
102. I. Svare, F. Borsa, D.R. Torgeson, S.W. Martin, Phys. Rev. B **48**, 9336 (1993)
103. K. Ngai, Solid State Ionics **105**, 225 (1998)
104. K.L. Ngai, J. Chem. Phys. **98**, 6424 (1993)
105. K. Ngai, C. León, J. Non-Cryst. Solids **315**, 124 (2003)
106. W. Dieterich, D. Knödler, P. Pendzig, J. Non-Cryst. Solids **172–174**, 1237 (1994)
107. P. Maass, M. Meyer, A. Bunde, Phys. Rev. B **51**, 8164 (1995)
108. M. Villa, J.L. Bjorkstam, Phys. Rev. B **22**, 5033 (1980)
109. K.L. Ngai, C. Leon, Phys. Rev. B **60**, 9396 (1999)
110. S. Estalji, R. Küchler, O. Kanert, R. Bölter, H. Jain, K.L. Ngai, J. Phys. IV **02**, C2 (1992)
111. H. Scher, M. Lax, Phys. Rev. B **7**, 4491 (1973)
112. M. Lax, H. Scher, Phys. Rev. Lett. **39**, 781 (1977)
113. K.L. Ngai, A.K. Jonscher, C.T. White, Nature **277**, 185 (1979)
114. K. Tsang, K. Ngai, Phys. Rev. E **56**, R17 (1997)
115. K.L. Ngai, J. Non-Cryst. Solids **162**, 268 (1993)
116. C.T. Moynihan, L.P. Boesch, N.L. Laberge, Phys. Chem. Glas. **14**, 122 (1973)
117. F.S. Howell, R.A. Bose, P.B. Macedo, C.T. Moynihan, J. Phys. Chem. **78**, 639 (1974)
118. I.M. Hodge, K.L. Ngai, C.T. Moynihan, J. Non-Cryst. Solids **351**, 104 (2005)
119. C. Moynihan, Solid State Ionics **105**, 175 (1998)
120. K.L. Ngai, C.T. Moynihan, MRS Bull. **23**, 51 (1998)
121. K.L. Ngai, C. Leon, Solid State Ionics **125**, 81 (1999)
122. K. Ngai, U. Strom, Phys. Rev. B **38**, 10350 (1988)
123. C. Cramer, M. Buscher, Solid State Ionics **105**, 109 (1998)
124. K.L. Ngai, J. Non-Cryst. Solids **248**, 194 (1999)
125. L.P. Boesch, C.T. Moynihan, J. Non-Cryst. Solids **17**, 44 (1975)
126. I. Svare, S.W. Martin, F. Borsa, Phys. Rev. B **61**, 228 (2000)
127. C. León, M. Lucia, J. Santamaria, M. París, Phys. Rev. B **54**, 184 (1996)
128. K. Funke, R.D. Banhatti, D.M. Laughman, L.G. Badr, M. Mutke, A. Santic, W. Wrobel, E.M. Fellberg, C. Biermann, Zeitschrift Für Phys. Chemie **224**, 1891 (2010)
129. K. Funke, R.D. Banhatti, S. Brückner, C. Cramer, C. Krieger, A. Mandanici, C. Martiny, I. Ross, Phys. Chem. Chem. Phys. **4**, 3155 (2002)

Chapter 6
Nanoionics

Recently, the development of nanotechnology and the possibility of obtaining artificially nanostructured materials have led to new strategies to find materials with high ionic conductivity values [1]. When decreasing the size of the solid below typically 100 nm, at least in one dimension, surface, interface, and, finite size effects may appear and result in enhanced ionic transport [2–4]. Nanotechnology is thus expected to have a large impact on the next generation of fuel cells and solid state batteries, and the term nanoionics has been coined to embrace the new concepts in ion transport and electrochemical storage resulting from nanoscale effects [5]. Today it is possible to grow ultrathin films with a thickness of just a few nanometers and of high crystallinity in large lateral lengthscales of at least several microns [6]. It is also possible to reduce crystallite size in all three dimensions to obtain nanocrystalline materials, and polycrystalline materials with an average grain size in the range from 5 to 100 nm. In nanocrystalline materials, the presence of a large number of grain boundaries or interfacial regions may result in drastic changes of the ionic conductivity [7]. Note that, assuming that the thickness of the grain boundary is about 1 nm, reducing the crystallite size to just a few nanometres results in an increase of the volume fraction of interfacial regions that can be as high as 50 % [8]. In grain boundaries or interfaces many atoms have a reduced coordination number with respect to the bulk, which may lead to an enhanced electronic or ionic diffusion.

In the pioneering work by Tuller and coworkers, a quite remarkable enhancement of the electronic conductivity was discovered on mixed ionic-electronic conductor CeO_2 nanocrystalline samples, which was ascribed to the accumulation of oxygen vacancies at the grain boundary cores [9]. In that work, the conductivity of micro- and nanocrystalline samples was measured as a function of the oxygen partial pressure over a range of about 25 decades (see Fig. 6.1). Two different regimes are found for the microcrystalline sample with grain size of about 5 μm. At high oxygen partial pressure the conductivity is dominated by ionic transport and thus is rather independent of the oxygen partial pressure. At low oxygen partial pressure, the conductivity increases by decreasing the oxygen partial pressure, which

J. Habasaki et al., *Dynamics of Glassy, Crystalline and Liquid Ionic Conductors*,
Topics in Applied Physics 132, DOI 10.1007/978-3-319-42391-3_6

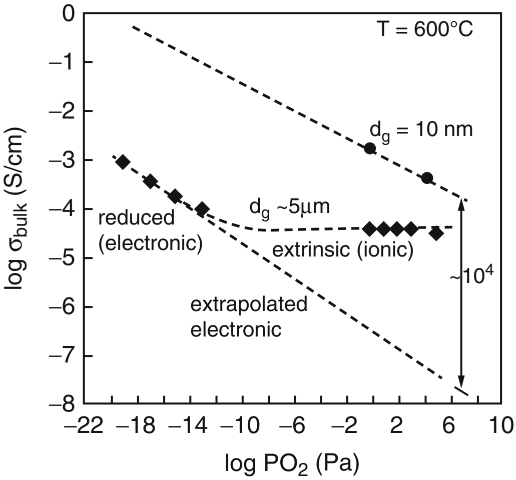

Fig. 6.1 Bulk conductivity of a coarsened CeO_{2-x} polycrystal exhibits electronic and ionic regimes as a function of oxygen partial pressure PO_2. In contrast, the nanocrystal conductivity shows electronic behavior characteristic of a reduced oxide even at high PO_2, and is about four orders of magnitude greater than the extrapolated electronic conductivity of the coarsened polycrystal at 600 °C. Reproduced from Ref. [13] by permission

is taken as evidence that the electronic contribution becomes dominant [10]. In the case of the nanocrystalline sample, with a grain size of 10 nm, the electronic conductivity is enhanced by about four orders of magnitude, and dominates the total conductivity even at high oxygen partial pressures. The result can be explained in terms of the higher concentration of oxygen vacancies in the nanocrystalline sample.

6.1 Space Charge Effects

Not much later, Maier and colleagues [11] broke new grounds in the field of nanoionics by obtaining a large increase of the ionic conductivity in layered BaF_2/CaF_2 heterostructures, grown by molecular beam epitaxy, with layer thicknesses in the nanometre range (see Fig. 6.2). They found that the thinner the layers the larger is the enhancement of the conductivity. They explain the enhancement as a result of an interfacial effect resulting from the transfer of fluorine ions into the CaF_2 side due to the gradient of the electrochemical potential across the interface. This yields enhanced vacancy concentration in the Ba side when the thickness of the individual layers become comparable to the size of the space charge region, i.e. ~ tens of nanometers. Since CaF_2 and BaF_2 are ionic conductors with mobile F^- ions, ion redistribution and the formation of a space-charge region at the interface between the two materials is required from the thermodynamical point of view (uniformity of electrochemical potential) [12].

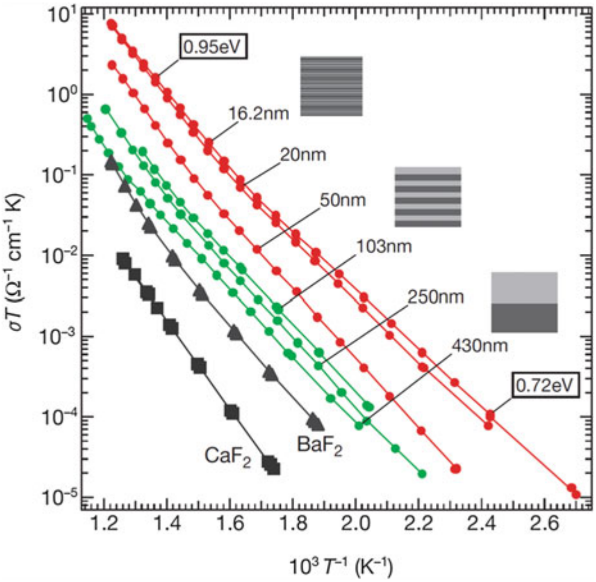

Fig. 6.2 Arrhenius plot of parallel ionic conductivity measured for several layered BaF_2/CaF_2 heterostructures, with an overall film thickness approximately the same in all cases (about 500 nm), but with different bilayer thickness. Reproduced from Ref. [11] by permission

A large ionic conductivity enhancement, of several orders of magnitude, has also been reported for nanocrystalline BaF_2 and CaF_2 as well as in BaF_2:CaF_2 composites with grain sizes between 10 and 30 nm prepared by high-energy ball milling [14], which is much easier to perform than molecular beam epitaxy (MBE). In addition to space-charge effects, the presence of a large concentration of defects in these mechanically prepared samples compared to the thin films might be also relevant for the observed increase in the ionic conductivity.

More recently, an increase of the lithium ion conductivity of about three orders of magnitude has been found by performing impedance spectroscopy measurements in amorphous lithium borate films, with nominal composition $0.2\ Li_2O \cdot 0.8\ B_2O_3$, when decreasing the film thickness from 700 to 7 nm [15]. The authors found that space-charge effects are able to explain their findings, though they favour an interpretation based on the formation of ionic pathways shorting the electrodes that are more numerous as the thickness of the layer is decreased. Heitjans et al. [16] studied lithium ion diffusion in nanocrystalline $(1-x)Li_2O{:}xX_2O_3$ ($X = B$, Al) composite materials formed by mixing nanocrystalline ion conductor with a nanocrystalline insulator. By using ^{7}Li nuclear magnetic resonance (NMR) line shape analyses and spin-lattice relaxation measurements, they found an increase of the lithium ion diffusivity due to Li ions at the hetero-interfaces between the ionic conducting and insulating nanocrystals. NMR technique allows discriminating between slow ions located inside the grains and fast ions at the interfacial regions.

Solid protonic conductors are also very relevant because of their applications in sustainable energy technologies through efficient fuel cells, electrolyzers, and gas-separation membranes [18]. Several nanocrystalline oxide ceramics, such as yttria-doped zirconia or gadolinium-doped ceria have been recently reported to

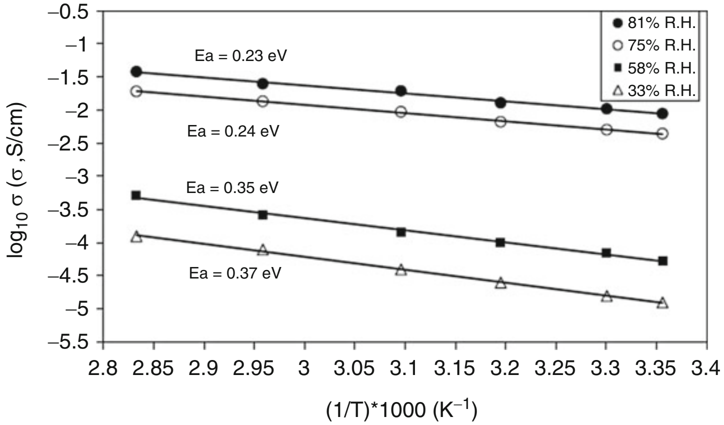

Fig. 6.3 Proton conductivity vs. inverse temperature and corresponding activation energies for TiO_2 anatase thin films at different relative humidity (RH) values. Reproduced from Ref. [17] by permission

present high proton conductivity values near room temperature [19–21]. It has been proposed that protons may diffuse easily along grain-boundary cores as a result of a space-charge layer effect, but it is also possible that adsorbed water at the less dense nanocrystalline ceramics results in the enhanced proton conduction [22]. In this regard, a comparison of electrical conduction experiments in porous and dense nanocrystalline Gd-doped ceria thin films has shown that the residual open porosity, rather than the presence of grain boundaries, is the key factor for the higher protonic conductivity observed near room temperature [23]. Other relevant example of a strong enhancement of the protonic conductivity at the nanoscale is found in TiO_2 anatase and solid acid $CsHSO_4$ composites, where very large hydrogen concentrations in TiO_2 of the order of 10^{21} cm^{-3} have been reported [24]. Nanoporous TiO_2 anatase thin films (see Fig. 6.3) have shown comparable proton conductivity, lower cost, and higher hydrophilicity than Nafion membranes used in proton-exchange membrane fuel cells [17]. First principles density functional theory calculations have indeed shown that proton insertion from $CsHSO_4$ into TiO_2 is favourable, with a negative formation enthalpy, and the estimated average proton concentration in TiO_2 is in good agreement with experimental findings [24].

In contrast to the above mentioned results for BaF_2/CaF_2 heterostructures and composites, as well as for lithium borate nanocrystals and thin films, and proton conducting thin films, controversial results have been reported on the occurrence of an enhancement of the ionic conductivity at the interfaces or grain boundaries of oxide ion conductors such as yttria stabilized zirconia (YSZ), xY_2O_3: $(1-x)ZrO_2$, characterized by a much larger concentration of mobile ions. Among oxide-ion conductors, those of anion-deficient fluorite structure like YSZ are extensively used today as electrolytes in SOFCs [25, 26]. Doping with Y_2O_3 is known to stabilize at room temperature the cubic fluorite structure of ZrO_2, and also to supply the oxygen vacancies responsible for its ionic conductivity [27]. While some authors have reported an increase of the ionic conductivity in nanocrystalline samples [28], others found no changes [29] or even a decrease [30, 31] of the conductivity. For example, Durá et al. [32] reported on the effects of decreasing the grain size between 900 and 17 nm on the oxide-ion conductivity of nanocrystalline YSZ ceramics with 10 % mol yttria content prepared by ball milling. It is worthwhile to mention that they measured X-ray absorption near edge structure (XANES) and extended X-ray absorption fine structure (EXAFS), and found that at the grain boundary the coordination of the absorbing atoms decreases due to the surface effect but without affecting the local structure. They reported also that microstructure and composition of the grain boundary are rather independent of the grain size and similar to that of the bulk [33]. Concerning the results of the ionic conductivity, they used the Brick Layer Model [2, 34, 35] to analyse experimental impedance spectroscopy data and obtain that the specific grain boundary conductivity is rather independent of the grain size, while the bulk conductivity values decrease when decreasing grain size (see Fig. 6.4).

However it is not clear how the implicit oversimplifications made by using the Brick Layer Model in the data analysis might affect the determination of the specific conductivity values for the bulk and grain boundary contributions in such ceramic samples with nanometer grain sizes. ^{18}O tracer diffusion experiments assisted by secondary ion mass spectroscopy also yield contradictory results in YSZ: while 3 orders of magnitude increase of the diffusion coefficient was reported in nanocrystalline thin films as compared with bulk samples [36], no change was found in bulk nanocrystalline ceramics [37]. Furthermore, since the theoretical value of the Debye screening length in these materials is very short, of the order of 0.1 nm for typical dopant concentrations (8 % YSZ) and at intermediate temperatures (500 °C), it is not straightforward to explain the observed increases in ionic conductivity as due to a space-charge effect.

Within the space-charge model [35], the profiles of mobile defects in the space-charge layers are governed by the Poisson equation. The electrochemical potential of any mobile defect species j with an effective charge z at a distance x from the interface plane ($x = 0$) is given by

$$\eta_j(x) = \mu_{0j} + k_\mathrm{B}T\ln c_j(x) + ze\phi(x), \tag{6.1}$$

where $c_j(x)$ is the defect concentration, $\phi(x)$ is the electrostatic potential, μ_{0j} the standard chemical potential, e is the electron charge, k_B the Boltzmann constant, and T the temperature. Far from the interface the electrochemical potential of the defect is

$$\eta_j(\infty) = \mu_{0j} + k_\mathrm{B}T\ln c_j(\infty) + ze\phi(\infty). \tag{6.2}$$

In equilibrium the condition $\eta_j(x) = \eta_j(\infty)$ must be satisfied, and therefore:

$$e\Delta\phi(x) = e\phi(x) - e\phi(\infty) = \frac{k_\mathrm{B}T}{z}\ln\left[c_j(\infty)/c_j(x)\right], \tag{6.3a}$$

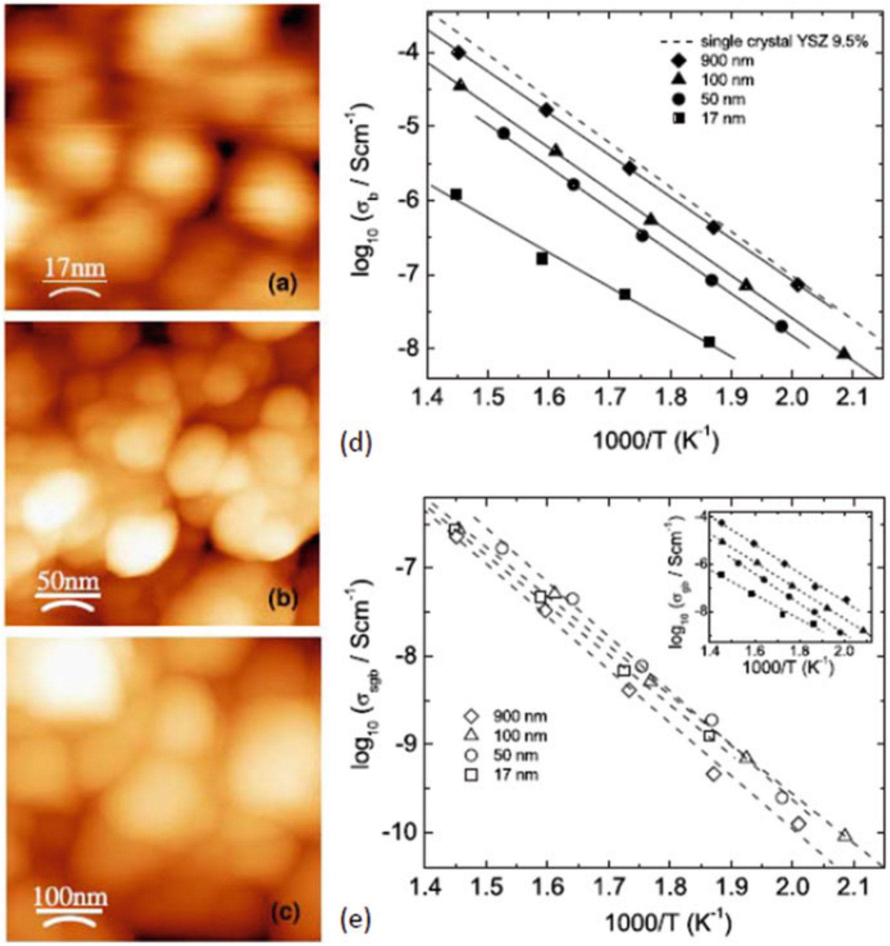

Fig. 6.4 Atomic force microscope images for nanocrystalline 10 % mol YSZ samples with nominal grain size of (**a**) 17 nm, (**b**) 50 nm, and (**c**) 100 nm. (**d**) Arrhenius plot of the bulk ionic dc conductivity for nanocrystalline 10 % mol YSZ samples with different grain sizes. *Dashed line* represents the conductivity data of a 9.5 % mol-YSZ single-crystalline sample for comparison (Ref. [38]). (**e**) Arrhenius plot of the specific grain boundary (*main panel*) and grain boundary (*inset*) conductivities for the same set of samples. Data after Ref. [32]

$$c_j(x)/c_j(\infty) = \exp[-ez\Delta\phi(x)/k_\mathrm{B}T]. \tag{6.3b}$$

In Eq. (6.3a) $\Delta\phi(x) = \phi(x) - \phi(\infty)$ represents the difference between the value of electrostatic potential at a distance x from the interface and the value of electrostatic potential at equilibrium for the bulk (far enough from the interface). $\Delta\phi(x)$ can be solved from the Poisson equation, given by

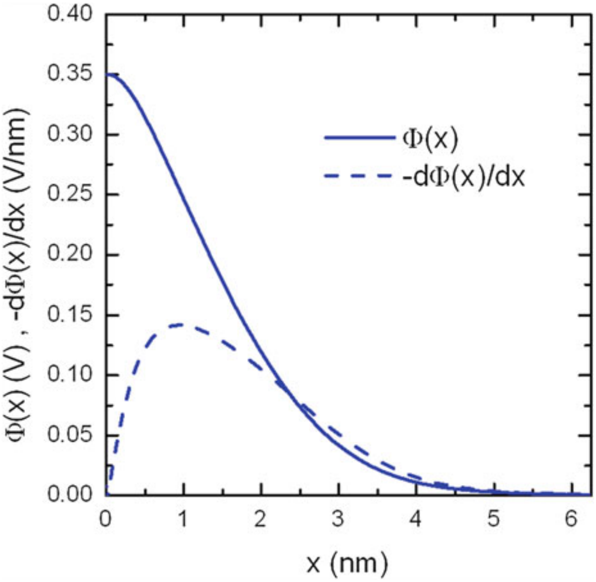

Fig. 6.5 Simulation of the electrostatic potential (*solid line*) and electric field (*dashed line*) as a function of the distance from the interface or grain boundary core in a YSZ bicrystal, as obtained from the numerical solution of the Poisson equation [39]. Here it is assumed that the total net charge is zero and the potential barrier is set to 0.35 eV

$$\frac{\mathrm{d}^2 \Delta\phi(x)}{\mathrm{d}x^2} = -\frac{Q(x)}{\varepsilon\varepsilon_0}, \tag{6.4}$$

with appropriate boundary conditions (see Fig. 6.5). In Eq. (6.4) ε is the dielectric permittivity, ε_0 is the permittivity of a vacuum, and $Q(x)$ is the charge density.

The built-in electrostatic barrier, $\Delta\phi = \phi(0) - \phi(\infty)$, arising at interfaces between ionic conductors where redistribution of electric charge takes place, has been used to explain the observed decrease of ionic conductivity across grain boundaries in polycrystalline materials [5, 35, 40]. Such effects are especially relevant in nanoionic systems, due to the increasing influence of grain boundaries and interfaces compared to the bulk [3, 11, 41]. At grain boundaries the energy for defect generation generally differs from the bulk value and charge neutrality may be broken as a result of defect accumulation or segregation of chemical species. Within the Mott-Schottky model, where the charge density is assumed to be approximately constant in the whole space-charge region, the ensuing electrostatic fields are screened by mobile charges over the space charge layer thickness λ^* determined by the height of the potential barrier $\Delta\phi$, and the Debye screening length L_D of the material [35]. L_D can be estimated from the dopant concentration n_∞ and the dielectric permittivity of the material ε according to the Debye-Hückel theory [42] as:

$$L_D = \left(\frac{\varepsilon\varepsilon_0 k_B T}{2z^2 e^2 n_\infty}\right)^{1/2}. \tag{6.5}$$

According to the Schottky model, the Poisson's equation can be used to obtain the thickness of the space charge layer λ^* given by [12]:

$$\lambda^* = \left(\frac{2\varepsilon\varepsilon_0\Delta\Phi}{zen_\infty}\right)^{1/2}. \tag{6.6}$$

Thus, the relation

$$L_D = \lambda^* \left(\frac{k_B T}{4ze\Delta\Phi}\right)^{1/2}, \tag{6.7}$$

is obtained by combining Eqs. (6.5) and (6.6), which allows an experimental determination of L_D from the Mott-Schottky model. However, a discrepancy between experiment and theory is often encountered, and constituted a long-standing problem in ionic conductors [35]. Such disagreement may arise from a more complex structure of the space charge layer at the grain boundaries, possibly containing a Gouy-Chapman layer instead or besides a Schottky one [2, 43], or from an inhomogeneous charge distribution at an atomic scale due to differences in strain along the grain boundary direction. Furthermore, the existence of multiple grain boundaries, varying grain boundary properties, and unknown ionic pathways *across* as much as *along* grain boundaries are being averaged when measuring the electrical response of grain boundaries in macroscopic ceramic samples. The poor knowledge of the structure and composition changes at the grain boundaries further obscures interpretation of the data. A paradigmatic case is YSZ, where for typical dopant concentrations (10^{27} to 10^{28} m^{-3}) at intermediate temperatures (500 °C), a relatively small value of the Debye screening length of the order of 1 Å is predicted theoretically. However, much higher values of about 1 nm are inferred experimentally from dielectric spectroscopic measurements on YSZ ceramics [35]. These findings cast some doubt on the occurrence itself of space charge layers in YSZ and, consequently, the overall validity of the Debye model in YSZ has been disputed [37, 44, 45].

In order to gain more insight on this issue, Frechero et al. [39] performed a detailed study of the chemistry, structure and transport of a *single* grain boundary in a YSZ bicrystal combining state-of-the-art electron microscopy and spectroscopy, contact microscopy with electrochemical contrast, dielectric spectroscopy on artificially patterned microstructures, and density functional theory (DFT) based calculations. They used a commercial YSZ bicrystal with a doping concentration $y = 0.09$ in moles of Y_2O_3 per formula and a symmetrical $-12°/12°$ [110] tilt grain boundary. Their results were found to be at odds with the conventional understanding of ion transport through grain boundaries based on charge screening by mobile ions as described in terms of Gouy-Chapman or Mott-Schottky models for a space-charge region. They found that ion conductivity across the boundary is indeed strongly depressed. This is shown in Fig. 6.6 where the complex impedance is plotted at several temperatures and the dielectric relaxations of the bulk, grain boundary, and electrodes can be separated and are observed at the highest, intermediate and lowest frequencies respectively. If a space-charge region were associated with each side of the grain boundary, when the frequency of the ac electric field

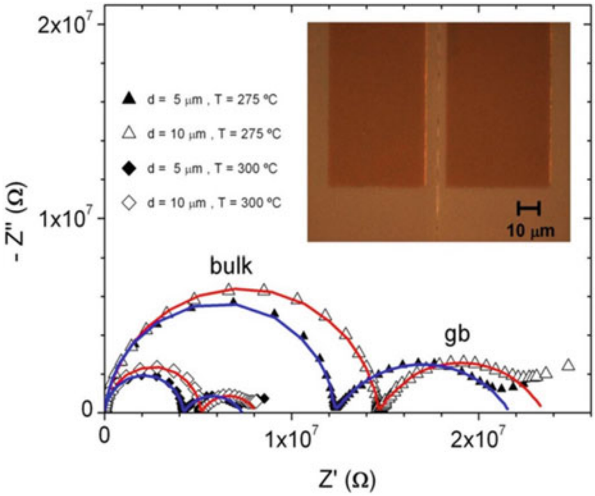

Fig. 6.6 Complex impedance plots at 275 °C (*triangles*) and 300 °C (*diamonds*) showing the contributions to ionic transport due to the bulk (*left semicircle*) and to the grain boundary (gb) (*right semicircle*) in YSZ bicrystals with electrodes separated d = 10 μm (*open symbols*) and 5 μm (*solid symbols*). The *inset* shows an optical microscopy image of the bi-crystalline boundary between the two gold electrodes. Data taken from Ref. [39]

is low enough, positive and negative charge would alternately accumulate at each side of the grain boundary, separated by a distance $2\lambda^*$, due to the blocking of mobile ions. λ^* would be the thickness of the space charge layer at each side of the grain boundary. From the ratio between the bulk (C_b) and grain boundary (C_{gb}) capacitance values (see Fig. 6.7), by using the expression $C_b/C_{gb} \approx 2\lambda^*/d_e$, where d_e is the effective distance between electrodes, a value of $\lambda^* \approx 4 \pm 1$ Å was estimated, of the order of the size of one unit cell. This value is about one order of magnitude smaller than previous estimates from ceramic samples [35]. Moreover, Scanning Transmission Electron Microscopy–Electron Energy Loss Spectroscopy (STEM-EELS) results for the extent of the oxygen depletion on either side of the grain boundary are in excellent agreement with this short λ^* value, pointing to an intimate connection between the structural vacancies and the observed blocking of ion transport, and that the underlying thesis of the Schottky model is not applicable for such short λ^* value [39].

This result evidences that oxygen vacancies found at the grain boundary are structural and not the result of space-charge formation according to the Schottky model. Moreover, the experimental profiles of oxygen vacancies measured by EELS do not show any depletion of oxygen vacancies (see Fig. 6.8), and thus the data cannot be rationalized in terms of conventional space-charge models. It is important to remark that the absence of space charge layers found in YSZ for this particular grain boundary orientation may not be a general result for all grain boundaries in ionic conductors. The formation of space charge layers is more probable to occur in ionic conductors with much lower concentration of mobile

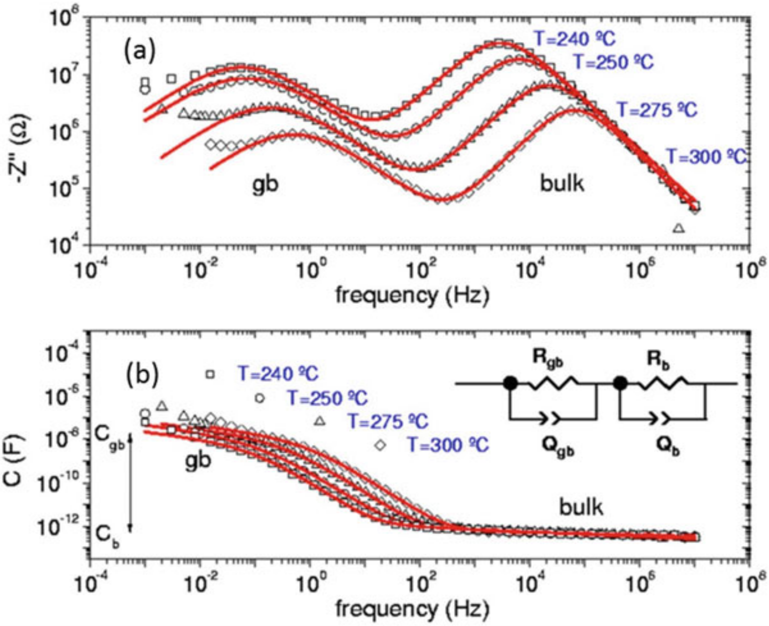

Fig. 6.7 Frequency dependence of the imaginary part of the impedance (*top panel*) and of the capacitance (*bottom panel*) at several temperatures (240 °C, 250 °C, 275 °C, 300 °C from *left to right*) for the same sample shown in Fig. 6.6 with electrode separation d = 10 μm. *Solid lines* are fits to the equivalent circuit shown in the sketch. Data taken from Ref. [39]

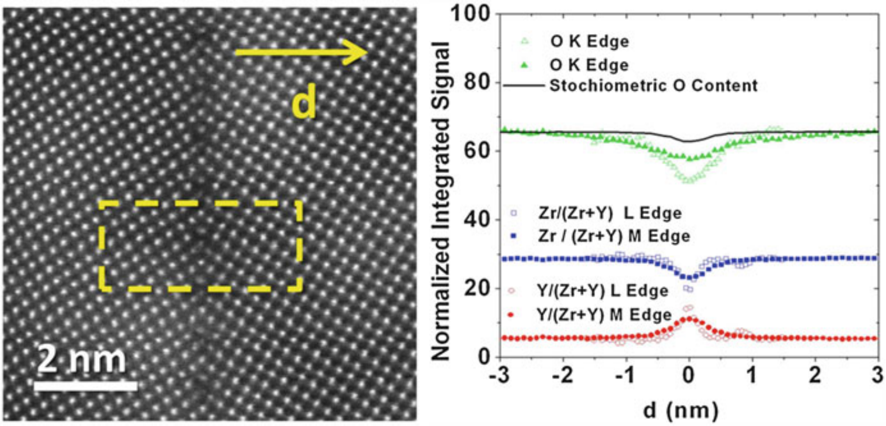

Fig. 6.8 The *left panel* shows a Z-contrast image of the grain boundary region in a YSZ bicrystal with 9 % yttria concentration in moles per formula and a symmetrical −12°/12° [110] tilt grain boundary. The image was obtained in a Nion UltraSTEM 200 electron microscope operated at 200 kV, the *yellow dashed box* marks the area where an EEL spectrum image was acquired. The *right panel* shows normalized integrated signal profiles across the direction marked with an *arrow* on the *left panel*. *Open symbols* correspond to the quantification based on the analysis of the O K and Zr and Y $L_{2,3}$ edges. *Solid symbols* result from a quantification performed on a spectrum image including the O K and the Zr and Y M edges instead. Zr and Y profiles have been normalized to the total cation concentration. The *black line* is the stoichiometric O content that would be expected from the measured Zr and Y signals alone. Data taken from Ref. [39]

ions since it results in longer values of the Debye length. The observed absence of depletion of oxygen vacancies in the YSZ grain boundary by Frechero et al. [39] requires a different explanation for the observed barrier of ion transport at the grain boundary. They performed density functional theory (DFT) calculations and showed that charge neutrality is not achieved by an oxygen-depleted vacancy layer, but rather by a negatively charged core created by acceptor states at the grain boundary. Thus, oxygen vacancies arriving at one side of a grain boundary initially face an attractive potential because of the mild negative charge on grain boundaries. However, for vacancies to depart from the other side they would have to climb out of an electrostatic well that attracts them toward the grain boundary, naturally resulting in an increase of the barrier for ion transport.

Frechero et al. [39] conducted also nanoscale mapping of electrochemical activity using electrochemical strain microscopy (ESM) in order to probe local ion conductivity close to the grain boundary plane, and found that the mobility of oxygen ions is indeed much lower than in the bulk [46, 47]. ESM provided a direct image of how the grain boundary acts as a barrier for ion transport and showed the power of this new technique to study ion dynamics at a microscopic scale.

6.2 Oxide Thin Films and Interfaces

Whether or not space-charge effects are always relevant to explain ionic transport at interfaces, the possibility of an enhanced ionic conductivity in YSZ nanostructures triggered large activity in the field, since it may result in a significant impact in the design of solid oxide fuel cell (SOFC) electrolytes with operation temperatures closer to room temperature [48] or in materials with higher oxygen exchange rates that could be used as novel electrodes [49]. Tuller et al. [28] reported a two orders of magnitude increase of the ionic conductivity of thin films of YSZ deposited by spin coating on Al_2O_3, when their thickness is reduced into the 10 nm range. Later, Kosacki et al. [44] also reported a large increase of the conductivity of 10 % mol yttria-doped YSZ epitaxial thin films grown on MgO substrates when the thickness is reduced down to 15 nm. Interestingly, they found that the increase by more than two orders of magnitude of the dc conductivity at 400 °C is accompanied by a concomitant reduction of the activation energy down to 0.62 eV, and propose that the conductivity increase is due to a highly conducting 1 nm layer at the YSZ/MgO interface (see Fig. 6.9). These results have been explained in the framework of the Coupling Model in terms of weaker ion-ion interactions in the diffusion process at the interface (see Sect. 6.3.1).

Karthikeyan et al. [50] have measured a more moderate conductivity increase, of about one order of magnitude, on 17 nm YSZ polycrystalline multiphase thin film samples grown on MgO. On the other hand, Guo et al. [51] found a decrease of the ionic conductivity of 12 nm thick nanograined polycrystalline YSZ thin films deposited on MgO as compared to 8 % mol yttria-doped bulk ceramics, and essentially no change of the activation energy. Altogether, these results suggest

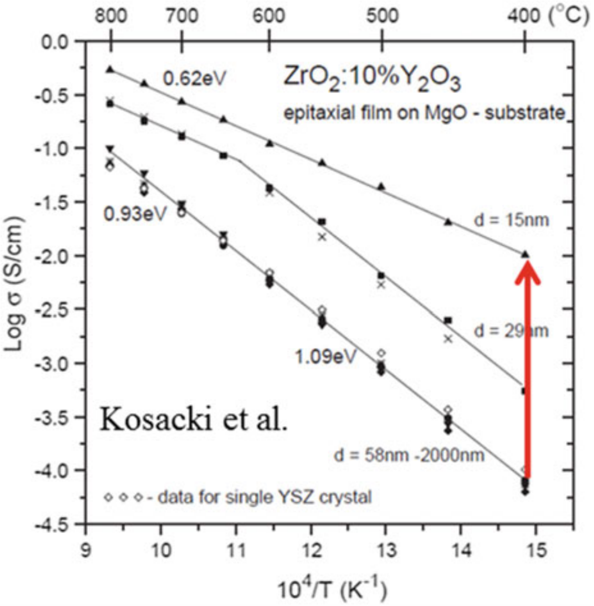

Fig. 6.9 Temperature dependence of the electrical conductivity determined for epitaxial 10 % mol YSZ thin films with different thicknesses. Reproduced from Ref. [44] by permission. The *vertical arrow* indicates the change of about 2 decades in reducing the thickness down to 15 nm, which will be revisited in Fig. 6.11

that epitaxial growth is an important step in attaining the enhanced ionic mobility [52]. In fact, several papers have reported conductivity enhancements at fluorite based heterostructures and superlattices, that have been explained in terms of an increase of the migration volume resulting from misfit dislocations at the interface [53–56], and indicate that the higher conductivity values at epitaxial interfaces involving nanometer thick YSZ may arise not (only) from space charge effects but from epitaxial strain or atomic reconstruction reported to appear at interfaces between correlated oxides [57, 58].

In an attempt to isolate a true interface effect on ion conductivity at oxide heterostructures, Garcia-Barriocanal et al. [6] grew highly strained multilayers combining STO and ultrathin YSZ layers with controlled thickness down to the unit cell level (0.3–1 nm) (see Fig. 6.10). They found conductivity values from dielectric spectroscopy measurements as large as eight orders of magnitude higher than bulk YSZ conductivity values at room temperature, which they attributed to enhanced oxide ion conductivity [6]. The dc conductivity determined by ac methods was independent of the YSZ layer thickness, which was taken as an indication of its interfacial origin. Guo has proposed [60] the electronic origin of the large conductivity values found in this experiment, but the possibility that the enhanced conductivity originated in electron doping of the substrate or STO layers was eliminated by measuring the dc (electronic) contribution of the conductivity, which turned out to be almost three orders of magnitude smaller than the global conductivity measured with ac methods [45]. Garcia-Barriocanal et al. [6] discussed the conductivity enhancement in terms of a decrease of the activation energy from values of about 1 eV for bulk samples to 0.6 eV for the ultrathin

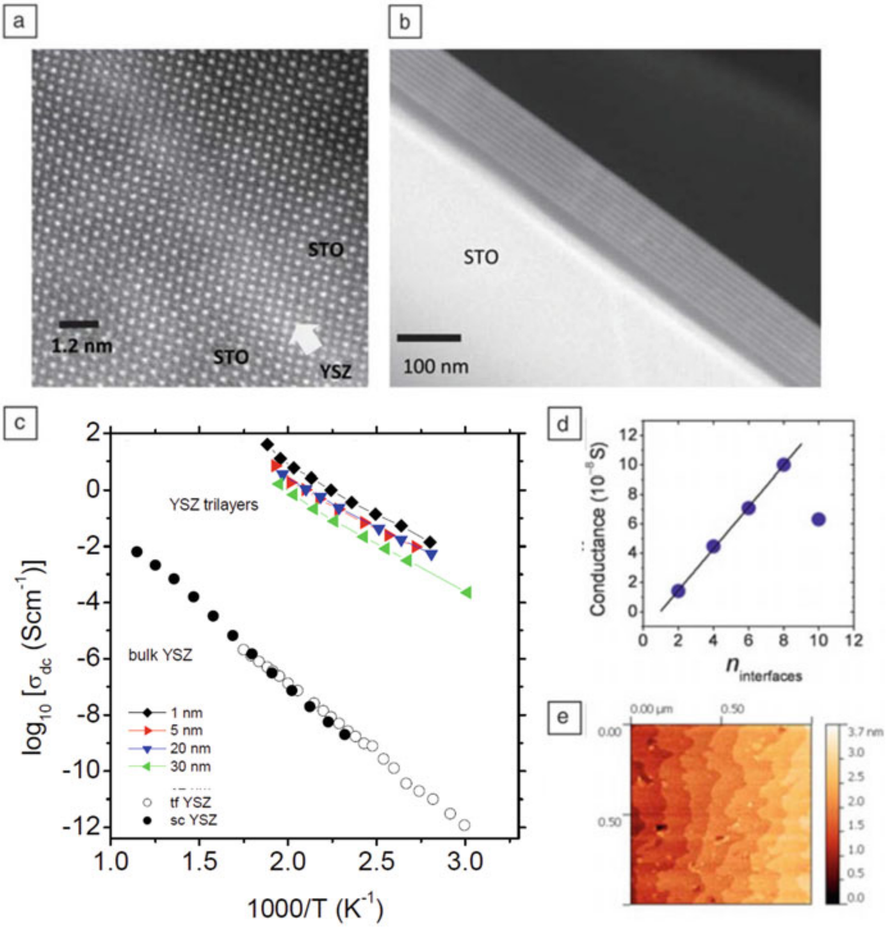

Fig. 6.10 (**a**) Z-contrast STEM image of an epitaxial 1-nm-thick YSZ layer (marked by the *arrow*) between 10 nm STO layers in a $[YSZ_{1nm}/STO_{10nm}]_9$ superlattice (with nine repeats). (**b**) Low magnification image of the same superlattice. (**c**) Arrhenius plot of the conductivity of the trilayers STO/YSZ/STO. The thickness range of the YSZ layer is 1–30 nm. Also included are the data of a single crystal (sc) of YSZ and a thin film (tf) 700 nm thick. (**d**) Conductance at 400 K of $[YSZ_{1nm}/STO_{10nm}]_{ni/2}$ superlattices (with ni/2 repeats) as a function of the number of interfaces ni. (**e**) AFM image of a 1 nm-thick YSZ layer grown on TiO_2 terminated 0.1 % wt. Nb-doped $SrTiO_3$ showing a two-dimensional growth mode. Figure adapted with permission from References [6, 59]

trilayers (see Fig. 6.10) and of the large conductivity pre-exponential factor of the STO/YSZ/STO trilayer samples, which may result from an increase in the concentration of oxygen vacancies, and/or a large entropy term related to disorder [45]. A reduction of the activation energy for oxygen ion diffusion has been obtained from an ab initio-based kinetic Monte Carlo model for ionic conductivity in YSZ [61]. The decrease in the activation energy has been interpreted in terms of weaker ion-ion interactions in the ultra-thin YSZ layers within the Coupling Model (see Sect. 6.3.2). Ionic interactions are found to be essential in reproducing the effective activation energy [62] and the enhanced oxygen ion mobility may result from a non-random distribution of the dopant Y ions at the interfacial planes [61], to structural disorder [63], or from a decrease of ionic interactions when the layer thickness goes down to the nanometer range [64]. An important point might be the effect of epitaxial strain on defect association, which in YSZ is known to immobilize oxygen vacancies at temperatures lower than 1000 K. Hence, the conductivity is controlled by both the mobility and the defect association constant. Generally it is believed that associates are formed between $Y_{zr}{}'$ and $V_{O}^{\cdot\cdot}$ (in Kröger-Vink notation), although oxygen vacancies could also be immobilized by a strain field due to the size difference between Zr^{4+} and Y^{3+} cations [65]. An interesting possibility is that the apparent mobility could increase significantly when this strain field is alleviated by externally induced strain (although not by several orders of magnitude).

Other authors have also reported substantial enhancement (though smaller than in Ref. [6]) of the ionic conductivity in ultrathin epitaxial YSZ layers. Sillassen et al. [66] reported more than three orders of magnitude enhancement of the oxide ion conductivity at low temperatures (lower than 350 °C) in epitaxial YSZ films grown on MgO substrates. Their results also indicate that the observed enhancement is due to an interfacial effect, and related to a combination of misfit dislocation density and elastic strain in the interface. The importance of epitaxial strain in determining an increase in the ionic conductivity at oxide interfaces and nanolayers has been very recently addressed experimentally by several groups. Janek et al. [67] have reported on the influence of strain on ion conduction at oxide interfaces, finding small conductivity enhancements in samples grown by pulsed laser deposition (PLD) with partially or non-coherent interfaces. Hertz et al. [68] have reported improved oxide ion conductivity on ultra-thin films of YSZ (below 10 nm thick) grown by sputtering on Al_2O_3 substrates. There is an increase in the out-of-plane lattice parameter in these films due to tensile strain, which may assist in-plane ionic conduction. Lian et al. [69] have reported a two order of magnitude increase in oxide-ion conductivity, as compared with bulk YSZ, in YSZ/$Gd_2Zr_2O_7$ heterostructures with 3 % tensile strain and dislocation-free interfaces upon the manipulation of the layer thickness down to 5 nm. Hyodo et al. [70] study $Pr_2Ni_{0.71}Cu_{0.24}Ga_{0.05}O_4/Sm_{0.2}Ce_{0.8}O_2$ (PNCG/SDC) layer-by-layer nano-sized laminated films and found a significant increase of oxide ion conductivity compared to bulk SDC values that they proposed to be due to the expanded lattice of SDC in these heterostructures. An enhancement of ^{18}O tracer diffusion coefficient for transport along strained YSZ films in YSZ/Y_2O_3 multilayer samples has been reported by Janek et al. [71] From the functional course of the measured mean oxygen ion diffusion coefficient vs. layer thickness between 12 and 45 nm, they estimate an elastically strained interface region thinner than 5 nm with modified ionic transport properties. One has to be careful with interpreting impedance measurements when using active electrodes like Ag or Pt. Gold is a better option to block oxygen ions [72]. Furthermore, measurement of the in-plain conductivity of thin films could be influenced by surface diffusion (conduction). The critical point about enhanced oxygen ion conductivity is proof by ^{18}O-exchange experiments preferably under current flow. There are also some controversial results regarding the conductivity enhancement of epitaxially strained layers. Pergolesi et al. [73] have studied YSZ-CeO_2 heterostructures on MgO substrates, where interfaces were found to be non-uniformly but significantly strained, and they reported no detectable contribution to the total conductivity even in the case of layers as thin as about 10 unit cells. By using PLD, Fleig et al. [74] grew YSZ layers with larger thickness ranging from 30 to 300 nm onto MgO, Al_2O_3 and $SrTiO_3$ substrates, with different lattice parameters, and did not find an enhancement in ionic conductivity. They attribute this result to the presence of grain boundaries in the films that strongly block ion transport. Cavallaro et al. [75] have grown YSZ/STO heterostructures by using PLD and found that the layers were discontinuous and YSZ islands had mixed crystalline orientations. They found enhanced values of the electronic conductivity that they attributed to an interfacial alloyed oxide resulting from zirconium/strontium intermixing. These results suggest the possible importance of crystalline orientation of the YSZ growth in order to obtain coherent and epitaxial films with enhanced ionic conductivity. By using different temperatures during the growth of YSZ films on STO with a sputtering technique, Rivera-Calzada et al. [59] were able to control their crystalline orientation what allowed stabilizing different morphologies, layer continuity and epitaxy, and as a result achieved different degrees of ion mobility enhancement. Despite the 7 % mismatch between both highly dissimilar structures, $\langle 001 \rangle$ YSZ growth yields coherent interfaces by stabilizing a disordered oxygen sublattice with an increased number of accessible positions for oxygen which promote oxygen diffusion. On the other hand, the $\langle 110 \rangle$ YSZ orientation results in the growth of connected islands, whose boundaries block the long range diffusion of ions. Moreover, the fact that conductance of superlattices with coherent interfaces scaled with the number of interfaces evidences that enhancement of ion conductivity is an interfacial effect (see Fig. 6.10). These results demonstrate that epitaxial strain is an important parameter in designing a high mobility landscape at the interfaces in addition to space charge effects [76, 77].

In fact, several theoretical groups have proposed that epitaxial strain provides an avenue to increase the conductivity of ion conducting solids, and understanding its effect and uncovering the microscopic mechanism has become an important challenge [64, 67, 78–82]. One important direction has been the use of static models based simulations to evaluate changes in the migration volume. Korte and co-workers, from a qualitative model of ion diffusion along hetero-interfaces based on the increased of activation volume associated to the density of misfit dislocations and the interfacial strain have pointed out that strain by itself can only account for 2–3 orders of magnitude conductivity increase in YSZ/STO heterostructures [67, 78]. This model predicts linear increase of the conductivity with lattice mismatch for tensile strained interfaces while compressive strain will decrease the ionic conductivity. On the other hand Roger de Souza and colleagues [83, 84], made use of static lattice simulation techniques using phenomenological potentials to describe lattice relaxation. The effect of strain affects the free energy for migration through its effect on the free migration volume. This model would account for a conductivity increase up to 5 orders of magnitude using the experimental values of the activation energy in YSZ/STO heterostructures by Garcia-Barriocanal et al. [6]. It is concluded that lattice strain alone cannot be responsible for the total conductivity increase found experimentally [84]. Furthermore, a recent paper by Bilge Yildiz and collaborators [80] has examined the effect of biaxial strain on the oxygen diffusivity using combined density functional theory DFT calculations and kinetic Monte Carlo (KMC), and conclude that bonds reconfiguration poses an upper limit to the effect of epitaxial strain in enhancing the conductivity by expanding the conduction path. A problem with these models may result from the fact that they tackle the issue of epitaxial strain by stressing bulk structure, i.e., they do not explicitly include the presence of interfaces which may incorporate interesting ingredients related to the chemical and structural compatibility of the merging lattices. Density-functional calculations have been used to investigate the influence of the (001) oriented interface on the conductivity increase in YSZ/STO superlattices explicitly considering the presence of the interface by introducing mixed YSZ/STO supercells [79]. The authors of that work proposed that the combination of epitaxial strain and oxygen sublattice incompatibility between both structures are key in yielding the highly conducting interface. They report that 7 % strain produces a drastic change in the O sublattice of YSZ, which becomes as disordered as expected from an increase of the temperature up to 2000 K. The O ion mean square displacement (mobility) is strongly enhanced (by a factor of over 10^6) as a result of the combined presence of oxygen vacancies and disorder. The incompatibility of the oxygen positions in the interface planes (octahedral in STO vs tetrahedral in YSZ) are proposed to play a key role in stabilizing the highly conducting interface by introducing extreme disorder in the oxygen sublattice in the region close to the interface. EELS experiments (both spectroscopy and imaging) have provided evidence for the oxygen disorder [82]. Moreover, density functional simulations show that a new YSZ phase is stabilized at epitaxially strained heterostructures for mismatch strain levels in excess of 5.2 % [79]. This result explains in fact why these high levels of strain do not result in strain relaxation by mismatch dislocations and islanding and evidences that lattice relaxation plays a dominant role in phase stabilization. Very recently, Li et al. [85] performed DFT and first-principles molecular dynamics simulations to examine the strain effect on oxygen conductivity in $KTaO_3$/YSZ/$KTaO_3$ sandwich structure with 9.7 % lattice mismatch. They found a large decrease of the activation energy for ionic conduction, and estimated the oxygen ionic conductivity for KTO-strained zirconia to be 6.4×10^7 times higher than that of the unstrained bulk zirconia at 500 K. Interestingly, by using Al_2O_3 and $SrTiO_3$ instead of $KTaO_3$ in the simulations, a nearly linear relationship is identified in that work between the energy barrier and the lattice mismatch in the sandwich structures.

Aside from epitaxial strain, polarity mismatch may play an important role in determining the atomic reconstruction at the interface [86]. In the case for example of (100) YSZ/STO superlattices, the non-polar STO (100) planes alternate with strongly polar YSZ (100) planes with a sequence $(Zr)^{4+}$-$(O_2)^{4-}$-$(Zr)^{4+}$-… This plane sequence is in fact a very energetically unstable situation, and it cannot be settled by electron transfer to the interface since STO interfaces are found to be always terminated in a TiO_2 plane [6]. In this case, it has been suggested the possibility that oxygen vacancies nucleate at the interface to avoid polarity mismatch and to restore charge neutrality [52]. This might actually explain the nucleation of a large number of oxygen vacancies at YSZ/STO interfaces. Another possibility is the formation of an $(ZrO)^{2+}$-plane with rocksalt structure, as proposed recently by Dyer et al. [87] from theoretical arguments. This interface termination preserves charge neutrality, avoids polarity mismatch, and is also consistent with experimental observations. This reconstruction may be in fact related to the formation of a zirconate compound at the interface [75]. In a related context, molecular dynamics simulations have shown [63] that in YSZ films on MgO substrates there is a slight enrichment of dopant, and that the extent of dopant enrichment is greater for lower thickness YSZ films. This would give rise to an increase of the interfacial conductivity by 2 orders of magnitude as the YSZ film size decreases from 9 to 3 nm due to the concomitant decrease in activation energy barrier from 0.54 to 0.35 eV in the 1200–2000 K temperature range. These results show that, apart from epitaxial strain, atomic reconstruction arising at interfaces (due to polarity mismatch or other forms of chemical incompatibility) may give rise to modified coordination and stoichiometry at epitaxial interfaces and are important to understand changes in ionic conductivity.

6.3 Nano Ion Dynamics

In Chaps. 4 and 5 many anomalous dynamic properties of ionic conductors with high ionic concentrations are presented and their origin is attributed to cooperative motion of ions due to ion-ion interaction. The dynamics of ions changes with increasing time progressively from roughly four time regimes. (1) Initially all ions are caged. (2) Thermally activated single ion hops out of cage with the primitive relaxation time $\tau_{\sigma 0}(T)$, the onset of which terminates the caged ion dynamics regime. (3) The number of ions hopping successfully and simultaneously increase with time, the rate of which is controlled by the ion-ion interaction and correlation because the process is cooperative. (4) The averaged maximum number of ions hopping cooperatively N_{dif} or the maximum length-scale of cooperativity L_{dif} is finally reached at times of the order of t_{dif}. This terminal conductivity α-relaxation has correlation function given by the Kohlrausch stretched exponential function, $\phi(t) = \exp\left[-(t/\tau_\sigma)^{1-n_\sigma}\right]$, with the conductivity α-relaxation time $\tau_{\sigma\alpha}(T)$ determining the d.c. conductivity σ_{dc} and the diffusion D. Stronger the ion-ion interaction, larger is N_{dif} or L_{dif} and longer is t_{dif}. This evolution of ion dynamics with time is the precept of the Coupling Model (CM) and substantiated by experiments as well as molecular dynamics simulations of the motion of Li ions in

Li_2SiO_3 shown by Fig. 4.59 in Chap. 4. This description of ion dynamics together with the CM relation between $\tau_{\sigma\alpha}(T)$ and $\tau_{\sigma 0}(T)$,

$$\tau_{\sigma\alpha} = \left[(t_{\sigma c})^{-n_\sigma}\tau_{\sigma 0}\right]^{1/(1-n_\sigma)}, \tag{6.8}$$

explain many properties of the ion dynamics in bulk ionic conductors in Chaps. 4 and 5.

Notwithstanding, the size of L_{dif} can be of the order of nanometer in many ionic conductors with large concentration of mobile ions. Therefore cooperativity in nanoionics, where one or more dimensions of the material is reduced to nanometer size, can be severely reduced and ion dynamics modified. In thin films deposited on a substrate, ion mobility is expected to be much enhanced at or near the free surface due to absence of ions on the other side of the free surface. Thus some changes of the ion dynamics in bulk of ionic conductors are expected when size is reduced to nanometer. This section is written to show the changes in some ionic conductors for which the ion dynamics are well characterized both in the bulk and in thin films. The CM explanation of the bulk ion dynamics is examined whether it can continue to account for the changes in thin films. There are lot more studies of change of structural α-relaxation and viscosity in non-ionic glass-formers confined to nanometer size and in thin films with the presence of free surface. For this reason it is worthwhile to show some examples to heighten the awareness that the phenomenology as well as the underlying physics is the same in the two fields of ionic conductivity relaxation and glass transition [88–92].

6.3.1 Oxygen Ion Dynamics in YSZ Thin Films

6.3.1.1 Thin Films of YSZ Deposited on MgO Substrates

Yttria-stabilized zirconia (YSZ), ($(1-x)ZrO_2{:}xY_2O_3$), has high oxygen ion conductivity at high temperatures, making the material attractive in technological applications including oxygen sensors, solid oxide fuel cell (SOFC) electrolytes, and etc. The oxygen ion dynamics in bulk YSZ have been amply discussed in Chap. 4, and at Fig. 4.33 therein the reader can find the $\tau_{\sigma\alpha}(T)$ or $\tau^*(T)$ experimental data, and $\tau_{\sigma 0}(T)$ calculated by the CM equation. Here we consider the oxygen ion dynamics in thin films of YSZ with thickness in the nanometer scale [64].

In highly textured thin films of YSZ with 9.5 mol% Y_2O_3 deposited on MgO substrates and thicknesses between 60 and 15 nm, Kosacki et al. [44] found enhanced conductivity. Their results were shown before in Fig. 6.9. The d.c. conductivity, σ_{dc}, in the 15 nm film is about 2 orders of magnitude higher than 2000 nm thick films at 673 K. Its activation energy is 0.62 eV, which is significantly lower than 1.09 eV of the 2000 nm thick film, and 1.16 eV of the bulk samples with about the same composition. The d.c. conductivity, σ_{dc}, data of the 15 nm film from Kosacki et al. are converted to $\tau_{\sigma\alpha}(T)$ via the relation,

$$\sigma_{dc} = \epsilon_0 \varepsilon_\infty / \langle \tau_{\sigma\alpha}(T) \rangle, \tag{6.9}$$

where $\varepsilon_o = 8.854 \times 10^{-14}$ F/cm is the permittivity of free space, and the results are shown by purple closed squares lying just above the dotted line representing $\tau_0(T)$ in Fig. 6.11. From the dependence of σ_{dc} on film thickness, Kosacki et al. concluded that the bulk conductivity and the surface/interface conductivity contribute in parallel. The surface/interface contribution becomes more important in thinner film. Using a mixture model to separate one contribution from the other, Kosacki et al. deduced that the surface/interface conductivity is about three to four orders of magnitude higher than that of the bulk, and its activation energy is 0.45 eV. These results are interesting but one should be mindful that they are dependent on the mixture model used to analyze the data. How exactly the two contributions have to be put together to become the observed σ_{dc} in the thin films is an open question. Notwithstanding, the results suggest the activation energy of the surface/interface conductivity is 0.62 eV as observed or less. This experimental fact is important for the CM explanation. At the surface/interface of YSZ, interaction between oxygen ions is weaker than in the bulk because of the absence of mobile oxygen ions (i.e. absence of oxygen vacancies) across the surface/interface. Weaker ion-ion interaction at the surface/interface leads to coupling parameter, n_S, smaller than $n_b = 0.55$–0.57 for the bulk. It follows from the CM equation (6.8) and relation (6.9) that the activation energy of the surface/interface conductivity, $E_{\sigma,S}$, and bulk conductivity $E_{\sigma,b}$ is given by

$$E_{\sigma,S} = E_a/(1 - n_S) \quad \text{and} \quad E_{\sigma,b} = E_a/(1 - n_b), \tag{6.10}$$

From these expressions, $E_{\sigma,S}$ is smaller than $E_{\sigma,S} = 1.15$ eV, because n_S is less than n_b, and the actual energy barrier, E_a, is the same in the bulk or at the surface/interface. This feature, i.e. $E_{\sigma,S} < E_{\sigma,b}$, is consistent with the experimental data as shown in Fig. 6.11.

From Eq. (6.8), the bulk and surface/interface conductivity relaxation times $\tau_{\sigma,b}(T)$ and $\tau_{\sigma,S}(T)$ can be rewritten as,

$$\tau_{\sigma,b}(T) = \tau_0(T)[\tau_0(T)/t_c]^{n_b/(1-n_b)} \tag{6.11}$$

and

$$\tau_{\sigma,S}(T) = \tau_0(T)[\tau_0(T)/t_c]^{n_S/(1-n_S)} \tag{6.12}$$

Since the exponent, $n/(1-n)$, is a monotonic increasing function of n, and $(\tau_0/t_c) \gg 1$, it follows from Eqs. (6.11) and (6.12) and n_S is less than n_b that $\tau_{\sigma,S}(T)$ is much shorter than $\tau_{\sigma,b}(T)$ in agreement with the experimental data.

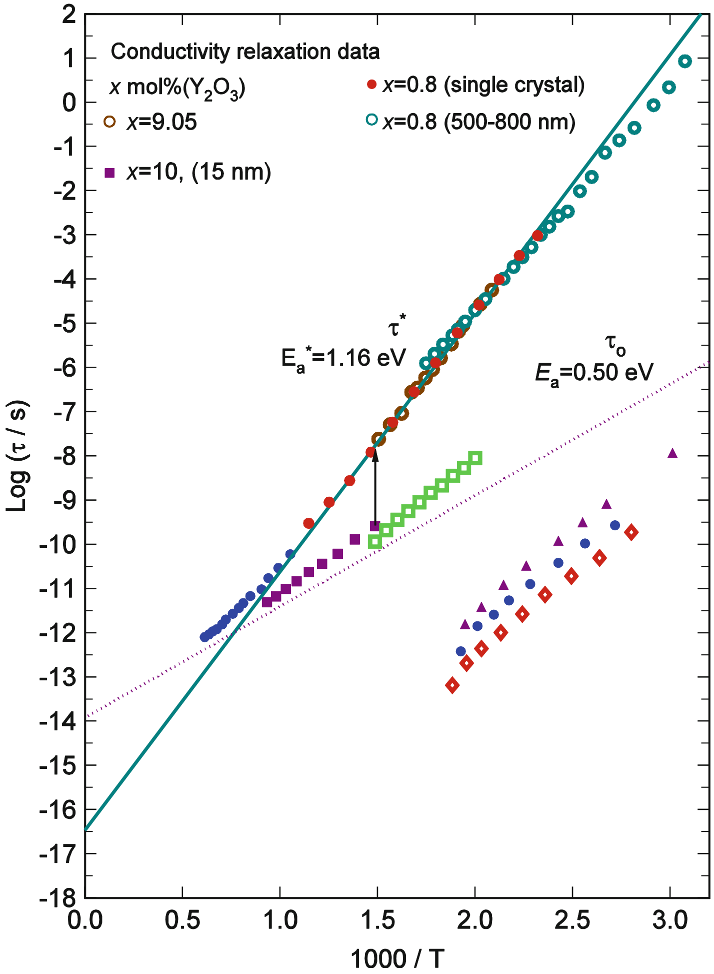

Fig. 6.11 Arrhenius plots of various relaxation times of oxygen ions in bulk YSZ and thin films of YSZ. The *blue closed circles* within the range, $0.6 < 1000/T < 1.1$ are $\tau^*(T)$ calculated from high temperature d.c. conductivity data. The *purple dotted line* are the independent ion hopping relaxation time $\tau_0(T)$ calculated from bulk $\tau^*(T)$ with $t_c = 1$ ps. The data of the conductivity relaxation times, $\tau_{\sigma,S}(T)$, of 15 nm YSZ thin film deposited on MgO are shown by *closed purple squares* located just above the *purple dotted line* representing $\tau_0(T)$. The $\tau_{\sigma,S}(T)$ of 62, 30, 5, and 1 nm YSZ thin film sandwiched between two 10 nm STO layers are shown by *green open squares* (near and above the *green dashed line*), *closed purple triangles*, *closed blue circles*, and *open red diamonds* (below the *green dashed line*) respectively

6.3.2 Interfaces of Epitaxial ZrO_2:Y_2O_3/$SrTiO_3$ Heterostructures

Thinner the YSZ film, more important is the influence of the surface/interface in reducing the ion-ion interaction, and naturally n_S becomes smaller. The consequences are larger decrease in $E_{\sigma,S}$ to approach the actual energy barrier, E_a, and higher d.c. conductivity or shorter $\tau_{\sigma,S}(T)$. These trends were found by Garcia-Barriocanal et al. [45, 59] in a trilayer heterostructure where a film of YSZ with 8 mol% Y_2O_3 were sandwiched between two 10-nm-thick layers of insulating $SrTiO_3$ (STO). The YSZ film thickness ranges from 62 nm down to 1 nm. In addition, superlattices alternating 10-nm thick STO layer with the YSZ film were fabricated. The interfaces between the STO and the YSZ are atomically flat, with the YSZ perfectly coherent with the STO. Due to large mismatch between the lattice constants of STO and YSZ, the epitaxial growth of the YSZ on top of the STO engenders a large expansive strain in the thin YSZ layers of 7 % in the *ab* plane. As already mentioned in Sect. 6.2, Garcia-Barriocanal et al. performed conductivity relaxation measurements to determine the d.c. conductivity, which they ascertained by other measurement that it comes from oxygen ionic diffusion, and (non-dispersive) electronic contribution is negligible. In the following discussion it is assumed that the observed conductivity is in fact due to an enhanced ionic conductivity. Garcia-Barriocanal's data of σ_{dc} are converted here to $\tau_{\sigma,S}(T)$ via Eq. (6.9), and the temperature dependence of $\tau_{\sigma,S}(T)$ for [STO_{10nm}/YSZ_{Xnm}/STO_{10nm}] trilayers with $X = 62$, 30, 5, and 1 nm thick YSZ films are shown in Fig. 6.11. Represented by open green squares, $\tau_{\sigma,S}(T)$ of the 62 nm YSZ film show a decrease of about two orders of magnitude than $\tau_{\sigma,b}(T)$ at the measurement temperature range, and the activation energy of $\tau_{\sigma,S}(T)$ decreases to 0.72 eV from 1.16 eV for $\tau_{\sigma,b}(T)$. On decreasing the thickness of the YSZ layer to 30 nm, $\tau_{\sigma,S}(T)$ decreases another three orders of magnitude, and the activation energy decreases to 0.6 eV. On further decrease of the thickness to 5 nm and all the way down to 1 nm (two unit cells of YSZ), the conductivity increases and the corresponding $\tau_{\sigma,S}(T)$ decreases inversely as the thickness of the YSZ layer. The dc conductivity of the 1-nm YSZ layer shows a exceedingly high value of 0.014 S/cm at 357 K, with an activation energy of 0.64 eV. Garcia-Barriocanal et al. also made ac and dc conductance measurements on YSZ/STO superlattices and from the collection of data they concluded that the high conductivity measured comes from the interface of the YSZ film with the STO. The activation energies of the interface conductivity of the 30, 5 and 1 nm thin YSZ films in the range, $0.60 \leq E_{\sigma,S} \leq 0.64$ eV, are nearly the same as the independent ion hopping activation energy $E_a \approx 0.52$ eV deduced from bulk conductivity relaxation data of YSZ with slightly higher mole % of Y_2O_3, and $E_{a,QELS} = 0.63$ eV from quasielastic light scattering in bulk YSZ with similar mol% of Y_2O_3 [93]. This is unsurprising because of the expected large reduction of ion-ion interaction at the interface and hence also n_S for the interface conduction in nm thin films of YSZ. It follows from Eq. (6.10) that as $n_S \rightarrow 0$ on decreasing film thickness down to 1 nm, we have $E_{\sigma,S} \rightarrow E_a$.

By inspection of Fig. 6.11, it can be seen that $\tau_{\sigma,S}(T)$ of the nm thin YSZ films are about 2–3 orders of magnitude shorter than the independent ion hopping relaxation time, τ_0, deduced from bulk ionic conductivity. Garcia-Barriocanal et al. suggested the cause of this enhancement is the large in-plane expansive strain on the YSZ interface plane (see Sect. 6.2), which give rises to higher concentration of vacant oxygen positions and probable positional disorder. Pennycook et al. [79, 82] performed simulated annealing to determine the structure of the STO-YSZ multilayers and confirm that the oxygen sublattice near the interface remains highly disordered all the way down to 360 K. From their examination of the energetic of oxygen vacancies at the YSZ interfacial plane, Pennycook et al. concluded that vacancy hopping, and therefore ionic conduction, occurs preferentially in a region adjacent to the interfacial plane, where the O atoms are perturbed but unconstrained by the STO. The importance of structural disorder in determining ionic transport properties in YSZ films with nanoscale thickness has been recently highlighted from a recent atomistic simulation study by Ramanathan et al. [63]. Because the oxygen sublattice near the interface is highly disordered, an activation entropy enters into determination of the independent hopping frequency, $1/\tau_0$, which becomes

$$1/\tau_0(T) = (\tau_\infty)^{-1}\exp(-E_a/kT)\exp(\Delta S/k). \tag{6.13}$$

The activation entropy term, $\exp(\Delta S/k)$, increases the independent hopping frequency of oxygen at the interface of the nm thin film of YSZ, and accounts for the observation that $\tau_{\sigma,S}(T)$ of the nm thin YSZ films are about 2–3 orders of magnitude shorter than the independent ion hopping relaxation time, τ_0, deduced from bulk ionic conductivity.

6.3.3 Computer Simulations Data Compared with Theoretical Interpretation

Computer simulations of oxygen ion dynamics in YSZ using various methods have been published by many groups. The results generated have fundamental significance and are critical for testing the predictions of the CM. The migration energy barriers and the self-diffusion of oxygen at macroscopic time-scale had been calculated by kinetic Monte Carlo (kMC) simulation with density functional theory [94]. The method assumes that oxygen diffusion is well-represented by oxygen vacancy hopping through the edges of cation tetrahedra. The advantage of this method is that it is not restricted to relatively short times, like molecular dynamics simulations. For example, the smallest of all the activation barriers for oxygen vacancy migration is across the Zr–Zr edges, and it is 0.58 eV. Activation energy for oxygen self-diffusion, E_{Ka}, increases with y, the mol % of Y_2O_3, from nearly 0.58 eV for x less than 2.5 to ≈0.59 eV for $x = 8$, ≈0.60 eV for $x = 10$, and ≈0.61 eV for $x = 12$. It was pointed out in Ref. [61] that these migration energy barriers were calculated without including ionic interactions. This may explain why the calculated migration energy barriers E_{Ka} are smaller than bulk $E_{\sigma,b}$ found in conductivity and quasielastic light scattering experiments, say for 8–10 mol% of Y_2O_3. Notwithstanding, these smaller activation energies E_{Ka} calculated without ion-ion interaction is the actual energy barrier, and hence it can be identified with the energy barrier for independent oxygen hop, E_a, of the CM in Eq. (6.10). It is clear that $E_{Ka} \approx 0.59$ eV for $y = 8$ mol % lies close and in between the two values of the energy barrier for independent oxygen hop: $E_a \approx 0.52$ eV and $E_{a,QELS} = 0.63$ eV deduced from conductivity relaxation and quasielastic light scattering respectively. Thus, the result of $E_{Ka} \approx 0.60$ eV from the simulations in Ref. [94] supports the prediction of the CM that the true energy barrier E_a of oxygen ion hopping is in the range $0.52 \leq E_a \leq 0.63$ eV, which has not been tested before.

Recognizing the importance of accounting for ionic interactions, a kinetic Monte Carlo model was used to calculate ionic conductivity in single-crystal YSZ. The kinetic Monte Carlo model [61] was based on combining density functional theory with the cluster expansion method. The results of ionic conductivity of YSZ with 8 mol% of Y_2O_3 showed an increase of the activation energy to 0.74 eV at high T and 0.85 eV at low T, as compared with $E_{Ka} \approx 0.59$ eV. The enhancement of the activation energy found by including ion-ion interaction in the simulations of Lee et al. is in accord with the prediction of the CM in Eq. (6.10), although the size is still smaller than $E_{\sigma,b} = 1.16$ eV found by conductivity relaxation data.

Another molecular dynamics simulation in which the interaction between oxygen ions was included was published by Tarancón et al. [95]. The potential energy chosen is a function of the distance between ions, Zr^{4+}, Y^{3+}, and O^{2-}. It is composed of a Born–Mayer–Buckingham potential for short range interactions, and Coulomb terms to describe the long-range electrostatic interactions between the ions of YSZ. These authors obtained the oxygen tracer diffusion coefficient of YSZ with 8 mol% Y_2O_3 at high temperatures ranging from 1159 to 1959 K. From the Arrhenius temperature dependence, they obtained the activation energy of 0.68 eV, which is significantly smaller than $E_{\sigma,b} = 1.16$ eV of d.c. conductivity at lower temperatures. Expressed in terms of $1000/T$, the temperature range of the simulations corresponds to $0.51 \leq 1000/T \leq 0.86$ K^{-1}. As can be seen by inspection of Fig. 6.11, in this temperature range, overall the conductivity relaxation time τ^* has a much weaker T-dependence than its Arrhenius T-dependence established at lower temperatures with $E_{\sigma,b} = 1.16$ eV. Its apparent activation energy is significantly smaller than 1.16 eV, but still a bit larger than $E_a \approx 0.52$ eV and 0.63 eV from light scattering [93]. Therefore, the activation energy of 0.68 eV found by Tarancón et al. is due to τ^* not long compared with $t_c \approx 1$ to 2 ps in the temperature range of simulations, consistent with the existence of the crossover from many-ion relaxation to independent ion hop in the CM discussed in Chap. 4.

Similar molecular dynamics simulations of YSZ were carried out by Devanathan et al. with the same potential [96] also at high temperatures from 1125 to 2500 K. The diffusion coefficients of oxygen obtained over this range have activation energies of 0.59, 0.60, and 0.73 eV for YSZ with 6, 8, and 10 mol% Y_2O_3 respectively. Again, τ^* is close to $t_c \approx 1$ to 2 ps in the measurement temperature range, and the activation energies obtained by Devanathan et al. are the actual energy barriers opposing oxygen hopping consistent with the values deduced by the CM.

Mean square displacements of oxygen in YSZ were obtained by Chang et al. [97] over the temperature range, $873 \leq T \leq 1473$ K for times up to 500 ps in another molecular dynamics simulation using the same potential. For the YSZ with 7 mol%

Y_2O_3, we obtain the activation energy of about 0.5 eV. For the same reason as discussed in the above, the proximity of τ^* to $t_c \approx 1$ to 2 ps in the simulation temperature range justifies interpreting the deduced activation energy of 0.5 eV as the actual energy barrier of oxygen vacancy hopping.

Another similar molecular dynamics simulation by Lau and Dunlap [98] up to 2.5 ns reported d.c. conductivity of single crystal YSZ with 8 mol% Y_2O_3 having Arrhenius temperature dependence over about 15 orders of magnitude in the wide temperature range from 300 to 1400 K, and have activation energy of 0.59 ± 0.05 eV. This activation energy is similar to $E_a \approx 0.52$ eV and 0.63 eV and is consistent with the interpretation of actual energy barrier as long as temperature is higher than say 1000 K. However, the results of Lau and Dunlap at temperature below say 800 K are at odds with the much larger activation energy, $E_{\sigma,b} = 1.16$ eV, of d.c. conductivity observed by experiments of single crystal YSZ with 8 mol% Y_2O_3.

There is a finite-temperature dynamical simulations of the oxygen vacancy dynamics in bulk cubic zirconia by Pennycook et al. [79, 82], where the oxygen vacancies were generated by applying 7 % strain to change the oxygen sublattice. At high temperatures the oxygen structure becomes disordered. The mean-square-displacements were calculated up to 6 ps, and hence the diffusion coefficients of oxygen in the strained structure were obtained from the simulations. The activation barrier extracted from an Arrhenius plot of the diffusivities is 0.4 ± 0.1 eV, identical to $E_a \approx 0.50$ to 0.52 eV within the error estimated. Since the simulations were carried out only up to 6 ps and close to $t_c \approx 1$ to 2 ps, this activation energy from simulation of strained bulk cubic zirconia can be taken as another source of information on the actual energy barrier for oxygen diffusion. The effect of strain has been also recently examined by using static atomistic simulations, based on empirical pair-potentials (EPP) [82] to determine the energetic barriers for oxygen-vacancy migration in a fluorite-structured lattice without considering ion-ion interactions. Authors of that work find a migration activation enthalpy of 0.59 eV in unstrained material (in good agreement with the estimates using the CM). They further propose that strain may account for large increases (up to 6 orders of magnitude) of the oxygen conductivity and that increased migration entropy (preserving the fluorite structure) may account for an additional order of magnitude conductivity increase.

6.4 Nanoionics for Energy

As already mentioned, nanotechnology and nanostructured materials are expected to have a strong impact on the next generation of energy conversion and storage devices. There is no doubt of the relevance of the scientific and technological challenge of finding new, low-cost, and environmentally friendly, alternatives to current fuel cells, batteries and supercapacitors for energy applications. For example, lithium batteries are currently reaching their limits in performance, and it is necessary to develop alternative technologies for commercially competitive hybrid electric vehicles. We will mention here recent developments in the design and fabrication of energy devices based on the use of nanoionics to improve their performance [99].

Concerning the use of nanostructured materials in battery's electrodes, it is expected that they could result in a longer cycle life since they accommodate better the strain of ion insertion and removal during charge and discharge cycles. Nanostructured electrodes can also lead to shorter charging times due to higher electrode/electrolyte contact area. Several authors have demonstrated improvements in cycling response of lithium batteries, avoiding cracking after repeated cycles by using nanocomposites based on Si-C, or on glasses containing tin oxide or different tin alloys, as anodes [100–104]. It has been also shown an improvement of capacity retention on cycling by using TiO_2 nanowires of only 40–60 nm in diameter, which can accommodate up to $Li_{0.91}TiO_2$ (305 mA h/g) at 1.5–1.6 V vs Li^+(1 M)/Li [105]. It is worthwhile to remark that electrochemical reaction paths may be radically different when dealing with nanoscale particles. This is for example the case of haematite, which shows an irreversible phase transformation when using large particles (1–2 μm) that avoids its use as anode material, but shows remarkable properties for Li insertion in the form of nanoparticles (20 nm) [106]. Another route to enhance electrode capacities is the use of porous materials to increase the surface-area of the electrodes. V_2O_5 aerogels have shown better performance as cathodes in lithium batteries than polycrystalline non-porous powders of the same composition [107, 108]. Another example is the greatly improved electrochemical response of phospho-olivine $LiFePO_4$ in the form of carbon-coated nanoparticles, since the formation of inactive regions in the bulk form of this electronically insulating material is thus prevented [109]. The search of new electroactive materials in lithium batteries has been strongly fostered by the use of nanotechnology, since we have realized that it is not necessary that the materials show high electronic conductivity, nor high lithium diffusivity, since these demands can be circumvented by the use of smart designs at the nanoscale. The performance of supercapacitors can also be enhanced by using nanostructured electrodes. Supercapacitors are somehow similar to batteries but are designed to have longer cycle life and power (discharge rates) at the expense of lower energy density. Their operation is based on surface charge accumulation at the electrode/electrolyte interface instead of inserting and removing ions in the electrodes, and therefore the electrode requirements are less demanding than for batteries. Several studies have already shown how the use of nanostructured carbons can indeed improve the capacitance and the cyclability of supercapacitors [110–112].

Similar achievements have been made in the improvement of the electrolyte transport properties in lithium batteries. The use of nanocomposites have led to large increases of the lithium ion conductivity in polymer electrolytes, particularly by using polymer-in-salt nanostructures [113] and ionic liquids [114]. It has been well established for many years that ionic conductivity in polymer electrolytes occurs only in the amorphous phase above the glass transition, and crystalline polymer electrolytes were considered to be insulators. However, recent studies have demonstrated high ionic conductivity in the crystalline 6:1 complexes PEO_6:$LiXF_6$ (X = P, As, Sb) on reducing the chain length to the nanometer range, opening new pathways to the optimization of electrolytes [115]. The use of nanostructured materials in order to increase the ionic conductivity of electrolytes is also very relevant in the case of fuel cell devices [116]. The inclusion of small amounts of SiO_2 nanoparticles inside the membrane have been shown to help retaining the water produced in the electrochemical reaction [117], which promotes proton conduction at operation temperatures in the range 130–150 °C at low humidity [118]. Intermediate-temperature solid oxide fuel cells (IT-SOFCs) have also benefited from the use of nanostructured ceramic materials. YSZ and ceria-based (YDC, SDC, CGO) nanocrystalline powders allows a reduction in the sintering temperature of the membrane (electrolyte), and nanocrystalline ceria, characterized by mixed electronic-ionic conduction, enhances charge transfer at the electrode/electrolyte interface [25].

A different scenario where nanoionics has recently shown their potential for energy applications, is oxygen exchange. It is usually found in current solid oxide fuel cells that if the conductance of the electrolyte is increased, either by increasing its conductivity or by reducing its thickness, electrode polarization losses become the dominant cause in limiting the device performance [119]. This is mostly due to the slow kinetics of the thermally activated oxygen reduction reaction at the cathode and results to be one of the critical factors limiting the operation of SOFCs at lower temperatures [120]. Epitaxial strain has been shown to be very effective in accelerating oxygen exchange [121–123], and its role on surface chemistry and ion exchange needs to be further investigated. First principles calculations have shown that epitaxial strain favors oxygen vacancy formation and enhanced oxygen mobility in $LaCoO_3$ [124, 125], a well studied material used as fuel cell cathode. Sase [126] have shown that oxygen surface exchange in heterointerfaces $La_{0.6}Sr_{0.4}CoO_3/(La, Sr)_2\ CoO_4$ is increased by three orders of magnitude as compared to single cobaltite surfaces, and they interpreted this result in terms of local strain effects at the interface. It has been also shown that quite significant chemical modifications occur at the surface of $La_{0.7}Sr_{0.3}MnO_3$ epitaxial films resulting from strain, namely Sr enrichment and enhanced oxygen vacancy formation [127]. Kubicek et al. [128] have performed tracer diffusion experiments with isotopically in tensile strained $La_{1-x}Sr_xCoO_{3-\delta}$ layers grown on $SrTiO_3$ as compared to compressively strained ones grown on $LaAlO_3$ substrates. They interpret these results as due to enhanced oxygen diffusion through reduced activation barriers for diffusion and/or energy for oxygen vacancy formation. Also very recently, an increase in the oxygen surface exchange coefficient of single-crystal YSZ has been reported on optimizing the dopant concentration at the surface with the help of atomic layer deposition of a 5–10 nm YSZ layer [129]. All these results demonstrate the potential of nanoionics to optimize the performance of batteries, supercapacitors, fuel cells, as well as other electrochemical devices.

6.5 Outlook

An interesting new field, nanoionics, is emerging in connection with nanostructured ionically conducting materials. In particular, the enhanced ionic conductivity found at heterostructures involving solid electrolytes may impact the performance of energy generation, conversion, and storage devices. They could provide an avenue to optimize the performance of solid state batteries as well as to reduce the high operation temperatures of current solid oxide fuel cells, which imposes severe constraints to materials selection and to conditions and durability of devices. Critical (limiting) factors are the ionic conductivity through the electrolyte and the exchange rate at the electrodes, and both of them could be drastically improved by using nanostructured materials, engineering interfaces, and designing smart new concepts based on nanoscale characteristic lengths of the device. Epitaxial growth of heterostructures seems to play an important role in determining the increase of the ionic conductivity at interfaces, but the ultimate reason behind the enhancement remains to be elucidated. As described in this text, different scenarios have been proposed as relevant to explain experimental data, namely charge transfer and space charge effects, the effect of epitaxial strain in opening diffusion paths, and the influence of atomic reconstruction at the interface in stabilizing new phases with increased carrier concentration.

Apart from its application for energy conversion and storage devices, nanoionics has been proposed to be used in other relevant technology, the design of future non-volatile memories [3]. Some metal–insulator–metal (MIM) systems show ion-migration induced resistive switching that has been proposed as an alternative to current solid state memory devices. The ion-migration effects are coupled to redox processes which cause the change in resistance [5]. One example is based on transition metal oxides, and operates through the migration of mobile oxygen ions towards the anode, with a subsequent change of the stoichiometry and a valence change of the cation sublattice associated with a modified electronic conductivity (see Fig. 6.12). If the cathode blocks ion exchange reactions, an

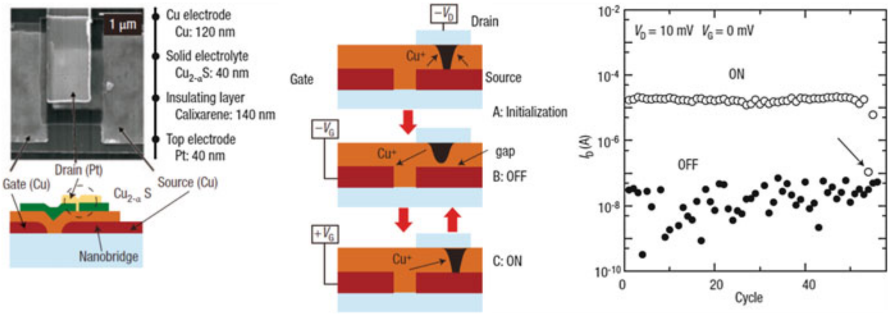

Fig. 6.12 Three terminal solid electrolyte switch. The electrochemical reaction forming and breaking a metallic filament between source and drain electrodes is controlled by the applied gate voltage. Reproduced from Ref. [5] with permission

oxygen-deficient region starts to build and to expand towards the anode. Transition metal cations accommodate this deficiency by trapping electrons emitted from the cathode. In the case of TiO_2 or $SrTiO_3$, for example, this results in a reduction reaction which is equivalent to filling the Ti 3d band. The presence of Ti^{3+} gives rise to enhanced electronic conductivity and eventually to a metallic behavior. This 'virtual cathode' moves towards the anode and will finally form a conductive path [130]. At the anode, the oxidation reaction may lead to the evolution of oxygen gas or the anode material may be oxidized. The actual electroforming conditions depend on the MIM system. The total charge has been found to control the electroforming [131], and once the electroforming is completed, bipolar resistive switching occurs by forming or breaking the conductive pathway between the virtual cathode and the anode. By controlling the charge transfer during the switching, the resistance of the system can be established at intermediate levels, which might help in creating memristive behavior and multibit storage in a single memory cell [132].

Much research effort is still needed to explore the potential of nanoionics-based resistive switching and to exploit this potential in commercial memory devices. In particular, it is needed to understand the microscopic mechanism of the switching, the ion migration and coupled redox process, and optimize the materials selection and fabrication technology [5, 133].

Finally, we want to mention the possibility to use nanoionics devices to dynamically control interfacial oxidation state, allowing the control of interface electronic properties, with an electric field. A relevant example is the voltage control of magnetic properties in a Co/metal-oxide bilayer by inducing oxygen migration to and from the interface (see Fig. 6.13) [134]. The interfacial magnetic anisotropy energy can be reversibly toggled by >0.75 erg cm^{-2} by applying just 2 V. In the virgin state (Fig. 6.13a), the coercive field H_c is uniform across the measured area. After applying a gate voltage $V_g = -4$ V for 240 s and then setting $V_g = 0$ V, H_c exhibits an abrupt step at the electrode edge (Fig. 6.13c) and increases to $\sim$340 Oe beneath the electrode. This is attributed to oxygen migration near the electrode perimeter, where ionic transport is typically most efficient. This would locally reduce the magnetic anisotropy energy by over-oxidizing the Co interface, creating potential wells at the electrode edge (Fig. 6.13d) that trap propagating domain walls and increase the coercive field. Since voltage-induced oxygen ion migration is thermally activated, voltage application at elevated temperature should result in exponentially higher drift velocities, and activation of bulk oxygen migration on an observable timescale. S. D. Beach et al. proposed that relatively small changes in temperature and gate voltage can improve device response times by orders of magnitude, and that by simply varying the thickness and morphology of the gate oxide and electrode, the magneto-ionic switching time drops from hundreds of seconds to hundreds of microseconds. Considerable further improvements in performance and functionality can be anticipated by examining oxides with higher ionic conductivity such as yttria-stabilized zirconia, or by designing

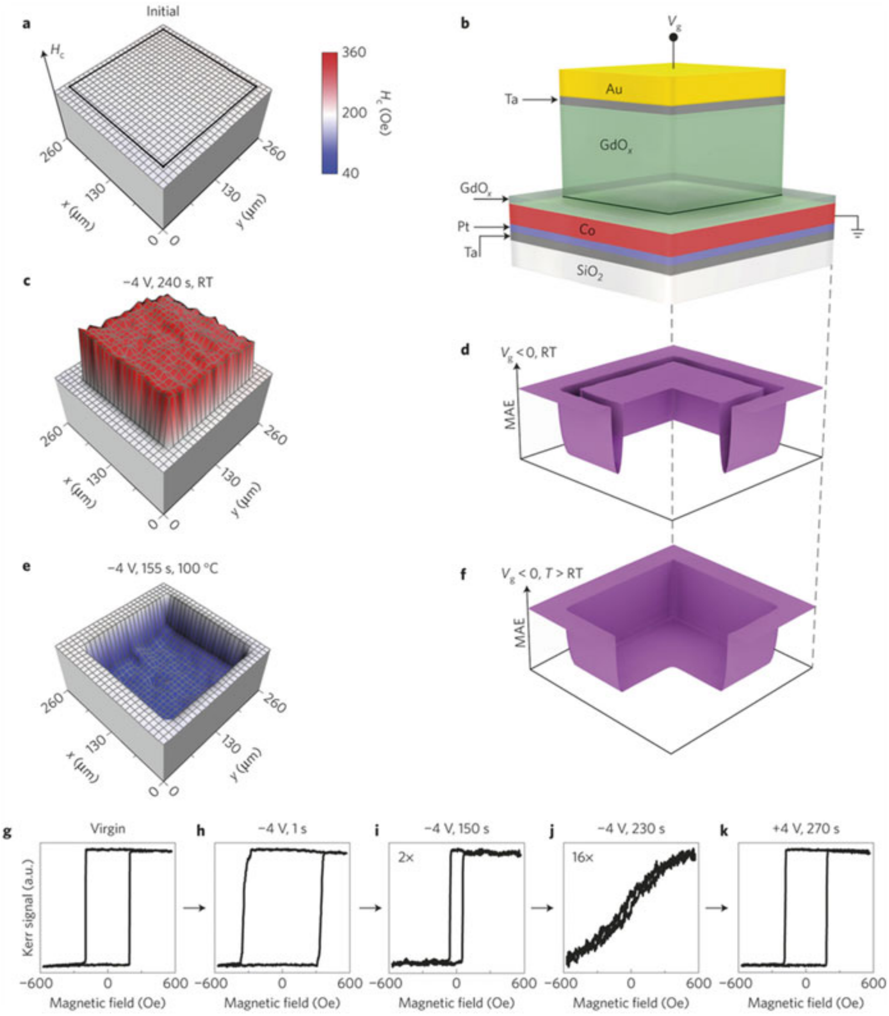

Fig. 6.13 (**a**) Topographic map of the coercivity (H_c) in the virgin state, in the vicinity of a gate electrode. (**b**) Schematic view of gate-electrode structure. (**c**, **d**) H_c and magnetic anisotropy energy landscape, respectively, after applying a gate voltage $Vg = -4$ V for 240 s at room temperature (RT). (**e**, **f**) The same as in (**c**, **d**) after applying $Vg = -4$ V for 155 s at 100 °C. (**g**–**k**) Polar MOKE hysteresis loops measured at room temperature at the centre of the gate electrode showing the device in its virgin state (**g**), after applying $Vg = -4$ V at 100 °C for 1 s (**h**), 150 s (**i**) and 230 s (**j**), and after applying $Vg = +4$ V at 100 °C for 270 s (**k**). The Kerr signal intensity in (**i**) is reduced by a factor of 2 and in (**j**) by a factor of 16, as indicated by inset number. Reproduced from Ref. [134] with permission

gate-oxide heterostructures that include separately optimized oxygen storage and ion conducting layers. These results suggest a new avenue in the nanoionics field towards the implementation of voltage-programmable materials based on solid-state switching of interface oxygen chemistry.

Novel experimental results in the emerging field of nanoionics are growing exponentially, together with a theoretical effort aimed to understand the conductivity enhancement. Ultimately, understanding the mechanism underlying enhanced ion diffusivity at nanostructured ionically conducting materials should help in selecting the suitable materials and designing the appropriate nanostructures for future nanoionic devices.

In closing this Chapter, it is beneficial to point out the enhancement of mobility of ions at surface and in nanometer thin films of ionic conductors have analogues in the structural α-relaxation of non-ionic glass-formers [135, 136], as well as similar explanation by the Coupling Model [137, 138]. This is another example of the same physics governing the dynamics of ions in ionic conductors and sructural relaxation in non-ionic glass-formers.

References

1. S. Kim, S.Yamaguchi, J. Elliot, (editorial article) "Solid State Ionics in the 21st Century: Current Status and Future Prospects", MRS Bull. **34**, 900 (2009)
2. H. Tuller, Solid State Ion. **131**, 143 (2000)
3. R. Waser, M. Aono, Nat. Mater. **6**, 833 (2007)
4. J. Maier, Solid State Ion. **175**, 7 (2004)
5. J. Maier, Nat. Mater. **4**, 805 (2005)
6. J. Garcia-Barriocanal, A. Rivera-Calzada, M. Varela, Z. Sefrioui, E. Iborra, C. Leon, S.J. Pennycook, J. Santamaria, Science **321**, 676 (2008)
7. P. Heitjans, S. Indris, J. Phys. Condens. Matter **15**, R1257 (2003)
8. M. Winterer, *Nanocrystalline Ceramics: Synthesis and Structure*, 2002
9. E.B. Lavik, I. Kosacki, H.L. Tuller, Y.-M. Chiang, J.Y. Ying, J. Electroceram. **1**, 7 (1997)
10. Y.-P. Xiong, H. Kishimoto, K. Yamaji, M. Yoshinaga, T. Horita, M.E. Brito, H. Yokokawa, Electrochem. Solid-State Lett. **13**, B21 (2010)
11. N. Sata, K. Eberman, K. Eberl, J. Maier, Nature **408**, 946 (2000)
12. X. Guo, I. Matei, J. Jamnik, J.-S. Lee, J. Maier, Phys. Rev. B **76**, 125429 (2007)
13. Y.-M. Chiang, E.B. Lavik, I. Kosacki, H.L. Tuller, J.Y. Ying, Appl. Phys. Lett. **69**, 185 (1996)
14. B. Ruprecht, M. Wilkening, S. Steuernagel, P. Heitjans, J. Mater. Chem. **18**, 5412 (2008)
15. F. Berkemeier, M. Abouzari, G. Schmitz, Phys. Rev. B **76**, 024205 (2007)
16. P. Heitjans, M. Wilkening, MRS Bull. **34**, 915 (2009)
17. M.T. Colomer, Adv. Mater. **18**, 371 (2006)
18. T. Norby, Mater. Res. Soc. Bull. **34**, 923 (2009)
19. S. Kim, U. Anselmi-Tamburini, H.J. Park, M. Martin, Z.A. Munir, Adv. Mater. **20**, 556 (2008)
20. H.J. Avila-Paredes, J. Zhao, S. Wang, M. Pietrowski, R.A. De Souza, A. Reinholdt, Z.A. Munir, M. Martin, S. Kim, J. Mater. Chem. **20**, 990 (2010)
21. J. Hinterberg, A. Adams, B. Blümich, P. Heitjans, S. Kim, Z.A. Munir, M. Martin, Phys. Chem. Chem. Phys. **15**, 19825 (2013)
22. M.J. Pietrowski, R.A. De Souza, S. Kim, Z.A. Munir, M. Martin, Solid State Ion. **225**, 241 (2012)
23. G. Gregori, M. Shirpour, J. Maier, Adv. Funct. Mater. **23**, 5861 (2013)
24. L.A. Haverkate, W.K. Chan, F.M. Mulder, Adv. Funct. Mater. **20**, 4107 (2010)
25. B.C. Steele, A. Heinzel, Nature **414**, 345 (2001)

26. A.V. Chadwick, Nature **408**, 925 (2000)
27. T.H. Etsell, S.N. Flengas, Chem. Rev. **70**, 339 (1970)
28. I. Kosacki, T. Suzuki, V. Petrovsky, H.U. Anderson, Solid State Ion. **136–137**, 1225 (2000)
29. C. Peters, A. Weber, B. Butz, D. Gerthsen, E. Ivers-Tiffée, J. Am. Ceram. Soc. **92**, 2017 (2009)
30. P. Mondal, H. Hahn, Berichte Der Bunsengesellschaft Für Phys. Chemie **101**, 1765 (1997)
31. S. Jiang, W.A. Schulze, V.R.W. Amarakoon, G.C. Stangle, J. Mater. Res. **12**, 2374 (1997)
32. O.J. Durá, M.a. López de la Torre, L. Vázquez, J. Chaboy, R. Boada, A. Rivera-Calzada, J. Santamaria, C. Leon, Phys. Rev. B **81**, 184301 (2010)
33. O.J. Dura, R. Boada, M.a. López de la Torre, G. Aquilanti, A. Rivera-Calzada, C. Leon, J. Chaboy, Phys. Rev. B **87**, 174109 (2013)
34. T. Dijk van, A.J. Burggraaf, Phys. Status Solidi A Appl. Res. **63**, 229 (1981)
35. X. Guo, R. Waser, Prog. Mater. Sci. **51**, 151 (2006)
36. G. Knoner, K. Reimann, R. Rower, U. Sodervall, H.-E. Schaefer, Proc. Natl. Acad. Sci. U. S. A. **100**, 3870 (2003)
37. R.A. De Souza, M.J. Pietrowski, U. Anselmi-Tamburini, S. Kim, Z.A. Munir, M. Martin, Phys. Chem. Chem. Phys. **10**, 2067 (2008)
38. C. León, M. Lucia, J. Santamaria, Phys. Rev. B **55**, 882 (1997)
39. M.A. Frechero, M. Rocci, G. Sánchez-Santolino, A. Kumar, J. Salafranca, R. Schmidt, M.R. Díaz-Guillén, O.J. Durá, A. Rivera-Calzada, R. Mishra, S. Jesse, S.T. Pantelides, S.V. Kalinin, M. Varela, S.J. Pennycook, J. Santamaria, C. Leon, Sci. Rep. **5**, 17229 (2015)
40. Y. Lin, S. Fang, D. Su, K.S. Brinkman, F. Chen, Nat. Commun. **6**, 6824 (2015)
41. M. Saiful Islam, Peter R. Slater, **34,** 935 (2009)
42. P. Debye, E. Hückel, Phys. Zeitschrift **24**, 185 (1923)
43. H.L. Tuller, S.J. Litzelman, W. Jung, Phys. Chem. Chem. Phys. **11**, 3023 (2009)
44. I. Kosacki, C. Rouleau, P. Becher, J. Bentley, D. Lowndes, Solid State Ion. **176**, 1319 (2005)
45. J. Garcia-Barriocanal, A. Rivera-Calzada, M. Varela, Z. Sefrioui, M.R. Díaz-Guillén, K.J. Moreno, J.A. Díaz-Guillén, E. Iborra, A.F. Fuentes, S.J. Pennycook, C. Leon, J. Santamaria, ChemPhysChem **10**, 1003 (2009)
46. A. Kumar, F. Ciucci, A.N. Morozovska, S.V. Kalinin, S. Jesse, Nat. Chem. **3**, 707 (2011)
47. A.N. Morozovska, E.A. Eliseev, N. Balke, S.V. Kalinin, J. Appl. Phys. **108**, 053712 (2010)
48. S.J. Litzelman, J.L. Hertz, W. Jung, H.L. Tuller, Fuel Cells **8**, 294 (2008)
49. N.P. Brandon, S. Skinner, B.C.H. Steele, Annu. Rev. Mater. Res. **33**, 183 (2003)
50. A. Karthikeyan, C.-L. Chang, S. Ramanathan, Appl. Phys. Lett. **89**, 183116 (2006)
51. X. Guo, E. Vasco, S. Mi, K. Szot, E. Wachsman, R. Waser, Acta Mater. **53**, 5161 (2005)
52. C. Leon, J. Santamaria, B.A. Boukamp, MRS Bull. **38**, 1056 (2013)
53. C. Korte, A. Peters, J. Janek, D. Hesse, N. Zakharov, Phys. Chem. Chem. Phys. **10**, 4623 (2008)
54. A. Peters, C. Korte, D. Hesse, N. Zakharov, J. Janek, Solid State Ion. **178**, 67 (2007)
55. C. Wang, M. Engelhard, S. Azad, L. Saraf, D. McCready, V. Shutthanandan, Z. Yu, S. Thevuthasan, M. Watanabe, D. Williams, Solid State Ion. **177**, 1299 (2006)
56. S. Azad, O.A. Marina, C.M. Wang, L. Saraf, V. Shutthanandan, D.E. McCready, A. El-Azab, J.E. Jaffe, M.H. Engelhard, C.H.F. Peden, S. Thevuthasan, Appl. Phys. Lett. **86**, 131906 (2005)
57. A. Ohtomo, D.A. Muller, J.L. Grazul, H.Y. Hwang, Nature **419**, 378 (2002)
58. S. Thiel, G. Hammerl, A. Schmehl, C.W. Schneider, J. Mannhart, Science **313**, 1942 (2006)
59. A. Rivera-Calzada, M.R. Diaz-Guillen, O.J. Dura, G. Sanchez-Santolino, T.J. Pennycook, R. Schmidt, F.Y. Bruno, J. Garcia-Barriocanal, Z. Sefrioui, N.M. Nemes, M. Garcia-Hernandez, M. Varela, C. Leon, S.T. Pantelides, S.J. Pennycook, J. Santamaria, Adv. Mater. **23**, 5268 (2011)
60. X. Guo, Science **324**, 465 (2009). author reply 465
61. E. Lee, F.B. Prinz, W. Cai, Phys. Rev. B **83**, 052301 (2011)
62. K.L. Ngai, J. Non-Cryst. Solids **203**, 232 (1996)

63. S.K.R.S. Sankaranarayanan, S. Ramanathan, J. Chem. Phys. **134**, 064703 (2011)
64. K.L. Ngai, J. Santamaria, C. Leon, Eur. Phys. J. B **86**, 7 (2013)
65. S.T. Norberg, S. Hull, I. Ahmed, S.G. Eriksson, D. Marrocchelli, P.A. Madden, P. Li, J.T.S. Irvine, Chem. Mater. **23**, 1356 (2011)
66. M. Sillassen, P. Eklund, N. Pryds, E. Johnson, U. Helmersson, J. Bøttiger, Adv. Funct. Mater. **20**, 2071 (2010)
67. N. Schichtel, C. Korte, D. Hesse, J. Janek, Phys. Chem. Chem. Phys. **11**, 3043 (2009)
68. J. Jiang, X. Hu, W. Shen, C. Ni, J.L. Hertz, Appl. Phys. Lett. **102**, 143901 (2013)
69. B. Li, J. Zhang, T. Kaspar, V. Shutthanandan, R.C. Ewing, J. Lian, Phys. Chem. Chem. Phys. **15**, 1296 (2013)
70. J. Hyodo, S. Ida, J.a. Kilner, T. Ishihara, Solid State Ion. **230**, 16 (2013)
71. H. Aydin, C. Korte, M. Rohnke, J. Janek, Phys. Chem. Chem. Phys. **15**, 1944 (2013)
72. S.P.S. Badwal, M.J. Bannister, M.J. Murray, J. Electroanal. Chem. Interfacial Electrochem. **168**, 363 (1984)
73. D. Pergolesi, E. Fabbri, S. Cook, V. Roddatis, E. Traversa, J. Kilner, ACS Nano **6**, 10524 (2012)
74. M. Gerstl, G. Friedbacher, F. Kubel, H. Hutter, J. Fleig, Phys. Chem. Chem. Phys. **15**, 1097 (2013)
75. A. Cavallaro, M. Burriel, J. Roqueta, A. Apostolidis, A. Bernardi, A. Tarancón, R. Srinivasan, S.N. Cook, H.L. Fraser, J.A. Kilner, Solid State Ion. **181**, 592 (2010)
76. E. Fabbri, D. Pergolesi, E. Traversa, Sci. Technol. Adv. Mater. **11**, 054503 (2010)
77. J.L.M. Rupp, Solid State Ion. **207**, 1 (2012)
78. C. Korte, N. Schichtel, D. Hesse, J. Janek, Monatshefte Für Chemie - Chem. Mon. **140**, 1069 (2009)
79. T.J. Pennycook, M.J. Beck, K. Varga, M. Varela, S.J. Pennycook, S.T. Pantelides, Phys. Rev. Lett. **104**, 115901 (2010)
80. A. Kushima, B. Yildiz, J. Mater. Chem. **20**, 4809 (2010)
81. G. Dezanneau, J. Hermet, B. Dupé, Int. J. Hydrogen Energy **37**, 8081 (2012)
82. T.J. Pennycook, M.P. Oxley, J. Garcia-Barriocanal, F.Y. Bruno, C. Leon, J. Santamaria, S.T. Pantelides, M. Varela, S.J. Pennycook, Eur. Phys. J. Appl. Phys. **54**, 33507 (2011)
83. J. Hinterberg, T. Zacherle, R.a. De Souza, Phys. Rev. Lett. **110**, 205901 (2013)
84. R.A. De Souza, A. Ramadan, S. Hörner, Energy Environ. Sci. **5**, 5445 (2012)
85. F. Li, R. Lu, H. Wu, E. Kan, C. Xiao, K. Deng, D.E. Ellis, Phys. Chem. Chem. Phys. **15**, 2692 (2013)
86. N. Nakagawa, H.Y. Hwang, D.A. Muller, Nat. Mater. **5**, 204 (2006)
87. M.S. Dyer, G.R. Darling, J.B. Claridge, M.J. Rosseinsky, Angew. Chem. Int. Ed. Engl. **51**, 3418 (2012)
88. S. Capaccioli, K.L. Ngai, M. Paluch, D. Prevosto, Phys. Rev. E. Stat. Nonlin. Soft Matter Phys. **86**, 051503 (2012)
89. K.L. Ngai, H. Bin Yu, J. Appl. Phys. **113**, 103508 (2013)
90. W. Zhang, C.W. Brian, L. Yu, J. Phys. Chem. B **119**, 5071 (2015)
91. K.L. Ngai, J. Polym. Sci. B: Polym. Phys. **44**, 2980 (2006)
92. L. Zhu, C.W. Brian, S.F. Swallen, P.T. Straus, M.D. Ediger, L. Yu, Phys. Rev. Lett. **106**, 256103 (2011)
93. K.L. Ngai, Philos. Mag. B **77**, 187 (1998)
94. R. Krishnamurthy, Y.-G. Yoon, D.J. Srolovitz, R. Car, J. Am. Ceram. Soc. **87**, 1821 (2005)
95. A. Tarancón, A. Morata, F. Peiró, G. Dezanneau, Fuel Cells **11**, 26 (2011)
96. R. Devanathan, W. Weber, S. Singhal, J. Gale, Solid State Ion. **177**, 1251 (2006)
97. K.-S. Chang, Y.-F. Lin, K.-L. Tung, J. Power Sources **196**, 9322 (2011)
98. K.C. Lau, B.I. Dunlap, J. Phys. Condens. Matter **23**, 035401 (2011)
99. A.S. Aricò, P. Bruce, B. Scrosati, J.-M. Tarascon, W. van Schalkwijk, Nat. Mater. **4**, 366 (2005)

100. J. Yang, B.F. Wang, K. Wang, Y. Liu, J.Y. Xie, Z.S. Wen, Electrochem. Solid-State Lett. **6**, A154 (2003)
101. J. Graetz, C.C. Ahn, R. Yazami, B. Fultz, Electrochem. Solid-State Lett. **6**, A194 (2003)
102. L.Y. Beaulieu, J.R. Dahn, J. Electrochem. Soc. **147**, 3237 (2000)
103. O. Mao, J. Electrochem. Soc. **146**, 423 (1999)
104. Y. Idota, Science **276**(80), 1395 (1997)
105. A.R. Armstrong, G. Armstrong, J. Canales, R. García, P.G. Bruce, Adv. Mater. **17**, 862 (2005)
106. D. Larcher, C. Masquelier, D. Bonnin, Y. Chabre, V. Masson, J.-B. Leriche, J.-M. Tarascon, J. Electrochem. Soc. **150**, A133 (2003)
107. W. Dong, Electrochem. Solid-State Lett. **3**, 457 (1999)
108. D.B. Le, J. Electrochem. Soc. **143**, 2099 (1996)
109. H. Huang, S.-C. Yin, L.F. Nazar, Electrochem. Solid-State Lett. **4**, A170 (2001)
110. P.A. Nelson, J.R. Owen, J. Electrochem. Soc. **150**, A1313 (2003)
111. J. Wang, S.Q. Zhang, Y.Z. Guo, J. Shen, S.M. Attia, B. Zhou, G.Z. Zheng, Y.S. Gui, J. Electrochem. Soc. **148**, D75 (2001)
112. C. Niu, E.K. Sichel, R. Hoch, D. Moy, H. Tennent, Appl. Phys. Lett. **70**, 1480 (1997)
113. C.A. Angell, C. Liu, E. Sanchez, Nature **362**, 137 (1993)
114. P.C. Howlett, D.R. MacFarlane, A.F. Hollenkamp, Electrochem. Solid-State Lett. **7**, A97 (2004)
115. Z. Stoeva, I. Martin-Litas, E. Staunton, Y.G. Andreev, P.G. Bruce, J. Am. Chem. Soc. **125**, 4619 (2003)
116. *Nanotechnology for the Energy Challenge* (Wiley, 2010), p. 440.
117. M. Watanabe, J. Electrochem. Soc. **143**, 3847 (1996)
118. A.S. Aricó, V. Baglio, A.D. Blasi, V. Antonucci, Electrochem. Commun. **5**, 862 (2003)
119. E.D. Wachsman, K.T. Lee, Science **334**, 935 (2011)
120. J. Fleig, Annu. Rev. Mater. Res. **33**, 361 (2003)
121. M. Burriel, G. Garcia, J. Santiso, J.A. Kilner, R.J. Chater, S.J. Skinner, J. Mater. Chem. **18**, 416 (2008)
122. Z. Gao, L.V. Mogni, E.C. Miller, J.G. Railsback, S. Barnett, Energy Environ. Sci. (2016)
123. H.-I. Ji, J. Hwang, K.J. Yoon, J.-W. Son, B.-K. Kim, H.-W. Lee, J.-H. Lee, Energy Environ. Sci. **6**, 116 (2013)
124. A. Kushima, S. Yip, B. Yildiz, Phys. Rev. B **82**, 115435 (2010)
125. J.W. Han, B. Yildiz, J. Mater. Chem. **21**, 18983 (2011)
126. M. Sase, Solid State Ion. **178**, 1843 (2008)
127. H. Jalili, J. Han, Y. Kuru, J. Phys. Chem. Lett. **2**, 801 (2011)
128. M. Kubicek, Z. Cai, W. Ma, B. Yildiz, H. Hutter, J. Fleig, ACS Nano **7**, 3276 (2013)
129. C.-C. Chao, J.S. Park, X. Tian, J.H. Shim, T.M. Gür, F.B. Prinz, ACS Nano **7**, 2186 (2013)
130. T. Baiatu, R. Waser, K.-H. Hardtl, J. Am. Ceram. Soc. **73**, 1663 (1990)
131. Y. Watanabe, J.G. Bednorz, A. Bietsch, C. Gerber, D. Widmer, A. Beck, S.J. Wind, Appl. Phys. Lett. **78**, 3738 (2001)
132. A. Beck, J.G. Bednorz, C. Gerber, C. Rossel, D. Widmer, Appl. Phys. Lett. **77**, 139 (2000)
133. N. Banno, T. Sakamoto, T. Hasegawa, K. Terabe, M. Aono, Jpn. J. Appl. Phys. **45**, 3666 (2006)
134. U. Bauer, L. Yao, A.J. Tan, P. Agrawal, S. Emori, H.L. Tuller, S. van Dijken, G.S.D. Beach, Nat. Mater. **14**, 174 (2015)
135. G.B. McKenna, Eur. Phys. J. Special Topics **189**, 285 (2010)
136. W. Zhang, C.W. Brian, L. Yu, J. Phys. Chem. B, **119**, 5071 (2015)
137. K. L. Ngai, J. Polym. Sci., Part B: Polym. Phys. **44**, 2980 (2006)
138. S. Capaccioli, K.L. Ngai, M. Paluch, D. Prevosto, Phys. Rev. E **86**, 051503 (2012)

Chapter 7
Ionic Liquids: Physics Bridging Two Fields

7.1 Introduction

When considering the ionic liquids (ILs) in general, and especially the room temperature ionic liquids (RTIL), the interest is naturally focused on the ionic conductivity and ion dynamics. Nonetheless, many ionic liquids are glass-formers, and undergo glass transition at T_g on cooling at ambient pressure or at P_g on elevating the applied pressure at constant temperature. In the supercooled liquid state, both the structural relaxation and the ionic conductivity relaxation are present and observable. Thus glass-forming ILs confer the bonus of studying ionic conductivity relaxation and structural relaxation in the same material. If the two processes are decoupled, the relation between the structural relaxation on the conductivity relaxation and possible effect of the former on the latter is of interest in basic research as well as in applications. Some general and interesting properties of the two relaxation processes are brought out in this chapter. The challenge to theory is the explanation of not only the properties of the conductivity relaxation but also the structural relaxation, and their relations. As it turns out, the properties of the two relaxation processes are similar, in dynamic properties indicating that they stem from some common physics that bridge the two fields. Proposed specifically for ionic conductivity relaxation and diffusion, some theory or model may run into difficulty in adapting it to explain the similar property of structural relaxation and viscosity of glass-formers. This problem casts doubt on the physics of the theory because it is common to the two fields, and should be easy to adapt it to address the other field. Therefore it is beneficial for those engaged in research of ionic conductivity relaxation and particularly in ionic liquids to be aware of the wealth of properties of glass-forming systems and the explanations.

The purpose of the following sections is to bring out the general and fundamental properties of ion dynamics that should have great impact on the two research fields. The similarity of the properties in the two fields are made clear by presenting each found in the non-ionic glass-formers to be followed immediately by the same in ionic conductivity relaxation.

J. Habasaki et al., *Dynamics of Glassy, Crystalline and Liquid Ionic Conductors*,
Topics in Applied Physics 132, DOI 10.1007/978-3-319-42391-3_7

7.2 Invariance of the Structural α-Dispersion to Various Combinations of T and P with τ_α Kept Constant

Studies of changes of relaxation dynamics of glass-formers with temperature at ambient pressure (0.1 MPa) have traditionally been the way to study glass transition. This practice is due largely to experimental convenience in varying temperature. Most of the experimental data of structural α-relaxation in the literature are ambient pressure measurements carried out at different temperatures. From the experimental data, it is well established that the time dependence of the correlation function of the α-relaxation is well described by the Kohlrausch function. Recently, the technique of applying high pressure in various spectroscopy has been greatly improved. By now, pressure from 0.1 MPa up to several GPa can be routinely employed as an experimental variable in light scattering, neutron scattering and broadband dielectric relaxation to probe the dynamics of the glass-formers. Consequently, experimental measurements can be made at different combinations of P and T over wide ranges of both variables. The specific volume V corresponding to any combination of P and T can be inferred from P-V-T measurements made separately. Elevated pressure increases τ_α, but the increase can be compensated by raising temperature. Hence, various combinations of P and T can be chosen for which the α-loss peak frequency ν_α and the corresponding relaxation time τ_α are the same.

By examining the large amount of experimental data from combined pressure P and temperature T studies of many different glassformers in various classes, an important experimental fact has emerged since 2005 [1, 2]. At any chosen constant value of the structural relaxation time τ_α or frequency ν_α, the frequency dispersion of the structural α-relaxation is invariant to different combinations of P and T. The frequency dispersion of the α-relaxation usually is well fitted by the Fourier transform of the Kohlrausch function, $\phi(t) = \exp\left\{-[t/\tau_\alpha(T,P)]^{1-n(T,P)}\right\}$, hence the general result can be restated as the invariance of the Kohlrausch exponent, 1-$n(T,P)$, to different combinations of P and T that keep $\tau_\alpha(T,P)$ constant. In addition to the large collection of glass-formers in the 2005 and 2006 publications, since then many more glass-forming systems have been found showing this property. Some combinations of T and P with contrasting values entail large differences in specific volume V and entropy S which follows from the thermodynamic relation, $(\partial S/\partial P)_T = (\partial V/\partial T)_P$ [3]. Thus the frequency dispersion or $n(T,P)$ at constant $\tau_\alpha(T,P)$ is independent of thermodynamic condition. In all the glass-formers having this property, the intermolecular potential is unchanged on varying T and P. Glass-formers with hydrogen bonds dominating the structure are excluded because high temperature associated with high pressure breaks hydrogen bonds and alters the structure and interaction.

Some examples of data published after the 2005 and 2006 papers [1, 2] are given here to show this spectacular property continue to hold in more glass-formers investigated up to date. The systems studied by dielectric spectroscopy at ambient and elevated pressure are mixture of 25 wt% of 2-picoline with tri-styrene [4], and

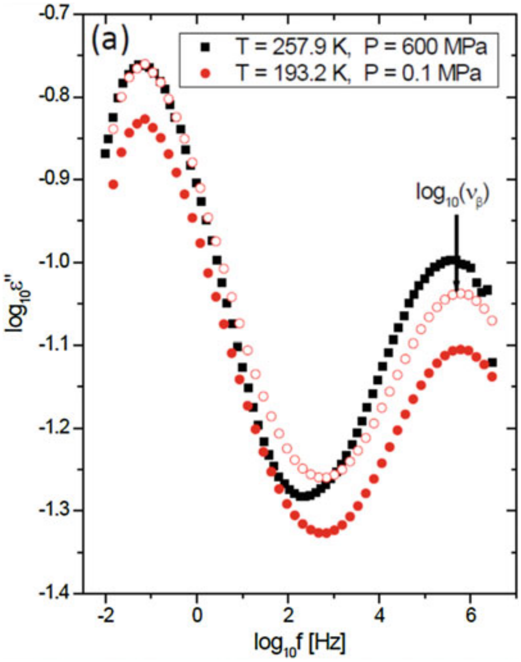

Fig. 7.1 Comparison of two spectra of 2-picoline in 25 wt% mixture with tri-styrene having the same α-relaxation frequency but measured at different thermodynamic conditions (see labels in figure). The *open circles* are obtained by shifting the data at 0.1 MPa vertically by a constant. The *arrow* indicates that JG β-relaxation frequency remains practically unchanged. Data from Ref. [4] are replotted here

mixture of 10 wt% of quinaldine with tri-styrene [5]. Since the dipole moments of picoline and quinaldine are much larger than tri-styrene, the observed spectra are contributed effectively by the motions of picoline or quinaldine. Both picoline and quinaldine are rigid molecules without any internal degree of freedom. In each mixture, the shape of the α-loss peak of picoline or quinaldine is invariant to T and P when τ_α is held constant. The invariance of the shape was found to hold for more than one constant τ_α value. Examples of superposed spectra from the two mixtures are shown in Figs. 7.1 and 7.2. In Fig. 7.3, the α-relaxation of the polar rigid molecule benzonitrile with 10 wt% in mixture with polystyrene with molecular weight of 370 show perfect superposition at all frequencies for several combinations of P and T [6].

Moreover, the data show not only the dispersion of the α-loss peak, but also the Johari-Goldstein (JG) β-relaxation time $\tau_{JG}(T,P)$ of picoline or quinaldine in the mixtures are invariant to different combinations of T and P while keeping τ_α constant, like the neat glass-former benzoin-isobutylether (BIBE) shown here in Fig. 7.4.

The primitive relaxation time τ_0 of the Coupling Model (CM) presented in Chap. 4 is calculated from the CM equation,

$$\tau_\alpha(T,P) = \left[(t_c)^{-n(T,P)}\tau_0(T,P)\right]^{1/(1-n(T,P))}, \tag{7.1}$$

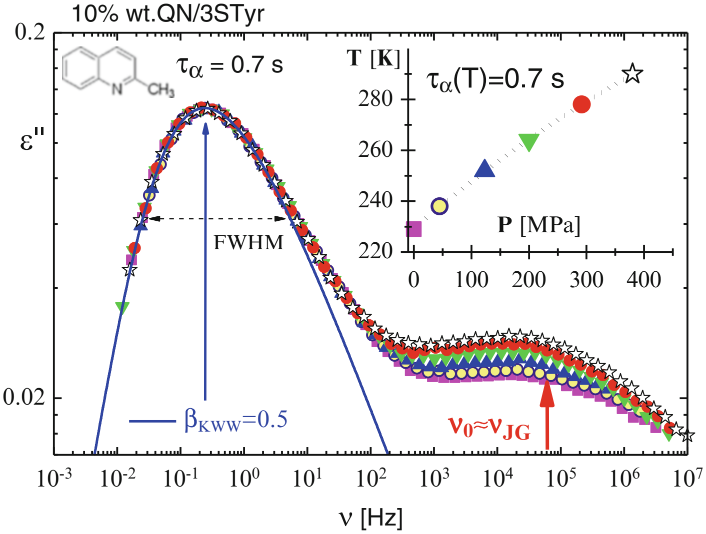

Fig. 7.2 *T-P* superposition of loss spectra for 10 % QN in tristyrene measured for different *T* and *P* combinations shown in the *inset* but the same $\tau_\alpha = 0.67$ s. The line is a Fourier transformed of the Kohlrausch function with $\beta_{KWW} \equiv (1\text{-}n) = 0.5$. The results demonstrate the co-invariance of three quantities, τ_α, n, and τ_{JG}, to widely different combinations of T and P. Data from Ref. [5] and redrawn

Fig. 7.3 Superposition of loss spectra for 10 % BzNtr in PS370 measured for different *T* and *P* combinations but the same τ_α. Reproduced from Ref. [61] by permission

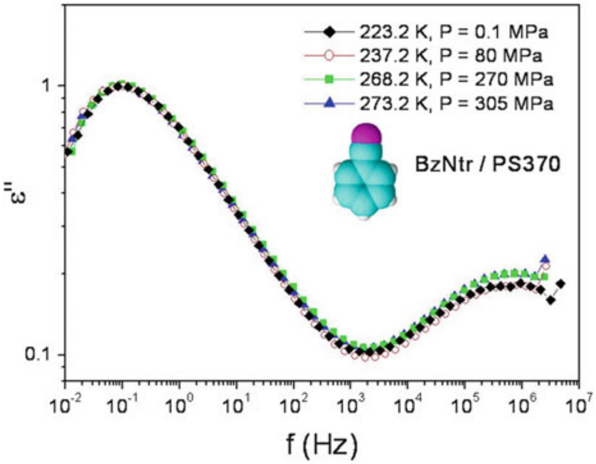

with the values of $\tau_\alpha(T,P)$ and $n(T,P)$ determined by the Kohlrausch fit, and $t_c = 2$ ps. In all three figures, the calculated $\tau_0(T,P)$ is in good agreement with $\tau_{JG}(T,P)$, which is one of the predictions of the CM [7–10]. This means that τ_α, τ_0 (or τ_{JG}), and the frequency dispersion (or n) of picoline, quinaldine or benzonitrile in the mixtures and BIBE are co-invariants to changes in T and P while keeping either τ_α or $\tau_\beta \approx \tau_0$ constant, exactly as prescribed by the CM Eq. (7.1).

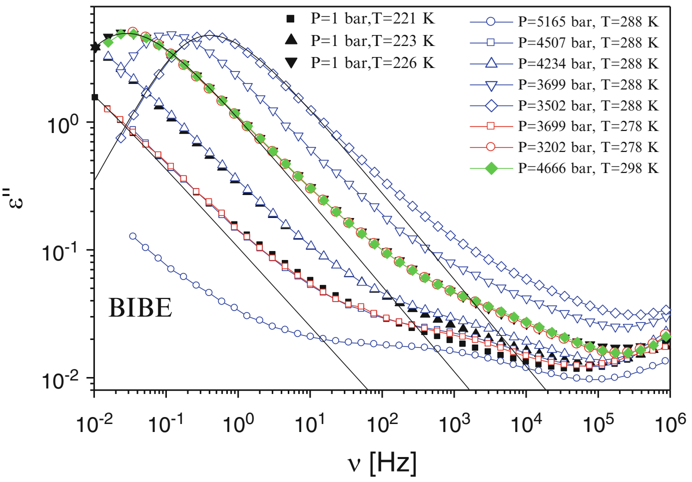

Fig. 7.4 *T-P* superposition of both α- and JG β-relaxation of benzoin-isobutylether (BIBE) showing invariance of the ratio τ_{JG}/τ_α at constant τ_α for widely different combinations of *P* and *T*. Note that when the 1 bar data are near coincident with the data at elevated pressures, the former are hidden and cannot be seen

7.3 Invariance of the Conductivity α-Dispersion of ILs to Various Combinations of *T* and *P* with $\tau_{\sigma\alpha}$ Kept Constant

In this section we shall show ionic conductivity α-relaxation in ionic liquids (ILs) in general has its frequency dispersion invariant to variations of the *T* and *P* while keeping the conductivity relaxation time, $\tau_{\sigma\alpha}$, constant. This is the exact analogue of the property of the structural α-relaxation in non-ionic glass-formers discussed in the previous Sect. 7.2.

7.3.1 $0.4\mathrm{Ca(NO_3)_2}$-$0.6\mathrm{KNO_3}$ (CKN)

We start with the *T* and *P* dependence of the conductivity relaxation in the canonical ionic glass-former $0.4\mathrm{Ca(NO_3)_2}$-$0.6\mathrm{KNO_3}$ (CKN) [11] discussed in detail before in Chap. 4 (see Figs. 4.3, 4.4, 4.5 and 4.6 therein). Measurements at ambient pressure were presented in terms of frequency dependent complex electric modulus, $M^*(f) = M'(f) + iM''(f)$. The $M''(f)$ loss peak narrows on lowering temperature or increasing $\tau_{\sigma\alpha}$, towards $T_g = 333 \pm 2$ K. The trend on lowering *T* (cooling) or elevating pressure (squeezing) is reflected by the increase of $\beta_\sigma(T,P) \equiv [1 - n_\sigma(T, P)]$, acquired from fits of the spectra to the Fourier transform of the Kohlrausch function, $\phi_\sigma(t) = \exp\left\{-[t/\tau_{\sigma\alpha}(T,P)]^{1-n_\sigma(T,P)}\right\}$, as shown in Fig. 7.5. This plot

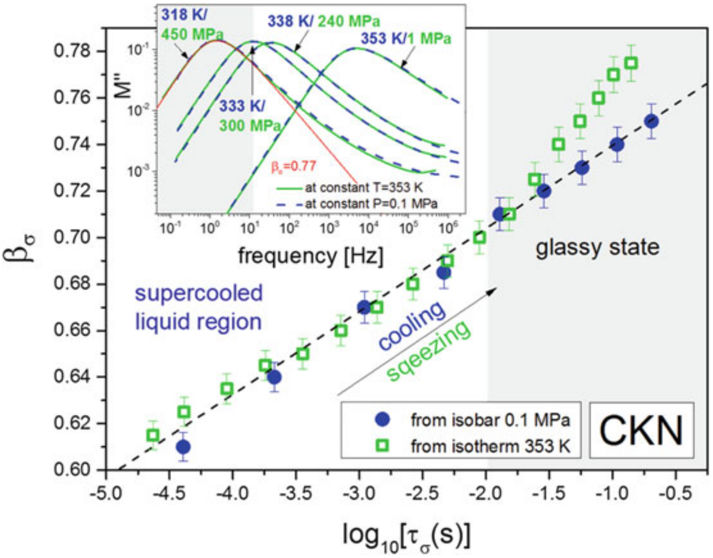

Fig. 7.5 Plot of β_σ versus $\log\tau_{\sigma\alpha}$. *Circles* and *squares* are obtained from fitting the isobaric and isothermal $M''(f)$ loss peaks in Fig. 7.1a, b, respectively. The *inset* presents the comparison of dielectric spectra recorded at different temperature and pressure conditions and at the same conductivity relaxation time. *Solid red line* is the fit to the KWW function with $\beta = 0.77$

shows that for any fixed $\tau_{\sigma\alpha}(T,P)$, the value of $\beta_\sigma(T,P)$ or $n_\sigma(T,P)$ is the same independent of the different combinations of T and P. Examples are shown by the superposition of the $M''(f)$ loss peaks at several fixed values of the peak frequency, $f_{\sigma\alpha}(T,P)$, and the Kohlrausch fit with $\beta_\sigma = 0.77$ for the two combinations of $T = 318$ K and $P = 0.1$ MPa, and $T = 353$ K and $P = 450$ MPa. This general property, shared by structural α-relaxation in non-ionic glass-formers and ion conductivity relaxation in IL, is remarkable.

The secondary β-conductivity relaxation of CKN is not resolved but its presence is suggested by the excess wing at higher frequencies than α-conductivity loss peak frequency $f_{\sigma\alpha}(T,P)$. The CM relations for ionic conductivity relaxations are given by

$$\tau_{\sigma\alpha} = \left[(t_{\sigma c})^{-n_\sigma}\tau_{\sigma 0}\right]^{1/(1-n_\sigma)}, \tag{7.2}$$

and

$$\tau_{\sigma 0} \approx \tau_{\sigma\beta} \tag{7.3}$$

where $\tau_{\sigma 0}$ and $\tau_{\sigma\beta}$ are respectively the primitive and secondary conductivity relaxation times. and $t_{\sigma c}$ is typically about 1 ps [9, 10]. From Eq. (7.2) and relation (7.3), it follows that

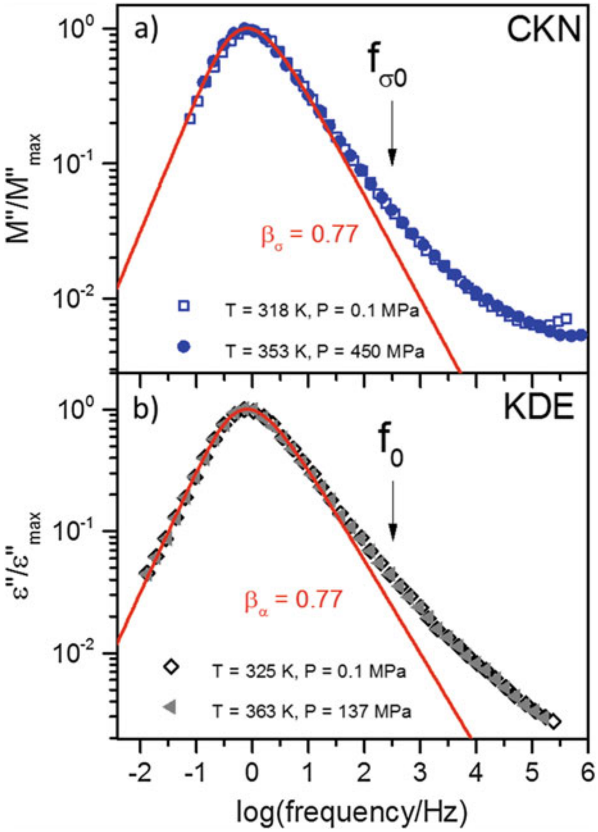

Fig. 7.6 $M''(f)$ spectra of CKN (panel **a**) and $\varepsilon''(f)$ spectra of KDE (panel **b**) recorded at different temperature and pressure conditions while maintaining the relaxation time constant. A small horizontal shift of 0.05 decade to lower frequencies of the $\varepsilon''(f)$ data is applied to have its maximum at the same frequency as $M''(f)$ of CKN. *Solid lines* are the fits to the KWW function with β_σ and $\beta_\alpha = 0.77$. The *arrow* indicates the primitive relaxation frequencies, $f_{\sigma 0}$ and $f_{\alpha 0}$ calculated by Coupling Model

$$[\log\tau_{\sigma\alpha} - \log\tau_{\sigma 0}] = \left[\frac{n_\sigma}{1 - n_\sigma}\right]\log\left(\frac{t_{\sigma c}}{\tau_{\sigma 0}}\right) \approx [\log\tau_{\sigma\alpha} - \log\tau_{\sigma\beta}] \tag{7.4}$$

The coupling parameter $n_\sigma = (1 - \beta_\sigma) = 0.23$ of CKN from the fit in the inset of Fig. 7.5 is small. Hence the separation between α- and the β-relaxation times on the log-scale, $\log\tau_{\sigma\alpha} - \log\tau_{\sigma\beta}$, from Eq. (7.4) is not large. The primitive frequency, $f_{\sigma 0} = 1/(2\pi\tau_{\sigma 0})$, with $\tau_{\sigma 0}$ calculated by Eq. (7.2) is indicated by the arrow in the upper panel of Fig. 7.6. The proximity of $f_{\sigma 0}$ to $f_{\sigma\alpha}$ is the reason why the β-conductivity relaxation is not resolved and instead showing up as an excess wing. Nevertheless, the entire frequency dispersion, including the α-conductivity loss peak and the excess wing representing the unresolved β-conductivity relaxation, superpose perfectly. This fact suggests that $\tau_{\sigma\alpha}$, $\tau_{\sigma 0}$ (or $\tau_{\sigma\beta}$), and the frequency dispersion (or n_σ) of CKN are co-invariants to changes in T and P while keeping either $\tau_{\sigma\alpha}$ or $\tau_{\sigma\beta} \approx \tau_{\sigma 0}$ constant, exactly as predicted by the by the CM Eq. (7.2) and relation (7.3).

Analogue of the conductivity relaxation in CKN can be found from the structural α-relaxation of many non-ionic glass-formers. The lower panel of Fig. 7.6 presents the structural α-relaxation of the non-ionic glass-former, cresolphthalein-dimethylether (KDE), which has almost the same frequency dispersion of its dielectric loss, $\varepsilon''(f)$ as that of $M''(f)$ of CKN, i.e. $n_\sigma = n_\alpha = 0.23$. Data of $\varepsilon''(f)/\varepsilon''_{\max}$ from KDE were taken at two combinations of T and P, ($T = 325$ K and $P = 0.1$ MPa) and ($T = 363$ K and $P = 137$ MPa). The primitive $f_0 = 1/(2\pi\tau_0)$ of KDE indicated by the arrow is also too close to the peak frequency, and hence the β-relaxation is not resolved. Like $M''(f)$ of CKN, the frequency dispersion of $\varepsilon''(f)$ is the same for two different combination of T and P, including the α-loss peak and the excess wing of KDE.

Presented in Fig. 7.7 are the isothermal and isobaric τ_σ of CKN. The change of τ_σ in T-dependence isobarically seen in the left panel is due to crossing the glass transition temperature T_g at $P = 0.1$ MPa. The data and the change are the same as that found by Howell et al. [12] in CKN reproduced in Fig. 7.8. The change of τ_σ in P-dependence in the right panel is due to it crossing the glass transition pressure P_g at constant temperature of 353 K. The broken line indicates that τ_σ has the same value at the two ways of reaching glass transition, and the frequency dispersion is the same or n_σ has the same value. The ratio, $\tau_\alpha/\tau_{\sigma\alpha}$ is the same at T_g and P_g, independent of whether glass transition occurs isobarically or isothermally. This indicates that the decoupling of the conductivity relaxation from the structural relaxation, discussed in Chap. 4, is also independent of thermodynamic factors, and is determined by n_σ.

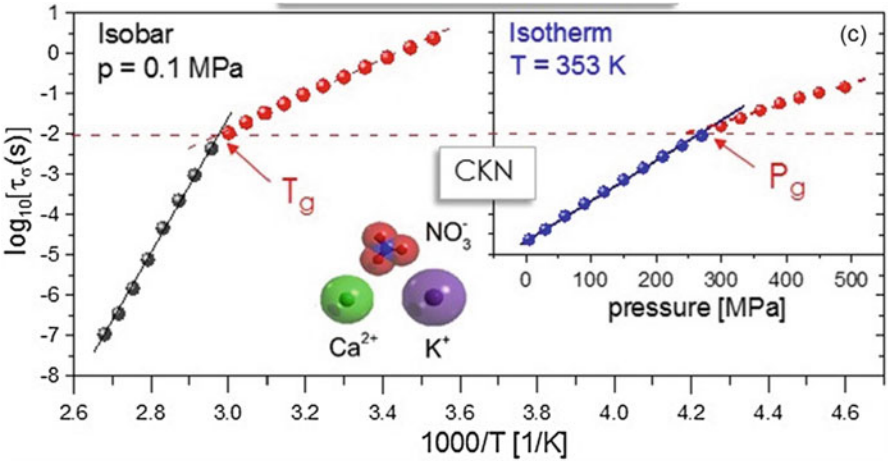

Fig. 7.7 Isobaric and isothermal dielectric measurements of conductivity relaxation time of CKN. The ratio, τ_α/τ_σ is the same at T_g and P_g, independent of whether glass transition occurs isobarically or isothermally. Data from Ref. [11] replotted

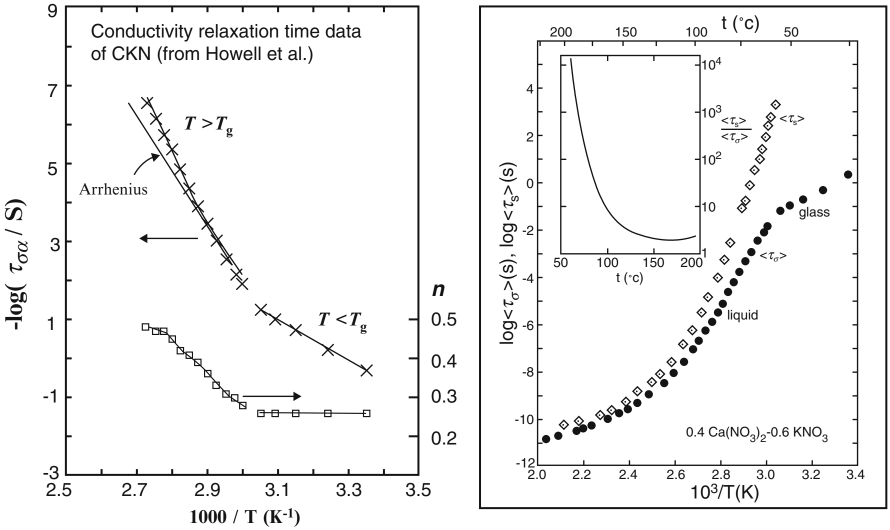

Fig. 7.8 (*Left*) Plot of $\log\tau_{\sigma\alpha}$ and n_σ against 1000/T of CKN showing changes of T-dependence of both quantities at T_g. Data are taken from Howell et al. and reproduced on the (*Right*)

7.3.2 Narrowing of the Conductivity Relaxation Dispersion of CKN on Decoupling: An Observation Challenging for Explanation

In most glass-forming ionic conductors including CKN [12, 13], CdF2-LiF-AlF3-PbF2 (CLAP) [14], and the room temperature ionic liquid, 1-butyl-3-methylimidazolium hexafluorophosphate (BMIM-HFP) [15–17], ion conduction or diffusion involves either the most mobile ionic part, while the structural α-relaxation involves the motion of all parts of the structural units. More generally, the translation of ions and structural α-relaxation are different modes of relaxation. For these reasons, the correlation function of ionic conductivity can be different from that of the structural α-relaxation. Due to this difference, the ion-ion interaction and correlation is less effective in slowing down the ionic conductivity relaxation than the molecular-molecular interaction and correlation in slowing down the structural α-relaxation. In the context of the Coupling Model (CM), the difference means that the coupling parameter n_σ of conductivity relaxation is smaller than n of structural relaxation. Two CM equations govern the structural relaxation time, τ_α, and the conductivity relaxation time, $\tau_{\sigma\alpha}$, which are Eqs. (7.1) and (7.2) respectively. If $n > n_\sigma$, the two relaxations are decoupled, and $\tau_{\sigma\alpha}$ has a weaker temperature dependence than τ_α. On the other hand, if the two are fully coupled, then $n = n_\sigma$ and $\tau_{\sigma\alpha} = \tau_\alpha$.

Phenomenologically, in CKN and the other glass-forming ionic conductors, the decoupling of conductivity relaxation from structural relaxation starts in the equilibrium liquid state when temperature falls below T_i (see the right panel of Fig. 7.8). At temperatures above T_i, $R_\tau(T) \equiv <\tau_\alpha(T)>/<\tau_{\sigma\alpha}(T)> = 0$ since $<\tau_\alpha(T)>$ and $<\tau_{\sigma\alpha}(T)>$ are equal, and structural and conductivity relaxations are essentially the same process, and hence $\tau_{\sigma 0}(T) = \tau_0(T)$ and $n_\sigma(T) = n(T)$. In other words, the two are fully coupled together to appear as one and the same process. As temperature decreases below T_i, there is separation of $<\tau_{\sigma\alpha}(T)>$ from $<\tau_\alpha(T)>$. The decoupling of the conductivity relaxation is caused by $n_\sigma(T)$ to start falling below $n(T)$. Further decrease in temperature leads to monotonic decrease of $n_\sigma(T)$. This continues until $R_\tau(T)$ becomes large enough for complete decoupling of the conductivity relaxation from the structural relaxation. At this point and beyond, the values of n_σ and $\tau_{\sigma 0}$ in Eq. (7.2) are for the optimally decoupled conductivity relaxation. This is a possible explanation of the narrowing of the α-conductivity relaxation dispersion on increasing decoupling. The idea was sketched out in a paper published many years ago [18, 19]. The data of CKN from Howell et al. [12] was used to demonstrate the decrease of $n_\sigma(T)$ with increasing decoupling on decreasing temperature, and how it determines $\tau_{\sigma\alpha}(T)$ according to Eq. (7.2). As shown for temperatures below T_g in the left panel of Fig. 7.8, $n_\sigma(T)$ is constant while the temperature dependence of $\tau_{\sigma\alpha}(T)$ is Arrhenius. By applying Eq. (7.2), the Arrhenius temperature dependence of $\tau_{\sigma 0}(T)$ is determined. Assuming that this Arrhenius dependence of $\tau_{\sigma 0}(T)$ holds above T_g, applying once more Eq. (7.4) with the values of $n_\sigma(T)$, we have calculated $\tau_{\sigma\alpha}(T)$. The results are in agreement with the experimental data (see left panel of Fig. 7.8).

Hasz et al. [14] had reviewed the explanations given by others than that of the CM of the narrowing of the α-conductivity relaxation dispersion on increasing decoupling from structural relaxation in various systems, and found them not capable to explain the experimental data including CKN. They also expressed reservation on the explanation for CKN sketched out before by Ngai and Mundy in Ref. [19], and elaborated here in the above. The main point made by Hasz et al. is based on the comparison of the decoupling of CKN with that of CdF_2-LiF-AlF_3-PbF_2 (CLAP) and alkali silicates. For CLAP melt, R_τ is $10^{7.1}$ at T_g (=277 °C) and decreases with increasing temperature to a value of $10^{5.2}$ at 325 °C. Hasz et al. pointed out the similarity as well as difference between the decoupling found in CLAP and CKN. The similarity is that R_τ exhibits the same type of temperature dependence, and β_σ decreases with increasing temperature. The difference is that R_τ in CLAP remains much greater than unity, and the electrical and structural relaxation processes remain highly decoupled in the temperature range where the CLAP melt β_σ decreases with increasing temperature. In other words, in CLAP, the conductivity relaxation remains highly decoupled and yet there is broadening of the dispersion or β_σ values decreasing with increasing temperature, while in the CKN melt the conductivity relaxation has gone from decoupled from to fully coupled with the structural relaxation. What Hasz et al. forgot is to compare the size of the change of the β_σ values in CLAP and in CKN. In CLAP the change is from 0.77 to 0.69. On the other hand, the change in CKN is from 0.74 to 0.52, which is much larger. Also the corresponding change of the conductivity relaxation time, $\tau_{\sigma\alpha}$, from one limiting value to another is much larger in CKN than in CLAP according to Eq. (7.2). Hasz et al. also considered the alkali silicate melt above T_g as an even more extreme case than CLAP because of larger R_τ. However the β_σ values they used to show the decrease with increasing temperature for the melt near T_g were obtained by very long extrapolation of data taken deep in the glassy state [20], and hence the conclusion cannot be considered as definitive or valid.

After the publication of the paper by Hasz et al., Moynihan [21] reexamined the problem of decoupling. He proposed a dynamic heterogeneity model for structural relaxation in glassforming liquids which assumes that the non-exponential structural relaxation kinetics are due to a distribution of independently relaxing nanoregions which relax at different rates. From the model, he gave an estimate of the contribution of microscopic heterogeneity to the non-exponentiality of the conductivity relaxation in ionically conducting glasses. For ionically conducting inorganic glasses with large R_τ near T_g such as the alkali silicate glasses, the microscopic heterogeneity makes at best a very minor contribution to the non-exponentiality of the electrical relaxation. From this he concluded that the source of this non-exponentiality is primarily correlations among the mobile ions, which is consistent with the CM applied to ionic conductors in general [10, 22, 23]. However for CKN, his result indicates that microscopic heterogeneity should make increasing contributions to non-exponential electrical relaxation in melts as the temperature is increased above T_g, in accord with the decrease of β_σ. It should be noted that heterogeneous dynamics is consistent with the CM as made clear in Refs. [24, 25], although this property is not emphasized when Eqs. (7.1) and (7.2) are employed. Thus the two approaches, one by Moynihan and the other by the CM, can be considered to be closely related, as expressed by Moynihan in the statement "It should be noted that this account of the temperature dependence of β_σ for the CKN melt is not phenomenologically inconsistent with that proposed earlier by Ngai and Mundy", and "The main difference between the treatment of Ngai and Mundy and that suggested in the present manuscript is the assumption made here that microscopic heterogeneity continues to be a prime contributor to non-exponential structural relaxation in very fluid melts at high temperatures.".

The ambient pressure data of CKN in Fig. 7.7 are within errors the same as found earlier by Howell et al. [12]. The glass-liquid transition temperature T_g is around 60 °C. The M'' vs frequency data at a number of temperatures from 25.3 to 93.2° C are well accounted for at each temperature by Fourier transform of a Kohlrausch function. As mentioned above, the frequency dispersion narrows on cooling from 93.2° C down to T_g, but becomes constant at temperatures below T_g. This trend is represented by the temperature dependence of $n_\sigma(T)$ in Fig. 7.8 where [1-$n_\sigma(T)$] is the fractional exponent of the Kohlrausch function, $\phi_\sigma(t) = \exp\left\{-[t/\tau_{\sigma\alpha}(T)]^{1-n_\sigma(T)}\right\}$, used to fit the dispersion. Plotted in the left panel of Fig. 7.8 are the conductivity relaxation times, $\tau_{\sigma\alpha}(T)$, from the fits. The change from Arrhenius T-dependence of $\tau_{\sigma\alpha}(T)$ in the glassy state to a stronger temperature dependence in the liquid state is apparently correlated with the change of $n_\sigma(T)$ from the constant and small value of 0.26 in the glassy state to a monotonically increasing function of T above T_g. According to the CM Eq. (7.2), this T-dependence of $n_\sigma(T)$ can contribute to the T-dependence of $\tau_{\sigma\alpha}(T)$, as discussed in Ref. [18].

7.3.3 *Analogy from the IL, 1-Butyl-3-Methylimidazolium Hexafluorophosphate (BMIM-PF$_6$)*

The decoupling of the conductivity relaxation from the structural relaxation in CKN and CLAP in the liquid state was found also in the supercooled liquid state of the room temperature IL, 1-butyl-3-methylimidazolium hexafluorophosphate (BMIM-PF$_6$), by Ito and Richert [15], and the data analyzed by the CM [17]. The conductivity relaxation time, $\tau_{\sigma\alpha}(T)$, determined from the Kohlrausch fits of $M''(f)$ (shown by one example in the inset) are shown in Fig. 7.9. The Kohlrausch exponent $\beta_\sigma = (1-n_\sigma)$ is equal to 0.60 or $n_\sigma = 0.40$.

The structural relaxation times were deduced from the response of BMIM-PF$_6$ in the solvation of the solute molecule Quinoxaline (QX) at a probe level concentration of around 10^{-4} mol/mol. The solvation dynamics monitored as a function of time and the result was fit by the Kohlrausch function, $C(t) = \exp\left[-(t/\tau_{sol})^{\beta_{sol}}\right]$, The characteristic solvation time, τ_{sol}, was obtained for 15 different temperatures between 194 and 205 K. The exponent, β_{sol}, is temperature independent and equal to 0.30 ± 0.03, or $n_{sol} \equiv (1-\beta_{sol}) = 0.70 \pm 0.03$. The rotational motion of the probe molecule QX in BMIM-PF$_6$ also was measured. The orientational correlation function of the probe molecule, $r(t)$, was fit by the Kohlrausch function, $r(t) = r(t=0)\exp\left[-(t/\tau_{rot})^{\beta_{rot}}\right]$, with β_{rot} temperature independent and equal to 0.37 ± 0.05, or $n_{rot} \equiv (1-\beta_{rot}) = 0.63 \pm 0.05$. Thus, within experimental error, n_{sol} and n_{rot} are about the same. Plotted against reciprocal temperature, Fig. 7.9 shows that τ_{sol} and τ_{rot} are nearly the same, indicating that both are good estimates of the structural relaxation time of the BMIM-PF$_6$. The decoupling of $\tau_{\sigma\alpha}(T)$ from τ_{sol} and τ_{rot} is evident by inspection of Fig. 7.9. Moreover, n_{sol} and n_{rot} are larger than $n_\sigma = 0.40$. Thus the characteristics of the decoupling in BMIM-PF$_6$ is the analogue of that found in CKN, and explained in the same way by the CM equations (7.1) and (7.2) through the difference in the coupling parameters of structural relaxation and conductivity relaxation [17].

The decoupling of conductivity relaxation from structural relaxation in ionic conductors is similar to the decoupling of self-diffusion coefficient D from rotational relaxation time τ_c or viscosity η of non-ionic glass-formers. In fact, in BMIM-PF$_6$ $\tau_{\sigma\alpha}(T)$ follows a fractional Stokes-Einstein law, $\tau_{\sigma\alpha}(T) \propto \eta^{0.73}/T$, similar to the relation between self-diffusion coefficient D and viscosity, $D \propto T/\eta^{\xi}$ with $\xi < 1$, observed in many non-ionic glass-formers. The latter is commonly referred to as breakdown of Stokes-Einstein (SE) relation or Debye-Stokes-Einstein (DSE) relation, i.e. the products $D\eta$ and $D\tau_c$ increase as the temperature is lowered towards T_g. This was seen in 1,3-bis-(1-naphthyl)-5-(2-naphthyl)benzene (TNB), ortho-

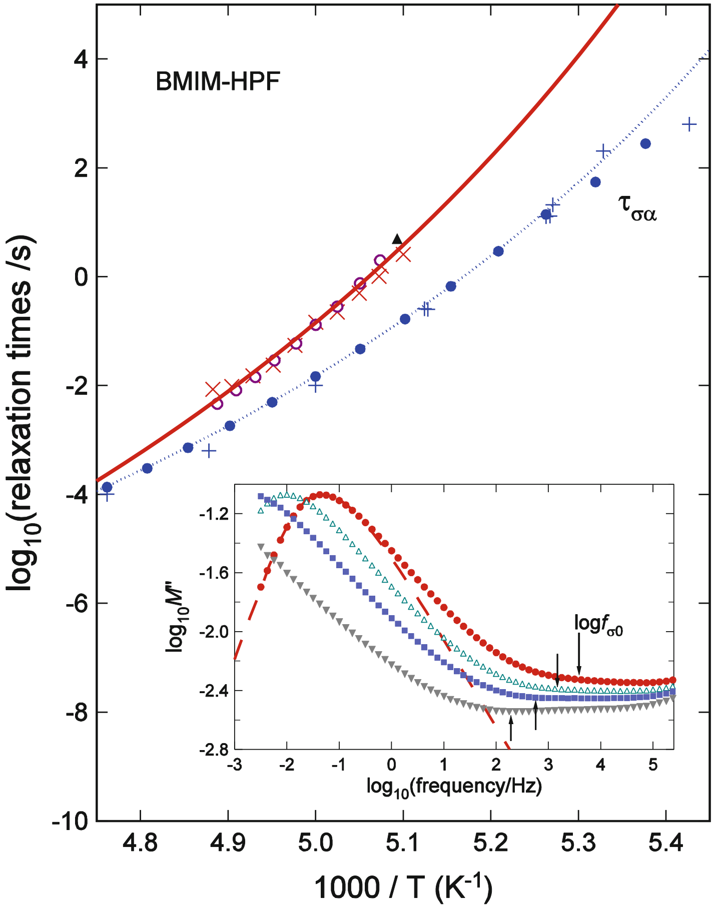

Fig. 7.9 Temperature dependence of various measured and calculated relaxation times of BMIM-HFP. *Solid circles* are the electric loss modulus peak time constants $\tau_{\sigma\alpha}$ measured by Ito and Richert [15], and the plus signs are the $\tau_{\sigma\alpha}$ values from them, the *dotted line* is a VFTH fit to $\tau_{\sigma\alpha}(T)$. *Open circles* show the solvation times (τ_{sol}) based on QX, crosses represent the probe rotation times $\tau_{rot}(T)$ for QX in BMIM-HFP. *Solid triangle* represents logarithm of viscosity, log(η/P), after 10.3 has been subtracted from it to match the log(τ/s) scale. The *inset* are the electric loss modulus data at 182, 188, 190, and 192 K of Ref. [17] The *dashed line* is the fit to the Fourier transform of the Kohlrausch function with $n_\sigma = 0.40$. The calculated primitive frequencies $f_{\sigma 0}$ at the four temperatures are indicated by the *arrows*. Apparently, the nearly constant loss is present at higher frequencies than $f_{\sigma 0}$

terphenyl, sucrose benzoate and other glass-formers [26–32]. For a long time, explanation of the breakdown of the SE and DSE relations was based on spatial and dynamic heterogeneity of the structural α-relaxation. By now it is recognized [33] that this explanation is contradicted by other experiments and hence is defunct. On the other hand, the CM explanation based on the coupling parameter of diffusion, n_D, being smaller than that of viscosity, n_{rot}, continues to hold [31, 32], and more generally when comparing different dynamic variable with different correlation functions [34]. The physics behind this explanation is fundamentally the same as for the decoupling of conductivity relaxation from structural relaxation in CKN and BMIM-PF$_6$ discussed in Sect. 7.3.2 and 7.3.3, as well as the explanation of the difference of ion dynamics in glassy ionic conductors probed by conductivity relaxation and NMR in Chap. 5. The correlation function of ion dynamics probed by NMR is conducive to enhanced ion-ion correlation than conductive relaxation, leading to the coupling parameter of NMR, n_{NMR}, being larger than n_σ. The primitive relaxation time and its activation energy is the same for NMR and conductivity. This together with the CM equation for NMR $\tau_{NMR\alpha} = \left[(t_{\sigma c})^{-n_{NMR}} \tau_{NMR0}\right]^{1/(1-n_{\sigma NMR})}$ and the companion Eq. (7.2) for conductivity relaxation, the difference between $\tau_{\sigma\alpha}$ and $\tau_{NMR\alpha}$ found by experiments [35–40] and simulations [41, 42] was explained [42–45].

The ability of the CM to explain with the same physics the decoupling phenomena between different processes and in diverse systems is worth notice.

7.3.4 1-Butyl-1-Methylpyrrolidinium Bis[Oxalato]Borate (BMP-BOB)

Dielectric relaxation measurements were reported on the ionic liquid, 1-butyl-1-methylpyrrolidinium bis[oxalato]borate (BMP-BOB), over wide temperature (123–300 K) and pressure ranges (0.1–500 MPa) [46]. The measured complex dielectric susceptibility $\varepsilon^*(\nu)$ was presented in terms of the electric modulus M^*

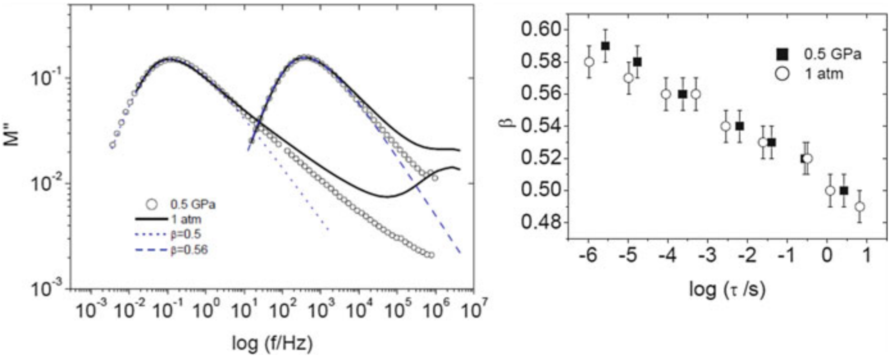

Fig. 7.10 (*Left*) Electric modulus relaxation spectra (M'') of the ionic liquid BMP-BOB at ambient pressure and 231 and 245 K are plotted as *solid lines*. High pressure M'' data (0.5 GPa) at the temperatures that yield relaxation times similar to those of the ambient pressure data, 283 and 308 K, are included in the figure as squares. Data at 0.5 GPa data are slightly shifted in frequency to match perfectly the atmospheric peak frequencies. Long and short dashed lines are fits to a Kohlrausch relaxation function with $\beta \equiv (1\text{-}n) = 0.56$ and 0.50, respectively. (*Right*) The figure shows the co-invariance of β and the relaxation time at different temperatures and at atmospheric pressure and at elevated pressure of 0.5 GPa. Data from Ref. [46] are replotted here

$(\nu) = 1/\varepsilon^*(\nu)$. The frequency dependence of the imaginary part of $M^*(\nu)$, $M''(\nu)$, is shown in the left panel of Fig. 7.10. Data at ambient pressure were taken at 231 and 245 K. At the high pressure of 0.5 GPa, the M'' data were taken at 283 and 308 K, which were chosen such that the loss peak frequencies $f_{\sigma\alpha}$ match those at ambient pressure. The prominent loss peak comes from the conductivity α-relaxation. Shown by the dashed lines are fits to the frequency dispersions by the Fourier transforms of the Kohlrausch functions. The loss peak observed at high frequencies does not shift much with temperature and its intensity is suppressed by pressure. It is not the conductivity β-relaxation and comes from some intramolecular relaxation. The conductivity β-relaxation of BMP-BOB is not resolved, and appear as the excess wing loss over and above that the Kohlrausch fit in the left panel of Fig. 7.10.

Dielectric study of another IL, BMIM-BMSF [16, 47], at ambient pressure have found two secondary relaxations, with the slower secondary relaxation proposed as the JG β-conductivity relaxation. The authors of Refs. [16, 47] made this conclusion based on its relaxation time having an activation energy $E_a = 24RT_g$ obeyed by JG β-relaxation in some non-ionically conducting glass-formers. However this criterion for JG β-relaxation is loose because it has been shown that non-JG β-relaxation in some glass-formers also obey the relation $E_a = 24RT_g$, and there is a large spread in the ratio of E_a/RT_g for genuine JG β-relaxations [48]. The critical test was made by applying pressure to BMIM-BMSF, and it was found that the purported JG β-relaxation does not shift in frequency on elevating pressure, and thus the resolved secondary relaxations of BMIM-BMSF have nothing to do with the β-conductivity relaxation, which is not resolved.

The width of the frequency dispersion of the α-loss peak broadens with increase of $\tau_{\sigma\alpha}$ on lowering temperature or by elevating pressure. Remarkably, at constant $f_{\sigma\alpha}$ or $\tau_{\sigma\alpha}$, its shape is the same whether the pressure is 0.1 or 500 MPa, as demonstrated in Fig. 7.10. The trend on lowering T or elevating P is reflected by the decrease of $\beta_\sigma(T,P) \equiv [1\text{-}n_\sigma(T,P)]$ with increase of $\tau_{\sigma\alpha}$ as shown in the right panel of Fig. 7.10. Within experimental errors, the values of $\beta_\sigma(T,P)$ at constant $\tau_{\sigma\alpha}$ are the same whether at 0.1 or 500 MPa.

7.3.5 1-Hexyl-3-Methylimidazolium Chloride

The invariance of the shape of the $M''(\nu)$ loss peak to P and T combinations that maintain τ_α constant was also found in another room temperature ionic liquid, 1-hexyl-3-methylimidazolium chloride (or bromide), by M. Mierzwa (unpublished). The data shown in Fig. 7.9 were not published due to some technical difficulty that cannot determine exactly the value of the applied pressure, and hence the values of pressure given in Fig. 7.11 may not be the actual applied ones. Nevertheless, the data are adequate for demonstrating the invariance of the frequency dispersion of the conductivity α-relaxation to changes of T and P at constant $f_{\sigma\alpha}$ or $\tau_{\sigma\alpha}$ in 1-hexyl-3-methylimidazolium chloride.

Fig. 7.11 Invariance of the shape of the electric modulus $M''(\nu)$ loss peak to P and T combinations that maintain τ_α constant in the room temperature ionic liquid, 1-hexyl-3-methylimidazolium bromide. Courtesy of M. Mierzwa

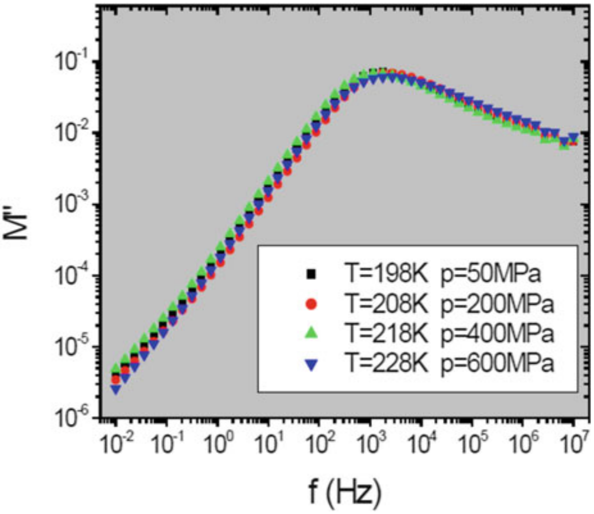

7.3.6 1-Methyl-3-Trimethylsilylmethylimidazolium Tetrafluoroborate ([Si-MIm][BF$_4$])

The conductivity relaxation dynamics of room temperature ionic liquid, 1-methyl-3-trimethylsilylmethylimidazolium tetrafluoroborate ([Si-MIm][BF$_4$]), have been studied by broadband conductivity relaxation measurements at ambient pressure and elevated pressures up to 600 MPa by Jarosz et al. [49] For the first time, several novel features of the dynamics have been found in a room temperature ionic liquid. Data of conductivity relaxation in most ionic conductors when represented by the electric loss modulus, usually a single conductivity α-loss peak is observed in the electric modulus loss $M''(f)$ spectra. However, in [Si-MIm][BF$_4$] found additionally is another well resolved loss peak at higher frequencies at ambient pressure as shown in Fig. 7.12, analogous to the presence of the Johari-Goldstein (JG) -β-relaxation accompanying the structural α-relaxation in many non-ionic glass-formers. The analogy of the β-conductivity relaxation in [Si-MIm][BF$_4$] with JG β-relaxation in non-ionic glass-formers goes further by the finding that its β-conductivity relaxation time τ_β shifts on applying pressure in concert with the relaxation time τ_α of the primary α-conductivity relaxation. The measurements were made at fixed $T = 253$ K and varying pressure, starting at the ambient pressure of 0.1 MPa and increasing up to 600 MPa (see Fig. 7.11). Naturally the analogy leads to the naming of the slower and faster processes resolved in [Si-MIm][BF$_4$] as the primary conductivity α-relaxation and the secondary β-conductivity relaxation respectively. The fits to the frequency dependence of the conductivity α-loss peak can be found at two temperatures in Fig. 7.12 and two pressures in Fig. 7.13, whereby the Kohlrausch exponent, $\beta_\sigma \equiv 1 - n_\sigma = 0.57$ is determined. Utilizing the CM Eqs. 7.2–7.4, the primitive relaxation frequency, $f_{\sigma0}(T)$, were calculated.

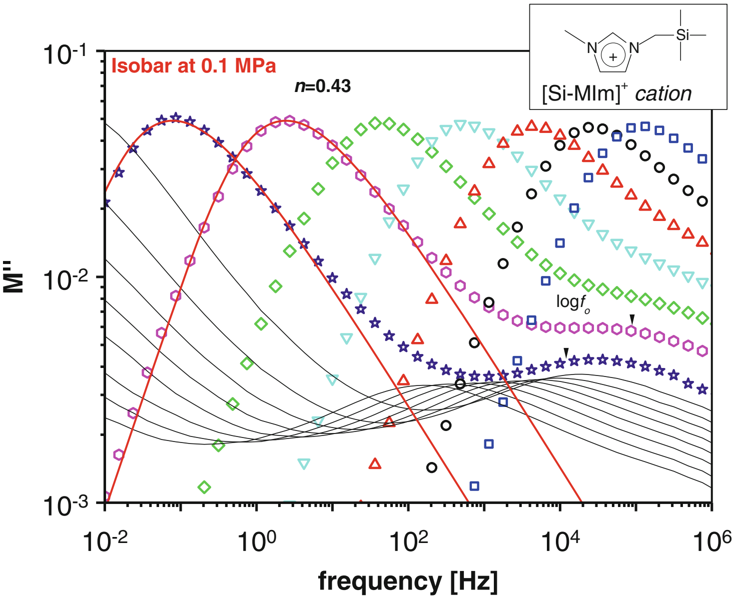

Fig. 7.12 Imaginary part of the complex electric modulus, $M''(f)$, of [Si-MIm][BF$_4$] versus frequency at ambient pressure and temperatures in the range 243–173 K, spanning across T_g. The spectra were measured at interval of 5 K each. The data represented by *symbols* range from 243 to 213 K. Data from 208 to 173 K are not shown by symbols for otherwise they overlap and the features cannot be clearly discerned. To avoid this undesirable situation, the data are interpolated by *black lines* to show the shift of the secondary β-conductivity relaxation on decreasing temperature. The *red lines* are fits to the slower primary α-conductivity relaxation loss peak at two temperatures by the Fourier transform of the Kohlrausch function. The secondary β-conductivity relaxation are resolved above and below T_g. The *arrows* indicate the locations of the logarithm of the primitive conductivity relaxation frequencies, logf_0, which are in agreement with the most probable β-conductivity relaxation frequencies within a factor of about 2. This figure has been shown before in Chap. 4 to emphasize the utility of the electric modulus

The arrows in Figs. 7.12 and 7.13 indicate the locations of the logarithm of log$f_{\sigma 0}$. The agreement of log$f_{\sigma 0}$ with the most probable β-conductivity relaxation frequencies within a factor of about 2, and thus validates the prediction of the CM on the evolution of ion dynamics from caged ions to the primitive or β-conductivity relaxation, and finally to the α-conductivity relaxation and d.c. conductivity. It further proves that the β-conductivity relaxation is the precursor of the α-conductivity relaxation, and the two are inseparable when considering the dynamics of ions. The spectrum taken at 600 MPa (closed inverted triangles) in Fig. 7.13 is in the glassy state. On aging the sample after 12 h while keeping pressure at 600 MPa and $T = 253$ K, the entire data (closed inverted triangles) shifts to lower frequencies (open inverted triangles). The shifts are not uniform, higher the frequency lesser is the shift. The shift of the β-conductivity relaxation on aging is indication that it is sensitive to density, and like the α-relaxation.

The $M''(f)$ loss peak at ambient pressure in Fig. 7.12 and at elevated pressure in Fig. 7.13 do not have exactly the same height. For comparison of the frequency

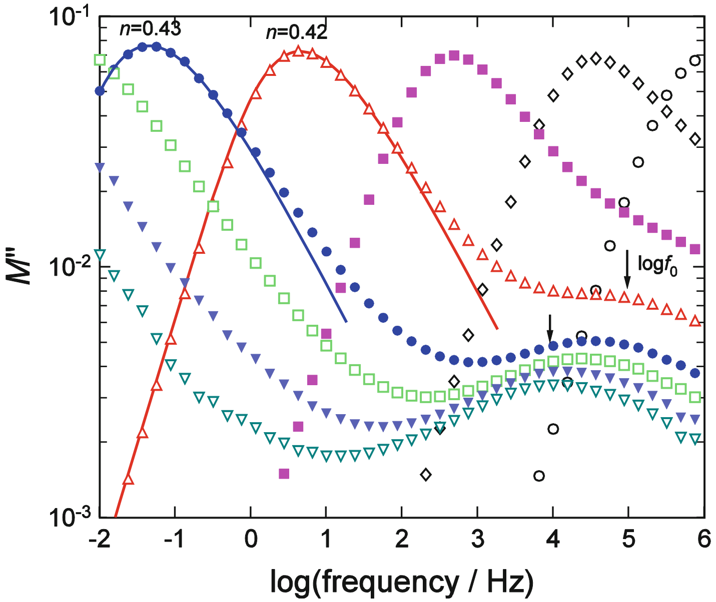

Fig. 7.13 Imaginary part of the complex electric modulus, $M''(f)$, of [Si-MIm][BF$_4$] versus frequency at fixed $T = 253$ K and variable pressure, starting at the ambient pressure of 0.1 MPa on the *far right* (*open circles*) and at elevated pressures from 100 (*open diamonds*) to 600 MPa (*closed inverted triangles*) with increment of 100 MPa each in going from *right to left*. The *open inverted triangles* are the data at 600 MPa and $T = 253$ K after aging the sample for 12 h while keeping pressure temperature constant. The *arrows* indicate the locations of the logarithm of the primitive conductivity relaxation frequencies, logf_0, which are in agreement with the most probable β-conductivity relaxation frequencies within a factor of about 2

dispersion of the α-relaxation at $P = 0.1$ MPa and $T = 213$ K with that at $P = 600$ MPa and $T = 253$ K, we normalize both spectra by the maximum loss, and the normalized spectra are shown in Fig. 7.14. There is a small difference in the frequencies of the loss maxima in the two spectra, and hence the relaxation times τ_α are not exactly the same. Ignoring this small difference in τ_α, it can be seen from the data and the fits by the KWW function with the same exponent, $(1-n)$, in Fig. 7.14 that the frequency dispersion of the α-conductivity relaxation is the same for these two combinations of P and T. Both are well fitted by the Fourier transform of the stretched exponential correlation function with the same $n = 0.43$. Furthermore, the resolved secondary relaxation remains at the same location, and hence τ_β is practically unchanged. Hence, the properties observed can be summarily stated as co-invariance of the three characteristic quantities, $\tau_{\sigma\alpha}$, $\tau_{\sigma\beta}$, and n_σ, to changes in pressure and temperature.

Also shown in Fig. 7.14 is the α-loss peak at ambient pressure of 0.1 MPa and $T = 253$ K. There is shift of more than 7 decades of τ_α on elevating ambient pressure to 600 MPa at $T = 253$ K. Since the JG β-conductivity relaxation is located at higher frequencies than the α-loss peak at $P = 0.1$ MPa and $T = 253$ K, we can infer there is a shift of more than 2.5 decades of τ_β on elevating pressure from 0.1 to 600 MPa.

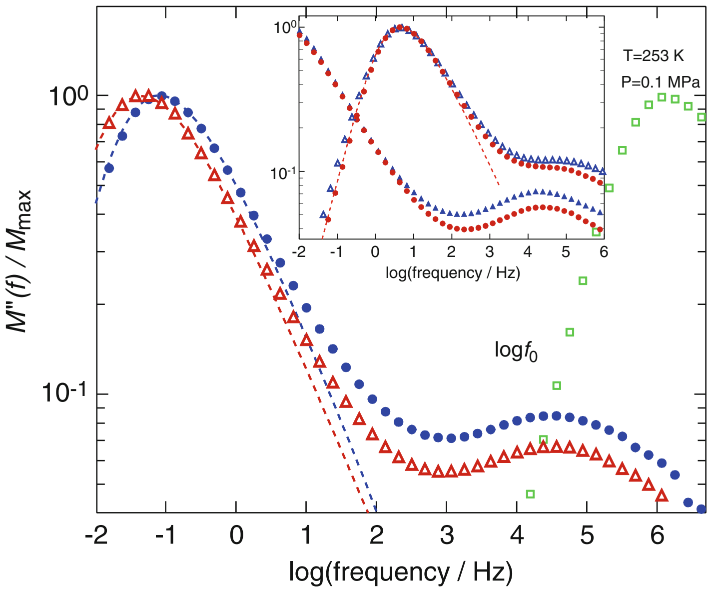

Fig. 7.14 Normalized $M''(f)$ spectra at different combinations of P and T to show co-invariance of τ_α, τ_β, and n at constant τ_α. *Red open triangles* ($P = 600$ MPa, $T = 253$ K). *Blue circles* ($P = 0.1$ MPa, $T = 213$ K). *Green open squares* ($P = 0.1$ MPa, $T = 253$ K). *Blue and red lines* are fits by Fourier transform of stretched exponential correlation function given by Eq. (7.2) with $n = 0.43$. The *inset* show co-invariance at two more constant values of τ_α. *Blue triangles* are data at ambient pressure and $T = 218$ and 208 K from *right to left*. *Red filled circles* are data at constant $T = 253$ K and $P = 300$ and 500 MPa from *right to left*. There is not a perfect match of the peak frequency of data taken at $T = 218$ K and $P = 0.1$ MPa with that taken at $T = 253$ K and $P = 300$ MPa. The comparison is made by shifting the ambient pressure data to higher frequencies by a factor of 1.5. Note that the width of the α-conductivity relaxation loss peak increases slightly on increasing τ_α towards glass transition. The *arrows* indicate the locations of the logarithm of the primitive conductivity relaxation frequencies, logf_0, which are in agreement with the most probable β-conductivity relaxation frequencies within a factor of about 2

This estimate demonstrates the high sensitivity of τ_β to pressure. The inset in Fig. 7.14 shows the co-invariance of τ_α, τ_β, and n holds at two other situations with different values of these parameters, and thus the co-invariance is general.

7.3.7 Caged Ion Dynamics in Ionic Liquids

The β-conductivity relaxation of [Si-MIm][BF$_4$] continues to be observed at temperatures below T_g as shown by a few examples in Figs. 7.12 and 7.13. Its $M''(f)$ spectra at temperatures within the range $163 \leq T \leq 123$ K and deep into the glassy state in Fig. 7.13 show the β-loss peak gives way at higher frequencies to the power law dependence of $M''(f) \propto (f)^{-0.1}$. This feature at higher frequencies of the loss, is

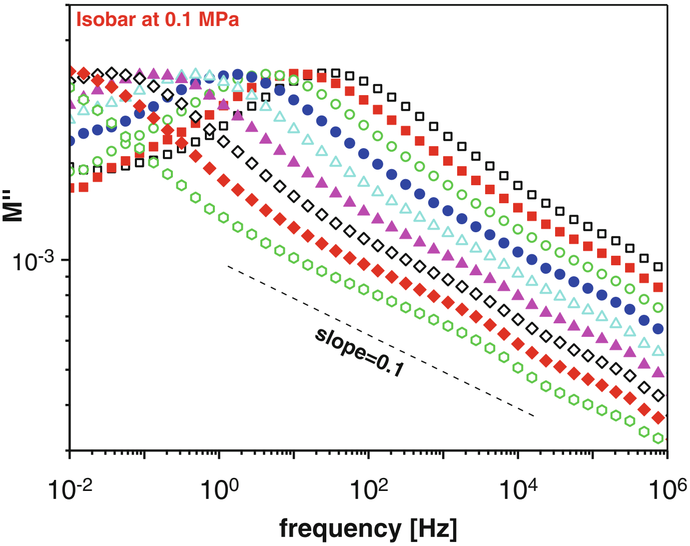

Fig. 7.15 Imaginary part of the complex electric modulus, $M''(f)$, of [Si-MIm][BF_4] versus frequency at ambient pressure and constant temperature with temperature in the range 163–123 K, way below T_g. The spectra, measured at every 5 K, show the presence of the slower and well resolved secondary β-conductivity relaxation and the nearly constant loss (NCL) at higher frequencies

appropriately called the nearly constant loss (NCL) because of the small exponent in the power law, and is commonly observed in many glass-formers, and ionic conductors [9, 50] of different types. The NCL of procainamide HCl was shown before in Figs. 4.8 and 4.10 of Chap. 4. It is the manifestation in susceptibility of caged ions at times before the onset of the primitive or the β-conductivity relaxation. Its properties, fundamental importance, and relation to the β-conductivity relaxation have been discussed in detail in Chap. 4.

Finding the NCL from conductivity relaxation in [Si-MIm][BF_4] is particularly rewarding because the β-conductivity relaxation is resolved, and thus the termination of the NCL by the onset of the β-conductivity relaxation predicted by the Coupling Model can be checked. This property is clearly observed as shown in Fig. 7.15, and hence the prediction is directly verified. The NCL was found in other ILs including BMIM-PF_6 [16] (see Fig. 7.9 inset), and in 1-alkyl-3-methylimidazolium ionic liquids, $(EMIm)_2[Co(NCS)_4]$ and $(BMIm)_2[Co(NCS)_4]$ [51].

7.3.8 Protic Ionic Liquids

In Chap. 4, the isothermal electric loss modulus $M''(f)$ and $\sigma'(f)$ spectra of the protic ionic liquid, procainamide HCl, at ambient pressure were shown in Figs. 4.9

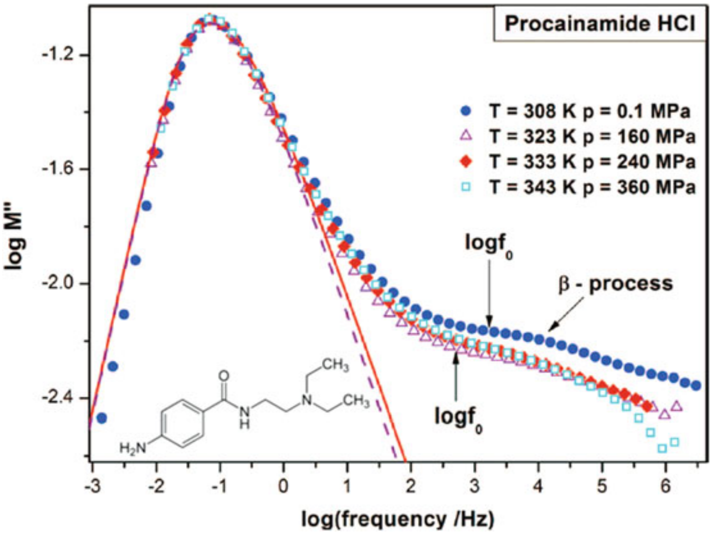

Fig. 7.16 Comparison of electric loss modulus spectra for different temperature and pressure combinations at constant loss peak frequency of procainamide HCl. The secondary β-conductivity relaxation is seen at higher frequencies. The *solid line* is the fit by the Fourier transform of the KWW function with $(1\text{-}n) = 0.64$ to the main peak of the data (*black circles*) taken at 308 K and 0.1 MPa. The *upper arrow* indicates $\log f_0$ calculated by the CM equation with $(1\text{-}n) = 0.64$. The main peak of the data taken at 323 and 160 K (*blue open triangles*) is slightly narrower, and the best fit by the KWW function requires $(1\text{-}n) = 0.66$ (*dashed line*). The *lower arrow* indicates $\log f_0$ calculated by the CM equation with $(1\text{-}n) = 0.66$. The *inset* shows the chemical structure

and 4.10 therein as a demonstration of the advantage of $M''(f)$ in revealing the presence of the β-conductivity relaxation, while the same data represented by $\sigma'(f)$ fail to do so. In Figs. 4.9 and 4.11 of Chap. 4, demonstrated is the good agreement between the β-conductivity relaxation time, $\tau_{\sigma\beta}$, and the primitive conductivity relaxation time, $\tau_{\sigma 0}$, calculated by Eq. (7.2) with the n_σ and $\tau_{\sigma\alpha}$ determined by the Kohlrausch fit [52]. The agreement was also found in procaine HCl and lidocaine HCl [53], and hence it is a general property.

Here we add the property of invariance of frequency dispersion of the α-conductivity relaxation in procainamide HCl to different combinations of T and P while keeping $\tau_{\sigma\alpha}$ constant. This feature is presented in Fig. 7.16. The β-conductivity relaxation shows up as a shoulder in this plot, and its shape does not seem to change on varying T and P, suggesting that not only n_σ but also the β-relaxation time, $\tau_{\sigma\beta}$, is also invariant, like in the case of [Si-MIm][BF$_4$] shown in Fig. 7.14.

7.4 Thermodynamic (TV^{γ}) Scaling of α-Relaxation Time and Viscosity of Non-ionic Glass-Formers

We shall consider another general property of the dependence of the dynamics on thermodynamic parameters, temperature T and specific volume V, which is shared by non-ionic glass-formers and glass-forming ionic conductors. For the former, the dynamics are the structural α-relaxation (or viscosity) and the primitive or the JG β-relaxation, while for the latter the dynamics include the structural α-relaxation (or viscosity), the conductivity α-relaxation and the conductivity primitive/β-relaxation. This property of thermodynamic scaling of dynamics with the product variable TV^{γ}, or alternatively T/ρ^{γ}, for non-ionic glass-formers is introduced first.

If intermolecular potential $V(r)$ for liquids is a repulsive inverse power potential (IPP), $U(r)=\varepsilon(\sigma/r)^{q}$ where r is the intermolecular distance, q is a constant, and ε and σ have respectively the dimensions of energy and length, it was shown by Hoover et al. [54, 55] and Hiwatari et al. [56] that the canonical partition function and hence also all thermodynamic properties depend on a single density-temperature variable, $\rho(\varepsilon/kT)^{1/\gamma}$ with $\gamma=q/3$, rather on T and density ρ (or volume V) separately. If distance is scaled by $\rho^{\,-1/3}$, and time scaled by the characteristic time $\rho^{\,-1/3}(m/kT)^{1/2}$, Hoover and Ross pointed out that the scaled equations of motion of the particles are simplified to show that the forces depend only on the density-temperature product variable $\rho(\varepsilon/kT)^{1/\gamma}$ with $\gamma=q/3$. Hence, for a fixed value of $\rho(\varepsilon/kT)^{1/\gamma}$ with $\gamma=q/3$, the dynamics variables of the system when expressed in terms of the scale distance and time at any density or temperature are the same. In other words, all dynamical quantities can be cast in the forms that depend on the single combined variable ρ^{γ}/T or alternatively $T^{-1}V^{-\gamma}$ with $\gamma=q/3$ [56]. Experimentally, the dependence on ρ^{γ}/T was demonstrated by the dynamic structure factor of OTP from quasielastic neutron scattering (QENS) being invariant when measured over several combinations of T and P, subject to the condition that the quantity TV^{γ} with $\gamma=4$ remains constant by Tölle and coworkers [57]. Dynamic light scattering α-relaxation times for OTP, measured at various T and P, were shown to superpose when plotted as a function of ρ^{4}/T or $1/TV^{4}$ by Dreyfus et al. [58] A related but different approach to examine temperature, density, and pressure dependence of relaxation times in supercooled liquids was proposed by Alba-Simionesco et al. in 2002 [59], and Tarjus et al. [60] The influence of density on the α-relaxation time τ_{α} or the viscosity η is simply described via a single parameter, an effective density-dependent interaction energy $E_{\infty}(\rho)$ characteristic of the liquid in the high-temperature, short relaxation time, or low viscosity regime. The scaling hypothesis is simplified by writing τ_{α} and η (represented by x) in the following forms, $\log[x(\rho,T)]=\Psi[E_{\infty}(\rho)/T]$, where $\Psi(x)$ is a material specific scaling function. As explained in Ref. [61], thermodynamic scaling by $E_{\infty}(\rho)/T$ can be considered as based on the primitive relaxation of the CM, which has the $E_{\infty}(\rho)$ as activation energy at high temperatures/short relaxation times, as discussed in Chap. 4.

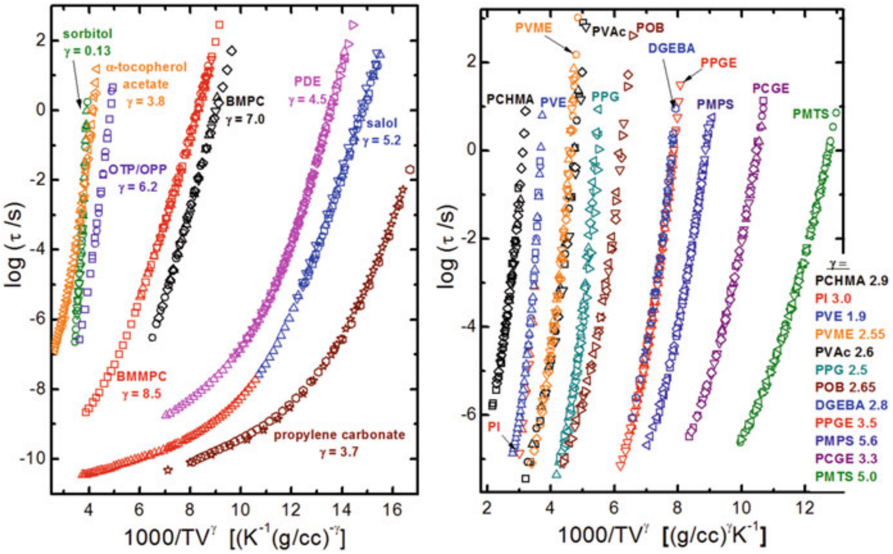

Fig. 7.17 (*Left*) Dielectric α-relaxation times of molecular liquids as a function of the reciprocal of temperature times the specific volume, with the latter raised to the indicated power of γ [65]. (*Right*) Dielectric α-relaxation times of polymers as a function of the reciprocal of temperature times the specific volume, with the latter raised to the indicated power of γ [62–64]. Data from publications are collected together and replotted in the two figures here

Casalini and Roland [62–65] investigated possible TV^{γ} scaling of other glassformers mainly by broadband dielectric spectroscopy, and their effort was joined in by Alba-Simionesco et al. [66] Treating the exponent γ as a material-specific constant, the α-relaxation times τ_α from different combinations of T and P for various molecular and polymeric glass-formers can be expressed as a unique function of ρ^{γ}/T, with the exponent varying in the range $0.13 \leq \gamma \leq 8.5$. The scaling of some of the glass-formers investigated [64, 65, 67] are shown in Fig. 7.17.

Here we show by experimental results that the JG β-relaxation time τ_{JG} also depend on the variable $T^{-1}V^{-\gamma}$ with the same γ as that of τ_α. Let us first consider the small molecular glassformers that have narrow α-loss peak and an excess wing on the high frequency flank (but otherwise no other resolved secondary relaxation in their dielectric spectra). There are experimental evidences indicating that the excess wing is an unresolved JG β-relaxation. The glassformer, phenylphthalein-dimethylether (PDE) is an example with its τ_α obtained at different T and P successfully scaled to become a function of ρ^{γ}/T with $\gamma = 4.4$ as shown in Fig. 7.18. The inset shows in the liquid state, the entire dispersion including the α-loss peak and the excess wing or the unresolved JG β-relaxation is invariant to various combinations of T and P at constant τ_α. This property immediately implies that τ_{JG} must also be a function of ρ^{γ}/T with the same γ.

Next we consider glass-formers that have a resolved JG β-relaxation in the liquid state. Experimental data of these glass-formers (see Sect. 7.2 and Figs. 7.1, 7.2, 7.3 and 7.4) have shown that τ_{JG} is invariant to changes in T and P while maintaining τ_α

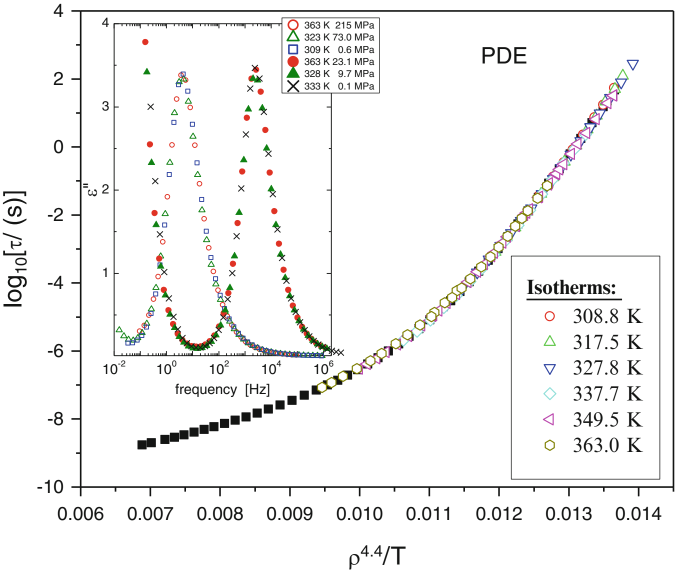

Fig. 7.18 Shown in the *inset* is perfect superpositioning of the dielectric loss spectra of a van der Waals glass-former, PDE, at different combinations of P and T for two given values of constant τ_α. Consequently, ρ^γ/T-scaling of τ_α holds as shown in the main figure

constant. Hence, for these glassformers, τ_{JG} must also be a function of ρ^γ/T with the same γ. Here we show the invariance of the co-invariance of τ_α and τ_{JG} in a different way by Fig. 7.19a, b for diglycidyl ether of bisphenol-A, $M_w = 380$ g/mol, also known as EPON 828. In Fig. 7.19c, the simultaneous scaling of τ_α and τ_{JG} to become a function of ρ^γ/T with $\gamma = 3.5$. It follows directly from Eq. (7.1) of the Couping Model and the property that n is invariant to variations of T and P at constant τ_α that the primitive relaxation time τ_0 is a function of ρ^γ/T with the same γ as τ_α. The figure also displays the values of the primitive relaxation times $\tau_0(\rho^\gamma/T)$ at several state points calculated by the Coupling Model Eq. (7.1) with the stretch exponent $\beta_K \equiv (1-n) = 0.52$ obtained by fitting the frequency dispersion of the α-relaxation by the Fourier transform of the Kohlrausch function. The CM relation, $\tau_0 \approx \tau_{JG}$, is also verified.

Written by their dependence on ρ^γ/T with the same γ, the CM relations between τ_α and $\tau_0 \approx \tau_{JG}$ become

$$\tau_\alpha\left(\frac{\varrho^\gamma}{T}\right) = \left[t_c^{-n}\tau_0\left(\frac{\varrho^\gamma}{T}\right)\right]^{1/(1-n)} \approx \left[t_c^{-n}\tau_{JG}\left(\frac{\varrho^\gamma}{T}\right)\right]^{1/(1-n)} \tag{7.5}$$

This is a CM prediction that both τ_α and τ_{JG} (or τ_0) depend on the same variable T^{-1} $V^{-\gamma}$, but their dependences are different and related by the equation above.

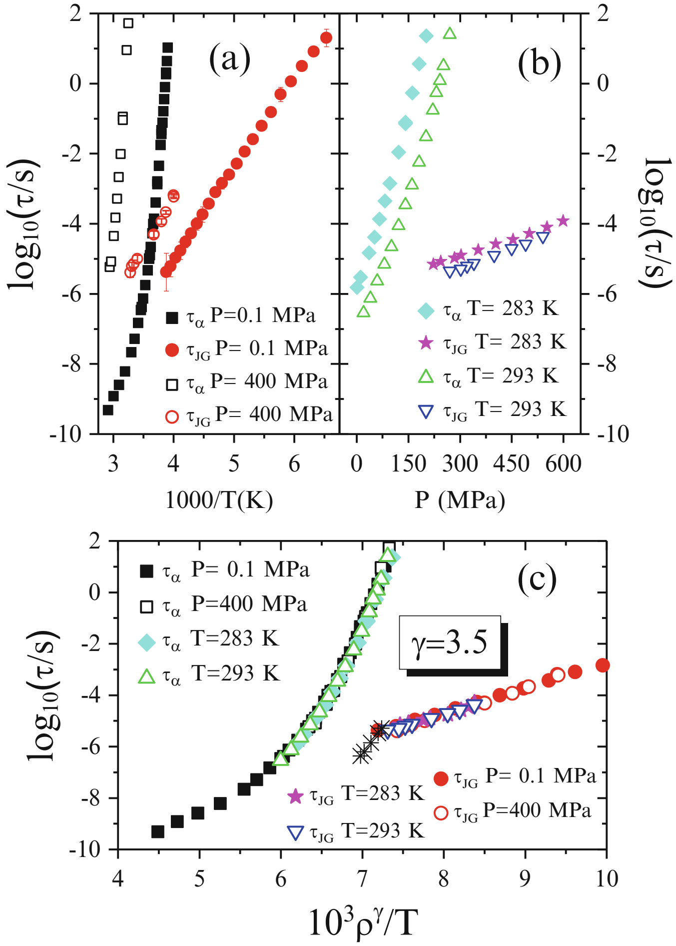

Fig. 7.19 Logarithm of characteristic time of dielectric loss maximum of DGEBA (diglycidyl ether of bisphenol-A, $M_w = 380$ g/mol, also known as EPON 828) for α-relaxation and JG-relaxation in isobaric condition versus reciprocal temperature (**a**), in isothermal condition versus pressure (**b**), and an overall plot of the same data versus ρ^γ/T (c). When not shown, error bars are smaller than symbol size. *Black asterisks* in panel (**c**) indicates the values for $\log_{10}(\tau_0)$ at several state points calculated by the Coupling Model Eq. (7.1) with the stretch exponent $\beta_K \equiv (1-n) = 0.52$ obtained by fitting the frequency dispersion of the α-relaxation by the Fourier transform of the Kohlrausch function. Density data in the glassy state have been extrapolated from the values of glass compressibility and expansivity

7.4.1 Causality Implies the ρ^{γ}/T-Dependence Originates from That of the Primitive or JG β-Relaxation

The experimental evidences given above have clearly shown that τ_{JG} (or τ_0) depend on the same variable ρ^{γ}/T as τ_{α}. From this and the fact that the JG β-relaxation or the primitive relaxation have transpired long before the α-relaxation, it follows from the principle of causality that the dependence of τ_{α} on the variable ρ^{γ}/T originates from the same of τ_{JG} (or τ_0).

7.4.2 No Correlation Between γ and the Characteristics (n, m_P, ξ_{het}) of the α-Relaxation: Another Support of Its ρ^{γ}/T-Dependence Originating from That of τ_0 or τ_{JG}

The discussions in the above summarized by Eq. (7.5) suggest that the ρ^{γ}/T-dependence originates from that of τ_0 or τ_{JG}, and the stronger dependence of τ_{α} on ρ^{γ}/T is due to the slowing down of the α-relaxation by the many-body effects. In the context of the CM, $\tau_{\alpha}(\rho^{\gamma}/T)$ is obtained from $\tau_0(\rho^{\gamma}/T)$ in Eq. (7.5) by raising the $\tau_0(\rho^{\gamma}/T)$-dependence to the superlinear power of 1/(1-n), i.e. $\tau_{\alpha}(\rho^{\gamma}/T) \propto [\tau_0(\rho^{\gamma}/T)]^{1/(1-n)}$. From this relation, it is clear that the nonexponentiality index n of the α-relaxation and γ are *independent* parameters and they bear no obvious correlation with each other. This relation also indicates that the isobaric fragility index m_P (say at ambient pressure) of the α-relaxation is determined by both n and γ, and therefore like n, m_P bears no correlation with γ.

The values of γ and m_P of many glassformers have been given in Tables 2 and 3 in Ref. [67]. In some glassformers, different values from more than one source are given. We use exclusively the data from Ref. [67], and by Alba-Simionesco et al. [66], and whenever there is a choice between the two we take the data from the works of Casalini, Paluch, and Roland [62–65, 67] for the sake of consistency with the results from the same group of collaborators. Added are new dielectric data of vitamin E ($\gamma = 3.9$, $n = 0.35$, $m_P = 63$, $m_V = 41.6$) [68], diphenyl-vinylene carbonate (DPVC) ($\gamma = 3.3$, $n = 0.29$, $m_P = 92$, $m_V = 61$) [69], heptapropylene glycol dimethylether (7PGDE) ($\gamma = 3.1$, $n = 0.52$) [70], benzoin-isobutylether (BIBE) ($\gamma = 3.8$, $n = 0.39$, $m_P = 78.4$, $m_V = 44.3$) [71], decahydroisoquinoline (DHIQ) ($\gamma = 3.95$, $n = 0.65$, $m_P = 156$) [72, 73], Squalene, ($\gamma = 4.2$, $n = 0.58$, $m_P = 77$) [74, 75].

In Figs. 7.20 and 7.21 we plot n against γ, and m_P against γ to test if there is any correlation between γ and n or m_P, which are the characteristics of the α-relaxation. Since DHIQ and squalene stand out among other small molecular glass-formers in having large n values, they are picked out in the figures. It is clear from the plots that neither there is any correlation between γ and n, nor between γ and m_P. Thus, the observed ρ^{γ}/T-dependence of τ_{α} bears no relation to fragility m_P and nonexponentiality of the structural α-relaxation even if glycerol and sorbitol in

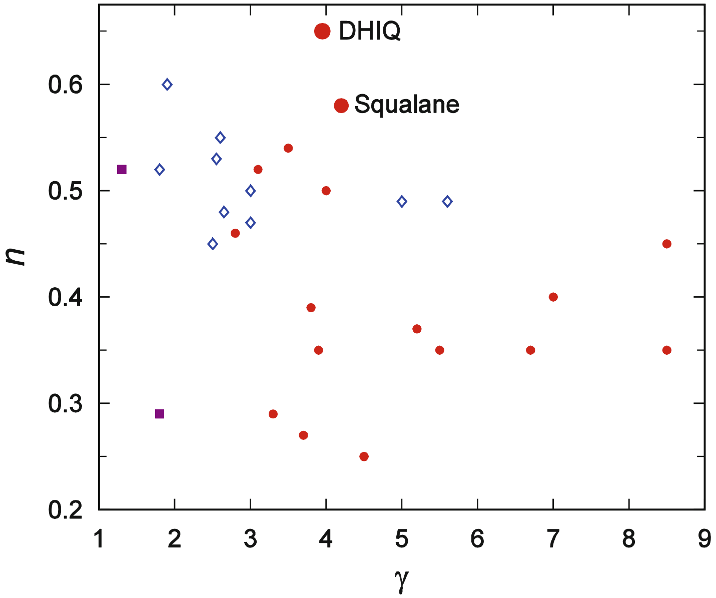

Fig. 7.20 Plot of n against γ, where the *closed red circles* are data of small molecular van der Waals glassformers, the *open blue diamonds* are polymeric glassformers, and the two *closed purple squares* are data of glycerol (smaller n value) and sorbitol (larger n value)

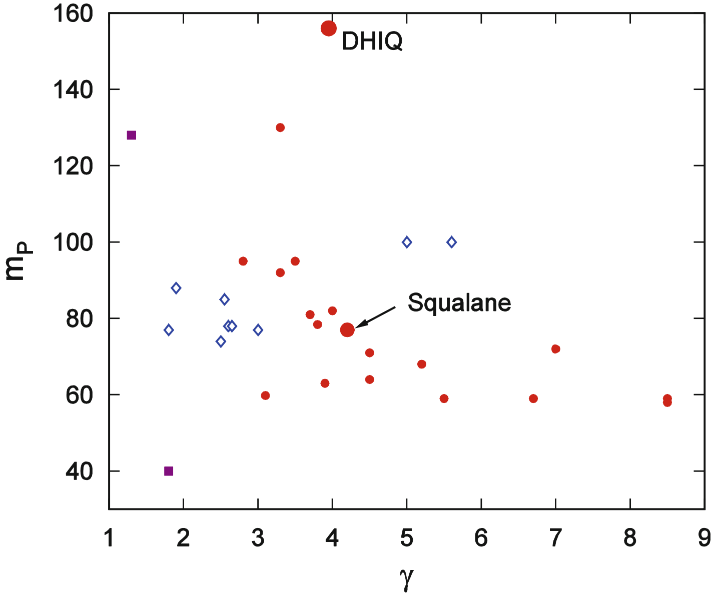

Fig. 7.21 Plot of isobaric fragility index, m_P, against γ. The *symbols* stand for the same glassformers as in Fig. 7.20, and the two *closed squares* are data of glycerol (smaller n value) and sorbitol (larger n value). There is neither any correlation between n and γ, nor between m_P and γ

the figures are excluded from consideration. The results indicate that γ in the ρ^γ/T-dependence of τ_α is unrelated to the characteristics of α-relaxation, and hence the ρ^γ/T-dependence of τ_α does not originates from structural α-relaxation itself. Instead the ρ^γ/T-dependence originates from τ_0 or τ_{JG}, which is passed onto the α-relaxation by Eq. (7.1). This is unsurprising because the JG β-relaxation and its relaxation time τ_{JG} is density and entropy dependent as evidenced by the pressure dependence [8] and the detection of a secondary glass transition at $T_{g\beta}$ by positronium annihilation lifetime spectroscopy (PALS) [76–78] and calorimetry [79–84] when $\tau_{JG}(T_{g\beta})$ reaches a long time [85–87]. The dependence of density and entropy of τ_0 as well as the ρ^γ/T-dependence of τ_0 automatically follows from the dependence of τ_α according to the CM because of the relation between τ_0 and τ_α by Eq. (7.1). Thus, from either the properties of τ_{JG}, or the relation of τ_0 to τ_α, we are assured that the origin of the ρ^γ/T-dependence of τ_α is at the level of τ_0 or τ_{JG}.

In the next section, we shall show that ρ^γ/T-scaling applies also to the d.c. conductivity and the conductivity relaxation time τ_σ in ionic liquids. The same physics govern this property shared by τ_α (viscosity) and τ_σ (conductivity).

7.5 Thermodynamic (ρ^γ/T) Scaling of Conductivity α-Relaxation Time and Viscosity of IL

Studies of the dynamics of some ILs at isobaric and isothermal conditions carried out by some groups had enabled them to test if ρ^γ/T-scaling also applies to the d.c. conductivity, σ_{dc}, and conductivity relaxation time, τ_σ. Their data confirms that ρ^γ/T-scaling works for σ_{dc} and τ_σ in several ILs. Moreover in some ILs, the viscosity also obeys ρ^γ/T-scaling. The similarity of scaling properties of σ_{dc} and τ_σ in ILs to that of the structural α-relaxation in non-ionic glass-formers implies the same physics and same explanation for both systems. In the following we present some examples of the experimental findings.

7.5.1 *RTIL [C_8MIM][NTf_2]*

Paluch and coworkers [88] made broadband dielectric studies of the IL, 1-octyl-3-methylimidazolium bis[(trifluoromethyl) sulfonyl]imide [C_8MIM][NTf_2]. Electrical conductivity of the supercooled IL was determined as a function of temperature and pressure. The σ_{dc} measured as a function of temperature over nearly 11 decades of magnitude exhibits a change from one VFT temperature dependence at lower temperatures to another VFT dependence at higher temperatures (see right panel of Fig. 7.22). The crossover from one VFT dependence to another at T_B is well-known in low molecular van der Waals liquids [28, 89–94], but now it has been found in one of ILs.

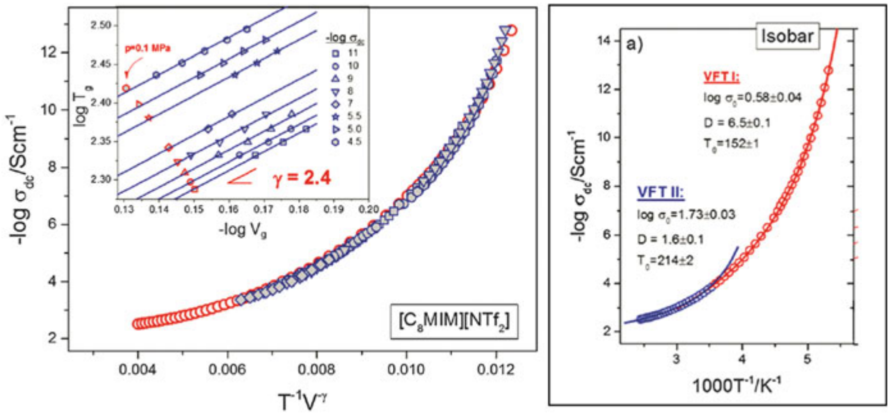

Fig. 7.22 (*Left*) The electrical conductivity data for [C_8MIM][NTf_2] plotted versus $T^{-1}V^{-\gamma}$ with the scaling exponent calculated herein as $\gamma = 2.4$. The *inset* shows the scaling exponent determined from the linear regression of the logarithmic dependence of glass transition temperature on volume. The *solid lines* denote the regression lines. (*Right*) Arrhenius plot of d.c. conductivity and the two VFT equations needed to fit the data over the entire range

The cause of the crossover at T_B was traced to the corresponding change of the magnitude as well as the T-dependence on crossing T_B of the stretch exponent $\beta_K(T) \equiv [1-n(T)]$ of the Kohlrausch function used to fit the frequency dispersion of the α-relaxation, and explained by the CM [93]. Based on a single primitive VFT temperature dependence of τ_0, the change of $n(T)$ on crossing T_B when substituted into Eq. (7.1) was shown to explain the two VFT dependences of τ_α. This explanation was reinforced by the observation of the relaxation time τ_α associated with the change in dynamics is found to be invariant to using either temperature T or pressure P to see the crossover at T_B or P_B respectively. That is, the relaxation time $\tau_\alpha(T,P)$ determines the onset of strong intermolecular cooperativity at temperature below T_B or pressure above P_B and the accompanying dynamical changes, but not T and P. Already in Sect. 7.2 we have demonstrated that the frequency dispersion of the α-relaxation or $n(T,P)$ is the same for the same $\tau_\alpha(T,P)$. Thus, the coupling parameter $n(T,P)$ determines the crossover of $\tau_\alpha(T,P)$ at T_B or P_B. Although $n_\sigma(T,P)$ of conductivity α-relaxation in [C_8MIM][NTf_2] are not available, the possibility remains that the cause of the crossover of T-dependence of $\tau_{\sigma\alpha}(T)$ from one VFT dependence to another is the same as $\tau_\alpha(T,P)$.

Thermodynamic scaling with the variable $T^{-1}V^{-\gamma}$ was performed on the isobaric and isothermal d.c. conductivity data of [C_8MIM][NTf_2] by Paluch et al. [88] In the operation, these authors separately scaled the high above (i.e., for $T > T_B$) and low conductivity (i.e., for $T < T_B$) data. The results of the two regimes are presented altogether in Fig. 7.22. All isothermal and isobaric curves collapsed into a master curve using a common value of the scaling exponent $\gamma = 2.40 \pm 0.05$. As pointed out by Paluch et al., the most interesting outcome of this analysis is that the two sets of σ_{dc} data, above and below T_B, were both successfully scaled by $T^{-1}V^{-\gamma}$ with the *same* value of γ, while two *different* VFT functions are needed to fit the entire temperature dependence of $\sigma_{dc}(T)$. This means that the $T^{-1}V^{-\gamma}$-dependence of σ_{dc} or $\tau_{\sigma\alpha}$ is insensitive or unrelated to the crossover of T-dependence of σ_{dc} or $\tau_{\sigma\alpha}$. This interesting fact is analogous to total lack of correlation between γ in the $T^{-1}V^{-\gamma}$-scaling of the structural α-relaxation time τ_α and the Kohlrausch's non-exponentiality parameter $\beta_K \equiv (1-n)$ and fragility index m_P, found in non-ionic glass-formers (see Figs. 7.20 and 7.21). Likewise, this can be taken as evidence that the $T^{-1}V^{-\gamma}$-dependence originates in the primitive relaxation time, $\tau_{\sigma0}$, or the secondary β-relaxation time, $\tau_{\sigma\beta}$, of the IL.

Paluch et al. mentioned that the value of the scaling exponent γ can also be determined from model independent analysis. At a given value of σ_{dc} the product $T_\sigma V_\sigma^\gamma = \text{const}$, which follows directly from the density scaling law. Some specific value of σ_{dc} was chosen to define T_g and the volume V_g at T_g can be taken as the pair satisfying $T_\sigma V_\sigma^\gamma = \text{const}$. This leads to the relation, $\log T_g = \text{const.} - \gamma \log V_g$, and a simple method for determining the scaling exponent γ. From the linear regression to the data of $\log T_g$ vs. $\log V_g$ shown in the inset of Fig. 7.22, they found $\gamma = 2.4$ exactly the same value obtained by scaling the isothermal and isobaric data of σ_{dc}.

Fig. 7.23 (**a**) Isothermal and isobaric data for $[C_4mim][NTf_2]$ plotted as a function of volume. (**b**) The molar conductivity data plotted against $T^{-1}V^{-\gamma}$ with $\gamma = 3.05$. The *inset* shows the scaling exponent determined from the linear regression of the logarithmic dependence of glass transition temperature on volume. The *solid lines* denote the regression lines. Data from Ref. [95]

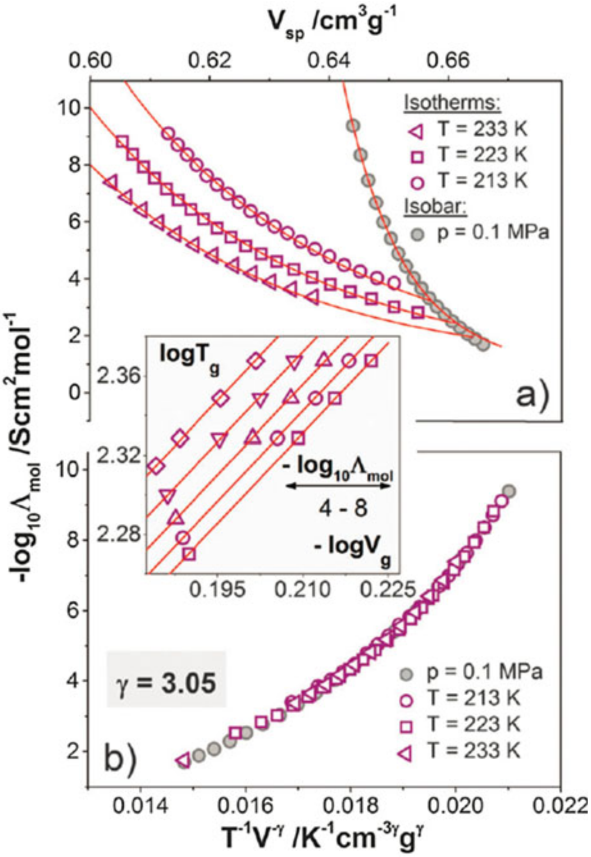

7.5.2 RTIL [C_4mim][NTf_2]

Wojnarowska et al. [95] studied the room temperature ionic liquid 1-butyl-3-methylimidazolium bis[(trifluoromethyl)sulfonyl]imide, [C_4mim][NTf_2], which differs from [C_8MIM][NTf_2] in having a shorter alkyl chain. They performed thermodynamic scaling of d.c. conductivity σ_{dc} data by the variable $T^{-1}V^{-\gamma}$ and determined the value of scaling exponent γ as shown in Fig. 7.23. The value of the conductivity scaling exponent $\gamma_\sigma = 3.05 \pm 0.01$ obtained from the numerical fitting procedure corresponds perfectly well to the one determined in an alternative, model independent way by using the simple linear regression of the relation, $\log T_g = \text{const.} - \gamma \log V_g$. The results are presented in the inset of Fig. 7.23.

For [C_4mim][NTf_2], thermodynamic scaling with $T^{-1}V^{-\gamma}$ has been performed on viscosity η of by López et al. [96] The value of the viscosity scaling exponent, γ_η, has the value of 2.89, which is practically the same as $\gamma_\sigma = 3.05$. We do not think this happens by accident. Rather, the $T^{-1}V^{-\gamma}$-scaling of σ_{dc} and η having the same γ is once more telling us that the $T^{-1}V^{-\gamma}$-dependence originates at the primitive relaxation time level. Although conductivity ($\propto 1/\tau_{\sigma\alpha}$) and viscosity ($\propto \tau_\alpha$) have different coupling parameters, n_σ and n_η, they all inherit the $T^{-1}V^{-\gamma}$-dependence of the primitive relaxation because of the respective Eq. (7.1) and Eq. (7.5) for $\tau_{\sigma\alpha}$ and τ_α.

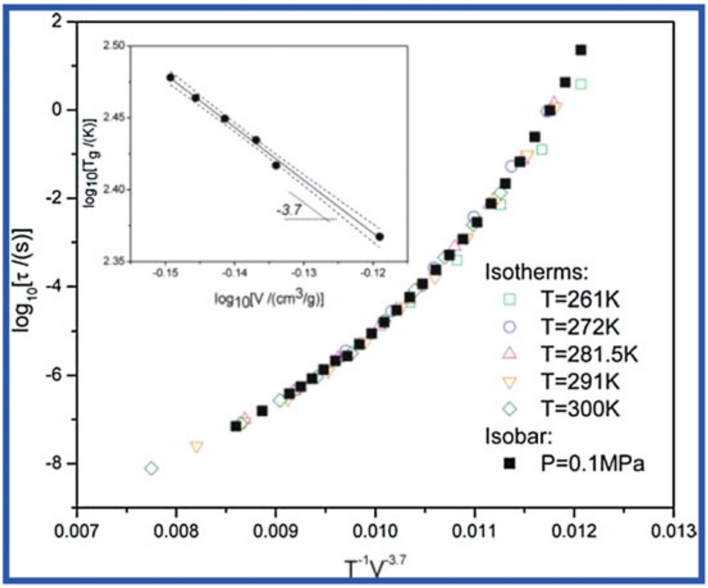

Fig. 7.24 Scaling of isothermal and isobaric BMP-BOB data of $\tau_{\sigma\alpha}$. The *inset* shows the scaling exponent determined from the linear regression of the logarithmic dependence of glass transition temperature on volume. The *solid line* denotes the regression line, and the *dashed lines* outline its 95 % confidence band. Reproduced from Ref. [75] with permission

7.5.3 RTIL BMP-BOB

The invariance of the frequency dispersion, or n_σ, of the conductivity α-relaxation in the room temperature ionic liquid, 1-butyl-1-methylpyrrolidinium bis[oxalato] borate (BMP-BOB) to variations of T and P at constant $\tau_{\sigma\alpha}$ was presented in Sect. 7.2. Paluch et al. [97] took the isobaric and isothermal data of BMP-BOB and plotted them against specific volume. From there they performed thermodynamic scaling of ionic liquids by plotting $\log\tau_{\sigma\alpha}$ as a function of TV^γ shown in Fig. 7.24. The optimal value of exponent $\gamma = 3.7$ was determined from a linear regression of $\log T_g$ on $\log V_g$, as shown in the inset. The glass transition T_g and V_g are defined as the temperature and volume, respectively, in which the relaxation time $\tau_{\sigma\alpha}$ assumes the value of 1 s. The rescaled experimental data shown in Fig. 7.24 do not all collapse into a single master curve, with the isothermal data measured at the lowest temperature slightly deviate from it.

For BMP-BOB, Paluch et al. [97] found good agreement between T_g's determined from calorimetric and conductivity relaxation measurements. Consequently the dc-conductivity mimics the structural relaxation process. For this reason, Paluch et al. used the term of dielectric structural relaxation time in the paper.

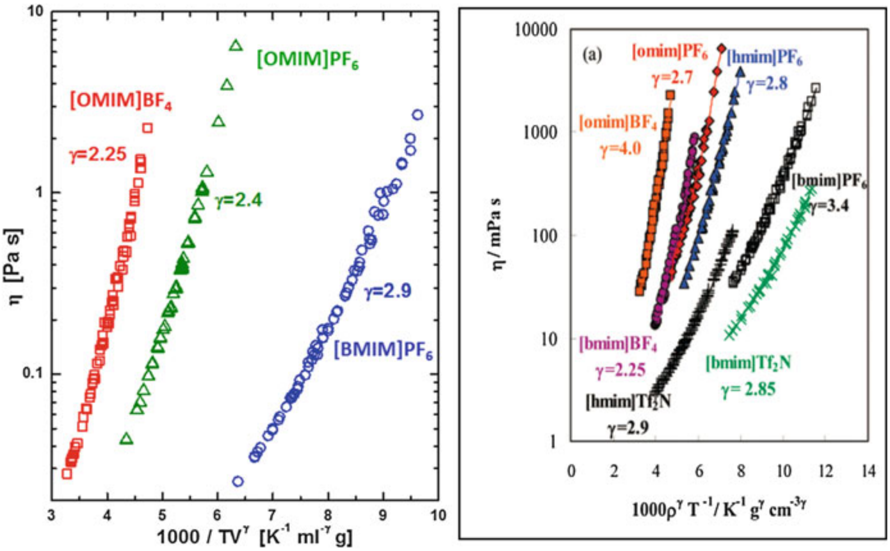

Fig. 7.25 Superpositioned viscosities of the ionic liquids. (*Left*) 1-methyl-3-octylimidazolium tetrafluoroborate ($\gamma = 2.25$), 1-methyl-3-octylimidazolium hexafluorophosphate ($\gamma = 2.4$), and 1-butyl-3-methylimidazolium hexafluorophosphate ($\gamma = 2.9$), from Ref. [75] and redrawn. (*Right*) from Pensado et al. [98]

7.6 Thermodynamic Scaling of Viscosity of RTILs

Although there is only one IL, namely [C_4mim][NTf_2], for which thermodynamic scaling with $T^{-1}V^{-\gamma}$ had been performed for both viscosity η and conductivity relaxation of ILs, it is worthwhile to cite the works of $T^{-1}V^{-\gamma}$-scaling of the viscosity of other ILs. If the $T^{-1}V^{-\gamma}$-scaling of conductivity of these ILs becomes available in the future, we can check if the scaling exponents γ_σ and γ_η are the same or not. Moreover, by showing the $T^{-1}V^{-\gamma}$-scaling of viscosity we are assured that the ILs are no different from non-ionic glass-formers.

The isothermal and isobaric viscosity of three RTILs were successfully scaled to function of $T^{-1}V^{-\gamma}$ by Roland et al. [75] as shown in the left panel of Fig. 7.25. The value of γ_η is 2.25 for 1-methyl-3-octylimidazolium tetrafluoroborate ([OMIM] BF_4). The value of γ_η is 2.4 for 1-methyl-3-octylimidazolium hexafluorophosphate ([OMIM]PF_6). The value of γ_η is 2.9 for 1-butyl-3-methylimidazolium hexafluorophosphate ([BMIM]PF_6). Shown also in the right panel are the superposed viscosity data of several ILs taken from Pensado et al. [98].

Independently López et al. reported $T^{-1}V^{-\gamma}$-scaling of the viscosity of more ILs [96]. The values of γ_η they obtained are 2.83 for [C4C1im][BF4]; 2.34 for [C6C1im][BF4]; 3.25 for [C4C1im][PF6]; 2.54 for [C6C1im][PF6]; 2.28 for [C8C1im][PF_6]; 2.89 for [C4C1im][NTf_2]; 2.36 for [C6C1im][NTf2]; and 2.43 for [N(C4H9)4][B(C4H9)4]. The notations of the ILs used by López et al. is different from others. For example, [C4C1im][NTf_2] in López et al. is [C_4mim] [NTf_2] in Paluch et al. [88], and [C8C1im][PF_6] is [OMIM]PF6 in Roland et al. [75].

7.7 Scaling of Other ILs

To show the generality of thermodynamics $T^{-1}V^{-\gamma}$-scaling of the α-conductivity relaxation time $\tau_{\sigma\alpha}$ of ILs, two more examples from pharmaceuticals are presented here.

The first is the protic ionic liquid verapamil hydrochloride by Wojnarowska et al. [99] The results are shown in Fig. 7.26 in the same manner as in Fig. 7.24. The value of the scaling exponent γ_σ is 2.45.

The other is the supercooled and glassy states of the protic ionic liquid lidocaine hydrochloride monohydrate [100]. The results of the $T^{-1}V^{-\gamma}$-scaling of the α-conductivity relaxation time $\tau_{\sigma\alpha}$ are shown in Fig. 7.27 in the same manner as in Fig. 7.24. The value of the scaling exponent γ_σ is 2.69.

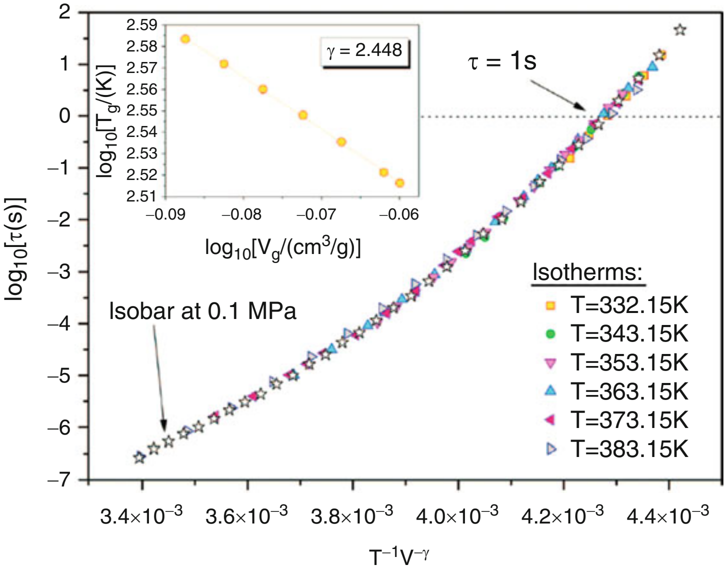

Fig. 7.26 The thermodynamic scaling vs the quantity $T^{-1}V^{-\gamma}$ with $\gamma_\sigma = 2.45$ of verapamil hydrochloride. The *inset* presents the double logarithmic plot of T_g *vs* V_g. The thermodynamic scaling exponent γ_σ obtained from the slope of this curve is equal to 2.448 [99]

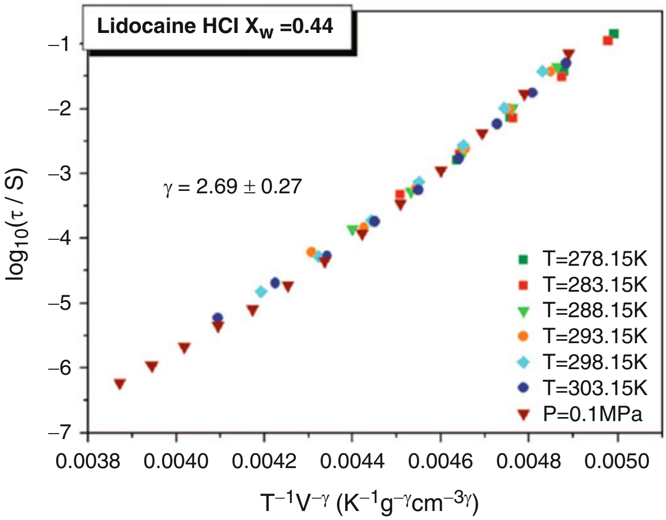

Fig. 7.27 The thermodynamic scaling vs the quantity $T^{-1}V^{-\gamma}$ with $\gamma_\sigma = 2.45$ of lidocaine hydrochloride monohydrate [100]

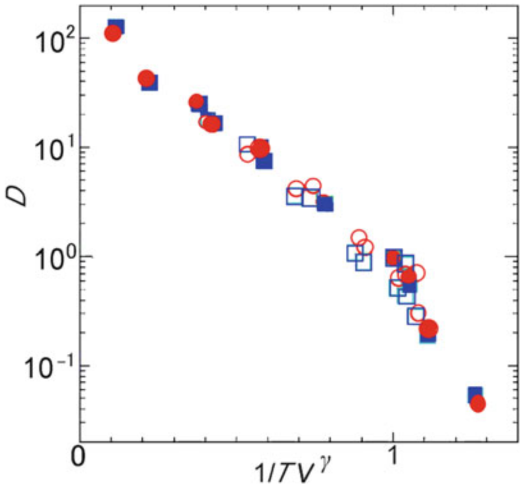

Fig. 7.28 Scaled plots against $1/TV^{\gamma}$ of the diffusivity for the cation and anion. Diffusion coefficients of cation are plotted against $1/TV^4$ by *red marks*. *Blue marks* are for anion. Both temperature dependence and pressure dependence are included. The scaling behavior for the anion is similar to that of cation but its γ is 3.8 ± 0.2

7.8 Molecular Dynamics Simulations of Thermodynamic Scaling of EMIM$^+$-NO$_3$$^-$

Molecular dynamics (MD) simulations were performed by Habasaki et al. [101] over wide temperatures and pressures ranges to study the scaling of dynamics by ρ^{γ}/T near the glass transition regime of ionic liquid, 1-ethyl-3-methylimidazolium nitrate (EMIM-NO$_3$). Diffusion coefficients of the cations and anions are well described by master curves with $\gamma = 4.0 \pm 0.2$ and 3.8 ± 0.2 respectively. Here we present the results of the anions and show them in Fig. 7.28. The complete results will be shown in the Chap. 11 on molecular dynamics simulations.

The potential used is a sum of bond, angle, and dihedral deformation energies, pairwise standard $p = 12$ and $q = 6$ L-J potential, and Coulomb interactions between atoms with charges. To explain the scaling, Habasaki et al. [61, 101] have suggested the use of the concept of the potential of mean force (PMF), rather than the bare potential parameters. This is because they found that the corresponding states on the master curve obtained after the scaling have similar pair correlation functions of ion-ion pairs, especially for the first coordination shell, and these functions bear correlation with the PMF.

The PMF, $W_{\mathrm{ij}}(r)$, was introduced by Kirkwood [102], and is used in statistical mechanical theories of liquids. $W_{\mathrm{ij}}(r)$ is obtained from the ion-ion pair correlation function $g_{ij}(r)$ by,

$$W_{ij}(r) = -k_B T \ln g_{ij}(r) \tag{7.6}$$

The functions $g_{ij}(r)$ obtained by simulations were accurate enough for the calculation of $W_{\mathrm{ij}}(r)$ directly by Eq. (7.6). In Fig. 7.29, $W_{\mathrm{ij}}(r)$s for the cation-cation pair (blue dashed-dotted curve), anion-anion pair (red dashed curve) and cation-anion pair (green solid curve) obtained at 400 K are shown with the corresponding pair

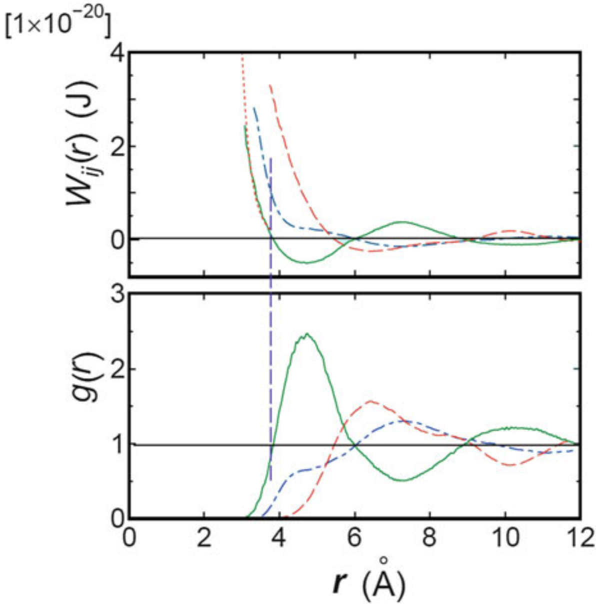

Fig. 7.29 *Upper panel*: Potentials of mean force, $W_{ij}(r)$s, for the cation-cation pair (*blue dashed-dotted curve*), anion-anion pair (*red dashed curve*) and cation-anion pair (*green solid curve*) obtained at 400 K for EMIM-NO_3. A fitted curve in the power law form ($r^{-\lambda}$ with $\lambda = 11$ (*red dotted curve*)) is shown for cation-anion pair. *Lower panel*: Corresponding pair correlation functions, $g_{ij}(r)$s. The power law region ends at distance r_λ, where $W_{ij}(r) \sim 0$ and $g_{ij}(r) \sim 1$ [61]

correlation functions, $g_{ij}(r)$. As a first approximation, it is probable that the $g(r)$ of cation-anion pair having the shortest distance is important for the scaling The results show that $W_{ij}(r)$ for the cation-anion pair, $EMIM^+$-NO_3^-, has power law dependence of $r^{-\lambda}$ with $\lambda = 11$ (red dotted curve) at distance r_λ less than the separation between the ion pairs. Dividing the value of this slope λ for the cation-anion pair by 3, the result is 3.7, which is near the value of the exponent $\gamma = 4.0$ for cations, and 3.8 for anions that were used to scale their diffusion coefficients. Based on the short distance in the repulsive part of the potential that determines the scaling exponent γ, [10, 61] we conclude that the dependence of the diffusivity of the ionic liquid on ρ^γ/T starts at the local level, i.e. at the primitive conductivity relaxation or the β-conductivity relaxation.

7.9 Molecular Dynamics Simulations of Thermodynamic Scaling of $2Ca(NO_3)_2 \cdot 3KNO_3$ (CKN)

Ribeiro et al. [103] performed MD simulations on the ionic glass-former, $2Ca(NO_3)_2 \cdot 3KNO_3$ (CKN), at various T and P. The non-polarizable pairwise potential was given by a Born-Mayer function. Diffusion coefficient, D, relaxation time of the intermediate scattering function, τ_α, and NO_3^- anion re-orientational time, τ_r,

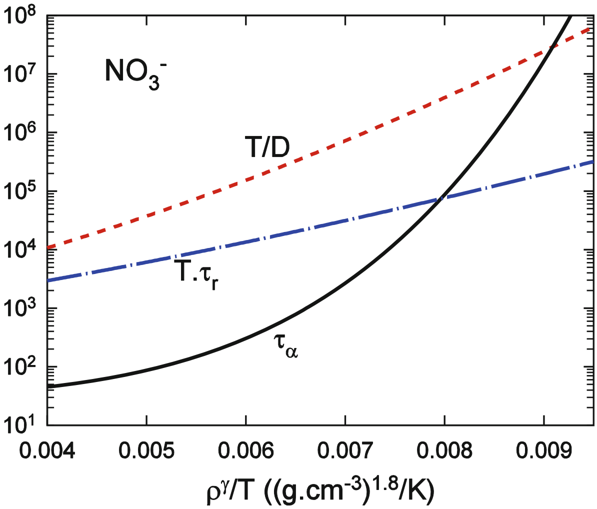

Fig. 7.30 Fit by $x = F(\rho^\gamma/T) = A\exp(B\rho^\gamma/T)^C$ to three dynamic quantities and plotted against ρ^γ/T with $\gamma = 1.8$ for NO_3^- in CKN obtained by simulation at 0.1, 0.5, 1.0 and 2.0 GPa. Data are not shown. *Black line* is for the relaxation time τ_α of the incoherent intermediate scattering function of anions, and the parameters are $A = 30.2$ ps, $B = 202.5$, and $C = 4.3$. *Dashed red line* is for *T/D*, and the parameters are $A = 584.4$ K.10^{-8} m^2 s^{-1}, $B = 487.1$, and $C = 1.6$. *Dashed-dotted blue line* is for the product of temperature and reorientational relaxation time, $T\tau_r$, and the parameters are $A = 402.2$ K.ps, $B = 408.5$, and $C = 1.4$

were obtained as a function of T and ρ. All these three dynamical properties of CKN scale as ρ^γ/T with a common value $\gamma = 1.8 \pm 0.1$. They have shown that effective potential $V(r)$ of interaction between Ca^{2+}, and oxygen atoms of NO_3^- can be represented by a sum of a term proportional to r^{-1} for long-range attraction due to Coulomb interaction, and another term proportional to r^{-p} to account for repulsion at short distance. The best fit to $V(r)$ gives the repulsive exponent $\hat{p} = 4.7$. Once again $\hat{p}/3 = 1.6$ is close to $\gamma = 1.8$ obtained from thermodynamic scaling of CKN dynamic properties. This finding is consistent with our conclusion that the scaling parameter γ is determined by the exponent of the repulsive part of an effective intermolecular potential between the atoms of the cation and anion at distance shorter than that of the first peak of the radial distribution function of Ca–O correlations, and hence dependence on ρ^γ/T of dynamic properties starts with the local process or the primitive relaxation of the Coupling Model. This point was well recognized by Ribeiro et al. from their own study. They also cited the Coupling Model [104] result that the ρ^γ/T scaling of viscosity or τ_α is a consequence of the more fundamental ρ^γ/T scaling of the primitive relaxation time τ_0 with the same γ.

Most experimental or simulation studies of ρ^γ/T scaling of dynamic properties consider only a single property to demonstrate the scaling. The simulations by Ribeiro et al. were able to consider scaling of four different dynamic quantities: the diffusion constants D of Ca^{2+} and NO_3^-, the relaxation time τ_α of intermediate scattering function of NO_3^-, the reorientational time, τ_r, of NO_3^-, and the ionic mean squared displacement $<u^2>$ at short time of 10 ps of each species, Ca^{2+}, and

NO_3^-. Ribeiro et al. found all these dynamic properties obey ρ^γ/T scaling with the *same* $\gamma = 1.8$, albeit in *different* functions $F_x(\rho^\gamma/T)$ for different properties x. In the present case, x stands for any of the quantities, τ_α, $T\tau_\mathrm{r}$, and T/D. This remarkable feature of the simulation results are shown in Fig. 7.30, where $F_x(\rho^\gamma/T)$ that fitting the data for different properties, τ_α, $T\tau_\mathrm{r}$, and T/D, of NO_3^- are shown without the actual data themselves. Note that the axis is ρ^γ/T with $\gamma = 1.8$ common to all three properties. Also density scaling holding for more dynamic properties with the same γ has been demonstrated by computer simulations of binary LJ particles in Ref. [105]

The fact that the same $\gamma = 1.8$ applies to several dynamic quantities of CKN implies the different scaling functions stem from one fundamental scaling function, which can be the primitive process of the Coupling Model [104]. All the primitive processes of the different dynamic properties obey ρ^γ/T scaling with the same γ. This is because the primitive processes of all properties x are local and their primitive relaxation or diffusion times, τ_{0x}, have the same γ is determined roughly by the slope $\widehat{p}$ of the repulsive part of the potential. As discussed by Ribeiro et al., in the framework of the Coupling Model, different dynamic properties can weigh differently the many-body cooperative dynamics, and hence can have different coupling parameters [25, 28, 31, 32, 34]. This is already found before in the simulation of CKN by Signorini et al. [106] and also by Ribeiro [103] at ambient pressure. The correlation functions of the reorientation of the NO_3^- described by the first order and second order Legendre polymers have different Kohlrausch exponents, β_K, or different n because $\beta_K \equiv (1-n)$. The same is true for the different properties x studied for ρ^γ/T scaling by Ribeiro et al. [103] The exponent γ in the dependences on ρ^γ/T of the primitive relaxation/diffusion/reorientation times, τ_{0x}, are the same because it is determined by the same slope $\widehat{p}$ of the repulsive part of the potential. Notwithstanding, the Kohlrausch stretch exponents, $\beta_{K\mathrm{x}}$, of their correlation functions and hence the coupling parameters, n_x, can be different. These different values of n_x appearing in the Coupling Model Eq. (7.5) for different dynamic variable x,

$$\tau_x\left(\frac{\rho^\gamma}{T}\right) = \left[(t_c)^{n_x}\tau_{0x}\left(\frac{\rho^\gamma}{T}\right)\right]^{\frac{1}{1-n_x}}, \tag{7.7}$$

readily explains why different dynamic properties τ_α, $T\tau_\mathrm{r}$, and T/D are functions of ρ^γ/T with the same γ, but the functional forms of $\tau_x(\rho^\gamma/T)$ are different because n_x are different.

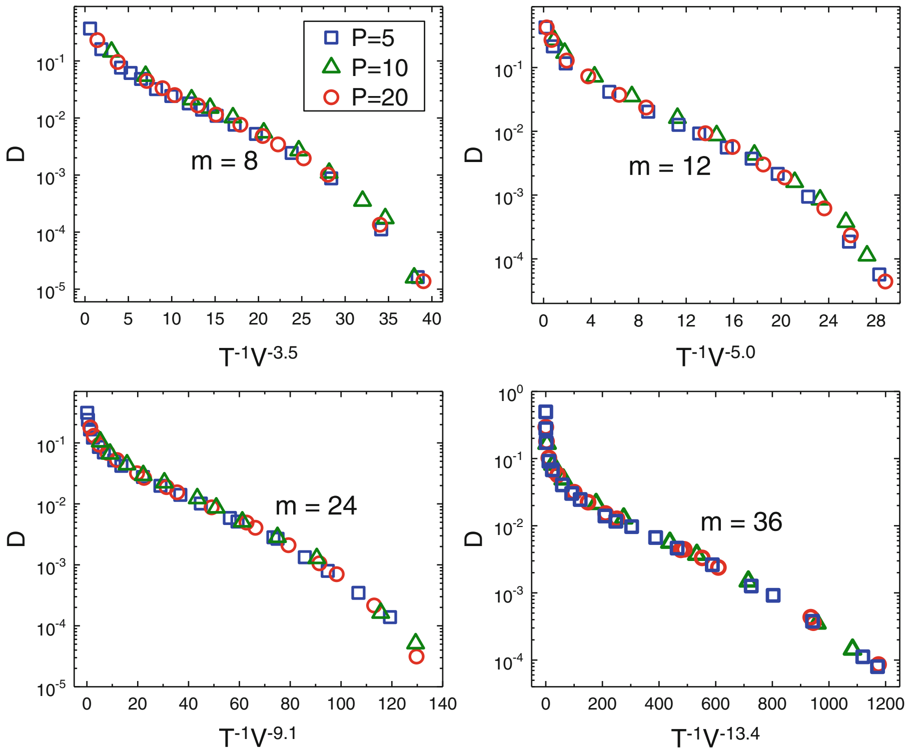

Fig. 7.31 Reduced diffusion coefficients D as a function of $1/(TV^{\gamma})$ for different values of the repulsive exponent m at different pressures: P = 5 (*squares*), P = 10 (*circles*), and P = 20 (*triangles*). For $m = 36$ ($\gamma = 13.4$), $m = 24$ ($\gamma = 9.1$), $m = 12$ ($\gamma = 5.0$), and $m = 8$ ($\gamma = 3.5$). The estimated uncertainty on γ is ±0.1 (±0.2 for $m = 36$). Reproduced from Ref. [110] by permission

7.10 Molecular Dynamics Simulation: Indication of $T^{-1}V^{-\gamma}$-Dependence Originating from the Primitive or JG β-Relaxation

Before ending this chapter, we cite the results from other studies that support the $T^{-1}V^{-\gamma}$ -dependence of dynamic quantities actually originate from that of the primitive relaxation of the CM or the JG β-relaxation. Earlier it was found is that the static structure factor and the local structure in non-associated liquids are sensitive to the repulsive part of the potential at short distance [107–109] but not the nature of the attractive potential extending to longer distance. Recently, Coslovich and Roland [110] simulated binary Lennard-Jones liquids with intermolecular potential $U(r) \propto \left[(\sigma/r)^{m} - (\sigma/r)^{6}\right]$, with the attractive exponent fixed at the value of 6, and the repulsive exponent m varied over the values of 8, 12, 24, and 36. In agreement with experimental results of various glassformers, the

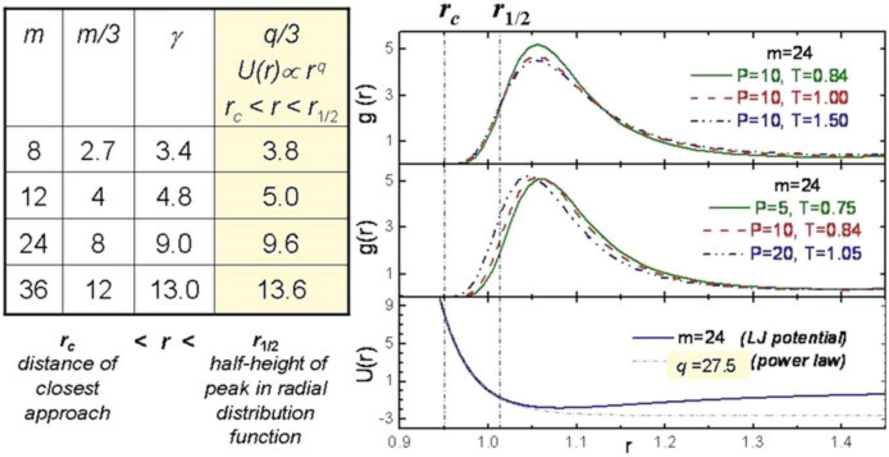

m	$m/3$	γ	$q/3$ $U(r) \propto r^q$ $r_c < r < r_{1/2}$
8	2.7	3.4	3.8
12	4	4.8	5.0
24	8	9.0	9.6
36	12	13.0	13.6

Fig. 7.32 *Top panel*: Radial distribution functions between large particles $g_{11}(r)$ at $P = 10$ for $T = 1.50$ (*dotted line*), $T = 1.00$ (*dashed line*), and $T = 0.84$ (*solid line*). *Middle panel*: $g_{11}(r)$ at the lowest equilibrated T: $T = 0.75$ at $P = 5$ (*dotted line*), $T = 0.84$ at $P = 10$ (*dashed line*), and $T = 1.05$ at $P = 20$ (*solid line*). *Bottom panel*: Pair potential $U_{11}(r)$ (*solid line*) and the intermediate power law, r^q, (*dotted line*) that fits $U_{11}(r)$ in the range from $r_c = 0.95$ to $r_{1/2} = 1.01$. This range is bounded by the two *vertical dotted lines* in all panels. The extreme *right column* of the table lists the values of q of the fits. The exponent γ that scales the diffusion coefficient in Fig. 7.31 given in the third column are close to q. Redrawn from data of Ref. [110]

diffusion coefficients for the simulated Lennard-Jones liquids in normal and moderately supercooled states are a unique function of the variable ρ^γ/T as shown in Fig. 7.31.

The magnitude of the exponent γ is always larger than $m/3$ due to the contributions of the attractive term, but not far from it. For $m = 36$ ($\gamma = 13.4$, and $m/3 = 12$), $m = 24$ ($\gamma = 9.1$, and $m/3 = 8$), $m = 12$ ($\gamma = 5.0$, and $m/3 = 4$), and $m = 8$ ($\gamma = 3.5$, and $m/3 = 2.7$). Thus γ is determined by the steepness of the repulsive part of $U(r)$ in the region bounded by r_c and $r_{1/2}$, which are respectively the *closest* approach distance between the particles and the separation corresponding to half-height of the radial distribution functions between large particles $g_{11}(r)$ in the supercooled regime. This is illustrated in Fig. 7.32.

The distance within the range $r_c < r < r_{1/2}$ is smaller than the average separation between the large particles corresponding to the first peak of the pair distribution function $g_{11}(r)$. At such small distances the primitive or the JG β-relaxation is more directly related to the repulsive part of $V(r)$ than the cooperative α-relaxation which involves more particles and longer length scale. Thus, this can be taken as evidence that the dependence of dynamic quantities on ρ^γ/T originates in the primitive relaxation of the CM or the JG β-relaxation. This original dependence of τ_{JG} (or τ_0) on $T^{-1}V^{-\gamma}$ is passed onto τ_α and magnified in τ_α of the structural α-relaxation at later times through action of the many-body dynamics. The stronger dependence of τ_α on $T^{-1}V^{-\gamma}$ than τ_{JG} (or τ_0) also follows directly from the CM

Eq. (7.1) by raising the dependence to the superlinear power of $1/(1-n)$. The remarks made in the above for non-ionic glass-forming model systems applied as well to ionic liquids and melts, in particular to the simulation data of CKN by Ribeiro et al. In Sect. 7.9 we have mentioned the potential $V(r)$ they used gives the repulsive exponent $=4.7$. Once again $4.7/3=1.6$ is close to $\gamma=1.8$ obtained from thermodynamic scaling of CKN dynamic properties. Thus the scaling parameter γ is determined by the exponent of the repulsive part of an effective intermolecular potential between the atoms of the cation and anion at distance shorter than that of the first peak of the radial distribution function, and hence the dependence on ρ^{γ}/T of dynamic ionic properties originates from the local ionic process or the primitive ionic relaxation of the Coupling Model.

7.11 Conclusion

Ionic liquids (ILs) differ from glassy and crystalline ionic conductors in the opportunity of studying the dynamics not only how it changes with temperature T but also at elevated pressure. One of the most remarkable properties found in some of the ILs is the invariance of the frequency dispersion of electric modulus, $M^*(f)$, of the primary or α-conductivity relaxation to variations of T and P that maintain the α-conductivity relaxation time $\tau_{\sigma\alpha}$ constant. This is exactly the property generally established in the structural α-relaxation in the non-ionic van der Waals glass-formers, i.e. the frequency dispersion of the structural α-relaxation is invariant to variations of T and P that maintain the structural α-relaxation time τ_α constant.

In some of these ionic conductors appearing together with the α-conductivity relaxation in $M^*(f)$ is a resolved secondary or β-conductivity relaxation with relaxation time $\tau_{\sigma\beta}$. In these ILs, the separation in time scale between the two relaxations given by $\left(\log\tau_{\sigma\alpha} - \log\tau_{\sigma\beta}\right)$ is constant to variations of T and P that maintain $\tau_{\sigma\alpha}$ constant. Putting the two properties together, we have the remarkable overall property that $\tau_{\sigma\alpha}$, $\tau_{\sigma\beta}$, and the frequency dispersion of the α-conductivity relaxation are co-invariants to variations of T and P. Since the Fourier transform of the Kohlrausch function fits well the frequency dispersion of $M^*(f)$, and the exponent, $1\text{-}n_{\sigma\alpha}$, of the Kohlrausch function defines the frequency dispersion, the overall property can be restated as co-invariance of $\tau_{\sigma\alpha}$, $\tau_{\sigma\beta}$, and $1\text{-}n_{\sigma\alpha}$. This property is exactly the same found in non-ionic glass-formers of the co-invariance of τ_α, τ_β, and $1\text{-}n_\alpha$. Thus the physics behind these analogous properties in the ion dynamics of ILs and molecular dynamics of non-ionic glass-forming liquids must be the same. The same physics bridging the two fields require for explanation a theory that is applicable to both fields. The Coupling Model is one such theory.

Moreover, the isothermal and isobaric α-conductivity relaxation time $\tau_{\sigma\alpha}(T,P)$ and d.c. conductivity $\sigma(T,P)$ of ILs obey thermodynamic scaling to master curve as function of the product variable $T^{-1}V^{-\gamma}$ or ρ^{γ}/T. For those ILs having a resolved

β-conductivity relaxation, both $\tau_{\sigma\alpha}(T,P)$ and $\tau_{\sigma\beta}(T,P)$ are scaled by ρ^{γ}/T with the same γ. Again this scaling property of conductivity relaxation in ILs is exactly the analogue of τ_{α} and τ_{β} of non-ionic glass-forming liquids, and the CM gives a consistent explanation for both.

References

1. K.L. Ngai, R. Casalini, S. Capaccioli, M. Paluch, C.M. Roland, J. Phys. Chem. B **109**, 17356 (2005)
2. K.L. Ngai, R. Casalini, S. Capaccioli, M. Paluch, C.M. Roland, in *Adv. Chem. Phys. Part B, Fractals, Diffusion and Relaxation in Disordered Complex Systems*, vol. 133, ed. by Y.P. Kalmykov, W.T. Coffey, S.A. Rice (Wiley, New York, 2006), pp. 497–585. Chapter 10
3. G.N. Lewis, M. Randall, *Thermodynamics*, 2nd edn. (McGraw-Hill, New York, 1961)
4. M. Mierzwa, S. Pawlus, M. Paluch, E. Kaminska, K.L. Ngai, J. Chem. Phys. **128**, 044512 (2008)
5. K. Kessairi, S. Capaccioli, D. Prevosto, M. Lucchesi, S. Sharifi, P.A. Rolla, J. Phys. Chem. B **112**, 4470 (2008)
6. M.S. Thayyil, K.L. Ngai, D. Prevosto, S. Capaccioli, J. Non-Cryst. Solids **407**, 98 (2015)
7. K.L. Ngai, J. Chem. Phys. **109**, 6982 (1998)
8. K.L. Ngai, M. Paluch, J. Chem. Phys. **120**, 857 (2004)
9. K.L. Ngai, J. Phys. Condens. Matter **15**, S1107 (2003)
10. K.L. Ngai, *Relaxation and Diffusion in Complex Systems* (Springer, New York, 2011)
11. Z. Wojnarowska, K.L. Ngai, M. Paluch, Phys. Rev. E **90**, 062315 (2014)
12. F.S. Howell, R.A. Bose, P.B. Macedo, C.T. Moynihan, J. Phys. Chem. **78**, 639 (1974)
13. A. Pimenov, P. Lunkenheimer, H. Rall, R. Kohlhaas, A. Loidl, R. Böhmer, Phys. Rev. E **54**, 676 (1996)
14. W.C. Hasz, C.T. Moynihan, J. Non-Cryst. Solids **172–174**, 1363 (1994)
15. N. Ito, R. Richert, J. Phys. Chem. B **111**, 5016–5022 (2007)
16. A. Rivera, E. Rössler, Phys. Rev. B **73**, 212201 (2006)
17. K.L. Ngai, J. Phys. Chem. B **110**, 26211–26214 (2006)
18. K.L. Ngai, Solid State Ionics **5**, 27–34 (1981)
19. K.L. Ngai, J.N. Mundy, in *Physics of Non-Crystalline Solids*, ed. by L.D. Pye, W.C. LaCourse, H.J. Stevens (Taylor and Francis, Washington, 1992), p. 342
20. L.P. Boesch, C.T. Moynihan, J. Non-Cryst. Solids **17**, 44 (1975)
21. C.T. Moynihan, J. Non-Cryst. Solids **235–237**, 781–788 (1998)
22. K.L. Ngai, J. Habasaki, C. León, A. Rivera, Z. Phys Chem. **219**, 47 (2005)
23. C. León, J. Habasaki, K.L. Ngai, Z. Phys Chem. **223**, 999 (2009)
24. K.L. Ngai, R.W. Rendell, in *Relaxation Complex Systems and Related Topics*, ed. by I.A. Campbell, C. Giovannella (Plenum Press, New York, 1990), pp. 309–316
25. K.L. Ngai, J. Phys. Chem. B **103**, 10684 (1999)
26. M.T. Cicerone, P.A. Wagner, M.D. Ediger, J. Phys. Chem. B **101**, 8727 (1997)
27. M.K. Mapes, S.F. Swallen, M.D. Ediger, J. Phys. Chem. B **110**, 507 (2006)
28. K.L. Ngai, J.H. Magill, D.J. Plazek, J. Chem. Phys. **112**, 1887 (2000)
29. D. Chakrabarti, B. Bagchi, Phys. Rev. Lett. **96**, 187801 (2006)
30. J.R. Rajian, W. Huang, R. Richert, E.L. Quitevis, J. Chem. Phys. **124**, 014510 (2006)
31. K.L. Ngai, S. Capaccioli, J. Phys. Condens. Matter **20**, 244101 (2008)
32. K.L. Ngai, Philos. Mag. **87**, 357 (2007)
33. M.D. Ediger, P. Harrowell, J. Chem. Phys. **137**, 080901 (2012)
34. K.L. Ngai, S. Mashimo, G. Fytas, Macromolecules **21**, 3030 (1988)
35. M. Tatsumisago, C.A. Angell, S.W. Martin, J. Chem. Phys. **97**, 6968 (1992)

36. S. Estalji, O. Kanert, J. Steinert, H. Jain, K. Ngai, Phys. Rev. B **43**, 7481 (1991)
37. C. Angell, Annu. Rev. Phys. Chem. **43**, 693 (1992)
38. K. Kim, D. Torgeson, F. Borsa, J. Cho, S. Martin, I. Svare, Solid State Ionics **91**, 7 (1996)
39. M. Trunnell, D.R. Torgeson, S.W. Martin, F. Borsa, J. Non-Cryst. Solids **139**, 257 (1992)
40. F. Borsa, D.R. Torgeson, S.W. Martin, H.K. Patel, Phys. Rev. B **46**, 795 (1992)
41. M. Meyer, P. Maass, A. Bunde, Phys. Rev. Lett. **71**, 573 (1993)
42. K.L. Ngai, Phys. Rev. B **48**, 13481 (1993)
43. K.L. Ngai, J.N. Mundy, H. Jain, O. Kanert, G. Balzer-Jollenbeck, Phys. Rev. B **39**, 6169 (1989)
44. K.L. Ngai, Solid State Ionics **61**, 345 (1993)
45. K.L. Ngai, J. Chem. Phys. **98**, 6424 (1993)
46. A. Rivera-Calzada, K. Kaminski, C. Léon, M. Paluch, J. Phys. Chem. B **112**, 3110 (2008)
47. A. Rivera, A. Brodin, A. Pugachev, E.A. Rössler, J. Chem. Phys. **126**, 114503 (2007)
48. K.L. Ngai, S. Capaccioli, Phys. Rev. E **69**, 031501 (2004)
49. G. Jarosz, M. Mierzwa, J. Ziozo, M. Paluch, H. Shirota, K.L. Ngai, J. Phys. Chem. B **115**, 12709 (2011)
50. K.L. Ngai, J. Habasaki, Y. Hiwatari, C. León, J. Phys. Condens. Matter **15**, S1607 (2003)
51. S. Hensel-Bielowka et al., J. Phys. Chem. C **119**, 20363 (2015)
52. Z. Wojnarowska, A. Swiety-Pospiech, K. Grzybowska, L. Hawelek, M. Paluch, K.L. Ngai, J. Chem. Phys. **136**, 164507 (2012)
53. S. Hensel-Bielowka, K.L. Ngai, A. Swiety-Pospiech, L. Hawelek, J. Knapik, W. Sawicki, M. Paluch, J. Non-Cryst. Solids **407**, 81 (2015)
54. W.G. Hoover, M. Ross, Contemp. Phys. **12**, 339 (1971)
55. W.G. Hoover, M. Ross, K.W. Johnson, D. Henderson, J.A. Barker, B.C. Brown, J. Chem. Phys. **52**, 4931 (1970)
56. Y. Hiwatari, H. Matsuda, T. Ogawa, N. Ogita, A. Ueda, Prog. Theor. Phys. **52**, 1105 (1974)
57. A. Tölle, H. Schober, J. Wuttke, O.G. Randl, F. Fujara, Phys. Rev. Lett. **80**, 2374 (1998)
58. C. Dreyfus, A. Aouadi, J. Gapinski, M. Matos-Lopes, W. Steffen, A. Patkowski, R.M. Pick, Phys. Rev. E **68**, 011204 (2003)
59. C. Alba-Simionesco, D. Kivelson, G. Tarjus, J. Chem. Phys. **116**, 5033 (2002)
60. G. Tarjus, D. Kivelson, S. Mossa, C. Alba-Simionesco, J. Chem. Phys. **120**, 6135 (2004)
61. K.L. Ngai, J. Habasaki, D. Prevosto, S. Capaccioli, M. Paluch, J. Chem. Phys. **137**, 034511 (2012)
62. R. Casalini, C.M. Roland, Phys. Rev. E **69**, 062501 (2004)
63. C.M. Roland, R. Casalini, J. Chem. Phys. **121**, 11503 (2004)
64. R. Casalini, S. Capaccioli, C.M. Roland, J. Phys. Chem. B **110**, 11491 (2006)
65. R. Casalini, C.M. Roland, Colloid Polym. Sci. **283**, 107 (2004)
66. C. Alba-Simionesco, A. Cailliaux, A. Alegria, G. Tarjus, Europhys. Lett. **68**, 58 (2004)
67. C.M. Roland, S. Hensel-Bielowka, M. Paluch, R. Casalini, Rep. Prog. Phys. **68**, 1405 (2005)
68. K. Kaminski, S. Maslanka, J. Ziolo, M. Paluch, K.J. McGrath, C.M. Roland, Phys. Rev. E **75**, 011903 (2007)
69. S. Capaccioli, D. Prevosto, K. Kessairi, M. Lucchesi, P.A. Roland, Philos. Mag. **87**, 681 (2007)
70. C.M. Roland, R. Casalini, R. Bergman, J. Mattsson, Phys. Rev. B **77**, 012201 (2008)
71. S. Capaccioli, R. Casalini, D. Prevosto, P.A. Rolla, unpublished
72. M. Paluch, S. Pawlus, S. Hensel-Bielowka, S. Kaminska, D. Prevosto, S. Capaccioli, P.A. Rolla, K.L. Ngai, J. Chem. Phys. **122**, 234506 (2005)
73. R. Casalini, C.M. Roland, J. Chem. Phys. **144**, 024502 (2016)
74. R. Richert, K. Duvvuri, L.-T. Duong, J. Chem. Phys. **118**, 1828 (2003)
75. C.M. Roland, S. Bair, R. Casalini, J. Chem. Phys. **125**, 124508 (2006)
76. J. Bartoš, O. Šauša, G.A. Schwartz, A. Alegría, J.M. Alberdi, A. Arbe, J. Krištiak, J. Colmenero, J. Chem. Phys. **134**, 164507 (2011)

77. J. Bartoš, P. Bandzuch, O. Šauša, K. Kristiakova, J. Kristiak, T. Kanaya, W. Jenninger, Macromolecules **30**, 6906 (1997)
78. H.A. Hristov, B. Bolan, A.F. Yee, L. Xie, D.W. Gidley, Macromolecules **29**, 8507 (1996)
79. C.L. Wang, T. Hirade, F.H.J. Maurer, M. Eldrup, N.J. Pedersen, J. Chem. Phys. **108**, 4654 (1998)
80. N. Qi, Z.Q. Chen, A. Uedono, Radiat. Phys. Chem. **108**, 81 (2015)
81. H. Fujimori, M. Oguni, J. Chem. Thermodyn. **26**, 367 (1994)
82. S. Vyazovkin, I. Dranca, Pharm. Res. **23**, 422 (2006)
83. V.A. Bershtein, V.M. Egorov, *Differential Scanning Calorimetry of Polymers* (Ellis Horwood, New York, 1994)
84. D.P.B. Aji, G.P. Johari, J. Chem. Phys. **142**, 214501 (2015)
85. S. Capaccioli, K.L. Ngai, M. Shahin Thayyil, D. Prevosto, J. Phys. Chem. B **119**, 8800 (2015)
86. K.L. Ngai, S. Capaccioli, D. Prevosto, L.M. Wang, J. Phys. Chem. B **119**, 12502 (2015)
87. K.L. Ngai, S. Capaccioli, D. Prevosto, L.M. Wang, J. Phys. Chem. B **119**, 12519 (2015)
88. M. Paluch, Z. Wojnarowska, P. Goodrich, J. Jacquemin, J. Pionteck, S. Hensel-Bielowka, Soft Matter **11**, 6520 (2015)
89. F. Stickel, E.W. Fischer, R. Richert, J. Chem. Phys. **102**, 6251 (1995)
90. F. Stickel, *Untersuchung der Dynamik in niedermolekularen Flüssigkeiten mit Dielektrischer Spektroskopie* (Shaker, Aachen, 1995)
91. K.L. Ngai, C.M. Roland, Polymer **43**, 567 (2002)
92. K.L. Ngai, L.-R. Bao, A.F. Yee, C.L. Soles, Phys. Rev. Lett. **87**, 215901 (2001)
93. R. Casalini, K.L. Ngai, C.M. Roland, Phys. Rev. B **68**, 014201 (2003)
94. R. Casalini, M. Paluch, C.M. Roland, J. Chem. Phys. **118**, 5701 (2003)
95. Z. Wojnarowska, G. Jarosz, A. Grzybowski, J. Pionteck, J. Jacquemin, M. Paluch, Phys. Chem. Chem. Phys. **16**, 20444 (2014)
96. E.R. López, A.S. Pensado, J. Fernández, K.R. Harris, J. Chem. Phys. **136**, 214502 (2012)
97. M. Paluch, S. Haracz, A. Grzybowski, M. Mierzwa, J. Pionteck, A. Rivera-Calzada, C. Leon, J. Phys. Chem. Lett. **1**, 987 (2010)
98. A.S. Pensado, A.A.H. Padua, M.J.P. Comunas, J. Fernandez, J. Phys. Chem. B **112**, 5563 (2008)
99. Z. Wojnarowska, M. Paluch, A. Grzybowski, K. Adrjanowicz, K. Grzybowska, K. Kaminski, P. Wlodarczyk, J. Pionteck, J. Chem. Phys. **131**, 104505 (2009)
100. A. Swiety-Pospiech, Z. Wojnarowska, S. Hensel-Bielowka, J. Pionteck, M. Paluch, J. Chem. Phys. **138**, 204502 (2013)
101. J. Habasaki, R. Casalini, K.L. Ngai, J. Phys. Chem. B **114**, 3902 (2010)
102. J.G. Kirkwood, J. Chem. Phys. **3**, 300 (1935)
103. M.C.C. Ribeiro, T. Scopigno, G. Ruocco, J. Chem. Phys. **135**, 164510 (2011)
104. K.L. Ngai, R. Casalini, C.M. Roland, Macromolecules **38**, 4363 (2005)
105. D. Coslovich, C.M. Roland, J. Chem. Phys. **131**, 151103 (2009)
106. G.F. Signorini, J.-L. Barrat, M.L. Klein, J. Chem. Phys. **92**, 1294 (1990)
107. J.-P. Hansen, I.R. McDonald, *Theory of Simple Liquids* (Academic, London, 1986)
108. J.D. Weeks, D. Chandler, H.C. Andersen, J. Chem. Phys. **54**, 5237 (1971)
109. D. Chandler, J.D. Weeks, H.C. Andersen, Science **220**, 787 (1983)
110. D. Coslovich, C.M. Roland, J. Phys. Chem. B **112**, 1329 (2008)

Chapter 8
Molecular Dynamics Simulations

8.1 Molecular Dynamics Simulations in Ionic Systems

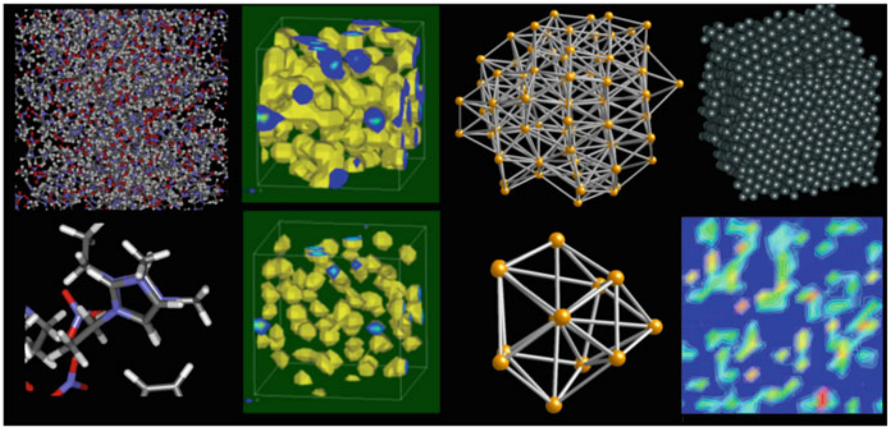

8.1.1 Purpose and Goals of the Molecular Dynamics Simulations

Molecular dynamics (MD) simulations are one of the methods of the computational science. One can study the structure and dynamics of the system in the computer by solving the equation of motion. Utilization of MD simulations has spread over many fields, such as biophysics, drug designs, as well as fundamental research areas in chemistry and physics. Systems and materials covered include proteins, liquid crystals, colloidal systems, polymers, glass-forming liquids.

The purpose of the simulation is not necessarily the faithful reproduction of the real system. Simulation is also used to examine the essential part of the dynamics

J. Habasaki et al., *Dynamics of Glassy, Crystalline and Liquid Ionic Conductors*,
Topics in Applied Physics 132, DOI 10.1007/978-3-319-42391-3_8

and/or structures of the model, and such a simulation is not required to be fully realistic. Therefore, it is necessary to understand the possible limitations of the methods and judging them according to the purpose. As already mentioned, MD simulations can treat the dynamics, because the equation of motion is numerically solved. For other properties such as equilibrated structures, the results of MD simulations are compatible with those by the Monte Carlo (MC) method.

Some of possible purposes, for which MD simulations are favorable or useful, are given as follows.

1. Simulation can be used to examine some commonly recognized as the essential parts of the dynamics and/or structures, such as the mechanism of ion diffusion and conductivity, the glass transition, the mixed alkali effects, the non-exponentiality and dynamical heterogeneity of the ion dynamics.
2. Simulations can be used for the prediction of the properties of systems not previously known by experiments. Simulations can provide properties not easily accessible by experiments such as the spatial information from wave number (q)-dependence of the intermediate scattering function.
3. Simulations can be used to examine systems under more extreme conditions including high pressures and high temperatures, which might be difficult to reach by experiments.
4. Sometimes, real experiments bring environmental pollution by the emission of heat, effusion of materials, and they might be hazardous. Simulations can examine the systems without environmental pollution or such danger.
5. Simulations can be used for screening various systems in the search for desired properties. In such cases, crude levels of the simulations are not necessarily a drawback, particularly if the time required is short.
6. Simulations can be used to treat changes of properties of systems when the structure, composition, mass, size, and/or other parameters, is modified.
7. Simulations can be used systematically to design new materials with improved performance in applications.
8. Of course, simulations can be used for comparison with the results obtained from experiments, and for validation of predictions from theory. Recently, they are also used to be a basis of construction and/or refinement of theories and models.

In the field of ionics, they are also applied for understanding dynamics and structures of new materials as well as composites or functional materials such as solid state batteries, actuators, and nano-machines in recent works and will be more applied in future works. It is expected that applicability of MD simulations will spread over wider fields of both fundamentals and applications.

8.1.2 History of MD Simulations in Ionics

Applications of MD simulations to ionics have a long history, and some early developments are introduced here. As far as we know, the first MD work for ionic system seems to be that by Woodcock in 1971 [1], in which alkali chlorides in the liquid state are treated by using the empirical potentials by Tosi and Fumi [2, 3]. Soon after, Rahman et al. [4] examined the structure and motion in liquid BeF_2, $LiBeF_3$ and LiF, assuming purely ionic interactions. It is worth to mention that the former two systems can be regarded a model of silica and silicate, because of comparable size ratio of constituent atoms. After these works, vitreous state for silica was examined by Woodcock et al. [5], where even individual motions of Si and O atoms were examined. Soules also examined the structure and dynamics of glasses including silicate [6]. These pioneer works of MD and/or Monte Carlo Simulation (for example see Ref. [7]) take important roles to understand the structure and dynamics of ionic systems including those in the glassy states.

Although the formal charge models used in almost of early works can pick up some essential character of the ionic motion or structures, still they were not good enough for comparison with experimental ones. A large discrepancy can be found in formal charge model. For example, the glass transition temperature, T_g, tends to be extremely different, and/or pressure becomes several orders larger or smaller than the ambient pressure. Therefore, the history of classical MD simulations is also a history of developments of reliable potential parameters, when used for comparison with experiments. The system size and time scale covered were limited in early works due to the limited power of computers. Furthermore, treatment of Coulombic force needs larger cost of calculation than with repulsive force of short length scale. As a result, the simulation times of early works on ionic systems were of the order of several pico seconds and the system size was also small (~several hundreds). This limitation of size and time scale caused several problems such as undesirable effect of periodic boundary conditions, insufficient equilibration time and insufficient sampling of rare events. In spite of such limitations, many new insights had been brought forth.

Empirical potential model for MD was usually derived from the information on crystal structures and related information such as compressibility, expansivity, structure of polymorphs. Although the models enable important tasks to be carried out by simulations, more realistic potential models have been sought after, since the quality of the available models was not necessarily good enough for some purposes. Many researchers have tried the determination of better potential parameters for different systems. Modeling by *ab-initio* quantum mechanical potential surfaces has been used for calculations in physics by several authors. In 1988, the simple pair additive potential derived from the quantum mechanical calculation was shown to be effective enough to reproduce polymorphs of silica by Tsuneyuki et al. [8, 9] (hereafter referred to as TTAM). Effective parameters used to reproduce the several Mg silicates were also derived by them using the potential energy surfaces of model clusters of both SiO_2 and MgO. Their method for the silicate is applicable only when the condition $q\mathrm{M} = -q\mathrm{O}$ is a good approximation, where q is the charge number. In 1990, the progress of the modeling methods in mineralogy has been reviewed by Catlow and Price [10]. Thus far, many MD works have been done for ionic systems for both molten [11] and glassy states using several kinds of potential parameters.

Although alkali silicates are typical glass-forming materials and a study of the structures and properties is important not only for industrial use but also for the fundamental understanding of minerals, ceramics and glasses, an adequate potential model for predicting the unknown properties had not yet been established for a long time. In 1992, Habasaki and Okada derived parameters for some alkali silicates [12], which have a different stoichiometry from Mg silicates, based on the ab initio MO calculation (see Sect. 9.1), by using the method similar to the approach in deriving TTAM. Because of the additivity of the different atomic species, the parameters are suitable for the study of the mixed alkali effect as well (see Chap. 10). The effect was reproduced by MD simulations successfully and jump paths (ion channels) for ionic motion were visualized for the first time as far as we know [12–14] and elaborated further in Refs. [15, 16]. Dynamic heterogeneity in the ionically conducting glass is observed in the motion of Li ions in lithium metasilicate [17, 18]. (See Sects. 9.5 and 11.5 for details.) This characteristic property is shared by structural relaxation of glass forming liquids, and the commonality has drawn attentions in the relation with the mechanism of the glass transition. Nowadays, the potential parameters are widely used by several other groups [19–22].

MD simulations have been used to examine a variety of nature of ionic systems. Using small angle X-ray diffraction and MD simulations, Greaves [23] has shown the clustering of alkalis in mixed alkali disilicate. By Jund et al. [24] and by Horbach and Kob [25], channel diffusion of sodium in silicate glass and melt was examined, and the relationship with the mode coupling theory also was discussed [26, 27]. Details of structures and dynamics are also examined in related systems. Recently, ionic liquids are actively examined by MD simulations and many common views with glass forming liquids are reported (see Chap. 11 for details).

With rapid developments of computer and technology for acceleration of calculations, the classical MD can now cover wider range of materials, compositions, temperatures, pressures and time scales. In recent years, ab initio molecular orbital (MO) calculation or calculation by density functional theory (DFT) can be done for the relatively larger systems [28, 29]. Furthermore, works using ab initio MD went the dawn, although some cautions might be necessary for the treatment of it, especially for the case of the slow dynamics as discussed in the next section.

Using ab initio MD methods, Tilocca [29] has examined the phosphosilicate glass, which is bioactive material. Recently, Payal and Balasubramanian [30] have performed the ab initio MD of dissolution of cellulose in ionic liquids. Such works will increase the importance and reliability with further development of computer technology in enabling the larger size and longer time scale calculations.

8.2 Methods in Molecular Dynamics Simulations

Nowadays, many MD programs are available and researchers are not necessarily to be programmers themselves. However, the contents of programs aimed for general purposes tend to be too complicated and often they seem to be a black box. In this section, the essence of methods used in the molecular dynamics simulation is explained, enabling the reader to understand the outline of it, and what is done in the programs. Our attention is mainly focused on the treatment of ionic systems by classical MD. In Chap. 12, practical introduction for MD simulations is given with some examples of the treatments of MD data.

For planning research using MD, the researcher is recommended to consider the characteristics of the problem to be examined as well as requirements of system size and time scale carefully. Then one can choose the most suitable method within the available resources, because classical and *ab-initio* methods as well as other methods all have their own advantage and limitation. Although needless to say, for a meaningful comparison of methods, reasonable choices of initial configurations, equilibration, suitable choice of conditions such as cooling schedules as well as good statistics are required. Therefore careful judgment for the usefulness and limitations of them is required. Even in the classical method, the covered space and time region might not be large enough, and consequently the results are problematic in such cases. This problem appears remarkably in ab initio MD, which requires larger calculation cost and also the "real time" required for the calculations. The problem will be discussed in the following section.

8.2.1 Classical and Ab Initio Methods

Here we compare classical and ab initio methods in the study of ionics briefly, although mainly the former method is treated in the present book. In classical MD simulations, equations of motion are solved numerically, based on a given potential model. When large scale simulations of long time are necessary, classical MD using empirical force field or effective force field derived from the ab initio molecular orbital calculation or density functional calculations are the practice because of lower calculation costs and time. For realistic simulations comparable to experiment, potential parameters with good quality are required; however, researchers of classical MD often encounter a problem of "missing parameters". Situation becomes worse in the complex systems with many interactions. In such works, it is difficult to find out suitable parameters and their combinations for the system to be examined. Although there are several approaches to treat general parameters and/or combination rules, careful judgement for the quality of the potential model is necessary. In such cases, derivation of suitable parameters for each problem is expected. Thus, in the classical MD simulations or hybrids of quantum and classical methods, one needs to critically examine the quality of the potential parameters, and the functions used, as well other conditions. Of course, more realistic simulations are better for some purposes. Ab initio MD methods such as the Car-Parrinello (C-P) methods [2] are contributing to recent developments of the computational science. In C-P, electrostatic states of the system are calculated using the density functional theory (DFT) with solving the equation of motions, at the same time. The method is particularly applicable if there are the time dependent changes of electronic states during the simulation as in the case of occurring chemical reaction. It is useful to examine the structures and dynamics in details, provided suitable conditions are fulfilled. Considering above situation, one may consider that the ab initio method is always the best choice. However, tractable ab initio methods have serious limitation in the following situations. In the case of ion dynamics in ionically conducting in molten and glassy states or in ionic liquids, dynamics observed are slow, similar to the super cooled liquids near the glass transition temperature [31], and therefore long time simulations as well as large size are required. Unfortunately, it is not easy to perform ab initio MD in suitable conditions, because of huge calculation resources and time required. For example, activation energy obtained from the short time ab initio MD seems to be used as a guide of material designs such as lithium batteries [32]. Although such approaches are useful, one should note that the obtained short time activation energy is for each jump motion and is not the same as that for diffusion (and/or conduction) of long time scale (see Sect. 9.4.2), in the case of densely packed materials such as supercooled liquids, crystals and glasses. That is, long time scale is required to examine transport properties in low temperature regions or in high pressure regions. In recent works in ab initio MD, typically system containing tens to hundreds particles during several ps ~ several tens of ps are examined. In contrast, in classical MD simulations of ionic systems, typically several thousand ~ several tens of thousands particles during ns ~ several tens of ns are examined. This situation of ab initio MD is similar to that in the beginning of the classical MD, where many problems were found due to the limited system sizes and the limited simulation time. Because of such limitations of *ab-initio* MD, the result obtained for slow dynamics in some systems may not be reliable, although challenges to larger system and longer time scale are continuing. The difference of several orders of magnitude in time scales and system size of the two methods are non-negligible and it will not be removed easily even by the further development of the computational technology. Nowadays, such limitation of ab initio MD seems to begin to be recognized well and many kinds of hybrid methods or combinations of methods tend to be used for each targeted problem. For the treatment of slow dynamics, classical MD simulation using the potential (force field) based on the ab initio MO calculation or DFT is a one of the suitable approaches for covering longer time region and larger system size with a relatively low cost. Our and related works using the approach will be explained in the Chaps. 9–11. When the potential curves or surfaces are not time dependent, classical MD simulations using reliable potential are good enough to examine the structure and dynamics of systems. Thus when applied to model systems, this method is capable of generating a “computational experiment” to uncover the principles of structure formation and/or the mechanism of the dynamics under well controlled conditions. In the studies of ionics in glasses [33–35] and ionic liquids [36], comparisons of ab initio and classical methods are reported. Pópolo et al. have argued that the local structure around the cation obtained from ab initio MD in dimethyl imidazolium chloride [DMIM][Cl] shows significant differences compared to both the classical calculations and the neutron results [36]. The author suggests ways in which the classical potentials may be improved. Recently, Carré et al. [37] derived the effective potential for silica based on the C-P MD [38] amenable for the larger and longer scale simulations. On the other hand, classical MD can also provide initial configurations for ab initio MD simulations, MO and DFT calculations, after long time equilibration. In this sense, both methods are complementally each other. Other approaches to cover the long time and large system size are also in progress. In the case of ionic liquids which have inner structures, coarse-grained models [39, 40] are the possible choices to extract the essential part of the structure or dynamics besides the fully atomistic simulations.

8.2.2 *Models Used in MD Simulations*

Potential functions and their parameters are the main "input" of the MD simulation, which determine the characteristics of the system. Here typical models used in the classical MD are summarized. Several functional forms of potential (force field) are used for MD simulation. Soft-sphere and Lennard-Jones are frequently used as model systems for examining liquids, crystals and glasses including the problem of the glass transition. They are also used as a part of ionic models having more complicated form. For the simulation of realistic systems, unknown parameters can be determined from the experimental data such as expansibility, compressibility, structures and/or from quantum mechanical methods.

8.2.2.1 Soft-Sphere Model

The model consists of the repulsive term in the following form [41–47] is traditionally called as soft-core (SC) model.

$$\varphi_{ij} = \varepsilon\left(\frac{\sigma}{r_{ij}}\right)^{n}, \tag{8.1}$$

where the r_{ij} is the distance between particle i and j. The parameter ε, and σ determine the depth and the size of the potential well, respectively. The reduced units are often used for describing general properties and for comparison with results. For example, the reduced unit of length, l (= $(V/N)^{1/3}$), and time τ $(=l(m/\varepsilon)^{1/2}(l/\sigma)^{n/2})$ are used, so that the equation of the motion becomes simple. Here V, N and m stand for system volume, total number and mass of particle, respectively.

Recently, this functional (inverse power law) form is considered as a basis for understanding the thermodynamic scaling (TV^{γ} scaling) of dynamical properties known for many systems including ionic liquids [48] and ionically conducting systems and importance of the model seems to be increasing (see Chap. 7). In the scaling law for the inverse power law (SC) potential, exponent n in Eq. (8.1) is connected to γ value of the system.

The SC system satisfies "dynamical scaling law" [44, 45], which is an extension of the scaling law of the hard sphere (HS) system. For the HS system, one considers N hard spheres of radius σ in the box of volume V ($=L^3$) and starts to move with given initial coordinates and velocities. If the initial coordinates, velocities, L, and σ are multiplied by a constant C (>0), the trajectory in the configuration space of $3N$ dimension is similar to that of the original one. If only the initial velocities are multiplied by C, the trajectory is unchanged through time intervals between collisions and is reduced by the factor of $1/C$. This is the dynamical scaling law of the HS system. In a similar manner, in the SC model, dynamic scaling law holds exactly and even a non-equilibrium relaxation can be represented by analytical expression.

In experiments, going back to the early days, several one component systems such as glycerol and/or ethanol are known to be excellent glass formers [49–51] and the simplicity of the one component system was recognized in the study of the glass transition problem. However, in early MD works around 1970, one-component SC system was found to crystallize within a short run, and hence binary system tends to be used for the study of glass transition [52–54]. In spite of this historical situation, one-component SC system can be a good model to study glass transition due to its simple theoretical treatment, if the crystallization is suppressed. Fortunately, when the system size is large enough (>500), the crystallization seem to be suppressed at long time and almost systems become metastable ones after non-equilibrium relaxation [45]. Actually, in many runs in the system larger than 2000 particles, one-component SC model with $n = 12$ shows non-equilibrium relaxation towards metastable states (called as a glass branch), which can be regarded as the (stabilized) glassy states, from both structural [45] and thermodynamical [46] properties. In the metastable glassy state, different local structures (face-centered cubic (fcc) like and body-centered cubic (bcc) like) are found to be mixing. Because of the mixing of different local structures, disordered structures can be formed without introducing different kinds of particles to form binary systems. Thus the glass transition can be mapped on a phase-diagram using the compressibility factor plotted against reduced density. When the system is rapidly quenched along the liquid branch of the phase-diagram, the system tends to be trapped on the midway towards the glass branch.

Recently, several one component systems including the ones with special types of potential functions are examined to understand the glass transition [55, 56].

8.2.2.2 The Lennard-Jones Model

The Lennard-Jones (LJ) model [57] has the following form.

$$\phi(r_{ij}) = 4\varepsilon\left[\left(\frac{\sigma_{ij}}{r_{ij}}\right)^{12} - \left(\frac{\sigma_{ij}}{r_{ij}}\right)^{6}\right], \tag{8.2}$$

The function becomes 0 at $r_{ij} = \sigma$ and the minimum is observed at $r_{\mathrm{ij}} = \sqrt[6]{2}\sigma$, where the function becomes $-\varepsilon$. The former is regarded as the size of the particle, and therefore, σ is used as a unit of length r.

The parameters for argon, $\sigma = 3.405$ Å and $\varepsilon/k_{\mathrm{B}} = 119.8$ K, where k_{B} is the Boltzmann constant, have been used in many theoretical works [58]. Several new parameters are proposed for argon (or other materials). The values $\sigma = 3.345$ Å and $\varepsilon/k_{\mathrm{B}} = 125.7$ K bring a better agreement between theory and experiment for thermodynamic behaviors of the system [59]

Generalized forms of LJ model [60, 61] consists of repulsive and attractive terms,

$$\phi(r_{ij}) = 4\varepsilon\left[\left(\frac{\sigma_{ij}}{r_{ij}}\right)^{n} - \left(\frac{\sigma_{ij}}{r_{ij}}\right)^{m}\right] \tag{8.3}$$

with powers n and m replacing the 12 and 6 respectively are also used in recent studies of the dynamics of glass-formers.

Binary LJ System

In recent years, starting from the study by Kob and Andersen, binary systems of LJ systems have been used as a model system exhibiting the glass transition and there are accumulated numbers of MD works based on these systems [62–65]. Bordat et al. have compared three different interaction models [63, 64], where the structures and dynamics of the system composed of 1500 particles (1200 for species A and 300 for species B) are discussed related to the glass transition problem. General forms of the binary LJ used in their work are represented by

$$V(r) = \frac{E_0}{(q-p)}\left[p\left(\frac{r_0}{r}\right)^{q} - q\left(\frac{r_0}{r}\right)^{p}\right], \tag{8.4}$$

where E_0 and r_0 are respectively a parameter for energy depth and position of the minimum of the potential well. In the model I, $q = 12$ and $p = 11$. In the model III, $q = 8$ and $p = 5$. The parameters for $q = 12$ and $p = 6$ for model II corresponds to the Kob-Anderson model [62], which has been extensively examined as a model of glass transition (see Table 8.1).

The anharmonicity of the potential for A-A interaction is increasing in the order of I (12-11), II (12-6) and III (8-5). The ‘fragility’ obtained from several methods is increasing in order of I, II and III. It parallels to the change of stretching exponent β of I, II and III, which are 0.69, 0.65 and 0.60, respectively. That is, the capacity of

Table 8.1 Parameters of the Lennard-Jones potentials in the Kob-Andersen model, where ($\sigma = \frac{r_0}{2^{1/6}}$) in Eq. (8.4)

Interaction	A-A	B-B	A-B
E_0	1.0	0.5	1.5
σ	1.0	0.88	0.8

intermolecular coupling and anharmonicity of the potential has the effect in increasing fragility and the non-exponentially parameter ($1-\beta$), which is the same as the coupling parameter, n, in the coupling model.

Even for the binary LJ systems, one may expect the existence of some mixing effect for the dynamics and structures. This is because the glassy system like silicates shows a large non-linear change of the dynamics by mixing of different kind of alkali ions, known to be "mixed alkali effect" (see Sect. 4.8 and Chap. 10). In this case, it was well established that the mixing of different sizes of alkali metal ions causes the mutual interception of jump paths in a certain time scale and suppression of the cooperative motion which enhances the effect [65]. For example, in the case of lithium potassium silicates, mutual interception means that the Li ion cannot enter the site previously occupied by K ion, while K ion cannot enter the site previously occupied by Li ion. Similar situations are found in the generalized LJ mixtures [66, 67]. The ionic liquids also can be regarded as the binary system of cation and anion. Comparison of generalized binary Lennard-Jones (LJ) systems with different potential parameters is helpful to understand the dynamics of ionic liquids, especially for the physical meaning of the coupling of the anion and cation or the role of charges [31].

Other functional forms used in inorganic materials especially for Ionics will be introduced hereafter.

8.2.2.3 Huggins-Mayer Potential

Fumi and Tosi [3, 68] developed potential parameters for alkali halide such as NaCl, by fitting the Huggins-Mayer dispersive energy to crystallographic data. The function form is as follows.

$$\varphi(r_{ij}) = A_{ij} e^{-\frac{r_{ij}}{\sigma_{ij}}} - \frac{C_{ij}}{r_{ij}^6} - \frac{D_{ij}}{r_{ij}^8} + \frac{q_i q_j}{4\pi\varepsilon_0\, r_{ij}}, \tag{8.5}$$

where the exponential term is for repulsive interaction, while inverse power-law terms represent the attractive interaction. A_{ij} is called the Pauling factor, defined by $1 + Z_i/n_i + Z_j/n_j$, where n_i is number of electron of the most outer shell of the ion i and Z_i is for electric charge on species i. The second and third term is for dipole-dipole and dipole-quadrupole interactions, respectively. The fourth term for the right hand side is for Coulombic interaction term with charges q.

Several functional forms for ionic systems are suggested so far, and both empirical and ab initio based potential parameters are developed.

8.2.2.4 Born-Mayer-Huggins Potential

The following similar in form to the previous one is called as Born-Myer-Huggins model.

$$\varphi\left(r_{ij}\right) = A_{ij}e^{\frac{\sigma_i+\sigma_j-r_{ij}}{\rho}} - \frac{C_{ij}}{r_{ij}^6} - \frac{D_{ij}}{r_{ij}^8} + \frac{q_iq_j}{4\pi\varepsilon_0 r_{ij}} \tag{8.6}$$

The first term on the right-hand side represents the Born-Myer repulsive term. The value of r represents the distance between atoms, and σ_i is a size of i ion. Here, ρ is the softness parameter.

8.2.2.5 Gilbert-Ida Type Potential

Gilbert-Ida type [69, 70] repulsive potential combined with Coulombic force has been successfully used for silica [8] and lithium, sodium and potassium silicates [12]. It is given by

$$\phi\left(r_{ij}\right) = \frac{q_iq_j}{r_{ij}} + f_0\left(b_i + b_j\right)\exp\left(\frac{a_i + a_j - r_{ij}}{b_i + b_j}\right) - c_ic_j{r_{ij}}^{-6} \tag{8.7}$$

The first term on the right-hand side represents the Coulombic interaction. The value of r_{ij} (Å) represents the distance between atoms, and a_i (Å) and b_i (Å) are the effective radius and the softness parameter, respectively, of atom i. the value f_0 is a constant (=1 kcal mol^{-1} Å^{-1}). The parameters c_ic_j (kcal Å^6 mol^{-1}) are for the correction of the curvature for the interaction of pairs including oxygen atom, and therefore may be treated as a part of repulsive potential term. Units in the function are as in original papers [8, 12], to avoid the loss of numerical accuracy by changing units. This potential form is additive for pair as well as atomic species. The latter property enables us to treat the mixed alkali system while keeping consistency with the single alkali systems. Therefore it is useful to study the “mixed alkali effect” (see Chap. 10). Examples of MD simulations of silicate crystals and glasses using this kind of potential will be shown in Chap. 9.

8.2.2.6 Potential Including Inner Structures

The following potential forms for representing both intermolecular and intramolecular interactions are frequently used for organic systems as well as ionic liquids [31, 71–73].

$$U(R) = \sum_{\text{bonds}} K_{\text{r}}\left(r - r_{\text{eq}}\right)^2 + \sum_{\text{angles}} K_{\theta}\left(\theta - \theta_{\text{eq}}\right)^2 + \sum_{\text{dihedrals}} \frac{V_{\text{n}}}{2}(1 + \cos[n\phi - \gamma]) + \sum_{\text{i<j}}^{\text{atoms}} \left(\frac{A_{\text{ij}}}{R_{\text{ij}}^{12}} - \frac{B_{\text{ij}}}{R_{\text{ij}}^{6}}\right) + \sum_{\text{i<j}}^{\text{atoms}} \frac{q_{\text{i}}q_{\text{j}}}{\varepsilon R_{\text{ij}}} \tag{8.8}$$

The model uses a sum of bond, angle, and dihedral deformation energies, a pairwise standard (6,12) Lennard-Jones potential, and Coulombic interactions between atoms with charges q_{i} and q_j.

Our and related works for ionic liquids using MD simulations are shown in Chap. 11.

8.2.2.7 Reactive Force Field

Reactive force fields, such as ReaxFF, have been used in several related works [74, 75], where the charge on the atom changes with the position. Such approaches will be useful in the investigation of the details of reactions on the surfaces of colloids, gels or related systems.

Other MO or DFT based potential model may be applicable for representing bond breaking of reconnection even if the charge seems to be fixed in the simulation. Actually, Habasaki and Ishikawa have observed that the clusters or gels can be formed in silica colloid-water-salt system [76] using the silica model by Tsuneyuki et al. [8] with a fixed charge. This is because the charge is fixed in the fitted parameters but not in the quantum mechanical calculations used for derivation of it. Therefore the model allows reconstruction of bonds.

8.2.2.8 Other Models

Models for Water

Many kinds of water model such as SPC, SPC/E [77, 78], TIPS3P, TIPS4P, TIPS5P [79, 80] are proposed so far. Comparison of some properties among different water models was reported in Refs. [81, 82]. Each model has both drawback and advantage and therefore researcher should select suitable one by any particular purpose. It may be useful for the researchers of glasses to mention that the structure and phase diagram of water is analogous to the silica due to network formation by hydrogen bonds in many points. Therefore, comparison of related systems will be useful for studies in both research fields.

8.2.3 Units Used in MD and Combination of Potential Models

It is recommended to use International System of Units (SI) in many fields; however, potential parameters or functions for MD simulations found in literatures are not necessarily given in SI. This is probably because values used in SI are not always appropriate for numerical treatments in order of magnitude. Many different units appear in MD programs and papers. Furthermore, reduced units are also used by physical reasons. Therefore, careful treatment of units is necessary. Because simulated systems are sensitive for the given potential parameters, it is better to avoid repeating conversions of units to keep numerical accuracy.

Quality of the potential parameters (for example, the size of the basis set used for derivation if it were based on ab initio MO calculation) should be good enough and comparable when one uses the combination of parameters taken from different sources. Sometimes, one may encounter the difficulty to combine the parameters because of different potential forms. In some cases, it is possible to change from one to the other. Gilbert-Ida type parameters can be easily changed to the Born-Mayer-Huggins form, although the merit of the additivity of the parameters is lost. The parameters in LJ form can be changed into those for Gilbert-Ida type, by a requirement of having the same energy minimum separation, depth and the same behavior for the large r region [83].

In treatment of ionic system (similar situation may happen in other systems), careful treatment of the term "mole" is required. For example, the system "Li_2SiO_3" is the same composition as "$x$$Li_2O$-$(1-x)$$SiO_2$" with $x = 0.5$. The former expression may be used to compare the different phases such as glass and crystal. The latter expression is often used for glasses to include composition dependence of the system. However, the system energy "per mole" for these system becomes different due to the different definition of "mole", because it is defined by the weight (represented by grams) of the Avogadro numbers of "specified groups of particles". In an MD program, the former expression may be chosen for mole because the smallest number of species (Si in this case) being an integer is preferred. In a certain MD program, ions included in a basic MD cell seem to be used as a group to define "mole". In ionic liquids, ion pair seems to be used as the group by many researches at least for simple systems. For comparison of works, it may be necessary to mention what unit is chosen for the definition of "mole" or changing the units to adjust it to conventional ones.

8.2.4 Solving the Equation of Motion

In principle, MD simulations describe the motions of particles (ions or atoms) by solving the equation of the motion. That is, the position of the particle is predicted from the previous and present ones by adding the forces acting from other particles.

In the case of classical MD, it would not be an exaggeration to say that potential functions and its parameters (force fields) determine the fate of the particles, if other conditions are reasonably selected.

The equation of the motion for i-th numbered particle can be written as,

$$\frac{d^2\mathbf{r}_i}{dt^2} = \frac{\mathbf{F}_i}{m}, i = 1, 2, \ldots N \tag{8.9}$$

8.2.4.1 Algorithm

In classical MD simulations, the equation of the motion is solved numerically. In other words, the next position of i-th particle is calculated based on the position at t and that of one or several steps before. Several algorithms to solve the equation of motions have so far been proposed. Here we explain the Verlet algorithm [84], which is simple and known to be symplectic [85, 86]. This method is suitable for calculation of motion including sudden changes of displacements (jumps or hops) found in melts and glasses, because it is not affected by the information of many steps before. The Gear's method, which is one of predictor-corrector methods with several steps, is also used for MD simulation [87]. In this case, slow dynamics by jump motions might be affected by the several steps before the motions. In other words, the method is not necessarily suitable when the sudden change occurs in the system. Although the method is known to be accurate in other cases and useful at least for a short time scale, drift of the motion might be non-negligible during long runs because of its non-symplectic nature.

In the Verlet method, the positions of i-th particle after Δt and that before Δt are

$$\mathbf{r}_i(t + \Delta t) = \mathbf{r}_i(t) + \Delta t\dot{\mathbf{r}}_i(t) + \frac{(\Delta t)^2}{2}\frac{\mathbf{F}_i(t)}{m} + O\left((\Delta t)^3\right) \tag{8.10}$$

$$\mathbf{r}_i(t - \Delta t) = \mathbf{r}_i(t) - \Delta t\dot{\mathbf{r}}_i(t) + \frac{(\Delta t)^2}{2}\frac{\mathbf{F}_i(t)}{m} + O\left((\Delta t)^3\right). \tag{8.11}$$

From the sum of Eqs. (8.10) and (8.11), one can obtain the following relation.

$$\mathbf{r}_i(t + \Delta t) + \mathbf{r}_i(t - \Delta t) = 2\mathbf{r}_i(t) + (\Delta t)^2\frac{\mathbf{F}_i(t)}{m} + O\left((\Delta t)^4\right), \tag{8.12}$$

On the other hand, from the difference of Eqs. (8.10) and (8.11), one can obtain the following equation,

$$\mathbf{r}_i(t + \Delta t) - \mathbf{r}_i(t - \Delta t) = 2\Delta t\dot{\mathbf{r}}_i(t) + O\left((\Delta t)^3\right), \tag{8.13}$$

That is, new position is,

$$\mathbf{r}_i(t+\Delta t) = 2\mathbf{r}_i(t) - \mathbf{r}_i(t-\Delta t) + (\Delta t)^2\frac{\mathbf{F}_i(t)}{m} + O\Big((\Delta t)^4\Big), \tag{8.14}$$

and a new velocity is,

$$\dot{\mathbf{r}}_i(t) = \frac{1}{2\Delta t}\{\mathbf{r}_i(t+\Delta t) - \mathbf{r}_i(t-\Delta t)\} + O\Big((\Delta t)^2\Big), \tag{8.15}$$

A numerical error in solving equation of motion thus depends on the time of each step, Δt.

8.2.4.2 Periodic Boundary Conditions (PBC)

Periodic boundary condition (PBC) is frequently used in typical MD simulations of bulk systems. Schematic description of the periodic boundary conditions used in the simulations is shown in Fig. 8.1, where the basic cell containing particles is surrounded by the periodically repeating image cells infinitively.

The figure is for the two dimensional case; however, similar conditions are also used for three dimensional cases. (One should be careful to use 2D system for comparison with experiments except for a special purpose, because motions of atoms might be affected by the dimensionality of the space.) For a particle within

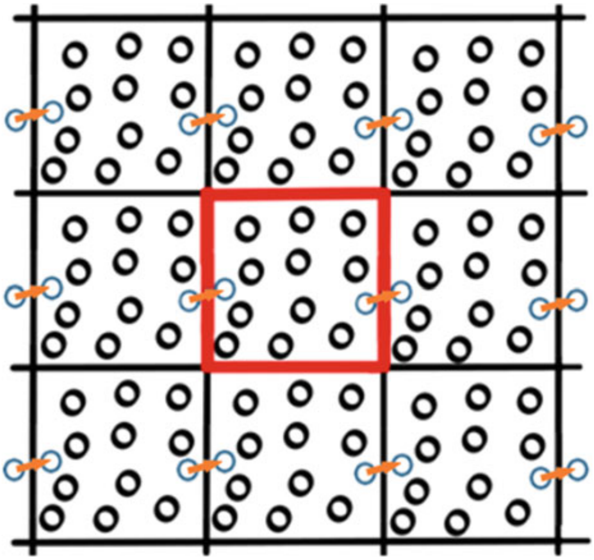

Fig. 8.1 Schematic description of the periodic boundary conditions used in the simulation. Image cells continue infinitively. When a particle moves out the basic cell of the MD simulation, another particle moves in from the image cell as shown by *orange arrows*

the basic cell, interactions from particles within the sphere with a certain cutoff length (typically chosen to be $L/2$, where L is a length of basic cell) are taken into account including ghost particles (images of the same particle found in the basic cell) in image cells.

By this treatment, we have the following benefit.

1. Properties of the bulk can be simulated by the limited number of particles. That is, effect of the surface can be removed.
2. If the particle moved beyond the boundary, the ghost particle comes into the basic cell. Therefore, in the case of constant number simulations such as NVE or NPT ensembles, the number of the particles is kept constant.
3. The periodicity like crystals makes it possible to calculate the long ranged Coulombic force using the Ewald method or related ones, even in the case of liquid or glasses. In many cases, minimum image (within $2/L$) is used for calculation of short range forces (and for real part of the Ewald summation explained later).

Following characteristics of the system should be kept in mind when one uses PBC. Even when we considered the infinitive system using PBC, the wave number accessible by the simulation is limited by the size of the simulation box. Furthermore, when one considered the motion of particle in the system with PBC, it is repeated as well and some artificial waves or vibrations in the particle motions will be formed. If the system size is too small, the particle might be affected by its own ghost in an image cell, which is moving in the same directions. Especially in the case of crystals, basic box of the MD is formed by several repeating basic lattices of the crystal and therefore the number of repetition of them in each axis direction will affect the periodicity of the motions. To reduce such effects, the system size used has to be large enough to the possible extent while ensuring the practical usability. It is useful to change the system size to check the effect.

For the study of glasses, further caution is required to avoid crystallization in the system. If only a small number of particles were contained in each basic box of the simulation, system may easily crystallize and/or behaves like crystals because of PBC. In the case of network glasses, long ranged oscillation tends to be formed and continued by PBC.

8.2.5 Treatment of Coulombic Force

Coulombic force is a long ranged force and has essential importance to consider in the ionic systems. The repulsive force is usually a short ranged force, and for it in MD simulations, using a certain cutoff length is a reasonable choice. Corrections by shifted force can also be used. The cutoff length should be chosen, so that the wave like structures of $g(r)$ for ion-ion converge (typically 8–15 Å). When the ion (molecule or residue) has an inner structure, the distance among the center of unit structures can be considered as that for ionic structures.

As well known, the Madelung energy of simple crystal is represented as

$$E_{Madelung} = -N\alpha' Z^2 e^2 / r_0, \tag{8.16}$$

where α' is known to be Madelung constant [88]. The system energy is affected from the ions located at long distances. For isolated system such as small clusters or nano-crystals, one can use the direct sum or multipole expansion [89] of it.

If parameters and functions are given in SI, the Coulomb's constant is defined and given by $k = 1/(4\pi\varepsilon_0\varepsilon)$, where the constant ε_0 is the permittivity of free space and ε is a relative permittivity for the material concerned. The Coulombic potential formed by N ions around an ion is given by

$$\phi(r) = \frac{1}{4\pi\varepsilon_0} \sum_{n=1}^{N} \frac{q_n}{|r - r_n|}. \tag{8.17}$$

Convergence of the long range force for the Coulombic term needs a large cost in calculation. The calculation cost of direct sum of N particle is $N(N-1)$ when all combinations are counted, and is of the order of N^2 (i.e. $O(N^2)$). Order of N^2 means that, if the system size (particle number within the basic cell) is 100 times larger, the calculation cost is 10,000 times larger.

Coulombic force is treated by several methods in MD simulations as shown below.

8.2.5.1 The Ewald Method

The Ewald method [90–92] is a standard method for calculation of Coulombic term used in the MD simulations, which mimics the periodicity of the crystal structure by using a PBC of the MD cells. Many methods to reduce the cost have been developed and still are developing. Recently, particle-particle-particle-mesh (P^3M) Ewald [93, 94], particle mesh Ewald method (PME) [95], and multipole expansion method are also used. These methods will be explained in the following subsections.

In MD simulations of bulk system, all forces from the particles in the basic cell and those from image cells at infinitive distances are taken into account to eliminate surface effects. The Ewald method is applicable to both crystalline and non-crystalline materials such as liquids, super-cooled liquids and glasses. In non-crystalline systems, the method is used with the periodic boundary conditions (PBCs), where the system has a periodic charge distribution similar to crystals. With this condition, Coulombic potential of the system is represented by

$$\varphi_C = \frac{1}{2}\sum_{\mathbf{n}}\sum_{i}\sum_{j}{}' \frac{Q_i Q_j}{4\pi\varepsilon_0}\frac{1}{|\mathbf{r}_i - \mathbf{r}_j + \mathbf{Ln}|}, \tag{8.18}$$

where $\boldsymbol{L}$ is a vector to represent the size of basic cell of MD simulations and **n** is a vector consists of integers such as (1,1,1) to represent the image cells.

The summation for **n** is taken to consider the contribution of all image cells. The vector (0,0,0) mean a basic cell for the simulation and the term $(i = j)$ in the cell is excluded and this restriction is represented by Σ' in the summation.

The Ewald method takes into account infinitive numbers of ions using PBC without considering all image cells in the real space. In the method, Coulombic potential is separated into three parts, which is the real, the reciprocal and a constant (self) part as shown in the following equation.

$$\varphi_C = \varphi_{real} + \varphi_{recip} - \varphi_{self}. \tag{8.19}$$

The First Term of the Ewald Method, φ_{real}

Here we considered the *j* point charges around an ion "*i*". The first term φ_{real} is the sum of the real part for point charges around an "*i*" ion and the Gaussian distributions having the opposite sign for the system. The term for the real space is given by

$$\varphi_{real} = \frac{1}{2}\sum_{i}\sum_{j}{}' \frac{Q_i Q_j}{4\pi\varepsilon_0}\frac{erfc\left(\alpha\left|\boldsymbol{r}_i - \boldsymbol{r}_j\right|\right)}{\left|\boldsymbol{r}_i - \boldsymbol{r}_j\right|}. \tag{8.20}$$

Here the summation is taken for the sphere within a cut-off length, typically radius of *L*/2 from "*i*" particles, and not for all image cells. In the expression for φ_{real}, "erfc()" stands for the complementary error function defined by,

$$\mathrm{erfc}(\mathrm{x}) = 1 - \mathrm{erf}(\mathrm{x}) = \frac{2}{\sqrt{\pi}}\int_{x}^{\infty} e^{-t^2} dt \tag{8.21}$$

The term α in the expression is a setting parameter to determine the shape of the Gaussian distribution of the charge and also determines convergence of the term.

The Second Part of the Ewald Summation, φ_{recip}

A part not sufficiently taken into consideration in real space is compensated by the reciprocal lattice term φ_{recip}, which includes the Gaussian distributions having the same sign as the point charges considered, and is given by

$$\varphi_{recip} = \frac{2\pi}{V}\sum_{G\neq 0}\frac{exp\left(-\frac{|\boldsymbol{G}|^2}{4\alpha^2}\right)}{|\boldsymbol{G}|^2}\sum_i\sum_j\frac{Q_iQ_j}{4\pi\varepsilon_0}\cos\left\{\boldsymbol{G}\cdot\left(\boldsymbol{r}_i-\boldsymbol{r}_j\right)\right\} \tag{8.22}$$

Here $\boldsymbol{G}$ is a reciprocal lattice vectors. This summation can be done for one half of the vectors, because terms (h, k, l) and $(-h,-k,-l)$ in the reciprocal space have the same values. The Gaussian distribution introduced guarantees the convergence of the summation in the reciprocal lattice vectors.

The Third Term of the Ewald Summation, φ_{self}

In the reciprocal term, φ_{self}, extra electrostatic potential by the ion "i" having a Gaussian distribution is included and the following term should be subtracted off.

$$\varphi_{self} = \sum_i\frac{Q_iQ_i}{4\pi\varepsilon_0}\frac{\alpha}{\sqrt{\pi}}, \tag{8.23}$$

Setting of the Ewald Method

The error in the Ewald summation is determined by the choice of α and L values. The optimal choice can be done by several methods [96]. For example, when $L \sim 20$ Å is used, 125 vectors are necessary to carried out the simulation with a tolerance of 10^{-5} in the energy of the Ewald sum. In several software of MD, the combination can be selected automatically or set by the choice of a value of tolerance.

The reciprocal lattice term has the factor $1/|\mathbf{G}|^2$, which diverges at $\mathbf{G} = 0$. To avoid the divergence of the second term, $\mathbf{G} = 0$ is omitted and this procedure is justified by the condition of the charge neutrality of the system. Thereby the method does not hold exactly in system with defects. It may be better to consider the charge redistribution to fulfill the neutrality in such a case, or to use other method such as the multipole expansion.

8.2.5.2 Particle Mesh Ewald (PME) and Particle-Particle-Particle-Mesh (P^3M) Ewald Method

Instead of the Ewald method with the $O(N^{3/2})$ character [90, 92], particle-particle-particle-mesh (P^3M) method was developed as the $O(N)$ method [93, 94]. In the case of P^3M, interaction of short length is treated by particle-particle, while the long ranged interaction was treated by particle-mesh interaction. To obtain the $O(N)$

condition in this method, real space region is more limited than the optimized one for the Ewald summation, and the calculation times of real space and reciprocal space are set to be comparable. Particle-Mesh Ewald [95], which is an $O(N\log N)$ method, is a special case of P^3M method, although it was independently developed.

8.2.6 Multipole Expansion and Tree Method

Usually, the force from particles located at the long distance is weak. One of the possible ways to reduce the calculation cost is to handle some numbers of particles together. The group can be represented by the sum of multi-poles. To distinguish the distant particles from the particles close by, the "tree method" has been proposed. The "multipole method" with a multipole expansion is typically used with the "tree method" or "hierarchy tree method" [97–99, 100], which can separate groups by a distance effectively, without calculating the distance among particles. For example, the "Quad tree code" (for 2D case) repeats the division of the system into four until each region contains less than a certain number of particles (0 or 1) (see Fig. 8.2). "Oct tree code" is for the case of 3D.

If both the particles acting and those being affected on are treated as groups, it is called "fast multipole method (FMM)" and is shown to be an $O(N)$ method. The method using multipoles is effective for extremely large system and also for the system without a periodic boundary, since one can consider the force acting from the sub-regions or grids (cells) of the system instead of individual particles. Now we considered a case of interaction from M particles in a sub-region to the outer point

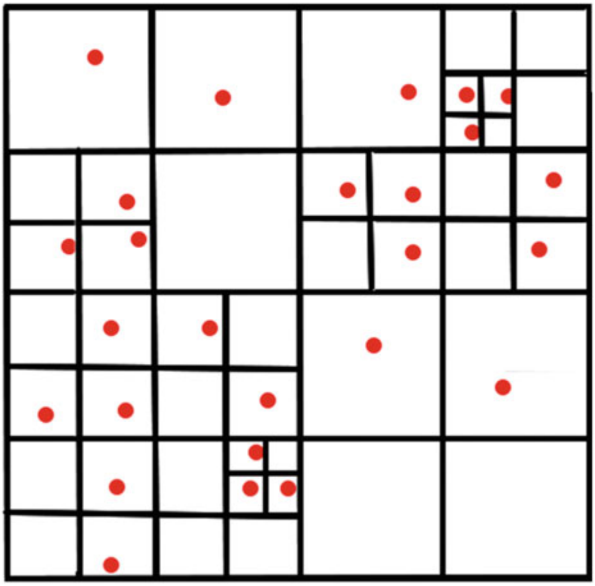

Fig. 8.2 Schematic description of the "Quadtree code" for the 2D structure, which can separate group of particles without calculating the distance

P to understand the merit of using multipoles. Here the center of the cell is represented as $\mathbf{r}_c$ and the relative positions of particles k ($k = 1, 2$----M) to the center are taken as $\mathbf{r}_k$. A Coulombic potential formed at the point *P* is represented as,

$$\varphi_C(\boldsymbol{r}) = \sum\nolimits_{k=1}^{M} \varphi_C(|\boldsymbol{r}_{k-}\boldsymbol{R}|) = \sum\nolimits_{k=1}^{M} \frac{q_k}{|\boldsymbol{r}_{k-}\boldsymbol{R}|}, \tag{8.24}$$

The vector $\boldsymbol{R}$ is a relative position of *P* from the center of the sub-region and q_k is a point charge. At the arbitrary chosen position $\boldsymbol{r}$, the potential function can be approximately represented as follows.

$$\varphi_C(\boldsymbol{r}) = \frac{Z}{R} + \frac{\mu_\alpha R_\alpha}{R^3} + \frac{Q_{\alpha\beta} R_\alpha R_\beta}{R^5} + \cdots, \tag{8.25}$$

In the right hand side of the equation, *Z* is a sum of charge within a grid, $Z = \sum_k q_k$, μ_α is a dipole moment, $\mu_\alpha = \sum_k q_k \boldsymbol{r}_{k\alpha}$, and $Q_{\alpha\beta}$. is a quadrupole, given by $Q_{\alpha\beta} = \sum_k q_k \frac{m}{2} \left\{ \left(3\boldsymbol{r}_{k\alpha} - \delta_{\alpha\beta} \boldsymbol{r}_k^2 \right) \right\}$.

The strength of the charge decreases with $1/r$, while that of dipolar decreases ~$1/r^2$ and so on. In this expression, $\mu_\alpha R_\alpha$ is for a sum of $\alpha = x,y,z$; while $\boldsymbol{r}_{k\alpha}$ is a $\alpha = x,y,$z component of vector $\mathbf{r}_k$. This treatment, which dividing the basic cell into sub-regions, is also useful for the parallel computing.

8.2.7 General Description of the Multipole Expansion

One can represent any charge distribution by using multipole expansion and this kind of treatment is also applicable for $1/r^m$ type potentials besides the Coulombic term. Therefore, more general treatment using spherical harmonics [101] will be useful in some situations. Outside of the ionic system, one assumes that the electrostatic potential ϕ(r) satisfies the following Laplace equation,

$$\nabla^2 \phi(r) = 0 \tag{8.26}$$

Under the condition that "at the long r limit, φ(r) becomes 0", the solution of the equation can be expanded as follows.

$$\phi(r) = \frac{1}{4\pi\varepsilon_0} \sum_{l=0}^{\infty} \sum_{m=-l}^{l} \frac{4\pi}{2l+1} q_{lm} \frac{Y_{lm}(\theta, \varphi)}{r^{l+1}} \tag{8.27}$$

Here the terms $Y_{lm}(\theta, \varphi)$ are the spherical harmonics (i.e., the angular part of the solution). One may be familiar with the graphical representation of the spherical harmonics, because it is frequently used to represent the shape of orbital of electrons such as π-orbitals or *d*-orbitals. For example, one can see the shape of the spherical harmonics. [For example, see Wolfram Demonstration Project, Spherical Harmonics, http://demonstrations.wolfram.com/SphericalHarmonics/ (The address was confirmed to be valid on 14th Feb., 2016.)]. The function is also used to characterize structures of bond ordering, local or intermediate structures in super-cooled liquids, glasses or crystals [66, 102].

The Eq. (8.27) as well as (8.25) is called a multipole expansion of the electrostatic potentials, where the q_{lm} is a multipole moment, which is related to the distribution of the density ρ(*x*') as shown in,

$$q_{lm} = \int_{\Omega} Y^{*}_{lm}(\theta', \phi') r'^{l} \rho(r') dr'. \tag{8.28}$$

When the total charge is denoted by q and the dipole moment is denoted by $p = \int\limits_{\Omega} x' \rho(x') dx'$, then the following relations are obtained.

$$q_{00} = \frac{1}{\sqrt{4\pi}} \int\limits_{\Omega} \rho(x') dx' = \frac{q}{\sqrt{4\pi}} \tag{8.29}$$

$$q_{l,\pm 1} = \mp \sqrt{\frac{3}{8\pi}} \int\limits_{\Omega} (x' \mp iy') \rho(x') dx = \mp \sqrt{\frac{3}{8\pi}} (p_x \mp ip_y) \tag{8.30}$$

$$q_{l0} = \sqrt{\frac{3}{4\pi}} \int\limits_{\Omega} z' \rho(x') dx = \sqrt{\frac{3}{4\pi}} p_z \tag{8.31}$$

Here $l = 0$ is for point charge ($m = 0$), $l = 1$ is for dipole moment($m = -1$, 0, 1), $l = 2$ corresponds to quadrupole ($m = -2$, -1, 0, 1, 2), and $l = 3$ corresponds to 8-pole moment and so on. The concept of multipoles is useful not only for calculations of Coulombic terms during simulation but also for understanding the force affecting the ions.

8.2.8 Multipoles as an Origin of Nearly Constant Loss (NCL) of Caged Ion Dynamics

Usually, interaction of neighboring ions or atoms is directly summed up in MD; however, it is possible to consider the multipole expansion of interaction from surrounding particles as a cage. Let us consider the cage formed by oxygen atoms around Li ions as in silicate or related systems. Each Li ion is trapped inside the cage formed by oxygen atoms and rocked. Instead of direct interaction between Li ion and oxygen atoms, the same potential (Coulombic term) can be represented as the sum of multipoles up to l_{max}. Here the accuracy becomes better if the l_{max} is larger, where the first term (charge-charge interaction) is considered for the center of mass position of oxygen atoms. As already mentioned, contribution of the dipole ($\sim 1/r^2$) decays faster than that of point charge ($\sim 1/r$), while contribution of quadrupole ($\sim 1/r^3$) decays faster than that of the dipole. Thus the potential of the cage, consisting sum of these terms, is anharmonic. In previous chapters, we have shown that anharmonic potential acting on the ions causes caging of the ions at short times, and observed experimentally in susceptibility as the nearly constant loss (NCL).

Here we do not exclude the contribution of repulsive terms, and note that representation by the multipoles is also applicable to the repulsive part. Represented by the multipoles and their time dependence, the anharmonic potential is effective in caging the ions, and the loss from motion of ions confined within the cages is manifested as the NCL in susceptibility (See Sects. 4.5, 4.7 and 9.4.2.). Previously, Dieterich and Maass considered the asymmetric double well potential, and/or random dipole interaction as an origin of NCL [103]. If the total charge in the caging region is 0, then the main term will be dipole (if it is not 0). Although this might be a good approximation in some cases, further terms will be necessary to represent the situation more precisely. In the ionic structures, alternative oscillation of positive and negative charges are observed at longer length scales than neighboring distance and this means that the charge neutrality does not hold within the neighboring distance. When the total sum of q is not 0, point charge term cannot be neglected. Actually, we have previously shown that the motion of Li ions in the lithium metasilicate system is well correlated with the motion of center of mass position of polyhedral formed by caging oxygen atoms [3, 68]. Contribution of further terms also will not be negligible especially in the short distance region. We also note that the cage is moving in NCL region and therefore its motion is characterized as dynamic anharmonicity as discussed in Sect. 9.5.2.

Generally, the nature of cages is also related to the problem of glass transition [104, 105], because the rigidity or softness of the cages determines the motion of ions, atoms, or molecules trapped within [106].

8.2.9 Treatment of Rotational Motion

8.2.9.1 Euler Angles

When ions or molecules of the system have internal structures, methods to include consideration of rotational motion are necessary in MD simulations. In such cases, motions of ion or molecule are regarded as a combination of translational motion of the center of mass position, P, and rotational motion around it. The rotational motion is represented by the Euler's equations [91, 107] named after Leonhard Euler using Euler angles, where the coordinates (P-$\widetilde{x}\widetilde{y}\widetilde{z}$) fixed on body, centered at P are used.

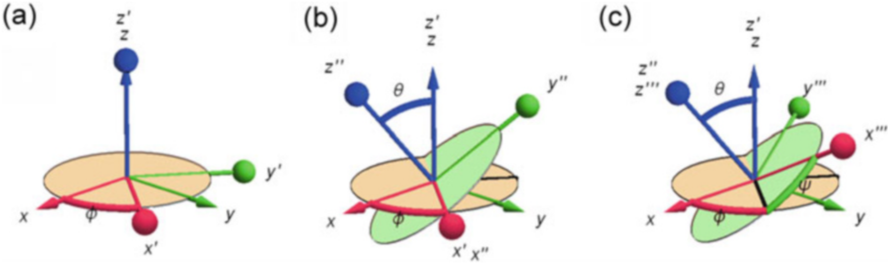

Fig. 8.3 Orientation of rigid body is represented by the Euler angles, ϕ, θ and ψ. Definition of Euler angles by Goldstein is shown here. The rotation is measured in counterclockwise direction. In this example, ϕ, θ and ψ used are 0.92, 0.67 and 0.87, respectively

The coordinate ($P\text{-}\widetilde{x}\widetilde{y}\widetilde{z}$) is transformed from the space coordinate (O-xyz) as follows, where P and O are overlapped. There are several notations and definitions for the treatment of angles. Here we used ones by Goldstein [108]. In these procedures, the rotation is counterclockwise and is in three steps as shown in Fig. 8.3.

1. The coordinate (O-xyz) is rotated around z axis with angle φ (see Fig. 8.3a).
2. A resultant coordinate (O-x$'$y$'$z$'$) is rotated around x$'$ axis with angle θ (see Fig. 8.3b).
3. A resultant coordinate (O-x$''$y$''$z$''$) is rotated around z$''$ axis with angle ψ (see Fig. 8.3c). The final coordinate after the rotations is O-x$'''$y$'''$z$'''$ (=$P\text{-}\widetilde{x}\widetilde{y}\widetilde{z}$) in Fig. 8.3c.

Rotational transformation of the vector **A** in (O-xyz) coordinate to **B** in $P\text{-}\widetilde{x}\widetilde{y}\widetilde{z}$ coordinate is represented as follows.

$$\mathbf{B} = \mathbf{AR}. \tag{8.32}$$

Here **R** is a transformation matrix shown below.

$$\begin{aligned}\mathbf{R} &= \mathbf{R}_\varphi \mathbf{R}_\theta \mathbf{R}_\psi \\ &= \begin{pmatrix} \cos\psi\cos\phi - \cos\theta\sin\phi\sin\psi & \cos\psi\sin\phi + \cos\theta\cos\phi\sin\psi & \sin\psi\sin\theta \\ -\sin\psi\cos\phi - \cos\theta\sin\phi\cos\psi & -\sin\psi\sin\phi + \cos\theta\cos\phi\cos\psi & \cos\psi\sin\theta \\ \sin\theta\sin\phi & -\sin\theta\cos\varphi & \cos\theta \end{pmatrix},\end{aligned} \tag{8.33}$$

where $\mathbf{R}_\phi = \begin{pmatrix} \cos\phi & \sin\phi & 0 \\ -\sin\phi & \cos\phi & 0 \\ 0 & 0 & 1 \end{pmatrix}$

$$\mathbf{R}_\theta = \begin{pmatrix} 1 & 0 & 0 \\ 0 & \cos\phi & \sin\phi \\ 0 & -\sin\phi & \cos\phi \end{pmatrix}$$

And $\mathbf{R}_\psi = \begin{pmatrix} \cos\psi & \sin\psi & 0 \\ -\sin\psi & \cos\psi & 0 \\ 0 & 0 & 1 \end{pmatrix}$.

A transformation from **B** to **A** is by using transpose matrix,

$$\mathbf{A}={}^t\mathbf{R}\mathbf{B} \tag{8.34}$$

8.2.9.2 Euler's Equations

Kinetic energy, K_R of the rotational motion of rigid body is represented as follows by using the inertia tensor.

$$K_R = \frac{1}{2}\Big[I_{xx}\omega_{\tilde{x}}{}^2 + I_{xy}\omega_{\tilde{x}}\,\omega_{\tilde{y}} + I_{xz}\omega_{\tilde{x}}\,\omega_{\tilde{z}} + I_{yz}\omega_{\tilde{y}}\,\omega_{\tilde{x}} + I_{yy}\omega_{\tilde{y}}^2 + I_{yz}\omega_{\tilde{z}} + I_{zx}\omega z\omega_{\tilde{x}} \\ + I_{zy}\omega_{\tilde{z}}\,\omega_{\tilde{y}} + I_{zz}\omega_{\tilde{z}}^2\Big]. \tag{8.35}$$

If the $P\text{-}\widetilde{x}\widetilde{y}\widetilde{z}$ is chosen to be coincident with the principal axes of inertia, inertia tensor is simplified to be represented by the diagonal elements, and time dependence of the angular momentum can be represented by the Euler's equations.

Time derivative of the angular momentum $\mathbf{L}_\mathrm{R}$ in O-xyz coordinate is,

$$\frac{d\mathbf{L}_R}{dt} = \mathbf{T}_R, \tag{8.36}$$

here $\mathbf{T}_R$ is torque vector and total angular momentum of the rigid body (molecule, ion, etc.) consists of N particles can be obtained by $\mathbf{L}_R = \sum_{i=1,N} m_i\mathbf{r}_i \times d\mathbf{r}_i/dt.$

While the angular momentum $\mathbf{L}_\mathrm{P}$ in the $P\text{-}\widetilde{x}\widetilde{y}\widetilde{z}$ coordinate is represented by

$$\mathbf{L}_P = \begin{pmatrix} L_{P\widetilde{x}} \\ L_{P\widetilde{y}} \\ L_{P\widetilde{z}} \end{pmatrix} = \begin{pmatrix} I_1 & 0 & 0 \\ 0 & I_2 & 0 \\ 0 & 0 & I_3 \end{pmatrix} \begin{pmatrix} \omega_{P\widetilde{x}} \\ \omega_{P\widetilde{y}} \\ \omega_{P\widetilde{z}} \end{pmatrix} = \begin{pmatrix} I_1\omega_{P\widetilde{x}} \\ I_2\omega_{P\widetilde{y}} \\ I_3\omega_{P\widetilde{z}} \end{pmatrix}, \tag{8.37}$$

where I_1, I_2, I_3 are the components of the principal moment of inertia in the $P\text{-}\widetilde{x}\widetilde{y}\widetilde{z}$ coordinate and $\omega_{P\widetilde{x}}$, $\omega_{P\widetilde{y}}$ and $\omega_{P\widetilde{z}}$ are the components of angular velocity about these principal axes.

Euler's equations can be derived from the transformation of time derivative of angular momentum $d\mathbf{L}_\mathrm{R}/dt$ in O-xyz coordinate to that ($d\mathbf{L}_\mathrm{P}/dt$) in $P\text{-}\widetilde{x}\widetilde{y}\widetilde{z}$ coordinate,

$$\frac{d\mathbf{L}_P}{dt}\left(in\ \ P-\widetilde{x}\widetilde{y}\widetilde{z}\ \text{coordinate}\right) = \frac{d\mathbf{L}_P}{dt}\left(in\ \ O-xyz\ \text{coordinate}\right)+\omega\times\mathbf{L}_P. \tag{8.38}$$

Taking each component along principal axis of Eq. (8.38) for left hand side, Euler's equations are given as follows.

$$I_1\frac{d\omega_{P\widetilde{x}}}{dt}-\omega_{P\widetilde{y}}\omega_{P\widetilde{z}}(I_2-I_3)=\mathbf{T}_{P\widetilde{x}} \tag{8.39a}$$

$$I_2\frac{d\omega_{P\widetilde{y}}}{dt}-\omega_{P\widetilde{z}}\omega_{P\widetilde{x}}(I_3-I_1)=\mathbf{T}_{P\widetilde{y}} \tag{8.39b}$$

$$I_3\frac{d\omega_{P\widetilde{z}}}{dt}-\omega_{P\widetilde{x}}\omega_{P\widetilde{y}}(I_1-I_2)=\mathbf{T}_{P\widetilde{z}} \tag{8.39c}$$

8.2.9.3 Relation Between Angular Velocity and Euler Angles

The derivatives of angles $\dot{\varphi}$, $\dot{\phi}$ and $\dot{\theta}$, are z', x'' and z''' components of angular velocity vectors ω'_{ϕ}, ω''_{θ} and ω'''_{ψ} in the P-$x'y'z'$, P-$x''y''z''$ and P-$x'''y'''z'''$(=P-$\widetilde{x}\widetilde{y}\widetilde{z}$) coordinates, respectively. Therefore, the following relation holds.

$$\boldsymbol{\omega}=\mathbf{R}_{\phi}\mathbf{R}_{\theta}\omega_{\phi}^{'}+\mathbf{R}_{\phi}\omega_{\theta}^{''}+\omega'''_{\psi} \tag{8.40}$$

By solving Eq. (8.40) for each derivative of angle, the following results

$$\begin{aligned}
\dot{\theta} &= \omega_{\tilde{x}}\cos\psi-\omega_{\tilde{y}}\ \sin\psi,\\
\dot{\phi} &= \frac{1}{\sin\theta}\left(\omega_{\tilde{x}}\ \sin\psi+\omega_{\tilde{y}}\ \cos\psi\right),\\
\dot{\psi} &= \omega_{\tilde{z}}\ -\frac{\cos\theta}{\sin\theta}\left(\omega_{\tilde{x}}\ \sin\psi+\omega_{\tilde{y}}\ \cos\psi\right),
\end{aligned} \tag{8.41}$$

are obtained.

8.2.9.4 Relation Between Quaternion and Euler Angles

Since the temporal derivative of the Eulerian angle contains singular point (the term 1/sin θ in Eq. (8.41) becomes ∞ and −∞, at 0 and π, respectively.), the Quaternion parameters [109] are used to avoid it. Quaternion parameters (ξ,η,ζ,χ) are connected to Goldstein's Euler angles θ,ψ,ϕ as follows.

$$\xi=\ \sin\left(\theta/2\right)\bullet\sin\left((\psi-\varphi)/2\right)$$

$$\begin{aligned}
\eta &= \sin(\theta/2) \bullet \cos\left((\psi-\phi)/2\right) \\
\zeta &= \cos(\theta/2) \bullet \sin\left((\psi+\phi)/2\right) \\
\chi &= \cos(\theta/2) \bullet \cos\left((\psi+\phi)/2\right)
\end{aligned} \tag{8.42}$$

Because of the relation, $\xi^2+\eta^2+\zeta^2+\chi^2=1$, these four parameters are not independent and therefore, the degree of freedom does not change with the transformation.

8.2.10 Ensembles Used for MD Simulations

Several ensembles are used in MD simulations including extended ones. Some typically used ensembles are introduced here.

8.2.10.1 Constant Energy Condition

Constant number of atoms, volume and energy (NVE) ensemble (micro-canonical ensemble) is achieved without modification of system, while extended ensemble such as NPT, NVT (P: pressure, T: temperature) requires additional parameters to control the pressure and/or temperatures.

8.2.10.2 Constant Pressure Condition (Andersen Method)

Andersen [110] developed the method to control the pressure by introducing the wall (a three dimensional piston) in the MD cell. This treatment is explained here for the case of soft-core (SC) model.

The Hamiltonian of the SC system interacting pair-wise force is

$$H(p,r)=\sum_j p_j^2/2m+\sum_{i<j}\varepsilon\left(\sigma/r_{ij}\right)^n \equiv K+U, \tag{8.43}$$

where the m and σ are the mass and a size parameter of the particle, respectively. Hamiltonian in the extended system can be written as follows,

$$H(\mathbf{s},\boldsymbol{\pi},V,\Pi)=\sum_i(\boldsymbol{\pi}_i\bullet\boldsymbol{\pi}_i)/\left(2mV^{2/3}\right)+U\left(\left[V^{1/3}\mathbf{s}\right]\right)+\frac{1}{2M}\Pi^2+P_{ex}V, \tag{8.44}$$

where $\mathbf{s}\left(=s_{ix},s_{iy},s_{iz}\right)$, $\boldsymbol{\pi}_i\left(=\frac{\partial L}{\partial \dot{s}_i}\right)$ and $\Pi\left(=\frac{\partial L}{\partial \dot{V}}=M\dot{V}\right)$ are normalized ($\mathbf{r}_i=L\mathbf{s}_i$) coordinates, momentum of particle i and momentum of the wall respectively, and

$P_{ex}V$ is a potential energy by the wall. Here we consider the isotropic system with $L = V^{1/3}$. The system is conservative.

In the equilibrated system with a constant pressure, the term $\frac{1}{2M}\Pi^2$ becomes negligibly small, where M has the dimension of [mass][(length)$^{-4}$]. Then one can use the reduced mass M' which is given by the relations [91]

$$M' = M\sigma^4/m. \tag{8.45}$$

The system under the constant pressure condition is controlled by the difference of external pressure and internal pressure.

From Eq. (8.9), equations of motions are obtained as follows.

$$\frac{d\mathbf{s}_i}{dt} = \frac{\partial H}{\partial \boldsymbol{\pi}_i} = \frac{1}{m_i V^{2/3}}\boldsymbol{\pi}_i \tag{8.46a}$$

$$\frac{d\boldsymbol{\pi}_i}{dt} = -\frac{\partial H}{\partial \mathbf{s}_i} = \frac{\partial U}{\partial \mathbf{s}_i}, i = 1, 2, 3, \ldots, N \tag{8.46b}$$

$$\frac{dV}{dt} = \frac{\partial H}{\partial \Pi} = \frac{\Pi}{M}, \tag{8.46c}$$

$$\frac{d\Pi}{dt} = -\frac{\partial H}{\partial V} = \frac{\Pi}{M} = \frac{1}{3V}\left(V^{-2/3}\sum_i \frac{\dot{\boldsymbol{\pi}}_i \bullet \dot{\boldsymbol{\pi}}_i}{m_i} - V^{1/3}\frac{\partial U}{\partial\left(V^{1/3}\right)}\right) - P_{ex} \tag{8.46d}$$

These equations of motion for the scaled system are solved numerically to give the time development of coordinates and momenta.

The correspondence between the scaled system and the original system is taken into account through the following relations.

$$\mathbf{r}_i = L\mathbf{s}_i \tag{8.47}$$

$$\mathbf{p}_i = L^{-1}\boldsymbol{\pi}_i. \tag{8.48}$$

$$\frac{d\mathbf{r}_i}{dt} = \frac{\mathbf{p}_i}{m} + \frac{\mathbf{r}_i}{3V}\frac{dV}{dt}, \tag{8.49a}$$

$$\frac{d\mathbf{p}_i}{dt} = \frac{\partial U}{d\mathbf{r}_i} - \frac{\mathbf{P}_i}{3V}\frac{dV}{dt}, \tag{8.49b}$$

$$\frac{dV}{dt} = \frac{\Pi}{M}, \tag{8.49c}$$

$$\frac{d\Pi}{dt} = \frac{1}{3V}\left(\sum_i \frac{\mathbf{p}_i{}^2}{m_i} - \sum_{i=1}^{N-1}\sum_{j>i}^{N} \frac{\phi(r_{ij})}{dr_{ij}} \frac{\mathbf{r}_{ij} \bullet \mathbf{r}_{ij}}{r_{ij}}\right) - P_{ex} \tag{8.49d}$$

The first term in Eq. (8.49d) represents the instantaneous internal pressure. When the internal pressure equals to the external pressure P_{ex}, $\frac{d\Pi}{dt} = 0$ and then the system volume becomes constant. In other cases, the instantaneous pressure (and volume) fluctuates around the P_{ex} set in the simulations. This situation can be regarded as the thermally equilibrated state, with the use of a suitable M. Time average of any function (which corresponds to NVH ensemble), F, can be calculated from the trajectories obtained by the Eq. (49).

8.2.10.3 Constant Temperature Condition (Nosé Method)

For controlling temperature, thermostat using a fictive time with a new degree of freedom, (s, p_s), is introduced by Nosé [86, 111–114]. Here, s and p_s correspond to the coordinate and its canonically conjugate variable, momentum, of the new degree of freedom having mass represented by Q. The coordinate and its canonically conjugate variable, momentum, in the extended (fictive) system are represented by $\mathbf{r}'$ and $\mathbf{p}'$, respectively.

The Hamiltonian of the extended system is defined by

$$H(\mathbf{p}', \mathbf{r}', p_s, s) = \sum_i \left(\mathbf{p}_{\mathrm{i}}'^2 / \left(2ms^2\right) + U(\mathbf{r}') + \frac{{p_s}^2}{2Q} + gk_B T \ln s, \tag{8.50}$$

where g is a parameter used to represent the degree of freedom.

In this case, T is a parameter to give the targeted value of the temperature, and Nosé has proved that the microcanonical ensemble of the extended system corresponds to the canonical (NVT) ensemble in the real system if one choose $g = 3N + 1$.

The values in the real and extended systems are assumed to be connected by

$$\mathbf{r}_i = \mathbf{r}_i', \quad \mathbf{p}_i = \frac{\mathbf{p}_i'}{s}, \quad t = \int^t \frac{dt'}{s}, dt = \frac{dt'}{s}$$

The last two equations represent the relation between the time in the extended system, t', and that in the real system, t.

Then the velocity of these systems are connected by,

$$\frac{d\mathbf{r}_i}{dt} = \frac{d\mathbf{r}_i}{dt'} \frac{dt'}{dt} = s \frac{d\mathbf{r}_i'}{dt'}. \tag{8.51}$$

The Hamilton's canonical equations for the extended system are derived from (Eq. 46) are given by,

$$\frac{d\mathbf{r}_i'}{dt'} = \frac{\partial H}{\partial \mathbf{p}_i'} = \frac{\mathbf{p}_i'}{ms^2}, \tag{8.52a}$$

$$\frac{d\mathbf{p}_i'}{dt'} = -\frac{\partial H}{\partial \mathbf{r}_i'} = -\frac{\partial U}{\partial \mathbf{r}_i'}, \tag{8.52b}$$

$$\frac{ds}{dt'} = -\frac{\partial H}{\partial p_s} = \frac{p_s}{Q}, \tag{8.52c}$$

$$\frac{dp_s}{dt'} = -\frac{\partial H}{\partial s} = -\frac{\partial W(s)}{\partial s} = \sum\nolimits_i \frac{\mathbf{p}_i'^2}{ms^3} - \frac{gk_BT}{s}. \tag{8.52d}$$

In Eq. (8.52d), $W(s)\ \left(= \frac{K}{s^2} + gk_BT\ln s \text{ with } K = \sum_i \frac{\mathbf{p}_i'^2}{2m} \right)$ corresponds to the potential energy relating to the giving and receiving the heat.

From Eq. (8.50), the equation of motion in the real system is derived as [91, 111],

$$\frac{d\mathbf{r}_i}{dt} = \frac{\mathbf{p}_i}{m}, \tag{8.53a}$$

$$\frac{d\mathbf{p}_i}{dt} = -\frac{\partial U}{\partial \mathbf{r}_i} - p_s\mathbf{p}_i/Q, \tag{8.53b}$$

$$\frac{ds}{dt} = s\frac{ds}{dt'} = sp_s/Q, \tag{8.53c}$$

$$\frac{dp_s}{dt} = s\frac{dp_s}{dt'} = \sum\nolimits_i \frac{\mathbf{p}_i^{\ 2}}{m_i} - gk_BT. \tag{8.53d}$$

The equations of motion in the real system are slightly modified to

$$\frac{d\mathbf{r}_i}{dt} = \frac{\mathbf{p}_i}{m}, \tag{8.53a$'$}$$

$$\frac{d\mathbf{p}_i}{dt} = -\frac{\partial U}{\partial \mathbf{r}_i} - \zeta\mathbf{p}_i, \tag{8.53b$'$}$$

$$\frac{d\zeta}{dt} = \frac{2}{Q}\left[\sum\nolimits_i \frac{\mathbf{p}^2{}_i}{2m} - \frac{gk_BT}{2}\right], \tag{8.53c$'$}$$

where $ds/dt = s\zeta$. Under the conditions, $x_s = \ln s$ and $\zeta = \dot{x}_s = \frac{p_s}{Q}$, these equations are equivalent to Eqs. (8.53a–8.53d).

This form of the thermostat, which is by eliminating s, is called the Nosé-Hoover thermostat [112], and it can reproduce the canonical distribution in the coordinate space.

Because the variable s for the scaling of time of whole system is eliminated, the friction coefficient ζ can be defined for each substructure of the system and it is useful for the controlling temperatures in complex systems. Sampling of data intervals used in a virtual system in the Nosé algorithm corresponds to the unequal sampling of that in the real space. The Nosé-Hoover algorithm also removes this difficulty, although the resulting system is not Hamiltonian. Recently, the Nosé-Poincaré method [86, 114] was introduced to solve this problem.

8.2.10.4 Combination of Conditions

Nosé generalized the work to include both thermostat and barostat. Nowadays, many kinds of extended ensembles are introduced and used [87, 91, 115].

In Sect. 8.5.3, our attention will be focused on the problem of the choice of ensembles to study structures and dynamics in super-cooled liquids or glasses including non-equilibrium situations. Some other problems concerned with the system showing slow dynamics will be also discussed there. Dynamics in crystals are also slow process and similar treatment seems to be required.

8.2.11 Parrinello-Rahman Methods

It is useful for the simulation of the crystal and its transformation, additional degree of freedom is taken into account. In the Parrinello-Rahman (and Parrinello-Rahman-Ray) methods [116–118], angles as well as axis lengths in the basic cell (with parallelepiped structure) can be changed during the MD runs. Practically, it seems to work in several conditions after the equilibration, although it is known that the collapse of the parallelepiped structure occurs in some cases. It may be helpful to consider the geometrical degree of the freedom [119] of the basic cell of MD to treat this problem.

8.2.12 High Performance Computation

If one would like to treat large system and for long times in a straightforward manner, acceleration of the calculation is desired, as well as the developments of computer technology itself. Another possible way is to reduce the amount of calculation itself. Coarse-graining by several methods and scaling concepts are effective for estimation and prediction of long time behavior of the system, and may save the calculation times. Here we mention the means for accelerating the calculations.

8.2.12.1 Parallel Computing, Acceleration Boards, and Graphic Processing Unit (GPU)

In MD simulations, each particle moves by the sum of forces from other particles. This calculation is the most time consuming part for the simulations. Many particles can be treated by several kinds of parallel computing, using Message Passing Interface (MPI), graphic processing unit (GPU), *etc*. Several methods for parallel computing both by manipulating software and hardware can be applied.

The GRAPE (Gravity Pipe) board was developed for solving the 'Gravitational Many-Body Problem', where the common algorithm with molecular dynamics is used. Then, MDGRAPE [120] chip was designed for acceleration of MD simulation.

Recently, graphic processing unit (GPU) pioneered by NVIDIA in 2007 [http://www.nvidia.com/object/what-is-gpu-computing.html (The address was confirmed to be valid on 14th Feb. 2016).] is widely used for acceleration of computation including MD and is called GPGPU (General-purpose computing on graphics processing units) (see also Appendix 8). GPU boards named Tesla and/or GeForce are included in many computing systems, not only super-computers but also in personal computers. Because of its generality and relatively lower cost, the methodology is rapidly spreading. Such developments will make an MD simulation suitable for personal use in the near future. An example of coding for the main loop of MD by Fortran using Compute Unified Device Architecture (CUDA) is shown in the Appendix A.8.1.

There are several problems for each technology. Sometimes, heat released on the boards causes many problems such as instability of the system. Noises coming from the fan for cooling may cause another problem. Therefore, controlling the heat release is an important problem for using acceleration boards. If the board is occupied by a job in an exclusive manner, it will prevent the execution of parallel computing jobs. Parallel calculations are effective to use for large system but not necessarily being effective enough for long runs. This is because the MD run of slow dynamics is essentially sequential to cover the different time regions. Therefore the technology different from the parallel computation may be desirable. Parallel computing of completely independent runs (of different conditions) is one of the alternative approaches. "Array job" can be used in some systems for parameter survey.

8.2.12.2 Difference in Numerical Results Using Parallel Computations

If one uses the symplectic integrator, the drift of the energy can be avoided in the equilibrium system. Nevertheless, drift may occur due to different origins such as the overlaps of non-equilibrium relaxations and/or aging. When calculated values in parallel calculations are accumulated into one, resultant data will have larger numerical errors compared with calculation on the single machine. Besides these problems, in the case of slow dynamics in supercooled liquids or glasses, further caution seems to be required for the deterministic nature of the motion.

Ionics in the glassy state is dominated by jump motion of ions and it has intermittent and sporadic nature related to chaos. Consequently, each motion is quite sensitive for the small difference of the initial value. Each ionic motion tends to show the different trajectory by this. This situation occurs regardless of single precision or double precision of the calculation and therefore it is not a problem of the number of significant digits. It is not a problem of the quality of GPU itself as well, although it occurs when the calculation is just moved from CPU to GPU.

This is because similar situation also occurs just by changing the order of the calculation within a Do loop [The view discussed here is obtained by the assistance of the staffs of the project of acceleration of the program using GPU in the Global Scientific Information and Computing Center in Tokyo Institute of Technology. Here we appreciate it]. Sometimes one needs extremely long time runs for calculation of properties such as transport coefficients and their fluctuations, and one may have to worry about the propagation of errors during the run. Fortunately, the dynamic properties of long time, such as transport coefficients, tend to converge to certain values during a long run (for example, diffusion coefficient of ionic motion converges within 10 ns runs at 800 K in lithium disilicate) and this is also represented by using the local expansion rate [121], which can be a measure of the propagation of the error in non-linear dynamics [122, 123] (see also Sect. 8.4.2). It means that the short time fluctuation of motions does not affect the structure of the attracter for the long time dynamics. In other words, characteristics of the ion channels are not changed by the local motion in the caging region. In our opinion, the short time discrepancy does not necessarily affect the long time behavior of the mean dynamics and that is why we can use a long time run of MD simulations for the calculation of transport properties. Of course, each researcher has responsibility to check it for the result of MD runs in each system when parallel computation and/or long runs are used.

8.2.12.3 Perspective of Computational Technology in MD Simulations

During a long run of MD, one may encounter the situation of run being stopped by the problem of the machine or supply of electricity. To avoid such troubles, further developments for acceleration of long time runs will be helpful. One may also encounter the problem of coding in calculations for adjusting available resources. Although some compilers have an option for parallel computing, still it requires some modification of the code for efficient treatment. When a new hardware is developed, a new coding might be necessary. To improve the performance, developments of machine independent coding seem to be desirable. Recent development of “Xeon Phi co-processor” by Intel seems to show one of the promising ways for this direction, because it does not require the special coding.

8.3 Physical Quantity and Properties Obtained from MD Simulations

In typical classical MD simulations, input of the MD simulations is the “potential parameters” and the output is essentially the “time series of coordinates of particles (and velocities)”, that is the “trajectories”. Typical input files in the MD simulations of glasses contain the following items:

1. Setting of potential parameters and functions,
2. Setting of ensemble (NPT, NVE, etc.).
3. Preparation of initial configuration (and velocity) (system size).
4. Setting of runs (step time and steps for equilibration and those for analysis)

In the case of study of glasses or glass transition, cooling schedule is also required.

In typical output files, fundamental information such as temperature, energies, pressure, pair correlation functions are included in most of MD programs for checking the data and/or further treatment.

From the trajectories, further analyses can be done. Available information is concerned with the structures, dynamics and thermodynamics. Researcher can define any functions to obtain specific information suitable for their purpose. Visualization of the structures, motions, vectors is also useful. Furthermore, potential functions or parameters can be artificially modified if necessary. For example, mass, ionic size, and functional forms can be changed to examine the effects of each factor. These methods are useful to separate possible mechanisms responsible for the problem treated, and to check the results or prediction from models or theories. The model of the system can be tuned up for desired properties and hence MD simulations are applicable for material designs. In this sense, MD simulations are a tool of experimental investigations as well as of theoretical treatment. Some typical functions or properties obtained from MD are summarized in the next subsections. We hope that from the example of the research on silicate systems and ionic liquids in Chaps. 9–11, readers can have a good idea of how to use MD simulations.

8.3.1 Structural Properties

8.3.1.1 Pair Correlation Function: g(r)

Liquids have homogeneous structure at longer length scales and characteristics of them can be well represented by the pair correlation function [87, 91], where the structure is represented by a function of r only. This can be also used for characterizing super-cooled liquids and glasses, although further terms might be required in some circumstances.

Pair correlation function among different kind of particles i and j is obtained by

$$g_{ij}(r) = \frac{V}{N_i \bullet N_j} \left\langle \sum_{i=1}^{N_i} \frac{n_i(r - \Delta r/2, r + \Delta r/2)}{4\pi r^2 \Delta r} \right\rangle, \tag{8.54}$$

where V is a volume of the system, N_i and N_j are the number of the species i and j and $n_i(r - \Delta r/2, r + \Delta r/2)$ is the number of j particles within the shell with width Δr at distance r from particle i. The term $4\pi r^2$ is for the surface area of the sphere.

When the species *i* and *j* are the same one, the function is,

$$g_{ii}(r) = \frac{V}{N_i \bullet (N_i - 1)} \left\langle \sum_{i,=1}^{N_i} \frac{n_i(r - \Delta r/2, r + \Delta r/2)}{4\pi r^2 \Delta r} \right\rangle, \tag{8.55}$$

where now $n_i(r - \Delta r/2, r + \Delta r/2)$is the number of *i* particles within the shell with width Δr at distance *r*. Practically, it can be calculated during the MD run and it is useful to check the status of the calculation. In this case, distances among *i* and *j* particles appeared are not ordered and this may prevent the effective coding for parallel computation. A part using random access may be better to put it out of the loop of the calculation of force, if necessary. The $(N_i - 1)$ term is the number of surrounding particles, which does not include the central particle *i*.

For example, in the case of ionic liquids with internal structures, the function $g(r)$ for each pair can be determined for the center of mass position (or center of charges) of each ion. Alternative arrangement of cation and anion in ionic system tends to neutralize structure at a certain length scale. This behavior is regarded as screening in the strongly-coupled system such as NaCl [124, 125] and charge radial distribution in the following form is suggested.

$$q(r) = \frac{A}{r} \exp(-r/\lambda_D) \sin(2\pi r/d + \varphi), \tag{8.56}$$

where A/r is the amplitude, φ is the phase shift and *d* is the period of the oscillations.

In ionic structures, one can consider the charge distribution function $Q(r)$ and the density distribution function $G(r)$ defined by the following equations [124–127] by assuming that the charge is simply on the center of mass (or charge) position,

$$Q(r) = Q_+(r) + Q_-(r) = \{g_{++}(r) + g_{--}(r) - 2g_{+-}(r)\}e \tag{8.57}$$

$$G(r) = G_+(r) + G_-(r) = \{g_{++}(r) + g_{--}(r) + 2g_{+-}(r)\}/4 \tag{8.58}$$

The former is related to the structures of layers of charges (charge density wave, CDW), while the latter is related to structures of ionic positions regardless the charges (density wave, DW). Typical length scales for these functions are informative due to the difference of the main factors controlling them. These functions become 1 when the value becomes the mean density of species of the surrounding particles.

If the plots of $\ln|Q(r)r|$ against *r* have a straight line when the maxima of the peaks (envelopes) are connected, the characteristic length λ_Q, which corresponds to the Debye length for the screening of the Coulombic term in the simple dilute ionic systems, can be determined from the slope, $-1/\lambda_Q$. However, the values in dense ionic systems are not necessarily the same one as in a dilute system. The interaction observed is a renormalized one by the interactions from the other ions.

In the theory of liquids, the pair correlation function is fundamental to understand their structure [128, 129] and we note that the function can be obtained with good statistics in MD because it can be averaged in many steps.

8.3.1.2 Structure Factor and Intermediate Scattering Functions

Comparison of structures with experiments can be done through the structure factor $S(k)$. The function is a Fourier transform of $g(r)$ [128–132].

$$S(k) = 1 + 4\pi\rho \int_0^{r_{\max}} r^2 \{g(r) - 1\} \frac{\sin kr}{kr} dr. \tag{8.59}$$

Obtained by X-ray diffraction, the function is modified by the weight of atomic scattering factor, $f(k)$ [131, 132], while for neutron diffraction it is modified by scattering length, b. Details of the treatment of data is slightly different by different researchers. For example, the following form was used in some X-ray diffraction works, where $I(k) = S(k) - 1$.

$$kI(k) = \frac{\sum_i \sum_j x_i x_j f_i(k) f_j(k)}{\left\{\sum_i x_i f_i(k)\right\}^2} \times \int_0^{r_{max}} 4\pi\rho_0 \left\{g_{ij}(r) - 1\right\} \sin(kr) dr \tag{8.60}$$

Here ρ is the number density of the system and ρ_0 is the average of it.

For comparison of the structural details of glasses (such as Q_n where n is the number of bridging oxygen in the SiO_4 unit, the distributions or statistics of rings) from simulations with experiments, one should be careful to consider not only the cooling rate, but also the history of the system on the *PVT* phase-diagram (see Sect. 9.2). Otherwise, the results of the MD simulations might deviate from the experimental ones. This is because the partial structure (such as Q_n structure) has its specific partial volume [133, 134].

The formation of three dimensional networks is observable directly in MD simulations.

8.3.1.3 Running Coordination Numbers

To examine the coordination shells of other particles or solvent, the pair correlation function is accumulated as represented by the running coordination numbers, $N_{\mathrm{coord}}(r)$. The function for the species j around species i is defined as follows.

$$N_{coord}(r) \equiv \rho_j \int_0^r 4\pi r^2 g(r) dr. \tag{8.61}$$

This function also can be calculated during the MD runs.

Coordination number is often defined by the cutoff values corresponding to the distance of the first minimum position of $g(r)$. The function also can be used to obtain the fractal dimension of the structures in different length scale regimes.

8.3.1.4 Angular Distribution Function

Distribution of angles in the structure can be examined by MD simulations. The angular correlation function may be defined by using the number of particles, dN, located between $\theta - d\theta/2$ and $\theta + d\theta/2$, within a certain distance r.

$$P(\theta) = CdN/\sin\theta\, d\theta. \tag{8.62}$$

C is a normalization constant so that the integration over 2π becomes 1.

When the data points are uniformly spreading, the number of points on the polar is smaller than that of points on the peripherals. The term $\sin\theta$ is used to take into account this situation. Namely, such correction is used, when the distribution in a three dimensional (3D) space is a target of the problem. The absence of the modification by the sine term is also found in literatures, such as the case when the frequency of the appearance of the angle (for example, that among bonding) is the problem to be examined.

8.3.2 Dynamic Properties

8.3.2.1 Mean Squared Displacement (MSD) and Diffusion Coefficient (D)

The Mean Squared Displacement (MSD) of species a is obtained by the expression [87, 91],

$$< {r_a}^2(t) > = \left\langle \left\{ \sum_{i=1}^{N_a} (r_{ai}(t) - r_{ai}(0))^2 \right\} / N_a \right\rangle. \tag{8.63}$$

Here the angled brackets represent the average for different initial times or independent runs.

Using a sequence of particle positions during a run of T_1 period, we prepared N arrays of data sequence with slightly shifted initial time t_0 values and the data for N arrays were averaged. Wide time window covering fluctuation of dynamics is required in the case when dealing with heterogeneous dynamics. In the case of equilibrated system, it is the same as the ensemble average. However, in the case of non-ergodic system, it is not necessarily the same.

For each species, the MSD starts to become proportional to time t at times longer than t_{dif}. From the slope of the MSD at times longer than t_{dif}, the diffusion coefficients, D, can be obtained using the Einstein relation [135].

$$D = \frac{1}{6} \lim_{t\to\infty} \frac{d}{dt} < [r_i(t) - r_i(0)]^2 > . \tag{8.64}$$

The onset time of steady state diffusion, t_{dif}, is a characteristic and fundamental time of the dynamics. Here the denominator 6 is used for the case of diffusion in three dimensional systems.

In slow dynamics of super-cooled liquids near the glass transition regimes, quasi-diffusive regime, where the MSD is proportional to time, can be found before the fractional power law regime, if one closely examine the data (see Sect. 9.4.2 for details). Therefore, it is necessary to distinguish it from the true long term diffusive regime, particularly if the observation time is limited. If the system has hierarchy structures, diffusive regime is not be easily attained. For example, particles might be located in different domains with different sizes, when observation is started.

Diffusion coefficients can also be obtained from the velocity autocorrelation function.

$$D = \frac{1}{3} \int_0^\infty \langle \mathbf{v}(t) \bullet \mathbf{v}(0) \rangle . \tag{8.65}$$

This equation is known as the Kubo formula [136].

The function may seem to be converging at a short time (several ps) at a first glance even in glasses. However, this is not for a true diffusive regime. Thus, to ensure correct result for D, the times for the integration should be long enough to cover steady state diffusive motion.

8.3.2.2 Conductivity

Conductivity is connected with the complex frequency dependence of the ion dynamics and is related to the time dependence of the MSD by the relation [136, 137],

$$\sigma^*(\omega) = -\omega^2 \frac{Nq^2}{6H_R k_B T} \int_0^\infty < r^2(t) > e^{-i\omega t} dt, \tag{8.66}$$

where N is the number density of mobile ions, q the ion charge, k_{B} the Boltzmann constant, H_R the Haven ratio [138] and T the temperature.

In MD, the Haven ratio, $H_R = D_t/D_b$, is obtained from the tracer diffusivity, D_t, and the bulk (or charge) diffusivity D_b. Its time dependency is defined by [136],

$$\mathrm{H}_R(t) = \sum_i <\mathbf{v}_i(0) \bullet \mathbf{v}_i(t)> / <\sum_i \mathbf{v}_i(0) \bullet \sum_j \mathbf{v}_j(t)> \tag{8.67}$$

Typical value of the Haven ratio is at around 0.2–0.5 for ionically conducting glasses and therefore the correction by this is not so large although the value gives useful information for mechanism of the transport properties. The value is known to decrease in increasing content of alkali metal, in alkali silicates or related materials [139, 140]. The ratio represents the geometric correlations in the case of single particle motion, while it is also affected by the collective or correlated motions of particles (ions) [141]. Doliwa and Heuer [142] argued that the value is an inverse of the number of particles (ions), which moves in cooperative manner. That is, typical Haven ratio means that 2–5 ions move in cooperative manner. Direct calculation of conductivity or Haven ratio from MD simulation runs were performed in some works [143, 144].

For single particle properties, statistics can be improved by taking the average of large number of particles or ions, while for collective properties such as conductivity or Haven ratio, it is not easy to obtain good statistics, especially when dealing with heterogeneous dynamics. In taking average of heterogeneous ionic motions, the use of large time windows covering different initial situations is recommended.

In principle, electric conductivity can be calculated directly from the electric current of ions, **J**(t) defined by

$$\mathbf{J} = \sum_i Q_i \dot{\mathbf{r}}_i(t), \tag{8.68}$$

where Q is the charge of the species and $\mathbf{r_i}$ is a displacement vector of the ith-ion. From the linear response theory [136], frequency dependent conductivity is given by

$$\sigma(\omega) = \frac{1}{3k_BTV} \int_0^\infty \langle \mathbf{J}(t) \bullet \mathbf{J}(0) \rangle \exp(i\omega t) dt, \tag{8.69}$$

and the direct current conductivity at the low frequency limit is given by

$$\sigma(0) = \frac{1}{3k_BTV} \int_0^\infty \langle \mathbf{J}(t) \bullet \mathbf{J}(0) \rangle dt. \tag{8.70}$$

If one compared this expression with Eq. (8.66), it is easily found that the time region for this limit corresponds to the long time limit of the MSD and/or the displacement of bulk diffusion. In the molten salt or in ionic "liquids", the time region is usually far beyond the ps region except for extremely high temperature region. At a first glance, the velocity auto-correlation function or that of the electric current might appear as if it has converged at short time (ps) region as already mentioned. Even if apparent convergence of the auto-correlation function in a short time was found, it does not mean that the motion corresponds to low frequency limit of Eq. (8.70). Careful sampling of the data is required with considering above situations. Similar situations will be found in many systems, liquids, glasses and crystals. Some further problems for the sampling of heterogeneous and intermittent dynamics near the glass transition regimes will be discussed in Sect. 8.5.7.

8.3.2.3 Viscosity

Viscosity, η, can be obtained from the Stokes-Einstein relation [135, 145] from the diffusivity. The relation for 3D liquids is given by

$$D = k_B T / c\pi\eta R, \tag{8.71}$$

where R is the effective diameter of the particle and c is a constant. The value c is known to be 2 and 3, in slip and stick hydrodynamic boundary condition, respectively.

Near the glass transition temperature, the deviation from the Stokes-Einstein relation is often found (see Sect. 7.3.3) and fractional power law relation between D and η can be a better description (Several fractional power laws are suggested. For example, $D = A'\left(\frac{k_B T}{\eta}\right)^{\gamma}$ was assumed in Ref. [67].).

The viscosity η can be calculated from the Green-Kubo formula

$$\eta = \frac{V}{k_B T}\int_0^{\infty} dt < P_{\alpha\beta}(0) \bullet P_{\alpha\beta}(t) > \tag{8.72}$$

where αβ stands for *xy, xz, yx, yz, zx*, or *zy*, and

$$P_{\alpha\beta} = \frac{1}{V}\left[\sum_i m_i v_{i\alpha} v_{i\beta} + \sum_i \sum_{j>i} (r_{i\alpha} - r_{j\alpha}) F_{ij\beta}\right]. \tag{8.73}$$

Non Equilibrium Molecular Dynamics (NEMD) and Reverse Non-Equilibrium Molecular Dynamics (RNEMD) are also useful to derive such transport properties (see Sect. 8.6).

8.3.3 Space-Time Correlations

8.3.3.1 Self- and Distinct-Part of Van Hove Functions

Space time correlation of the particles can be brought out by the self and distinct part of van Hove functions respectively defined as follows [146, 147],

$$G_s(\mathbf{r},t) = (1/N)\sum_{i=1}^{N}\left\langle\delta\left(\mathbf{r}_i(t) - \mathbf{r}_i(0) - \mathbf{r}\right)\right\rangle \tag{8.74}$$

$$G_{\mathrm{d}}{}^{\alpha,\beta}(\mathbf{r},t) = (1/N_\alpha)\sum_{\mathrm{i}=1}^{\mathrm{N}_\alpha}\sum_{\mathrm{j}=1}^{\mathrm{N}_\beta}\left\langle\delta\left(\mathbf{r} - \mathbf{r}_i^\alpha(0) + \mathbf{r}_j^\beta(t)\right)\right\rangle \tag{8.75}$$

The former is concerned with a self-motion of a particle, while the latter is for the mutual motion of different species α and β. Usually, results in figures are shown as a function of $r = |\mathbf{r}|$. If the self-part of the van Hove function is multiplied by $4\pi r^2$, the area under the curve corresponds to the number of particle and therefore $4\pi r^2 G_{\mathrm{s}}(r)$ tends to be used for the plot.

In the distinct part of the van Hove function, new peak appears at $r = 0$ if the particle of species β comes into the site previously occupied by a particle of species α and this feature is useful to examine the jump events. (See Sects. 10.1–10.3.) During this period, structures shown by $g(r)$ are kept unchanged although at $t = 0$, the distinct part of the van Hove function is the same function as $g(r)$ of the $\alpha-\beta$ pair.

This difference of the time development is due to the fact that the origin of the coordinate is fixed on the initial position of species α in the space in the former, while relative positions of α and β species are measured in the latter.

8.3.3.2 Intermediated Scattering Functions: $F_s(k,t)$

The intermediate scattering function is defined by [147]

$$F_s(k,t) = \left\langle\sum_{j=1}^{N}\exp\left\{i\mathbf{k}\cdot\left(\mathbf{r}_j(t) - \mathbf{r}_j(0)\right)\right\}\right\rangle / N \tag{8.76}$$

The function is useful for comparison with experiments as well as many kinds of theoretical treatments in the problem of slow dynamics.

8.3.3.3 Fluctuation of the Order Parameter

Lačević et al. defined the overlap susceptibility χ_4 (which is related to the four point correlation function) as follows [148] to investigate the spatial heterogeneity in the glass forming liquids. A time dependent order parameter $Q_p(t)$, which measures the number of "overlapping particles in two configurations separated by a time interval t" is defined by

$$Q_p(t) = \int d\mathbf{r}_1 d\mathbf{r}_2 \rho(\mathbf{r}_1, 0)\rho(\mathbf{r}_2, t)\delta(\mathbf{r}_1 - \mathbf{r}_2)$$
$$= \sum\nolimits_{i=1}^{N} \sum\nolimits_{j=1}^{N} \delta(r_i(0) - r_j(t)), \tag{8.77}$$

where $\rho(\mathbf{r}, t) = \sum_i \delta(\mathbf{r} - \mathbf{r}_i)$.

The order parameter is related to the distinct-part of the van Hove function by, $\langle Q_p(t) \rangle = NG_{\mathrm{d}}(r, t)$, with $r = 0$. In other words, this order parameter is concerned with the probability of substituting α and β species in Eq. (8.75) (for the case of single component, it is defined with α = β).

The function $\chi^{\mathrm{p}}{}_4(\mathrm{t})$, the fluctuation of the order parameter, is represented by

$$\chi^p{}_4(t) = \frac{\beta V}{N^2}[\langle Q_p^2(t)\rangle - \langle Q_p(t)\rangle^2], \tag{8.78}$$

where $\beta = (k_B T)^{-1}$.

It is rewritten as

$$\chi_4(t) = \frac{\beta V}{N^2}[\langle Q^2(t)\rangle - \langle Q(t)\rangle^2] \tag{8.79}$$

using a modified $Q(t)$ by a substitution of $\delta\big(\mathbf{r}_i(0) - \mathbf{r}_j(t)\big)$ in Eq. (8.77) by the "overlap" function $\mathrm{w}\big|(\mathbf{r}_1 - \mathbf{r}_2)\big|$. The "overlap" function is unity when $\big|(\mathbf{r}_1 - \mathbf{r}_2)\big| \leq a$ and zero otherwise. Here the parameter "a" is for typical amplitude of vibrational motion. This function can pick up the correlation length concerned with jumps or jump-like motions.

8.3.4 Thermal Properties

Thermal properties can be also determined from MD simulations. Pressure, temperature, volume, energies, and forces (each component of the kinetic and potential energies can be separated.), their time dependent behavior, and their derivatives or integral as well as fluctuations can be analyzed. In several systems such as the SC model, analytical treatment of the thermodynamic properties is possible [See Refs. [41–47] and references therein.].

8.3.5 Thermodynamic Scaling and Other Scaling Rules

The system may obey several kinds of scaling rules. Details for the thermodynamic scaling of the ionic systems are found in Chap. 7 and Sect. 11.10. Application of such rules will be helpful (see also Sect. 13.2) to predict or interpolate the properties of materials to a different condition or state. In this manner, the scaling rules make it easier to estimate or predict the properties under a different condition, and also useful to understand the mechanism underlying them.

8.3.6 Further Possible Analyses

There are many other possible analyses of the results from MD simulations. For example, individual motion of particles (ions, molecules), rotational dynamics, 3-, 4- (or higher order) time correlation functions, details of inner and inter structures of ions or molecules, correlation among angles and/or distances, can be analyzed and examined. Furthermore, possible analyses are not limited to the ones mentioned above. One can define any kind of functions or representations. Simulations also could be done under extreme conditions such as high pressure, negative pressure, and extremely high or low temperatures. For the purpose of material designs, or examination of the mechanism of dynamics, one can change freely the mass, particle size of the constituents of the system.

8.4 Errors in the Molecular Dynamics Simulations

There are several source of errors that can occur during the MD simulations and analyses of them [149, 150]. Here we treat three kinds of errors. One is concerned with the treatment of digits in the computer. Second one is concerned with the treatment of the numerical integration during the MD runs and of the averaged quantities. The third one is concerned with the propagation of small error during MD runs related to deterministic properties of the system especially in the case of slow dynamics.

8.4.1 Errors Occurred in the Numerical Treatment

In computers, the real number with infinitive digits is approximated by the floating point numbers having a limited number of digits. There exists a round-off error due to the limit. There are several standards to treat it such as IEEE 754-2008. The value x_f can be represented by [151],

$$x_f = \pm f \times \beta^m, \quad f = \frac{x_1}{\beta} + \frac{x_2}{\beta^2} + \cdots + \frac{x_n}{\beta^n}, \tag{8.80}$$

The base for the scaling can be two, ten, or sixteen in almost all cases.

Here x_k $(k = 1, \cdots, n)$ are integers with $1 \leq x_1 \leq \beta - 1$ and $0 \leq x_k \leq \beta - 1 (k = 2, \cdots, n)$.

For example, 3.14159 is represented by 0.314159×10^1. In this example, 0.314159 corresponds to the fraction f and 10 corresponds to the base, β, of the scaling and 1 corresponds to the exponent m. The parameter m is integer within the range, $L \leq m \leq U$.

The largest and the smallest values ($F_{\max}$ and $F_{\min}$), which can be treated in the machine are represented by

$$\begin{aligned} F_{\max} &= \beta^U (1 - \beta^{-n}), \\ F_{\min} &= \beta^{L-1} \end{aligned} \tag{8.81}$$

Thus the system can be characterized by β (base), n (number of significant digits), L (minimum exponent) and U (maximum exponent). These values depend on the system. For example, β = 16, n = 14, $L = -64$, and $U = 63$ may be used in the case of double precision for a certain system.

For the treatment of MD simulations, one needs to be careful for the loss of significant digits and trailing digits. The former situation occurs when the difference of comparable large values is taken. The latter situation occurs when the sum or difference of large value and extremely small value is taken.

8.4.2 Numerical Errors Occurred During MD Runs

For example, in Eq. (8.14), the third term in the right hand side of the equation is much smaller compared with other terms. To avoid the loss of trailing digits, calculation will be done by preparing the following values for $i = 1{,}2$ ---N

$$\Delta \mathbf{r}_i(t) = \mathbf{r}_i(t) - \mathbf{r}_i(t - \Delta t)$$

Then Eq. (8.14) was divided into two steps,

$$\Delta \mathbf{r}_i(t + \Delta t) = \Delta \mathbf{r}_i(t) + (\Delta t)^2 \frac{\mathbf{F}_i(t)}{m} \tag{8.14a}$$

and

$$\mathbf{r}_i(t + \Delta t) = \mathbf{r}_i(t) + \Delta \mathbf{r}_i(t + \Delta t) \tag{8.14b}$$

By this transformation, the values in Eq. (8.14a) become comparable in magnitude and furthermore, the error in Eq. (8.14b) will not propagate to longer times.

Pressure of the system is usually obtained from the difference of large comparable values and therefore, the loss of significant digits tends to occur. These losses as well as rounding error may be diminished by changing the order of calculations.

For example, for averaging of heterogeneous quantities for long runs, small values are better to sum up before performing the summation that includes large values. Error of the numerical integration also depends on the algorithm of the integrator used [152, 153]. For energy conservation of long time scale, symplectic integrator such as Verlet algorithm is known to be better compared with the method such as predictor-corrector method, which might be more accurate for short time runs. For the stability of the calculations, time reversible methods are also favored. Several methods with symplectic and/or time reversal properties have been proposed.

8.4.3 Propagation of Small Error and Lyapunov Exponent

As will be discussed in the Sect. 8.5 and Appendix A.2, (see also Example 2 in ESM) deterministic motion of ions causes the large fluctuation of the dynamics and such characteristics are common to other non-linear systems. Lorenz [154] has studied a predictability of non-linear dynamics of atmospheric model. In a similar manner, one can consider a propagation of the small error in MD simulations, although further problems remain as to be discussed later.

If the time evolution of the system is governed by a function $\boldsymbol{F}$ of the variables, $\boldsymbol{r}_{\mathbf{i}}(t)_, i = 1, \ldots, N$, in N dimensional system (i.e., the positional vectors of MD), and time evolution is determined by the following equation,

$$\frac{d}{dt}\boldsymbol{r}_i(t) = \boldsymbol{F}\left[\boldsymbol{r}_1(t), \ldots, \boldsymbol{r}_N(t)\right]; i = 1, \ldots, N, \tag{8.82}$$

The propagation of error in the basic solution, $\boldsymbol{r}_{\mathrm{i}}(t)$, beginning with initial time t_0 with a small initial error $\boldsymbol{e}_{0\mathrm{i}}$ can be approximated by the linear equations by taking the first term of the Taylor expansions,

$$\frac{d}{dt}\boldsymbol{e}_i(t) = \sum_{j=1}^{N}\frac{\partial \boldsymbol{F}}{\partial \boldsymbol{r}_j}\boldsymbol{e}_j, \tag{8.83}$$

in which the coefficient $\frac{\partial \boldsymbol{F}}{\partial \boldsymbol{r}_j}$ is time dependent.

Using Jacobian matrix of $\boldsymbol{F}$ at $\boldsymbol{r}$(t), $\left(\boldsymbol{J}_{ij} = \frac{\partial \boldsymbol{F}}{\partial \boldsymbol{r}_j}\right)$, it can be written as,

$$\frac{d}{dt}\boldsymbol{e}_i(t) = \boldsymbol{J}(\boldsymbol{r}(t))\boldsymbol{e}(t), \tag{8.84}$$

Integrating Eq. (8.84), we have at the time after τ_e of initial time,

$$\boldsymbol{e}(t_0 + \tau_e) = \boldsymbol{M}(\boldsymbol{r}(t_0), \tau_e)\boldsymbol{e}(t_0), \tag{8.85}$$

The matrix $\boldsymbol{M}$ is called as error matrix and it depends on the $\boldsymbol{r}(t)$ during this time interval.

Then one can consider the mean expansion rate of error. If initial error is randomly and spherically distributed in the N dimensional phase space, the distribution of error with size ε is represented by

$$\mathbf{e}^T(t_0)\mathbf{e}(t_0) = \varepsilon^2. \tag{8.86}$$

Here the superscript T indicates the transpose. From Eqs. (8.85) and (8.86), the distribution of error becomes an ellipsoid after τ_e, represented by,

$$\mathbf{e}^T(t_0+\tau_e)\left[\boldsymbol{M}(\boldsymbol{r}(t_0),\tau_e)\boldsymbol{M}^{\boldsymbol{T}}(\boldsymbol{r}(t_0),\tau_e)\right]^{-1}\mathbf{e}(t_0+\tau_e) = \varepsilon^2 \tag{8.87}$$

The amplification rate, α, during this time is given by [123, 155]

$$\alpha(\boldsymbol{r}(t_0),\tau_e) = \sqrt{\frac{1}{N}\sum_{i=1}^{N}\Gamma_i(\boldsymbol{r}(t_0),\tau_e)}, \tag{8.88}$$

where $\Gamma_i = \lambda_1{}^2, \ldots, \lambda_N{}^2$ is a N real and non-negative eigen values of the matrix $\boldsymbol{M}(\boldsymbol{r}(t_0),\tau_e)\boldsymbol{M}^{\boldsymbol{T}}(\boldsymbol{r}(t_0),\tau_e)$ and $\Gamma_i{}^{1/2}$ corresponds to the local Lyapunov exponent [123, 154].

The error doubling time is inversely proportional to the leading Lyapunov exponent, a common view in the meteorological community [156]. As shown above, the error propagation in complex systems is related to the Lyapunov exponent.

There are some further problems concerning it for the above treatment. The first problem is the non-spherical distribution of the initial error, which is related to the dimensionality of the jump paths, which can be less than 3. Another problem is that the functional form of $\boldsymbol{F}$ being time dependent. Especially for slow dynamics at low temperature regions, the fluctuation of the cage in local region is larger than that for the whole system. The third problem may be a contribution of neglected terms in Eqs. (8.83) and (8.84).

8.4.4 Backward Error Analysis of the Averaged Properties

Mathematicians are interested in the numerical integration of ordinary differential equations. Backward error analysis [150, 153, 157] seems to be an important tool for understanding the long time behavior of numerical integration methods and have shown the usefulness of the symplectic integrator used in MD simulations. Traditional ‘forward error analysis’ describes the difference between the exact trajectory and numerical trajectory, while in the ‘backward error analysis’, the difference between the numerical and exact solution is expressed in terms of a perturbation of the problem or the vector field.

Bond and Leimkuhler [153] have done the backward analysis of the accuracy for numerically computed averages of MD. The history for the numerical treatment in MD was also summarized in this reference. Reich [150] has shown the long time integration of chaotic Hamiltonian systems and discussed the approximation of time averages along numerically computed trajectories. These works seem to be encouraging to use in long time MD simulations for obtaining averaged quantities.

8.5 Treatments of Slow and Fast Dynamics in Ionic Systems

Dynamics of ions in both ionically conducting glasses and ionic liquids are quite heterogeneous. That is, both fast and slow ions coexists, while the mean of the dynamics is slow, similar to dynamics of liquids in the glass transition regimes, where the rare event is not negligible. This situation makes it difficult to treat the heterogeneous dynamics in molecular dynamics simulations.

In this section, several requirements to observe such dynamics and the resultant structures will be discussed, although sometime they are difficult to fulfill by a limited calculation resource. Sampling method of such dynamics or structures is also a matter of debate here. If the system was trapped in the local metastable state on the complicated potential well, many runs with independent cooling schedule might be required. However, for the ionics with a measurable diffusivity within several ns, delayed time series with many initial times obtained by a long run, covering the phase-space, is more useful than a limited number of short time runs.

8.5.1 System Size Requirements (Relationship with Fragility and Confinement)

In MD simulations, periodic boundary condition (PBC) is often used. This is useful to treat the infinitive size of system and long ranged interactions. However, the nature of the system might be affected by the size of the basic cell. This is because the motions of particles are repeated by the periodic boundary conditions, and consequently the resultant structures also are restricted. Of course, the system size required in MD simulations depends on the problem to be treated, and researcher should select suitable size for the purpose and within the restriction of the available calculation resources. Here, some general requirements for the study of the structure and dynamics including those in the case of the silicate glasses are discussed.

8.5.1.1 General Requirements of System Size in MD

The size of the basic cell determines the largest length scale and smallest wave number accessible by MD simulations. In the case of crystal, motion of particles including vibrational mode is considerably affected by the cell size and how the unit crystal structure is repeated in the basic MD cell.

In liquids or glasses, the structure shown by pair correlation function $g(r)$, decays within a certain length. For ion-ion interactions, the correlation of the structure (deviation from the line of $g(r) = 1$) is not clear at distance longer than 8–12 Å in ionic systems such as lithium silicate glass. Therefore, twice this length is a minimum length of the unit cell for MD simulations to avoid the ionic structure being affected by the PBC. In the case of ionic liquid, longer correlation is observed as shown in Fig. 8.4. The correlation is small at around ~18 Å. Therefore the system size with ~36 Å of L will be a good choice for many purposes. However, larger system size might be necessary depends on the purpose of the simulations.

Angell has introduced a concept of "fragile" and "strong" to characterize glass forming materials [158, 159] and the system size required to examine the network glasses depends on the fragility of it. The fragile system shows a non-Arrhenius behavior, while the strong system shows an Arrhenius behavior. In the fragile liquid, the Arrhenius plot of structural relaxation time as a function of T_g/T increases rapidly near $T_g/T = 1$, and the "fragility" or fragility index m is usually defined by the slope at $T_g/T = 1$. Fragile (strong) glass-formers have large (small) value of m. In general, system size effect of the basic MD cell for dynamics is known to be larger in the "strong" system [160].

Generally, fragility is larger when the alkali content is larger and this affects the required system size of MD. For lithium silicate, experimental fragility index, m, of

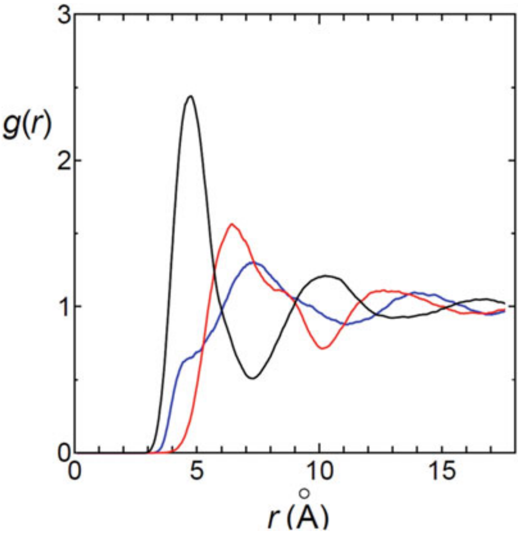

Fig. 8.4 Example of the structure of ionic liquid (EMIM-NO_3 at 400 K for system with 512 ions) examined by the center of mass positions of ions. *Black*: Cation-Anion pair, *Red*: Anion-Anion pair, *Blue*: Cation-Cation pair. Correlation of the structures is diminished but is continuing ~18 Å

silica, lithium trisilicate, lithium disilicate, and lithium metasilicate is reported to be 17.9, 26.3, 34.7 and 33.9, respectively [161]. As expected from its fragility, larger size effect on the network statistics is found in silica rich region than in the lithia rich region and therefore larger system size is required in the silica rich region.

In a confined system such as thin films, mobility of the mobile species (ions) tends to be affected by the immobile species or walls (see Sect. 10.7.1). Using the dependence of dynamics on the distance from the wall, one can obtain a length scale to characterize it. If the system is smaller compared with this length scale, particle motion is affected by its ghost particles in the image cells. Therefore this is related to the minimum size of the system required for the study of the mobile particles.

In the case of more complex systems with several domains, larger system size may be required to represent regions with different length scales. For example, in colloid-water-salt systems, domains or clusters, gels are formed by a coagulation process and the fractal dimension of local regions and connections between them are different in the cluster or gel [76].

8.5.1.2 System Size Required for the Study of Q_n Structures or Other Network Statistics

For determination of the structures in network systems with long life time, both system size dependency and cooling schedules play roles. In the case of strong system, long (and medium) ranged structure at the high temperature may remain in the system after the vitrification. As a result, the system will show the fictive glass transition temperature which depends on the cooling rate. Fixing of the high temperature structure causes a problem of how to get good statistics for the network structures. One may consider that extremely large number of runs is required to obtain statistically meaning quantity in a glass.

For the statistics of the networks, required numbers of runs may depend on the possible sub-structural units to be considered and their combinations. For Q_n (where n is the number of bridging oxygen in the SiO_4 unit) distribution in lithium disilicate, the system size (3456 particles) seems to be large enough to represent any combinations of structural units of the networks, even when the exchanges among structural units are slow. If one would like to examine the structures at longer range such as the connectivity of the Q_n units, larger size may be required. Some differences of the distribution are found by each quenching schedule and ensemble due to the existence of polyamorphism (see Sect. 9.2 for more details). In a limiting case of high pressure region, the statistics of the distribution can be well represented by the binomial distribution as a first approximation [134, 162] and this resulted in good reproducibility of the structures and dynamics of ions in the glassy state from the works of different researchers.

Thus the system sizes should be large enough for the purpose of simulations. However, due to practical reasons such as the calculation time, the required storage and the cost, extremely large system is not necessarily recommended. One should consider the balance of several factors to choose the condition of simulations.

8.5.2 Equilibration and Cooling Schedules in the MD Simulation of Glasses

Generally, different length scale motions have different time scales and therefore larger system requires longer equilibration time. Some characteristics observed near the glass transition of the system can be understood by existence of these different time scales of substructures.

When the temperature or pressure of the system is changed, shorter length scale motion of local structure can rapidly follow it, while the longer length scale motion of long ranged structure occurs after that. For example, formation of glass starts from short length scale, and spreads to the long length scale [163]. As a result, the system near T_g shows some cooling rate dependence. Actually, Vollmayr et al. [164] found that the glass transition temperature T_g in silica is in accordance with a logarithmic dependence on the cooling rate γ. The rate γ seems to have a much more marked effect on the radial distribution function, the bond-bond angle distribution function, the coordination numbers, and the distribution function for the size of the rings, than density and thermal expansion coefficients. Recently, Forero-Martinez et al. [165] found the trend such as $T_g(vol) > T_g(ene)$ (vol and ene stand for volume and energy, respectively.) for the glass transition temperatures in ionic liquids and it was rationalized in terms of the different relaxation times of energy and volume. It was pointed out that the volume is an intrinsically N-body property, depending on the relative position of far-away particles, while energy depends primarily on the local arrangement of particles, whose relaxation in response to temperature variations is faster than in the case of volume. As a result, energy provides an estimate of T_g somewhat less affected than $T_g(vol)$ by fast quenching rates. Thus the cooling schedule should be designed with considering the different length scales. It is probable that reproducibility of the glass transition temperature becomes better, if the system was maintained just above the glass transition regimes for a long time and then the system was cooled down further. In this condition, long (and medium) ranged structures are equilibrated enough and glass transition temperature is determined mainly by the short length scale structures.

8.5.3 Ensembles Used in the Simulations of Super-Cooled Liquid, Glass, and in the Treatment of Glass Transition

Mostly experiments have been done under constant pressure conditions; while constant energy condition (micro canonical ensemble) is obtained in MD, as long as one does not use modification by additional degrees of freedom. Therefore, the extended ensembles are useful for direct comparison of MD and experiments for some purposes. However, details of the thermodynamics (and its fluctuation) and motion of particles near the glass transition regimes depends on the ensemble used. Therefore suitable conditions should be chosen dependent on the purpose.

When the system is sensitive for thermodynamic condition in the preparation of glass, question arises is what condition should be used in the study of glass transition. So far, many MD works for the glass transition seem to be done in the fixed volume condition and structures prepared in such a manner are not the same as that obtained at ambient pressure. There are reasons to select such conditions. Binder [166] pointed out that "It is essential to carry out simulations for examining the glass transition at constant density (taken from experiment) and not at constant pressure, because in the latter case, there is a too strong dependence of the simulated properties on the cooling rate of the simulation." It seems to be reasonable for those with this point of views. Still one may ask how the system depends on the volume change during the cooling schedule, because the strong dependence can be characteristics of the glass transition.

As will be shown for the Q_n distribution of the network of the silicates (see Sect. 9.2), it depends on the pressure or volume of the system considerably. This is explained by the fact that a local structural unit has its own specific volume as already mentioned. Furthermore, the system may show polyamorphism [167] in the certain region of the phase-diagram [134]. Therefore, the resultant structure of glasses depends on the path on the P-V-T diagram during the cooling schedules.

Since the different ensemble causes differences in the pathway and direction of the fluctuation on the phase-diagram during the non-equilibrium relaxation as shown for SC model [45, 46, 168], caution should be paid to the ensembles used during the cooling schedules.

Thus, one of the possible choices comparable to experiments may be the following conditions. The cooling is performed by constant pressure conditions with temperature scaling or gradual changes in temperatures and the following run is performed in the NVE condition at each target temperature and under a target pressure. If the temperature spontaneously increases during NVE runs, it means the system is under the non-equilibrium relaxation (aging) [45]. Therefore, further control of temperature may be necessary during this period. An NPT ensemble will be also useful, if the overlap with the aging is small or distinguished clearly.

8.5.4 Sampling of Structures and Dynamics Near the Glass Transition Regimes and Glasses

For adequate sampling of the structure of glasses and jump motions including cooperative ones, long time scale simulations and large system size are required especially near the glass transition regimes. Here adequate sampling means that the trajectories cover whole region in the phase space. In other words, the effective sampling is concerned with the "ergodicity" of the system. For MD performed for a limited time scale, is this condition achieved? Is the system trapped in a certain position in the phase space? Fortunately as shown in Sect. 9.9, the transport properties of ions obtained MD are comparable to the experimental ones and such sampling seems to be possible. This is understandable as discussed in the following subsections.

8.5.5 Non-ergodicity of the Dynamics for Network Former

At first, we consider the case of network former in the silicate glass as an example. Since the reconstruction of Si-O bonding is a slower process than ionic motion, it will be more affected by the cooling rate and the characteristics of the structure in the molten state will remain in the structures of glasses. That is, their structures are affected by the fictive temperature as known in experiments. Due to this reason, network structure represented by Q_n (n means number of bridging oxygen atoms in a SiO_4 unit) distribution shows large fluctuations in each quenching run. However, the rearrangement of Si-O bonding is relatively fast process above the glass transition temperature (for example at 1000 K in lithium disilicate, rearrangement occurs within several tens ps), in the conventional MD system with a periodic boundary condition. Thereby one can obtain quasi-equilibrated Q_n distribution, which is approximately represented by the binomial distributions. This means that the different substructures of the network is mixed well and can be sampled enough in these systems. (See Sect. 9.2 for more details for the observed Q_n distribution). If one examined the structure of longer length scale (such as rings), larger system size and longer relaxation time may be required. However, at least for examining the ionics in the system, non-ergodicity of the network structure does not cause severe problems. If suitable cooling schedules are used, reproducibility of dynamics is also good. (See Sect. 9.9 for the comparison of ion dynamics in MD and experiments.) This fact implies that the effect of rapid cooling rate in MD is compensated by the system size effect with periodic boundary conditions at least partially.

8.5.6 Relation Between Ion Dynamics and Chaos

Even for ionic motion, obtaining good statistics in slow dynamics is sometimes a difficult task due to strong heterogeneity with intermittency of the jump motions. At first, here we discuss how ion dynamics are related to the deterministic chaos to understand such characteristics of ionic motions. In the super-cooled liquid states or in the glass, the motion of ions occurs through jump motions among ionic sites (see Sect. 2.4 for examples of such motions in ionic systems). Larger fluctuation of the ion dynamic is observed compared with simple liquids. Similar situation occurs in the ionic liquids, molten salt, crystals, bio-materials, colloidal systems and so on.

Strong heterogeneity with intermittency mentioned above is related to the deterministic character of the motion.

Researchers may encounter such motion even in a simple system such as the SC model [46] or the Lennard-Jones model [168, 169]. Simonazzi and Tenenbaum [169] have reported that the kinetic energy fluctuations exhibit an anomalous behavior in LJ microcrystals at low temperature and attributed them due to weak chaos. Deterministic nature of the system resulted in the intermittent and sporadic behaviors [171] frequently observed near the glass transition regimes.

8.5.7 Sampling of Rare Event with Dynamic Heterogeneity-Ergodicity of Ionic Motion

For ionics in the glassy state, system shows exchanges between vast or laminar states and cooperative motions of several ions emphasize such a behavior [172]. For averaging such properties, many independent initial positions and/or wide time window are required [173], if the calculation resources and times allow it to be performed. Deterministic behaviors of the system are also found in extended ensembles. Holian et al. [174] have pointed out that the Toda "demon" is hidden in the Nosé-Hoover thermostat, which can cause the noncanonical undulations. Therefore, if one used extended dynamics, it is better to check if the dynamics are affected by it or not. In the case of slow dynamics, sampling of the rare events such as cooperative motions of several ions is always problematic [17, 171]. It also means the difficulty of averaging the heterogeneous dynamics.

How can we cover the wide region of the phase-space and how can we check it? One possible method to cover the wide phase-space is using a lagged time series as shown below. To reduce the effect of fluctuation of dynamic heterogeneity related to the cooperative nature of jumps for statistic treatment of the system, average for many number of lagged time series**,** $\mathbf{r}(t)$, $\mathbf{r}(t+\tau'')$,····· and $\mathbf{r}(t+(m-1)\tau'')$, can be used for the analysis of MD data. Large time windows and many initial times are required because MD trajectories have correlations between successive motions. If the time window, $m\tau''$, covered by the many initial times is wide enough, long correlated motion with strong dynamic heterogeneity can be smoothed out. This procedure using lagged time series is similar to the "embedding" [175, 176] to find out the deterministic chaos in the time series. That is, the procedure can cover the trajectories in the phase-space.

Once sampling time is long enough with wide time windows, results of transport properties of ions obtained by different runs starting from different configurations or those by different researchers are comparable when the same potential model and comparable cooling schedule was used. This suggests that the long time ionic motion in ionically conducting glasses has "ergodicity" at least approximately, once the whole phase-space structure can be covered during the observation time. By this method, one can reproduce well the transport properties such as diffusion coefficient of ions.

Exceptional case is observed at quite low temperatures, where the aging (non-equilibrium relaxation) overlaps the observed dynamics. If permanently trapped particle exists, non-ergodicity of the dynamics might be found.

Of course, accumulation of independent runs is one of the possible choices for the sampling method. However, how may runs are required for this kind of sampling?

In Fig. 8.5, the van Hove functions of cations in the ionic liquid, EMIM-NO_3 obtained at 370 K, which shows a medium degree of heterogeneity is compared with the randomly sampled data from the original curve in (a). The shape strongly depends on the number of the samples, N_S. Many independent samples are required

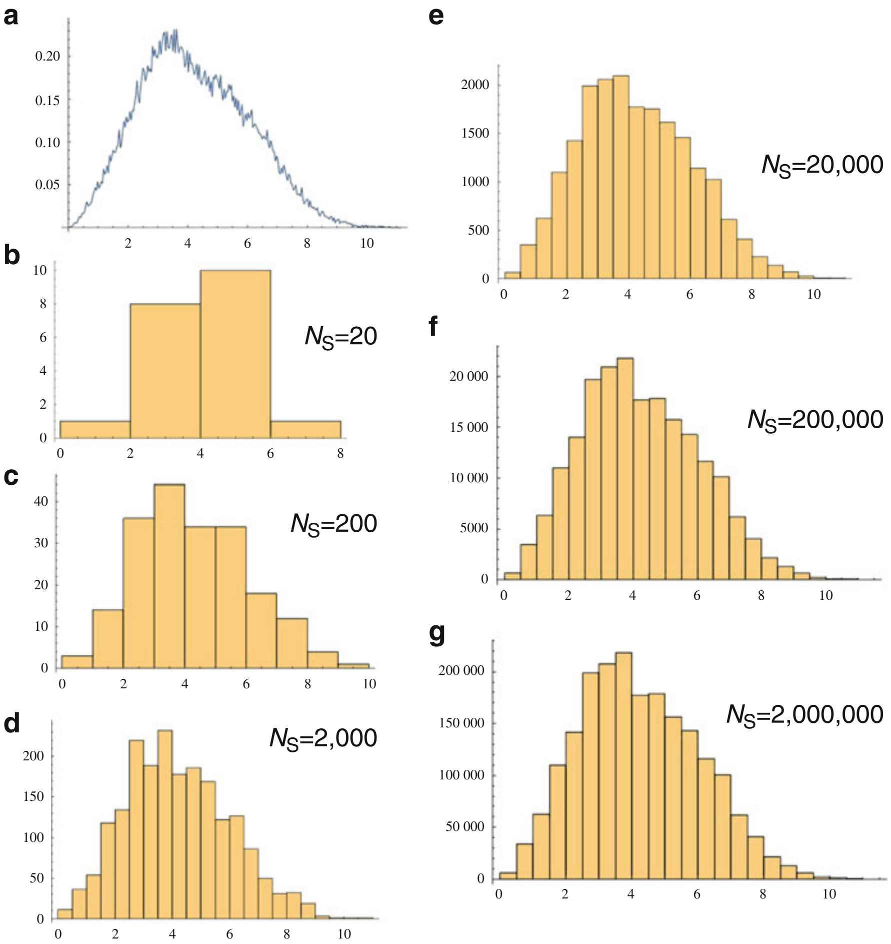

Fig. 8.5 (**a**) Distribution curve taken from the self-part of the van Hove functions of cations in EMIM-NO_3 at 370 K at 2.5 ns determined by using many lagged time series. (**b**)–(**g**) Reproducibility of the functional form by random sampling from the original distribution, where N_s data points are used. Many data points are necessary to reproduce the original functional form

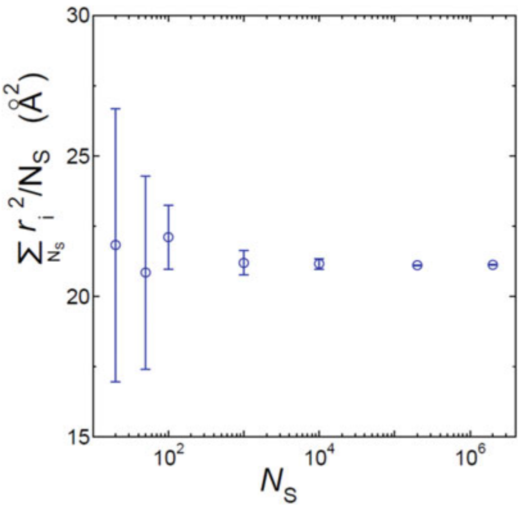

Fig. 8.6 Dependence of mean squared displacement on number of random sampling, N_S. Error bars are obtained from three or four runs using different random numbers. Distribution is taken from the same original function shown in Fig. 8.5a

to reproduce the original curves including power law tail and an exponential truncation.

In Fig. 8.6, the mean squared displacement at 2.5 ns calculated from reproduced distributions was plotted against N_S. Error bars are for three or four examples with the same N_s. For obtaining the mean value, ~10^4 of N_S may be enough; while to reproduce the functional form in details, more than 10^5 independent samples are required. More heterogeneous the system, the larger number of samples will be required. It is not easy to do so many runs and furthermore, independent short time runs are not necessarily better than the small number of long runs to understand the dynamics of the system. This is because they cannot cover the low frequency mode, which is responsible for the transport properties of the glass and they cannot recover the functional form concerned with the slow dynamics. Long time run is also useful for sampling of rare events. If the observation time is not long enough, it is difficult to observe the rare events such as correlated motion of ions of long time scales in spite of the fact that its contribution to the dynamic properties are non-negligible.

For the single particle motions, sampling for the space can be done by many ions spread out in the system. Therefore the average can be taken for many ions. Existence of the large fluctuation is more serious problem for the collective motion compared with the single particle motion. For example, enhanced heterogeneity seems to be observed for molecular motion in bio-systems, where a small number of molecules or units tend to be treated.

The cooling rate dependency of ion dynamics is smaller compared with that of network [177] due to higher relaxation rate, but still it is non-negligible when it is accompanied with the relaxation of networks. (See Sect. 9.9.)

8.6 Non-equilibrium Molecular Dynamics and Reverse Non-equilibrium Molecular Dynamics

In slow dynamics, it is not easy to attain the region of constant transport coefficient in MSD or other dynamic properties. In such a case, Non-Equilibrium Molecular Dynamics, NEMD can be useful. In this method, the system is treated by the external force such as that giving rise to shear viscosity [178]. Reverse Non-Equilibrium Molecular Dynamics [179, 180], RNEMD, is also useful for investigating the transport properties of glass-forming systems, because it provides faster convergence than the usual numerical non-equilibrium or equilibrium methods. The RNEMD method is based on the phenomenological relation:

$$J_Z(p_x) = -\eta\left(\frac{\partial v_x}{\partial z}\right), \tag{8.89}$$

where $\left(\frac{\partial v_x}{\partial z}\right)$ is the shear, $J_Z(p_x)$ is the transverse momentum flux, and η is the shear viscosity. In this method, different from the usual techniques, $J_Z(p_x)$ is **imposed** and the shear is **measured**.

References

1. L.V. Woodcock, Phys. Chem. Lett. **10**, 257 (1971)
2. F.G. Fumi, M.P. Tosi, J. Phys. Chem. Solids **25**, 31 (1964)
3. M.P. Tosi, F.G. Fumi, J. Phys. Chem. Solids **25**, 45 (1964)
4. A. Rahman, R.H. Fowler, A.H. Narten, J. Chem. Phys. **57**, 1 (1972)
5. L.V. Woodcock, C.A. Angell, P. Cheeseman, J. Chem. Phys. **65**, 1565 (1976)
6. T.F. Soules, J. Non-Cryst. Solids **49**, 29 (1982)
7. L.V. Woodcock, K. Singer, Trans. Faraday Soc. **67**, 12 (1971)
8. S. Tsuneyuki, M. Tukada, M. Aoki, Y. Matsui, Phys. Rev. Lett. **61**, 869 (1988)
9. S. Tsuneyuki, Thesis of Ph. D of physics, University of Tokyo, 1989
10. C.R.A. Catlaw, G.D. Price, Nature **347**, 243 (1990)
11. H. Ogawa, Y. Shiraishi, K. Kawamura, T. Yokokawa, J. Non-Cryst, Non-Cryst. Solids **119**, 151 (1990)
12. J. Habasaki, I. Okada, Mol. Simul. **9**, 319 (1992)
13. J. Habasaki, I. Okada, Y. Hiwatari, J. Non-Cryst. Solids **183**, 12 (1995)
14. J. Habasaki, I. Okada, Y. Hiwatari, J. Non-Cryst. Solids **208**, 181 (1996)
15. J. Habasaki, K.L. Ngai, Y. Hiwatari, J. Chem. Phys. **121**, 925 (2004)
16. J. Habasaki, K.L. Ngai, Y. Hiwatari, C.T. Moynihan, J. Non-Cryst. Solids **349**, 223 (2004)
17. J. Habasaki, I. Okada, Y. Hiwatari, Phys. Rev. **B55**, 6309 (1997)
18. J. Habasaki, I. Okada, Y. Hiwatari, Phys. Rev. **E52**, 2681 (1995)
19. H. Lammert, M. Kunow, A. Heuer, Phys. Rev. Lett. **90**, 215901 (2003)
20. C. Mueller, E. Zienicke, S. Adams, J. Habasaki, P. Maass, Phys. Rev. **B75**, 014203 (2007)
21. R.A. Montani, C. Balbuena, M.A. Frechero, Solid State Ion. **209–210**, 5 (2012)
22. L.G.V. Gonçalves, J.P. Rino, J. Non-Cryst. Solids **402**, 91 (2014)
23. G.N. Greaves, Solid State Ion. **105**, 243 (1998)

24. P. Jund, W. Kob, R. Jullien, Phys. Rev. B **64**, 134303 (2001)
25. J. Horbach, W. Kob, Phys. Rev. B **60**, 3169 (1999)
26. A.N. Cormack, Top. Mol. Organ. Eng. **15**, 227 (2002)
27. A.N. Cormack, J. Du, T.R. Zeitler, Phys. Chem. Chem. Phys. **4**(14), 3193 (2002)
28. J. Du, R. Devanathan, L.R. Corrales, W.J. Weber, Comput. Theor. Chem. **987**, 62 (2012)
29. A. Tilocca, Phys. Rev. B **76**, 224202 (2007)
30. R.S. Payal, S. Balasubramanian, Phys. Chem. Chem. Phys. **16**, 17458 (2014)
31. J. Habasaki, K.L. Ngai, J. Chem. Phys. **129**, 194501 (2008)
32. C.Y. Ouyang, S.Q. Shi, Z.X. Wang, H. Li, X. J. Huang, L.Q. Chen, Europhys. Lett. **67**, 28 (2004)
33. S. Ispas, T. Charpentier, F. Mauri, D.R. Neuville, Solid State Sci. **12**, 183 (2010)
34. A. Tilocca, J. Chem. Phys. **133**, 014701 (2010)
35. A. Tilocca, N.H. de Leeuw, J. Mater. Chem. **16**, 1950 (2006)
36. M.G. Del Pópolo, R.M. Lynden-Bell, J. Kohanoff, J. Phys. Chem. B **109**, 5895 (2005)
37. A. Carré, J. Horbach, S. Ispas, W. Kob, EPL **82**, 17001 (2008)
38. R. Car, M. Parrinello, Phys. Rev. Lett. **55**, 2471 (1985)
39. Y. Wang, W.G. Noid, P. Liu, G.A. Voth, Phys. Chem. Chem. Phys. **11**, 2002 (2009)
40. D. Jeong, M.Y. Choi, H.J. Kim, Y. Jung, Phys. Chem. Chem. Phys. **12**, 2001 (2010)
41. W.G. Hoover, M. Ross, K.W. Johnson, D. Henderson, J.A. Barker, B.C. Brown, J. Chem. Phys. **52**, 4931 (1970)
42. Y. Hiwatari, H. Matsuda, T. Ogawa, N. Ogita, A. Ueda, Progress Theor. Phys. **52**, 1105 (1974)
43. M. Tanemura. Y. Hiwatari, H. Matsuda, T. Ogawa, N. Ogita, A. Ueda, Progress Theor. Phys. **58**, 1079 (1977); ibid. **58**, 3070 (1977)
44. A. Ueda, Butsuri **62**, 769 (2007). in Japanese
45. J. Habasaki, A. Ueda, J. Chem. Phys. **134**, 084505 (2011)
46. J. Habasaki, A. Ueda, J. Chem. Phys. **138**, 144503 (2013)
47. M. Tanemura, H. Matsuda, T. Ogawa, N. Ogita, A. Ueda, J. Non-Cryst. Solid **117/118**, 883 (1990)
48. J. Habasaki, R. Casalini, K.L. Ngai, J. Phys. Chem. B **114**, 3902 (2010)
49. F. Simon, F. Lange, Z. Physik, **38**, 227 (1926)
50. G.E. Gibson, G.S. Parks, W.M. Latimer, J. Am. Chem. Soc. **42**, 1542 (1920)
51. G.S. Parks, J. Am. Chem. Soc. **47**, 338 (1925)
52. B. Bernu, Y. Hiwatari, J.P. Hansen, J. Phys. C **18**, L371 (1985)
53. T. Muranaka, Y. Hiwatari, J. Phys. Soc. Jpn. **67**, 1982 (1998)
54. J. Matsui, T. Odagaki, Y. Hiwatari, Phys. Rev. Lett. **73**, 2452 (1994)
55. T. Mizuguchi, T. Odagaki, Phys. Rev. E **79**, 051501 (2009)
56. E.A. Jagla, Phys. Rev. **E63**, 061509 (2001)
57. J.E. Lennard-Jones, Proc. R. Soc. Lond. A **106**, 463 (1924)
58. D. Brown, J.H.R. Clarke, Mol. Phys. **51**, 1243 (1984)
59. J.A. White, J. Chem. Phys. **111**, 9352 (1999)
60. G. Mie, Ann. Physik. Lpz. **11**, 657 (1903)
61. M. Edalat, S.S. Lan, F. Pang, G.A. Mansoori, Int. J. Thermophys. **1**, 177 (1980)
62. W. Kob, H.C. Andersen, Phys. Rev. **E51**, 4626 (1995)
63. P. Bordat, F. Affouard, M. Descamps, K.L. Ngai, Phys. Rev. Lett. **93**, 105502 (2004)
64. P. Bordat, F. Affouard, M. Descamps, K.L. Ngai, J. Non-Cryst. Solids **352**, 4630 (2006)
65. J. Habasaki, K.L. Ngai, Phys. Chem. Chem. Phys. **9**, 4673 (2007). and references cited therein
66. L.C. Valdes, F. Affouard, M. Descamps, J. Habasaki, J. Chem. Phys. **130**, 154505 (2009)
67. J. Habasaki, F. Affouard, M. Descamps, K.L. Ngai, IAP Proc. **982**, 154 (2008)
68. F.G. Fumi, M.P. Tosi, J. Phys. Chem. Solids **25**, 31 (1964)
69. T.L. Gilbert, J. Chem. Phys. **49**, 2640 (1968)
70. Ida, Phys. Earth Planet Inter. **13**, 97 (1976)
71. M.G. Del Pópolo, G.A. Voth, J. Phys. Chem. **B108**, 1744 (2004)

72. T.I. Marrow, E.J. Maginn, J. Phys. Chem. **B106**, 12807 (2002)
73. J.N.C. Lopes, J. Deschamps, A.A.H. Pa’dua, B**108**, 2038 (2004)
74. A.C.T. van Duin, A. Strachan, S. Stewman, Q. Zhang, X. Xu, W.A. Goddard III, J. Phys. Chem. **107**, 3803 (2003)
75. H. Manzano, S. Moeini, F. Marinelli, A.C.T. van Duin, F.-J. Ulm, R.J.-M. Pellenq, J. Am. Chem. Soc. **134**, 2208 (2012)
76. J. Habasaki, M. Ishikawa, Phys. Chem. Chem. Phys. **16**, 24000 (2014)
77. H.J.C. Berendsen, J.P.M. Postma, W.F. van Gunsteren, J. Hermans, in *Intermolecular Forces*, ed. by B. Pullman (Reidel, Dordrecht, 1981), p. 331
78. H.J.C. Berendsen, J.R. Grigera, T.P. Straatsma, J. Phys. Chem. **91**, 6269 (1987)
79. M.W. Mahoney, W.L. Jorgensen, J. Chem. Phys. **112**, 8910 (2000)
80. S.W.A. Rick, and references therein. J. Chem. Phys. **120**, 6085 (2004)
81. J. Zielkiewicz, J. Chem. Phys. **123**, 104501 (2005)
82. M.W. Mahoney, W.L. Jorgensen, J. Chem. Phys. **114**, 363 (2001)
83. V.A. Bakaev, W.A. Steele, J. Chem. Phys. **111**, 9803 (1999)
84. L. Verlet, Phys. Rev. **159**, 98 (1967)
85. In the symplectic integrator, time propagator is decomposed into a product of easily obtainable propagators, where each time evolution can be solved rigorously. The methods are known to conserve energy for long time; J.M. Sanz-Serna, *Proceedings of the International Congress of Mathematicians, Zürich, Switzerland 1994* © (Birkhäuser Verlag, Basel, 1995)
86. S. Nosé, J. Phys. Soc. Jpn. **70**, 75 (2001)
87. M.P. Allen, D.J. Tildesley, *Computer Simulation of Liquids* (Oxford University Press, New York, 1989)
88. E. Madelung, Phys. Z. **19**, 524 (1918)
89. K.S. Thorne, Rev. Mod. Phys. **52**, 299 (1980)
90. P.P. Ewald, Ann. Phys. **64**, 253 (1921)
91. A. Ueda, *Molecular Simulations -from Classical to Quantum Method* (SHOKABO, Tokyo, 2003). in Japanese
92. C. Kittel, *Introduction to Solid State Physics*, 5th edn. (Wiley, New York, 1976)
93. R.J.W. Eastwood, L. Hockey, D.N. Lawrence, Comput. Phys. Commun. **19**, 215 (1980)
94. W. Eastwood, L. Hockey, *Computer Simulation Using Particles* (McGraw-Hill, New York, 1985)
95. T. Darden, D. York, L. Pedersen, J. Chem. Phys. **98**, 10089 (1993)
96. For example, see Toukmaji, J.A. Board Jr. Comput. Phys. Commun. **95**, 73 (1996); http://www.ccp5.ac.uk/DL_POLY_CLASSIC/FAQ/FAQ2.shtml The address is confirmed to be valid on 14th Feb. 2016
97. J.E.L. Barnes, P. Hut, Nature **324**, 446 (1986)
98. V. Greengard, J. Rokhlin, Comput. Phys. **73**, 325 (1987)
99. T.J. Giese, D.M. York, J. Comput. Chem. **29**, 1895 (2008)
100. J. Carrier, L. Greengard, V. Rokhlin, SIAM J. Sci. Stat. Comput. **9**, 669 (1988)
101. E.T. Newman, R. Penrose, Phys. Rev. Lett. **15**, 231 (1965)
102. P.J. Steinhardt, D.R. Nelson, M. Ronhetti, Phys. Rev. B **28**, 784 (1983)
103. W. Dieterich, P. Maass, Solid State Ion. **180**, 446 (2009)
104. J. Habasaki, Mol. Phys. **70**, 513 (1990)
105. K.L. Ngai, J. Habasaki, J. Chem. Phys. **141**, 114502 (2014)
106. J. Habasaki, K.L. Ngai, J. Chem. Phys. **142**, 164501 (2015)
107. *The Molecular Dynamics of Liquid Crystals*, ed. by G.R. Luckhurst, C.A. Veracini (Kluwer, Nato Science Series C 1994)
108. H. Goldstein, *“The Euler Angles” and “Euler Angles in Alternate Conventions.” in Classical Mechanics*, 2nd edn. (Addison-Wesley, 1980), pp. 143 and 606
109. W.R. Sir, *Hamilton, Lectures on Quaternions* (Hodges & Smith, Dublin, 1853)
110. H.C. Andersen, J. Chem. Phys. **72**, 2384 (1980)
111. S. Nosé, Mol. Phys. **52**, 511 (1984)

112. W.G. Hoover, Phys. Rev. **A31**, 1695 (1985)
113. J.M. Haile, S. Gupta, J. Chem. Phys. **79**, 3067 (1983)
114. S.D. Bond, B.J. Leimkuhler, B.B. Laird, J. Comput. Phys. **151**, 114 (1999)
115. J.M. Thijssen, *Computational Physics* (Cambridge University Press, 1999)
116. M. Parrinello, A. Rahman, Phys. Rev. Lett. **45**, 1196 (1980)
117. A. Rahman, N. Parrinello, J. Appl. Phys. **52**, 7182 (1981)
118. J.R. Ray, A. Rahman, J. Chem. Phys. **80**, 4423 (1984)
119. A.L. Loeb, *Space Structures* (Addison-Wesley, 1976)
120. J. Makino, M. Taiji, *Simulations with Special-Purpose Computers* (Wiley, 1997)
121. J. Habasaki, K.L. Ngai, to be published
122. E.N. Lorenz, J. Atoms. Sci. **20**, 130 (1963)
123. S. Yoden, M. Nomura, J. Atmos. Sci. **50**, 1531 (1993)
124. P. Keblinski, J. Eggebrecht, D. Wolf, S.R. Phillpot, J. Chem. Phys. **113**, 282 (2000)
125. B.P. Lee, M.E. Fisher, Europhys. Lett. **39**, 611 (1997)
126. M.G. Del Pópolo, G.A. Voth, J. Phys. Chem. B **108**, 1744 (2004)
127. J. Habasaki, K.L. Ngai, J. Non-Cryst. Solids **357**, 446 (2011)
128. D. Chandler, *Introduction to Modern Statistical Mechanics* (Oxford University Press, New York, 1987)
129. J.P. Hansen, I.R. MacDonald, *Theory of Simple Liquids*, 2nd edn. (Academic, London, 1990)
130. C.G. Gray, K.E. Gubbins, *Theory of Molecular Fluids*, vol 1 (Clarendon, Oxford, 1984)
131. S.K. Chatterjee, *X-ray Diffraction: Its Theory and Applications* (PHI Learning, 2010)
132. Y. Waseda, E. Matsubara, K. Shinoda, *X-Ray Diffraction Crystallography: Introduction, Examples and Solved Problems* (Springer, 2011)
133. H. Doweidar, J. Non Cryst. Solids **194**, 155 (1996)
134. J. Habasaki, K.L. Ngai, J. Chem. Phys. **139**, 064503 (2013)
135. A. Einstein, *Investigations on the Theory of Brownian Motion* (Dover, New York, 1956)
136. R. Kubo, J. Phys. Soc. Jpn. **12**, 570 (1957)
137. T. Odagaki, M. Lax, Phys. Rev. B **24**, 5284 (1981)
138. Y. Haven, B. Verkerk, Phys. Chem. Glasses **6**, 38 (1965)
139. G.E. Murch, Solid State Ionics **7**, 177 (1982)
140. J.O. Isard, J. Non-Cryst. Solids **246**, 16 (1999)
141. B. Hafskjold, X. Li, J. Phys. Condens. Matter **7**, 2949 (1995)
142. B. Doliwa, A. Heuer, Phys. Rev. E **61**, 6898 (2000)
143. G.A. Evangelakis, V. Pontikis, Europhys. Lett. **8**, 599 (1989)
144. A. Heuer, M. Kunow, M. Vogel, R.D. Banhatti, Phys. Chem. Chem. Phys. **4**, 3185 (2002)
145. Some researchers suggest to call it Stokes-Einstein-Sutherland relation. See, W. Sutherland, Phil. Mag. **9**, 781 (1905)
146. A. Rahman, K.S. Singwi, A. Sjolander, Phys. Rev. **126**, 986 (1962)
147. L. Van Hove, Phys. Rev. **95**, 249 (1954). The same basic ideas were earlier put forward by Glauber. R.J. Glauber, Phys. Rev. **8**7, 189 (1952); **94**, 751 (1954); **98**, 1692 (1955)
148. N. Lačević, T.B. Schrøder, F.W. Starr, S.C. Glotzer, J. Chem. Phys. **119**, 7372 (2003)
149. R.A. Lippert, K.J. Bowers, R.O. Dror, M.P. Eastwood, B.A. Gregersen, J.L. Klepeis, I. Kolossvary, J. Chem. Phys. **126**, 046101 (2007)
150. S. Reich, SIAM J. Numer. Anal. **36**, 1549 (1999)
151. M. Sugihara, K. Murota, "Mathematical principle of numerical calculation methods", second version (in Japanese. The title was translated.), Iwanami, 1994. ISBN4-00-005518-6
152. S. Toxvaerd, O.J. Heilmann, T. Ingebrigtsen, T.B. Schrøder, J.C. Dyre, J. Chem. Phys. **1**, 064102 (2009)
153. S.D. Bond, B.J. Leimkuhler, Acta Numer. **16**, 1 (2007)
154. E.N. Lorenz, J. Atoms. Sci. **20**, 130 (1963)
155. H. Mukougawa, M. Kimoto, S. Yoden., J. Atmos. Sci. **48**, 1231 (1991)
156. E.N. Lorenz, *Predictability –a Problem Partly Solved. Predictability,* ed. by T. Palmer, European Center for Medium Range Forecasting, (Shinfield Park, Reading, 1996);

Predictability of Weather and Climate, ed. by T. Palmer, R. Hagedorn, (Cambridge University Press, 2006)
157. G. Benettin, A. Giorgilli, On the Hamiltonian interpolation of near to the identity Symplectic mappings with application to symplectic integration algorithms. J. Statist. Phys. **74**, 1117 (1994)
158. C.A. Angell, J. Non-Cryst. Solids **73**, 1 (1985)
159. R. Böhmer, K.L. Ngai, C.A. Angell, D.J. Plazek, J. Chem. Phys. **99**, 4201 (1993)
160. J. Horbach, W. Kob, K. Binder, C.A. Angell, Phys. Rev. E. **54**, R5897 (1996)
161. M.L.F. Nascimento, C. Aparicio, J. Phys. Chem. Solids **68**, 104 (2007)
162. E.D. Lacy, Phys. Chem. Glasses **6**, 171 (1965)
163. J. Habasaki, Mol. Phys. **1990**, 513
164. K. Vollmayr, W. Kob, K. Binder, Phys. Rev. B **54**, 15808 (1996)
165. N.C. Forero-Martinez, R. Cortes-Huerto, P. Ballone, J. Chem. Phys. **136**, 204510 (2012)
166. K. Binder, J. Non-Cryst. Solids **274**, 332 (2000)
167. O. Mishima, L.D. Calvert, E. Whalley, Nature **314**, 76 (1985)
168. J. Habasaki, A. Ueda, J. Non-Cryst. Solids, **447**, 212 (2016)
169. R. Simonazzi, A. Tenenbaum, Phys. Rev. E54, 964 (1996)
170. F. Calvo, J. Chem. Phys. **108**, 6861 (1998)
171. X.-J. Wang, Phys. Rev. A**45**, 8407 (1992)
172. J. Habasaki, Y. Hiwatari, Phys. Rev. **E59**, 6962 (1999)
173. J. Habasaki, Y. Hiwatari, Phys. Rev. **E65**, 021604 (2002)
174. B.L. Holian, A.F. Voter, R. Ravelo, Phys. Rev. **E52**, 2338 (1995)
175. The method of "embedding" is used to reconstruct the attractor of the non-linear motion; N.H. Packard, J.P. Crutchfield, J.D. Farmar, R.S. Shaw, Phys. Rev. Lett. **45,** 712 (1980)
176. F. Takens, Dynamical Systems and Turbulence, Warwick 1980 (Coventry, 1979/1980), Lecture Notes in Mathematical, vol 898 (Springer, Berlin, 1981), pp. 366–381
177. J. Tilocca, Chem. Phys. **139**, 114501 (2013)
178. G. Ciccotti, G. Jacucci, Phys. Rev. Lett. **35**, 789 (1975)
179. P. Bordat, F. Müller-Plathe, J. Chem. Phys. **116**, 3362 (2002)
180. P. Bordat, F. Affouard, M. Descamps, F. Müller-Plathe, J. Phys. Condens. Matter **15**, 5397 (2003)

Chapter 9
Molecular Dynamics Simulation of Silicate Glasses

9.1 Derivation of the Potential Parameters from Ab Initio Calculations

Modeling techniques using molecular dynamics simulation can contribute to the design and improvement of materials, and the methods can be used for predicting properties of them and compare with experiments and theory. Recently, potential models based on the ab initio MO calculations or DFT are used in many cases. However, the potential parameters are not necessarily uniquely determined from the ab initio calculation. To understand the quality of the parameter set, its limitation and applicability of it to each problem, it is useful to learn how it is derived and how it is checked. Although recently many methods are developing, here we explain how the parameters for alkali silicates [1], mentioned in Sect. 8.1.2, had been determined.

At first, the partial structures of Si surrounded by O are treated as follows. For the charge number of Si, the value obtained for TTAM potential [2] was adopted, that is $q_{\mathrm{si}} = +2.40$. In their works, Hartree-Fock level calculation using a Gaussian type basis set (12s8p)/[5s3p] with two d orbitals ($\alpha = 0.118$, 0.424) was used for silicon, while (9s5p)/[3s2p] with a diffuse function (with $\alpha = 0.0059$) was used for negative ion states of oxygen. They calculated the total energy of ${\mathrm{SiO}_4}^{4-}$ cluster surrounded by four positive point charges, which mimic the Madelung potential from the rest of the crystal. Then the potential energy surface is obtained by changing Si-O distance or O-Si-O angles with three different modes.

The potential function used in their work is

$$\phi_{ij} = \frac{q_i q_j e^2}{r} + f_0 \left(b_i + b_j\right) \exp\left(\frac{a_i + a_j - r}{b_i + b_j}\right) - c_i c_j r^{-6} \tag{9.1}$$

J. Habasaki et al., *Dynamics of Glassy, Crystalline and Liquid Ionic Conductors*,
Topics in Applied Physics 132, DOI 10.1007/978-3-319-42391-3_9

where q is the charge number and e the elementary charge; a, b and c are the parameter characteristic of each atom, f_0 is a normalization constant (1 kcal Å^{-1} $\text{mol}^{-1} = 4.184$ kJ Å^{-1} mol^{-1}) and r is the distance between the centers of atoms.

The parameters a, b and c, of Si and O of TTAM were used without change, because the cluster surrounded by point charges seems to be a good model not only for silica but also for silicates.

The other parameters for silicate is that derived from the Molecular Orbital calculation of $(e^+\text{-O-M-O-}e^+)^{-1}$ cluster. Total energies of the cluster were calculated using an *ab-initio* Hartree-Fock self-consistent-field method using the Huzinaga-Dunning type [3, 4]. Contractions are [721/31], [631111/6111] and [4321/421] for Li, Na and K, respectively. The same basis set used by Tsuneyuki was applied for O. The interaction energies thus obtained with changing M-O distances in clusters were fitted to the potential function represented by Eq. (9.1). In addition to the Coulombic terms, the Gilbert-Ida type repulsive function, and an r^{-6} term were used, since the potential form of this type is successfully used for TTAM model.

The partial structures of the alkali metal ions surrounded by oxygen atoms are treated as follows. From the fitting of the obtained potential energy to the assumed functional form, several data sets representing the potential surface can be obtained. In such treatment, the best fitted values for the cluster are not necessarily the best one for the simulation of the bulk structure. This difficulty is coming from the non-linearity of the functional form and difference between the cluster and the bulk. To select the best one among these parameter sets to represent the system, MD simulations of lithium metasilicate (Li_2SiO_3) in crystalline state at constant pressure (0.1 MPa) were performed. If the balance of the parameters is not good enough, the crystal structure will be broken and therefore reproducing crystal structure under constant pressure (NPT) condition is a severe test of the quality of the parameters. Several polymorphs should be tested if structures are known.

Partial charge model was found to be better than the formal charge model.

Among several sets, a set of q_{Li}, a_{Li}, b_{Li}, and c_{Li} reproducing the experimental density of the crystal within ±0.10 g cm^{-3} was chosen and this parameter set can reproduce the structures well. The values of the parameters thus obtained are given in Table 9.1. Behaviors of the systems using these parameters were also checked by MD simulations in liquid and glassy states starting from the configurations obtained by the earlier work using an empirical potential model [5, 6]. The structures are consistent with the results by X-ray diffraction analysis [7]. Parameters for the sodium and potassium salts are obtained by similar procedures, where the c_{Na} and c_{K} terms were not necessary. The sets of parameters obtained for the sodium and potassium salts are also listed in Table 9.1. In MD programs available, many kinds of units are used including reduced ones. Since conversion of units itself brings some errors for the result of MD, we show it in the unit appeared in the original paper in Table 9.1.

Table 9.1 Parameters of the potentials for alkali silicates

Species	Q	a/Å	b/Å	c/Å^3 kcal$^{1/2}$ mol$^{-1/2}$
For lithium silicates				
Si[a]	2.40	0.8688	0.03285	23.18
O[a]	[b]	2.0474	0.17566	70.37
Li	0.87	1.0155	0.07321	10.87[c]
For sodium and potassium silicates (parameters of Si and O are commonly used)				
Na	0.88	1.0805	0.08461	0.0
K	0.85	1.4081	0.10070	0.0

[a] Taken from the TTAM model [2]

[b] Charge of the oxygen atom should be modified for charge neutrality of the bulk

[c] For the term $c_{Li}c_O$

Table 9.2 Atomic coordinates for lithium metasilicate (Li_2SiO_3) crystal

Atomic coordinates	Close packing	Our model (Partial charge model [1])	Experimental [8]	Experimental [9]
Li				
x	0.167	0.1722	0.160	0.170
y	0.333	0.3387	0.320	0.330
z	0.0	−0.0240	0.0	0.0
Si				
x	0.0	0.0004	0.0	0.0
y	0.167	0.1653	0.164	0.167
z	0.500	0.4986	0.537	0.496
O(1)				
x	0.167	0.1389	0.141	0.147
y	0.333	0.3062	0.321	0.310
z	0.375	0.4156	0.450	0.406
O(2)				
x	0.0	−0.0002	0.0	0.0
y	0.167	0.1056	0.100	0.108
z	0.875	0.8432	0.860	0.845

The atomic configurations in the metasilicate crystal obtained by our model are listed in Table 9.2 together with the experimental values [8, 9]. The atomic coordinate for the sodium salt and the potassium salt were also shown in Ref. [1]. Some other characteristics for crystal structure of the lithium metasilicate are given in Table 9.3.

The parameter set shown in Table 9.1 has following characteristics.

In this modeling, it was assumed that the repulsive parameters *a*, *b*, and *c* for the cluster are applicable for these crystals and that the difference in the parameters between cluster and bulk is mainly due to the different charges on the oxygen atoms. Thus the charge of the oxygen atom should be determined by the charge neutrality in the system even if the composition was different. Recently, the parameters were also checked for two polymorphs of $Li_2Si_2O_5$ crystals

Table 9.3 Structural parameters of the lithium metasilicate crystal

Characteristics	Ref. [8]	Ref. [9]	Our model (Partial charge model [1])
a/Å	9.36	9.38	9.55
b/Å	5.395	5.40	5.44
c/Å	4.675	4.68	4.68
Density/g cm^{-3}	2.52	2.52	2.45
Average distance Si-O/Å	1.60	1.65	1.61
Average distance Li-O/Å	2.08	2.01	2.00

[10, 11]. The assumption seems to work well including these systems. That is, in MD, the value q_O for each composition of crystals or glass is determined according to the charge neutrality of the system and not to that of clusters. For example, $q_O = -1.38$ is used for Li_2SiO_3 composition. This procedure brings some arbitrariness; however, charges assumed are reasonable when compared with several experimental works and theoretical work for related systems [12, 13] including recent ones on related systems. These parameter sets presented here can be applicable for systems with different M_2O: SiO_2 ratios, and even systems with different kinds of M only by changing the charge on the oxygen.

It is noteworthy that the potential include the charge transfer effect between alkali metal ion and oxygen atom. This is because the fixed charges are used in the fitted parameter sets, but not in the MO calculations of clusters. This also means that the effect of fixed charge is compensated by other terms in the function.

The parameter thus obtained can be used for the prediction of the unknown structures. Probably because of the deliquescent character, the crystal structure was unknown for potassium salt. Therefore, the parameters for the salt were selected to reproduce the density of the melt under 0.1 MPa (at 1673 K). Crystal structure starting from that for the sodium is found to be stable for potassium salt. Thus we can predict the structure of crystal by MD simulation [1].

Densities of these salts in the crystalline, molten and glassy states were also reported in Ref. [1]. The pair correlation functions for glassy and liquid lithium metasilicate by our model are quite similar to those obtained from MD simulation based on the empirical potential parameters in our previous work [5].

The functional form can be easily changed to the following one, which consists of the sum of a Buckingham potential and a Coulomb pair potential,

$$U(r_{ij}) = \frac{q_i q_j e^2}{r_{ij}} + A_{ij}\left[\exp\left\{-B_{ij} r_{ij}\right)\right\}\right] - C_{ij} r^{-6} \tag{9.2}$$

as found in Ref. [14].

There repulsive term can be also easily changed to the Born-Myer-Huggins form. Therefore, the parameters can be used by many kinds of MD simulations programs available.

9.1.1 Quality of the Parameters

So far, these parameters are successfully applied to silicate systems, and extended to some related systems for structures and dynamics. For example, diffusive dynamics of lithium and potassium disilicates were shown to be in semi-quantitative agreement with experimental ones [15]. Diffusion coefficient and viscosity in lithium disilicate system is comparable to the experimental values [16]. (See Sect. 9.9 for details.) Therefore the parameters seem to be good enough to discuss the mechanism of the dynamics and even to be able to predict properties. In spite of these successes, caution is required if one would like to use the potential parameters in the region, which is different from that used for the determination of the potential parameters. For the lithium and sodium salts, calculated thermal expansion rate seem to be smaller than the experimental ones. The charge distribution based on the very simple assumption may cause this discrepancy. Differences of effective charge distributions among crystal, liquid and glassy states were also neglected in the work. Therefore, applicability of the parameters to other situations should be checked sufficiently, depending on the purpose of each work.

Recently, Voigt et al. [17] has examined the network and clustering of Li ions in the silicate systems by both NMR experiment and MD simulations using the same potential parameters. For the region of low lithia contents ($x \leq 0.17$), the NMR data and the MD simulations were found conceptually to be in excellent agreement. They pointed out that the clustering found in MD simulations is generally less pronounced than that indicated by the NMR results, and a significant difference in the structure is observed for the lithium disilicate ($0.333Li_2O$–$0.667SiO_2$) glass. Their value of 39 % for Q_3 content (which is a measure of the distribution) is smaller than experimental one (~55 %). Interestingly, similar results are obtained from other potential parameters with different origins. Therefore, it is not clear if the discrepancy is caused by the potential parameters. Recently, Habasaki and Ngai have shown that there is poly-amorphism related to the different Q_n distribution in lithium disilicate [11]. The Q_n distribution observed for the system near 0 (or slightly negative) pressure is not far from the experimental result. It was also shown that the Q_n structure is sensitive for the system volume because each Q_n structure unit has its own specific volume. Therefore, the path during cooling schedule in P-V-T diagram better has to be taken into account for the discussion of the distribution (see Sect. 9.2 for more details).

One should note that further developments of long range structures or the possibility of the phase-separation, and partial crystallization were neglected in the MD simulations of limited time scale. One of the causes of the discrepancy from the experiments may be the difference in the cooling rate (or annealing time) between experiment and simulation, as already been pointed out by several authors [17, 18].

Although the effect of the cooling rate exists, dynamics in the rapidly cooled lithium disilicate is comparable to the experimental ones and this suggests that the effect of the rapid cooling rate is at least partially compensated for the effect of the small system size with periodic boundary condition (see, Sect. 9.9).

Of course, further refinement of the parameters is always desirable when more realistic simulations are required. Actually, for silica, which is the end composition of the silicate, development of the new potential parameters is still in progress. TTAM silica is known to give the slightly (~7 %) larger density than experimental ones. Beest et al. [19] have pointed out that the adjustment of short-range parameters to bulk properties is inevitable to improve the potential model of silica. Further efforts for improving the potential of silica are continuing [20–22].

9.2 Characteristics of the Structure

9.2.1 Statistics of the Framework Structures

Molecular dynamics simulations are useful to study the characteristics of the structures of glasses like the statistics of the framework (3D network) structure. Here we introduce one of such studies.

Zachariasen [23] assumed a random network structure for oxide glasses. In 1985, Greaves [24] examined the structure of glasses with ionic modifier by EXAFS. He proposed a modified random network (MRN) model. In this model, the alkali and non-bridging oxygen ions are micro-segregated to form regions rich in alkali (i.e., channels) within the network structure, and transport of alkali ions occurs inside the channels formed. In the case of the silicate systems, the ionic channels are formed by the network connected SiO_4 units. This structure is strongly related to the ionic dynamics and transport. For example, in mixed alkali silicate glasses, reduction of ionic diffusion coefficient is caused by mutual interception of paths by different alkali species [25–29], and this reduction is accompanied by the loosening of the glass structure [30] as will be explained in Chap. 10.

The MRN model seems to be successful for explaining many features of glasses and widely accepted. However, still one can ask the question: “Are the structures of glasses completely random?” and “How can we characterize the disorder?” Relevant to the consideration of the network structure is the presence of Q_n, which stands for an SiO_4 tetrahedron with n bridging oxygen linked to the silicon atom, and in principle n assumes integer values ranging from 0 to 4. The distribution of Q_n is useful to characterize the structure of molten, crystalline and glassy systems in the studies by experiments [31–34] and simulations [11, 35–39]. Therefore, our attention was focused on the distribution of Q_n structures here, although other characteristics such as number of rings or of its constituents, connections of Q_n structures can be also used for characterization of the network.

Typical Q_n strictures for $n = 1$–4 taken from our MD work is shown in Fig. 9.1. The coordination number of Si atoms around an Si atom has the same physical meaning as the n in the Q_n structure and can be used as a measure of the networks.

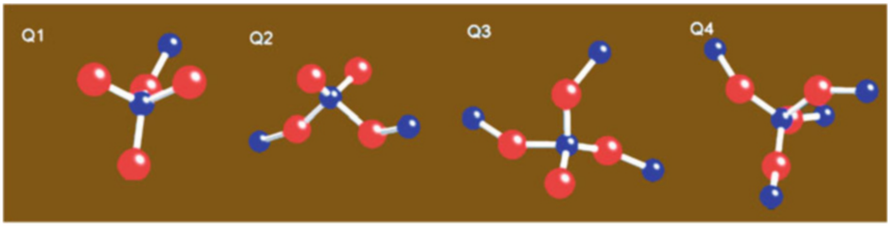

Fig. 9.1 Q_n structures observed in the MD simulations of lithium disilicate. Neighboring Si atoms connected with bridging oxygen are also shown. The partial volume of the SiO_4 unit is in the order of $Q_1 > Q_2 > Q_3 > Q_4$, because each bridging oxygen is shared by neighboring units

In alkali silicates, networks consisting of SiO_4 units are interrupted by the alkali metal ions of the network modifiers. Equilibration of Q_n species is governed by the following disproportionation reaction,

$$2Q_n \Leftrightarrow Q_{n-1} + Q_{n+1} \tag{9.3}$$

as well as that for the oxygen species,

$$2\mathrm{O}- \Leftrightarrow -\mathrm{O}- + \mathrm{O}^{2-} \tag{9.4}$$

Here −O− and O− stand for bridging and non-bridging oxygen, respectively.

9.2.1.1 Theoretical Backgrounds

Binomial Distribution and Hypergeometric Distribution of Q_n Units

In our previous work [25], distribution of −O− and O− in the lithium metasilicate and lithium-potassium silicate glasses has been examined and the mixing is found to be almost random, in the sense that the combinations of oxygen species around the alkali ions are as expected from the ratio of these species. Some theoretical models of Q_n structures are based on such randomness. Distribution of Q_n structures was derived by the disproportionation reactions [40–42] based on the mixing of the −O− and O− species with and without some modifications. Q_n distribution obtained by MD simulations is well represented by the binomial distribution, which is the simplest case of the multifractal. (See Appendixes A.4–A.6).

At first, the probability of finding −O− and O− is considered for each SiO_4 unit in lithium disilicate. We assume the oxygen show two states, −O− and O−, and all Si are in fourfold coordination as observed in the typical glassy state. In this case, the resultant distribution is binomial and the connection of Q_n units also can be binomial.

In this case, the Q_n distribution obtained from a mixing of two states is explained as follows [43]. When the probability of oxygen being −O− is represented as p_1, the probability of oxygen being O− is p_2 (=1−p_1). The probability for finding Q_1 species is represented by $p_1p_2{}^3$, where the −O− can be one of the four oxygen atoms in each unit. Therefore the number of the combination is $_4C_1 = 4$. In a similar manner, one can determine the probability and frequency (the binomial coefficient) for each Q_n value, where the iteration number n corresponds to the number of bridging oxygen atoms. Binomial distribution with equal probability is symmetrical, while we include the probability different from $p_1 = p_2 = 0.5$, which results in the asymmetrical distribution. Thus the joint probability of the distribution for Q_n with $n = 1$–4 is,

$$P(Q_n, n = 1, N) = \frac{N!}{n!m!} p_1{}^n p_2{}^m, \tag{9.5}$$

where, N (maximum number of oxygen atoms for each unit, 4) and $m = (N\text{-}n)$.

In this case, $P(Q_n)$ is a direct function of p_1.

Note that the probability p_2 is concerned with the oxygen around the Si and bonding oxygen is shared by two Si. It means that the same oxygen was counted twice in the Q_n distribution, and it also means that the volume of the oxygen is shared by two units. Therefore, when observed from oxygen atoms, the actual ratio of −O− to O− (p_1':p_2') is not p_1:p_2, but is $p_1/2$:p_2. In Fig. 9.2, a schematic description of the mixing of probability is shown for the $p_1 = 0.3$.

In the case of SiO_4 unit, the maximum step is 4. In general, with increasing number of mixing steps, the system becomes more heterogeneous. In this sense, binomial is a limit distribution having the maximum heterogeneity. If one compare this situation and the Cantor sets used for the explanation of multifractal, it is clear that the situation means the multifractal mixing of more than one exponent (for structures or states). A hypergeometric distribution is also possible for the combination of these species. In contrast to the binomial distribution, where the choice is

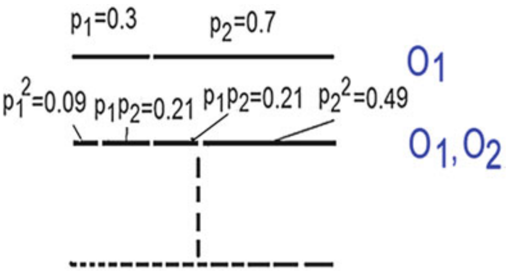

Fig. 9.2 Schematic description of binomial mixing of structures in glasses. One can suppose that p_1 is a probability for one oxygen atom being a bridging one. Two lines in the first column show the probability of the first oxygen (O_1) to be bridging (p_1) and non-bridging (p_2), respectively. In this case, $p_1 = 0.3$. In the next line, joint probability for O_1 and O_2 are shown and so on. The joint probability for oxygen atoms of SiO_4 unit determines the limit distribution of Q_n. See explanation of multifractal in Appendix A.4 for more general cases

taken with replacement, hypergeometric distribution is a discrete probability distribution, where the choice is from a finite population without replacement. Therefore, the distribution is possible in the case when the system is not fully equilibrated.

9.2.1.2 How Can We Examine the Statistics of Networks?

Here we consider the condition to examine the Q_n distribution to compare the result of MD with experimental values. Conventional procedures to examine the statistics of structures of glasses are by repeating the preparations of glasses by cooling or compression of the systems. In each run, the network structures of the system are almost fixed to one of the configurations at high temperature (or low pressure). Such procedure corresponds to the use of the "fictive temperature" in the MD simulations. Unfortunately, it is not so clear how many runs are enough for the sampling of the structures. It will depend on the system size, length scale of the structures to be examined and on the cooling schedule employed. It may also depend on the quality of the potential parameters. When we examined the system under different cooling conditions, the resultant Q_n structure has large standard deviations (i.e., percentage of Q_3 structure $P_{\mathrm{Q3}} = 42.8 \pm 3.1\ \%$, here probability of Q_3 structure, P_{Q3} was used as a measure of the Q_n distribution), which means that the resultant distribution in the quenched system fairly changes in each run.

Another possible ways to study the statistics is to examine the equilibrated or quasi-equilibrated structures near or above T_g. In Ref. [11], the distribution of the Q_n structures in lithium disilicate was examined near or above T_g, where the rearrangements of the Q_n structure are possible. As a long time averaged value at 1000 K and after the rapid cooling and further quasi-equilibration, the value of $P_{\mathrm{Q3}} = 39.5 \pm 1.0\ \%$ was obtained from 10 regions during 100,000 steps (100 ps) runs. These values are smaller than the recent experimental value ~55 %. The value $P_{\mathrm{Q3}} = 42.2\ \%$ is expected from the binomial distribution in lithium disilicate and therefore this structure of limiting case can be a basis to compare the observed Q_n distribution in MD and that in experiments. To consider the different situation in MD and experiments, we consider the effect of pressure, volume and history of the system as shown in the following sections. This is because each Q_n structure has specific volume, as explained in the caption of Fig. 9.1 and in following subsections.

9.2.2 Changes in the Q_n Structure Under Pressure

In following subsections, MD simulations are used for examination of Q_n distribution under pressure is introduced and roles of pressure or volume for determining the distribution will be discussed. Structural properties of lithium disilicate systems ($0.333\mathrm{Li_2O}{-}0.667\mathrm{Si_2O}$) were examined [11], where the presence of Q_n with $n = 2$, 3, and 4 is critical. The system studied consists of 768 Li, 768 Si, and 1920 O atoms in the basic cell with periodic boundary condition. Structural changes along the pressure-volume (*P*-*V*) diagram of lithium-silicate in the silica rich region have been examined. The assumption of two states in oxygen atoms nearly hold for lithium disilicate as found in the experimental observation by X-ray Photoelectron Spectroscopy (XPS) [44]. For the case of the disilicate composition, thus p_2' for the disilicate is 0.4, which is expected from the ratio of $Li_2O:SiO_2 = 1:2$, where 2 lithium ions can cut one bond to form 2 non-bridging oxygen atoms, as is well known from experiments.

Experimentally, Kitamura et al. [45] studied the densification of the lithium disilicate glass by pressure. The densification was explained as the change of packing caused by the distortion of the tetrahedral units. The question that arises is what happened to the Q_n with this densification? At first, the experimentally observed *P*-*V* relations were reproduced by MD simulation as shown in Fig. 9.3. Structural changes found in experiments are reproduced as well.

Then it was confirmed that the Q_n structure of the network glasses changes with densification. Some examples of the Q_n distributions obtained are shown in Fig. 9.4, where the distribution depends on temperature, as well as pressures.

In the work shown in Ref. [11], maximum of the Q_3 content was found near the $P \sim 0$ (or $P < 0$) region. This result is explained by the following arguments considering the specific volume of each Q_n structure. The relation between density and Q_n structures in alkali silicate glasses was previously suggested by Doweidar [46] by comparing the densities of systems with different alkali contents. The volume, V_n, of structural units Q_n are related in the order of $V_2 > V_3 > V_4$. With decreasing volume or increasing pressure, more compact structure with larger *n* value will be formed (see Fig. 9.1 and its explanation of the partial volume of units). Thus changes of Q_n distribution are driven by the changes of volume (or pressure). As reported in Ref. [11], some pairs of network structures with equi-volume, but having

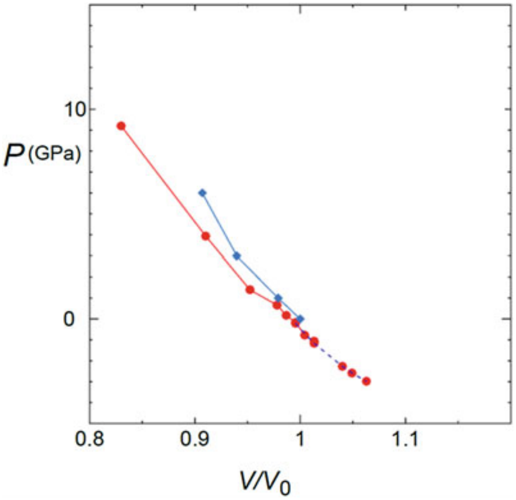

Fig. 9.3 Pressure against volume curves. *Red*: The trend obtained from MD simulation at 1000 K. *Blue*: Experimental value by Kitamura et al. at room temperature. The curvature reflect the trend of the changes in the repulsive energy in the system

Fig. 9.4 Example of Q_n distribution obtained at several conditions. *Brown*: $V = 18.8$, *Blue*: $V = 20.5$, *Purple*: $V = 21.4$, *Green*: $V = 24.4$ ($cm^3 mol^{-1}$), at 1000 K. *Red*: $V = 21.9$ ($cm^3 mol^{-1}$) at 1200 K. *Black* (*dotted*) : Binomial distribution for $p_2' = 0.4$, which is the simplest case of the multifractality

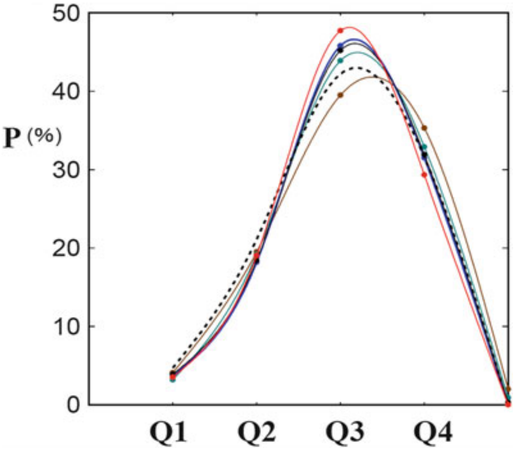

different distributions of Q_n (or different heterogeneity) were found when different compression (or expansion) schedule on the phase diagram was used, and this is related to the existence of polyamorphism and also the liquid-liquid phase transition in the system. This is understandable from the relation among the volumes of structural units, where the sum of the V_2 and V_4 is comparable to twice of V_3.

9.2.3 Time Dependence of the Q_n Distribution After Compression

It is interesting to learn how fast Q_n distribution can follow the volume change. In Fig. 9.5, time dependence of Q_n values is shown after a sudden change of V (in $cm^3 mol^{-1}$) at an initial time (t_0) at 1000 K. The initial configuration is the quasi-equilibrated state with $V = 22.4$. Volume was changed to 18.8 at t_0 with temperature kept constant. The percentages of Q_3, Q_4, Q_2, and Q_1 structures are shown from top to bottom. Changes in Q_n distributions occurred in two steps. At the early times from 0 to 15 ps, Q_3 and Q_4 increase, while Q_2 decreases. For the Q_3 structures, the maximum appears at around 15 ps. After that, the content of Q_3 decreases and that of Q_4 increases.

A structural change occurs within a short time even near the (computer) glass transition temperature.

9.2.4 Comparison with Experimental Q_n Distribution

Experimentally obtained Q_n values [32–34] and those by MD simulations [36] for the disilicate by several authors are not necessarily comparable directly, although the peak value of the distribution has been commonly observed at around Q_3.

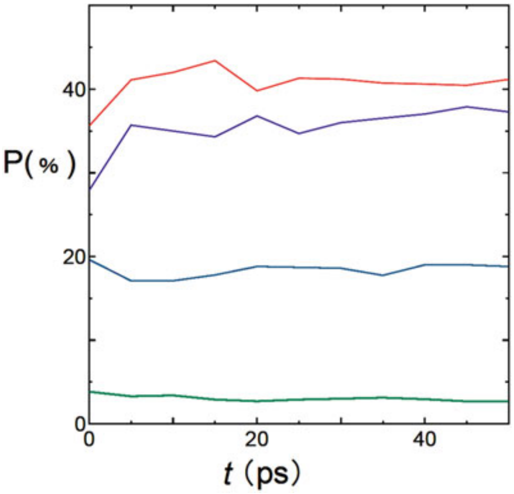

Fig. 9.5 Time dependence of the Q_n distribution with the compression of the volume (Percentages of Q_3 (*red*), Q_4 (*purple*), Q_2 (*blue*) and Q_1 (*green*) structures are shown) after the volume change of the system from $V = 22.4$ to 18.8 (cm^3 mol^{-1}). In this case, changes in Q_n distributions occur in two steps. At the early period, (0–15 ps) The Q_3 and Q_4 increases, while Q_2 decreases. Later Q_3 decreases. After the short time relaxation shown here, structures are nearly stable up to several ns regions

Recent experimental works tend to show ~55 % of Q_3 content, while typical classical MD simulations tend to show ~40 % including the value previously reported by Vogt et al., using our potential model. Du and Corrales [37, 38] showed quite similar trends for the distribution of Q_n. The results seem not depend on the details of the potential parameters used. The value ~40 % is not far from the expected value of the binomial distribution with 40 % of O−.

What is a cause of this discrepancy? The problem can be solved at least partially if we take into account of the position of the system in the *P*-*V*-*T* diagram. As expected from the specific volume of each Q_n structure, larger content of Q_3 species (~48 %) was obtained near the $P \sim 0$ region in our simulation. This value is larger than the typical value for the binomial mixing, although the value is slightly lower than the experimental value [34] (~55 %). That is, for molecular dynamics simulations of the Q_n distributions, it seems to be important to consider the different cooling schedule on the *P*-*V*-*T* relation and the complex phase behavior including poly-structures.

Several different causes of the discrepancy have been suggested so far and are summarized in Ref. [11]. For example, some works emphasize the role of cooling rate [36].

For the soda lime silicate glass, the Q_n distribution (P_{Q3} is ~63.7 %, while experimental value [34] is 70 %) in the formal charged potential with polarization term was reported [47] and importance of polarization term was suggested. For this point, further clarification seems to be required, because the term may be just compensating for the insufficient quality of the formal charge model.

We note here that the comparison of the experimental and MD value should be done at the comparable volume and pressure of the system (with modification by considering the quality of the potential model). This condition is not so obvious for the non-equilibrium situation under different cooling schedules and different ensembles.

In some of the MD or MC simulations, the structure seems to be forced to adjust to the experimental one by modifying the potential parameters; however, this procedure is not necessarily recommended due to the quasi-equilibrated nature of the glasses. Careful consideration and treatment of the result of such simulations seem to be necessary.

9.3 Are the Structures Random or Fractal?

When more species are taken into account, multifractal distributions are formed by the similar procedure to obtain binomial distribution. That is, binomial distribution is considered to be just the simplest case of the multifractal. Actually, other species such as (O^{2-}) can contribute, at high alkali content glasses and the species, SiO_5 also contributes at high pressure region. This multifractality of the Q_n distribution can be considered as a measure of the heterogeneity of the network structures and similar situation is found in the heterogeneous density profile made by ions [48]. In other words, different structural units (with different exponents) in the glasses form a multifractal structure rather than random one, which is modified by several conditions.

9.4 Temporal and Spatial Aspects of the Dynamics

9.4.1 Mean Squared Displacement (MSD) of Li Ions in Lithium Metasilicate

Experimentally observed complex frequency dependence of the conductivity is a function of the time development of mean squared displacement (MSD). Therefore, if we examined each process found in MSD, we can understand the process in each frequency region. In this section, several distinct time regions of ionic motions are characterized and then the temporal and spatial aspects of the dynamics are discussed based on the results of MD simulations [49, 50]. The MSD of the lithium metasilicate, which is located in the lithium rich region, is shown first in details.

The MSD can be obtained from the MD simulations data using the following relations.

$$<r^2(t)>= \left\langle \left\{ \sum_{i=1}^{N_i} (r_i(t) - r_i(0))^2 \right\} / N_i \right\rangle \tag{9.6}$$

Here the angled brackets represent the average over initial times. Using a sequence of particle positions during a run in period T_1, we prepared N arrays of data sequence with slightly shifted initial time t_0 values. The data for N arrays were averaged. The time range covered by chosen t_0 values is the time window δt. In a rapidly decaying system such as a normal liquid, the time window δt. of several tens pico seconds is long enough to obtain the macroscopic values. However, in the super-cooled liquid or glassy state, some properties depend on the time scale of observation, which is determined by the value of δt. A large time window, δt, and many numbers of initial times, N, are required especially at low temperature (and also under the pressure). This situation is common for systems showing slow dynamics.

If one knows the details of the MSD and nature of the motion during each time regions, then a full understanding of the time evolution of the ion conductivity relaxation as a function of time or frequency is gained. The ion dynamics changes with frequency because the complex frequency dependence of the conductivity, $\sigma'(\omega)$ are related to the MSD by Eq. (9.7) [51, 52].

$$\sigma^*(\omega) = -\omega^2 \frac{Nq^2}{6H_R kT} \int_0^\infty <r^2(t)> e^{-i\omega t} dt, \tag{9.7}$$

where N is the number density of mobile ions, q the ion charge, k the Boltzmann constant, H_R the Haven ratio and T the temperature.

9.4.2 Several Time Regions in the Mean Squared Displacement

MD simulations of lithium metasilicate system were performed using our potential model [53] previously derived on the basis of ab initio molecular orbital calculations (see Sect. 9.1). Pair potential functions of Gilbert-Ida type [54, 55] and r^{-6} terms were used. Typical cooling schedule used for obtaining the glass in our early works is described as follows. The system consists of 432 particles was used in early works. In more silica rich region, usually larger system size is required. The system with 3456 particles were used later.

The smaller system was equilibrated at 3000 K for more than 1 ns starting from a random configuration. The system was cooled to lower temperatures from high

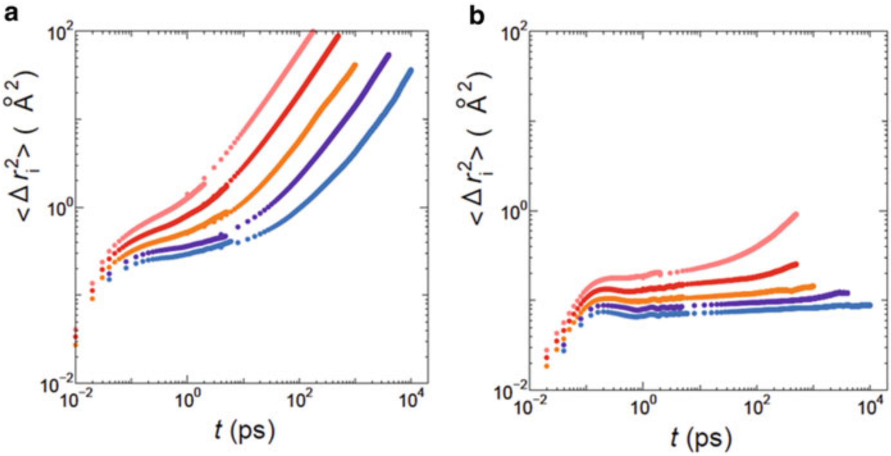

Fig. 9.6 (**a**) Temperature dependence of MSD of Li ions in lithium metasilicate (Li_2SiO_3) in molten and glassy states. Temperatures are 1200, 1000, 800, 720 and 630 K from *upper* to *lower curves*. (**b**) Temperature dependence of MSD of Si atoms in lithium metasilicate (Li_2SiO_3)

temperature to low temperature in the order of 3000, 2000, 1673, 1473, 1200, 1000, 900, 800, 700, 600 and 500 K. Typical cooling rate used ranges from 0.2 to 1 K/ps. At each temperature, the system was equilibrated adequately (~1 ns or longer) by NPT ensemble, and then the condition was switched to NVE, where the volume was fixed to the one obtained from the NPT run. The glass transition temperatures obtained by *T*-*V* relation was approximately 830 K.

Here we will show the results of the system with 3456 particles, i.e. the particles contained in the unit cell are 1152 Li, 576 Si and 1728 O for Li_2SiO_3. In this case, similar cooling schedule in the order of 3000, 2000, 1673, 1473, 1200, 1000, 900, 800, 720, 630 and 500 K, but with longer time was used for the equilibration at each stage. The results are almost the same as previous works for $N = 432$ systems, while the statistics are better [56]. In Fig. 9.6a, temperature dependence of MSD of Li ions in lithium metasilicate (Li_2SiO_3) is shown. The temperatures of the MSD curves are 1600, 1000, 800, 720 and 600 K from top to bottom.

The corresponding MSD for Si atoms are shown in Fig. 9.6b. At low temperature (<830 K) the motion of Si atoms are negligibly small, so that the system is in the (computer) glassy state in the sense that the motion of network is essentially suppressed during the observation time. The MSD of O atoms are slightly (about twice) larger than Si atoms at each temperatures, but show similar trend as the Si atoms and hence not shown here. Here we focus our attention only on the motion of the Li^+ ions.

In Fig. 9.7, MSD of Li ions, $<r^2>$, at 800 K is shown from 0.01 ps to a few ns. At the very short times we see the ballistic motion that has $<r^2> \propto t^2$ and then a combination of vibrational and relaxation contribution at longer times. Vibrational contribution to the MSD becomes constant after about 1 ps. The Li^+ time dependence of the MSD can be divided according to differences in properties into four

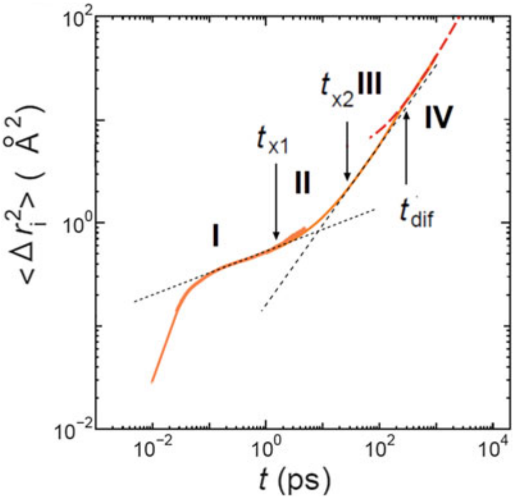

Fig. 9.7 Typical behaviors of the MSD of Li ions in silicate glass exemplified by lithium metasilicate glass at 800 K. *Dotted line* (*black*) means power law dependence in the region I. Short *dashed line* is power law in the region III. *Dashed curve* (*red*) means a linear dependence of the MSD in region IV. Characteristic times separating these time regions are also shown

time regimes, I to IV. Each region becomes longer and longer with decreasing temperature. The four time regimes of the MSD are delineated by three characteristic times, t_{x1}, t_{x2} and t_{dif}, and are shown in the figure.

It is useful to examine the van Hove functions and the intermediate scattering function in conjunction with the MSD to understand the behaviors of ions in each time regime.

The self-part of the van Hove function for the Li ion is defined by

$$G_s(\mathbf{r},t) = (1/N)\sum_{i=1}^{N}\langle\delta((t) - \mathbf{r}_i(0) - \mathbf{r})\rangle, \tag{9.8}$$

and the number of ions remaining in the original sites can be also calculated from

$$N(t) \equiv \int_{o}^{r_c} 4\pi r^2 G_s(r,t)dr, \tag{9.9}$$

where r is the distance traveled by the Li ion in a time t and $\mathbf{r}$ is the corresponding positional vector. The cut off distance r_c was chosen to be 1.7 Å. In Fig. 9.8a, b, the van Hove function of Li ions at 1673 and 800 K are shown, respectively.

If the motion is Gaussian type with diffusion coefficient D, the van Hove function is

$$G_s(r,t) = \frac{1}{(4\pi Dt)^{3/2}}\exp\left(-r^2/4Dt\right). \tag{9.10}$$

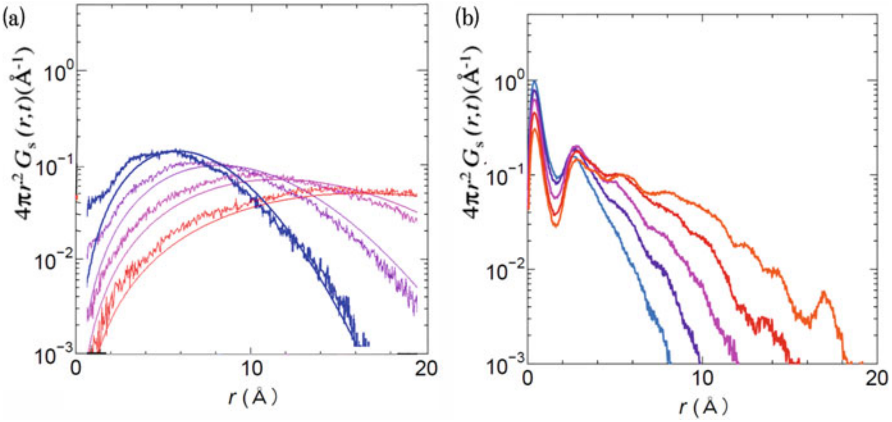

Fig. 9.8 Self-part of the van Hove function of Li ions (**a**) at 1673 K (for $t = 16$, 32, 64 and 128 ps from *left* to *right* in the curves of long ranged region), and (**b**) at 800 K (for $t = 50$, 100, 200, 400, 800 ps from *left* to *right* in the curves of long ranged region) in lithium metasilicate, respectively. Smooth curves in (**a**) are for the Gaussian type distribution having the same diffusion coefficient as the observed function. Same Colors are used when the time is the same

In Fig. 9.8a, the smooth curves are the Gaussian type distributions having the same diffusion coefficient as the simulation data are also shown. The same color is used to indicate the pair with the same time. At 1673 K, the function at short time region deviates from the Gaussian but soon becomes comparable to the Gaussian functions. On the other hand, at 800 K near the glass transition temperature in Fig. 9.8b, the deviation from the Gaussian function is clearly observed as well as slowing down of the dynamics. The first peak tends to remain for long time by caging and other peaks due to the jump motions were observed. Existence of the both first peak remaining long time and the long tail observed here means the heterogeneity of the dynamics [57] and will be discussed later in details. With the aid of these functions, each of the four time regimes of MSD is characterized as follows.

I. (The NCL region) An early time regime between approximately 0.2 and 2 ps, a power law behavior of $<r^2> \propto ct^{\alpha}$, with small and positive exponent α ($\approx$0.2) was found. From Eq. (9.7), this MSD corresponds to $\sigma'(\omega) \propto \omega^{1-\alpha}$ and $\varepsilon''(\omega) \propto \omega^{-\alpha}$ by the Maxwell's relation are also power laws. Thus this early time region corresponds to a nearly constant loss (NCL) [58–61], since α is small. Actually from our data we can only say that the increase of MSD is very slow in the regime. In this region, almost all ions are still in the cage formed by matrix oxygen atoms. This NCL region ends when the contributions of jumps to the MSD becomes clear starting at about t_{x1} (~2 ps at 800 K). Thus, the regime I exists in the time period of 0.2 ps $<t<t_{x1.}$

II. (Primitive ion jump region) In the intermediate time regime of about $2<t<20$ ps, the MSD rises more rapidly than t^{α} of NCL regime defined by 0.2 ps$<t<t_{x1.}$ In this region, MSD is almost linear when plotted against time, and the behavior is evidence of independent (i.e. non-cooperative) jumps or

the primitive relaxation of the Coupling Model of some Li ions. This linearity is brought by the accumulated number of jumps increasing almost proportional to time. End of the regime II is denoted by t_{x2}.

III. (Sublinear Diffusion Regime) After 20 ps and up to about 300 ps, the MSD has a time dependence well described by t^{θ} with $\theta \approx 0.77$. This is the time regime III, which corresponds to the ω^n power law in ac conductivity for cooperative ion hopping well described by the stretched exponential time correlation function of Kohlrausch, $\varphi(t) = \exp[-(t/\tau)^{1-n}]$, and with β identified with $1-n$. The slope $\theta = 1-n$ here is important to determine the time scale of the diffusive motion. In this region, jump to the next sites occurs more frequently and back correlated jumps are also frequently observed. This motion includes jumps of longer lengths with cooperative characteristics. (See Sect. 9.7 and Fig. 2.12 in Sect. 2.4.1 for the meaning of long jumps.)

    The exponent θ corresponds to $1-n$ in the coupling model. Experimentally, it is known for many systems that the near equality exist between E_a and βE_σ, where β is Kohlrausch exponent, E_σ is the activation enthalpies of conductivity relaxation and E_a is a short time activation energy observed in the same glasses [62]. Our observations for the single alkali systems mean that the apparent E_σ in the activation enthalpies of conductivity is a modified one by the geometrical correlations and not for each jump motion, while short time activation energy E_a is related to the jump motion.

IV. (Diffusive regime) It starts at time longer than about 300 ps, where the root MSD, $\sqrt{\langle r^2 \rangle}$, is about 3 Å, the average distance between neighboring Li sites. In this time regime, the steady state of the cooperative ion hopping has been established after coarse graining heterogeneous motions and the MSD corresponds to the frequency independent dc conductivity. The onset time of this regime, t_{dif} (about 300 ps at 800 K), is not exactly the same as the characteristic time scale, τ, in the stretched exponential correlation function but equal in order of magnitude. Thus approximately, regime III is defined by $t_{x2} < t < t_{\mathrm{dif}}$, and regime IV correspond to $t > t_{dif}$. Even in the regime IV, still the motion is heterogeneous, but is coarse-grained gradually by exchange of slow and fast ions.

Heuer and coworkers [63] also have performed molecular dynamics simulation on lithium metasilicate using the similar potentials based on our potential model. In many ways their results are similar to ours [49, 50]. One major difference is that long and/or successive jumps are missing in their representation of trajectories. We note that such motions are rare but the contribution to the MSD is large, because the distance is squared in MSD. Existence of such a motion, explains the functional form with a long tail of the self-part of the van Hove function well (see Sects. 9.5, 11.5, 11.10 and Appendix A.2 for more details). Many experimental findings are also comparable to the results of MD [64].

9.4.3 Intermediate Scattering Functions

The signature of cooperative ion hopping motion in time regime III also can be inferred from the time dependence of the self-part of the Li ion density correlation (or intermediate scattering) function defined by

$$F_s(k,t) = \left\langle \sum_{j=1}^{N} \exp\left\{i\mathbf{k}\cdot\left(\mathbf{r}_j(t) - \mathbf{r}_j(0)\right)\right\} \right\rangle \Big/ N \tag{9.11}$$

In Fig. 9.9a, the wave number dependence of the function of Li in lithium metasilicate at 800 K is shown for $k = 2\pi/0.8$, $2\pi/1.0$, $2\pi/1.5$, $2\pi/2.0$, $2\pi/3.0$, $2\pi/5.0$, $2\pi/10.0$ and $2\pi/15.0$ Å^{-1}. A faster decay is observed for larger wave number (short length scale motion) at short time scale, while the decay of the smaller wave number (long length scale motion) start at longer time scale. Corresponding plots of log[-ln($F_s(k,t)$)] against log$t$ are shown in Fig. 9.9b. In this plot, stretched exponential form shows a straight line. Curves with small wave numbers in Fig. 9.8b have straight portion that starts at about 10 ps. The lines for $2\pi/5.0$, $2\pi/10.0$ and $2\pi/15.0$ Å^{-1} are also shown in the figure. Obviously, the stretched exponential region corresponding to the region III of the MSD is clearly found in the $F_s(k,t)$ with smaller k or at longer length scale. This means that the stretched exponential decay function and power law dependence of MSD are contributed mainly by ionic motions longer than neighboring distance. The time scale t_{dif} in MSD is comparable

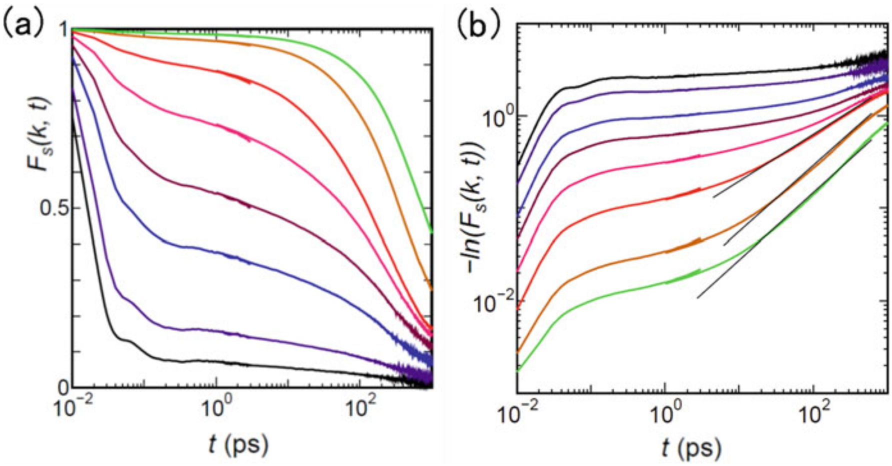

Fig. 9.9 (**a**) Wave number dependence of the intermediate scattering function of Li in lithium metasilicate at 800 K is shown for $k = 2\pi/0.8$, $2\pi/1.0$, $2\pi/1.5$, $2\pi/2.0$, $2\pi/3.0$, $2\pi/5.0$, $2\pi/10.0$ and $2\pi/15.0$ Å^{-1} from *bottom* to *top*. (**b**) log[−ln($F_s(k,t)$)] against log t plot of the same data. The color of the curve for each wave number is the same as in (**a**). In such a plot, stretched exponential form looks like lines. Note that the stretched exponential decay is clearer in the small wave number regions

to the effective time scale, τ, of the stretched exponential decay in the intermediate scattering function.

It is to be noted that the stretch exponent in the stretched exponential time dependence of $F_s(k,t)$ is k-dependent. For $k = 2\pi/10$ Å^{-1} the stretch exponent of $F_s(k,t)$ determined from the slope for $t > 20$ ps is not too different from the exponent in the t^{1-n} dependence of the MSD in time regime III. On the other hand, for larger $k = 2\pi/3.0$ Å^{-1}, the stretched exponent of $F_s(k,t)$ is noticeably smaller than that of the MSD. This difference as well as the dependence of $(1-n)$ on k may originate from the stronger effect of ion-ion interaction in slowing down the dynamics at shorter distances (larger k). An analogy of these findings is the difference between the ion dynamics probed by nuclear magnetic resonance and d.c. conductivity [65, 66] which had been explained by the same reasoning (see Chap. 5). In any case, the stretched exponential time dependences of $F_s(k,t)$ for several values of k are further indications of the onset of cooperative ion hopping motion at about 20 ps. The value of the onset time seems to become shorter for larger wave numbers and the change in the slope becomes less clear. Such plots of $F_s(k,t)$ were used to also determine the onset of cooperative ion hopping at other temperatures.

The starting point of stretched exponential decay at 1200 K and at 1000 K (both not shown) was found to be equal to approximately 1 and 2 ps, respectively. The change of van Hove function at 1200 K with time in the time regime of 0.2–2.2 ps is similar to that observed at longer times between 2 and 20 ps, i.e. regime II ($t_{x1} < t < t_{x2}$) at 800 K.

9.4.4 Time Regions Found in Lithium Disilicate Glass

Li ions in the lithium disilicate system in more silica rich region show the comparable regions for MSD but with smaller diffusivity. MD simulations have been also done for the lithium disilicate system with 3456 particles. The particles contained in the unit cell are 768 Li, 768 Si and 1920 O for $Li_2Si_2O_5$. Time regions found in the lithium disilicate at 800 K are shown in Fig. 9.10. Behaviors of MSD of Li ions in the lithium disilicate glass are summarized as follows.

Region I (NCL): An early time regime between approximately 0.2 and 2 ps where the MSD increases with time as t^{α} with $\alpha \approx 0.07$, and the ions are caged.

Region II (primitive jump region): In the intermediate time regime of about $t_{x1} < t < t_{x2}$, the MSD rises more rapidly than t^{α} of regime (I). MSD is nearly proportional to time here.

Region III (Power law region) MSD depends on t^{θ}. Both fast and slow ions are found here and the slope is affected by the back-correlated motion of jumps.

Region IV (Diffusive region): At time longer than about 2 ns, the MSD assumes the linear t dependence, where MSD reaches to the square of the typical neighboring distance of ion sites.

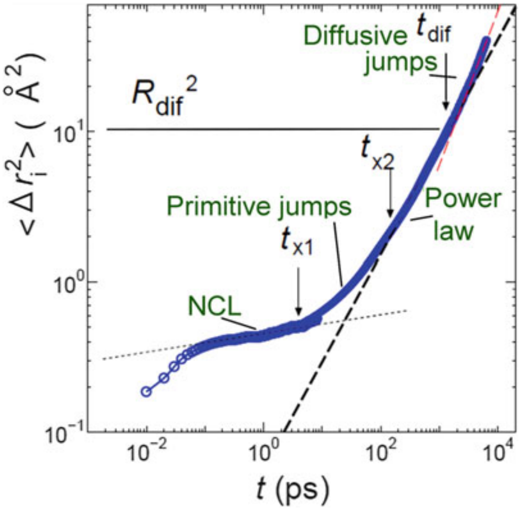

Fig. 9.10 Typical behaviors of the MSD of Li ions in lithium disilicate glass at 800 K

Comparison with Figs. 9.7 and 9.10 reveals that there is a quite similar feature but with different time scales. Namely, the time scale of each region becomes longer with decreasing LiO_2 content. (See Sect. 9.9 for the composition dependence of the diffusion coefficient.)

Common features of development of MSD are also seen in other compositions and are related to the decay of the cage, and the gradual transition (or broad crossover) at longer times to ion hopping ac conductivity and the terminal transition to the dc conductivity region.

9.5 Dynamic Heterogeneities

Dynamics of ions are found to be quite heterogeneous. To illustrate the heterogeneous dynamics of the Li^+ ions, the ions were divided into two groups in some works [57, 67]. The particles showing a squared displacement less than the square of the distance equal to the first minimum of the Li-Li static structure factor $g(r)$ is defined as type A. Namely, the ion is located within neighboring sites during a given time, t_{local}. Particles showing a squared displacement greater than the square of the distance equal to the first minimum of $g(r)$ are defined as type B, which can contribute to the long time and longer range dynamics.

The criterion used is consistent to the trend observed in the self-part of the van Hove function. As shown in Fig. 9.8b, change of the height of the second peak is small for a certain time period. The decreases of the initial peak seem to be balanced with the development of the third and further peaks and the latter is found after the saturation of the second peak. In other words, particle moved to the next shell tends to be localized within the neighboring sites, and after that further peaks are developed due to the longer scale motion. That is, the dynamics have hierarchical structure consisting of localized motion and forward correlated motions. This feature is different from the behavior at high temperature, where the peak position itself moves from left to right with elapse of time.

For example, types A and B particles are distinguished by MSD using time window, δt of 80 ps (100 points of initial t) during t_{local} of 920 ps (~$2t_{\text{dif}}$) at 700 K in Ref. [57]. The MSD of all Li ions shown in Fig. 9.6 is the weighted average of MSDs for type A and type B particles, i.e.,

$$\left\langle r^2(t)\right\rangle = \left(N_A\left\langle r_A{}^2 > +N_B\left\langle r_B{}^2\right\rangle\right)/N, \tag{9.12}$$

where $<r_A{}^2>$ and N_A are the MSD and number of type A ions respectively. Similar definitions apply to the quantities for the type B ions.

In the first jump, the jump distance is nearly the same for both types A and B. The MSDs of the ions of both types are almost the same until t_{x2} is reached. Both A particles (with high probability of backward correlated jumps) and B type particles (with high probability of forward correlated jumps) behave as if they jumped freely or independently before t_{x2}. Even if we start the observation from any jump, the first jump looks like a free jump, since the displacement is not modified by jump angles. In this sense, the first jump is a special jump that the influence of the other ions is not detected for the single particle motion, and microscopically this is the origin of the region II. At time t_{x2} there is the change from primarily apparent free independent jump to the correlated jump process with modified jump angles. This fact is consistent with the independent ion jump relaxation time (i.e. the primitive relaxation time of the Coupling Model) τ_{o} being about the same as t_{x2} (see Figs. 9.7 and 9.10), because we expect the jumps are independent for $t \ll \tau_{\text{o}}$ and more or less independent for $t < \tau_{\text{o}}$. After t_{x2}, slow and fast ions contribute to the MSDs with time dependences t^p with $p < 1$, and t^q with $q > 1$, respectively. The "mean" squared displacement is less than the distance of the first minimum of $g(r)$ at t_{dif}, however the fast ions moves longer distance as found in the self-part of the van Hove functions. Type A and type B ions show dynamics with different wave number dependences, naturally because mainly type B ions contribute to the long time diffusion. Both fast and slow dynamics have been observed in the stretched exponential region. The cause of the fast dynamics of type B ions in the stretched exponential region and in the longer time region is the cooperative jump motion. This property has been deduced from the observation of a tracer ion, where we find that the angle of the next jump is affected by the other ions.

Although some arbitrariness always exist for the definition, we note that the existence of the localized and accelerated motions corresponds to the laminar and burst states as observed in the deterministic chaos [68] caused by external field. Such dynamics with a length scale distribution has a characteristic of Lévy flight [57, 69] dynamics (see Sect. 11.2 and Appendix A.2.2–A.2.4). For each ionic motion, the force from other ions plays roles as an external force, which causes anomalous diffusion.

Recently, Montani et al. [70] have analyzed the same system using our potential model, by using the concept of the propensity. Isoconfigurational Method (IC) and the associated concept of particle propensity introduced by Widmer-Cooper et al. [71]. Highest propensity particles (HPPs) are taken as those particles that at time t^* (It corresponds to t_{x2} in our definition) have a displacement greater than one half of the distance of the first maximum of the pair correlation function. The result shows the existence of the cluster of the high-propensity and this is consistent with our results. Some differences are observed due to different definition of the fast and the slow categories. In their definition, the localized ions within neighboring sites are included as the fast ions. It was also shown that the distinction of fast and slow ions already starts at the early time region. The overall behaviors observed are consistent with our findings.

9.5.1 The Non-Gaussian Parameter

The non-Gaussian (N-G) parameter [72],

$$\alpha_2(t) = (3/5) < r^4(t) > / < r^2(t) >^2 - 1, \tag{9.13}$$

characterizes the deviation of $G_s(r,t)$ from the Gaussian form. We have evaluated $\alpha_2(t)$ of the Li^+ ions from their displacement distribution function of time at several temperatures. In Fig. 9.11, the N-G parameters of Li ions for lithium metasilicate at

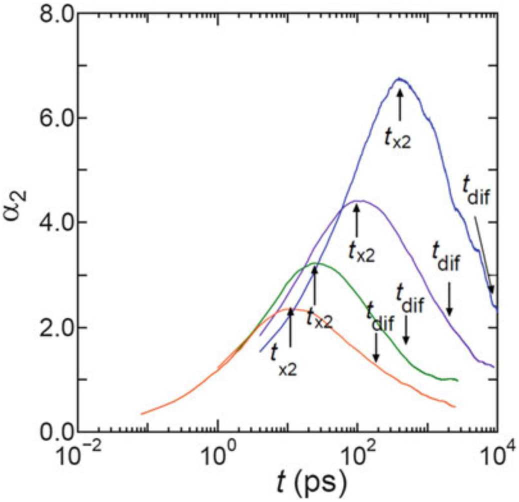

Fig. 9.11 Non-Gaussian parameters of Li ions in lithium metasilicate at 800, 700, 600 and 500 K from *bottom* to the *top*. Peaks are found at t_{x2}. The parameter tends to decreases at 800 K towards 0. The parameters become plateau values at several times longer than t_{dif} ~τ at 600 and 700 K, while the plateau is not attained at 500 K during the observation time. In the glassy state the plateau value is greater than 1

800, 700, 600 and 500 K are shown. For each temperature, the $\alpha_2(t)$ starts out from small values at short times, increases throughout regimes I and II and attains the maximum value. The value $\alpha_2(t)$ of Li^+ ions in metasilicate peaks near t_{x2}. At higher temperatures, the maximum of $\alpha_2(t)$ of Li^+ moves to shorter times and it is also located near t_{x2} and τ_o.

The maximum of $\alpha_2(t)$ observed near the t_{x2} is due to the some ions having jumped out to just the neighboring sites. Therefore it does not mean that the largest heterogeneity due to coexistence of slow and fast ions is observed at t_{x2}. The parameter tends to decreases at 800 K or higher temperatures towards 0. In a time scale longer than t_{dif}, fast ions are changed to slower ones and vice versa, and after several times of t_{dif}, mixing of the dynamics is observed as an average.

The parameter reaches a plateau value at several times longer than $t_{\mathrm{dif}} \sim \tau$ at 600 and 700 K, while at 500 K the plateau has not been attained during the full observation time. From the trend at 800 and 500 K, one may expect that the dynamics becomes Gaussian at long times and the non-Gaussianity it merely the problem of the limiting time scale of observation. However, there is no reason to assume that the situations at 800 and 500 K are entirely the same. In the glassy state at 700 and 600 K, plateau value is greater than 1 and the value increases with decreasing temperature. It suggests that the non-Gaussianity ion dynamics remains at long times in the glassy state. This scenario with non-ergodic character is possible when the permanently localized ions remain in the system. With decreasing temperatures, the value of α_2 at t_{dif} increases and the value at the plateau also increases. Therefore it is probable that the value of α_2 in the long time limit deviates from 0 at the quite low temperature.

Even the long time limit behavior is Gaussian, one should note that the dynamics of the system are always heterogeneous. This is because one can observe the heterogeneous dynamics always by using an arbitrary chosen initial time in the MD simulations after equilibration.

9.5.2 Some Characteristics of the Dynamics in NCL Region

So far we have considered the motions of the Li ions in Regime I and relate them to caged ions dynamics and the NCL in susceptibility loss. However, in the NCL region, matrix atoms, oxygen and silicon, are moving at the same time. Their mean square displacements are smaller than that of Li and do not contribute to the NCL directly. Instead their motions cause deformation of the cages, which in turn affect the trajectories of Li ions. In particular, the Li ions having large displacements experience what we call “dynamic anharmonicity” originating from the fluctuating cage potential. After a large amplitude motion and a back correlated jump, the Li ion may not necessarily return to the original position because of changes in positions of surrounding atoms accompanying the cage drift. In turn, the dynamic anharmonicity causes dissipation or relaxation of the Li ions in the form of the NCL.

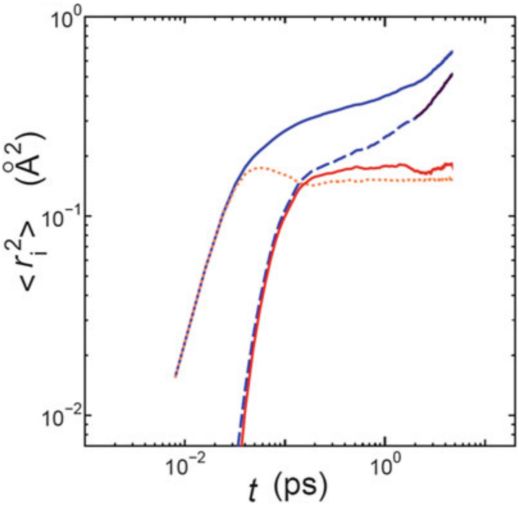

Fig. 9.12 In short time region including NCL, components of the MSD for Li in Li_2SiO_3 at 700 K are separated. *Blue solid curve*: MSD of Li ions. *Orange dotted curve*: MSD of Li ions in a cage, where the motion of all oxygen atoms are frozen. Difference of the above two curves is shown by *blue dashed curve*. Black part of this curve is for contribution of independent jumps. The t-linear contribution shown by the *black curve* was subtracted from the difference. The final *red curve* is due to the oscillation (boson) and the relaxation (NCL)

In fact, without the influence from the motions of the matrix atoms, the slightly positive slope of MSD in NCL of the Li ions does not appear in our simulations [73]. This was shown by the component analysis with the results presented in Fig. 9.12.

Mean square displacement of the Li ions from a simulation at 700 K, wherein all oxygen atoms are frozen, was shown by an orange dotted curve. It is clear by comparing this result with the normal $<r^2>$ (blue solid curve) that the NCL is no longer there. Subtracting $<r^2>$ of fixed cages from $<r^2>$ of mobile cages, the result (dashed blue curve) exhibits the $t^{1.0}$-dependence (black part of the curve) of jump contribution in the region $t_{x1} < t < t_{x2}$ of Li ions. Subtracting once more this term, the final result shown by red solid curve should be the mean square displacement corresponding solely to the NCL and oscillation (related to the boson peak). Hence, the origin of the NCL, though from Li ion motions within their cages, is indirectly related to the motion of the matrix atoms since it disappears when the motions of the matrix (deformation and drift of the cage) are frozen out. Thus the result in Fig. 9.12 demonstrates that the NCL involves the correlated motions of the caged Li ions with the matrix atoms, and originates from the dynamical anharmonicity incurred during such motions.

Effect of correlated motion in NCL region is also clear from the fractal dimension analysis of trajectories of ions. In the method, complexity of the trajectories is measured by N_T, how many times are required to cover the trajectory using the ruler of length L_r. Further details of the method are described in Appendix A.1. For the frozen oxygen atoms case, the plot for N_T against L_r for the trajectories of Li ion has an exponential form, for L_r less than about 2 Å. This is in contrast to the fractal character in the normal case of mobile oxygen atoms. Therefore it is also clear that the power law dependence usually found is caused by the perturbation by the surrounding matrix atoms.

In ionic system, interaction among Li ions and with other surrounding atoms is dominated by the ion-ion interaction. Therefore it is interesting to consider the electrostatic field around each ion. As shown in Sect. 8.2.8, the field can be represented by the summation of the multipoles but with moving cages.

9.5.3 Characteristics of Jump and Separation of Temporal and Spatial Term

9.5.3.1 Definitions of Jump Motions

Jump like character of the motion is found even at high temperature regimes and it becomes clearer at lower temperatures. This is a natural result of the motion among the clearly separated peaks in the $g(r)$ or the van Hove functions. Among several possible definitions of jumps, we used the following one in some of our works [27]. Because of the existence of these peaks, the motion with a displacement greater than 1/2 of the distance of the first maximum, $g(r)_{\mathrm{maxM\text{-}M}}$, can be used as a criteria of jumps. Algorithm used in this analysis is simple and is summarized as follows. Large scale motion was picked up by using a critical velocity, v_c. The region with $\Delta|r|/\Delta \mathrm{t} \geq v_c$ can be regarded as jumps, while that with $\Delta|r|/\Delta \mathrm{t} < v_c$ can be regarded as waiting times. Time interval Δt and a critical velocity v_c determine the magnitude of coarse graining of the fine motions. The values of v_c and Δt were chosen so that the characteristics of the displacements are well reproduced ($\Delta t = 0.8$ ps and $v_\mathrm{c} = 1.7$ Å/ps in the analysis of that presented here). It is useful to separate the contribution of temporal and spatial terms of the dynamics as shown next.

9.5.3.2 Separation of Temporal and Spatial Term

Jump motion of ions can be characterized by the temporal (jump frequency) term and spatial term (geometrical correlation among successive jumps) [See Sect. 2.4]. Here it will be shown how we can distinguish these two contributions [74].

The MSD is considered as a product of the “number of jumps against time plot” and the “MSD against number of jumps plot”. The former is concerning with the temporal characteristic of the jump motion, while the latter is for the spatial character of the jump. For the MSD of Li ions in metasilicate system shown in

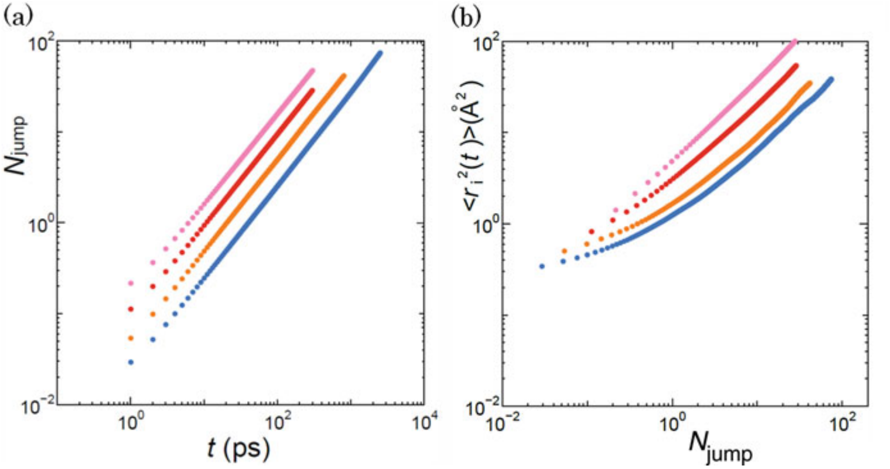

Fig. 9.13 Separation of temporal and spatial terms in MSD of Li ions in lithium metasilicate. Temperatures are 1200, 1000, 800 and 630 K from *top* to the *bottom*. Colors are the same as in Fig. 9.6. (**a**) Accumulated numbers of jumps were plotted against time. (**b**) MSD is plotted against accumulated number of jumps. The plots in (**a**) are almost linear functions for all temperatures examined. Therefore, the curvature found in the MSD is due to spatial term (geometrical correlation among successive jumps)

Fig. 9.6, both terms were separated at four selected temperatures as illustrated in Fig. 9.13. The method is applicable for both the jump motions in the slow dynamics and the jump-like motion at higher temperatures. In Fig. 9.13a, the mean values of the accumulated jump number, N_{jump}, per ion are plotted against times. In Fig. 9.13b, the MSD is plotted against the mean accumulated number of jumps. In Fig. 9.13b, curvatures of the function comparable to the time dependence of the MSD, including a power law exponent are observed. Therefore, changes of the slope of the time dependence of the MSD are due to those in the spatial term, that is, geometrical correlation among successive jumps. Small MSD found at the low temperature is clearly in the region where a mean number of jumps is less than 1 for Li ions. That is the changes in the "regions" and the "slopes" in the time dependence of the MSD and corresponding power law exponent is caused by the spatial term.

For the temporal term, one may consider the possibility that the long time trapping in the glassy state can affect the slope. However, it is not the case for the equilibrated or quasi-equilibrated state. Almost linear relation (slope ~ 1 in log-log plot) is found at all temperature examined. This means that the number of jumps in each time interval is unchanged during the observation time at each temperature. In fact, this is quite natural because one can start the observation at any arbitrary chosen time. In other words, jump motions of ions are renewal process, which can start again from the next ion site, and the number of the jumps per unit time is kept unchanged. In Fig. 9.13b, the mean displacements of ions reaches the typical neighboring distance (~3 Å) at t_{dif}. This situation is attained not by single jumps but after several motions among the neighboring sites. Here the time scale, t_{dif} is much longer than the time sale of each jump motion especially at low temperatures. In both kinds of plots, the absolute values decrease with decreasing temperature. Both the number of jumps per unit of time and the effective distance per each jump change with temperature, while the curvature of the plot and the change in the slope is controlled by the spatial term. The diffusive motion is modified by the back correlated motions and not only determined by the jump rate. Furthermore, the power law exponent of MSD can modify the dynamics by many orders of magnitude. Such characters of the temporal and spatial terms seem to be quite common for a variety of systems including bio-systems.

9.5.4 Heterogeneity Shown by Fractal Dimension Analysis of Trajectories

Generally, geometrical character of the jump motions can be directly examined from the trajectories of ionic motions obtained from MD simulations [73, 75]. Fractal dimension of the random walk, d_{w} [76], is one of the measure of the complexity of the trajectories (see Appendix A.1).

The power law dependence $\sim t^{\theta}$ of the MSD, is characterized by d_{w} from the relation $\theta = 2/d_w$ [77] when the geometrical term governs the slope. For free random walk, one can expect that $d_{\mathrm{w}} = 2$. The values of d_{w} larger than 3 mean that the trajectories are folded many times by backward correlation. On the other hand, strong forward correlation reduces the values of d_{w}.

The fractal dimension of random walk, d_{w}, is defined by

$$N_T = A{L_r}^{-d_w}, \tag{9.14}$$

where L_r is a length of the divider and N_T is how many times are required to cover the trajectories. Thus the value can be determined from the slope of the N_T against L_r plot in a double logarithmic scale.

When this kind of analysis was applied in the results of MD simulations, two different length scales were found in the trajectories in single alkali silicates. In the case of ionic motion in lithium metasilicate [75, 78, 79], the slope of the plot is found to change at about 3 Å, the distance between neighboring Li sites. At 700 K, $d_{\mathrm{w}} = 3.09$ for $L_r < 3$ Å and $d_{\mathrm{w}} = 2.61$ for $L_r > 3$ Å. On the other hand, at 500 K, $d_{\mathrm{w}} = 3.57$ for $L_r < 3$ Å and $d_{\mathrm{w}} = 6.75$ for $L_r > 3$ Å. From these results, we find the motion in the NCL regime has fractal character up to large lengths. The dimension >3 means a strong localization. The large value found for d_{w} at 700 K is consistent with the motions at 500 K having larger backward correlation. Thus exponent d_{w} is a parameter that characterize the motions of caged Li ions as well as diffusive motion. Existence of more than one exponent means the presence of multifractality of the dynamics.

9.5.5 Different View for the Temporal and Spatial Terms

In above discussions, we have explained the origin of the power law dependence of MSD by the geometrical correlations among successive jumps. However, different views might be found in literatures.

From the concept of the continuous time random walk (CTRW) [80, 81], one might expect that jump rate decrease gradually, when the residence time has some distribution with a tail [82, 83]. Then the power law behavior of the MSD might be explained by the existence of waiting time distribution with a power law. Actually, the existence of the waiting time distribution of jump motion is directly observed in several systems using the molecular dynamics simulations [84–88] both in real and configurational spaces. However, existence of the waiting time distribution does not mean it is a cause of the power law dependence of the MSD (see also Sect. 2.4.2). This situation will be discussed in the present section.

In the case of waiting time distribution, further behaviors of the ion (or particle) are not considered after that the marked ion is moved out the initial site. This situation is not the same as the measurement of MSD, where the ion moved out the initial site returns back to the previous site or continues further jumps. That is, jump motion is a renewal process in the quasi-equilibrated situation and in MSD, successive motions of ion (or particle in general) should be taken into account again after the jump to the neighboring site [87]. Therefore, the motion is affected by the angles between successive jumps. Furthermore, the time dependence of MSD in Fig. 9.6 is observed from any arbitrary chosen initial times. It means that mean behavior of many ions in ionically conducting glasses in the quasi-equilibrated state are kept constant, because ions with long residence time can change into the one having a short residence time and *vice versa*. Similar change also occurs for different length scales of motions.

That is, only when one observe a jump of the ion marked at time 0, but do not observe the motion of it after that, the waiting time looks like a time dependent one.

Lammert et al. [88] have determined the ion sites (or the cluster containing them) and tried to characterize the ionic motion from the property of them. Different impression may be acquired when the observers' view point is on the ion sites instead of ions themselves. In their analysis, characteristics of cooperative or successive motions as well as single jumps are divided into sites without considering the renewal of the process [87]. In the analysis shown in Fig. 9.4 in Ref. [88], both the waiting time and back correlation probabilities are represented as a function of time. Thus the apparently different view from Lammert et al. originates from the different observation method but not necessarily contradicting ours. Further differences due to the different definitions of sites and jumps are discussed in the Sect. 10.3. Caution has to be exercised in accepting their characterization of the ionic motions by division into sites because this way obscures the role of cooperative dynamics by successive jumps, although in some cases such coarse-graining may be useful.

Situation with the non-equilibrium relaxation is different from that discussed above. If non-equilibrium relaxation towards the more localized state occurs during the observation time, one can expect increase of the number of the particles trapped in the specific sites with time. This situation is revealed by the dependence of the MSD on the absolute observation time. Such situation is found for the early work of ionic system by Soules and Busbey [89] and also observed in the non-equilibrium relaxation in the SC system [90].

This kind of behaviors can be observed during equilibration in the MD runs of ionically conducting glasses or during a long time run in a quasi-equilibrated situation.

The KWW relaxation observed in many kinds of experiments can be explained by the distribution of relaxation times in several theories. It is noteworthy that the relaxation time discussed there does not correspond to each jump motion, but to the time scales modified by the geometrical correlation among successive jump motions.

9.6 Comparison with Other Systems

It is interesting to point out the same properties, such as several time regimes found in the MSD of lithium ions in lithium silicate glass, are found in the MSD of colloidal particles, reported by Weeks et al. [91]. Time regions observed here can be divided into four regimes, demarcated by t_{x1}, t_{x2}, and τ, in exactly the same manner as for the MSD of the Li ions. In the time regime $t_{x1} < t < t_{x2}$, the cage correlation function decays faster than when $t < t_{x1}$. The decay is even faster when $t > t_{x2.}$ The similarity between the Li ion dynamics in Li silicate glasses and colloidal supercooled liquids goes further than their MSD. The maximum of $\alpha_2(t)$ at a time near t_{x2} is found also in the colloidal supercooled liquids. The analogous properties have been shown for colloidal suspensions with volume fractions $\phi = 0.56$ in Fig. 4.55 of the Chap. 4.

Similar time and temperature dependences of $\alpha_2(t)$ were found in molecular dynamics simulation of a supercooled binary Lennard-Jones liquid as well as ionic liquids. For the binary L-J liquid, the time dependence of the mean square displacement $<r^2(t)>$ of the A particles and the non-Gaussian parameter $\alpha_2(t)$ at several temperatures are taken from the work of Donati et al. [92], and shown in Fig. 9.14. The heterogeneous dynamics in colloidal suspension and Lennard-Jones supercooled liquids are thus quite similar to the ionics in the ionically conducting system. The common dynamics governing these interacting systems are consistent with the universal dynamics predicted by the Coupling Model by one of the authors [93]. Moreover, based on the view point obtained from MD simulation, it is probable because all these systems show the jump motion which has rather common deterministic characters.

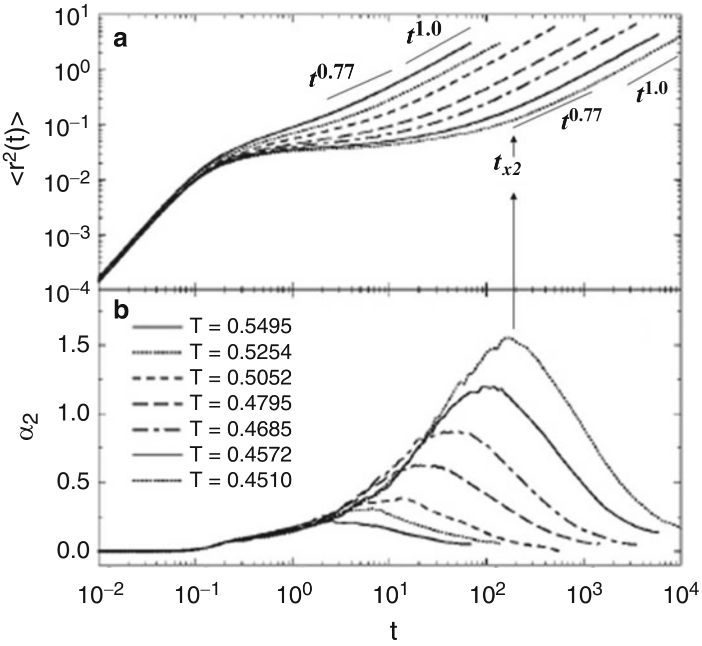

Fig. 9.14 (**a**) Mean square displacement $<r^2(t)>$ of the A particles of binary L-J liquid versus time for several values of T. (**b**) Non-Gaussian parameter $\alpha_2(t)$ vs time for the same values of T as in (**a**). From Ref. [92] and reproduced by permission

9.7 Cooperativity of the Motion and Vacancy Dynamics

One of the possible methods to examine the ionics is based on the analysis of sites and paths of ions. Lammert et al. have characterized the alkali ion sites in lithium silicate glasses by MD from the probability density of ions accumulated during MD runs using our potential model [88]. They found the number of sites is only slightly bigger (~2 or 3 %) than the number of ions, when a certain cut off value is used to pick up sites or clusters. For a coarse-grained description of the dynamics, such analysis is useful.

Existence of the limited numbers of sites is natural in the glassy state, because almost all the free volume in the molten state is lost when the system is vitrified. This character of the sites affect a waiting time distribution and back correlation probability of the jump motion; that is, in a dense material, ions or atoms must wait until destination becomes empty before it can jump over. If the neighboring sites are occupied, ion tends to be bounced back to the original sites. When the neighboring sites tend to be occupied by other ions, it is difficult for ions to move independently. Therefore, it is closely related to the occurrence of the cooperative motion of ions.

In a longer time scale, exchange of fast and slow ions occurs. Exchange of mobile and immobile ions requires~several ns in the case of lithium metasilicate at 700 K [94], which is several times longer than t_{dif}. Therefore, accumulation time used for the analysis of sites and paths by the density profile should be long enough to cover the exchanges of fast and slow ions, otherwise, only the sites for strong localization of ions will be found.

Qualitatively, the small number of sites discussed above are reasonable. Notwithstanding, if we counted all possible sites visualized, more sites (~10 %) were found [95] for the same system, in spite of the fact that the same potential model is used. This difference of the result is coming from the multifractal character of the density profile (see Ref. [76] and Appendixes A.3–A.5) formed by the mixing of localized and accelerated motions with different exponents. Characterization of such sites and paths can be done using the multifractal analysis of the density profile. By this analysis, the fractal dimension of the structure is represented by the singularity ($f(\alpha)$) spectrum where the densest part (α_{min}) is related to the localized sites, while the rare part even near α_{max} is related to the diffusive motion. In this situation, small sites (in size) mean that the ion visit the site for only short period and moves to the different sites soon. Such sites can contribute to the diffusive dynamics significantly. This description of jumps by vacancy is closely related to the cooperativity of ionic motions. Example of cooperative jumps of three ions is shown in Fig. 2.11 of Chap. 2. In this example, the first ion shows a long jump (~twice of the typical distance among ion sites) without a clear trapping. The second ion is found to be located between the sites for a while, until the vacant site is available. Thus availability of the vacancy is closely related to the cooperative jumps. Compared with single jump, which tends to return to previous site, cooperative jumps of several ions are rarer events but they form ion channels [33, 85–87].

As mentioned above, the small number of ion sites reasonably explains a long waiting time of the jump motions and the successive motions of ions using the same vacancy. As easily understood, the motion of vacancy means that the atom moves in the opposite direction of it. If the c_v of vacancies diffuses with the diffusion coefficient D_{v}, the diffusion coefficient of atoms, D is represented by $c_v D_{\text{v}}$ which is well known. Therefore, it is possible to map the ion dynamics by vacancy dynamics [96] using effective back correlation probability of ions. In this case, the probability includes the effect of cooperative motions. Of course, the apparent vacancy dynamics is a result of particle-particle interactions because usually in the molecular dynamics simulations the interactions between a particle and a vacancy or that among vacancies are not included.

With the measure of the cooperativity at t defined by

$$N_{coop}(t) = \frac{\sum\limits_{ij} X_i(t) X_j(t)}{\sum\limits_{i} X_i(t) X_i(t)}, \tag{9.15}$$

where $X_i(t) \equiv (\mathbf{r}_i(t) - \mathbf{r}_i(0))^2 - <r^2(t)>$, Heuer et al. observed [62] that N_{coop} is about 2–5 in the lithium metasilicate from 1200 to 600 K. These values are consistent with our findings [57, 67] and also with the expected value for the Haven ratio ($=1/N_{\mathrm{coop}}$) [97]. It is known that the Haven ratio decreases with concentration of alkali ions and the ratio is ~0.3 in high alkali content glasses [98, 99]. The number of N_{coop} is relatively small as a value but it does not mean the cooperative motion is negligible.

Comparison of the role of vacancies in glasses and crystals [10] is briefly mentioned here and will be discussed in details in Sect. 9.10. In the perfect crystalline lithium disilicate, diffusion coefficient of Li ions is several orders smaller than the glasses, although the situation remarkably changes by introducing vacancies. Although the vacancy mechanism is common for glasses and crystals, the mechanism in the glass is different from that in the crystal. In the latter, the characteristics of sites are rather homogeneous and the dynamics is more Gaussian like.

Importance of available volume as revealed by the vacancy is consistent to the validity of thermodynamic scaling (see Chap. 7 and Sect. 8.3.5). Interestingly, the thermodynamic scaling represented by the TV^{γ}, where V is the specific volume and γ is a material constant is found to hold in substructure of ion channels in the ionically conducting glasses [100] and it means the importance of the available volume for the motion, which affects the complexity of trajectories of ionic motion. In this sense, the concept of "free volume" still works.

9.8 Mixing of Heterogeneity and Its Life Time

The fast and slow dynamics tend to mix with each other, and the behavior becomes more the averaged one governed by the law of large number. That is, mean value of the sample $\mathrm{u}_1,\mathrm{u}_2$,--- $\underline{\mathrm{u}}_{\mathrm{N}} = (1/N)(\mathrm{u}_1 + \mathrm{u}_2 + \text{---} + \mathrm{u}_{\mathrm{N}})$ converges to a certain value <u> by the law, if the events occur randomly at longer time scale than t_{dif}. Even if the deviation from the mean behaviors is large as found in the glass or super-cooled liquids, one can expect the existence of distribution of fluctuation represented by the following equation [101], based on the large deviation theory (The above law of large number resulted in the Gaussian form in the case of small deviation of order $N^{-1/2}$. If the deviation is order N, it obeys the large deviation theory).

$$S(u) = -\lim_{N\to\infty}\frac{1}{N}\ln P_N(u) \tag{9.16}$$

where $P_N(\mathrm{u})$ is a probability density of the mean value of u. Thus the long time limit behavior after the mixing of fast and slow motions is not necessarily a Gaussian form. This is consistent with the non-zero value of the non-Gaussian parameters of long time, at least in the long time accessible in our MD simulations.

Mixing behaviors of fast and slow dynamics are common with other glass forming materials. Recently, three or four time correlation functions or related experiments are used to extract life times of heterogeneity and/or mechanism of it [102, 103] related to the glass transition problem. If the slowest motion of some species (i.e., the immobile ones) does not change to the fast one, the behaviors of ions (or atoms or molecules) cannot be averaged. Therefore, the life time of the heterogeneity is determined by the slowest species and existence of permanently localized component makes the system non-ergodic one. To consider this mixing, it is interesting to learn how the temporal change is being correlated with the spatial change, while the conventional multi-time correlation function does not distinguish these two terms. For the ionic system, direct determination of the life time of the components was performed [85–87]. It was also examined how the temporal heterogeneity correlate with spatial heterogeneity. In lithium metasilicate, temporal term and spatial term are found not necessarily being correlated [94], although some correlations might be assumed in theoretical treatment. Similar analyses are possible in other systems.

9.9 Comparison of Dynamics Obtained by MD and Experiments

Direct comparison of MD data with experiments is important to make in order to guarantee the applicability of the MD simulations for some problems. In the beginning of the history of MD simulations, comparison of the dynamics obtained with experimental values was not easy because of limited time scales of observation and/or of poor quality of the potential parameters. Furthermore, in the study of glasses or glass transitions, one may consider that the extremely rapid cooling rate used in MD might cause a problem when one compares them with experimental values. Nowadays, direct comparison becomes easier. In this section, it will be shown that the diffusion coefficients obtained from a rapid quench in MD using the reasonable potential parameters are comparable to experimental values. This observation suggests that smaller system size with a periodic boundary condition has compensated for the effect of rapid cooling. For this purpose, comparison of MD data and experimental values in lithium disilicate is made. In MD simulation shown here, our potential parameters (see Sect. 9.1) are commonly adopted by other researchers and by us.

9.9.1 High Temperature Region

So far, several authors have compared the experimentally obtained transport properties and those by MD simulations in the high temperature regime. For the lithium disilicate composition, many experimental data have been reported.

Kawakami et al. reported the experimental electrochemical determination of cation interdiffusivity [104]. Diffusion coefficients obtained from MD simulations by Gonçalves and Rino [105] were consistent with the experimental result of the diffusion of Si atom in the molten state. In Fig. 9.16, their MD data (open circles, blue) are plotted against inverse of temperature. The data for oxygen atoms are also shown (open diamond, pink). Their viscosity data obtained by the Maxwell relation [106] using τ_α of intermediate scattering function of Si were also found to be consistent to the experimental values [107] at least for the high temperature region $T > 2000$. They also compared the diffusion coefficient for Si with the viscosity obtained from a relaxation and that obtained from experiment via Eyring relation [108]. Even nowadays, calculation of viscosity at lower temperature region is not easy, however, they suggest that the Stokes-Einstein (or the Eyring) relation seems a reliable measure except for near the glass transition. Diffusion coefficients of Li ions at high temperatures acquired by them (open squares, red) are comparable to experimental data by Bockris et al. [109], where conductivity data at high temperatures were used to calculate the diffusion coefficient of Li ions.

9.9.2 *Low and Medium Temperature Region*

Self-diffusion coefficients of Li ions represented by inverse triangles in Fig. 9.15 were obtained from the interpolation of our MD simulations data using a power law dependence of composition as to be explained later. Corresponding our MD data directly obtained for the disilicate composition (open inverse triangles, purple) with a high cooling rate (~10 ps/K) are also plotted in Fig. 9.16. They are in good agreement with each other. Approximate values (black line) of the experimentally obtained diffusion coefficients gathered from literatures by Nascimento et al. [111] are also shown in Fig. 9.16, for the sake of comparison. It is worth to note that they are comparable to each other, in spite of the different conditions of preparations of the sample. Our MD data obtained by the interpolation of other compositions seem to connect smoothly at low temperature data, while there seems to be a gap between our data thus obtained and those by Gonçalves and Rino, although they are located in a different temperature region. Therefore, we added the data between these values in Fig. 9.15.

9.9.3 *Role of Different Cooling Rate*

MD data obtained by interpolation were obtained by a rapid quench (10–100 K/ps), while the data in Ref. [105] were obtained by using relatively slow cooling rate of ~1 K/ps. In the case of slower cooling rate in Ref. [105], the results seem to be negatively deviated from the rapidly cooled cases. It suggests that a different behavior is introduced by the different cooling rate. To clarify it, we re-examined

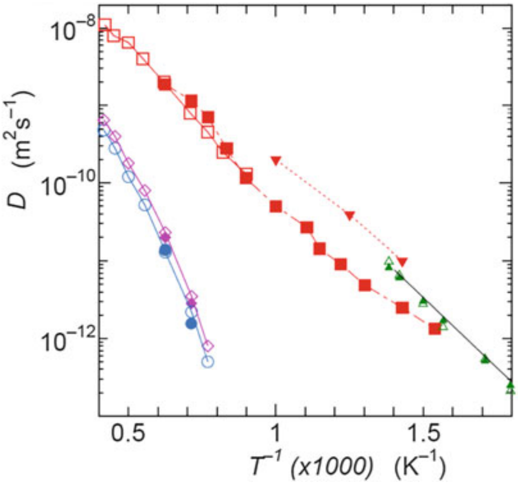

Fig. 9.15 Comparison of diffusion coefficients of lithium disilicate system obtained from experiments and MD works by several authors. Rapid cooling case: *Open reverse triangles* (*purple*) are for the MD data, while *filled reverse triangles* are obtained from interpolation based on the power law composition dependence of the MD obtained by rapid cooling of several systems. These values seem to be smoothly connecting experimental values (*filled* and *open triangles*) in Ref. [110] and the line (*black*) representing an approximate position of experimental data gathered in Ref. [111]. Slower cooling case: *Open squares* are taken from the data of MD [105], which is comparable to the experimental values (not shown) of melts by Bockris [109]. *Open circles* and *open diamonds* are MD data for Si and O in Ref. [105], respectively, where the data for Si is comparable to the experimental values (not shown) in Ref. [104]. MD data using the slower cooling rate than those in Ref. [105] are also shown (Li: *Filled squares*, *red*; Si: *filled circles*, *blue*; O: *filled diamond*, *pink*). The data show a concave shape and it accompanied with the decreases of system volume even in the super-cooled liquid regime (~1000 K). Errors in our MD data are within the size of marks. For errors for other data, see references

Fig. 9.16 Power law composition dependence of the diffusion coefficients [65] of Lithium silicate system $(Li_2O)_x$-$(SiO_2)_{1-x}$ 700 K: *open squares, green*; 800 K: *filled circles*, *blue*; 1000 K: *open circles*, *red*

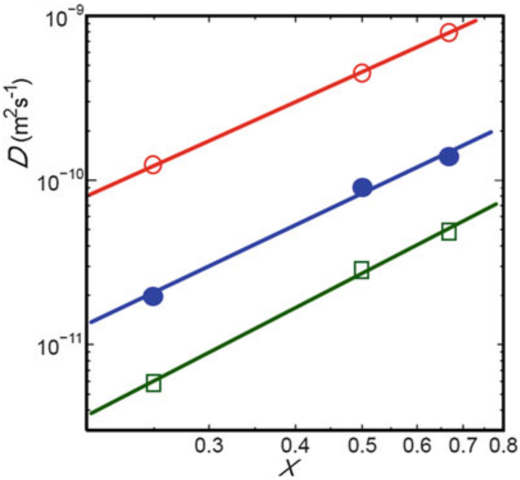

the diffusion coefficients of Li ions in a slower cooling rate. MD data for Li ions obtained by slower cooling rate of 0.2 (K/ps) were also plotted (filled squares, red) in Fig. 9.15.

As shown in this figure, the data at the high temperature region are comparable to the values given in Ref. [105] and the negative deviation was reproduced. The value decreases with decreasing temperature and deviation from the rapid cooling case increases in the medium temperature region. The deviation becomes smaller at low temperature region and the value becomes only slightly lower than the experimental value at $T \sim 600$ K. At the low temperatures, the diffusion coefficient might be affected by the non-equilibrated nature of the system even after quasi-equilibration of several ns, and it contributes to the curvature of the temperature dependence.

In other words, the values obtained by slower cooling rate have a concave shape in the medium temperature region.

We confirmed that the slower cooling rate accompanied the decrease of the system volume at around 1000 K, namely it occurs by annealing of the silicate frameworks during the slow cooling schedule [100]. It is in contrast to the fact that the volume change in the rapidly quenched system is negligibly small below 1000 K. Interestingly, thermodynamic scaling of the diffusion coefficient seems to hold well [100], i.e., the diffusivity is a function of the volume including the cases with different cooling rates.

Observed larger volume change in the slow cooling case is reasonably explained by the relatively smaller system size with periodic boundary condition of MD simulations, and effective cooling rate in this case is even slower than the experimental one. That’s why we mentioned that the effect of the smaller system size with a periodic boundary condition has compensated for that of rapid cooling rate.

9.9.4 Composition Dependence of the Diffusion Coefficient of Li Ions in Lithium Silicate

Maass [112] has predicted that the activation energy of DC conductivity decreases logarithmically with increase of alkali contents from critical path analysis, that is, this dependence is explained it by percolation of jump sites.

As shown in Fig. 9.16, the power law relation holds well for the composition dependence of diffusion coefficient of Li ions in lithium silicate systems by MD [95] and this is a basis of the interpolation used for the estimation of MD data in Fig. 9.15. We note that this dependence is accompanied with the contributions of cooperative jumps, especially in lithia rich region [95].

Recently, Bauer et al. [110] have reproduced the trend of composition dependence in lithium silicate experimentally and their data are in good agreement with our MD data. Interestingly, composition dependence seems to vanish [113, 114] in tempered samples (at 500 K) as pointed out in Ref. [110].

9.10 Comparison of Dynamics in Crystal and Glass

Dynamics in the glassy and crystalline states are markedly different, although coexistence of fast and slow ion dynamics is commonly observed in the same composition of the materials. The difference is worth a close examination in this subsection.

Comparison of the diffusion coefficient (or conductivity) in crystal and glass of the same composition reveals that the diffusivity of the glass is several orders of magnitude higher than the crystal [10, 115–117]. In lithium disilicate, Küchler et al. [115] have shown that conductivity in the glass is larger than the corresponding crystal. Similar trends are experimentally known for other systems.

In the case of $LiNbO_3$, the conductivity in the glass is many orders of magnitude greater than that of the single crystal of the same composition [116]. The same trend is also reported [117] for the conductivity in the glass formation region in AgI-Ag_2O-P_2O_5 system compared with the crystal of the same composition.

This trend found in experiment is well reproduced by the MD simulations in the comparison of lithium disilicate crystal and glass [10]. In the lithium disilicate crystal, both heterogeneity and anisotropy of the ionic motion are found. Because of small diffusion coefficient in the crystal, the motion was examined in a high temperature region.

In Fig. 9.17, trajectories of Li ions in the lithium disilicate crystal (stable form) at 1400 K are shown by projections onto the A-B and B-C planes, where the trajectories are overlapping because the motion started at (0, 0) position at $t = 0$. Both localized jumps within neighboring sites and longer jumps are observed there. In this figure, dense part of the plots near (0, 0) position for all ions means the strong localization within neighboring sites as exemplified by a trajectory in blue color. The dynamics of all the ions are anisotropic and the motion along the C-axis through zigzag paths exists as shown by an example of trajectories in light green color. Such zigzag motion is also found in other crystals. In the study of colloidal crystal, Derks et al. has argued [118] that such motion is an effect that arises *via* interaction with particles in the neighboring layers. At the same time, the long length scale motion contribute to diffusive motion is found shown by a trajectory colored purple, and thus the contribution from this rare event is non-negligible.

In Fig. 9.18, self-part of the van Hove Function of lithium ions in lithium disilicate crystal at 1400 K for $5 \times 2 \times 5$ system (1800 particles) in the stable form is shown. In this case, diffusive regime is attained after ~10 ns. Distinct peaks and overlaps of curves in the second peak are respectively evidence of the clear jump character and strong localization within neighboring sites. Although the motion is non-Gaussian even at the longest time (the non-Gaussian parameters is 0.6 at 64 ns), the power law tail of the van Hove function is not clearly developed. In the crystals, the existence of heterogeneity in the dynamics is related to the anisotropy of the crystal structure as shown in Fig. 9.18. Naturally, the motion in the crystal is highly cooperative since the simulated crystal is a perfect one without defects. Anisotropic motion is closely related to the dynamic heterogeneity in the

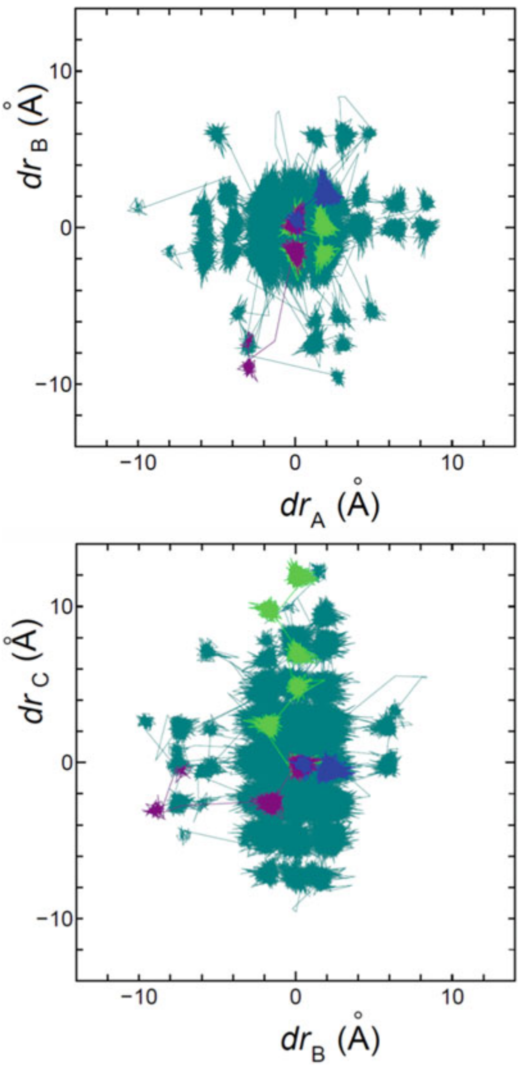

Fig. 9.17 Trajectories of Li ions in the lithium disilicate crystal in the stable form, during 32 ns at 1400 K for 5 × 2 × 5 system. *Upper panel* is projection onto the A-B plane, *bottom panel* is a projection onto the B-C plane, respectively. *Dark green*: all Li ions. The motion of arbitrary chosen three ions (one shows the largest mobility) are shown by different colors. Motions of ions are overlapped so that the motion start from (0,0) positions at t = 0. This kind of plot with a common origin for many particles is comparable to the self-part of the van Hove functions. One can imagine how the peaks of the function are formed by both localized and accelerated motions. Contribution of long jumps is found as in the glass

crystal. However, the diffusive motion in the glass is not merely the average of anisotropic motion of the corresponding crystal. Stronger deviation from the Gaussian dynamics in the glass is a proof of the contribution of the interactions from other ions (and atoms) in the system.

The difference of ion dynamics in glass and crystal has been brought out experimentally in a.c. impedance spectroscopy by Munro et al. [119] and in ^{7}Li-NMR spectroscopy by Franke and Heitjans [120]. They studied both the glass $Li_2O{\cdot}Al_2O_3{\cdot}4SiO_2$ and its crystalline counterpart β-$LiAlSi_2O_6$, (β-spodumene) by ^{7}Li-NMR. The frequency dispersion of the a.c. conductivity or the electric modulus of the crystalline samples is narrower than that of the glassy counterpart. The

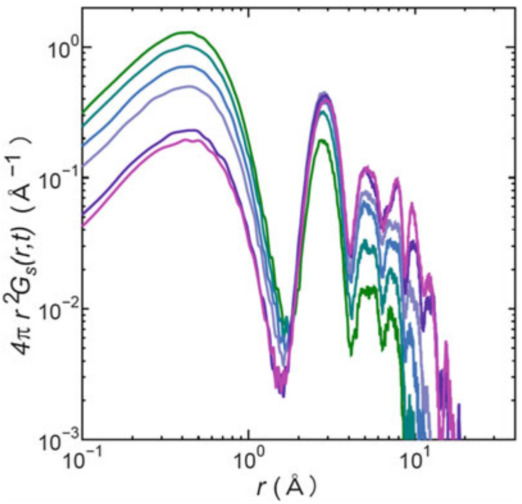

Fig. 9.18 Self-part of the van Hove Function of lithium ions in lithium disilicate crystal at 1400 K for 5 × 2 × 5 system in the stable form. From *upper* to *bottom curve* in the first peak corresponds to 3.2, 6.4, 12.8, 22.4, 44.8 and 60.8 ns, respectively. Distinct peaks and overlaps of curves in the second peak means that the clear jump character and strong localization within neighboring sites, respectively. Although the motion is non-Gaussian even the longest time, the power law region is not clear

difference indicates that the degree of cooperativity of ion dynamics is less in the crystal than in the glass. The spin lattice relaxation (SLR) time T_1 of ^{7}Li in the glass and the crystal shows a diffusion-induced peak in $T_1^{-1}(T)$. Comparison of the positions of the maxima and the slopes of the low-T sides of log T_1^{-1} vs $1/T$ curves shows that the Li$^+$ jump rate in the glass is higher and the activation energy is lower than in the crystal. These results are consistent with the MD simulations.

Comparison of the caged ion dynamics in polycrystalline and glassy $Li_2O{\cdot}Al_2O_3{\cdot}4SiO_2$ has been made by dielectric relaxation measurements at frequencies higher and temperatures lower than the conductivity relaxation by Rizos et al. [121]. The data show the near constant loss (NCL) is present in both the polycrystalline and glassy states of $Li_2O{\cdot}Al_2O_3{\cdot}4SiO_2$. Further, its magnitude and temperature dependence is comparable in both forms of the same substance. Again these experimental findings are consistent with MD simulations.

9.10.1 Role of Defects in the Crystal and Glass

By introducing defects in the crystal, diffusivity of ions drastically increased. This trend is also reproduced by MD [10]. It was found that the ion dynamics observed in the crystal with defects are more Gaussian-like as compared with the corresponding glass of the same composition. It means that the mechanism of the diffusion is not the same as in the glass as revealed by the different degree of non-Gaussianity. The motion in the glass is more heterogeneous than the crystal with or without defects, and the result again brings out that the ion dynamics in the glass is accelerated by the fast ions in the heterogeneous dynamics. One problem remains to discuss the dynamics of ions in the crystals by MD is that the number of jump events observed is too small during the observation time. Therefore high temperature tends to be used to examine it. This condition might cause a change of the mechanism of the ionic motion. Therefore further examination of long runs at low temperature regions is desired.

9.11 Conclusion

Structure and dynamics of ionically conducting glass are examined by MD simulations. For structure, importance of the history of the system in *PVT* relations is pointed out to explain the Q_n distribution, where n is a number of bridging oxygen atoms in SiO_4 units. This also suggests the existence of polymorphs in the lithium disilicate. Relation between the concept of the multifractal and Q_n distribution was discussed.

Jump motions of ions and characteristics of several functions can be also analyzed by MD. As discussed in Chap. 2, distinct time regions in MSD corresponds to the frequency dependent regions of the conductivity. The existence of the near constant loss (NCL) of caged ions has been established from the molecular dynamics simulation results of Li metasilicate glass. In the next or second time regime, $t_{x1} < t < t_{x2}$, the change of $4\pi r^2 G_s(r,t)$ with time is more rapid, indicating the inset of the jump motions to the neighboring sites. Concurrently an increasingly more rapid increase of $<r^2>$ is found in this time regime, but its time dependence is not a fractional power law until after $t_{x2.}$ In the third time regime, $t_{x2} < t < t_{dif}$, $<r^2>$ has the time dependence of a power law, t^{1-n}, with a fractional power. Here t_{dif} is a beginning of the diffusive regime, approximately the time after which $<r^2>$ is proportional to t. In this third time regime, a second and further peaks at a distance between Li^+ ion sites develop in $4\pi r^2 G_s(r,t)$ and grows with time, indicating significant number of Li ions have jumped out of their cages to neighboring and further sites to participate in cooperative motion to longer distances. Still many ions are localized and therefore the motion is heterogeneous.

The self-part of the Li^+ ion density correlation function, $F_{\mathrm{s}}(k,t)$, in the same time regime is a stretched exponential function of time, which also is the signature of cooperative or collective dynamics.

Generality of the dynamics is suggesting the common physics governing the relaxation and diffusion of interacting systems. Displacements of ions at tdif are not for the first jumps of ions but that several jumps as shown in Sect. 2.4.1. Therefore, the relaxation rate is affected by angles among successive jumps.

Generally, temporal and spatial contribution in MSD can be separated by the analysis of jump motions of ions. Some different views brought out by other workers using the same potential models were compared and the causes of the apparent differences were explained.

References

1. J. Habasaki, I. Okada, Mol. Sim. **9**, 319 (1992)
2. S. Tsuneyuki, M. Tsukada, M. Aoki, Y. Matsui, Phys. Rev. Lett. **61**, 869 (1988)
3. H. Dunning, P.J. Hay, in *Gaussian Basis Sets for Molecular Calculations*, ed. by H.F. Schaefer. Modern Theoretical Chemistry, vol. 3 (Plenum Press, New York, 1977), p. 1
4. S. Huzinaga, J. Andzelm, M. Klobukowski, E. Radzio-Andzelm, Y. Sakai, H. Tatewaki, Gaussian Basis Sets for Molecular Calculations, *Physical Sciences Data,* 16 (Elsevier, 1984)
5. J. Habasaki, I. Okada, Y. Hiwatari, in *Molecular Dynamics Simulations*. ed. by F. Yonezawa. Springer Series in Solid-State Sciences, vol. 103 (Springer-Verlag, 1992)
6. J. Habasaki, I. Okada, Y. Hiwatari, Mol. Simul. **9**, 49 (1992)
7. H. Hasegawa, K. Adachi, I. Yasui, M. Imaoka, X-ray diffraction study of Li_2O-SiO_2 glass. Yogyo-Kyokai-Shi **88**, 51 (1980) (in Japanese)
8. V.H. Seemann, Acta Cryst. **9**, 251 (1956)
9. B.A. Maksimov, Y.A. Kharitonov, V.V. Ilyukhin, N.V. Belov, Sov. Phys. Dokl. **13**, 85 (1968)
10. J. Habasaki, K.L. Ngai, J. Electroceram. **34**, 43 (2015)
11. J. Habasaki, K.L. Ngai, J. Chem. Phys. **139**, 064503 (2013)
12. D.K. Swanson, C.T. Prewitt, Am. Mineralogist **68**, 581 (1983)
13. S. Sasaki, K. Fujino, Y. Takeuchi, R. Sadanaga, Acta Cryst. **A36**, 904 (1980)
14. R.D. Banhatti, A. Heuer, Phys. Chem. Chem. Phys. **3**, 5104 (2001)
15. J. Horbach, S.K. Das, H. Knoth, K. Binder, in *NIC Symposium 2004*, Proceedings, NIC Series, vol. 20, 215 (2003)
16. L.G.V. Gonçalves, J.P. Rino, J. Non-Cryst. Solids **402**, 91 (2014)
17. U. Voigt, H. Lammert, H. Eckert, A. Heuer, Phys. Rev. B **72**, 064207
18. J. Du, R.L. Corrales, Phys. Rev. B **72**, 092201 (2005)
19. B.W.H. van Beest, G.J. Krarner, R.A. van Santen, Phys. Rev. Lett. **64**, 1955 (1990)
20. A. Takada, P. Richert, C.R.A. Catlow, G.D. Price, J. Non-Cryst. Solids **354**, 181 (2008)
21. P. Tangney, S. Scandolo, J. Chem. Phys. **117**, 8898 (2002)
22. A. Carré, J. Horbach, S. Ispas, W. Kob, Eur. Phys. Lett. **82**, 17001 (2008)
23. W.H. Zachariasen, J. Am. Chem. Soc. **54**, 3841 (1932)
24. G.N. Greaves, J. Non-Cryst. Solids **71**, 203 (1985)
25. J. Habasaki, I. Okada, Y. Hiwatari, J. Non-Cryst. Solids **183**, 12 (1995)
26. J. Habasaki, I. Okada, Y. Hiwatari, J. Non-Cryst. Solids **208**, 181 (1996)
27. J. Habasaki, K.L. Ngai, Phys. Chem. Chem. Phys. **9**, 4673 (2007)
28. S. Balasubramanian, K.J. Rao, J. Phys. Chem. **97**, 8835 (1993)
29. S. Balasubramanian, K.J. Rao, J. Non-Cryst. Solids **181**, 157 (1997)
30. J. Habasaki, Y. Hiwatari, Phys. Rev. E **58**, 5111 (1998)
31. Bruckner, H.-U. Chun, H. Goretzki, Glastechn. Ber. **51**, 1 (1978)
32. R. Dupree, D. Holland, M.G. Mortzuka, J. Non-Cryst. Solids **116**, 148 (1990)
33. C.M. Schramm, B.H.W.S. de Jong, V.E. Parzialet, J. Am. Chem. Soc. **106**, 4397 (1984)
34. H. Maekawa, T. Maekawa, K. Kawamura, T. Yokokawa, J. Non-Cryst. Solids **127**, 53 (1991)
35. J. Du, A.N. Cormack, J. Non Cryst. Solids **349**, 66 (2004)
36. U. Voigt, H. Lammert, H. Eckert, A. Heuer, Phys. Rev. B **72**, 064207 (2005)
37. J. Du, R.L. Corrales, Phys. Rev. B **72**, 092201 (2005)
38. J. Du, L.R. Corrales, J. Chem. Phys. **125**, 114702 (2006)

39. A. Tilocca, J. Chem. Phys. **139**, 114501 (2013)
40. M.E. Brandriss, J.F. Stebbins, Geochim. Cosmochim. Acta **52**, 2659 (1988)
41. J. Tan, S. Zhao, W. Wang, G. Davies, X. Mo, Mater. Sci. Eng. B **106**, 295 (2004)
42. G.N. Greaves, S. Sen, Adv. Phys. **56**, 1 (2007)
43. E.D. Lacy, Phys. Chem. Glasses **6**, 171 (1965)
44. T. Sasaki, M. Kawaguchi, M. Yamane, Y. Suginohara, J. Jpn. Inst. Met. **45**, 790 (1981) (in Japanese)
45. N. Kitamura, K. Fukumi, H. Mizoguchi, M. Makihara, A. Higuchi, N. Ohno, T. Fukunaga, J. Non Cryst. Solids **274**, 244 (2000)
46. H. Doweidar, J. Non Cryst. Solids **194**, 155 (1996)
47. A. Tilocca, N.H. de Leeuw, A.N. Cormack, Phys. Rev. **B73**, 104209 (2006)
48. J. Habasaki, K.L. Ngai, J. Chem. Phys. **122**, 214725 (2005)
49. J. Habasaki, I. Okada, Y. Hiwatari, Phys. Rev. **E52**, 2681 (1995)
50. J. Habasaki, K.L. Ngai, Y. Hiwatari, Phys. Rev. **E66**, 021205 (2002)
51. R. Kubo, J. Phys. Soc. Jpn. **12**, 570 (1957)
52. T. Odagaki, M. Lax, Phys. Rev. B **24**, 5284 (1981)
53. J. Habasaki, I. Okada, Mol. Simul. **9**, 319 (1992)
54. T.L. Gilbert, J. Chem. Phys. **49**, 2640 (1968)
55. Y. Ida, Phys. Earth Planet Inter. **13**, 97 (1976)
56. J. Habasaki, K.L. Ngai, J. Chem. Phys. **122**, 214725 (2005). Some difference is obtained for the both right and left ends of the multifractal spectrum of the density profile, which is related to the most dilute part and densest part of it
57. J. Habasaki, I. Okada, Y. Hiwatari, Phys. Rev. B **55**, 6309 (1997)
58. W.K. Lee, J.F. Liu, A.S. Nowick, Phys. Rev. Lett. **67**, 1559 (1991)
59. C. León, A. Rivera, A. Varez, J. Sanz, J. Santamaria, K.L. Ngai, Phys. Rev. Lett. **86**, 1279 (2001)
60. J. Habasaki, K.L. Ngai, J. Non-Cryst. Solids **352**, 5170 (2006)
61. D.M. Laughman, R.D. Banhatti, K. Funke, Phys. Chem. Chem. Phys. **11**, 3158 (2009)
62. K.L. Ngai, G.N. Greaves, C.T. Moynihan, Phys. Rev. Lett. **80**, 1018 (1998)
63. A. Heuer, M. Kunow, M. Vogel, R.D. Banhatti, Phys. Chem. Chem. Phys. **4**, 3185 (2002)
64. K.L. Ngai, J. Habasaki, Y. Hiwatari, C. León, J. Phys. C Condens. Matter **15**, S1607 (2003)
65. K.L. Ngai, Phys. Rev. B **48**, 13481 (1993)
66. K.L. Ngai, C. León, Phys. Rev. B **66**, 064308 (2002)
67. J. Habasaki, Y. Hiwatari, I. Okada, Fall MRS (Material Research Society) Meetings, Boston, Proceedings 455, ed. by C.A. Angell, K.L. Ngai, J. Kieffer, T. Egami, G.U. Nienhaus. p. 91 (1996)
68. R. Ishizaki, H. Mori, Prog. Theor. Phys. **97**, 201 (1997)
69. J. Klafter, M.F. Shlesinger, G. Zumofen, Phys. Today 33 (1996) and references therein
70. R.A. Montani, C. Balbuena, M.A. Frechero, Solid State Ion. **209–210**, 5 (2012)
71. Widmer-Cooper, P. Harrowell, H. Fynewever, Phys. Rev. Lett. **93**, 135701 (2004)
72. A. Rahman, Phys. Rev. **136**, A405 (1964)
73. J. Habasaki, K.L. Ngai, Y. Hiwatari, J. Chem. Phys. **120**, 8195 (2004)
74. J. Habasaki, I. Okada, Y. Hiwatari, J. Phys. Soc. Jpn. **67**, 2012 (1998)
75. J. Habasaki, Y. Hiwatari, J. Non-Cryst. Solids **307–310**, 930 (2002)
76. B. Mandelbrot, Science **156**, 636 (1967)
77. S. Havlin, D. Ben-Avraham, Adv. Phys. **51**, 187 (2002)
78. J. Habasaki, K.L. Ngai, J. Chem. Phys. **122**, 214725 (2005)
79. J. Habasaki, K.L. Ngai, Flow Dynamics, IAP Conference Proceedings **832**, 199 (2006)
80. E.W. Montroll, G.H. Weiss, J. Math. Phys. **6**, 167 (1965)
81. J. Klafter, A. Blumen, M.F. Shlesinger, Phys. Rev. A **35**, 3081 (1987)
82. T. Odagaki, J. Matsui, Y. Hiwatari, Physica **A204**, 464 (1994)
83. B. Doliwa, A. Heuer, Phys. Rev. E, **67**, 030501(R) (2003)
84. H. Miyagawa, Y. Hiwatari, Phys. Rev. **A44**, 8278 (1991)

85. J. Habasaki, Y. Hiwatari, Phys. Rev. **E59**, 6962 (1999)
86. J. Habasaki, Y. Hiwatari, J. Non-Cryst. Solid **307–310**, 930 (2002)
87. J. Habasaki, K.L. Ngai, J. Chem. Phys. **129**, 034503 (2008)
88. H. Lammert, M. Kunow, A. Heuer, Phys. Rev. Lett. **90**, 215901 (2003)
89. T.F. Soules, R.F. Busbey, J. Chem. Phys. **75**, 969 (1981)
90. J. Habasaki, A. Ueda, J. Chem. Phys. **134**, 084505 (2011)
91. E.R. Weeks, J.C. Crocker, A.C. Levitt, A. Schofield, D.A. Weitz, Science **287**, 28 (2000)
92. C. Donati, S.C. Glotzer, P.H. Poole, W. Kob, S.J. Plimpton, Phys. Rev. E **60**, 3107 (1999)
93. K.L. Ngai, *Relaxation and Diffusion in Complex Systems* (Springer, New York, 2011)
94. J. Habasaki, Y. Hiwatari, Phys. Rev. E **65**, 021604 (2002)
95. J. Habasaki, Y. Hiwatari, Phys. Rev. B **69**, 144207 (2004)
96. H. Lammert, A. Heuer, Phys. Rev. Lett. **104**, 125901 (2010)
97. B. Doliwa, A. Heuer, Phys. Rev. E **61**, 6898 (2000)
98. H. Jain, N.L. Peterson, H.L. Downing, J. Non-Cryst. Solids **55**, 283 (1983)
99. J.E. Kelly III, J.F. Cordaro, M. Tomozawa, J. Non-Cryst. Solids **41**, 47 (1980)
100. J. Habasaki, AIP Conf. Proc. **1518**, 170 (2013)
101. H. Fujisaka, M. Inoue, Phys. Rev. A **39**, 1376 (1989) and references therein
102. A. Heuer, K. Okun, J. Chem. Phys. **106**, 6176 (1997)
103. K. Kim, S. Saito, J. Chem. Phys. **138**, 12A506 (2013)
104. M. Kawakami, K. Nagata, K.S. Gato, J. Electrochem. Soc. **125**, 395 (1978)
105. L.G.V. Gonçalves, J.P. Rino, J. Non-Cryst. Solids **402**, 91 (2014)
106. A. Heuer, J. Phys. Condens. Matter **20**, 373101 (2008)
107. L.L. Burgner, M.C. Weinberg, Phys. Chem. Glasses **42**, 184 (2001)
108. I. Gutzow, J. Schmelzer, *The Vitreous State* (Springer, Berlin, 1995)
109. J.O'M. Bockris, J.A. Kitchener, S. Ignatowicz, J.W. Tomlinson, Trans. Faraday Soc. **48**, 75 (1952)
110. U. Bauer, A.-M. Welsch, H. Behgrens, J. Rahn, H. Schmidt. I. Horn, J. Phys. Chem. B **117**, 15184 (2013)
111. M.L.F. Nascimento, V.M. Fokin, E.D. Zanotto, A.S. Abyzov, J. Chem. Phys. **135**, 194703 (2011)
112. P. Maass, J. Non-Cryst. Solids **255**, 35 (1999)
113. W. Beier, G.H. Frischat, J. Non-Cryst. Solids **73**, 113 (1985)
114. W. Beier, G.H. Frischat, Glastech. Ber. **57**, 71 (1984)
115. R. Küchler, O. Kanert, T. Vereget, H. Jain, J. Non-Cryst. Solids **353**, 3940 (2007)
116. A.M. Glass, K. Nassau, T.J. Negran, J. Appl. Phys. **49**(9), 4808 (1978)
117. T. Minami, Y. Takuma, M. Tanaka, J. Electrochem. Sci. Technol. **124**, 1659 (1977)
118. D. Derks, Y.L. Wu, A. van Blaaderen, A. Imhof, Soft Matter **5**, 1060 (2009)
119. B. Munro, M. Schrader, P. Heitjans, Ber. Bunsunges. Phys. Chem. **96**, 1718 (1992)
120. W. Franke, P. Heitjans, Ber Bunsenges. Phys. Chem. **96**, 1674 (1992)
121. A.K. Rizos, J. Alifragis, K.L. Ngai, P. Heitjans, J. Chem. Phys. **114**, 931 (2001)

Chapter 10
The Mixed Alkali Effect Examined by Molecular Dynamics Simulations

10.1 Overview and Brief History

When more than one kind of mobile ions are mixed in ionic conducting glasses, crystals and melts, there is non-linear decrease of conductivity or diffusivity, which can be as large as several orders of magnitude compared with the transport coefficient of either kind of ions. What is a cause of such a large effect? The phenomenon is known as mixed mobile ion effect or Mixed Alkali Effect (MAE) [1–4]. MAE is also known as common properties for ionic conductors including fast ion conductors such as β”-aluminum systems [5] and is considered as a key feature of the common physics governing the dynamics. Molecular dynamics simulation is useful to study the complex ion dynamics giving rise to the MAE in ionically conducting glasses. Many researchers tackled this problem for a long time and it was called as “permanent challenge” [6] during nearly over one century. The problem is still unsolved in the sense that “ a common view among researchers has not established yet”, although many features have become clearer in recent years. The experimental aspects of MAE are covered in details in Sect. 4.8. The difficulty of the problem is to solve all the following properties and features consistently.

The slowing down by MAE is larger at lower temperatures.

The effect is larger when the size difference of the two alkali ions is larger.

The effect is larger in the systems with higher concentration of alkali ions, and vanishes at extremely dilute concentration, suggesting that the effect is enhanced by the suppression of the cooperative motions of like ions in the mixture.

In the dilute foreign alkali region with small concentration x of foreign ions, the MAE is known to be the largest [7], and $\log(D(x)/\mathrm{D}(0)) = -E/k_BT$ exhibits a curvature [8–10]. In the reference [8], it was pointed out that the large MAE in the dilute foreign-alkali region is one of the most critical tests for any explanation of MAE, where large numbers of majority ions are immobilized by a single foreign ion.

J. Habasaki et al., *Dynamics of Glassy, Crystalline and Liquid Ionic Conductors*,
Topics in Applied Physics 132, DOI 10.1007/978-3-319-42391-3_10

The viscosity of the mixed alkali system is smaller than the single alkali systems. This suggests that the loosening up of the network by the presence of different kinds of alkali ions.

The effect is larger at low frequency than at high frequencies [11]. That is, the effect is remarkable in DC but not found or weak in AC at higher frequencies.

Several authors [12, 13] pointed out that the maximum of the Haven ratio exists in the mixed alkali systems. Namely, Haven ratio of the mixed alkali system tends to be larger than the single alkali systems. In other words, the effect is larger in the conductivity than in diffusivity.

MD simulations have been taking as the means to understand the MAE for a long time. Vessal et al. [14] have visualized the structure of the mixed alkali system. The changes in the activation energy by mixing were observed as well as a segregation of ions from the frameworks. Existence of nearly independent jump paths for different alkali species in the molten state or in the glassy state was found by Balasubramanian and Rao [15, 16], and by Habasaki et al. [17, 18], independently. In these works, distinct-part of the van Hove functions was used to study the motion of ions among different kind of ion sites. This short time observation needs further examination of the long time behavior, unless the connection between short and long time behavior is established. This is because the peak observed at $r \sim 0$ of the van Hove function includes the localized jumps and hence it is not necessarily for the diffusive motion if the observation time was too short. In early works, time scales, system sizes and compositions covered, were limited because of the limitation of the power of the computer. Mixed alkali effect is known to be remarkable in high alkali content glass where the ion dynamics is decoupled with the motion of the matrix. Therefore, we have chosen the meta-silicate glasses. The system is more fragile than silica rich systems and this allows one to treat a relatively small system. Actually, the system size effect is reported to be larger in strong system than in fragile system [19]. With a rapid development of computers or methodology, such as parallel computing, this situation changed considerably. Later, researches of the MAE were expanded to longer time scales and/or different composition including lower alkali content glass [20, 21].

In this section, our attention is focused on the results of MD simulations for metasilicate composition, where the mixed alkali effect is remarkable.

MD simulations were performed for $(Li_{1\text{-}x},K_x)_2SiO_3$ ($x = 0$, 0.1, 0.25, 0.5, 0.75, 1.0.) Contained in the unit cell are 1152 M, 576 Si and 1728 O for M_2SiO_3, where M = Li or K. The smaller systems with 432 particles used in early works are still useful for graphic representation and some other treatments. The volume was fixed as that derived by NPT (constant pressure and temperature) ensemble simulation under atmospheric pressure and the results of NVE ensemble are analyzed. Pair potential functions of Gilbert-Ida type [22, 23] and r^{-6} terms were used. The parameters of the potentials used were previously derived on the basis of *ab initio* molecular orbital calculations [24] (see Sect. 9.1). The glass transition temperatures obtained by the *T*-*V* relation for the Li_2SiO_3 was approximately 830 K. The runs for $(Li_{1-x},K_x)_2SiO_3$ systems at 600, 700, 800 and 1673 K were analyzed.

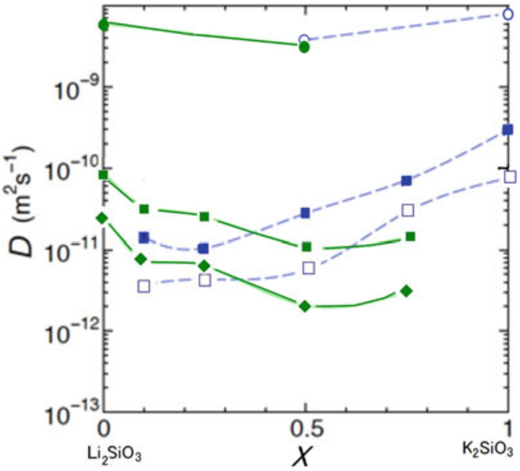

Fig. 10.1 Mixed alkali effect reproduced by MD simulations. Isotherms of diffusion coefficients of in the mixtures of lithium metasilicate and potassium metasilicate, at three temperatures, 1673, 800 and 700 K from *upper to lower*. *Green marks* are for Li ions and *Blue marks* are for K ions. *Curves* are for a guide of eyes

The MAE observed in the diffusivity reproduced by MD for the mixture of lithium and potassium metasilicate glasses of several compositions is shown in Fig. 10.1 [17, 21]. The top curve for each Li and K is for the molten state, where the effect is small. At lower temperatures, the effect becomes clearer. In a low K concentration region, large decrease of the diffusivity of Li ions was observed, which means the one K ion causes the suppression of many Li ions. Thus, known features including an effect in a dilute foreign region can be reproduced well in our model. Different from other models used in the beginning of such works, our model can reproduce MAE effects at reasonable temperature regions with a reasonable glass transition temperature of the system.

10.2 Evidence of the Interception of Jump Paths Among the Ion Sites of Different Kinds of Alkali Ions: Distinct-Part of the Van Hove Function

The distinct part of the van Hove function [25] is useful to understand the different behaviors of ions among different kind of ion sites.

The function is defined by,

$$G_d^{\alpha,\beta}(\mathbf{r},t) = (1/N_\alpha)\sum_{i=1}^{N_\alpha}\sum_{j=1}^{N_\beta}\left\langle\delta\left(\mathbf{r}-\mathbf{r}_i^{\alpha}(0)+\mathbf{r}_j^{\beta}(t)\right)\right\rangle \tag{10.1}$$

where in the summations the self-term $i=j$ is left out if $\alpha=\beta$. N_α and N_β are the number of particles of species α and β, respectively. In the function, if the ion

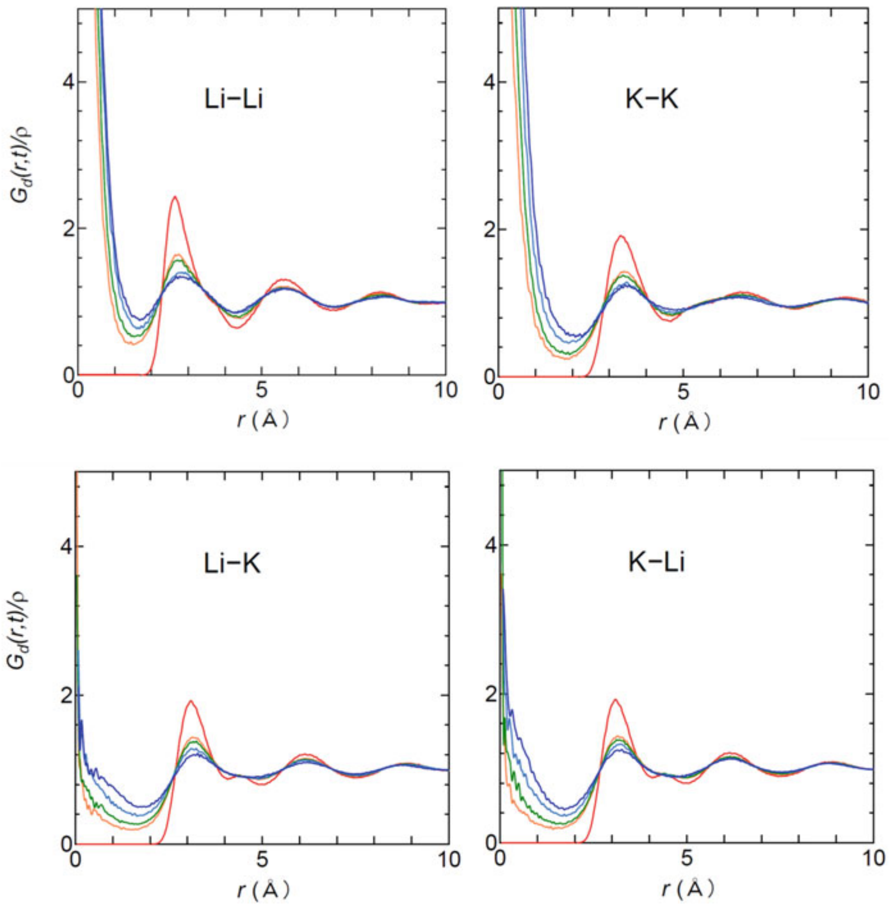

Fig. 10.2 Distinct part of the van Hove functions at 700 K in lithium-potassium metasilicate ($(\mathrm{Li}_{1\text{-x}},\mathrm{K}_\mathrm{x})_2\mathrm{SiO}_3$ with x = 0.5) for Li-Li, K-K, Li-K and K-Li pairs, respectively. The *red curves* are the function at $t = 0$, which corresponds to g(r) by the definitions. *Orange, green, pale blue and blue curves* are the function at t = 320, 640, 1600 and 2880 ps, respectively

species β comes into the site previously occupied by species α at an initial time t_0, a new peak developed at around $r = 0$.

The function for $(\mathrm{Li}_{1\text{-}x},\mathrm{K}_x)_2\mathrm{SiO}_3$ with $x = 0.5$ at 700 K is shown in Fig. 10.2.

The peaks at $r \sim 0$ in the Li-Li and K-K pairs mean the occurrence of such jumps. For the Li-K and K-Li pairs, they were not observed until 192 ps in Ref. [17]. That is, the jump to the site previously occupied by a different kind of ion site is rare. In a longer time scale, contribution of jumps is found [21] as shown in Fig. 10.2. From this result, one can say that in the mixed alkali system, the motions among different kinds of ion sites are suppressed. This means the characteristic of each site remain in the system and the path for each ion are nearly independent. This suppression is clearer at lower temperatures. The MAE effect and its temperature dependence is explained by such characteristics. By introducing fictive mass for Li ions, it was confirmed that the effect is essentially caused by a size difference of Li and K ions and not by the difference of masses [17]. The function for Li-K is the same as the function for K-Li and at $t = 0$, it is the same as the pair correlation function $g(r)$, from the definition.

By reverse Monte Carlo methods, it was shown that mixed mobile ion effect in silver-sodium phosphate glasses are weak [26], where both ions used common jump paths. This can be explained by the comparable ionic radii for silver and sodium ions. For the former, the radii 1.0 or 1.02, while for the latter the value 0.99 (in Å), both for the monovalent 4 coordinated ions were reported by Shannon [27, 28].

Considering the size difference of alkali metal ions, it is easy to understand why the larger ion cannot enter the site for the smaller ion, while the opposite case is not so obvious. From the many body configurations during MD run, activation energies of jumps have been estimated. A Li ion in a fully relaxed site is found to be more stable (about 200 kJ mol^{-1}) than the one put in the site previously occupied by K. Large distortion energy for the rearrangement of the environment is required to induce the jump to unlike ion site due to the large site mismatch [9, 15, 16, 18]. This explains why the jumps among unlike ion sites are rarer than the jumps among like ion sites.

10.3 Composition Dependence of the Mixed Alkali Effect

One can determine the exact number of ions moving among dissimilar or similar kinds of ion sites. The function, $R_d(r,t)$ defined by

$$R_d(r_c, t) \equiv \int_o^{r_c} 4\pi r^2 G_d(r, t) dr, \tag{10.2}$$

represents an accumulated number of M_2 ions at t within the distance r observed from the original sites ($r = 0$) at $t = 0$ of the M_1 ion. By using a suitable distance r_c, the number of the M_2 ions coming into the original site of M_1 ion can be obtained. The function $R_d(r,t)$ for the mixed alkali system was examined for longer time scales and different compositions. From this analysis, the following findings were reported to explain the trend observed in the isotherms [21]. In these systems, the number of events for Li-Li and K-K is obtained by the product of the number densities of both species concerned, that is, the probability of the meeting. The number of events for Li-K and K-Li are exactly the same in the $(\text{Li}_{1\text{-}x},\text{K}_x)_2\text{SiO}_3$ with $x = 0.5$. The equality of the number is necessary to keep the system stable. This conclusion is different from results by other MD work [20] for disilicate system, where asymmetry of the motions was observed. This difference of the explanation seems to be coming from the different treatment of jump sites. In their work, the site was defined by the dense part of the density profile using an arbitrary chosen cut-off value, while in the function $R_d(r,t)$, the minimum position of $g(r)$, which is common for Li-K and K-Li pairs, was used for r_c.

In the case of $(Li_{1-x},K_x)_2SiO_3$ with $x = 0.1$, asymmetry of the motion is observed even using $R_d(r,t)$ because of different number of ions; that is, number of jumps of Li ions into the site previously occupied by a K ion is larger than the opposite case because of the larger contents of Li ions. In the opposite case, where the potassium ions are the major component, the decrease of the dynamics of potassium ions is weaker, because of larger size of the potassium ions. This result explains the asymmetry found in the isotherm of the MAE and is related to the mechanism of the large MAE effect in a dilute foreign region (see Sects. 10.5.3 and 10.7).

10.4 Visualization of the Ion Trajectories and Paths in the Mixed Alkali System

Li ion cannot enter easily the site previously occupied by K site and opposite is also true. Therefore path for each ionic species is nearly independent and thereby cut each other. Existence of independent paths and trajectories of ions were visualized by several methods from MD simulations. Trajectories for the mixed alkali system have been shown in several papers [18, 21].

In Fig. 10.3, trajectories of atoms and ions of $(Li_{1-x},K_x)_2SiO_3$ with $x = 0.5$ for lower temperature and longer time scale (at 600 K during 8 ns runs) are shown. During the runs, Si atoms are essentially immobile, while local motions of oxygen atoms are observed. It is clearly found that the trajectories of Li and K ions are almost independent. Both localized clusters and overlap of trajectories along the path are observed. Such complicated motions form the heterogeneous (multifractal) density profile of ions. In our previous work, structure of the paths and ion sites can be visualized by using a density profile [29] and multifractal analysis (Appendixes A.3–A.5) has been done for such structures. Accumulated positions of ions during 1 ns runs for $(Li_{1-x},K_x)_2SiO_3$, $x = 0.5$ at 700 K was shown in Fig. 10.4 by the contour map for a slice of the MD basic cell of the smaller system.

In the left column, the profile for Li ions is shown. In the middle column, the profile of K ions within the same plane is shown. In the third column, the sum of both contributions is shown. In these figures, red color corresponds to the concentrated part (localized ions) and blue color means the rarified regions. In other words, region accessible by each species are restricted within the substructure of ion channel by the volume fraction of M_2O. This suggests the validity of the thermodynamic (TV^γ) scaling in each substructure (see Ref. [30] for the validity of the scaling in silicate glass. We also obtained preliminary results to support the validity of it in substructures.). In some cases, positions of Li and K ions overlap (not exactly the same because of the size difference) and this may be regarded as common sites, although this may depend on the definition of them [31].

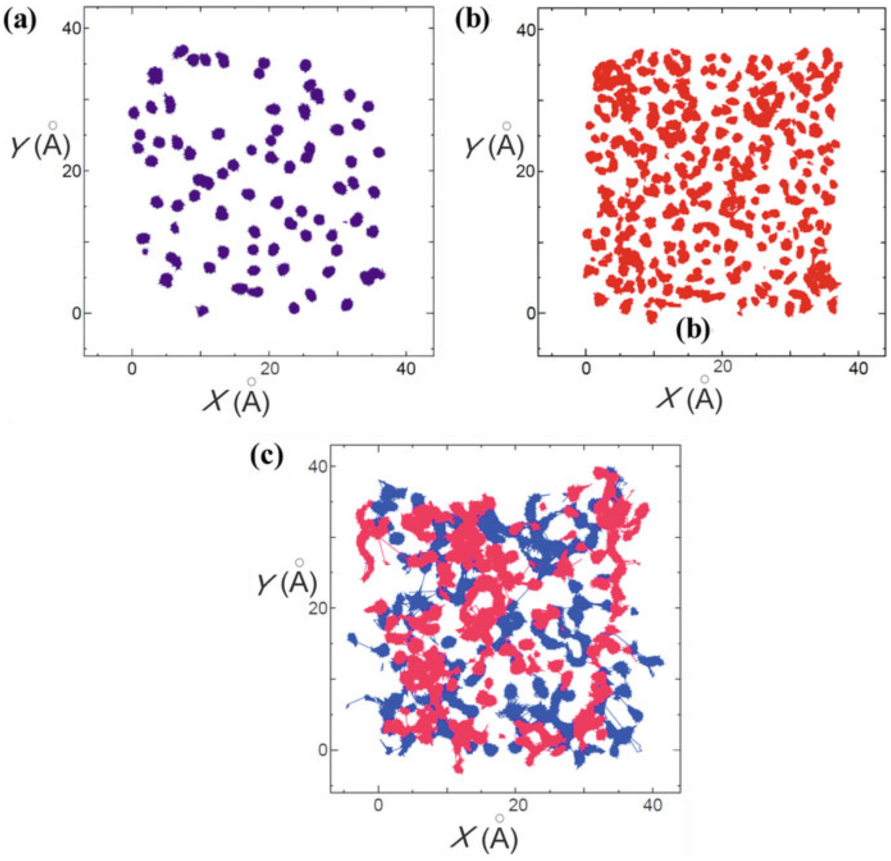

Fig. 10.3 Trajectories at 600 K during 8 ns for a slice of 5 Å projected on x-y plane for (**a**) Si (*Purple*), (**b**) O (*Red*) (**c**) Li (*dark pink*) and K (*blue*) ions in the ((Li$_{1\text{-x}}$,K$_x$)$_2$SiO$_3$ with $x = 0.5$)

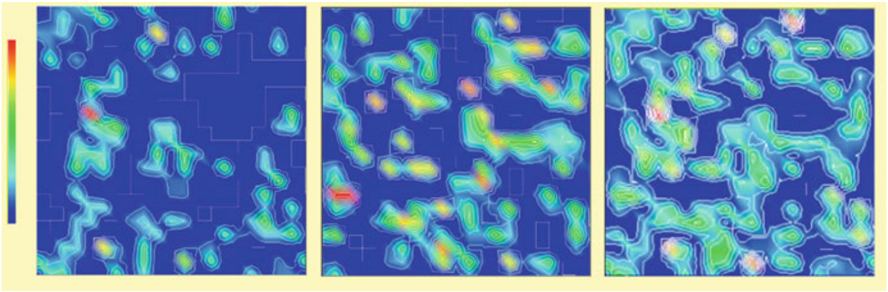

Fig. 10.4 Contour plots of density profile for (Li$_{1\text{-x}}$,K$_x$)$_2$SiO$_3$ with x = 0.5 at 700 K for the slice of the MD cell. The positions of ions during 1 ns of MD run are accumulated with an interval of 400 fs. *Left panel*: Li ions, *Middle panel*: K ions and *Right panel*: Sum of Li and K ions. The *red part* corresponds to a concentrated part while and *blue* one corresponds to a rarified part of the profile. The profile shows a multifractal nature. That is, substructures such as ion sites, ion paths have different fractal dimensions. The substructures for Li and K ions is nearly independent and hence intercepting each other

10.5 Quantitative Characterization of the Slowing Down of the Dynamics

As shown in Fig. 10.1, in the mixed alkali metasilicate with $x = 0.5$, the diffusivity of Li ions is one order of magnitude smaller than that of the single alkali system. Even if one half of the paths for an ion is intercepted by the other kind of alkali metal ion or its site, the possibility of finding the way is nearly one half. Therefore a change of the transport property is not linear to the number of available sites nor volume of possible occupation regions for each ion. Non-linear character of the dynamics is an important feature of the MAE that needs to be explained. To understand this non-linearity, it is expedient to consider the fractal dimension of random walks and that of the paths.

10.5.1 Combination of Fractal Dimension of Paths and Walks

In Table 10.1, the fractal dimensions of the random walks and the jump paths for single and mixed alkali systems are compared [32]. These values are relative ones obtained from the same period of runs (1 ns) for all systems. Both the increase of d_{w} and the decrease of d_{f} were observed in the mixed alkali system. The method to determine these exponents are described in the following subsection (see also Appendix A.1 for d_{w}.). The mechanism of MAE, where both the change in fractal dimension of the random walks and the change in the fractal dimension of the jump paths was observed, is easily understood by the concept similar to the "fracton" discussed by Alexander and Orbach [33]. Generally, the number of visited sites by an ion during N steps, $V(N)$, of a simple fractal system is given by

$$V(N) \sim R^{Df} \sim N^{ds/2}, \tag{10.3}$$

where the fracton dimension d_s is defined by

Table 10.1 Fractal dimensions of the jump path and that of random walk calculated from the accumulated (1 ns) density around ions and trajectories for Li ions, respectively

Systems in the glassy states	Temperature	d_{fc}	d_{w}
Li_2SiO_3	700 K	2.98	2.71
$LiKSiO_3$	700 K	2.21	3.25
	800 K	2.47	2.94
K_2SiO_3	700 K	2.78	2.31

For K_2SiO_3, values are for K ions

$$d_s = 2d_f/d_w, \tag{10.4}$$

where d_f is a dimension of the jump path and d_w is a fractal dimension of the random walk, and R is a distance from the original position of the ion after N steps and D_f is a dimension of the space.

The probability $<P_0(t)>$ of finding the particle at the origin at time t is given by

$$<P_0(N)>\sim [V(N)]^{-1} \tag{10.5}$$

when the particle was located at the origin at time $t = 0$. Here we use N instead of t to remove the effect of the waiting time distribution of jump motions. From these relations, it is clear that the increase in the fractal dimension of the random walk and the decrease in the dimension of the jump path resulted in a localization.

10.5.2 Fractal Dimension of Jump Path and Walks

As shown in the previous subsection, dimensionality of paths and walks determine localization of ions. Therefore, method to characterize the jump paths and trajectories is explained here [17, 32, 34]. Fractal dimension of the path can be determined from the number of surrounding ions in the accumulated position of ions.

In Fig. 10.5, an example of such analysis is shown. From the slope of the power law region, one can estimate the dimension for the possible connections of the path

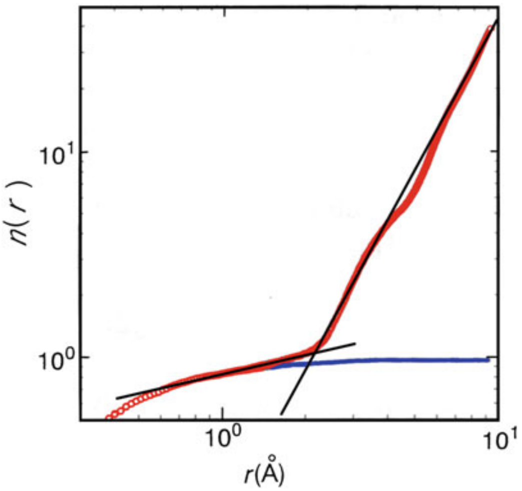

Fig. 10.5 An example of fractal dimension analysis of jump path. Number of Li ions (accumulated during 1 ns) around Li ions within the distance r is plotted against the distance r for $LiKSiO_3$ glass at 800 K (*Red curve*). *Blue curve* is for the self-term (that is for localized ions). The plot was normalized, so that the number of centered ion is 1. The slope is 0.31 for local region and 2.47 for clustering region

during a certain time of MD runs. Time scale (several times) longer than t_{dif} is necessary for accumulation to judge the percolation of the path.

Fractal dimension of the random walk, d_{w}, was determined from the trajectories of each ion by using a divider method (see Sect. 9.5.4 and Appendix A.1). This dimension represents the complexity of the trajectory and is defined by the following equation as already mentioned.

$$N_T = A' L_r^{-d_w}. \tag{10.6}$$

In this analysis, trajectories were obtained by the MD simulation during a run of time t_{run}. For determination of saturated value of d_{w} for both fast and slow ions, long run is better to be used, if calculation resources allowed it. For example $t_{run} = 4$ ns at 700 K for $x = 0$, which is about 8 times longer than t_{dif}, was used in Ref. [34]. The time scale covers exchange between fast and slow ions or saturation of the relative intensity in the density profile related to it.

In the lithium metasilicate, the slope of N_T against L_r plot was found to change at around 3 Å at lower temperatures. The d_{w} for shorter length scale (<3 Å) was named d_{w1} and d_{w2} for longer length scale ($3 \leq L_{\mathrm{r}} < 10$ (Å)).

In Fig. 10.6a, changes of the d_{w1} and d_{w2} of Li ion by mixing with K ions at 700 K are shown. It was found that d_{w1} for the short scale motion and d_{w2} values for

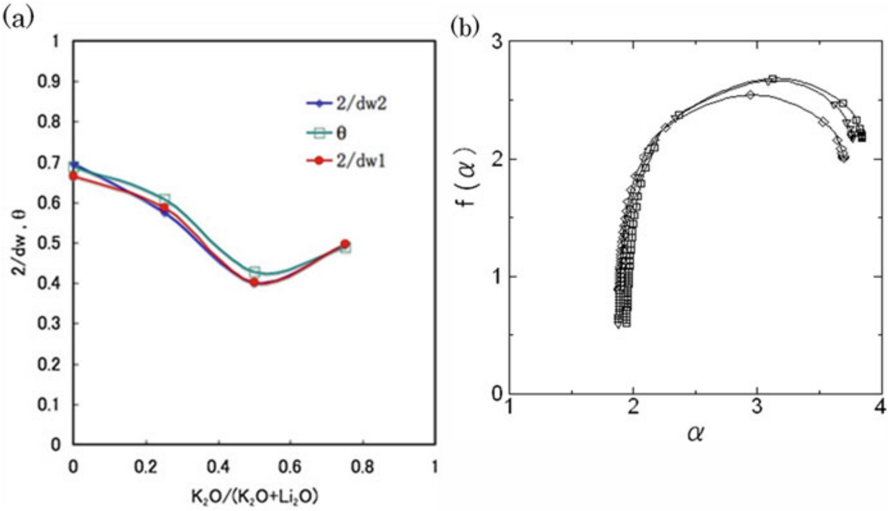

Fig. 10.6 (**a**) Changes of $2/d_{\mathrm{w}}$ compared with power law exponent θ of MSD. The fractal dimension of random walk in single alkali system shows two values ($2/d_{\mathrm{w1}}$ and $2/d_{\mathrm{w2}}$) for shorter and longer scale regions, while such difference was not observed for the mixed alkali system. That is, accelerated motion observed in the Li_2SiO_3 system is missing in the mixed alkali system. (**b**) Singularity spectrum of Li ions in $(Li_{1-x},K_x)_2SiO_3$, (*squares*: $x = 0.$, *triangles*: $x = 0.25$, *diamonds*: $x = 0.5$) obtained from 1 ns runs at 700 K

longer scale motion are non-distinguishable in the mixed alkali system. This means that the fast ionic motion with cooperative characters are suppressed by an addition of small amount of foreign alkali metal ions.

The value $2/d_w$ is compared with the exponents, θ, in the power law dependence, t^{θ}, of the MSD. As well known, the decrease in the value of θ represents the slowing down of the dynamics. From the comparable trends found in θ and $2/d_w$, the main cause of the slowing down with increasing potassium content is inferred as originating from the geometrical correlation of the successive motions, that is spatial term. In contrast, in the usual theory of fractal [35], θ correspond to $2/d_w$', where the d_w' is considered to be more general one including both temporal and spatial terms. Thus it is proved [36] that the origin of the remarkable slowing down in the mixed alkali system is related to the suppression of the cooperative motions and changes of the complexity of the trajectories. Naturally, the changes of the slope in the "power law" dependence of the MSD due to complexity of the trajectories explains "the large non-linear effect of the slowing down" in the mixed alkali system.

We note that the β in the $F_s(k,t)$ is comparable to θ and from this relation, we can expect the decrease of β with mixing of foreign alkali ions for the single particle motion. It is noteworthy that this mechanism of the slowing down through θ and/or β by mixing does not necessarily require the direct modification of activation energy of each jump motion.

In the conductivity of the mixed alkali system, the relation in β and θ is not simple, because both kinds of ions and cooperative motions of them are affected by the mixing, as discussed in the next section for the motion in the dilute foreign alkali region and in Sect. 10.6 for the Haven ratio.

Related changes are found in the variation of the exponent β with x obtained from fits using the Kohlrausch function to the electric modulus of data. Ngai and coworkers [8] have argued for the mixed alkali silicate glasses $[xK_2O(1-x)\,Na_2O]$–$3SiO_2$ that the increase of $\beta \equiv (1\text{-}n)$ of the Kohlrausch function with x and a maximum at some intermediate composition are expected based on the coupling model.

10.5.3 Rapid Decrease of the Diffusivity in the Dilute Foreign Alkali Region

The difference of $2/d_{w1}$ and $2/d_{w2}$ becomes negligibly small in mixtures and this trend already exists in a dilute foreign region. Therefore, the suppression of the fast ions (in the diffusivity) by addition of foreign ions is responsible for the rapid decrease of the dynamics at dilute foreign region. As discussed in Sect. 10.3, in the $x = 0.1$ case, the motion of K ion to the site previously occupied by Li ion needs a motion of a plural number of Li ions in the dilute foreign ion region. We also note that the strong localization of K ions is found with $x = 0.1$. Therefore, cooperative motion of like ions is affected by introducing the larger ions considerably and rapid increase of d_{w2} is observed by mixing with a small amount of foreign alkali ions. As discussed later in the Sect. 10.7.1, such effects propagate to longer distances and this explains the immobilizing the dynamics of majority ions found in a dilute foreign alkali content region.

Thus changes in the diffusivity are dominated by the change in the geometrical correlation between successive jumps and not by the change in the relaxation rates in the high frequency region, and the motion less than 1 ps is not affected by the mixing as it is easily confirmed by MSD. Experimentally, Jain [11] has examined the low temperature ac conductivity in $x\mathrm{Na_2O}$-(1-x)$\mathrm{Rb_2O}$-4$\mathrm{GeO_2}$ glasses and found that the mixed alkali effect is essentially absent at high frequencies. This feature is consistent to our findings.

10.5.4 Multifractality of Jump Path and the Percolative Aspect of MAE

Here we make the importance of the geometrical structure of the pathway clearer. In a single alkali glass, large fluctuations in the heights of the density profile, due to the hierarchy dynamics of fast and slow ions [37, 38], were found [29]. Different fractal dimension is found for each substructure (ion sites or paths connecting them) or the mixture. Therefore, multifractal analysis using singularity spectrum, $f(\alpha)$, (see Appendix A.5) is useful to characterize the changes in the profile by mixing with foreign alkali metal ions. Singularity spectra of the Li ions in the mixed alkali systems $(\mathrm{Li}_{1\text{-}x},\mathrm{K}_x)_2\mathrm{SiO}_3$ ($x = 0.$, 0.25, 0.5) is shown in Fig. 10.6b, where the run of 4 ns at 700 K was analyzed [21]. Each singularity spectrum, $f(\alpha)$ shows a convex shape, which indicates the multifractal character. The $f(\alpha)$ value at the maximum corresponds to the capacity dimension of the percolated jump paths and the value decreases with the increasing foreign alkali metal ions (the threshold value in 3D is known to be ~2.53). The largest value of α corresponds to the most rarified part of the density profile, which corresponds to the accelerated (long ranged) motion, while the left part is concerning with the localization. Therefore, the smooth convex curve means the smooth mixing of the localized motion and accelerated motion to form the density profile. Changes in the dynamics forming the density profile can be also found in the spectra. With increase of K ion content, the right hand part of the spectrum is suppressed accompanied with the decrease of the capacity dimension. This means the motion becomes more localized one.

When the heterogeneity of the dynamics is weaker, it is expected that the spectrum becomes narrower.

The capacity dimension with $x = 0.5$ is near the percolation threshold (~2.53) at 700 K.

Generally, singularity spectra are representative of the density profile formed by both fast and slow dynamics and are useful to examine different systems on the same basis.

For example, for the lower alkali content glass such as Li_2SiO_3-$3SiO_2$, similar change in the spectrum $f(\alpha)$ showing slowing down of the dynamics was found [20]. This is a direct evidence to show that the situation of each ionic species in mixed alkali system is similar to the low alkali content glass.

10.5.5 Self-Part of the Van Hove Functions

The self-part of the van Hove function is also useful to characterize the difference or similarity of the single alkali and mixed alkali systems. The function for ions is defined by

$$G_s(\mathbf{r},t) = (1/N)\sum_{i=1}^{N}\langle\delta(\mathbf{r}_i(t) - \mathbf{r}_i(0) - \mathbf{r})\rangle, \qquad (10.7)$$

where $\mathbf{r}$ is the vector to show the travel by the ion in a time t.

Figure 10.7a, b show the comparison of the evolution of $4\pi r^2 G_s(r,t)$ for Li ions in single alkali metasilicate and that of the mixture with potassium metasilicate at 700 K. In the plot, the function is shown as a function of r with time, where r is $\|\mathbf{r}\|$. The different functional forms in the mixed alkali systems (for $x = 0.1$ and 0.5) are found as shown below.

In the single alkali glass, the curves are the functions for 80, 160, 320, 640, 1280 and 2240 ps from top to the bottom of the first peak. With a decrease of the height of the first peak, peaks at larger r develop. In Fig. 10.7a, the brown and red curves are

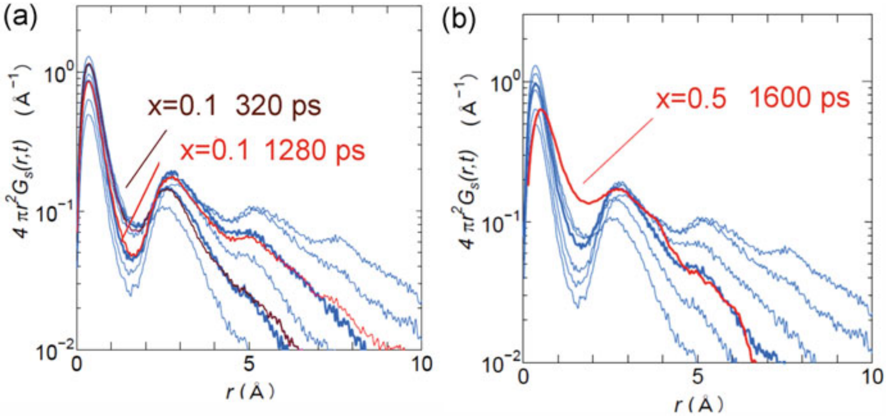

Fig. 10.7 Comparison of the self-part of the van Hove function of Li ions in Li_2SiO_3 glass and that in $Li_{1-x}K_xSiO_3$ glasses both at 700 K. *Blue curves* are for single alkali system (80, 160, 320, 640, 1280 and 2240 ps from *top to the bottom* for the first peak. (**a**) *Brown and red curves* are the functions for the mixed alkali system with $x = 0.1$ at 320 ps and 1280 ps. (**b**) *Red curve* is for the mixed alkali system with $x = 0.5$ at 1600 ps

the functions of the mixed alkali system for $x = 0.1$ at 320 and 1280 ps, respectively. These two curves cross each other at around 2.5 Å. Similar behavior in the single alkali system, at 160 and 640 ps are shown by the thick curves. The time scale for developing of the function becomes about 2 times longer by the addition of 10 mol % of potassium salt. For $x = 0.1$, the scaling of the dynamics by an effective time will hold because of the similarity of the functional forms. The situation is slightly changed in the case of $x = 0.5$. In Fig. 10.7b, the red curve at 1600 ps for the mixture is comparable to that at 320 ps of the single alkali system shown by the blue thick curve in the long r region. However, the red curve at small r region is fairly different from that of the blue thick curve. The function is broader and the height is lower in the mixed alkali system. Moreover, the dip between the first and second peaks are not as clear. These results suggest that additional motion such as jump toward ion site previously occupied by a different kind of alkali ion or increased number of localized jumps contributes to the functional form.

10.6 Haven Ratio in the Mixed Alkali System

The complex conductivity $\sigma^*(\omega)$ is related to the MSD by the following equation [39, 40],

$$\sigma^*(\omega) = -\omega^2 \frac{N_\rho {q_c}^2}{6 H_R k T} \int_0^\infty < r^2(t) > e^{-i\omega t} dt, \tag{10.8}$$

where N_ρ is a number density of mobile ions, q_c is a charge of ion, k is the Boltzmann constant, H_R is Haven ratio , and T is temperature. Using this relation, the $\sigma^*(\omega)$ spectra in frequency domain can be connected to the motion in each stage in MSD [41]. The Haven ratio [42] is experimentally obtained from the ratio of tracer diffusion and conductivity. It is represented by the ratio, $\sum_i < \mathbf{v}_i(0) \bullet \mathbf{v}_i(t) > / < \sum_i \mathbf{v}_i(0) \bullet \sum_j \mathbf{v}_j(t) >$ as shown the linear-response theory by Kubo [39]. Since the cross terms is included in the denominator, the Haven ratio is another indicator of the cooperativity in the ionic motions.

Experimentally, the change of the Haven ratio (H_R) is found by mixing of foreign alkali and a maximum is found as some intermediate value of the mixing ratio [11, 43]. This is in contrast to the expectation of decreasing ratio by mixing when one considered the geometrical correlation of motions only. This problem is solved if we considered the cooperative motion of ions [18].

In the MD simulation of Mg-stabilized Na-β” aluminum, Hafskjold and Li [44] have pointed out that a small H_R value corresponds to highly correlated velocities of different conducting ions, indicating that ions move in the same direction simultaneously. In their work, the ratio was obtained using the tracer diffusion coefficient and bulk diffusion coefficient at $f = 0$, where f is frequency.

They are defined by

$$D^t(f) \equiv \frac{1}{zN}\int_0^{\infty} dte^{i2\pi ft}\left\langle \sum_{i=1}^{N} \mathbf{v}_i(t) \cdot \mathbf{v}_i(0) \right\rangle$$

and

$$D^b(f) \equiv \frac{1}{zN}\int_0^{\infty} dte^{i2\pi ft}\left\langle \sum_{i=1}^{N} \mathbf{v}_i(t) \cdot \sum_{i=1}^{N} \mathbf{v}_i(0) \right\rangle, \tag{10.9}$$

where z is the dimensionality of the system. In the case of the β”-alumina, the value 2 was used.

Such cooperative jumps are found in both lithium (see Fig. 2.12) and potassium metasilicate glasses, and the maximum of the Haven ratio in the mixed alkali system is explained by the suppression of the cooperative motion found in the mixed alkali system [17]. Therefore, the term “cooperativity blockage” is appropriate to represent such situation and was used in Ref. [45].

In the single alkali glass, the value is known to be 0.2–0.5 and this value is inversely correlated with the cooperatively of the mobile ions [46]. Therefore, 2–5 ions move cooperatively. On the other hands, the ratio is larger in the mixed alkali glasses than the single alkali systems [11, 43], indicating that the cooperative motions of same kinds of ions are suppressed in the mixture.

Recently, Voss et al. [47] has shown the relationship between activation enthalpy of the ionic conductivity and the mean separation distance of cations, $<d_{\mathrm{ion}}>$ in Na- and Rb-oxide, and also that the Haven ratio decreases with the decreasing $<d_{\mathrm{ion}}>/<d_{\mathrm{network}}>$. The relation was confirmed by the Monte Carlo simulations including single and collective jumps on the random field and importance of cooperative motions was also argued.

10.7 MAE as a Cooperativity Blockage

Suppression of the cooperative jumps and resultant propagation of the blockage effect is found to be essential in MAE and this has been identified as the origin of the rapid decrease of the mobility in the diluted foreign region or the large magnitude of the mixed alkali effect. Namely, suppression of motions propagates to longer distances [35, 45, 48]. Prof. C.T. Moynihan suggested to us to describe the mechanism as “cooperativity blockage”. These features are consistent with the results in the fractal dimension analysis and explanation of Haven Ratio, with considering the cooperativity. This mechanism is related to the dynamics in the confined materials as discussed in the next subsection.

10.7.1 Relation with Confined Systems

Recently, many kinds of confined systems draw attentions. This includes water in gel, molecule in the tube, systems with fixed walls. Some effect of fixed particles introduced artificially to block the paths of the mobile ions [48] is remarkably similar to the mixed alkali effect [21]. Such blockage effect is found to be emphasized on the cooperative jumps as shown by the Monte Carlo Simulation [49], where Lennard-Jones particles (i.e. argon like ones) were used instead of ions. As far as the mechanism of blocking of the path, there is no difference between ionic system and non-ionic system. This mechanism is not limited for ions and is rather general for interacting systems.

In Fig. 10.8, changes of the intermediate scattering functions of the majority of lithium ions in lithium metasilicate glass, where the 10 % of block particles (fixed Li ions) [45] has been introduced, are shown. As shown by the blue dotted curves, the decay of the function is slowed down by the small number of block particles. The effect is observed for all wave numbers examined but seems to be larger for smaller wave number at the long time region. In this case, one can consider both the block of the path and suppression of the cooperative motions. Effect of the fixed wall can be used to distinguish these effects. MD simulations of the binary Lennard-Jones (L-J) system by Scheidler et al. [50] have shown that the fixed wall affects dynamics of confined particles considerably and over longer distances from the

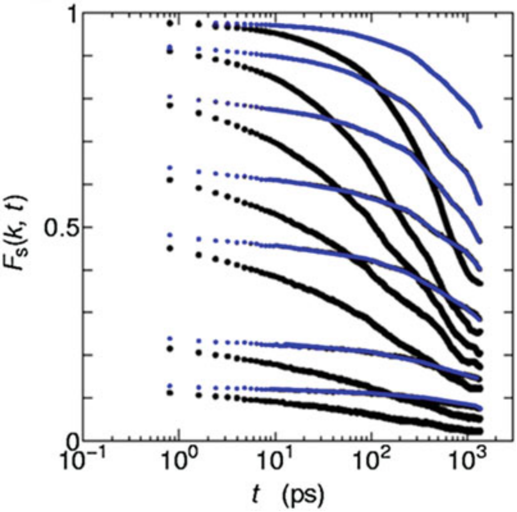

Fig. 10.8 Changes of self-part of the intermediate scattering function, $F_s(k, t)$ by introducing block particles are shown. *Black, large dotted curve*: $F_s(k, t)$, in Li_2SiO_3 as a standard for $k = 2\pi/n$ (Å^{-1}) ($n = 10, 5, 3, 2, 1.5, 1.0, 0.8$ from *top to bottom*) at 700 K. *Blue, dotted curve*: $F_s(k, t)$, of mobile Li (a major part) ions in Li_2SiO_3, where randomly chosen 10 % of Li ions are fixed. Wave numbers and temperatures are the same in both cases. Slowing down of the majority ions is caused by the small number of fixed ions

wall. Here the walls are formed by frozen L-J particles. The dynamics shown by the intermediate scattering function become more stretched by the continuously changing mobility with distance. In this case, the fraction of paths for the majority of mobile particles was not changed by the fixed ions. Therefore, their effects cannot be explained without a propagation of the effects for other particles. Similar result showing the propagation of effect was obtained for the motion of Li ions affected by the frozen ions in the wall [45]. This interesting property was fully explained by the Coupling Model [51, 52].

Maass et al. [9, 10] reproduce the behaviors of mixed alkali systems including dilute foreign region by considering the propagation of the mismatch effect with direct modification of barrier height with foreign character of the site. The mechanism has some similarity to that discussed here, because it includes the propagation of the effect, but not entirely.

Interestingly, fixing particles can cause the slowing down of dynamics, without changing structures [45]. Recently, effect of the pinned particles in LJ system was used to study the “true glass transition temperature” by their definition at higher temperature [53].

10.8 Motions Among Unlike Ion Sites

In spite of the fact that the interception of the jump path among the unlike alkali ion sites in a short time scale is observed well as clarified from MD simulations, jump motions among unlike ion sites were observed in a longer time scale or at higher temperatures near Tg [17, 18, 54]. Namely, Li ion can enter the site previously occupied by K ion and opposite is also true as confirmed for $LiKSiO_3$ system during a long time run or at high temperature region near Tg. These motions are rarer event compared with the jumps using like ion sites. However, it can contribute to the long time behaviors or more macroscopic behaviors such as viscosity. Details such as composition dependence of the number of events examined by MD seem to be helpful to understand this issue better.

10.8.1 Loosening of the Structure in the Mixed Alkali System

Ingram [3, 4] pointed out that mixing of different kinds of cations leads both to a loosening of the structure and, at the same time, to immobilization of cations. This seems to occur concurrently with the large change in the diffusivity in the dilute foreign region. There are several models explaining such phenomena. The mixed alkali defect model by LaCourse [55] has considered that the exchanges of ions with different sizes cause a relaxation of the whole system. The model postulates that the type A ions can enter the site for type B ions and vice versa, and the number of both events are the same. The structure of this site commonly used both kinds of ions is called the mixed alkali defect and this causes mechanical and electrical distortion of the local structures. Mutual ionic motion observed in MD simulations supports the existence of the common site for both kinds of ions, which has been often assumed to explain the friction peak and/or MAE itself. Ingram and Roling [56] suggested the concept of matrix mediated coupling and MAE have been explained to be caused by that the stress due to the jumps among unlike ions. In their model, attention is focused what happens when the cation moves into the "wrong" sites.

So far, following key features are confirmed in the mixed alkali system from MD, for the motion of network accompanied with the mutual jumps of the alkali ions to unlike sites.

1. In the mixed alkali glass, the size difference among unlike cations causes the successive and/or simultaneous relaxation of network structure, and therefore the relaxation time due to jumps among unlike sites is comparable to that for the network. In other words, jumps among unlike ion sites make the network looser.
2. The number of jumps among unlike sites becomes larger at high temperature or long time scale and these numbers can be quantitatively counted by MD.
3. Equality of the amount of motions among unlike sites holds for 1:1 mixture but does not hold for other compositions.

10.8.2 Internal Friction Peak in the Mixed Alkali System

These motions among unlike ion sites discussed in the previous subsection can be related to the experimental fact that the internal friction peak [57] in the mixed alkali system shows some peculiar behaviors. The intensity of the so called 'mixed alkali peak' is known to become quite large when mixing with only a small amount of the foreign alkali. Maass et al. [9, 10] argued that the small number of ion sites is essential to explain the observed ratio of the intensity of single and mixed alkali internal friction peak. In their model, jumps among unlike ion sites are considered to be the origin of the mixed alkali friction peak. The strong intensity of the "mixed alkali peak" at the dilute foreign alkali region is considered to be caused by small number of vacancy, which makes the number of ion-vacancy jumps being comparable to that of unlike ion pair.

These explanations [55, 56] of the mixed alkali peak and its property have the common problem of not able to simultaneously explain the large decrease of conductivity or diffusion coefficient in the dilute foreign alkali limit. On the other hand, the explanation of the MAE and its various properties including the large decrease in this limit by the immobilization of a large number of host ions by a single foreign ion [8] provides a natural explanation of this mixed alkali peak by the elastic dipoles formed by the immobilized host and foreign alkali ions. Details of this explanation and many other properties of the MAE can be found in the Chap. 4.

Although, direct observation by MD simulations has not been done yet for the origin of the mixed alkali peak, localization of majority ions caused by small number of foreign ions and its propagation were confirmed from MD as well as the strong localization of foreign ions [21]. Further examination of the roles of the motion among unlike sites might be necessary with considering the different time scales of these processes.

10.9 Temporal and Spatial Aspect of MAE

For understanding of details of transport properties in MAE, analysis of individual jumps is useful [38]. Analysis of each jump has been done by picking up that having displacement greater than 1/2 of the distance of the first maximum of the pair correlation function $g(r)_{\mathrm{maxM\text{-}M}}$ by checking the data with elapsed time for every interval of $\Delta t = 0.8$ ps. The algorithm used in this analysis is simple and summarized as follows. Large scale motion was picked up by using a critical velocity, v_c. The region with $\Delta|r|/\Delta t \geq v_c$ can be regarded as successful jump, while that with $\Delta|r|/\Delta t < v_c$can be regarded as waiting. Time interval Δt and a critical velocity v_c determines the magnitude of coarse graining of the microscopic motions, The values of v_c and Δt were chosen so that the characteristics of the displacements are well reproduced ($\Delta t = 0.8$ ps and $v_c = 1.7$ Å /ps). Based on the jumps defined by this velocity category along the trajectories, we examined the mechanisms for the mixed alkali effect. Both the increasing backward correlation of jumps with the suppression of accelerated dynamics and the decreasing jump rate can be related to the reduction in the transport properties. The former property is related to the geometrical correlation of the jumps (spatial term), while the latter is concerning with the waiting times (temporal term). The changes in the spatial terms are dominant in the mixed alkali effect, although changes in the waiting time also exist. Similar conclusion (but much weighted by the temporal factors) has been obtained by Lammert and Heuer for a related system [20]. Some differences of explanations were caused by the definitions of jumps. Their jumps are the coarse-grained ones compared with that obtained directly from the trajectories of ions, since density profile they considered does not distinguish localized motion and strong localization directly. In their treatment, time spent for localized motion around the clusters is regarded as residence time. That is, the spatial factors in the short length scale regions are transformed into the temporal factor in such treatment. If larger region is defined as a site, it resulted in a longer waiting time, since the back-correlated motion tendency becomes larger in the mixed alkali glass as shown by the fractal dimension analysis of the trajectories.

Namely, in a course-grained description, it is possible to treat the strong back-correlated motions as the long residence time. However, arrest of motion in a deep trap is not necessarily the same as the localized motion within a cage, when we consider the mechanism of the ionic motion.

The difference of the definition of the jump motion affects the explanation of MAE as follows. When foreign alkali metal ions are mixed, the change in fractal dimension of the random walk, d_w, in a shorter region can be a cause of the apparent longer residence time.

10.10 Role of the Motion of Matrix Oxygen Atoms

Propagation of the dynamics through matrix oxygen atoms is also expected, because the motion of ions is cooperative with oxygen atoms in the NCL region. The jump motion of Li ions is accompanied with changes in the coordination number of surrounding oxygen atoms, which have the characteristics of a pre-jump motion. Previously, motion of Li ion was linked to the movement of the center of mass of the coordination polyhedron formed by surrounding oxygen atoms [58], where the vector for the center is determined by the summation of the positional vectors of surrounding oxygen atoms. This observation means that the motion of Li is cooperative with surrounding oxygen atoms. Naturally, if the motion of the oxygen atoms are suppressed, the motion of Li ion is also suppressed as found in Refs. [45, 59]. In this sense, the local fluctuations of oxygen atoms are necessary for the Li ion dynamics. However, the correlation at short distance does not necessarily mean that the long time and longer range dynamics of the Li ion is also governed by the oxygen motion. By using the steepest descent methods of Stillinger and Weber [60], we have shown that [18] the activation energy of the cooperative jumps are different from the one for the single jump.

This conclusion is consistent with the Coupling Model. This is another evidence that although the short time and short length scale motion of oxygen is necessary for the ion jump motion, but it is not enough to explain the long time and long range dynamics. For the same reason, the large MAE concerning conductivity and diffusion observed in the high alkali content glass is expected when the motion is decoupled with the relaxation of the matrix chain motion.

10.11 Comparison with Other Methods

Interception of the jump paths in the mixed alkali system we found was also confirmed for phosphate glasses by Swenson and Adams [59] using the bond-valence technique to Reverse Monte Carlo (RMC) produced structural models. They have visualized the pathway of Li and Rb ions with several composition of $Li_xRb_{1-x}PO_3$. In the mixture, the paths are mutually intercepted and the trend observed is essentially the same as ours, although some details including the shapes of the ion sites and paths seem to depend on the assumptions (such as geometric constraints) used in the technique. The following relation was found by Adams and Swenson [61–63]

$$\ln\left(\sigma_{\exp T}\right) \propto \sqrt[3]{F} \propto -\frac{E_\sigma}{k_B T} \tag{10.10}$$

They have also shown that the activation energy of the conductivity in the mixed alkali system is related to the cube root of the pathway volume fraction F, multiplied by the square root of the mobile cation mass M. In these observations, non-linear decrease of the dynamics is related to the cubic root dependence of the pathway volume. Therefore, the observations by them seem to be consistent with the changes in the fractal dimension of path and walks in our findings, at least qualitatively. It suggests that general characteristics of the percolation paths such as the volume fraction can be used for estimation of dynamics, irrespective for the detailed shape of the pathways. However, if one compared the examples of structures of paths obtained by MD and RMC, quite different impression might be brought. For example, please compare the left panel of Fig. 4.31 of Chap. 4 and Figs. 10.3 and 10.4.

For more detailed comparison, it is interesting to see how the pathways or ion sites and other related structures can be correctly reproduced by the technique. Recently, Mueller et al. [64] have examined the quality of structural models generated by the RMC method applied to the structure obtained MD of lithium metasilicate as input. It was found that the RMC modeling can reproduce well the short ranged structures such as the coordination numbers and bond angles, while, medium range order such as ring size distribution were not captured well and affected by initial configurations used in the method. In their work, MD simulation was used as a standard for the comparison. In such a case, it is not necessarily required to be more reliable than the structures obtained by other methods. This seems to be a good example how MD simulation can be used.

A volume change of substructure causes a change in the complexity of trajectory as suggested by the thermodynamical scaling, where the quantities of the dynamics obey scaling by the product variable TV^γ. Therefore, it will be helpful to consider that the transport property changes with TV^γ with a certain γ, which is a characteristic of the system even for the partial structures in the mixed alkali system.

10.12 Conclusion

Using molecular dynamics simulations, improved understanding of the mixed alkali effect has been obtained. In the mixed alkali system, the long range motion tends to be suppressed and the contribution of the local motion increases. Both increased complexity of the motion and decreased dimension of the paths cause a slowing down of the dynamics. Power law exponent of MSD is determined mainly by geometrical correlation between the jumps, and the change of it in mixed alkali glasses governs the slowing down of ionic motion in a non-linear manner. Therefore, the percolative aspects of the jump paths play roles in the MAE.

These descriptions are supported by the time dependence of the self-part and distinct part of the van Hove function of the Li ion, $G_s(r,t)$ and $G_d(r,t)$, in single and mixed alkali systems as well as fractal dimension analysis of the system for both the paths and the walks. Many majority ions are immobilized by the "cooperativity blockage" by the minority ions, while the motion among different kinds of ion sites weakens the blockage effect.

Involvement of the dynamics of the matrix oxygen atoms is expected in NCL region because of coupling of the ion motion with oxygen atoms. Thus the caged ion dynamics is important property of the system to be examined. Naturally, if the motion of the oxygen atoms is suppressed, the motion of Li ion is also suppressed. In this sense, local fluctuations of oxygen atoms are necessary for Li ion dynamics, although the cooperative nature of the motions among like ions should not be forgotten.

Dynamical heterogeneity and "cooperativity blockage" originating from ion-ion interaction and correlation are fundamental for understanding the observed ion dynamics and the MAE. Structural disorder such as in glasses is not essential in causing the MAE since these features of ion dynamics are common to other ionic conductors, which have not glassy networks and yet they all exhibit the MAE.

References

1. J.O. Isard, J. Non-Cryst. Solids **1**, 235 (1969)
2. D.E. Day, J. Non-Cryst. Solids **21**, 343 (1976)
3. M.D. Ingram, Phys. Chem. Glasses **28**, 215 (1987)
4. M.D. Ingram, Ber. Glass Sci. Technol. **67**, 15 (1994)
5. G.V. Chandrashekhar, L.M. Foster, Solid State Commun. **27**, 269 (1978)
6. G. Tomandl, H.A. Schaeffer, J. Non-Cryst. Solids **73**, 179 (1985)
7. C.T. Moynihan, N.S. Saad, D.C. Tran, A.V. Lesikar, J. Am. Ceram. Soc. **63**, 458 (1980)
8. K.L. Ngai, Y. Wang, C.T. Moynihan, J. Non-Cryst. Solids **307–310**, 999 (2002)
9. P. Maass, R. Peibst, J. Non-Cryst. Solids **352**, 42 (2006)
10. R. Peibst, S. Schott, P. Maass, Phys. Rev. Lett. **95**, 115901 (2005)
11. H. Jain, X. Lu, J. Non-Cryst. Solids **196**, 285 (1996)
12. H. Jain, N.L. Peterson, H.L. Downing, J. Non-Cryst. Solids **55**, 283 (1983)
13. R. Terai, H. Wakabayashi, H. Hamanaka, J. Non-Cryst. Solids **103**, 137 (1988)
14. B. Vessal, G.N. Greaves, P.T. Marten, A.V. Chadwick, R. Mole, S. Houde-Walter, Nature **356**, 504 (1992)
15. S. Balasubramanian, K.J. Rao, J. Phys. Chem. **97**, 8835 (1993)
16. S. Balasubramanian, K.J. Rao, J. Non-Cryst. Solids **181**, 157 (1995)
17. J. Habasaki, I. Okada, Y. Hiwatari, J. Non-Cryst. Solids **183**, 12 (1995)
18. J. Habasaki, I. Okada, Y. Hiwatari, J. Non-Cryst. Solids **208**, 181 (1996)
19. J. Horbach, W. Kob, K. Binder, C.A. Angell, Phys. Rev. **E54**, R5897 (1996)
20. H. Lammert, A. Heuer, Phys. Rev. **B72**, 214202 (2005)
21. J. Habasaki, K.L. Ngai, Phys. Chem. Chem. Phys. **9**, 4673 (2007)
22. T.L. Gilbert, J. Chem. Phys. **49**, 2640 (1968)
23. Y. Ida, Phys. Earth Planet Inter. **13**, 97 (1976)
24. J. Habasaki, I. Okada, Mol. Simul. **9**, 319 (1992)
25. L. Van Hove, Phys. Rev. **95**, 249 (1954)

26. A. Hall, J. Swenson, S. Adams, C. Meneghini, Phys. Rev. Lett. **101**, 195901 (2008)
27. R.D. Shannon, C.T. Prewitt, Acta Cryst **B25**, 925 (1969)
28. R.D. Shannon, Acta Cryst **A32**, 751 (1976)
29. J. Habasaki, K.L. Ngai, J. Chem. Phys. **122**, 214725 (2005)
30. J. Habasaki, AIP Conf. Proc. **1518**, 170 (2013)
31. J. Habasaki, Y. Hiwatari, Phys. Rev. **B69**, 144207 (2004)
32. J. Habasaki, I. Okada, Y. Hiwatari, Mat. Res. Soc. Symp. Proc. **455**, 91 (1996)
33. S. Alexander, R. Orbach, J. Phys. Lett. **43**, L625 (1982)
34. J. Habasaki, K.L. Ngai, Y. Hiwatari, J. Chem. Phys. **120**, 8195 (2004)
35. D. ben-Avraham, S. Havlin, *Diffusion and Reactions in Fractals and Disordered Systems* (Cambridge University Press, Cambridge, 2000)
36. J. Habasaki, Y. Hiwatari, J. Non-Cryst. Solids **307–310**, 930 (2002)
37. J. Habasaki, Y. Hiwatari, Phys. Rev. E **59**, 6962 (1999)
38. J. Habasaki, I. Okada, Y. Hiwatari, Phys. Rev. B **55**, 6309 (1997)
39. R. Kubo, J. Phys. Soc. Jpn. **12**, 570 (1957)
40. T. Odagaki, M. Lax, Phys. Rev. **B24**, 5284 (1981)
41. J. Habasaki, K.L. Ngai, Y. Hiwatari, Phys. Rev. **E65**, 021604 (2002)
42. Y. Haven, B. Verkerk, Phys. Chem. Glasses **6**, 38 (1965)
43. R. Terai, J. Non-Cryst. Solids **6**, 121 (1971)
44. B. Hafskjold, X. Li, J. Phys.: Condens. Matter **7**, 2949 (1995)
45. J. Habasaki, K.L. Ngai, Y. Hiwatari, C.T. Moynihan, J. Non-Cryst. Solids **349**, 223 (2004)
46. A. Heuer, M. Kunow, M. Vogel, R.D. Banhatti, Phys. Chem. Chem. Phys. **4**, 3185 (2002)
47. S. Voss, S.V. Divinski, A.W. Imre, H. Mehrer, J.N. Mundy, Solid State Ionics **176**, 1383 (2005)
48. J. Habasaki, K.L. Ngai, Y. Hiwatari, J. Chem. Phys. **121**, 925 (2004)
49. J. Habasaki, Y. Hiwatari, Phys. Rev. E **62**, 8790 (2000)
50. P. Scheidler, W. Kob, K. Binder, Europhys. Lett. **52**, 277 (2000)
51. K.L. Ngai, Philos. Mag. B **82**, 291 (2002)
52. K.L. Ngai, *Relaxation and Diffusion in Complex Systems* (Springer, New York, 2011)
53. M. Ozawa, W. Kob, A. Ikeda, K. Miyazaki, Proc. Natl. Acad. Sci. **112**, 6914 (2015)
54. J. Habasaki, Y. Hiwatari, Phys. Rev. **E58**, 5111 (1998)
55. W.G. LaCourse, J. Non-Cryst. Solids **95&96**, 905 (1987)
56. M.I. Ingram, B. Roling, J. Phys. Condens. Matter **15**, S1595 (2003)
57. J.E. Shelby Jr., D.E. Day, J. Am. Ceram. Soc. **52**, 169 (1969)
58. J. Habasaki, I. Okada, Y. Hiwatari, in *Transport and Dynamical Correlations in Glassy States and the Liquid-Glass Transition of Li_2SiO_3*, ed. by F. Yonezawa. Molecular Dynamics Simulations, Springer Series in Solid State Science, vol. 103 (Springer, Berlin, 1992), pp. 98–108
59. E. Sunyer, P. Jund, R. Jullien, J. Phys.: Condens. Matter **15**, L431 (2003)
60. F.H. Stillinger, T.A. Weber, Phys. Rev. **A25**, 978 (1982)
61. J. Swenson, S. Adams, Phys. Rev. Lett. **90**, 155507 (2003)
62. S. Adams, J. Swenson, Phys. Rev. Lett. **84**, 4144 (2000)
63. S. Adams, J. Swenson, Phys. Chem. Chem. Phys. **4**, 3179 (2002)
64. C.R. Mueller, V. Kathrirachchi, M. Schuch, P. Maass, G. Petkov, Phys. Chem. Chem. Phys. **12**, 10444 (2010)

Chapter 11
Molecular Dynamics Simulations of Ionic Liquids

11.1 Brief Introduction and History

Typical ionic salts such as NaCl have high melting point. However, different from the classical salt, some newly developed molten salts are liquids even at room temperature. They form a new class of chemical compounds, and are now called the room-temperature ionic liquids (RTIL) or simply ionic liquids (ILs). Typical ILs of interest are salts each of which is constituted by an organic cation and an inorganic anion, and their melting points are below or near the room temperature [1–4]. Sometimes they are defined by the melting point <100 °C. Recently, the term "ionic liquids" might be used to include traditional "molten salts" with higher melting points and is distinguished from "room temperature ionic liquids" in that case.

We note that there was a class of room temperature molten salts before developments of ILs; however, the new class of ILs have attracted much attention in the research community because they possess many desirable properties. The properties include high thermal stability and a good solvent action for many substances with negligible vapor pressure, making them ideal replacements for volatile organic solvents in various applications. For example, cellulose was shown to be solved up to 25 wt% with 1-butyl-3-methylimidazolium chloride, [bmim]Cl, at 100 °C, where the cellulose can be cracked or modified [5]. Therefore ILs are expected to take a role for making biomass fuel effectively and many technology concerning with it is developing. In such cases, the process in preparation will be also important in its contribution to green chemistry [6]. The ILs also have high ionic conductivity values suitable for use as electrolytes. Moreover, the ILs are designable to suit the need because of the many possible combinations of cations and anions with different structures and properties including the bulky ones, and therefore are expected to play roles for various applications in many fields. The system tends to be viscous, because the situation is similar to liquid near the glass transition regimes, and therefore the system has the general characteristics of glass-formers to

J. Habasaki et al., *Dynamics of Glassy, Crystalline and Liquid Ionic Conductors*,
Topics in Applied Physics 132, DOI 10.1007/978-3-319-42391-3_11

study the glass transition. Molecular dynamics (MD) simulations are useful methods to learn more about the mechanism of the ionic transport properties as well as structural glass transition macroscopically and microscopically. The knowledge of the microscopic mechanism slowing down the dynamics in ILs will be useful for the application of them in many branches of science. The models of ionic liquid systems used in MD simulations are in most cases realistic enough to compare the results with experimental findings.

The following potential form is frequently used in MD simulation studies of ILs by different groups [7–12],

$$\begin{aligned} U(R) = & \sum_{\text{bonds}} K_{\mathrm{r}}\left(r - r_{\mathrm{eq}}\right)^2 \\ & + \sum_{\text{angles}} K_{\theta}\left(\theta - \theta_{\mathrm{eq}}\right)^2 \\ & + \sum_{\text{dihedrals}} \frac{V_{\mathrm{n}}}{2}(1 + \cos\left[n\phi - \gamma\right]) \\ & + \sum_{\mathrm{i<j}}^{\text{atoms}} \left(\frac{A_{\mathrm{ij}}}{R_{\mathrm{ij}}^{12}} - \frac{B_{\mathrm{ij}}}{R_{\mathrm{ij}}^{6}}\right) \\ & + \sum_{\mathrm{i<j}}^{\text{atoms}} \frac{q_{\mathrm{i}} q_{\mathrm{j}}}{\varepsilon R_{\mathrm{ij}}} \end{aligned} \tag{11.1}$$

The model potential is composed of a sum of bond, angle, and dihedral deformation energies, a pairwise standard (6,12) Lennard-Jones potential, and Coulombic interactions between atoms with charges q_{i}. Used by Lopes et al. [13], and by Wang et al. [14], they were able to reproduce by simulations the domain structures, suggested by the results from experiments [15]. Some researchers pointed out the importance of the polarization term to explain the deviations of MD simulations result from experimental dynamics in ionic liquids [16]. Viscosity of 1-ethyl-3-methylimidazolium nitrate (EMIM-NO_3) system in the polarizable model at 400 K is in better agreement with the experimental values than non-polarizable model [17]. Bagno et al. [18] have compared the interaction energy of two clusters of the 1,3-dimethylimidazolium tetrafluoroborate made of four and eight ions by DFT of B3LYP/6-311G(d,p) level and have shown the importance of the many body effects. They also discussed the role of polarizability.

In most of classical MD simulations of IL, partial charge had been used for each atom based on the MO calculations, while the formal charge had been assumed for each ion. Sometimes, polarization term was used just for improving the formal charge potential, when the deviation from the experiments was found. Importance of using a partial charge for each ion in more realistic MD simulations is pointed out by several authors including us [19, 20]. Actually, it is known that the partial charge model is good for reproducing other ionic systems [21]. Nowadays, parameters using partial charges have been proposed for several ILs and seem to be good enough without the polarization terms [20, 22, 23]. Yasaka et al. have pointed out that scaled charge in an ionic liquid is effective to reproduce the rotational dynamics found in experiment by NMR [24]. Employing the Quantum Theory of Atoms In Molecules (QTAIM) approach, recent theoretical work by Beichel et al. [25] have obtained the charge density of [C1MIM][C1SO_4]. Integrated QTAIM charges of the experimental (calculated) charge density of the cation and anion resulted in non-integer values of ±0.90 (±0.87) e. Therefore revision or further study of importance of the polarization term may be necessary. In either case, the role of the polarization term is considered to be just shifting the position in the phase diagram [17] and it is not necessarily required for the discussion of general property of ILs such as the mechanism of the glass transition. This is because such properties are common to materials with and without polarization terms.

Several kind of coarse-grained models are also used for simulation of IL. Attempts including the replacement of the long range electrostatic potential energy by the short range effective potential have been reported so far for ILs and related materials. One of the successful approaches is damped shifted (DS) potential [26] having the following form

$$V_{DS}(r) = \left(\frac{erfc(\alpha r)}{r} + P(r - R_{cut})\right) \tag{11.2}$$

In the approach in Ref. [27], inverse-power law type potential has been applied for water and NaCl by the force matching method. In this approach, interaction potential is obtained for each interaction and therefore the information for the structure of the atomic level is kept.

Another possible approach is to use the concept of the potential of mean force (PMF) [28] for the coarse-graining of the potential. Pair-correlation functions, $g(r)$ of the pairs of ions or part of the ions derived from atomistic simulations can be transferred to the coarse-grained model, because the force is a function of $g(r)$. Caution is necessary because the force is essentially having a collective property including multi particle effects. Namely, if one uses the PMF as an effective force in a conventional MD program, the forces from other particles may have been counted twice. Therefore, modification of the program or further refinements of the parameters using some cost functions are useful.

One of the problems for studying of ionic liquids may be the rapidly increasing numbers of papers and data. This makes it difficult in catching up to understand the system. Combination of different cation and anion and more complex systems introduced are increasing with time. IUPAC prepared the data base named "ILThermo" [29] where data are now being gathered. Recently, extensive investigation of [Tf_2N^-] ILs have been done including experimental, molecular modeling of their structure, thermodynamics and transport (self-diffusion coefficient, viscosity, etc.) properties, because IUPAC has selected bis(trifluoromethylsulfonyl)imide, [Tf_2N^-], as a benchmark anion in ILs (for example, see Ref. [30]). Such standardization of the system is helpful for comparison of systems and understanding them. However, caution is required for understanding the nature of the MD simulations among these works, because the purpose of the simulation is not necessary to faithfully reproduce the real system. One should choose proper model depending on the purpose of the work, and one needs to understand correctly the type of simulations.

11.2 MD Study of 1-Ethyl-3-Methyl-Imidazolium Nitrate (EMIM-NO_3)

Habasaki and Ngai studied the dynamics of the IL, 1-ethyl-3-methyl-imidazolium nitrate (EMIM-NO_3) by using the potential functions of the same form as Eq. (11.1) [19, 31–33]. In these works, formal charge had been used for each ion. The parameters for the IL were taken from the General Amber Force Field and the system can be regarded as a useful model system for considerations of structures, dynamical properties, glass transitions, and dynamic heterogeneity. Optimized structure of ion pair obtained by ab initio MO calculations is shown in Fig. 11.1. The imidazolium ring is rather bulky and the cation is larger than the anion, while the iso-electrostatic potential surface seems to have comparable sizes.

Our attention was focused on the heterogeneous dynamics and changes of dynamics near the glass transition. The general Amber potential field used is good enough to understand what kind of microscopic dynamics is responsible for the slow dynamics near the glass transition. Although the slow dynamics in the

Fig. 11.1 Optimized structure of ion pair of an ionic liquid (EMIM-NO_3) obtained by ab initio MO calculation (using a double zeta + p + d basis). Electrostatic potentials (iso-surface 0.05) are shown

ionic liquids have similarities to that of molecular glass forming materials, caution is needed in examining the slow and fast categories of the heterogeneity. In the present work, “fast and slow” is concerned with the transport properties of long times, rather than short times and short length scales behavior, while the fast and slow categories are also used for the relaxation time in the discussion of the glass transition problems.

MD simulations were performed using this force field on smaller systems having 64 $EMIM^+$ and 64 NO_3^-, and on a larger system having 256 $EMIM^+$ and 256 NO_3^- with a total of 5888 atoms. PBC were imposed, and Coulomb interactions were calculated using the particle mesh Ewald method. The system was equilibrated at 3000 K and the temperature was gradually decreased. The time step was either 1 or 2 fs, and the simulations of NVE ensemble were carried out up to 2.5 or 10 ns at temperatures of 0, 250, 300, 350, 370, 400, 500, 600, 800 and 1000 K after equilibration with a more than 1 ns run of NPT ensemble at each temperature. The equilibrated density was found to be 1.206 at 400 K. We found that the system size dependence of the diffusivity of the system is small, and hence we use results of both systems for discussion.

11.2.1 Heterogeneity in the Structure of Ionic Liquid, EMIM-NO_3

Instantaneous structure of EMIM-NO_3 at 400 K is shown in Fig. 11.2. Structure represented by balls and sticks can be found in Fig. 11.2a, while in Fig. 11.2b, imidazolium rings are shown by tubes and other structures are shown by wire frames. Clustering of imidazolium rings with several sizes can be clearly seen in the figure. Clustering of anions with several sizes is also found. Some of the pairs of cations (i.e. parallel imidazolium rings) within 5 Å are found and this corresponds to the shoulder found in the $g(r)$ of the $EMIM^+$-$EMIM^+$ correlation shown later.

So far there are several reports for the heterogeneous structures of ionic liquids related to the segregation of the chain part of the cations [15, 34] and it is suggested to be important for characterizing the ionic liquids as a solvent. As found in Fig. 11.2, heterogeneous structure already exists for the system with a cation having a short chain like $EMIM^+$ ions, and therefore it is not necessarily based on the specific character of the chains. We also note that the heterogeneity discussed here depends on temperature strongly.

11.2.2 Pair Correlation Functions

Pair correlation function, $g(r)$, of ionic liquid at 400 K is shown in Fig. 11.3a. Those of at 600 K, 370 K, and 250 K (glassy system) are shown in Fig. 11.3b.

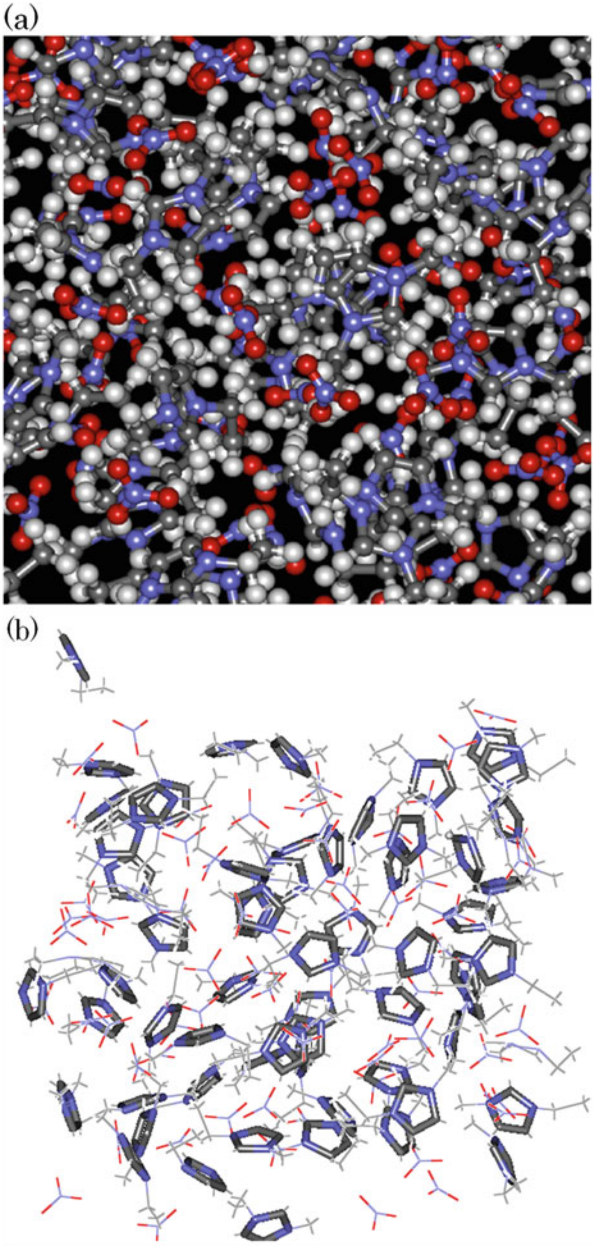

Fig. 11.2 Instantaneous structure of an ionic liquid (EMIM-NO_3) at 400 K. (**a**) In ball and stick representation. (**b**) In wire representation, where the imidazolium rings were emphasized by the tubes. Clustering of structures with several sizes are found

MD simulations for the same system had been done previously by Del Popolo and Voth [11] and the behaviors at 400 K were examined. The pair correlation function of center of mass, $g(r)$ and the diffusion coefficient of both cation and anion at 400 K shown here are comparable to those obtained by them. The quality of

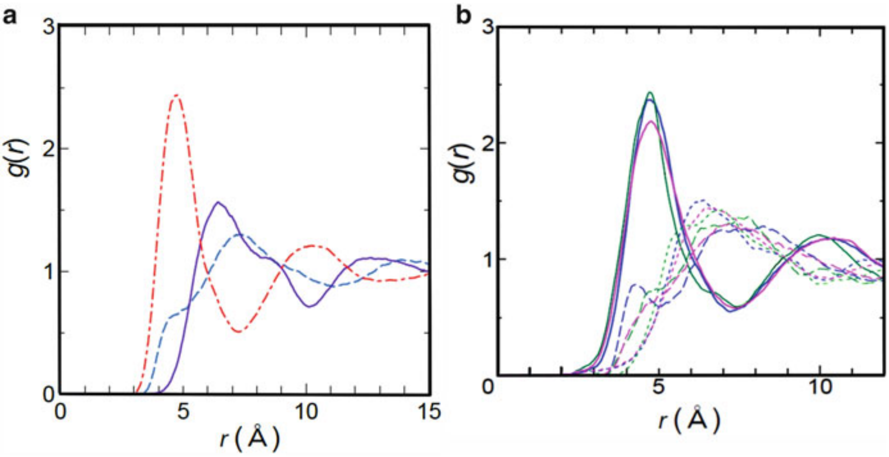

Fig. 11.3 (**a**) Pair-correlation g(r) of EMIM-NO_3 at 400 K for anion-anion (*purple solid*), cation-cation (*blue dashed*) and cation-anion (*red dot-dashed*) pairs, respectively. (**b**) Temperature dependence of the pair correlation functions of ionic liquids and its vitrified system. Temperature examined was 600 K (*pink*), 370 K (*blue*), and 250 K (*green*)

the potential parameters used seems to be comparable to the ones used by them. Pair correlation functions also are comparable with those of a similar system, $DMIM^+Cl^-$ (1,3-dimethyl imidazolium chloride), obtained by neutron diffraction experiments [35].

Increases in the coordination number in these pairs with lowering temperatures are found by integrating the peaks. Coordination number for $EMIM^+$-$EMIM^+$ pair within the first coordination shell (determined at 7.5 Å) is increasing from 6.4 to 7.7 when temperature is decreased from 400 K to 250 K. Coordination number of anion around anion also increases from 6.6 to 8.1. The change of coordination number from 7.0 to 8.4 is found for the $EMIM^+$-NO_3^- pair. The first peak of $g(r)$ of the pair tends to be sharper and narrower with decreasing temperature. Except for bumps and sharpness, the structures at low temperature seem to keep the liquid like structure from the appearance of $g(r)$ at a first glance. (For more discussions of the structural (topological) change of the system, go to Sect. 11.11.)

11.3 Several Time Regions in MSD

Mean squared displacement (MSD) of ionic liquids shows different behaviors in several time regions. The behavior of the MSD indicates changes from caging at short times to diffusive motion at long times through power law time dependence regime caused by back correlated motion within neighboring sites.

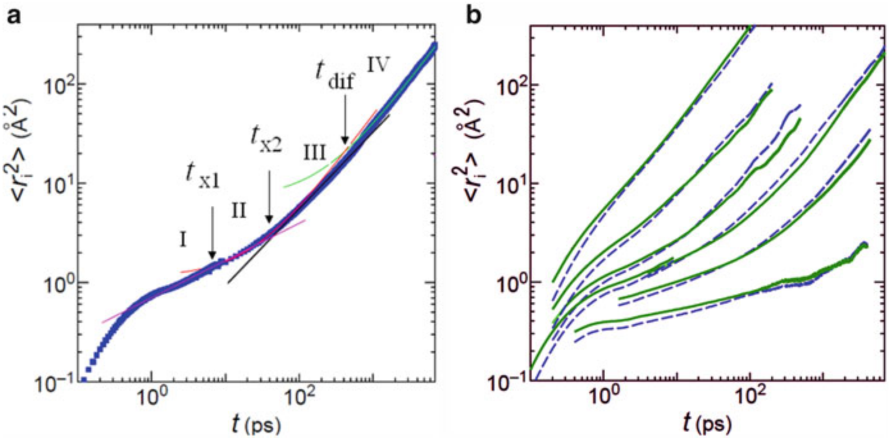

Fig. 11.4 (**a**) Time regions in mean squared displacement for the center of mass motion of cations in ionic liquid (EMIM-NO_3) at 400 K. Regions observed are comparable that in the lithium ions in the lithium silicates. The slope in the NCL region is larger than the ion in the glass due to the larger local motions of bulky ions. (**b**) Temperature dependence of MSD for cations (*blue*) and anions (*green*). 1000, 600, 500, 400, 370, 300 K from top to bottom

Typical MSD of EMIM^+ ion at 400 K is shown in Fig. 11.4a.

In the Region I (NCL), $t < t_{x1}$, the relation $\ln <r_\mathrm{i}^2> = -0.38 + 0.38\ln(t)$ was obtained.

In Region II, $t_{x1} < t < t_{x2}$, quasi-linear relation due to independent jumps was obtained $<r_\mathrm{i}^2> = 1.14 + 0.048t$.

In region III (power law region), $t_{x2} < t < t_{df}$, $\ln <r_\mathrm{i}^2> = -1.86 + 0.77\ln(t)$, the fractional power law was obtained.

Power law exponent is proportional to t^θ, where $\theta = 2/d_\mathrm{w}$ for the mean behavior of fast and slow ions, if temporal term can be neglected. Here d_w is a fractal dimension of random walks. (See Sect. 9.5.4 and Appendix A.1.)

In region IV (diffusive region), $t_{df} < t, <r_\mathrm{i}^2> = 7.02 + 0.032t$ was obtained.

(Here t is in ps and MSD is in $\text{Å}^2\ \text{ps}^{-1}$.)

These situations are comparable for the ionics in the ionically conducting glasses [36] except for larger slope in the NCL region in the IL, which is related the motion of bulky ions. The qualitatively identical dynamics of the IL and the glassy ionic conductors is a special case of the universal dynamics of interacting systems predicted by the Coupling Model and supported by experiments in different fields [37–39].

11.4 Temperature Dependence of the Dynamics

Temperature dependence of the MSD of ions in EMIM-NO_3 was shown in Fig. 11.4b at several temperatures. Behaviors of cation and anion in the present system are similar and it is probably due to comparable effective sizes. The difference will become larger if the size difference is larger. Tokuda et al. [40] have reported the physicochemical properties of the nine ILs with varying ionic structures. In their works, the microscopic ionic diffusion is found to be significantly influenced not only by the relative cationic and anionic size but also by the geometric shape.

11.4.1 Origin of the Fragile Behaviors Characterized by the Temperature Dependence of the Diffusivity

From the slope of the MSD in diffusive regimes, the diffusion coefficient can be obtained by the Einstein equation. Slowing down of the dynamics on decreasing temperature is well characterized by the change of the diffusion coefficients. At high temperature regimes, the diffusive regimes are rapidly attained. With decreasing temperature, each region in Fig. 11.4a becomes longer and longer. At the lowest temperature of 300 K, in the short time region, the MSD increases weakly with time because the $EMIM^+$ or NO_3^- ions are caged, and it corresponds to the nearly constant loss (NCL) [41–44] regime observed by dielectric loss in a conductivity relaxation experiment or MD simulations of ionically conducting glasses. NCL has been found experimentally in conductivity relaxation data of a room temperature ionic liquid, 1-methyl-3-trimethylsilylmethylimidazolium tetrafluoroborate, ([Si-MIm][BF_4]) [45]. This caged regime extends to longer times and the diffusive regime was not attained up to the longest time of the simulation. For more discussion of NCL, go to Chap. 4.

Although ILs are liquids over wide temperature ranges, they can be vitrified at sufficiently low temperatures or elevated pressures. In this simulation, at temperatures less than 260 K, the system is in the glassy state deduced from the change of the temperature dependence of the density. Between 260 K and about 360–370 K, the system can be regarded as being in the super-cooled liquid state.

In general, dynamics of ions in disordered materials show large dynamical heterogeneity in both the temporal terms (waiting time distribution of jumps) and the spatial terms (geometrical correlation among successive motions) [46, 47]. Temperature dependences of diffusion coefficients are shown in Fig. 11.5a and in b, where semi-logarithmic plot and double-logarithmic plot are used, respectively. Diffusivity above 800 K seems to show the Arrhenius type temperature dependence. Below this temperature the system shows the slowing down by following the Vogel-Fulcher-Tammann-Hesse (VFTH) dependence;

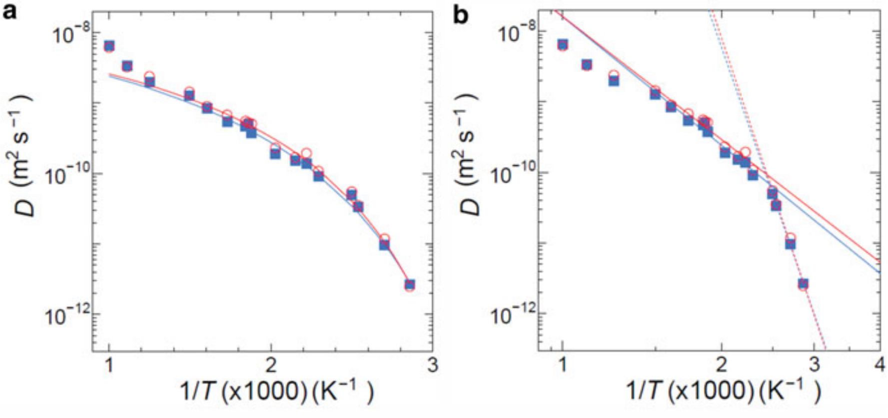

Fig. 11.5 (**a**) VFTH fit of the temperature dependence of diffusivity for cation (*red circles*) and anion (*blue squares*) in ionic liquid (EMIM-NO$_3$) obtained by MD simulations. (**b**) Double-logarithmic plot of the same data used in the VFTH plot. Inflections of the plots are found at around 410 K for both cations and anions. Lines are fitted ones for the power law in each region. Slowing down of the dynamics near the glass transition can be characterized by the different slopes and not necessarily mean the rapid decrease near T_0

$$D = D_0 \exp\left(\frac{E}{T - T_0}\right). \tag{11.3}$$

In several ionic liquids so far, diffusivity as well as conductivity can be well fitted [38, 48] to the VFTH equation [49–51]. The VFTH fit to the MD simulation data is shown by the curve in Fig. 11.5a.

11.4.2 *Fragility Characterized by the Different Slopes of Two Regions*

For cations and anions, T_0 obtained from the fits for EMIM-NO$_3$ are 243.2 and 256.5 K, respectively. The value of T_0 in Eq. (11.3), at which the diffusion coefficient is practically 0, is slightly lower than the glass transition temperature obtained from the density-temperature plot. The relation $T_0 < T_g$ is also known for the viscosity η, which was also fitted to $\eta \propto \exp[DT_0/(T - T_0)]$ [49–51]. The results in the present work are consistent with the analysis in previous works using VFTH type equation; however, the T_0 value is not necessarily a true characteristic temperature of the system for the following reasons. Although the VFTH relation holds approximately, data for both high and low temperature regions can also be well fitted by power laws as shown in Fig. 11.5b. Thus the VFTH fit is not necessary the best fit in both the high and low temperature regions and existence of T_0 is due to a choice of the functional form. In both fits using exponential functions and in those using power law functions, we have observed an inflection point at around 410 K. From the observation of the inflection, the rapid slowing down of the dynamics at lower temperature region is attributed to the coexistence of a gentle slope at higher temperature and a steeper slope at lower temperature regimes rather than to the characteristics near the specific temperature T_0. Due to the limited range of each temperature region, it is difficult to judge which expression is the best by the quality of the fitting only. As shown in the following section, inflections of the dynamics correspond to changes in the fractal dimension of the random walk, d_w, obtained from trajectories of ions.

The concept of "fragility" is proposed by Angell to characterize the glass transition [52]. The fragile system shows super-Arrhenius behavior of the dynamics, while the strong system shows temperature dependence closer to the Arrhenius behavior. It can be concluded that the large "fragility", shown by the curvature of diffusion coefficients, can be explained by the changes in the slopes in both temperature regions rather than the suddenly caused rapid decrease of dynamics near T_0. From this view, the acceleration of the dynamics with heterogeneity near the inflection points, which resulted in the gentle slope in the high temperature region, ensures the large changes in the slopes.

If we use the exponential function at lower temperature region, extrapolated value of the diffusion coefficient of cation becomes $3.8 \times 10^{-40}\ \mathrm{m}^2\ \mathrm{s}^{-1}$ at 100 K. It must be difficult to observe the diffusion in the MD simulation up to several nano seconds. In this situation, phase transition to explain the glass transition is not necessary, although the results do not exclude the possibility of the existence of other characteristic temperatures nor starting of the non-equilibrium relaxation. In the ionic liquid, liquid like structure with small modifications are obtained by the rapid cooling down (~1 degree/ps) as shown in $g(r)$ at low temperatures. Therefore, the systems at low temperatures are regarded as (computational) quenched glasses. In this case, the structure is not so much different from liquids unless the system was deeply cooled down. We note that we observed a non-equilibrium relaxation starting at around 410 K in EMIM-NO_3 during a long run. It may cause a crystallization or stabilization of the glasses after longer runs. This situation may be comparable to the SC (see 8.2.2.1) system [53, 54]. With a rapid quench of the SC model, a quenched glass keeping the liquid like structure was obtained, while it seems to be inevitable for the system to start non-equilibrium relaxation near or larger than $\rho^* = 1.4$, in many of runs, where ρ^* is a reduced density of the system. When the system was kept for long time at a certain temperature region near $\rho^* = 1.3$, non-equilibrium relaxation toward the glass branch (or crystal branch below it in the phase-diagram) starts. It is also interesting to note that the effective potential underlying the TV^γ scaling behaviors of the ionic liquid is considered to arise from the inverse-power law type potentials as in the SC model.

Dynamical slowing down similar to the present work has been found in other systems such as binary Lennard-Jones systems [55, 56].

11.5 Dynamic Heterogeneity in Ionic Liquid

11.5.1 Heterogeneity Observed in the Trajectories of Ions

Dynamics of these systems at several temperatures are characterized by the fractal dimension of random walks obtained from the trajectories of ions, van Hove functions, intermediate scattering functions and multifractal analysis of the density profiles. Trajectory of ions were visualized and characterized by the fractal dimension of the random walk by the divider method shown in the Appendix A.1.

In Fig. 11.6, trajectories of arbitrary chosen ions of both kinds at the much lower temperature of 370 K during 9.5 ns runs are shown. They were averaged every 25 ps and shown by the projection onto the x-y plane. The jump connecting the localized regions becomes clearer after the short time scale motion has been averaged. One can see that some ions are localized for long periods, while some ions tend to show larger scale motions. The heterogeneity shown in the trajectories are quite similar to the ones shown in the motion of Li ions in the ionically conducting glasses. The most mobile ion in Fig. 11.6 (cation) shows the successive jumps during the 9.5 ns time span, while some ions tend to be localized near the initial positions. The heterogeneity observed in the lower temperature region is related to the slower rate of exchange between the fast and slow components.

11.5.2 Fractal Dimension of the Random Walks

Fast and slow ions, as found in Fig. 11.6, can be characterized by their geometrical characteristics of trajectories and thereby fractal dimension of the random walk [57], d_w, which represent the complexity of the trajectory, was determined by the

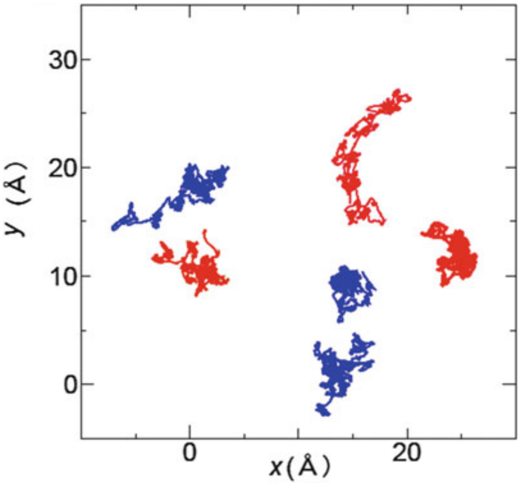

Fig. 11.6 Examples of trajectories of ions at 370 K during 9.5 ns runs. Cations (*red*) and anions (*blue*) are arbitrary chosen

divider method (see Appendix A.1). MSD in the power law region is proportional to t^{θ}, where $\theta = 2/d_{\mathrm{w}}$ for the mean behavior of fast and slow ions. The fractal dimension is concerned with the spatial term determined from the following equation,

$$N_T = AL_r^{-\mathrm{dw}}, \tag{11.4}$$

where L_r is a length of the divider and N_T is a count how many times are required to cover the trajectories by it. Since the slope of the plots of N_T against L_r in double logarithmic scale changes at around 3 Å in wide temperature ranges, one can obtain d_{w1} for the shorter length scale motion and d_{w2} for the longer length scale motion.

Temperature dependence of both values is shown in Fig. 11.7. The d_{w} values at higher temperature than 600 K is about 2 (typical value for free random walks) and it increases with decreasing temperature. At 600 K, $d_{\mathrm{w}} = 2.08$ for $1 < L_r < 3$ Å and $d_{\mathrm{w}} = 2.02$ for $10 > L_r > 3$ Å. A rapid increase of d_{w} with decreasing temperature is observed at around 400 K, and at lower temperatures the short length scale motion becomes dominant. Increase of both d_{w} values with decreasing temperature means the existence of the anomalous diffusion (i.e. in the power law region) due to stronger back-correlated motion. The temperature dependence of the long range motion is stronger than that of the short range motion, because motion of fast ions is fairly suppressed at low temperature regions. In particular, the contribution of the

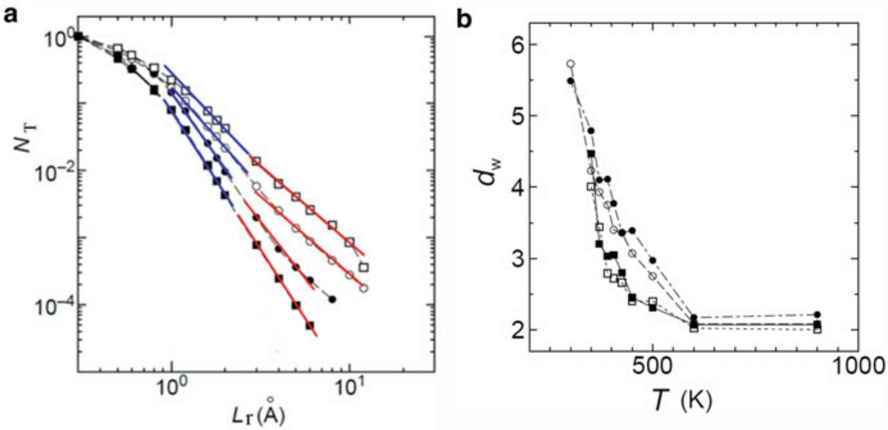

Fig. 11.7 (**a**) Examples of temperature dependence of the N_T against L_r plot obtained from the trajectories for EMIM ions at 600 K, 400 K, 370 K, and 350 K. The slopes of each short and long L_r region are different at most temperatures. The fitted lines at 600 K in each region shows inflection at around $L_r = 3$. (**b**) Fractal dimension of the random walks is obtained from the slope. (**b**) Temperature dependence of fractal dimension of the random works for short length (d_{w1}) and for long length scale (d_{w2}). *Circles* are for d_{w1}, while the *squares* are for d_{w2}. *Filled marks* are for EMIM^+ ions while the *open marks* are for $\mathrm{NO_3}^-$ ions. The value 2 is expected for the free random walks, while larger values than 2 means stronger back correlations. Rapid increase of d_{w2} begins at around 410 K and dominant component becomes d_{w1} at lower temperatures than 350 K

long range motion rapidly decreases with lowering temperature and N_T of $L_r > 3$ Å is less than 10^{-3} at 350 K. At this temperature, difference of the slopes for the two regions is small. At temperatures higher than 350 K, $d_{\mathrm{w}2}$ for longer length scale motion is smaller than $d_{\mathrm{w}1}$ due to stronger forward correlated motion. Long range motion is essentially absent at 250 K. In general, the back correlation probability of ions depends on the fracton dimension [58] defined by $2d_{\mathrm{f}}/d_{\mathrm{w}}$, where d_{f} is the dimension of the path. In the present system, the mobility of the ions is of the same order as that of the surrounding ions. Therefore, the changes in the path for ionic motion occur on a time scale similar to that of the motion of the ion itself, and hence d_{f} is comparable to the dimension of the space at high temperature region.

Existence of the characteristic value of the fractal dimension of the random walk, ($d_{\mathrm{w}} = 3$) to separate the localization and delocalization of ion is worth notice. With decrease in temperature, d_{w} gradually increases at the beginning, and a rapid increase is found at around 400 K, where the values of d_{w} for longer scale motion exceed 3. For example, at 370 K, we find $d_{\mathrm{w}} = 3.93$ for $L_r < 3$ Å and $d_{\mathrm{w}} = 3.44$ for $L_r > 3$ Å. Value of d_{w} larger than 2 is due to the motion having backward correlation. The number of the space dimension 3 is the limit for d_{w}, if overlaps of trajectories are not allowed. The value can be greater than 3 at lower temperatures, because d_{w} is a latent dimension which includes the folding of the trajectories. Thus values of d_{w} larger than 3 mean that the trajectories of ions are folded many times and do not easily spread over space at lower temperatures. These changes in d_{w} values and changes in the contribution of long range motion reasonably explain the inflection observed in the temperature dependence of the diffusion coefficients.

The complex conductivity is a function of the mean squared displacements [59, 60],

$$\sigma^*(\omega) = -\omega^2 \frac{N_{\mathrm{ion}} q^2}{6 H_{\mathrm{R}} kT} \int_0^\infty < r^2(t) > e^{-\mathrm{i}\omega t} dt, \tag{11.5}$$

where N_{ion} is the number density of mobile ions, q the ion charge, k the Boltzmann constant, and T the temperature. H_{R}, the Haven ratio, is the ratio of the self-diffusion and the bulk diffusion given by [59]

$$H_{\mathrm{R}} = \sum_{\mathrm{i}} \langle \mathbf{v}_{\mathrm{i}}(0) \bullet \mathbf{v}_{\mathrm{i}}(t) \rangle \Big/ \left\langle \sum_{\mathrm{i}} \mathbf{v}_{\mathrm{i}}(0) \bullet \sum_{\mathrm{j}} \mathbf{v}_{\mathrm{j}}(t) \right\rangle \tag{11.6}$$

Therefore, the trend observed for tracer diffusion should be related to the collective motion, unless a sudden change in the Haven ratio occurs near the glass transition region of ILs. It is worth mentioning that when both anion and cation can move by cooperative jumps in the same direction, this contributes to the diffusion but not the conductivity, and thus this kind of motion also affects the behavior of the Haven Ratio. In the present IL, the motions of the anion and cation are strongly coupled with each other and their motions are directly related to the structural relaxation, except for a modification by the dynamical heterogeneity. The motions of cation and anion are only slightly decoupled near the glass transition temperature, as shown by the van Hove function. Therefore, the behaviors of the tracer diffusion and the collective motion are connected to each other in the present system. When the ionic motion is decoupled from the structural relaxation, the length scale of the cooperative motions for viscosity can be different from that of conductivity or diffusion. Examples of decoupling of the conductivity relaxation from the structural relaxation experimentally found in real systems can be found in Refs. [61, 62].

11.5.3 Self-Part of the Van Hove Functions

Low viscosity ionic liquids based on organic salts are rare and are sought after for some purposes [63]. The high viscosity originates from the fact that the motion of ions in the ionic liquid is similar to a super-cooled liquid near the glass transition regimes. Therefore, it is natural that the dynamic heterogeneity similar to the glass forming materials is found in the trajectories or in the self-part of the van Hove functions. The self-part of the van Hove function is useful for understanding the heterogeneity of the dynamics. The function is defined as follows.

$$G_s(\mathbf{r}, t) = (1/N)\sum_{i=1}^{N} \langle \delta(\mathbf{r}_i(t) - \mathbf{r}_i(0) - \mathbf{r}) \rangle \tag{11.7}$$

Example of the data obtained from MD for EMIM-NO_3 is shown in the following subsection.

11.5.3.1 Lévy Distribution

In Fig. 11.8a, b, the function for the center of mass of $EMIM^+$ ions in the EMIM-NO_3 obtained by MD at 400 K is shown in linear-scale and in double-logarithmic scale, respectively. Both plots are useful to show shapes to characterize the functional form. Deviation from the Gaussian form is clearly found in both plots. Observed functional form of the self-part of the van Hove function of ions is affected by trapping in the cages, back correlated motions with distribution of the length scales and exponential truncation of it (see Fig. 11.8b).

In the power law region of MSD, the distribution shows an inverse-power law tail (see red dashed line in Fig. 11.8b) of the following form for large X ($=d|r|/dt$ or r) region,

$$P(X) = \frac{1}{|X|^{\alpha+1}} \tag{11.8}$$

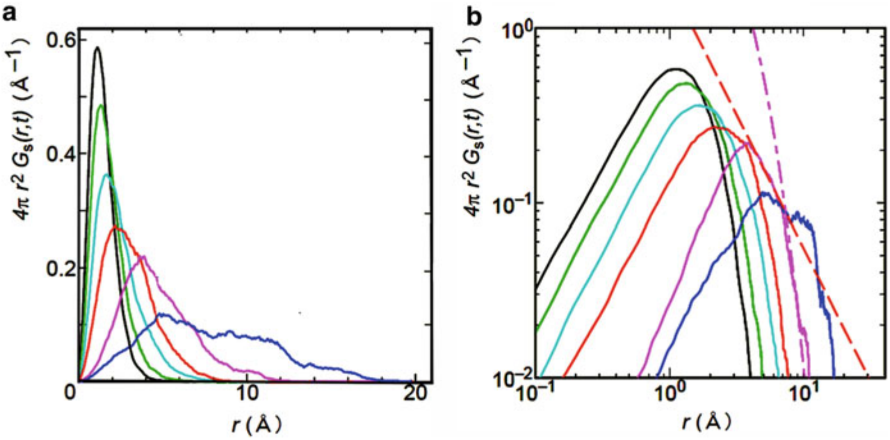

Fig. 11.8 (**a**) Self-part of the van Hove function at 400 K for EMIM$^+$ ions. t = 20, 40, 100, 200, 400 and 1000 ps from *left* to *right*. (**b**) The same data shown in a log-log plot. In the power law region, inverse power law tail (fitted line is shown by a *dashed line*) is followed by the exponential truncation (shown by the *dash-dotted curve*) as found in the data at 400 ps

with an exponential tail (see dashed dotted curve in Fig. 11.8b). This part of the van Hove functions is related to the Lévy (alpha stable) distribution (when $\alpha < 2$) [64–66] (see Appendix A.2 for details) as found [67] in molten and glassy Li_2SiO_3. The broadening of the peak found in a short time region represents the motion within a cage and the fluctuations of the cage itself, while the decreased area of the first peak represents the motion to the next shell. With the decay of the first peak, the tail part of the function develops with elapse of time. The long tail with large *r* is related to the long range motion as found in the trajectory, i.e., by fast ions with successive jump-like motions.

The decay of first peak is faster than that in the case of Li$^+$ ions in glassy lithium metasilicate (Li_2SiO_3) at 700 K in spite of the comparable relaxation rates at longer length and time scales; however, it is similar to the Li_2SiO_3 in the super-cooled liquid state at higher temperatures. In Li_2SiO_3 and related glasses, the first peak remains for a long time due to long waiting time of the jump motions. This strong localization enhancing the dynamical heterogeneity is not obvious at least at 400 K of ILs. These differences are natural because the matrix atoms, Si and O, in Li_2SiO_3 have the chain structure with much slower relaxation rates than Li ions, while the EMIM$^+$ and NO_3^- have comparable mobility. Jumps in the EMIM-NO_3 at these temperatures are not the typical ones among well-defined ion sites, because the mobility of the ions at short time and length scales contributes even in the supercooled liquid state.

Figure 11.9 show the evolution of the self-part of the van Hove function, $4\pi r^2 G_s(r,t)$, as a function of *r* with time at (a) 400 K, and (b) 370 K for both cation and anion in linear-log scales. In this IL, the behaviors of cation and anion are quite similar. Deviation from the Gaussian form is found for the functions at 370 and 400 K and both at short and long times. Peaks due to long time localization together

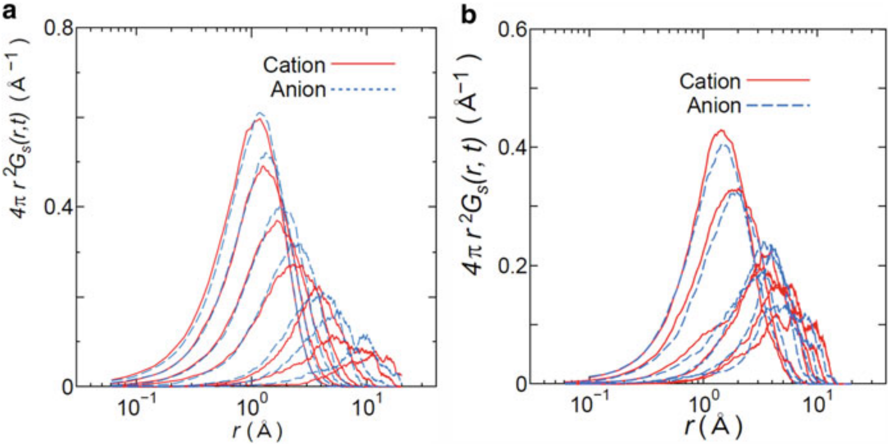

Fig. 11.9 (**a**) Self-part of the van Hove function at 400 K for EMIM$^+$ ions. t = 20, 40, 100, 200, 400, 1000 and 2600 ps from *left* to *right*. Inverse power law tail is followed by the exponential truncation. (**b**) The same function at 370 K at 0.5,1.0, 2.5, 3.0, 4.0 and 8.5 n from *left* to *right*. Jump character of the motion becomes clearer and the tail at longer r region is suppressed

with the jump character of the motion become clearer at lower temperature. Peaks of the function is more prominent at 370 K than at 400 K and the developments of the peaks at further distances are brought out by the net changes after overlap of jumps of many ions at different times. The long tail begins to be suppressed at around 370 K. At 400 K, contribution of fast ions is dominant and gives rise to non-Gaussian dynamics, while the tails tend to be suppressed at lower temperatures. The difference of the mobile and less mobile ions becomes more distinct in the longer time scale. The deviation from the Gaussian form is found in both the shorter and longer r regions at 370 K, while the dynamics at 400 K is dominated by fast ions corresponding to the thicker tail in the self-part of the van Hove function. In the liquid state, the ion in the ionic liquid shows diffusive jumps as well as large motion in the so-called nearly constant loss (NCL) region, while in the super-cooled liquid state, the short length scale motions are dominant.

Decrease of the diffusion coefficients with decreasing temperature is related to the suppression of the successive jumps with long length scales. At 300 K, both ions are located within 3 Å during 2 ns (only a small contribution is found at around 3–4 Å of the self-part of the van Hove function.) and therefore they are practically trapped in the cage during the observation time.

11.5.3.2 Exponential Truncation of the Lévy Distribution

As found in Fig. 11.8b, the functional form of the self-part of the van Hove function consists of inverse-power law part and exponential truncation. Although the inverse-power law tail of the function is related to the stable Lévy distribution at least for a certain time scale, the shape of the function gradually changes over a longer time scale. This situation is just the same as that found in several theoretical works for the Lévy distribution with a truncation [68–70]. That is, with elapse of the time, the Lévy distribution is affected by the truncation in a multifractal manner due to the mixing of behaviors of different length scales.

11.5.4 Distinct-Part of the Van Hove Function

Typical ILs can be regarded as a mixture of two species, the cation and the anion. Generally, in the binary system, the localization is governed not only by the local structure of the potential function but also by the mutual interception of paths of different kind of species, resulting in the suppression of the cooperative motions at lower temperatures. The situation is similar to that in the mixed alkali glasses (see Chap. 10), where the mutual interception of jump paths of different kinds of alkali metal ions causes the slowing down of the dynamics. To examine the motion among the two species α and β, distinct part of the van Hove function is useful.

The distinct part of the van Hove function is defined by

$$G_{\mathrm{d}}{}^{\alpha,\beta}(\mathbf{r},t) = (1/N_{\alpha})\sum_{\mathrm{i}=1}^{\mathrm{N}_{\alpha}}\sum_{\mathrm{j}=1}^{\mathrm{N}_{\beta}}\left\langle \delta\left(\mathbf{r}-\mathbf{r}_i^{\alpha}(0)+\mathbf{r}_j^{\beta}(t)\right)\right\rangle, \tag{11.9}$$

where in the summations the self-term $i = j$ is to be left out if $\alpha = \beta$. N_{α} and N_{β} are the number of particles of species α and β, respectively. In the function, if the ion species β comes into the site previously occupied by species α at an initial time t_0, a new peak develops at around $r = 0$.

Examples of such analyses can be found in several papers [19, 71, 72].

In the dynamics of EMIM-NO$_3$ [19], the mobility of both kinds of ions are comparable at high temperature region and therefore, mutual interception is not remarkable. In other words, motions among unlike ion sites occur when the system behaves as liquids, otherwise the mobile region (volume of the substructure) for each species are restricted. This result is also consistent with the observed changes in d_{w} values. We can expect larger mixing effect if the size difference is larger as in the case of MAE.

11.6 Multifractal Structure of the Density Profile

Multifractal analysis [73, 74] is a general and useful tool to characterize the complex heterogeneity having sub-ensembles with different fractal dimensions.

In this section, we will show that the density profile of ions in IL has a multifractal nature (see Appendixes A.3–A.5). At fist, density profile obtained

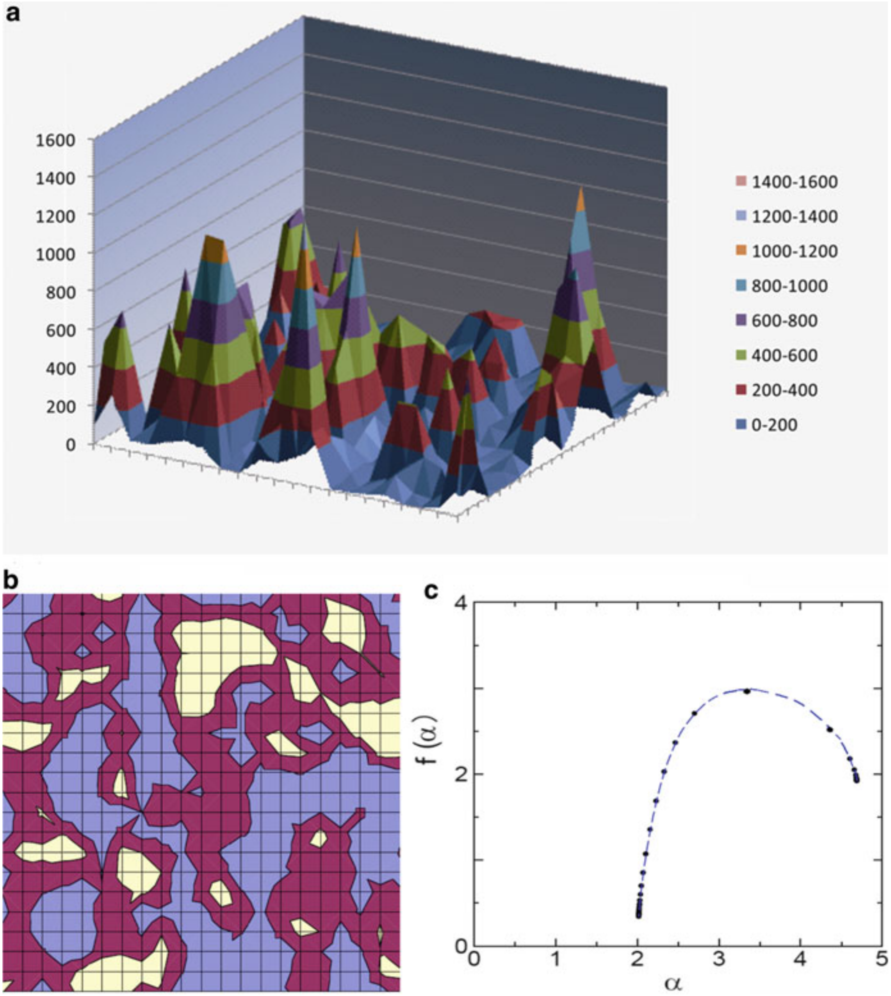

Fig. 11.10 (**a**) An example of density profiles of EMIM$^+$ ions at 370 K for a slice (L/20) of the basic cell of MD Positions of EMIM$^+$ ions are accumulated during 2 ns. (**b**) a profile at 370 K projection on a plane. Colors are changed by a logarithmic scale. (**c**) An example of the singularity spectrum for the density profiles of EMIM$^+$ ions found in the EMIM-NO$_3$ at 370 K. Convex shape of the curve means the multifractality. The maximum position with $q = 0$ corresponds to the capacity dimension of the profile. The value 3 mean the three dimensional connections of the paths in the liquid state. The α_{max} and α_{min} correspond to the most rarefied part and the densest part of the density profile, respectively

from MD for ions will be shown. The profile for the EMIM ions at 370 K is shown in Fig. 11.10a, b for a slice of the MD basic cell. The ion sites (high peaks in a and white part in b) with different sizes are connected by paths. Both the sites and the paths connecting sites have different fractal dimensions. As shown by these figures, the density profile is complex one with heterogeneity. To represent the complex structure and/or dynamics, multifractal analysis was applied for the present system [32].

The singularity spectrum, $f(\alpha)$, for this system is shown in Fig. 11.10c. It can represent all the fractal dimensions of the sub-ensembles by a single curve. For example, using the capacity dimension at the peak position ($q = 0$), one can understand how the density profile spread over the three dimensional space. In this case, the value is found to be 3. It represents that the ion sites are connected three dimensionally and this characteristic of the system is similar to the liquid state. The largest singularity α is concerned with the most dilute part of the profile, while the smallest α is related to the densest part, which is related to ion sites. Therefore, the difference between $\alpha_{\max}$ and $\alpha_{\min}$ in the singularity spectra [73, 74] is a measure of the spatial heterogeneity of the density profile. As found in lithium metasilicate and its mixture with potassium salt (see Sect. 10.5.4), multifractal (i.e., mixing of more than one exponent) pattern of the density profile of ions is formed by the coexistence of localized and delocalized ions. Thus the system has multifractal density profiles, similar to the lithium silicate.

11.7 Multifractality in the Walk

The singularity spectrum $D(h)$ for the motion can be defined in a similar manner as $f(\alpha)$ (cf. Appendix A.6). The time dependence of the displacement of a cation and a corresponding singularity spectrum for an arbitrary chosen EMIM$^+$ ion at 370 K is shown in Fig. 11.11. As shown in Fig. 11.11a, localized motions and strongly forward correlated motions are mixing; that is the motion has more than one Hurst

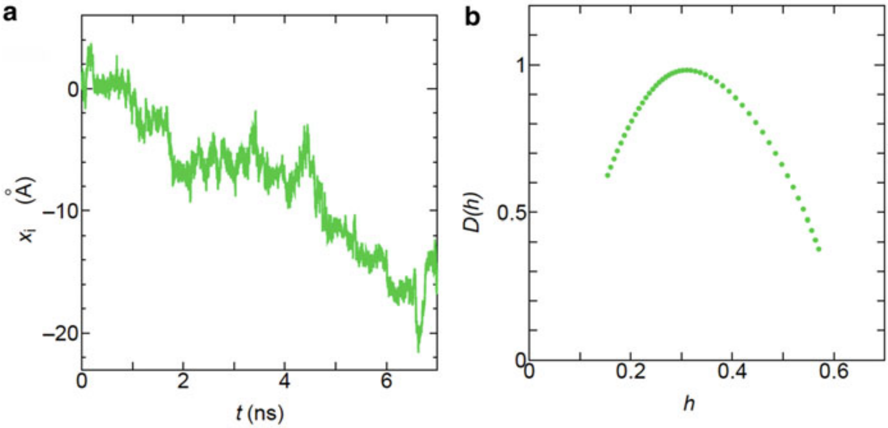

Fig. 11.11 (**a**) An example of the changes in the position of an EMIM$^+$ ion along X axis at 370 K. The motion consists of fast and slow motions. (**b**) A singularity spectrum $D(h)$ for the motion shown in (**a**). A convex shape of the spectrum means the multifractality of the dynamics

exponents (see Eq. (A.17) in the appendix). The curved shape of the spectrum $D(h)$ in Fig. 11.11b is due to the mixing of several exponents resulted in a distribution of the Hurst exponents; and therefore it also means the multifractality (In this case, units in a transverse and a vertical axis are different and therefore it is called multiaffinity in the strict sense). This result is consistent to the existence of different fractal dimensions found in the fractal dimension of the random walks of the trajectories. From the definition of the Hurst exponents, it is obvious that the distribution of the Hurst exponent is related to the power law exponent in the MSD. That is, power law exponent of MSD is closely related to the multifractality of the dynamics.

If the motion is simple Brownian, the Hurst exponent, h, is always 0.5 and the displacement is self-similar at everywhere. As is well known, fractional Brown motions are also characterized by the single Hurst exponent. However, in that case, a trend of forward correlated motions in the time development of the MSD continues for long time. In the case of Lévy motion, the different length scales are considered to be mixed randomly, although the Lévy index is inversely correlated to the Hurst exponent. Therefore, the fast ions can switch to become the slow ones and opposite is also true in a longer time scale. Such mixing of the short and long length scales motions can be characterized as the multi-fractal walks. With elapse of time, short length scale motion is found to be mixed with longer scale motion to form multi-fractal walks.

This mechanism is rather general as shown by the comparison of the dynamics in ionic liquids and in ionically conducting glasses. The fact that ionic liquids and other glass forming liquids show similar dynamics related to structural relaxation and glass transition is pointed out by several authors [11, 75].

The density profile formed by the motion is also multifractal as already shown. Therefore, time developments of the heterogeneous dynamics are governed by both the Lévy distributions and multifractality. Here we have elucidated the similarity of the dynamics of ions in ionic liquids and ionically conducting glasses. Similarities are also found in other glass forming systems. Robledo [76] has pointed out that the multifractality is relevant to glassy dynamics characterized by the two step relaxations and the heterogeneity. Sakikawa and Narikiyo [77] have reported the multifractality of the ‘bond’ in the two-dimensional binary soft sphere supercooled liquid, which is related to the heterogeneity of the dynamics.

Thus overall their dynamics in every respect are rather general, which are expected by the Coupling Model [39]. The dynamics observed have long memory of the motion, and we found that the phase space plots for the motions are also quite similar (see Sect. 11.9).

Thus the concept of the multifractal explains how these systems have common properties characterized by a small number of exponents as a result of the mixing of several exponents.

11.8 Intermediate Scattering Function, $F_s(\mathbf{k},t)$

Multifractal nature of the dynamics is also found in the wave number dependence of the intermediate scattering functions, $F_s(\mathrm{k},t)$, defined by

$$F_s(k,t) = \left\langle \sum_{j=1}^{N} \exp\left\{ i\mathbf{k} \cdot \left(\mathbf{r}_j(t) - \mathbf{r}_j(0)\right)\right\} / N \right\rangle. \tag{11.10}$$

The function for the center of mass of cation at 370 K is shown in Fig. 11.12 together with the MSD associated with it. The curves from bottom to top have values of the wave number $k = \|\mathbf{k}\|$ equal to 2π/2, 2π/3, 2π/4, 2π/5, 2π/6, 2π/8, 2π/10, and 2π/15 (Å^{-1}). Anions behave in quite a similar manner as cations, especially at longer times and small wave numbers. The function $F_s(\mathrm{k},t)$ is connected to the self-part of the van Hove function by the Fourier transform [78],

$$F_s(k,t) = \int 4\pi r^2 G_s(\mathbf{r},t) \frac{\sin(\mathbf{k} \bullet \mathbf{r})}{\mathbf{k} \bullet \mathbf{r}} dr. \tag{11.11}$$

In Fig. 11.12, the dashed lines represent t_{x1} and t_{dif}. By comparing the function of different wave number in each region, the following results were obtained. The function with larger wave number decays faster than that with smaller wave number at shorter time scale than t_{x1}, while the smaller wave number decays faster than larger one at longer time scale than t_{dif}. In between t_{x1} and t_{dif}, the early times belong to the primitive relaxation regime of independent jumps and are followed by the power law regime of MSD. In the latter regions, different length scale motions are mixing. Therefore, existence of two length scale region is clear in the function. The function $F_s(k,\mathrm{t})$ can be approximated by the following equations [79].

$$F_s(k,t) \approx \exp\left[-\frac{k^2}{2d} < r_i^2(t) > + \frac{k^4}{2} \left(\frac{r_i^2(t)}{2d} \right)^2 \alpha_2(t) \right], \tag{11.12}$$

where α_2 is the non-Gaussian parameter and d is the spatial dimension. This approximation as well as the non-Gaussian parameter can be useful to determine the magnitude of the deviation from the Gaussian form but the k^2 and k^4 terms in Eq. (11.12) may not be sufficient to fully represent the dynamics.

Instead of this kind of "so called standard" analysis, here we suggest a different kind of analysis based on the fractional exponent. Experimentally, stretched exponential form of the function has been found in a certain regime for many systems,

$$F_s(k,t) \propto \exp\left[-(t/\tau_k)^{\beta_k} \right] \tag{11.13}$$

In some systems such as polymers [39, 80, 81], it was reported that the τ in the function obeys in the following forms,

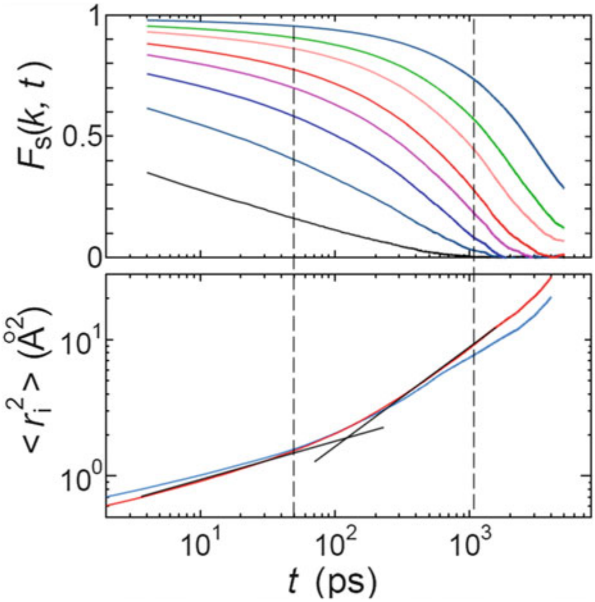

Fig. 11.12 *Upper column*: Wave number dependence of the self-part of the intermediate scattering function of the EMIM$^+$ ions at 370 K. Wave numbers are 2 π/2, 2 π/3, 2 π/4, 2 π/5, 2 π/6, 2 π/8, 2 π/10, 2 π/15 A^{-1} from *bottom* to *top*. MSD of EMIM$^+$ ion (*red*) and NO$_3^-$ ions (*blue*) are shown with the common time axis. *Dashed lines* are for t_{x1} and t_{dif}. *Black lines* for the power law slopes in NCL region and power law region for cation. The slope for anion is slightly smaller in each region. *Lower column*: MSD of EMIM$^+$ ion (*red*) and NO^{3-} ion (*blue*). The *black lines* are fitted by power laws

$$\tau \propto k^{-\nu} \tag{11.14}$$

From Eqs. (11.13) and (11.14), the wave number dependence of the function can be shown [80, 81]

$$F_s(k,t) \propto \exp\left[-\left(k^{\nu\beta}t^{\beta}\right)\right] \tag{11.15}$$

When the wave number dependence of β_k is negligible, the time dependence of the t^{β_k} will explain the power law dependence of MSD. If the dynamics is normal, i.e. Gaussian with Debye type relaxation, then $\beta_k = 1$ and $\nu\beta_k = 2$ are expected, while, it does not necessarily hold in the power law regime, where the non-Gaussianity of the dynamics is found. The following relation was checked to hold in the stretched exponential region,

$$F_s(k,t) = \exp\left[-g(k)\left\langle r^2(t)\right\rangle\right] \tag{11.16}$$

This relation is also given by the coupling model description [39, 82] as well as the MIGRATION concept of Funke [83] for ion dynamics.

The plot of $g(k)$ against k has shown the power law behavior as expected and therefore $F_s(k, t)$ can be represented by a product of the fractional power of wave number $k^{\beta'}$ ($\beta' = \nu\beta_k < 2$) and MSD with a fractional power law of time in this region. The exponent β' (at 160 ps) was determined to be 1.6. Therefore, the separation of the part depending on the length scale distribution (k dependent) and that depending on the geometrical correlation of particle motions found in MSD can be done. It is interesting to note that both are based on the geometrical character of jump motions rather than the temporal character (jump rate). As shown in Sect. 9.4.3, complicated behavior of $F_s(k,t)$ of Li ions in Li_2SiO_3 has been explained by the existence of slow and fast ions [36, 67]. General trend observed in ILs at around 400 K are similar to the Li_2SiO_3 at around 1000 K slightly above the glass transition temperature, where the fast (diffusive) ions are dominating. IL is a mixture of anion and cation with similar mobility, while Li_2SiO_3 has network structures composed by SiO_4 units, which have considerably lower mobility than the Li ions. Hence, some differences between ILs and Li_2SiO_3 systems are found. These include larger motion in the cage ions or the NCL regime and larger coupling between the motions of cation and anion in the ILs.

11.9 Deterministic Nature of the System: Phase Space Plot

Although the existence of heterogeneous dynamics with non-Gaussian characters has been already reported in Ref. [11] for the same IL, EMIM-NO_3, the time scale of the observed heterogeneity found by us is longer than that discussed there. Our heterogeneity is related to the deterministic motion of ions of long range and up to long time scale. This situation becomes clear if we examined the phase-space structure of the ionic motion. Phase-space plot of the ions was found to be useful to characterize the structure of dynamics such as in chaos. Here we used the plot of the velocity of each ion against its displacement. Reconstruction of the attractor can also be done by using the delayed time series [84] even one did not know the characteristics of the time series. In such a plot, if the motion is random, the curves will fill the space while. If the motion is oscillating, oval structure will be found.

In the case of time series obtained by MD simulations, thermal motion overlapped to the dynamics may make the direction of the long range motion unclear. To de-noise the data, singular spectrum analysis (SSA) (see Appendix A.7), which is principal component analysis of the time series [85], is useful to examine an ionic motion [86]. The method looked for the most probable direction of the data without a generating function. If the motion is deterministic, clear pattern (attractor) will appear in the phase-space plot after denoising.

Example of de-noised data for the displacement of ions and phase-space plot is shown here. Figure 11.13 shows a displacement during 9.5 ns at 370 K (black curve) in the direction for an arbitrary chosen cation, which exhibited successive jumps as shown in the inset. The blue curve overlapping the black one is obtained

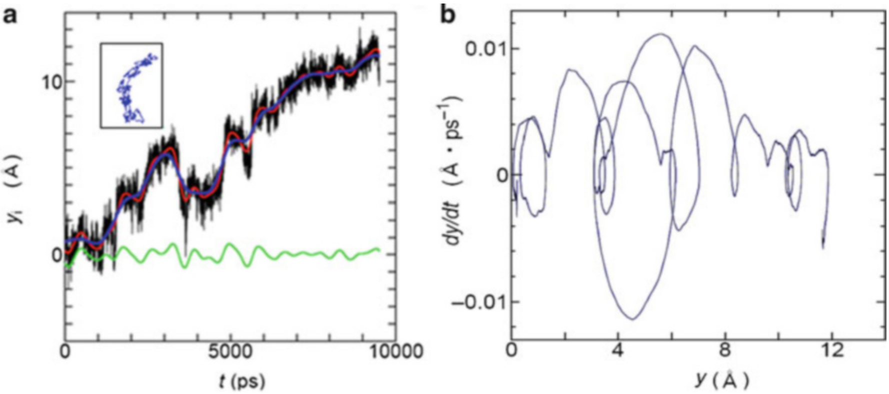

Fig. 11.13 (**a**) Displacement during 9.5 ns at 370 K of an EMIM ion, for which trajectory is shown in the inset. The *blue curve* is for the reconstruction from the first principal component. *Green* one is that for the second principal component. *Red* one is the sum of these components. (**b**) Phase-space plot of the same ion in (**a**) using the reconstructed data by SSA (for sum of the first and the second principal components)

by the reconstruction from the first principal component. The green one is that for the second principal component and the red one is the sum of these components. As shown this figure, a few numbers of components are enough to represent the trend of the trajectories and this suggests a deterministic nature of the motion. This is confirmed by the clear structure in the phase-space plot. Figure 11.13b shows the phase space plot for this motion. Namely, the first derivative of the displacement in the *y*-direction is plotted against the displacement by the reconstructed data using the first and second principal components. Smaller ovals mean the local motion while the longer curve or oval represent the jumps connecting ion sites. The motion within a cage is oval-like in the plot with some distortions, and its size is larger compared with that of Li^+ in Li_2SiO_3 in the glassy state. Thus by using de-noised data, the jump-like motion can be distinguished from the local motion. However, in the MSD, such motions by several ions overlap. The relatively larger size of the circle like structure in the plot reflects the larger amplitude of the mean square displacement of motion of ions in the caged regime, and this explains why the caged dynamics region in MSD is not clearly separated from the region by jump motions in ionic liquids even in the super cooled liquid state.

If memory of the direction of the motion is lost during the localization time, the direction is randomized and therefore no continuous trend will be found in the phase space plot. However, the short time motion tends to be smoothly connected to that at long times in the plot in many cases. That is, the memory of the direction of the motion is not lost by each jump even after long intervals. This picture of the dynamics is much different from the thermal activation process with stochastic nature, and indicates the importance of long range and long time scale correlations. The continuous motion without trapping long time can be regarded as the long jump, which contributes to the Lévy distribution.

11.10 Thermodynamic Scaling of Ionic Liquids

Recently, the existence of the thermodynamic scaling of dynamic quantities and transport coefficients has been well established (see Chap. 7). Examination of the thermodynamic scaling by MD simulations enables one to establish how dynamic properties depend on the thermodynamic properties, potential parameters, structures, and other variables. For example, the presence of strong correlations between equilibrium fluctuations of the configurational parts of (instantaneous) pressure and energy for a number of model liquids in NVT ensemble has been shown by the Roskilde group [87] using simulations. An effective inverse law type potential dominating fluctuations (in the equilibrium system) is argued to be responsible for the thermodynamic scaling, based on the pressure-energy correlations. From this point of view, the system with hydrogen bonds and ionic systems were excluded for the thermodynamic scaling. However, both experiments [88–91] and simulations [32, 92–95] show that ionic systems such as ionic liquids are not exceptional.

In this section, thermodynamic scaling based on the diffusion coefficient tested for the EMIM-NO_3 system [32] will be discussed. Obviously, the r^{-1} dependence of the Coulombic force present cannot explain the observed scaling. One of the possible explanations is based by a concept of potential of mean force (PMF), introduced by Kirkwood [28] as shown in Chap. 7 and in this section.

The scaling behaviors are tested as follows. At first, MSD for EMIM$^+$ ions in several conditions used in the scaling are shown in Fig. 11.14. Temperature dependent MSDs are overlapped with those of the data obtained under high pressure. If the diffusivity is comparable, MSD is also comparable starting from the short time region. That is, the scaling stems from short time region of the dynamics [94, 95].

In Fig. 11.14, the slope of MSD of ions becomes 1 for high temperature data at long times. Meanwhile, a deviation from the slope 1 is found at long time

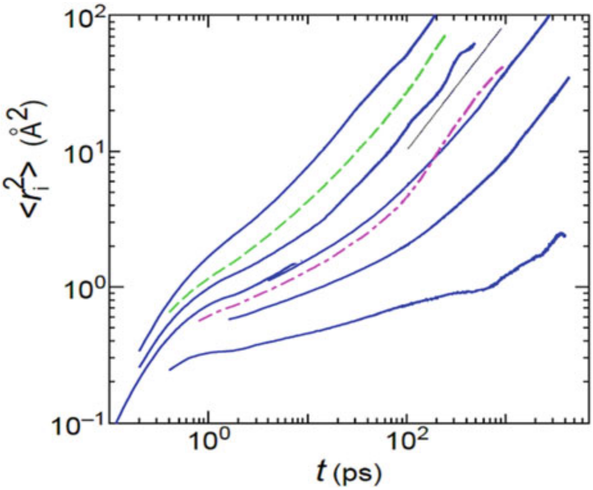

Fig. 11.14 Temperature dependence of MSD for EMIM$^+$ ions (*blue*) at 600, 500, 400, 370 and 300 K at 0.1 MPa from *top* to *bottom*. A *dash-dotted* (*pink*) *curve* is for the data at 510 K (500 MPa) and a *dashed curve* (*green*) is for the data at 800 K (1 GPa). The *black line* is for the slope 1 in the double logarithmic scale

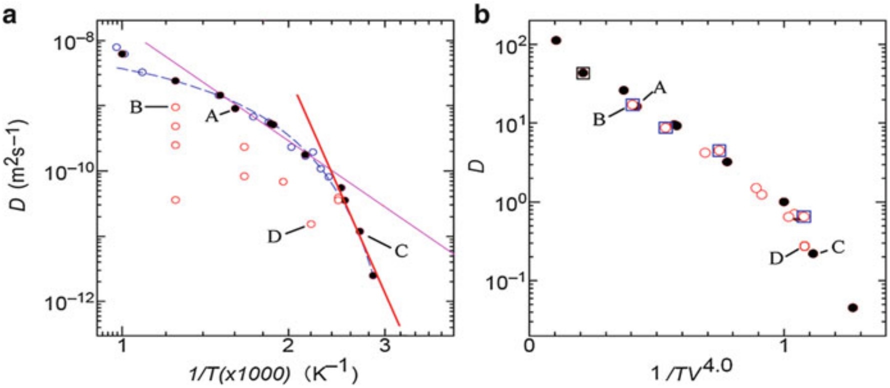

Fig. 11.15 (**a**) Diffusion coefficients of EMIM$^+$ ions at several conditions for the center of masses motion in EMIM-NO_3 is shown by solid (*brown*) circles. Data obtained under high pressure conditions are also shown by *red open circles*. *Dashed blue curve*: Temperature dependence of the diffusion coefficient of EMIM$^+$ ion fitted to Vogel-Fulcher-Tammann-Hesse (VFTH) type. *Solid pink* and *red lines* are for power law type functions. Some additional data points (*open circles*, *blue*) were also used for fitting. (**b**) Diffusion coefficients in (**a**) are plotted against $1/TV^4$. Isothermal data at 800 K are shown by *open red circles* within *open blue squares*. Two sets of data, A (600 K, ~0.1 MPa) and B (800 K, 500 MPa), C (370 K, ~0.1 MPa) and D (450 K, 500 MPa) shown in these figures are located nearby on the master curve and have comparable structures and dynamics. Data are normalized for the 400 K under ~0.1 MPa

(after ~1 ns) even after the subdiffusive regime at 370 K. In Fig. 11.15a, the diffusion coefficients for EMIM$^+$ ion are plotted against inverse temperature. Temperature dependence of the diffusion coefficients at ambient pressure (~0.1 MPa) is shown by the solid (brown) filled circles. These results can be fitted to Vogel-Fulcher-Tammann-Hesse (VFTH) [49–51] as well as double power laws. The best fitted parameters obtained for VHTH are $D_0 = 1.22\text{E}{-8}$ ($\text{m}^2\ \text{s}^{-1}$), $E = -907.69$ (K) and $T_0 = 243.24$ (K). Here D is given in $\text{m}^2\ \text{s}^{-1}$ and T is in K. In the power law fits, the best fit parameters obtained in the form of $\ln(D) = A_0 + A_1(1000/T)$ are, $A_0 = -17.94$, $A_1 = -5.78$ for the high temperature regime and $A_0 = -6.44$, $A_1 = -19.05$ for the low temperature regime.

The validity of the scaling behavior $D = \mathfrak{J}(TV^\gamma)$, of the data shown in this figure is demonstrated in Fig. 11.15b, where the data are plotted against $1/TV^\gamma$, with $\gamma = 4.0$. In the plot, the data points at $T = 800$ K and $P = 0.1$, 500, 1000, 2000 and 4000 MPa are represented by the open red circles within open blue squares. All data points are found to fall on a master curve, and therefore diffusion coefficients are well thermodynamically scaled with $\gamma = 4.0 \pm 0.3$. Similarly, TV^γ relation for the diffusivity for anion with similar but slightly smaller γ value (=3.8) was obtained for anion. This is as expected from the similar behavior of diffusion coefficients of EMIM$^+$ ion and NO_3^- ions and this suggests the comparable effective sizes of cation and anion in EMIM-NO_3. Thus we could reproduce the scaling behaviors of data obtained by MD simulations. The exponent obtained for EMIM$^+$-NO_3^- is similar to the value for the soft-core (SC) potential with $n = 12$ and $\gamma = n/3$.

Thus, the thermodynamic scaling was confirmed to hold in this model. Different experimental values of γ for other ILs were observed [88]. This scaling is concerned with the effective potential among ions, and not specifically for the repulsive term with r^{-n}-dependence for each atom-atom interactions. It is certainly not related to the r^{-1} dependence of Coulomb term.

Next we considered the diffusion coefficients, D as a target to examine the thermodynamic scaling. In the experiments, scaling has also been confirmed for the viscosity or the relaxation time. The appropriate quantity can be D/T rather than D based on the Stokes-Einstein law or the related fractional Stokes-Einstein law. We have confirmed the similar scaling behavior is obtained when D/T was used albeit the deviation from the master curve is slightly larger. Recently, Lopez et al. [89] have discussed that the results by considering D/T is slightly better and the γ value obtained by D/T is comparable with those for viscosity and conductivity.

The validity of the scaling suggests the existence of the underlying effective potentials in the form of the inverse-power law. Therefore, it is useful to refer the physics to that of the soft-core (SC) model to understand the thermodynamic scaling, In the SC-model, the scaling by TV^{γ} should be exact if the reduced units are used (see Sect. 8.2.2). The scaling in the real units was found to be based on the similar response of the system to temperature and pressure, which can be connected through the density-temperature variable in the form of TV^{γ}. Correspondence of the different states on the master curve in the present work is found for the diffusion coefficients not in the scaled units but in the real units. It is interesting to compare the situation of this scaling to the exact scaling in the SC system. In the model SC system, the scaling is due to the self-similarity of the system and trajectories in the phase space, while the observed scaling law in the present work is valid for the temperature and pressure dependence within a system and related to the similarity of the structure of $g(r)$ for small r region in the real unit and we pointed out the difference of these scalings in Ref. [32]. We note here that it is also pointed out by Prof. A. Ueda. Later, several authors have used reduced variables or residual reduced variables [96–98], and the scaling is found to hold slightly better.

11.10.1 Comparison Between Corresponding States on a Master Curve

To understand the scaling, comparison of the data points located nearby on the master curve will be useful. Two sets of data points characterized by closely equal values of D at different combinations of T and P (A-B pair and C-D pair) in Fig. 11.15b are compared. These two pairs are located in different regimes of the master curve.

We found that the Coulombic energy for A (600 K ~0.1 MPa), $E_{\mathrm{Coul}} = -281.15$ kJ mol^{-1}, is comparable to that for B (800 K, 500 MPa), $\mathrm{E}_{\mathrm{Coul}} = -278.92$ kJ mol^{-1}. While the potential energy of A, $E_{\mathrm{ptot}} = -139.68$ kJ mol^{-1}, which is a sum of terms in Eq. (11.1), is considerably smaller than for B,

$E_{\text{ptot}} = -93.31$ kJ mol^{-1}. For the other pair we found the Coulombic energy, E_{Coul} of C (-299.0 kJ mol^{-1} at 370 K, 0.1 MPa) and D (-298.6 kJ mol^{-1} at 450 K, 500 MPa) are comparable. E_{ptot} for C (-228.6 kJ mol^{-1}) is again different from that for D (-207.6 kJ mol^{-1}). This result suggests that the Coulombic term plays a major role for the scaling behaviors. Here the energy terms at 400 K obtained by our MD simulations are comparable to those obtained by Popolo and Voth [11].

The systems in corresponding states on the master curve have comparable electrostatic energy. This statement was proved in Ref. [32], by plotting TV^{γ} ($\gamma = 4.0$) against Coulombic energy of the system, for which the master curve remains almost stable. That is, The slope for the relation between Coulombic energy and TV^{γ} changes near the glass transition point (~260 K). It is found that structures located nearby on the master curve shown by the pair correlation functions, $g(r)$, of EMIM$^+$-NO$_3{}^-$, NO$_3{}^-$-NO$_3{}^-$ and EMIM$^+$-EMIM$^+$ pairs are comparable for both the A-B and the C-D pairs. Furthermore, temperature and pressure dependence of the pair correlation function for the A-B pair or the C-D pair also was found to be comparable. It is interesting to note that the characteristics of temperature dependence of the diffusion coefficients shown in Fig. 11.5 are kept on the master curve. As discussed before, dynamical slowing down represented by the empirical VFTH temperature dependence, or by the inflection of the temperature dependence of the diffusion coefficient is related to the change from longer to shorter length scale dynamics. The fact that the master curve maintains these characteristics mean that the many body character of the dynamics common for temperature dependence and pressure dependence is retained after the scaling.

11.10.2 Potential of Mean Force

The potential of mean force (PMF), $W_{\text{ij}}(r)$, introduced by Kirkwood [28] is playing an important role in statistical mechanical theories of liquids [99, 100]. Habasaki and coworkers suggested [32] that the scaling behaviors observed in the ionic liquid can be explained by the softness of the PMF. This is because nearby points on the master curve have quite similar pair correlation functions of ion-ion pairs, and the function bears correlation with the PMF.

The PMF is connected to the pair correlation function $g_{\text{ij}}\,(r)$ by the relation,

$$W_{ij}(r) = -k_B T \ln g_{ij}(r) \tag{11.17}$$

The force acting for an ith particle, is represented by [99, 100]

$$-\frac{\partial W}{\partial \mathbf{r}} = \frac{k_B T}{g(r)} \bullet \frac{\partial g(r)}{\partial \mathbf{r}} = \frac{\int \cdots \int \left(-\dfrac{\partial U_N}{\partial \mathbf{r}_i} \right) \exp\{-\beta U_N\}\, d\mathbf{r}_{n+1}, \ldots, d\mathbf{r}_N}{\exp\{-\beta U_N\}\, d\mathbf{r}_{n+1}, \ldots, d\mathbf{r}_N}, \tag{11.18}$$

where U_N is for internal energy for n body potentials of N particles. In the case of the pair potential, $n = 2$.

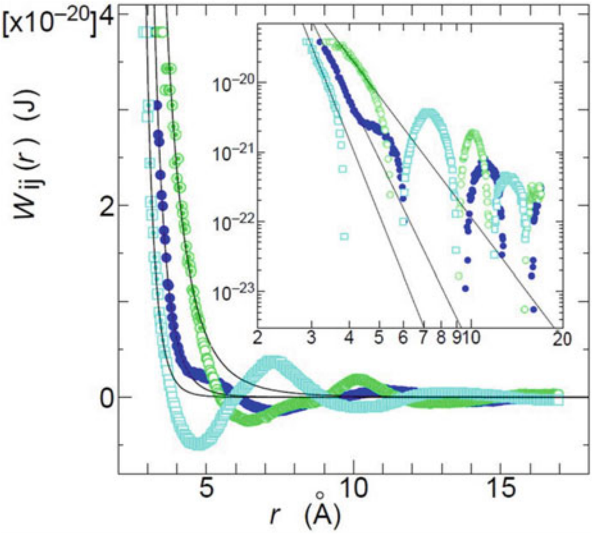

Fig. 11.16 Potential of mean force calculated from the pair correlation functions of cation-cation, cation-anion and anion-anion pairs. Double logarithmic plots of the same data are shown in *inset*. Slope obtained for the cation-anion interaction is reasonable to explain the observed scaling exponent. *Pale blue*: cation-anion pair, *Dark blue*: cation-cation pair; *Blight green*: anion-anion pair

As shown in Eq. (11.18), the concept of the potential of mean force contains many body effects a priori. In the low density limit, the mean force potential becomes comparable to a bare potential among ions.

In our simulations, we calculate the PMF from the pair correlation function directly using Eq. (11.17). The potentials, $W_{\mathrm{ij}}(r)$, calculated for cation-cation, anion-anion and cation-anion pairs from the corresponding $g_{\mathrm{ij}}(r)$ for the center of masses of ions at 400 K are shown in Fig. 11.16. The PMF can be regarded as an effective potential among ions. Effective potential thus obtained has the inverse power law dependence and similar type of potential parameters is derived in several works as discussed before in Sect. 11.1. The fits by straight lines in the double logarithmic plot of $W_{\mathrm{ij}}(r)$ against r are also shown in the inset. Since the linear regions are clearly found for every pairs, the power law exponents can be determined from the plot. The power law exponents of cation-cation, anion-anion and cation-anion are found to be −9.00, −6.97 and −11.10, respectively. From the slope for cation-anion pair, γ can be estimated by $(11.10/3) = 3.7$. Thus these results explain the existence of scaling exponent by relating it to the PMF.

11.11 Temperature Dependence of Topological Structures of Ionic Liquids

As generally observed in many systems, diffusion coefficients of ILs show the slowing down of dynamics with decreasing temperature. In the present section, relation between dynamics and topological structure of ILs are shown exemplified by EMIM-NO_3.

The problem treated here is closely related to the glass transition of the system. There are many theories or models to explain the glass transitions and related dynamics [101–107]. Some of them describe the glass transition as the localization and trapping within a free energy landscape, while others consider it as due to the rapid increase of cooperatively rearranging regions or some length scales near the glass transition temperature. In the present section, we don't directly compare the results with these theories or models because they are beyond the scope of this book and are controversial, however, the dynamics of ions is quite similar to that in other glass forming liquids and therefore, observation and discussion here is expected to be applicable to other systems. Namely, we suggest that the changes of packing of local structural units (coordination polyhedra) and topological changes of fictive bonds explain important features of the glass transition.

Before discussing for the topological changes focused in the present section, here we briefly discuss the relation between diffusion coefficient and viscosity, because the glass transition tends to be discussed with both transport properties.

One might expect that the behavior of the diffusivity is connected to the viscosity, η, through the Stokes-Einstein relation [108].

$$D = \frac{kT}{3\pi\eta d} \tag{11.19}$$

where the d is an hydrodynamics diameter of particles placed in the solvent. In MD simulations, the value η can be obtained from the off-diagonal elements of the stress tensor [109] or by a non-equilibrium method [110, 111]. If one defines the glass transition by the changes in the viscosity, the situation is slightly changed from the discussions for the diffusivity or conductivity. Different slopes of temperature dependence of diffusivity and viscosity with a collective character resulted in a deviation from the Stokes-Einstein relation as discussed for the ionic liquids [112], molten salts [113] and in the generalized binary Lennard-Jones systems [114].

11.11.1 Rigidity and Soft Percolation of Fictive Networks: Infinitive Networks Found in the Ionic Liquid Based Glass

Topological structure and packing of the local structure determines the stiffness of the system as well as slowing down of the system. Since ionic liquid is the important linchpin, connecting the two research fields of ionics and glass transition, Habasaki and Ngai [115] examined the fictive networks (formed by contact ion pairs) in 1-ethyl-3-methyl imidazolium nitrate (EMIM-NO_3) by MD simulations by an all-atomistic model to clarify the relationship between the characteristic structures and slowing down of the dynamics. As shown in the next subsection, the system shows changes of dynamics at two characteristic temperatures [116], T_B and the glass transition temperature T_g, as found in other fragile glass forming liquids. This behavior is related to the fragility [117] and nonexponentiality (or coupling parameter n of the Coupling Model) [118] of the system. In the fragile system with larger n, the T_g-scaled temperature dependence of structural relaxation time or transport coefficient has steep slope at $T_g/T = 1$ and the fragility can be defined by the slope. Existence of two characteristic temperatures is a typical behavior near the glass transition of fragile glass-formers. On the other hand, systems such as silica, which has rigid three dimensional networks, are typical strong system, where the Arrhenius behaviors are observed. The dynamics and thermodynamic properties of strong and fragile glass-formers are very different, although glass transition is commonly observed.

In the models or theories, glass transitions of fragile systems and strong systems tend to be treated separately, however, there are other glass-formers having properties that are intermediate between the strong and fragile extremes. This suggests us the existence of a common explanation of glass transition in both fragile and strong systems. In looking for an alternative way to understand glass transition based on concept that is common to all glass-formers irrespective of whether they are fragile, intermediate, or strong, the approach of this section was taken. That is, we consider the networks of the fragile system formed by fictive bonds and packing of coordination polyhedra.

In Fig. 11.17a, an instantaneous network structure for anion-cation bonds is shown for EMIM-NO_3 in the glassy state (at 150 K), where the nodes are chosen to be the center of mass positions of ions (Blue: $EMIM^+$ ion; Red: NO_3^- ions) and bonds are connecting ions within the distance of the first $g(r)_{min}$. Of course, there is no direct bond among center of mass positions of cation and anion, however, one can find network of closely packed anion and cation interacting through Coulombic interaction. Since the system is analyzed using the position of center of mass of each ion, details of the inner structures have no significant roles in the glass transitions observed here, although some details of the packing of the system may depend on them.

In Fig. 11.17b, clusters within $g(r)_{min}$ of the cation-anion the central cation (left) and anion (right) are shown. As shown in these figures, cations surrounding anion forms a coordination polyhedron and vice versa. These coordination polyhedra are not separated each other but is mixing in a complex manner because the same kind of ions as the central ions are also included in the cluster defined by the same cut-off distance.

As shown in Fig. 11.17b, both anions around cation and cations around anion form closely packed coordination polyhedra in the glass. In these structures, cation-cation or anion-anion pairs form an edge of the coordination polyhedron. Of course, there is no direct bond between anion and anion, or between cation and cation and therefore, the bond is fictive one for the neighboring contact ion pairs. These bonds and coordination polyhedra are used to characterize the system. Generally, mixing of networks found for the ionic fragile systems are also expected for non-ionic fragile systems and the concept of overlapping networks are valid in many systems.

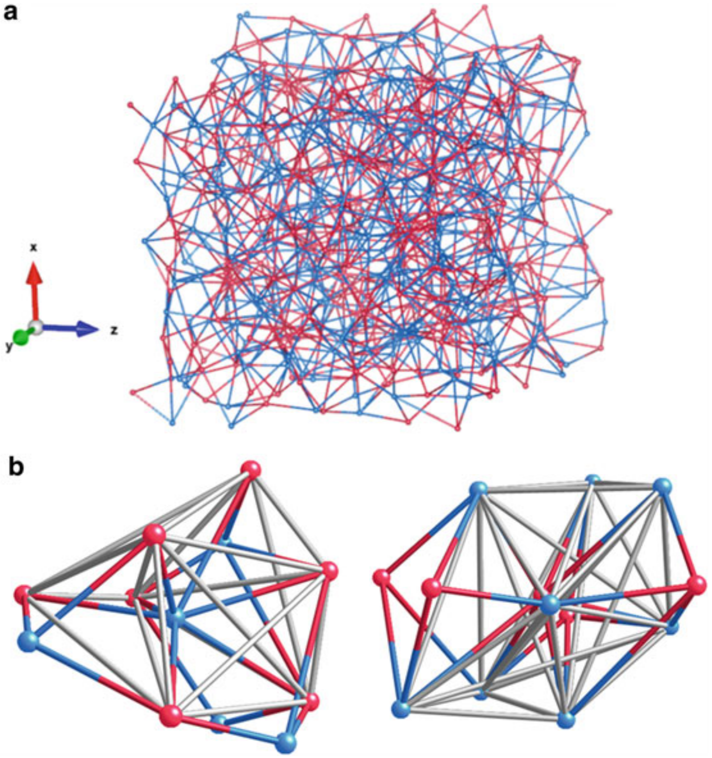

Fig. 11.17 (**a**) Structure of the network found in the glassy state of EMIM-NO_3 at 150 K (based on the full atomistic MD consists of 5888 atoms (256 ion pairs)). Positions of the center of mass of anions (NO_3^-: *red*) and surrounding cations ($EMIM^+$: *blue*) within the distance of $g(r)_{\min}$ of cation-anion pair are connected. The structure is repeated by the periodic boundary condition applied to form an infinite network. (**b**) Examples of clusters for the cases, anions around anion (*left*) and cations around anion (*right*). The same kind of ions as the central ion within $g(r)_{\min}$ of cation-anion distance are also shown. *Colored sticks* are connecting cation and anion, while *gray sticks* are connecting the same kind of ions within $g(r)_{\min}$ of anion-anion (*left*) or cation-cation (*right*) for each coordination polyhedron

If a trapped particle is the same kind as the surrounding particles, it can form a cage of the other particles. That is, even in a one component system, distinguishable substructures are found and the system can exhibit the glass transition having the same origin.

11.11.1.1 Structural Changes Near T_B and T_g and Definitions of N_V, N_b and N_B

As already shown in Fig. 11.3a, g(r) of the ionic liquid changes with temperature gradually. This change is accompanied with that for the coordination number N_V for both cations around anion and anions around cation. The changes also occurred for the coordination by same kind of species. Topological examination of the system and polyhedra were performed typically at the onset time, t_{dif}, of the diffusive regime shown by the mean squared displacement (MSD), however, the essential features of networks obtained during $t \sim t_{\mathrm{dif}}$ can be observed already from the instantaneous structure. Since changes of the first minimum positions are relatively small, we used fixed cutoff values to determine the bonds of network and polyhedra. Namely, the first minimum positions of $g(r)$ at 7 Å, 10 Å and 11 Å were used for the cation-anion, anion-anion and cation-cation pairs, respectively.

Here, we distinguish the total number of bonds, N_{B}, counted without redundancy for the system from the number of bonds, N_{b} in each polyhedra, which have a redundancy with other polyhedra. This is because vertices of polyhedra are usually shared with other polyhedra and as a result, $N_B < \sum N_b$ holds. This relation is important because it suggest that temperature dependence of the packing of the polyhedra and that of bonds behaves in a different manner.

At first, how system volume changes with temperature and how it is related to the changes in N_{B} will be discussed.

11.11.2 Existence of $\mathrm{T_B}$ *and* $\mathrm{T_g}$ *in the System Volume and in the Diffusivity*

In Fig. 11.18a, the volume of the system obtained by MD simulations in NPT conditions at each temperature after equilibration is plotted. When it is plotted against reciprocal temperature, changes in the slope at around ~410 K and ~250 K are found. These characteristics are common with other ionic liquids and similar trend is found in Ref. [119], where Forero-Martinez et al. examined voids in three ionic liquids ($[\mathrm{C_4mim}][\mathrm{PF_6}]$, $[\mathrm{C_4mim}]$ $[\mathrm{Tf_2N}]$ and $[\mathrm{C_3mim}][\mathrm{Tf_2N}]$) by MD simulations. The free volume of fragile systems measured by the positronium annihilation lifetime spectroscopy (PALS) [120, 121] is also comparable.

The inflection point T_{B} found in the system volume is closely related to the change in the dynamics summarized below. As discussed in Sect. 11.2, our diffusion coefficient data of ions in ILs can be fitted to Vogel-Fulcher-Tammann-Hesse (VFTH) equation (see Fig. 11.5a). If the same data are plotted in log-log scale (or semi-log scale), temperature dependence of the diffusion coefficients of the cation in the present system shows an inflection point at around 400 K (see Fig. 11.5b) and this point is assigned as T_{B}. That is, the fragile behavior is characterized by the slower decrease of the diffusion coefficient at higher temperature region above T_B, and the change to a more rapid decrease below T_B. This finding suggests that it is not necessarily required to consider the sudden changes of dynamics near Tg for understanding fragile behavior. Diffusivity near the inflection point (~410 K) is of the order of 10^{-10} m^2/s and is measurable within ~ns runs. While at T_g (~250 K) determined by change of the temperature

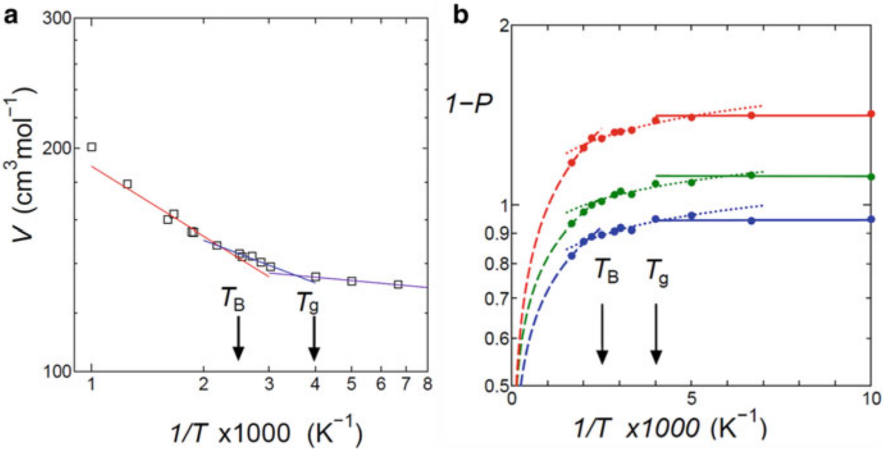

Fig. 11.18 (**a**) Temperature dependence of volume of the system. Lines are fitted ones using power laws for three temperature regions. *Red*: above T_B, *Blue*: between T_B and T_g, *Purple*, Below T_g. (**b**) The probability, $1-P=\frac{N_B}{(3N-6)}$, is shown as a function of reciprocal temperature in a semi-log plot, where the total number of bonds (contact pairs) within $g(r)_{\min}$ of anion-cation (*blue*), anion-anion (*green*) and cation-cation (*red*) pairs are counted without redundancy. The curves are obtained by the power law fitting. At around T_B (~410 K) and T_g (~250 K), the change of slopes for the three kinds of networks is observed. The saturation of the number of bonds is observed for the cation-anion network at around T_g and followed by others. Error bars estimated at 250 K from three independent cooling schedules are within the size of the mark

dependence of the density, diffusive regime of MSD was not attained during the observation time. Estimated value (from the extrapolation of the fitted lines in the lower temperature regimes) at T_g is of the order of 10^{-16} m^2/s for both cation and anion in the present system. Each time region of the MSD becomes longer and longer with decreasing temperature and NCL region becomes to cover the whole region of the observation time. The kinetic glass transition temperature, $T_{g\text{-}k}$, obtained from simulations up to ~10 ns by the condition that the diffusive regime is not attained during the observation time, is higher than $T_g = 250$ K but lower than T_B. This can be regarded as the "computer glass transition", although it does not necessarily mean the absence of structural change at T_B or at T_g. In Sect. 11.4.2, by using the fractal dimension of the random walk, it was also shown that the inflection of the diffusion coefficient at T_B is related to the restriction of the trajectories in the local space at low temperatures. Therefore, the change in the dynamics is directly related to the available region for the motion of ions. This view is not against with the traditional concept of the free volume. It is note worthy again that there is a characteristic value of the fractal dimension of the random walk, ($d_w = 3$) to separate the localization and delocalization of each ion.

11.11.3 Structural Change at T_g as a Rigidity Percolation: Number of Bonds and Degree of Freedom of the Whole System

How are the dynamics related to the geometrical freedom of the system? As shown in the present section, the structural change at T_g is characterized by the saturation of the number N_B of cation-anion bonds (followed by saturation of the other kinds of bonds) with the corresponding decrease of the degrees of freedom of the system as shown below.

The degrees of freedom of the system consisting of N particles, F_system, can be defined by,

$$F_\mathrm{system} = [(3N - 6) - N_B] \tag{11.20}$$

Here counting is taken over all bonds (contact pairs) without redundancy.

$3N$ is the degrees of freedom of the motion for N particles in 3 dimensions (here we consider the coordinate space only), and 6 is that for the rotational and translational motion of the system. Then the probability P of finding a mode with $N_\mathrm{B} < 3N - 6$, is defined by

$$P = F_\mathrm{system}/(3N - 6) = 1 - \frac{N_B}{(3N - 6)} \tag{11.21}$$

The probability of finding a part without the mode is the complement,

$$1 - P = \frac{N_B}{(3N - 6)} \tag{11.22}$$

If the value exceeds 1, it means that the inner structures of the system have extra bonding compared with the value of $3N - 6$. In the present work, analysis has been done for each pair of species.

In Fig. 11.18b, results of $1 - P$ plotted against the inverse of temperatures for cation-anion, anion-anion, and cation-cation pairs are shown. Here N stands for the number of all ions, although the number of bonds is counted among the cations (or anions) in the case of cation-cation (anion-anion) pairs. Remarkable features found are the saturation of the $1 - P$ values for these pairs near the glass transition temperatures. This means the system becomes rigid by the saturated number of bonding.

This result means that even for a fragile system, glass transition can be described by the formation of rigid networks formed by ion pairs. Especially, attractive interaction for cation-anion pair seems to be important. For other combinations, even larger saturated values were observed. This is because fictive bonds examined are loose ones having several lengths. Changes in the network of the system are found at both T_B and T_g.

11.11.4 Geometrical Degree of the Freedom in the Polyhedron

To consider the different changes of volume and dynamics at T_B and T_g, we introduce here the geometrical degree of freedom [122], f_g, of each coordination polyhedron, which can be defined by $f_g = [(3N_V - 6) - N_b]$. This kind of analysis was previously applied for the coordination polyhedra made of oxygen atoms around Li ions in the molten and glassy Li_2SiO_3 system and can characterize the dynamics and topological change at Tg, successfully [123–125]. Here $3N_V$ is the degree of freedom of N_V vertices of the polyhedron in three dimensions, 6 is the degree of freedom for translational and rotational motion of the polyhedron. In other words, "$3Nv - 6$" bonds are necessary to fix the shape of the polyhedron. The concept is schematically shown in Fig. 11.19a for the case of $N_V = 4$. That is, if $N_b < 3N_v - 6$, system has a floppy part (and/or free volume) in the coordination polyhedron. The present explanation is not specific to the structures with a fixed N_v such as icosahedra, although they are included in the concept of the distribution of coordination polyhedra.

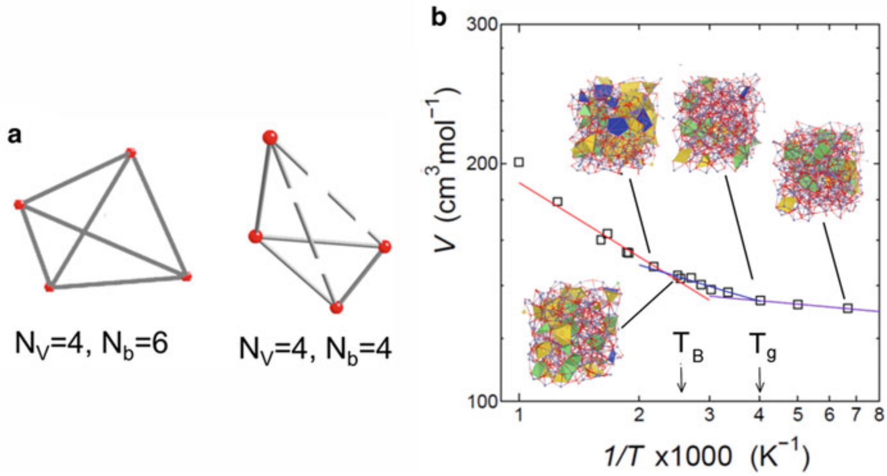

Fig. 11.19 (**a**) Schematic description of the concept of geometrical degree of freedom of the coordination polyhedron [122] for the structure with $N_V = 4$. Trapped ions are not shown. Here N_V is a number of vertices, and N_b is number of fictive bonds (contact pairs). Broken bonds have lengths longer than a certain criterion (the first minimum position of $g(r)$ for the anion-anion pair is used here). When $N_b = 3N_V - 6$, the freedom for the deformation of the polyhedron is lost. (**b**) Temperature dependence of the coordination polyhedra (anions around cation) are mapped on the corresponding volume change. Characteristics of coordination polyhedra of anions around cation are shown by colors. *Blue*: polyhedron with $N_b < 3N_V - 6$. *Yellow*: polyhedral with $N_b = 3N_V - 6$. *Green*: polyhedra with the maximum number of bonds, $N_b = 1/2N_V(N_V - 1)$. Structures between $N_b = 3N_V - 6$ and $N_b = (1/2)\ N_V\ (N_V - 1)$ are not colored. Decrease of the structure with $N_b < 3N_V - 6$, becomes clearer at around T_B. At the glass transition temperature (~250 K), the saturated N_b structures increase

11.11.5 Temperature Dependence of the Distributions of N_V

Following changes were found in the distribution of coordination number, N_{V} (see Ref. [115]). Peak position of the distribution tends to shift to the right with decreasing temperature. Contribution of $N_{\mathrm{V}} = 4$ structure is almost totally missing below 400 K. The distribution at higher temperature has a tail of larger N_{V} values, while in the glassy state at 150 K, the distribution is rather symmetrical and centered at $N_{\mathrm{V}} = 7$. We also note that the corresponding changes of peak heights are found in g(r) and are detectable in experiments.

11.11.6 Changes of the Distribution of N_V and N_b at Around T_B and T_g

Structural change accompanying glass transition is sometimes not emphasized in the study of glass transition. This is probably because the sudden structural changes at T_{g} was looked for and changes at these characteristic temperatures are not easily observed in the experiments. However, to explain the change of the slope of the dynamics at T_{B} towards to T_{g}, only a gradual structural change is required. As shown below, in the distribution of N_V and N_b, one can clearly observe the characteristic temperature dependence in each region separated by both T_B and T_g.

To characterize the local and medium range packing, here we considered coordination polyhedra formed by anions around cation. Their remarkable changes on decreasing temperature were observed at around T_{B} and T_{g} by using the coordination number, N_{V}, and the number of bonds, N_{b}, within the coordination polyhedron. Temperature dependence of the characteristics of the polyhedra is shown for the anions around cation in Fig. 11.19b.

Blue polyhedra have a character with $N_{\mathrm{b}} < (3N_{\mathrm{V}} - 6)$. Yellow ones are for the structure with $N_{\mathrm{b}} = (3N_{\mathrm{V}} - 6)$, while green ones are for polyhedra with maximum number of bonds, $N_{\mathrm{b}} = (1/2)N_{\mathrm{V}}(N_{\mathrm{V}} - 1)$. Polyhedra with the N_{b} between $N_{\mathrm{b}} = 3N_{\mathrm{V}} - 6$ and $N_{\mathrm{b}} = (1/2)N_{\mathrm{V}}(N_{\mathrm{V}} - 1)$ are not colored. As shown in this figure, the change at T_{B} is related to the disappearance of polyhedra with $N_b < (3N_{\mathrm{V}} - 6)$. Therefore above T_{B} ~400 K, there is a geometrical degree of the freedom for polyhedra, and the change in the structure is accompanied by the decrease in the free volume with increase of N_{b} and N_{V}. Large N_{b} structures become dominant at lower temperatures. At T_g, the characteristics of polyhedra change again by the saturations of the shortest connections by the cation-anion pairs followed by the other pairs. Below T_{B} ~400 K, the change is mainly observed in the distribution in N_{b} and N_{V} of the polyhedra within the limited region of N_{v}.

Near the glass transition point, inner structure becomes more rigid because of saturation of possible connections within the polyhedra as well as the saturation of the number of bonds shown before. That is, the structures with $(1/2)N_{\mathrm{V}}(N_{\mathrm{V}} - 1)$, which is the maximum number of bonds for each polyhedron, are found frequently near and below T_g. Even if each cage had enough number of bonds to stabilize the shape of the structure, further increase of fictive bonds are allowed below T_B. Thus the system volume can decrease even below T_B, by increasing number of contact ion pairs. Below T_g, the change of the pattern of distribution of N_b is small and the sharpening of each peak is the dominant effect. These results are consistent with the change of the compressibility of the system with temperatures and therefore, the locations of the "free volume" are represented well. To characterize the packing, coordination polyhedra of cations around anion are also examined [109] and are summarized below. The peaks for the distribution of N_b are sharper and seem to be more separated with $\delta N_b \sim 5$. The structure with $N_b < (3N_V - 6)$ was not so clear at the high temperature region. If the difference between the effective sizes of cation and anion is larger, such differences in the mutual coordinations will become more important.

11.11.7 The Concept of Rigidity and Soft Percolation

Topological aspects of the glass structure formed after glass transition has been repeatedly discussed in the literatures [39, 126–141] after the suggestion of the concepts of rigidity by Phillips [126, 139–141]. He introduced the constraint theory for SiO_2 and the binary and ternary chalcogenide glasses As_2Se_3 and $Ge_aAs_bSe_c$ to address glass forming ability. It seems to be quite natural to apply it to the problem of the glass transition. Actually, Thorpe [127, 128, 137] reformulated the constraint theory as a problem of rigidity percolation. In random networks, numerical calculations have shown that a floppy-to-rigid transition occurs when the mean coordination number <r> increases to a value quite close to the predicted mean-field value of 2.40. Experimentally, Boolchand [138] has observed an intermediate phase in binary Ge-Se glass. Existence of the intermediate phase seems to be similar to the intermediate temperature region between T_B and T_g found in our work.

The concept of percolation concerning a fictive bond (contact pair) is slightly different from the rigidity percolation involving direct bonding. We call it soft percolation. As already mentioned, fictive bonds are defined by the neighboring pairs of cation-cation (or anion-anion), where the interactions are via the repulsive force modified by the other terms of the potential. Such fictive bonds can increase in number even after the condition $N_b = (3N_V - 6)$ has been attained. As a result, gradual change of the topology of cages continues below T_B until the system has been deeply cooled. In other words, the volume of the system is reduced until the more rigid bonds by cation-anion interaction, which connects the loose networks of anion-anion and cation-cation, are formed.

Here we considered the characteristics of the soft percolation, which causes the complexity of the dynamics and structure in the fragile system. Often large coordination numbers and “fictive” bonds are found with the soft percolation. The large coordination number of the system and mixing of different networks means the existence of variety of structures with different N_b and N_V. This will result in wide distributions of life-times of the structures as well. Cages of anions are formed by cations, while the cages of cations are formed by anions and these networks are highly intertwined. Such multiple networks make the system a complicated one. The first changes at T_B are the characteristics of the fragile system, which is related to the packing of networks and coordination polyhedra around the anion or the cation. That is, the “soft percolation” characterizes the gradual changes in volume and the non-Arrhenius behavior of diffusivity in the fragile system.

It is interesting to compare this situation of the fragile liquid with the strong liquid. In typical strong system, silica, the equality, $3N_V - 6 = (1/2)N_V(N_V - 1)$, for the tetrahedron holds for each SiO_4 unit, and therefore further change of the number of bonds in the unit is not allowed after the loss of geometrical degree of the freedom, and this explains the Arrhenius behavior of the strong system. It is also understandable that the mixing of modifier such as alkali metal ions, which brings a distribution of coordination numbers of oxygen atoms, resulted in more fragile character to the system.

11.11.8 Relation of the Structure of Polyhedron with the Dynamics

As already shown in Sect. 11.2, MSD of ILs shows a caging region in a short time scale as found in other glass forming liquids. It means that the mobility of trapped particle and its cage are closely connected to the property of the polyhedron. This brings us an idea that dynamics of the trapped ion in the cage can be related to the deformation of cages, which is characterized by the fluctuation of N_V and/or N_b. By using the MTM (multi taper method) spectra of the motion of the central ions, it was shown that it is comparable with those of the motion of the cage characterized by N_b, although contribution from outer shells of the cages is not negligible [115]. If we examined the fast ion at 400 K, both the zero frequency mode corresponds to the diffusive motion, and the power law frequency dependence (caused by back correlated motion of ions) at around $f = 0.002$–0.03 are found, while the both regions are naturally missing for the slower (localized) ion. (Here the Nyquist frequency ($f = 0.5$) corresponds to $1/(2\delta t)$ (THz), where δt is chosen to be 0.8 (ps).) For the case of the localized ion taken near T_g, situation is similar to the localized ion found at 400 K. Thus the decrease in the diffusive mode is related to the stability of the polyhedron, and they are accompanied by the volume change at both T_B and T_g.

11.11.9 Relation with Thermodynamic Scaling

One of other possible approaches for the glass transition is based on the observation of the property of thermodynamic scaling as discussed in Sects. 7.4 and 11.10. Temperature and pressure dependences of the system are well described by the master function of the product variable, TV^{γ}, with $\gamma = 4.0$ and 3.8 for cation and anion respectively. Pair correlation functions show similar trend. The master curve of TV^{γ} shows an inflection at around T_{B} and the scaling seems to break down near the T_g. Existence of the inflection point implies a change in the compressibility of the system, and this is naturally related to the packing of the polyhedra.

Validity of the thermodynamic scaling of dynamic properties in many glass forming liquids suggests we should consider the packing of the coordination polyhedra in relation to the glass transition problem. This is because the dynamics having inflection points at temperatures T_B and T_{g} are associated with the corresponding changes in temperature dependence of volume.

11.11.10 Formation of the Infinitive Networks and the Glass Transition

To understand the mechanism of glass transition, one may assume the formation of infinitive network of some structural or dynamical units or domains at T_g, but it is not clear what is the length scale of the structural units that characterizes the glass transition. In the present section, we explained the glass transition as the soft and rigidity percolation of bonds and polyhedra including fictive bonds. This explanation is closely related to the structural and volume changes of the system with temperature or pressures.

Sometimes, the glass transition might be regarded as purely kinetic phenomenon, where the relaxation time of the metastable liquid state becomes longer than the observation time, while we considered here the structural changes near the glass transition regimes. In MD simulations, the former situation is expected and may be regarded as a “computer glass transition”, caused by the short time scale of the observation. We note that this situation occurs even for the ionics in the ionically conducting glass, where the ion is still mobile in the longer time scale. That is, only NCL region is observed in the MD simulation in low temperature region, however, of course, this is not a true glass transition of ions. This concept related to the observation time does not exclude further structural changes with non-equilibrium relaxation. The change accompanied with that for the free volume of the system is still possible.

Disorder found in the glass is considered to be the one brought by the mixing of different structures and/or different coordination numbers and this is related to the multifractality of the system discussed in Sect. 11.6.

In ionic liquid, several findings for dynamics such as details of the dynamic heterogeneity and relaxations with several steps are similar to those found in the ionic motion in ionically conducting glasses as well as other glass forming liquids. Thus the study of the ionic liquid bridges of the field of ionics and glass transition. These common features mean the existence of general physics underlying. Especially, the glass transition in an ionic liquid may be informative for the glass transition in other materials and therefore, it is summarized below. We have considered the network structures formed by bonds and cages to address the glass transition problem in the fragile ionic liquid, 1-ethyl-3-methyl imidazolium nitrate (EMIM-NO_3). The existence of the changes of network properties at T_B and T_g are shown. With decrease in temperature, we have observed the increase of the shortest cation-anion (Coulombic) bonds resulting in the saturation of the degrees of the freedom of the system near T_g as well as increase in the number of connections of fictive bonds. Thus the glass transition is similar to the rigidity percolation for these bonds.

Then we have characterized the cages, and the local structures in the network, and their changes on decreasing temperature by using the coordination number, N_{V}, and the number of bonds, N_{b}, within the coordination polyhedron. We introduced a concept of soft percolation of the cages with fictive bonds to characterize changes in the volume and dynamics near T_B higher than T_g. Coordination polyhedra with fictive bonds play a role to determine the packing of the local structures. That is, the structure with $N_{\mathrm{V}} = 4$ and $N_{\mathrm{b}} < (3N_{\mathrm{V}} - 6)$ with other N_{V} values almost disappeared at T_{B}, where the system still have measurable diffusivity in MD simulations. Soft percolation of cages can explain the further change of the system volume after the geometrical degree of the freedom was lost in each cage. Dynamics of ions are well correlated to the fluctuation of the cage characterized by using N_{V} and N_{b}. The rigidity and/or softer percolation of bonds or cages can explain the structural and dynamical changes accompanied with the glass transition in the system with different fragility.

11.12 Further Details of the Dynamic Heterogeneity

Because the heterogeneity is related to the existence of fast ions, some points for designing new materials with high conductivity and accelerated motions on the surface of the materials will be discussed. The problem is now common for both ionically conducting systems and ionic liquids.

11.12.1 Accelerated Dynamics in Ionic Systems

As explained in Sects. 9.4 and 11.3, the short time behavior of dynamics reflect the character of the jumps, while the diffusion or conduction is a mean behavior of both the fast and slow ions at times after t_{dif} when the MSD assumes the linear time dependence. This averaged behavior attained after t_{dif} determines diffusion. Changes from cage decay to diffusion regimes through the intermediate power law time dependence of MSD and the corresponding changes in frequency dependence of susceptibility are commonly found in the dynamics of ions in ionically conducting glasses and ionic liquids. In all cases, with decreasing temperature, the jump character of the motion becomes clearer. Thus the activation energy of each individual jump of ion is different from that for the steady state diffusion.

As found for these systems, existence of the Lévy stable distribution is rather general to characterize the dynamics of ions at certain time regimes. If consideration is confined to the localized motion only, Gaussian like motion might be found (example is given in Sect. 12.2.5) and this functional form is a special case of the Lévy distributions. It was also shown that the origin of the power law behaviors of MSD and stretched exponential behavior of the intermediate scattering functions are coexistence of fast and slow dynamics.

When considering the ionics in glass one may encounter the following questions.

1. In the field of glass transition problem, existence of the power law, t^{θ} dependence of MSD with $\theta < 1$, is regarded as the signature of the slow dynamics. Why the ions can show the large displacement in the glass in spite of the large back correlation probability of jumps?
2. Why the power law region in MSD can persist over many orders of time and how it changes to the diffusive regime?

The functional form of Lévy distribution with truncation is relevant for providing answers to these questions. When the van Hove function spreads to a distance r_{c}, the mean squared displacement $< r_i(t)^2 >$is represented by

$$< r_i(t)^2 > = \int_0^{r_c} r^2 \bullet 4\pi r^2 G_s(r,t)dr \tag{11.23}$$

From this equation, we can see that dynamics of ions are affected considerably by the small number of fast ions in the tail part of the function. In other words, the existence of the fast ions is an origin of the relatively large diffusion coefficient of ions, although the localized ions also make some contribution. Existence of the vacancies or ion channel related to this characteristics of $<r_i(t)^2>$ are observed, but is not sufficient to explain the commonly found behavior. Even if more coarse-grained model is considered and neglecting dynamic heterogeneity, the mean behavior of diffusion in the model was already affected by the fast ions, through the increase of the effective length scale or decrease of back correlation probability. For the second question, the stable character of the Lévy distribution explains why the power law region can continue many orders of magnitude in time. This is because of the truncation and multifractal mixing in the stable Lévy distribution, the change to the diffusive regimes proportional to time can take place over a longer time scale.

11.12.2 Origin of the Lévy Distribution: Fractional Fokker-Planck Equation

If the motion is random without interaction with other atoms or ions, its correlation function should show exponential decay with time, and Gaussian dynamics is expected. The Lévy distribution is a result of the deterministic motion affected by other ions. This view is consistent with the nature of the relaxation and diffusion of interacting species in ionic conductors and other systems espoused by the Coupling model by one of the authors [39]. Here we introduce some other approaches explaining the existence of Lévy distribution.

One of the possible methods to argue for the Lévy distribution is based on the fractional diffusion equation. Chaves [142] started the discussion from the ordinary Fokker-Planck equation based on the Fick's law and has analyzed the motion by the skew Fokker-Planck equation as follows. The stream, **j**, caused by the difference of the concentration n is taken into account here. By combining the continuity equation

$$\nabla \bullet \mathbf{j} + \frac{\partial n}{\partial t} = 0. \tag{11.24}$$

with the Fick's empirical law,

$$\mathbf{j} = -D\nabla n + \mathbf{v}n, \tag{11.25}$$

where D is diffusion coefficient, the result is the ordinary Fokker-Planck equation

$$\partial_t P(x,t) = -v\partial_x P(x,t) + D\partial x^2 P(x,t), \tag{11.26}$$

In one dimension, the probability density $P(x,t)$ of a particle, initially ($t = 0$) located at $x = 0$, is represented by the Gaussian form,

$$P(x,t) = (4\pi Dt)^{-1/2}\exp\left(-x^2/4Dt\right), \tag{11.27}$$

By generalization of the equation (11.25),

$$\mathbf{j} = -\frac{D}{2}\left(\nabla_r^{\alpha-1} - \nabla_{-r}^{\alpha-1}\right)n + \mathbf{v}n, \tag{11.28}$$

with $1 < \alpha \le 2$.

$$\frac{\partial n}{dt} = \frac{D}{2}\left(\nabla_r^{\alpha-1} - \nabla_{-r}^{\alpha-1}\right)n - \mathbf{v} \bullet \nabla n. \tag{11.29}$$

In one dimension,

$$\frac{\partial n}{dt} = \frac{D}{2}\left(\partial_x^{\alpha} + \partial_{-x}^{\alpha}\right)n - v\frac{\partial n}{\partial x}, \tag{11.30}$$

where the operator ∂_x^α is defined by the eigenvector equation,

$$\partial_{bx}^{\alpha}\exp(ax) = \left(\frac{a}{b}\right)^{\alpha}\exp(ax), \tag{11.31}$$

Here, a, b, and α are complex numbers.

The solution was obtained by using the Fourier transform,

$$n(x,t) = \int_0^\infty \frac{dk}{\pi}\Phi(k,t)\exp(ikx), \tag{11.32}$$

as,

$$n(x,t) = \int_{-\infty}^{\infty} \frac{dx'}{2\pi} n(x',0)P(x-x',t), \tag{11.33}$$

where the kernel P(x,t) is

$$P(x,t) = \int_0^\infty \frac{dk}{\pi}\cos k(x-vt)\times\exp\left[\cos\left(\alpha\frac{\pi}{2}\right)Dtk^{\alpha}\right]. \tag{11.34}$$

Further generalization with a skewness is introduced by different diffusivity depending directions, although it remains to prove that P(*x, t*) is positive. Later Almeida [143] commented that this probability kernel is a positive one, which is exactly the characteristic function of the stable distribution. Thus the Lévy distribution is a natural result of the generalized Fokker-Planck equations. The distribution is also a natural result of the Tsallis statistics [144].

11.13 Acceleration of the Motion on Surfaces

Here we note that the accelerated dynamics represented by the Lévy flight dynamics is also observed on the surface of material as shown by both experiment [145] and simulations [146]. Some works related to this problems are introduced here. Deltour et al. [146] have examined the fast diffusion of LJ clusters on the crystalline surface by MD simulation. Luedtke and Landman [147] reported the Lévy type power law distribution in the anomalous diffusion of a gold nanocrystal by using extensive molecular dynamics simulations. Maruyama [148] has analyzed temperature dependence of stick-slip diffusion of Au cluster on graphite. Chen et al. [149] have examined a Brownian particle in a two-dimensional periodic potential (force field). When the potential is separated into the independent two one-dimensional potentials, the friction η dependent on the diffusivity is $D \sim 1/\eta$, while for non-separable and anisotropic potential, $D \sim 1/\eta^{0.5}$. They found that the dependence of D on η in the low friction regime is directly related to the occurrence of long jumps.

Thus, acceleration of the motion in the nano crystals or grain boundaries, which discussed in Chap. 6, seems to be closely related to the Lévy distribution. Further studies by molecular dynamics simulations for such systems with and without periodic boundary condition will be useful to understand the effects of surface.

11.14 Conclusion

Studies of structure and dynamics of ionic liquids exemplified by EMIM-NO_3 using molecular dynamics simulation are described and discussed in the present chapter. Since the ionic liquid is ionic and also glass forming, this can make clear connections of the physics of ionics with that of the glass transition.

Time development of MSD of ions shows several distinct time regions and ions show a dynamic heterogeneity of long time scale. They are characterized by van Hove functions, intermediate scattering function and fractal dimension analysis. The self-part of the van Hove function has an inverse power law tail followed by the exponential part. That is, it has characteristics of the Lévy distribution with a truncation [see A.2.2–A.2.4]. Multifractal mixing of such motions explains both the time development of dynamics and frequency dependence of them related to it. From the phase-space plot, it was shown that such motion is rather deterministic and it is related to chaos.

Topological changes of the system and coordination polyhedra, which are related to the packing and geometrical degree of the freedom of the system were observed in the temperature dependence of the system by MD. Such features would be useful to understand the glass transition of the system.

The dynamics shows common features with ions in ionically conducting glass.

References

1. T. Welton, Chem. Rev. **99**, 2071 (1999)
2. M.J. Earle, K.R. Seddon, Pure Appl. Chem. **72**, 1398 (2000)
3. P. Wasserscheid, W. Keim, Angew. Chem. Int. Ed. **39**, 3772 (2000)
4. T. Kitazume, J. Fluorine Chem. **105**, 265 (2000)
5. R. Swatloski, S. Spear, J. Holbrey, R. Rogers, J. Am. Chem. Soc. **124**, 4974 (2002)
6. Q.-P. Liu, X.-D. Hou, N. Li, M.-H. Zong, Green Chem. **14**, 304 (2012)
7. T.I. Morrow, E.J. Maginn, J. Phys. Chem. B **106**, 12807 (2002)
8. J.N.C. Lopes, J. Deschamps, A.A.H. Pádua, J. Phys. Chem. B **108**, 2038 (2004)
9. C.G. Hanke, S.L. Price, R.M. Lynden-Bell, Mol. Phys. **99**, 801 (2001)
10. C.J. Margulis, Mol. Phys. **102**, 829 (2004)
11. M.G. Del Popolo, G.A. Voth, J. Phys. Chem. B **108**, 1744 (2004)
12. X.P. Wu, Z.P. Liu, S.P. Huang, W.C. Wang, Phys. Chem. Chem. Phys. **7**, 2771 (2005)
13. A. Canongia Lopes, A.A.H. Pádua, J. Phys. Chem. B **110**, 3330 (2006)
14. Y. Wang, W. Jiang, T. Yan, G.A. Voth, Acc. Chem. Res. **40**, 1193 (2007)

15. A. Triolo, O. Russina, H.-J. Bleif, E. Di Cola, J. Phys. Chem. B **111**, 4641 (2007)
16. M.G. Del Popolo, R.M. Lynden-Bell, J. Kohanoff, J. Phys. Chem. B **109**, 5895 (2005)
17. T. Yan, C.J. Burnam, M.G. Del Popolo, G.A. Voth, J. Phys. Chem. B **108**, 11877 (2004)
18. A. Bagno, F. D'Amico, G. Saielli, J. Phys. Chem. B **110**, 23004 (2006)
19. J. Habasaki, K.L. Ngai, J. Chem. Phys. **129**, 194501 (2008)
20. G.-E. Logotheti, J. Ramos, I.G. Economou, J. Phys. Chem. B 7211 (2009)
21. J. Habasaki, I. Okada, Mol. Simul. **9**, 319 (1992)
22. V. Chaban, Phys. Chem. Chem. Phys. **13**, 16055 (2011)
23. M. Lísal, Z. Chval, J. Storch, P. Izák, J. Mol. Liq. **189**, 85 (2014)
24. Y. Yasaka, M.L. Klein, M. Nakahara, N. Matubayasi, J. Chem. Phys. **136**, 074508 (2012)
25. W. Beichel, N. Trapp, C. Hauf, O. Kohler, G. Eickerling, W. Scherer, I. Krossing, Angew. Chem. **126**, 1 (2014)
26. D. Wolf, P. Keblinski, S.R. Phillpot, J. Eggebrecht, J. Chem. Phys. **110**, 8254 (1999)
27. S. Izvekov, J.M.J. Swanson, G.A. Voth, Phys. Chem. B **112**, 4711 (2008)
28. J.G. Kirkwood, J. Chem. Phys. **3**, 300 (1935)
29. IL-Thermo (see http://ilthermo.boulder.nist.gov/) The address was confirmed to be valid in Sep. 2014
30. G.-E. Logotheti, J. Ramos, I.G. Economou, J. Phys. Chem. B **2009**, 7211 (2009)
31. J. Habasaki, K.L. Ngai, J. Non Cryst. Solids **357**, 446 (2011)
32. J. Habasaki, R. Casalini, K.L. Ngai, J. Phys. Chem. B **114**, 3902 (2010)
33. J. Habasaki, K.L. Ngai, J. Chem. Phys. **133**, 124505 (2010)
34. J.N.A.C. Lopes, A.H. Padua, J. Phys. Chem. B **110**, 3330 (2006)
35. C. Hardacre, J.D. Holbrey, S.E.J. McMath, D.T. Bowron, A. Soper, J. Chem. Phys. **118**, 273 (2003)
36. J. Habasaki, K.L. Ngai, Y. Hiwatari, Phys. Rev. E **66**, 021205 (2002)
37. K.L. Ngai, J. Phys. Condens. Matter **15**, S1107 (2003)
38. J. Habasaki, K.L. Ngai, J. Non Cryst. Solids **353**, 5170 (2006)
39. K.L. Ngai, *Relaxation and Diffusion in Complex Systems* (Springer, New York, 2011)
40. H. Tokuda, K. Hayamizu, K. Ishii, A.B.H. Susan, M. Watanabe, J. Phys. Chem. B **108**(42), 16593 (2004)
41. K.L. Ngai, C.T. Moynihan, Bull. Mater. Res. Soc. **23**, 51 (1998)
42. X. Liu, H. Jain, J. Phys. Chem. Solid **55**, 1433 (1994)
43. K.L. Ngai, J. Chem. Phys. **110**, 1576 (1999)
44. J. Habasaki, K.L. Ngai, Y. Hiwatari, J. Chem. Phys. **120**, 8195 (2004)
45. G. Jarosz, M. Mierzwa, J. Ziolo, M. Paluch, H. Shirota, K.L. Ngai, J. Phys. Chem. B **115**, 12709 (2011)
46. J. Habasaki, I. Okada, Y. Hiwatari, Phys. Rev. E **52**, 2681 (1995)
47. J. Habasaki, I. Okada, Y. Hiwatari, Phys. Rev. E **67**, 2012 (1998)
48. J. Vila, P. Ginés, J.M. Pico, C. Franjo, E. Jiménez, L.M. Varela, O. Cabeza, Fluid Phase Equilib. **242**, 141 (2006)
49. H. Vogel, Z. Phys. **22**, 645 (1921)
50. G. Tammann, G. Hasse, Z. Anorg. Allg. Chemie **156**, 245 (1926)
51. G.S. Fulcher, J. Am. Ceram. Soc. **8**, 339 (1925)
52. C.A. Angell, Nature **393**, 521 (1998)
53. J. Habasaki, A. Ueda, J. Chem. Phys. **134**, 084505 (2011)
54. J. Habasaki, A. Ueda, J. Chem. Phys. **138**, 144503 (2013)
55. P. Bordat, F. Affouard, M. Descamps, K.L. Ngai, Phys. Rev. Lett. **93**, 105502 (2004)
56. P. Bordat, F. Affouard, M. Descamps, K.L. Ngai, J. Non Cryst. Solids **352**, 4630 (2006)
57. B. Mandelbrot, Science **155**, 636 (1967)
58. S. Alexander, R. Orbach, J. Phys. (Paris) Lett. **43**, L625 (1982)
59. R. Kubo, J. Phys. Soc. Jpn. **12**, 570 (1957)
60. T. Odagaki, M. Lax, Phys. Rev. B **24**, 5284 (1981)
61. K.L. Ngai, Solid State Ion. **5**, 27 (1981)

62. Z. Wojnarowska, K. Kołodziejczy, K.J. Paluch, L. Tajber, K. Grzybowska, K.L. Ngai, M. Paluch, Phys. Chem. Chem. Phys. **15**, 9205 (2013)
63. D.R. MacFarlane, J. Golding, S. Forsyth, M. Forsyth, G.B. Deacon, Chem. Commun. 1430 (2001)
64. W. Feller, *An Introduction to Probability Theory and its Applications*, vol. 2 (Wiley, New York, 1971)
65. M.F. Shlesinger, G.M. Zaslavsky, J. Klafter, Nature, London, U.K., **363**, 31 (1993)
66. J. Klafter, M.F. Shlesinger, G. Zumofen, Phys. Today **49**(2), 33 (1996)
67. J. Habasaki, I. Okada, Y. Hiwatari, Phys. Rev. B **55**, 6309 (1997)
68. H. Nakao, Phys. Lett. A **266**, 282 (2000)
69. R.N. Mantegna, H.E. Stanley, Phys. Rev. Lett. **73**, 2946 (1994)
70. I. Koponen, Phys. Rev. E **52**, 1197 (1995)
71. W. Kob, H.C. Andersen, Phys. Rev. E **51**, 4626 (1995)
72. J. Habasaki, K.L. Ngai, Phys. Chem. Chem. Phys. **9**, 4662 (2007)
73. A. Chhabra, R.V. Jensen, Phys. Rev. Lett. **62**, 1327 (1989)
74. C. Halsey, M.H. Jensen, L.P. Kandanoff, I. Procaccia, B.I. Shraiman, Phys. Rev. A **33**, 1141 (1986)
75. O. Yamamuro, Y. Minamimoto, Y. Inamura, S. Hayashi, H. Hamaguchi, Chem. Phys. Lett. **423**, 371 (2006)
76. A. Robledo, Phys. Lett. A **328**, 467 (2004)
77. W. Sakikawa, O. Narikiyo, J. Phys. Soc. Jpn. **72**, 450 (2003)
78. L. Van Hove, Phys. Rev. **95**, 249 (1954)
79. A. Rahman, K.S. Singwi, A. Sjölander, Phys. Rev. **126**, 986 (1962)
80. J. Colmenero, A. Alegria, A. Arbe, Phys. Rev. Lett. **69**, 478 (1992)
81. K.L. Ngai, J. Colmenero, A. Alegria, A. Arbe, Macromolecules **25**, 6727 (1992)
82. K.L. Ngai, L.-M. Wang, J. Chem. Phys. **135**, 194902 (2011)
83. K. Funke, R.D. Banhatti, J. Non Cryst. Solids **353**, 3845 (2007)
84. F. Takens, Detecting strange attractors in turbulence, in *Dynamical Systems and Turbulence, Lecture Notes in Mathematics*, vol. 898, ed. by D.A. Rand, L.-S. Young (Springer-Verlag, 1981), pp. 366–381
85. R. Vautard, P. Yiou, M. Ghil, Physica D **58**, 95 (1992)
86. J. Habasaki, K.L. Ngai, Y. Hiwatari, J. Chem. Phys. **122**, 054507 (2005)
87. U.R. Pedersen, N.P. Bailey, T.B. Schroder, J.C. Dyre, Phys. Rev. Lett. **100**, 015701 (2008)
88. C.M. Roland, S. Bair, R. Casalini, J. Chem. Phys. **125**, 124508 (2006)
89. E.R. López, A.S. Pensado, J. Fernández, K.R. Harris, J. Chem. Phys. **134**, 144507 (2011)
90. E.R. López, A.S. Pensado, J. Fernández, K.R. Harris, J. Chem. Phys. **136**, 214502 (2012)
91. A.S. Pensado, A.A.H. Pádua, M.J.P. Comuñas, J. Fernández, J. Phys. Chem. B **112**, 5563 (2008)
92. M. Paluch, S. Haracz, A. Grzybowski, M. Mierzwa, J. Pionteck, A. Rivera-Calzada, C. León, J. Phys. Chem. Lett. **1**, 987 (2010)
93. M.C.C. Ribeiro, T. Scopigno, G. Ruocco, J. Chem. Phys. **135**, 164510 (2011)
94. K.L. Ngai, J. Habasaki, D. Prevosto, S. Capaccioli, M. Paluch, J. Chem. Phys. **137**, 034511 (2012)
95. K.L. Ngai, J. Habasaki, D. Prevosto, S. Capaccioli, M. Paluch, J. Chem. Phys. **140**, 019901 (2014)
96. G. Galliero, C. Boned, J. Fernández, J. Chem. Phys. **134**, 064505 (2011)
97. R. Casalini, R.F. Gamache, C.M. Roland, J. Chem. Phys. **135**, 224501 (2011)
98. D. Fragiadakis, C.M. Roland, J. Chem. Phys. **134**, 044504 (2011)
99. D. Chandler, *Introduction to Modern Statistical Mechanics* (Oxford University Press, New York, 1987)
100. J.P. Hansen, I.R. MacDonald, *Theory of Simple Liquids*, 2nd edn. (Academic, London, 1990)
101. J. Habasaki, K.L. Ngai, Anal. Sci. **24**, 1321 (2008)
102. G. Adams, J.H. Gibbs, J. Chem. Phys. **43**, 139 (1965)

103. E. Leutheusser, Phys. Rev. A **29**, 2765 (1984)
104. T. Odagaki, Y. Hiwatari, Phys. Rev. A **41**, 929 (1990)
105. K.L. Ngai, R.W. Rendell, D.J. Plazek, J. Chem. Phys. **94**, 3018 (1991)
106. F. Sciortino, J. Stat. Mech. **05**, 5015 (2005)
107. T. Odagaki, T. Ekimoto, J. Non Cryst. Solids **353**, 2928 (2007)
108. A. Einstein, Ann. Phys. **322**(8), 549 (1905)
109. G.K. Batchelor, *An Introduction to Fluid Dynamics* (Cambridge University Press, Cambridge, 1967)
110. F. Müller-Plathe, Phys. Rev. E **59**, 4894–4898 (1999)
111. P. Bordat, F. Müller-Plathe, J. Chem. Phys. **116**, 3362 (2002)
112. K.L. Ngai, J. Phys. Chem. B **110**, 26211 (2006)
113. P. Singh, R.D. Banhatti, K. Funke, Phys. Chem. Chem. Phys. **7**, 1096 (2005)
114. J. Habasaki, F. Affouard, M. Descamps, K.L. Ngai, in *Proceedings of AIP Conference* **982**, 154 (2008)
115. J. Habasaki, K.L. Ngai, J. Chem. Phys. **142**, 164501 (2015)
116. K.L. Ngai, J. Habasaki, J. Chem. Phys. **141**, 114502 (2014)
117. C.A. Angell, J. Non Cryst. Solids **73**, 1 (1985)
118. R. Casalini, K.L. Ngai, C.M. Roland, Phys. Rev. B **68**, 014201 (2003)
119. N.C. Forero-Martinez, R. Cortes-Huerto, P. Ballone, J. Chem. Phys. **136**, 204510 (2012)
120. K.L. Ngai, L.-R. Bao, A.F. Yee, C.L. Soles, Phys. Rev. Lett. **87**, 215901 (2001)
121. G. Dlubek, Y. Yu, R. Krause-Rehberg, W. Beichel, S. Bulut, N. Pogodina, I. Krossing, C. Friedrich, J. Chem. Phys. **133**, 124502 (2010)
122. A.L. Loeb, *Space Structures* (Addison-Wesley, Reading, 1976)
123. J. Habasaki, Mol. Phys. **70**, 513 (1990)
124. J. Habasaki, I. Okada, Y. Hiwatari, Mol. Dyn. Simul., Springer Series in Solid-State Sciences **103**, 98 (1991)
125. J. Habasaki, Z. Naturforsch. **46a**, 616 (1991)
126. J.C. Phillips, J. Non Cryst. Solids **34**, 153 (1979)
127. M.F. Thorpe, J. Non Cryst. Solids **57**, 355 (1983)
128. H. He, M.F. Thorpe, Phys. Rev. Lett. **54**, 2107 (1985)
129. R. Böhmer, C.A. Angell, Phys. Rev. B **45**, 10091 (1992)
130. D.G. Georgiev, P. Boolchand, M. Micoulaut, Phys. Rev. B **62**, R9228 (2000)
131. W. Bresser, P. Boolchand, P. Suranyi, Phys. Rev. Lett. **56**, 2493 (1986)
132. P. Boolchand, R.N. Enzweiler, R.L. Cappellett, W.A. Kamitakahara, Y. Cai, M.F. Thorpe, Solid State Ion. **39**, 81 (1990)
133. M. Tatsumisago, B.L. Halfpap, J.L. Green, S.M. Lindsay, C.A. Angell, Phys. Rev. Lett. **64**, 1549 (1990)
134. W.A. Kamitakahara, R.L. Cappellett, P. Boolchand, B.L. Halfpap, F. Gompf, B.A. Neuman, H. Mutka, Phys. Rev. B **44**, 94 (1991)
135. E. Aharonov, E. Bouchbinder, H.G.E. Hentschel, V. Ilyin, N. Makedonska, I. Procaccia, N. Schupper, Eur. Phys. Lett. **77**, 56002 (2007)
136. R. Fabian Jr., D.L. Sidebottom, Phys. Rev. B **80**, 064201 (2009)
137. D.J. Jacobs, M.F. Thorpe, Phys. Rev. Lett. **75**, 27 (1995)
138. P. Boolchand, X. Feng, W.J. Bresser, J. Non Cryst. Solids **293–295**, 348 (2001)
139. J.C. Phillips, J. Non Cryst. Solids **43**, 37 (1982)
140. J.C. Phillips, Solid State Phys. **37**, 93 (1981)
141. J.C. Phillips, Rep. Prog. Phys. **59**, 1133 (1996)
142. A.S. Chaves, Phys. Lett. A **239**, 13 (1998)
143. M.P. Almeida, Phys. Lett. A **249**, 560 (1998)
144. C. Tsallis, J. Stat. Phys. **52**, 479 (1988)

145. L. Bardotti, P. Jensen, A. Hoareau, M. Treilleux, B. Cabaud, A. Perez, F. Cadete, S. Aires, Surf. Sci. **367**, 276 (1996)
146. P. Deltour, J.-L. Barrat, P. Jensen, Phys. Rev. Lett. **78**, 4597 (1997)
147. W.D. Luedtke, U. Landman, Phys. Rev. Lett. **82**, 3835 (1999)
148. Y. Maruyama, Phys. Rev. B **69**, 245408 (2004)
149. L.Y. Chen, M.R. Baldan, S.C. Ying, Phys. Rev. B **54**, 8856 (1996)

Chapter 12
Practical Introduction to the MD Simulations of Ionic Systems

12.1 Examples of MD Simulation of Ionic System

For anyone interested in performing molecular dynamics simulations, there are many possible approaches. Nowadays, many kinds of MD programs and those for analysis are available. Choice of the method of the calculations depends on the objective of the researcher and the application of MD depends on scientific background of the researcher. Due to large number of possible selections, it may be difficult to choose the most suitable programs or conditions for starting the MD simulations.

In such situations, fundamental steps taken in the study of simpler system with a minimum setting will be useful as a start for learning how to perform MD simulations. Then one can select the suitable methods for one's purpose. Therefore, in Sect. 12.1, we will show some examples and carry out the exercise of MD simulations of ionic systems using a short program. Although the program is not optimized one for your machine, it is essentially the same one used in our studies and can be used for other purposes. In this exercise, we planned that one can run MD simulations and treat the data on "windows machine" by oneself. Some programs and examples will be found in Electronic Supplementary Material (ESM) (http://extras.springer.com) You will be able to find materials by searching the book's ISBN. Please use contents of ESM at your own risk.

In Sect. 12.4, fundamental setting in MD programs is explained. How to prepare initial configurations of melt, crystals and glasses are also explained with examples. After that, introduction of several products of software of MD simulations and for visualization available freely or commercially are given. For advanced features to acquire, one may need to consult with experts of related systems, manuals of programs.

In principle, it should be avoided to use addresses of WEB sites in publication. However, especially in the present section, addresses of some WEB sites are included for convenience of users, in spite of the fact we cannot guarantee the validity of the address.

J. Habasaki et al., *Dynamics of Glassy, Crystalline and Liquid Ionic Conductors*,
Topics in Applied Physics 132, DOI 10.1007/978-3-319-42391-3_12

Example 1: MD simulations of lithium metasilicate glass on "Windows"

In the first example, we use a program for the lithium silicate glass that works on "Windows" with a personal computer.

STEP 1 (Preparation of Linux like environment on Windows)

Unfortunately, the situations of the readers (for machines, OS etc.) can be different case by case. Here we assume the case of the "Windows 8.1 or 10" machine with 64 bit, while most of MD programs work on the "Unix" or "Linux" platform with suitable compilers. Therefore, at first, linux-like environment is introduced on windows by "Cygwin" [1]. Cygwin user can skip this step; although addition of some options may be required later.

Cygwin is a large collection of GNU and Open Source tools which provide functionality similar to a Linux distribution on Windows. Please visit the WEB page (Ref. [1]) and follow the instruction there. Please include GCC and Gfortran compilers. Additional installations of editors (such as vi) may be useful for modification of the input files, although one can also use the text editor on windows. This environment can be used for many purposes. Some knowledge for Linux or UNIX may be required, although usages of some commands (appeared after the prompt $) are included below. Caution may be required for the difference of code (for example, it is found in carriage return (CR) or line feed (LF)), in using different systems.

- If you are a user of the Linux or Unix and Intel compilers, please try to use the file named "mdintel.exe" in the ESM instead of "lsomd.exe".
- If your environment is not suitable for using exe files found in the ESM, please skip step 1–4.

STEP 2 (Preparation of files on your home directory)

Put all files within "Example 1" folder in ESM in your home directory of Cygwin (You can do it by the usual operation on windows). By the default installation, the home directory may be located at C:\cygwin64\home\"User Name". For starting the program, one can prepare some shortcuts during the installation.

For example, click "Cygwin64Terminal" created on the desktop for starting Cygwin.
Input the following command and then depress the enter key to see file list.

```
$ls –al
```

File names with information will appear.

STEP 3 Structure of Files

lsomd.exe is a binary code of the MD Program LSOMD for M_2SiO_3 systems. The test data used is for $M = Li$.

Input files

Initial configuration of the system of 3456 atoms (Li 1152, Si 576, O 1728) is given in lslarsinf800ini.data.

Please copy the configuration data to "lslarinfini.data" for the input of the program by the following procedure.

For copying the data from A to B files, put the command “cp A B” after the prompt, $, then depress a return key. In this trial, please input the following.

```
$cp lslarinf800ini.data lslarinfini.data
```

The data included in this file are initial coordinates of ions and atoms, x_n, y_n, z_n in Å.

That is, x_1, y_1, z_1, x_2, y_2, z_2, ----x_{3456}, y_{3456}, z_{3456} followed by dx_1,dy_1,dz_1,dx_2, dy_2,dz_2-----dx_{3456}, dy_{3456}, dz_{3456}. Here dx_1 is for a difference of $x_1(t)$ and $x_1(t+dt)$ and similar definitions are used for dy, dz for $n = 1, 2,\text{---}3456$.

Several parameters are necessary to be set in “lslarset.data”.

“lslarset.data”: Setting of total steps, temperature, pressure, delta *t*, etc.

Initial setting in the file is as follows.

```
===== lslarset.data=====
5000 100 33.15 800. 1.00E−15 0.
6.941 28.0806 15.9994
0.87 2.40 −1.38
1.0155 0.8688 2.0474
0.07321 0.03285 0.17566
10.87 23.18 70.37
================
```

For the first line, number of steps, *N*, interval of steps, m_{itv}, length of the cell (in Å), target temperature (in K), and step time (in s) and parameter for setting conditions. In the last figure, ‘0.’ means NVE condition, while ‘1.’ means NVT condition (using Gaussian thermostat). The value ‘target temperature’ does nothing when the NVE condition is chosen. In the following lines, potential parameters (see Sect. 9.1) for lithium metasilicate are given. In the second line, mass of Li, Si and O are given. In the third line, effective charges of Li, Si and O are given, respectively. In line 4, (5 and 6), potential parameters in Gilbert-Ida type for these species, a_i, (b_i, and c_i) are given in the order of Li, Si and O in this case. Please distinguish integer and real figures carefully.

Setting of these parameters depends on the problem to be examined as well as the properties of the system. For example, one needs to modify the setting considering following situations.

Usually longer total time steps will be necessary for slow dynamics in melts, glasses, and crystals. The highest frequency accessible depends on the m_{int} of the output. Shorter step time is required for the system with faster dynamics. If the system includes light atom such as hydrogen, it should be less than 0.5–1 fs.

Step 4 Run the program

Please run the program “lsomd.exe” using the lslarset.data. Configuration file lslarinfini.data is also used by the program. Put the following command.

```
$./lsomd.exe <lslarset.data
```

Here “./” is for using a current directory for execution of the program.

After pressing the “enter key”, the program will start.

At first the content of “lslarset.data” is repeated for confirmation.

Please wait for a while.

Then the status of the run with interval of m_{itv} steps will be appeared on screen.

Count, Temperature for Li, Si, O and total (in K), Pressure (in GPa),

Energies (Total, Coulombic, Repulsive and for c_ic_j term (in J/mol).

The following is an example.

```
------------------------------------------------------------------------------------------
    COUNT T_Li T_Si T_O Tmean P Etot Ecoul Erepul Ecc
    10   822.208   808.818   804.311   811.027   −0.9078E-02   −0.7689E+07
−0.8087E+07 0.2975E+07 −0.2576E+07
------------------------------------------------------------------------------------------
```

The execution time depends on your machine.

You can see temperature and energy fluctuate during the run. Total energy of the system is maintained if NVE condition is chosen.

Pressure of the system tends to show large fluctuations including negative values. Note that the pressure is sensitive to the setting of the box size and also the potential parameters used. The value has a relatively large error because it is obtained from a difference of large comparable values.

OUTPUT FILES

When a run stops, the following files will be found.

lslar2traj.data: Coordinate of atoms obtained for every m_{itv} steps are accumulated in this file. The data have similar sequences as lslarinfini.data but is repeated for N steps with interval of m_{itv} steps. The data for dx, dy, dz are not included here.

lslar3thermo.data: This output is the same one, which is shown on the screen during the run.

“lslarinflast.data” is the last configuration for the input of continuing run.

The structure of the file is the same as the “lslarinfini.data”.

Pair correlation function, $g(r)$ of the system was stored in lslar-gr.data.

Please examine the size of output files and “real time” required for the calculation of 5000 steps in your system. If your file space is enough and run time is acceptable, further longer runs can be done by your own choice.

Before starting the second run, copy the lslarinflast.data to lslarinfini.data.

```
$./cp lslarinflast.data lslarinfini.data
```

Please try further the longer runs for better statistics. During the following runs, output files are overwritten by new data. Such “overwriting” seems to be used in several MD programs and caution may be required if you need long successive runs. When you need old data, rename the old files. Probably it is better to prepare the script file for renaming or modify programs to add the run number.

It may be also useful to add the name of the system, temperature, date, etc. to the file name with some rules of order and abbreviations.

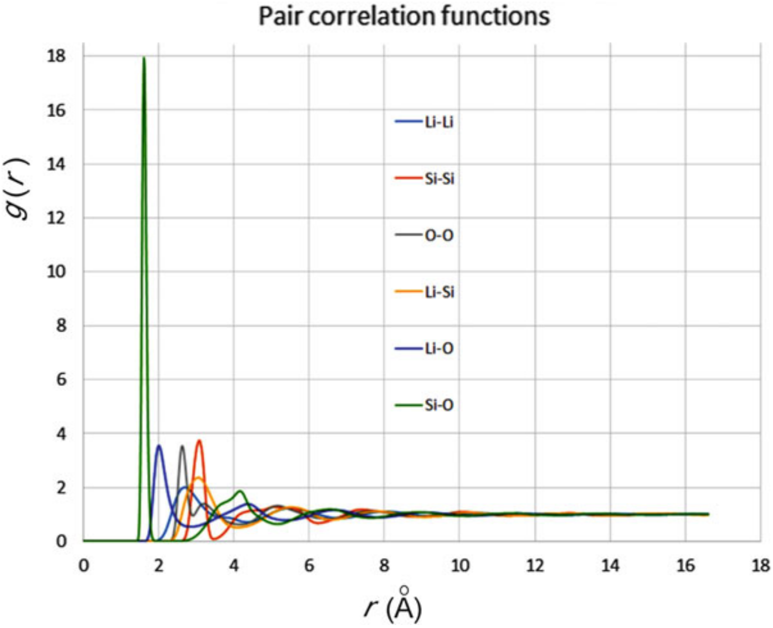

Fig. 12.1 Example of the plot of *g*(*r*) using the "lslar-gr.data" obtained by the 100,000 steps run (Li_2SiO_3 system at 800 K) using "Excel"

STEP 5 Visualization of data

After finishing run, one can plot the *g*(*r*) for each combination of ion pairs using the file named "lslar-gr.data" (or "lslar-gr.csv" if you skipped step 1–4) by several plotting programs.

For example, the plot using "Microsoft Excel" after some setting of the appearance can be found in Fig. 12.1.

In the "lslar-gr.data", the first column of the data is a distance *r*. The values of *g*(*r*) are found from the 2nd to 7th column for Li–Li, Si–Si, O–O, Li–Si, Li–O and Si–O pairs, respectively.

Please examine the characteristics of the structures.

An example of the output file "lso.pdb" will be found in the ESM. The pdb file can be read from many visualization programs. One can use it to examine the structural details such as angles, distances, etc. Please try to use VESTA (**V**isualization for **E**lectronic and **ST**ructural **A**nalysis) [2] and open the pdb file. Select "Edit" tab and "bonds" tab and set Si–O bonds (connecting the atoms within 2.1 Å is useful in almost all cases) in the case of VESTA. Then select the "ball and stick" model. You can also use other styles such as "space filling model", "polyhedra (after setting bonds)". The file "lso.vesta" will be found in the same location, where the Si-O bonds are connected and polyhedra of SiO_4 units are shown as in Fig. 12.2.

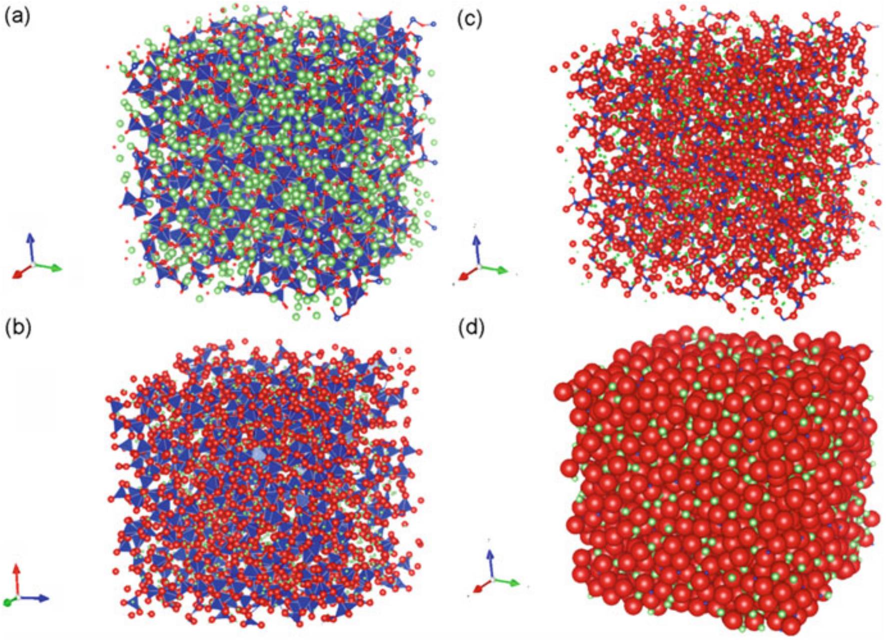

Fig. 12.2 Examples of the visualization of the Li_2SiO_3 system (3456 particles) (near the glass transition temperature) at 800 K. (**a**) SiO_4 units are shown by polyhedra. Li ions are shown with atomic radius to emphasize the positions and existence of ionic paths. (**b**) The same structure as (**a**) but with ionic radius of Li ion. (**c**) The same structure in ball and stick model. (**d**) The same structure in space filling model. *Green*: Li ions, *Red*: Oxygen atoms and *Blue*: Si atoms (and SiO_4 units). These figures are visualized using the file "lso.vesta" (or "lso.pdb") in ESM and the program "VESTA" [2]

Please change the size of atoms or ions by yourself. You can also Zoom, Rotate and Move it. You can also measure distances or angles in the structures. Please follow the manual of VESTA or other programs used for further details.

You can also visualize the structure obtained by the run you have performed.

Please run the program inftoxyz.exe to change the "lslarinflast.data" to "lso.xyz" by the following command.

```
./inftoxyz.exe <lslarinflast.data
```

The file named "lso.xyz" was created in the same directory. Many programs for visualization can read "xyz" format. Please modify the appearance by your own choice.

STEP 6 Further analysis of the system

Change temperature or box size gradually. How does the structure change?

You can also examine more details by your own programs.

12.2 Example 2: Analysis of the Lévy Flight and Lévy (Alpha Stable) Distribution

12.2.1 *Example of Analysis for a Mobile Ion*

In this subsection, an example for the ionic motion in the lithium “metasilicate” is shown, and after that examples included in the ESM will be explained.

It shows a Lévy distribution as found in the functional form of the self-part of the van Hove functions for all ions. This result shown here is another proof of the existence of Lévy flight with $\alpha < 2$. Original time series for ionic motion is plotted in Fig. 12.3, where the absolute value of the displacement for Li ion $|r_i(t)|$ in lithium metasilicate at 500 K during 1 ns runs is used. Here t is a sampling time measured by an interval of dt. (In this example, dt is taken as 4 ps).

12.2.2 *Log Return of Data*

For examining the functional form of vibrational motions and jumps, one can use “log return” defined by following relation, which is often used in the analysis of financial time series (for example, see Ref. [3]).

For the time series, $|r_i(t)|(=|r_t|)$, log-return, $\Delta\ln|r_t|$ is given by,

$$\begin{aligned}\Delta\ln|r_t| &= \ln|r_{t+1}| - \ln|r_t|,\\ &= \ln\left(1 + \frac{|r_{t+dt}| - |r_t|}{|r_t|}\right) \sim \frac{|r_{t+dt}| - |r_t|}{|r_t|}\end{aligned}$$

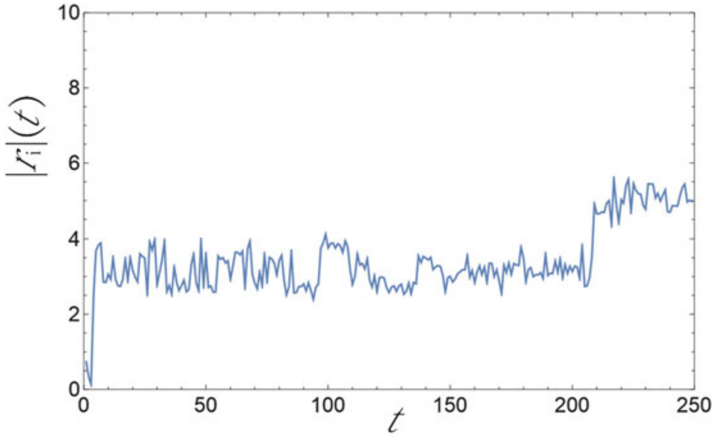

Fig. 12.3 Time series of absolute value of the displacement for Li ion $|r_i(t)|$ in lithium metasilicate at 500 K during 1 ns runs plotted against t. Here t is a sapling time measured by an interval of dt (in this example, dt is taken as 4 ps), plotted by using Mathematica

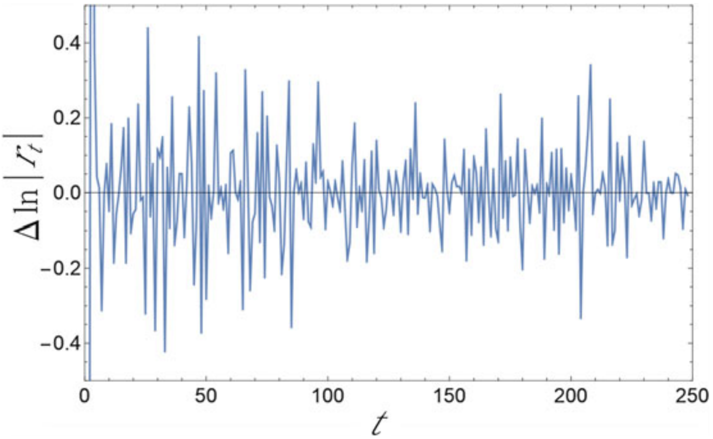

Fig. 12.4 Log-return of the time series of absolute value of the displacement for Li ion shown in Fig. 12.3

Therefore, the log-return is an estimation of the expansion rate of $|r_t|$.

The distribution of $|r_t|$ is affected by the sudden jumps of the data, and the change of the absolute value of the $|r_t|$ is affected by the distance from the initial position, while the log-return does not depend on the absolute value of the $|r_t|$. Log return of the time series in Fig. 12.3 is shown in Fig. 12.4.

12.2.3 Comparison of the Distribution of Log-Return and the Fitted Curve

In Fig. 12.5, histogram for the probability distribution for the log-return (denoted by Z here) (orange) is shown, where a fit by the stable distribution is represented by the blue curve (blue). Thus the motion of ion is represented by the Lévy flight dynamics with $\alpha = 1.46$.

12.2.4 Further Analysis of Cumulative Distribution and Comparison of Lévy (Alpha Stable with $\alpha < 2$) and Gaussian Distribution (Alpha Stable with $\alpha = 2$)

To check the quality of the fit, cumulative distribution function is useful. In the long time scale, the distribution is affected by the exponential truncation of the tail.

One should note that the exponential truncation (see Appendix A.2) in the self-part of the van Hove functions is found in the log-log scale (For example, see Fig. 9.8 of Chap. 9), where the contribution is less than ~1 %, but is emphasized in the log-log scale.

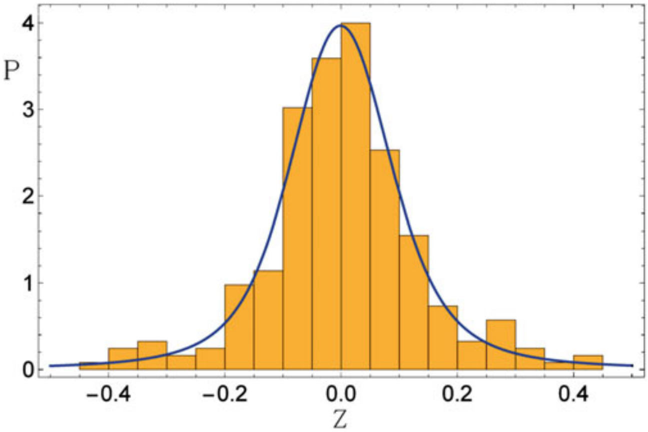

Fig. 12.5 Probability distribution, P, of the log return (denoted Z here) of the time series of absolute value of the displacement for Li ion shown in Fig. 12.3. Histogram (*orange*) is for the data obtained by MD, while the *blue curve* is for the fitted one with the stable distribution. Parameters for $(\alpha, \beta, \gamma, \delta)$ is found to be (1.46, 0.039, 0.073, 0.028) by the maximum likelihood method. Here the tail found in longer distance was omitted

Fig. 12.6 Comparison of the pattern of the cumulative distribution of the log-return (*blue dots*) and that of the fitted one for stable distribution (*red curve*)

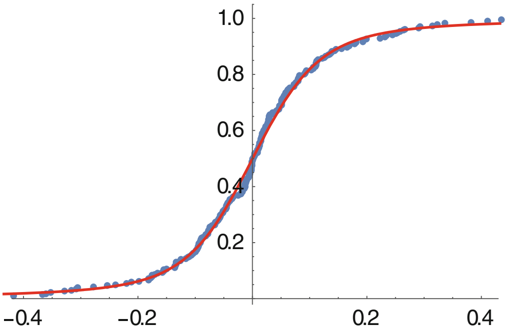

In Fig. 12.6, the function of the log-return of the time series (blue dots) and the fitted one for stable distribution (red curve) by the maximum likelihood method [4] obtained by using Mathematica are shown.

In Fig. 12.7, comparison of the stable α distribution with $\alpha = 1.46$ (red) and corresponding distribution with $\alpha = 2.0$ (blue dot) is shown. The difference is observed in both the tail and the sharpness of the function.

12.2.5 Free CDF Files with Manipulation

We prepared free Computable Document Format (CDF) files using Mathematica [5] for treatment of the data in the folder named “Example 2” in the ESM. It works on Windows. Please copy the contents of the folder in your Documents directory (by usual procedures on your machine).

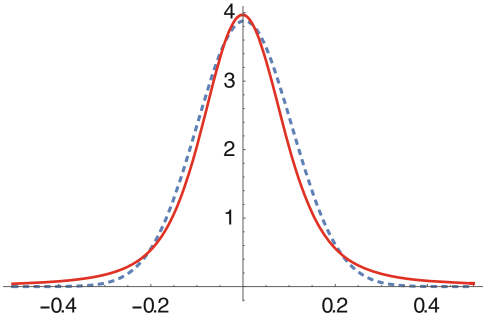

Fig. 12.7 Comparison of the pattern of the distributions. *Red curve* is the fitted one with (α, β, γ, δ) = (1.46, 0.039, 0.073, 0.028) and *blue dashed* one is α = 2 (other parameters are set to be the same as *red* one)

If you don't have Mathematica, you can use a free CDF-Player which can be available at Ref. [6].

There is a free CDF file named "**Levy -stable alpha- distribution of type 1. cdf**". It includes interactive manipulation of four parameters in the stable distribution (see Appendix A.2 for details of the distribution). If the file does not work well in your environment, please try "**Levy -stable alpha- distribution of type 1_9.cdf**" files. You can check how the distribution changes with parameters by yourself.

There are several examples of CDF files **(Analyses ---.cdf)** for time series, $|r_i(t)|$ data of some arbitrary chosen particle obtained by MD runs, which were fitted to the stable distribution.

You can treat the file using the CDF player. Please change the size of figures to see the details for the motions

Sample 1: Jump motion for a Li ion in lithium "metasilicate" glass at 700 K. Lévy flight dynamics is clearly observed.
Sample 2: For an EMIM ion in the ionic liquid, EMIM-NO_3 at 300 K. The motion is not a clear jump but the Lévy (alpha stable) distribution is clearly observed.
Sample 3: For the arbitrary chosen Li ion at 800 K in lithium "disilicate" glass. The ion is localized for a long time (The time series during 12 ns run is shown here.). In this case, both fittings to normal and Lévy stable distributions are compared. The distribution is Gaussian like except for the contribution of the peak due to the jump found at the last of the time series. Note that the numbers of the sampling points are not the same in each example.

The file named **"Simulation using stable distribution.cdf"** (and/or that with_9) is for the simulation of the displacement of ion reproduced by the random sampling of 1000 points from the stable distribution with a characteristic index α chosen by you. When α = 2, the motion is the Brownian motion.

You can find strong heterogeneous motions with intermittency with a smaller (<2) value of the index α. You can compare the actual data and the randomly sampled data.

The free CDF file named **"MD-Soft-Core Model.cdf"** is for the MD simulations of soft-core model (exponent $n = 12$). Although this is not an ionic system, readers can have some idea of what is done in the MD simulations. In this example, the periodic boundary condition is not used and particles are bounced back from the wall. Except for this point, the program do the MD simulation by the Verlet algorithm with your choice of the number of particles, temperatures and system size. Color of particle changes when the velocity of the particle changes.

12.3 Example 3: Examining Movies

Two examples of movies are included in the "Example 3" directory in the ESM. Since their visibility depend on your machine environments, we prepared two files with different formats. We hope that you can see at least one of them.

The file named "**EMIM-NO3 100 K-1.wmv**" is for EMIM-NO_3 glass at 100 K shown by the stick model. This can be open by the "media player". Try to click the file name on Windows.

In these movies, periodic boundary condition is used as usual. If the center of mass position of the ion moves to the next image cell, the ion disappeared and the corresponding ion comes in at the same time. Thus the number of ions is kept constant.

The file named "**disilicate crystal.swf**" is for lithium disilicate crystal in the metastable form at 1400 K. The format is for adobe flash player. Please try to open it from Internet Explorer. If it does not work, please check if the adobe flash player was installed in your system or not, by visiting the WEB site of adobe (Ref. [7]) and follow the instruction there.

It can be seen that how the mobility of atoms depends on the direction of the crystal.

For explanation of other files, see readme.txt or Readme---.docx in each folder in the ESM.

12.4 Fundamental Usage of MD Programs

In followings, we explain a general (and may be minimal) example for input and output in MD programs.

12.4.1 INPUT of the MD Programs

If you use a program suitable for your purpose, each MD program has its own input and output format and may have examples to show how to use it.

Typical input files in the works using MD simulations of glasses contain

1. Setting of potential parameters and functions
2. Setting of ensemble (NTP, NVE, etc.) and some options such as the shape of the MD cell.
3. Initial configuration, velocity and system size.
4. Setting of runs for analysis (step time and total number of steps at each temperature).

In the case of MD simulation of super-cooled liquids and/or glasses, cooling schedule must be planned.

5. Several settings for cutoff values (for repulsive term and/or Ewald summation).

12.4.2 Preparation of Initial Configurations for Crystals

Crystal structures can be used for checking the quality of the potential parameters, for the preparation of initial configuration for liquids or glasses, as well as examination of crystals themselves.

Here we briefly explain how initial configuration for MD simulations of crystal is prepared as exemplified by lithium or sodium metasilicate crystals.

These crystals are orthorhombic and space group is $C_{mc}2_1$ with $Z = 4$ [8].

Li_2SiO_3 $a_0 = 9.36$; $b_0 = 5.395$, $c_0 = 4.675$ (in Å)

Na_2SiO_3 $a_0 = 10.52$; $b_0 = 6.07$, $c_0 = 4.825$ (in Å)

Space group: $C_{mc}2_1$,

where the meaning of each notation is as follows.

C: ***base-centered lattice.***
m: ***mirror planes***
c: ***glide planes*** (mirror planes involving reflection and a translation parallel to the plane). (The plane can be **a**, **b**, **c**, **n** or **d**)
2_1: ***screw axis***

Treatment of crystal structure is based on the "International Tables for Crystallography" volume A [9].

General coordinate of the present systems are given by,

1. x,y,z
2. −x,−y,z + 1/2
3. x,−y, z + 1/2
4. −x, y, z
5. x + 1/2, y + 1/2, z
6. −x + 1/2,−y + 1/2, z + 1/2
7. x + 1/2,−y + 1/2, z + 1/2
8. −x + 1/2, y + 1/2, z

Some software can generate the crystal structure by choosing the space group and input of coordinate in the unit cell. As an alternative way to obtain the basic cell for MD runs, the atomic coordinate, $\mathbf{r}_\alpha$, within an asymmetric unit is expanded to $\mathbf{r}_\mathrm{i}$ in the whole crystal lattice by using symmetry operators.

$$\mathbf{r}_\alpha \bullet \mathbf{P}_m + \mathbf{T}_m = \mathbf{r}_i, \tag{12.1}$$

where $\mathbf{P}_m$ and $\mathbf{T}_m$ are (3×3) matrix of linear part and (3×1) column matrix (translational vector), respectively for general transformation.

The linear part (orientation or length, or both) of the basis vector **a**, **b**, **c** can be transformed into new vector **a′**, **b′**, **c′** by the (3×3) matrix $\mathbf{P}_\mathrm{m} = \begin{pmatrix} P_{11} & P_{12} & P_{13} \\ P_{21} & P_{22} & P_{23} \\ P_{31} & P_{32} & P_{33} \end{pmatrix}$, that is, $(\mathbf{a}',\mathbf{b}',\mathbf{c}') = (\mathbf{a},\mathbf{b},\mathbf{c})\mathbf{P}_\mathrm{m}$. This is combined with translational transformation.

For example, obtaining the coordinates x, y, z + 1/2, from atomic coordinate x_α, y_α, z_α, following operation

$$\begin{array}{ccccccc} & \mathbf{P}_\mathrm{m} & & \mathbf{T}_\mathrm{m} & & & \\ (\mathrm{x}_\alpha, \mathrm{y}_\alpha, \mathrm{z}_\alpha) & \begin{pmatrix} 1 & 0 & 0 \\ 0 & 1 & 0 \\ 0 & 0 & 1 \end{pmatrix} & + & \begin{pmatrix} 0 \\ 0 \\ 1/2 \end{pmatrix} & = & \begin{pmatrix} x_i \\ y_i \\ z_i \end{pmatrix} \end{array} \tag{12.2}$$

is applied for the (8b) positions in the atomic coordinates shown in the next Table 12.1 [8].

Both matrix and general forms also can be found in the WEB site [10]

In Fig. 12.8, primitive cell for the lithium metasilicate crystal is shown.

Usually, basic unit of MD simulations is chosen to have equal (or comparable) axis lengths by repeating the crystal units.

In this example of lithium metasilicate crystal, a supercell formed by repetition of axis length as $a_0 \times 2$, $b_0 \times 3$, $c_0 \times 3$ is taken as the basic cell of MD simulations. The cell contained $2 \times 3 \times 3$ of $Z = 4$, namely 72 of Si atoms, 144 of Li ions, and 216 O atoms, and the total number of atoms is 432. The space group of the system is $C_{mc}2_1$. The supercell thus prepared is shown in Fig. 12.9. This system size can be used to examine some characteristics of crystal structures, but might be too small for examining dynamics of them because of long length scale repetitions of the structures affect the dynamics.

Table 12.1 Atomic coordinate of lithium (and sodium) metasilicate crystal [8]

Atom	Position	X	Y	Z
Li(Na)	(8b)	0.160(0.166)	0.320(0.339)	0.000(0.000)
Si	(4a)	0.000(0.000)	0.164(0.166)	0.537(0.564)
O(1)	(8b)	0.141(0.130)	0.321(0.286)	0.450(0.500)
O(2)	(4b)	0.000(0.000)	0.100(0.077)	0.860(0.895)

Fig. 12.8 Unit of crystal in Li_2SiO_3 system [8]. *Pale blue*, *blue* and *red* spheres are for Li, Si and O, respectively

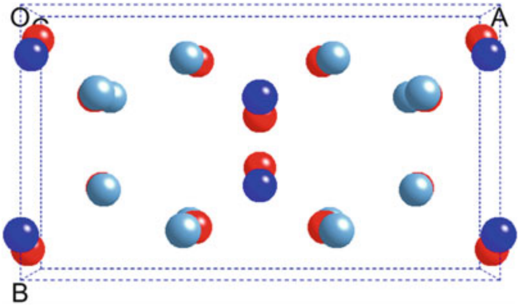

Fig. 12.9 Example of basic cell of MD for Li_2SiO_3 crystal. Supercell consists of 2 × 3 × 3 of primitive cells. *Colors* are the same as in Fig. 12.8

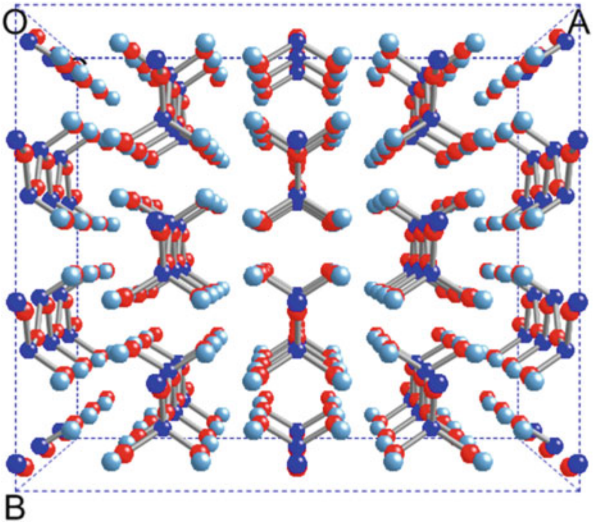

The required system size depends on the property to be examined and it should be judged by the purpose of the work. Especially, oscillation of the system is affected by the symmetry of environments as well as that of the inner structure of the crystal unit, and therefore caution is required in how to prepare the supercell.

12.4.3 Data Base for Crystal Structures

In the case of crystals, one can use the data from data bases such as

AMCSD (**A**merican **M**ineralogist **C**rystal **S**tructure **D**atabase) [11],

COD (**C**rystallography **O**pen **D**atabase) [12], **WWW**-MINCRYST (Crystallographic and Crystallochemical Database for Minerals and their Structural Analogous) [13]. Several data format (in xyz, cif and pdb) are used for initial configurations and changes of the format may be necessary to adjust the MD code.

Configurations in the basic cell of crystal structure can be prepared by using the information of the space group as already mentioned. It can be done by using software, such as, "CrystalMaker®" [14], which can create a supercell of $n_1 \times n_2 \times n_3$. Usually, it seems convenient to set the length of three axes to be comparable in 3D system as already mentioned; otherwise, different setting for calculations of cut off length, Coulombic force by directions will be required.

Some other cautions are required in the preparation of the super cell.

1. Number of repeating cell may affect the properties of the crystal especially the dynamics.
2. Some atoms may be automatically added at the edge of the crystal by a software. It is usually unnecessary, when one uses PBC. One needs to eliminate them.
3. Some crystals contain several sites for one atom, with occupation number being less than 1. This should be carefully treated when it is used for an initial configuration of MD.

12.4.4 Initial Configurations for Melts and Glasses

For melts and glasses, it can be started from the crystals or random configurations equilibrated at high temperatures. One may need to check if the final configurations after equilibration are affected by the initial configuration or not, especially when using crystal structures. For example, in the case of silica, it is known that the long range network structure remains for a long time in the structures. This trend is more remarkable in the strong system than in fragile systems [15]. Of course, several kinds of molecular structure editors can be used for preparing and/or modifying structures.

The system in the glassy state is obtained by cooling or by compressing the melt.

Some details of the glassy state depend on the cooling schedule. Example of a configuration of lithium silicate glass (after equilibration) is found in the ESM, and such a structure can be used for the initial structures of other melts.

Required system size depends on the properties and status of the system considerably (see Sect. 8.5.1 for more details). Generally, in the melt and glass, the structure has shorter length scale than the crystal. Therefore in the former with periodic boundary condition, relatively smaller system can be used, as long as the effect of ghost particle (image of the particle in the basic cell) in the surrounding cells of MD simulations is negligibly small.

In the lithium silicate glass, if one fixed the particle within a wall (for one of the 6 faces) of the basic cell, it affects mobility of other particles. The length scale thus determined was about ~8 Å at around 700 K for lithium metasilicate and the system size of $L \sim 17$ Å (longer than twice the length scale) for 432 particles seems to be the minimum size for examining of structure and dynamics of the present system in the liquid and glassy states. The larger size is required for stronger (rich in network formers) systems even for the liquid and glass [16], and it also means necessity of longer equilibration time of the system. Of course, practical system size depends on the available resources for calculations and "real" times necessary to do simulations.

For the initial configuration of melts or glasses, random configurations at high temperature (for example, ~3000 K in silicate) are used frequently.

If one start from the random configurations, it may be better to remove or change the position of particles being too close to other particles in the beginning of runs. The problem depends on the characteristics of potential parameters used. In the beginning of equilibration of the system, several pre-relaxation methods, which may be included in the software, can be used. Smaller time steps or modification of mass will be helpful to suppress unstable motion in the beginning.

MD programs may have examples of initial configurations, tutorials and exercises, which are useful to begin simulations with/without some modifications, although check of the quality of parameters or methods used is the responsibility of the user.

12.5 Output of the MD Programs

Most fundamental output of MD is time series of particle positions, that is, trajectories. From these values, many secondary outputs can be drawn. Further analyses by the user also can be done. In typical output files, fundamental information such as temperature, energies, pressure, pair correlation functions are included and they will be useful for checking the setting and/or for further treatment.

12.6 Software for MD Simulations

Many kinds of MD programs have been developed including commercial ones and researchers can choose the ones suitable for their own purpose. It also depends on the available potential parameters, the functional forms and the ensembles to be used.

Some of them, which can be used for the study of ionics, are introduced here, although for details the user should consult the developer.

Amber [17] is a collective name of program. It is designed for the biomaterials but can be used for the ionic materials such as ionic liquids. Several force fields such as, general amber force field [18] can be used for the simulation of ionic liquid. Of course, other potential parameters tuned for individual systems are also useful. The "sander" code was for the classical molecular dynamics for **CPU**, while "pmemd" code was for **GPU** and is included in the version 11. After the Amber 12, "sander" has been added to the "pmemd" coding for both **CPU** and **GPU**. Official support for the Intel Xeon Phi architecture also started in Amber 14.

DL_POLY is a general purpose serial and parallel molecular dynamics simulation package (DL_POLY_4.08 is the latest version (March 2016)) [19, 20], which can be used for ionic systems and several exercises and demonstrations for them can be found.

The Car-Parrinello Molecular Dynamics (CPMD) [21] is a code designed for the ab initio MD simulations, where the parallelized plane wave/pseudopotential implementation of Density Functional Theory is used.

Large-scale Atomic/Molecular Massively Parallel Simulator, LAMMPS [22] is a molecular dynamics package and $\text{LAMMPS}_{\text{CUDA}}$ is a molecular dynamics package, which can use **GPU** and have been applied for ionically conducting glasses [23].

The OCTA [24] [**OCTA** is Greek “8”, which is a 90° rotation of the mathematical symbol of infinity.] is flexible and expandable programs for meso-scale simulation and it seems to be suitable for the multiscale simulations of polymer etc.

MODYLAS [25] is a general-purpose, molecular dynamics simulation program suited for the simulation of very large physical, chemical, and biological systems. In the program, the Coulombic term can be calculated by the multipole method.

Many of MD programs have been coded by Fortran (The name “Fortran” tends to be used for after Fortran 90, although “FORTRAN” had been used before.) and/or C (C++). Therefore, some knowledge of them may be required. Traditionally, the former has been used for long time because of suitableness of numerical processing and there are many cumulative programs related to it. Its method for memory allocation has said to have merits for parallel computation. Some comparison of Fortran and C has been done by several authors. For example, see Ref. [26].

12.7 Software for Visualization

Nowadays, there are many software including commercially available ones and free ones for visualization of structures obtained by MD. One can select the suitable software for any particular purpose. Some of them are introduced here.

Some tools can treat the output of MD codes, directly. For example, the program VESTA [2] can be used for the visualization of many kinds of files including CONFIG file used in DL_POLY code.

VMD (**V**isual **M**olecular **D**ynamics) [27] can be used for visualization of instantaneous structures as well as making movies (for example, using HISTORY file obtained by DL_POLY and/or other trajectory files).

References

1. http://www.wolfram.com/index.php. Accessed 12 Aug 2016
2. K. Momma, F. Izumi, J. Appl. Crystallogr. **44**, 1272 (2011). http://jp-minerals.org/vesta/en/. The address was confirmed to be valid on Oct. 2015
3. C. Brooks, *Introductory Econometrics for Finance*, 2nd edn. (Cambridge University Press, 2008)
4. http://www.wolfram.com/cdf-player/. Accessed 12 Aug 2016
5. http://www.adobe.com/software/flash/about/. Accessed 12 Aug 2016
6. "International Tables for Crystallography" volume A. WEB version is available at http://it.iucr.org/. Accessed 12 Aug 2016
7. http://www.adobe.com/software/flash/about/. The address was confirmed to be valid on 12th Aug. 2016
8. V.H. Seemann, Acta Cryst. **9**, 251 (1956)
9. "International Tables for Crystallography" volume A. WEB version is available at http://it.iucr.org/. The address was confirmed to be valid on 12th Aug. 2016
10. http://www.cryst.ehu.es/cgi-bin/cryst/programs/nph-getgen?list=new&what=gen&gnum=36. In this address, the number 36 means $C_{mc}2_1$. Please put the number of the space group in that page (These URLs are conformed to be valid on 26th Dec. 2014.)
11. http://rruff.geo.arizona.edu/AMS/amcsd.php. The address was confirmed to be valid on 19th Feb. 2016
12. http://www.crystallography.net/. The address was confirmed to be valid on 19th Feb. 2016
13. http://database.iem.ac.ru/mincryst/index.php. The address was confirmed to be valid on 19th Feb. 2016
14. http://www.hulinks.co.jp/software/c-maker/. The address was confirmed to be valid on 19th Feb. 2016. After the version 9.2.2, CrystalMaker® can treat STL files, which are supported by many 3D printers
15. J. Horbach, W. Kob, K. Binder, C.A. Angell, Phys. Rev. E **54**, R5897 (1996)
16. J. Habasaki, K.L. Ngai, Y. Hiwatari, J. Chem. Phys. **121**, 925 (2004)
17. http://ambermd.org/. The address was confirmed to be valid on 26th Apr. 2016. The latest version is Amber 14. Amber 14 was developed by D.A. Case, V. Babin, J.T. Berryman, R.M. Betz, Q. Cai, D.S. Cerutti, T.E. Cheatham, III, T.A. Darden, R.E. Duke, H. Gohlke, A.W. Goetz, S. Gusarov, N. Homeyer, P. Janowski, J. Kaus, I. Kolossváry, A. Kovalenko, T.S. Lee, S. LeGrand, T. Luchko, R. Luo, B. Madej, K.M. Merz, F. Paesani, D.R. Roe, A. Roitberg, C. Sagui, R. Salomon-Ferrer, G. Seabra, C.L. Simmerling, W. Smith, J. Swails, R.C. Walker, J. Wang, R.M. Wolf, X. Wu and P.A. Kollman (2014), University of California, San Francisco
18. J. Wang, R.M. Wolf, J.W. Caldwell, P.A. Kallamn, D.A. Case, J. Comput. Chem. **25**, 1157 (2004)
19. I. Todorov, W. Smith, Phil. Trans. R. Soc. Lond. A **362**, 1835 (2004)
20. I. Todorov, W. Smith, Phil. Trans. R. Soc. Lond. A **2**, 161 (2004)
21. CPMD is available at http://www.cpmd.org/. The address was confirmed to be valid in Oct. 2015
22. S. Plimpton, J. Comp. Phys. **117**, 1 (1995). See http://lammps.sandia.gov/, the address was confirmed to be valid in Oct. 2015
23. Thesis of Doctor Courses, C. R. Trott, Technische Universität Ilmenau. GPU code of MD using C was introduced there.
24. http://octa.jp/OCTA/whatsOCTA.html. The address was confirmed to be valid on 19th Feb. 2016
25. http://www.modylas.org/. The address was confirmed to be valid on 19th Feb. 2016
26. http://www.ibiblio.org/pub/languages/fortran/ch1-2.html. The address was confirmed to be valid on 19th Feb. 2016
27. http://www.ks.uiuc.edu/Research/vmd/. The address was confirmed to be valid on 19th Feb. 2016

Chapter 13
Some Applications and Further Problems

13.1 Fabrication of Porous Structures in Molecular Dynamics Simulations: For Design and Examination of Solid State Batteries

The importance of porous materials in applications to batteries has attracted the attention of researchers in many fields. Many materials having not only microscopic and mesoscopic pores but also macroscopic pores are the subjects of studies by researches. They are beneficial to use in electric devices as electrode, insulator, and other components. Especially for the use as electrode or electrolyte, porous materials are expected to increase the reaction rate, because of the large surface areas. The subject is closely related to the nanoionics discussed in Chap. 6. In this section, application of molecular dynamics (MD) simulations to such fields is described.

Recently, all solid-state lithium batteries using porous materials are proposed by Kanamura et al. [1–3]. Almost ordered porous $Li_{0.35}La_{0.55}TiO_3$, which shows the electric conductivity larger than 10^{-4} S cm^{-1}, was prepared in their work. It acts as the electrolyte of the solid state battery with inclusion of $LiCoO_2$ (or $LiMn_2O_4$) as a cathode material, and $Li_4Ti_5O_{12}$ as an anode material.

Experimentally, porous silica can be prepared by sol–gel methods or by chemical vapor deposition (CVD) methods, where some templates for pores can be used, although the fabrication of suitable porous materials for practical use is not necessarily an easy task. Under this circumstance, modeling of porous structures and their composites by MD simulations should be beneficial for understanding the details of the structures including shapes, types (open/closed pores, or channels), size and its distribution, and details of dynamics, as well as for the design of new composites.

Furthermore, porous materials are expected to be useful for storage and transportation of gaseous substances [4] and also for drug delivery [5, 6]. Therefore, the MD methods will be relevant for these related fields.

J. Habasaki et al., *Dynamics of Glassy, Crystalline and Liquid Ionic Conductors*,
Topics in Applied Physics 132, DOI 10.1007/978-3-319-42391-3_13

In the following subsection, modeling of porous silica by MD simulation will be introduced, although the methods used are not limited to silica. Obtained porous structures by these methods can be used as templates for modeling of other porous systems. Quasi-equilibrated structures thus prepared by the large scale molecular dynamics can be used as the initial structures for ab initio calculations of electronic states if necessary.

13.1.1 Modeling of Porous Silica in MD

So far, several methods to prepare computational models of porous silica have been proposed. Kieffer and Angell [7] prepared a porous model by the expansion of a dense silica system. The method is later refined by Nakano et al. [8] and Beckers and De Leeuw [9] have prepared a nano-porous silica model using the charge scaling procedure. Aggregation of silicic acid in water is studied by Bhattacharya and Kieffer using a reaction force field [10]. Rimsza and Du [11] have compared two protocols (by expansion and charge scaling) in modeling of porous systems and found several differences in the structures and/or mechanical properties.

In Fig. 13.1, another protocol by Habasaki and Ishikawa for preparing the porous system based on the spontaneous formation of gel from silica nanocolloids [12] is shown schematically. Using the TTAM model of silica, which allows the reorganization of Si–O bonds, several aqueous systems with different NaCl concentrations were examined. As reported in Ref. [12] in details, infinitive three

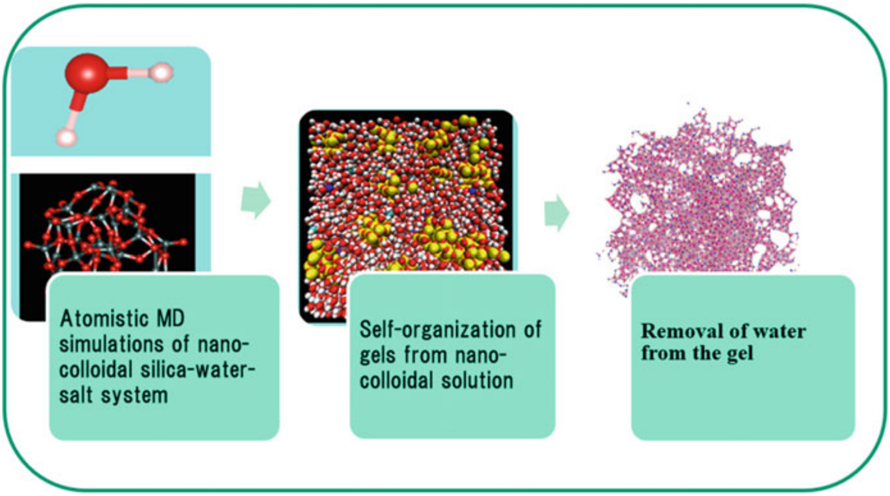

Fig. 13.1 A new protocol to prepare a porous model (before annealing) in MD simulations. Spontaneous formation of infinitive network of silica including open pores filled with water was observed and this structure was regarded as gel

dimensional network (with a periodic boundary) of the silica part was formed in MD at a certain composition and it includes open pores filled with water. This structure with immobile water (and salt) was regarded as a gel. It is worthwhile to note that the structure of the-pore part can be obtained at the same time, because it corresponds to the water part in gels (before further annealing of the system). Therefore it is easy to visualize the structure of the silica part having open pores and channels as shown in the right panel of Fig. 13.1. Further details of the porous structures thus obtained will be reported elsewhere in the near future.

The porous structure obtained by this protocol is not necessarily the same as the ones prepared by other protocols and comparison of them are in progress. Further studies for effects of surface modifications, details of morphology, mechanical properties, and etc. are waiting for researchers to explore.

In order to represent the different length scale regions in gels and related aggregates, the use of a MD basic cell as large as possible is preferred even to examine the pores of nano-scales. Around the gelation composition, the dynamics of the components including water becomes slower. Therefore, long time of calculation is required to make possible quasi-equilibration of the system with slow dynamics. Since dynamics of the water confined in pores are different from the pure water [12, 13] (see also arguments in Sect. 10.7 for systems with particles blocked or confined by walls), the change of mobility of solvent is non-negligible in the formation of gels.

13.1.2 MD Simulations of Porous Lithium Disilicate

The ionic motion in the porous structure is known to be accelerated and its mechanism is a topic of discussion. Some examples of porous materials intended to increase the conductivity have already been introduced in Chap. 6. Some other examples are shown here. When the AgI and AgBr are mixed with Al nano particles or mesoporous alumina, large increase of ionic conductivity was observed [14]. It is interesting to note that our MD simulations predict considerable increase of mobility of Li ions in porous lithium disilicate as well [15]. In this case, the porous structure was prepared by scaling the volume [7, 8] at 600 K and the resultant density is 0.74 times of original (glassy lithium disilicate before expansion) system. In the left column of Fig. 13.2, example of trajectories of ions and atoms in porous lithium disilicate obtained by MD simulations is shown. The last position of these atoms and ions are shown in the figure on the right column. Quite a heterogeneous character of the motions of ions is observed. Diffusion coefficient of Li ions is found to be one order of magnitude higher than the original system, and the motion of network is also found to be affected by the expansion. As found in the trajectories, the mobile region is not necessarily along the boundary of the pore. Further examination of dynamics including the motion of network part is in progress to understand the mechanism of the acceleration.

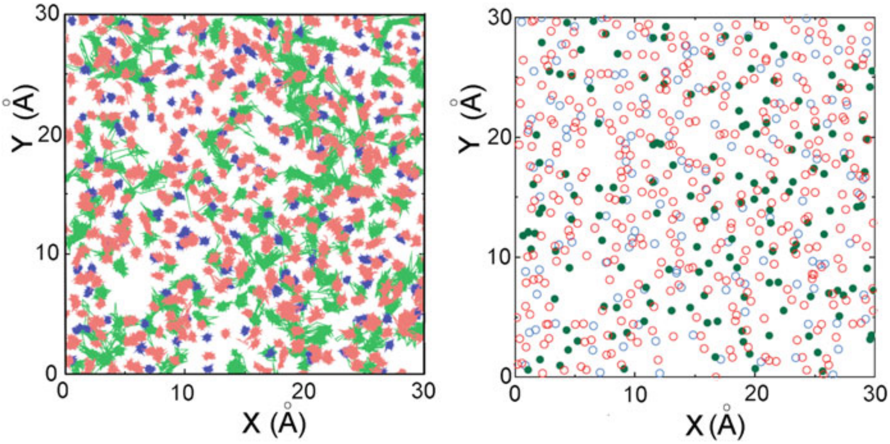

Fig. 13.2 Accelerated dynamics in porous lithium disilicate at 600 K. *Left panel*: Trajectories during 400 ps for the slice of the MD cell (width is chosen to be 10 Å) *Red*: O atoms, *Blue*: Si atoms and *Green*: Li ions. *Right panel*: The last position of ions and atoms in these trajectories. *Red circles*: O atoms, *Blue circles*: Si atoms, *Green filled circles*: Li ions. In this case, density of the system is 0.74 times of the original system and diffusion coefficient of Li ions is one order higher than the original system

In References [1] and [2], opal (fcc) like porous structures are used for the solid state battery. The role of ordering (or disordering) and dimensionality of the structure in the porous materials, especially in electrochemical devices, are also interesting problems to examine.

13.2 Application of Thermodynamic Scaling to the Material Design

From the generality of dynamics as suggested by the Coupling Model (CM) [16] as well as the explanations given in Chaps. 7 and 11 on ionic liquids, one can expect the thermodynamic TV^{γ} scaling of conductivity relaxation time and transport coefficients will hold in general. Actually, the CM gave in Ref. [16] that the TV^{γ} scaling of the structural α-relaxation and transport coefficients stems from the primitive relaxation of the CM or the associated Johari-Goldstein (JG) β-relaxation. More details are given in a Chap. 7 on pressure dependence of ionic liquids and glass-formers. Ribeiro et al. [17] showed by MD simulations in CKN that diffusivity, viscosity and the structural relaxation time τ_{α} obey TV^{γ} scaling with a common value of $\gamma = 1.8$. Therefore, once a master curve for one of the dynamical variable such as the diffusivity is obtained as a function of a known physical quantity (temperature and volume or density), it can be used to predict the behavior of the system under different conditions, and it is also expected that the scaling holds for other physical quantities than diffusivity.

Therefore the thermo-dynamical scaling will provide a general and promising method to design materials having desired properties. This is especially useful for the ionic liquid, which has many possible combinations of cations and anions. For example, López et al. [18] have pointed out that the values of the scaling exponent for the ionic liquids containing the $[BF_4]^-$ anion is lower than those for the ILs with the $[PF_6]^-$ anion. They also pointed out that increasing the length of the side alkyl chain of the cations leads to a decrease in the scaling exponent for both imidazolium and ammonium ILs. This trend is comparable to that of the scaling exponent in alkanes examined by Pensado et al. [19]. The value $\gamma = 13$ for hexane decreases with chain length to $\gamma = 6.3$ in octadecane. Thus the guideline for the selection of material designed for application with certain purpose is simplified by using the γ value.

Scaling based on the potential of mean force discussed in Sect. 11.10 means the coarse-grained model using the effective potential functions also work well in the ionic liquids as well as other glass forming liquids. Therefore, naturally it can be connected to the theories related to the coarse-graining [20] and entropy scaling [21].

13.3 Applicability of Effective Potential Parameters for Coarse-Grained Dynamics

For the study of systems with complex structure such as ionic liquids, coarse-graining description of the system is useful. Several attempts to replace a long range electrostatic potential energy by the short range effective potential have been reported. Izvekov et al. [20] have obtained a soft-sphere type potential by the force matching methods for water and NaCl, where interaction potential are determined on an atomic level. Thus the long range Coulombic potential is replaced by the effective soft-type potential. This success seems to be related to the generality of the thermodynamic scaling. Thus coarse grained potential can be obtained from the scaling properties and/or from the pair correlation function both by experiment and simulations in principle. When it is used for modeling of multi-scale systems, different levels of systems can be connected without changing the dynamic properties, if the coupling among systems at different levels is correctly taken into account.

Recently, Shell [22] suggests that the potential energy landscapes of arbitrary fluids can be mapped onto effective soft-sphere landscapes in a systematic way using a recently introduced coarse graining formalism based upon the relative entropy [23–25]. This approach can also be considered to be related to the thermodynamic scaling.

13.4 Application of the Mixed Alkali Effect

The mixed alkali effect (MAE) is exploited for various purposes and applications in industry and society [26]. Therefore, a fundamental understanding the mechanism of the mixed alkali effect is useful for the design and control the transport properties and/or dielectric and thermodynamic properties. Furthermore, the low diffusivity in the mixed alkali glass is useful to increase the strength of the glass. The knowledge obtained from the MD simulation works has been used to obtain the materials with the desired level of conductivity.

13.4.1 Low Dielectric Loss Glasses

Materials with low dielectric loss are useful as components in electric devices such as mobile phones. Low dielectric loss in materials can be obtained effectively in glasses with low content of alkali ion [26]. For the same concentration of the ions, mixed alkali glasses can be used, although the MAE at high frequencies is weaker than that in the low frequency region.

13.4.2 Modification of Surface by Ion Exchange Process

Surface of the glass can be modified by ion exchange process when it is immersed in a molten salt bath. This technique is convenient to change the strength or optical properties of glasses [26]. How are the properties of the mixed alkali glass in the surface different from that of the bulk mixed alkali system? Interestingly, it is known that the conductivity of both are comparable [27]. After a certain immersion time, the gradient glass behaves as if it were a composite of stacked layers of mixed alkali glass with a varying ratio of the two alkali ions [28]. Ion exchange can occurs even at temperature below the glass transition temperature T_g because of the high mobility of the alkali ions by decoupling from the structural relaxation. This may suggest that the details of the long ranged structure of ion channel are not necessarily important for the controlling diffusivity or conductivity, although the percolation of it is a precondition of this statement.

Empirically, after the exchange process of alkali metal ions in the glass, the mutual diffusion coefficient, $\overline{D}$, is given by [29]

$$\overline{D} = D_1 D_2/(x_1 D_1 + x_2 D_2), \tag{13.1}$$

where D_1 and D_2 are the diffusion coefficients of species 1 and 2, while x_1 and x_2 mean their fractions, respectively.

13.4.3 *Toward the Design of the Materials with High Conductivity*

Both theory and MD simulations have the power of predictability, and it can be used profitably in some applications. For designing the material of high conductivity, knowledge of the mechanism of diffusion or conduction of the ionic system is of course fundamental and seems to be already used for design. Importance of the dimensionality of paths of ion migration seems to be well recognized nowadays. Percolation of ionic channels is a necessary condition for the high conductivity materials. It has been already shown that the related volume of the partial structures governs the transport coefficients as expected from the TV^{γ} scaling. Some further hints to design the materials with high conductivity is presented next in this section.

At first we pointed out that the short time activation energy of ionic motion for jump motion is different from the observed activation energy in the diffusive regions because the cooperative nature of jumps are important determining factor for the d.c. conductivity.

1. Effective transport is caused by the cooperative jumps with strong forward correlations. Therefore effectiveness of cooperative jumps should be taken into account (Sects. 4.4 and 9.7). For the effective transport of ions, controlling the dimensionality of paths as well as the optimal concentration of vacancies enabling the cooperative jumps are useful.

In single alkali oxide system, the mobility of the smaller cation is not necessarily larger. For the glass and melt of this system, Habasaki and coworkers predicted [30, 31] larger diffusivity of potassium ions than the lithium ions in the alkali metasilicate. This trend is confirmed by the experiment for the disilicate composition at 1000 K [32, 33] including the reproducibility of the mixed alkali effect.

2. Although the mixed alkali effect (MAE) discussed in Chap. 10 is concerned with non-linear decrease of the dynamics, one can find from research some other controlling factors of the ion dynamics. For example, the importance of the dimensionality of the paths and walks was clarified. It is consistent with the fact that the interception of the ion jump paths is enhanced by the large difference of the ion sizes of the two species. The analysis of paths and walks enable us to characterize the details of the transport properties.
3. The power law increases of the diffusion coefficient on the composition of alkali metal ions are found in MD simulations in single alkali silicate glasses and this result is consistent to the experimental observation (see Sect. 9.9).
4. It is also interesting to consider the role of mobility of the network in the design. In silicate and related materials, ions in the glassy state still have mobility in spite of the slowing down of the dynamics of the framework structures. When we consider the system with networks, based on the conservation of the momentum of the system, it is clear that a flexible part such as rotational motions of O around Si atoms, which can move in the opposite direction of ions, is desirable.

We also pointed out the importance of the structure of the cages in determining the mobility of ions.

5. From the arguments of gradual topological changes found in the ionic liquids and related argument for the silicate glasses (see Sect. 11.11), one can understand why the ions in a cage still can have mobility in the glass.
6. From the experiments performed on nano particles and porous structures, we learn that there are many possibilities in the preparations of new materials and composites. From our MD simulations of porous lithium disilicate systems, we predict that the ionic motion of Li ions is also accelerated in the porous structures [15] and the simulations will enable us to examine details of the ion dynamics.
7. In the ionically conducting glasses, ionic motion tends to be enhanced when the two kinds of network former is mixed. The "Mixed former effect" [34–36] is another example of cooperative motions of ions and matrix atoms. It is possible to examine how trajectories of ions change with structure by MD simulations of different mixed network formers.
8. As shown in the comparison of glass and crystal of $Li_2Si_2O_5$ with the same composition, we reproduced the large enhancement of mobility of lithium ions in the former (see Sect. 9.10). Roles of disorder and defects played in the ionic glass is made clear by the comparison.
9. MD simulations are useful for design as well as screening of the materials that can operate under special conditions including the extreme ones, while these tasks cannot be performed by experiments. Systematic changes of the system by varying the ionic size, mass, and compositions can be easily carried out in MD simulations, and hence the importance of simulations in the design of materials will increase in the future.

Of course, the considerations of ionic diffusivity and conductivity given in the above conditions are modified by other factors such as electromotive force of ions, densities, availability of ions, durability, safety and cost in practical use.

A multicomponent analysis including all factors will be useful in optimizing the performance of the material.

13.5 Relation with the Glass Transition Problems

In Chap. 7 and Sect. 11.11.10, we have shown TV^{γ}-scaling is applicable to conductivity relaxation of ionic liquids. From this fact and since TV^{γ}-scaling is known to apply to structural relaxation of glass-forming liquids, we have inferred that the physics governing ion dynamics in ionic conductors are similar to glass transition. Furthermore, in Sect. 11.11, we have argued for the changes in the topological characteristics of the system. Because the structure and its fluctuation via the coordination polyhedra correlate well with the dynamics of the caged ion, these characteristics of ion dynamics can explain the slowing down of the structural relaxation in the glass transition problem reasonably. This explanation shares a view with the constraint theory related to the rigidity percolation, but it is not necessarily the same as other conventional theories or models of glass transition.

Several distinct time regions in the mean square displacement as well as dynamic heterogeneity discussed in the present book on ionics are commonly observed in glass-forming materials. Therefore, theories or models of glass transition may share common grounds with ionics in the basic physics. Some additional important issues to consider in the glass transition problem are pointed out here based on the results obtained in ionic systems.

13.5.1 What Is a Cause of the Rapid Slowing Down of Dynamics Near T_g?

Many theories of the glass transition put emphasis on the super-Arrhenius or the Vogel-Fulcher-Tammann-Hess (VFTH) temperature dependence of the structural relaxation time and viscosity, prompting some researchers to assume a divergence of the length and time scales at the glass transition temperature (or a characteristic temperature before it). However, as shown in Sects. 11.4 and 11.11.8, the VFTH behavior of the transport properties found in the Arrhenius plot of the diffusion coefficient can be also represented by two regions of the dynamics separated by T_B with different temperature dependences. This result suggests that the cause of the slope change at T_B is relevant to understand the rapid slowing down of the dynamics on decreasing temperature to approach T_g. Actually, below T_B, long ranged motion by cooperative jumps are found to be suppressed. This feature is quite general because similar slope change is found even for the master curve of the TV^{γ} scaling of the dynamics in different kinds of materials and therefore not limited to ionics. When the smaller negative slope is found above T_{B}, it is combined with the larger negative slope below it, and it enhances the fragile behavior. In other words, acceleration of the dynamics compared with the Arrhenius behavior at high temperature region resulted in the rapid slowing down near Tg. Therefore change in the dynamics at T_B is a problem to be explained together with the rapid increase of viscosity and the possibility of existence of divergent dynamic length scales near T_g.

13.5.2 Is the Slowing Down of Dynamics Comes Without Any Change in the Structure?

Glass transition is often assumed to occur without a structural change. Of course, due to the limitation of the observation time, "computational" glass transition might be observed especially in MD, where the diffusive regime is not attained within the observation time. However, the existence of this limitation of time scale observation does not exclude the existence of structural changes at T_g.

As shown in Sect. 11.11, several structural changes have been found for the ionic liquid, EMIM-NO_3, by MD. That is, a gradual change of structures concerned with the rigidity percolation formed by fictive bonds (contact ion pairs) was found. Namely, geometrical degree of freedoms for the coordination polyhedra and number of fictive bonds changes in the regions separated by characteristic temperatures, T_B and T_g. The change in the coordination polyhedra is not well known experimentally for glass forming materials, however, corresponding changes in the system volumes [37–39] and changes in the peak height in $g(r)$ or the related $S(q)$ [40–43], which corresponds to the changes in the coordination can be detectable in experiments as well as in MD. In a model system such as soft-core and LJ systems, changes in the $g(r)$ such as splitting of the second peak in the glass is well known among researchers [44]. The splitting means the dynamical changes among several structures are suppressed and particle tends to be trapped in the potential well [40, 42, 43]. Therefore, such structural changes are naturally accompanied with the dynamic slowing down.

With decreasing temperature and/or increasing pressure of the system, delocalized motion changes to well defined jumps among cages, and then trapping within cages. These structural changes in the topological structure of coordination polyhedra are related to the change in dynamics with temperature and/or pressure. Importance of topological modeling has been pointed out in several approaches. For example, as a generalization of Thorpe [45–48] and Phillips [49, 50], Gupta and Mauro [51] have argued for the composition dependence of the glass transition temperature and fragility in Ge_xSe_{1-x} using the concept of topological constraints. Moreover, many properties of glasses such as thermodynamics, mechanical properties and rheological properties are well represented by the constraint theory [52].

13.5.3 How Structural (Topological) Changes Are Related to the Dynamics?

Using the concept of coordination polyhedra and its fluctuation, the relation between the caged ion dynamics and their structures are clarified for EMIM-NO_3 in Sect. 11.11. If one's standpoint or emphasis is on the dynamics only, it seems to be difficult to explain why the caged ion dynamics by jump motions remains at lower temperature than T_B. Is the existence of the thermal fluctuation enough to explain the temperature dependence of it?

13.5.4 *Is the Structure and Dynamics of the Glass Random or Fractal?*

As discussed in Sects. 9.3, 11.6, 11.7, structure and dynamics of supercooled liquids and glasses are multifractal rather than random. This feature is concerned with the mixing of different units or length scales. Mixing of the dynamic heterogeneity naturally explained the existence of different dynamical regions as shown by the slope changes in diffusivity at the same time. Structural change from liquids to glasses can occur while keeping multifractal nature of the structure. If one assumes the structure of the glass is just random, it is difficult to understand how the random structure can change.

13.5.5 *How Can We Detect Non-Equilibrated Relaxation Before the Glass Transition?*

In MD, if one used NVE condition (here we distinguished the NVE ensemble and NVE condition, because the latter does not necessarily means the NVE ensemble in a non-equilibrated process), gradual increase of the temperature during the run is observed if the system is in non-equilibrium (see Sects. 8.2.2.1 and 8.5.3). This also means the gradual structural changes with decreasing potential energies. Related changes are also observed in the dynamics. It is also accompanied with gradual slowing down of the dynamics with elapse of time. These changes might be overlooked when temperature control is always applied. For examining related changes, careful treatment of cooling schedule is required.

References

1. K. Kanamura, N. Akutagawa, K. Dokko, J. Power Sources **146**, 86 (2005)
2. M. Hara, H. Nakano, K. Dokko, S. Okuda, A. Kaeriyama, K. Kanamura, J. Power Sources **189**, 485 (2009)
3. K. Dokko, N. Akutagawa, Y. Isshiki, K. Hoshina, K. Kanamura, Solid State Ion. **176**, 2345 (2005)
4. R. Morris, Angew. Chem. Int. Ed. **47**, 4966 (2008)
5. S. Wang, Micropor. Mesopor. Mater. **117**, 1 (2009)
6. M. Vallet-Regí, ISRN Mater. Sci. (2012), Article ID 608548
7. J. Kieffer, C.A. Angell, J. Non Cryst. Solids **106**, 336 (1988)
8. A. Nakano, L. Bi, R.K. Kalia, P. Vashishta, Phys. Rev. B **94**, 4991 (1994)
9. J.V.L. Beckers, S.W. De Leeuw, J. Non Cryst. Solids **261**, 87 (2000)
10. S. Bhattacharya, J. Kieffer, J. Phys. Chem. C **112**, 1764 (2008)
11. J.M. Rimsza, J. Du, J. Am. Ceram. Soc. **97**, 772 (2014)
12. J. Habasaki, M. Ishikawa, Phys. Chem. Chem. Phys. **16**, 24000 (2014)
13. P. Scheidler, W. Kob, K. Binder, Europhys. Lett. **52**(3), 277 (2000)

14. H. Yamada, A.J. Bhattacharyya, J. Maier, Adv. Funct. Mater. **16**, 525 (2006)
15. J. Habasaki, to be published
16. K.L. Ngai, J. Habasaki, D. Prevosto, S. Capaccioli, M. Paluch, J. Chem. Phys. **137**, 034511 (2012)
17. M.C.C. Ribeiro, T. Scopigno, G. Ruocco, J. Chem. Phys. **135**, 164510 (2011)
18. E.R. López, A.S. Pensado, M.J.P. Comuñas, A.A.H. Pádua, J. Fernández, K.R. Harris, J. Chem. Phys. **134**, 144507 (2011)
19. A.S. Pensado, A.A.H. Pádua, M.J.P. Comuñas, J. Fernández, J. Phys. Chem. B **112**, 5563 (2008)
20. S. Izvekov, J.M.J. Swanson, G.A. Voth, Phys. Chem. B **112**, 4711 (2008)
21. G.X. Li, C.S. Liu, Z.G. Zhu, J. Non Cryst. Solids **1–11**, 946 (2005)
22. M.S. Shell, J. Chem. Phys. **137**, 084503 (2012)
23. M.S. Shell, J. Chem. Phys. **129**, 144108 (2008)
24. A. Chaimovich, M.S. Shell, Phys. Rev. E **81**, 060104 (2010)
25. A. Chaimovich, M.S. Shell, J. Chem. Phys. **134**, 094112 (2011)
26. D.E. Day, J. Non Cryst. Solids **21**, 343 (1976)
27. G.H. Frischat, in *Proceedings of the 10th Glass Congress*, Versailles, France, Sect. Ai., vol. 1, p. 37 (1971)
28. A.K. Varshneya, J. Non Cryst. Solids **19**, 355 (1975)
29. G.H. Frischat, R. Kirchmeyer, J. Am. Ceram. Soc. **56**, 552 (1973)
30. J. Habasaki, I. Okada, Y. Hiwatari, J. Non Cryst. Solids **183**, 12 (1995)
31. J. Habasaki, Y. Hiwatari, I. Okada, Mater. Res. Soc. Sym. Proc. **455**, 91 (1997)
32. Landolt-Börnstein, *Diffusion in Semiconductors and Non-Metallic Solids*, vol. 33, subvolume B1 (Springer, Berlin, 1999)
33. D. Wolf, G. Münster, M. Kremer (eds.), *NIC Symposium 2004, Proceedings*, NIC Series, vol. 20 (John von Neumann Institute for Computing, Jülich, 2003), p. 215
34. M. Schuch, C.R. Müller, P. Maass, S.W. Martin, Phys. Rev. Lett. **102**, 145902 (2009)
35. H. Yamamoto, N. Machida, T. Shigematsu, Solid State Ion. **175**, 707 (2004)
36. M. Tatsumisago, N. Machida, T. Minami, J. Ceram. Soc. Jpn. **95**, 197 (1987)
37. N.C. Forero-Martinez, R. Cortes-Huerto, P. Ballone, J. Chem. Phys. **136**, 204510 (2012)
38. K.L. Ngai, L.-R. Bao, A.F. Yee, C.L. Soles, Phys. Rev. Lett. **87**, 215901 (2001)
39. G. Dlubek, Y. Yu, R. Krause-Rehberg, W. Beichel, S. Bulut, N. Pogodina, I. Krossing, C. Friedrich, J. Chem. Phys. **133**, 124502 (2010)
40. J. Habasaki, Mol. Phys. **70**, 513 (1990)
41. N.A. Mauro, M. Blodgett, M.L. Johnson, A.J. Vogt, K.F. Kelton, Nat. Commun. **5**, 5616 (2014)
42. J. Habasaki, I. Okada, Mol. Simul. **8**, 179 (1992)
43. J. Habasaki, K.L. Ngai, J. Chem. Phys. **142**, 164501 (2015)
44. Y. Hiwatari, H. Matsuda, T. Ogawa, N. Ogita, A. Ueda, Prog. Theor. Phys. **52**, 1105 (1974)
45. M.F. Thorpe, J. Non Cryst. Solids **57**, 355 (1983)
46. H. He, M.F. Thorpe, Phys. Rev. Lett. **54**, 2107 (1985)
47. Y. Cai, M.F. Thorpe, Phys. Rev. B **40**, 10535 (1989)
48. M.F. Thorpe, J. Non Cryst. Solids **182**, 135 (1995)
49. J.C. Phillips, J. Non Cryst. Solids **34**, 153 (1979)
50. J.C. Phillips, M.F. Thorpe, Solid State Commun. **53**, 699 (1985)
51. P.K. Gupta, J.C. Mauro, J. Chem. Phys. **130**, 094503 (2009)
52. J.C. Mauro, Am. Ceram. Soc. Bull. **90**(4), 31 (2011)

Afterword

We have presented a plethora of experimental data and simulations results on the dynamics of ions in various ionic conductors. The finding is the universal patterns followed by their properties, independent of the chemical composition and physical structure, liquid, glassy or crystalline. From our point of view, this is a remarkable phenomenon in condensed matter physics and materials science, and is worthwhile of recognition by the research communities from different disciplines. Surprisingly this recognition has not yet been given, possibly because of the broad spectrum of materials studied and the publications of results are scattered over various research journals with diverse emphases. Perhaps the main reason for the lack of recognition is the absence of any serious effort in the past of analyzing and comparing the properties of different ionic conductors to bring out the universality until now after this book has been written. Thus one purpose of writing this book is to make the research communities fully aware of the universal properties of ion dynamics.

Another possible reason why the universality has not been recognized in the past is the influence from theories and models proposed in the past to explain the ion dynamics. These theories did not cover all the properties collected in this book and naturally are not able to indicate universality we found. Examples including those theories based on distribution of ion jump relaxation rates or random energy barriers will not either expect or be able to address the universal properties. Also, in the current literature, there is the fixation on the frequency dependence of the conductivity as the major property to be explained, as well as the unjustified claim of a.c. conductivity of different ionic conductors can be scaled to a master curve. These works unfortunately have diverted attention of the research community from the universality of many more important properties of ionic conductors in the past 2 decades.

The universal ion dynamics must originate from some fundamental feature common to all ionic conductors considered in this book. A common feature is that most of the conductors have high density of ions, and ion-ion interactions are naturally one of the determining factors on the ion dynamics. This factor is clear to anyone familiar with molecular dynamics simulations as presented in several

J. Habasaki et al., *Dynamics of Glassy, Crystalline and Liquid Ionic Conductors*,
Topics in Applied Physics 132, DOI 10.1007/978-3-319-42391-3

chapters of this book. The very first step in carrying out the simulation is to determine the potential function, which necessarily has the ion-ion interactions term in it. From this step it is clear that the ion dynamics and the ion conductivity relaxation and diffusion problem is a many-body problem of irreversible process in statistical mechanics. Of course the many-body relaxation problem common to all ionic conductors is just a hint to the occurrence of universal properties. There is no assurance that this is true until the many-body relaxation problem has been solved to show the universal properties. Unfortunately, many-body relaxation and diffusion is an unsolved problem in statistical mechanics and condensed matter physics as far as we know. The well-known Brownian diffusion is a one-body diffusion problem and it was solved in 1905 by Einstein. Astonishingly, 110 years have gone by but a complete solution of the many-body relaxation and diffusion problem is still nonexistent. The only feeble substitute at the present time is the Coupling Model. Although far from a full solution of the problem, based on classical chaos originating from ion-ion interactions and other terms in the potential function, the Coupling Model has proven that it can generate and explain the observed universal properties of ion dynamics, as well as the dynamics of glass-forming systems. It may be used as a stepping stone for others to solve the problem completely.

We have written the chapters with the intention of meeting the diverse backgrounds of the potential readers of the book. Chapter 2 is devoted to describe some commonly known theoretical models for ion diffusion. It presents the basics of linear response theory, and introduces the Debye model and other phenomenological descriptions of relaxation phenomena. These descriptions are typical not only for dielectric relaxation originating from bound charges in some systems, but also for conductivity relaxation in materials with mobile ions. A detailed discussion is provided of the use of conductivity formalism and of electric modulus formalism, the connection to linear response theory, and the application for the analysis of the electrical response of ionic conductors. Chapter 3 presents the basics of Impedance Spectroscopy (IS) and Nuclear Magnetic Resonance (NMR) techniques and their applications in experimental study of ion dynamics in ionic conductors. Special emphasis is given to IS due to its extremely wide spectral range that spans from frequencies of just a few nHz ($\tau \sim 1$ year) to above 1 THz ($\tau \sim 10^{-1}$ ps). Besides the description of the experimental techniques, we have tried to provide the reader with some useful hints for extracting information of ion dynamics from the experiments. Chapters 4 and 5 contain a multitude of experimental data, obtained by IS and NMR, showing the relevant properties of ionic conductivity relaxation and ion diffusion. The universal patterns in the dynamics of ionic conductors emerge from the collection of the data. The experimental data are discussed in terms of different proposed models for ion diffusion, and in particular the Coupling Model, which helps the reader to gain a global perspective of all the different experimental findings.

Chapter 6 deals with the emerging research field of nano-ionics and applications. Spectacular changes of ionic conductivity relaxation and diffusion were observed in experimental studies and by simulations. These changes are important concerns in the development of nano-ionics for applications, as well as critical in judging theories proposed for bulk ionic conductors. It is desirable for a theory to be able to predict the changes when dimension of the material is reduced to nano-meter dimension. Even better if the theory can predict quantitatively the changes from the known dynamics of the bulk. In this Chapter we show the Coupling Model has done just that, but not any other theory or model discussed in Chaps. 2 and 4 as far as we know.

Ionic liquids, and especially the room temperature ionic liquids, have recently become an active research area of ionic conductivity relaxation. These ionic liquids and molten salts are also glass-formers. Therefore the study of the ionic dynamics in these materials necessarily involves both ionic conductivity relaxation and structural relaxation which leads to glass transition. The results from experiments and simulations in ionic liquids challenge simultaneous explanations of the two aspects of the dynamics. So far no theory of ionic conductivity relaxation has done so except the Coupling Model.

Molecular dynamics (MD) simulation is a powerful tool to examine the structures, the dynamics and the mechanism behind them. The technique might be regarded as a microscope probe, where the magnification can be changed freely, and even the dynamics of each ion can be observed. The essentials of the technique necessary for understanding the properties of ionic materials by MD simulations are explained, and a practical introduction for that newcomers to engage in research using MD simulations are also included in the book. By these means we hope MD simulation techniques will become more familiar to researchers and accessible to beginners of ionics and related fields, and our book can serve as a guide for starting new research to gain deeper understanding.

In Chap. 9, the structures and dynamics of ionically conducting glasses for lithium silicate glasses (Li_2SiO_3 and $Li_2Si_2O_5$) examined by MD simulations were discussed. In Chapter 10, the lithium metasilicate mixed with potassium metasilicate was examined to clarify the mechanism of the mixed alkali effect (MAE). In Chap. 11, ionic liquids are examined from several points of views, using the system EMIM-NO_3 as an example. The glass transition of the system was also examined and behaviors are explained by the changes of the topological constraint of the system. Transport properties obtained by MD simulations are compared with experiments and theory in these chapters. A limited number of systems are examined by different approaches with references given to related works. The method and style of research carried out by simulations is quite different from that in Chaps. 4–7, where experimental data from studies of a variety of ionic conductors are accumulated and analyzed to show the generality of properties implying the existence of common underlying physics, and compared with predictions from theory. The results of some simulations overlap that presented in Chaps. 4–7 despite the difference of styles and time scales. The results obtained by these two different approaches should be consistent if the underlying physics are common. In fact this is the case, and this should make the readers more convinced of the existence of universal properties of ionic conductors and the underlying common physics.

From Chaps. 9–11, one can understand there are some remarkable differences between dynamics of glasses and crystals of the same composition. Difference between single alkali and mixed alkali systems can be also found in the mixed alkali effect (MAE). The dynamics of ionically conducting glasses and glass forming ionic liquids are also different. Comparisons of these different systems for distinguishing their properties will be useful to understand and to predict the properties of new materials. The non-linear MAE is a key feature of ionic dynamics critical in judging the validity of any theoretical explanation of ion dynamics. One of the remarkable contributions of MD simulations to ionics is concerned with identifying the mechanism of the mixed alkali effect. Existence of independent paths of unlike ions in mixed alkali glasses was proven by distinct part of the van Hove functions, and the paths of ions were visualized in the simulations. At longer time scales, existence of jumps among unlike ion sites are found and it causes a loosening of the network structures.

Non-Gaussian dynamics found in the real space is closely related to the stretched exponential decays in the intermediated scattering function, as revealed by examinations of the mean square displacement (MSD), the van Hove functions, the non-Gaussian parameters, and by the fractal dimension analysis. Ionic motion shows dynamic heterogeneity (coexistence of fast and slow ions) similar to the glass forming materials near the glass transition temperature. Each motion found in several distinct time regions of MSD was characterized by these functions and fractal dimensions (or exponents).

Development of the mean square displacement (MSD) with time starts from local caged ion dynamics, independent and local ion jumps, changes to ion jumps participated by increasing number of ions, mixing of fast and slow motions of ions, and culminating in the long ranged diffusive motions which defines the diffusion constant. We have successfully separated spatial (related to the geometrical correlations among successive jumps) and temporal (related to the waiting time distribution of jumps) contributions to the MSD. Thus the relationship between the jump motions and the relaxation rate of stretched exponential relaxation is clarified.

In room temperature ionic liquids, ionic motion also shows dynamic heterogeneity and the several distinct time regions of mean squared displacement (MSD) similar to that found in ionic glasses, as reported for the case of EMIM-NO_3. Moreover, the ion dynamics obey thermodynamic scaling similar to that found in structural relaxation of glass-formers and there are similar relation between topological structure and dynamics for the ions and for the structural relaxation responsible for glass transition.

We clarified that the heterogeneous ion dynamics have a multifractal nature. By the multifractal nature of walks, heterogeneous density profile of ions is formed. Heterogeneous motions and structures can be well characterized by the multifractal analysis using singularity ($D(h)$ or $f(\alpha)$) spectra. Thus mutifractality is a measure of the heterogeneity and can be used as a general framework to describe the universality of the dynamics and structures.

Applications of MD in several fields were also discussed. For example, in nanoionics, MD simulations are expected to play a role for understanding the mechanism of ion transport and for optimization of them as devices. Design of solid state batteries totally by MD simulations is a promising approach, if the required system size and time scales are fulfilled. Such emerging fields are not fully explored so far, and they await new efforts from other researchers. With further developments of the methodologies and computational techniques, MD simulations will be able to study the ion dynamics of larger size systems to longer time scales, as well as more complicated systems with hierarchy structures.

Before starting writing this book, when we first explored the ideas of undertaking this project, we strongly felt indeed useful to have such a monograph on the dynamics in ionic conductors. We agreed that it should be a book presenting comprehensively the many experimental results, the theoretical developments and modeling, and the progress made by MD simulations in ionically conducting materials during the last few decades. The book written indeed covers experimental data from a large variety of materials obtained by using different experimental techniques, and various theories and models. Most importantly, the theories and models are discussed in connection with experimental results to emphasize their strength and weakness. Many examples of MD simulations are given to examine the dynamics of mobile ions and to understand them.

Our purpose was to write a self-contained book which could be of interest to both beginners and experienced researchers in dynamics of ions in ionic conductors, and serve as a basis of future developments in the field. It is written in such a way that it may be used as a text-book for university students in a postgraduate course and, at the same time, used as a reference book for active researchers in academic institutions and industries. We have tried to provide the fundamentals for an introduction to the field, explaining the basics of experimental techniques, theories of ion diffusion, and MD simulations applied to ion dynamics, together with an overview of the recent research results and current activities in the field. And we have also gathered many relevant scientific results from experiments, theories and simulations, and discuss them by using general concepts that shed light on the universal patterns found in the properties of the dynamics of ionic conductors, independently of its chemical composition or physical state, and the role played by many-body interactions in generating this universal response.

We believe the subject of the book is currently of great interest for the broad and diverse communities of condensed matter physicists, chemists, materials scientists and engineers working in many different systems, and making contributions to both fundamental and applied research. Driven by technological application of ionic conductors in fuel cells, supercapacitors, and lithium-ion and other solid state batteries, the interest in the subject is expected to increase in the years to come. Energy generation, transport, and storage is one of the most important challenges of the world. Realization of a "green economy" in the future also depends on advances in research and development of ionics. We sincerely hope this book will contribute to progress in science and technology of the ionically conducting materials.

Appendix

A.1 Fractal Dimension of Random Walks

The motion of ions in the molten state (including ionic liquids) or in glasses is quite heterogeneous. Abnormal diffusion can be found in certain time regimes due to coexistence of fast and slow ions. Diffusivity of particle is related to how its trajectory spreads in the space. How can we characterize the motion from the trajectory?

Mandelbrot has determined the fractal dimension of random walk, such as in representing the complexity of the coast line by using a divider method [1]. The method is applicable to the trajectories of ions obtained by MD simulations; i.e. fractal dimension of random walks is a measure of the complexity of the trajectory. Trajectory is not an exact fractal in the sense of the self-similarity but has the characteristic of statistical fractal dimension. In general, dynamics of ions in disordered materials show large dynamical heterogeneity both temporally (waiting time distribution of jumps) and spatially (geometrical correlation among successive motions). The fractal dimension analysis of the trajectories is concerned with the spatial term.

A schematic description how to measure the fractal dimension of the random walk from the trajectory of ion is shown in Fig. A.1.

With using a divider method or related ones, one can determine the fractal dimension of the random walks. Using divider (*i.e.*, a straight ruler) of length L_r, one can count how many times, N_{T}, are required to cover the trajectory. From the slope in the double logarithm plots we determine the fractal dimension of random walk, d_{w}, defined by

$$N_T = A{L_r}^{-\mathrm{d_w}}. \tag{A.1}$$

For the system with many ions, we used the following method. When the length of a complicated trajectory obtained by simulation during t_{run} is measured by a divider, the number of times needed for the divider to cover the entire trajectory is ν.

J. Habasaki et al., *Dynamics of Glassy, Crystalline and Liquid Ionic Conductors*,
Topics in Applied Physics 132, DOI 10.1007/978-3-319-42391-3

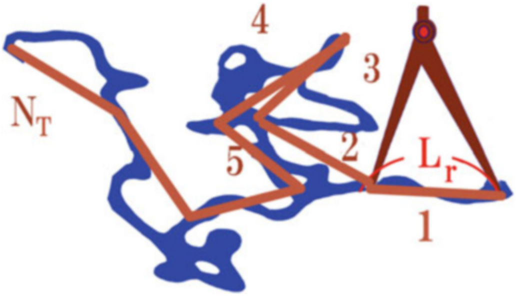

Fig. A.1 Complexity of the trajectory determines how particle diffuses. Using a ruler of length L_r, fractal dimension of the random walk (see Eq. A.1), which represents the complexity of the trajectory, can be measured

The total length of the trajectory is νL_r, which depends on the choice of L_r. For more complicated trajectories, a larger νL_r is obtained if a smaller L_r is used. Then, N_T, which is determined as a function of L_r, is the number of times required for the divider of length L_r to cover all the trajectories obtained after a run up to t_{run}. In this manner we can examine all the trajectories of the ions obtained during runs at several temperatures, with L_r ranging from 0.3 to 10 ~ 20 Å.

Normal random walk like in Brownian diffusion has $d_{\text{w}} = 2$. The value increases if the trajectories are more complex and localized, while the value decreases if the trajectories were simpler and delocalized. The trajectory curves can overlap each other and therefore the obtained fractal dimension is a latent one, which can be larger than the dimensionality of space.

The slope with θ (=2/d_{w}) is expected for the fractional power law region of the MSD (before the onset of the diffusive regime) in the case of infinitive network. That is, if the ionic site is visited by the walk with d_{w} in a monofractal manner, the mean squared displacement in the power law regime is given by

$$\left\langle r^2(t) \right\rangle \sim t^{2/dw}. \tag{A.2}$$

The value can be modified if we consider every particle on clusters of different sizes.

In many cases, more than one region will be found in the plots of N_T against L_r for trajectories examined. Then the walks are "multifractal walks" as explained in Appendix A.6.

A.2 Dynamic Heterogeneity: Coexistence of Slow and Fast Ions

The fractal dimension of random walk with $d_{\text{w}} = 2$ corresponds to Brownian diffusion. Fast ions with accelerated motion show smaller d_{w} value ($d_{\text{w}} < 2$), which means the trajectories are more linear like and this also means the acceleration is achieved by the geometrical terms. On the other hand, localized motion tends to have larger d_w (>2) values, which means the trajectories are folded many times. On path with small dimensionality, such motion can be understood as "fracton" [2], coming from the complicated motion and small dimensionality of the paths.

A.2.1 Concept of Fracton

When the motion of ions are examined along the trajectory, the numbers of sites, $V(N)$, visited during the N steps is represented by

$$V(N) \sim R^{df} \sim N^{ds/2}, \tag{A.3}$$

where d_f is the density dimension of the cluster formed by the visited sites and R is a linear size of it. Vibrational state on the fractal structure depends on both the fractal dimension of the visited sites and the walk as follows.

"Fracton" dimension, d_s, is defined by

$$d_s = 2d_f/d_w, \tag{A.4}$$

The back correlation probability, $<P_0(t)>$, of finding a walker, which is located at an origin initially at time t_0 and back to the initial position at time t, is given by,

$$<P_0(N)> \sim [V(N)]^{-1}. \tag{A.5}$$

In the case of slow dynamics, both long waiting time and localized motion contribute. On the other hand, for the fast ions, the Lévy flight [3, 4] dynamics play important roles as explained in the next section.

Although heterogeneous motion is omnipresent at least in the observed temperature regions, long time diffusive motion is a coarse-grained one after the mixing of fast and slow motions of ions, and that is why the complex motion of ions at long times can be represented by the mean behaviors of fast and slow ions.

A.2.2 Concept of Lévy distribution and Lévy flight

The self-part of the van Hove functions often shows a long (inverse power law) tail deviating from the normal Gaussian dynamics, near glass transition. The characteristics of the motion represented by such a function are explained here.

Existence of such tail means that the motion involves large length scale, which is a rare event, but is non-negligible. The heterogeneous dynamics observed can be represented by a Lévy (alpha stable) distribution [5] with a truncation (note that without truncation or other mechanisms, the distribution will have infinitive second or higher moments).

The stable distribution is defined by the characteristic function $\varphi(\alpha, \beta, \gamma, \delta)$. Here α is index of stability or characteristic index (exponent), $\alpha \in (0, 2]$, β is a skewness parameter, $\beta \in [-1, 1)$ (where, $[a, b) = \{x | a \leq x < b\}$ and $(a, b] = \{x | a < x \leq b\}$) and γ is a scale parameter, $\gamma > 0$, and δ is a location parameter, $\delta \in \mathbb{R}$. Some caution is required because of the different parameterizations and or the naming of the distribution.

One can find the different types of parameterization in Ref. [6]. The term "Lévy distribution" may be used for narrower meaning, specifically for the case of $\alpha = 0.5$ and $\beta = 1$ [7]. In this book, we use the term "Lévy distribution" with a wider sense (that is for alpha stable distribution) and the following figures are prepared by the "type 1" parameterization in Ref. [7].

For the stable distribution of the random variable X with distribution function F(X), the characteristic function is defined by $\phi(u) = E\exp(iuX) = \int_{-\infty}^{\infty} \exp(iuX) dF(X)$.

The stable distribution of random variable X has the characteristic function $\varphi(\alpha, \beta, \gamma, \delta)$ given by

$$E \exp(iuX) = \exp\left(iu\delta - \gamma^{\alpha} |u|^{\alpha} \left(1 - i\beta \,\mathrm{Sign}(u) \tan\left(\frac{\pi\alpha}{2}\right)\right)\right), \quad \text{when } \alpha \neq 1. \quad \text{(A.6)}$$

$$E \exp(iuX) = \exp\left[iu\delta - \gamma |u| \left(1 + \frac{2i\beta \ln |u| \mathrm{Sign}(u)}{\pi}\right)\right], \quad \text{when } \alpha = 1. \quad \text{(A.7)}$$

Here the Sign function returns the sign (plus or minus) of the value. Here our attention is focused on the situation with $1 < \alpha \leq 2$.

Figure A.2 shows the Lévy distribution S(α, β, γ, δ) with several α values (1.0, 1.2, 1.4 and 2.0). The shape gradually changes with the Lévy (or α) index and the Gaussian dynamics is just a special case of the distribution with $\alpha = 2$.

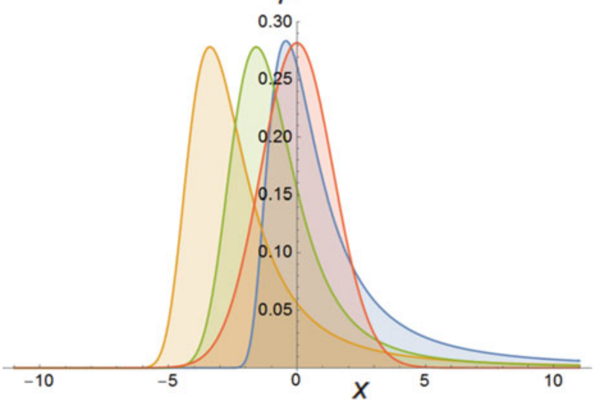

Fig. A.2 Example of Lévy distribution $S(\alpha, \beta(=1), \gamma(=0), \delta(=1))$ with several α values (1.0 (*Yellow*), 1.2 (*Green*), 1.4 (*Blue*) and 2.0 (*Red*)), where 2.0 corresponds to Gaussian distribution. You can manipulate the parameters of the function using free CDF file in ESM (see Sect. 12.2)

When temperature is lowered or pressure is increased, motion of ions becomes jump like. In this case, the distribution is related to the Lévy flight dynamics of the jump motion of ions. Essence of the Lévy flight dynamics can be explained as follows [3] by considering the motion (walk or flight for clear jumps) of an ion (a particle or a molecule in general) in a real space. For the probability for the sum of N steps $P_N(X)$, where $X = x_1 + x_2 + ---- + x_N$, one can say the distribution is stable when the same probability $p(x)$ is found in the individual steps.

As a simple example of the Lévy flight dynamics, Weierstrass random walk represented by

$$p(x) = \frac{\lambda - 1}{2\lambda} \sum_{j=0}^{\infty} \lambda^{-j} [\delta(x, b^j) + \delta(x, -b^j)], \tag{A.8}$$

where $b > \lambda > 1$, is known. This probability means that there are jumps with size of $x = 1, b, b^2, b^3$--, where the b time longer jump is λ times less probable. Here $\delta(x, y)$ means the Kronecker delta, which equals 1 when $x = y$ and otherwise vanishes. The Fourier transform of this equation results

$$\tilde{p}\,(k) = \frac{\lambda - 1}{2\lambda} \sum_{j=0}^{\infty} \lambda^{-j} \cos\,(b^j k) \approx \exp[-N|k|^{\alpha'}] \text{for small k}, \tag{A.9}$$

where $\alpha' = \ln \lambda / \ln b$.

In the example 2 of ESM, some examples of analysis of jumps in proving the existence of Lévy flight dynamics are shown (see Sect. 12.2).

A.2.3 Lévy Walk and Lévy Flight with Strong Back Correlated Motions

Lévy flight can be an origin of the accelerated motion. However, at temperature near the glass transition or in glassy state, it is related with slow dynamics on the average.

Klafter *et al.* [3] have examined the Lévy walk, where the Lévy flight is combined with the fractal waiting time distribution. The probability density, $\Psi(\mathbf{r}, t)$ of the displacement vector of particle $\mathbf{r}$ at t is represented by,

$$\begin{aligned} &\text{(i)} \quad \iint \Psi(\mathbf{r}, t) dt d\mathbf{r} = 1 \\ &\text{(ii)} \quad \Psi(\mathbf{r}, t) = \varphi(\mathbf{r}) \delta\big(t - |\mathbf{r}|/v(\mathbf{r})\big) \\ &\text{(iii)} \quad \varphi(\mathbf{r}) \underset{r \to \infty}{\sim} |\mathbf{r}|^{-\mu} \end{aligned} \tag{A.10}$$

Here the step length is $\varphi(r)dr = \varphi(\mathbf{r})d\mathbf{r}$.

This model can explain the enhanced dynamics in turbulence successfully. The Lévy motion can be combined with a fractal waiting time distribution having a long tail [5]. This temporal slowing down can be a mechanism to avoid the divergence of the Lévy flight.

Another possible mechanism causing slow dynamics is a strong back correlated ionic motion, observed in the fractional power law region of MSD in ionic liquids and in glasses [8–12]. The strong back correlation in the low temperature region, which is characterized by the large fractal dimension of the random walks, also causes the slowing down instead of waiting time distribution. In other words, tailed shape of the self-part of the van-Hove function is formed by the length scale distribution with $\alpha < 2$ folded by the strong back correlation [13]. Although the waiting time distribution of jump motions exists for both slow and fast components of the dynamics, mean number of jumps at a time is nearly constant for the ionic motions observed in the quasi-stable glass (see Sect. 9.5.5). Temporal and geometrical slowing down might be expressed by the similar expressions; however, the physical meaning is not necessarily the same.

A.2.4 Truncation of Lévy Distribution and Multifractal Mixing

As already mentioned, Lévy stable process has infinite variance and hence additional mechanism is necessary to explain the behavior in the abnormal diffusion. In MD simulations of ionic systems [13], exponential truncation of the self-part of the Van Hove functions is found and this is a possible mechanism to avoid the divergence of the dynamics. Corresponding upper cutoffs (abrupt one and a smooth exponential regression) are theoretically treated by several authors [14–16]. Mantegna and Stanley [14] have shown that the convergence of the truncated Lévy flight (TLF) with a sudden cutoff to a Gaussian process is a ultraslow process, because it requires a remarkable large number of independent TLF steps n (~10^4) in contrast to ~10 for common distribution. Nakao [16] has pointed out that the TLF shows multiscaling properties because of convolution of different length scale motions.

We note that similar mechanism to avoid the divergence of the dynamics is also possible for the temporal term. For the particles in the rigid heteronuclear bi-atomic system [17], the waiting time distribution was found to be exponential at higher temperatures, while at low temperatures, waiting time distribution function of the jump relaxation was found to obey power law at short times and the decay is faster than exponential at long times.

The systems with smooth truncation (with an exponential cut-off) exhibit bi-fractal behavior, which is the simplest case of multifractality [16]. The mechanism plays a role in the dynamics observed and is related to the multifractal nature of the walks [18], and the multifractal density profile shown in the Appendix A.3 is formed by such motions.

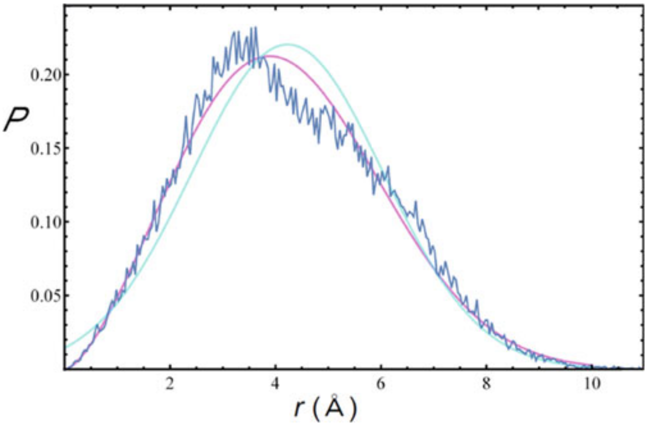

Fig. A.3 Self-part of the van Hove function (*blue*) of EMIM$^+$ ion at 370 K, at 600 ps compared with Weibull distribution (*pink*), where α, β and μ are 2.50, 4.75 and 0.0165, respectively. And normal distribution(pale blue) where μ and σ are 4.23 and 1.81, respectively

In the observation in a limited time scale of experiments and in the simulations, often the stable region (power law region in MSD) continues for long time; however, Lévy flight dynamics will not hold further at long times, because of the truncation of the distribution.

The form of the truncated Lévy distribution seems to be closely related to the Weibull distribution, W(x), with the following form [19],

$$W(x) = 1/\beta\left(\alpha\left(\frac{x-\mu}{\beta}\right)^{\alpha-1}\exp\left(-\left(\frac{x-\mu}{\beta}\right)^{\alpha}\right)\right), \tag{A.11}$$

which has both the power law term and the exponential tail. Here the α, β and μ are the shape, scale, and positional parameter, respectively.

In the case of ionic liquid, this functional form is useful for fitting of the data of the self-part of the Van Hove function as shown in Fig. A.3 (unpublished data) approximately.

A.3 Concept of Multifractal Density Profile

To envisage the structure of the ionic system or positions of ions in disordered system, it is convenient to consider the density profile of it.

An example of a density profile for the Li ions in the lithium metasilicate glass is shown in Fig. A.4.

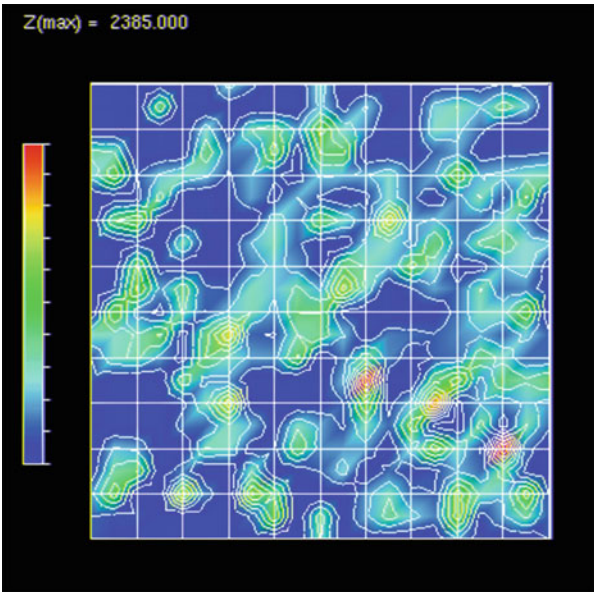

Fig. A.4 An example of a density profile of Li ion for a slice of the MD cell in lithium metasilicate glass. Positions of ions are accumulated during 1 ns MD run at 700 K. *Red part* has the high counts corresponding to the deepest well of the ion site. Such a pattern with heterogeneity can be characterized by the multifractal analysis

In such a density profile, localized sites and paths connecting them can have different fractal (Hausdorff) dimensions.

As can be seen from this figure, density profiles of systems in the liquid and glassy states are complex and heterogeneous. Such characteristics of the structure can be well represented by the multifractal (singularity) spectra explained in Appendix A.5. The analysis is applicable for any patterns with contrasting density and thereby it provides a common framework to study complex structures with heterogeneity. The theoretical structure of the analysis is comparable with the "thermodynamics" and is applicable in both time and space to many objects. So far it is applied for many systems such as chaos, turbulence, geophysics, bio materials and so on. Before explaining the multifractal analysis of the density profile, we explain the concept of multifractal.

A.4 Fractal and Multifractal Cantor Sets

In Figs. A.5 and A.6, mono-fractal and multifractal Cantor sets are shown to explain the concept. Uniform (mono fractal) Cantor set was constructed as follows. At first, a top bar of length 1 is prepared. The second stage is done by removing 1/3 of the middle part of the top bar (of probability 1) and the probability of right and left bars are the same (1/2). In the third stage, 1/3 of each bar was removed and the probability of both sides was the same. This procedure is repeated. After n generations, each segment has measure $p_0 = 1/2$ and scale $l_0 = 1/3$. In the n-th generation, the small bars with the same lengths are found. Thus the system is

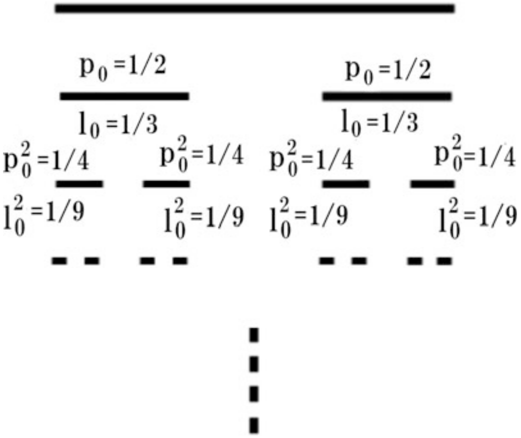

Fig. A.5 An example of a uniform (mono fractal) Cantor set. From a bar on the tip, 1/3 of the middle part was removed in the first stage. This procedure was repeated

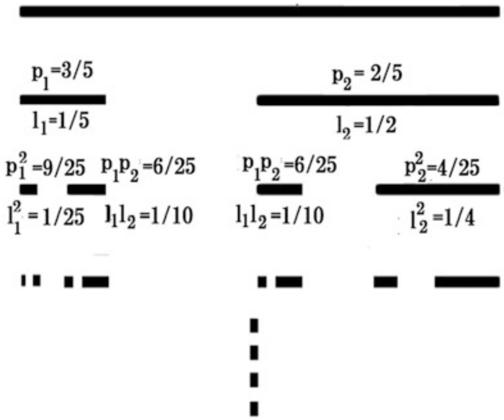

Fig. A.6 Example of a multifractal Cantor set. Length 1/5 and 1/2 remain in the first stage, where the measure is 3/5 and 2/5, respectively. This procedure was repeated. Resultant distribution after n stages is heterogeneous. That is, multifractal analysis gives a spectrum characterizing the heterogeneity

uniform. In Fig. A.6, an example of multifractal Cantor set is shown. In the case of multifractal Cantor set, similar procedure is repeated with different l and p values. Here we used the scales of $l_1 = 1/5$ and $l_2 = 1/4$, with measures $p_1 = 3/5$ and $p_2 = 2/5$. Resultant distribution after several stages is rather heterogeneous. Therefore, multifractality provides a general description of the heterogeneity.

A.5 Singularity Spectrum $f(\alpha)$

Multifractal nature of the probability density profile (or patterns in a general case) of ions can be represented by using a singularity spectrum, $f(\alpha)$, which is defined and obtained as follows [19].

Singularity spectrum, $f(\alpha)$, is obtained from the probability $\mu_i(\delta)$. The procedure to obtain the function from the (accumulated) density profile of Li ions is described as follows.

1. Pattern (density profile) was divided into cells with size δ.
2. Measure (probability) $\mu_i(\delta)$ $(=n_i/\sum n_i)$ of the cell is measured. In this case, the number "how many times ions visit the i-th cell during the run", are regarded as n_i.
3. The measure $\mu_i(\delta)$ is represented as

$$\mu_i(\delta) = \delta^\alpha, \tag{A.12}$$

where α is a strength of the singularity. The probability of α lying between α' and $\alpha' + d\alpha'$ is

$$\rho(\alpha') \propto \delta^{-f(\alpha')} d\alpha'. \tag{A.13}$$

Thus $f(\alpha)$ corresponds to the fractal dimension of the set of small cells with a singularity strength α and they are obtained as the function of the moment q, using $[\mu_i(\delta)]^q$,where the q-th moment emphasizes the concentrated region of the data points when it is positive and emphasizes the rarefied region when it is negative.

When $q = 0$, $f(\alpha(q))$ corresponds to the capacity dimension, D_0, while information dimension is given by $f(\alpha(q = 1)) = D_1$, and correlation dimension is given by D_2.

Using the normalized q-th moment, $\mu_i(q, \delta)$, the numerical values of $\alpha(q)$ and $f(\alpha(q))$ are obtained for a certain range of q ($-40 < q \le 30$ were used in our analysis) for several δ values using following relations.

$$\alpha(q) = \sum_{i=1}^{N} \mu_i(q, \delta) \ln \mu_i(\delta) / \ln(\delta/L), \tag{A.14}$$

$$f(\alpha(q)) = \sum_{i=1}^{N} \mu_i(q, \delta) \ln \mu_i(q, \delta) / \ln(\delta/L), \tag{A.15}$$

where $\mu_i(q, \delta)$ is defined by

$$\mu_i(q, \delta) = [\mu_i(\delta)]^q / \sum_{j=1}^{N} \left[\mu_j(\delta)\right]^q. \tag{A.16}$$

Typical singularity $f(\alpha)$ spectrum of the multifractal is found in Fig. A.7.

A convex shape of the curve in the $f(\alpha)$ spectrum means the multifractality (mixing of more than one exponent). That is, the structure is formed by the mixing of localized and accelerated motions having different exponents.

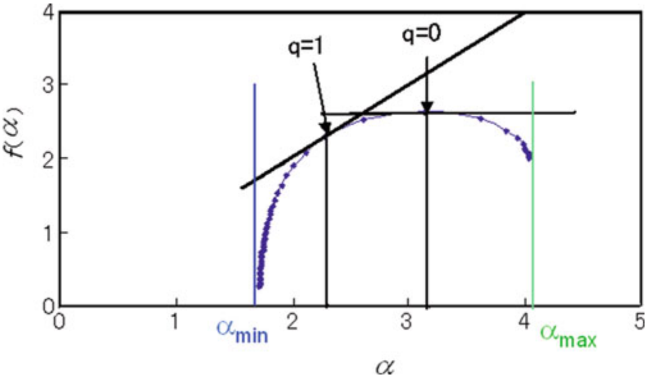

Fig. A.7 Example of the singularity ($f(\alpha)$) spectrum for the density profiles of Li ions found in the silicate glasses. Convex curve means the multifractality. The maximum position with $q = 0$ corresponds to the capacity dimension of the profile. The value for $q = 1$ corresponds to the information dimension. The α_{max} and α_{min} correspond to the most rarefied part and the densest part of the density profile, respectively. Therefore, it is a measure of the heterogeneity of the structures.

The generalized dimension, D_q, is related to $f(\alpha(q))$ by a Legendre transformation, $\tau(q) = (q - 1)D_q$, where $\tau(q)$ and q are conjugate thermodynamic variables to $f(\alpha)$ and α. These relations have the similar structure as the thermodynamic formalism of equilibrium thermodynamics. In other words, the multifractal analysis has the thermodynamic framework and generally applicable to many systems. Using the singularity spectra, one can compare the heterogeneity of different systems.

A.6 Multifractal Walks

A multifractal density profile is formed by the multifractal motion of many ions. Therefore, each ionic motion has also a multifractal character. Such process named multifractal random walk was introduced by Bacry [18].

Multifractality of the walks can be characterized by singularity spectrum using Hurst exponent [20, 21], h, defined by the following equation.

$$\delta x_i(t_0, \delta t) = |x_i(t_0 + \delta t) - x_i(t_0)| \approx (\delta t)^{h(t_0)} \tag{A.17}$$

In the power law region of the MSD,

$<r^2(t)> = 2D \times t^{\theta}$, then $\theta = 2H$, here H is the Hurst exponent for the mean behavior of particles. Since the fractal dimension of the random walk d_w is related to θ by $\theta = 2/d_w$, the value of d_w for the mean behavior corresponds to the inverse of the Hurst exponent [22].

If the motion is simple Brownian, the Hurst exponent, h, is always 0.5 and the displacement is self-similar at everywhere. The singularity spectrum $D(h)$ for the motion can be defined by a similar manner as $f(\alpha)$. Example of such spectrum is found in Fig. 11.11 of Chap. 11 for ionic liquid.

The curved shape of the spectrum is due to the mixing of several exponents resulting in the distribution in the Hurst exponents; and therefore it also means multifractality (multiaffinity in the strict sense) [16]. The density profiles with multifractal natures are thus formed by the multifractal walks. From the definition of the Hurst exponents in (Eq. A.17), it is obvious that the distribution of the Hurst exponent is related to the power law exponent in the MSD. As shown by the example of this figure, short length scale motion is mixed with the longer scale motion to form multi-fractal walks. This result is consistent to that found in the fractal dimension analysis of random walks of the trajectories [23], where two different length scale regions are found in the N_T against L_r plot explained in Appendix A.1.

A.7 Time Series Analysis: De-Noising of Data by Singular Spectrum Analysis (SSA)

Ions in glasses tend to be localized at the initial sites, when we start observation at an arbitrary chosen initial time. With elapse of time, the vectors indicating the displacement of the moving ions tend to be grouped together in domains and the size of the domains grows with time (see Sect. 4.6). Although time series of such vectors or other data obtained from MD simulations contain useful information on the dynamics of the system, they tend to be affected by short time thermal noises considerably.

How can we extract the characteristics of motion without noises?

Previously, using the phase-space plot of de-noised data, similarity of the dynamics in ionic liquids and ionically conducting glasses are clarified, where both show a long term memory of the motion and deterministic characters. These plots exhibited clear topological structures with a complicated and dissipative character (see Sect. 11.9).

Singular Spectrum Analysis (SSA) [24] is a principal component analysis of time series, which can extract the de-noised data from raw data. SSA non-parametrically provides a robust method of separating an arbitrary signal from noise, and finds the most probable equation to represent the data to maximize the variance of the data. When it is applied to the MD simulations, it is useful to extract the structure of motion in the phase-space and/or in the real space by de-noising the MD data.

In Fig. A.8a, an example of the de-noising applied for the ionic motion is shown. By using the reconstructed data, phase-space plot and return map are obtained. When applied to the jump motion of ions, SSA can effectively extract the characteristic of it for both within and among sites as shown in Fig. A.8b. In this figure, small circles are for localized motion and these regions are connected by larger

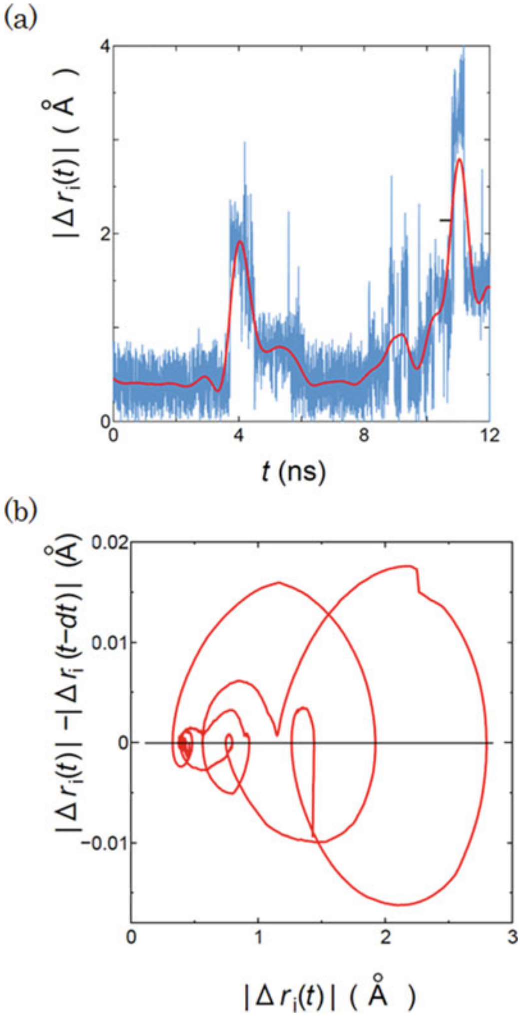

Fig. A.8 (**a**) Example of de-noising of data using singular spectrum analysis (SSA) for ionic motion. The data is the absolute value of the displacement of arbitrary chosen Li ion at 800 K in lithium disilicate glass. The ionic motion is localized within 12 ns run. A *blue curve* is for the original data sampled every 1000 step. A *red curve* is for the reconstructed data using the 1 ~ 3 principal components. (**b**) Phase-space plot obtained from the reconstructed data. Here the difference of the absolute value of the displacement with an interval of dt (=4 ps) is plotted against the value at t. The clear pattern of the dynamics hidden in the noise was clarified

circle like motions for delocalized motion. Even a longer scale motion is found during a long run. The clear pattern means that the deterministic characters of jump motions. This means that ion moves along a kind of strange attractor both in the short time (NCL) regime and the longer time (jump diffusion) regimes (see Sect. 11.9).

As shown in this figure, time series analysis was successfully applied for the development of the length of these vectors, that is, the absolute value of the displacements of ion. From MD simulations, several kinds of time series x (t) ($t = 1$,---,N) of data, where x can be positions, velocities, temperatures, and other variables, are available and the method is applicable to other time series.

The analysis can be done as follows. The sampled time series $x\ (t)$ ($t = 1$,---,N) are embedded in a vector space of dimension M by considering M lagged copies. $x(t, j), j = 1$,-----M.

1) the M x M lag-covariance matrix C_{D} of the data was computed using the trajectory matrix D,

$$C_D = N^{-1}DD^T. \tag{A.18}$$

Eigenvector E_{k} (empirical orthogonal functions, EOF) and the eigenvalues λ_k are obtained by the diagonalization of the covariance matrix C_{D} from the N sample points. The eigenvalues λ_k are obtained are ranked in a decreasing order. The eigenvalue gives the variance of the time series in the direction specified by the corresponding eigenvector.

2) For each EOF, we can construct the k-th principal component $A_{\mathrm{k}}(\mathrm{t})$ of length N, as follows.

$$A_k(t)\sum_{j=1}^{M} x(t+j)E_{k,j}\ t = 0,\ - - -\ , N - M, \tag{A.19}$$

Partial reconstruction $R_K(t)$ of the original data series can be obtained by

$$R_K(t) = \frac{1}{M_t}\sum_{k\in K}\sum_{j=1}^{M} A_k(t-j)E_{k,j}, M \le t \le N - M + 1. \tag{A.20}$$

Here N means $N - \mathrm{M} + 1$.

The time series $x(t)$ can be represented by

$$x(t) = \sum_{k=1}^{M} x_k(t), \tag{A.21}$$

where the function x_k ($=R_K(t)$), which is a k-th component of $x(t)$, form a complete orthogonal set. The eigenvalue λ_k in SSA gives the variance of the time series in the direction specified by the corresponding k_{th} eigenvector, thus the reconstructed data using the first component by SSA is a most probable direction of the data.

The function x_k in Eq. (A.21) forms a complete orthogonal set. For example, the direction of the second principal component is perpendicular to the first component. This gives us useful information for the characteristics of the motion.

The probability of the system being in the state x_k is P_k and it is defined by

$$P_k = \left(\int x_k^2 dt\right)^2 = {\lambda_k}^2 \tag{A.22}$$

Thus λ_k is a measure of the importance of the mode x_k in the expansion of $x(t)$.

This approach is promising not only to learn more about the dynamics of ions but also for the understanding of molecular motions from the MD simulation of glass-forming substances. In principle, it can be used to prepare the model to represent on the coarse-grained level while keeping the phase-space structure of the dynamics.

A.8 Acceleration of MD Simulations by GPU

There are several ways to use the Graphic Processing Unit (GPU) (see Sect. 8.2.12.1). One is through using the library, in which some functions are accelerated by GPU. In such a case, each function seems to be well tuned for the devices by experts of GPU coding. Second one is to use OpenACC, which are directives for accelerator.

Compiler (for example, PGI Compiler [25]) can treat the parallel computation by addition of OpenACC to the source codes as follows.

------------Example of coding using OpenACC----------

```
!$acc parallel loop !OpenACC
DO j = 1,M
   DO i = 2,N-1
      Codes for a parallel computation
   END DO
END DO
!$acc end parallel loop
```

As shown here by bold fonts, OpenACC directives are inserted both in the beginning and the end of the target Do loop. Then the codes between them are compiled for parallel computation by the compiler. The acceleration by this method is not always successful and not necessarily better than using programming language, but is useful to use GPU with a small effort. The third one is to use programming language such as CUDA [26]. This allows fine tuning of each program.

GPU can be used in several programming languages such as C, FORTRAN (or Fortran) and/or in several applications such as MATHEMATICA and/or MATLAB.

Nowadays, C or C++ languages seem to be more frequently used than FORTRAN; however, many MD programs traditionally use FORTRAN as well. It depends on the store of knowhow and related programs etc. For the numerical calculations, the FORTRAN seems to have some reasons for it to be used. After FORTRAN 77, structured programming was introduced and modules can be used in Fortran 90, 95, and 2003. Probably, it depends on the problem in judging of which language is the best. For example, see Ref. [27] for the comparison of C and FORTRAN.

Here we show an essence of CUDA coding for an example of FORTRAN program of MD of ionic system [28], while similar coding is possible in other languages.

A.8.1 Example of CUDA Coding of the MD Program for Lithium Silicates, lso.f

The following is a part of MD code named “lso.f” using CUDA FORTRAN.

A structure of MD program coded by CUDA is as follows.

Here “DO 9999 loop” is a main loop for MD steps and the CUDA program was found to be 26 times faster than the original code for this main loop.

In this program, the loop 200 is a hot spot, which should be parallelized.

The loops 200 and 98 (not shown) are treated by GPU and other parts are treated CPU in this code.

```
-----------------------

Reading module
Setting of the initial values

| Setting of input and output files
| Input from files
|--- Setting of device
|
|--- Reserving the device memory (cudaMalloc)

|--- 0 clear of device parameters (cudaMemset)
|--- Data transfer from host to device (cudaMemcpy)
| C < < < START SIMULATION > > >
|-- + DO 9999 COUNT = 1,STEP ----Main loop for MD steps
| |--- 0 clear of device parameters (cudaMemset)
| |--- Data transfer from host to device(cudaMemcpy)
| |--- loop98
| |--- Data transfer from device to host(cudaMemcpy)
| |--- loop200
|
|--- Data transfer from device to host(cudaMemcpy)
|--- Releasing the device memory (cudaFree)
|
|--- Output to files

---------------------------------------------------------
```

Setting of device can be done using the following command.

```
istat = cudasetdevice(0)
```

Here device number 0 is used.

In the program “lso.f”, GPU device was called as follows.

```
-------------------------------------
call malloc_device(NTT,NMAX)
~
C < < < START SIMULATION > > >
DO 9999 COUNT = 1,STEP
~
9999 CONTINUE
~
call free_device()
----------------------------------------------------------------------------------------------
```

Contents of the “lso.f” are as follows. The hot spot (DO 200 loop) was changed to a kernel and called from the following main program.

```
----------------------------------------------------------------------------
use cudafor
use kernel_func_mod
use reduction_sum_module
~
C < < < START SIMULATION > > >
DO 9999 COUNT = 1,STEP
DO 90 I = 1,NTT
EED(I) = 0.0
BER(I) = 0.0
90 CONTINUE
istat = cudaMemset(d_enp,0.0,ntt)
istat = cudaMemset(d_en2,0.0,ntt)
istat = cudaMemset(d_ttf,0.0,ntt*3)
istat = cudaMemcpy(d_q,q,ntt*3,cudaMemcpyHostToDevice)
call loop98 <<< NL,128 >>>
& (ntt,d_vm,d_vn,d_q,d_z,d_si,d_co,d_nw,d_en2,
& d_bl,d_bm,d_ttf,d_en1)
en1 = sum_gpu(nl,d_en1,d_wrk1,d_wrk2)
istat = cudamemcpy(EN2,d_en2,ntt,cudamemcpydevicetohost)
TT1 = 0.0
TT2 = 0.0
TT3 = 0.0
TTT = 0.0
TTA = 0.0
TT11 = 0.0
TED = 0.0
BBER = 0.0
call loop200 < << NTT-1,128 >>>
$ (NTT,
$ AL,ALH2,
```

```
$ d_KINNUM,d_IPAIR,d_JFR,
$ d_Q,d_ENP,
$ d_DEC,d_DER,d_DRFF,d_DEP,
$ d_EC,d_ER,d_RFF,d_EP,d_BR,d_TTF,
$ d_ECL,d_EDD,d_ERS,d_VIL)
ecl = sum_gpu(NTT*(NTT-1),d_ecl,d_wrk1,d_wrk2)
edd = sum_gpu(NTT*(NTT-1),d_edd,d_wrk1,d_wrk2)
ers = sum_gpu(NTT*(NTT-1),d_ers,d_wrk1,d_wrk2)
vil = sum_gpu(NTT*(NTT-1),d_vil,d_wrk1,d_wrk2)
istat = cudaMemcpy(TTF,d_TTF,NTT*3,cudaMemcpyDeviceToHost)
istat = cudaMemcpy(ENP,d_ENP,NTT,cudaMemcpyDeviceToHost)
~
9999 CONTINUE
-----------------------------------------------------------------------------------------------
```

Kernel of the DO 200 loop

Original DO loop is as follows.

```
-----------------------------------------------

   DO 200 I = 1,NTT-1
   ION = KINNUM(I)
   DO 201 J = I + 1,NTT
   IF (RR2.LE.ALH2) THEN ----If the distance dij is within L/2,
   JON = KINNUM(J)
   MF = IPAIR(ION,JON) --------Pair index for I and J
   R = SQRT(RR2)
   N = R*100
   NN = N/2 + 1

C------------

      ENP(I) = ENP(I) + EP(N,MF) + DEP(N,MF)*RFA
      ENP(J) = ENP(J) + EP(N,MF) + DEP(N,MF)*RFA
      EDQF = RFF(N,MF) + DRFF(N,MF)*RFA
      TTF(I,1) = TTF(I,1) + EDQF*AA1
      TTF(J,1) = TTF(J,1)-EDQF*AA1
      TTF(I,2) = TTF(I,2) + EDQF*AA2
      TTF(J,2) = TTF(J,2)-EDQF*AA2
      TTF(I,3) = TTF(I,3) + EDQF*AA3
      TTF(J,3) = TTF(J,3)-EDQF*AA3
ECL = ECL + EP(N,MF) + DEP(N,MF)*RFA
   BERS = ER(N,MF) + DER(N,MF)*RFA
   EDD = EDD-EC(N,MF)-DEC(N,MF)*RFA
   ERS = ERS + BERS
   VIL = VIL-BR(MF)*BERS*R
   ENDIF
201 CONTINUE
200 CONTINUE

-----------------------------------------------------------------------------------------------
```

For DO 200 loop, the blocks of the same number as the iteration (NTT-1)were used while for inner loop 201, threads were used for parallel computation.

For the summation of each energy (ECL, EDD, ERS) and virial (VIL) terms, new arrays were prepared for saving the values before summation was taken. A summation was performed in the "sum_gpu" kernel after the calculation of this loop.

For JFR (a summation of numbers of particles at distance r_{ij} for calculation of a pair correlation function), ENP, TTF (summation of force), atomic function of CUDA was used.

The kernel function for double loops (200 and 201) was prepared as follows.

```
-----------------------------------------------------------------------------------------------

attributes(global) subroutine loop200(NTT,
$ AL,ALH2,
$ KINNUM,IPAIR,JFR,
$ Q,ENP,
$ DEC,DER,DRFF,DEP,
$ EC,ER,RFF,EP,BR,TTF,
$ ECL,EDD,ERS,VIL)
INTEGER,value::NTT
REAL,value::AL,ALH2
INTEGER,device::JFR(3000,6)
INTEGER,device::IPAIR(3,3),KINNUM(NTT)
REAL,device::Q(NTT,3)
REAL,device::DEC(NTT,6),DER(NTT,6),DRFF(NTT,6),DEP(NTT,6)
REAL,device::EC(NTT,6),ER(NTT,6),RFF(NTT,6),EP(NTT,6),br(6)
REAL,device::ENP(NTT)
REAL,device::TTF(NTT,3)
REAL,device::ecl(NTT,NTT-1),edd(NTT,NTT-1),
& ers(NTT,NTT-1),vil(NTT,NTT-1)
integer I
I = blockIdx%x
ION = KINNUM(I)
DO 201 J = I + threadIdx%x,NTT,blockDim%x
ecl(j,i) = 0.0
edd(j,i) = 0.0
ers(j,i) = 0.0
vil(j,i) = 0.0
AA1 = Q(I,1)-Q(J,1) + 1.5*AL
AA2 = Q(I,2)-Q(J,2) + 1.5*AL
AA3 = Q(I,3)-Q(J,3) + 1.5*AL
AA1 = AMOD(AA1,AL)-0.5*AL
AA2 = AMOD(AA2,AL)-0.5*AL
AA3 = AMOD(AA3,AL)-0.5*AL
C
```

```
RR2 = AA1*AA1 + AA2*AA2 + AA3*AA3
IF (RR2.LE.ALH2) THEN
JON = KINNUM(J)
MF = IPAIR(ION,JON)
R = SQRT(RR2)
N = R*100
NN = N/2 + 1
iret = atomicadd(JFR(NN,MF),1)
RFA = AMOD(R,0.01)
C phy1i
ftmp = EP(N,MF) + DEP(N,MF)*RFA
fret = atomicAdd(ENP(i),ftmp)
fret = atomicAdd(ENP(j),ftmp)
EDQF = RFF(N,MF) + DRFF(N,MF)*RFA
ftmp = EDQF*AA1
fret = atomicAdd(TTF(I,1),ftmp)

20
fret = atomicSub(TTF(J,1),ftmp)
ftmp = EDQF*AA2
fret = atomicAdd(TTF(I,2),ftmp)
fret = atomicSub(TTF(J,2),ftmp)
ftmp = EDQF*AA3
fret = atomicAdd(TTF(I,3),ftmp)
fret = atomicSub(TTF(J,3),ftmp)
ECL(J,I) = EP(N,MF) + DEP(N,MF)*RFA
BERS = ER(N,MF) + DER(N,MF)*RFA
EDD(J,I) = -EC(N,MF)-DEC(N,MF)*RFA
ERS(J,I) = BERS
VIL(J,I) = -BR(MF)*BERS*R
ENDIF
201 CONTINUE
end subroutine
```

MD runs were performed on “Thin node” in TSUBAME2.5 at the Global Scientific Information and Computing Center of the Tokyo Institute of Technology.

CPU used is Intel Xeon 2.93 GHz and GPU used is NVIDIA Tesla K20X.

A.8.2 Compile of the CUDA Code

For the check of the performance of the original code, Intel compiler was used without any option, while PGI compiler was used for the code using CUDA.

Versions of the compilers are as follows.

Intel: Intel(R) Fortran Intel(R) 64 Compiler XE for applications running on Intel(R) 64, Version 13.0.0.079
PGI: 13.9-0 64-bit target on x86-64 Linux -tp nehalem

Compile options used for CUDA are as follows.

```
pgfortran -O2 -Mcuda kernel_func.f reduction_sum.f90 lso1.f-o lso.exe
```

A.8.3 Check of the Performance

The performance was checked for a 10,000 steps-run of 3456 particle system.

Measurement of time has been done using "system_clock" command (Table A.1).

Thus the DO 9999 loop is 26 times faster compared with the original code.

Using CUDA for other loops is not necessarily effective for the acceleration because of time loss by using kernels.

This check was done for single precision. In this condition, TSUBAME2.5 (in Tokyo Institute of Technology) has shown the best performance because the performance of "atomic functions" becomes better in Kepler architecture. While, when the double precision was used, the performance of the atomic functions becomes worse.

To obtain better performance in the calculation using double precision, avoidance of atomic function, criteria by distance may be necessary.

Generally, on GPUs warp divergence using **if** and **switch** statements, is to be avoided for better performance. In the case of loop 200, the judgment by distance corresponds to the case. Other possible changes are to do the execution without synchronization, if the dependency among treatments did not exist. Multiuse of GPUs for long loops is also useful.

Of course, the faster calculations enable us to treat larger system or long time simulations, which may expand systems or themes which can be examined. Nevertheless, it seems to be a good question for researcher of science, how fast is good enough for the purpose of the simulations.

Table A.1 Comparison of time required for MD run during 10,000 steps run of $Li_2Si_2O_5$

	Time required in serial computing using CPU (sec)	Time required in parallel computing using a GPU (sec)	Acceleration (time for CPU/time GPU)
DO 9999 loop	3088.42	118.73	26.01
DO 200 loop	3062.17	107.88	28.38
Memory copy	–	1.04	–

A.9 Fast Fourier Transform (FFT)

In experiments and simulations, one may need a procedure to do the Fourier transform of a signal. Particularly, treatment of numerical time series by Fast Fourier Transform (FFT) is useful and shows the dominant frequencies. Although there are many methods to treat it, here we introduce a simple method by using Microsoft Excel with an add-ins [28, 29], so that many readers can do the procedure by themselves and familiarize with the basics of the FFT. We will explain step by step how to perform the FFT and plot it. (We assume the reader is familiar with the general use of Microsoft Excel.)

When one considers the N data points $f(x_j)$ for $x_j = jL/N$ ($j = 0$,---,$N-1$) with an interval of $h = L/N$, Fourier transform of the data at $k_n = 2n\pi/L$ ($n = 0$,---,$N-1$), $\hat{f}\,(k_n)$, is defined by

$$\hat{f}\,(k_n) = \sum_{j=0}^{N-1} f\left(x_j\right)\exp\left(i2\pi n_j/N\right). \tag{A.22}$$

And inverse Fourier transformation is defined by

$$f\left(x_j\right) = \frac{1}{L}\sum_{j=0}^{N-1} \hat{f}\,(k_n)\exp\left(-i2\pi n_j/N\right) \tag{A.23}$$

Note that to do the FFT, the number of data points, N, must be a power of 2, that is, 4, 8, 16,---.

Step 1

We prepared a sheet of Microsoft Excel representing a Fourier transform of the sample data. Please copy the example of the sheet named “FFT1.xlsx” in ESM (example 4) to your Windows machine. First, please examine the following example carefully, to understand what is done in the procedure.

When you open the file by using Microsoft Excel, the Fourier transform of the simple data “0,1,0,−1,0,1,0,−1” (Column B) is found in the column D in complex number. In the sheet, column A is data number, and C is time.

Frequency of the n-th FFT data is n/(N h). The magnitude or amplitude of the FFT data can be obtained by the function IM.ABS($D) as shown in the column I.

In Fig. 1 on the sheet, the amplitude of FFT of the data is plotted against the frequency. Red and blue curves are symmetrical and it means that only the half of the values is meaningful. Note that it shows a peak at a value of $f = ¼ = 0.25$, since the data are periodic with time with a period of 4.

The sum of the values of the amplitude (column I) is found to be 8 as shown by the column marked by yellow. This sum is larger than the sum of the original values. In the column J, the values are modified by (N/2), so that the sum of the values, 2, corresponds to the column marked in red.

Step 2

In order to perform the Fourier analysis using Microsoft Excel you need an add-in named “The Analysis ToolPak”. If you cannot find it in the data tab, you must add it by clicking “File”, “Options”, “Add-ins”, “Setup” and check the “Analysis ToolPak” found there [30].

Step 3

The procedure to obtain the FFT of the data will be done using the same file “**FFT1.xlsx**”. Select “data” tab of the Excel ribbon. Then click the “Data Analysis” button.

Select the “Fourier Analysis” from the following window.

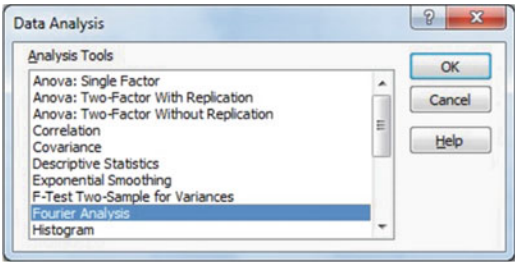

In the next window, select the region of the input data “$B$2:$B$9” and the place for the output “$D$2:$D$9”.

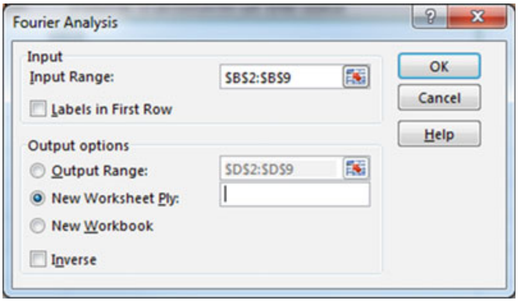

Input Range: $B$2:$B$9

☐ Labels in First Row

○ Output Range: $D$2:$D$9

● New Worksheet Ply:

○ New Workbook

☐ Inverse

The position “$D$2:$D$9” was used in the output of this example. Please select now “new work sheet” instead, so that you can compare the result to the example. Then the result will appear in the A column of the new sheet.

In the new sheet, please set the frequency in column C as in column H of the example.

In the new sheet, use the column D to calculate the amplitude of the complex data obtained by the Fourier transform by using the function “=IMABS ($A$1)” for D1. Please drag the equation down to fill every cell used.

Then you can plot the result of FFT by selecting the

“Magnitude” column (D) for Y axis against the “Frequency” column (C) for X axis.

Now, use the first half of the data for the plot. Magnitude can be also modified as explained in the step 1, if necessary.

Step 4

You can try to do the inverse Fourier transform using the Fourier transform tool by choosing the FFT values of the data as input and check the box of "inverse Fourier transform". This will allow you checking you did it right, since you must get the initial input data.

Step 5

Now you can use the tool for the analysis of your own data. Please input your data (remember that the number of data must be a power of 2 and if the data do not satisfy this condition, please add "0" values. If the Fourier noise is not negligible in your data, additional use of the window function may be necessary.) Try for example with the series "0, 1, 2, 1, 0, −1, −2, −1" in column B. Perform the FFT following the step 3 and see the FFT plot. Which are the dominant frequencies now?

We have also included in the ESM an Excel file (FFTKWW.xlsx) with an example to obtain the FFT of a signal whose time dependence follows a stretched exponential or KWW behavior of the form $\phi(t) = e^{-(t/\tau)^{\beta}}$. We have chosen the value of τ as 10 s (or 10 times the time interval, chosen as 1 s), and the exponent β can be chosen by changing the value in cell B4. Then you can perform the FFT as explained in the procedure above, and see the result of the amplitude of the FFT and also the frequency dependence of the real and imaginary parts of the FFT. You must be aware that while these examples give you the basic details on how to perform and analyze the FFT of a signal, the limited number of data results in relatively large errors in the FFT, particularly at the lowest and highest frequencies. If you are interested in using the FFT procedure for the analysis of your data you may consider using other software specifically designed for it or any general software to perform operations with a suitable window function.

References

1. B. Mandelbrot, Science **155**, 636 (1967)
2. S. Alexander, R. Orbach, J. Phys. (Paris) Lett. **43**, L625 (1982)
3. J. Klafter, M.F. Shlesinger, G. Zumofen, Phys. Today **49**, 33 (1996)
4. R. Metzler, J. Klafter, Phys. Rep. **339**, 1 (2000)
5. T. Odagaki, J. Matsui, Y. Hiwatari, Physica A **204**, 464 (1994)
6. http://academic2.american.edu/~jpnolan/stable/stable.html; the address is confirmed to be valid on 5 February 2016
7. http://academic2.american.edu/~jpnolan/stable/chap1.pdf, the address is confirmed to be valid on 5 February 2016.
8. J. Habasaki, I. Okada, Y. Hiwatari, Phys. Rev. **B55**, 6309 (1997)
9. J. Habasaki, Y. Hiwatari, Phys. Rev. **E59**, 6962 (1999)
10. J. Habasaki, K.L. Ngai, Y. Hiwatari, Phys. Rev. **E66**, 021205 (2002)
11. A. Heuer, M. Kunow, M. Vogel, R.D. Banhatti, Phys. Chem. Chem. Phys. **4**, 3185 (2002)
12. M. Vogel, Phys. Rev. B **68**, 184301 (2003)
13. J. Habasaki, K.L. Ngai, J. Chem. Phys. **129**, 034503 (2008)
14. R.N. Mantegna, H.E. Stanley, Phys. Rev. Lett. **73**, 2946 (1994)
15. I. Koponen, Phys. Rev. E **52**, 1197 (1995)
16. H. Nakao, Phys. Lett. A **266**(4–6), 28, 282 (2000)
17. C. De Michele, D. Leporini, Phys. Rev. E **63**, 036701 (2001)
18. E. Barcy, Phys. Rev. E **64**, 026103 (2001)
19. A. Chhabra, R.V. Jensen, Phys. Rev. Lett. **62**, 1327 (1989).
20. N.L. Johnson, S. Kotz, N. Balakrishnan, *Continuous univariate distributions*. Wiley series in probability and mathematical statistics: applied probability and statistics, vol. 1, 2nd edn. (Wiley, New York, 1994)
21. J. Feder, *Fractals* (Plenum Press, New York, 1988)
22. L.M. Zelenyǐ, A.V. Milovanov, Physics-Uspekhi **47**, 749 (2004)
23. J. Habasaki, K.L. Ngai, J. Chem. Phys. **122**, 214725 (2005)
24. R. Vautard, M. Ghil, Physica **D35**, 395 (1989); See also http://research.atmos.ucla.edu/tcd//ssa/guide/andy/ssatheory4.html, the address is confirmed to be valid on 19 September 2016
25. http://www.pgroup.com/, the address is confirmed to be valid on 5 February 2016
26. http://www.nvidia.co.jp/page/home.html, the address is confirmed to be valid on 5 February 2016
27. http://www.ibiblio.org/pub/languages/fortran/ch1-2.html, the address is confirmed to be valid on 5 February 2016

J. Habasaki et al., *Dynamics of Glassy, Crystalline and Liquid Ionic Conductors*,
Topics in Applied Physics 132, DOI 10.1007/978-3-319-42391-3

28. http://homepage1.nifty.com/gfk/fourier-transform.htm (in Japanese), the address is confirmed to be valid on 11 March 2016
29. http://news.techgenie.com/technology/how-to-do-a-fast-fourier-transform-fft-in-microsoft-excel/, the address is confirmed to be valid on 11 March 2016
30. https://www.add-ins.com/Analysis_ToolPak.htm, the address is confirmed to be valid on 11 March 2016

Index

J. Habasaki et al., *Dynamics of Glassy, Crystalline and Liquid Ionic Conductors*,
Topics in Applied Physics 132, DOI 10.1007/978-3-319-42391-3